Characterization of Pile Driving Induced Ground Motions

by

Athina Gkrizi

A dissertation submitted in partial fulfillment
of the requirements for the degree of
Doctor of Philosophy
(Civil Engineering)
in the University of Michigan
2017

Doctoral Committee:

Associate Professor Adda Athanasopoulos-Zekkos, Co-Chair
Emeritus Professor Richard D. Woods, Co-Chair
Professor Roman D. Hryciw
Professor Yin Lu Young
Associate Professor Dimitrios Zekkos

ACKNOWLEDGEMENTS

I feel the need to express my gratitude to many people that have helped me and made this dissertation possible. First and foremost, I would like to thank my doctoral advisor, Professor Adda Athanasopoulos-Zekkos, for her guidance and support during my doctoral studies. Overall, she has been a great advisor guiding me through many challenging technical aspects and difficulties I had to confront, and a great mentor with regard to other areas, such as improving my technical skills and developing my engineering judgement. Furthermore, I am also grateful for her support and understanding during a personal hardship I had and I cannot thank her enough for that.

I also would like to thank my Co-Chair Committee member, Professor Richard Woods. He has been an exceptional mentor, advisor and teacher to me and I feel I have learned a lot from his expertise in soil dynamics. Professor Woods has always been there for me to assist in any kinds of problems I encountered during this challenging research project. I feel blessed I had the opportunity to work with him.

I wish to extend my gratitude to my Master's advisor, Professor George Athanasopoulos, who has been my first mentor. Professor Athanasopoulos provided me the background in geotechnical engineering and guided me to find my way in this field. The other members of my Committee, Professor Hryciw, Professor Zekkos and Professor Young also deserve recognition for being excellent teachers and helping me with this research.

There are some people that I wish to acknowledge that helped me overcome difficulties encountered in this research and made everything work smoothly. These are Richard Endres and Tony Pietrangelo from Michigan Department of Transportation and Chris Naida from SME, Inc.. Rick Burch has come to my assistance many times for equipment issues and always provided very fast solutions, and I am grateful for his help.

In addition, I gratefully thank the Rackham Graduate School for supporting me financially during my final semester of studies.

I also would like to thank many of the current and former students at the University of Michigan. Their friendship, support and practical help through the years we have spent together at Michigan has been of great importance to me. Special thanks go to Adam Lobbestael, Jonathan Hubler, Xunchang Fei, Zhijie Wang and Sid Nadukuru.

Many thanks go to many of my friends in Greece and Ann Arbor that are always here for me during happy, but most importantly difficult times. Lampros, Dora, Lena, Konstantina, Xeni, Daphne, Stavros and godchild Dimitris: thank you for brightening my days, I feel honored I am your friend.

Finally, I want to express my deepest gratitude to my parents, my sister Nadia, my brother-in-law Alexis and my nephew Yannis for their continuous love, support and patience. It is with the values of this family that I walk through life and without them I would not have gotten this far.

TABLE OF CONTENTS

LIST OF TABLES

LIST OF FIGURES

LIST OF APPENDICES

ABSTRACT

Pile installation is a complicated, energy intensive process where codes and regulatory standards provide some guidance, but little is understood about coupling and transmission of pile driving energy into and through the ground in the form of vibrations. These vibrations can cause direct structural damage and damage due to settlement of granular soils. This thesis presents results that give insight to concepts that are still in question concerning pile driving induced vibrations using impact hammers. These results are the outcome of an innovative research comprised of three components: (1) full-scale ground monitoring during impact driving of H-piles in the field, (2) small scale pile driving testing in a controlled laboratory environment and (3) numerical analysis of the impact pile driving process using 3D finite element analysis.

Field pile driving vibration data were collected from five project sites. The mechanisms of energy propagation during impact pile driving were evaluated by installing sensors in the ground, starting very close from the pile (0.5 ft) and moving away at different radial distances and depths, generating the first data set of its kind. Analysis of the data reinforces the hypothesis of the wave propagation field generated by impact driven piles. Body waves radiate from the pile tip in a spherical wave front. Shear waves propagate outwards from the pile shaft in a cylindrical wave front. The shaft transfer starts only after the pile tip passes below and observation point (sensor). The Rayleigh wave development reported by various researchers is not verified.

Attenuation of the peak particle velocity and increase of the shear wave velocity at increasing distances from the pile is also confirmed. A widely used attenuation formula (Bornitz equation) was fitted to the recorded measurements and was found to be a good model to describe the energy degradation through the soil when impact driven piles are

used as a source. The attenuation coefficients are in agreement with earlier documented findings.

A process to evaluate the potential for a granular soil to undergo shakedown settlement is presented based on the field measurements from the tested sites. This concept can serve as a first guide for identifying potentially troublesome sites with similar site conditions. The order of magnitude of shear coupling assumed for soil behavior zones in the proximity of the pile is confirmed. A decrease of particle velocity and an increase of shear wave velocity with increasing distances from the pile is also verified.

Reduced-scale physical experiments of pile driving were conducted in the laboratory. The controlled environment of a homogeneous and properly characterized soil profile allowed for investigation of the mechanisms of energy transfer from the pile to soil without the complexities encountered in the field. The generated wave field follows the pattern found for field testing measurements. The contribution from shear waves is not “seen” by the installed sensors until the pile tip reaches their elevation. These trends substantiate the existence of two wave fields, spherical and cylindrical, generated from a linear source as the pile, a behavior also observed in the field.

The pile driving induced vibration field was modeled using a 3D finite element dynamic analysis. It is clearly shown that a cylindrical wave front emanates from the shaft and a spherical wave front radiates from the pile tip. Preliminary results of calculated ground motions in the very close proximity of the pile showed good agreement with recorded ground motions in the laboratory.

Pile driving induced vibrations can reach, depending on the size of the project, thousands of loading cycles. The vibration threshold strain assumed in the literature for seismic events needs to be reduced.

CHAPTER 1 INTRODUCTION

1.1 Background and Motivation

The construction and retrofit of bridges, retaining walls and other structures often includes driving piles for foundation support. This process induces vibrations into the ground which can be transmitted to nearby structures and underground utilities and threaten their integrity and serviceability. Specifically, these vibrations can cause ground settlements leading to differential settlements of foundations, when loose sand deposits are part of the soil profile. In rapidly growing cities, pile driving activities often take place close to existing infrastructure, thus it is critical to understand and quantify the mechanisms of the energy propagation and assess the potential for ground settlement. Geotechnical engineering has shown great progress towards studying the soil behavior when subjected to seismic motion. However, pile driving induced vibrations can reach, depending on the size of the project, thousands of loading cycles, whereas for seismic events the number of significant cycles is less than twenty. Therefore, there is a need to better understand coupling and transmission of the energy into the ground during pile installation.

Pile driving equipment can generate two types of vibration: impact vibrations and continuous vibrations. Impact pile driving, that is the subject of this research, falls in the first category, while vibratory pile drivers are examples of the second category. At this time, there are no specific regulations developed for pile driving operations. Various vibration limiting criteria proposed by researchers, governmental agencies and independent standards agencies are followed. The peak particle velocity (PPV) is often used as a measure to vibration intensity. In the United States, 4 in/sec for commercial

buildings and 2 in/sec for residential structures were considered for many years to be thresholds of possible damage. However, there are several reported cases in the literature that settlement and consequently structural damage occurred to structures adjacent to pile driving activities, with particle velocities much lower than the 2 in/sec limit. Settlement induced by pile driving installation can extend to as far as 1300 ft (400 m) from the pile driving area in the extreme case (Woods 1997).

There is a widely accepted strain threshold of γ=0.01% to cause settlement of granular soils. This threshold was derived from the geotechnical earthquake engineering research and has been adopted for construction activities. However, there is a need for a better evaluation of this threshold strain gained specifically from pile driving vibrations. Brandenberg et al. (2009) has shown that there is a low risk of settlement for shear strain levels of γ=0.001% for pile driving projects. This risk can increase for high numbers of loading cycles, which is typical for pile driving induced vibrations.

1.2 Research Objectives

Recent experience by the Michigan Department of Transportation (MDOT) during replacement operations has emphasized shakedown settlement of loose sand from pile driving as an important problem. MDOT funded a big part of this research to study and better understand the mechanisms of energy transfer to the ground from impact driven H-piles. The hypothesis that body waves radiate from the pile tip, shear waves propagate from the pile shaft and the Rayleigh wave front is developed on the surface, from the interaction of the first two, has not been proved with physical ground motion measurements in the close proximity of the pile, Figure 1-1.The current practice is to measure vibration intensities on the ground surface, starting around 5 ft from the pile, since placing a geophone closer than that could cause decoupling of the sensor from the ground as high ground motions occur in the vicinity of the pile.

The study presented in this dissertation focuses on confirming or modifying the hypothesis of the wave field generated during impact pile driving. Furthermore, vibration attenuation in three different soil behavior zones, plastic, non-linear and nearly elastic,

Figure 1-2 needs to be verified. As seen on the top of this Figure, particle velocities diminish with distance from the pile, while shear wave velocities increase while moving away from the pile. This behavior is of course attributed to the high strains that the soil experiences in the very close vicinity of the pile (plastic zone or near field) which decay as we move to elastic zones (far field). The potential of shakedown settlement for a granular soil is another objective that this research study tried to address.

This study was comprised of three significant research tasks: (a) full-scale ground motion monitoring during H-pile driving in the field, (b) small-scale pile driving testing in a controlled laboratory environment and (c) numerical modeling of the pile-driving process using 3D finite element analysis, validated using small-scale testing data. The first task included collection of field pile driving vibration data from five project sites in Michigan. The mechanisms of energy propagation during impact pile driving were evaluated by installing sensors in the ground, starting very close from the pile (0.15 m) and moving away at different radial distances and depths, generating the first data set of its kind. This work led to the development of an empirical criteria tool for prediction of the likelihood of shake-down settlement, using as inputs the soil conditions and the pile and hammer type. The tool has been implemented by the Michigan Department of Transportation (MDOT) in their Bridge Design Manual (Athanasopoulos-Zekkos et al. 2013).

Second, small-scale pile driving laboratory tests were conducted in an in-doors sand pit to supplement the data obtained during full-scale testing, in highly controlled conditions of known soil stratigraphy. These tests have provided the necessary data for the third task of this research project, validation of the 3D numerical finite element model. Simulation of the non-linear, time dependent and anisotropic behavior of the soil was analyzed. The combination of these components provided a unique database of results that assisted in answering many of the concepts that were not yet fully understood concerning impact pile driving induced vibrations.

1.3 Organization of Dissertation

This dissertation is organized as follows:

Chapter 2 presents fundamental principles of wave propagation in a medium, as well as the complexity of the energy transmission during impact pile driving.

In **Chapter 3** previous studies concerning pile driving induced vibrations are reviewed. Specifically, vibration limit criteria, empirical equations to predict ground vibrations, cases of recorded ground motions during pile installation, cases of reported settlement due to pile driving operations, and thresholds of cyclic shear strain that can pose a risk of ground settlement are discussed.

Chapter 4 has a summary of piles, hammers, wave equation analysis methods and basic hammer/pile energy concepts.

In **Chapter 5**, the configuration, equipment and instrumentation used in the field tests and the field testing procedures that were followed are discussed.

In **Chapter 6**, field monitoring of pile driving induced vibrations is discussed. Description of test sites and the geotechnical characterization at each site are presented. Ground motion measurements and analysis are also presented.

In **Chapter 7**, a process for estimation of the potential of the potential of ground settlement due to pile driving is presented. This concept is based on the field data collected in this study.

Chapter 8 presents results from the reduced-scale physical experiments of pile driving in the laboratory.

In **Chapter 9**, validation of the 3D numerical finite element model using ground motion measurements from the small-scale pile driving tests is discussed.

Chapter 10 presents a summary of the conclusions of this study and areas for further research.

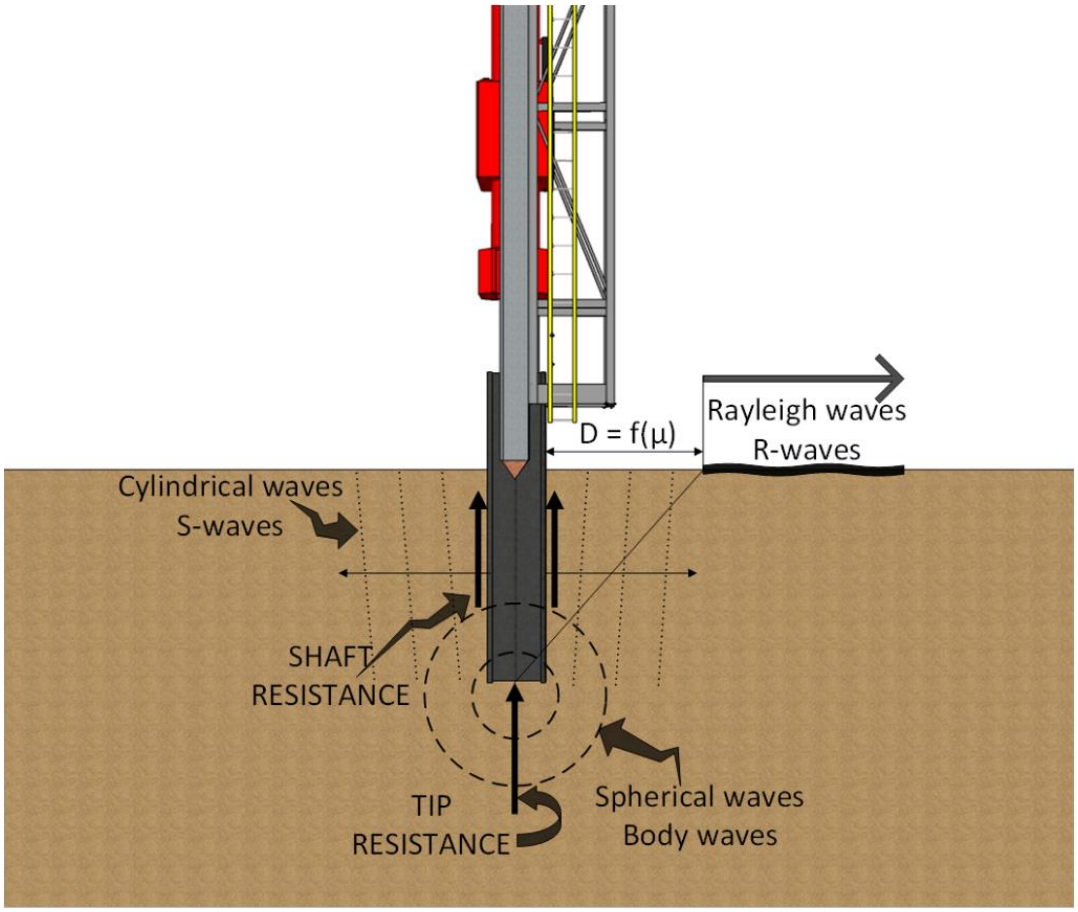

Figure 1-1 Mechanisms of energy transfer from impact driven pile to surrounding ground (from Grizi et al. 2016)

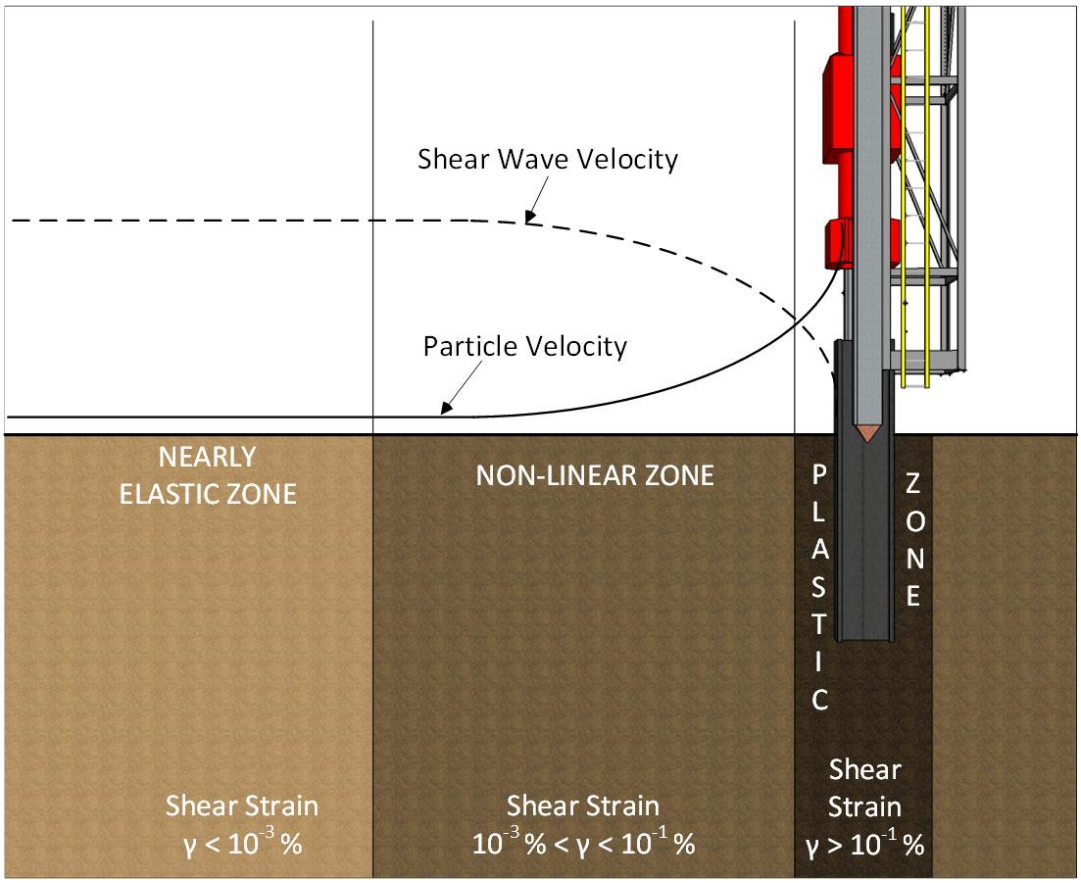

Figure 1-2 Assumed soil behavior zones near impact driven pile (from Grizi et al. 2016)

CHAPTER 2 WAVE MECHANICS AND PROPAGATION

Wave propagation is the transmission of energy through a medium when this medium is excited by a source. In order to study the pile driving wave propagation mechanism, it is important to understand the mechanics of ground motion. The wave propagation velocity is the velocity that the wave travels through a medium. As the wave propagates through a soil medium it oscillates the soil particles. This particle motion is usually monitored during construction activities. Pile driving produces a complex combination of wave types, where the inhomogeneity of the soil medium makes their characterization even more complex.

Construction operations produce three main types of waves: compressional or primary (P-waves), shear or secondary (S-waves) and surface (Rayleigh or Love waves). For P-waves, the particle motion is parallel to the direction of travel (Figure 2-1a). The particle motion is perpendicular to the direction of S-waves as shown in Figure 2-1b. Based on the direction of the particle movement, S-waves are further divided in SV-waves (vertical plane movement) and SH-waves (horizontal plane movement). The Rayleigh wave, which is the most important and complicated surface wave, produces motions both vertical and parallel to the direction of propagation forming a retrograde elliptical motion as shown in Figure 2-1c. Rayleigh waves are produced by the interaction of P-wave and S-wave and they dominate at farther distances from the impact source (Kramer 1996). A P-wave and S-wave will propagate into a soil medium at velocities:

P-wave $$V_P = \sqrt{\frac{G(2-2\nu)}{\rho(1-2\nu)}}$$ Eq. 2-1

S-wave $$V_S = \sqrt{\frac{G}{\rho}}$$ Eq. 2-2

$$\frac{V_P}{V_S} = \sqrt{\frac{2-2\nu}{1-2\nu}}$$ Eq. 2-3

where: V_P = P-wave velocity
V_S = S-wave velocity
G =shear modulus
v = Poisson's ratio
ρ = mass density of ground

Eq. 2-3 shows the ratio of the compressional to shear wave velocity as a function of Poisson's ratio. The variation of the three wave velocity types with Poisson's ratio is presented in Figure 2-2. The Rayleigh wave travels slightly slower than the S-wave, except when v=0.5 where V_S=V_R. P-wave velocity is higher than shear and Rayleigh wave velocity for all Poisson's ratios.

Surface waves travel below the ground surface only one to two wavelengths as indicated in Figure 2-3 which illustrates the decreasing amplitudes of both vertical and horizontal components with depth. The wavelength is defined as:

$$\lambda = \frac{V}{f}$$ Eq. 2-4

where: λ = wavelength
V = wave propagation velocity
f = frequency

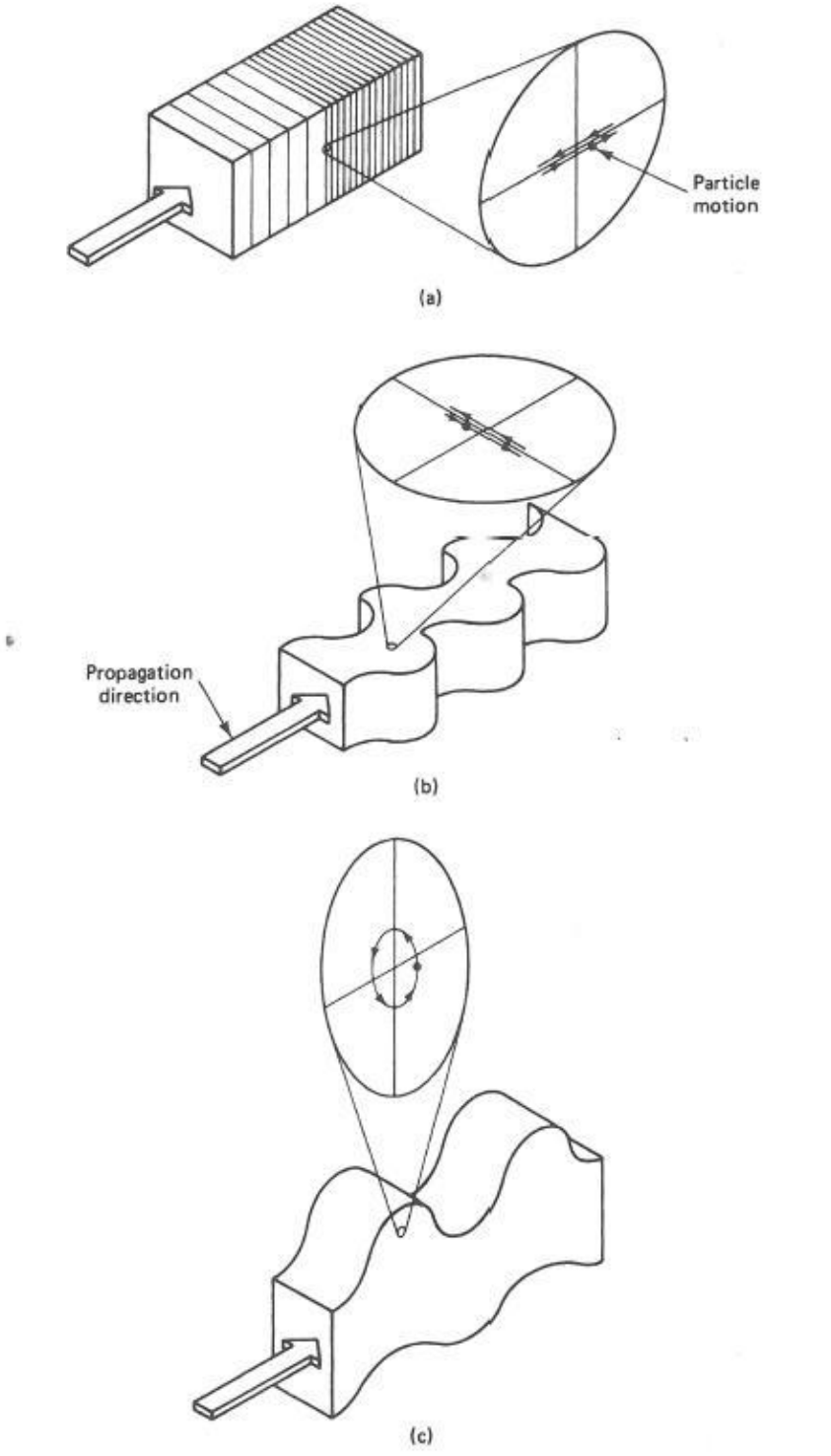

Figure 2-1 Particle motions for (a) P-wave, (b) S-wave and (c) Rayleigh wave (from Dowding 1996)

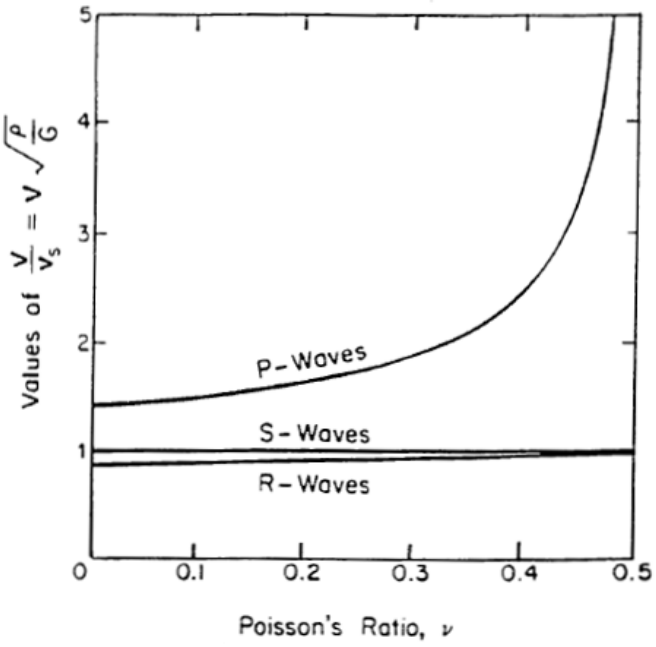

Figure 2-2 Variation of propagation velocities of P, S and Rayleigh waves as a function of Poisson's ratio (from Woods 1997)

Impact pile driving generates two different types of waves: spherical waves emanating from the pile tip and cylindrical waves travelling from the pile shaft. In Figure 1-1, an idealized uniform soil profile and the basic mechanisms of stress wave generation from an impact driven pile is presented. The hammer impact causes a volumetric displacement in the ground, resulting in primary and shear waves travelling outwards from the pile tip (Woods 1997). Shear waves spread their energy into the ground in a cylindrical wave front with the particle motion being parallel to the pile face. The interaction between these two wave types results in Rayleigh waves, travelling also in a cylindrical wave front, when they reach the ground surface. The decay of the Rayleigh wave amplitude is much slower than those of the P-wave and S-wave, thus a Rayleigh wave can propagate on the ground surface for hundreds of feet.

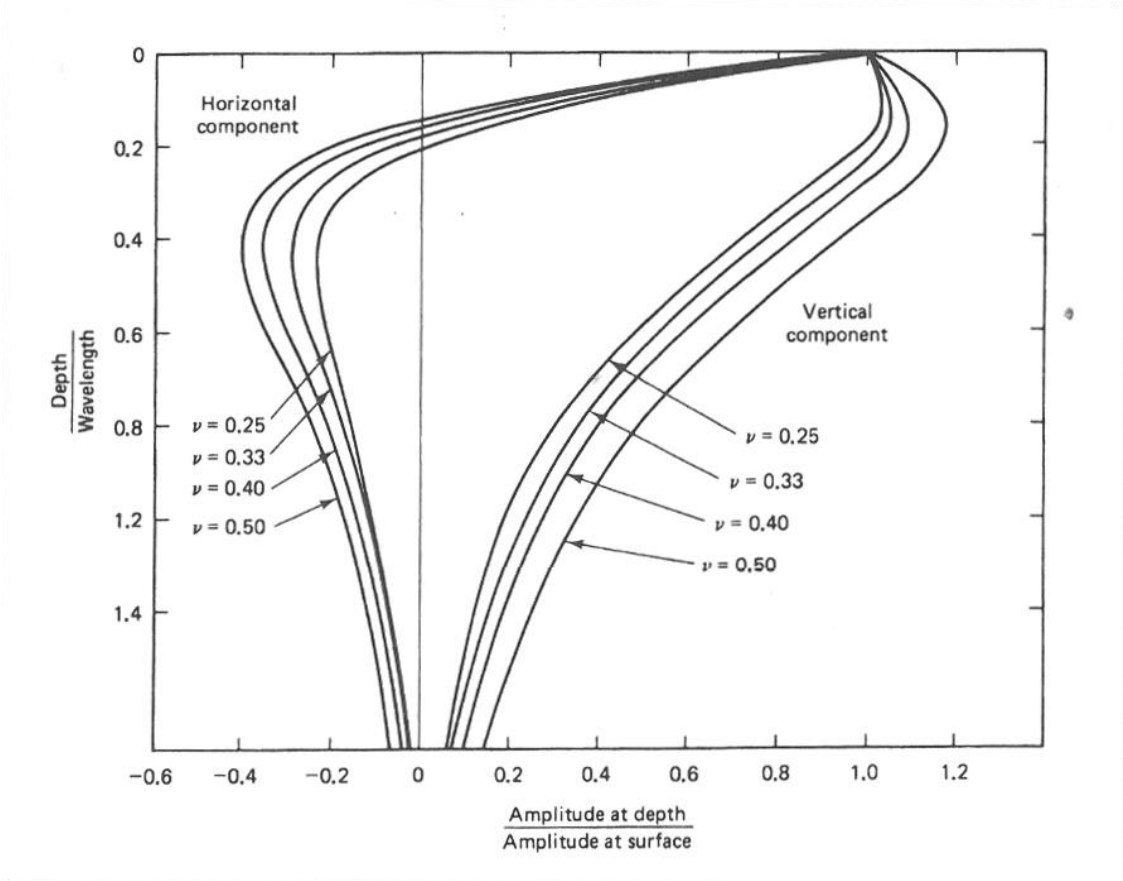

Figure 2-3 Vertical and horizontal motion of Rayleigh waves versus depth and Poisson's ratio (from Richart et al. 1970)

For a realistic layered ground, wave propagation from pile driving operations becomes much more complicated. When the P and S-waves encounter a boundary and enter a different soil layer, two reflected and two refracted waves will be generated from the incident waves. Figure 2-4 shows the complexity of the wave propagation from impact pile driving through a non-uniform soil profile (Woods 1997).

Figure 2-5 illustrates the development of Rayleigh waves which can be quite close to the pile driving source. The proximity of the surface wave formation is a function of the propagation velocities (Dowding 1996). An example of particle displacement paths for three different distances from a driven sheet pile is shown in Figure 2-6. The surface ground motions follow an elliptical form typical for a Rayleigh wave transmission.

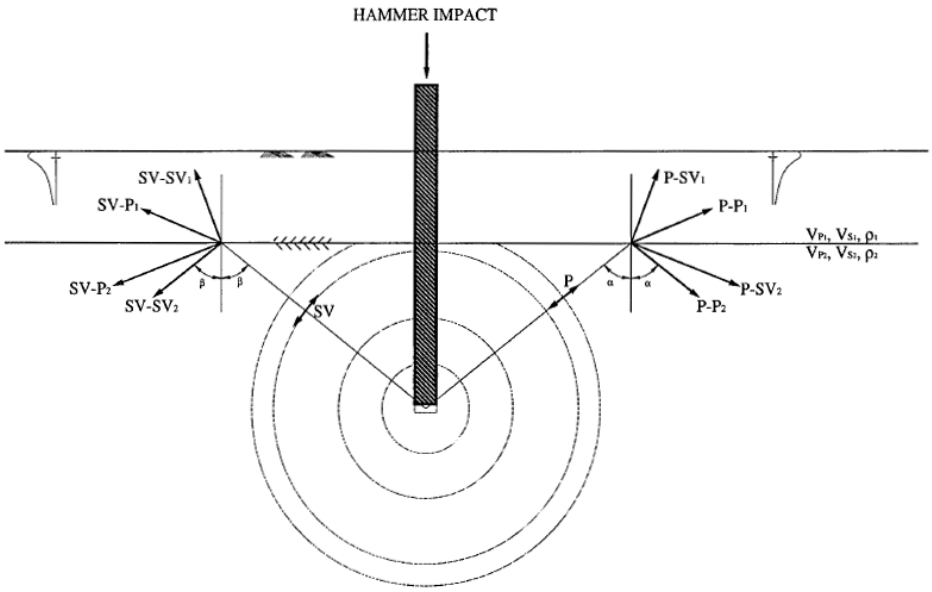

Figure 2-4 Wave propagation from impact driven pile at a layered soil medium (from Woods 1997)

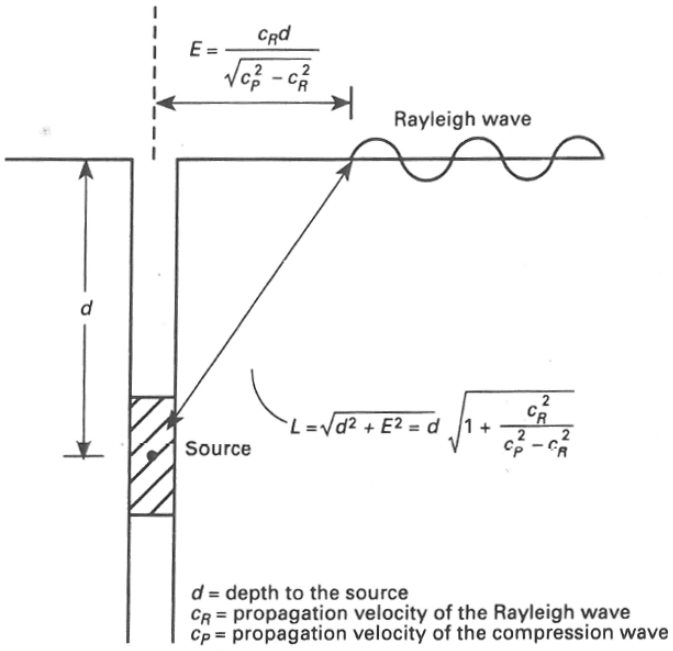

Figure 2-5 Rayleigh wave development from embedded source (from Dowding 1996)

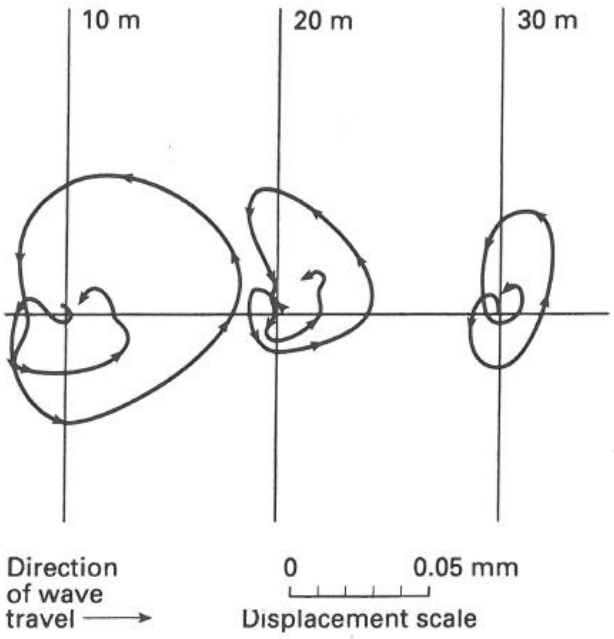

Figure 2-6 Particle displacement paths from a driven sheet pile (from Attewell and Farmer 1973)

To conclude, pile driving vibrations are induced by a linear source which is constantly lengthening as the pile is driven deeper into a layered soil profile. This makes the mechanism of energy transfer more complex and difficult to understand. However, it is important to characterize the wave propagation from pile driving to better understand how the large amounts of energy are transmitted through the ground.

CHAPTER 3 LITERATURE REVIEW

3.1 Vibration Criteria

Construction equipment can generate two different types of vibration: (1*) transient* or *impact vibrations* and (2) *steady-state* or *continuous vibrations.* Blasting and impact pile driving fall into the first category and represent high amplitude vibrations with short duration. Vibratory pile drivers and compaction equipment are examples of continuous vibration sources which produce steady state periodic motion consisting of a very large number of similarly shaped pulses. The primary types of vibration receivers that may be affected by construction operations are people, structures and sensitive equipment. Problems associated with vibration effects from pile installation, which is considered one of the most energy intense sources of vibrations, depend on the dynamics of the source and soil medium through which the waves will propagate. Vibration intensities reported from the operation of construction equipment are usually recorded on the surface of the earth. *Peak particle velocity (PPV)* is most often used as the measure of vibration intensity. There are no specific regulations developed for construction vibrations. Researchers, governmental agencies and independent standards agencies have proposed various vibration limit criteria. A brief discussion of the most important vibration criteria is provided in this section.

3.1.1 Human response

People sense and react to a much broader range of vibration intensities than do structures. Human perception is a rather subjective matter which depends on the sensitivity of the person involved, the duration of the event and the activity they are participating in at the time of disturbance; someone sleeping will be less tolerant to vibration than someone who is exercising. Reiher and Meister (1931) presented results

of vibration sensitivities of people to steady-state vibrations (Table 3.1). Table 3.2 is a summary from another study (Wiss and Nicholls,1974) of human response to transient vibrations. Thresholds for annoyance seem to be higher for transient than for continuous vibration.

The International Standards Organization (ISO 1989) published the *Guide to the Evaluation of Human Exposure to Vibration and Shock in Buildings (1 Hz to 80 Hz)* (ISO 2631). These standards suggest that people are sensitive to particle velocities in the range of 8–80 Hz. A summary of the ISO 2631 vibration criteria is found in Table 3.3. The vibration velocity level, L_v, in decibels (dB) is defined as:

$$L_v = 20log_{10}\left(\frac{v}{v_{ref}}\right) \qquad \text{Eq. 3-1}$$

where v is the root mean square (rms) velocity amplitude and v_{ref} is the reference velocity amplitude. The accepted reference quantities for vibration velocity are $1x10^{-6}$ in/sec in the United States and either $1x10^{-8}$ m/sec or $5x10^{-8}$ m/sec in the rest of the world. The abbreviation VdB is used for the vibration velocity level to distinguish it from the sound decibels. The Federal Transit Administration (FTA, 1995) developed vibration criteria based on building use and event frequency (Table 3.4). More than 70 events per day are defined as frequent events while less than 70 events per day are categorized as infrequent events. Overall, vibration intensities defined as disturbing by people are well below the intensities that can cause damage to structures.

Figure 3-1 to Figure 3-3 summarize guidelines of threshold values of vibrations with regard to human sensitivity. These values are in terms of frequency and peak values of acceleration (Figure 3-1), peak values of velocity (Figure 3-2) and peak values of displacement (Figure 3-3). It is important to notice that the threshold values expressed in terms of particle velocity and displacement are decreasing with the frequency of vibrations.

Table 3.1 Human Response to steady-state vibration (after Reiher and Meister, 1931)

PPV, in/sec (mm/sec)	Human Response
3.6 (91.4) at 2 Hz – 0.4 (10.2) at 20 Hz	Very disturbing
0.7 (17.8) at 2 Hz – 0.17 (4.3) at 20 Hz	Disturbing
0.10 (2.54)	Strongly perceptible
0.035 (0.89)	Distinctly perceptible
0.012 (0.31)	Slightly perceptible

Table 3.2 Human Response to transient vibration (after Wiss and Nicholls, 1974)

PPV, in/sec (mm/sec)	Human Response
2 (50.8)	Severe
0.9 (22.9)	Strongly perceptible
0.24 (6.1)	Distinctly perceptible
0.035 (0.89)	Barely perceptible

Table 3.3 Table 1.3 ISO 2631 Vibration Criteria

Building Use	Vibration Velocity Level (VdB)	Vibration velocity rms Amplitude (in/sec)
Workshop	90	0.032
Office	84	0.016
Residence	78 day/ 75 night	0.008
Hospital operating room	72	0.004

Table 3.4 Federal Transit Administration vibration criteria (FTA 1995)

Building Use	Vibration Impact Level for Frequent Events (VdB)	Vibration Impact Level for Infrequent Events (VdB)
Category 1: Buildings where low ambient vibration is essential for interior operations	65	65
Category 2: Residences and buildings where people normally sleep	72	80
Category 3: Institutional land uses with primarily daytime use	75	83

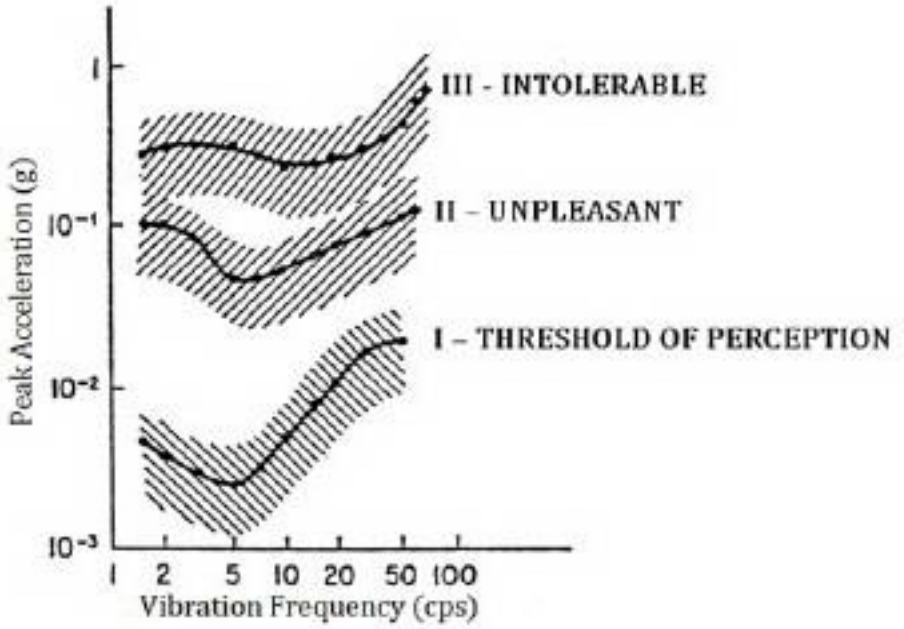

Figure 3-1 Human sensitivity to vibrations in terms of acceleration response (Gierke and Goldman 1988)

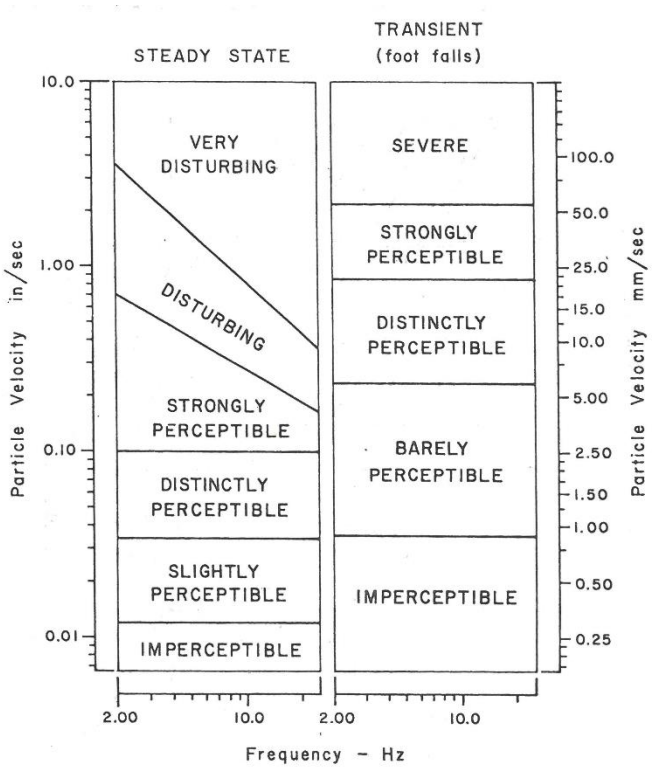

Figure 3-2 Human response to steady-state (Reiher and Meister 1931) and transient vibrations (Wiss and Parmelee 1974, source: Wiss 1981)

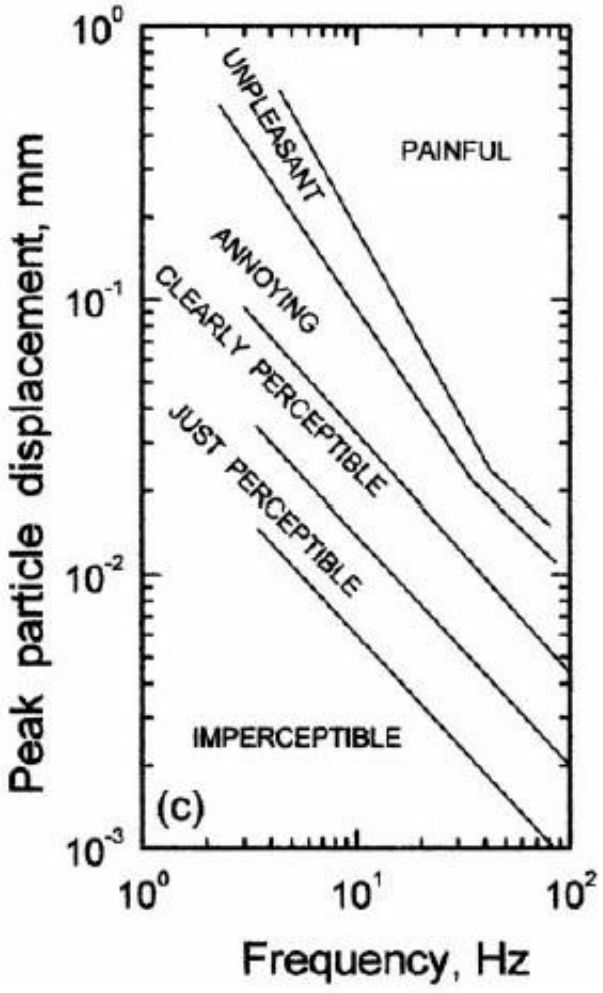

Figure 3-3 Human sensitivity to vibrations in terms of displacement (after Attewell and Taylor 1984, source: Athanasopoulos and Pelekis 2000)

3.1.2 Structures

Earthborne vibrations can cause, under the right conditions, architectural and/or structural damage to buildings and buried infrastructure. Direct structural damage is not the only consequence from vibration operations though. A combination of loose granular soils and ground vibrations can be the cause of liquefaction, densification and ground settlement and consequently damage to a building. Edwards and Northwood (1960) and Northwood et al. (1963) defined three categories of cracking in structures from blast vibrations: (1) *Cosmetic cracking* or *threshold damage* which includes opening of old cracks and formation of new plaster cracks and dislodging of loose structural particles such as loose bricks in chimneys; (2) *Architectural* or *minor damage* which is superficial damage not affecting the strength of the structure, such as broken windows, loosened or fallen plaster and hairline cracks in masonry; and (3) *Structural cracking* or *major damage* that results in serious weakening of the building (e.g. large cracks, shifting of foundations or bearing walls, major settlement resulting in distortion or weakening of the structure, walls out of plumb). These categories of cracking in structures are shown in Figure 3-4. Cosmetic cracking usually appeared at 76 mm/sec (3 in/sec), minor cracking appeared at 114 mm/sec (4.5 in/sec) and major cracking at 203 mm/sec (8 in/sec). The data in Figure 3-4 was collected by the U.S. Bureau of Mines from 718 blasts and 233 reported observations of cracking. The A zone represents the threshold damage, whereas zones B and C describe minor and major damage (Svinkin 2005).

In the United States, 4 in/sec for commercial buildings and 2 in/sec for residential structures were considered for many years to be thresholds of possible damage (Wiss, 1981). These criteria ignored the influence of frequency and have been supplanted with more advanced criteria that include frequency.

In the former USSR the safe vibration limits for sound structures were found as 30 to 50 mm/s (1.18 to 1.97 in/s) by the Moscow Institute of Physics of the Earth (Sadovskii 1946). This study was an assessment of the safety of structures from the explosive effects of various blasts in the air, on the ground, and under the ground at the time of the Second World War (Svinkin 2008).

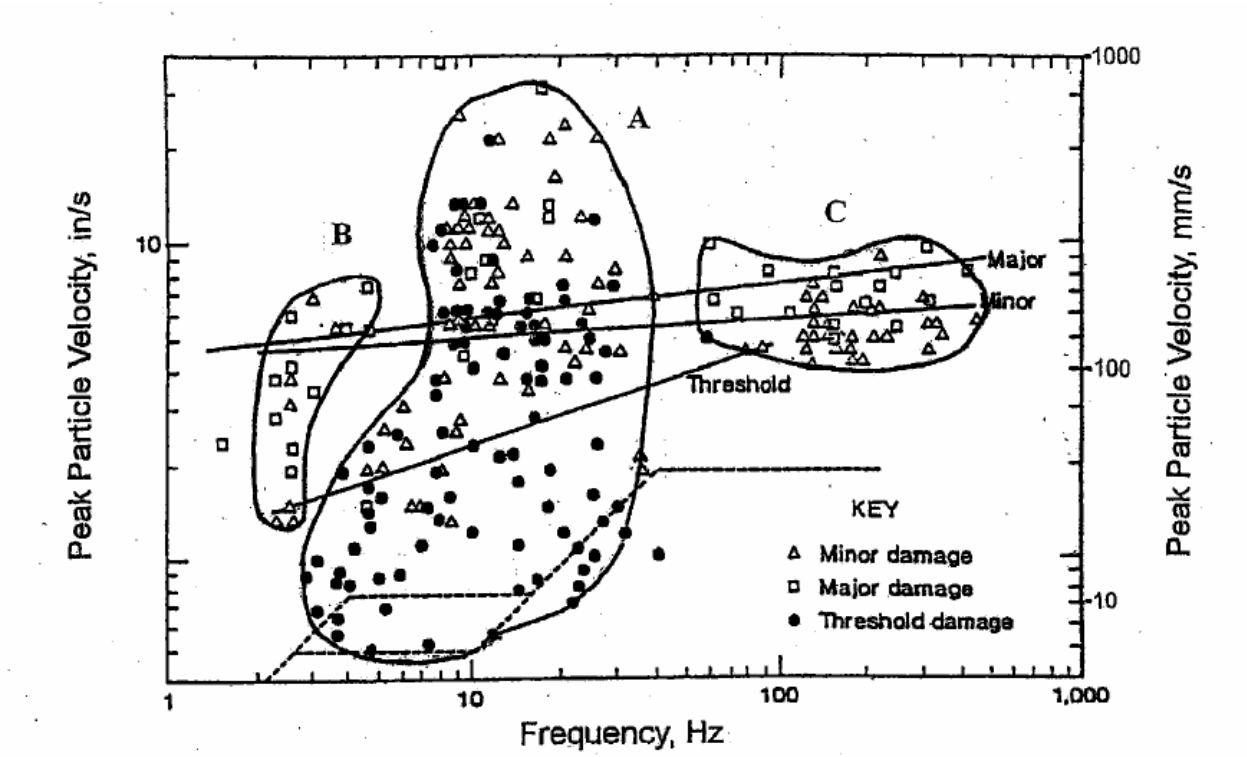

Figure 3-4 Reported data from observed cracks in buildings along with corresponding cracking thresholds (adapted from Siskind 2000)

Extensive research on the effect of vibrations in structures was conducted by the blasting industry. The United States Bureau of Mines (USBM) RI 8507 developed criteria for safe levels of surface blasting for typical residential structures (Siskind et al. 1980). This study was focused on preventing architectural damage (cosmetic cracking) in low-rise (1-2 story) residential houses with no distinction concerning the age of the structure. The USBM criteria were modified by the Office of Surface Mining (OSM 1983). The safe limits for cosmetic cracking by the USBM and the OSM are presented in Figure 3-5 for four ranges of the dominant frequency. Even though the USBM and OSM criteria are considered a great achievement for the assessment of blasting vibration effects, they are not relevant for the assessment of construction operations (Svinkin 2014). The ISO 4866 - 1990 has been adopted as the American National Standards Institute (ANSI) ANSI S2.47 – 1990, *Vibration of Buildings - Guidelines for the Measurement of Vibrations and*

Evaluation of their Effects on Buildings. This Standard provides guidelines for measurement of building vibrations and evaluation of their effects on buildings for different sources of vibration (Svinkin 2014).

The British Standard (BS) 7385 (BS 1990 and BS 1993) considers two types of buildings, industrial and residential, and specifies peak velocities from transient vibrations causing minor damage to buildings. The BS adopted the 2 in/sec threshold by the USBM for industrial buildings and suggested more conservative criteria for residential buildings. A comparison of the two criteria is shown in Figure 3-6. The German guidelines Deutsches Institut für Normung DIN-4150 (1986) are rather conservative and their basis is unknown, however, they are considered safe (AASHTO Designation: R8-96 2009). Figure 3-7 presents a comparison of the USBM and the DIN criteria. The Australian Standard (AS) 2187.2 (1983) also presented conservative vibration criteria suggesting 0.08 in/sec for historical buildings, 0.39 in/sec for residential buildings and 1 in/sec for industrial and commercial structures. In general, low frequency vibrations have lower limits of tolerance than high frequency vibrations.

The Swedish Standard SS 02 52 11, Vibration and Shock – Guidance levels and measuring of vibrations in buildings originating from piling, sheet piling, excavating and packing to estimate permitted vibration levels, was published in 1999 (Massarsch and Fellenius 2014). The vibration levels are based on experience of measured ground vibrations and observations of damaged buildings. The vibration level, v, is the peak vertical particle velocity multiplied by three correction factors:

$$v = v_0 F_b F_m F_g \qquad \text{Eq. 3-2}$$

where v_0 is the uncorrected vertical vibration velocity (mm/sec), F_b is the building factor, F_m is the material factor and F_g is the foundation factor. The limiting vibration values, v_0, are frequency independent. Values for v_0 for different soil conditions and construction activities are provided in Table 3.5, while correction factors for F_b, F_m, F_g are given in Table 3.6 toTable 3.8.

The Hong Kong Buildings Department published a Practice Note APP-137 (2004) providing guidelines on the control of ground-borne vibrations and ground settlements generated from pile driving and similar operations. This is the only Standard found in the literature indicating limiting values with regard to ground settlement and angular distortion. The effect of ground-borne vibrations from piling operations is assessed by the maximum peak particle velocity. The maximum PPV is assessed by the peak particle velocities at three orthogonal axes measured at ground levels of the evaluated structures. Guide values of maximum PPV suggested to give minimal risk of vibration-induced damage are given in Table 3.9. Due attention should also be paid to sensitive buildings close to the piling site such as hospitals, academic institutes, declared monuments, old buildings with shallow foundations, old tunnels/caverns, buildings installed with sensitive equipment, masonry retaining walls or sites with history of instability, monuments or buildings with historical significance etc. A more stringent control on the allowable limit of PPV for these buildings may have to be specified based on site and building conditions together with the duration and frequency of the exciting source. As different structures will have different tolerance in accommodating movements of their foundations, acceptance of estimated ground settlements should be considered on a case-by-case basis with respect to the integrity, stability and functionality of the supported structures. Provided that there are no particularly sensitive adjacent buildings, structures and services, the guide values in Table 3.10 may be taken as the trigger values in accordance with item 4(k) of PNAP APP - 18 for reference purpose.

Dowding (1996) proposed maximum allowable peak particle velocities depending on the structure type (Table 3.11). The Florida Department of Transportation (FDOT) uses the 0.5 in/sec criterion as the general PPV limit for their projects. The California Department of Transportation (Caltrans) has experienced minor damage from sustained pile driving at about 7.5 - 9 mm/s (0.30 - 0.35 in/sec) peak vertical particle velocity vibration on the ground next to an existing parking structure with the distance being slightly greater than 5 m (17 ft). The highest measured vibration amplitude was 73.1 mm/sec (2.88 in/sec) at 3 m (10 ft) from a pavement breaker. The criterion amplitude for pile driving is somewhere between 5 and 50 mm/sec (0.2 and 2 in/sec); the 50 mm/sec

(2 in/sec) criterion is being used for well-engineered and reinforced structures, for normal dwellings however vibrations should be limited to 7.5 mm/sec (0.3 in/sec). In any case, extreme care must be taken when sustained pile driving occurs within 7.5 m (25 ft) of any building, and 15-30 m (50-100 ft) of a historical or sensitive building (Hendriks 2004).

Criteria for vibration limits from continuous dynamic sources (e.g. highway traffic, trains) have also been published. The Transport and Road Research Laboratory (TRRL) in the United Kingdom has researched various vibration levels due to traffic vibrations (Whiffin and Leonard 1971). A summary of vibration amplitudes and reactions of people and the effects on buildings is found in Table 3.12. The Swiss Standards Association differentiates vibration limits between machines, traffic and blasting for four different building classes (Wiss 1981). The building classes are presented in Table 3.13, while Figure 3-8 and Figure 3-9 show the frequency dependent vibration limits for transient (blasting) and continuous (machines, traffic) vibrations, respectively. The USBM standard is also plotted for comparison. This standard is considered very conservative and introduces limits for historic structures. Konon and Schuring (1985) reviewed studies providing safe limits for historic and sensitive older buildings and recommended vibration criteria for transient and continuous vibrations (Figure 3-10). Overall, the safe limit for continuous vibrations is lower than that for transient vibrations.

Table 3.5 Uncorrected vibration velocity, v_0 (after Swedish Standard SS 02 52 11)

Foundation Condition	Piling, Sheet Piling,	Soil Compaction
Clay, silt, sand or gravel	9 mm/sec (0.35 in/sec)	6 mm/sec (0.24 in/sec)
Moraine (till)	12 mm/sec (0.47 in/sec)	9 mm/sec (0.35 in/sec)
Rock	15 mm/sec (0.59 in/sec)	12 mm/sec (0.47 in/sec)

Table 3.6 Building Factor, F_b (after Swedish Standard SS 02 52 11)

Class	Type of Structure	Building Factor,
1	Heavy structures such as bridges, quay walls, defense structures	1.70
2	Industrial or office buildings	1.20
3	Normal residential buildings	1.00
4	Especially sensitive buildings and buildings with high value or structural elements with wide spans, e.g. churches, museums buildings	0.65
5	Historic buildings in a sensitive state as well as certain sensitive historic buildings (ruins)	0.50

Table 3.7 Material Factor, F_m (after Swedish Standard SS 02 52 11)

Class	Type of Building Material	Material Factor,
1	Reinforced concrete, steel or timber	1.20
2	Unreinforced concrete, bricks, concrete blocks with voids, light-weight concrete elements	1.00
3	Light concrete walls, plaster	0.75
4	Limestone, lime-sandstone	0.65

Table 3.8 Foundation Factor, F_g (after Swedish Standard SS 02 52 11)

Class	Type of Foundation	Foundation
1	Slab, raft foundation	0.60
2	Buildings founded on friction piles	0.80
3	Buildings founded on end-bearing piles	1.00

Table 3.9 Guide values of maximum PPV (after APP-137)

Type of building	Transient Vibration (e.g. drop hammer)	Continuous Vibration (e.g. vibratory hammer)
Robust and stable buildings in general	15 mm/sec (0.59 in/sec)	7.5 mm/sec (0.30 in/sec)
Vibration sensitive/dilapidated buildings	7.5 mm/sec (0.30 in/sec)	3 mm/sec (0.12 in/sec)

Table 3.10 Empirical guidelines for tolerable ground settlement limits (after APP-137)

Instrument	Criterion	Alert	Alarm	Action
Ground Settlement marker	Total settlement	12 mm (0.47 in)	18 mm (0.71 in)	25 mm (0.98 in)
Services settlement marker	Total settlement and angular distortion	12 mm or 1:600	18 mm or 1:450	25 mm or 1:300
Building tilting marker	Angular distortion	1:1000	1:750	1:500

Table 3.11 Dowding vibration criteria for different structure types (Dowding 1996)

Structure	Limiting PPV, mm/sec (in/sec)
Bridges	50 (2)
Industrial buildings	50 (2)
New residential structures	25 (1)
Residential structures	12.5 (0.5)
Historic and old buildings	12.5 (0.5)

Table 3.12 Vibration Criteria for traffic vibration (after Whiffin and Leonard 1971)

PPV, in/sec (mm/sec)	Human Reaction	Effect on Buildings
0.4-0.6 (10-15)	Unpleasant	Architectural damage and possible minor structural damage
0.20 (5)	Annoying	Threshold risk of architectural damage to normal dwellings (plastered walls and ceilings)
0.10 (2.5)	Threshold of annoyance	Virtually no risk of architectural damage to normal buildings
0.08 (2.0)	Readily perceptible	Recommended upper limit to which ruins and ancient monuments should be subjected
0.006-0.019 (0.15-0.30)	Threshold of perception	Vibrations unlikely to cause damage of any type

Table 3.13 Building categories of Swiss Standard

Class	Building Type
I	Steel or reinforced concrete buildings, such as factories, retaining walls, bridges, steel towers, open channels, underground chambers and tunnels with and without concrete alignment
II	Buildings with foundation walls and floors in concrete, walls in concrete or masonry, stone masonry retaining walls, underground chambers and tunnels with masonry alignments, conduits in loose material
III	Buildings as mentioned previously but with wooden ceilings and walls in masonry
IV	Construction very sensitive to vibration, objects of historic interest

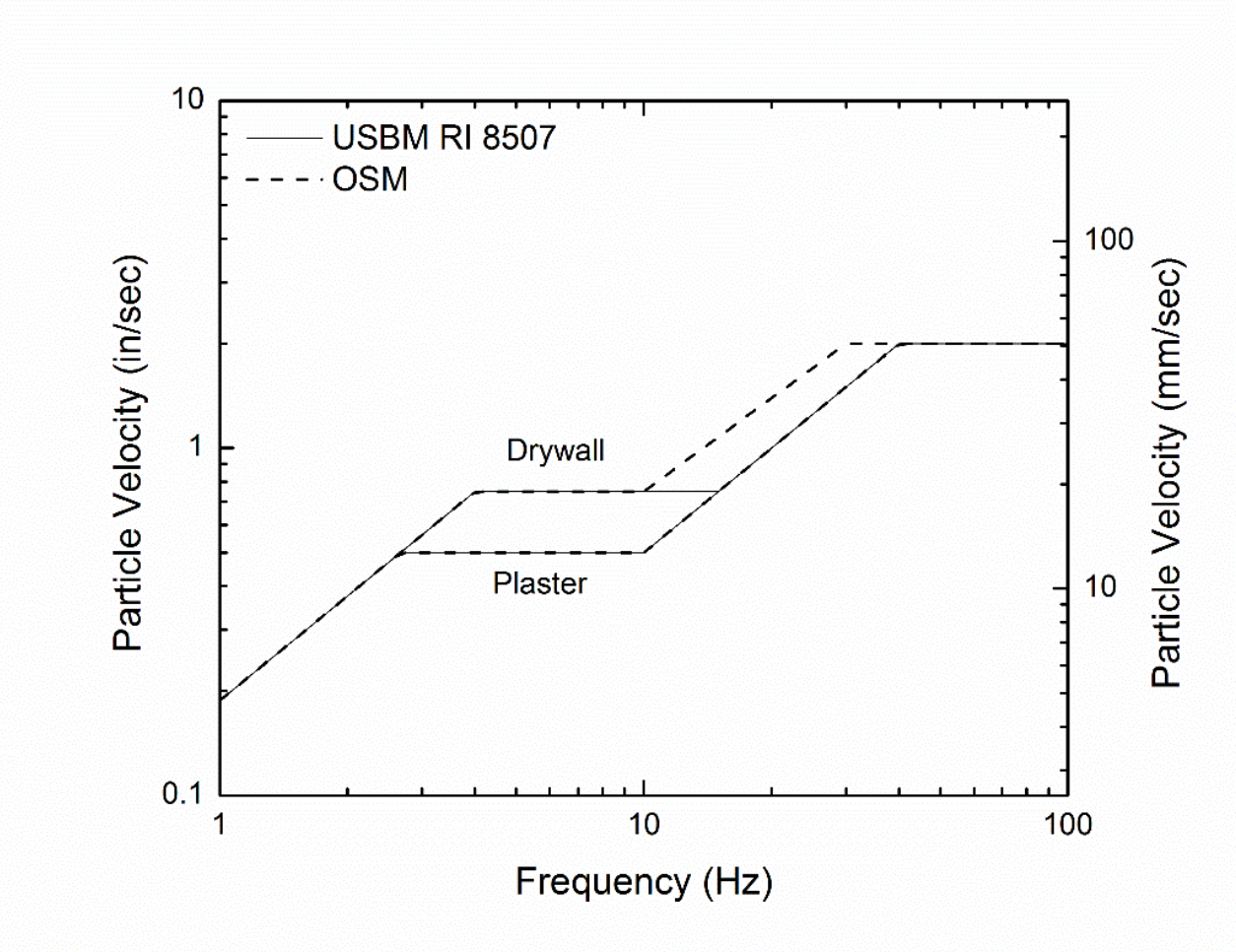

Figure 3-5 Safe vibration limit recommendations (after AASHTO Designation: R8-96, 2009)

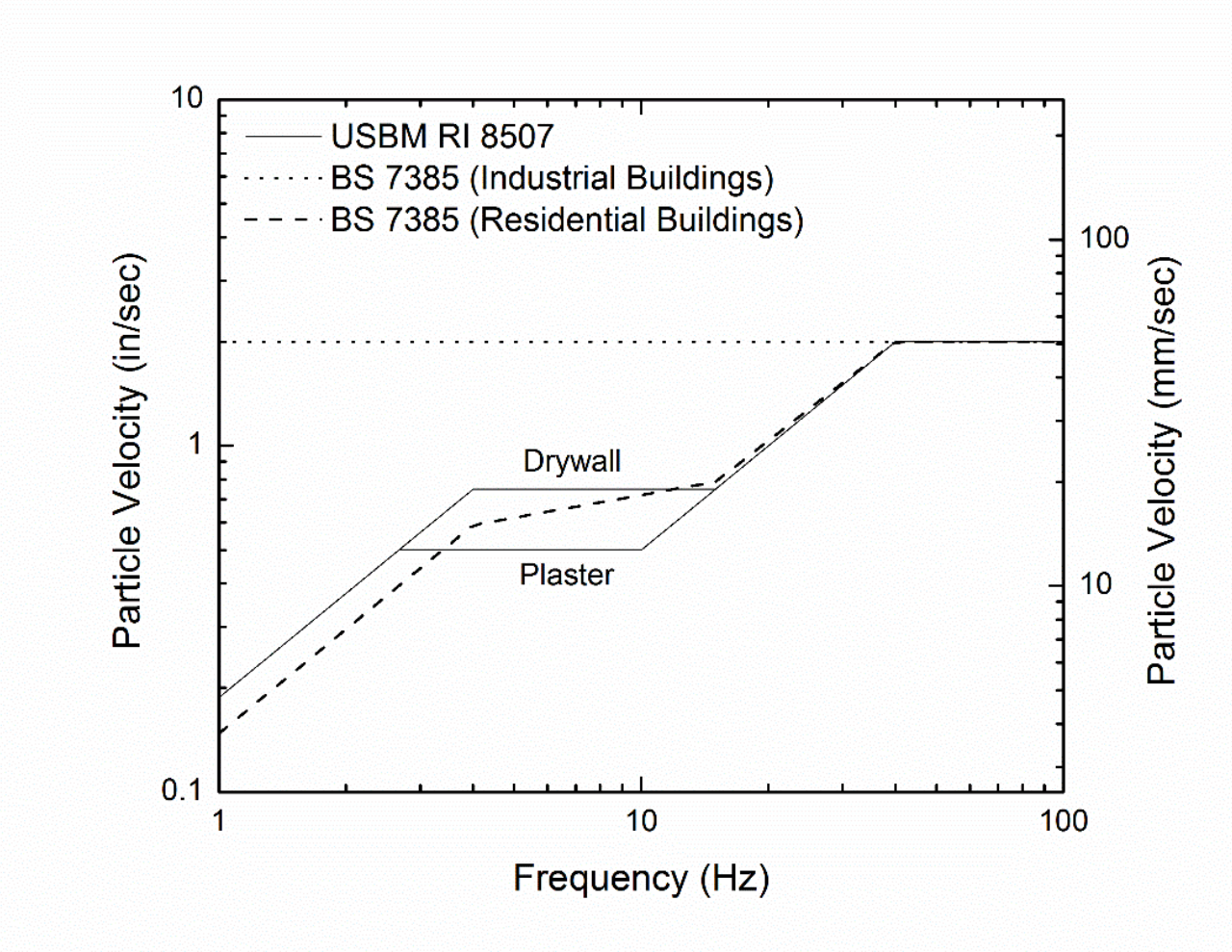

Figure 3-6 Comparison of the USBM RI 8507and the BS 7385 Standards (after AASHTO Designation: R8-96, 2009)

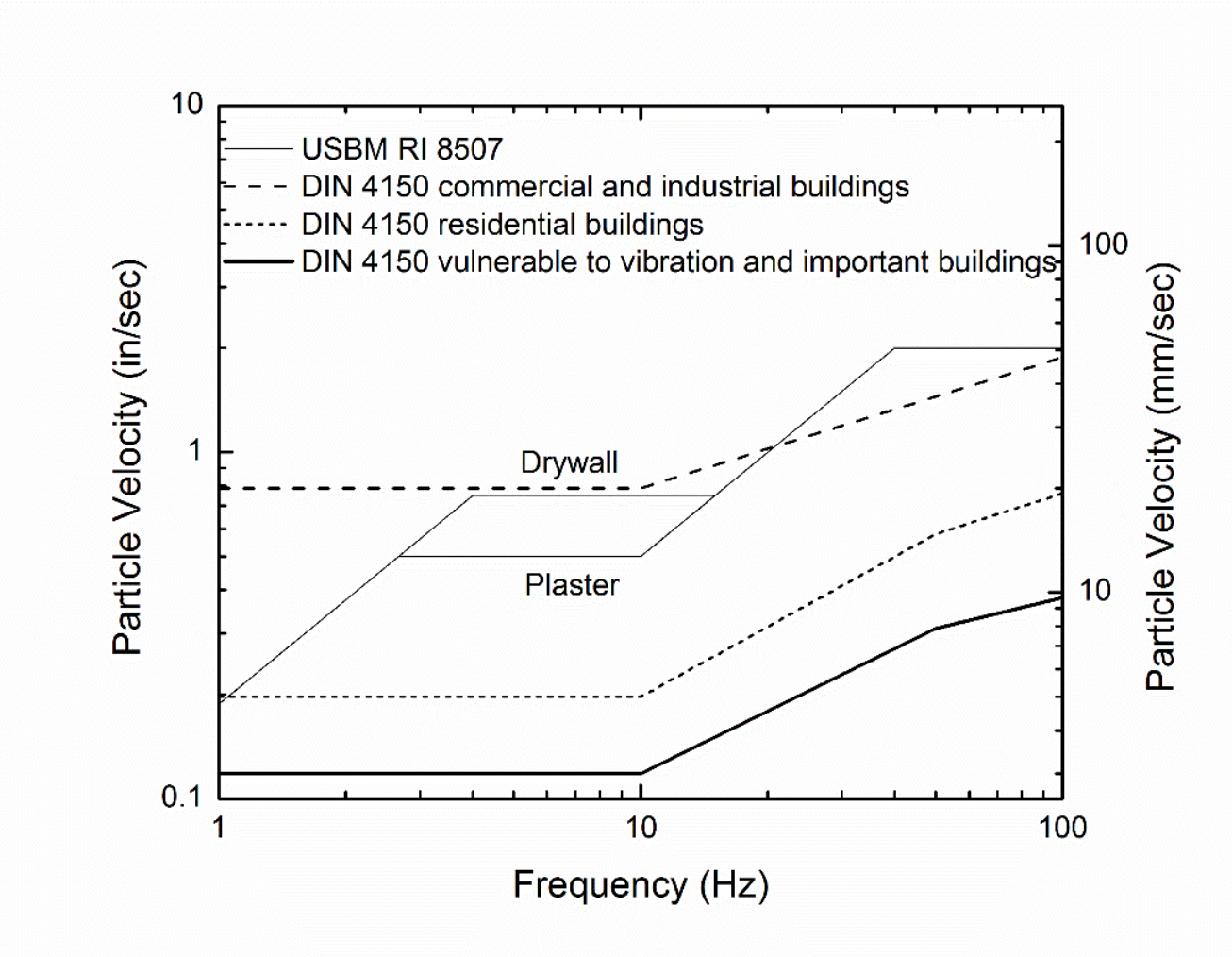

Figure 3-7 Comparison of the USBM RI 8507and the DIN 4150 Standards (after AASHTO Designation: R8-96, 2009)

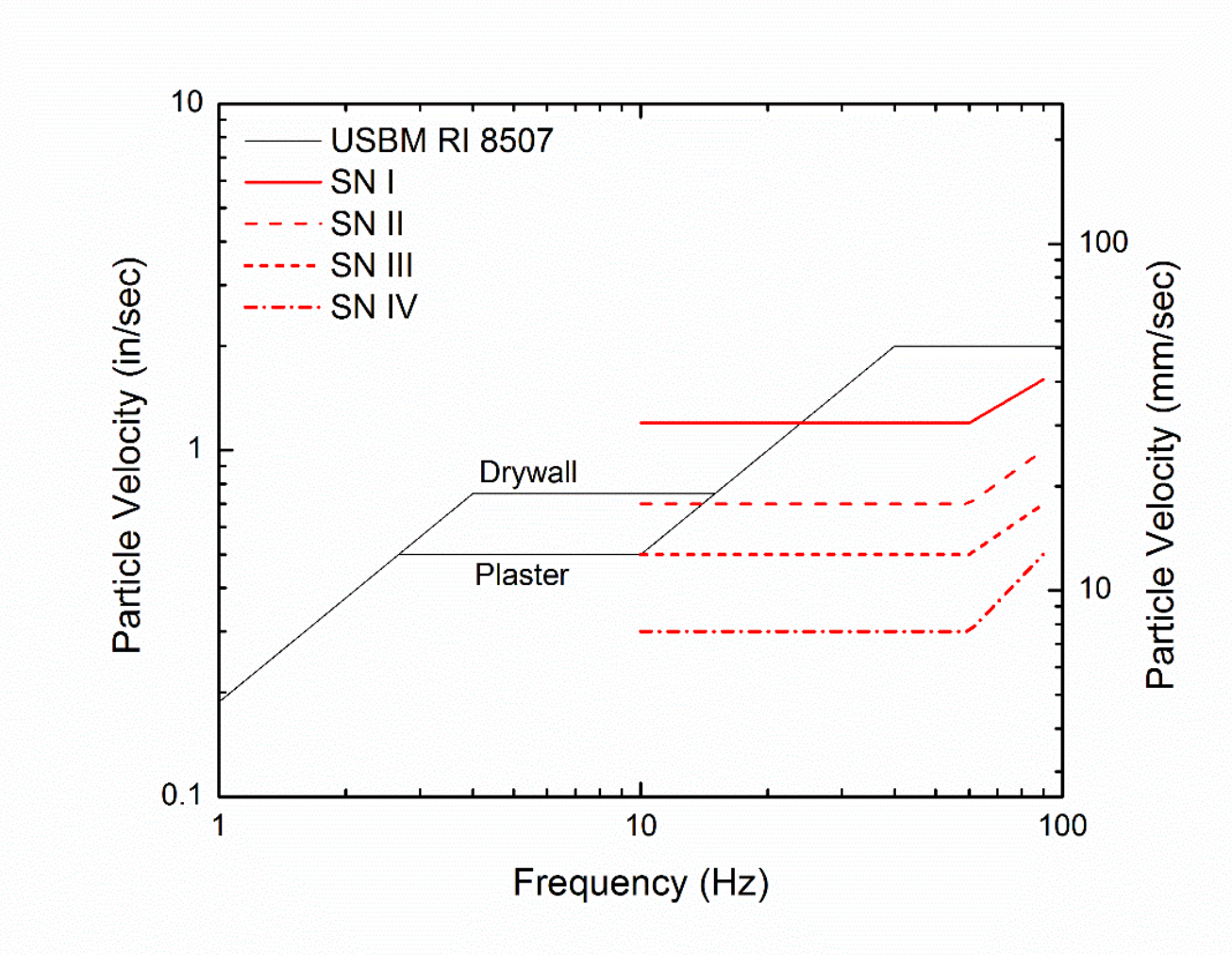

Figure 3-8 Swiss Standard for transient vibrations

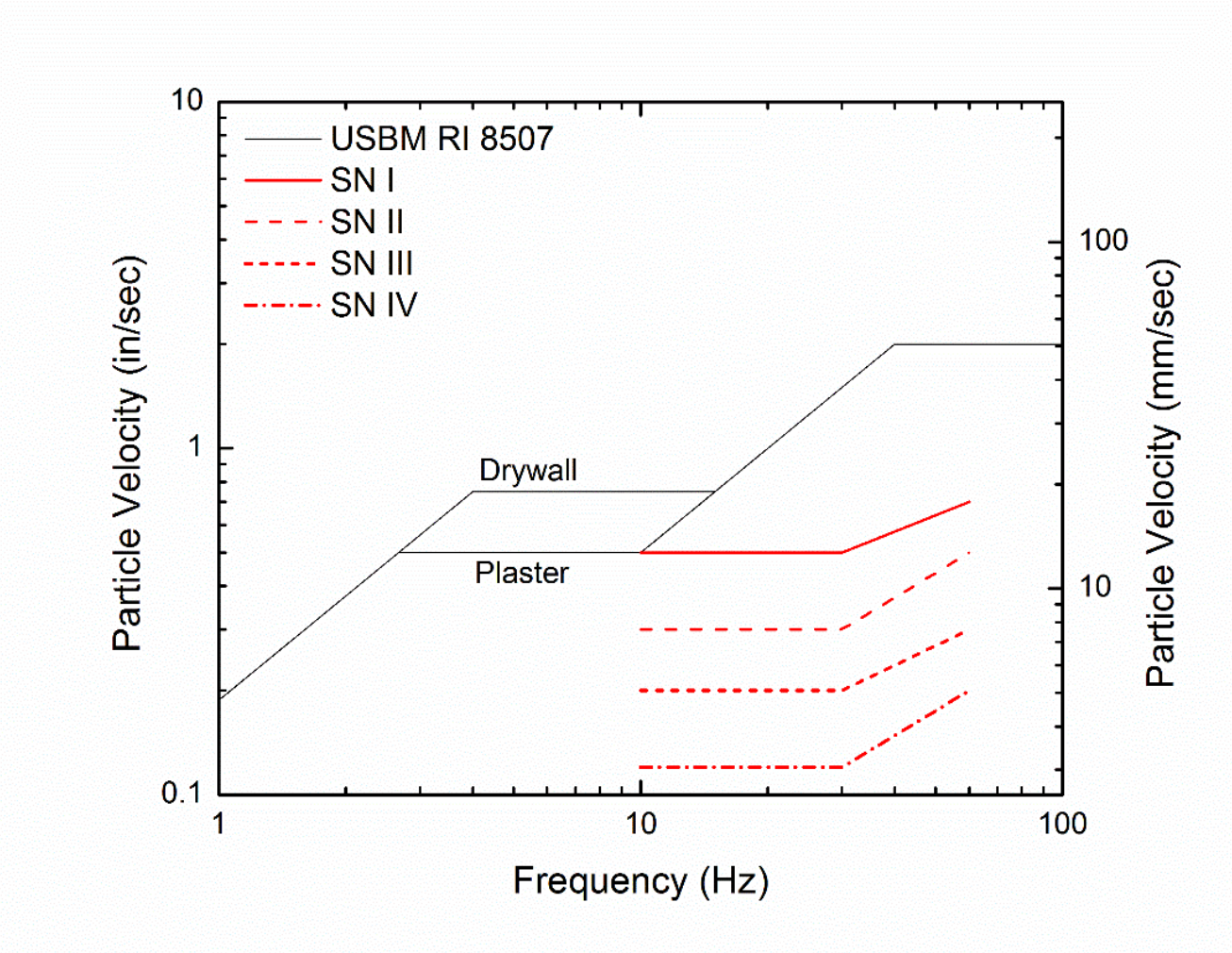

Figure 3-9 Swiss Standard for continuous vibrations

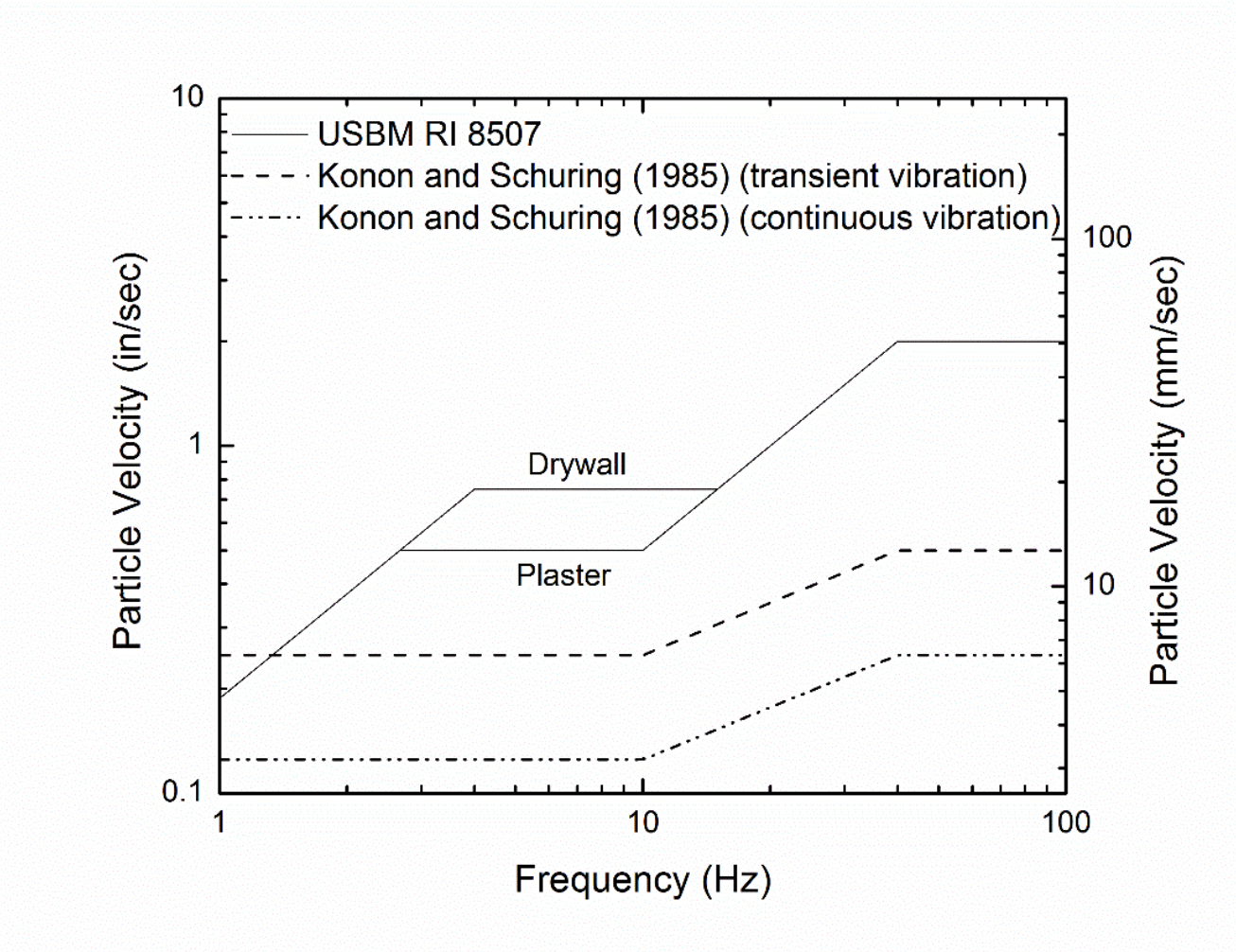

Figure 3-10 Vibration criteria for historic and sensitive older buildings (after Konon and Schuring 1985)

Massarsch and Broms (1991) reviewed existing vibration codes and suggested a simple relationship for the estimation of the critical *vertical* vibration velocity, v_v, that can cause damage to a structure as a function of the wave propagation velocity, c:

$$v_v = 4.7x10^{-5}\ x\ A_1\ x\ A_2\ x\ A_3\ x\ c \qquad \text{Eq. 3-3}$$

This equation was derived assuming a sinusoidal wave motion for impact loading and a building length that is half the wave length as this is considered a critical situation for the potential of distortion below the building. In order to account for other types of loading (different number of cycles and rate of loading), factor A_1 was introduced (Table 3.14). Factors A_2 and A_3 take care of the building category and the degree of acceptable damage, respectively (Table 3.15 and Table 3.16). Comparison of equivalent values calculated with this approach with the provisions existing vibration codes provided a good correlation (Figure 3-11).

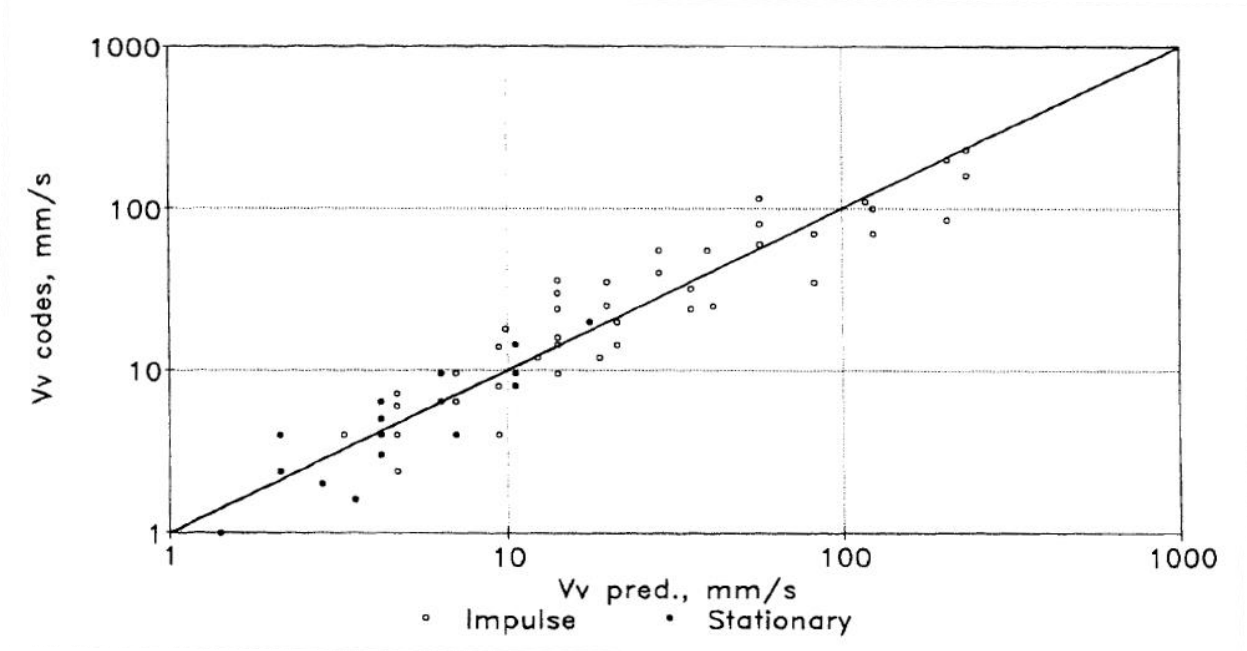

Figure 3-11 Comparison of vertical particle velocity from Massarch and Broms approach and vibration criteria (from Massarch and Broms 1991)

Table 3.14 Correction factor that takes into account the type of vibration source (after Massarsch and Broms 1991)

Vibration source	A_1
Impulse	1.0
Repeated	0.6
Stationary	0.3

Table 3.15 Correction factor that takes into account the type of building (after Massarsch and Broms 1991)

Building Category	A_2
Very sensitive structures, historic monuments	0.5
Vibration-sensitive buildings (with masonry walls and plaster), conventional foundations	1.0
Buildings with good foundations, concrete walls, structures not vibration sensitive	1.5
Steel or reinforced concrete structures, industrial premises	2.5

Table 3.16 Correction factor that takes into account the degree of acceptable damage (after Massarsch and Broms 1991)

Degree of acceptable damage	A_3
Negligible	0.7
Slight	1.0
Moderate	2.0
Severe	4.0

Damage categories due to construction activities were defined by Massarsch (2000) and are divided in four different mechanisms (Figure 3-12). This classification was made by Massarsch in order to clarify that other types of damage, other than ground vibration, exist and may have a contribution to a structural damage:

Category I, comprises static ground movements such as heave and lateral soil movements. Heave is a common phenomenon during installation of displacement piles in cohesive soils. Lateral soil movements are often encountered due to excavations or slope instability.

Category II, describes the problem of ground distortion. It is considered a static problem which happens when horizontally propagating waves cause a temporary distortion of the ground surface layer to a depth corresponding approximately to one wave length. During the construction works, like soil compaction and pile driving, the number of distortion cycles can be very high. Thus, the distortion magnitude depends on the wave length and the number of cycles of the propagating wave and the displacement amplitude.

Category III, covers permanent settlement (total and differential) and strength loss due to cyclic loading mainly in loose granular soils. Differential settlements that happen during pile driving are more critical than total settlement.

Category IV, considers building damage caused by dynamic effects in the building itself due to ground vibrations, and is the only category that is considered in most of the vibration standards.

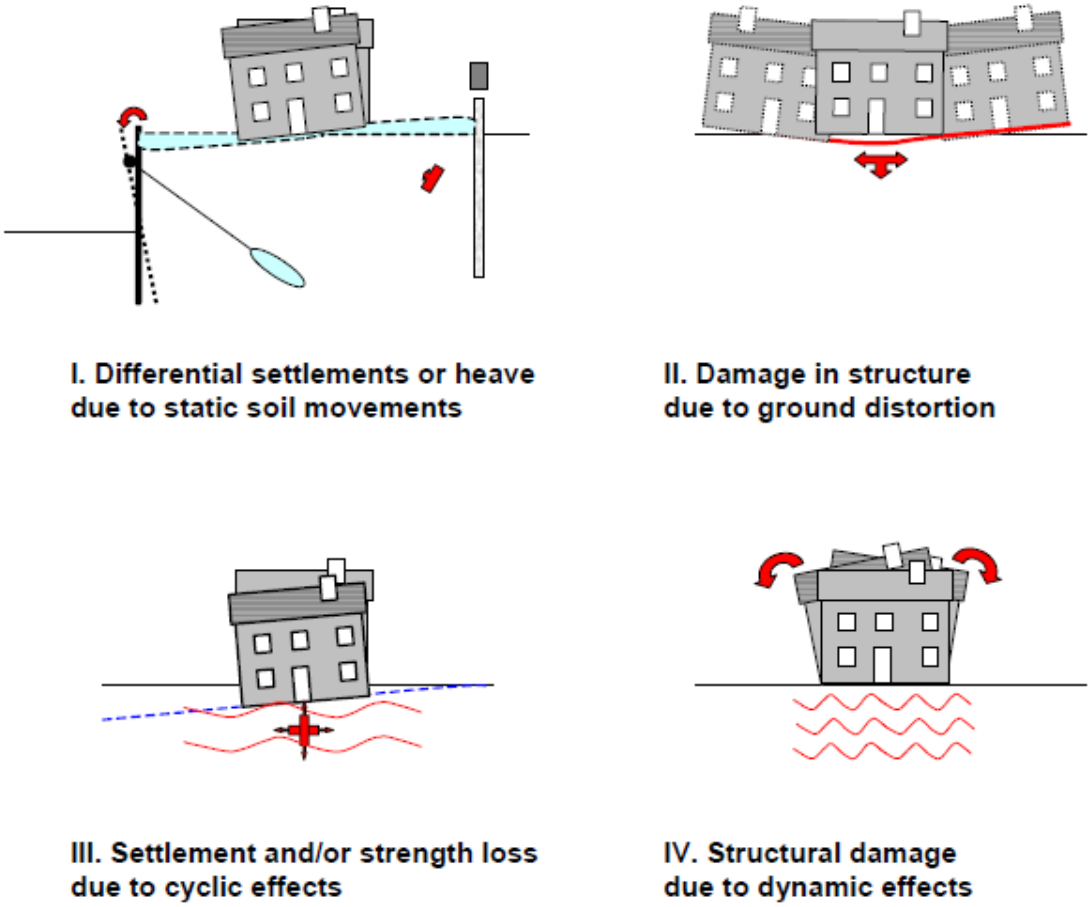

Figure 3-12 Types of building damage in connection with construction activities (after Massarsch 2000)

Svinkin (2004, 2005) discussed the different ways that ground vibration from construction sources may affect adjacent and remote structures:

Direct Vibration Effects to Structures: Direct damage to structures may be the result of soil-structure interaction when excitation frequencies of ground vibrations do not match the natural frequencies of structures. All the allowable vibration values for structures discussed above fall into this category. However, there are reported cases that

demonstrate no structural damage even if velocities of ground vibrations were higher than the cracking threshold levels (Oriard 1999, Siskind 2000).

Resonant Structural Vibrations: The proximity of the frequency of ground vibrations to one of the building's natural frequencies may generate the condition of resonance. Ground and structure vibrations with a frequency near the natural structure frequency are presented in Figure 3-13. The peak particle velocity of structure vibrations increased 2.7 times and structure vibrations started to increase after the first cycle of ground vibrations. A dynamic magnifying factor for low-rise residential structures at resonance, can reach 2 to 9 times the vibrations measured on the ground (Quense 2001). This factor can be much higher for multistory steel and concrete structures. Resonant structural vibrations can be triggered at large distances of a few hundred meters from a pile driving site and even more than one kilometer from a blasting site. Rausch (1950) reported a case where intolerable vibrations occurred in a building located 200 m from a foundation of a forge hammer with a falling weight of 14.7 kN. Svinkin (1993) described resonant structure vibrations of a five story building located at 500m from the foundation under a vibroisolated block for a forge hammer with a falling weight of 157 kN. Resonant horizontal building vibrations are the main cause of concern. Resonant vertical floor vibrations are important when sensitive devices are installed on the floors.

Resonance of Soil Layers: The coincidence of the occurrence of the dominant frequency of propagated waves with the frequency of a soil layer can create the condition of resonance and generate large soil vibrations. The relationship between the natural frequency, f_n, of a uniform soil with deposit thickness H according to Roesset (1977) is estimated by:

$$f_n = \frac{(2n-1)}{4}\frac{c}{H} \qquad \text{Eq. 3-4}$$

where n represents the number of modes c is the compression or shear wave velocity.

An interesting example of this case was described by Bodare and Erlingsson (1993). Two rock concerts were held at a soccer stadium in Sweden. The stadium is founded on precast concrete piles in soft clay. Sixty thousand people were present, with a good half of the audience in the stands, and more than twenty-five thousand people standing on the field. The audience jumped in time to the music and excited the clay layer of 25 m from the surface, with the same frequency as the beat of the music (around 2.4 Hz). The upper parts of the stands moved so violently that some people left their places. People assessed the heavy ground vibrations to have an amplitude of displacement between 2 and 20 cm. Damage to the roof and the building was documented after the concerts. Residents of buildings 400 m away of the stadium complained that the vibrations caused books to tumble from shelves. It was found that the beat of the music coincided with the second mode of the clay layer, thus the high vibration levels were due to resonance of the clay deposit. Concerts were not permitted at the stadium after that.

Dynamic Settlements: Ground and foundation settlements as a result of ground vibration levels much lower that the threshold cracking limit can occur at various distances from the source. Densification of sands is expected at short distances from the dynamic sources, but surface settlements extend beyond the zone of densification. Several cases of dynamic settlement in sands and clays are discussed in a later section.

Repeated Dynamic Loads: The accumulated effect of repeated dynamic loads should be taken into account for production pile driving (Crockett 1980). This approach is especially important for historic and old buildings. Lacy and Gould (1985) concluded that increasing the number of driven piles can change a situation from insignificant vibration effects to damaging settlements.

Non-Dynamic Construction Activities: Dewatering and excavation are very often involved in building projects. Under certain conditions they can cause important movement of the adjacent ground and damage to nearby structures (D'Appolonia 1971). Dowding (1996) observed that permanent excavation deformations can extend further away from the area of construction compared to those induced by pile driving vibrations.

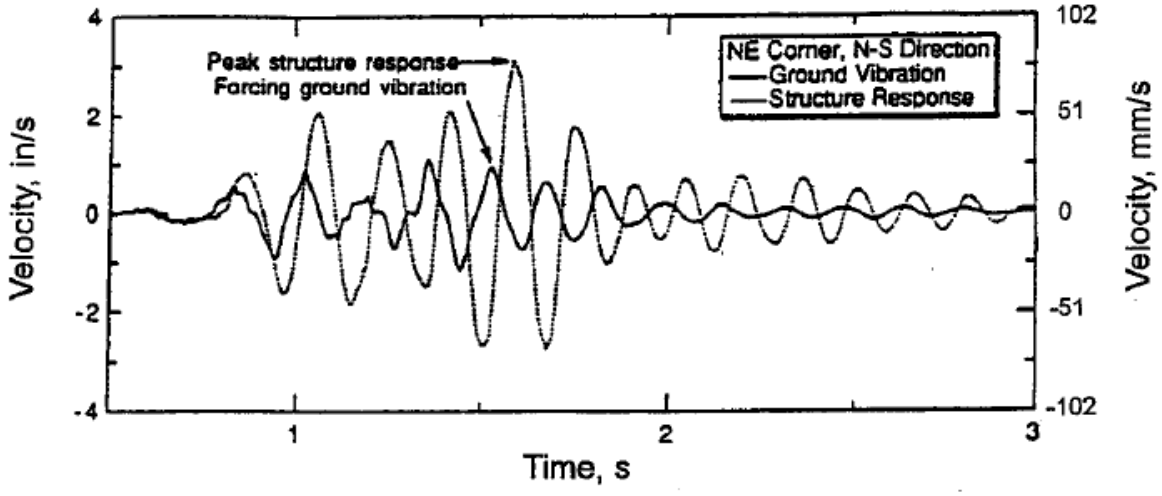

Figure 3-13 Ground and structure vibrations with frequency of 5.8 Hz near structure resonance (from Crum 1997)

3.1.3 Sensitive Equipment

Vibration-sensitive laboratories which use equipment for research, microelectronics and optoelectronics manufacturing, medical diagnostics, and similar activities must satisfy special vibration criteria. When the design of a facility is to house a sensitive device, the so-called generic criteria are applicable for a group of equipment. The Vibration Criterion (VC) curves (originally known as the "BBN" criteria) were developed in the early 1980s by Gordon and Ungar (1983) and published by the Institute of Environmental Sciences and Technology (IEST) (2005), while the NIST-A criterion was developed in the early 1990s for the Advanced Measurement Laboratory at the U.S. National Institute of Standards and Technology (NIST) (Soueid et al. 2005). The VC criteria were originally developed for use in the semiconductor industry, but have found application in a wide variety of technological applications. The NIST-A criterion was developed for metrology, but has gained popularity within the nanotechnology community (Amick et al. 2005). Figure 3-14 presents the two criteria along with the International Standards Organization guidelines (ISO 2631) for the effects of vibration on people in buildings. The settings for which the criteria are applicable are defined Table 3.17. Measured vibrations are to be processed in one-third octave bands of frequency, for which the bandwidth is 23 percent of the center frequency of each band.

Table 3.17 Application and interpretation of the generic Vibration Criterion (VC) curves

Criterion Curve	Amplitude[1], μm/sec (μin/sec)	Detail Size[2], μm	Description of Use
Workshop (ISO)	800 (32000)	N/A	Distinctly perceptible vibration. Appropriate to workshops and non-sensitive areas.
Office (ISO)	400 (16000)	N/A	Perceptible vibration. Appropriate to offices and non-sensitive areas.
Residential (ISO)	200 (8000)	75	Barely perceptible vibration. Appropriate to sleep areas in most instances. Usually adequate for computer equipment, hospital recovery rooms, semiconductor probe test equipment, and microscopes less than 40x.

Criterion Curve	Amplitude[1], μm/sec (μin/sec)	Detail Size[2], μm	Description of Use
Operating Theater (ISO)	100 (4000)	25	Vibration not perceptible. Suitable in most instances for surgical suites, microscopes to 100x and for other equipment of low sensitivity.
VC-A	50 (2000)	8	Adequate in most instances for optical microscopes to 400x, microbalances, optical balances, proximity and projection aligners, etc.
VC-B	25 (1000)	3	Appropriate for inspection and lithography equipment (including steppers) to 3 μm line widths.
VC-C	12.5 (500)	1-3	Appropriate standard for optical microscopes to 1000x, inspection and lithography equipment (including moderately sensitive electron microscopes) to 1 μm detail size TFT-LCD stepper/scanner processes.
VC-D	6.25 (250)	0.1-0.3	Suitable in most instances for demanding equipment including electron microscopes (TEMs and SEMs) and E-Beam systems.
VC-E	3.12 (125)	<0.1	A challenging criterion to achieve. Assumed to be adequate for the most demanding of sensitive systems including long path, laser-based, small target systems, E-Beam lithography systems working at nanometer scales, and other systems requiring extraordinary dynamic stability.
VC-F	1.56 (62.5)	N/A	Appropriate for extremely quiet research spaces; generally difficult to achieve in most instances, especially cleanrooms. Not recommended for use as a design criterion, only for evaluation.
VC-G	0.78 (31.3)	N/A	Appropriate for extremely quiet research spaces; generally difficult to achieve in most instances, especially cleanrooms. Not recommended for use as a design criterion, only for evaluation.

[1] As measured in one-third octave bands of frequency over the frequency range 8 to 100 Hz (VC-A and VC-B) or 1 to 80 Hz (VC-C through VC-G).

[2] The detail size refers to the line width in the case of microelectronics fabrication, the particle (cell) size in the case of medical and pharmaceutical research, etc. It is not relevant to imaging associated with probe technologies, AFMs, and nanotechnology.

The information given in this table is for guidance only. In most instances, it is recommended that the advice of someone knowledgeable about the applications and vibration requirements of the equipment and process be sought.

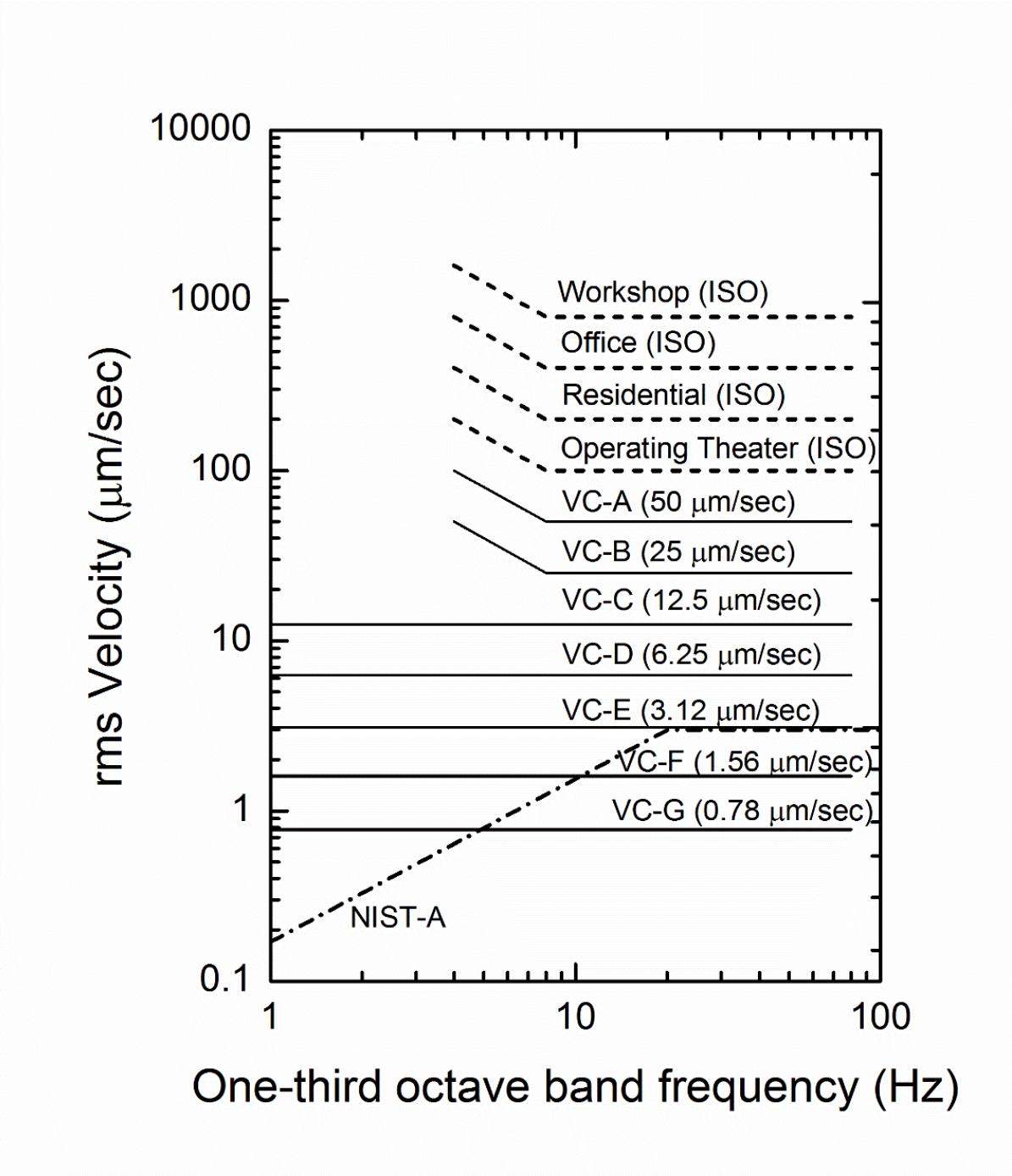

Figure 3-14 Generic Vibration Criterion (VC) curves for vibration-sensitive equipment, showing also the ISO guidelines for people in buildings

3.2 Prediction of ground vibrations

The *wave propagation velocity* is the rate that vibrations travel through the ground as waves of energy. Wave propagation velocity should not be confused with the *particle velocity* that is the excitation velocity of individual ground particles caused by travelling waves. The particle motion reaches a peak value before attenuating as the wave passes (Head and Jardine 1992). An example of a vertical particle velocity record during driving an H-pile is presented in Figure 3-15. The maximum value of particle velocity is usually extracted and is known as the peak particle velocity (PPV). The particle motion may be measured in three orthogonal directions, x, y and z. The intensity of the vibrations is expressed in several ways (Hiller and Hope 1998). The most popular definition for PPV used by many researchers, is the *maximum single value* of the three directional components or in some cases by the peak value attained by the vertical component. The *true vector sum* of the three components measured at the same time of impact has been also reported and can be calculated as:

$$v = \sqrt{{v_x}^2 + {v_y}^2 + {v_z}^2} \qquad \text{Eq. 3-5}$$

Some researchers calculate the *pseudo vector sum* of the three components which is based on the maximum value of each of the triaxial components irrespective of the time of occurrence:

$$v = \sqrt{{v_{xmax}}^2 + {v_{ymax}}^2 + {v_{zmax}}^2} \qquad \text{Eq. 3-6}$$

This is somewhat misleading though since it is very rare that v_{xmax}, v_{ymax} and v_{zmax} occur at the same time during pile driving (Mayne 1985) and can provide overly conservative values of vibration intensity (Athanasopoulos and Pelekis 2000). Figure 3-16 shows the comparison between the maximum single component velocity and the true vector sum of the triaxial components. The true vector sum can be 10 to 40% higher than the peak

single component velocity. The pseudo vector sum velocity can be even higher reaching a ratio of pseudo vector sum to maximum component of 1.6. It is important to indicate which definition of PPV is implemented in each study, since the magnitude of the nominal PPV depends on the definition used (Hiller and Hope 1998).

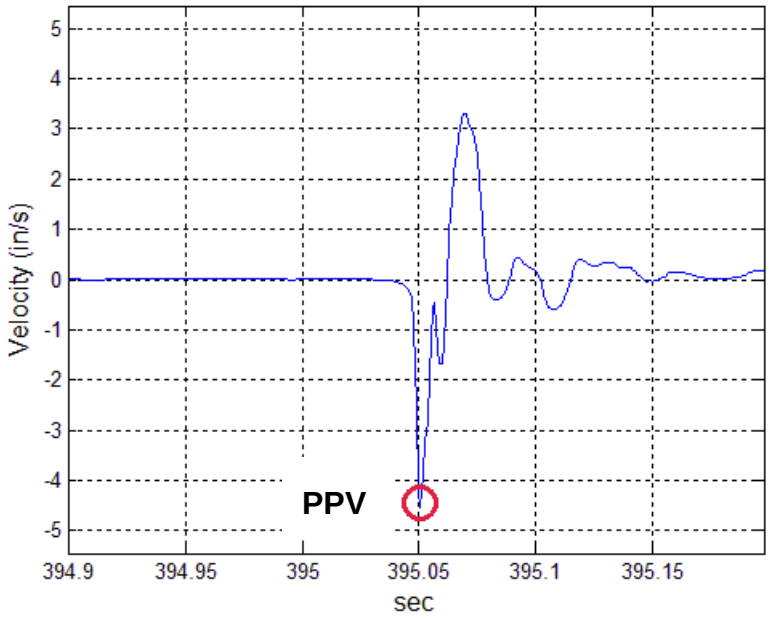

Figure 3-15 Example of vertical particle velocity record from H-pile driving

The peak particle velocity during construction operations has been recorded by many researchers who have, subsequently, suggested empirical equations to predict ground motion. These empirical correlations were developed after measuring vibration records on the ground surface during pile installation or other construction activities. The horizontal distance from the source to the measuring point is usually taken as the distance in these relations. However, when a source of vibration other than a point source, like the pile, is generating waves through the soil, the actual distance from the measuring point to the source point may not be the horizontal. For pile driving it is necessary to keep in mind that body waves are propagating outward from the tip and shaft of the pile, thus the

distance may be diagonal, changing during pile penetration. Also, if the target point is within the soil mass the distance needs to be correctly evaluated.

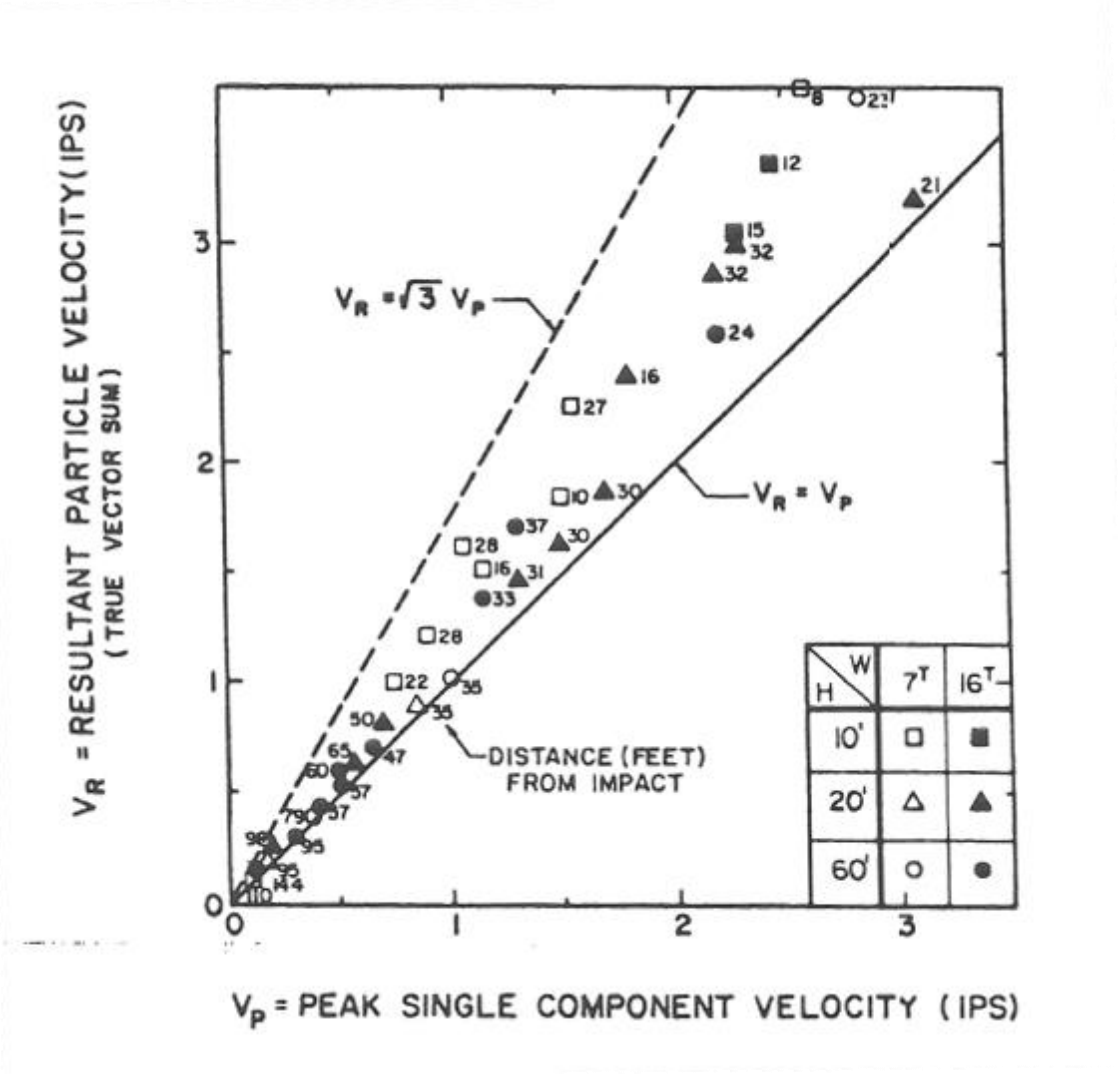

Figure 3-16 Trend between measured true vector sum velocity and peak single component velocity for dropped weights (from Mayne 1985)

Typical intensities of vibration from different construction equipment operation are presented in Figure 3-17. The data were collected by Wiss (1974) during actual construction operations at different distances on the ground surface. The monitored values depict specific soil conditions of the sites tested, but it is interesting to note the wide range over which the intensities are spread.

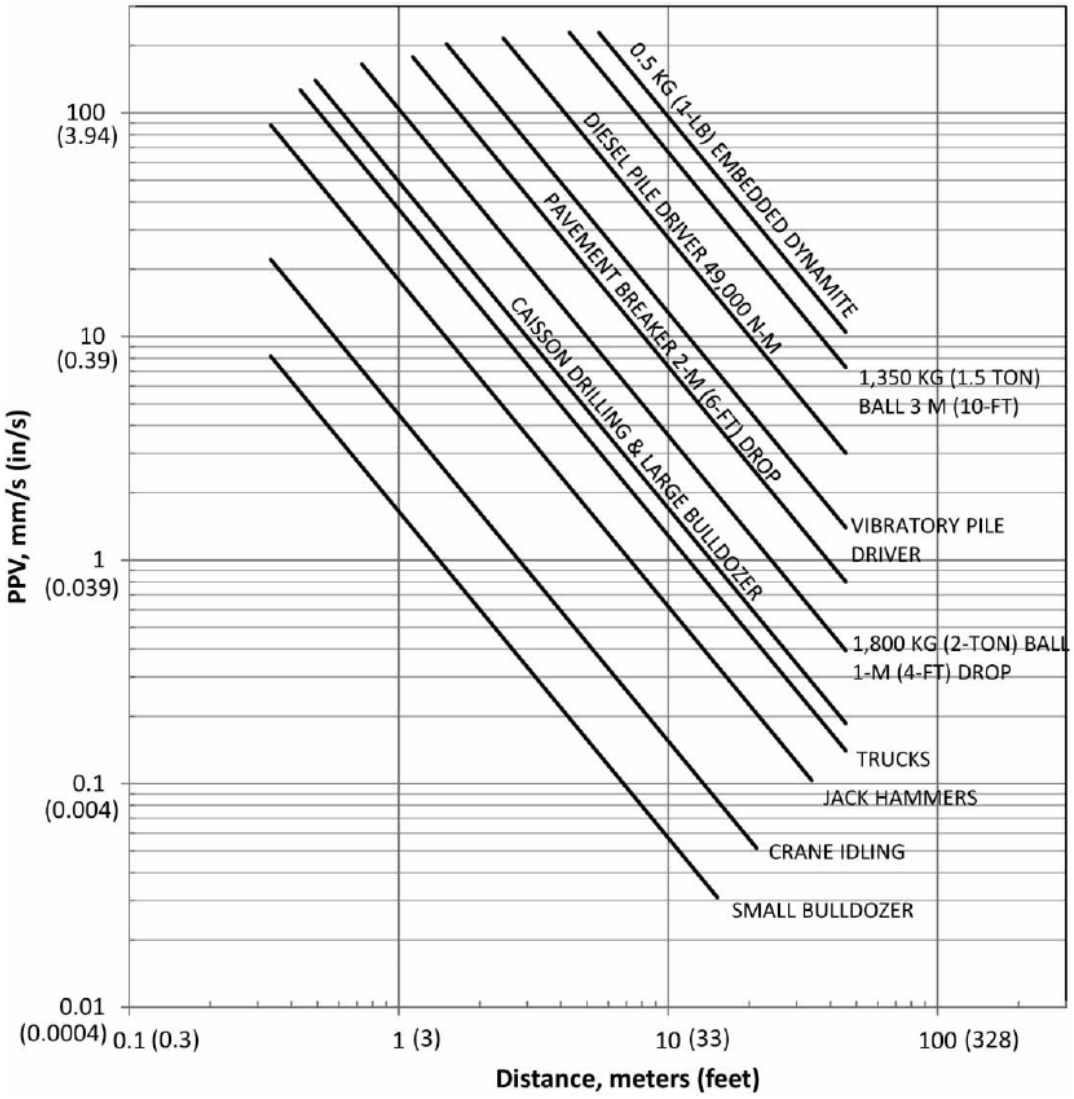

Figure 3-17 Typical intensities of construction vibrations (after Wiss 1974, from Johnson et al. 2013)

Wiss (1981) suggested a power equation for impact energy sources correlating energy and particle velocity as:

$$v = C(E)^{a} \qquad \text{Eq. 3-7}$$

where: v = peak particle velocity
C = velocity at energy of one unit
E = impact energy
a = slope of velocity increase

This relationship is applicable for a given distance from the source. Wiss suggests a rate of increase, a=0.5 in most cases.

The amplitude of the seismic waves decreases with increasing distance from the impact source. **Richart et al. (1970)** defined two components of the decay of vibration amplitudes: *geometric (radiation)* damping and *material (hysteretic)* damping. Geometrical decay with distance is described by:

$$A_2 = A_1 \left(\frac{r_1}{r_2}\right)^{n} \qquad \text{Eq. 3-8}$$

where: r_1 = distance from source to point of known amplitude
r_2 = distance from source to point of unknown amplitude
A_1 = vibration amplitude at distance r_1 from source
A_2 = vibration amplitude at distance r_2 from source
n = coefficient depending on wave type
n = 0.5 for Rayleigh waves
n = 1 for Body waves in the ground
n = 2 for Body waves on the ground surface

It is the pioneering work of Lamb (1904) who investigated analytically the response of homogeneous, isotropic, elastic half space to various harmonic and impulsive loads, that established the wave propagation due to point and line loads. If a *point load* is applied on the elastic half space, three types of waves will propagate from the point of source. The geometric decay of amplitude of the Rayleigh waves is proportional to the square root of distance, whereas the body waves' decay is proportional to the square of the

surface distance. The body waves traveling inside the medium will spread their energy spherically and will drop off proportionally to the radial distance. If the point load is buried within the elastic medium, the spherical spreading of the body waves will attenuate again proportionally to the first power of distance. For a *line load* applied to the half space, the Rayleigh waves do not drop off with distance along the surface, and progress out to infinity. It is noted again that this is true for the assumed undamped solid. On the surface, body waves will fall off in amplitude proportionally to the surface distance, while body waves travelling in the interior of the elastic space lose energy proportionally to the square root of the radial distance. If the line load is buried, the geometric decay of the amplitude is proportional to the square root of the cylindrical distance. The above spreading attenuation characteristics for various physical sources are summarized in Table 3.18 (Gutowski and Dym 1976).

Table 3.18 Geometric attenuation coefficients (after Gutowski and Dym 1976)

Physical Source	**Source Type**	**Wave**	**Source Location**	**n**
Highway/rail line footing array	Line	Rayleigh	Surface	0
		Body	Surface	1.0
Car in pothole, single footing	Point	Rayleigh	Surface	0.5
		Body	Surface	2.0
Tunnel	Buried Line	Body	Interior	0.5
Buried explosion	Buried Point	Body	Interior	1.0

When waves travel through the soil, energy is lost since soil is not a perfectly elastic material. This reduction of vibration amplitude is called material damping. **Mintrop (1911)** proposed a formula combining the geometric and material damping, which was presented by **Bornitz (1931)** and is known as the *Bornitz equation*:

$$A_2 = A_1 \left(\frac{r_1}{r_2}\right)^n exp[-\alpha(r_2 - r_1)] \qquad \text{Eq. 3-9}$$

where: exp = base of natural logarithm, e = 2.71828
α = attenuation coefficient (units of 1/distance)

The exponential decay express by $\exp[-\alpha(r_2-r_1)]$ represents the material damping and is characterized by the attenuation coefficient α. Figure 3-18 shows the Bornitz equation for Rayleigh waves (n=0.5) for different attenuation coefficients and a reference amplitude, r_1=1 m. It is clear that material damping has a great influence on the attenuation of ground vibration.

The attenuation coefficient, α, is frequency dependent. Low frequency vibrations will attenuate slower than high frequency vibrations when travelling the same distance, thus being more damaging to nearby structures. Energy is lost during deformation cycles in material damping, which indicates a frequency decline with distance for the same type of wave (Dowding 1996). Table 3.19 was prepared with data collected for twenty years from 36 sites by **Woods and Jedele (1985)** and presents values of the attenuation coefficient for a frequency of 5 Hz. As can be seen, softer materials have greater attenuation coefficients which means that the particle velocity attenuates faster with distance in these types of soil. Alpha values for different frequencies may be determined by:

$$\alpha_2 = a_1 \left(\frac{f_2}{f_1}\right) \qquad \text{Eq. 3-10}$$

where: α_1 = known attenuation coefficient at frequency f_1
α_2 = unknown attenuation coefficient at frequency f_2

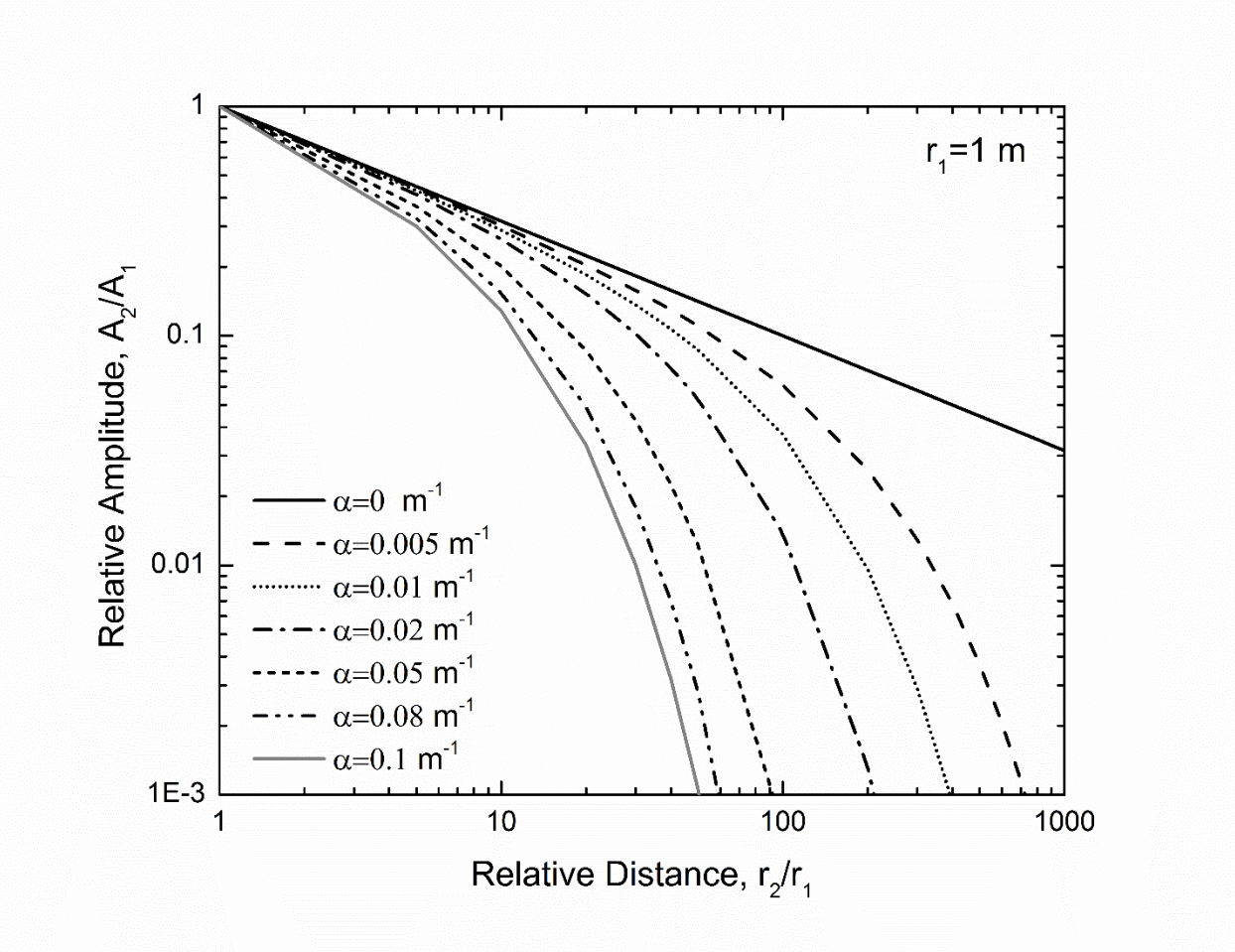

Figure 3-18 Reduction of vibration amplitude of Rayleigh waves due to material damping effect for different attenuation coefficients

An equation for the attenuation coefficient, α, based on damping ratio, vibration frequency and the shear, compressional or surface wave velocity was presented by **Haupt (1986)**:

$$\alpha = \frac{2\pi D f}{c} \qquad \text{Eq. 3-11}$$

where: D = material damping (%)
f = vibration frequency
c = wave propagation velocity

Table 3.19 Proposed Classification of Earth Materials by Attenuation Coefficient (after Woods and Sharma 2004)

Class	Attenuation Coefficient, α at 5 Hz		Description of material (N = SPT Blow Count)
	(1/m)	(1/ft)	
I	0.01 to 0.033	0.003 to 0.01	*Weak or soft soils* (shovel penetrates easily): lossy soils, dry or partially saturated peat and muck, mud, loose beach sand and dune sand, recently plowed ground, soft spongy forest or jungle floor, organic soils, topsoil. (**N<5**)
II	0.0033 to 0.01	0.001 to 0.003	*Competent soils* (can dig with shovel): most sands, sandy clays, gravel, silts, weathered rock. (**5<N<15**)
III	0.00033 to 0.0033	0.0001 to 0.001	*Hard soils* (cannot dig with shovel, need pick to break up): dense compacted sand, dry consolidated clay, consolidated glacial till, some exposed rock. (**15<N<50**)
IV	< 0.00033	< 0.0001	*Hard competent rock* (difficult to break with hammer): bedrock, freshly exposed hard rock. (**N>50**)

For vibration propagation in an elastic medium (far-field problem), the soil damping ratio, D, can be assumed to be in the range of 3 to 5% (Massarsch and Fellenius 2008). Near the vibration source (near-field problem) the material damping is higher. Figure 3-19 presents the variation of the attenuation coefficient versus the wave velocity for different values of frequency and a material damping of D=4%. The alpha coefficient decreases with increasing wave velocity and with decreasing frequency.

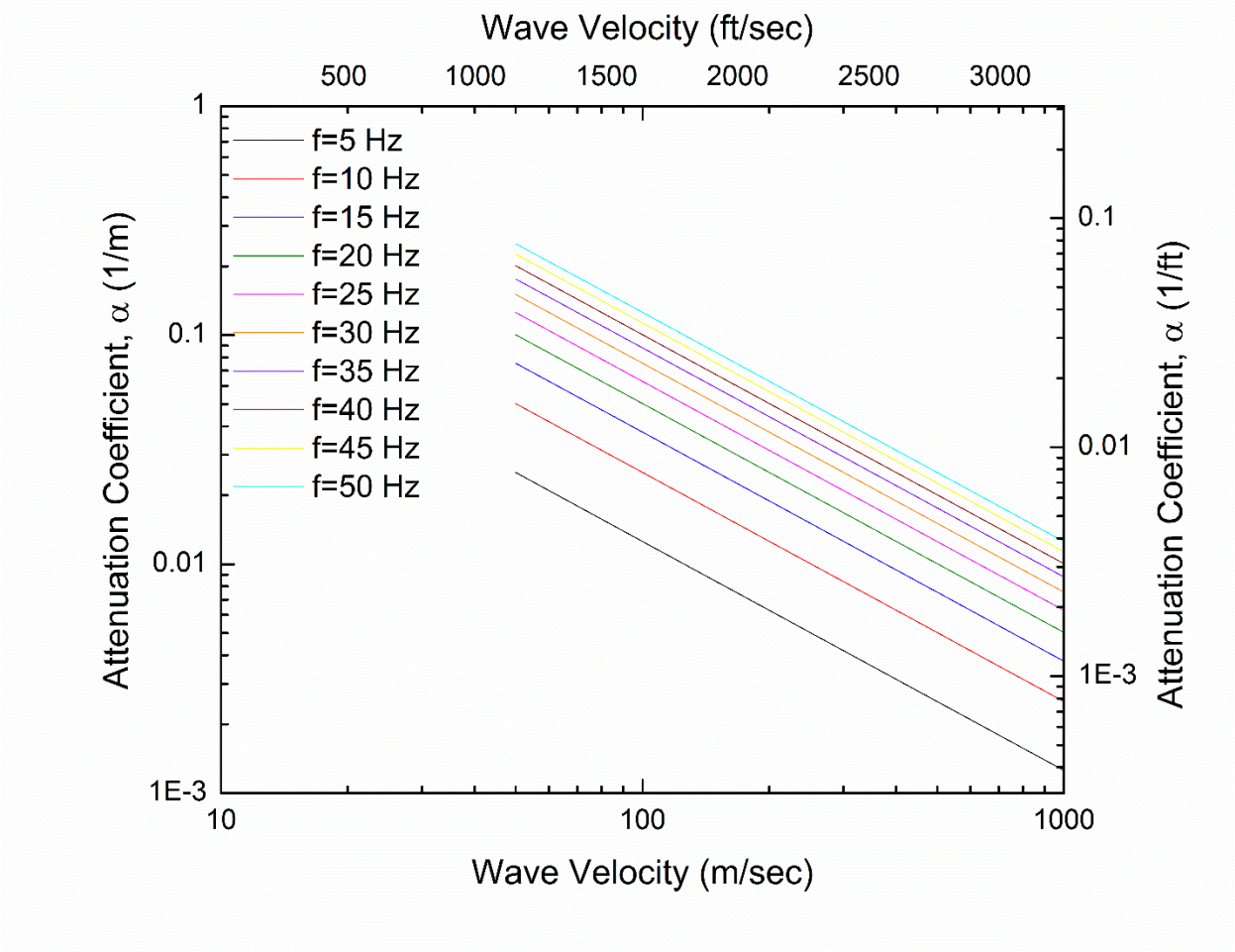

Figure 3-19 Attenuation coefficient as a function of wave velocity for different frequencies (D=4%)

Yang (1995) modified the Bornitz equation claiming that it is a surface wave attenuation formula (for n=0.5) without providing information about ground vibration near the source due to body waves. According to Yang, the Bornitz equation is suitable for the far field where r_1 of Eq. 3-12 is larger than $2.5\lambda_R$, where λ_R is the wavelength of the Rayleigh wave. In order to capture the wave propagation phenomena in the near field ($r_1<2.5\lambda_R$), the effect of geometry of vibration source and the dependency of attenuation on soil type, Yang proposed the following formula to calculate the vibration intensity at distance r from the source:

$$A_r = A_0\sqrt{\frac{r_0}{r}\left[1-\xi_0\left(1-\frac{r_0}{r}\right)\right]}\,exp[-\alpha_0 f_0(r-r_0)] \qquad \text{Eq. 3-12}$$

where: A_r = vibration amplitude on free surface of soil at a distance r from dynamic area source center
A_0 = vibration amplitude at exciting source
ξ_0 = coefficient of geometrical attenuation in relation to an area source
r_0 = radius of exciting source
$r_0 = \mu_1\sqrt{F/\pi}$, equivalent radius for rectangular or square area
F = exciting source area
μ_1 = coefficient for dynamic effects
$\mu_1 = 1.0$ for $F < 10$ m^2
$\mu_1 = 0.9$ for $F = 15$ m^2
$\mu_1 = 0.8$ for $F > 20$ m^2
f_0 = exciting frequency of source
α_0 = coefficient of energy attenuation of soil

It is interesting to notice that the attenuation coefficient, α_0, is independent of frequency, however the exciting frequency of the source is inserted in the equation. Values of coefficients of geometrical attenuation, ξ_0, and values of coefficient of energy attenuation, α_0, are presented in Table 3.20 and Table 3.21, respectively. This formula was derived for different vibration sources such as, highway, railway, subway traffic and pile driving. In Figure 3-20, measured vibration amplitudes at different sites are compared with the calculated results by the formula and the evaluation seems good. It should be noted here that the Bornitz formula can be used for the estimation of pile driving ground vibrations, even if Yang disagrees, with the appropriate geometric coefficient, n, depending on the source type and the type of waves that are transmitted through the ground.

Table 3.20 Coefficients of geometrical attenuation, ξ_0 (after Yang 1995)

Soil Group	Radius of exciting source, r_0 (m)							
	≤ 0.5	**1**	**2**	**3**	**4**	**5**	**6**	**≥ 7**
Clayey soil and sands	0.85-0.99	0.70	0.60	0.55	0.45	0.40	0.35	0.15-0.25
Saturated soft soil	0.85-0.99	0.65-0.70	0.50-0.55	0.45-0.50	0.35-0.40	0.30-0.35	0.25-0.30	0.10-0.20
Rocks	0.90-0.99	0.85-0.90	0.80-0.85	0.75-0.80	0.70-0.75	0.65-0.70	0.60-0.65	0.40-0.50

Table 3.21 Coefficient of energy attenuation of soils, α_0 (after Yang 1995)

Soil Group		α_0 ($x10^{-3}$ sec/m)
Rocks (covering layer within 1.5-2.0 m)	Shale, limestone	0.385-0.485
	Sandstone	0.580-0.775
Hard plastic clays		0.385-0.525
Broke stones of medium density cobbles		0.850-1.100
Plastic clays, coarse sands and gravels of medium density		0.965-1.200
Soft plastic clays, silts, slightly dense medium or coarse sands		1.255-1.450
Silty clays, silts and saturated fine sands		1.200-1.300
Recently deposited clays and unsaturated loose sands		1.800-2.050

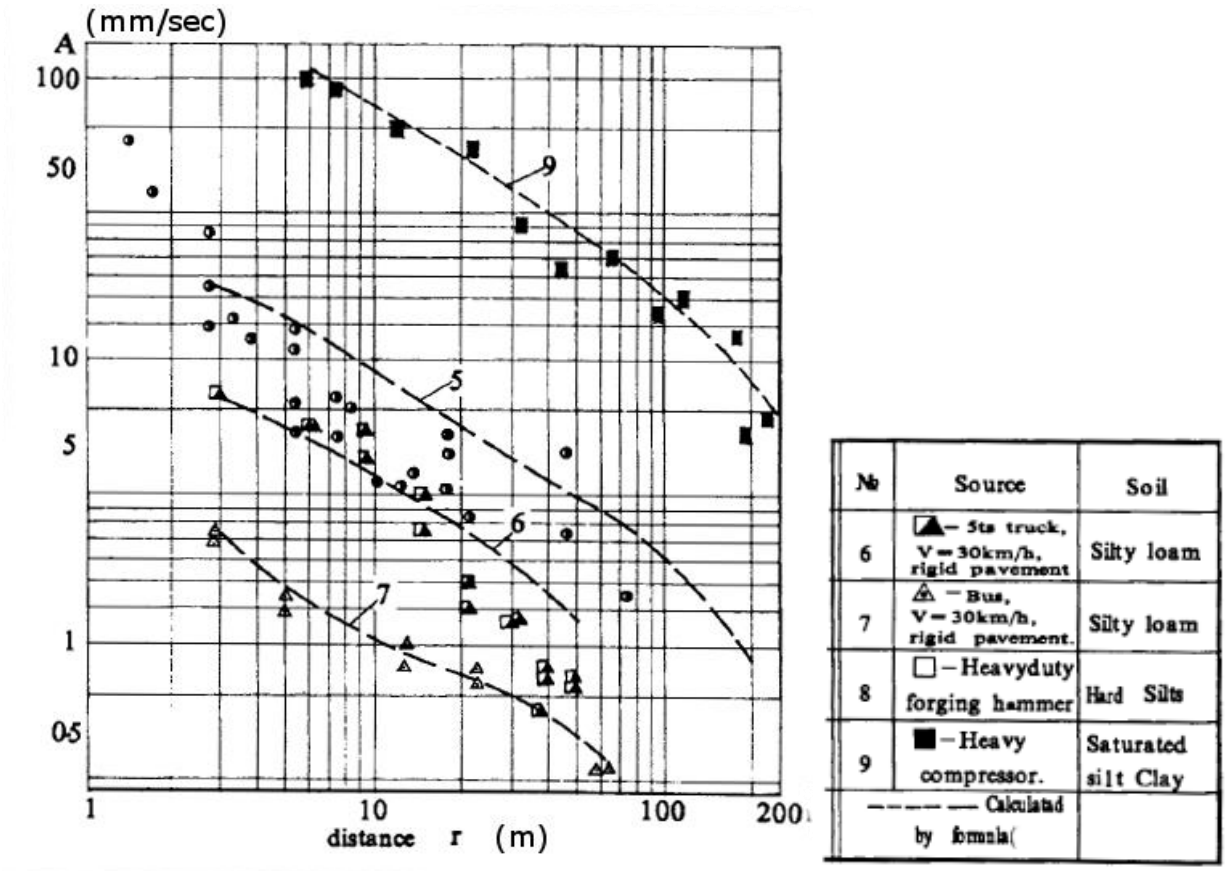

Figure 3-20 Measured vibration amplitudes compared with the Yang formula (after Yang 1985)

Another approach was suggested by **Wiss (1981)** in which a best fit line through a log-log plot determined the rate of attenuation of vibration with distance:

$$v = kD^{-n} \qquad \text{Eq. 3-13}$$

where: v = peak particle velocity of seismic wave
k = value of velocity at one unit of distance
D = distance from vibration source
n = slope or attenuation rate

The attenuation rate, n, is not the same as the material damping coefficient, α, but rather a pseudo-attenuation coefficient that accounts for both geometric and material damping.

Figure 3-21 shows the Bornitz relationship with (Eq. 3-9) and without (Eq. 3-8) the material damping component and the pseudo-attenuation power formula (Eq. 3-13) proposed by Wiss (1981) for measured vibrations in the field (Woods and Jedele 1985). As can be seen in Figure 3-21, the Bornitz equation with n=0.5 is the best fit through the field data. Woods and Jedele (1985) gathered vibration data for a wide range of construction activities which are presented in Figure 3-22 using the power pseudo attenuation formula by Wiss. The attenuation relationship for a detonation of ½ kg (1 lb) dynamite is included for comparison. Dynamic compaction with large energy sources produces the greatest ground motions. Table 3.22 has details for each project from which the data were collected, along with the calculated attenuation coefficient alpha and the pseudo-attenuation coefficient, n. The ranges of the pseudo attenuation factor, n, appear to be independent of soil type, energy level and energy source.

Attewell and Farmer (1973) investigated ground vibrations from pile driving operations with different hammers (impact and vibratory) and soil conditions. The peak particle velocity for metric units was related linearly with the scaled energy, where scaled energy is defined the square root of the rated hammer energy over the distance to the hammer.

$$v = 1.5\left(\frac{\sqrt{E}}{D}\right) \qquad \text{Eq. 3-14}$$

where: v = peak particle velocity in mm/sec
E = energy of source in Joules (rated energy of hammer)
D = distance from vibration source in meters

Attewell and Farmer reached the conclusion that “the influence of the geotechnical character of the ground can be largely ignored”, i.e. the attenuation of the ground vibration amplitude is independent of the soil type. Thus, material damping losses were treated as being insignificant with respect to geometrical losses. The researchers did not clarify if the distance from vibration source to be used in the equation, should be the horizontal distance to the measuring point or the diagonal distance from the pile tip to the point of

interest. It is the horizontal distance that is usually considered as an input for prediction of ground vibrations, even if the vibration source is constantly going deeper in the ground in pile driving.

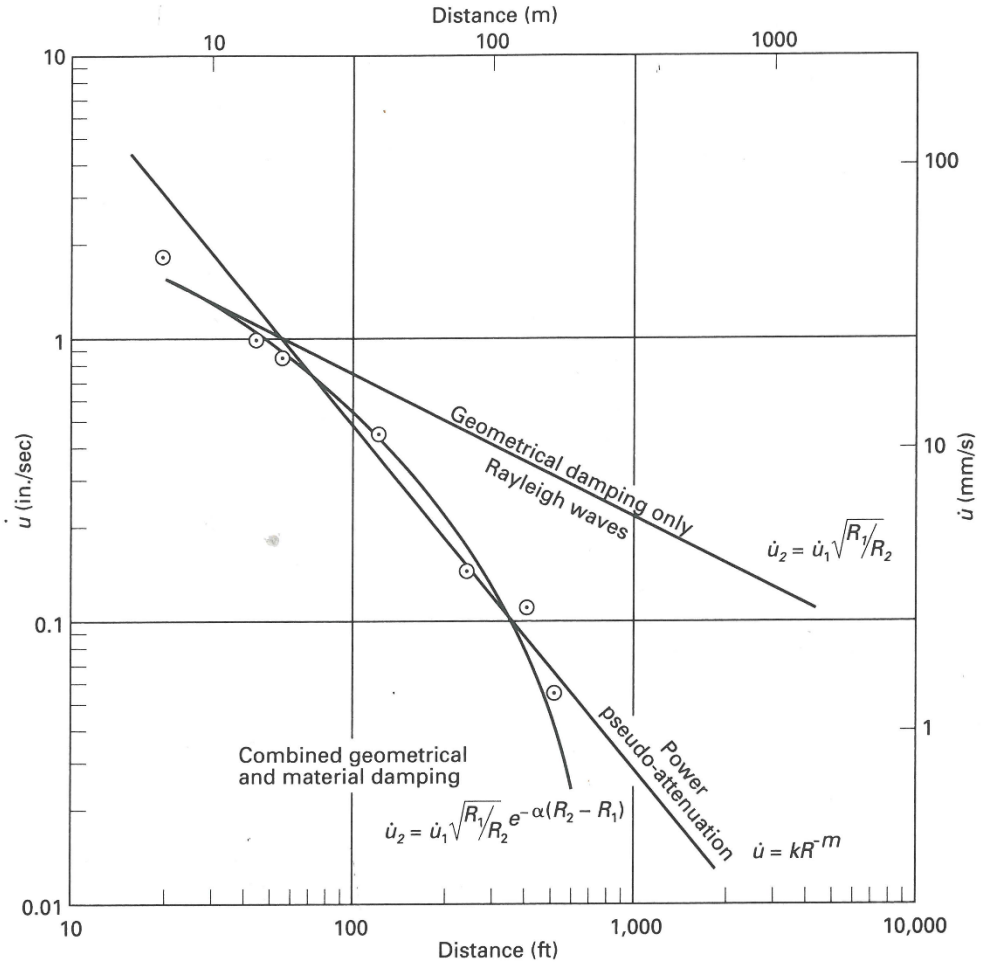

Figure 3-21 Attenuation relationships of ground vibrations (after Woods and Jedele 1985, from Dowding 1996)

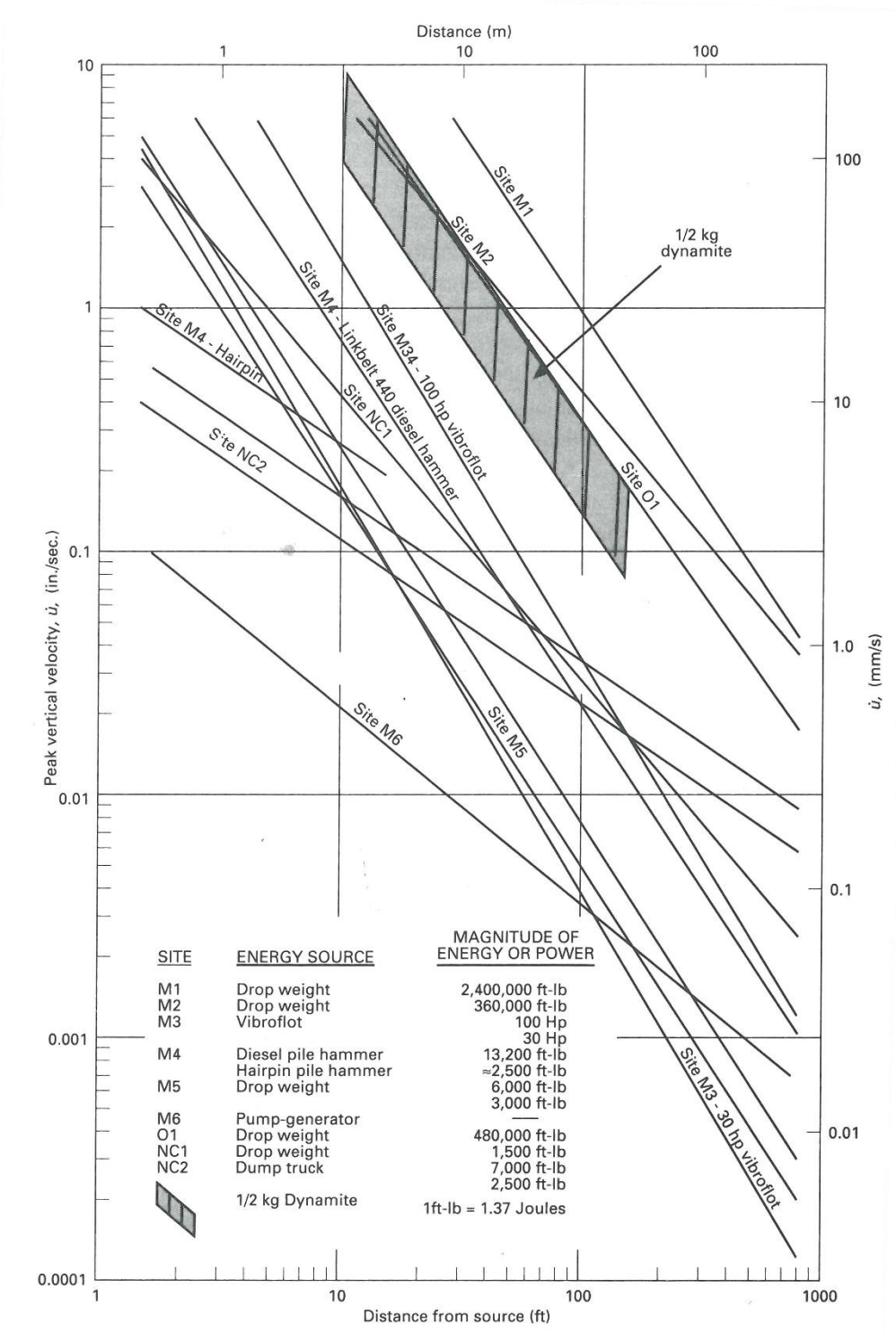

Figure 3-22 Magnitude of construction vibrations for different activities (after Woods and Jedele 1985, from Dowding 1996)

Table 3.22 Construction cases and attenuation coefficients (after Woods and Jedele 1985, from Dowding 1996)

Site	Soil Type	Energy Source/ Description	Energy or Power	Frequency Range (Hz)	Attenuation Factor, α (1/ft)	α Adjusted[a] to $f = 5$ Hz	Pseudoattenuation factor, m
M1	Sand	Drop weight/ 15 tons, 80 ft drop	2,400,000 ft-lb[b]	5–10.5	0.002–0.0025	0.0022	1.445
M2	Clay	Drop weight/ 6 tons, 30 ft drop	360,000 ft-lb	8.5–17	0.0041	0.0016	1.195
M3	Sand	Vibroflot	100 hp	31	0.0101	0.0016	1.65
			30 hp	31			1.65
M4	About 20 ft soil over bedrock	Diesel pile hammer, 700-lb hairpin	18,200 ft-lb 2,500 ft-lb	18–33 40–44	0.0319 0.0356	0.0063 0.0043	1.52 0.698
M5	Clay	Drop weight 13 ft. below G. S./1.5 tons, 1 ft and 2 ft drop	6,000 ft-lb 3,000 ft-lb	12–33 30–48	0.0102	0.0023	1.476
M6	Sand	Pump-generator	—	11–60	0.000707	0.0001	0.778
01	Clay	Drop weight/ 8 tons, 30 ft drop	480,000 ft-lb	9–12	0.0049	0.0023	1.412
NC1	Sand	Drop weight/ 300 lb, 5 ft drop	1,500 ft-lb	20–40	0.0103	0.0017	1.15
NC2	Sand	Dump truck driving over 3-in. high plank	7,000 ft-lb (loaded) 2,500 ft-lb (unloaded)	10–40	0.002	0.0004	0.666

[a] $\alpha_2 = \alpha_1 (f_2/f_1)$.
[b] 1 ft-lb = 1.37 joules

Heckman and Hagerty (1978) investigated eight pile driving cases with pipe piles, H-piles and sheet piles at different sites using different hammers. They used a modified relationship based on the studies of Attewell and Farmer (1973) and Wiss (1967):

$$v = K\left(\frac{\sqrt{E}}{D}\right) \qquad \text{Eq. 3-15}$$

where: K = factor dependent on pile impedance
E = impact energy transferred from hammer to pile
D = distance from vibration source

Heckman and Hagerty commented that the interaction of soil and vibrations produced is difficult to evaluate, however the effect of pile hammer and pile type in transmitting vibrations in the surrounding soil is not. An attenuation coefficient of α=0.03 1/ft (0.009 1/m) was found for all the tested cases. The important outcome of this study is the

influence of the pile impedance on the peak particle velocity. The pile impedance determines the maximum force that can be transmitted by the pile. Figure 3-23 shows the variation of K factor with different pile types for the eight cases tested by the researchers. The range of pile impedances for different pile types is shown on the top of the Figure. There is a very good fit between the pile impedance and the K factor, with increasing ground vibrations when the impedance of the pile is decreasing. The outlier point is from a case that the particle velocity was measured on a rubble fill in which the piles were also driven. This stiff layer had obviously a significant effect in the prediction of the particle velocity, but as mentioned before the researchers did not investigate the influence of soil in this research. However, the Figure implies that for the same site and distance from the pile, a pile impedance reduction (from 2000 to 500 kNs/m) can increase the ground vibrations by about eight times.

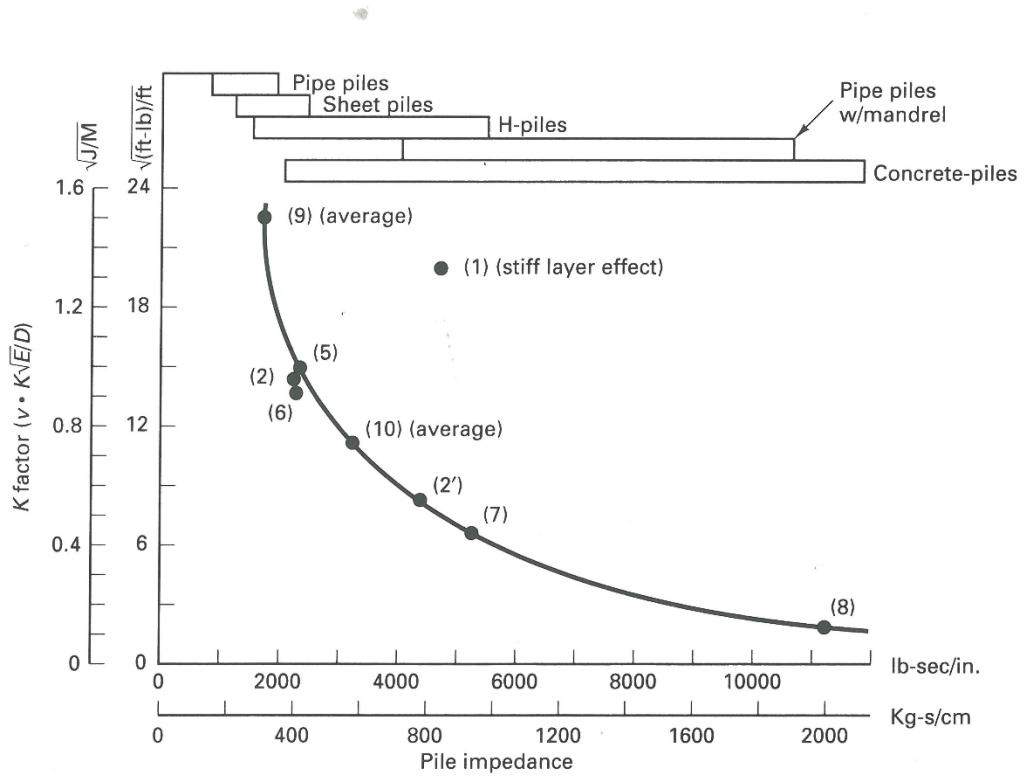

Figure 3-23 Influence of pile impedance on peak particle velocity (from Dowding 1996)

Parola (1970) investigated how matching hammer cushion and pile impedance can maximize the transfer of force to the pile. Specifically, he found that for an optimum pile-hammer combination with respect to maximum energy transmitted to the pile, the pile impedance (ρcA) ranged between 0.6 and 1.1 times the square root of the ram mass and the cushion stiffness

$$\rho cA = (0.6 - 1.1)\sqrt{mk} \qquad \text{Eq. 3-16}$$

where: ρ = density of the pile mass
c = wave propagation velocity
A = cross-sectional area of pile
m = ram mass
k = cushion stiffness

Figure 3-24 shows how a hammer cushion can maximize the energy transmitted to a pile. Long timber and H-piles are considered and are driven with a single-acting Vulcan hammer operating with a hammer efficiency of η=75%. For a specific pile (constant impedance), increasing the hammer cushion stiffness, by selecting aluminum-micarta instead of pine plywood, produces a much higher force than increasing the size of the hammer (Vulcan 1 to 010).

Analyzing the data from Heckman and Hagerty (1978) and modifying their equation yields a linear relationship between the inverse of pile impedance and the k factor (Massarsch and Fellenius 2015). The K-factor is a linear function of the inverse of the pile impedance. The prediction of ground vibration from pile driving then can be written as:

$$v = K\left(\frac{\sqrt{\eta W_0}}{D}\right) \qquad \text{Eq. 3-17}$$

where: v = vertical component of vibration velocity (m/sec)
η = hammer efficiency factor
W_0 = rated energy of hammer (N-m)
$D = \sqrt{(x^2+z^2)}$ (m)
x = horizontal distance from observation point to pile at ground surface (m)

z = pile penetration depth (m)
$K = 440/Z_P$ ($m^2/(sec\sqrt{Nm})$)
Z_P = pile impedance (N-sec/m)

This equation takes into account the actual distance, D, from the pile source (pile toe) which is constantly changing as the pile penetrates the ground. In addition, the energy used in this equation is the transferred energy to the pile and not the rated energy of the hammer. Figure 3-25 shows the K-factor as a function of the inverse of the pile impedance. It should be noted that this scaled distance expression of vibration velocity, would give good predictions if most of the waves are emanating as spherical waves from the pile tip.

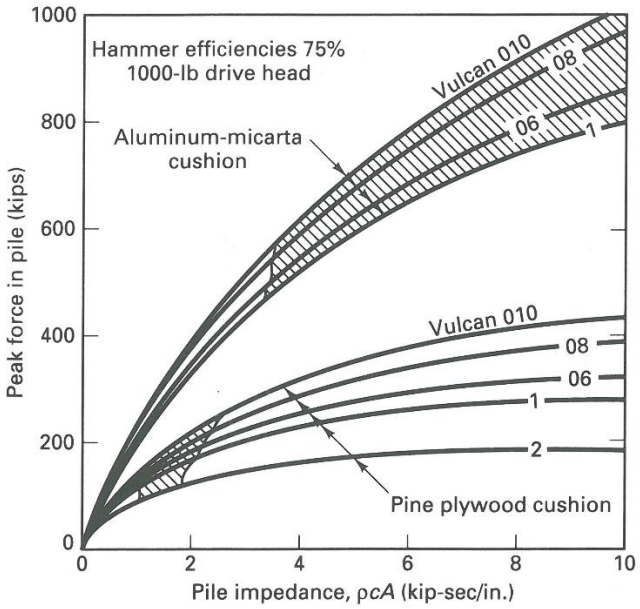

Figure 3-24 Transmitted force to pile with changing stiffness of cushion (from Dowding 1996)

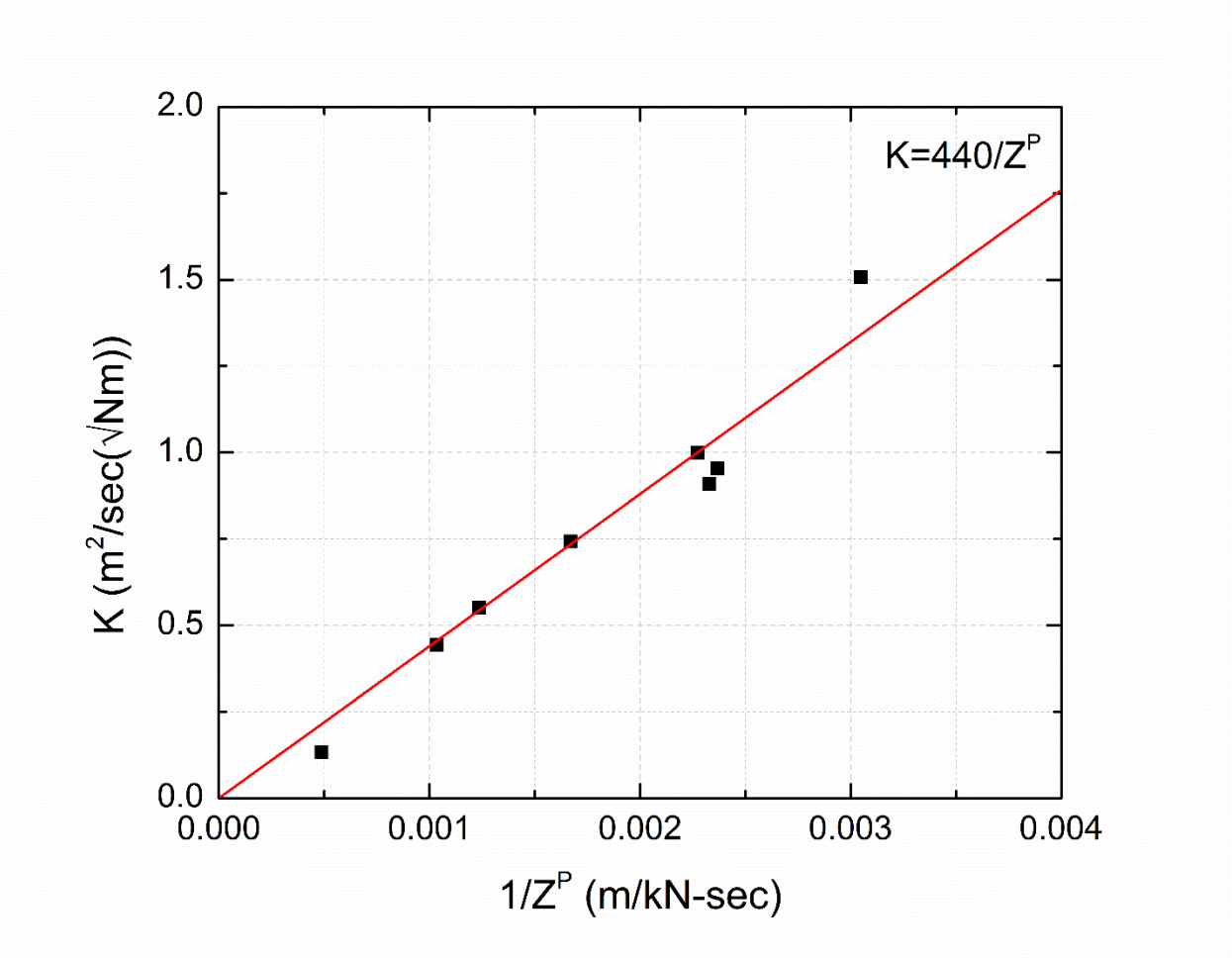

Figure 3-25 Relationship of K-factor and inverse of pile impedance (modified after Heckman and Hagerty 1978)

Wiss (1981) suggested a scaled-distance propagation equation to predict the peak particle velocity in terms of energy and distance:

$$v = k\left(\frac{\sqrt{E}}{D}\right)^{n} \qquad \text{Eq. 3-18}$$

where: k = value of velocity at D/√E=1
E = energy of source
√E/D = scaled distance
n = slope or attenuation rate

The square root scaling is commonly used in the blasting industry, where the charge is distributed in a long cylinder (Dowding 1996). Wiss adopted this theory to pile driving and other activities and developed square root attenuation plots. The value of the attenuation rate, n, is generally between one and two with a common value of n=1.5. Woods and Jedele (1985) calculated n values for collected data of construction operations in the field. Table 3.23 presents the n values from Woods (2016). **Jedele (2005)** presented additional ground motion attenuation data from various vibration sources and calculated alpha and pseudo attenuation coefficients for each case. An upper bound solution was provided combining the data of this and Woods and Jedele (1985) research, so as an estimate of the peak particle velocity at a site for a given energy and distance from the source can be made:

$$v = 0.137\left(\frac{\sqrt{E}}{D}\right)^{1.27} \qquad \text{Eq. 3-19}$$

where: D = distance from source (ft)
E = energy of source (ft-lb)
$\sqrt{E}/D$ = scaled distance ((ft-lb)$^{0.5}$/ft)

Figure 3-26 summarizes the compilation of the data. Jedele concluded that this solution is a first evaluation to assess if an activity will create potential problems, but site-specific ground motion data is recommended, especially for critical procedures.

Table 3.23 Attenuation rates, n, based on soil classes (after Woods 2016)

Class	Slope or attenuation rate, n	Description of material (N = SPT Blow Count)
I	1.4	*Weak or soft soils* (shovel penetrates easily): lossy soils, dry or partially saturated peat and muck, mud, loose beach sand and dune sand, recently plowed ground, soft spongy forest or jungle floor, organic soils, topsoil. (**N<5**)
II	1.3	*Competent soils* (can dig with shovel): most sands, sandy clays, gravel, silts, weathered rock. (**5<N<15**)
III	1.1	*Hard soils* (cannot dig with shovel, need pick to break up): dense compacted sand, dry consolidated clay, consolidated glacial till, some exposed rock. (**15<N<50**)
IV	1	*Hard competent rock* (difficult to break with hammer): bedrock, freshly exposed hard rock. (**N>50**)

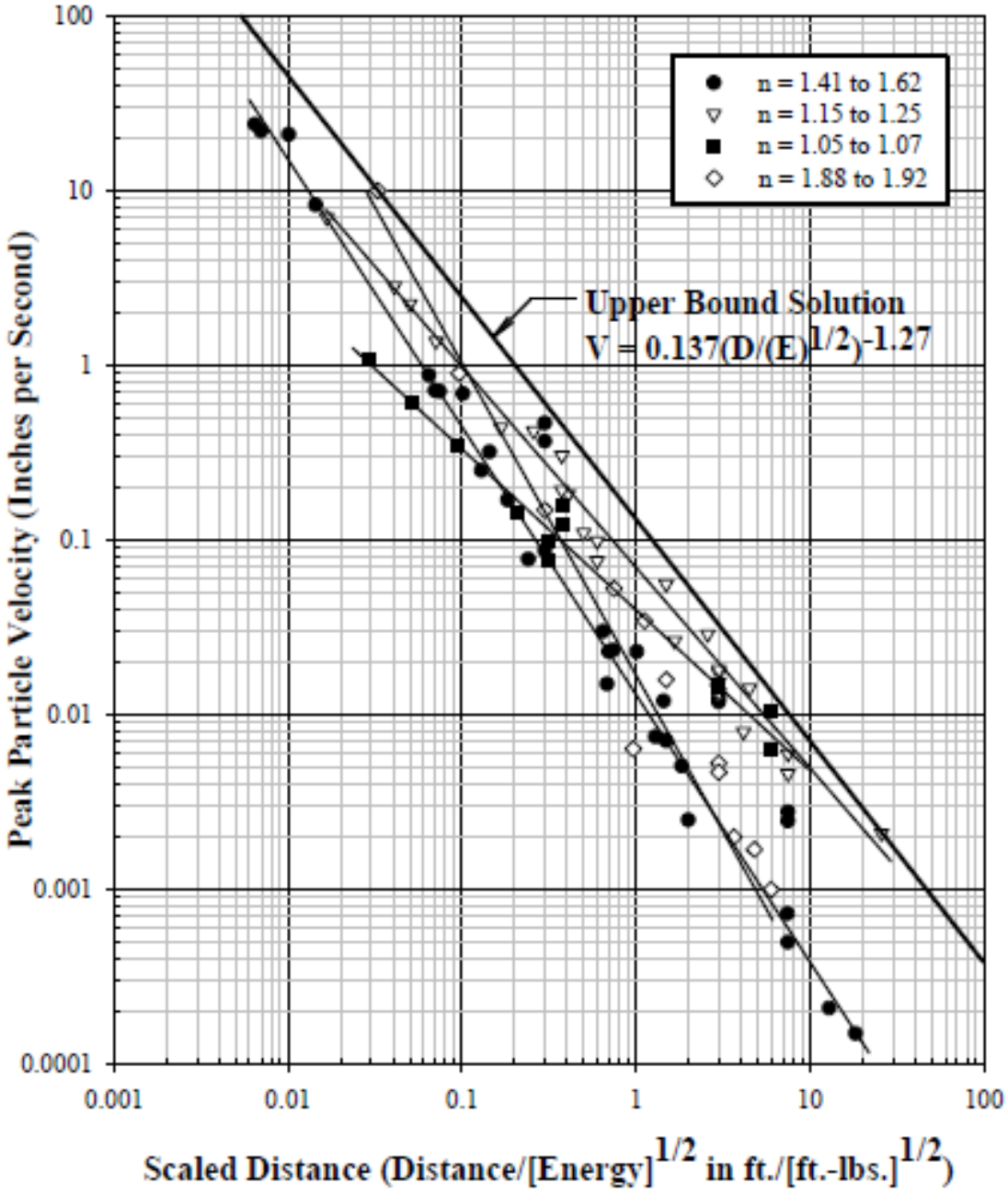

Figure 3-26 Accumulated ground motion attenuation data (from Jedele 2005)

Svinkin (1992) used the scaled-distance formula by Wiss and adapted the results from Woods and Jedele (1985) to calculate peak ground velocity during pile driving activities. Figure 3-27 depicts the peak vertical ground velocity versus scaled distance from steel, timber and concrete driven piles. The slope was kept at n=1, which is the upper limit for the rate attenuation. Extreme values of 4.6, 2.4 and 0.9 m/sec are marked on the left side of the lines. An equation that uses the scaled distance between pile and ground velocities was suggested by Svinkin:

$$v_g = v_p \frac{\sqrt{W_t}}{D} \qquad \text{Eq. 3-20}$$

where: v_p = peak particle velocity at the pile head
v_g = peak particle velocity of ground
W_t = transferred energy to the pile
D = distance from source

Values of the peak particle velocity at the pile head, v_p, can be determined by an equation also proposed by Svinkin (1996b):

$$v_p = \sqrt{2 \frac{c}{ZL} W_t} \qquad \text{Eq. 3-21}$$

where: c = wave propagation velocity in pile
Z = EA/c = pile impedance
E = elastic modulus of pile material
A = pile cross-sectional area
L = pile length
W_t = transferred energy to the pile

According to Svinkin, Figure 3-27 provides an opportunity to construct curves of the expected maximum peak ground velocity for various distances from pile driving sources and different magnitudes of the transferred energy. This new development of the scaled distance approach eliminates the need to know in advance the k factor and increases the accuracy of calculated ground velocity before pile installation.

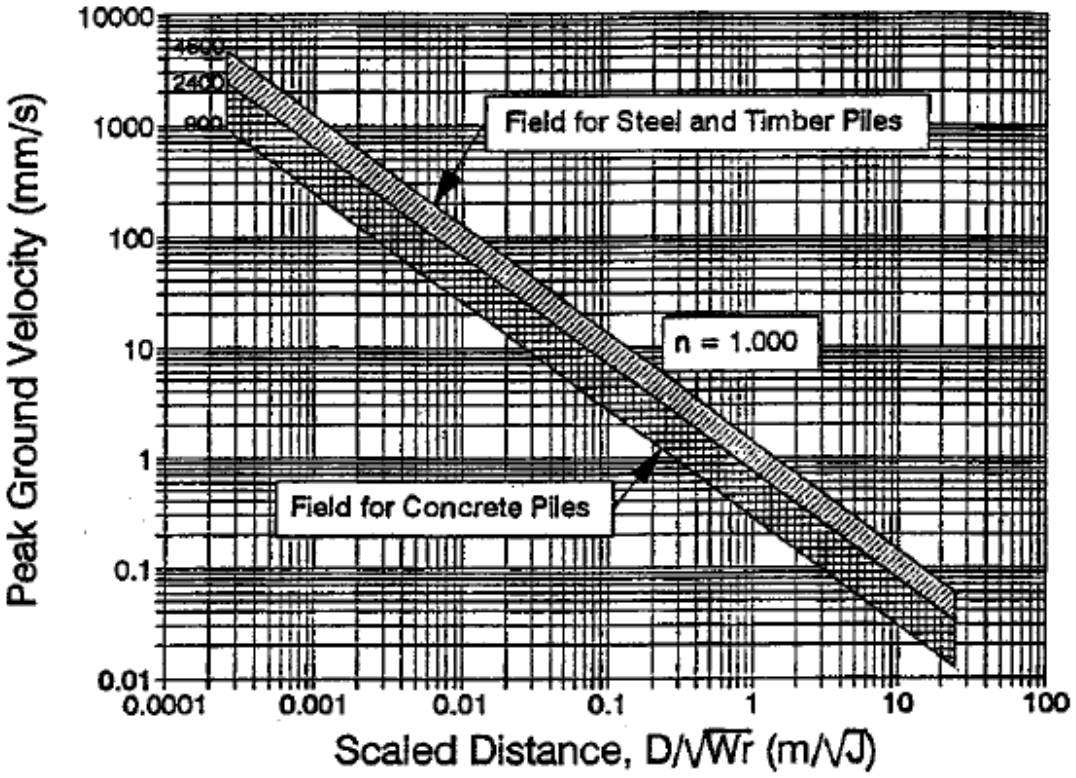

Figure 3-27 Peak vertical ground velocity versus scaled distance for pile driving (from Svinkin 1999)

Attewell et al. (1992a, 1992b) revisited vibration data from Attewell and Farmer (1973) along with new vibration data from impact and vibratory pile driving. They investigated best fit lines separately for impact hammers and vibratory hammers and suggested that a quadratic regression curve rather than the linear regression curve proposed in 1973 provides a better fit to the data sets for which they had access. A statistical analysis of the data was performed in order to get the mean (best fit), one half standard deviation line and one standard deviation line. That is because with the least squares line there is a 50% probability of the measured vibration exceeding the predicted one. However, the actual vibration has a 31% chance of exceeding the predicted vibration above a one half standard deviation line and only 16% chance of exceeding the predicted

vibration above a one standard deviation line. They recommended that the one half standard deviation quadratic lines can serve as vibration limit lines.

Impact hammers

$$\log v = -0.296 + 1.38 \log\left(\frac{\sqrt{W}}{r}\right) - 0.234 \log\left(\frac{\sqrt{W}}{r}\right)^2 \qquad \text{Eq. 3-22}$$

Vibratory hammers

$$\log v = -0.213 + 1.64 \log\left(\frac{\sqrt{W}}{r}\right) - 0.334 \log\left(\frac{\sqrt{W}}{r}\right)^2 \qquad \text{Eq. 3-23}$$

where: v = peak particle velocity in mm/sec
W = energy of source in Joules (rated energy of hammer)
r = horizontal distance from vibration source in meters

Attewell et al. recognized that most of the vibration energy emanates from the toe of the pile which means that the distance from between the tip and the measurement point should be specified for the above equations. However, the horizontal standoff distance is assigned for practical convenience. In Figure 3-28 and Figure 3-29 a family of curves for the prediction of particle velocities at distances up to 20 m is presented for the best fit and the one half standard deviation line, respectively.

Hendriks (2002) suggested a vibration decay relationship for pile driving operations:

$$v = v_0 \left(\frac{D_0}{D}\right)^k \qquad \text{Eq. 3-24}$$

where: v = particle velocity at distance D
v_0 = particle velocity at reference distance D_0
k = dimensionless soil parameter

This equation takes into account the significant proportion of the body waves and has a frequency independent coefficient, k. According to Hendriks, the assumption of a frequency independence material damping coefficient is acceptable because damage levels in terms of velocity in the frequency range of 1–80 Hz tend to be independent of frequency. The same applies for complaint levels within a range of 8–80 Hz. Typical vibration from transportation and construction sources typically falls in the range of 10–30 Hz and usually centers around 15 Hz. However, this method is not applicable in vibration-sensitive research facilities, where the frequency domain has a significant role in the assessment of the impact of vibration. Values of the k coefficient lie between 1 to 1.5; for sandy soils k is close to 1 while the k factor of clayey soils approaches 1.5. Clay soils are more resistant to advancing piles and generate higher vibration levels near the source than sandy soils. Vibrations tend to drop-off more rapidly with distance though in clay soils than those in sandy soils.

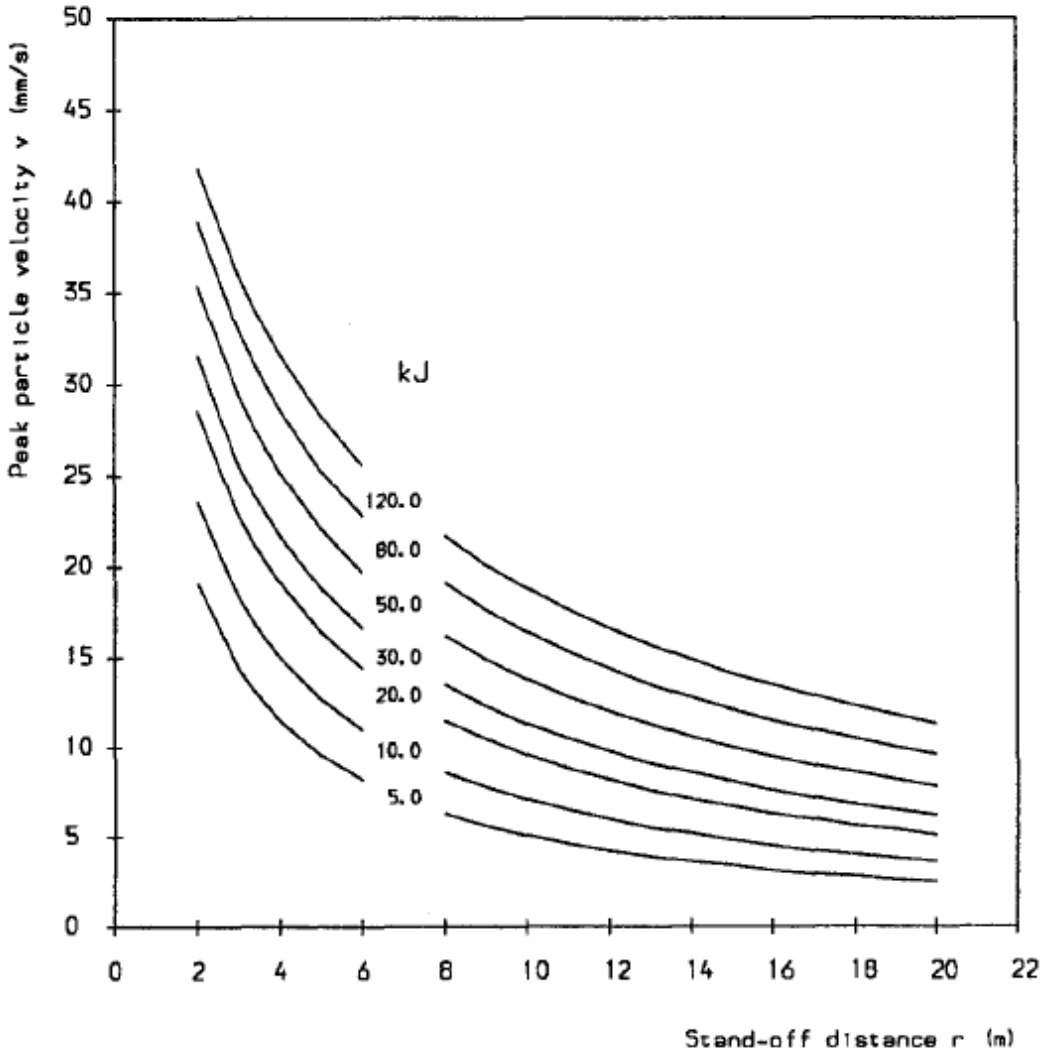

Figure 3-28 Best fit line for prediction of particle velocities with distance for impact hammers (from Attewell et al. 1992b)

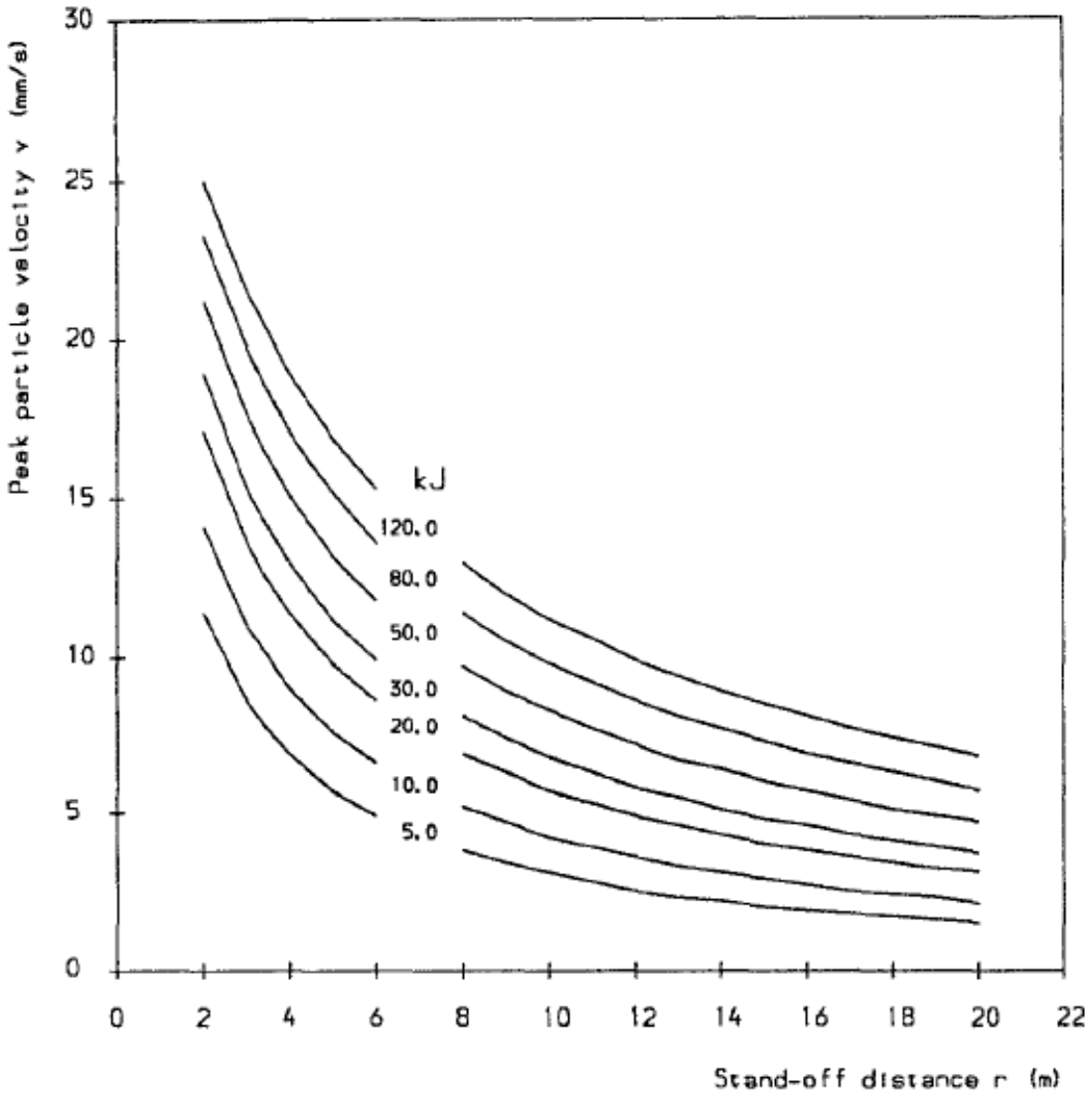

Figure 3-29 One half standard deviation line for prediction of particle velocities with distance for impact hammers (from Attewell et al. 1992b)

3.3 Reported Cases of Recorded Ground Motion Data

Ground borne vibrations generated by adjacent construction activity can be potentially damaging to nearby structures and sensitive equipment, as well as annoying to people. Vibration measurements are commonly recorded on the ground surface at different radial distances from the dynamic source without considering the propagation path. There are only a few studies that have presented data with measurements in-depth and in the close vicinity of pile driving operations. There is a need to better understand the mechanism of energy dissipation through the soil close to impact driven piles. Pile installation is a complex procedure with the dynamic source constantly changing location, going deeper in the ground as the pile penetrates the soil. Site-specific prediction techniques have been published in the literature, with vibration usually quantified in terms of the peak particle velocity. A review of cases where peak particle velocities were measured during pile installation is discussed in this Section.

Brenner and Viranuvut (1977) collected information, available at the time of their writing, of monitored ground motions during pile driving operations. In Figure 3-30 peak particle velocity versus the scaled distance is plotted from different researchers. Other than data from Peter (1953) and Dalmatov et al. (1967) that represent the resultant velocity of the three components, the other values are for the vertical component of the particle velocity. The upper regression line by Brenner and Chittikuladilok (1975) falls below almost all the values. This is attributed by the authors to the soil conditions in Bangkok which consist of a marine clay, designated as Bangkok clay. Some error exists though beacause the format of the particle velocities is different. The authors conducted measurements, while driving 0.35 m square precast concrete piles with a drop hammer on two sites in the Bangkok area, on the ground surface and on an adjacent building. The results were compared with those by Brenner and Chittikuladilok (1975) and were found to be similar, so the upper limit of total vibration in the Bangkok area proposed in 1975 was found to be sufficient:

$$v = 0.3\left(\frac{\sqrt{E}}{D}\right) \qquad \text{Eq. 3-25}$$

where: v = peak particle velocity in mm/sec
E = energy delivered by the hammer in Joules (rated energy of hammer)
D = horizontal distance from vibration source in meters

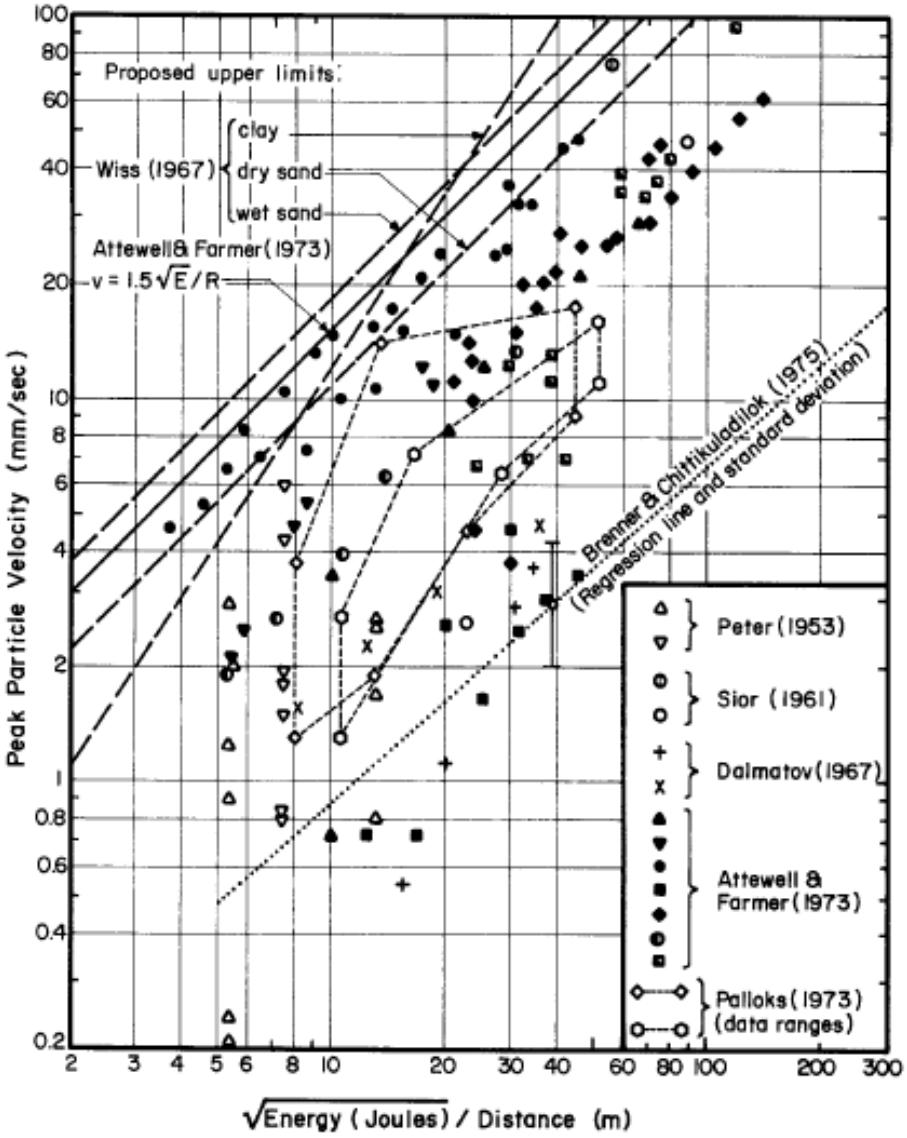

Figure 3-30 Measured of peak particle velocity versus scaled energy from various researchers (from Brenner and Viranuvut 1977)

Clough and Chameau (1980) measured vertical and horizontal ground vibrations during vibratory sheet pile driving. The soil profile consisted of deep soft bay mud and medium dense sands overlain by loose rubble sand fills. The piles were driven with an ICE 812 vibratory hammer operating at a frequency of 18 Hz. The recorded peak ground accelerations were in the range of 0.15g to 0.50g for hard driving when obstacles were encountered and around 0.10g to 0.30g for normal driving. Vertical accelerations attenuated rapidly with distance from the pile, with the phenomenon being more pronounced for soft soils rather than dense soils (hard driving), apparently due to their greater damping capacity. Peak vertical accelerations versus distance from pile at different test sites of the project are shown in Figure 3-31. It can be seen that hard driving led to ground accelerations twice as high as those that occurred during normal driving. The writers analyzed their data using the Bornitz equation, which they called it Barkan equation, to obtain alpha coefficients for Rayleigh waves. Figure 3-32 presents an example of their data fitting to the Bornitz equation. They found alpha coefficients varying from 0.008 1/ft to 0.06 1/ft and they concluded that there is little difference in α values for horizontal and vertical vibrations. Based on their findings structures at distances more than 80 ft from vibratory pile driving operations should not suffer structural damage, however residents in this case complained about high levels of noise and vibration.

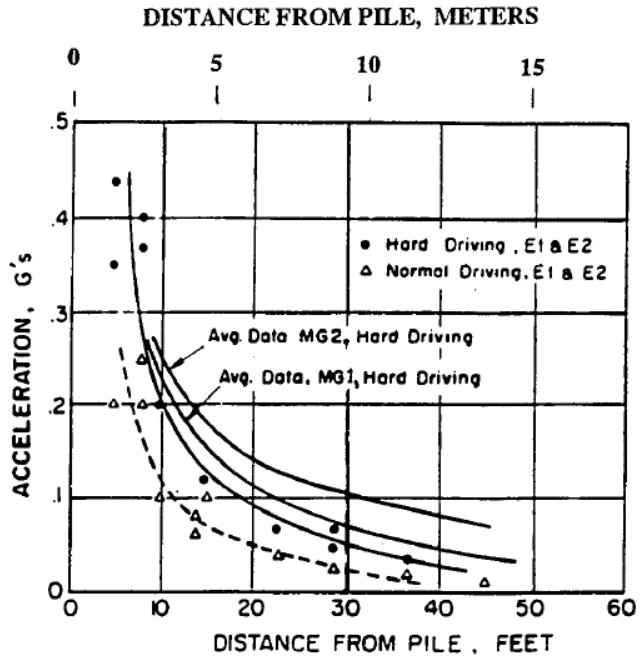

Figure 3-31 Peak vertical accelerations during sheet pile driving (from Clough and Chameau 1980)

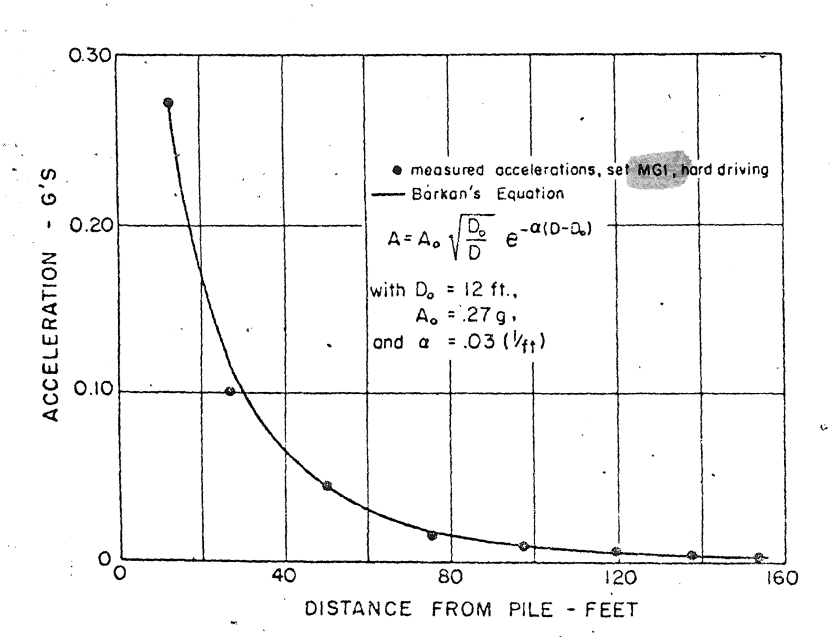

Figure 3-32 Measured accelerations fitted to Bornitz (or Barkan) equation (from Clough and Chameau 1980)

Mayne (1985) reported ground vibration data from dynamic compaction of granular materials. Dynamic compaction induces low frequency waves which can be more damaging than high frequency vibrations. Frequencies for dynamic compaction are usually in the range of 2 to 20 Hz. Low frequency vibrations are associated with loose soils, since such soils have a low shear modulus, and larger drop weights. With the available measured data, Mayne indicated that the drop height is slightly more influential to the particle velocity than the drop weight. Finally, the author provided an interesting correlation between the normalized vibration level (particle velocity divided by the impact velocity of the falling weight) and distance from the source normalized to the weight radius (d/r_0). The corresponding plot of the particle velocity attenuation, presented in Figure 3-33, showed a close approximation.

Selby (1991) reported a field test of driving H-piles near brick corner walls. Strain gages were placed on the walls and a line array of geophones was placed on the surface. A schematic of the test is shown in Figure 3-34 . A drop hammer and a vibrodriver were used while the pile was extracted and redriven closer to the walls up to 0.5 m. Ground vibrations of up to 70 mm/sec and transient strains of up to 100×10^{-6} were recorded on the walls , however the walls withstood and no damage was observed. Figure 3-35 shows a linear relation between the peak radial components of vibration and the maximum strains on the wall. Walls A and B were of standard half brick construction, wall C was of half brick construction with damp proof course (dpc) and some open joints and wall D was full brick thickness. The vibratory driver caused the least severe relation of strain per 1 mm/sec.

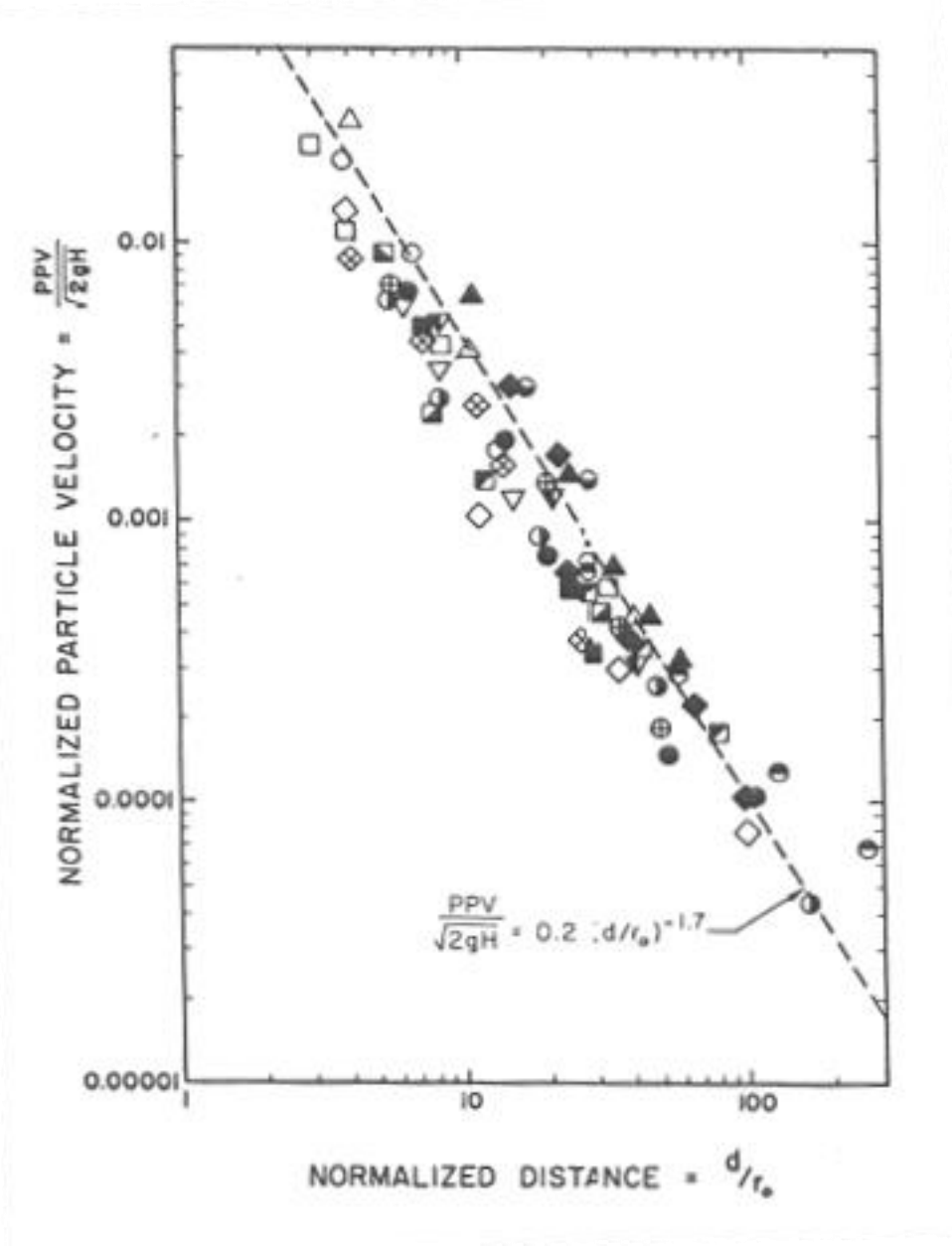

Figure 3-33 Normalized particle velocity versus normalized distance (from Mayne 1985)

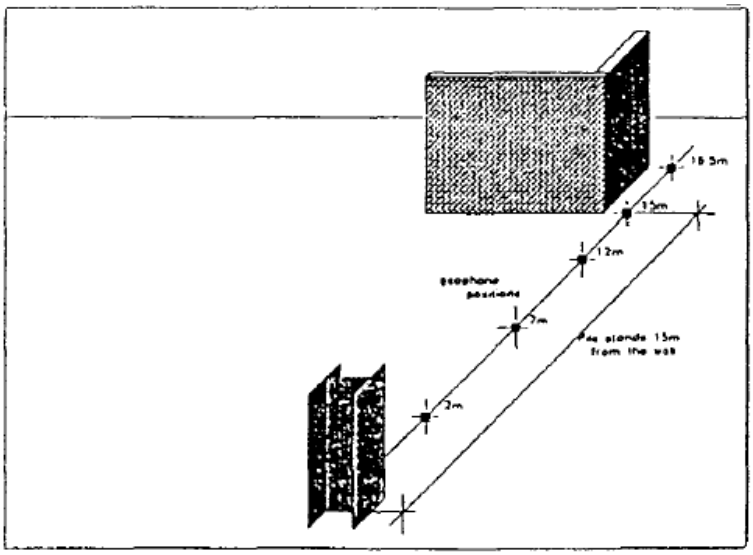

Figure 3-34 Schematic view of pile driving near brick corner wall (from Selby 1991)

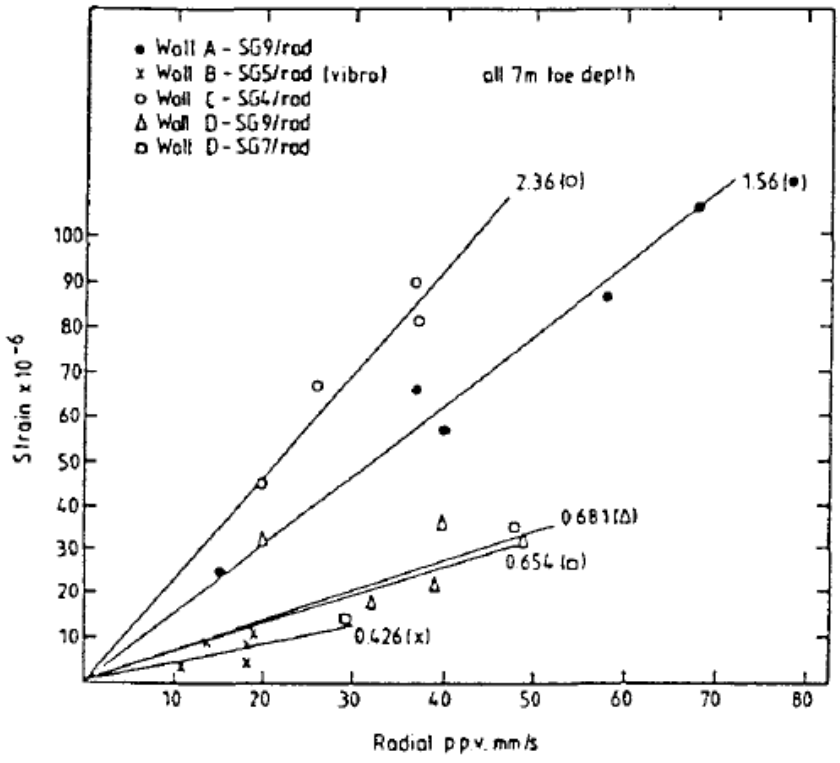

Figure 3-35 Relationship between radial ground vibrations and maximum strains on the wall (from Selby 1991)

Linehan et al. (1992) reported a project where potential vibration would become problematic when driving sheet pile cofferdam walls and H sections adjacent to a pressurized natural gas pipeline (the closest pile was driven 2 ft away from the pipeline). Soil boring data revealed loose sands and soft silt river deposits within 20 ft of the surface. A vibratory hammer with a rating of 333 ft-lb and driving frequencies in the range from 7 Hz to 27 Hz was used to install the sheet piles. It became apparent that the vibration amplitudes increased significantly during the startup and turnoff of the vibrator, since at these frequencies the hammer was operating at a frequency close to the natural frequency of the pipeline or the soil profile. Velocity transducers were mounted on the pipeline and in the ground. Vibration response of both the pipeline and the soil resulted in less restriction of construction activity than anticipated. Also, as can be seen in Figure 3-36 and Figure 3-37, surface soil motions were substantially greater than those measured on the pipeline, for both the vibratory and impact driving.

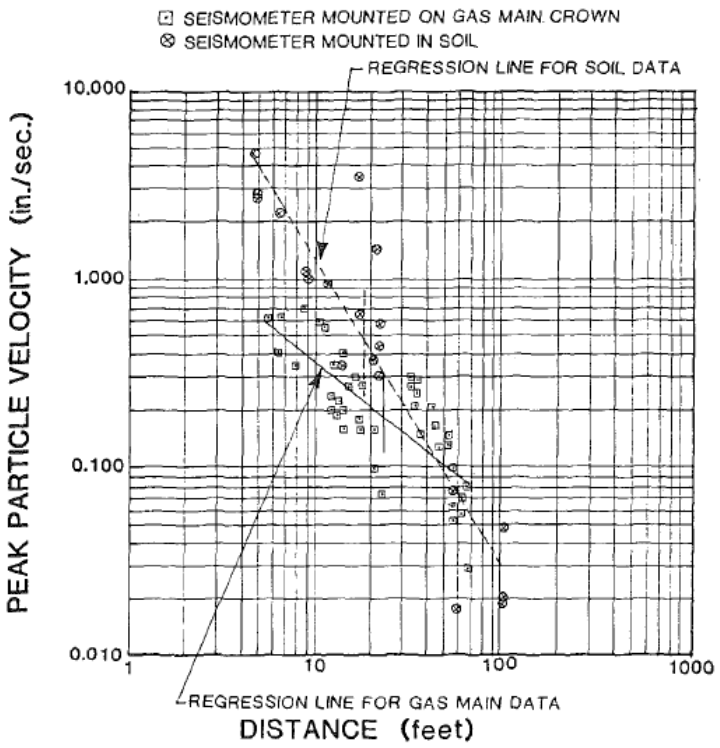

Figure 3-36 Attenuation relationships for vibratory hammer sheet pile driving (from Linehan et al. 1992)

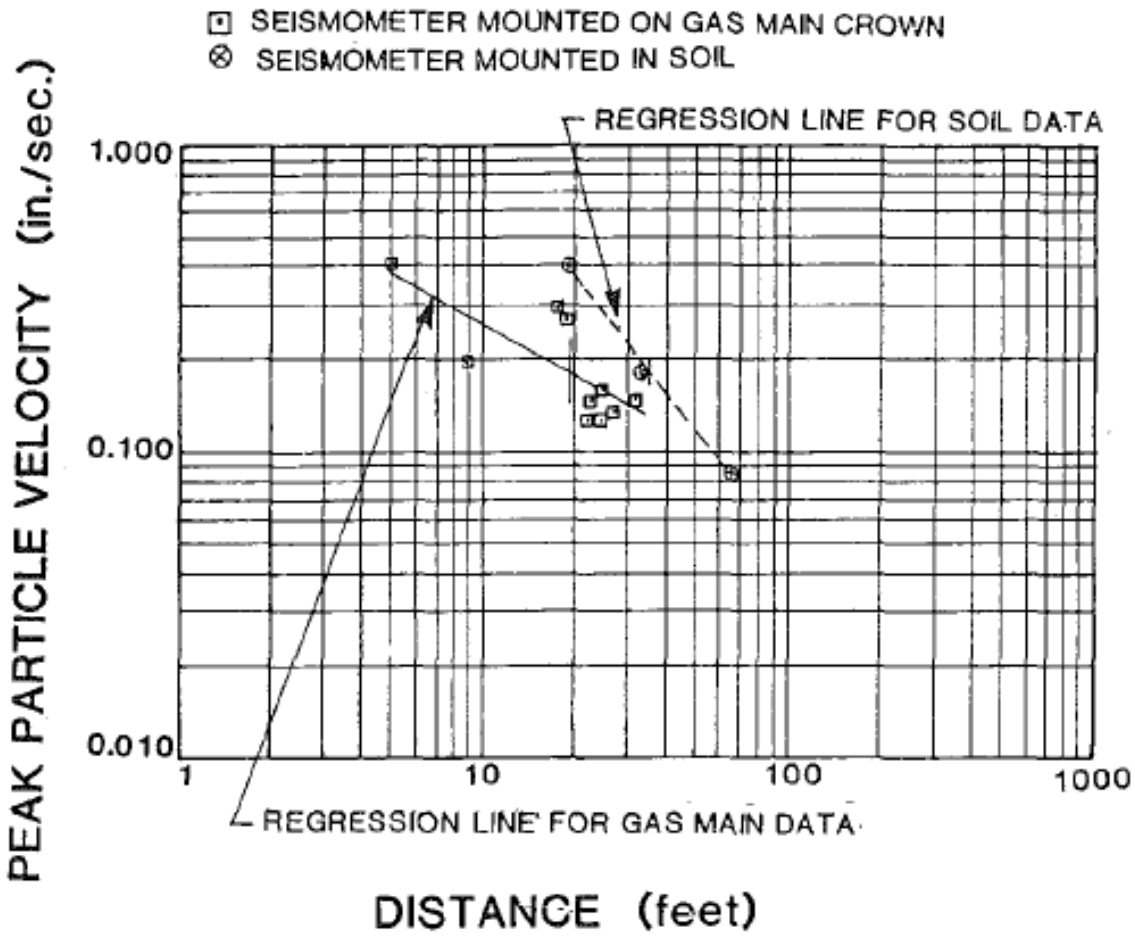

Figure 3-37 Attenuation relationships for impact hammer H-pile driving (from Linehan et al. 1992)

Lewis and Davie (1993) collected pile driving vibration data for 14 years. The authors used the scaled distance equation by Wiss (1981) to fit their data (Eq. 3-13). It should be noted that the resultant peak particle velocity was computed. Also, the hammer transferred energy rather the rated hammer energy was implemented. For the tested cases an average transferred energy of 10,000 ft-lb was calculated and assuming n=1, they found the intercept of k=0.1 (English units). The correlation was found good in order to predict the peak particle velocity. Measured data and the empirical equation are shown in Figure 3-38. In Figure 3-39 the results from settlement monitoring for site 1 are

presented. Precast, pre-stressed concrete piles with diameters of 14 in and length of 80 ft were driven with an ICE 640 closed-ended diesel hammer with rated energy of 40,000 ft-lb. The soil conditions consisted of loose to dense sands and silty sands with shell. Movements ranged from 0.5 in of heave to around 3 in of settlement (negative axis). At distances beyond one length of the pile, no movement occurred. This is supported also by earlier findings (Dowding 1991), however the authors recognize that when a big number of piles are to be driven in a site, cumulative settlement can be significant.

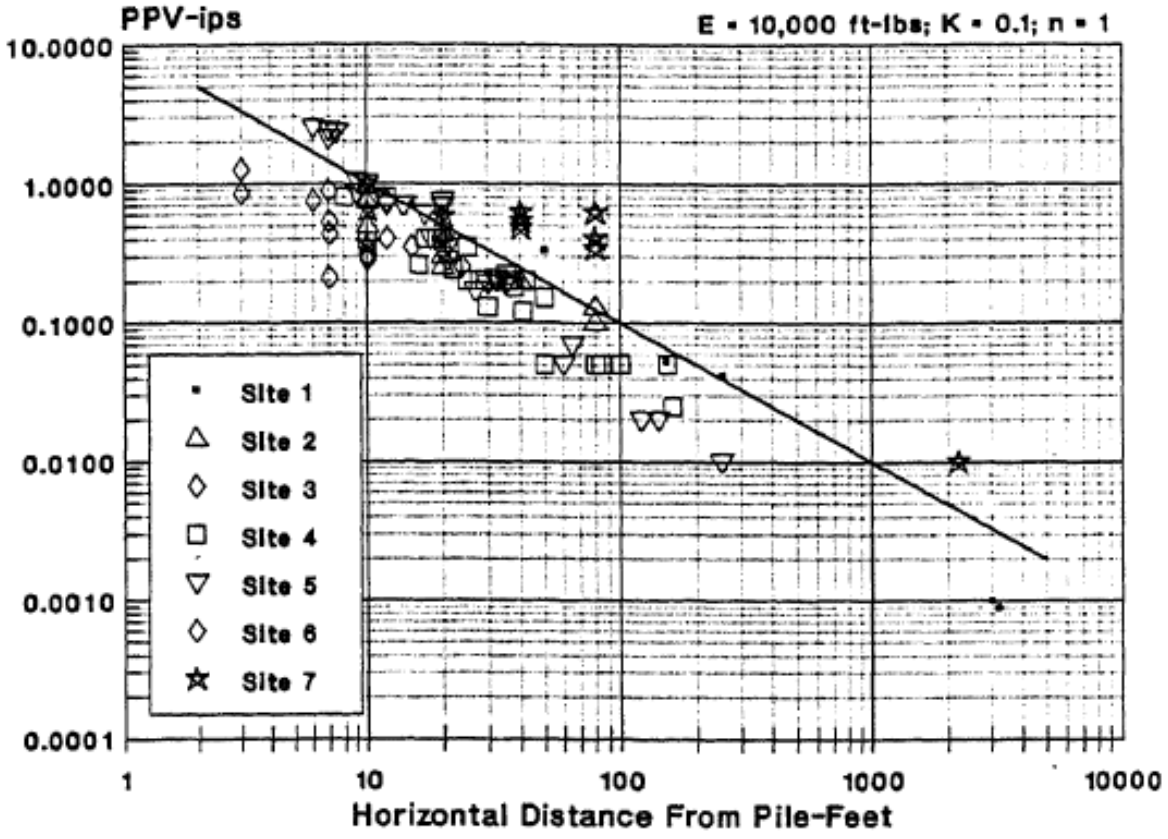

Figure 3-38 Particle velocity versus horizontal distance from pile (from Lewis and Davie 1993)

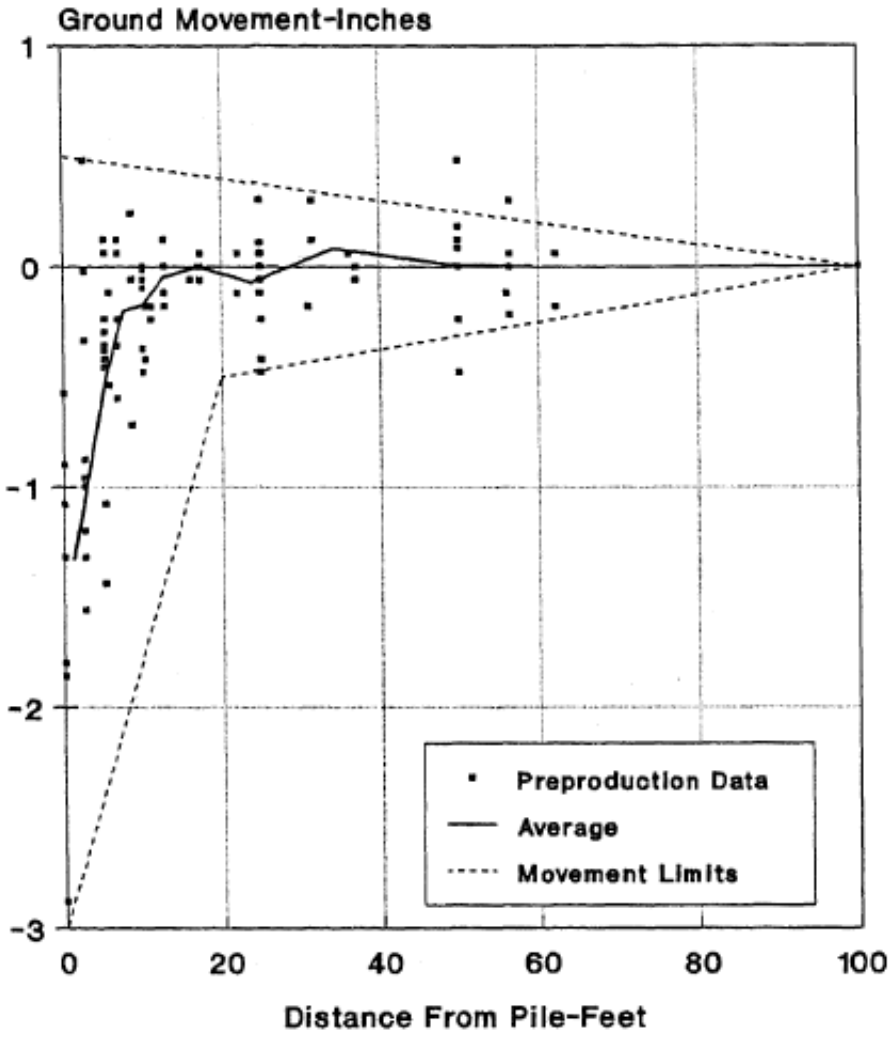

Figure 3-39 Ground movement versus distance from pile (from Lewis and Davie 1993)

Moore et al. (1995) presented measurements of small scale tests using a 50 kg steel ball drop weight and drop heights between 1 and 2 m. The weight was dropped either on a plate simulating impact from surface source or on a post driven into the ground, simulating impact from embedded source. A timber post of 0.82 m length and a steel post 0.62 m long were driven into sand and a clay soils. The simulation of the embedded source might not be very accurate though, with the short lengths selected for the posts. Figure 3-40 presents measured peak particle velocities and the regression lines for the

embedded source for both the sand and clay sites. The data are widely scattered and the regression lines are close to the upper limit lines of the existing empirical equations at the time. The authors recognized that the principal frequencies decreased with increasing distance from the source (Figure 3-41). Their proposed scaled distance relationships for wave attenuation of body and Rayleigh waves, predicted peak particle velocities considerably greater than those observed.

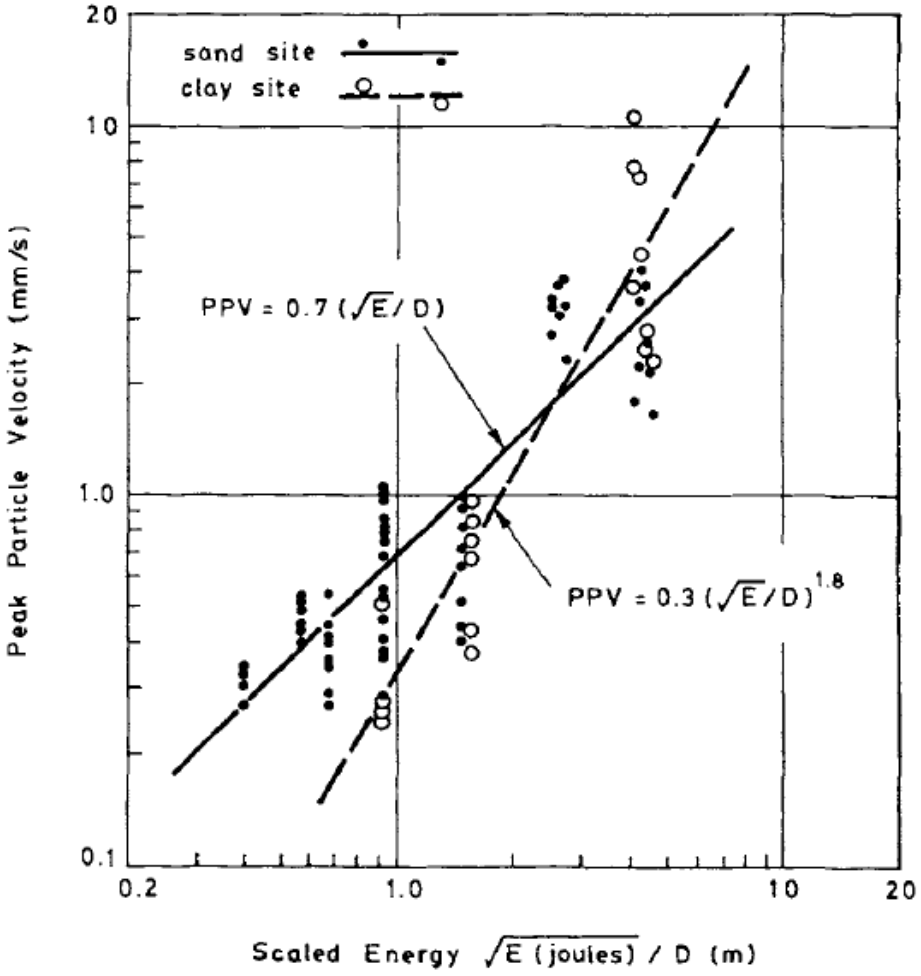

Figure 3-40 Ground motions-impact from an embedded source (from Moore et al. 1995)

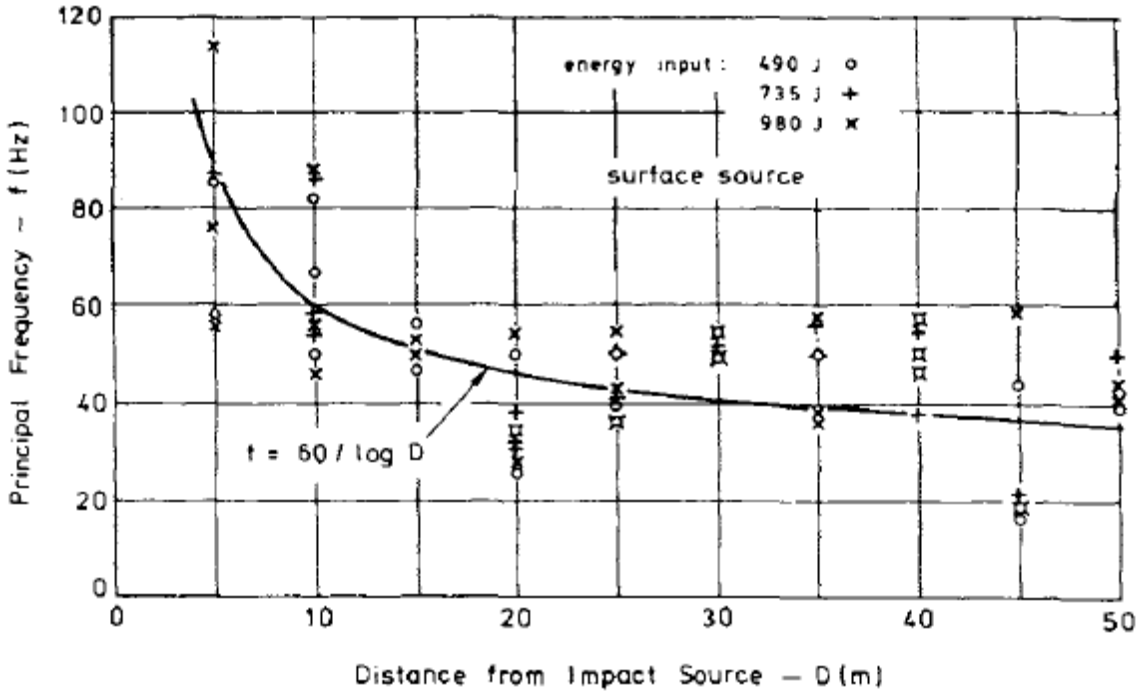

Figure 3-41 Observed principal frequencies at sand site (from Moore et al. 1995)

Kelley et al. (1998) reported vibration measurements at the ground level and on floor levels of two historic buildings adjacent to tunnel construction activities. Trenching of slurry wall panels within 12 ft of the building perimeter and vibratory installation of sheet piles within 25 ft of the building perimeter were monitored. The maximum recorded vibration levels were below the vibration criteria for historic buildings (0.2 in/sec). The important finding of this study is that the magnitude of the vertical velocity at an elevated floor can be amplified by a factor of two compared to the basement record. This is important for the prediction of occupant discomfort on elevated floors of buildings during construction vibrations.

Kim and Lee (1998) and **Kim and Lee (2000)** measured ground vibrations caused by train loading, blasting, friction pile driving and hydraulic hammer compaction, in an attempt to characterize the propagating waves and determine their attenuation characteristics. Triaxial geophones were on the ground surface as well as in-depth in

order to analyze the particle motions in the three directions and understand which types of waves emanate from each source and how they attenuate. The train induced vibration was found to be a mixture of surface and body waves, and the speed and length of train seemed to affect the vibration amplitudes and the rate of attenuation. The in-depth blasting vibration was transmitted predominantly as body waves attenuating on a spherical wave front. Friction pile driving developed a dominant vertical shear wave expanding around a conical wave front. The hydraulic hammer compaction transfers energy into the ground mainly by surface waves. The geometric damping coefficients from this study are summarized in Table 3.24 and are comparable with those suggested by Gutowski and Dym (1976).

Table 3.24 Geometric damping coefficients for various sources (after Kim and Lee 2000)

Physical Source	Source Type	Wave	Source Location	n
Short length and high speed train	Combination of point and infinite line	Body	Surface	1.5
Long length and high speed train	Line	Body	Surface	1.0
In depth blasting and friction pile driving	Point	Body	In depth	1.0
Hydraulic compaction	Point	Surface	Surface	0.5

Athanasopoulos and Pelekis (2000) collected ground motion amplitudes at different sites during vibratory sheet pile driving on pavements and sidewalks close to the source, as well as on the ground floor and higher floors of adjacent buildings. The hammers had rated energy ranging from 1000 to 3000 Nm and the soil conditions consisted of mixed

layers of gravels, sands, silts and clays in the upper 8 m and low plasticity clay below that depth. The braced sheet pile walls reached a penetration depth of 10 m below the ground surface. Many interesting conclusions can be drawn from this work. Figure 3-42 presents particle displacement paths during driving sheets 2.40 m from the source. Clearly the vertical component of the motion is greater than the horizontal component resulting in an elliptical shape like Rayleigh wave motion. The same trend was found at a greater distance from the source indicating that sheet pile driving generates mainly Rayleigh waves. Regression analysis of the measured data provided a linear log-log best fit and upper bound line described by:

Best-fit

$$v = 32D^{-1.5} \qquad \text{Eq. 3-26}$$

Upper bound

$$v = 80D^{-1.5} \qquad \text{Eq. 3-27}$$

where: v = peak particle velocity in mm/sec
D = distance from source in m

The above equations have the same form of Eq. 3-13 suggested by Wiss (1981) with a slope of n=1.5 which is also in agreement with the value proposed by Woods (2016) for similar soils (Table 3.23).

The authors estimated an attenuation coefficient α=0.091 m^{-1} (Athanasopoulos and Pelekis 1998). The alpha value for an average frequency of 20 Hz for the sites tested was close to the range proposed by Woods (2016) for similar soils (0.018 to 0.054 m^{-1}). Figure 3-43 shows the best-fit and upper bound attenuation lines derived from this study compared to other published empirical relationships for sheet pile driving. It is obvious that all relationships follow the same attenuation rate (n=1.5).

It is important to mention that a three-floor concrete frame building experienced architectural cracking of the brick walls while settlement and cracking of a sidewalk

adjacent to this building was also observed. The vibration amplitude for this case was 20 mm/sec which is the threshold limit for the USBM criterion. Soil densification and the excavation operations probably contributed to this damage but it is another indication that vibratory settlement of loose soils cannot be captured by the limiting values to levels the standards suggest. The amplification of vibrations at the higher floors of adjacent buildings is depicted in Figure 3-44. The vertical axis is the normalized peak particle velocity defined as the velocity measured on the ground floor of the buildings divided by the velocity measured at upper floors. It may be seen that the vibration amplitudes were amplified at the higher floors with an increasing amplification ratio (with an exception of one site). Plots like this are a tool for the assessment of the human perception during construction operations.

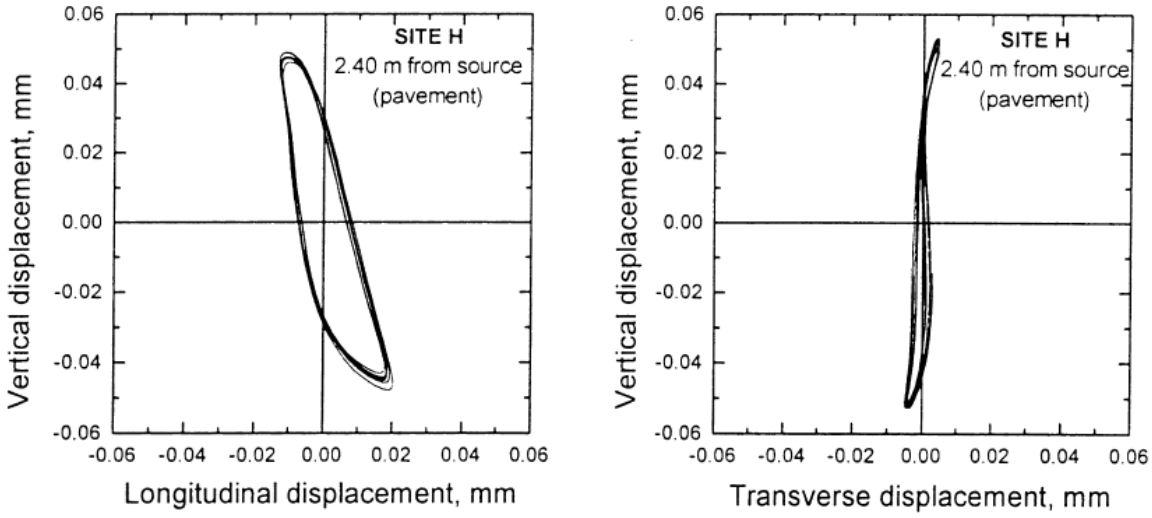

Figure 3-42 Particle displacement paths during pile driving 2.40 m from the source (from Athanasopoulos and Pelekis 2000)

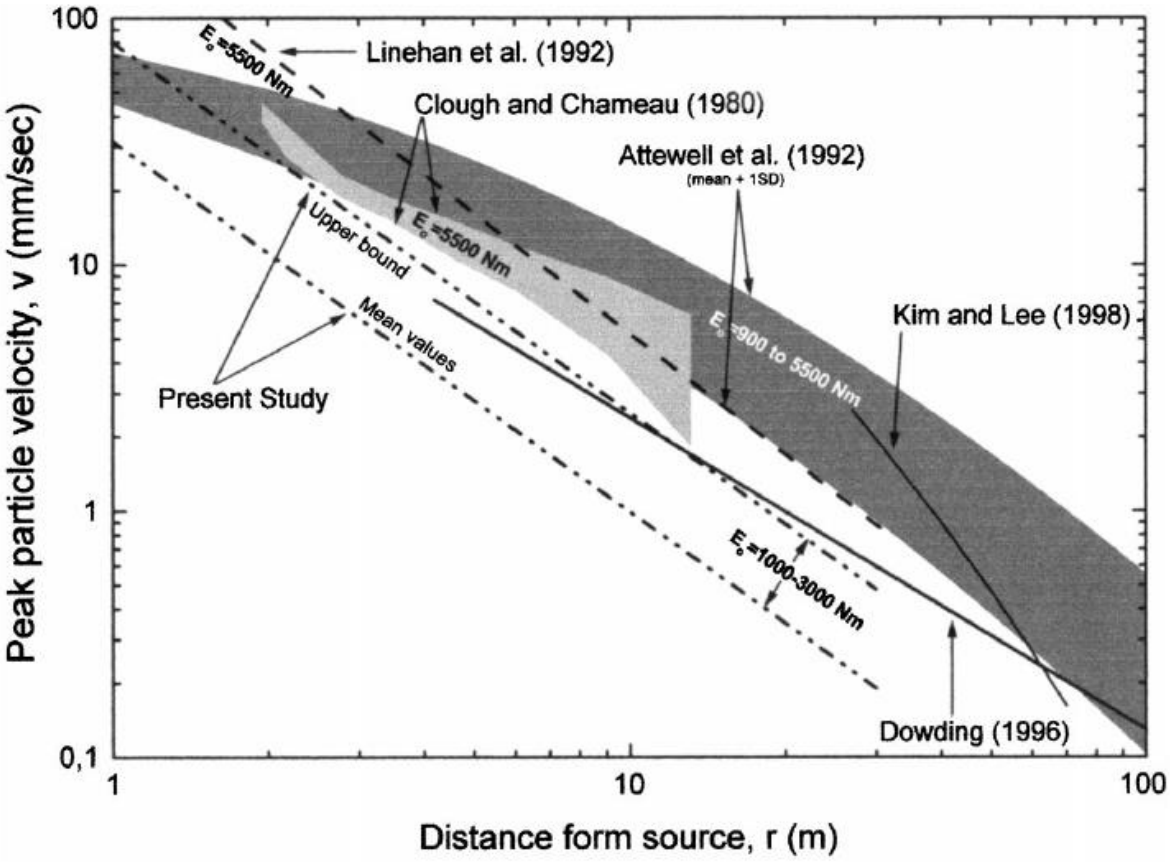

Figure 3-43 Attenuation of vibrations with distance from various studies (from Athanasopoulos and Pelekis 2000)

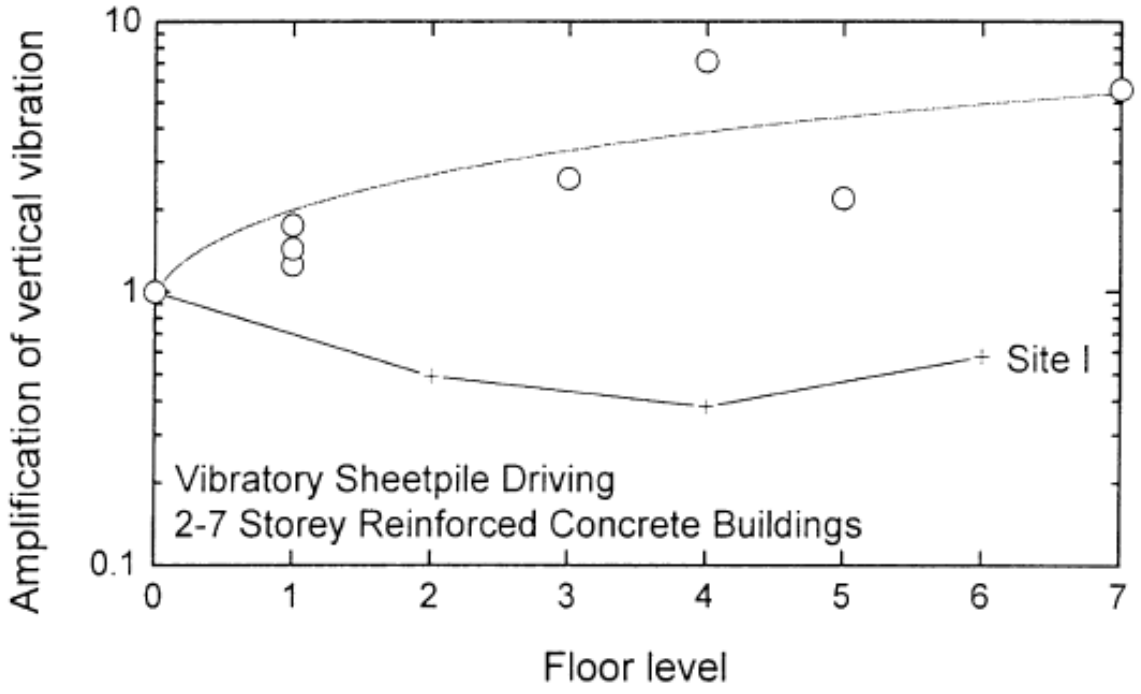

Figure 3-44 Amplification of vertical particle velocity at the elevated floors during vibratory sheet pile driving (from Athanasopoulos and Pelekis 2000)

Hajduk et al. (2000) investigated the soil motion mechanism during impact pile driving of a 32.4 cm diameter, 31.4 long closed ended steel pipe end-bearing pile. The pile was installed with a Delmag D30-32 single ended diesel hammer. The pile was instrumented with accelerometers and strain gages at the top, middle and tip. The Pile Driving Analyzer was used to record measurements. The test was performed at a bridge reconstruction site in the Boston area. The soil consisted of soft clay to a depth of 19 m and was underlain by a fine, medium dense sand from 26 m to bedrock at 30.5 m. Figure 3-45 shows the maximum middle (1-8-APCB-A) and tip (1-16-APCB-A) pile accelerations normalized to the maximum pile top accelerations with depth. The mean ratio between pile middle and pile top was found 0.85, while the mean ratio between the pile tip and pile top was 0.58. Unfortunately, the accelerometer mounted at the pile tip was destroyed when the pile tip was at a depth of 18.9 m. Also, the data acquisition system stopped

recording between depths 20.42 and 23.48 m, so a conclusive idea of the pile response could not be derived. However, the normalized accelerations suggest that there is a consistent drop between the values of the maximum pile top, middle and tip.

Three triaxial accelerometers were installed within the silty sand layer (19.3-21.6 m) Figure 3-46 depicts maximum and minimum vertical, horizontal and tangential velocities versus position of pile tip relative to sensors GA1 and GA2. GA1 was installed at depth 19.5 m and horizontal distance 1.4 m from the pile and GA2 at depth 19.34 m and horizontal distance 2.3 m from the pile. It can be seen that the peak velocities are maximized when the pile tip passes close to the installated depth of the sensors. The authors observed that when the pile tip is above the sensor elevation, the downward (negative) velocities are larger, while when the pile tip passes the accelerometer elevation, the upward (positive) velocities become larger.

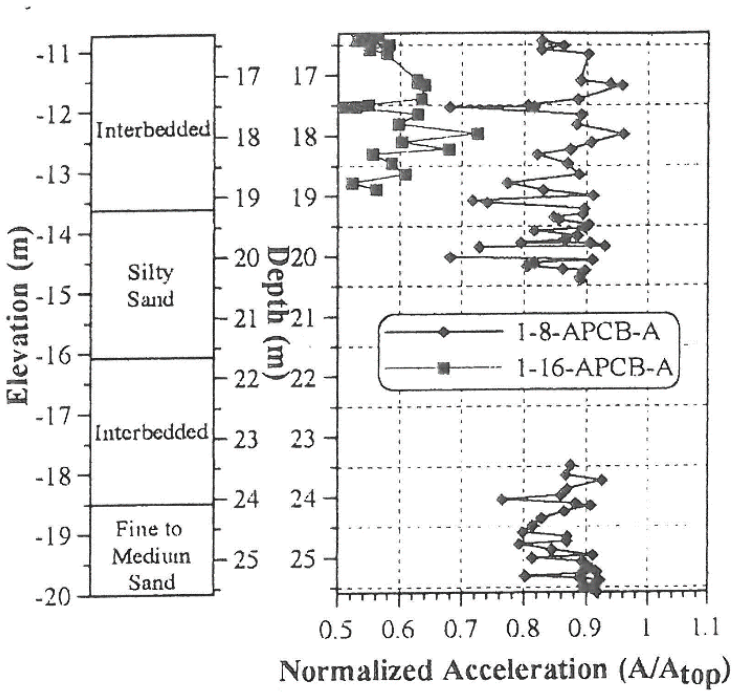

Figure 3-45 Normalized maximum acceleration measurements with depth (from Hajduk et al. 2000)

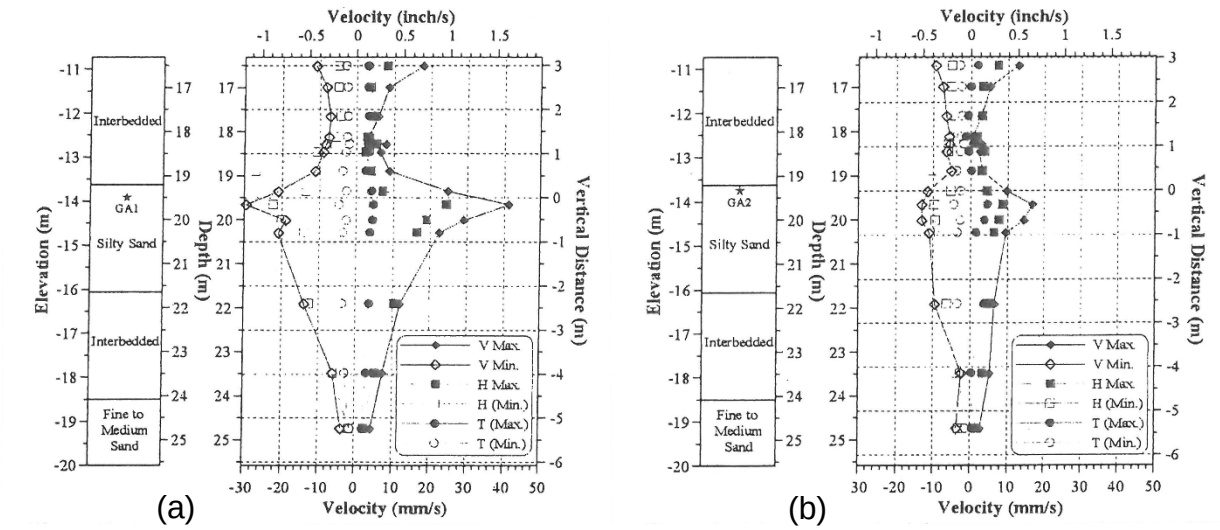

Figure 3-46 Maximum and minimum measured velocities with depth for (a) GA1 and (b) GA2 accelerometers (from Hajduk et al. 2000)

Hwang et al. (2001) presented a very well documented case of soil responses during driving of three precast concrete piles (DP1, DP2, DP3) with piezometers, inclinometers, level posts and velocity sensors installed. The diameter of the hollow closed-ended piles was 0.8 m and they were driven in two segments of 17 m each. A Delmag D100 diesel hammer was used. Standard Penetration tests, Cone and Seismic Cone Penetration tests and Dilatometer tests were conducted prior to pile driving and installation of instruments, revealing a soil profile consisting successively of sand and clay layers to a depth of 40 m (Figure 3-47). The piezometers were placed in the loose sand at 6 m depth and at a depth of 9 m in the soft clay. Surface horizontal and vertical velocity sensors were fixed at various distances from the piles. Locations of the driven piles and all the instrumentation is presented in Figure 3-48. It was found that the buildup of excess pore pressure is closely related to the penetration depth of the pile. The pore water pressure of soil (either sand or clay) began to rise when the pile tip was 4d to 7d above the piezometer location and reached the maximum value when the pile tip passed 4d below the piezometer; d being the pile diameter. After 3.5 min, static water pressure conditions were reached for the sand layer. However, it took 18 hours for the dissipation of the excess pore water

pressure of the clay layer. Figure 3-49 shows the maximum excess pore water pressure normalized to the in situ effective overburden stress versus the normalized distance, r/a, r being the distance to the pile center and a the pile radius. It is clear that the excess pore water pressure in the clayey layer is greater (3.5 times the overburden) than that in the sand layer (1.5 times the overburden), with the latter reaching liquefaction conditions. The phenomenon decreased rapidly with increasing distance, being negligible at r/a greater than 30. This study is in good agreement with other published results, also plotted in Figure 3-49. Lateral displacement of the ground caused by pile driving decreased with increasing distance from the pile. The maximum horizontal displacement occurred in the sandy layer, at depth 3.5 m, with a value of 29 mm. Lateral displacement became insignificant when r/a was greater than 24. Maximum heave of the ground surface of 36 mm was recorded at a distance 1.5d from the pile center. DP1 pile was installed first and experienced a total uplift of 13.7 mm after DP2 and DP3 piles were driven.

The ground vibrations caused by pile driving were primarily of high frequency. The response spectra of ground vibrations showed that pile driving induces short period responses with periods less than 0.5 sec. Signal analysis indicated that each driving blow contained a wave trace of high frequency (body waves), followed by a wave trace of lower frequency (surface waves). For all three horizontal accelerations recorded, the peak ground acceleration of surface waves exceeded that of body waves. Figure 3-50 presents the attenuation of peak ground acceleration as a function of distance from the driven DP1 pile in the sand layer (15 and 20 m penetration depth) and the clay layer (25 and 30 m penetration depth). The PGA values were plotted separately for total, body and surface waves. The results indicate that the decaying of PGA did not show any trend with the penetration depth but decreased rapidly with increasing distance from the pile. Body waves attenuate faster than surface waves in the horizontal direction.

In conclusion, the writers found a good correlation between the driving resistance and the geological profile. A similar trend was demonstrated after comparing the SPT profile, the cone resistance values, q_c, from the CPT test, the blow counts for each meter of penetration and the load cell readings installed at the tip of DP3 pile. All the above are

shown in Figure 3-47. Thus, the SPT and CPT values could be used for this specific site to estimate the blow counts required for the pile installation.

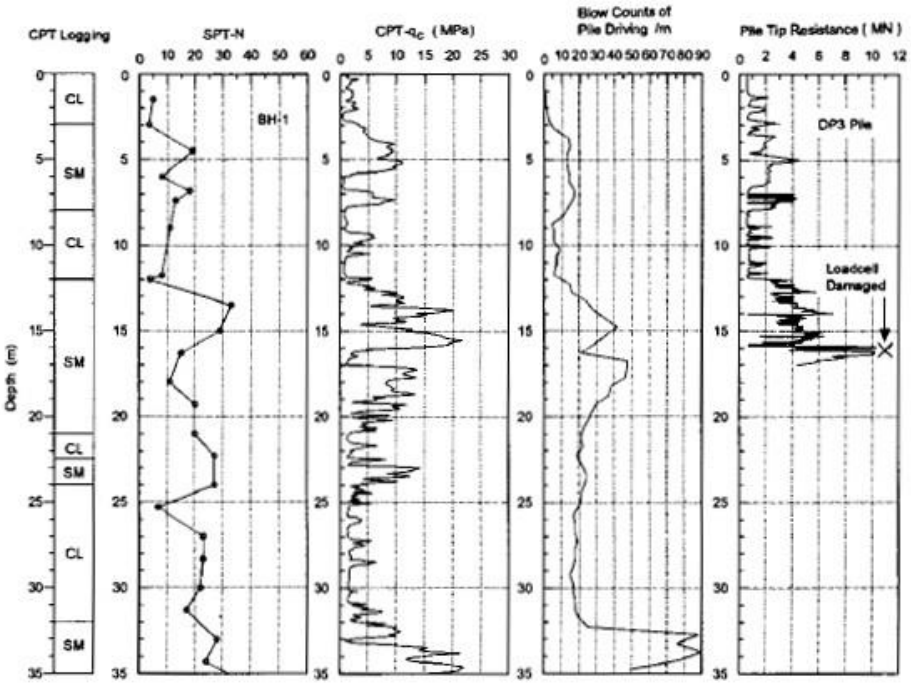

Figure 3-47 Profiles of SPT, CPT, blow counts and tip resistance of DP3 pile (from Hwang et al. 2001)

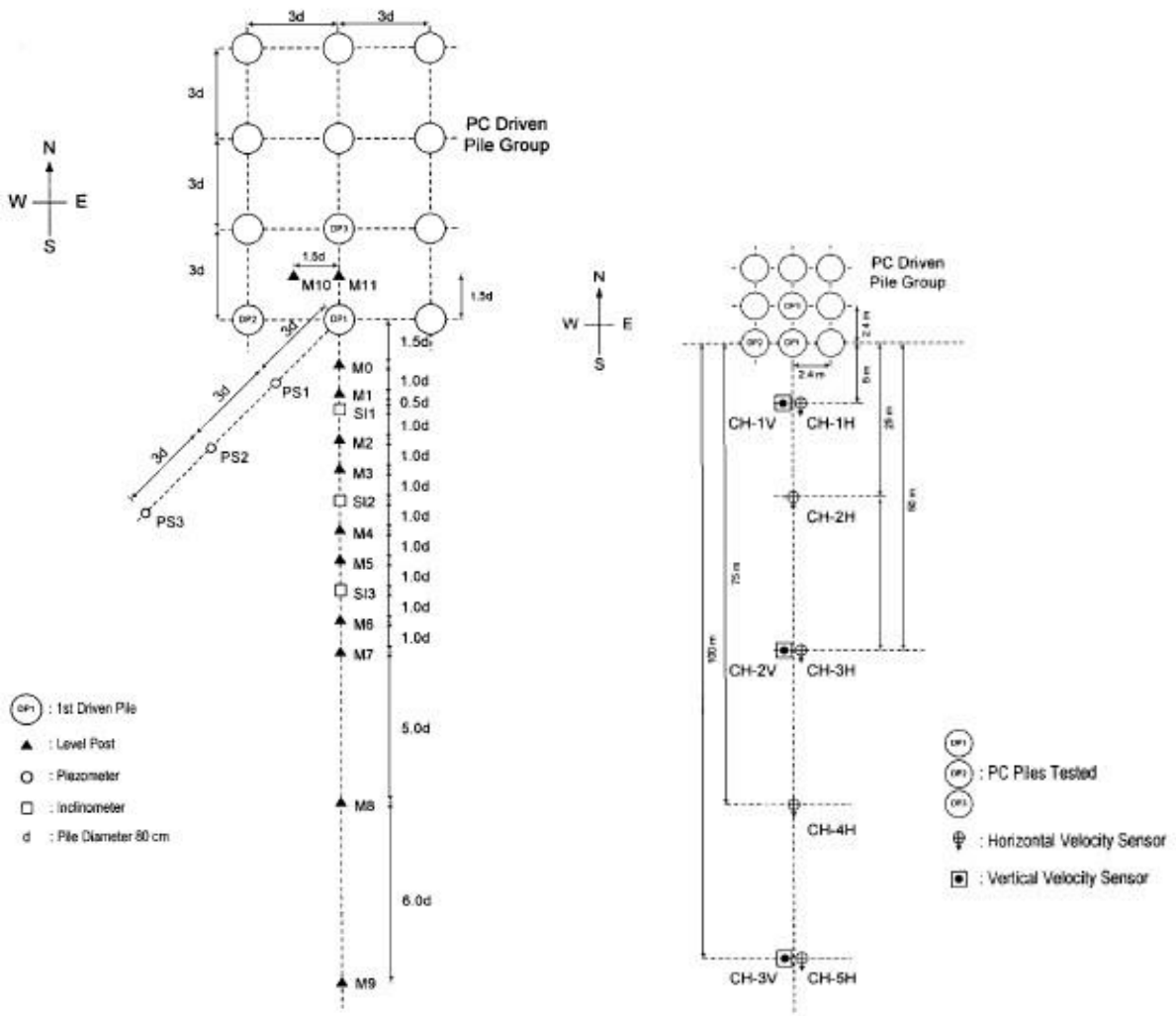

Figure 3-48 Site plan with arrangement of instruments (from Hwang et al. 2001)

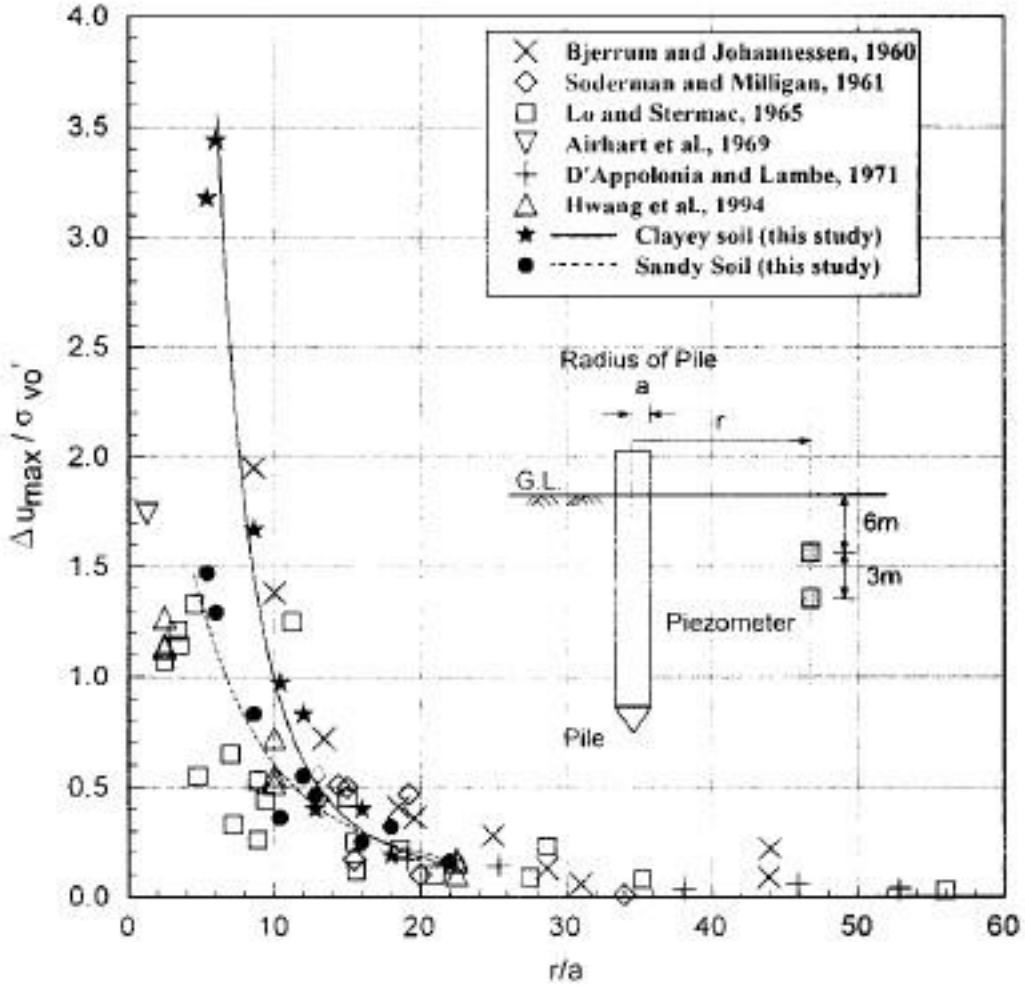

Figure 3-49 Normalized maximum excess pore pressure ratio with normalized distance to pile driving (from Hwang et al. 2001)

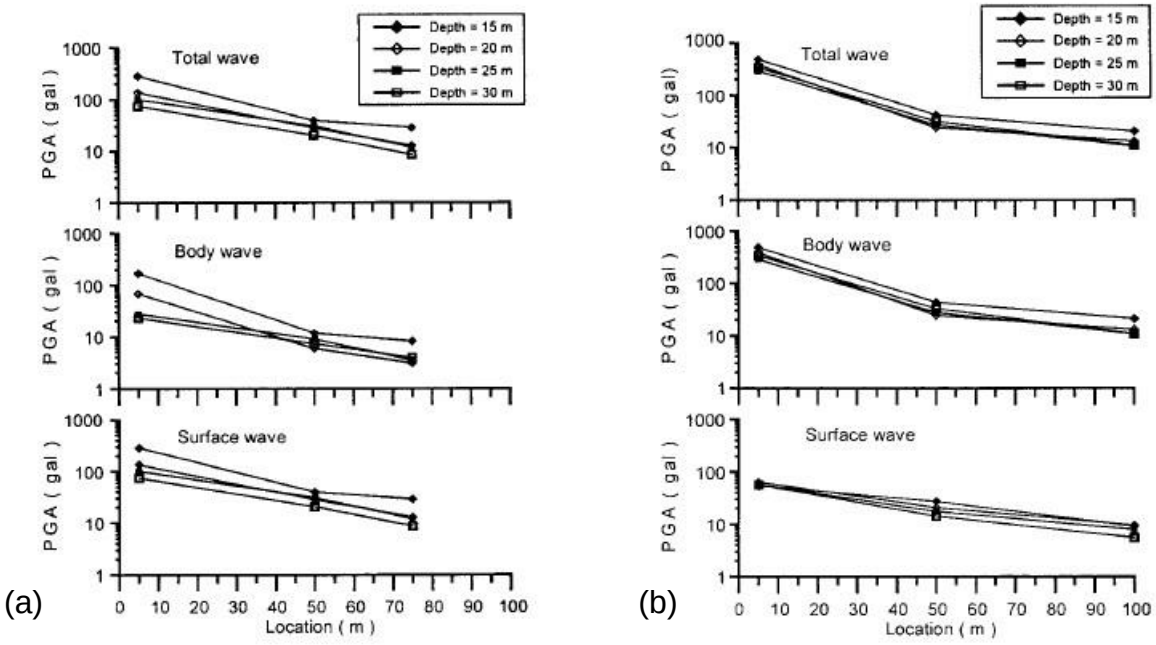

Figure 3-50 Attenuation of peak ground acceleration with radial distance: (a) Horizontal acceleration and (b) Vertical Acceleration (from Hwang et al. 2001)

Ashraf et al. (2002) presented a case of driving forty-two 14 in (356 mm) diameter concrete filled steel pipes for a newly constructed bridge near existing residential buildings located 9.7 ft (3 m) from the driving operations. A Vulcan 01 hammer with a rated energy of 14,970 ft-lb (20,300 J) was selected to drive the piles in pre-augered holes of 19.5 ft(6 m) depth; the top 7.8 ft (2.4 m) of the piles was encased in 20 in (508 mm) diameter steel shells filled with sand. A maximum peak particle velocity of 0.4 in/sec (11 mm/sec) was measured at a distance of 12 ft (3.7 m) from the driven piles. Figure 3-51 shows the monitored data plotted with the energy attenuation curves from Woods and Jedele (1985).

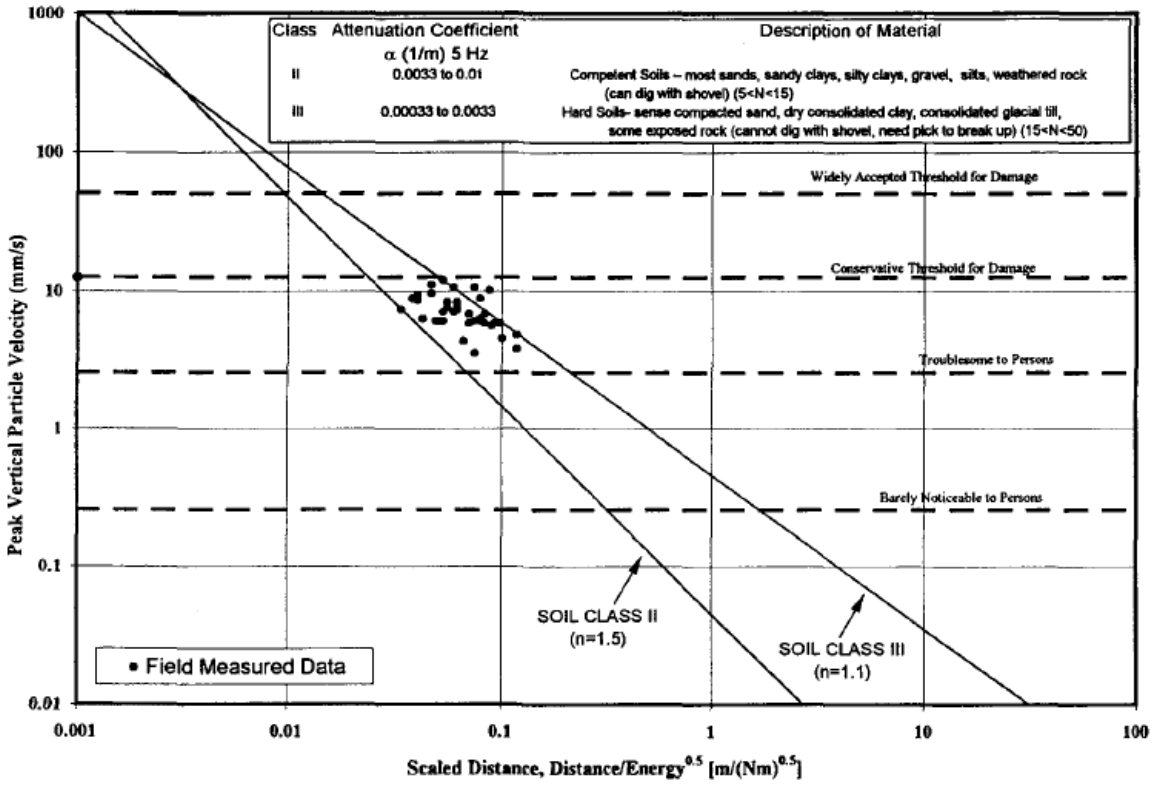

Figure 3-51 Monitored ground motion data with scaled distance curves from Woods and Jedele 1985 (from Ashraf et al. 2002)

Thandavamoorthy (2004) monitored surface ground vibrations and vibration of the top of an already installed concrete pile during impact driving of a closed ended steel pipe pile of 600 mm diameter and 20 m length. The soil was essentially fine and medium sand and the pile was installed by impacting a hammer of weight 41 kN dropped from a height of 2.4 m. Ground vertical vibrations at 3 and 15 m away from the pile are above the permissible velocity of 50 mm/sec for almost the entire penetration depth. The pile head vibration located at 6.25 m from the driven pile experienced very high values of accelerations, with a maximum of 123.42 m/sec^2, exceeding the acceleration permissible value of 7.1 m/sec^2. Figure 3-52 shows the variation of the vertical acceleration of the pile head of the concrete pile with the depth of penetration of the pipe pile. This high level of vibration of the existing pile is attributed to the resonance of the concrete pile. This is verified by examination of the frequency spectra where the horizontal ground acceleration has a dominant frequency of 25 Hz, which coincides with the vertical dominant frequency of the concrete pile. Horizontal ground surface vibrations were lower than the vertical values at a distance of 3 m from the pile. The duration of the horizontal accelerations is also longer than the vertical, indicating a lower frequency content of the horizontal vibrations.

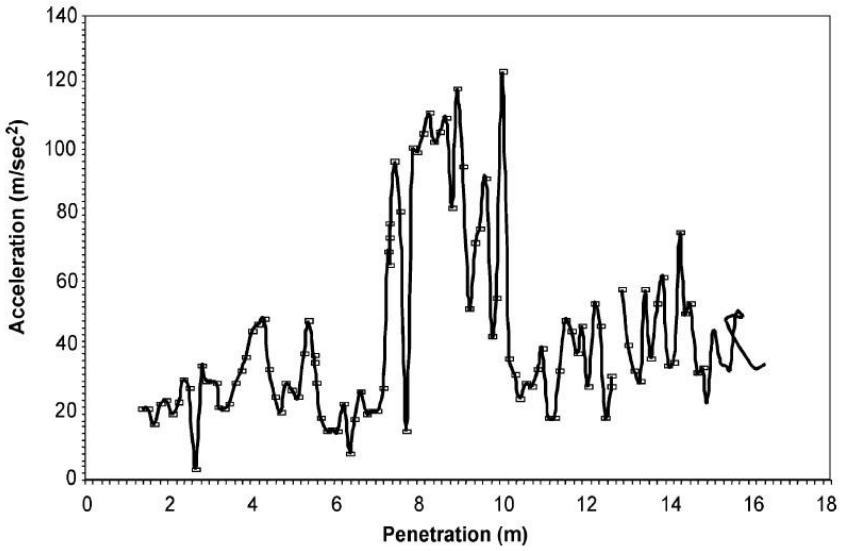

Figure 3-52 Penetration versus vertical acceleration of pile head of concrete pile at 6.25 m from the driven steel pipe pile (from Thandavamoorthy 2004)

Heung et al (2007) used ground vibration data during pile driving operations in central and south Florida as an input in the scaled distance equation. They established correlations between the scaled distance and the peak particle velocity, and the axial pile capacity and PPV. Seismographs were placed on the surface and were synchronized in real time with the Pile Driving Analyzer to get the pile capacities (RMX). Open-ended diesel hammers were used to drive mainly 455 mm square precast, pre-stressed concrete piles. The soil deposits consisted mainly of silty sands and clayey silts. Eq. 3-28 was used to calibrate the measured data; the estimated upper bound line was found as:

$$v = 0.8\left(\frac{\sqrt{E}}{D}\right)^{1.1} \qquad \text{Eq. 3-28}$$

where: v = PPV in mm/sec
E = actual hammer energy in J
D = horizontal distance between pile and seismographs in m
n = slope or attenuation rate

The authors compared the data with available correlations with horizontal and actual scaled distance. Figure 3-53a and Figure 3-53b show the correlations with the peak particle velocities and particle velocities (all readings) of the driven concrete piles. Data is compared with the Eq. 3-14 from Attewel and Farmer (1973) and the Eurocode 3 (1992) equation; Eurocode 3 adopts the scaled distance expression with k=1 for dense soils and k=0.5 for loose soils; n is equal to one. The correlation by Eurocode 3 for dense soils matches the data closely. Instead of the horizontal distance from the monitoring points to the pile, the actual distance from the pile tip to the geophones, which changes continuously as the pile penetrated deeper into the ground, is used in some correlations. The scaled actual distance equation by Wiss (1967) with k=2 for wet sand and the British Standard BS 5228-4 (1992) correlation with k=0.75 are implemented; n is equal to unity for both cases. Figure 3-54a and Figure 3-54b depict the peak particle velocity and all particle velocities from the monitored sites. It is observed that the data show more scattering when using the scaled actual distance approach.

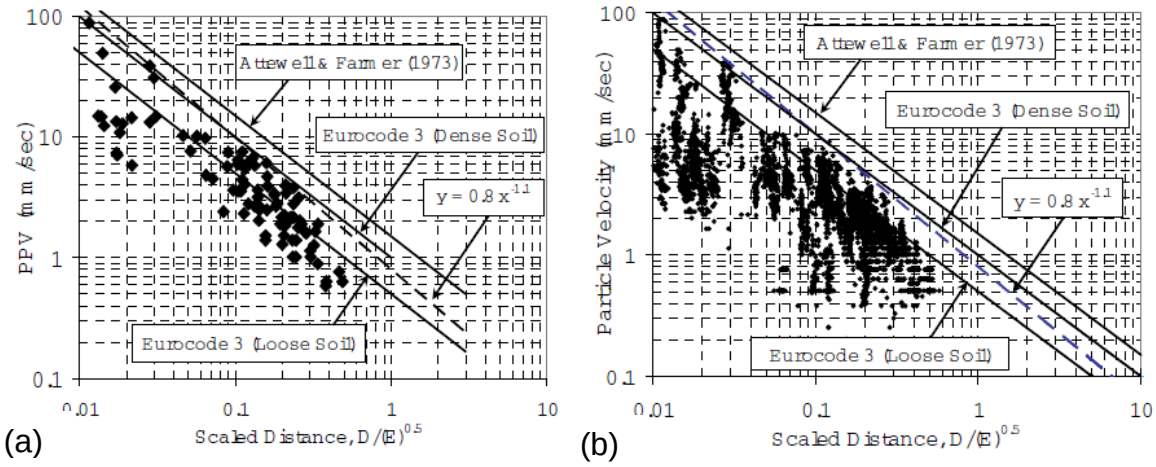

Figure 3-53 (a) Peak Particle Velocities and (b) Particle Velocities of 455 mm PPC piles versus scaled horizontal distance (from Heung et al. 2007)

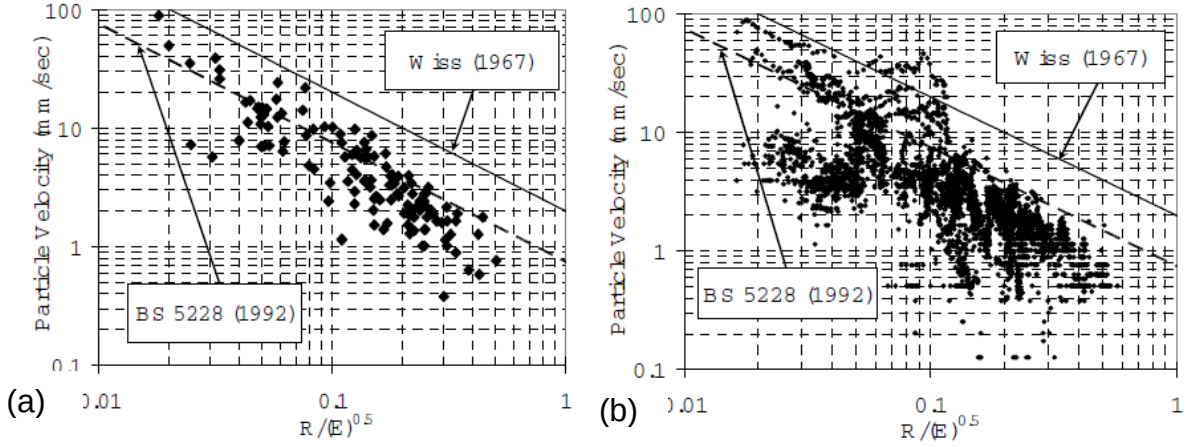

Figure 3-54 (a) Peak Particle Velocities and (b) Particle Velocities of 455 mm PPC piles versus scaled radial distance (from Heung et al. 2007)

The authors attempted to investigate a relationship between particle velocity and pile capacity. As can be seen in Figure 3-55a particle velocity increases with increasing pile capacity. This correlation would be a tool to engineers in order to estimate the peak particle velocity at a distance from a pile when information regarding the pile installation system is not available. The best estimate was found to be:

$$v = k\left(\frac{\sqrt{RMX}}{D}\right)^{n} \qquad \text{Eq. 3-29}$$

where: k = constant
RMX = ultimate pile capacity by PDA in kN
n = attenuation rate

The upper bound line for the measured data of the driven concrete piles resulted in k=4.5 and n=0.9. Figure 3-55 b depicts all the particle velocities with the estimated upper bound line.

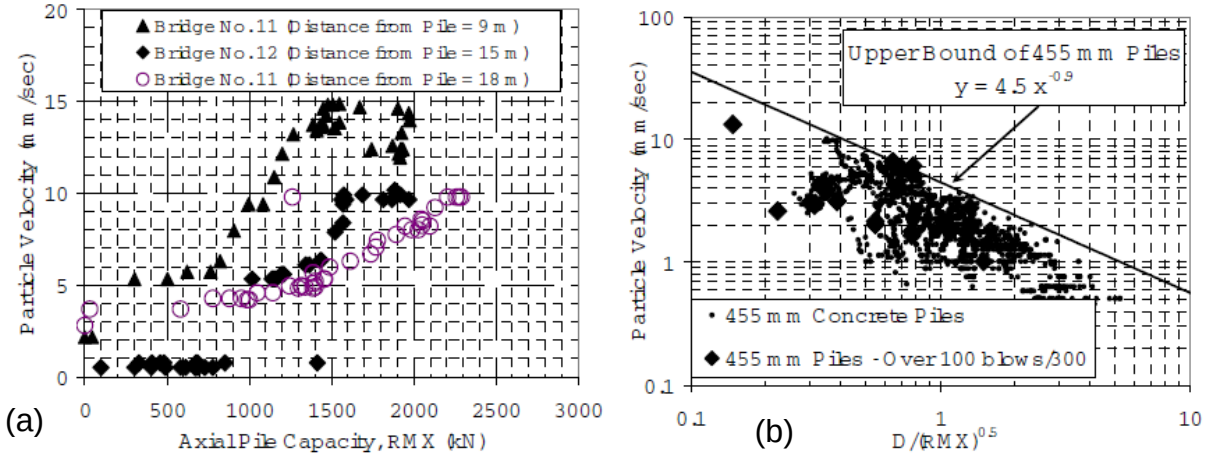

Figure 3-55 (a) Peak Particle Velocity versus PDA pile capacity and (b) Particle Velocity of 455 mm PPC piles versus scaled horizontal distance (from Heung et al. 2007)

Seo et al. (2014) recorded ground vibrations induced from driving steel pipe piles of 406 mm diameter and HP 306x174 piles installed with a Junttan HHK9S hydraulic hammer. Three pipe piles and one H-pile were installed at two different locations. Location 1 consisted of medium dense to very dense sands (N_{SPT} = 2 to 20) while Location 2 consisted of very dense sands (N_{SPT} = 10 to 80). Figure 3-56 depicts the peak particle velocities versus scaled distance at the two locations; hollow symbols represent Location 1 and solid symbols Location 2). The best fit lines for each location are also plotted along with the suggested expressions from Woods (1997) for competent (n=1.1) and hard soils (n=1.5). It can be seen that all data is below the line for hard soils suggested by Woods, while most of values at Location 2 (very dense sands) lie above the line for competent soils suggested by Woods. Figure 3-57 presents peak particle velocities for the same driving energy versus distance from pile and the corresponding fitted lines, separately for pipe and H-piles for the two different locations. H-piles showed higher vibration levels than pipe piles even though pipe piles had greater driving resistance. This is attributed to the higher ratio of shaft contact perimeter to pile diameter of H-piles than that of cylindrical piles.

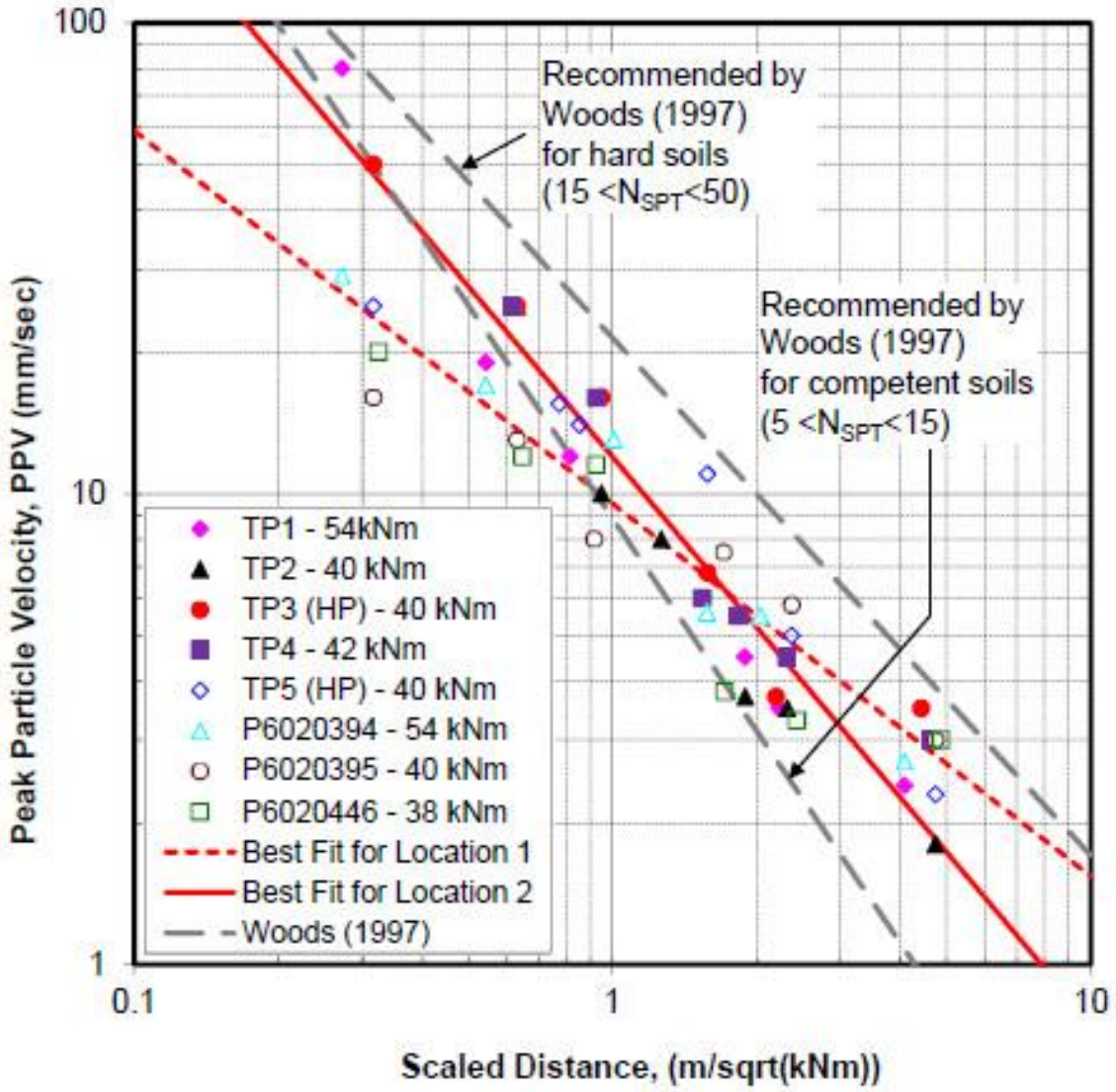

Figure 3-56 Measured peak particle velocities versus scaled distance with fitted lines (from Seo et al. 2014)

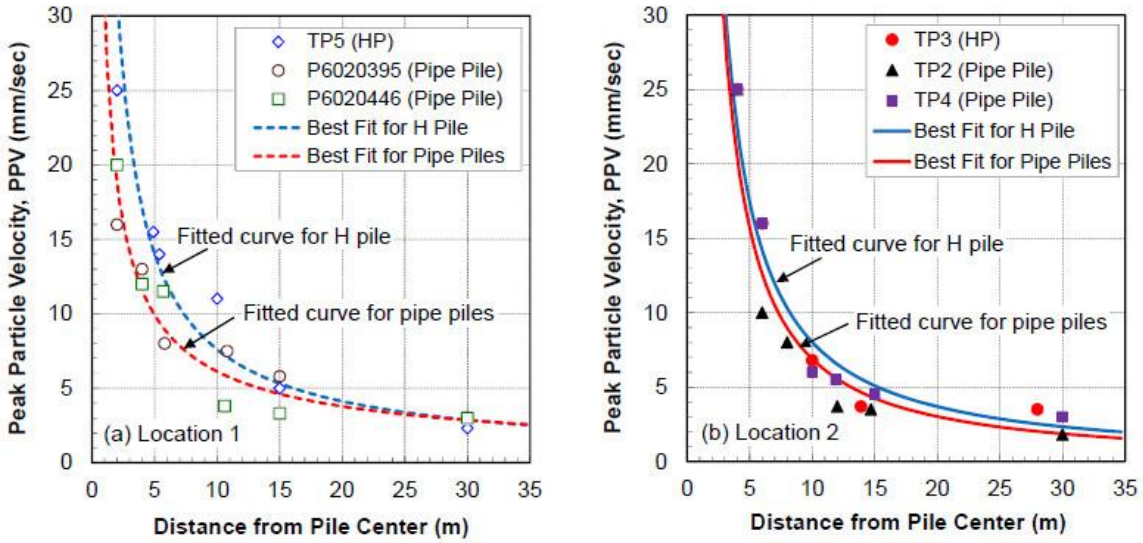

Figure 3-57 Peak particle velocities for pipe and H-piles for Locations 1 and 2 (from Seo et al. 2014)

3.4 Vibration Induced Settlements

Ground movements are an important side effect of construction activities. Poorly graded clean sands with relative densities less than 50% are susceptible to densification by vibration (Lacy and Gould 1985). Several researchers have reported settlement and structural damage when the aforementioned sands are part of the soil profile, with peak particle velocities less than the 2 in/sec safe limit for buildings. Total settlement or differential settlement, and not the high amplitude of ground vibrations, under a large number of vibration cycles, which is the case for pile driving operations, can be the cause of building damage. Settlement induced by pile driving activities can extend to as far as 1300 ft (400 m) from the pile driving area in the extreme case (Woods 1997). Understanding vibrations resulting from pile driving is essential to alleviate risk of damage to assets in the vicinity of pile driving activities. A discussion of reported cases of settlement due to pile driving and suggested methods of estimating settlements are provided in this Section.

Lynch (1960) reported a case where large settlements occurred at a site where piles had already been installed and additional piles were driven. Installation of 60 to 70 ft (20 to 23 m) long, 12 in (305 mm) diameter pipe piles and 14 in (350 mm) diameter shell piles was performed with a 30,000 ft-lb (40,680 J) Vulcan hammer. The soil consisted mainly of loose to medium dense sand layers. Monitoring of settlements indicated that the sand compacted by previously driven piles was further compacted up to 7 in (180 mm) by driving additional piles and the maximum distance of reported settlements was 20 ft (6 m) from the driven piles.

Heckman and Hagerty (1978) investigated a number of cases where large settlements occurred. In one of them, sheet piles were driven with a vibratory hammer in moist loose to medium dense sands causing extensive damage to several buildings. At the same site 12 in (305 mm) H-piles were driven with a 8,750 ft-lb (11,850 J) MKT 9B3 hammer and no settlement damage was observed. A PPV of 0.07 in/sec (1.8 mm/sec) was recorded at 30 ft (10 m) from the H-pile while a PPV of 0.25 in/sec (6.35 mm/sec) was monitored when driving a sheet pile at the same distance.

D'Appolonia (1971) investigated pile driving in clay soils. Pile driving in clay increases the lateral stress which in turn generates excess pore pressures and the ground surface heaves. After the pile is driven, the excess pore pressure dissipates, the soil consolidates under its own weight and the ground settles usually more than the heave during driving; the end result being a net settlement of the ground surface. D'Appolonia presented several cases of pile driving that caused movements of adjacent buildings and reduction of slope stability and retaining structures. Figure 3-58 presents a case studied by **Lambe and Horn (1965)** where it is clear that there is a close correspondence between excess pore pressure and movement of the adjacent building. In another case, end bearing pipe piles (12 in diameter) were driven into precored holes for foundations in the well-known Boston clay (**Lambe and Horn 1965; D'Appolonia and Lambe 1971**). The soil deposits in Boston consist mainly of sensitive soft to medium clay. Maximum measured heave and settlement of adjacent buildings on shallow foundations are shown as a function of distance from the nearest pile in Figure 3-59. The data points are the net settlements two to five years after the end of construction. Maximum heave was found to be 0.4 in (10 mm) and maximum settlement was up to 1.50 in (38 mm) at distances more than 100 ft (30 m) from the piles. Figure 3-59 also presents settlement of the nearby buildings for installation of H-piles at the same site; settlement was found to be 2 to 3 times larger than that of the pipe piles (**Casagrande and Avery 1959**). The number of piles per unit foundation area represents the average pile density and as can be seen, the bigger the density the larger the movement. The Figure is applicable to cases when high capacity piles are driven with low displacement through soft to medium clay.

Ireland (1955) summarized results from movements of nearby buildings during low capacity, high displacement timber pile driving in Chicago soft clay (Figure 3-60). The pile densities in Chicago were much larger than the Boston case, and the Chicago movements were greater. The main variables that have an important effect on the induced pore pressures and movements when driving piles in clays are: the spacing of the piles, the type of piles, the method of pile installation and the sequence of pile driving. Figure 3-61 shows how disturbance is reduced by preaugering at the Boston site. The measured maximum excess pore pressure divided by the vertical effective overburden stress is

compared with the theoretical maximum excess pore pressure that can be developed in undrained shear by increasing the lateral total stress. Preaugering to a depth of 85 ft is effective as the maximum excess pore pressure is about half of the theoretical maximum. The author concludes by stating that previously driven piles in soft clays act as a shield making the area stiffer, thus to minimize movements of nearby buildings, piles closest to the adjacent structures should be driven first and then the pile driving should proceed away from the structures being protected.

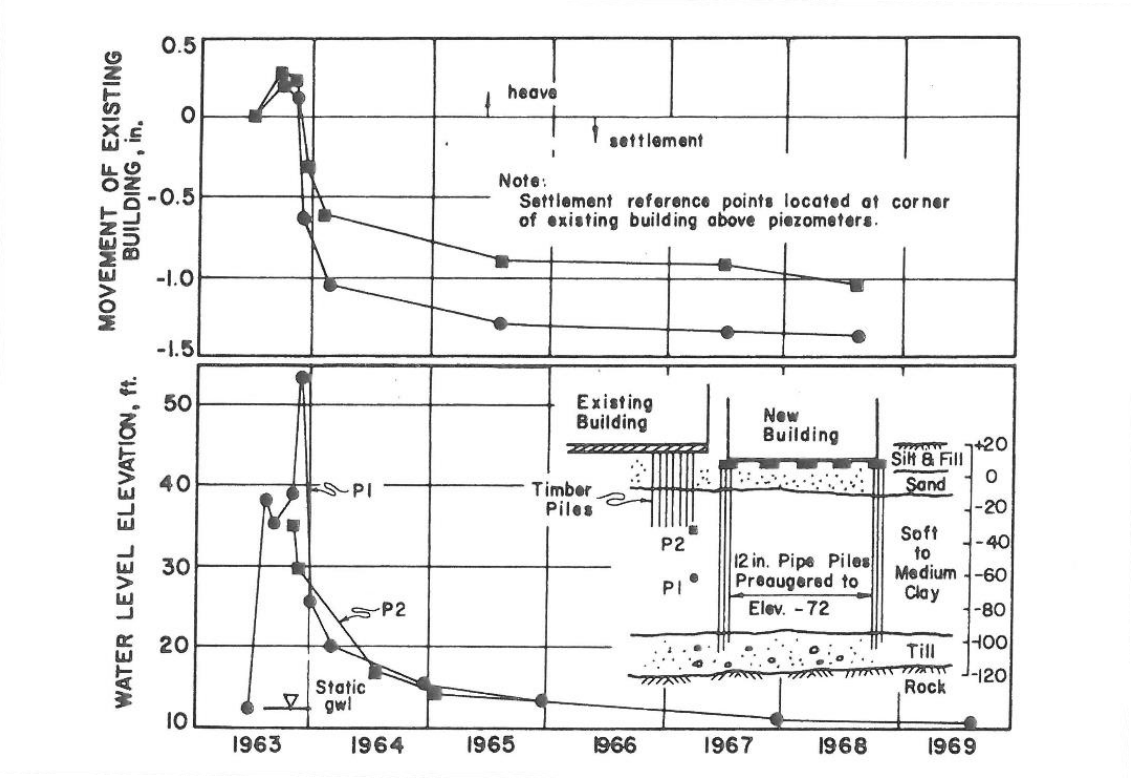

Figure 3-58 Excess pore pressures and movements of nearby building caused by pile driving (from D'Appolonia 1971)

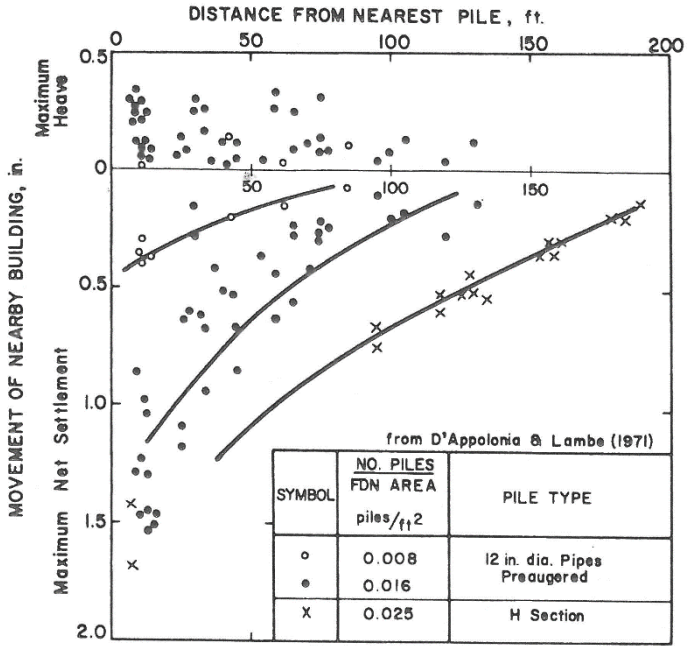

Figure 3-59 Heave and settlement of nearby structures caused by driving pipe piles and H-piles in Boston (from D'Appolonia and Lambe 1971)

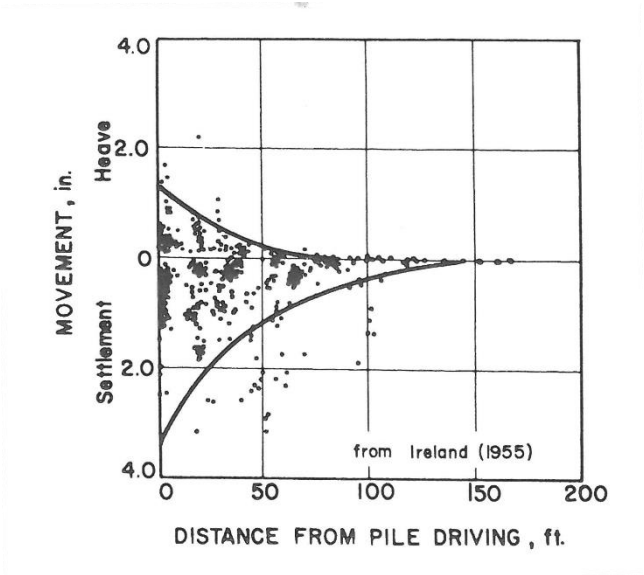

Figure 3-60 Movements of nearby structures by constructions of pile foundations in Chicago (from D'Appolonia 1971)

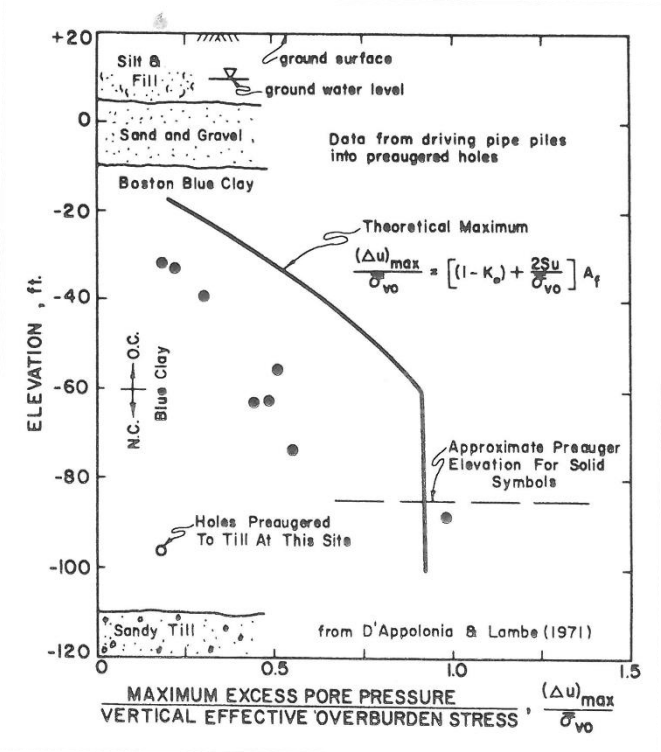

Figure 3-61 Effectiveness of precoring prior pile driving (from D'Appolonia 1971)

Brumund and Leonards (1972) conducted model footing tests using a vibrator actuating a 4 in diameter base plate which was on top of an Ottawa 20-30 sand at a relative density of 70%. The vibrator was designed so that the static weight, dynamic force and frequency could be varied independently. The authors concluded that the parameter that governs the ultimate residual settlement of a vibrating footing resting on the surface of a granular soil, is the steady-state transmitted energy. Data in Figure 3-62 include frequency ranges from 14 to 59.3 Hz, static pressure ranges between 0.27 and 0.55 of the static bearing capacity, ranges in ratio of maximum downward dynamic force to static weight from 0.3 to 1.0 and acceleration ranges from 0.05 to 1.60 times the acceleration of gravity. The impact tests, shown on the Figure, represent a ratio of dynamic force to static weight that exceeded one. It is obvious that the relationship is valid for a wide range of conditions and vibration variables. The finding that the transmitted energy, and not acceleration, controls sand densification is also shown in Figure 3-63. If the transmitted

energy is constant, the same settlement is produced over a wide range of accelerations and frequencies.

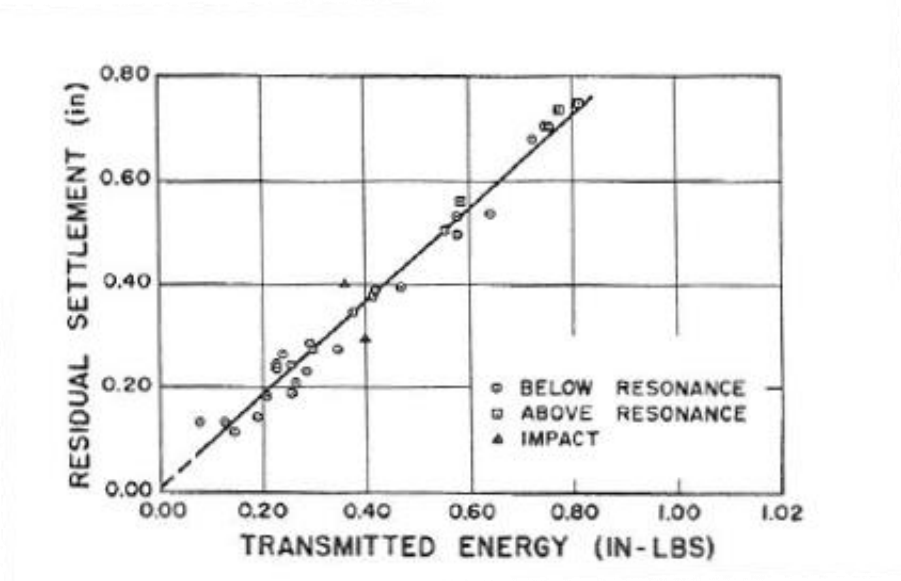

Figure 3-62 Transmitted energy versus ultimate residual settlement (from Brumund and Leonards 1972)

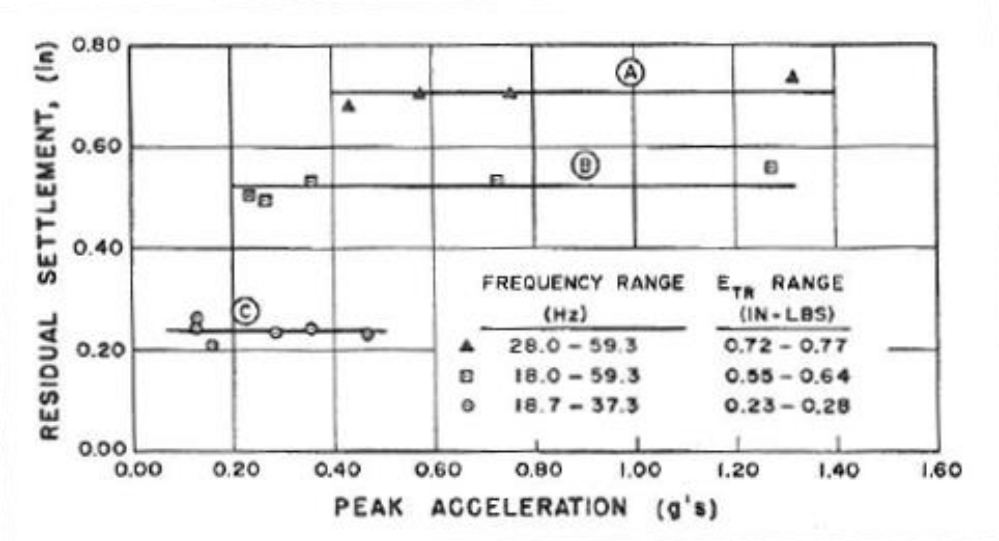

Figure 3-63 Acceleration versus residual settlement for three levels of transmitted energy (from Brumund and Leonards 1972)

Clough and Chameau (1980) described a case of measured settlement due to vibratory sheet pile driving. The soil deposits consisted mainly of loose and medium dense sands while the top 20 to 30 ft were loose rubble sand fills that were placed into the bay of San Francisco. Survey measurements were made during driving on the ground surface, and 6 ft (1.8 m) below the ground surface using settlement plates. Significant settlements occurred causing cracking of adjacent streets. Figure 3-64 presents results of the measured settlements at two test areas. Near the pile the settlements reached as high as 5 in (127 mm) but they diminished to zero 40 ft (12 m) from the pile (around one length of pile). The researchers calculated the average vertical ground strains as the amount of settlement at a point divided by the height of fill material beneath the measurement point and correlated them with the measured accelerations at these locations (Figure 3-65). They found a strong correlation between strain and acceleration. E2 site had higher strains since the sand deposits had lower densities (Dr = 30-50%) than site E1 (Dr = 50-60%). Strains are less than 0.3% (settlements are less than 0.5 in) when accelerations are less than 0.1 g. The trend of the strains with increasing acceleration, was compared to data from Silver and Seed (1972) from shake table tests of 10 cycles of loading at 4 cycles per second, for dry sand specimens with relative density of Dr=45%, and were found to be very similar. Seed and Silver also indicated that volume changes in sands are small when accelerations are less than 0.1 g.

Lacy and Gould (1985) analyzed 9 cases of settlement from pile driving; 5 cases dealt with bearing piles and 4 cases with sheet pile installation. All the cases involved driving in clean sands with a narrow gradation zone with relative densities less than 50 to 55%. In all case histories, vibration related settlement was observed and significant damage occurred even if the measured peak particle velocities were between 0.1 to 0.9 in/sec, less than the threshold of 2 in /sec that is taken as the safe limit for buildings. Pile driving superposes very small effects for many cycles and can produce much greater settlements than earthquakes with peak accelerations between 0.05 g to 0.1g. Silver and Seed (1971) performed laboratory tests that showed that a volume decrease can occur at low cyclic strain amplitude after many repetitions, as in pile driving, as well as under relatively few cycles at large strain, as in earthquakes. Dalmatov et al. (1968) also found

that settlements at building sites are insignificant if transmitted accelerations are less than 0.01g to 0.05g.

Other important findings from Lacy and Gould (1985), include the influence of job characteristics in the settlement magnitude. The increasing number of driven piles can change a situation from insignificant vibration effects to damaging settlements. The prediction of settlement in sands requires knowledge of gradation, relative density, site geometry, groundwater levels, depth of overburden, hammer energy and the scale of the project. In addition, soil properties that may influence settlement include: grain shape, permeability, anisotropy and magnitude of effective stress. It may be counterproductive to drive dewatering sheeting to great depths when later extraction of these piles can cause settlement of sewer pipes and other underground facilities. Potentially dangerous conditions arise when driving piles through granular materials, where these materials are relied on for passive resistance for stability (cofferdams or excavated slopes).

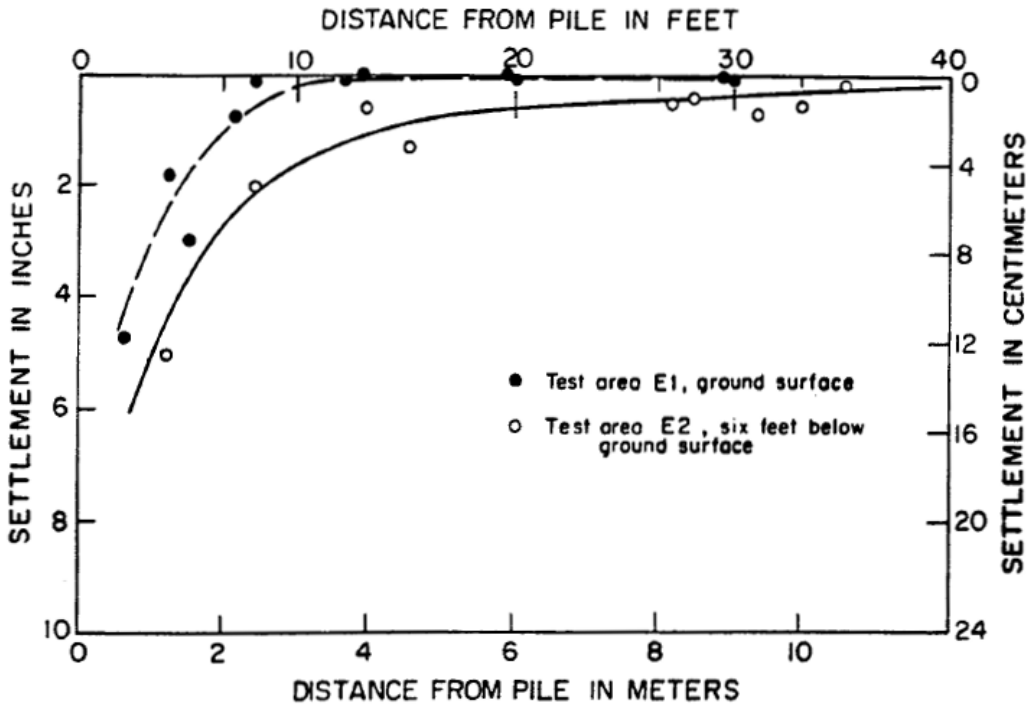

Figure 3-64 Settlements caused by sheet pile driving (from Clough and Chameau 1980)

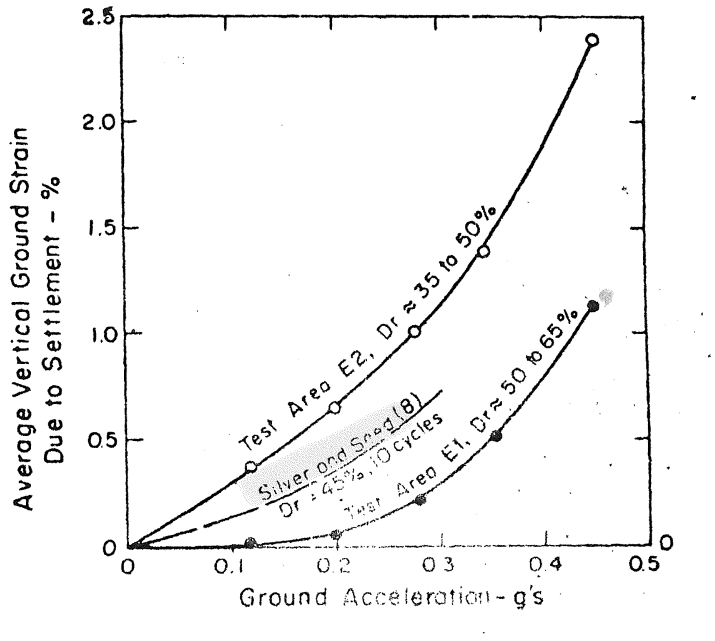

Figure 3-65 Correlation between strains due to settlements and accelerations during sheet pile driving (from Clough and Chameau 1980)

Picornell and Del Monte (1985) described settlement from driving steel H-piles that were needed for foundation support at a steel framed structure. The predominant soil was loose to medium dense sand underlain with limestone; boulders were found frequently in the sand stratum. Consolidation and load tests were performed to assess the compressibility of an upper gravel layer and the lower sand deposit. These tests indicated that despite the loose condition of both strata, they exhibited very low compressibility under the expected static loads. In addition, the field load tests indicated that the piers could withstand the static design load with total settlements less than 0.35 in (9 mm). However, upon driving the H-piles, one of the pier foundations of the building settled 10 in (254 mm) pointing to the dynamic compaction induced by pile driving as the cause of the settlement. The ground movements induced by pile driving drop from a maximum near the affected footing, to zero in the closest unaffected footing located 39 ft away. Observed attenuation rates by Dalmatov et al. (1968) indicated that the ground

movements were zero at distances beyond 26 ft from the pile center, at a site with similar soil conditions, which is in approximate agreement with this case.

Leznicki et al. (1992) reported a case of low-vibration, non-displacement continuous flight auger (CFA) piles selected for an inner urban area. The site was underlain by loose to medium dense sands overlying bedrock. After installing 19 CFA piles at distances as close as 4 ft (1.2 m) from a historic structure, settlements of 1.5 in (38 mm) were measured on the building. The movements were attributed to ground loss during augering. After implementing technical procedures to reduce the volume of soil removed from the boreholes, 200 CFA piles were successfully installed. The recorded settlements of the historic building adjacent to the construction site were 0.5 in (13 mm), assumed to be caused by the reduction in soil strength and density. These minor settlements should be expected within a radius of about 6 pile diameters.

Conversion to CFA piling system was made to the above project, after 780 open-ended pipe piles were impact driven at distances as close as 30 ft (9 m) from the historic building and caused settlement of its exterior wall up to 1.4 in (36 mm); the maximum allowable movement was set at 0.5 in (12 mm). A Vulcan 50C impact hammer was used with a rated energy of 15,000 ft-lb (20,300 J). Settlements from driving operations occurred over distances exceeding 50 ft (15 m) from the driven piles. Monitoring was conducted for 70 weeks from the beginning of the construction and revealed that time delayed settlement appears to occur after piling has been completed (in 22 weeks) and can be a significant contributor to total settlements. Results of the monitoring program for the southwest corner of the building are presented in Figure 3-66. As can be seen in this Figure, the total downward movement after all construction activities were completed, including time-delayed movement, was 3.8 in (96 mm). It is important to note that peak particle velocities were measured in the lower basement of the historic structure and were found to be less than 0.2 in/sec (5 mm/sec). Vibrations recorded on the ground were about 0.6 in/sec (15 mm/sec) within 10 ft (3 m) away of the pile and decreased to 0.05 in/sec (1.3 mm/sec) at a distance of about 100 ft (30 m) from the pile.

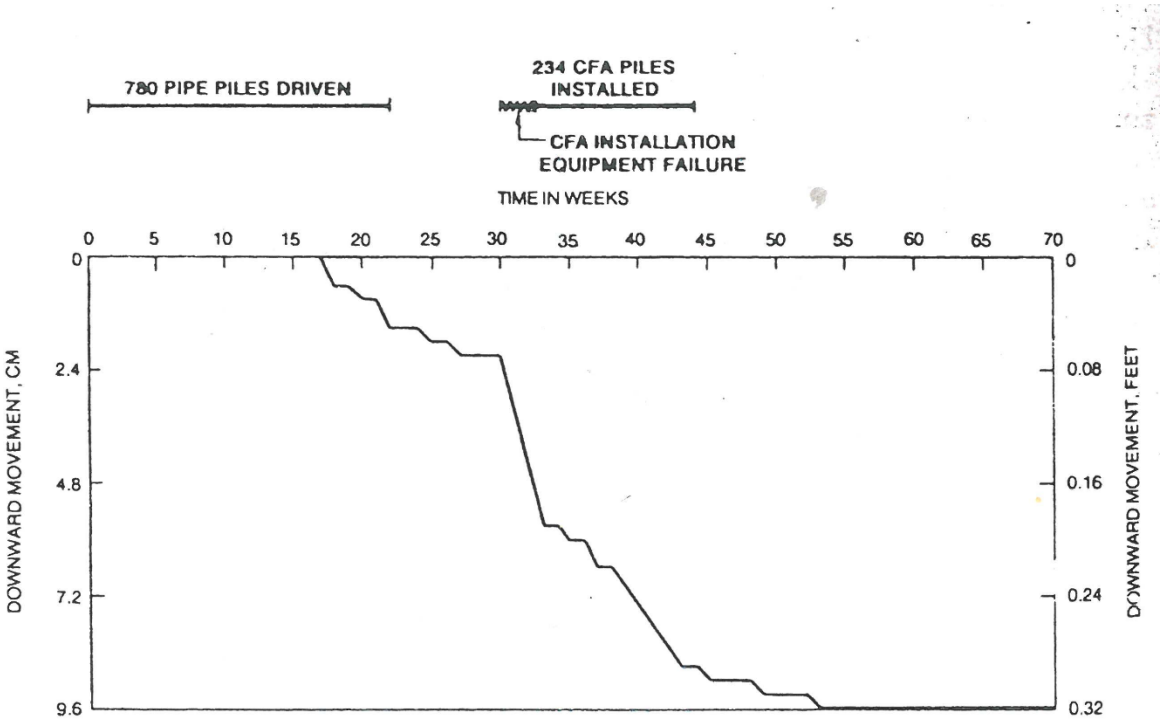

Figure 3-66 Vertical movement of southwest corner of historic structure (from Leznicki et al. 1994)

The case reported from **Linehan et al. (1992)** with vibratory and impact pile driving near a pressurized natural gas pipeline led to significant settlement and lateral deformation of the pipeline. Figure 3-67 and Figure 3-68 present the vertical and horizontal movements of the pipeline measured with survey monuments that were placed on an uncased segment of the pipe. Sheet driving and impact driving of the H-piles resulted in 0.5 in and 1 in of settlement, respectively. During driving the H sections, lateral movements of about 1 in occurred, which resulted in high bending stresses in the pipe. Soil was excavated around the pile to relieve the stresses following sandbag additions to offset buoyant forces. Subsequent driving at the east cofferdam produced additional settlement of about 1 in, making the total settlement of the pipe to be 2 in. Thus, the main risk in this project resulted again from pipeline settlement and lateral movement, and not vibration. There are far fewer documented failures from structural vibration effects than

from permanent displacement during construction activities close to buried pipelines (O'Rourke and Hall 1988).

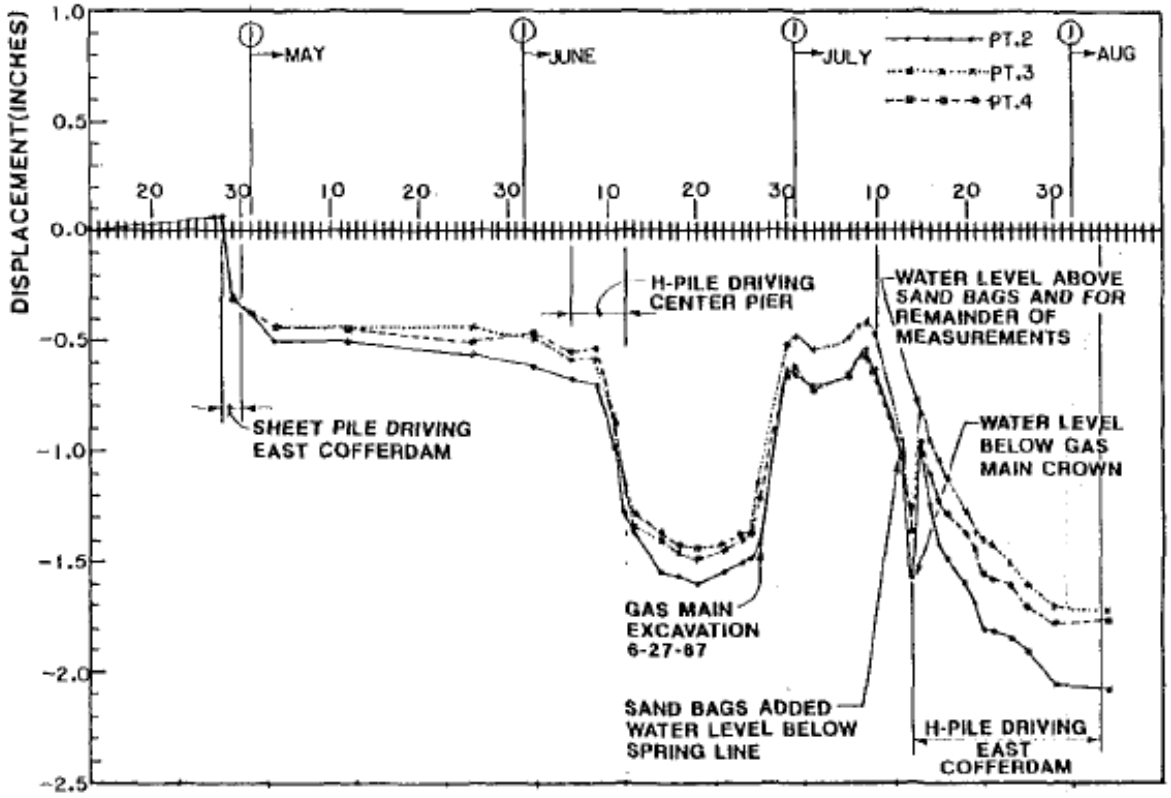

Figure 3-67 Time history settlement movements during construction work (from Linehan et al. 1992)

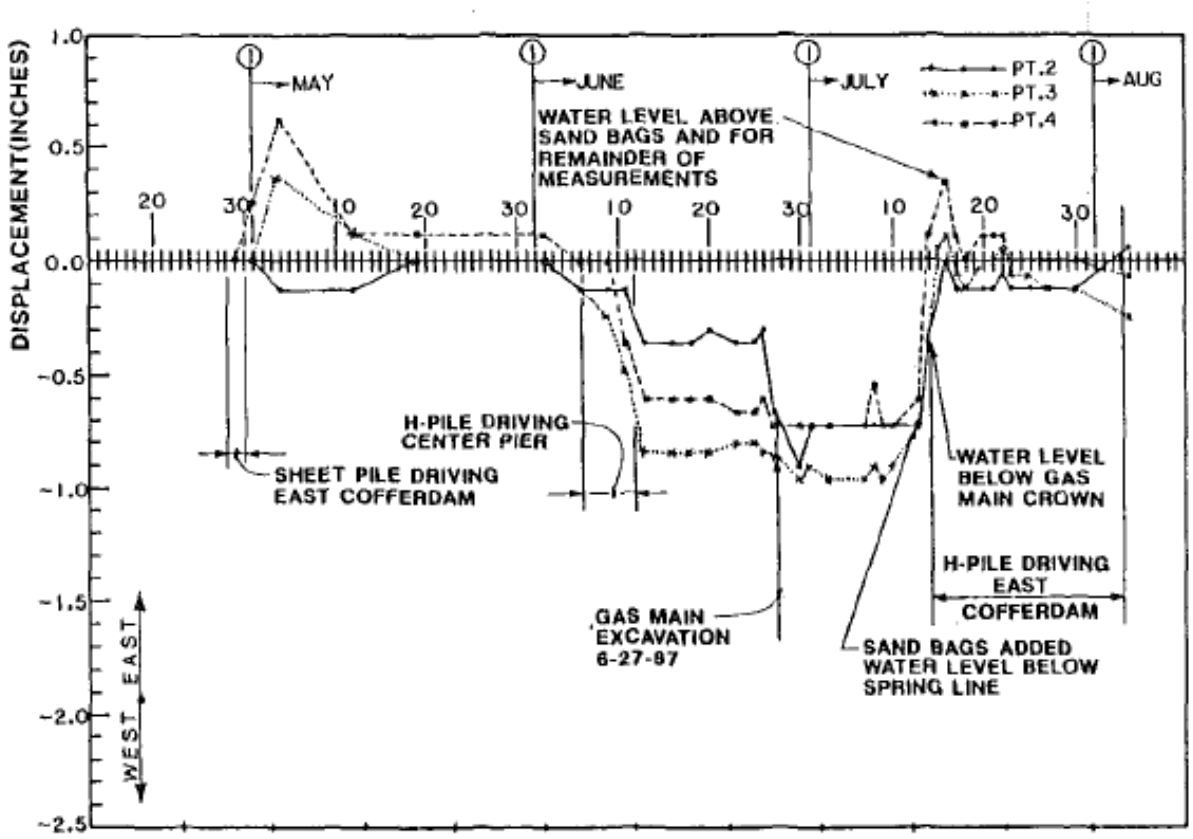

Figure 3-68 Time history lateral movements during construction work (from Linehan et al. 1992)

Leathers (1994) reported a case where significant settlement occurred under low vibration levels (max PPV was 6.4 mm/sec) during driving 360 mm square precast concrete piles with an ICE 640 diesel hammer, with a rated energy of 54,000 N-m. A total of 180 piles were driven immediately adjacent to two buildings. The primary soil strata consisted of granular fill, organic silt, silty clay with zones of clayey sand, sand and gravely sand and glacial till, from top to bottom. The thickness of the sand layer was about 23 m. A total of 31 settlement points were established close to the adjacent buildings (Figure 3-69). The maximum settlement after driving all piles was 54 mm and lateral movements of up to 18 mm toward the pile driving zone were measured. Settlements measured at the ground surface and the top of the sand layer were found to be identical, which confirms that there was no volume change in the fill and clay layers and settlement

occurred only in the lower sand stratum. The estimated volumetric densification of the sand layer ranged from 1.4% to 1.7%. The average volume change needed to offset the volume displacement of the piles, was about 1.3%, therefore a cumulative volume change of sand (densification) and the piles' displacement of 3% was predicted at the site. The volume of the sand stratum contributing to the settlements was assumed to extend an average of 3 m beyond the perimeter of the pile driving area. This assumption was based on the observation that driving piles about 3 m from an inclinometer, caused ground movements due to densification.

Dowding (1992) compared settlements and ground motions produced by blast densification and pile driving. Grain size distribution provides susceptible soils to densify as clean sands with less than 10% fines and relative densities of 50% to 55% or less. The sands fall within the range of gradation which defines which soils are liquefiable (Bhandari 1981). After studying other case histories, Dowding suggested that densification can extend approximately as far as the length of the driven pile and even more. Distinction between vibratory induced settlements and settlement resulting from loss of lateral support during adjacent excavation were discussed. The above two types of settlement are compared in Figure 3-70 as a function of distance from the driving or the excavation. Typical settlements for 6 and 12 m excavations were taken from Goldberg et al. (1976) and are similar to vibratory settlements from the Clough and Chameau (1980) study beyond 4 m (thin solid lines). At 2 m and less from the wall, vibratory densification gave higher amplitudes than excavation settlements.

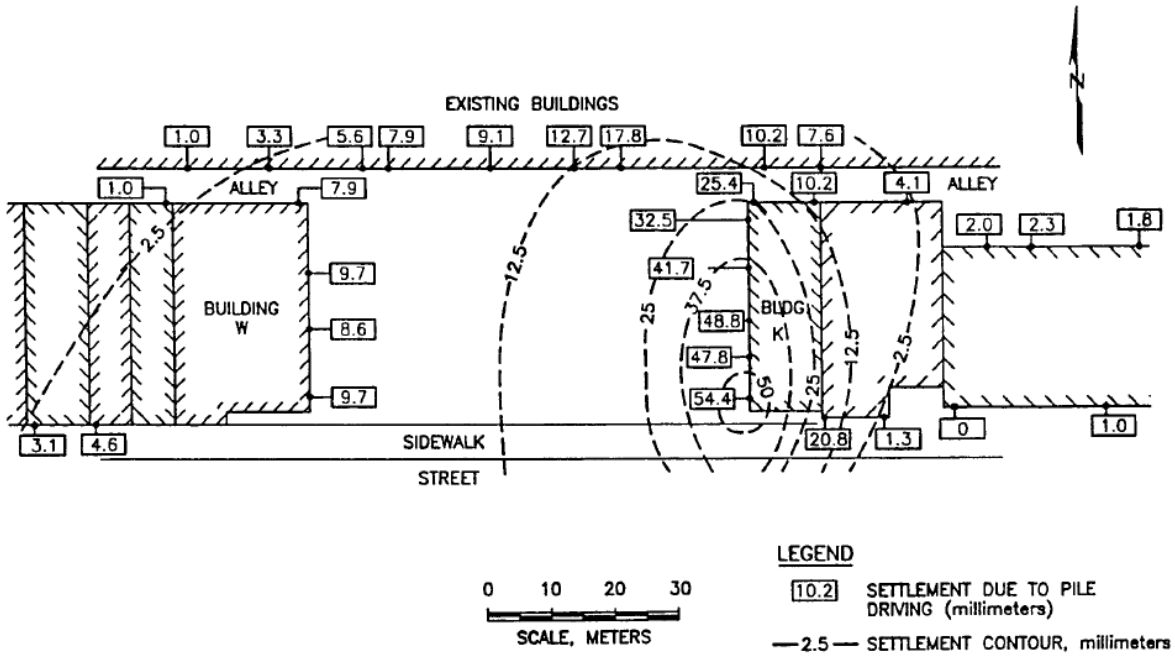

Figure 3-69 Settlements due to pile driving (from Leathers 1994)

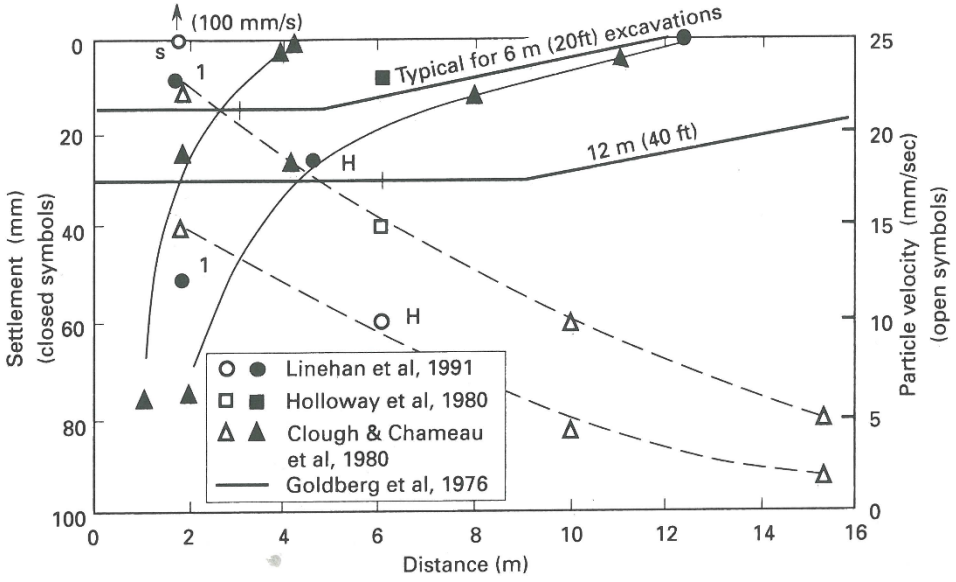

Figure 3-70 Comparison of settlement and particle velocities produced by pile driving vibrations (thin solid and dashed lines, respectively) with typical settlements produced by braced excavation in sand (thick solid lines) (from Dowding 1996)

Kim et al. (1994) developed a mathematical model for the evaluation and prediction of the vibration induced in-situ settlement of sands at low vibration levels (2.5 to 18 mm/sec). An experimental program was run using seven factors affecting settlement: vibration amplitude, number of cycles, confining pressure, deviatoric stress, grain size distribution, moisture content and relative density. The tests were in principle, vibration of a soil specimen with height 15 cm, using a shake table while differentiating the seven influencing factors. A regression polynomial was used to calculate the potential settlement with 27 different combinations of the 7 factors; the Multifactorial Experimental Design (MED) method was implemented. The predicted settlement from the model was directly extrapolated to the in-situ stress conditions to estimate the settlement of a vulnerable sand layer. The model was evaluated by comparing the predicted and measured settlements from two case histories and was found to match closely to the observed values.

An investigation of the factors implemented in the Kim et al. (1994) mathematical model was discussed by **Kim and Drabkin (1995a)**. The authors indicated that overburden stress from the superstructure and loss of lateral support can produce site conditions more vulnerable to vibration induced settlement than level ground. Therefore, stress anisotropy is taken into consideration in the prediction model with the deviatoric stress factor. Shallow depths, where the confinement is smaller than greater depths, are more susceptible to settlement. The latter was captured by varying the confining stress with different ranges of the earth pressure coefficient. Settlement increases with the increase of vibration amplitude and the number of cycles. Coarse sand specimens with small content of fines are more susceptible to vibration than fine sand specimens. The authors conclude by providing a parametric assessment of settlement for highway traffic, subway traffic and pile driving vibration. The attenuation characteristics of soils are also taken into account for the different types of vibration sources, indicating variations in the predicted settlement with depth. Therefore, for proper settlement assessment in urban environments, vibration amplitude should be monitored not only on the ground surface, but also within the ground.

More details about the laboratory developed statistical polynomial model are provided by **Kim and Drabkin (1995b)** and **Drabkin et al. (1996)**. The settlement evaluation of a 6 in height specimen is expressed by:

$$\ln Y = 2.27 + 1.19x_1 - 0.71{x_1}^2 + 0.49x_2 - 0.68{x_2}^2 - 0.80x_3 + 1.09{x_3}^2 - 0.46x_4 + 0.06{x_4}^2 + 0.45x_5 - 0.38{x_5}^2 - 0.19x_6 - 0.10x_7 \quad \text{Eq. 3-30}$$

where Y is the settlement in 0.001 in and x_1 to x_7 are the factors with their coded values. The coding formulas for the different factors are given in Table 3.25. By direct extrapolation, settlement, Δ, of an in-situ sand soil layer of height, H, can be estimated by:

$$\Delta = \frac{Y}{6}H \quad \text{Eq. 3-31}$$

According to Drabkin et al. (1996), pile driving operations can generate up to 500,000 cycles which is several orders of magnitude greater that earthquake cycles. An increase of number of vibration cycles can cause substantial settlement especially for large vibration amplitudes. If low-level vibrations are analyzed for long-term impact, the accumulation of vibrations may be sufficient to cause considerable densification of sandy soils. However, the authors point out that extrapolation of settlement observed during test pile driving might be inaccurate, since the number of cycles is much smaller when driving one or two test piles, than during construction where a large number of piles are driven. Test pile driving is important though in evaluation of vibration amplitudes and attenuation characteristics of the soil (**Drabkin and Lacy 1998**).

Table 3.25 Factors and coding for polynomial model (after Drabkin et al. 1996)

No.	Factor	Tested ranges	Coding of Factors
1	Vibration amplitude	v=0.1-0.7 in/sec	x_1= -1 + (v - 0.1)/0.3
2	Deviatoric Stress	s=2-15 psi $s=\sigma_v$-p	x_2= -1 + (s - 2)/6.5
3	Confining Pressure	p=10-30 psi $p=(1+2K_0)/3\sigma_v$	x_3= -1 + (p - 10)/10
4	Sand mixture	coarse	x_4= -1
		fine	x_4= 1
5	Number of cycles	N=60-500,000	x_5= -1 + (N - 60)/26,997
6	Moisture content	Dry	x_6= -1
		Saturated	x_6= 2
7	Relative density	Loose	x_7= -1
		Medium dense	x_7= 2

Pile installation in clay differs a lot from pile driving in sands as discussed above. Pile penetration in clay generates excess pore pressures and heave of the ground surface. After the dissipation of the excess pore pressures the ground surface settles as it reconsolidates and usually this settlement is much higher than the heave during the pile driving (Svinkin 2006). Pile driving of 16.1 in (410 mm) wide square precast prestressed concrete piles in soft marine clays in the Boston area produced unacceptable movement of an adjacent building (**Bradshaw et al. 2005**). The first phase of the construction included piles being driven up to 27 m from the closest building while in phase two, the closest distance of a structure was 15 m. Five deformation monitoring points (DMP) were installed along the perimeter of the closest building and the vertical deformation data are presented in Figure 3-71. In phase one, 44 mm was monitored as the greatest amount of heave which was above the maximum specified value of 25.4 mm. Mitigation measures were implemented for construction phase two; installation of wick drains and preaugering before pile driving to limit additional heave. None of the measures was effective as can

be seen in Figure 3-71 since heave continued to increase reaching a maximum amount of 81 mm.

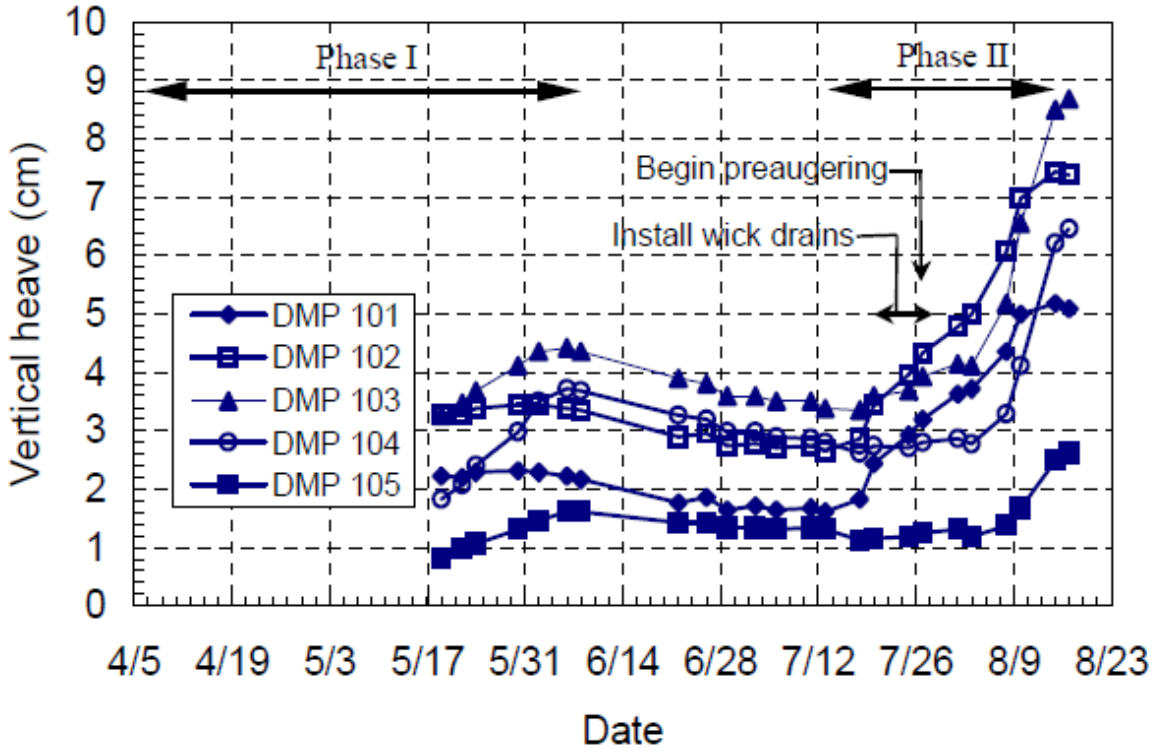

Figure 3-71 Vertical heave of adjacent building during pile driving (after MHD 1995, from Bradshaw et al. 2005)

Massarsch (1992) suggested an empirical relationship for estimating ground settlements as a function of ground acceleration, observed during vibratory compaction (Figure 3-72). The degree of ground settlement depends on the initial density of the soil which is expressed in terms of initial cone penetration resistance. Settlements, as a percentage of the soil layer thickness, can range between 1 % in dense sand and gravel, to 10 % in very loose sand and silt.

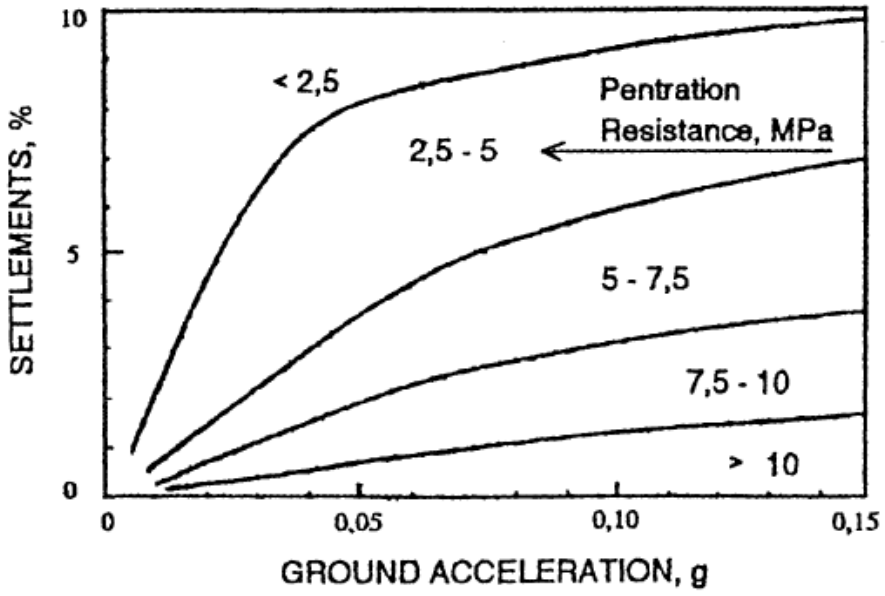

Figure 3-72 Settlements caused by vibratory pile driving and vibratory soil compaction (from Massarsch 1992)

Massarsch (2004) presented a simplified procedure to estimate settlements in a homogeneous sand deposit adjacent to a single pile (Figure 3-73). This approach is based according to the author, on experience from soil compaction projects. The intense densification due to pile penetration is assumed to occur within a zone corresponding to three pile diameters around the driven pile. The volume reduction resulting from ground vibrations will cause significant settlements in a cone with an inclination 2(V):1(H), with its apex at a depth of 6 pile diameters below the pile tip. Thus, the settlement trough will extend a distance of 3D + L/2 from the center of the pile, with maximum settlement at the

center of the pile. Maximum settlements, s_{max}, and average settlements, s_{av}, are estimated as:

$$s_{max} = a(L + 6D) \quad \text{Eq. 3-32}$$

$$s_{av} = \frac{a(L + 6D)}{3} \quad \text{Eq. 3-33}$$

where: L = pile penetration length
D = pile diameter
α = compression factor from Table 3.26

The displacement volume of the installed pile is not taken into account. The effect of incompressible layers should be considered by adjusting the effective pile length.

Table 3.26 Compression Factor, α, for sands for different soil densities and driving energies

Driving Energy	**Low**	**Average**	**High**
Soil Density	**Compression Factor, α**		
Very Loose	0.02	0.03	0.04
Loose	0.01	0.02	0.03
Medium	0.005	0.01	0.02
Dense	0.00	0.005	0.01
Very Dense	0.00	0.00	0.005

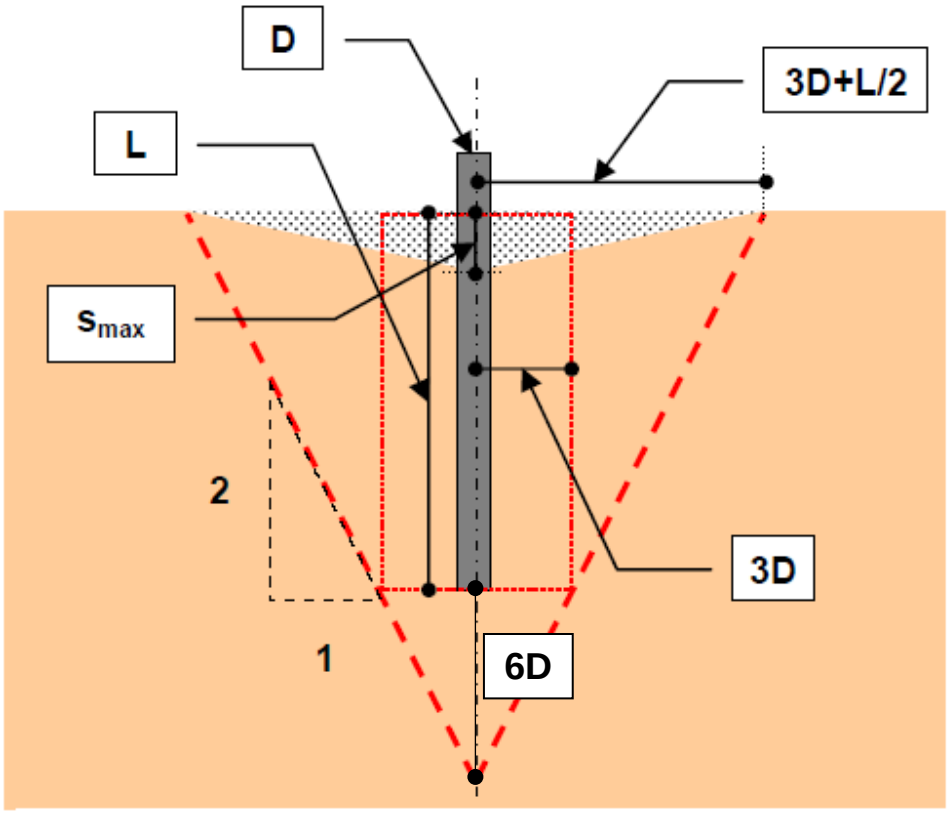

Figure 3-73 Simplified method of estimating settlements adjacent to a single pile in homogeneous sand deposit (after Massarsch 2004)

Borden et al. (1994) developed a procedure to predict ground surface settlement due to construction induced vibration. Settlement potential of 33 residual soil specimens from 8 sites in North Carolina, was evaluated by resonant column and torsional shear stress tests. The effect of confining pressure from 25 kPa to 100 kPa, shear strain amplitude from 10^{-4} % to 10^{-1} %, vibration frequency from 0.2 to 10 Hz and number of cycles up to 1 million on the dynamic densification of residual soils were investigated. The dynamic settlement caused by cyclic shear strain can be obtained by:

$$\Delta\varepsilon_{vol} = a(\gamma - \gamma_c)(logN)^b \qquad \text{Eq. 3-34}$$

where: $\Delta\varepsilon_{vol}$ = dynamic volumetric strain under N cycles of torsional shear
α, b = factors dependent on type of soil and confining pressure
γ = current shear strain amplitude (%)
γ_c = threshold shear strain amplitude (%)
N = number of cycles

For the same dynamic load (shear strain amplitude and number of cycles) the dynamic settlement is a function of the soil properties and confining pressure. The finer the particle size, the smaller is the settlement observed. The dynamic settlement is reduced by increasing confining pressure. Figure 3-74 shows best fit lines for the dynamic volumetric strain at 1000 cycles for MH, ML and SM soils. In order to use this approach however, determination of the α and b parameters by lab tests must be done.

Borden and Shao (1995) verified the above analytical model with pile driving tests in the field. In one of the field tests two timber piles of 10.7 m and 10.4 length were driven in residual soil profiles and an extensometer was used to measure settlement at different depths. A 3D borehole geophone system was used to record vibrations within the soil profile while geophones were also placed on the surface. A steel hammer of 1350 kg (3000 lb) was lifted to a height of 1.83 m (6 ft) and 3 m (10 ft) for the 2 piles tested.

The analytical model was implemented before the field test and predicted a ground surface settlement of 1.7 mm. Samples of the residual soils were collected during the field

test and resonant column and torsional shear stress tests were performed. The dynamic settlement according to the model was found to be 0.06 mm and 0.29 mm for the average and 95% confidence level, respectively. The measured settlement with the extensometer was negligible, thus the analytical model provides a conservative estimate of the ground surface settlement. Figure 3-75 presents the trend of vibration attenuation on the ground surface from the pile driving test. Compared to results from other researchers, it is observed that wave attenuation in residual soils is faster.

Data from the tests conducted by Borden and Shao (1995) are plotted in Figure 3-76. The importance of fines content on potential for settlement on granular materials is obvious. For fines content greater than about 10%, the threshold strain for vibration settlement increases.

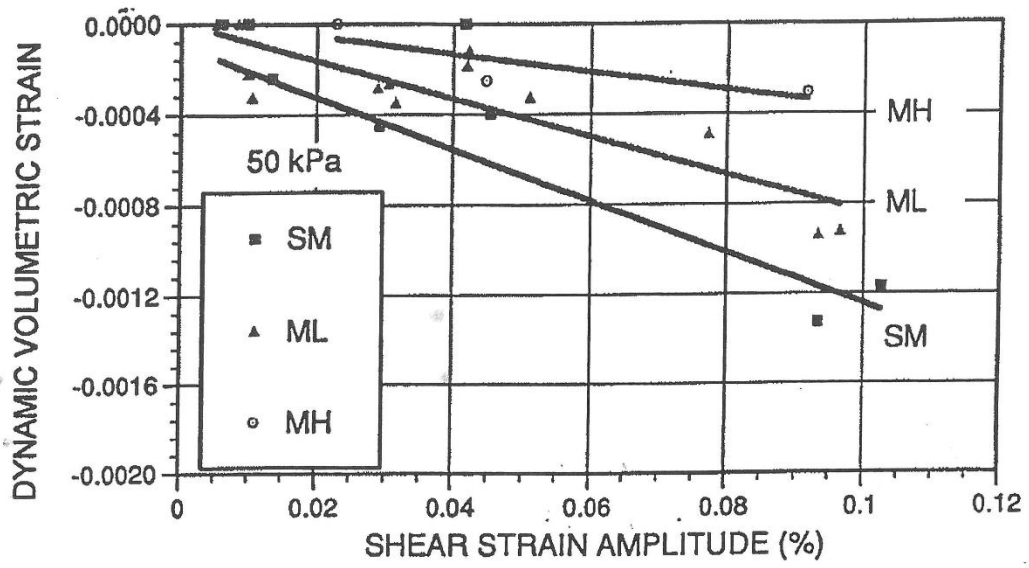

Figure 3-74 Effect of soil type on dynamic settlement at 1000 cycles (from Borden and Shao 1995)

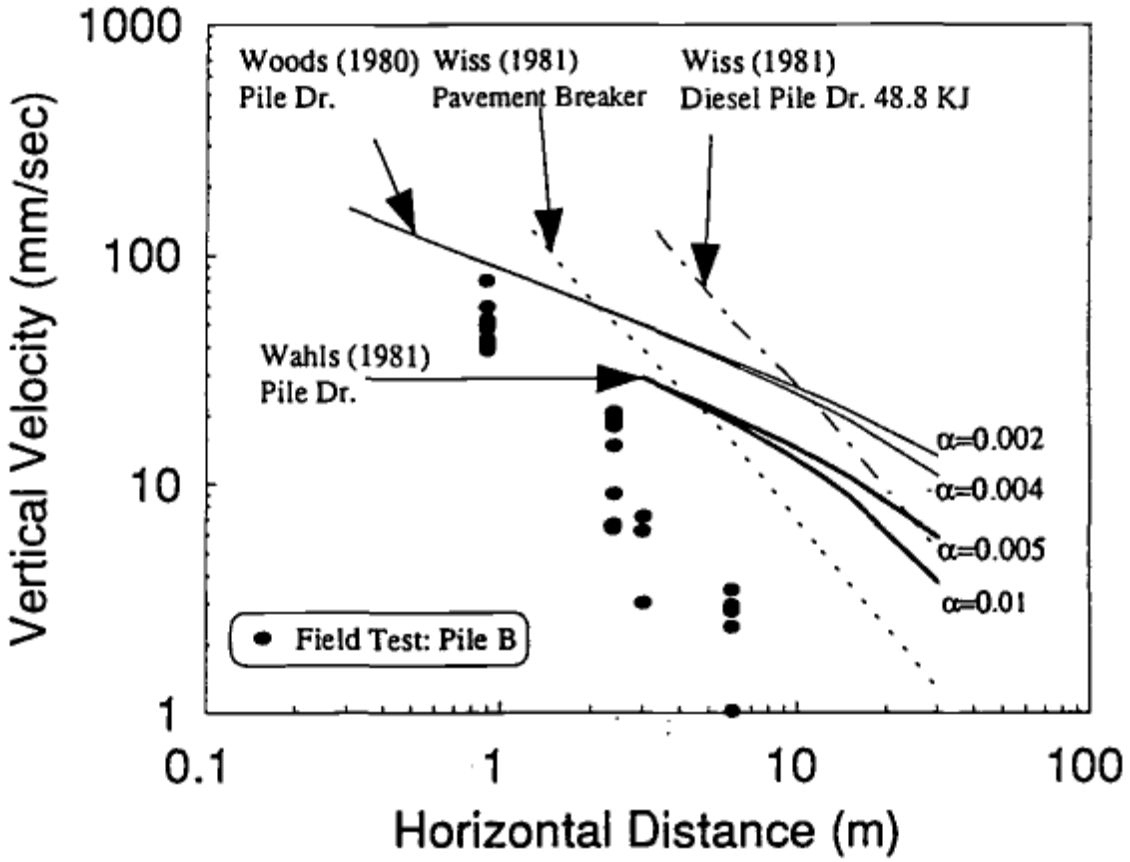

Figure 3-75 Vibration attenuation on the ground surface from pile driving test and literature reports (from Borden and Shao 1995)

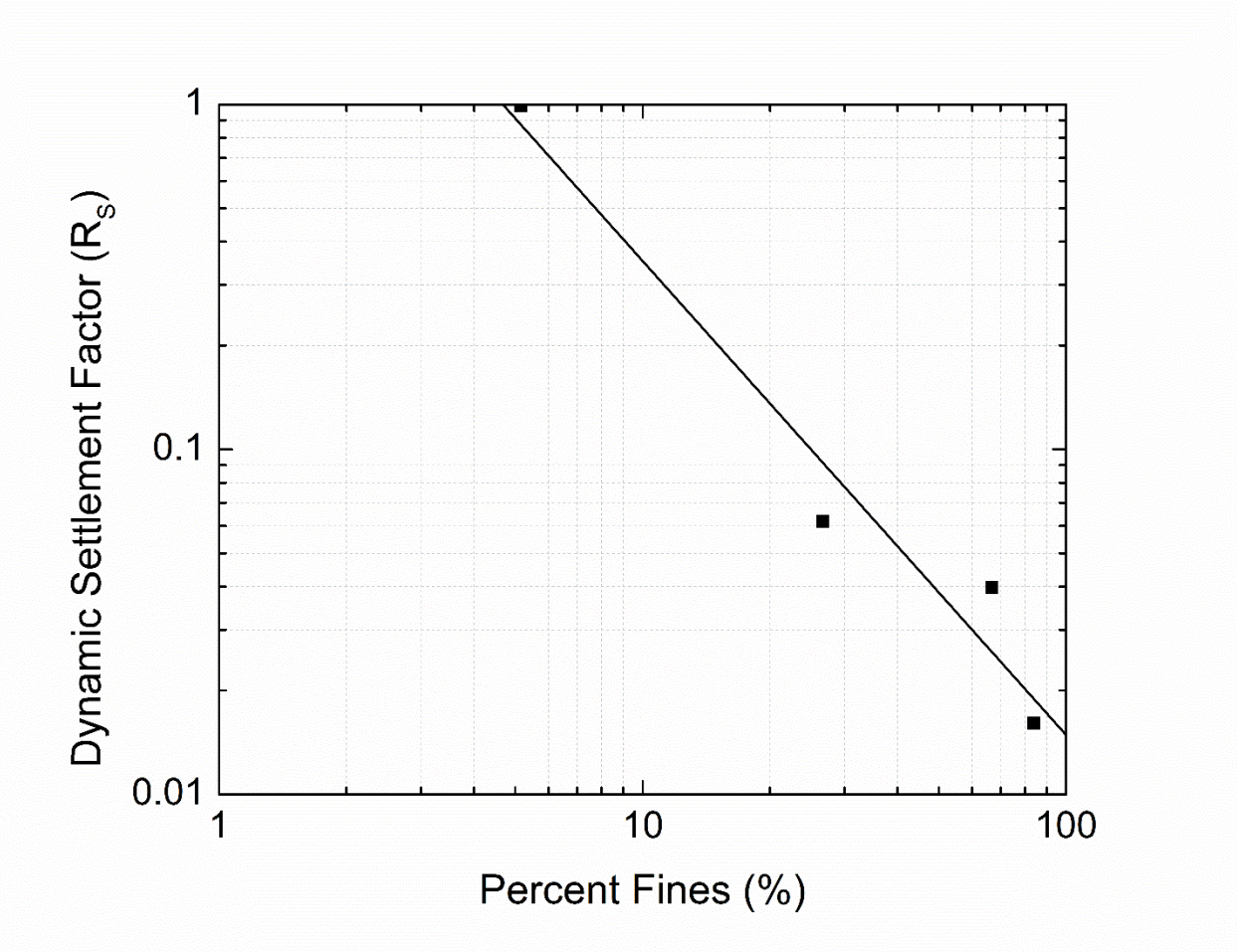

Figure 3-76 Effect of fines on dynamic settlement (after Borden and Shao 1995)

3.5 Shear strain and potential of settlement

In the past years a big portion of the geotechnical engineering research was focused on understanding the soil behavior when subjected to seismic motion. Specifically, the concepts of the behavior of cohesionless soils under dynamic loading and the corresponding dynamic stress-strain properties of granular soils (shear modulus and hysteretic damping) were investigated in depth providing interesting results. Studying these concepts can assist engineers to better understand ground vibrations generated by construction activities. Earthquakes of course, have a much higher intensity compared to that generated by man-made activities. The other major difference between vibrations by natural phenomena and human operations is the number of loading cycles. In most seismic events the number of significant cycles is likely to be less than 20 (Silver and Seed 1971). Pile driving induced vibrations can reach, depending on the size of the project, thousands of loading cycles. Some important findings mainly from the geotechnical earthquake engineering research are discussed in this Section. Thresholds of cyclic shear strain that can pose a risk of ground settlement are also discussed.

Seed and Silver (1972) presented a method of analysis for the estimation of the magnitude of settlements of dry sands deposits due to earthquake shaking. The method was based on a combination of simple shear and shaking table tests of a silica sand at different relative densities, stress conditions, number of cycles and intensities of the seismic motion. The tests on the shaking table showed an increase in settlement with increasing number of cycles and a reduction in settlement with increasing relative density (Figure 3-77). The settlement decreased when the sand layer was subjected to a surcharge (Figure 3-78). Figure 3-79 shows the effect of the base acceleration on the vertical settlement after 10 cycles of motion. Figure 3-80 shows the relationship between cyclic shear strain and vertical strain for different number of cycles, with and without the surcharge, obtained from the results of the simple shear tests for a loose specimen (Dr=45%). The threshold cyclic shear strain that corresponds to the start of the settlement

is approximately γ=0.01%. The authors then combined these results to obtain the distribution of the shear strain with depth which in combination of Figure 3-80 can give an estimate of the settlement in a sand layer. The authors conclude by stating that even under static load conditions, evaluations of settlements in sand deposits are subject to considerable error (in the order of ± 25% to 50%), so for the complex situation of dynamic loading it is unrealistic to expect that evaluations could be made with even this degree of accuracy. However, an approximate evaluation of the possible settlement is adequate for many purposes.

More details about the cyclic simple shear tests were provided by **Silver and Seed (1971)**. The authors modified the Norwegian Geotechnical Institute (NGI) simple shear device, which was developed for static strength tests (Bjerrum and Landva 1966), to obtain the dynamic properties of the silica sand. The dynamic shear modulus was found to increase slightly with increasing number of cycles and with increasing relative density and to decrease significantly with increasing values of shear strain amplitude. There is also an increase in modulus with increasing vertical stress; Figure 3-81 summarizes the above phenomena for the tenth loading cycle. The values of hysteretic damping were found to increase with increasing shear strain amplitude and decrease slightly with increasing number of cycles and increasing values of vertical stress. The relationship between damping and shear strain is independent of the relative density of the sand. Figure 3-82 shows the relationship between damping and shear strain amplitudes that is suggested to be used in response analysis for shallow layers. The results shown are for 5 cycles, representative for seismic events.

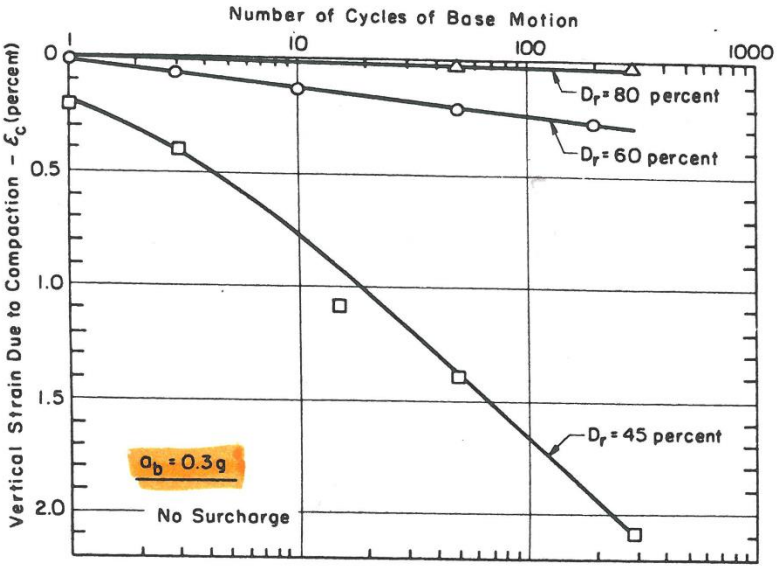

Figure 3-77 Effect of relative density and number of cycles on settlement of sand layer in shaking table test (from Seed and Silver 1972)

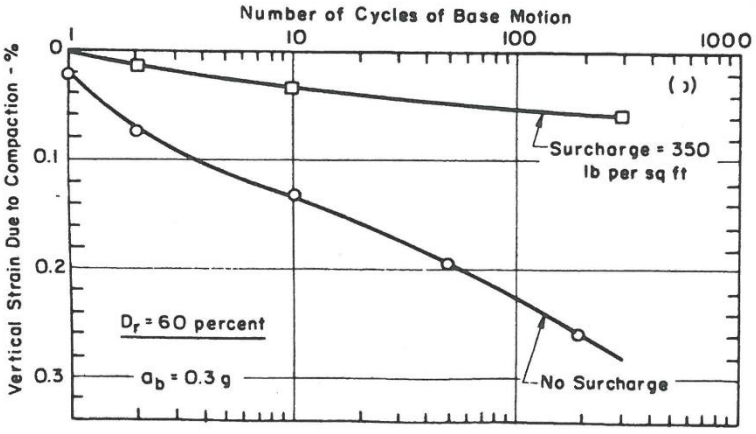

Figure 3-78 Effect of surcharge on settlement of sand layer in shaking table test for 10 cycles (from Seed and Silver 1972)

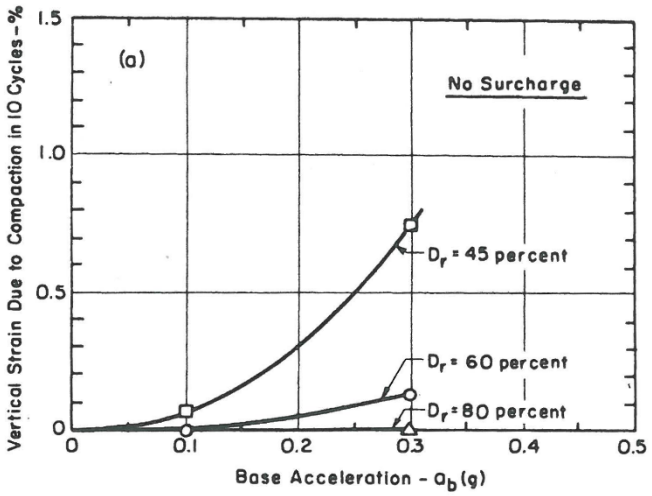

Figure 3-79 Effect of relative density on settlement of sand layer in shaking table test for 10 cycles (from Seed and Silver 1972)

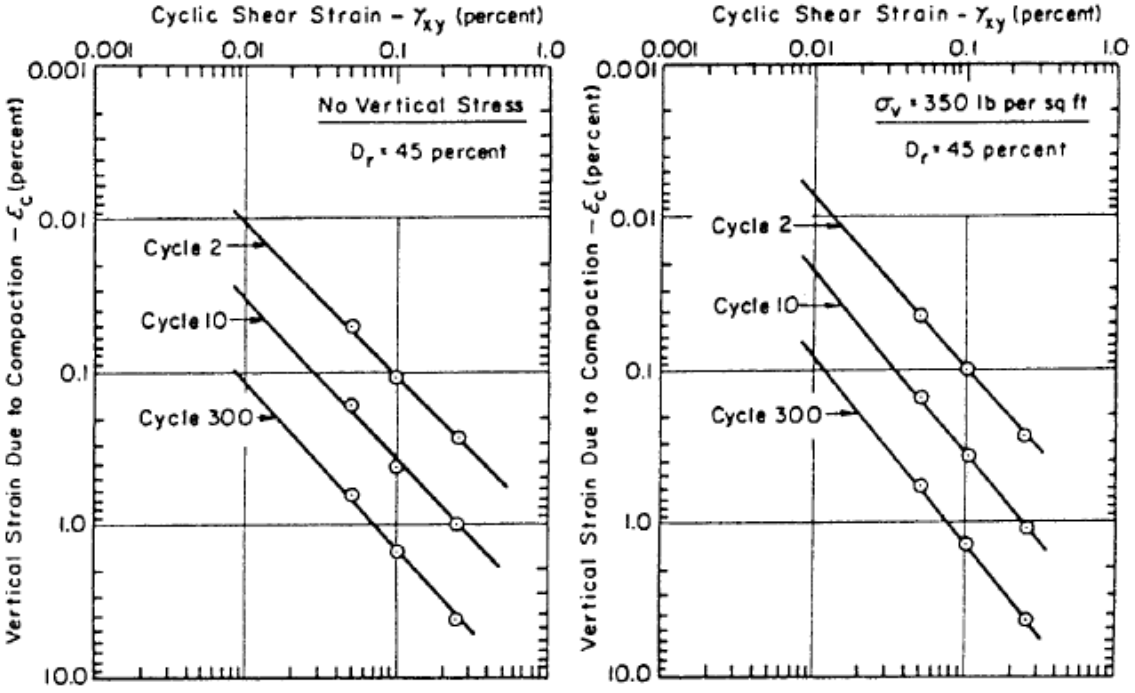

Figure 3-80 Vertical settlement versus shear strain for dry silica sand (from Seed and Silver 1972)

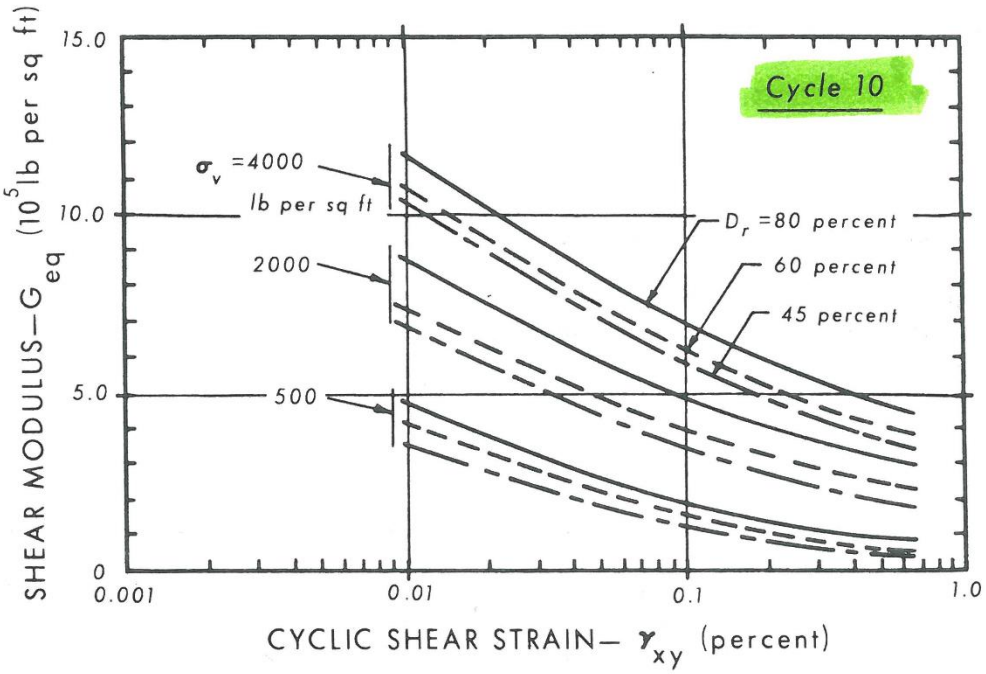

Figure 3-81 Effect of relative density and vertical stress on shear modulus in tenth loading cycle (from Silver and Seed 1971)

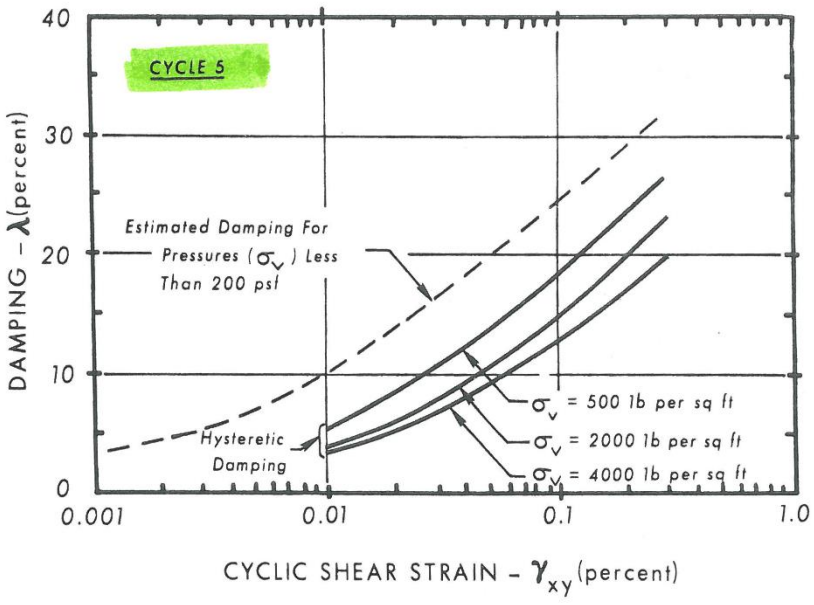

Figure 3-82 Effect of vertical stress on hysteretic damping in fifth loading cycle (from Silver and Seed 1971)

Youd (1972) conducted cyclic shear tests on dry and saturated (totally drained) Ottawa sand samples using an NGI simple shear apparatus to define their compaction behavior. Up to 150,000 cycles of shear were applied to samples at shear strain amplitudes ranging from 0.1% to 9% under vertical stresses ranging from 100 psf to 4,000 psf. This study overlaps in part the work by Silver and Seed (1971) who also performed cyclic shear tests on silica sand, for up to 300 cycles of shear at shear strains ranging from 0.01% to 0.63% under vertical stresses ranging from 500 psf to 4,000 psf.

Youd showed that the rate of compaction increased markedly with shear strain amplitude, while no significant influence of vertical stress on compaction rate was observed. The latter is shown in Figure 3-83 where the change of void ratio in a given number of cycles is plotted as a function of cyclic shear strain amplitude for different vertical loads. A lack of compaction at strains less than 0.01% is observed even at the extrapolated 1,000 cycle curve (the shear strain test limit was 0.1%). A significant influence of cyclic shear strain, γ, on compaction rate is also evident in the plotted data. In the 10 to 115 cycles/min (0.17 to 1.9 Hz) frequency of straining range, no significant effect on the compaction behavior of Ottawa sand samples was observed, as shown in Figure 3-84. Also, no significant differences between the compaction behavior of the saturated and totally drained samples and those tested dry were observed. The conclusions reported by Silver and Seed were confirmed by Youd's work; the rate of compaction increases with shear strain amplitude and compaction is not significantly affected by normal pressure for shear strains exceeding 0.05%. Drnevich and Richart (1970) also reported that sands can be vibrated for many cycles at shearing strains less than 0.01% without a significant effect on their density.

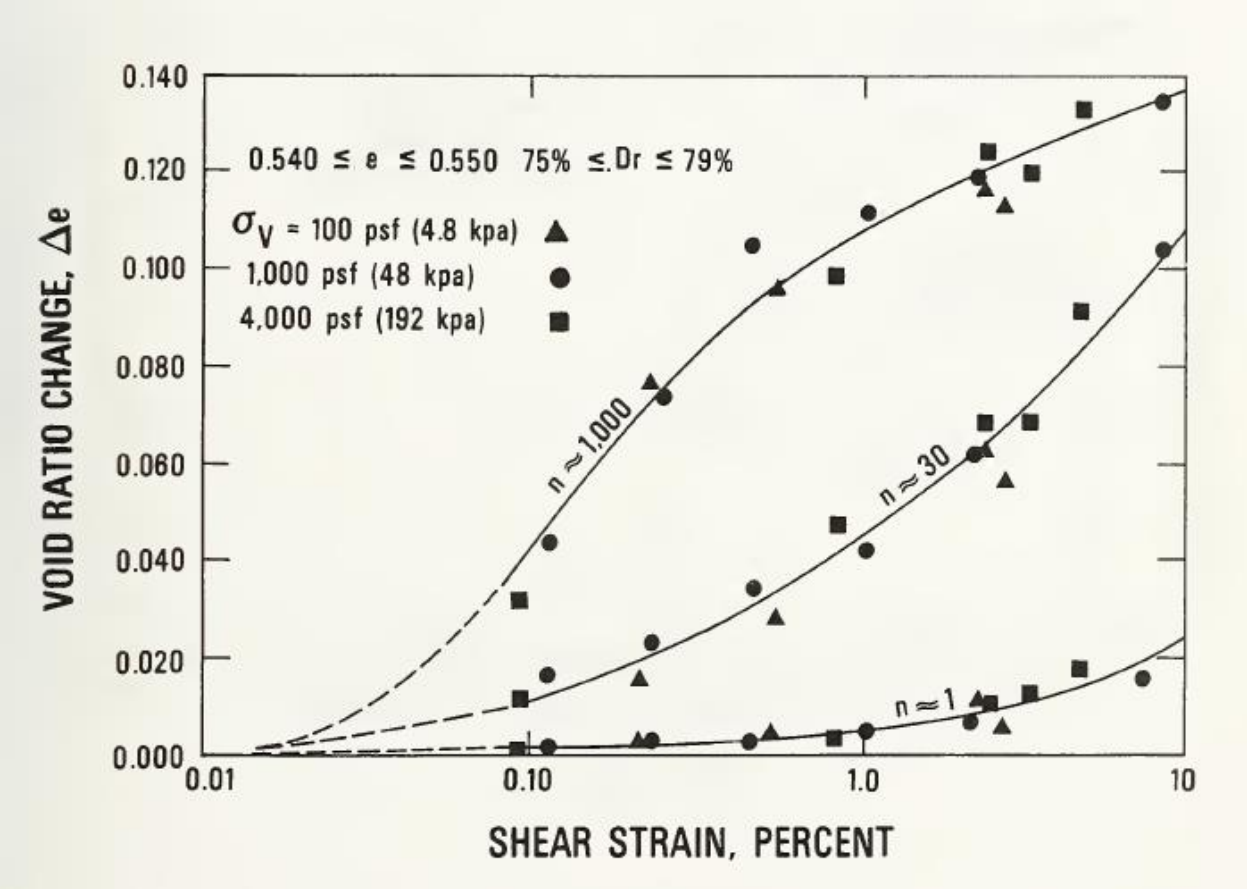

Figure 3-83 Void ratio change for a sand as a function of cyclic shear strain and number of cycles (from Youd 1972; after Dobry et al. 1982)

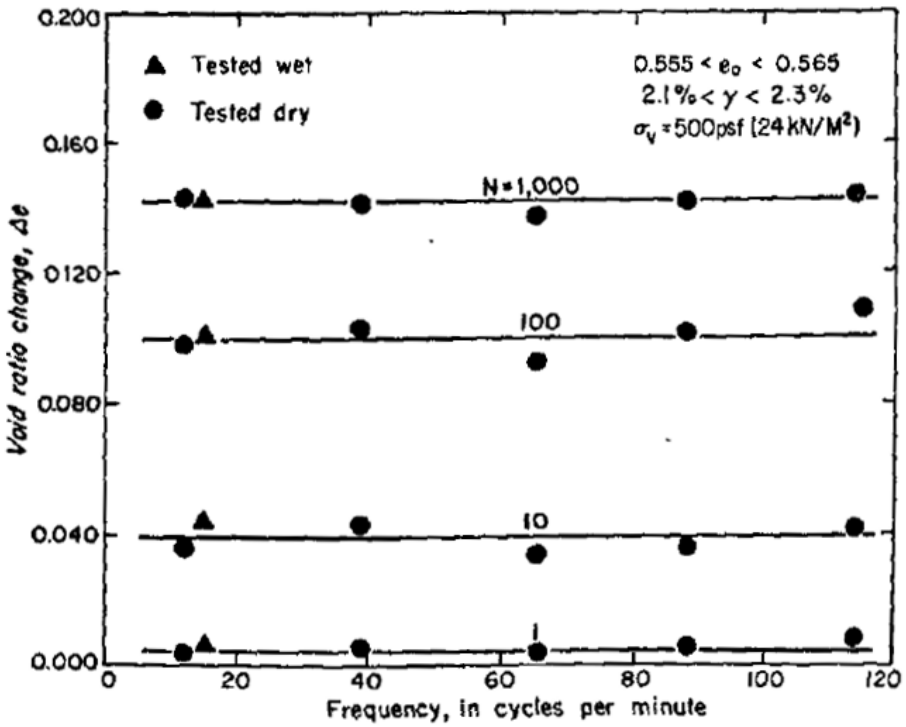

Figure 3-84 Non dependence of density change on frequency of straining (from Youd 1972)

Vucetic and Dobry (1991) reviewed a number of available cyclic loading test results of saturated specimens with different overconsolidation ratios (OCR) and different number of cycles. Figure 3-85 shows how the G/G_{max} curve moves up and the damping ratio curve moves down with increasing Plasticity Index (PI). Non-plastic soils like sands (PI=0) start to behave non-linearly at the smallest strain levels ($\gamma<0.001\%$), while soils with high plasticity behave linearly all the way to 0.01% shear strain. The effect of the number of cycles, N, on G/G_{max} for soils with PI=15 and 50 is shown in Figure 3-86. The relative effect of cyclic stiffness degradation, with respect to the initial G for N=1, is more significant for low plasticity than for medium or high plasticity soils. However, the modulus reduction curve is not affected as much as with the variation of the PI of the soil.

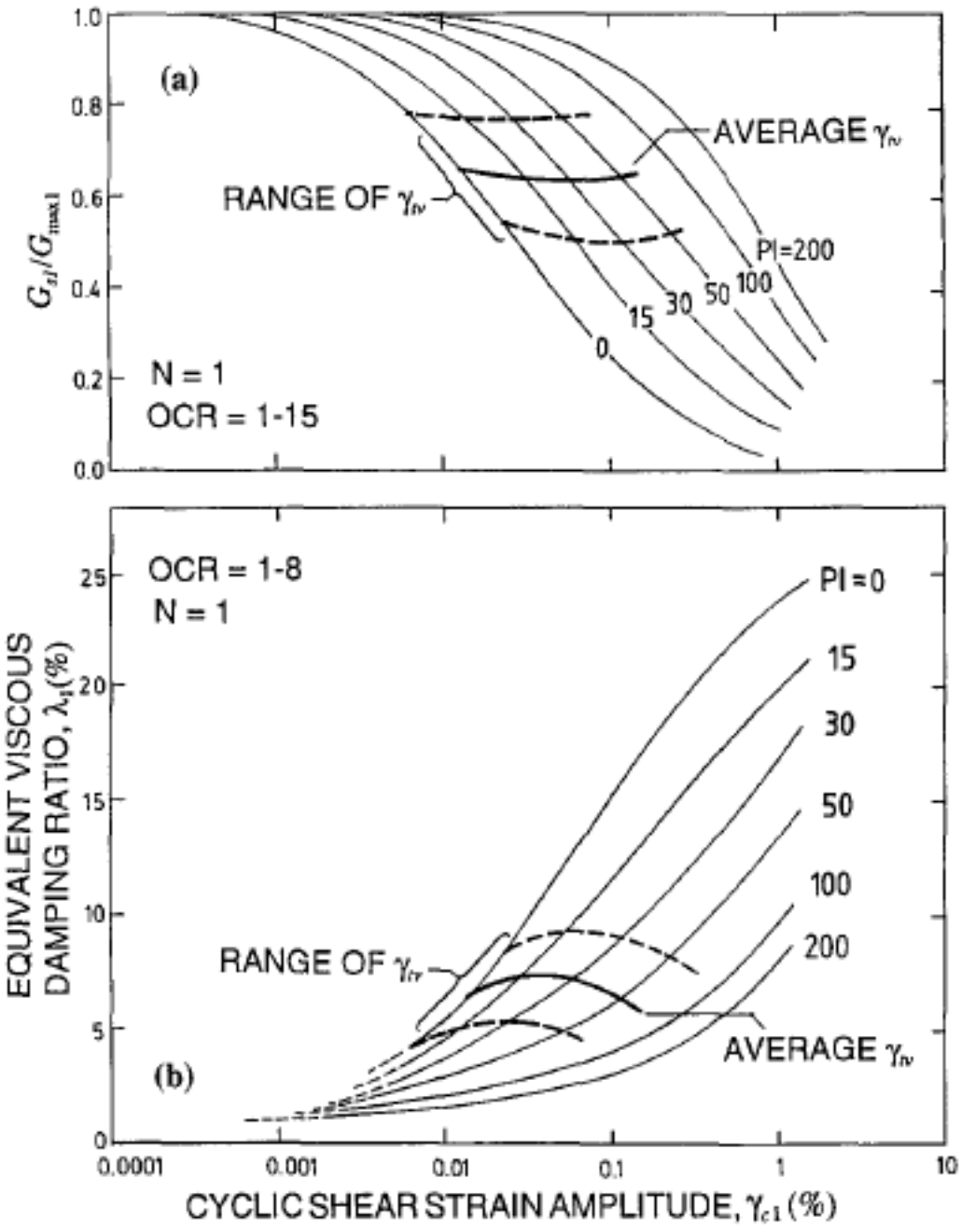

Figure 3-85 Relations between shear strain and modulus reduction and damping curves and soil plasticity for normally and overconsolidated soils (from Vucetic 1994)

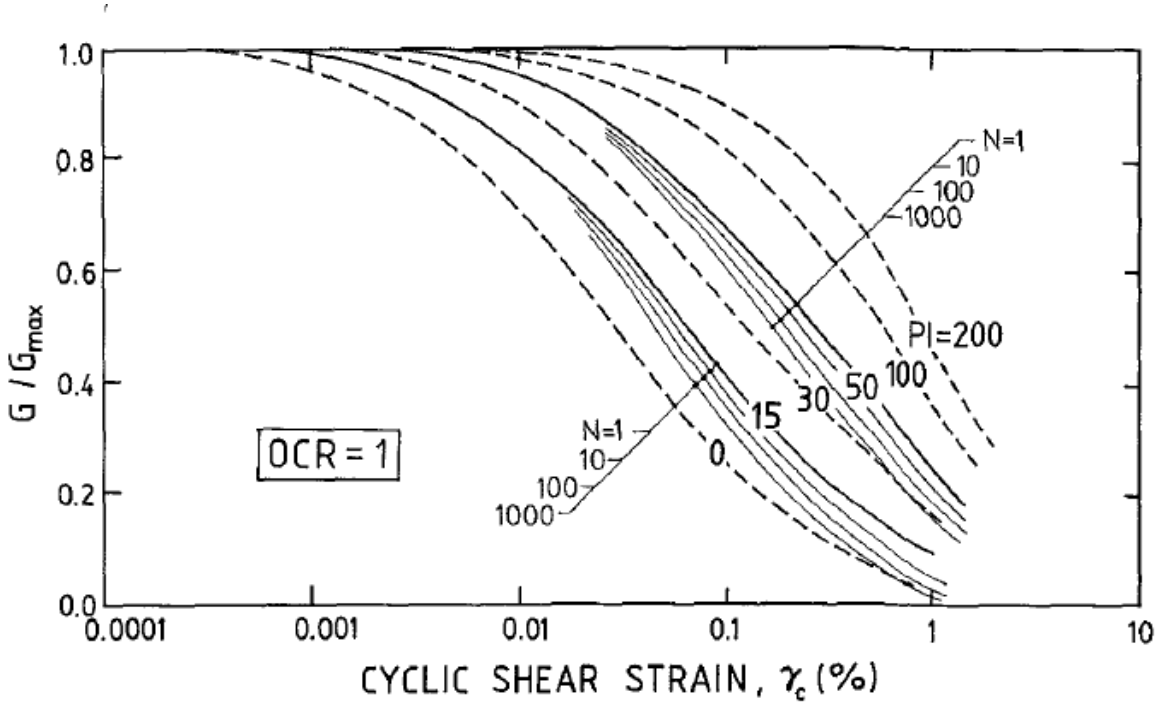

Figure 3-86 Effect of cyclic stiffness degradation on G/G_{max} versus γ_c curve for soils of different plasticity indices (from Vucetic and Dobry 1991)

Vucetic (1994) defined two types of cyclic threshold shear strain and discussed the influence of different parameters on them based on published laboratory data on different soils. The cyclic threshold shear strain above which a significant permanent volume change or permanent pore water pressure change may occur to the soil, is defined as the *volumetric threshold shear strain, γ_{tv}*. The *linear cyclic shear strain, γ_{tl}*, is defined the strain below which the soil behaves as a perfectly linearly elastic material. Ranges and definitions of the boundaries of the cyclic soil behavior are shown in Table 3.27. Figure 3-87 shows modulus reduction and damping curves for fully saturated soils in semilog scale; G_{sN} is the secant shear modulus at cycle N, G_{maxN} the maximum shear modulus at small strains and λ_N the damping ratio at cycle N. Values of the volumetric and linear shear strains were compiled from different studies (dry and fully saturated soils) and are presented versus the Plasticity Index in Figure 3-88. It is apparent that both strains increase with increasing PI and that the average curves of γ_{tv} and γ_{tl} are parallel and are

separated by about 1.5 log cycles. The approximate range and average line of γ_{tv} are incorporated in Figure 3-85. The horizontal trend of the threshold shear strain lines indicates that regardless of the soil type, the secant shear modulus must be reduced approximately by the same amount before the cyclic threshold shear strain is reached. The reduction obtained by this study is around 35%; G_{s1}/ G_{max1}=0.65. Another conclusion worth mentioning from this work is that sands have a lower threshold for volumetric strain, $\underline{\gamma_{tv} = 0.01\%}$, than clays, $\underline{\gamma_{tv} = 0.1\%}$ which makes them, of course, less flexible and more susceptible to densification.

Table 3.27 Ranges of γ_c (from Vucetic 1994)

Range of γ_c	**Linearity and Elasticity**	**Degradability for fully saturated soils cyclically sheared in undrained conditions**
$0 < \gamma_c \leq \gamma_{tl}$	Linear, Elastic	Essentially non-degradable
$\gamma_{tl} < \gamma_c \leq \gamma_{tv}$	Nonlinear, Slightly Elastoplastic	Practically non-degradable
$\gamma_c > \gamma_{tv}$	Nonlinear, Elastoplastic	Degradable

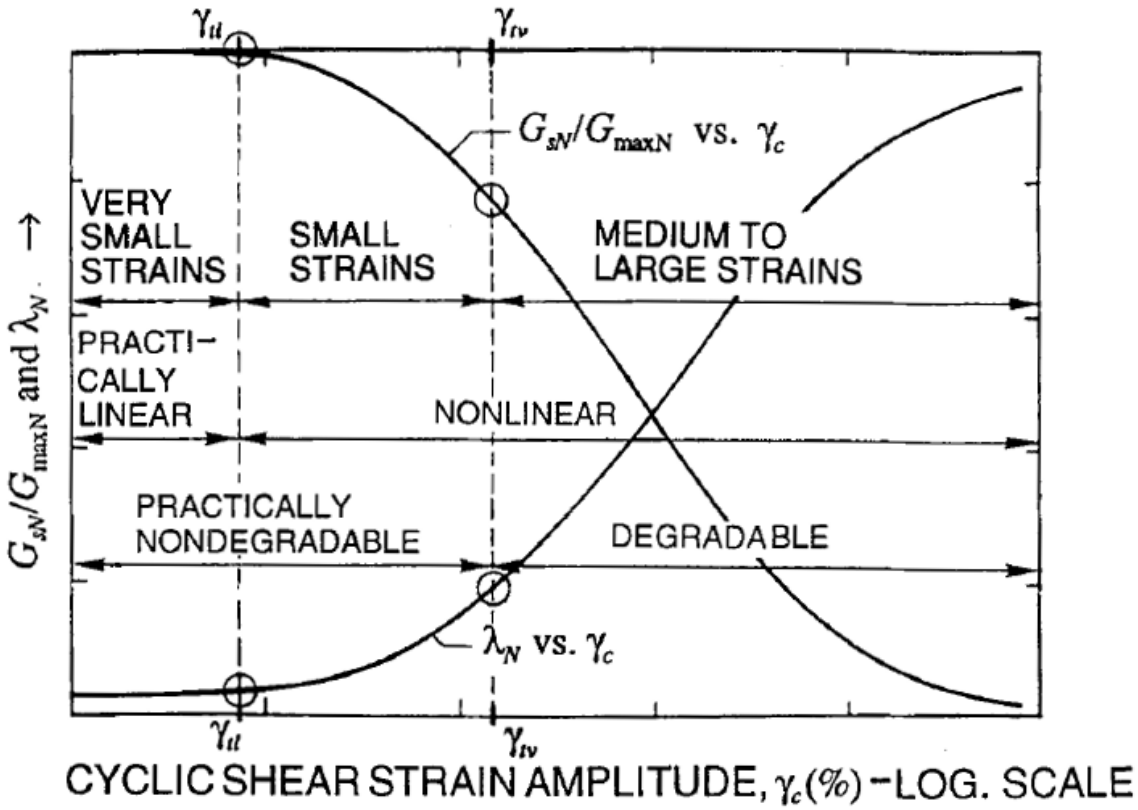

Figure 3-87 Secant shear modulus reduction curve and damping curve versus cyclic shear strain amplitude for fully saturated soils (from Vucetic 1994)

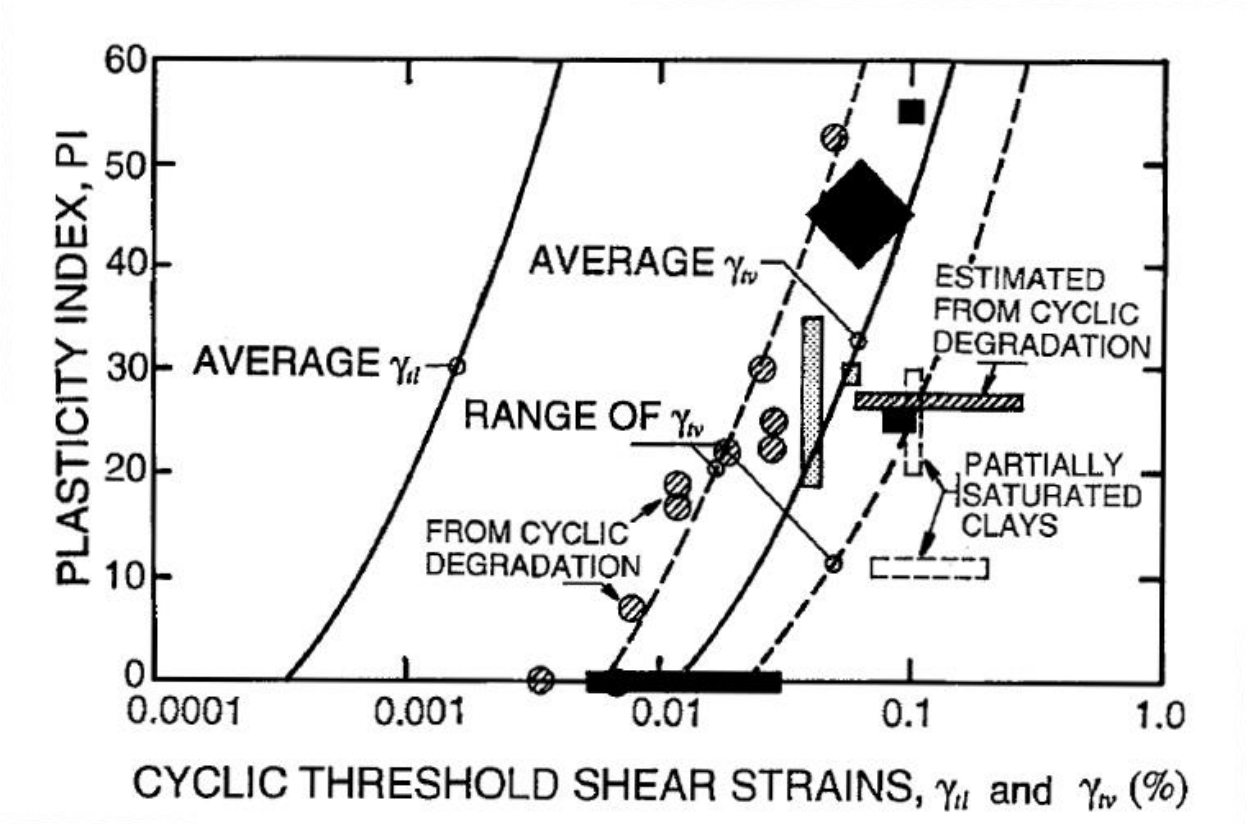

Figure 3-88 Effect of Plasticity Index on the cyclic threshold shear strains (from Vucetic 1994)

Hsu and Vucetic (2004) performed 11 multistage cyclic settlement tests on 7 different soils using the NGI direct simple shear device to investigate specifically the evaluation of the magnitude of the cyclic threshold shear strain. Each stage was conducted by applying a cyclic strain for a constant number of cycles, and then the strain was gradually increased. The number of cycles was varied in different tests which resulted in permanent, residual volume changes. The authors noticed that the rate of cyclic settlement was dependent on the permeability of the soil tested and for dry sands and soils with low degree of saturation was relatively high. Low rate of cyclic settlement was found for clayey soils. The cyclic threshold shear strain of sands is smaller than that of clays. Furthermore, γ_{tv} in clays generally increases with the plasticity index of the soil. The results were plotted along with data presented by others and are presented in Figure

3-89. The estimation of γ_{tv} values falls in a narrower range than previous findings, thus more consistent, but generally they are in a good agreement. No effect on γ_{tv} was found by varying the degree of saturation in one sand and the vertical consolidation stress in one of the clays. The shear modulus reduction versus the cyclic shear strain for 5 of their tests is shown in Figure 3-90. It is apparent that the soil behavior is considerably nonlinear at $\gamma_c = \gamma_{tv}$. The secant shear modulus, G_s, was reduced approximately by 20 to 45% from the G_{max} value (G_s=0.55 to 0.80 G_{max} at $\gamma_c = \gamma_{tv}$).

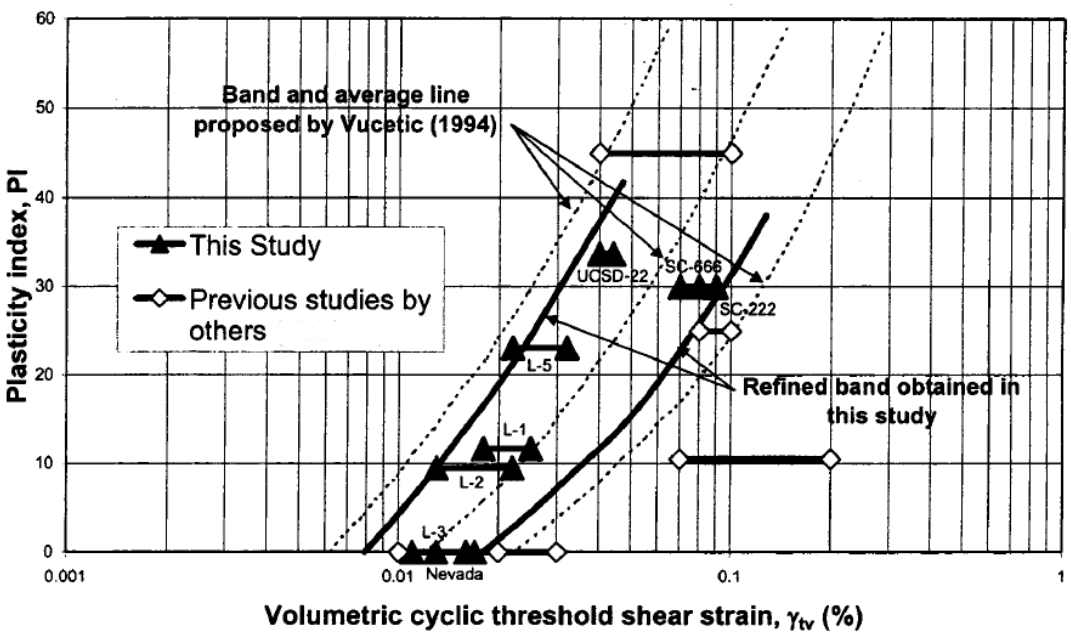

Figure 3-89 Effect of plasticity index on the volumetric cyclic threshold shear strain (from Hsu and Vucetic 2004)

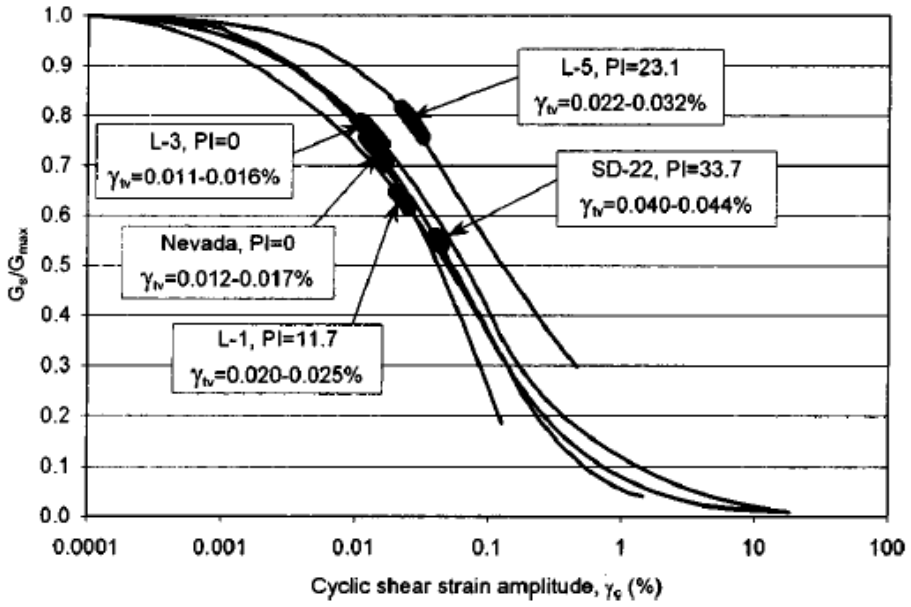

Figure 3-90 Relation between secant shear modulus and cyclic shear strain (from Hsu and Vucetic 2004)

Brandenberg et al. (2009) presented an interesting approach where they estimated shear strains during pile driving at a buried prehistoric archeological site. Measurements of ground motion were taken with triaxial surface accelerometers, and geophones embedded to depths of 1.2, 3.7 and 4.6 m at distances of 10 and 40 m from the pile driving operations. Eighty steel pipe piles were driven with a 180 kN impact hammer to depths around 20 m. Cone penetration tests provided the soil stratigraphy, whereas the shear wave velocity profile was measured using the seismic cone penetration test method. The upper 3 m of the soil consisted of gravelly sand fill, below which alluvial silty sand to sandy silt was encountered. Because this site was of historic significance the particle velocities from pile driving should not exceed the threshold of 2 mm/sec for such sensitive infrastructure. However, average maximum peak velocities reached values of 15.6 mm/sec indicating that potential damage was to be anticipated. The shear strain was taken approximately equal to the *displacement gradient,* du_z/dy, in this work.

The estimation of the displacement gradient was calculated with three different methods; (1) the difference of adjacent displacement records divided by the length between the two sensors, (2) the particle velocity divided by the wave velocity at the depth that the particle velocity was measured and (3) the particle velocity divided by the frequency dependent wave velocity from the dispersion curve. Methods 1 and 3 were generally in a good agreement, with method 2 exhibiting errors due to the use of the constant depth dependent wave velocity instead of the correct frequency dependent wave velocity. Figure 3-91 shows the plot of average peak displacement gradients versus depth computed with method 1 which ranged from 0.001 to 0.005%. Displacement gradients, hence shear strains, are larger at closer pile driving distances from the measuring point. Peak displacement gradients are plotted versus distance from pile driving in Figure 3-92. The Bornitz equation was fitted through the data with n=0.5 and α=0.01 m^{-1}. Measurements were taken only at two distances from the pile, so this is a very crude fitting, however, we can observe from this Figure that at a distance of 100 m from the pile, the peak amplitudes of strain will be lower than 0.001%. Even with the shear strains being less than the threshold strain associated to cause permanent vertical strains, 2-3 cm of settlement was observed in the vicinity of the pile driving activities (around 40 m). This indicates that construction vibrations that can induce tens of thousands of loading cycles in the soil, can potentially cause permanent settlement even with shear strains below the threshold value.

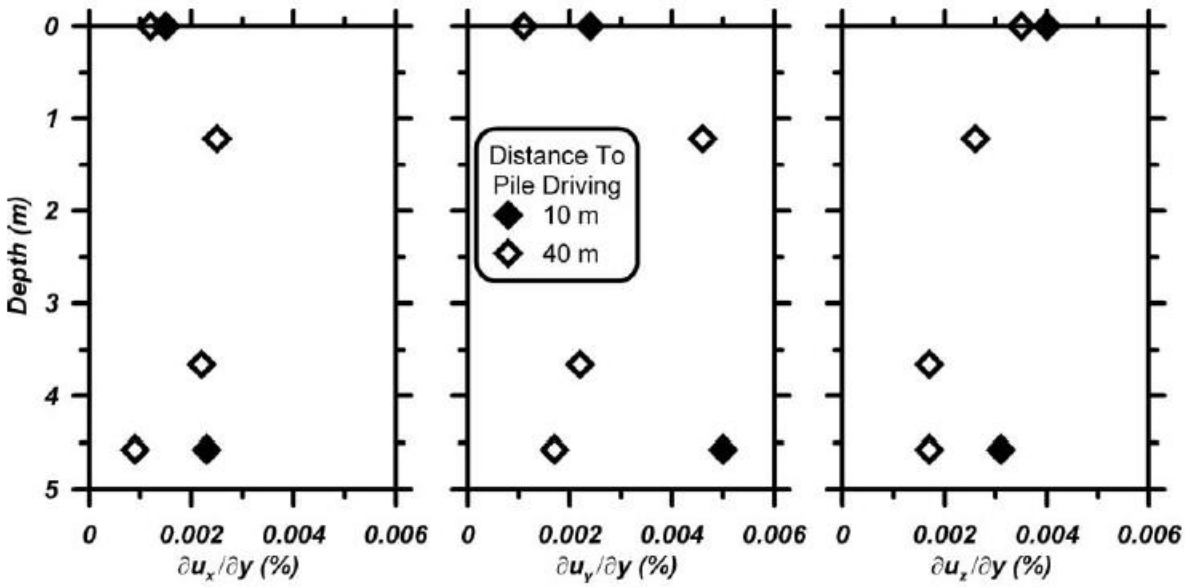

Figure 3-91 Average of peak displacement gradients versus depth (from Brandenberg et al. 2009)

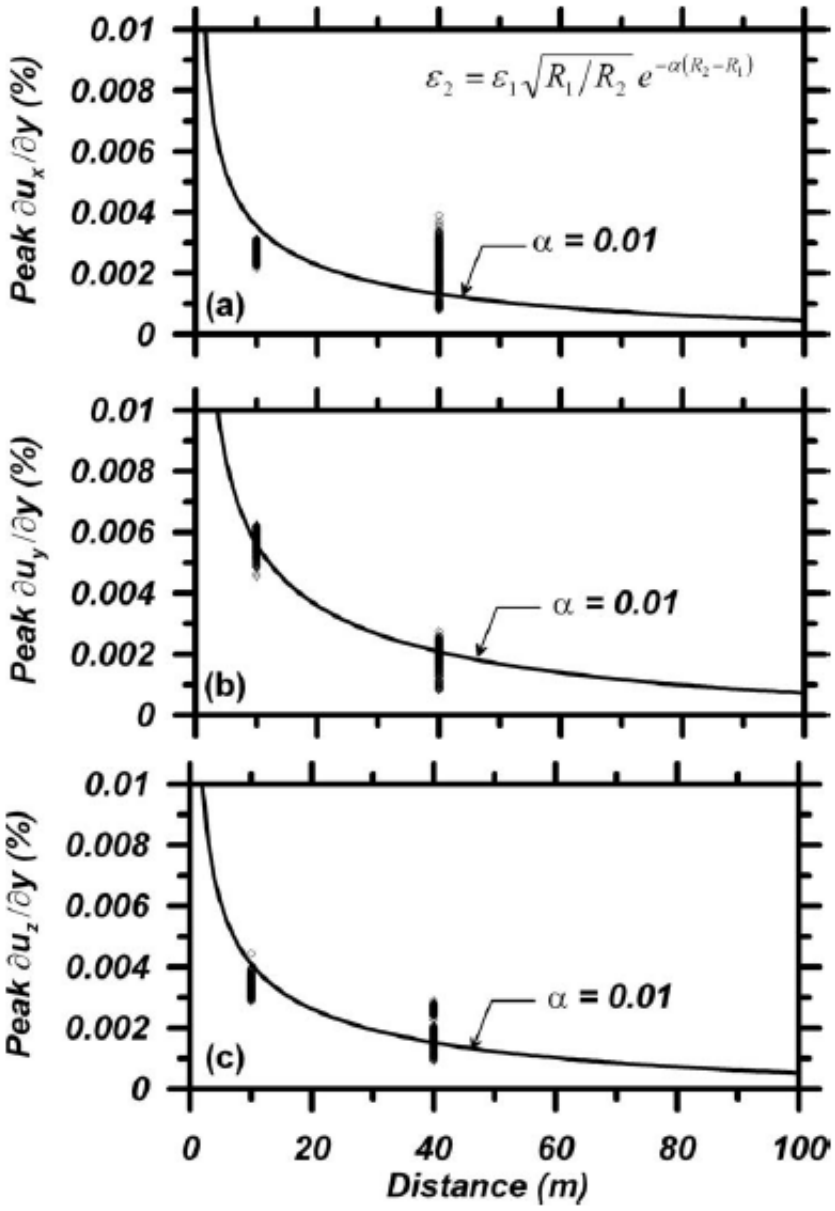

Figure 3-92 Attenuations of displacement gradients with distance from pile driving (from Brandenberg et al. 2009)

Mohamad and Dobry (1987) presented charts to determine the maximum cyclic shear strain induced by Rayleigh waves in terms of peak particle velocity and shear wave velocity of a soil deposit. The method is based on the strain approach developed to predict liquefaction potential due to earthquakes (Dobry et al. 1982). It is assumed that cylindrical Rayleigh waves can be approximated as plane Rayleigh waves, thus using expressions developed for the latter. The expression of maximum cyclic shear strain, γ_{max} is:

$$\gamma_{max} = \frac{v\ m}{V_S \sqrt{\left(\frac{G}{G_{max}}\right)_{max}}} \qquad \text{Eq. 3-35}$$

where: v = peak particle velocity, horizontal or vertical
m = shear strain factor, m_x for horizontal PPV and m_z for vertical PPV (taken from plots in Figure 3-93)
V_S = shear wave velocity at small strains
$(G/G_{max})_{max}$ = effective modulus reduction factor at cyclic shear strain $\gamma=\gamma_{max}$

Figure 3-93 shows the variation of the shear strain factors with depth and Poisson's ratio, v, where L is the wavelength of the Rayleigh wave. An iterative procedure is implemented to find the shear wave velocity corresponding on a shear strain level. Firstly, a value of γ_{max} is assumed and the value of G/G_{max} is obtained by available relations between γ and modulus reduction for a similar soil by reported studies (e.g. Vucetic and Dobry 1991). The value of γ_{max} is calculated and is compared with the assumed value. If the two values are close the iteration stops. If not, the iteration continues taking as γ_{max} the value calculated from the previous step. The value of G/G_{max} of the last step is the desired reduction factor for the shear wave velocity.

To evaluate the threshold surface particle velocity, v_t, with the intensity of which densification of the soil will occur, the above equation is rearranged substituting γ_t for γ_{max}:

$$v_t = \frac{\gamma_t V_S \sqrt{\left(\frac{G}{G_{max}}\right)_t}}{m} \qquad \text{Eq. 3-36}$$

where $(G/G_{max})_t$ is the effective modulus reduction factor of the soil corresponding to γ_t. The authors evaluated the accuracy of the above expression to predict the critical velocity above which settlement would be expected with the case study of Clough and Chameau (1980) which has been discussed already. The critical particle velocity was calculated as 16.8 mm/sec, corresponding to 0.19g. From the measured values of acceleration and settlement that Clough and Cheamau were able to make, it was found that the predicted value agreed with the measured below which settlement occurred.

Mohamad and Dobry suggested that for most sands, the threshold strain is γ_t = 0.01%.

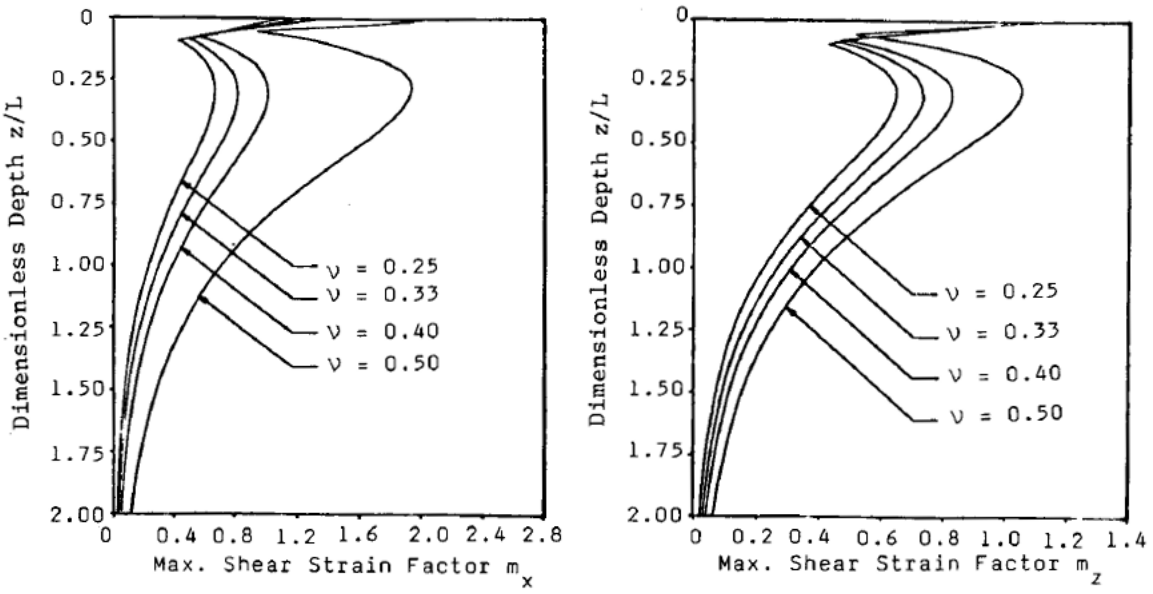

Figure 3-93 Shear strain factors for horizontal, m_x, and vertical, m_z, peak particle velocity (from Mohamad and Dobry 1987)

Massarsch (2000) reviewed studies from various researchers considering the threshold shear strain level, γ_t, and presented a simple chart showing the relationship between particle velocity and shear wave velocity due to ground vibrations for three different levels of shear strain in relation to the risk for settlement in sand (Figure 3-94). For a shear strain level of $\gamma = 0.001$ % there is almost no risk of ground settlement or strength loss. The shear strain level $\gamma_t = 0.01$ % indicates the threshold shear strain, which if exceeded the risk of settlement of sandy soils increases. At $\gamma = 0.1$ % and above, there is a significant risk of settlement. A first assessment of the risk of settlement when sandy soils are subjected to ground vibrations is possible by using this simple chart. It is important to note that this chart does not include the effect of the number of load cycles, which is important for man-made construction operations and would decrease the threshold level of shear strain.

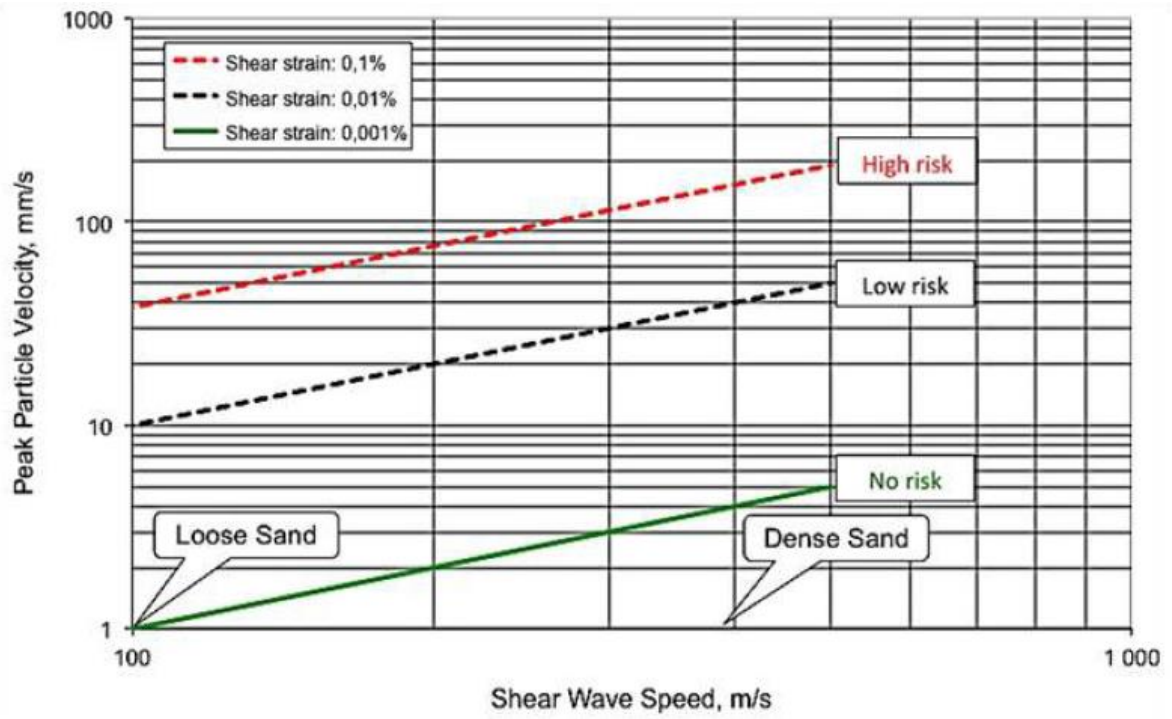

Figure 3-94 Settlement risk in sand as a function of shear wave speed and particle velocity (from Massarsch and Fellenius 2014)

The shear wave velocity that is measured in the far field by seismic tests at low shear strains, should be adjusted for large levels of shear strains. As seen from the above studies, the shear modulus, thus the shear wave velocity, at large strains is significantly lower than the elastic shear modulus. The decrease of the shear modulus and the shear wave velocity can be expressed by the following equations:

$$G = R_G G_{max} \quad \text{Eq. 3-37}$$

$$V_S = R_S V_{Smax} \quad \text{Eq. 3-38}$$

$$R_S = \sqrt{R_G} \quad \text{Eq. 3-39}$$

where: G = shear modulus at a given strain
G_{max} = shear modulus at low strain
V_S = shear wave velocity at a given strain
V_{Smax} = shear wave velocity at low strain
R_G = reduction factor of shear modulus
R_S = reduction factor of shear wave velocity

Figure 3-95 shows the result of a resonant column test on a medium dense sand. Once the critical shear strain level of 0.001 % is exceeded, the shear modulus and shear wave velocity decrease. For a shear strain of 0.1 %, the reduction factors R_G and R_S are calculated as 0.33 and 0.59, respectively. The shear wave velocity at shear strain levels of 1 % (very close to the source at a plastic zone) can decrease to 0.15 or 0.20 of the shear wave velocity at low strains (elastic zone). **Massarsch (1999)** identified three zones around the vibration source:

- *Plastic zone*: the soil is in failure condition and experiences large shear strain levels of $\gamma > 10^{-1}$ %
- *Elasto-plastic or non-linear zone*: some permanent deformations occur and the shear strain levels are between 10^{-3} % < γ < 10^{-1} %
- *Elastic zone*: no permanent deformations are expected; shear strain levels are below $\gamma < 10^{-3}$ %

The three zones in the vicinity of a driven pile are shown in a schematic in Figure 3-96. It is also seen in this Figure that the shear wave velocity is strain dependent and increases with increasing distance from the source. The opposite stands for the particle velocity; the vibration amplitude attenuates as the waves propagate through the ground and away from the source.

Döringer (1997) reviewed results from resonant column tests. A regression analysis of data from tests in cohesive and low-plastic soils provided a relationship for the shear modulus reduction factor as a function of the plasticity index and the shear strain:

$$\frac{G}{G_{max}} = \frac{1}{[1 + \alpha\,\gamma(1 + 10^{-\beta\gamma})]} \qquad \text{Eq. 3-40}$$

$$\alpha = \frac{794}{I_P{}^{0.36505}} \qquad \text{Eq. 3-41}$$

$$\beta = 0.046 + 0.5475\ \log I_P \qquad \text{Eq. 3-42}$$

where: I_P = plasticity index

The above relationship is shown in Figure 3-97 for the shear wave velocity reduction factor. Soils with low plasticity, such as sands and silty sands, experience the highest reduction of shear wave velocity. Again, there is a critical shear strain value above which the shear wave velocity starts to decrease and this reduction becomes more pronounced with increasing shear strain levels.

Table 3.28 has a summary of the reported thresholds of shear strains reported by different researchers. It is important to remember that this threshold can be much smaller for high numbers of cycles of loading, which is typical for pile driving induced vibrations.

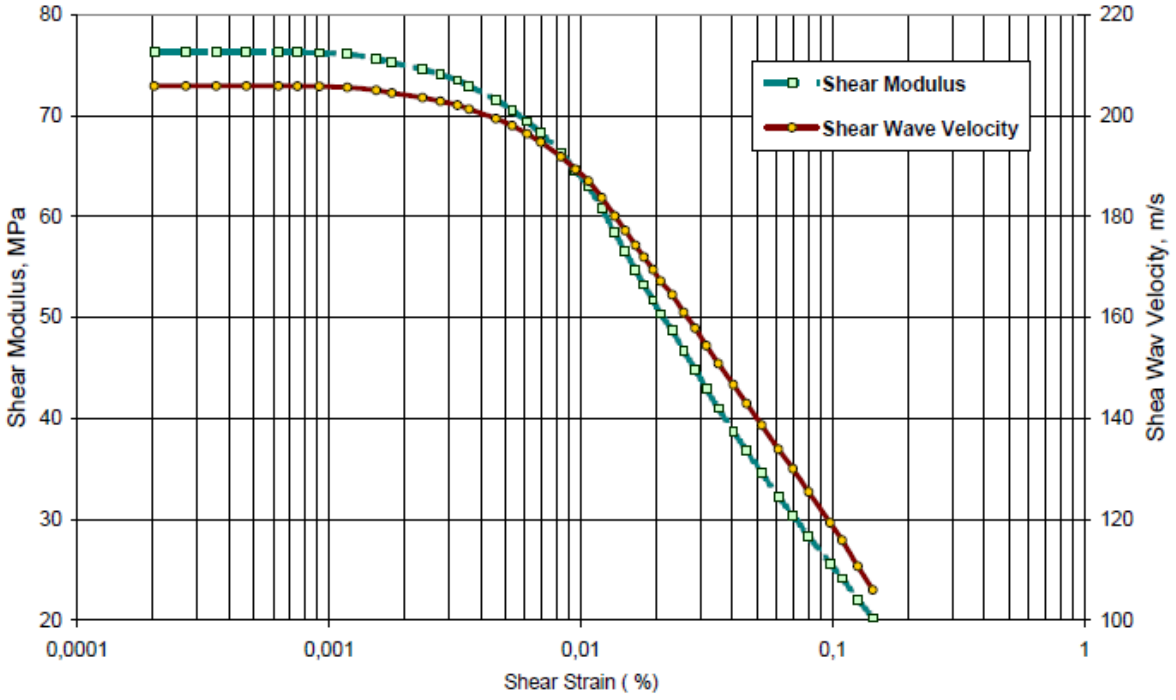

Figure 3-95 Resonant column test on a medium dense sand with the variation of shear modulus (left axis) and shear wave velocity (right axis) with shear strain (from Massarsch 2000)

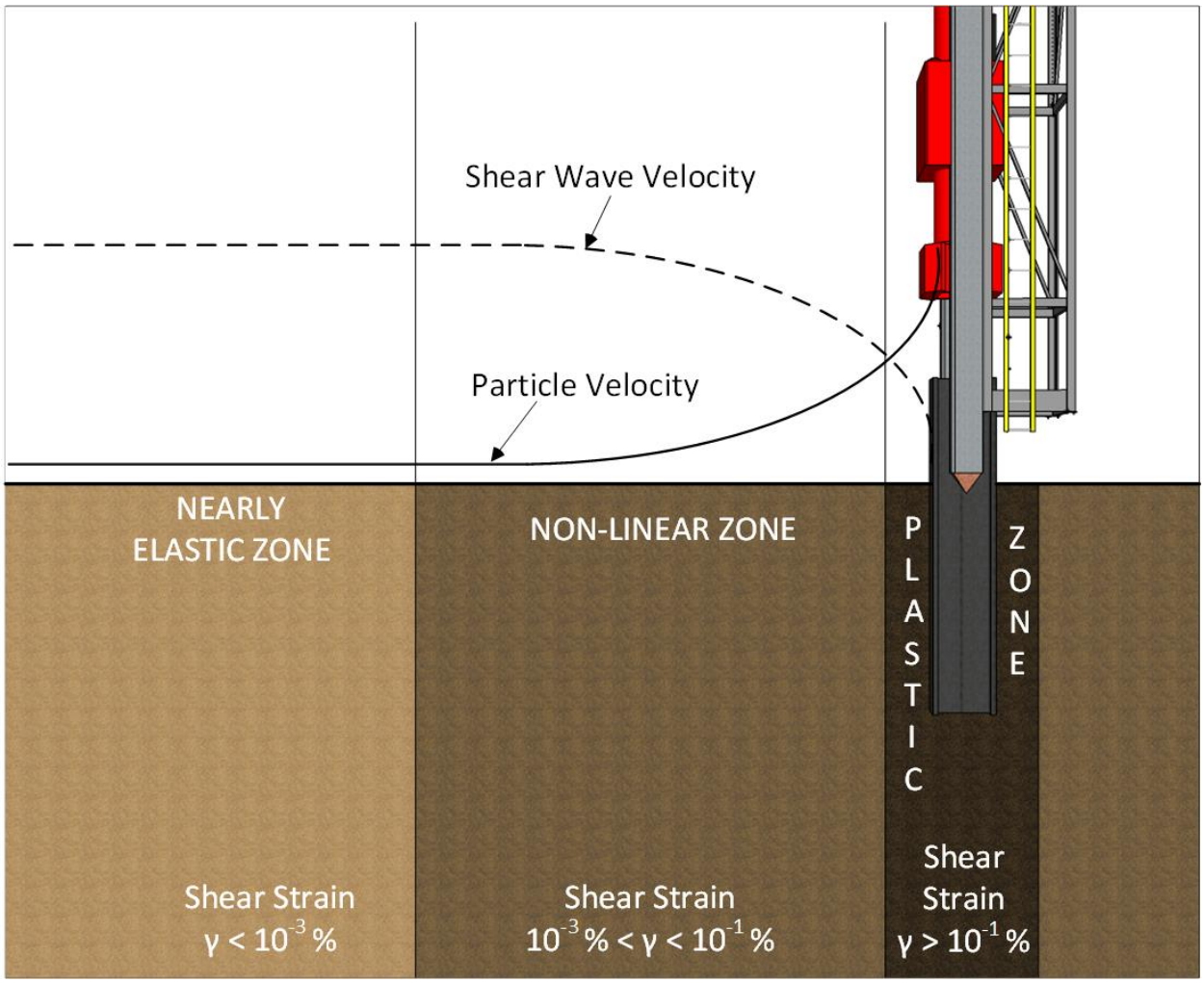

Figure 3-96 Hypothetical soil behavior zones near driven pile (modified after Massarsch 1999)

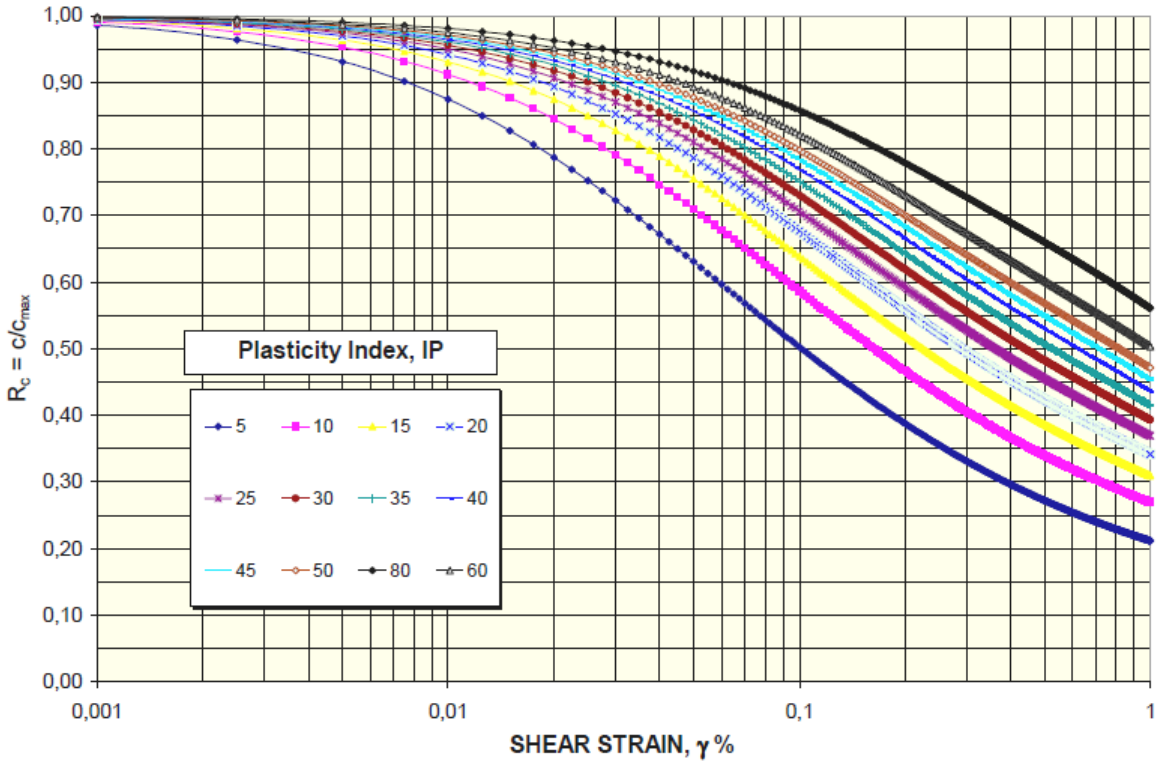

Figure 3-97 Shear wave velocity reduction factor as a function of shear strain and plasticity index (from Döringer 1997)

Table 3.28 Reported thresholds of cyclic shear strain, γ_t, on sands

Cyclic Shear Strain Threshold, γ_t	Reference	Notes
$\gamma_t \approx 0.01\%$	Seed and Silver (1972)	Cyclic shear tests; N ≤ 300
$\gamma_t = 0.01\%$	Youd (1972)	Cyclic shear tests; N ≤ 150,000
$\gamma_t = 0.01\%$	Dobry et al. (1982)	For liquefaction; N = 10
$\gamma_t = 0.001\%$	Massarsch (2000)	Review of studies; many cycles
$\gamma_t < 0.01\%$	Hsu and Vucetic (2004)	Multistage cyclic shear tests with 10 cycles each stage
$\gamma_t = 0.001\%$	Brandenberg et al. (2009)	Pile driving vibrations; many cycles

CHAPTER 4 PILING EQUIPMENT AND METHODS

Piles are structural elements of small cross-sectional area compared to their length, that transfer loads from weak soils to stronger and deeper soil layers. Piles are classified based on: (1) the type of material, (2) the mechanism of load transfer and (3) the method of installation.

4.1 Types of Piles

4.1.1 Classification of piles based on the pile material

The principal materials that piles are constructed of are timber, concrete and steel. Trees were used for piling from the Roman times. *Timber piles* are still being used as deep foundations with an average length of 33 – 66 ft (10 – 20 m) and are suitable for light loadings with a typical range of 18 – 55 kips (80 – 240 kN). They have low cost compared to steel and concrete piles and are either untreated or treated with preservatives to resist decay due to microbes, fungus and insects. When placed below the groundwater level, where there is not significant amount of oxygen, timber piles can technically last forever. Typical timber piles are shown in Figure 4-1.

Concrete piles can be divided in two main categories, precast and cast-in-place piles. Precast piles may be conventionally reinforced or prestressed. They are usually manufactured at the construction site in order to avoid intolerable tensile stresses, which can be caused in handling and transportation (Gunaratne 2006). Their use is very common in marine and river structures where the use of cast-in-place piles is impractical and uneconomical (Tomlinson and Woodward 2014). Typical lengths of precast piles range from 33 – 82 ft (10 – 25 m) and load bearing capacities can reach up to 200 kips

(900 kN) for reinforced and 1900 kips (8500 kN) for prestressed piles. Precast pile elements are shown in Figure 4-2. Cast-in-place piles may be cased or uncased. A hole is drilled into the ground (a steel tube is driven first for the cased type) and a reinforcement steel cage is inserted. The pile is then cast by pouring concrete into the hole. The constructions sequence is presented in Figure 4-3. Their principal advantage is that they can be readily formed to the desired depth of penetration. Typical load capacities range from 80 – 450 kips (350 – to 2000 kN). Another technique to install cast-in-place piles is by using a continuous flight auger (CFA or auger-cast piles). The auger has a hollow stem and once the soil is displaced, concrete is pumped down the stem while the auger is pulled up.

Steel pipes, H-sections and sheet piles are widely used especially if conditions call for hard driving, unusually great lengths or high working loads per pile (Peck et al. 1974). They can be readily shortened or extended by cutting or welding. Hollow-section piles are either cylindrical or of box type sections and can be driven either open-ended or closed-ended, where in the latter type the bottom of the pipe is closed with a steel plate or a tapered point welded to the pipe and is usually filled with concrete after being driven (Fuller 1983). A perspective of closed-ended steel pipes is shown in Figure 4-4. Box section piles are typically formed by welding two or four Z section or U section sheet piles, edge to edge, to form a box (Fleming et al. 2008). Typical cross-sections of U and Z sections are presented in Figure 4-5. Typical H sections, which are of interest in the current research, are given in Table 4.1. Figure 4-6 shows driven H-piles with one of them ready to be driven in one of the sites tested. H-piles are available in 8, 10, 12, 14, 16 and 18 inch sections in lengths up to 100 ft (30 m)

A combination of materials in driven piles can be used to overcome particular site or ground condition problems (Tomlinson and Woodward 2014). A precast concrete pile above a timber section is an example of a composite pile which is used to face the problem of decay in timber piles above the groundwater level. Micropiles are a special category of bored piles; their diameter is in the range of 6 – 10 in (150 – 250 mm) and their load capacities fall in the range of 4.5 – 110 kips (20 – 500 kN).

4.1.2 Classification of piles on the basis of load transfer

The two main categories that piles can be classified according to their load transfer mechanism are *end bearing piles* and *friction piles*. In end bearing piles, the pile acts as a column and carries the load to a bedrock or rock-like material. This is very important for sites that consist of weak soil layers, which the load has to bypass and be transferred to the hard stratum. On the other hand, friction piles transfer the load to the soil, across the full length of the pile, by friction of soil in contact with the shaft of the pile.

4.1.3 Classification of piles based on the installation technique

Piles can be classified into two categories depending on the degree of soil displacement during installation: (i) *replacement (or bored or drilled) piles* and (ii) *displacement (or driven) piles*. In the former, there is no removal of soil, while in the latter a hole is previously bored, and the removed soil is replaced by concrete (Viggiani et al. 2012). Cast-in-place and continuous flight auger piles are examples of replacement piles. Driven piles can be either large-displacement or small-displacement. Solid or hollow-sections with a close-ended displace the soil when driven and fall into the large volume displacement category. Steel open-ended piles and H sections are considered small volume displacement piles since they have thin cross sections. If the soil enters the pile section of an H pile (between the flanges and the web) during driving and moves down with the pile, the open end section becomes plugged. When this plug formation at the toe of the pile happens, they become large volume displacement piles.

Figure 4-1 Installation of timber piles (Courtesy of DEMLER Spezialtiefbau GmbH and Co.)

Figure 4-2 Precast concrete piles (Courtesy of Structural Concrete Industries)

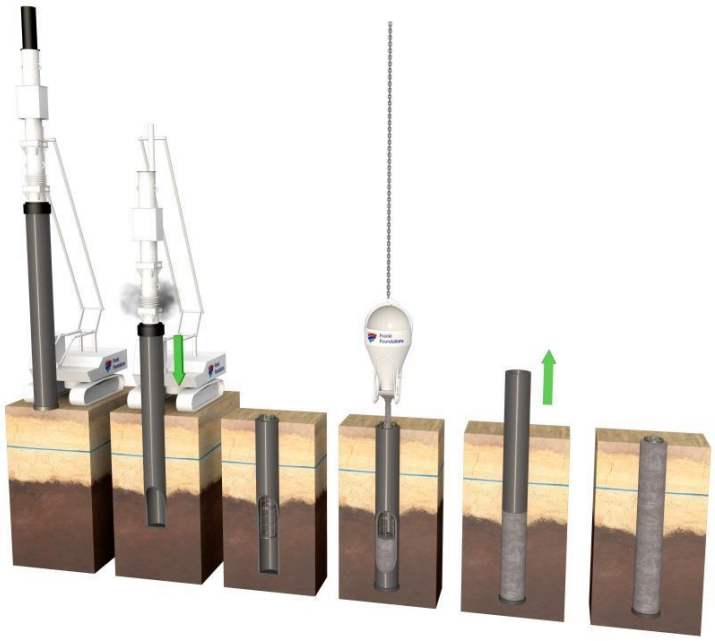

Figure 4-3 Cast-in-place concrete pile construction sequence (Courtesy of Franki Foundations S.A.)

Figure 4-4 Closed-ended steel pipes (Courtesy of Qiancheng Steel-Pipe Co., Ltd.)

(a)

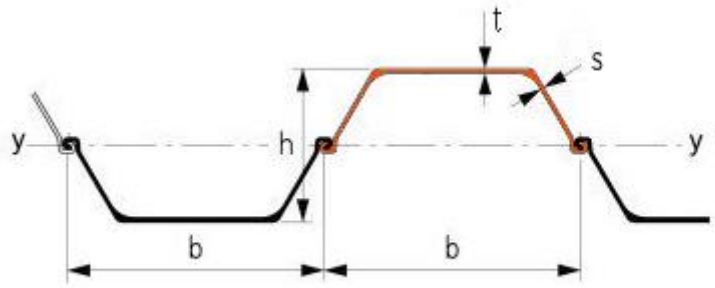

(b)

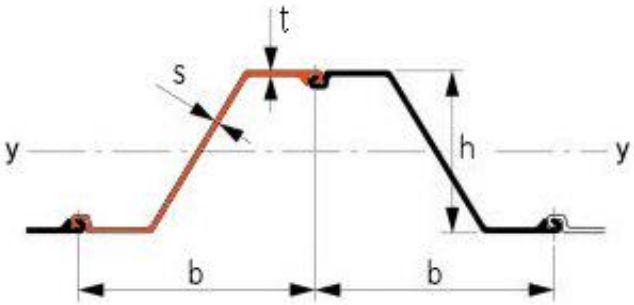

Figure 4-5 Typical cross sections of (a) U and (b) Z sheet piles (Courtesy of ArcelorMittal Commercial RPS Ltd.)

Figure 4-6 H-piles in one of the tested sites for this project

Table 4.1 Properties of H section piles (taken from R. W. Conklin Steel)

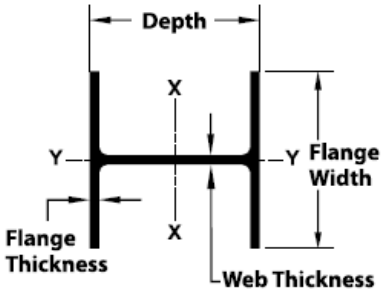

H-Piling is used in a variety of construction projects including, heavy highway, public works, marine, industrial, and more. We stock a wide variety of domestically produced H-Pile available in single lengths or multiple truckloads. H-Pile is available in 8, 10, 12, 14, 16 and 18-inch sections, and in lengths over 100 feet.

SECTION SIZE	WEIGHT	AREA	DEPTH	FLANGE WIDTH	THICKNESS: FLANGE	THICKNESS: WEB	COATING AREA	ELASTIC PROPERTIES: AXIS X-X I	AXIS X-X S	AXIS X-X r	AXIS Y-Y I	AXIS Y-Y S	AXIS Y-Y r
	lb/ft (kg/m)	in² (cm²)	in (mm)	in (mm)	in (mm)	in (mm)	ft²/ft (m²/m)	in⁴ (cm⁴)	in³ (cm³)	in (cm)	in⁴ (cm⁴)	in³ (cm³)	in (cm)
HP 8″ HP 200 mm	36 54	10.6 68.4	8.02 204	8.155 207	0.445 11.3	0.445 11.3	3.92 1.19	119 4950	29.8 487	3.36 8.53	40.3 1680	9.88 162	1.95 4.60
HP 10″ HP 250 mm	42 63	12.4 80.0	9.70 246	10.075 256	0.420 10.7	0.415 10.5	4.83 1.47	210 8740	43.4 711	4.13 10.5	71.7 2980	14.2 233	2.41 6.12
	57 85	16.8 108	9.99 254	10.225 260	0.565 14.4	0.565 14.4	4.91 1.50	294 12200	58.8 969	4.18 10.6	101 4200	19.7 323	2.45 6.22
	53 79	15.5 100	11.78 299	12.045 306	0.435 11.0	0.435 11.0	5.82 1.77	393 16400	66.9 1090	5.03 12.8	127 5290	21.1 346	2.86 7.26
HP 12″ HP 310 mm	63 94	18.4 119	11.94 303	12.125 308	0.515 13.1	0.515 13.1	5.86 1.79	472 19600	79.1 1290	5.06 12.9	153 6370	25.3 415	2.88 7.32
	74 110	21.8 141	12.13 308	12.215 310	0.610 15.5	0.605 15.4	5.91 180	569 23700	93.8 1530	5.11 13.0	186 7740	30.4 498	2.92 7.42
	84 125	24.6 159	12.28 312	12.295 312	0.685 17.4	0.685 17.4	5.97 1.82	650 27100	106 1730	5.14 13.1	213 8870	34.6 567	2.94 7.47
	73 109	21.4 138	13.61 346	14.585 370	0.505 12.8	0.505 12.8	6.96 2.12	729 30300	107 1770	5.84 14.8	261 10900	35.8 587	3.49 8.86
HP 14″ HP 360 mm	89 132	26.1 168	13.83 351	14.695 373	0.615 15.6	0.615 15.6	7.02 2.14	904 37600	131 2150	5.88 14.9	326 13600	44.3 726	3.53 8.97
	102 152	30.0 194	14.01 356	14.785 376	0.705 17.9	0.705 17.9	7.06 2.15	1050 43700	150 2480	5.92 15.0	380 15800	51.4 842	3.56 9.04
	117 174	34.4 222	14.21 361	14.885 378	0.805 20.4	0.805 20.4	7.12 2.17	1220 50800	172 2830	5.96 15.1	443 18400	59.5 975	3.59 9.12
	88 131	25.8 167	15.33 389	15.665 398	0.540 13.7	0.540 13.7	7.52 2.29	1112 46295	145 2378	6.56 16.7	347 14425	44.0 725	3.66 9.31
	101 151	29.8 192	15.50 394	15.750 400	0.625 15.9	0.625 15.9	7.56 2.30	1297 53978	167 2742	6.60 16.8	408 16971	52.1 848	3.70 9.40
HP 16″ HP 410 mm	121 181	35.7 230	15.75 400	15.875 403	0.750 19.1	0.750 19.1	7.62 232	1578 65675	200 3283	6.65 16.9	501 20859	63.1 1035	3.75 9.52
	141 211	14.7 269	16.00 406	16.000 406	0.875 22.2	0.875 22.2	7.69 2.34	1871 77859	234 3832	6.70 17.0	599 24923	75.2 1227	3.79 9.63
	162 242	47.7 308	16.25 413	16.125 410	1.000 25.4	1.000 25.4	7.75 2.36	2175 90542	268 4387	6.75 17.2	701 29167	87.0 1424	3.83 9.74
	183 272	53.8 347	16.50 419	16.250 413	1.125 28.6	1.125 28.6	7.81 2.38	2492 103738	302 4951	6.81 17.3	807 33595	99.0 1628	3.87 9.84
	135 202	39.8 257	17.50 445	17.750 451	0.750 19.1	0.750 19.1	8.54 2.60	2196 91423	251 4114	7.43 18.9	700 29143	78.8 1293	4.19 10.7
HP 18″ HP 460 mm	157 234	46.2 298	17.74 451	17.870 454	0.870 22.1	0.870 22.1	8.60 2.62	2583 107516	291 4772	7.48 19.0	829 34512	93.0 1521	4.24 10.8
	181 269	53.2 343	18.00 457	18.000 457	1.000 25.4	1.000 25.4	8.66 2.64	3017 125579	335 5493	7.53 19.1	974 40545	108.1 1774	4.28 10.9
	204 304	60.0 387	18.25 464	18.125 460	1.125 28.6	1.125 28.6	8.73 2.66	3450 143598	378 6196	7.58 19.3	1119 46585	123.0 2024	4.32 11.0

4.2 Hammer Types

Displacement piles are driven into the ground by means of a *hammer or ram*. The pile driving equipment that will be employed depends on the driven pile, the soil and site conditions. Figure 4-7 shows the components of a typical driving system. The hammer operates between a pair of parallel guides or *leads* suspended by a lifting crane. The *spotter or brace* fixes the bottom of the leads to the crane. The *helmet or cap* is attached to the top of the pile to protect it from possible damage caused by the hammer. *Hammer cushions* between the hammer and the helmet, and *pile cushions* between the helmet and the pile are used to relieve the impact shock. Helmet and cushions affect the energy that the hammer will transmit to the pile and therefore it is very important to be inspected before the pile driving operation. There are two main types of pile hammers: impact hammers and vibratory hammers. Impact hammers use different sources of power (gravity, air, steam, hydraulics and diesel) and advance the penetration of the pile into the ground by a series of short duration impacts. Vibratory hammers introduce continuous sinusoidal vibration into the pile during the procedure of driving. The following section is a discussion of the various types of hammers.

4.2.1 Drop Hammers

The drop hammer is the simplest and oldest type of driving hammer and consists of a weight which is suspended by a rope or cable, raised through a pulley and released to drop free on the pile head. The energy is adjusted by varying the drop height which varies between 0.2 to 2 m (Fleming et al. 2008). When driving to stiff soil, a drop hammer can cause damage to the pile head from excessive driving stresses. Its slow operating speed (blows per minute) does not make it a preferable choice over other more sophisticated hammers except for specific projects and applications (Deep Foundations Institute: Pile Inspector’s Guide to Hammers 1995).

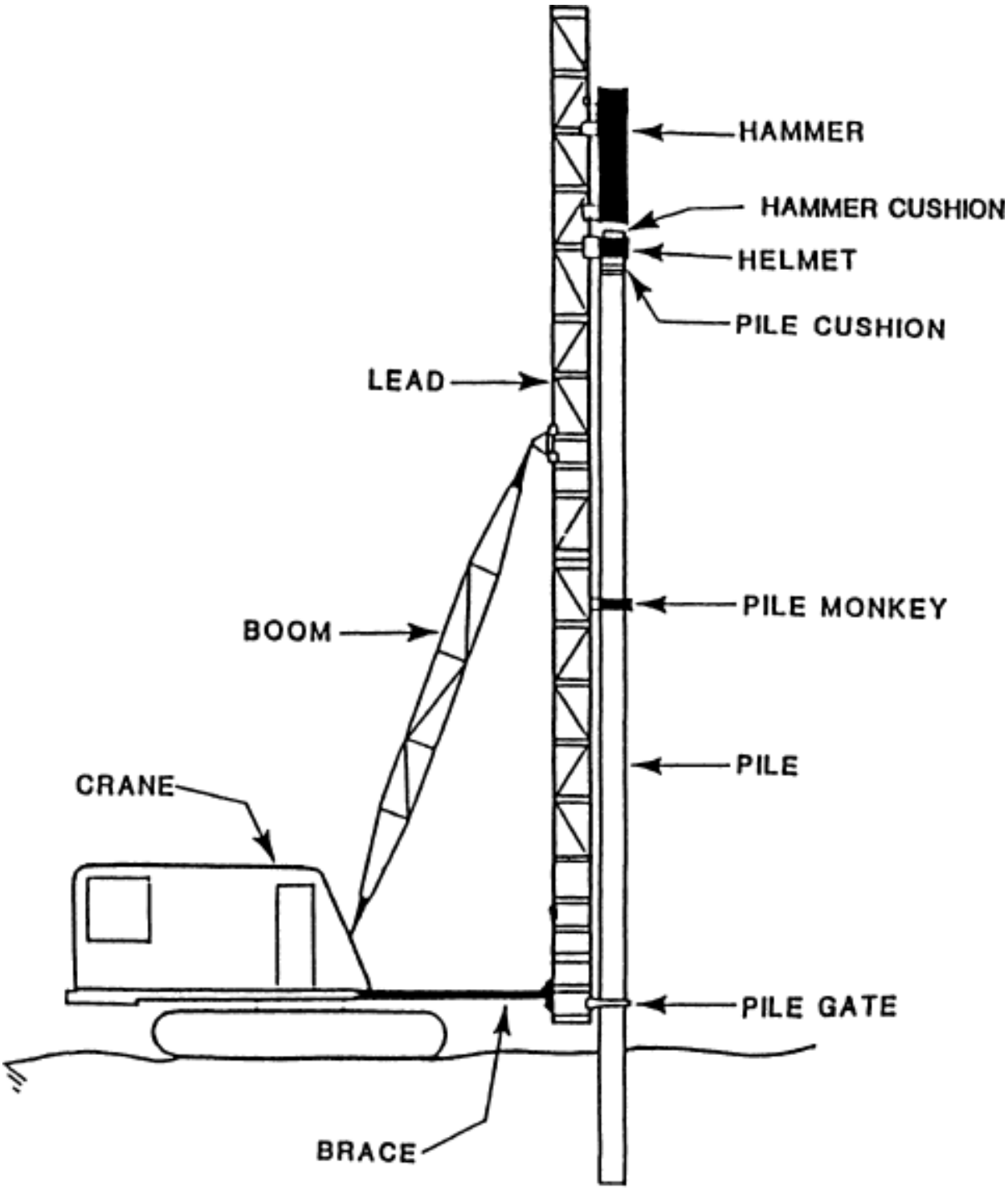

Figure 4-7 Components of pile driving system (from Pile Dynamics Inc.)

4.2.2 Air/Steam Hammers

The operation of the air/steam hammer lies in the use of pressurized medium. Originally it developed by employing steam power, but today most of these hammers operate on compressed air (Hannigan et al. 2006). There are three different types of air/steam hammers, *single-acting, double-acting or differential acting hammers*. A single-acting hammer consists of a ram which is lifted by the air or steam pressure acting against a piston housed in the hammer cylinder. Once the ram is raised a certain height, a valve is activated and the ram falls due to gravity forces. Figure 4-8 is a schematic of a typical single-acting air/steam hammer. The working principle of a double-acting hammer differs in the increased driving efficiency, as the down stroke is accelerated by a combination of the free fall of the ram and the pressurized air or steam. For this reason, these hammers have lighter rams and operate at a higher number of blows per minute than a single-acting air/steam hammer. Figure 4-9 is a schematic of a double-acting air/steam hammer. The differential acting hammer is another type of a double-acting hammer, which has two pistons of different diameter connected to the ram; the accelerating downward force results from the difference in areas between the top and bottom of the piston. These hammers perform at a high speed and a shorter stroke when compared to single-acting hammers. The working principle of a differential acting hammer is illustrated in Figure 4-10.

A single-acting air/steam hammer can perform at a rate of 60 blows per minute while a double-acting hammer can achieve twice this rate. Some double-acting air/steam hammers are fully enclosed and can be operated underwater. The stroke can vary affecting the hammer efficiency. The maximum stroke, and hence hammer potential energy, is therefore not constant and depends upon the pressure and volume of air or steam supplied, as well as the amount of pile rebound due to pile resistance effects (Hannigan et al. 2006). Commercially available single-acting air/steam hammers are available with ram weights from 3,000 lbs (1,300 kg) to over 300,000 lbs. (130,000 kg) and energy ratings of less than 10,000 ft-lbs (13 kJ) to 1.8 million ft-lbs (2500 kJ). Double acting air/steam hammers for pile driving are available with ram weights between 3,000

and 60,000 lbs (1,300 and 27,000 kg). Maximum energy ratings typically range from 7,000 to 180,000 ft-lbs (10 and 250 kJ) (DFI 1995).

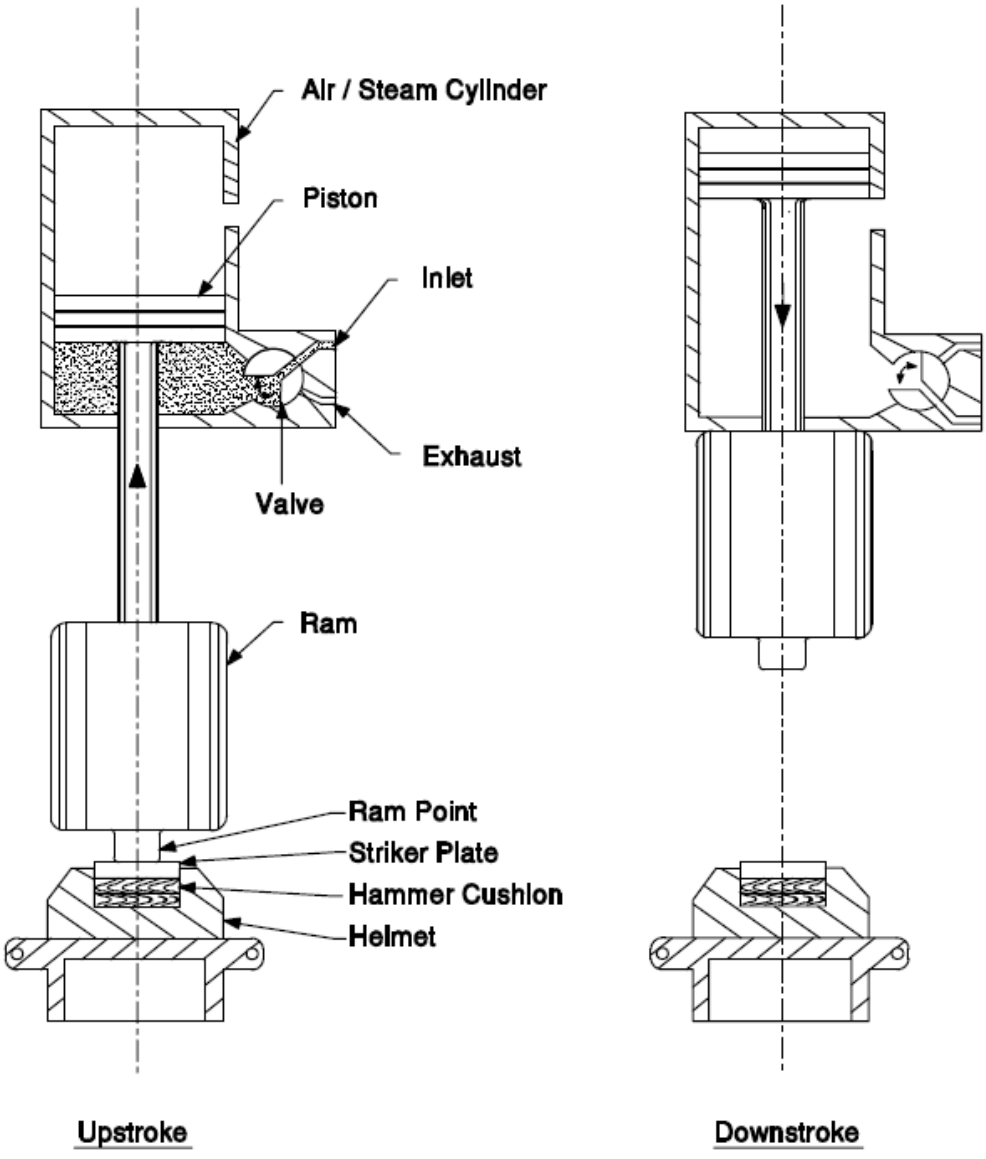

Figure 4-8 Schematic of Single-acting air/steam hammer (from DFI 1995)

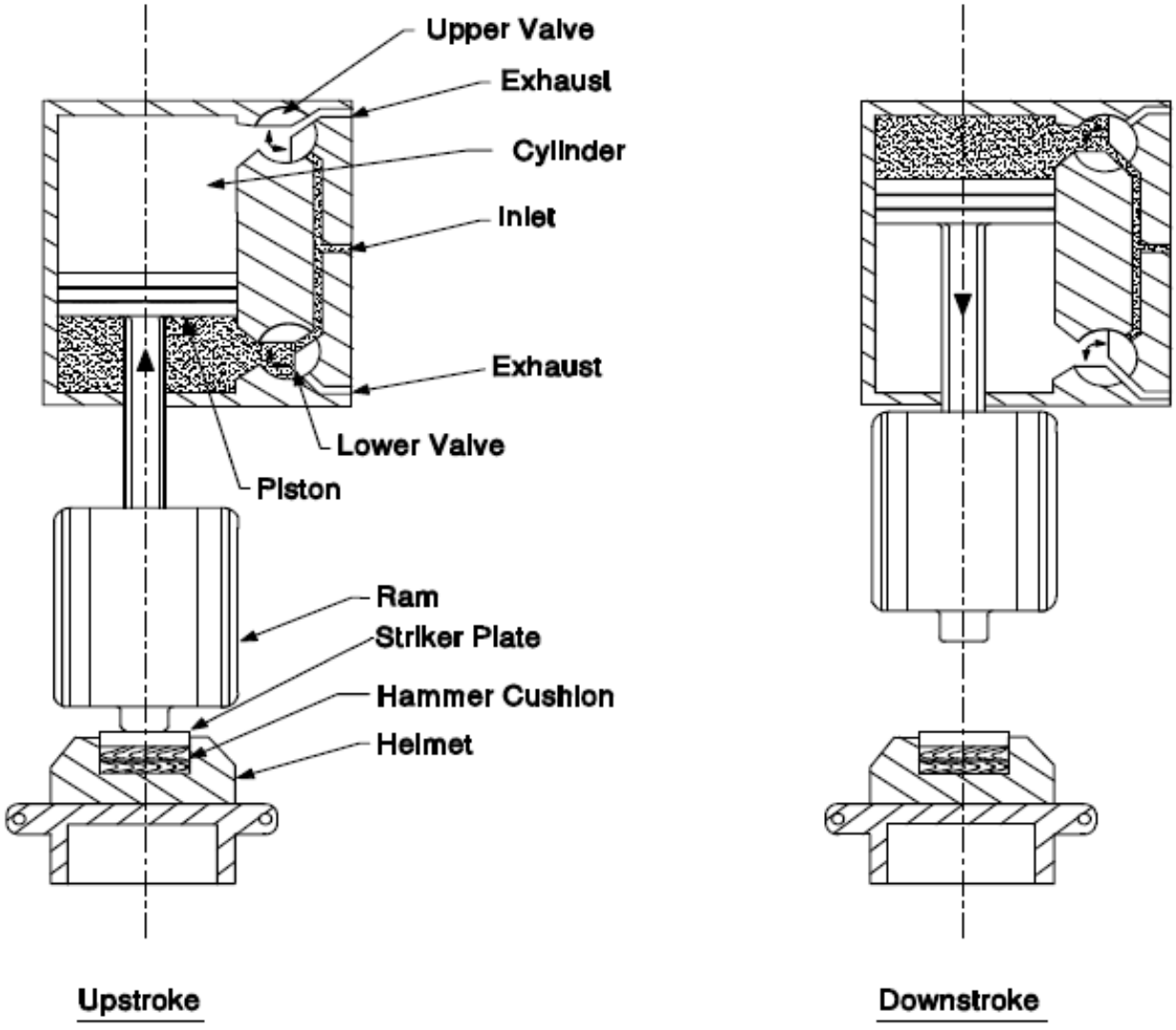

Figure 4-9 Schematic of Double-acting air/steam hammer (from DFI 1995)

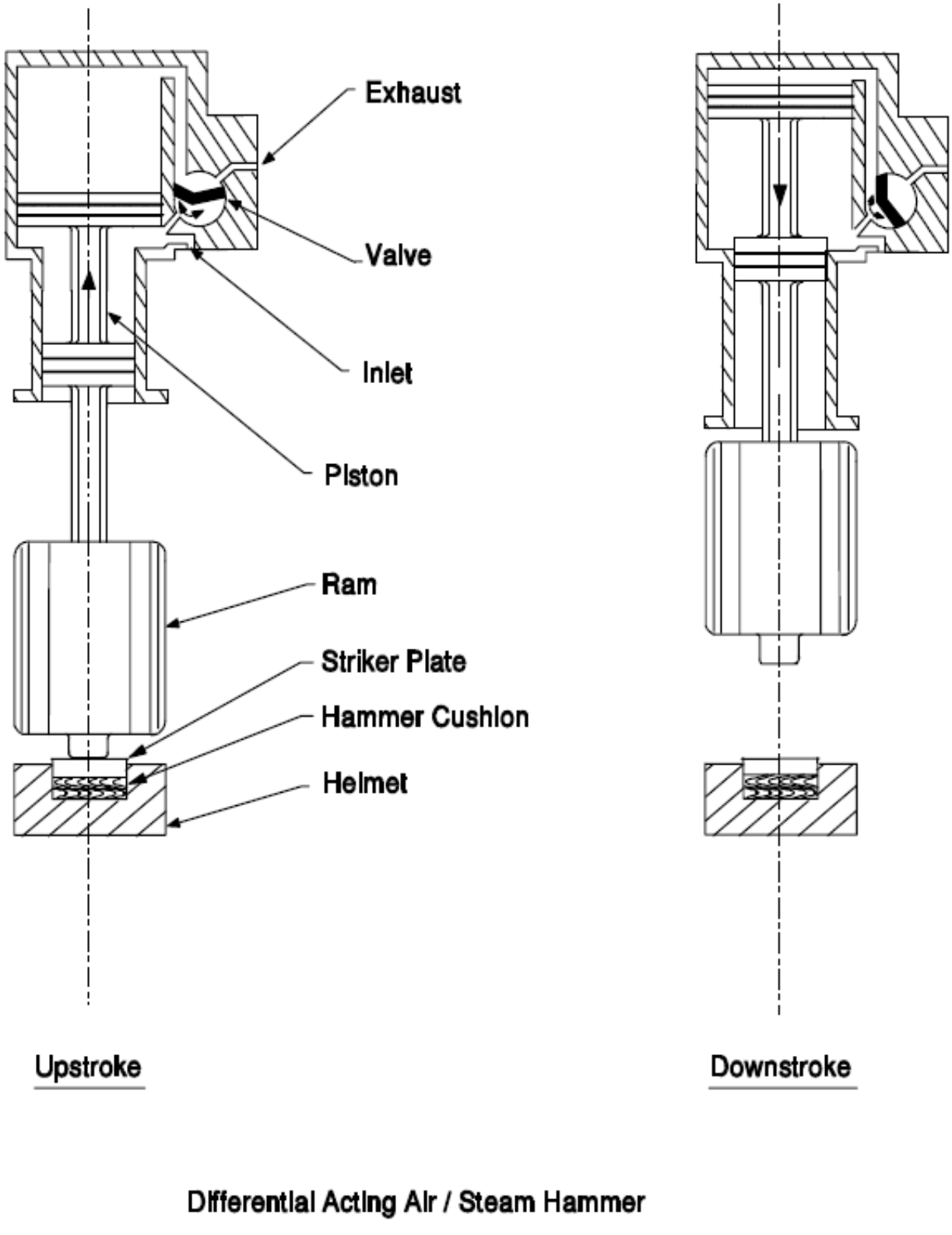

Figure 4-10 Schematic of Differential acting air/steam hammer (from DFI 1995)

4.2.3 Hydraulic Hammers

Hydraulic hammers are becoming popular nowadays and are considered the environmentally friendly version of the air/steam hammers, as they do not emit exhaust gases and they are less noisy than other impact hammers. They use hydraulic fluid to lift the ram. The simplest form of hydraulic hammer uses the hydraulic cylinders to raise the ram, which is then released to fall freely under gravity. Some models employ hydraulic accumulators to store a volume of the hydraulic fluid, arriving from the pump under pressure during the downward fall of the ram. This will speed up the ram lifting operation once impact takes place. Various ram weights are available, generally in the range of 4,400 pounds to 88,000 pounds (2,200 to 40,000 kg) and some hammers employ a segmental drop weight, so that the weight can be modified in increments (generally 1,000 kg per segment). Similar to air/steam hammers, hydraulic hammers are also made in both *single and double acting* versions. The ram is lifted up and pushed down by the hydraulic piston for the double-action hammers. Another complicated model is the nitrogen-assisted double-acting hammer which utilizes a nitrogen charged accumulator system to help drive the ram down, making it capable to increase the blow rate significantly. Figure 4-11 shows a schematic of the latter and of a single-acting hydraulic hammer.

Hydraulic hammers have many advantages in their use compared to other impact hammers. The main advantage is that they are very controllable; the ram stroke and the ram weight are adjusted to fit the energy needs of specific applications. Short strokes are preferred for soft driving or to minimize tension stresses in concrete piles, while high strokes are available for hard driving. Many models have a control unit which incorporates a stroke counter and the impact velocity of the ram, parameters that are important in the pile driving analysis. Most of the hammers are enclosed and capable of operating underwater and some include noise attenuation enclosures. Shock absorbers are sometimes incorporated to protect the hammer from rebound action. Double-acting hammers are effective for driving batter piles as the down stroke and up stroke are powered hydraulically. These types of hammers can also operate horizontally and can act as extractors (DFI 1995, Hannigan et al. 2006).

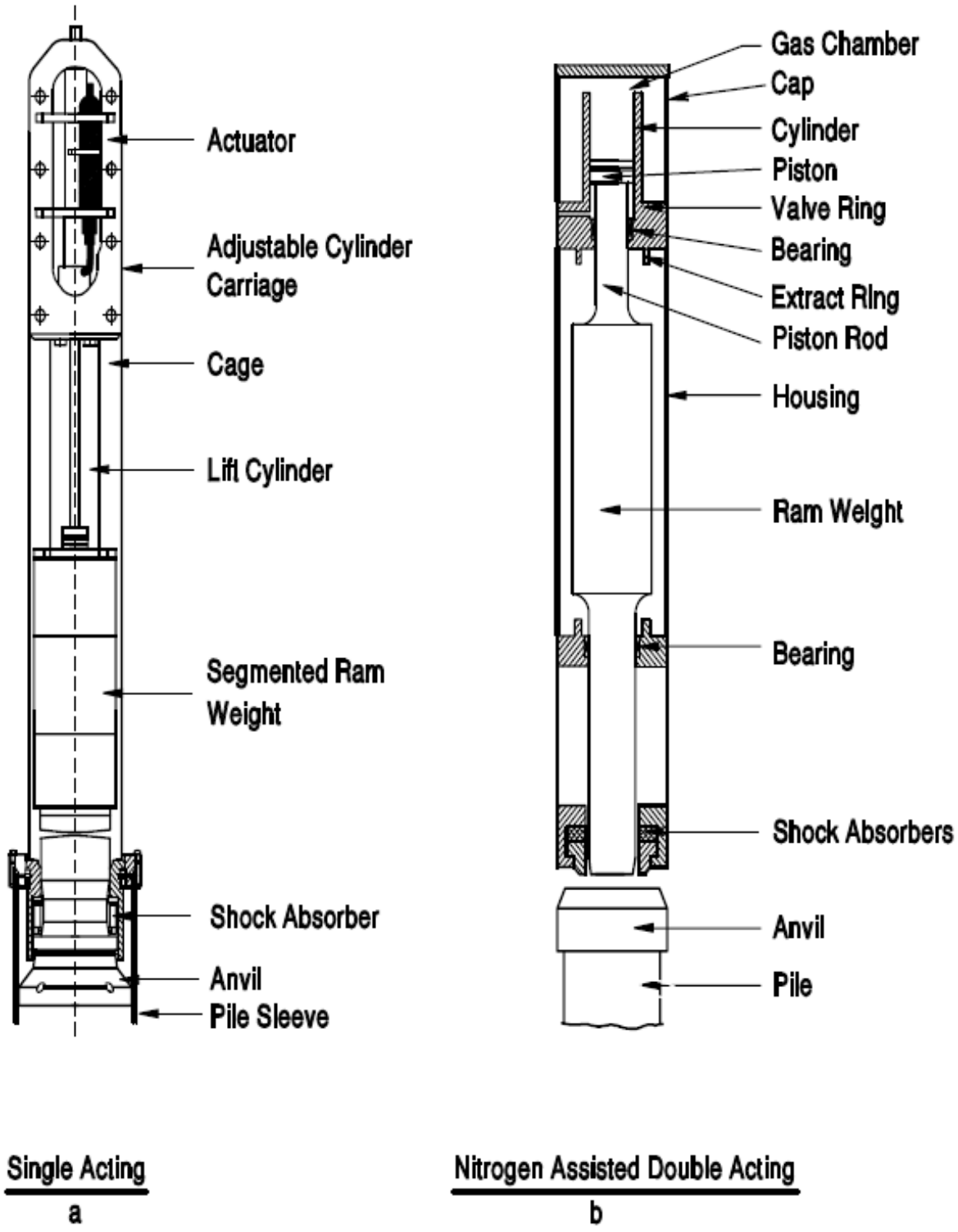

Figure 4-11 Schematics of (a) single and (b) double-acting hydraulic hammers (from DFI 1995)

4.2.4 Diesel Hammers

The basic difference between the diesel hammers and air/steam hammers is that, whereas the air or steam cylinder hammers have single-cylinder engines, requiring motive power from an external source; diesel hammers carry their own fuel from which they generate power internally. They are also smaller and lighter from an air/steam hammer of similar capability. Figure 4-12 shows the working principle of a **single-acting (or open-end)** diesel hammer. A cycle of the operation can be described beginning with the ram at the top of the stroke in Figure 4-12a. It falls freely under the action of gravity to the exhaust ports as shown in Figure 4-12b. When the ram passes the exhaust ports, a certain volume of air is trapped and begins compressing the gas in the combustion chamber (Figure 4-12c). During this stage, the ram starts to decelerate and finally will lose velocity due to the action of the pre-compression pressures under the ram. As it descends, the falling ram activates the fuel pump and causes a metered amount of fuel to be introduced into the combustion chamber. In some hammers the fuel is injected in liquid form, while in other hammers the fuel is atomized and injected later in the cycle and just prior to impact. At or near the time of impact, the fuel and the heated compressed air mixture in the combustion chamber begins to burn; the gas pressure in the combustion chamber increases dramatically when the fuel burns. It is the impact that does most of the pile driving but in very easy driving the pile is also pushed down into the ground by the force of the compressed gas in the combustion chamber acting down on the anvil. After impact, the ram begins to move back up in the chamber. The upward motion is generated by both the rebound of the pile and the gas pressure. In very easy driving conditions, some pile penetration is generated by the gas pressure directly, reducing the gas pressure available for raising the ram. Thus, the stroke of the Open-End Diesel hammer is dependent on *driving resistance, fuel charge, pile movement, and pile stiffness*. Under the action of the gas pressure, the ram is accelerated upward until it reaches the port where the excess gas pressure is exhausted to the atmosphere (Figure 4-12e). Since the ram has a velocity at that time, the ram continues upward against gravity, and fresh air is pulled into the cylinder scavenging the burned gases (Figure 4-12f). The cycle then repeats until the fuel input is interrupted (DFI 1995).

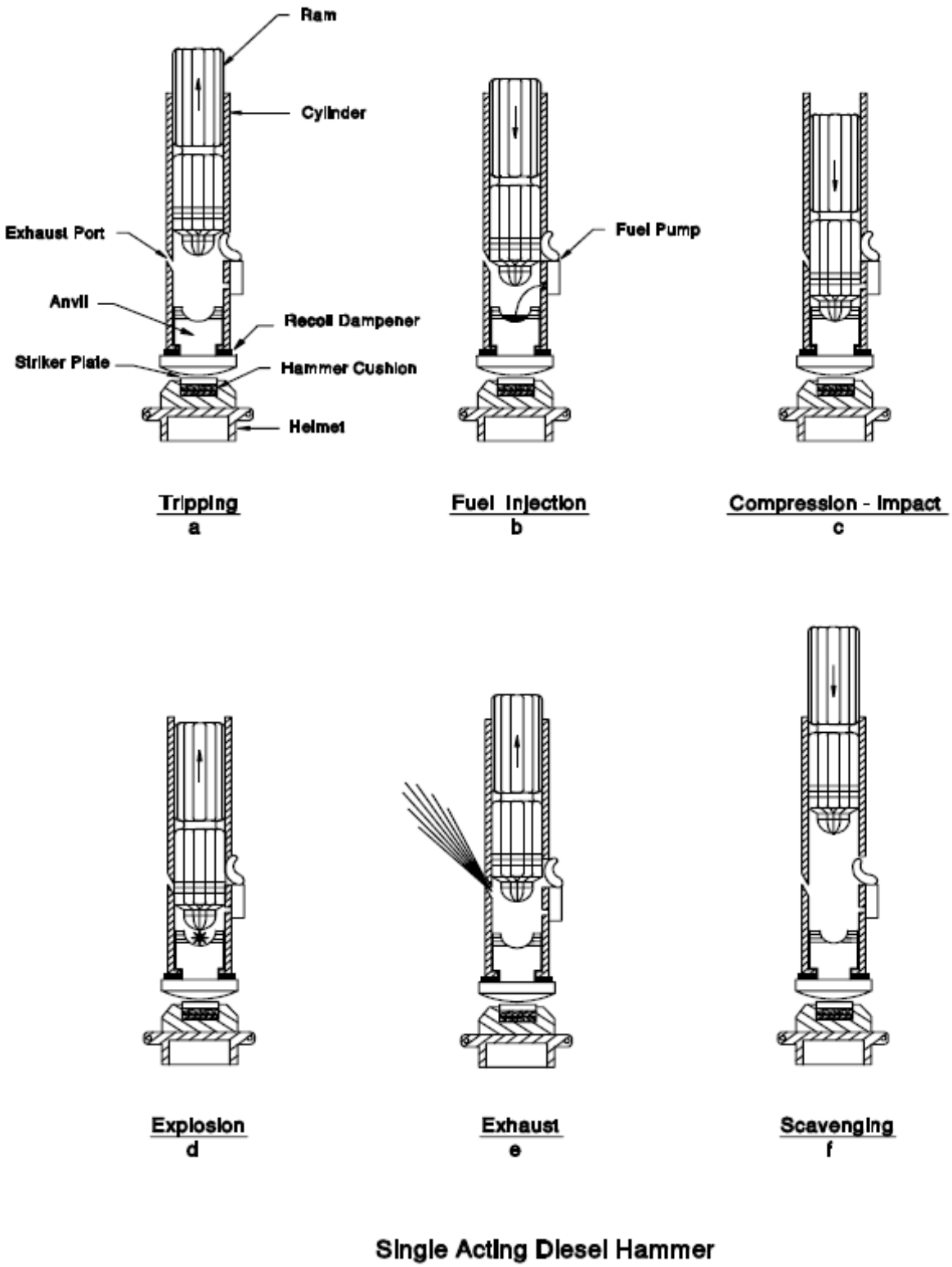

Figure 4-12 Working principle of a single-acting diesel hammer (from DFI 1995)

Diesel hammers are considered unpredictable in action, as there is no standard method of how they should be rated. Many manufacturers use the maximum potential energy computed simply from maximum stroke times the ram weight. The actual hammer stroke is uncontrollable because as mentioned before, it is a function of fuel charge, condition of piston rings containing the compressed gases, driving resistance, and pile length and stiffness. A set of driving conditions will produce a particular stroke. When driving resistance is very low, the upward ram stroke may be insufficient to scavenge (or suction) the air into the cylinder and the hammer will not run. Thus, the ram must be manually lifted repeatedly by the crane until resistance increases. The stroke can be reduced for most hammers by reducing the amount of fuel injected. The gases ignite when they attain a certain combination of pressure and temperature. Under continued operation, when the hammer's temperature increases due to the burning of the gases, the hammer fuel may ignite prematurely. This condition, called "pre-ignition", reduces the effectiveness of the hammer, as the pressure increases dramatically before impact, causing the ram to do more work compressing the gases and leaving less energy available to be transferred into the pile (Hannigan 2006). The stroke of a single-acting diesel hammer can be calculated from the formula:

SI units

$$H = \frac{4400}{BPM^2} - 0.09 \qquad \text{Eq. 4-1}$$

English units

$$H = \frac{14500}{BPM^2} - 0.3 \qquad \text{Eq. 4-2}$$

where H is the stroke in m for SI units and ft for English units, and BPM is the hammer blow rate in blows per minute. The hammer stroke for various hammer speeds is given in Figure 4-13.

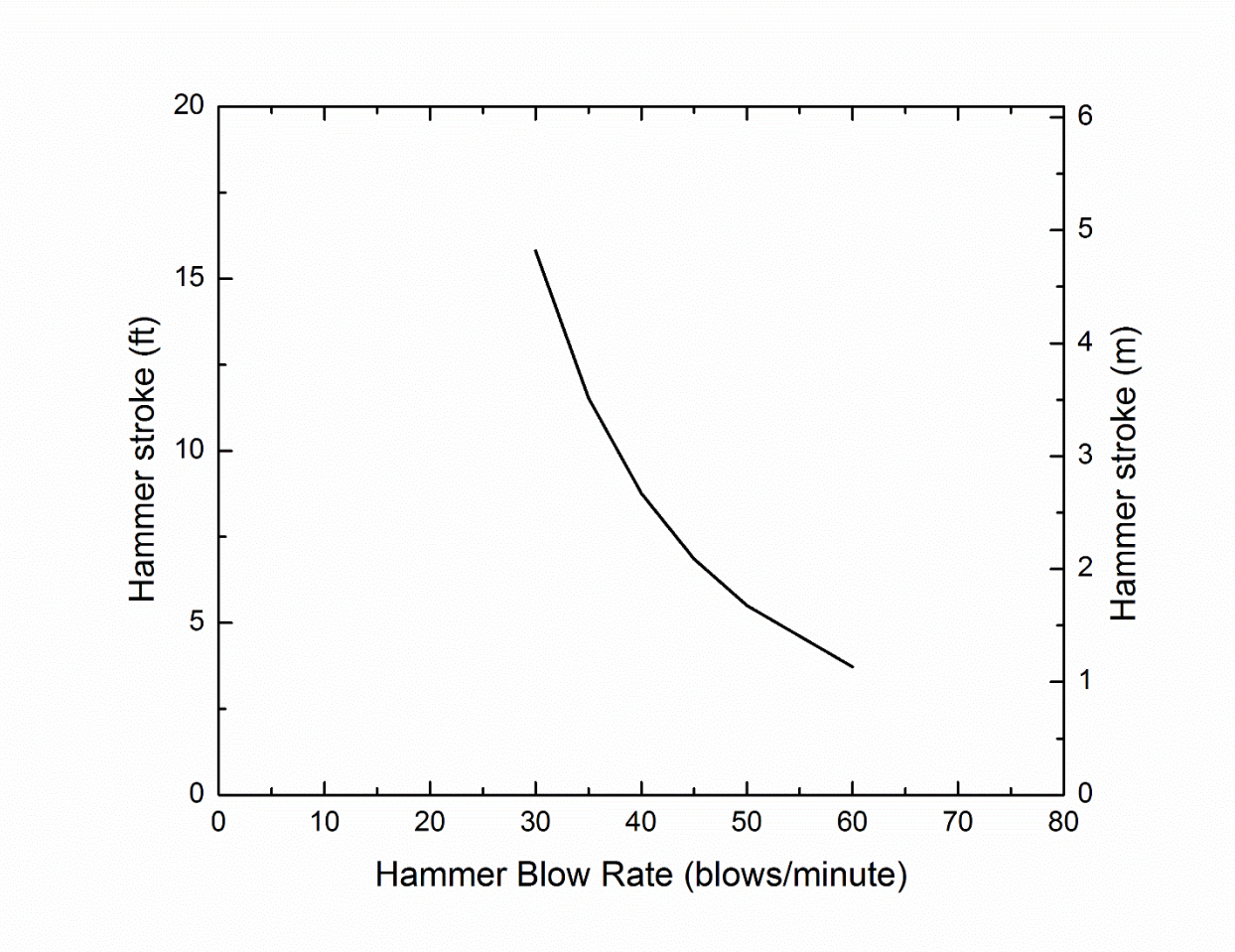

Figure 4-13 Hammer stroke as a function of blow rate for a single-acting diesel hammer

An electronic device is frequently employed to calculate the hammer rate and the stroke from the time between blows detected by sound. Proximity switches are attached to the body hammer and are connected to a transmitter mounted on the hammer that communicates with a wireless hand held unit. This unit is called E-Saximeter. A photograph of the equipment attached on the hammer and of the wireless device is presented in Figure 4-14a and Figure 4-14b.

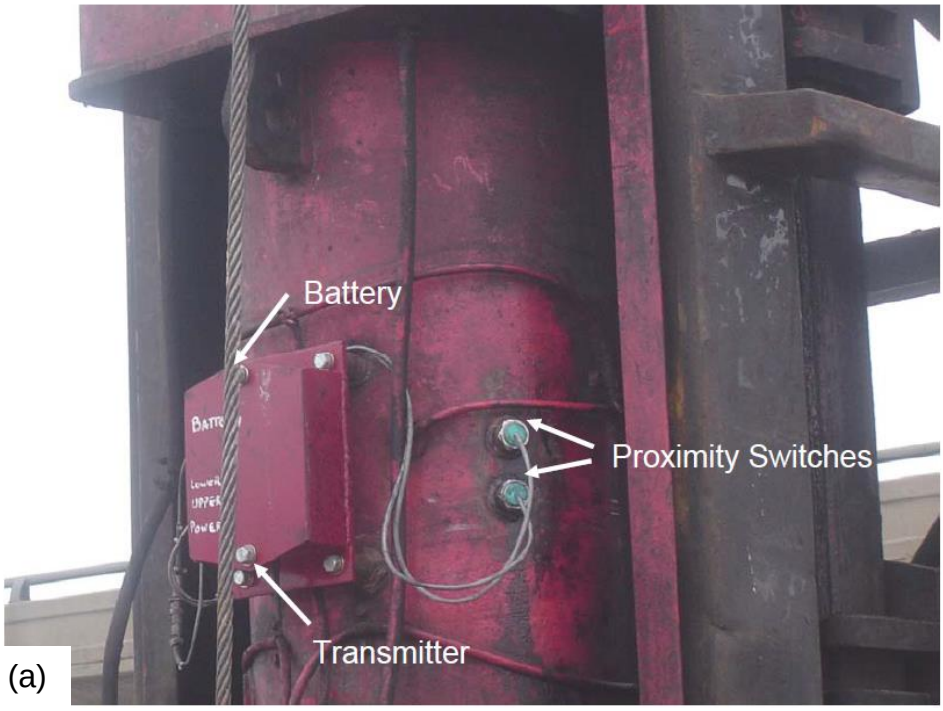

(a)

(b)

Figure 4-14 (a) Proximity switches and transmitter attached on diesel hammer and (b) E-Saximeter wireless device (from Hannigan 2006)

The **double-acting (close-end)** diesel hammer is very similar to the single-acting hammer, they differ in the closed cylinder on top. When the ram moves upward, air is being compressed at the top of the ram in the so called "bounce chamber" which causes a shorter stroke and therefore a higher blow rate. The operation of this hammer is shown in Figure 4-15. Hammer strokes, and therefore hammer energy, may be increased or decreased by the fuel pump pressure. The hammer is stopped by interrupting the fuel supply. Closed-end diesel hammers operate at up to twice the blow rate of an open-end diesel hammer in similar driving conditions.

Hammer suppliers usually categorize diesel hammers in D-series, where D designation means diesel hammer. The following number is the ram weight in metric tons. The series of the model number is following after the dash. For example, D25-21 has a ram weighing 2500 kg and 21 is the model number. Three of the largest diesel hammers in the market right now are the APE D300-42 with a ram weight of 30,000 kg (66,150 lb) and maximum rated energy of 1,005 kNm (744,188 lb-ft), the Delmag D400-32 with a ram weight of 40,000 kg (88,185 lb) and maximum rated energy of 1,335 kNm (984,645 lb-ft) and the Pileco D800-32 with a ram weight of 80,000 kg (176,370 lb) and maximum rated energy of 2,665 kNm (1,965,600 lb-ft). A diesel hammer driving a steel pipe pile is shown in Figure 4-16.

4.2.5 Vibratory Hammers

Vibratory hammers are basically generators which consist of a static weight and a pair of counter-rotating eccentric weights so that an axial force is applies to the pile, while the horizontal components of the centrifugal force are cancelled out. A schematic of a vibratory hammer is presented in Figure 4-17. The hammer is mounted by clamps on the pile head and is powered hydraulically or electronically by a power pack which is rested on the ground. The vibrations generate pore pressure build up which reduces the shear strength of the soil enabling the pile to penetrate. Vibratory hammers are classified as low-frequency drivers in resonance with the soil frequency or high-frequency drivers, operating at frequencies between 5 and 150 Hz.

Vibratory hammers are most effective in loose to medium dense granular soils as they displace more easily and are ideal to drive H-sections, steel pipe piles and sheet piles. They can be used as pile drivers or pile extractors. There is a critical frequency during starting and stopping the driving process, which may resonate with the natural frequency of the buildings and cause problems. For this reason, high frequency resonant-free vibrators have been developed to eliminate these high amplitudes during start-up and shutdown. Their main advantages over impact hammers is that they have lower driving noise, they cause less damage to the pile head, can achieve penetration at a very fast rate. However, they can produce high ground vibrations and they can cause problems by liquefaction or densification in specific occasions. Also, there is no reliable technique to estimate the pile capacity

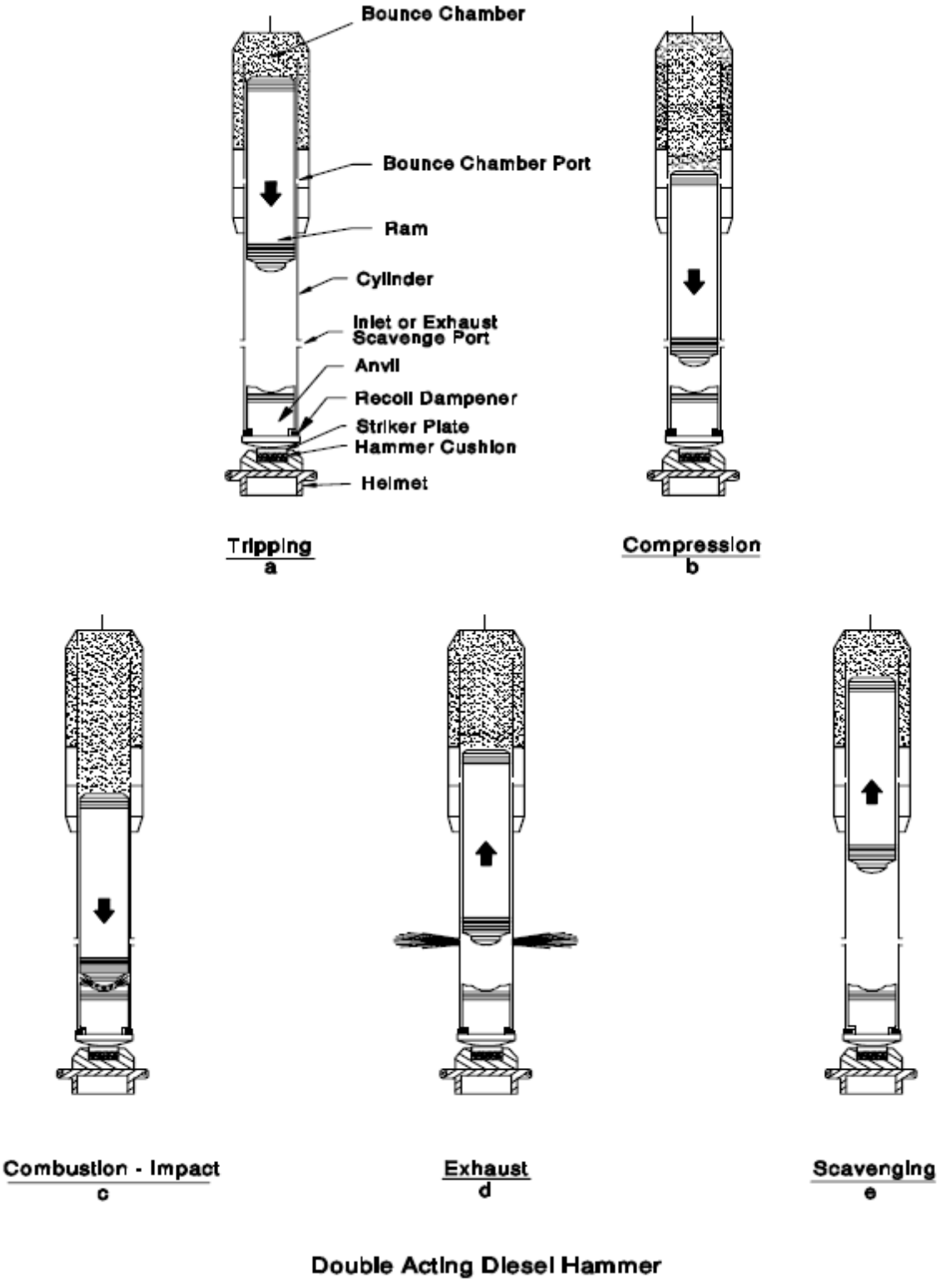

Figure 4-15 Working principle of a double-acting diesel hammer (from DFI 1995)

Figure 4-16 Diesel hammer driving pipe steel piles (courtesy of Delmag)

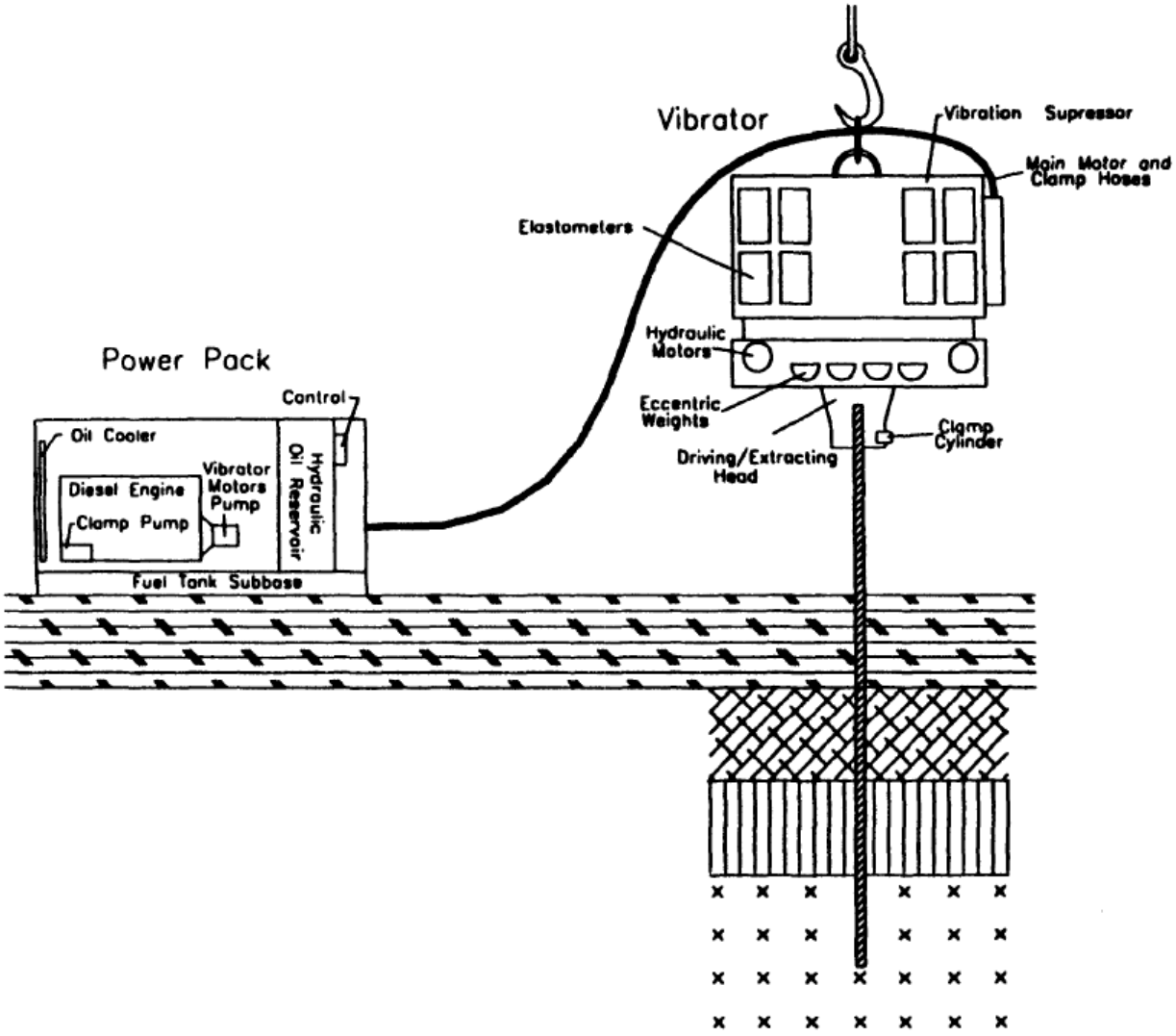

Figure 4-17 Vibratory driver/extractor (from DFI 1995)

4.3 Pile Driving Formulas

Engineers have been trying for many years to develop correlations that predict the capacity of a pile during driving based on pile penetration observations. These relationships are known as pile driving formulas. They are simply calculating the pile capacity based on the energy delivered by the hammer. The basic form of the dynamic formulas is:

$$P_{\alpha} = \frac{W_r h}{sF} \qquad \text{Eq. 4-3}$$

where: P_{α} = allowable downward load capacity
W_r = hammer ram weight
h = hammer stroke
s = pile set (penetration) per blow obtained from last blows of driving
F = factor of safety

Hundreds of dynamic formulas have been proposed. The first one published by Wellington in 1888, commonly known as the Engineering News Formula:

$$P_{\alpha} = \frac{W_r h}{F(s + c)} \qquad \text{Eq. 4-4}$$

where c is a coefficient and is taken as 1 in (25 mm). Wellington's approach was based on load test data for timber piles driven with drop hammers in sands only. This equation was revisited by many researchers and some other popular relationships are the Hiley Formula (1925), Janbu's Formula (1953), the Gates Formula (1957) and the Danish formula (Olson and Flaate 1967) among others. Though their simplicity made them been widely used in the past, nowadays it is recognized that these relationships are inaccurate and unreliable and should no longer be used. Their correlation to static load tests with driven piles is very poor (Peck et al. 1974). The shortcomings of the pile driving formulas lie in the many simplifying assumptions that are taken into account. More specifically, they do not consider any energy losses that take place in the various parts of the driving system. Also, the soil resistance is assumed to be a constant force which is not true. The pile is assumed to be rigid and its pile length is not considered. Finally, every formula was

developed for specific pile, hammer and soil types and it is not necessarily applicable to other cases.

4.4 Wave Equation Analysis

Since the pile driving formulas are inappropriate to predict pile capacities, alternative methods had to be developed. Dynamic analysis by the wave equation method was presented in the 1930s. The driving system which consists of the pile driving equipment, the pile and the soil is not oversimplified as in the pile driving formulas and stress wave propagation is now taken into account. The mathematical model was introduced by Smith (1960). The one-dimensional wave equation is defined as:

$$\frac{\partial^2 u}{\partial t^2} = \frac{E}{\rho}\frac{\partial^2 u}{\partial z^2} = c^2 \frac{\partial^2 u}{\partial z^2} \qquad \text{Eq. 4-5}$$

where: z = depth below ground surface
u = displacement of pile at depth z
t = time
E = modulus of elasticity of the pile
ρ = mass density of the pile
c = wave propagation in the pile

When digital computers became available, computer programs that incorporated the wave equation analysis of pile driving were developed. The Texas Transportation Institute (TTI) program (Hirsch et al. 1976) and the Wave Equation Analysis for Piles (WEAP) program (Goble and Rausche 1976) are two of the most important. The latter was improved several times and is now known as GRLWEAP (Pile Dynamics Inc. 2005).

In the wave equation analysis, the hammer and the pile are divided into discrete elements which are typically 1 m (3.3 ft) in length, have a mass equal to the corresponding segment and are connected to each other with weightless springs that have the stiffness of the corresponding element. The interface between the pile and the soil is modeled by a series of springs and dashpots along the sides and at the bottom of the pile. A representation of the model principle can be found in Figure 4-18. As seen in the lower

left corner of Figure 4-18, the soil resistance is represented by static and dynamic components. The static soil resistance is modeled by elastic, perfectly plastic springs, while the dynamic resistance is modeled with a linear dashpot. The displacement between the pile and the soil required to mobilized full plastic resistance is called **quake, q**. The dynamic soil resistance is a function of the pile velocity and according to Smith (1960) it is proportional to the static soil resistance times pile velocity by a damping factor, $\mathbf{J_s}$ with dimensions of inverse velocity. Goble et al. (1976) assumed that the damping resistance is proportional to pile impedance times pile velocity by a dimensionless factor defined as **viscous damping factor, $\mathbf{J_c}$**:

$$R_{dyn} = J_c \, Z \, v \qquad \text{Eq. 4-6}$$

where: R_{dyn} = dynamic pile resistance
J_c = depth below ground surface
Z = pile impedance
v = particle velocity of pile

The GRLWEAP analysis offers three options to present its output results, the bearing graph, the inspector's chart and the driveability analysis. The *bearing graph* is a curve of the ultimate resistance versus the penetration resistance (blow count). This plot is considering a certain driving equipment, pile, soil conditions and penetration depth. An example of a bearing graph is shown in Figure 4-19 (Hannigan et al. 2006). For this case, for an ultimate pile capacity of 333 kips, a penetration resistance of 83 blows/ft is required. A hammer stroke of 8.4 ft is predicted. The hammer stroke versus penetration resistance is also plotted. Higher or lower strokes, would require a lower or higher penetration resistance for the same capacity. The upper part of the graph provides the maximum compression and tension driving stresses as a function of the penetration resistance.

The *inspector's chart* (constant capacity analysis) calculates the blow count for a given ultimate capacity as a function of the hammer stroke. This graph helps an engineer to select the hammer stroke range that will give a reasonable penetration resistance and is helpful to determine if the operation of the field pile driver should stop in the case of an observed hammer stroke different than the predicted. An example of the result of a

constant capacity analysis is given in Figure 4-20. The upper half of the graph shows again the stress maxima associated with a particular driving resistance.

The *driveability analysis* calculates the penetration resistance at up to 100 depth values for a certain hammer performance (hammer stroke). This plot is a tool to the engineer as it helps him/her select the suitable hammer and pile for every project. Selection of the right hammer is very important as a small hammer might not be adequate to reach the design depth or a large hammer may overstress and damage the pile. Figure 4-21 presents the driveability analysis results for an H-pile The maximum penetration resistance calculated for the H-pile to penetrate the dense sand layer, which is at 5 m, is only 26 blows/0.25m (32 blows/ft).

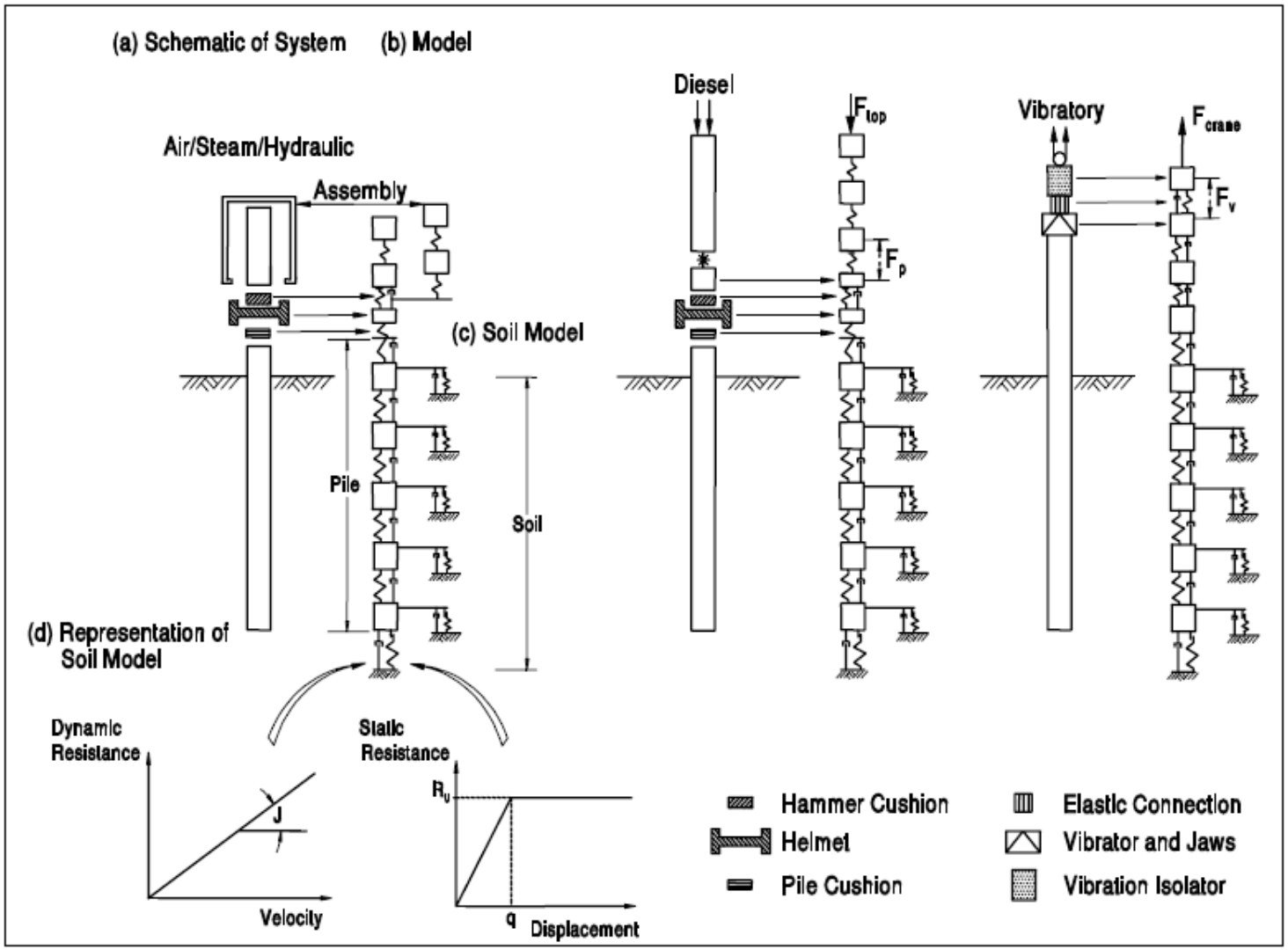

Figure 4-18 WEAP models (from Rausche et al. 2004)

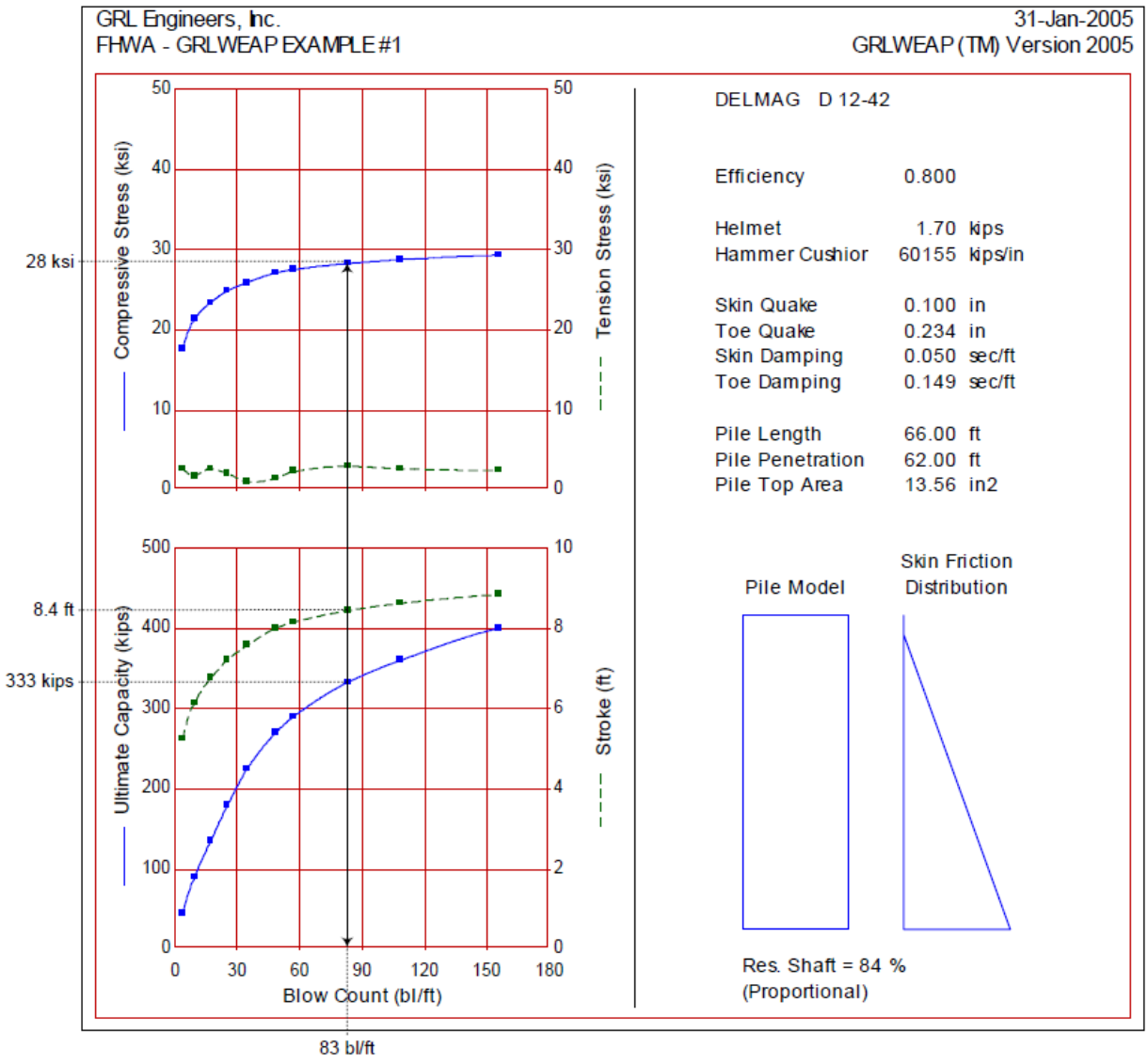

Figure 4-19 Example of a bearing graph (from Hannigan et al. 2006)

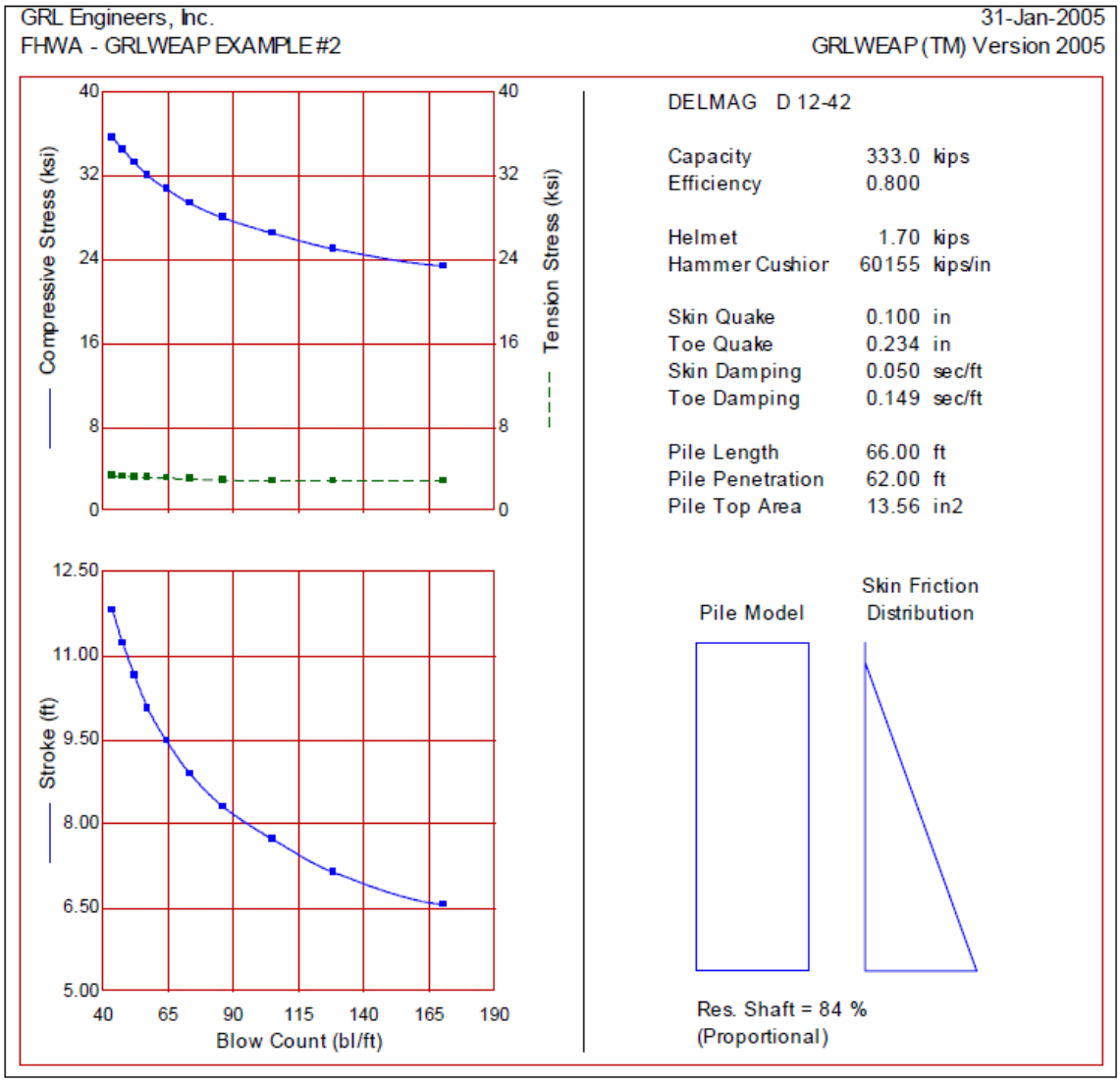

Figure 4-20 Example of constant capacity analysis (from Hannigan et al. 2006)

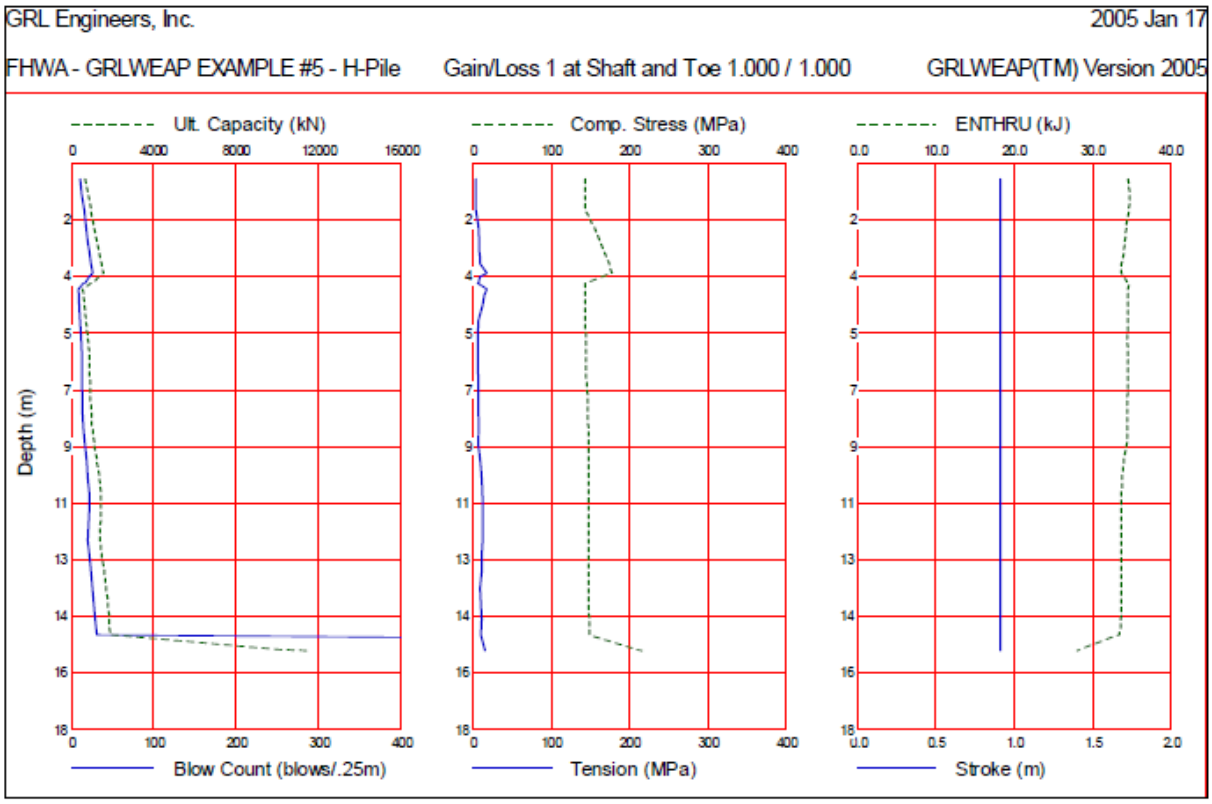

Figure 4-21 Driveability analysis results for an H-pile (from Hannigan et al. 2006)

4.5 High-strain Dynamic testing of piles

Dynamic test methods are an alternative way to evaluate the static load capacity of a driven pile. Force and velocity measurements obtained near the top of the pile are monitored during the pile driving operation. Except for estimating the static pile capacity, dynamic tests are used to evaluate the performance of the driving system, calculate pile installation stresses and determine pile integrity. The work on high-strain dynamic tests started in the 1960s at the Case Western Research University; the technique is known as the *Case Method*. The commercial use of the method started in 1972 with the *Pile Driving Analyzer* test, while a numerical model technique called CAPWAP (CAse Pile Wave Analysis Program) was also set in use.

4.5.1 Pile Driving Analyzer (PDA)

The *Pile Driving Analyzer* system, commonly known as PDA, was developed in the 1960s and consists of a minimum two strain transducers and a pair of accelerometers mounted near the top of the pile; two or three diameters below the pile head. A monitoring device called Pile Driving Analyzer is used to record and process the data which are transferred by a transmitter also attached close to the pile top. A photograph of a strain and accelerometer gage with their transmitter bolted on an H-pile is presented Figure 4-22. The data acquisition system is shown in Figure 4-23. The test is standardized and is given in ASTM Designation D4945-12 “Standard Test Method for High-Strain Dynamic Testing on Deep Foundations” and is used for almost any pile type (timber, concrete, steel pipe, H section, etc.). The axial pile force is computed from the measured strain, ε, times the pile elastic modulus, E, times the cross-sectional area of the pile, A. Velocity is obtained by integration of the acceleration data with time; integrating once more we obtain pile displacement. Results for each hammer blow are displayed on the screen of the PDA real-time and are stored for later processing.

Figure 4-22 Accelerometer (left), strain gage (middle) and transmitter mounted near the top of an H-pile (Pile Dynamics, Inc.)

Figure 4-23 Pile Driving Analyzer (Pile Dynamics, Inc.)

4.5.2 Wave Mechanics

In order to understand how the PDA test works and how to interpret its results, the wave mechanics principles for a driven pile and a discussion of PDA results will be given in this section. When the hammer hits the pile head, an impact force, F, is generated on the cross-sectional area, A, creating a compressive wave travelling down the pile with a speed, c. Pile particles will then have a particle velocity, v. Force and particle velocity are proportional by the impedance, Z_P = EA/c, where E is the elastic modulus of the pile. The time required for a wave to travel down the pile tip, be reflected and return and being captured by the strains and accelerometers on the pile head, is 2L/c, where L is the pile length below the gages. Force and particle velocity monitored by the PDA are presented in certain plot types called *wave traces.* Time is in L/c scale for convenience, since the wave reaches the gages at 2L/c as mentioned before.

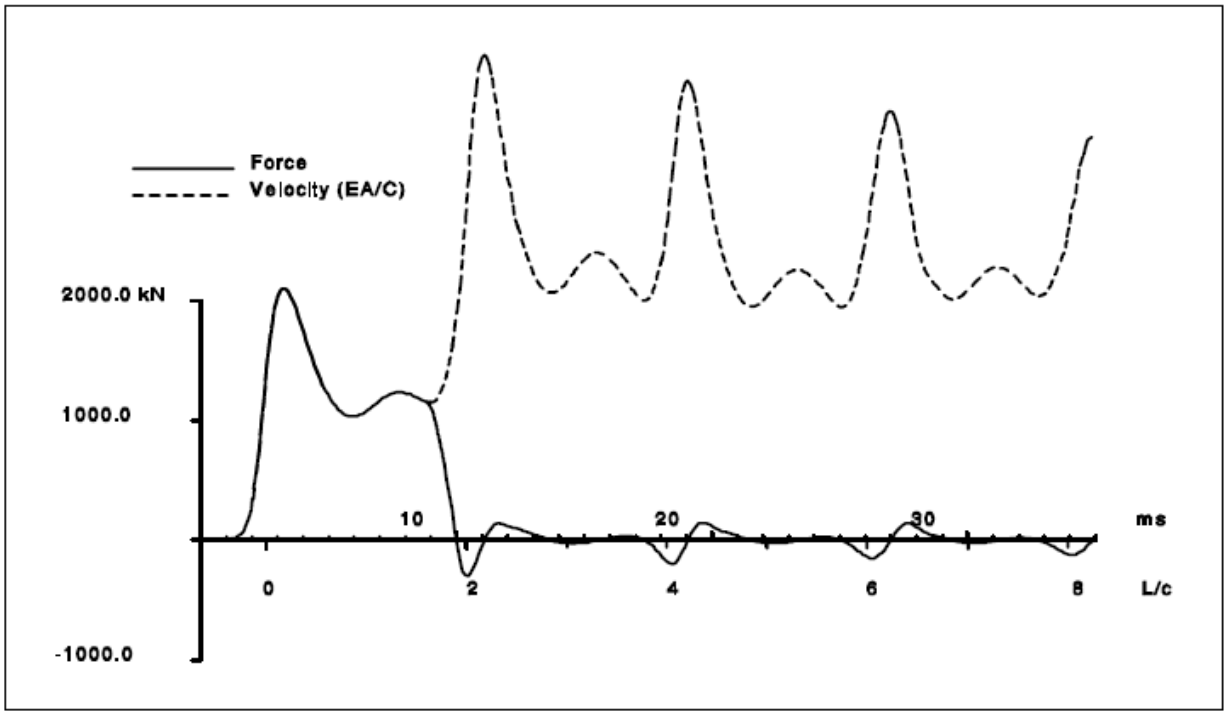

Figure 4-24 Force and particle velocity wave trace versus time for a Free-end condition (from Hannigan et al. 2006)

Figure 4-24 shows a typical plot of force and particle velocity captured by the PDA sensors near the pile top for a *free-end* condition. The free-end condition means that when the compressive wave reaches the toe of the pile at time L/c, little or no resistance is encountered. The compressive wave will be reflected back as a tension wave travelling upwards the pile. The force becomes zero and the particle velocity doubles at the pile tip. As illustrated in Figure 4-24 , force and velocity traces overlap (proportionality of F and v) until the wave reaches the pile top at time 2L/c, where the force will go to zero and the velocity will double. The same pattern is noticed at times 4L/c, 6L/c, etc. as the wave travels up and down the pile. The free-end condition is also known as *easy driving* and may be found if the pile tip is at soft soil.

Figure 4-25 presents wave traces of a *fixed-end* condition, which is typical when driving in hard soil or rock, also known as *hard driving*. The compressive wave will travel down the pile and when reaching the pile toe it will be reflected again as a compression

wave and will travel up the pile. The force at the pile tip will now double and the pile velocity will go to zero. This phenomenon can be seen in Figure 4-25 where at time 2L/c the force doubles and the velocity is decreased to zero.

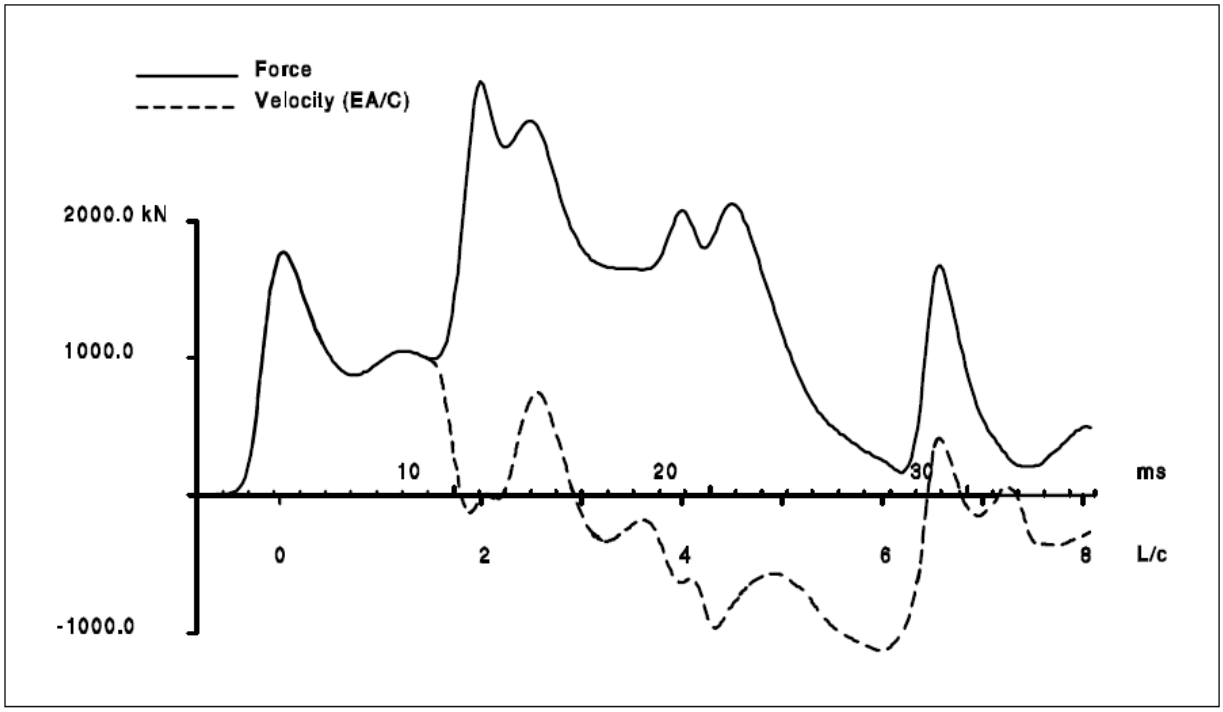

Figure 4-25 Force and particle velocity wave trace versus time for a Fixed-end condition (from Hannigan et al. 2006)

As mentioned previously, the force and particle velocity traces are proportional until a shaft or toe resistance is encountered on the pile. In Figure 4-26, a large separation between the two traces at the time range between 0 to 2L/c is an indicator of a large shaft resistance on the pile (Hannigan et al. 2006). The larger the separation of the wave traces, the higher the soil resistance.

Another reason that the force and velocity time histories will separate is cross sectional changes of the pile. A cross sectional reduction (decrease in pile impedance), which indicates pile damage on the pile, will cause a decrease in the force record and an increase in the velocity record. Thus, wave traces serve as pile integrity data to help an engineer determine the pile structural damage. The location of the impedance change on

the time scale will indicate the pile crack or bending. Figure 4-27 shows an extracted H-pile which was damaged due to buckling and bending, confirmed by the wave traces. Cross sectional increases will increase the force trace and decrease the velocity record.

Figure 4-26 Force and velocity wave traces for large shaft resistance condition (from Hannigan 1990)

Figure 4-27 Extracted H-pile after PDA damage indication (from Hannigan 2006)

The Pile Driving Analyzer uses the Case Method technique to determine the static pile capacity. Using real time information from the force and velocity wave traces, the total static and dynamic resistance, **RTL**, on the pile is derived from a closed form solution to the one-dimensional wave propagation theory:

$$RTL = \frac{[F(t_1) + F(t_2)]}{2} + \frac{[v(t_1) - v(t_2)]}{2}\frac{EA}{c} \qquad \text{Eq. 4-7}$$

Where:
F = Force at gage location
v = Velocity at gage location
t_1 = Time of initial impact
t_2 = Time of reflection from pile toe (t_1+2L/c)
E = Elastic modulus of the pile
c = Wave speed in pile
A = Cross-sectional area at gage location
L = Pile length below gages

The static pile capacity is calculated if we subtract the dynamic resistance (or damping) from the total resistance. The dynamic resistance is approximated as a linear function of a dimensionless damping factor, J_c, times the pile toe velocity which is estimated from the monitored values at the pile head (Goble et al. 1975). The standard Case Method capacity, **RSP**, is:

$$RSP = RTL - J_c\left[v(t_1)\frac{EA}{c} + F(t_1) - RTL\right] \qquad \text{Eq. 4-8}$$

The damping factor, J_c, depends on the soil type at the pile toe. Typical values are presented in Table 4.2. The selection of the Case damping factor should be refined by correlating the PDA's capacity with static load test results or CAPWAP analysis. For the case of displacement piles and for large tip resistances, the toe resistance will be slightly delayed in time in the wave trace plot. The maximum Case capacity method, **RMX,** is used in these cases; t_1 and t_2 times are shifted until the maximum Case Method capacity is found (Hannigan 1990). Other Case Methods are also available.

Table 4.2 Suggested Case Damping Factors (Pile Dynamics, Inc.)

Soil Type at Pile Tip	**Case Damping Ranges, J_c**
Clean Sand	0.10 to 0.15
Silty Sand, Sandy Silt	0.15 to 0.25
Silt	0.25 to 0.40
Silty Sand, Clayey Silt	0.40 to 0.70
Clay	0.70 or higher

One very important output from the PDA test is the energy transferred from the hammer to the pile. The transferred energy is calculated by the integral of the force and velocity records over time. The maximum value of the energy at the gage location, **EMX**, is an indicator of the hammer performance. Figure 4-28 presents the procedure of the transferred energy computation.

Another set of wave traces that the PDA analysis has as an output, are the Wave Up and Wave Down traces. The Wave Down force is the average of the measured force and the velocity times impedance:

$$WD = \frac{(F + Zv)}{2} \qquad \text{Eq. 4-9}$$

The Wave Up force is half the difference of the measured force and velocity times impedance:

$$WD = \frac{(F - Zv)}{2} \qquad \text{Eq. 4-10}$$

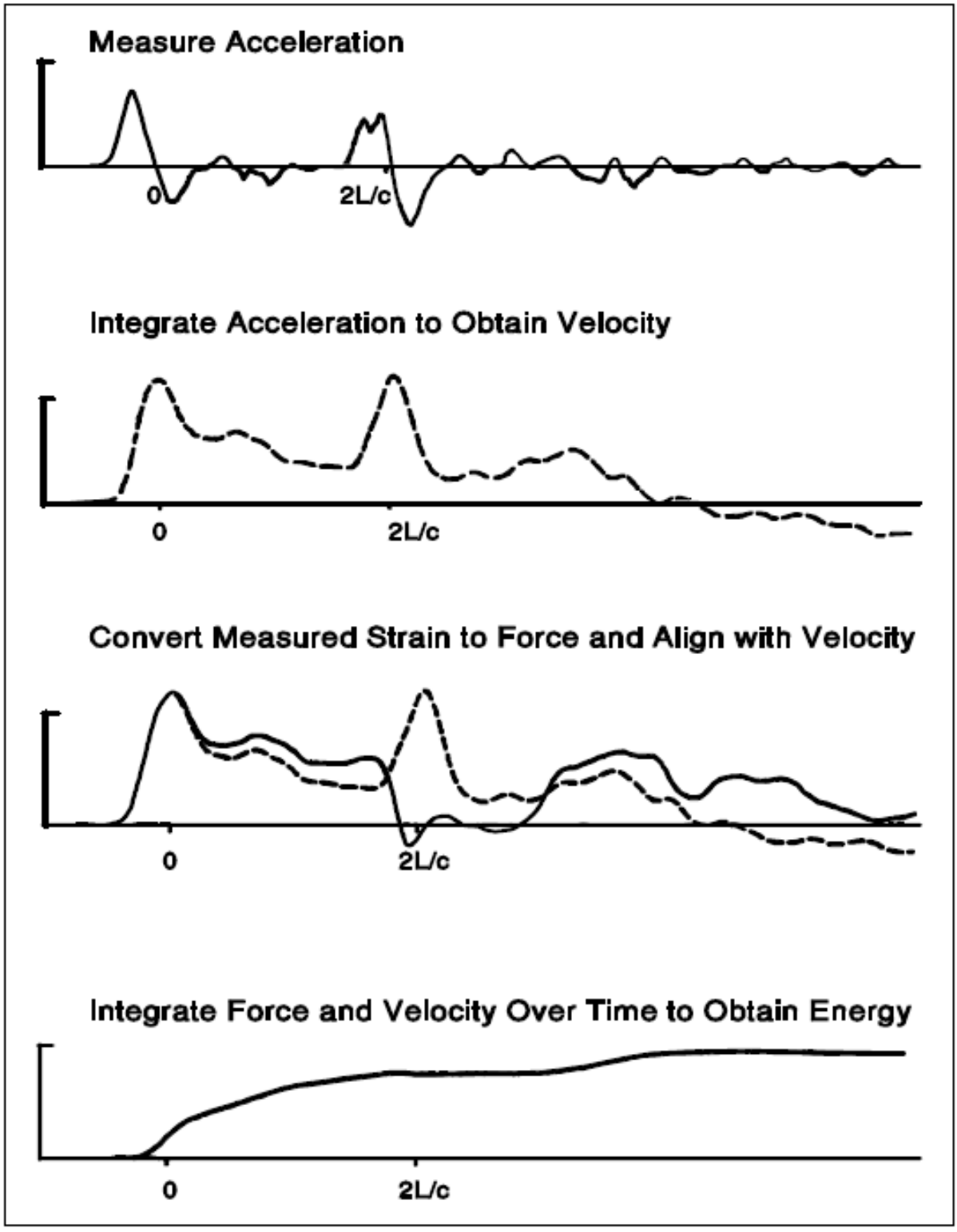

Figure 4-28 Energy transfer computation (from Hannigan 1990)

For the case of easy driving (Free-end condition), the compressive downward wave will be reflected as a tensile wave. An example of this condition is presented in Figure 4-29 where the upward travelling wave changes signal as it goes up the pile in tension after it passes the time 2L/c. On the other hand, for the hard driving case (Fixed-end condition) the wave will be reflected in compression (Figure 4-30).

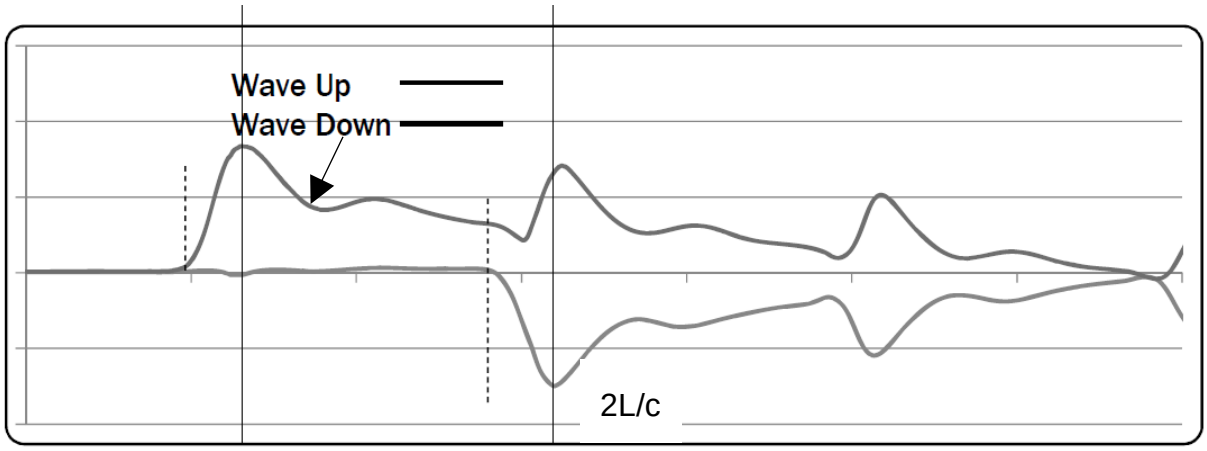

Figure 4-29 Wave Up and Wave Down traces for Free-end condition (after Pile Dynamics, Inc.)

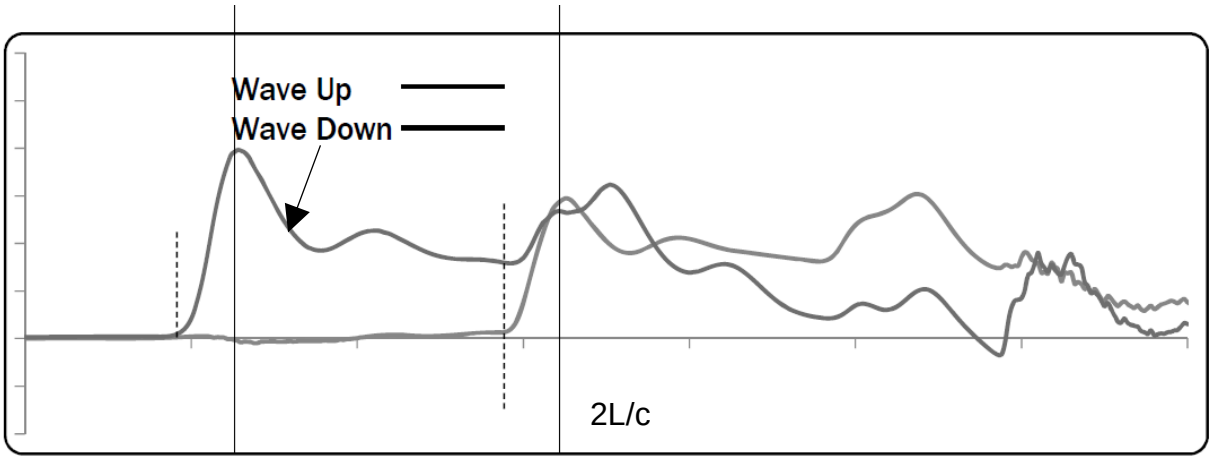

Figure 4-30 Wave Up and Wave Down traces for Fixed-end condition (after Pile Dynamics, Inc.)

Table 4.3 Most important PDA output quantities (after Pile Dynamics, Inc.)

Output	Quantit	Description
Force, Acceleration, Velocity, Displacement	FMX	Maximum compressive force at sensors
	AMX	Maximum acceleration at sensors
	VMX	Maximum velocity at sensors
	DMX	Maximum displacement at sensors
Stresses, Integrity	CSX	Maximum compression stress at sensors
	CSB	Maximum computed compression stress at pile toe
	TSX	Maximum computed tension stress below sensors
	BTA	Pile integrity factor
	LTD	Length to damage below sensors
Hammer performance	EMX	Maximum energy transferred to pile
	ETR	Energy transfer ratio (=EMX/rating)
	STK	Computed stroke (for open-end diesel hammers only)
	BPM	Blows per minute
Capacity Methods	RSP	Standard Case Method
	RMX	Maximum Case Method
	RSU	Case method with unloading correction
	RAU	Automatic Case Method – End bearing, no friction
	RA2	Automatic Case Method – Moderate friction

The dynamic quantities that the PDA provides as output are identified with three letter acronyms. Table 4.3 has a list of the most important quantities computed with the Case Method (Pile Dynamics, Inc.).

The energy transfer ratio is defined as the transferred energy to the pile divided by the manufacturer's rated hammer energy and is an indicator of the hammer and driving system performance. Figure 4-31 shows energy hammer ratios for diesel and open-end air/steam hammers for different pile types expressed as a percentile; the average hammer efficiency for a specific hammer-pile combination is found at the fifty percentile.

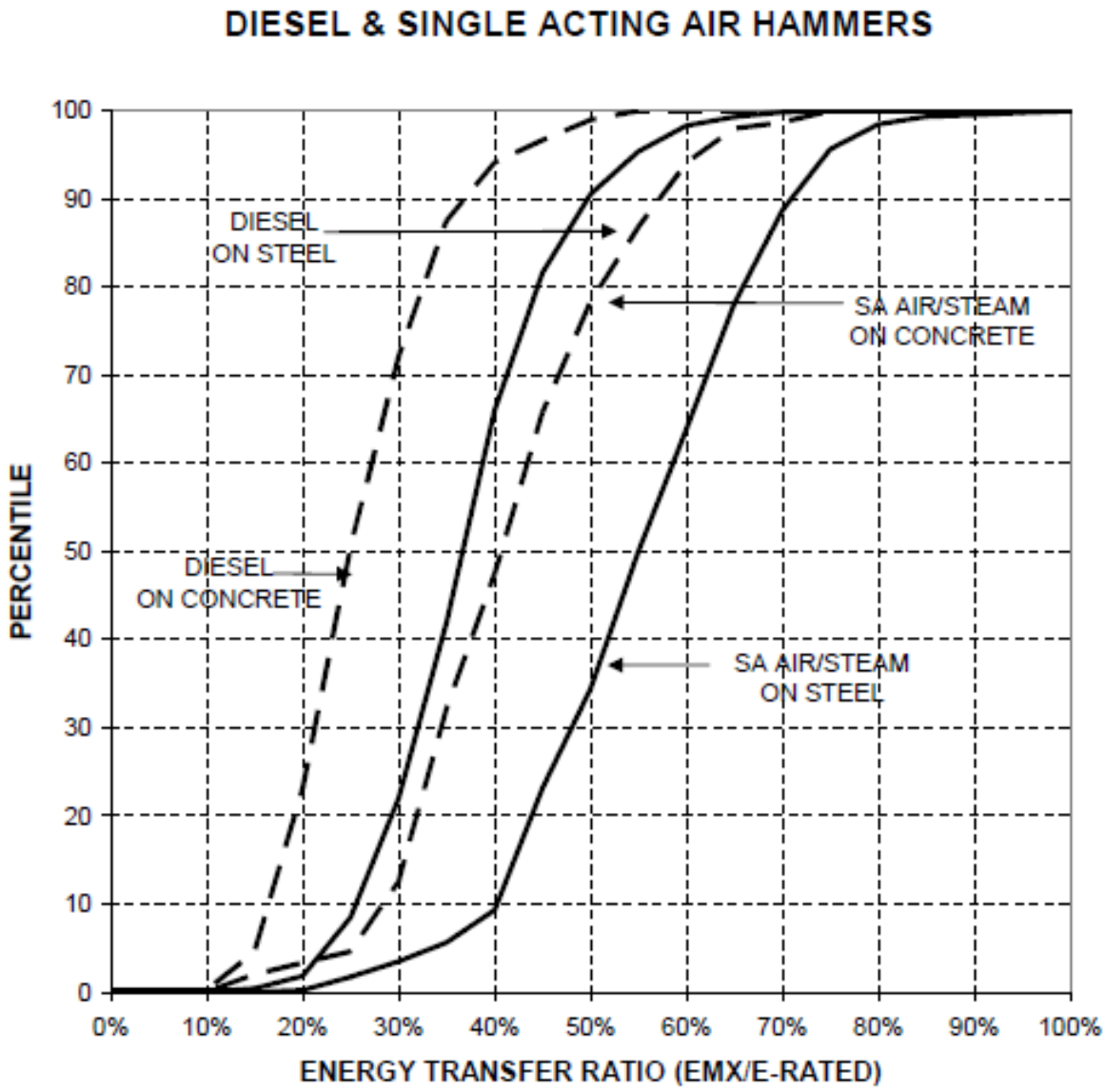

Figure 4-31 Energy transfer ratios for diesel and single-acting air/steam hammers for different pile types (from Hannigan et al. 2006)

4.5.3 CAPWAP (CAse Pile Wave Analysis Program)

The CAPWAP analysis method is a computer program that uses the measured force and velocity records from the PDA analysis from one hammer blow to calculate the ultimate static pile capacity, soil resistance distribution and soil quake and damping factor. This hammer blow is usually extracted at the end of driving. In principle, the CAPWAP numerical analysis makes use of the wave equation analysis and the PDA measured data through an iteration process of signal matching. The measured pile motion by the PDA test is used as an input and assuming a soil resistance distribution, the program derives a force wave trace at the pile head which is compared with the PDA measured force. Adjusting the soil model assumptions will provide finally a good match between the measured force wave trace and the computed one by the program (Hannigan 1990). Figure 4-32 presents an example of the CAPWAP iteration process. The best match soil model includes the static pile capacity, the soil resistance distribution and the soil quake and damping parameters.

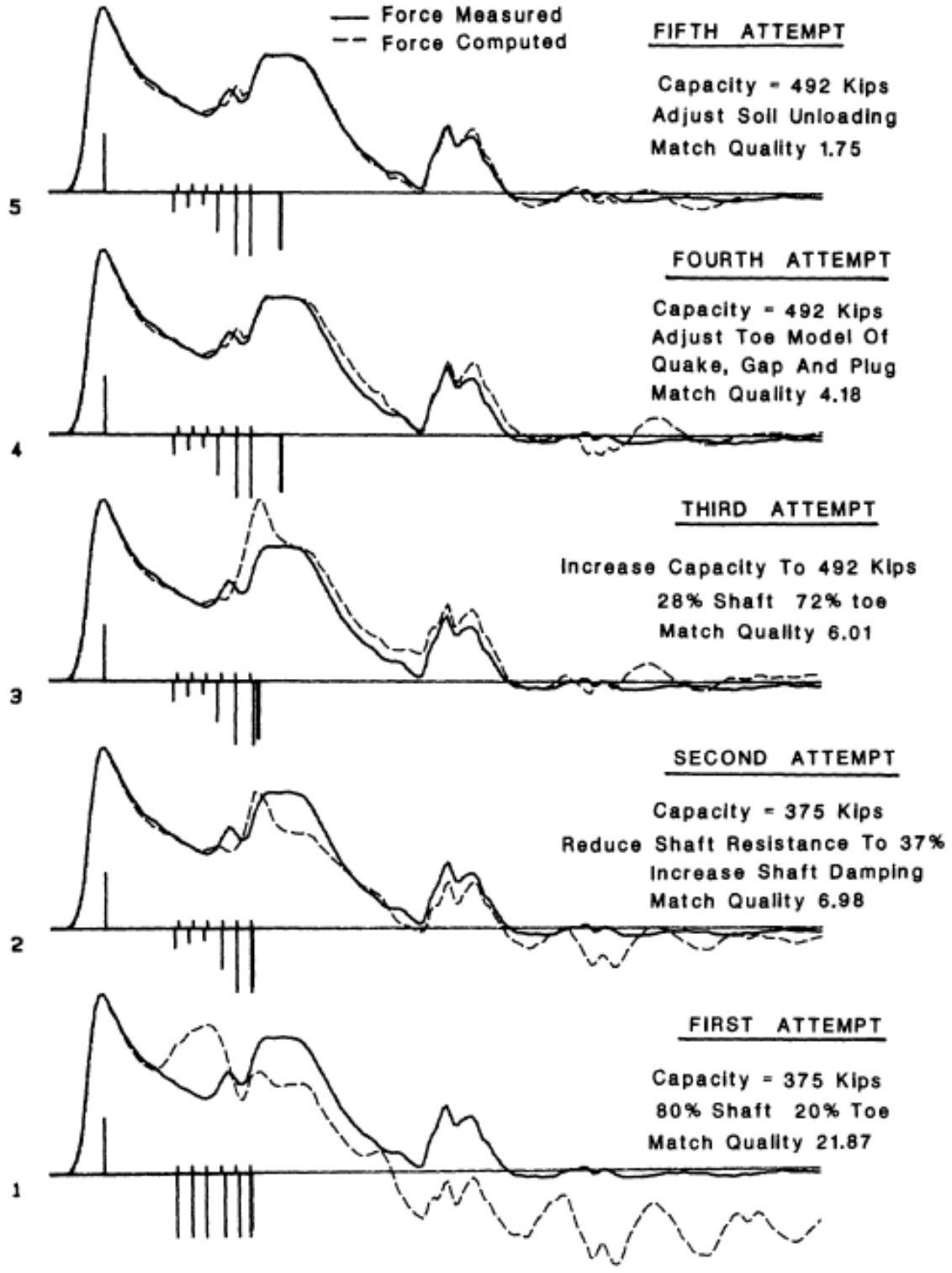

Figure 4-32 Schematic of CAPWAP iteration matching process (from Hannigan 1990)

4.6 Basic Hammer/Pile Energy concepts

The hammer performance is an important parameter that needs to be taken into account when driving a pile in order to ensure the proper hammer operation so as to install the pile to the designed depth. The **rated energy** or **potential energy, E_P**, of a hammer is the manufacturer's rating energy which is the ram weight, W, times the full stroke, h. Due to energy losses, only part of the potential energy will be transferred to the pile. Ideally, the impact velocity of the hammer immediately before the impact, v_0, would be:

$$v_0 = \sqrt{2gh} \qquad \text{Eq. 4-11}$$

Where: g = the acceleration due to gravity
h = maximum hammer stroke

The **kinetic energy, E_K**, is computed by:

$$E_K = \frac{1}{2}\left(\frac{W}{g}\right) {v_0}^2 = \frac{1}{2} m {v_0}^2 \qquad \text{Eq. 4-12}$$

Where: m = hammer ram mass

The actual energy delivered to the pile is calculated as the integral of the force times the velocity with time:

$$E_T(t) = \int_0^t F(t)v(t)\, dt \qquad \text{Eq. 4-13}$$

The **transferred energy** or **ENTHRU, E_T**, can be measured by the acceleration and strain records near the pile head with the PDA test. Figure 4-33 presents a schematic of the energy transfer process from a hammer to a pile.

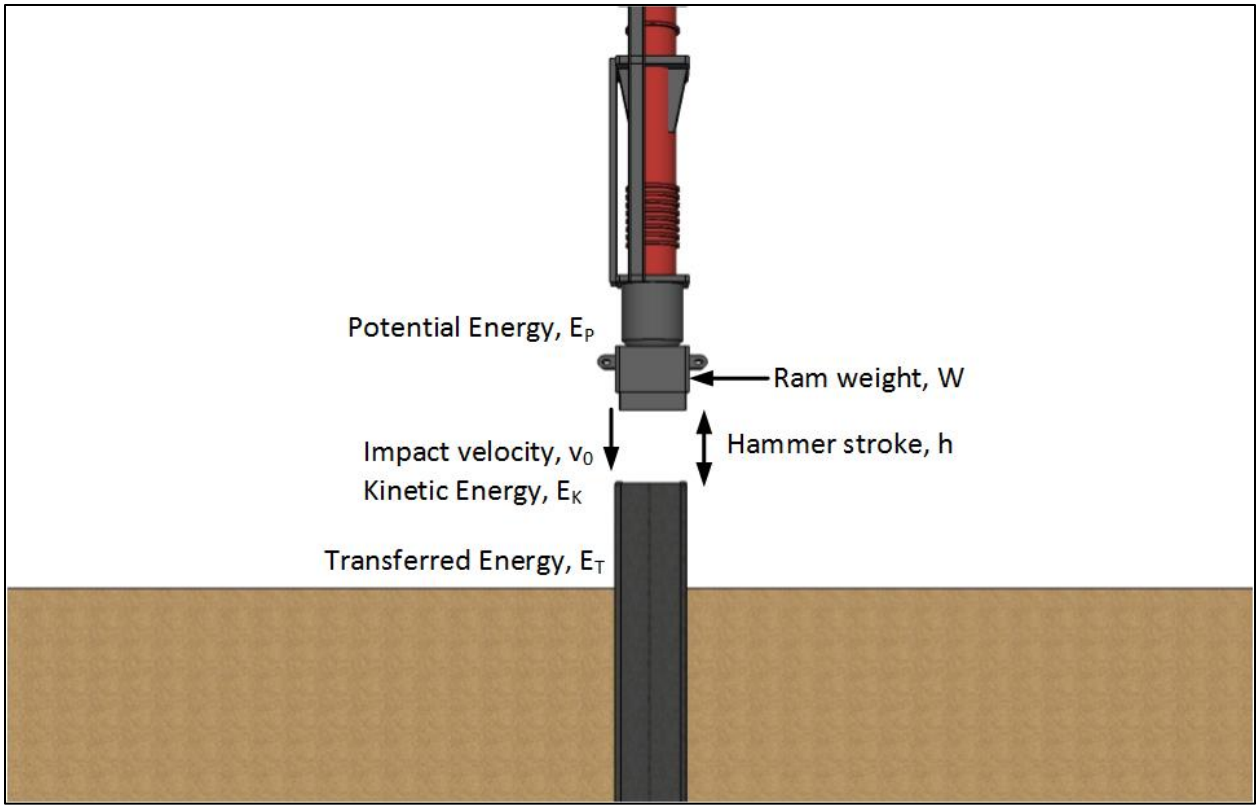

Figure 4-33 Schematic of energy transfer from the hammer to the pile

The **hammer efficiency, η**, is defined as the ratio of the actual kinetic energy of the ram to the potential energy of the hammer. A 100% efficiency would correspond to the ideal kinetic energy of the ram if no energy losses existed. The **energy ratio** is the ratio between the transferred energy to the pile and the potential energy. Histograms of transfer energy ratios for different hammer and pile combinations are presented in Figure 4-34 and Figure 4-35. These histograms provide the distribution and standard deviation of the drive system performance at the end of the drive condition. Table 4.4 presents recommended values of hammer efficiencies for different hammer types. Selecting the upper bound is recommended as it gives a conservative prediction.

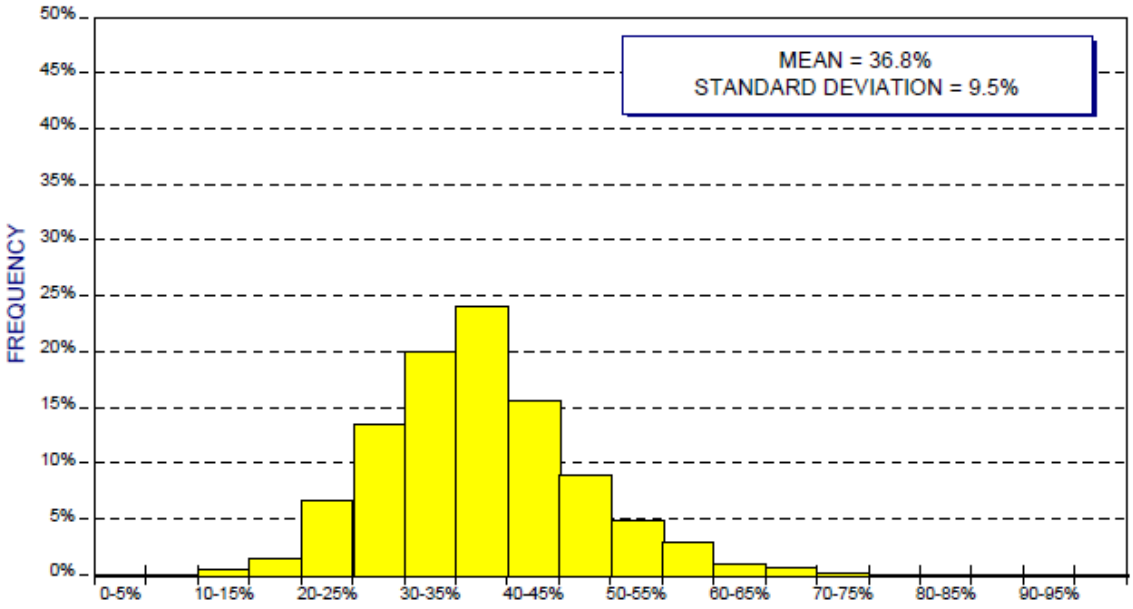

(a)

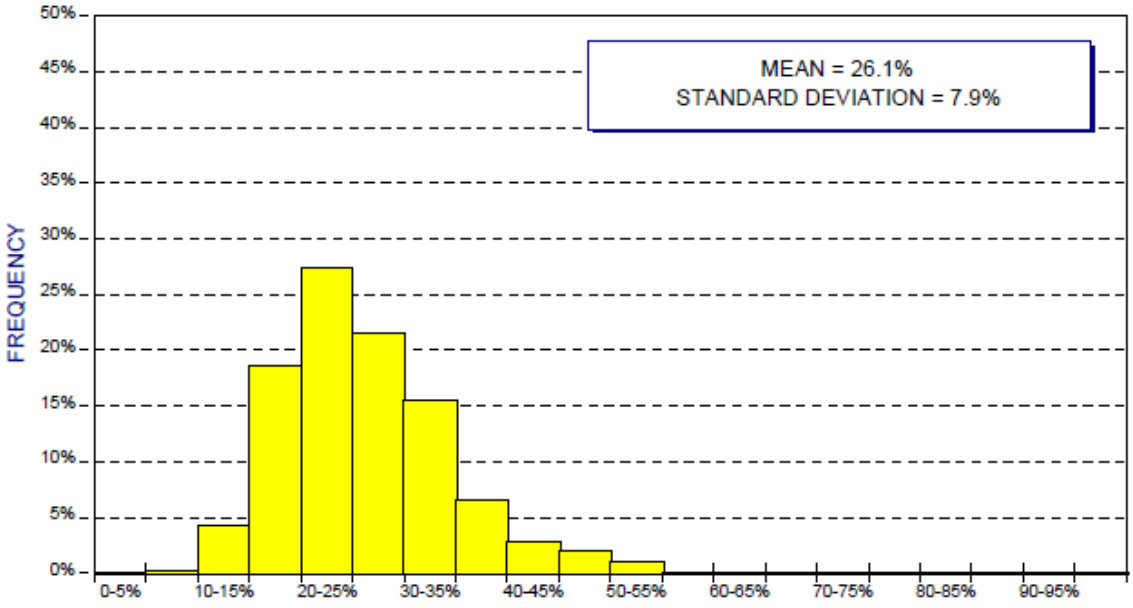

(b)

Figure 4-34 Histograms of energy transfer ratio for diesel hammers on (a) steel piles and (b) timber/concrete piles (from Hannigan et al. 2006)

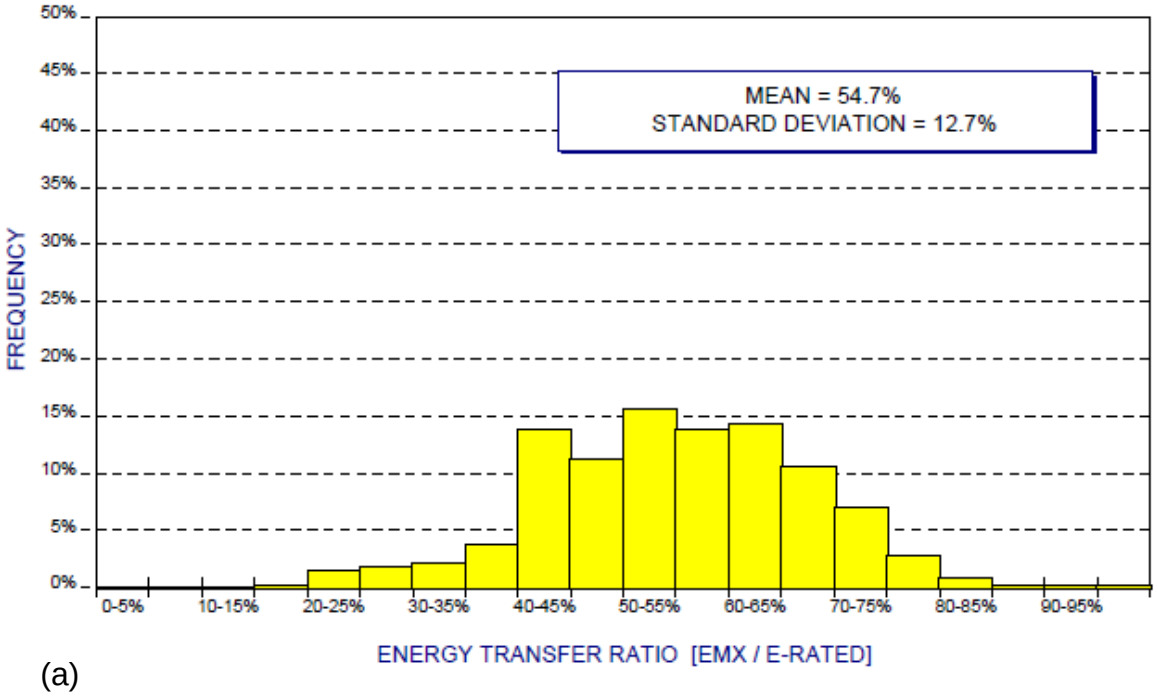

(a)

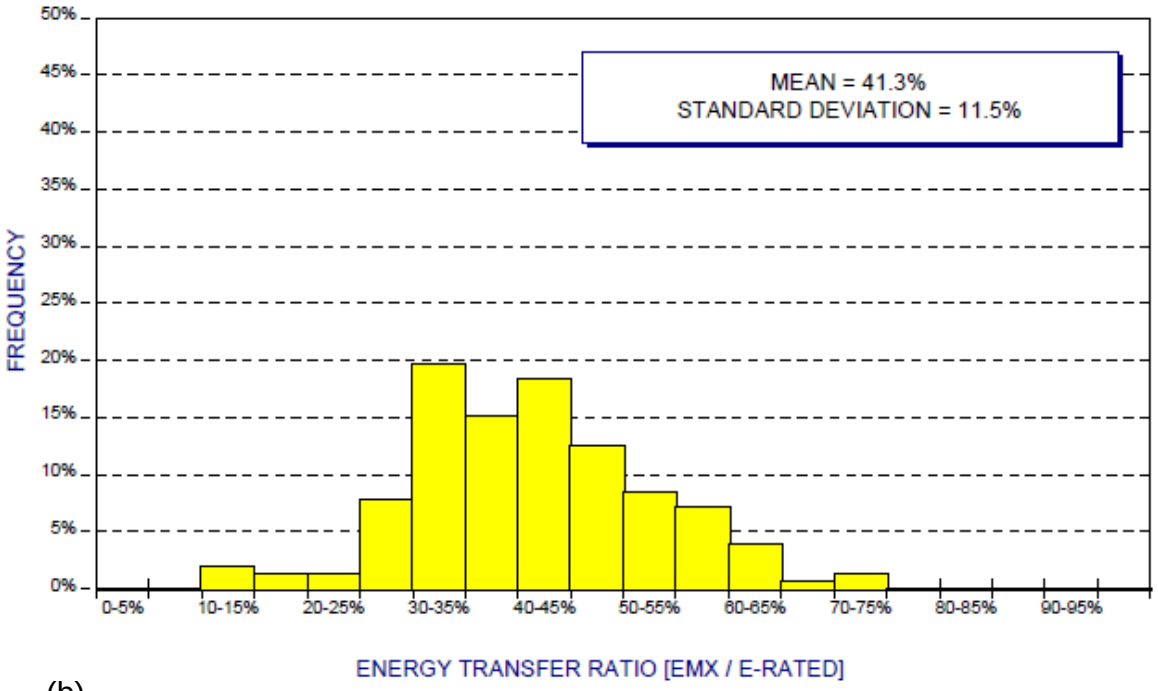

(b)

Figure 4-35 Histograms of energy transfer ratio for single acting air/steam hammers on (a) steel piles and (b) timber/concrete piles (from Hannigan et al. 2006)

Table 4.4 Recommended values of hammer efficiencies, η (after Rausche 2000)

Hammer Type	Pile Type	Hammer Efficiency, η
Drop hammer (free release)		0.95
Single-acting air/steam hammer	Steel piles	0.55 – 0.70
	Concrete and Timber piles	0.40 – 0.60
Double and Differential acting air/steam hammer	Steel piles	0.35 – 0.50
	Concrete and Timber piles	0.30 – 0.45
Diesel hammer	Steel piles	0.30 – 0.40
	Concrete and Timber piles	0.25 – 0.30
Hydraulic drop hammer (self-monitored)		0.95
Hydraulic drop hammer (other types)		0.55-0.85

When a hammer impacts on a pile top, a force is generated and a wave is propagated down the pile. The axial force, F_i, and the pile velocity, v_P, are proportional to the pile impedance:

$$F_i = Z v_P \qquad \text{Eq. 4-14}$$

The pile impedance is defined as:

$$Z = \frac{EA}{c} = Ac\rho \qquad \text{Eq. 4-15}$$

Where: Z = impedance of the pile
E = modulus of elasticity of pile material
A = pile cross section area
c = wave propagation speed in pile material

The stress in the pile at impact can be calculated as:

$$\sigma_P = \frac{E_P}{c_P} v_P \qquad \text{Eq. 4-16}$$

where: σ_p = stress in the pile
E_P = elastic modulus of the pile
c_P = propagation speed of compression wave in the pile
v_P = particle velocity in the pile

Assuming that the impedances of the hammer and the pile are equal, $\underline{Z_H = Z_P}$, yields that the particle velocity of the pile, v_P, is half the hammer velocity of the hammer just before touching the pile, v_0 (Fellenius 2016). Typical values of pile material properties are provided in Table 4.5.

Table 4.5 Pile material properties

Material	Elastic Modulus, E, GPa (ksi)	Wave Velocity, c, m/sec (ft/sec)	Density, ρ, kg/m^3 (lb/ft^3)
Steel	210 (30,500)	5,120 (16,800)	7,850 (490)
Concrete	40 (5,800)	4,000 (13,120)	2,400 (150)
Wood	16 (2,300)	3,300 (10,820))	1,000 (62.4)

The total soil resistance, R_{tot}, during pile driving is composed of a movement-dependent (static) component, R_{stat}, and a velocity-dependent (dynamic) component, R_{dyn}:

$$R_{tot} = R_{stat} + R_{dyn} \qquad \text{Eq. 4-17}$$

Soil resistances can be modeled as a spring and a slider representing the static resistance and a dashpot representing the dynamic resistance as shown in Figure 4-36. Ground vibrations are caused by the dynamic soil resistance.

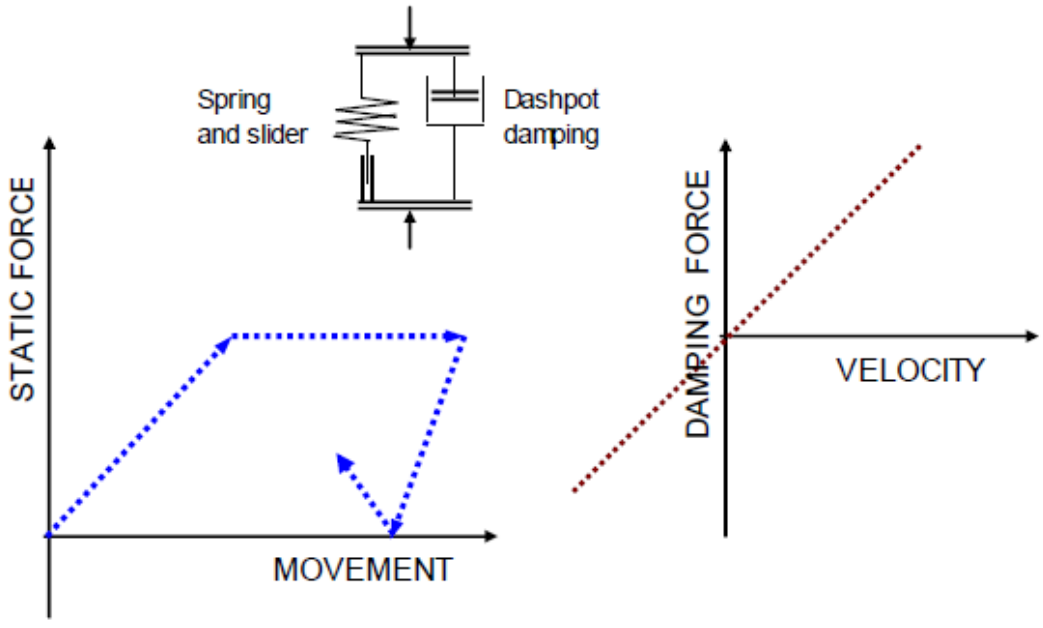

Figure 4-36 Static and dynamic soil resistance and model (from Fellenius 2016)

4.6.1 Dynamic Soil Resistance at Pile Tip

Goble (1980) assumed that the damping force at the pile tip, R_{dyn}^{TIP}, is proportional to the pile impedance times pile velocity by a dimensionless damping factor, J_c, called viscous damping factor:

$$R_{dyn}{}^{TIP} = J_c Z_P v_P \qquad \text{Eq. 4-18}$$

where: J_c = viscous damping factor
Z_P = pile impedance
v_P = particle velocity in the pile

Generally, it is assumed that J_c, is dependent only on the dynamic properties of the soil. Typical values of J_c for different soils are provided in Table 4.6.

Table 4.6 Viscous damping factor for different soils (after Rausche et al. 1985)

Soil Type	J_c
Sand	0.05-0.20
Silty Sand or Sandy Silt	0.15-0.30
Silt	0.20-0.45
Silty Clay or Clayey Silt	0.40-0.70
Clay	0.60-1.10

Iwanowski and Bodare (1988) derived the J_c analytically using the model of a vibrating circular plate in an infinite elastic body and found that it also depends on the ratio between the pile impedance and the soil impedance for P-waves at the pile tip:

$$J_c = 2\frac{\rho_{soil} c_{P-wave} A_{tip}}{\rho_P c_P A_P} = 2\frac{Z_{soil}}{Z_P} \qquad \text{Eq. 4-19}$$

where: ρ_{soil} = soil density
ρ_P = pile density
$c_{P\text{-}wave}$ = P-wave velocity
c_P = speed of the compression wave in the pile
A_{tip} = pile tip area in contact with soil
A_P = pile cross-sectional area
Z_{soil} = impedance of the soil
Z_P = impedance of the pile

The A_{tip} will be equal with the A_P, unless there is a case of closed-tip or plugged pipe or H-pile. The soil impedance is strain-dependent and needs to be adjusted for the strain level during pile driving. The dynamic force at the pile tip can then be written as:

$$R_{dyn}{}^{TIP} = 2Z_{soil}v_P = Z_{soil}v_0 \qquad \text{Eq. 4-20}$$

During pile penetration the stiffness at the pile tip, thus the impedance, will change. An empirical factor, $\mathbf{R_R}$ is introduced in the above equation to take into account disturbance and compaction effects (Massarsch and Fellenius 2008). It can be assumed that for loose and medium dense granular soils due to compaction and densification, R_R will increase with increasing driving resistance. For overconsolidated clays, pile driving will reduce the soil stiffness at the pile tip. Typical values that can be used if no field tests are available are:

- R_R = 2 for loose to medium dense granular soils
- R_R = 0.2-0.5 for overconsolidated clays (upper limits are preferable)

4.6.2 Dynamic Soil Resistance along Pile Shaft

The dynamic soil resistance along the pile shaft, R_{dyn}^{SHAFT}, can be estimated by:

$$R_{dyn}^{SHAFT} = A_{shaft}\rho_{soil}c_{S-wave}v_P \qquad \text{Eq. 4-21}$$

where: A_{shaft} = contact area between shaft and soil
ρ_{soil} = soil density
$c_{S\text{-}wave}$ = S-wave velocity of soil at the shaft-soil interface
v_P = particle velocity in the pile

A zone surrounding the pile shaft will be disturbed and remolded, a factor **R_R**, is introduced to the above Equation to take care of these effects. A reduction factor, **R_C**, needs to be applied to Eq. 4-21 in order to represent the reduction of the shear wave velocity at the shaft-soil interface (Massarsch and Fellenius 2008). Assuming that the pile length in contact with the soil is equal to the length of the stress wave in the pile, L_W, and for pile of cylindrical shape, the dynamic soil resistance along the pile shaft can be written as:

$$R_{dyn}^{SHAFT} = 0.5v_0\rho_{soil}R_R R_c c_{S-wave}\pi d L_W \qquad \text{Eq. 4-22}$$

where: R_R = reduction factor for disturbance/remolding effects
R_C = reduction factor for shear wave velocity at shaft-soil interface
d = diameter of pile
v_0 = particle velocity of the hammer at impact

The reduction factor, R_R, for disturbance and remolding effects along the pile shaft is different than that used at the pile tip. It is usually less than unity in most soils, in contrast to R_R of tip resistance which is equal to 2 for granular soils.

The maximum particle velocity at the pile-soil interface, $\mathbf{v_{max}}$, can be approximated by:

$$v_{max} = \frac{\tau_f}{\rho_{soil} R_c c_{S-wave}} \qquad \text{Eq. 4-23}$$

where: τ_f = maximum shear stress at the shaft-soil interface
ρ_{soil} = soil density
R_C = reduction factor for shear wave velocity at shaft-soil interface
$c_{S\text{-}wave}$ = S-wave velocity of soil at the shaft-soil interface

CHAPTER 5 FIELD SET-UP AND METHODOLOGY

5.1 Ground Motion Sensor Design and Fabrication

5.1.1 Sensors

Two types of sensors were used to measure ground motion vibrations, geophones and accelerometers. Triaxial and single axis seismometers, model L4 units supplied by Mark Products, were used to monitor ground motions on the ground surface near the driven pile. All of these seismometers have a natural frequency of 1 Hz and are ideal to measure the expected low frequencies from pile driving operations. Figure 5-1 and Figure 5-2 present the triaxial geophone package and a single axis vertical seismometer, respectively. Sandbags were placed on top of the two closest instruments from the pile to secure coupling with the ground.

Three-axis accelerometers and vertical geophones were installed in the ground. Model CXL10GP3, triaxial silicon micro-machined accelerometers, supplied by Crossbow were used at the first test site. This accelerometer has an acceleration range of ± 10 g and can be used with a 5.5 to 36 V power supply. The output requires no external signal conditioning and may be directly interfaced to a data acquisition system with a range between 0 to 5.5 V. These accelerometers were factory calibrated and tested. In order to lower the cost of the embedded accelerometers, since these sensors would be buried and would not be recovered, custom made triaxial accelerometer units were designed by Civionics, LLC and were used for all the other test sites. Model MMA7361LC, Micro-Electro-Mechanical Systems (MEMS) type accelerometers, supplied by Freescale were selected for this application. The acceleration range of this instrument is ±6g and the output can range between 0 and 3.3 V. A 3.3 voltage regulator was included to provide

any voltage source between 4 and 14 V. The MEMS sensing element was mounted on a 1 in x 1 in printed circuit board (PCB) as shown in Figure 5-3 .

Also, for the least expensive approach, single component (vertical) geophones, model RGI-4.5 Hz supplied by Racotech Geophysical Instruments, were implemented in this project. Figure 5-4 shows one of the geophone elements. Table 5.1 presents a summary of the main parameters of the aforementioned sensors. Specifications and amplitude response curves, where applicable, of all the sensors used are given in Appendix A. It should be noted that the sensors will be referred from here on with the sensor ID provided in Table 5.1.

Table 5.1 Sensors used in this research

Supplier	Crossbow	*Freescale	Racotech	Mark Products	Mark Products
Model	CXL10GP3	MMA7361LC	RGI-4.5Hz	L4	L4
Type	Accelerometer	Accelerometer	Geophone	Seismometer	Seismometer
Axes	Triaxial	Triaxial	Vertical	Triaxial	Vertical Longitudinal Transverse
Range	± 10 g	± 6 g			
Sensitivity	200 mV/g	206 mV/g	23.4 V/m/sec	7 V/in/sec	7 V/in/sec
Natural Frequency			4.5 Hz	1 Hz	1 Hz
Size	1.20 in x 1.20 in x 0.86 in	1.25 in x 1.25 in x 0.15 in	1 in x 1.3 in (diameter x height)	9.45 in x 9.45 in (diameter x height)	3 in x 6 in (diameter x height)
Sensor ID	**A**	**A**	**SG**	**BG**	**G**

*custom-made by Civionics, LLC.

Figure 5-1 Triaxial seismometer used to measure surface ground motions

Figure 5-2 Vertical seismometer used to measure surface ground motions

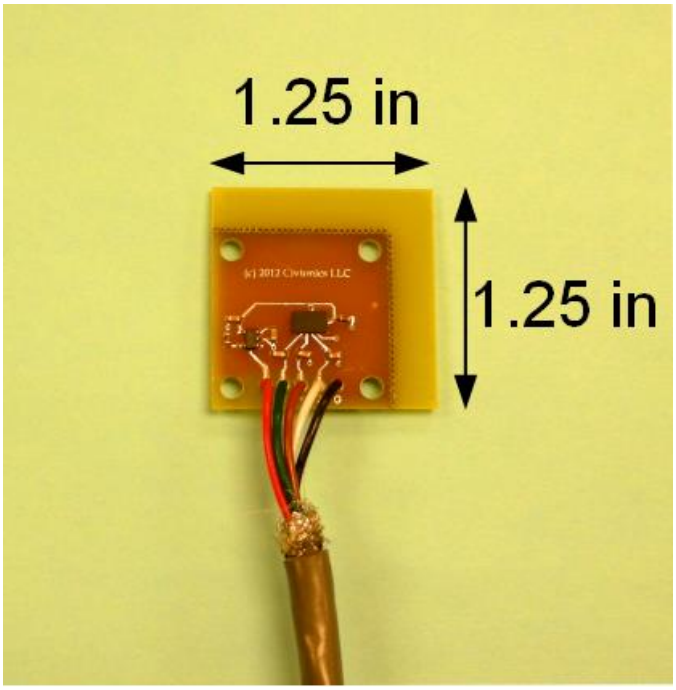

Figure 5-3 MEMS type accelerometer mounted on a PCB

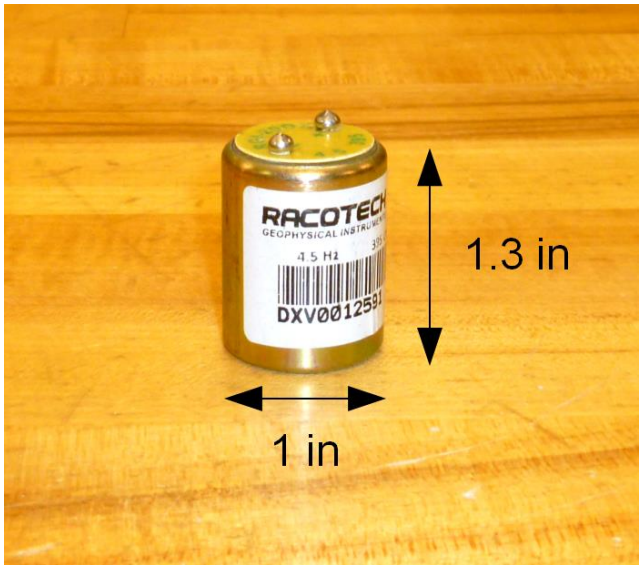

Figure 5-4 Low frequency geophone element

5.1.2 Data Acquisition System

A multi-channel data acquisition system was employed to record ground vibrations from both the embedded and the surface sensors. The National Instruments (NI), Model *NI CompactDAQ-9178* USB chassis was chosen. This eight-slot system has the capability to combine up to eight accelerometers or other voltage modules for simultaneous data acquisition. The chassis is connected to a field laptop with a USB cable. The NI cDAQ requires a 9 to 30 VDC power supply and uses a maximum load 15 W of power. It has four 32-bit counter/timers built in.

In order to record data from the accelerometers sensors, five *NI 9232* analog input modules were plugged in the cDAQ chassis. Each module has three input channels that can record signals at sampling rates up to 102.4 kSamples/sec (kHz) with built-in antialiasing filters. The voltage input range is ±30 V and the resolution is 24 bits. The input signal on each channel is buffered, conditioned, and then sampled by an isolated 24-bit Delta-Sigma ADC (Analog to Digital Converter). One triaxial accelerometer can be connected to each of these modules. A 12 V battery was used to provide power supply and excitation for the accelerometers.

One *NI 9205* analog input module was plugged in to acquire voltage signals from geophones. This module has 32 single-ended or 16 differential channels with a maximum sampling rate of 250 kSamples/sec (kHz). Each channel has voltage input ranges of ±200 mV, ±1 V, ±5 V and ±10 V and the ADC resolution is 16 bits. All channels share a common ground and a programmable instrumentation amplifier and are multiplexed to an ADC. The differential configuration was used in order to attain more accurate measurements and less noise, and since two inputs for each measurement was required, the number of available channels was reduced to 16.

Two *NI 9221* analog input modules were plugged in the cDAQ chassis to record voltage signals from geophones. Each module provides eight analog input channels with a maximum sampling rate of 800 kSamples/sec (kHz). The maximum voltage input range is ±60 V. There is a common terminal for all channels that is internally connected to the isolated ground reference of the module. The input signals are scanned, buffered,

conditioned, and then sampled by a single 12-bit ADC. This module was implemented to record voltage signals from geophones that were placed very close to the pile, since high amplitudes were expected from these sensors and this module has a maximum voltage input of 60 V. The NI 9205 module was used to acquire voltage signals from geophones that were further away from the pile. A summary of the different modules that were plugged in the DAQ system are presented in Table 5.2. Figure 5-5 shows the data acquisition system used for this research.

The NI LabVIEW SignalExpress software was used to acquire, view and store the data logs from the different modules and channels in a Panasonic Toughbook 53 laptop computer (Figure 5-6). Signals were then exported as text or Microsoft Excel files and were processed using the Matlab software.

Table 5.2 Summary of selected modules of the data acquisition system

Module	Signal Type	Channels	Sample Rate	Resolution (bits)
9232	IEPE (Integrated electronic piezoelectric accelerometer)	3	102.4 kS/sec	24
9205	Voltage	32 SE/16 DI	250 kS/sec	16
9221	Voltage	8	800 kS/sec	12

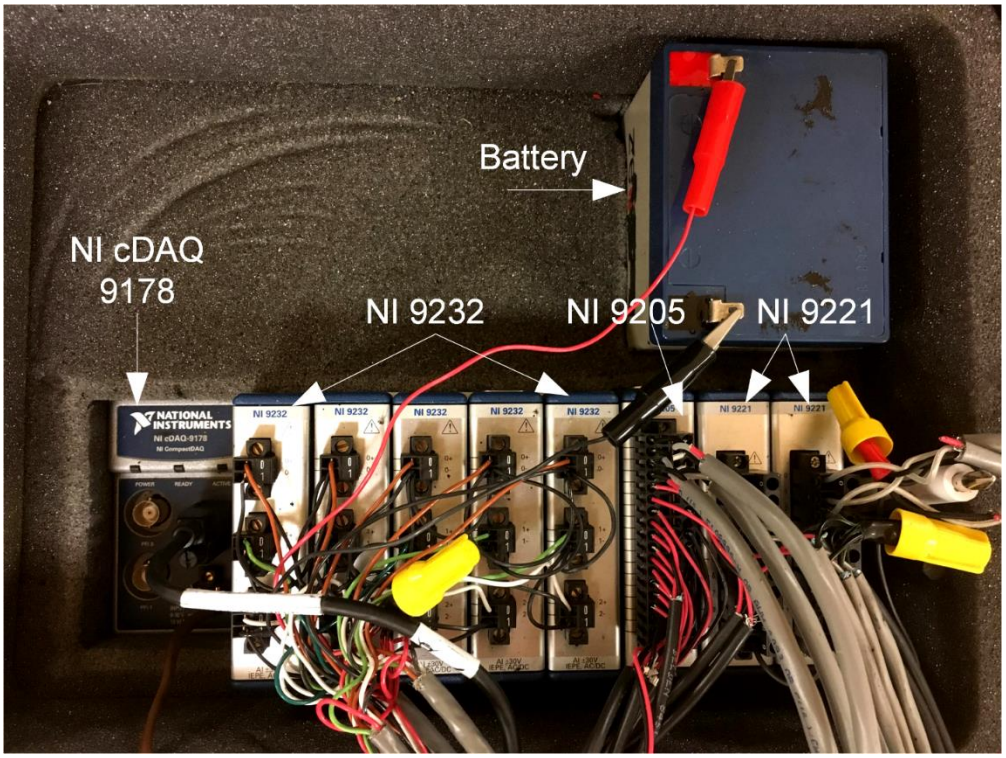

Figure 5-5 Data acquisition system used in field tests

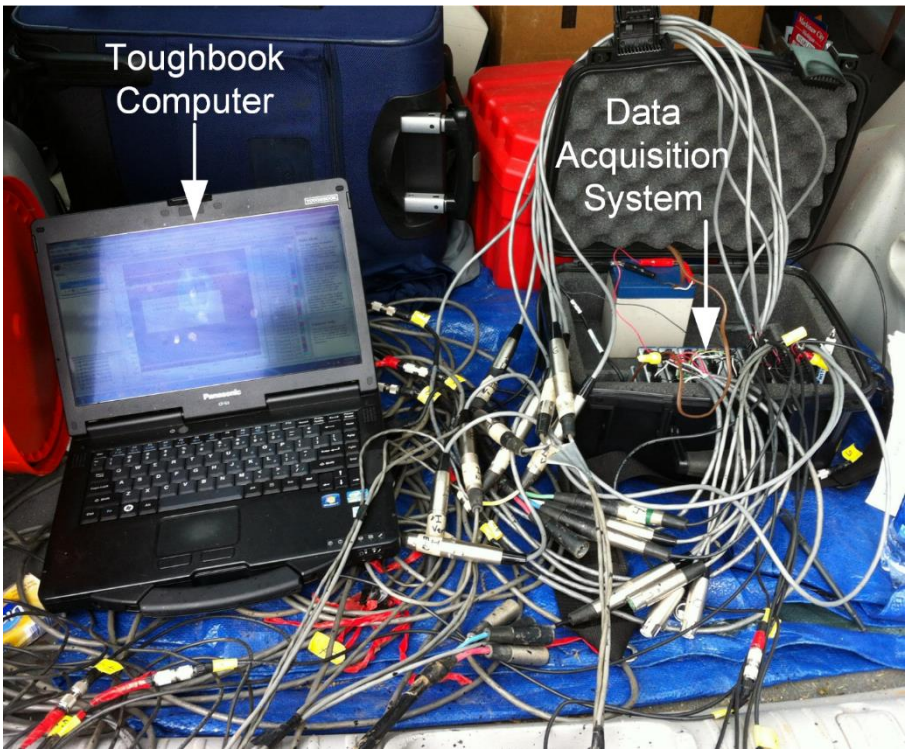

Figure 5-6 Data acquisition system and Toughbook computer

5.1.3 Sensor Cones

Since the buried transducers would be sacrificial, sensor packages had to be designed that could be pushed into and be left in the ground. Removing the embedded sensors would interfere with operations of the piling contractor, while the conductor cables are very vulnerable to breakage. Steel sensor cones were selected because they would be very robust for pushing into shallow or deep soil profiles. These cones had 60 degrees tapered tips and a hollow cylindrical center to house the sensors. Figure 5-7 shows an accelerometer chip being fitted into a cone cavity and Figure 5-8 presents views of the cone casing. The sensors were placed into the cone cavity, which was then filled with epoxy resin to protect the transducers and make them waterproof. A special adaptor was designed that would allow downward pushing of the cone with Standard Penetration Test (SPT) AW rods. A withdrawing force to the sensor cone would not be allowed with this design. Figure 5-9 depicts the adaptor and sensor casings with the sensing elements and the epoxy in place. Figure 5-10 shows a cross section and a view of the cone, adaptor and rod. As can be seen in this Figure, the shoulder of the cone was designed with a slightly larger diameter (2 in) than the outer diameter of the drill rod (1.75 in). This feature would help the cone to engage the soil and be held in place as the rod and adaptor were withdrawn. Other dimensions of the cone and the adaptor can be found in Figure 5-10.

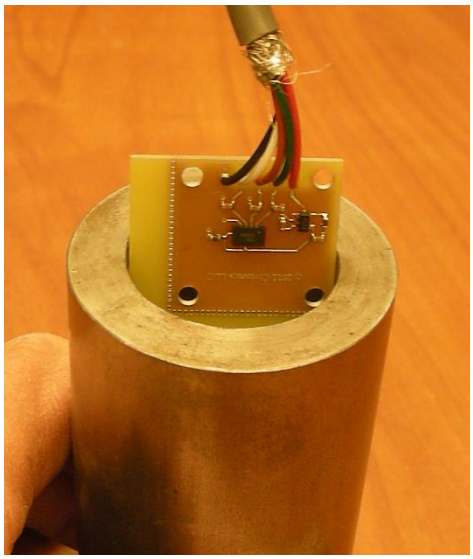

Figure 5-7 Accelerometer chip being fitted into cone cavity

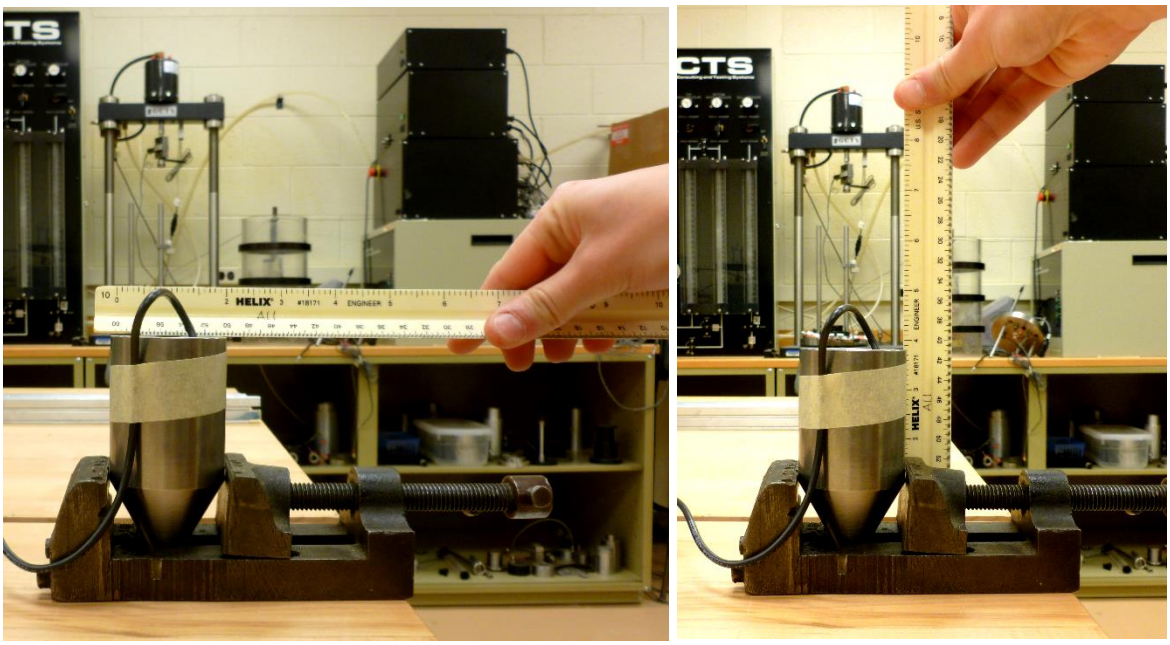

Figure 5-8 Sensor package (cone)

Figure 5-9 Sensor casings and rod to cone adaptor

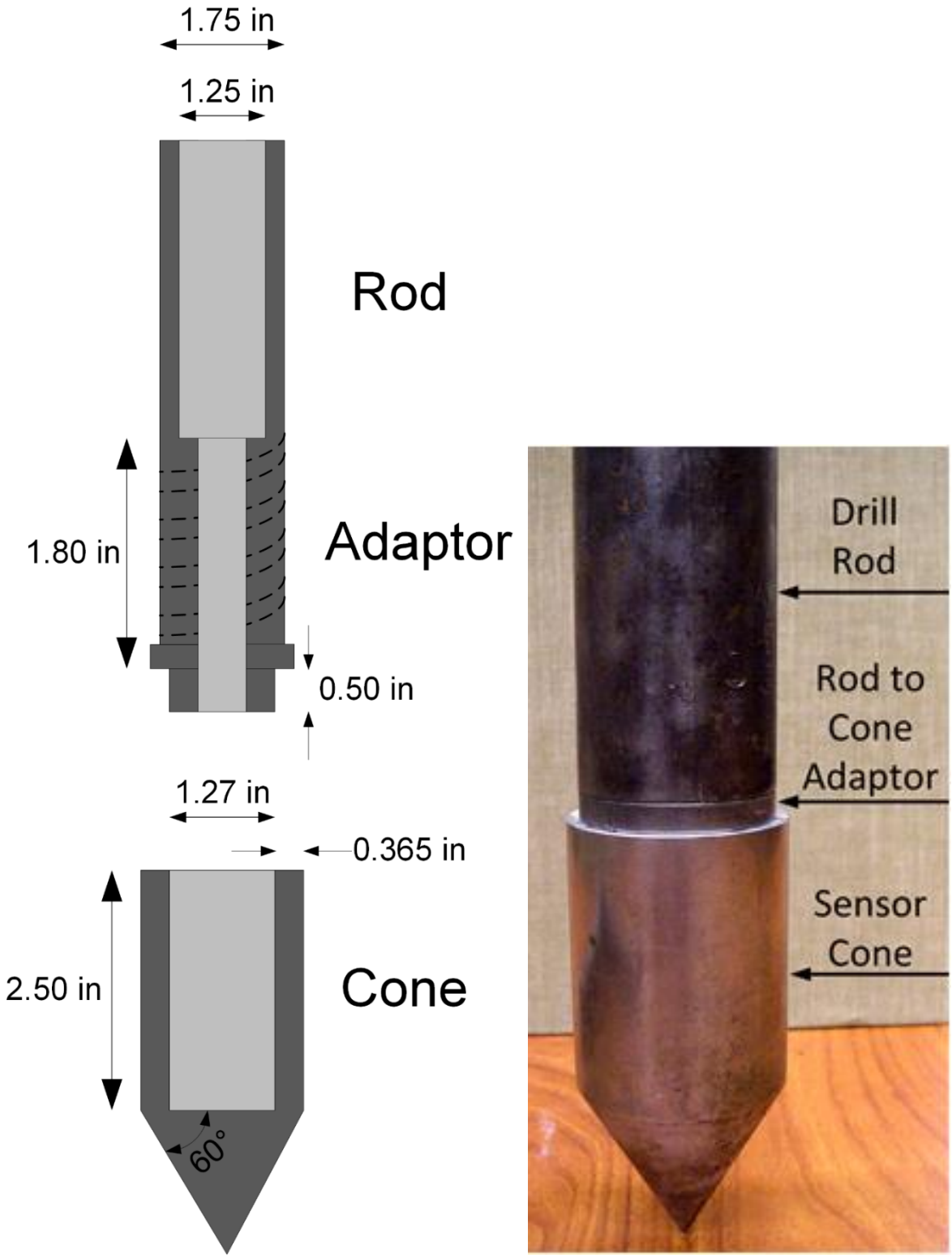

Figure 5-10 Cross section and view of cone, adaptor and rod (not to scale)

5.2 Ground Motion Sensor Installation

Pile driving contractors, of the selected tested sites recommended by MDOT, were approached and were asked to cooperate in order to make it possible to monitor ground motion vibrations in the vicinity of the pile. All contractors agreed to drive a pile in an appropriate location based on soil conditions, which would not interfere with the contractors' operations. Some of the piles were test piles that were then extracted or just left in place and some were production piles, part of the project. The installation of the embedded sensor packages started from the ones closest to the pile and continued outward from the pile for additional sensors. An MDOT drill rig was positioned over the sensor location and the sensor package was pushed into the ground. Sensor cones were pushed using the hydraulic thrust capabilities of the drill rig. Figure 5-11 shows a view of the drill rig at one of the test sites. After each sensor was installed to the desired depth, the above ground conductor cable was placed into a plastic bag to protect and identify the buried sensor location, while working on installing the rest of the sensors.

The sites that were selected to be tested in this project consisted mainly of sites with loose to medium dense sands so little difficulty was expected during the installation of the sensors. It was anticipated that sensor cones would be pushed into soil for which Standard Penetration Test blow count (N) would be less than 40. However, based on a dry run test that took place in order to practice the sensors' installation process, several difficulties were experienced. The full downward capacity of the drill rod could not be applied and pushing the cones worked for blow counts only up to 30. When the drillers encountered a thin gravel layer, they had difficulty to continue driving the sensor even in a layer with low blow counts (less than 10). Unsupported column action of the drill rod also limited how far the sensors could be pushed without bending the rods beyond their elastic range. Damage to the conducting cable during the withdrawal of the SPT rods also happened in some cases. As an alternative approach, installation of the sensor packages through the center of hollow stem flight augers was attempted. This method was found to be unsuccessful, since pulling the SPT rod upwards sometimes resulted in loss of either the sensor package or severing the conductor cable. Figure 5-12 illustrates an SPT rod inside a hollow stem flight auger and Figure 5-13 shows the removal of the hollow stem

flight auger, where flooding of the AW rod was used to help hold the sensor in place. Even if each sensor's depth was predetermined according to the soil conditions, in practice the local ground conditions and installation process often controlled the final depth of the sensors.

5.2.1 Sensors' Installation Procedure

The general installation process was as follows. First, the cable was threaded through the hollow core of the first SPT rod which was positioned along with the sensor package on the ground surface at a predetermined location (Figure 5-14). The wire was fed through the next rod which was aligned on top of the first one as shown in Figure 5-15a. A special designed adaptor, with a notch that would protect the cable, was attached on the top rod before positioning the rig over the head of the rod and start pushing (Figure 5-15b). The rods were pushed into the ground as depicted in Figure 5-16a; multiple SPT rods of 5 ft length were used to push the sensor packages to the desired depth. Figure 5-16b shows the extraction of the rods while the sensor cones were left in place. The rods were removed carefully one by one to make sure that the cable would not be damaged. The boreholes were backfilled with white sand as illustrated in Figure 5-17. This Figure shows how close to the driven pile the sensors were successfully installed.

5.2.2 Problematic installation due to soil conditions

The soil conditions that caused difficulties during the installation process were of two extreme types: very loose sand or very dense sand. In the case of very loose sand, the sensor cone would not remain in the planned location as the rods were withdrawn and would come upwards with the rods. This problem was solved by either filling the rods with water, to put hydraulic pressure on the cone and help it stay in place when pulling out the push rods, or by machining a very loose cone to adaptor fit, so that the sensor cone would fall out of the drill string. Sharpening the adaptor to sensor cone connection and using masking tape to hold the cone to the adaptor while keeping a loose fit was the most successful method. However, each test site had a unique behavior, so different attempts were tried to accomplish successful sensor installation every time. Dealing with the other

extreme, very dense sand, required other solutions. One of them, as mentioned above, was to install the SPT rod through a hollow stem flight auger. This approach was not very successful, because it was difficult to push the sensor package below the end of the hollow stem auger, thus below the zone of disturbance caused by the hollow stem auger's installation. Sand pinched the cone at the flight auger exit point and contact was lost between the cone and the push rod causing the cable to be cut. Predrilling a borehole with the hollow stem flight auger, removing the auger and then pushing the cone into the loosened sand worked in some cases.

Successful installation of the sensor packages did not always ensure successful operation of the sensor. In some cases, the driven pile would cut the wire of the sensors buried very close to the pile. That is because the sensors were not at a depth directly below the surface location where cables were coming out on the ground surface.

5.2.3 Specific Site Installation Experience

From the above discussion it is obvious that each site had its own sensor installation difficulties and there was no single solution to every problem. The actual experience was different than what was anticipated. The intention was to install two sets of sensors at two different elevations and three different distances from the pile face. Below there is a brief discussion of specific installation behavior at the test sites. More details, plan and elevation views of the successfully installed sensors will be provided in the next Section.

- **M-25 site over Harbor Beach Creek:** Two sensor cones were successfully installed at a planned depth of 6 ft. The third sensor in the row at this depth would not stick in place (very loose sand case) until a depth of 10 ft was reached. The 6 ft depth was found to be too shallow, because the pile penetrated about 12 ft with fewer than 10 blows. The deeper set of sensors was intended to be set at about 20 ft, but two of the sensor cones were lost due to breakage of the cable on installation and a third sensor installation at this depth was not attempted.
- **M-66 site over Wanadoga Creek:** Three sensor cones were successfully installed at different distances from the pile at 35 ft. For the shallow set of sensors, the first attempt

proved unsuccessful, as the sensor cone would not stay in place in the very loose sand material, and finally the wire was cut, so another attempt was not tried. A geophone sensor cone was pushed to a depth of 5.4 ft, which again is considered too shallow but gave a good comparison with the surface geophone placed right above it.

- **M-139 site over Dowagiac River:** Three deep sensor cones were pushed successfully at 25.5 ft. It was also difficult at this site to position the close-in casing at a shallow depth of 10 ft. Only one sensor cone stayed in place, another one was lost.
- **US-131 A site over St. Joseph River:** At abutment A of this site, trial installation methods were performed. Pre-augering with a small diameter solid stem flight auger was used to bore to the planned depth. Flights were then removed leaving loose sand in the hole and the sensor cone was pushed to the desired depth. This approach worked very well at this site and allowed sensor installation at two depths and three distances from the pile as planned.
- **US-131 B site over St. Joseph River:** At abutment B, the installation procedure used at abutment A, did not work for unknown reasons. Shallow depth sensor installation was not achieved as planned because the soil was very loose and the casing would not stick, while deep sensors did not reach the planned depth because of insufficient push capacity. At this site an attempt was made to determine if there was difference in vibration transmission based on the orientation of the pile. Sensors were set at 0.5 ft from both the open side and the flange side of the pile. Unfortunately, the open side sensors were destroyed during pile driving; conductor circuits were tested before the driving the pile and were found to operate.

Table 5.3 is a summary of the attempted and successful installation procedures for all the tested sites. As can be seen, 19 out of 23 accelerometer sensor casings and 8 of the 9 geophone sensor cones were successfully installed. Again, successful cone installation did not always provide successful signal acquisition. Also, these statistics do not reflect cases where the installation was abandoned due to obstacles. Table 5.4 presents a summary of the surface geophones that were used at each site.

It is important to note, that due to the uncertain construction schedule, best use of the learning curve installation experience could not be made. Most sensors, were fabricated

at the same time and were ready to go to be installed on short notice. A larger shoulder cone might be a solution to stick the cone in the very loose sand layers. The sensors were already potted in the cone and it was impossible to remove them without destroying them when the experience showed that another design would be more favorable.

Table 5.3 Success rate of embedded sensors at tested sites

Site	Embedded Sensors			
	Accelerometers		Geophones	
	Attempted	Successful	Attempted	Successful
M-25	5 Crossbow	3		
M-66	4 Freescale	3	1	1
M-139	5 Freescale	4		
US-131 A	5 Freescale	5	2	2
US-131 B	4 Freescale	4	6	5
TOTAL	23	19	9	8

Table 5.4 Summary of surface geophones used at each tested site

Site	Surface Geophones			
	Triaxial	**Vertical**	**Longitudinal**	**Transverse**
M-25	Geophones were plugged in other data acquisition system (not the NI) and the signals were clipped			
M-66	2	4		
M-139	2	2	2	
US-131 A	2	4	3	3
US-131 B	2	4	3	3

Figure 5-11 View of drill rig used to push sensor cones in desired depths

Figure 5-12 SPT rod inside the hollow stem flight auger

Figure 5-13 Withdrawal of the hollow stem flight auger

Figure 5-14 Rod and cone positioning on the ground surface

Figure 5-15 (a) Feeding of cable through the rod and (b) attachment of drill rig with rod

Figure 5-16 (a) Pushing the rods and (b) rod extraction

Figure 5-17 Conductor cables coming out on the ground surface

CHAPTER 6 GROUND MOTION FIELD MEASUREMENTS

6.1 Monitored Test Sites

Ground motions during pile driving were monitored at five project sites controlled by the Michigan Department of Transportation (MDOT) in the State of Michigan. The five sites that were visited and tested were selected based on their soil stratigraphy, specifically the presence of loose to medium dense sands.These sites are:

- M-25 over Harbor Beach Creek in Rubicon Township, Huron County
- M-66 over Wanadoga Creek in Pennfield Township, Calhoun County
- M-139 over Dowagiac Creek, in Niles Township, Berrien County
- US-131 over St. Joseph River, in Constantine Township, St. Joseph County (Abutment A)
- US-131 over St. Joseph River, in Constantine Township, St. Joseph County (Abutment B)

In addition to these sites, MDOT provided access to another site to be used as a dry-run site for the sensor installation and the testing procedure. This site was part of the reconstruction and expansion of the 112th Avenue bridge over I-96 in Crockery Township, Ottawa County, and consisted mostly of clayey soils which are not susceptible to settlement, and therefore are not within the scope of this research. However, geophones were installed close to the pile and the signal analysis provided valuable information for the next tested sites, in terms of the optimal transducers and data acquisition system to be used to capture the high level of vibrations near the pile.

The identification of every site will be according to the State or National highway number hereafter. The first three sites were associated with demolition and replacement

of the deteriorating existing bridges, while the fourth and fifth site, US-131, involved the construction of a new two-lane bridge over a river. Figure 6-1 shows the location of each site on Google Earth map. At sites M-25, M-66 and M-139, the pile driving contractors that had been awarded the contracts to build the replacement bridges, agreed to drive an extra test pile in a location where ground motion measurements would be easy to monitor. This made the installation process much easier since having access and pushing the sensors in the areas that had cofferdams would be difficult. This approach was also beneficial for the contractors because ground motion measurements could be made with minimal interruption of their operations. Production piles were monitored at the two bridge abutments of US-131 site. Access to this site easier and the installation process went smoothly.

In Figure 6-2 to Figure 6-6, the location of each site is presented in a more detailed view. The MDOT provided soil profile and groundwater elevation information based on borings and laboratory tests that were performed to explore the sites' soil conditions. Detailed information about the soil conditions at the test sites is provided in the next Section. Typical photographs during recording ground vibrations in the vicinity of pile driving are provided in Figure 6-7 to Figure 6-17. Technical data sheets for the diesel hammers used in this research project are available in Appendix B. More details about the location, soil boring data, pile layout plans and pile details can be found in Appendix C. Detailed description of each tested site with respect to pile driving procedure will be discussed in a following Section.

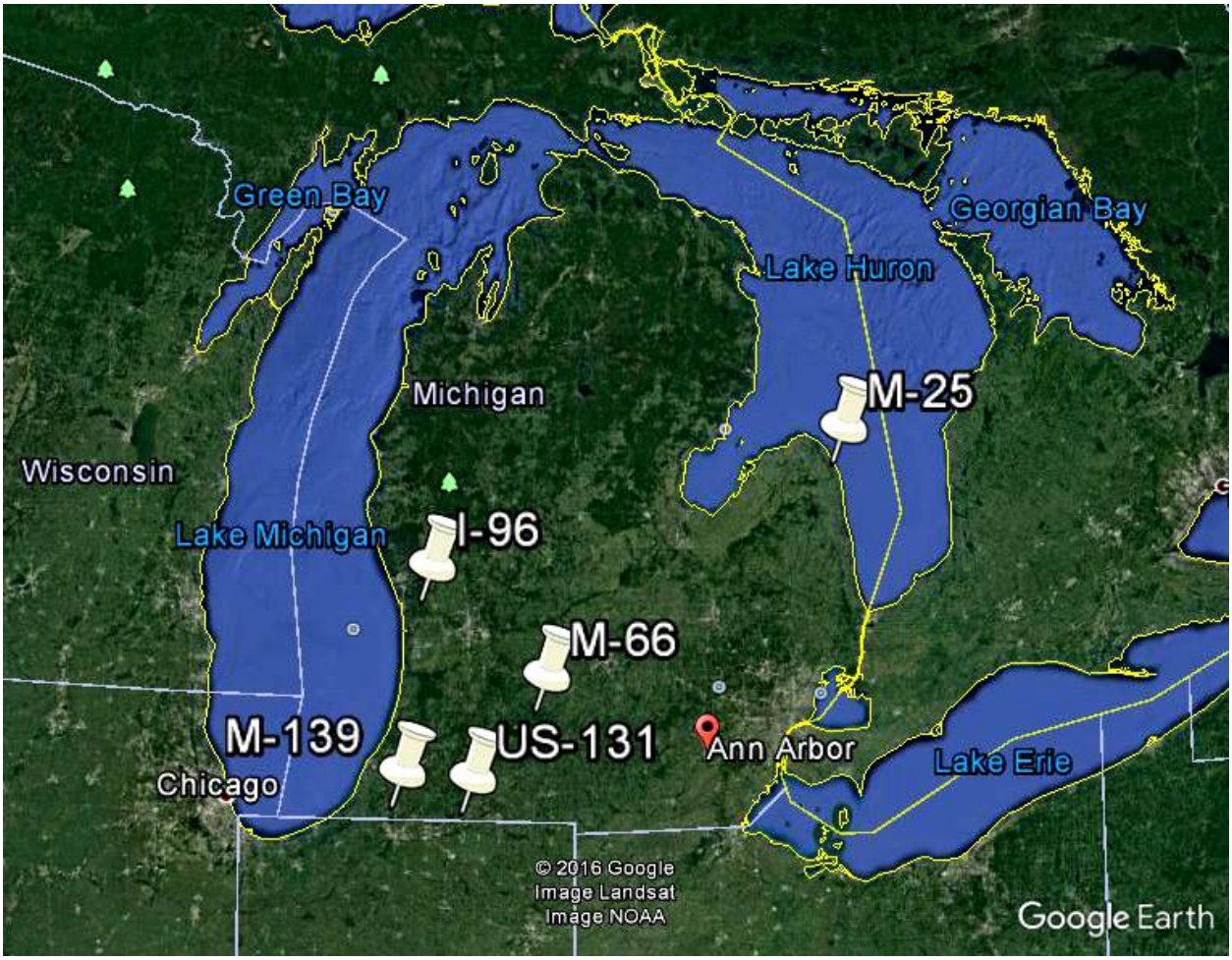

Figure 6-1 Location of tested sites on Google Earth map

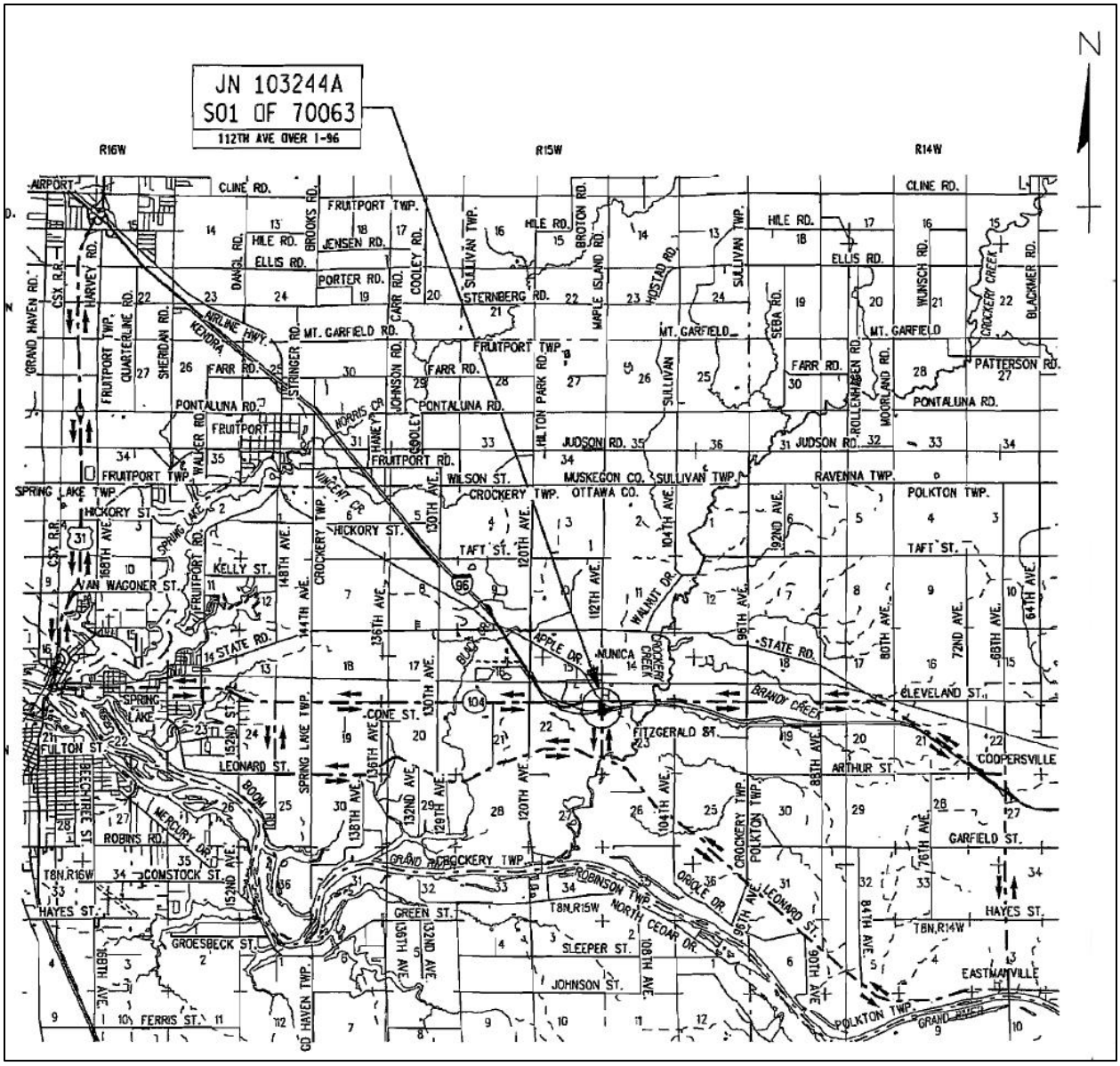

Figure 6-2 Location of I-96 site (dry-run)

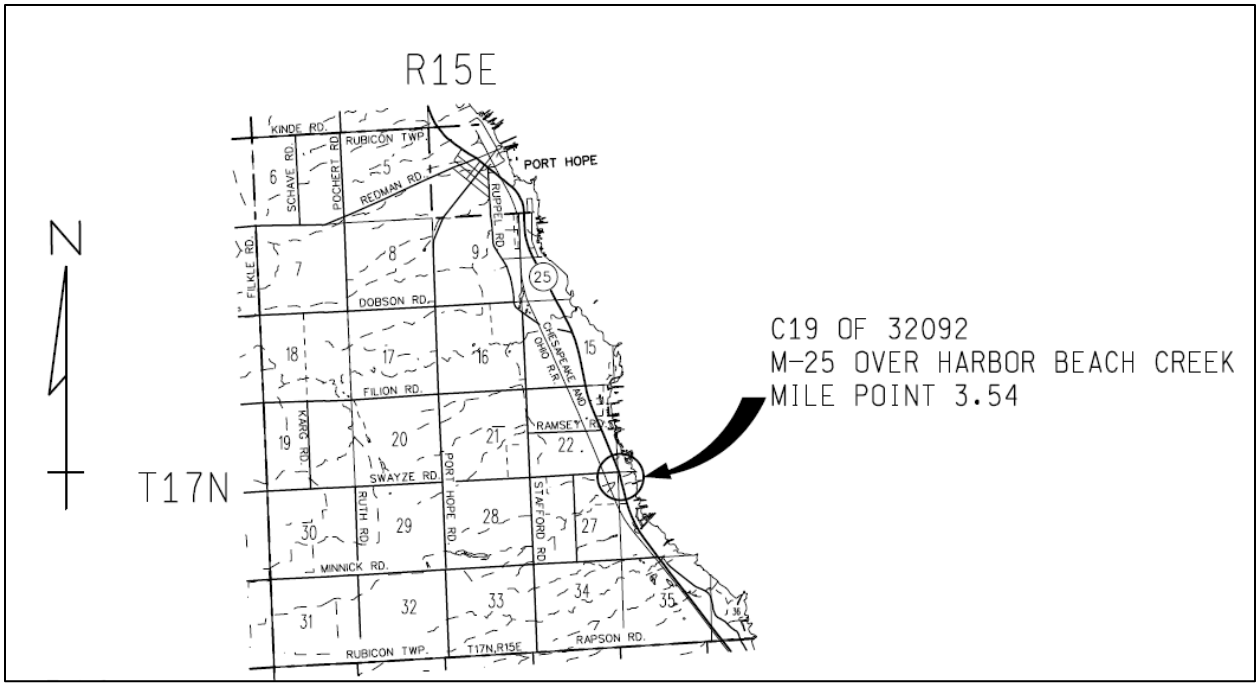

Figure 6-3 Location of M-25 site

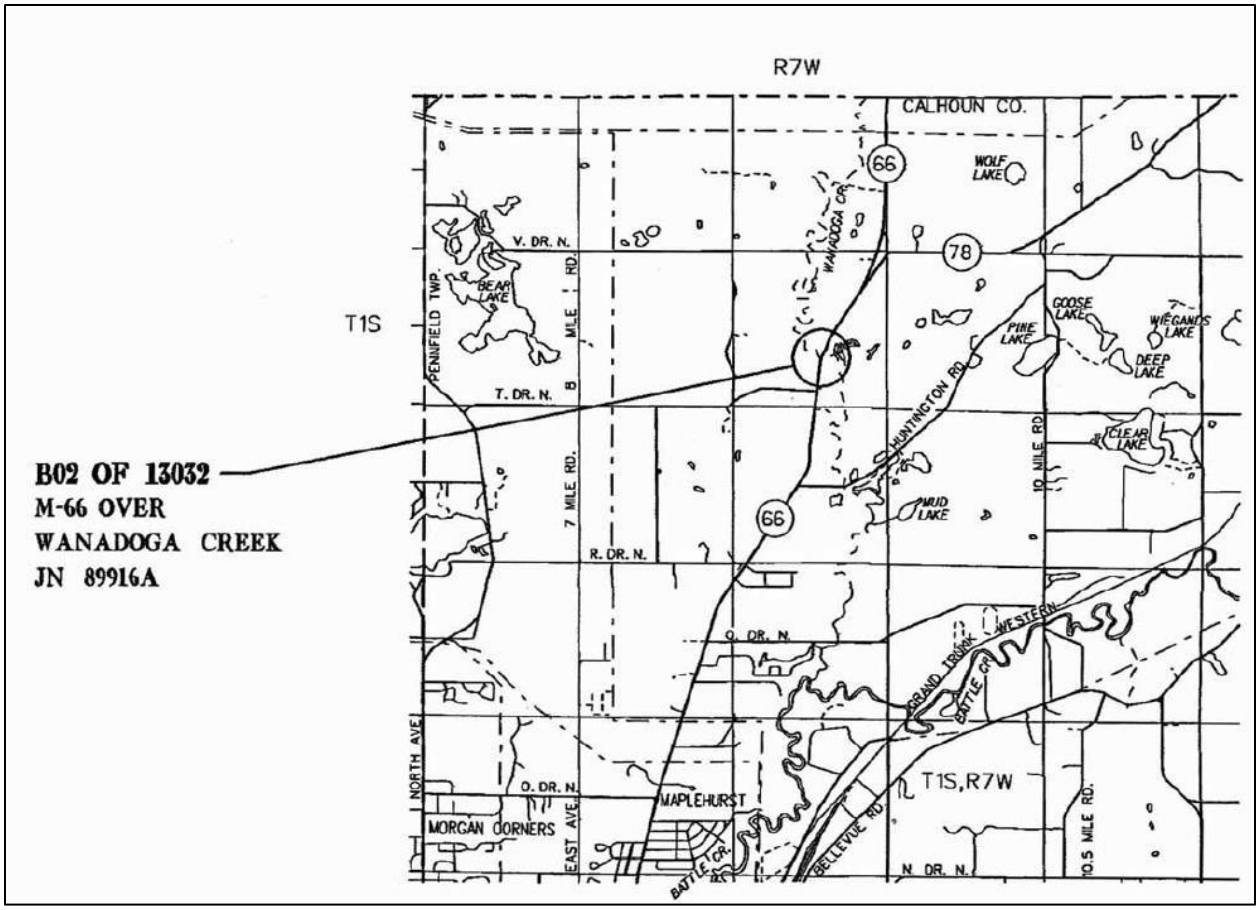

Figure 6-4 Location of M-66 site

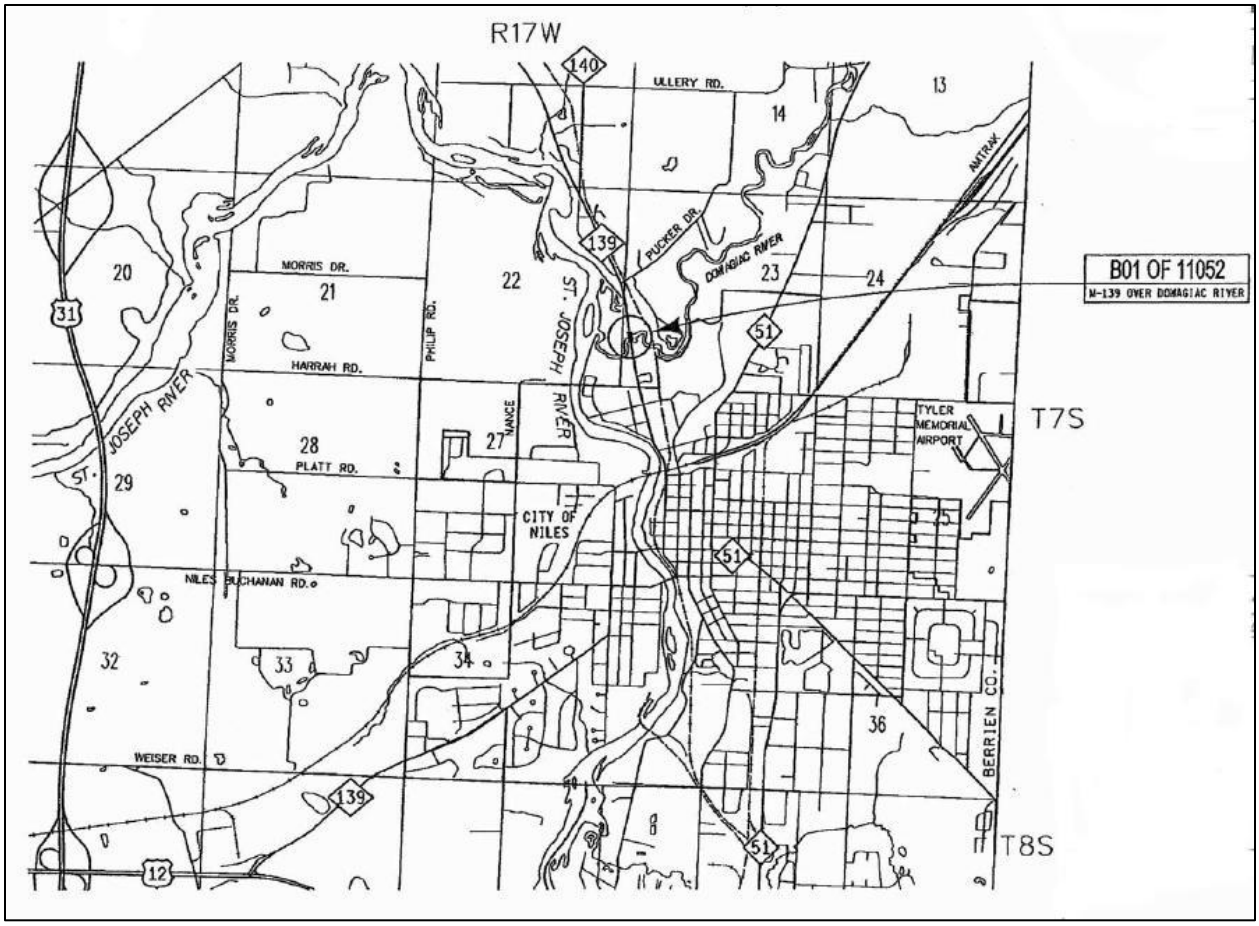

Figure 6-5 Location of M-139 site

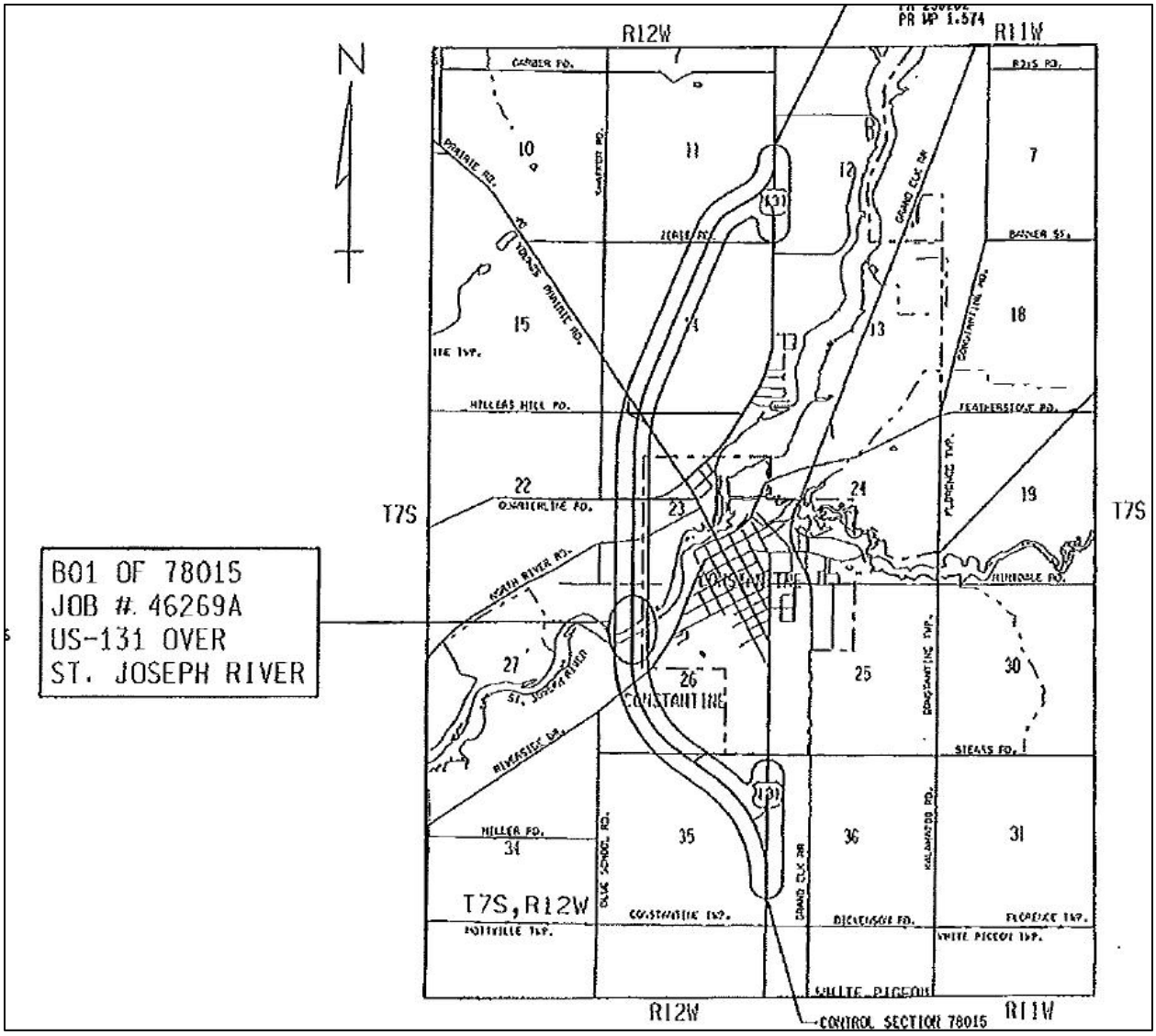

Figure 6-6 Location of US-131 site

Figure 6-7 Spotting the pile at I-96 site

Figure 6-8 Pile driving at M-25 site

Figure 6-9 Ground motion data collection at M-25 site

Figure 6-10 Welding a pile section on the test pile of M-66 site

Figure 6-11 Pile driving at M-66 site

Figure 6-12 Test pile after the end of driving at M-139 site

Figure 6-13 Extraction of test pile with vibratory hammer after the end of monitoring the installation process with the diesel hammer

Figure 6-14 Pile driving at US-131 site at bridge abutment A

Figure 6-15 Tested piles #1 (front) and #18 (back) after the end of driving at US-131 site at bridge abutment A

Figure 6-16 Lead and hammer preparation before pile driving at US-131 site at bridge abutment B

Figure 6-17 Positioning of pile #54 at US-131 site at bridge abutment B

6.2 Soil Conditions at Test Sites

Site characterization of the field test sites was performed by Standard Penetration Tests (SPT) and shear wave velocity measurements in-situ yielding both SPT and V_s profiles. The SPT testing was performed in accordance to the ASTM standard designation D1586-11 and results were provided by the Michigan Department of Transportation (MDOT). The soil samples were classified based on the Unified Soil Classification System (USCS) using primarily visual classification methods in accordance with ASTM D2488-09a. Details of all the soil borings near the area of the new structures of all sites are provided in Appendix C. In this Section the soil borings that were closer to the driven piles, will be discussed separately for each site. The small strain shear wave velocity was obtained using a combination of the Multichannel Analysis of Surface Waves (MASW) technique (Park et al. 1999) and the Microtremor Array Measurement (MAM) survey (Okada 2003).

The MASW testing was performed at all sites along a linear array of geophones at a selected distance that was very close to the tested pile. The configuration of the source, receivers and data acquisition system is illustrated in Figure 6-18. Vertical velocity transducers with a natural frequency of 4.5 Hz were used as the receivers and a sledge hammer was employed as the source. The ES-3000, Geometrics multichannel seismograph was used to record the signals and data analysis was performed with the software that comes together with the seismograph from the same supplier. In order to explore deeper soil layers, the MAM technique was implemented. The MAM uses surface waves from ambient activities or background noise. In this research project, background activities were present since construction operations were taking place at the tested sites. The same configuration as that of MASW test was used for the MAM survey.

The MASW (active) survey is adequate to collect information about shorter wavelengths (higher frequencies), while the MAM technique can capture longer wavelengths (lower frequencies). Records of both methods are transformed to a dispersion curve according to the Park et al (1996) method. An overlap over a frequency range of the MASW and MAM dispersion curve, allows for the development of a single

dispersion curve. The V_s profile is obtained by comparing the measured dispersion curve to a theoretical dispersion curve through an inversion process. Modifications to the Vs profile are made iteratively until the two dispersion curves match closely (Sahadewa 2012). The V_s profile provided one more site characterization, apart from the SPT profiles, and assisted to better understand the soil stratigraphy at each site. In addition, SPT data could be correlated with V_s values, as it will be discussed in the next Section, and the estimated equation could be compared with another widely used V_s relationship as a function of N values.

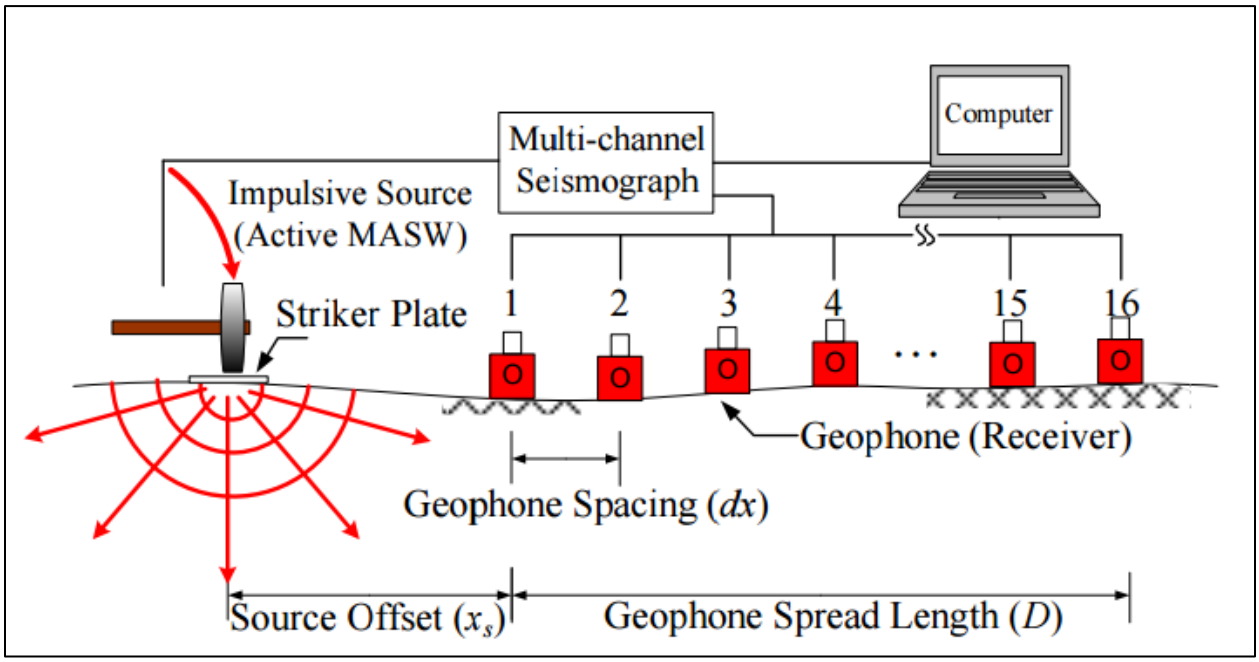

Figure 6-18 Schematic diagram of the general set-up for the MASW testing (from Sahadewa et al. 2012)

6.2.1 M-25 over Harbor Beach Creek

The construction work at this site consisted of replacing the Harbor Beach Creek crossing, near the city of Harbor Beach, Michigan, while the M-25 highway was detoured. Four test holes were drilled near the proposed structure as shown in Figure 6-19. The contractor agreed to drive an extra test pile near the location of test hole TH#5, which was located 17 ft right of the M-25 centerline. SPT blow counts were obtained at 5 ft depth intervals. The soil profile in test hole TH#5 can be generalized as 1 ft of Hot Mixed Asphalt (HMA) followed by 1 ft of medium dense gravel (GP). Beneath the medium dense gravel was 15 ft of loose sand (SP) underlain by 15 ft of dense silt (ML). Below the dense silt was 10 ft of hard clay (CL) followed by shale to the explored depth of 40 ft. The ground water level was found at a depth of 14 ft. Figure 6-20 shows the soil conditions based on the N values, the SPT profile of test hole TH#5 and the V_s profile. The soil profile has been adjusted to the ground surface elevation that the pile was driven.

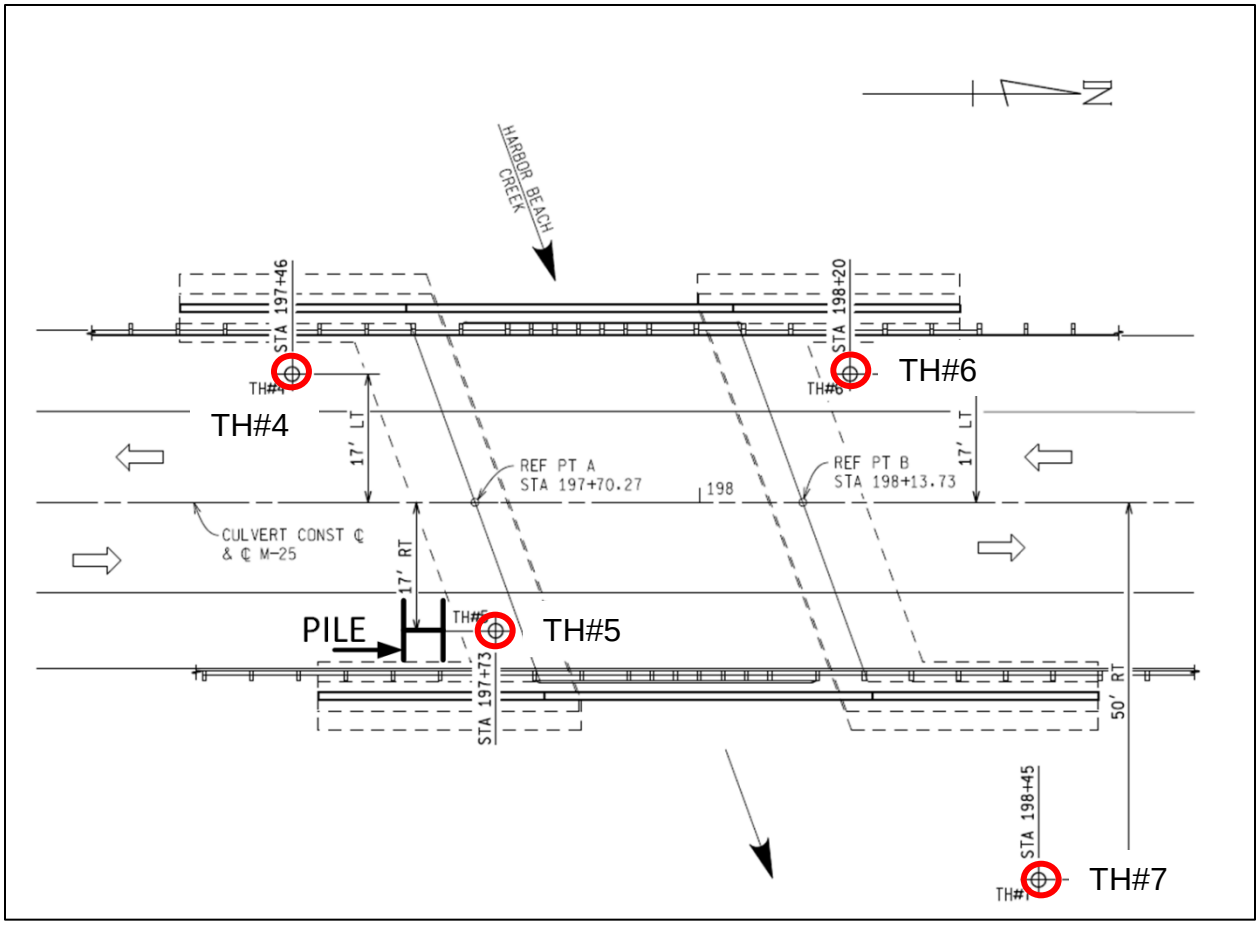

Figure 6-19 Location of tested pile and test holes at M-25 site

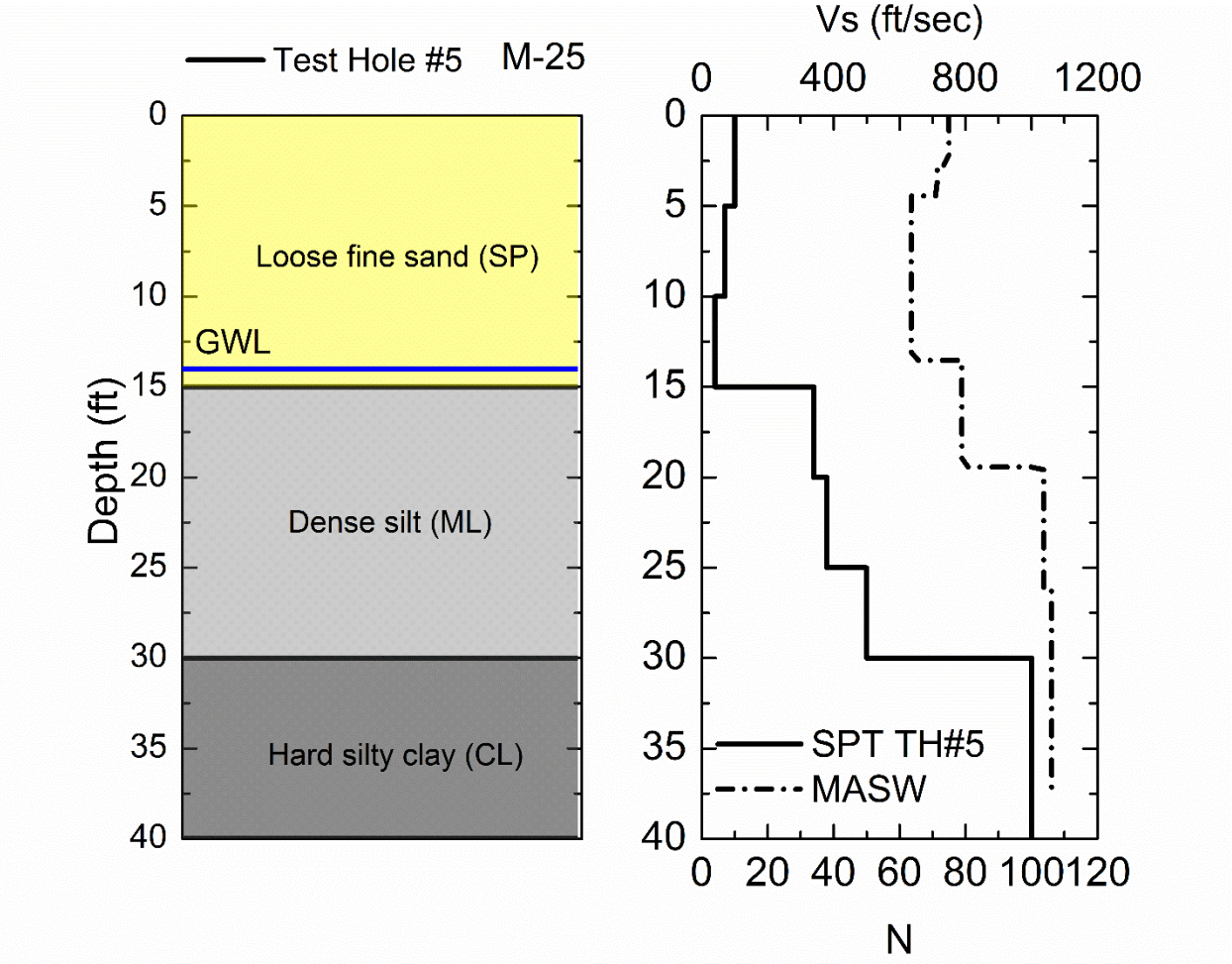

Figure 6-20 Soil conditions, SPT and Vs profile at M-25 site

6.2.2 M-66 over Wanadoga Creek

The work at this site consisted of replacing the M-66 bridge over Wanadoga Creek, near the city of Battle Creek, Michigan, while traffic on M-66 was detoured in both directions. Two soil borings were drilled for the design of this project. The contractor opted to drive an extra test pile near the location of test hole TH#1 for the purpose of this project, as shown in Figure 6-21. Test hole TH#1 was located 11 ft left of the M-66 centerline. SPT blow counts were obtained at 5 ft depth intervals. The soil profile in test hole TH#1 can be generalized as 0.5 ft of Hot Mixed Asphalt followed by 0.5 ft of medium dense gravel (GP). Below the medium dense gravel was 1 ft of concrete followed by 18 ft of very loose sand (SP). Underlying the very loose sand was 10 ft of loose sand (SP) followed by 21 ft of medium dense sand (SP). Below the medium dense sand was sandstone to the explored depth of 65 ft. The ground water level was found at a depth of 15 ft. Figure 6-22 shows the soil conditions based on the N values, the SPT profile of test hole TH#1 and the V_s profile. The soil profile has been adjusted to the ground surface elevation at which the pile was driven.

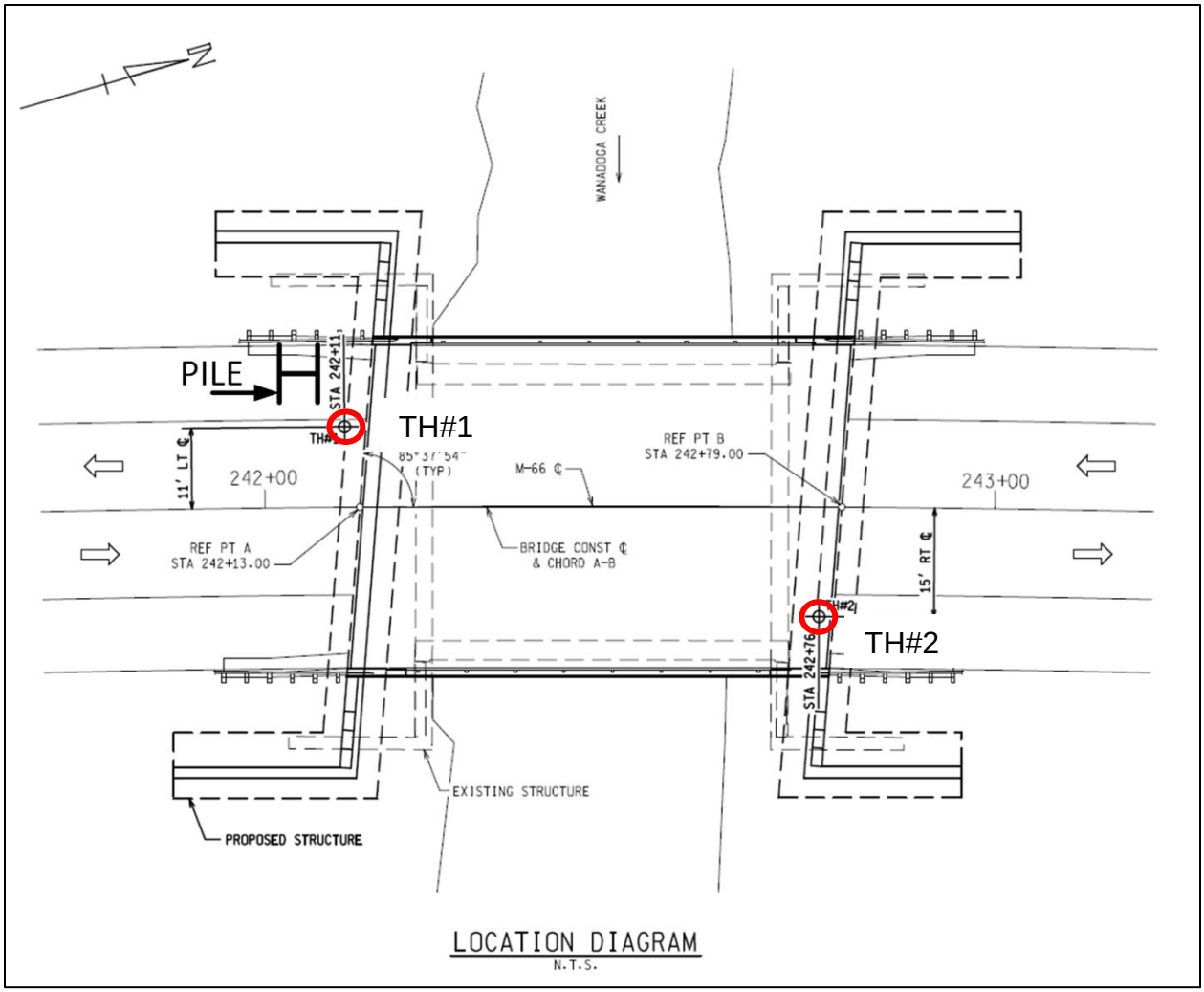

Figure 6-21 Location of tested pile and test holes at M-66 site

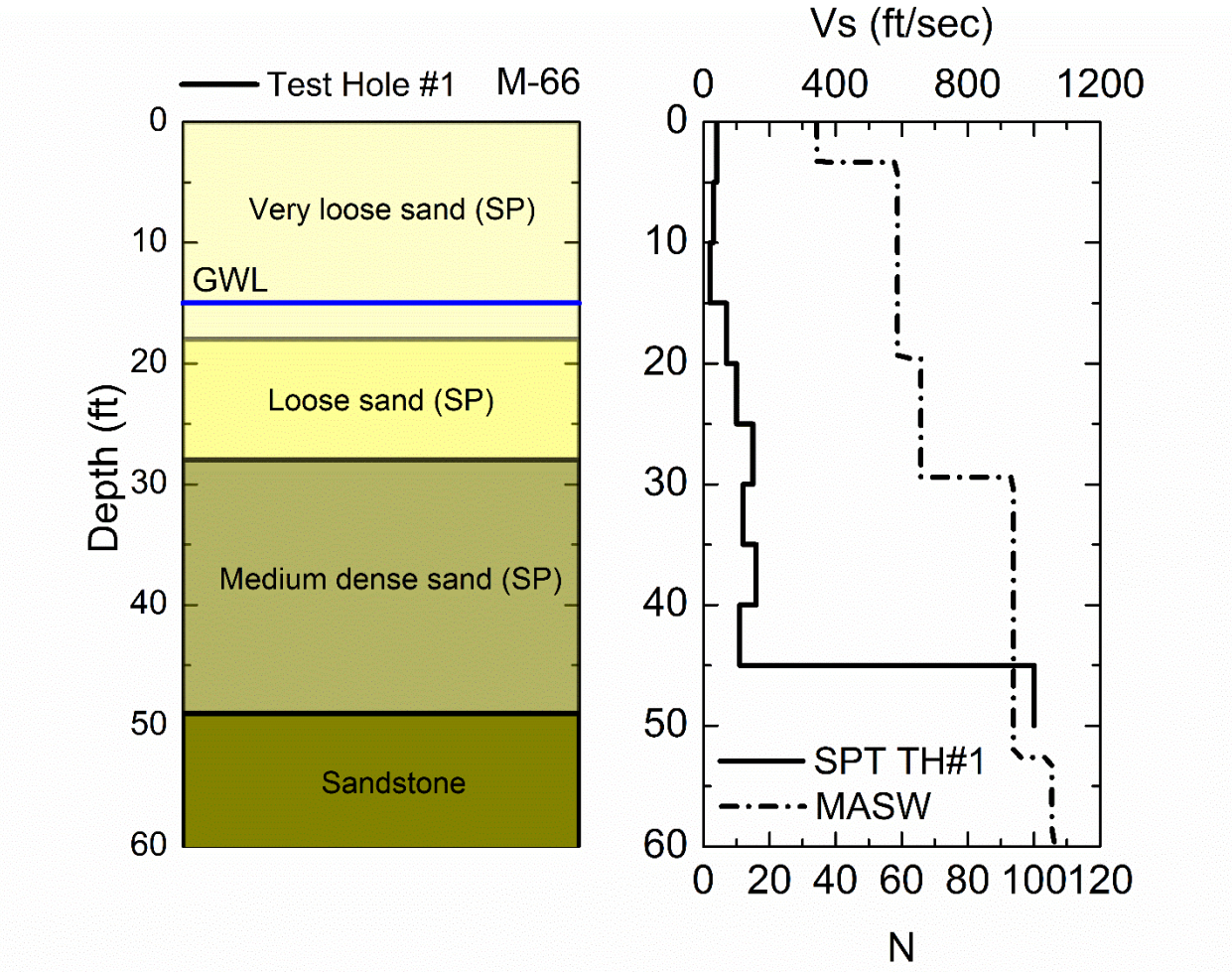

Figure 6-22 Soil conditions, SPT and Vs profile at M-66 site

6.2.3 M-139 over Dowagiac River

The work at M-139 site was associated with the replacement of a deteriorating river bridge near the city of Niles in Michigan. Throughout construction the bridge was open with one lane of alternating traffic. The geotechnical evaluation of the proposed replacement bridge was performed by Soil and Materials Engineers, Inc. (SME). Three test holes were drilled near the proposed abutment and pier locations of M-139. A drill rig No. 253 (75 CME) was used to conduct the SPT tests. Three particle size gradation analyses were performed on selected samples recovered near or below the proposed abutment and pier elevations of the upper channel sands. Details of the grain size distributions of these samples are provided in Appendix D. The generalized soil profile at M-139 site from the three soil borings is also provided in Appendix D. The contractor chose to drive a test pile with a diesel hammer close to test hole TH#1, which was extracted right after the end of driving with a vibratory hammer, and was used as a production pile for the project to its assigned location (Figure 6-23).

MDOT drillers made an extra test hole, TH#4, at the M-139 site, after the test pile had been driven, which was located 34 ft left of the M-139 centerline and 4.9 ft from the driven pile. The test pile was driven from an elevation of about 6 ft below the old bridge deck elevation. The soil profile in test hole TH#4 can be generalized as 6 ft of loose to medium sand (SP) followed by 4 ft of muck with silt sediments (ML). Below the muck was 5 ft of loose to medium sand (SP) followed by 6 ft of medium dense silt (ML). Underlying the silt was 7 ft of loose to medium dense sand (SP) followed by 10 ft of medium dense sand (SP). Below the medium dense sand was 15 ft of dense sand ft (SP) followed by 7 ft of very dense sand (SP). Beyond the very dense sand was 11 ft of dense silt (ML) followed by 5.5 ft of very dense silty sand (SP-SM) to the explored depth of 100 ft. The ground water lever was found at 5.5 ft below the ground surface. Figure 6-24 shows the adjusted soil conditions based on the N values, the SPT profile of test hole TH#4 and the V_s profile.

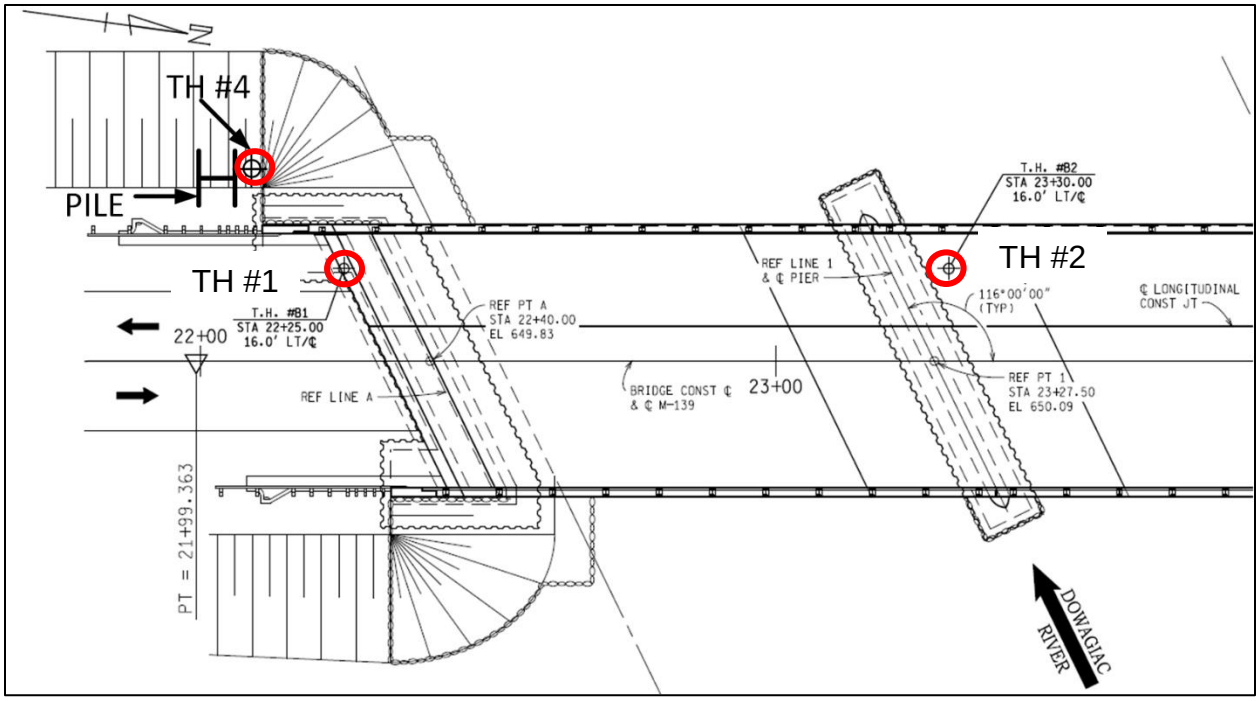

Figure 6-23 Location of tested pile and test holes at M-139 site

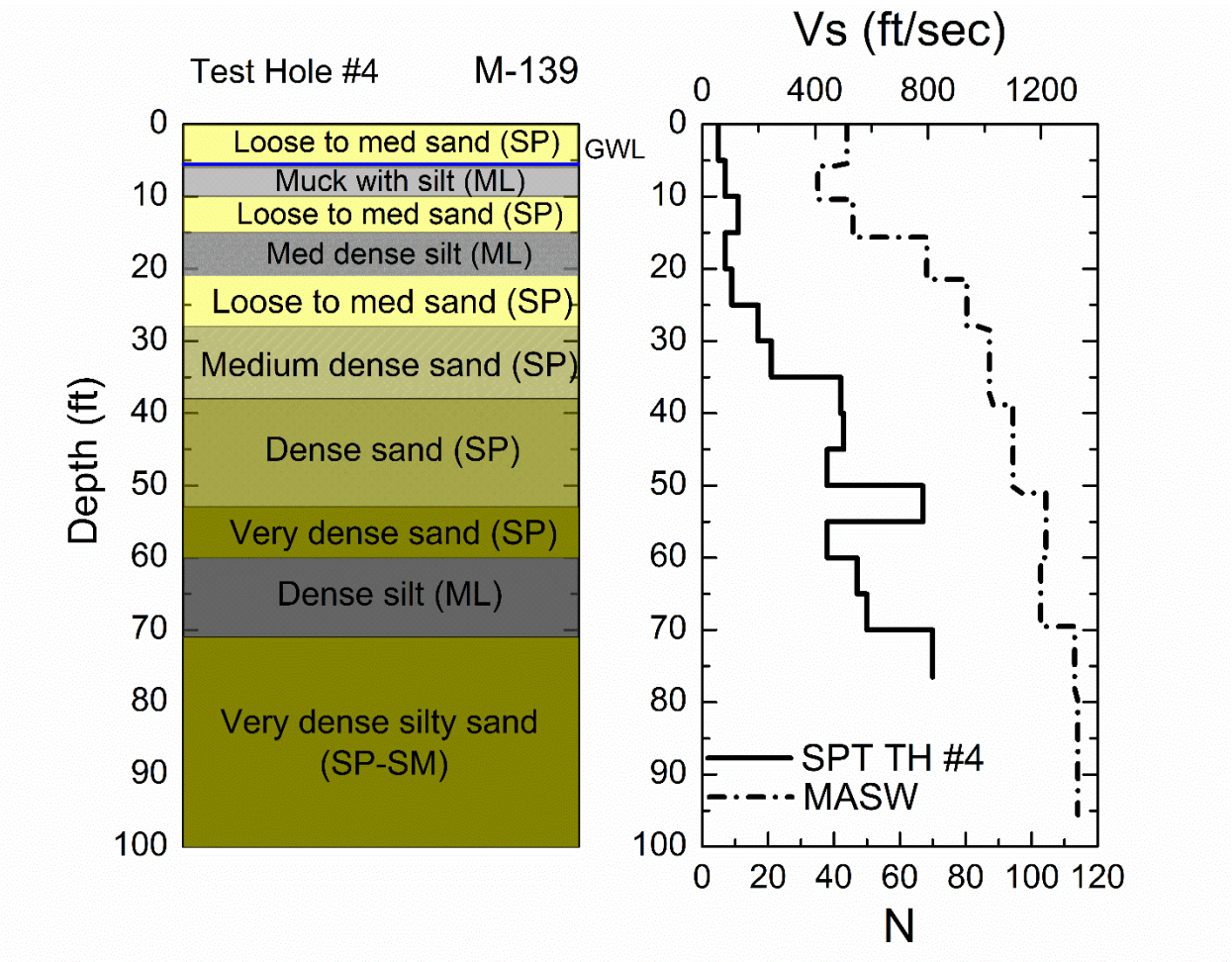

Figure 6-24 Soil conditions, SPT and Vs profile at M-139 site

6.2.4 US-131 over St. Joseph River

Work at this site consisted the construction of a new two-lane bridge over the St. Joseph River within the Village of Constantine in Michigan. The new bridge is a six span structure with a total length of 870 ft and individual span lengths of 145 ft. Fishbeck, Thompson, Carr and Huber, Inc. (FTCH) performed nine test holes in the field as shown in Figure 6-25. The test holes were performed using a rotary drill rig mounted on top of an all-terrain vehicle (ATV). Test holes B6 and B7 were performed by placing a barge in the river; a crane was used to lift the drill rig on the barge. The test holes were advanced to the sampling depths using hollow stem augers to a depth of 25 to 50 ft; wash rotary drilling was used below the hollow stem auger segments. The geotechnical evaluation of the proposed new bridge was performed by Soil and Materials Engineers, Inc. (SME). Four particle size gradation analyses were performed on soil samples near the proposed abutment and pier footing locations. The grain size distribution results are provided in Appendix E, along with the generalized soil profile of site US-131. Four piles were monitored at this site, two in each of the bridge abutments. The contractor allowed recording of ground vibrations during driving production piles at the two abutments. A trench for the construction of the abutments was excavated to the depth where foundation piles would be driven. Sensors were buried close to the first driven pile and surface ground vibration measurements were collected during the driving of the second pile at each abutment, A and B.

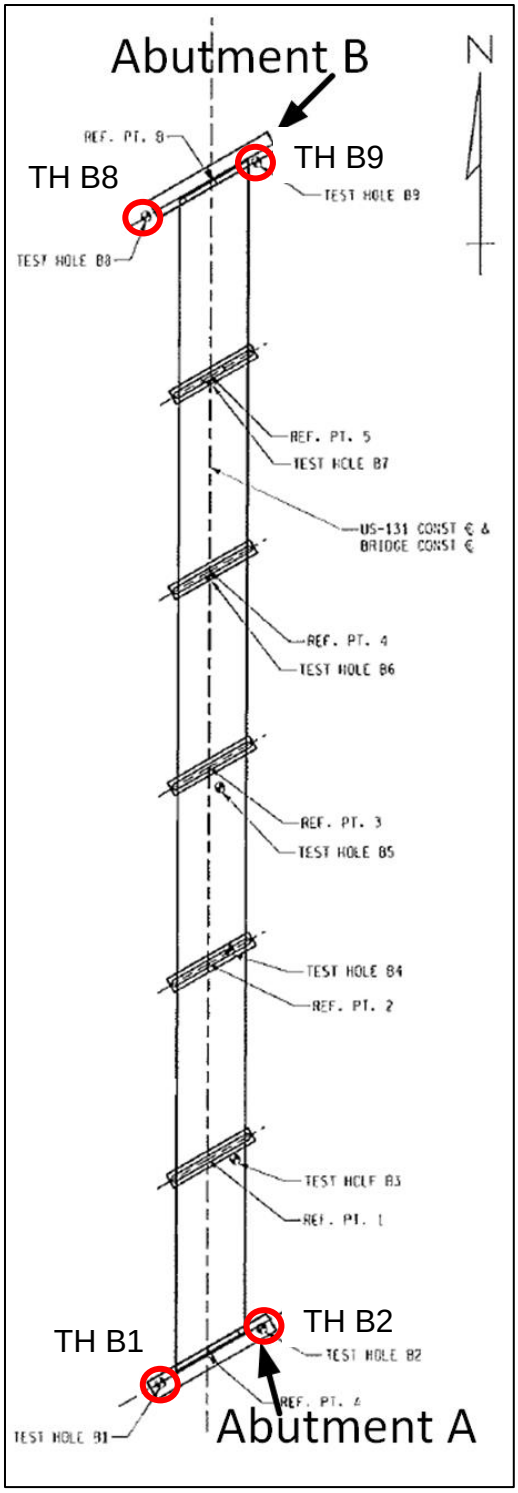

Figure 6-25 Locations of test holes at US-131 site

6.2.4.1 US-131 Abutment A

Test hole B1 was located 45 ft southwest of the US-131 centerline and was close to the first driven pile 1, as shown in Figure 6-26. The soil profile in test hole B1 can be generalized as 1 ft of marsh topsoil overlying 6 ft of loose to medium sand with some silt (SM). Underlying the loose to medium sand was 20 ft of loose to medium dense sand (SP) followed by 17 ft of hard sandy clay (CL). Beyond the hard sandy clay was 2.5 ft of dense clayey sand (SC) followed by 10 ft of very dense sand (SP). Below the very dense sand was 24 ft of hard sandy clay (CL) to the end of the soil boring at 80 ft. Ground water was encountered at 9 ft below the ground surface. Figure 6-27 presents the adjusted soil conditions, after the excavation of the trench, based on the N values, the SPT profile of test hole B1 and the V_s profile.

Test hole B2 was located 45 ft northeast of the US-131 centerline and was close to the second driven pile 18, as shown in Figure 6-26. The soil profile in test hole B2 can be generalized as 1 ft of marsh topsoil followed by 2 ft of loose to medium sand with trace silt (SP-SM). Below the loose to medium sand was 10.5 ft of loose to medium sand (SP) followed by 11.5 ft of medium dense sand (SP). Underlying the medium dense sand was 21 ft of hard silty clay (CL) followed by 10 ft of very dense to dense sand with trace silt (SP-SM). A layer of hard sandy clay 23.5 ft in thickness followed the very dense sand to the explored depth of 79.5 ft. Ground water was encountered at 7 ft below the ground surface. Figure 6-28 presents the adjusted soil conditions, after the excavation of the trench, based on the N values, the SPT profile of test hole B2 and the V_s profile.

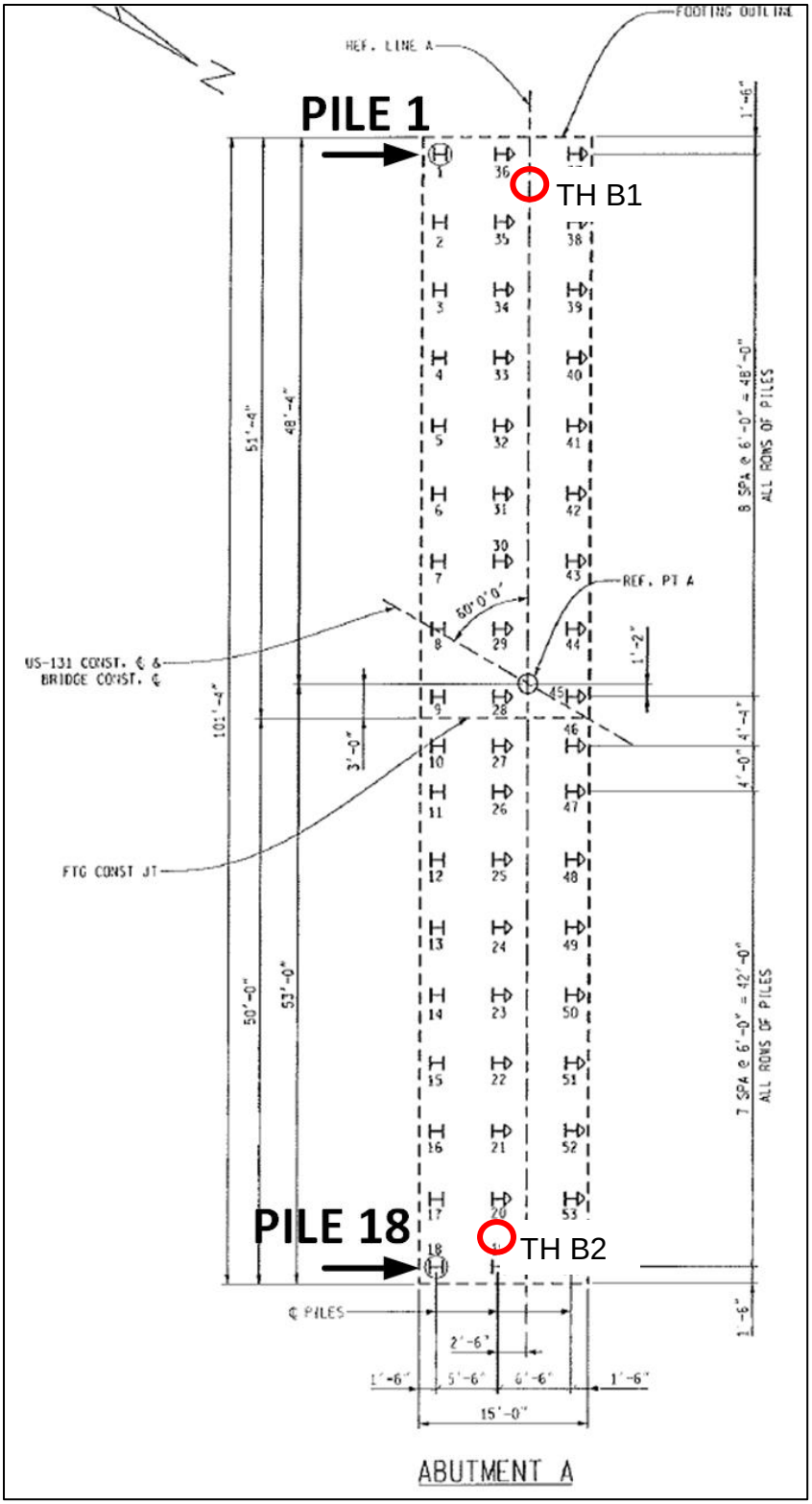

Figure 6-26 Locations of test piles 1 and 18 at US-131 A site

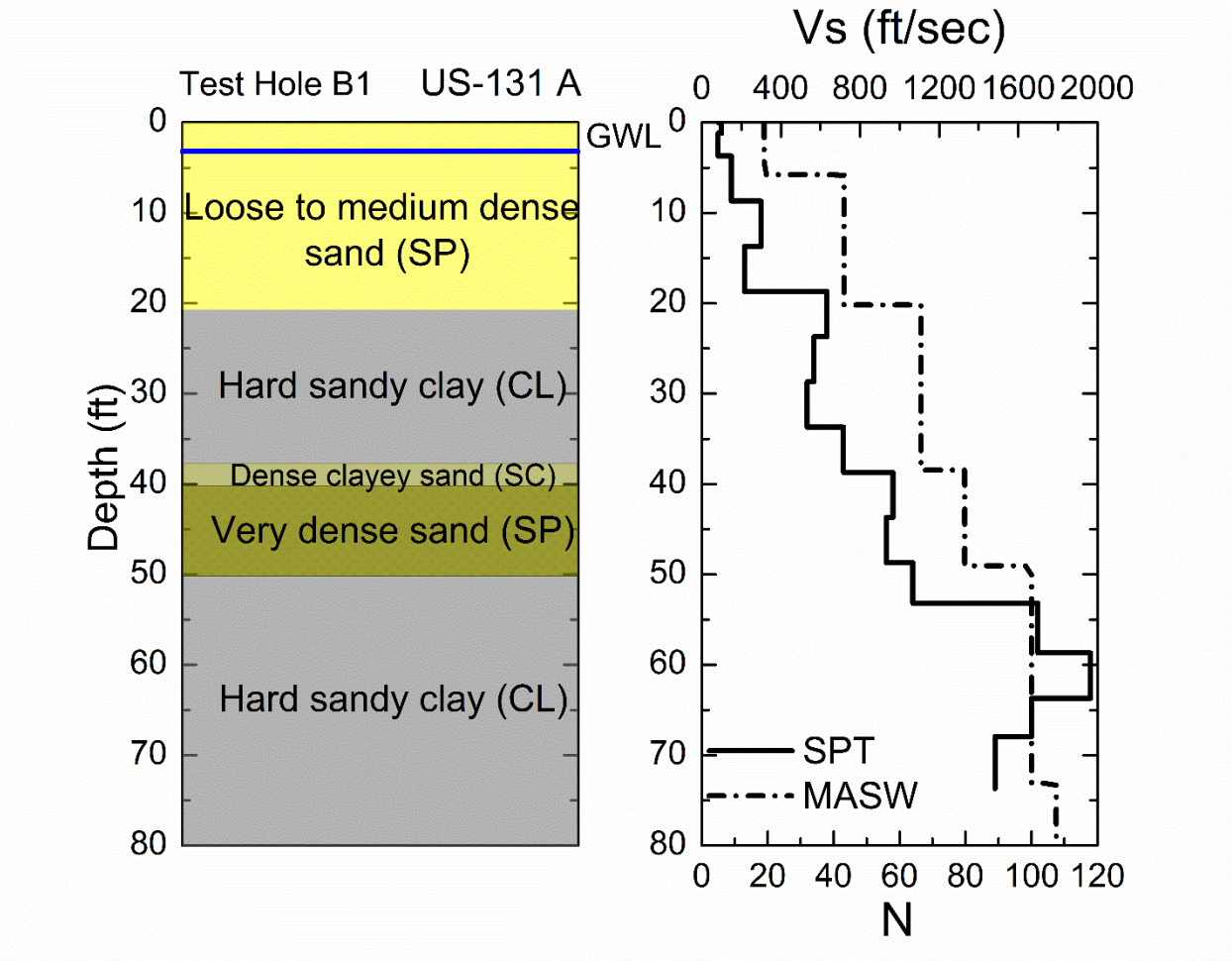

Figure 6-27 Soil conditions, SPT and Vs profile at US-131 A site; Pile 1

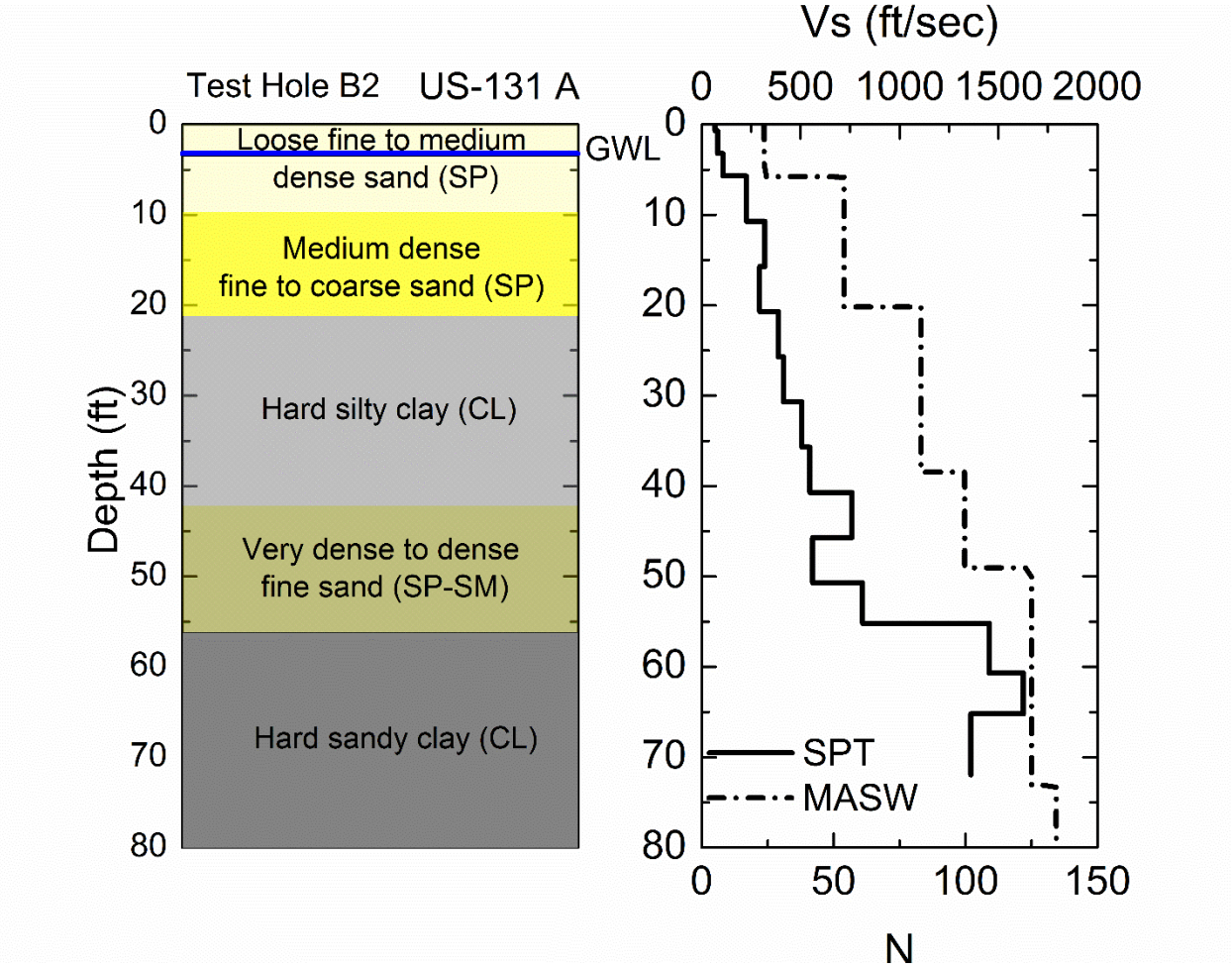

Figure 6-28 Soil conditions, SPT and Vs profile at US-131 A site; Pile 18

6.2.4.2 US-131 Abutment B

Test hole B9 was located 45 ft northeast of the US-131 centerline and was close to the first driven pile 54, as shown in Figure 6-29. The soil profile in test hole B9 can be generalized as 1 ft of marsh topsoil overlying 2 ft of loose to medium dense sandy fill (SM) and 3.5 ft of loose to medium dense sand with trace silt (SP-SM). Underlying the fill was 14.5 ft of loose to medium dense sand (SP) followed by 15 ft of medium dense to dense sand (SP). Beyond the medium dense to dense sand was 10 ft of hard sandy clay (CL) followed by 13.5 ft of very dense sandy silt (ML). Below the sandy silt was 17.5 ft of hard sandy clay (CL) followed by weathered shale until the end of the test hole at 78.75 ft. Ground water level was encountered at 12 ft below the ground surface. Figure 6-30 presents the adjusted soil conditions, after the excavation of the trench, based on the N values, the SPT profile of test hole B9 and the V_s profile.

Test hole B8 was located 45 ft southwest of the US-131 centerline and was close to the second driven pile 37, as shown in Figure 6-29. The soil profile in test hole B8 can be generalized as 1 ft of marsh topsoil overlying 6 ft of loose to very loose sandy fill (SP). Beyond the fill was 5 ft of medium dense to dense sand (SP) followed by 4.5 ft of hard silty clay (CL). Underlying the silty clay was 12 ft of loose to medium sand (SP) followed by 3 ft of dense sand (SP). Below the dense sand was 10.5 ft of hard sandy clay (CL) followed by 19.5 of very dense to extremely dense sand (SP) overlying 15.5 ft of hard sandy clay (CL) to the end of the exploration depth at 78.5 ft where weathered shale was encountered. The ground water level was found at 10 ft below the ground surface. Figure 6-31 presents the adjusted soil conditions, after the excavation of the trench, based on the N values, the SPT profile of test hole B8 and the V_s profile.

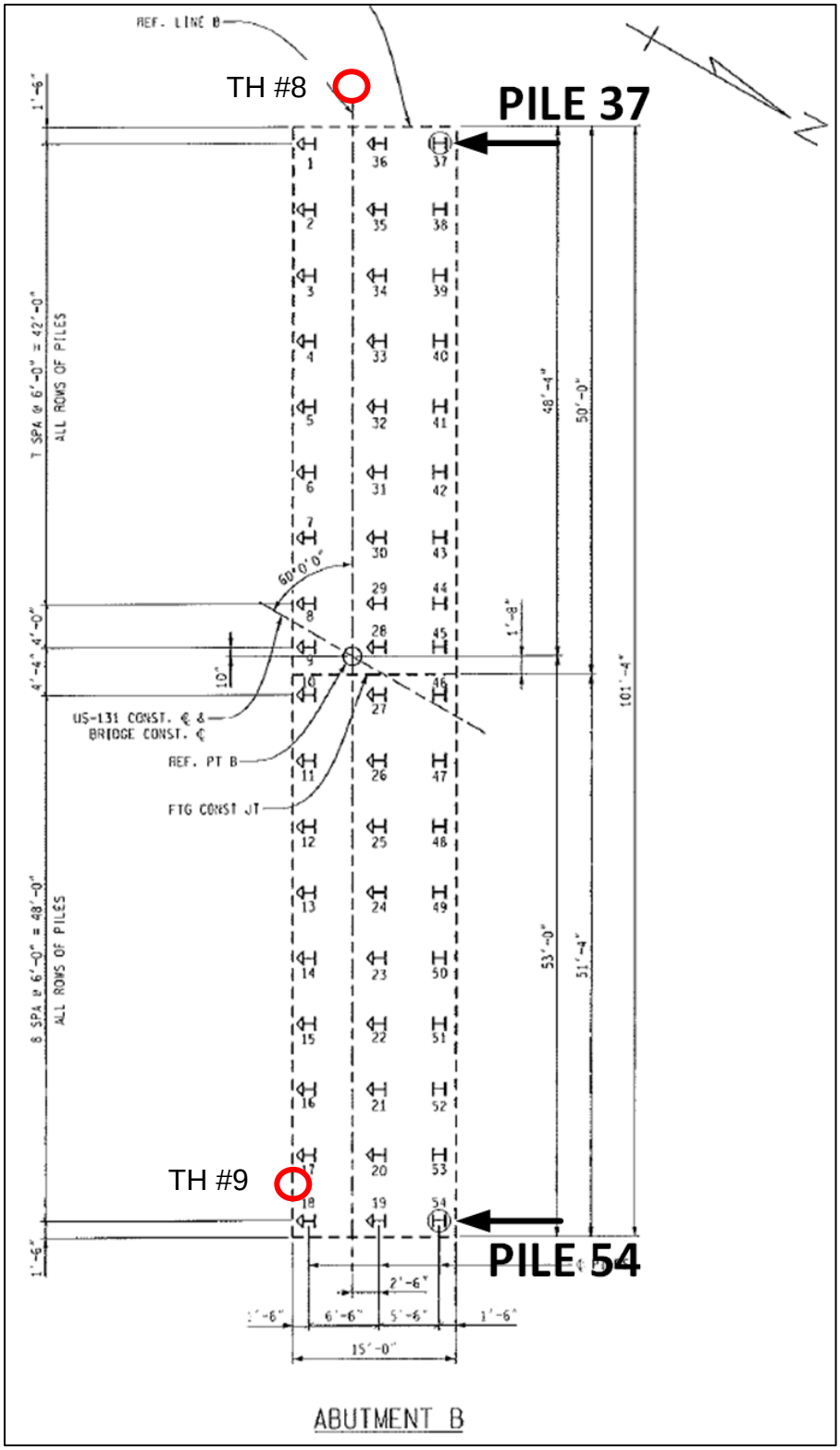

Figure 6-29 Locations of test piles 54 and 37 at US-131 B site

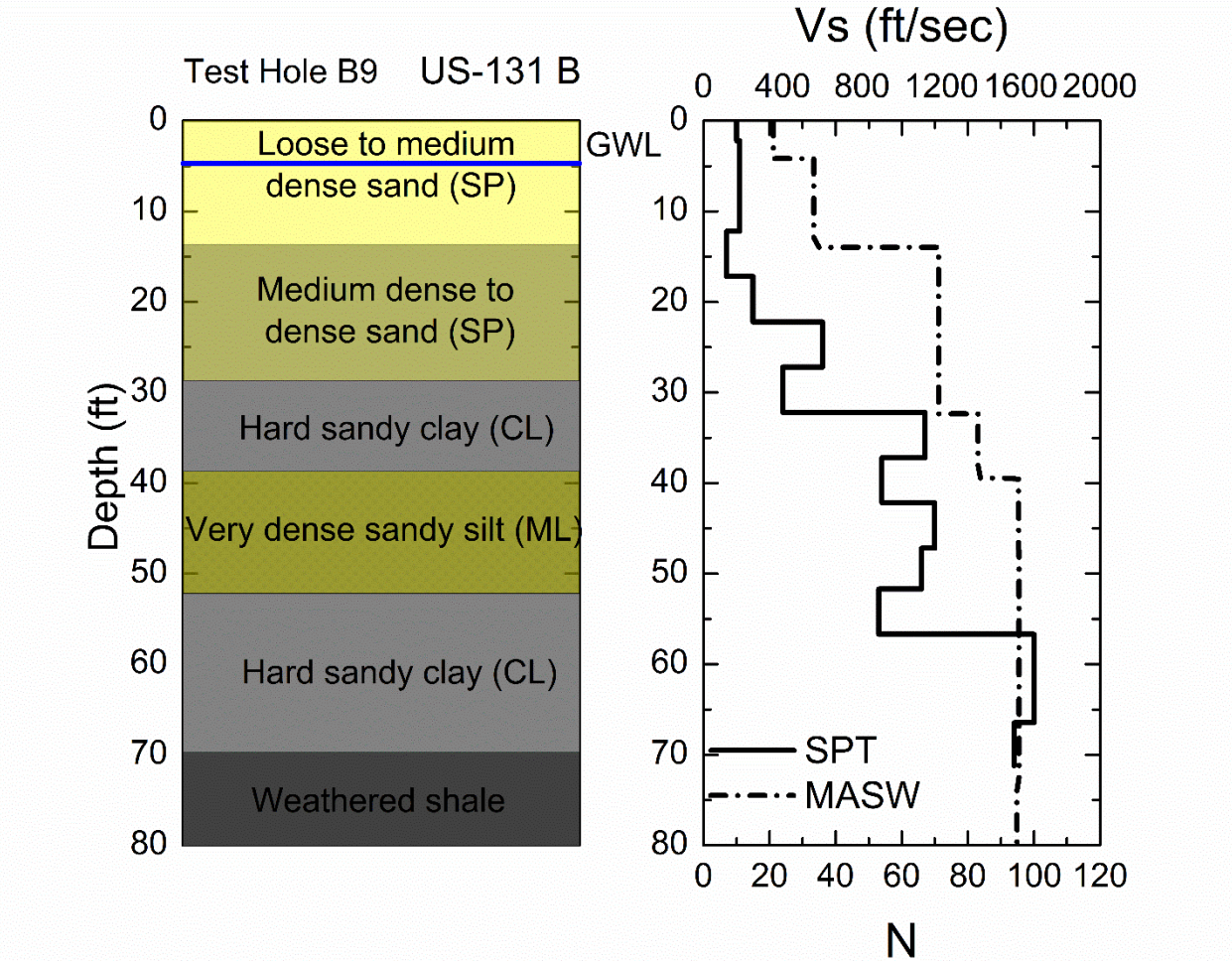

Figure 6-30 Soil conditions, SPT and Vs profile at US-131 B site; Pile 54

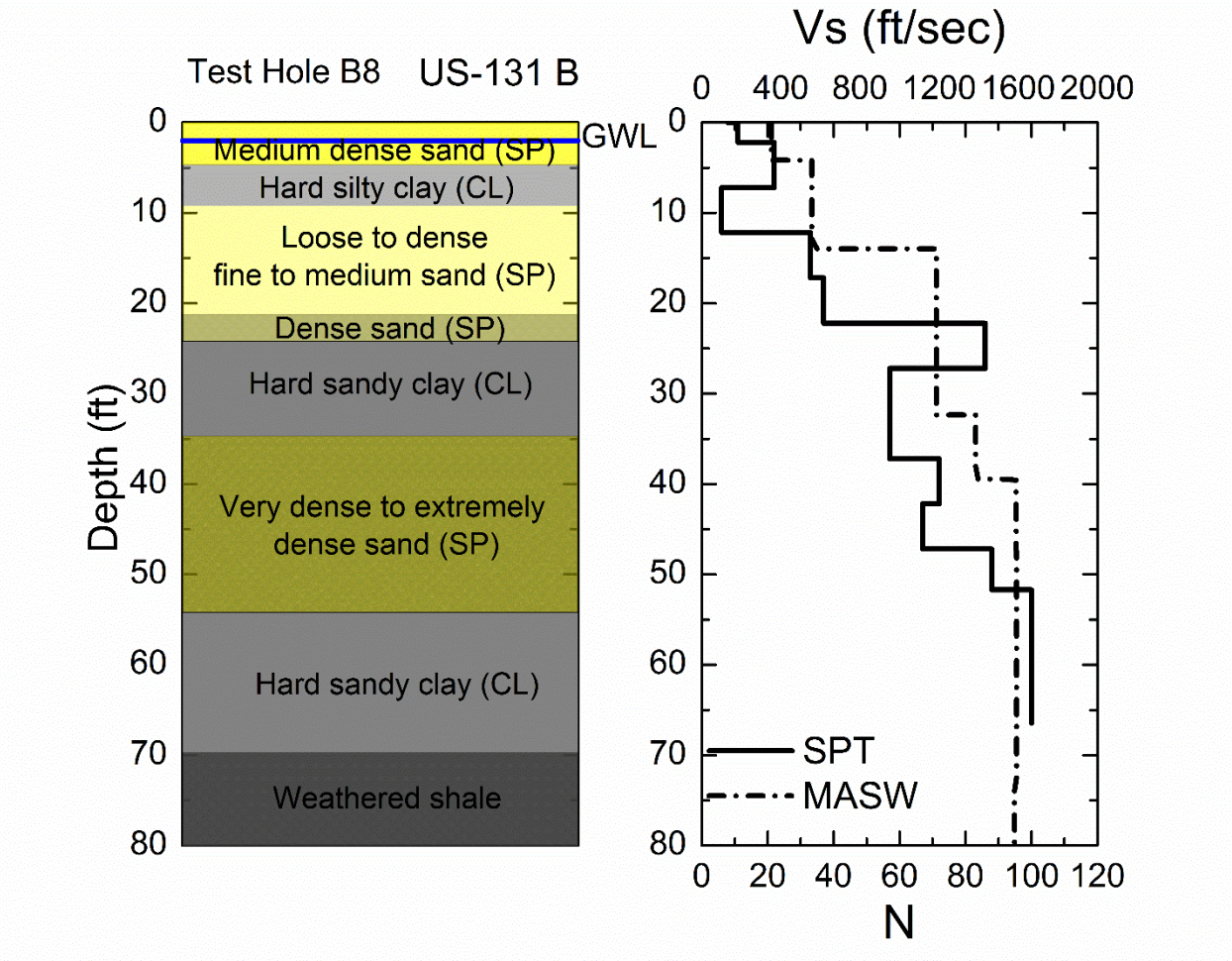

Figure 6-31 Soil conditions, SPT and Vs profile at US-131 B site; Pile 37

Figure 6-32 presents a summary of the SPT profiles for the sites that were tested and Figure 6-33 depicts the corresponding V_s profiles of all sites. As discussed above, the sites consisted primarily of loose to medium dense sand deposits in the top 20 to 30 ft, but showed greater variability of soil conditions with depth.

Researchers have developed relationships between the shear wave velocity and the SPT N values since the 1960s. Imai and Tonouchi (1982) collected the largest database, of 1654 data sets from 250 sites from different soil conditions throughout Japan. They developed a Vs correlation based on N-value, soil type and geologic age (Wair et al. 2012):

$$V_S = 318N^{0.314} \qquad \text{Eq. 6-1}$$

Where: Vs = shear wave velocity (ft/sec)
N = SPT blow count

Figure 6-34 shows values from all the tested sites of this research project, the regression line fitted to these values and the R-squared values:

$$V_S = 263N^{0.376} \qquad \text{Eq. 6-2}$$

Where: Vs = shear wave velocity (ft/sec)
N = SPT blow count

The above site specific equation is compared with the one developed by Imai and Tonouchi. In the low blow count region up to N=30, which is the most important region for this research, the coincidence of the two curves is good. For similar soil conditions, Eq. 6-2 can then be used along with the SPT profile to generate V_s profiles.

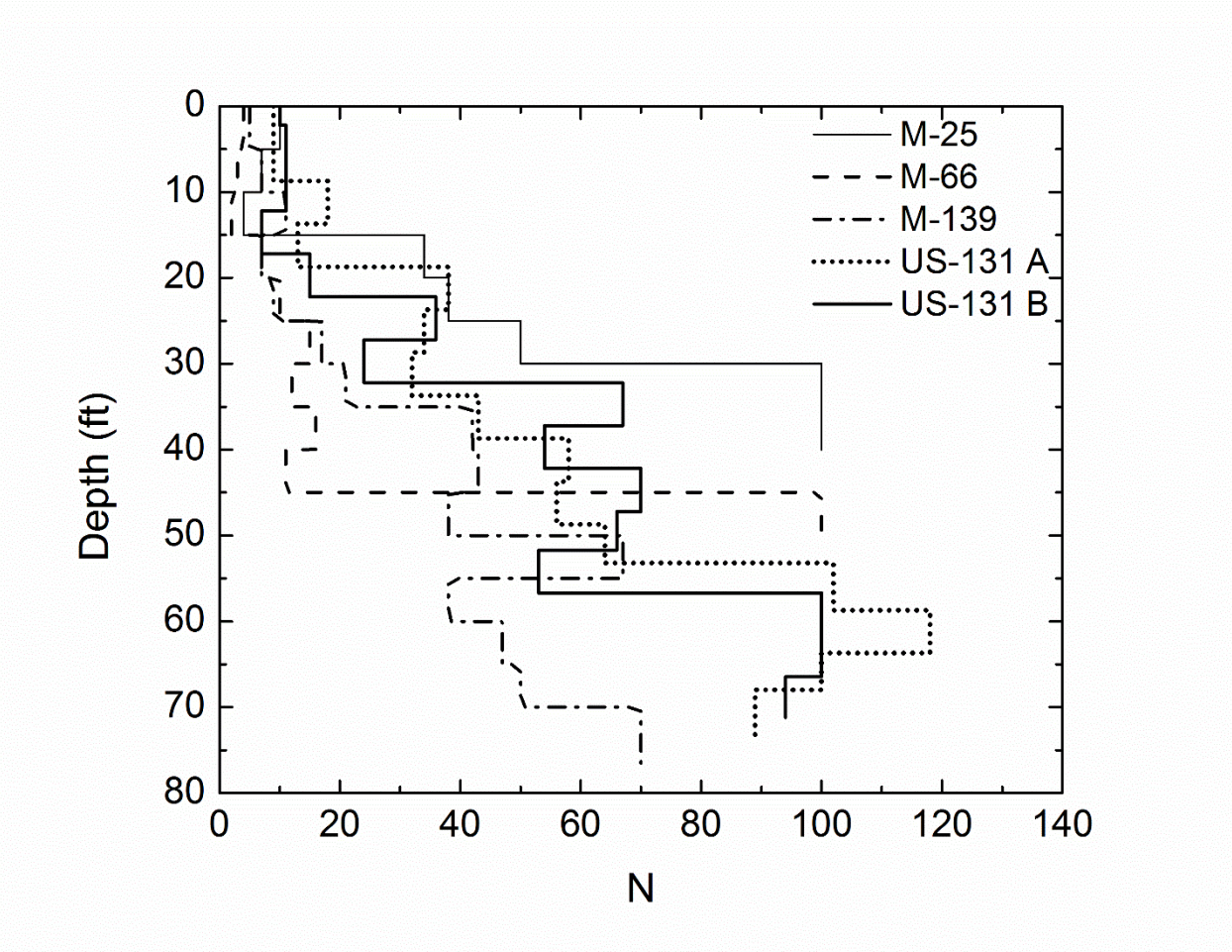

Figure 6-32 Summary of SPT profiles for all tested sites

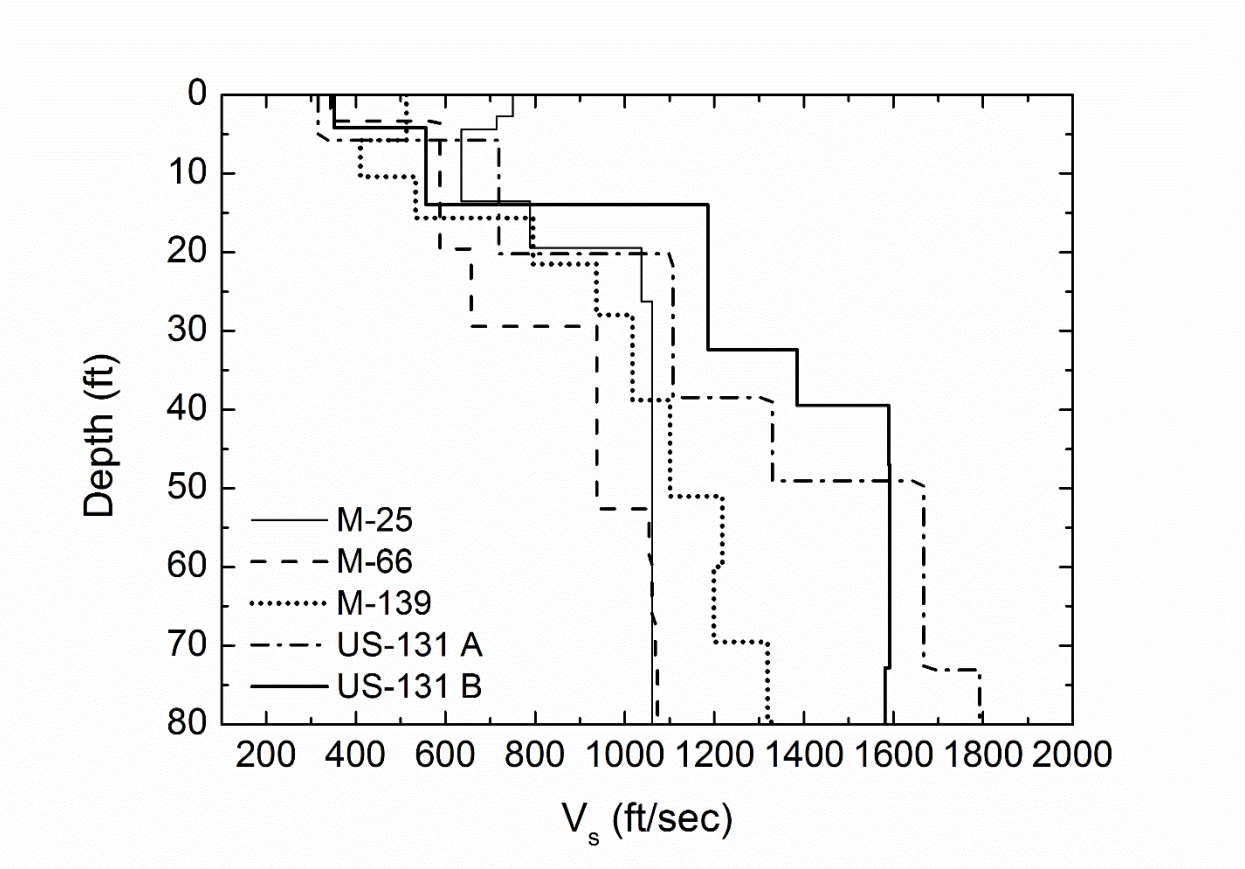

Figure 6-33 Summary of V_S profiles for all tested sites

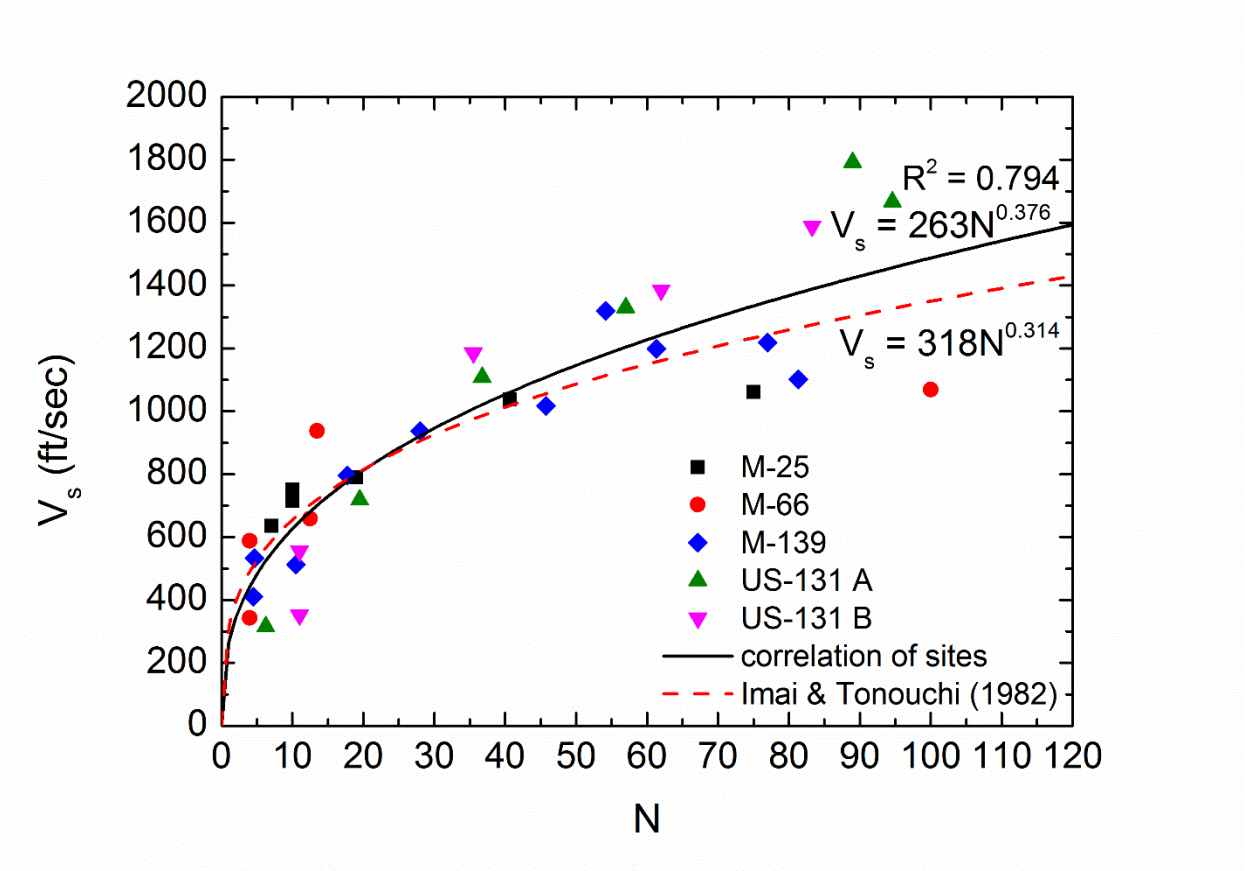

Figure 6-34 Site specific regression line of tested sites for V_s versus N and comparison with accepted equation

6.3 Ground Motion Measurements and Interpretation

Ground motion measurements from the embedded and the surface sensors were recorded simultaneously for the whole duration of pile driving using the cDAQ data acquisition system. This system enables recording of every single hammer blow, providing a complete database for every monitored site. A sampling rate of 1 kHz was used for recording the signals. This sampling rate was selected, as the Nyquist frequency, which is half of the sampling rate frequency, needs to be well in excess of the frequencies anticipated. It is critical to choose the correct sampling rate, depending on the dynamic operation, in order to record accurately the ground motion signals. The dominant frequency of impact motions typically ranges between 10 and 50 Hz for typical impact hammers (Dowding 1996). The dry-run site that was visited first, confirmed this by revealing the frequency content of the collected signals. Thus, the selected sampling rate of 1 kHz was found to be sufficient.

For most of the driven piles, an E-Saximeter unit was attached on the hammer. This instrument calculates the hammer operating rate in blows per minute, and for single acting diesel hammers it displays the hammer energy and hammer stroke. In addition to the E-Saximeter unit, a video was recorded during each pile installation to confirm the number of blows per 1 ft pile increments of pile penetration.

The signal processing of vibration records was performed using a Matlab code. Voltage output was recorded for all the sensors used. This voltage was converted to acceleration or velocity by using the appropriate calibration factor for each sensor. All acceleration signals were integrated to velocity for comparison with the velocity records from geophones. Vibration records in time domain were transferred into frequency domain using the Fast Fourier Transform (FFT). This process was done for the recorded signal for the whole time history of the pile driving installation, as well as for every single hammer blow in order to get a detailed signature of the frequency content. Low-pass filters were applied to remove the high frequency noise from the signals. Figure 6-35 shows an example of the Fourier amplitude spectrum of the whole time history response for one of the embedded sensors. In this example, a cutoff frequency of 100 Hz was used

to remove higher noise frequencies. Figure 6-36 presents the whole time history response of one of the sensors during pile driving, before and after applying the low-pass filter. A zoom-in view of one of the single blows extracted from the previous signal is shown in Figure 6-37. Figure 6-38 illustrates a single blow time history and its corresponding power spectrum.

The number of blows required to drive each pile every one foot increment was found from the recorded video at every tested site. The blow with the maximum amplitude was extracted for every foot. Figure 6-39 shows an example of the recordings of one of the accelerometers used. Driving this specific pile from 32 ft to 33 ft penetration depth, required 29 blows. The blow with the highest acceleration amplitude was found with the Matlab code and is shown in the same Figure. Finally, the acceleration signal was integrated to velocity time history. The above procedure was done for all sensors used in this research.

Table 6.1 has a summary of the pile hammers, H section pile sizes, pile lengths and penetration depths for every tested site. Table 6.2 shows a summary of the accumulated number of blows required to drive each test pile, the hammer rated energy and the average hammer efficiency determined by the Saximeter unit or PDA test for each driven pile.

Each of the sites will be discussed separately with respect to data collection and interpretation. The sites are listed in chronological order of investigation in Section 6.1 and the first two sites revealed unexpected complications when the research crew arrived and produced less than ideal records. Advanced reconnaissance was not possible because MDOT notified the researchers of an expected test pile drive by the contractor with only a short advance notice. Therefore, the discussion of the measurements and interpretations will proceed from the third chronological site, M-139, through US 131 A and US 131 B, and lastly, M-25 and M-66.

It is important to note that for the case of the buried triaxial accelerometers, the plan for controlling orientation of the two horizontal directions depended on keeping the push rod alignment constant with continual visual observation at the surface. It became evident

during installation of the sensors that this approach was too crude for accurate orientation control. This might have affected the actual orientations of the horizontal sensors.

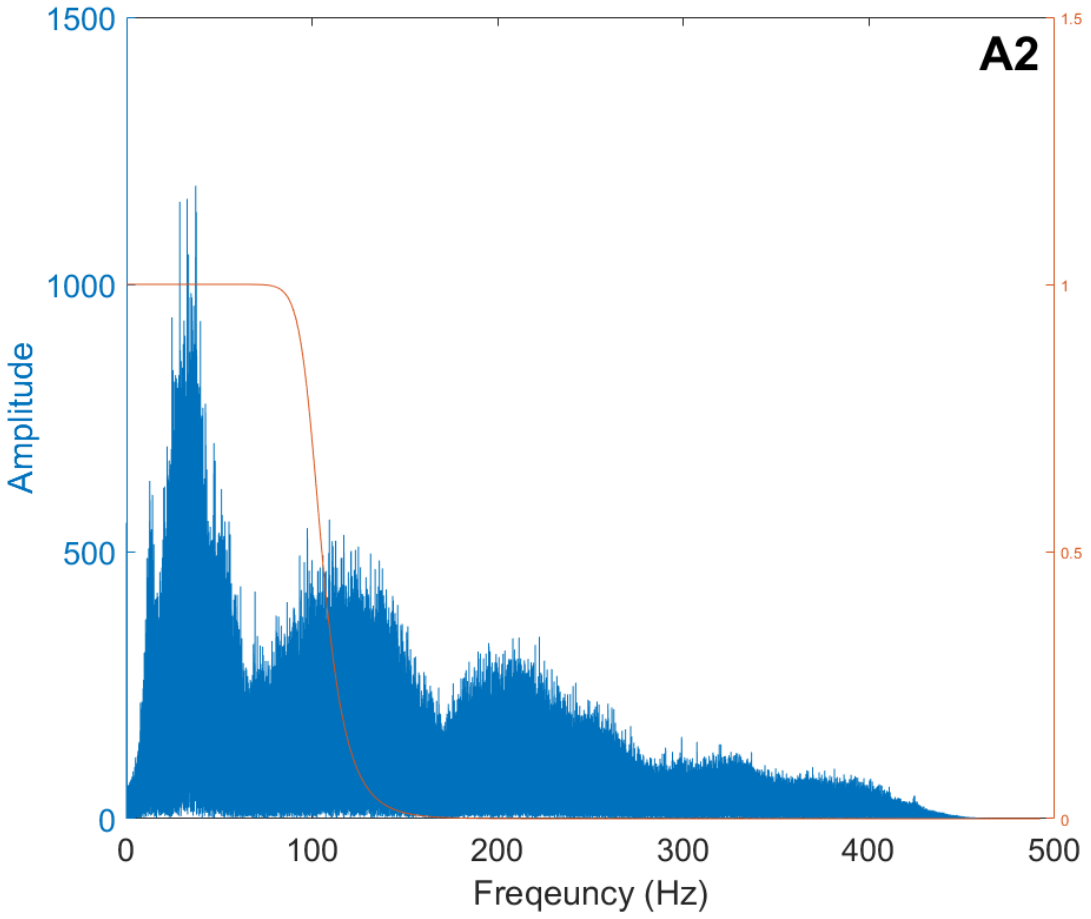

Figure 6.1

Figure 6-35 Fourier amplitude spectrum and cutoff frequency at 100 Hz of one of the embedded accelerometers

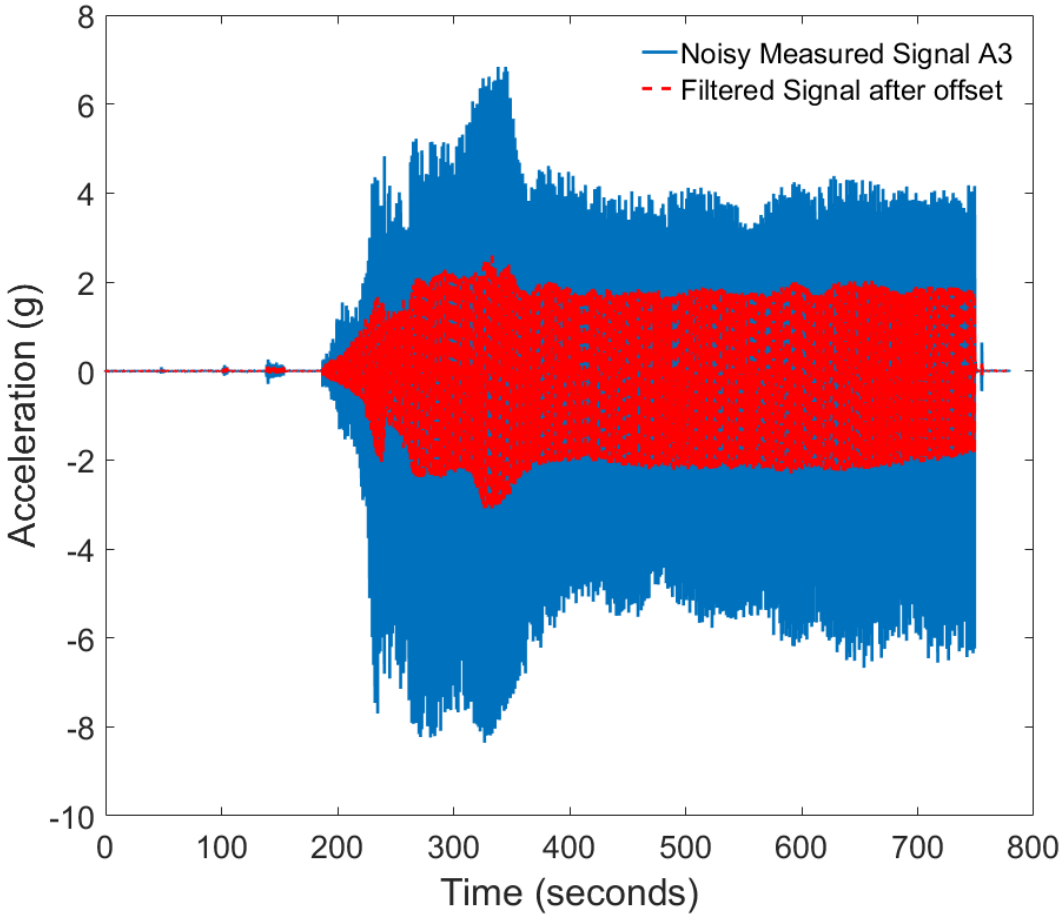

Figure 6-36 Whole time history recorded by one of the sensors before and after filtering

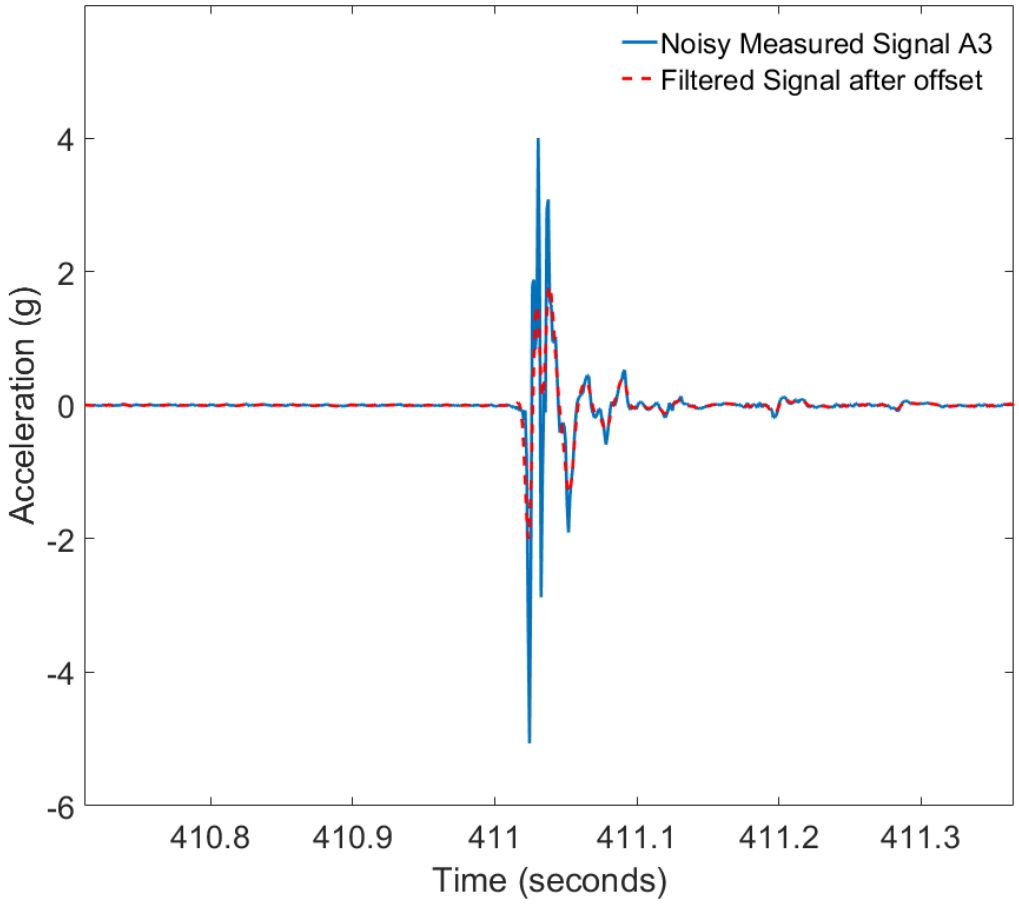

Figure 6-37 Single blow time history before and after filtering

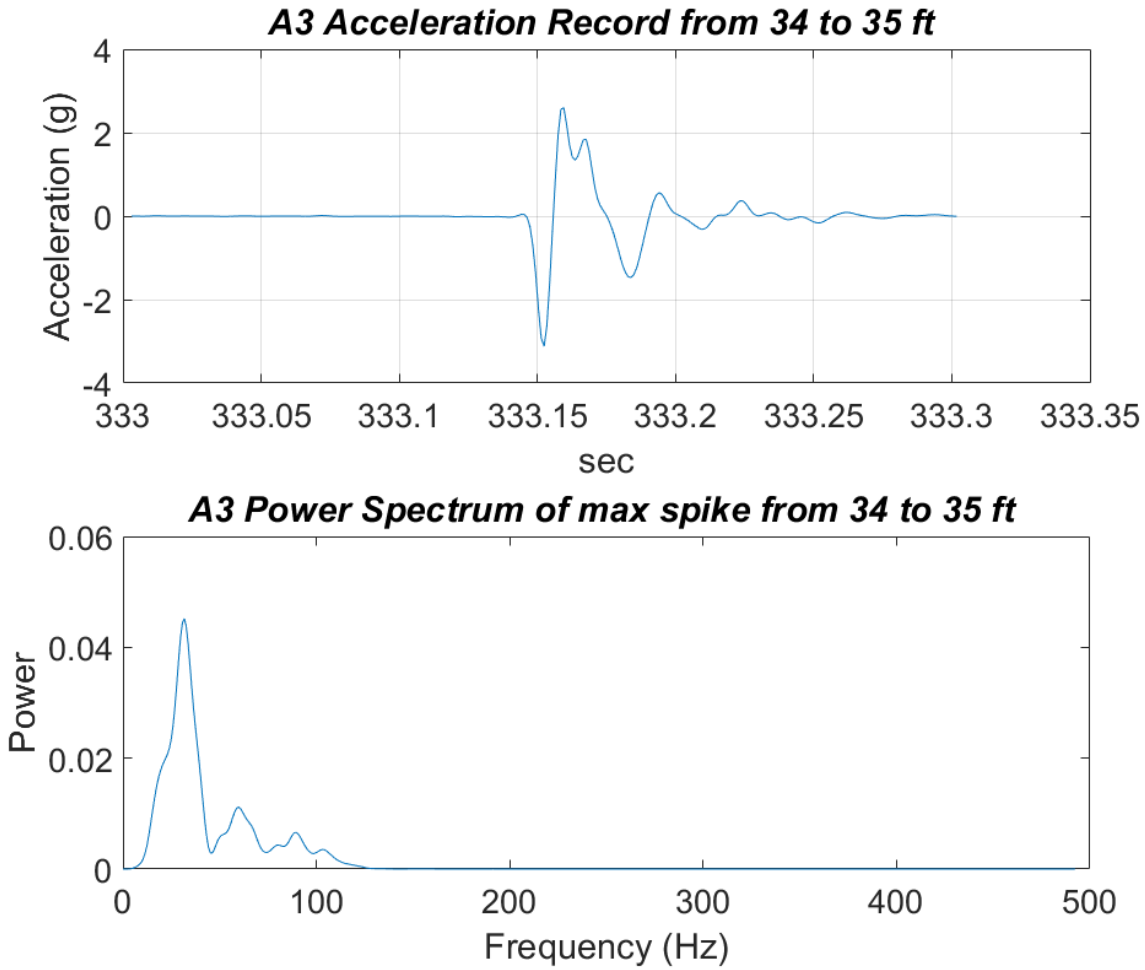

Figure 6-38 Single blow time history and corresponding power spectrum

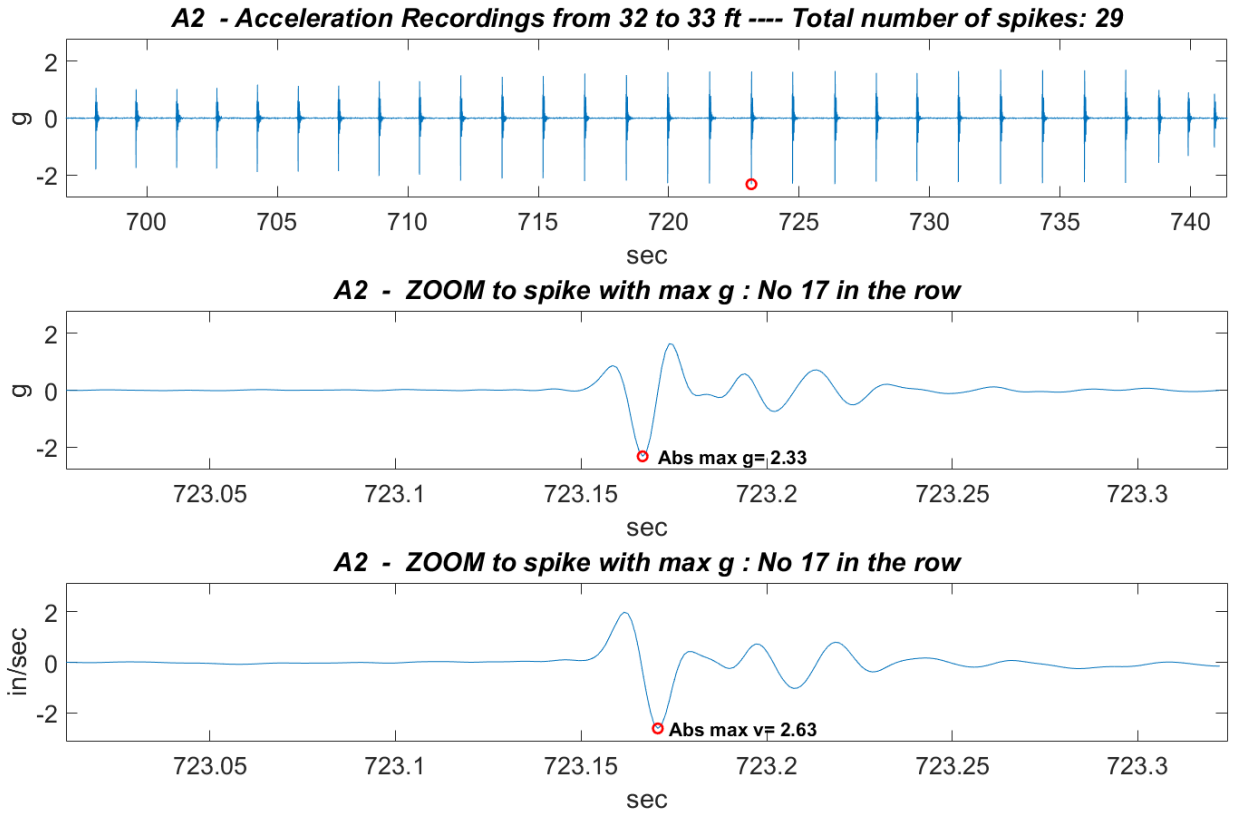

Figure 6-39 Example of selection of blow with the maximum amplitude

Table 6.1 Pile and Hammer information for field sites

Site	Pile Type (in x lb/ft)	Pile Length (ft) /Welding section length (ft)	Penetration Depth (ft)	Hammer
M-25	HP 12x53	40	32.5	Pileco D30-32
M-66	HP 12x53	40/49.5	47.5	Delmag D16-32
M-139	HP 14x73	55	53	Pileco D30-32
US-131 A	HP 14x73	55	43	Delmag D30-32
	HP 14x73	56.5	45.25	Delmag D30-32
US-131 B	HP 14x73	64.5	53.25	Delmag D30-32
	HP 14x73	61	54.75	Delmag D30-32

Table 6.2 Total number of blow count, hammer rated energy and hammer efficiency of tested piles

Site	Total Blow Count	Rated Energy of Hammer (lb-ft)	Hammer Efficiency, η (%)	Hammer
M-25	218	69,923	65	Pileco D30-32
M-66	430	39,830	48	Delmag D16-32
M-139	448	69,923	58	Pileco D30-32
US-131 A	457	75,970	43	Delmag D30-32
	576	75,970	40	Delmag D30-32
US-131 B	793	75,970	39	Delmag D30-32
	882	75,970	42	Delmag D30-32

6.3.1 M-139 Site

At this site the contractor had installed sheet piling to form cofferdams for driving structural support piles on both sides and in the middle of the river for the new northbound lanes, before monitoring driving of the test pile was conducted while driving the sheet piles and structural support piles, significant settlement was observed at the south approach to the bridge on the southbound lane. Figure 6-40 shows a bump that was formed on the road due to these settlements. Because of significant observed settlement before test pile driving, no conclusions about shakedown settlement can be made for this site.

A perspective view of the in-depth sensor locations at the M-139 near Niles, MI is shown in Figure 6-41. One accelerometer was installed in the loose to medium sand layer at a depth of 10.5 ft. Two additional sensors were attempted at this depth without success for the general reasons described earlier for loose sand. Three triaxial accelerometers were pushed to a depth of 25.5 ft at three different distances from the pile flange, into a loose to medium dense sand deposit. A 55 ft long HP 14x73 pile was driven using a Pileco D30-32 diesel hammer. The final depth of penetration of the pile was 53 ft.

Figure 6-42 presents the pile driving penetration resistance as the number of blows per pile foot increment and the accumulated number of blows versus depth of pile tip penetration. The total blow count to drive this pile section was 448. The driving resistance gradually increased with increasing penetration depth to denser sand layers. The spikes in penetration resistance at depths marked 1 and 2 on Figure 6-42 are at approximate depths where soil becomes significantly denser as indicated by the increase in blow counts, Figure 6-24. The drop off in pile penetration rate near the seating zone below 50 ft is currently unexplained. Actual count of the penetration rate from the pile driving video confirms the E-Saximeter readings so the count is not in question. Further confounding this behavior is the fact that the pile tip is penetrating very dense sand. Figure 6-43 illustrates the average actual hammer energy per pile foot increment and the hammer efficiency, η, from the E-Saximeter versus depth. The rated energy of the Pileco D30-32

hammer is 69,923 lb-ft. The average hammer efficiency when driving the test pile at M-139 site was around 58%.

Figure 6-44, Figure 6-46 and Figure 6-48 show the acceleration amplitudes of the three components of the sensors versus depth of the pile tip, while Figure 6-45,Figure 6-47 and Figure 6-49 present the velocity amplitudes versus depth for the three measured directions, i.e. vertical, longitudinal and transverse. The highest ground motion amplitudes are observed for the vertical component of the recorded values. It can be observed in Figure 6-44 and Figure 6-45 that the amplitudes increase smoothly as the pile tip approaches the depth of the embedded three sensor array (25.5 ft), with the trend being more evident for the sensor closest to the pile (A3). The spike in amplitude when the pile tip reaches the sensor depth is currently unexplained, but it occurs only for the nearest sensor to the pile. There may be some localized mechanical Poisson's effect of the steel pile on energy wave reflection precisely at the pile tip and that disturbance dissipates rapidly with distance. The increase in amplitude around 30 ft and 43 ft may be attributed to the higher driving resistance at these depths as was shown in Figure 6-42. After the pile tip passes the depth of the sensors, the amplitude of motion remains about constant until diminishing near the end of driving.

Another way of viewing the same data as presented in Figure 6-44 to Figure 6-49 is to plot the sensor acceleration or particle velocity versus the diagonal distance from the pile tip to the sensor. Plots of this type are shown in Figure 6-50 to Figure 6-52. Blue symbols represent ground motions when the pile tip is above the elevation of the sensors, while red symbols represent data collected when the pile tip had passed the sensors' depth (25.5 ft). For example, it can be seen in Figure 6-50 by viewing from the bottom right upward to the left that the amplitude of vibration increases as the pile tip comes closer to the sensor elevation where the diagonal distance is shortest, i.e. at the depth of the sensor. As the pile tip passes below the sensor, now reading in Figure 6-50 to the right of the sensor elevation, the vibration amplitude remains nearly constant but oscillates slightly until the end of driving. This behavior can be interpreted as the pile tip is causing all the vibrations at the sensor while the pile tip is above the sensor elevation. The pile tip is transmitting spherical body waves during that portion of the driving. As the

pile tip passes below the sensor, vibrations from the shaft begin to impact the sensor and increase as the length of the cylinder causing vibrations from the shaft becomes longer and exerts more influence on the sensor. At the same time, the pile tip still causing spherical body waves moves farther and farther away from the sensor causing diminishing vibrations. But the combined effect of the superposition of the shaft contributions to increasing vibrations and the tip contribution to diminishing vibrations combine to result in about a constant vibration amplitude at this site.

The cylindrical wave from the pile shaft does not contribute to vibrations when the pile tip is above the sensor as explained by Mooney (1974). He showed that a shear wave source (traction) inside an elastic body produces a wave front in the form of a torus as shown in Figure 6-53. The amplitude of the shear wave in the torus is proportional to the horizontal diameter of the torus with the maximum relative amplitude equal to one. At any other angle to the horizontal, the amplitude of the shear wave will diminish relative to the diameter as a line in the torus deviates from the horizontal. At a vertical or near vertical direction the amplitude of the shear wave will be very small, approaching zero. For this reason, it should not be expected that the cylindrical shear wave front from the pile shaft will encounter a vibration sensor until the pile shaft is nearly adjacent to or below the sensor. The same behavior as shown above for the vertical component of motion can be seen in subdued form for the longitudinal motion in Figure 6-54 and the transverse motion in Figure 6-55 to Figure 6-57.

These two general behaviors, i.e. gradual increase in amplitude as pile tip approaches sensor depth and the relative constant vibration amplitude after the pile tip passes the sensor depth, reinforce the hypothesis that the spherical waves from the pile tip dominate the wave field when the pile tip is above a point in the ground and the cylindrical wave from the pile shaft reinforces the pile tip vibrations to cause nearly constant vibrations after the pile tip goes below that same point in the field.

For this site, sensor accelerations decrease for the sensor closest to the pile face near the end of the drive in a similar but counterintuitive way as the pile penetration resistance in Figure 6-42. The reason for this behavior is unknown.

For the horizontal motion directions, longitudinal and transverse, there is a sharp increase, spike, of the amplitude of the nearest sensor to the pile (A3) when the pile tip reaches the sensor depth, Figure 6-46 to Figure 6-49, similar to the vertical direction, Figure 6-44 and Figure 6-45. When the pile tip is either above or below the sensor locations the amplitudes are lower, and have similar amplitudes for all the three sensors distances. For the longitudinal motion for example, Figure 6-46, acceleration increases to the depth of the sensor where the sensor nearest to the pile face spikes, but the further away sensors do not spike. Then the motion amplitudes remain approximately constant to the end of driving. It will be noticed that for some depths, the further away sensors record higher amplitudes of motion than the closer sensors. Some of this variation may come from the inaccuracy in orientation of the horizontal sensors, some from the influence of layering of the soil and some partly from a variable, slight torsion or twist that the pile hammer imparts to the pile (observed during driving). Figures for particle velocity show similar but subdued behavior due to the integration routine. The longitudinal direction of accelerometer A4 is not plotted because the signal was too noisy.

In order to compare the three component response of the accelerometers, the maximum accelerations for every pile foot of penetration of the vertical, longitudinal and transverse directions for each of the four buried sensors are shown in Figure 6-58a to Figure 6-60a. The longitudinal and transverse components showed similar behavior as the vertical component. Also, the transverse component values are higher than the longitudinal component.

It is evident that the amplitudes of the three components of acceleration shown in Figure 6-58a are different at most depths. The relative amplitudes in the three directions of motion are helpful in defining the type of motion occurring (body waves versus Rayleigh waves). Therefore, it is useful to examine the ratios of vertical to longitudinal (V/L) and vertical to transverse (V/T) components of acceleration as in Figure 6-58b to Figure 6-60b. For sensor A3, nearest to the pile face, Figure 6-58b, the vertical component of motion is greater than either the longitudinal or transverse components except for one depth, 27 feet, i.e. ratios greater than one. The next further away sensor, A4, Figure 6-59b, has only the vertical to transverse ratio (V/T) plotted and that ratio is greater than

one for the entire depth of the pile. And, finally, the furthest sensor from the pile, A5, Figure 6-60b reveals some depths where both the longitudinal and transverse components are greater than the vertical component, i.e. ratios (V/L) and (V/T) less than one. Additional discussion of ratios of components will come after introduction of data from the surface geophones.

Six geophones were also placed along the ground surface at the locations shown in Figure 6-61. The two closest geophones (BG1 and BG2) were triaxial units, while G1 had three single component geophones and the further out (G2) was a single vertical component geophone. Vertical peak particle velocity versus depth is shown for all the sensors in Figure 6-62. Ground motion records from the surface geophones follow a similar vibration pattern as the embedded sensors; the further the sensor from the pile the lower the peak particle velocity. There is a decrease in velocity amplitudes when the pile tip is about 15 ft and an increase in amplitudes at about 20 ft as the pile penetrates a medium dense silt layer, Figure 6-24, and the driving resistance increases. Figure 6-63 Figure 6-64 present the particle velocities for the longitudinal and transverse directions of these same surface sensors except G1 and G2 that did not have a transverse component transducer.

Figure 6-65a to Figure 6-67a show the three velocity components versus depth and Figure 6-65b to Figure 6-67b show the ratios of vertical to longitudinal (V/L) and vertical to transverse (V/T) components for sensors BG1, BG2 and G1, respectively. The red vertical line at the ratio value of 1 in Figure 6-65b to Figure 6-67b is the boundary below which vertical components of motion are smaller than either or both of the horizontal components of motion indicating that the wave motion at these sensors is not classical Rayleigh Wave form. This observation is very firm because there was no uncertainty with regard to horizontal sensor orientations for the surface sensors as there was for the buried sensors. Traditionally, researchers have assumed that the surface waves propagating from a vertical impact driven pile were Rayleigh waves and consequently, the vertical component had the greatest amplitude and this was not true for the surface measurements at this site. Another observation, the surface geophones recorded lower

velocities than the buried sensors, as expected, because they were at greater distances from the pile face than the buried sensors.

The amplitude ratios for the buried sensors presented in Figure 6-58b to Figure 6-60 are more variable with depth, and show smaller depth ranges for which V/L ratios are less than 1. Sensor A5 shows depth ranges where both longitudinal and transverse components of motion are greater than the vertical component.

Another way of investigating the types of waves propagating away from a vibration source and recorded by a surface geophone is by plotting the variation in particle motions with time. Figure 6-68a presents vertical versus longitudinal particle motion and Figure 6-68b shows a combination of the vertical and transverse time histories captured by the geophone BG2. It is evident that the particle motion path does not have the form of an elliptical shape with higher vertical particle motion, which is typical for a Rayleigh wave motion. This is an important finding from this research, contradicting the assumption that the vertical component amplitudes are greater than the horizontal components, thus a classical Rayleigh wave was not developed on surface based on the surface measurements at all the tested sites.

Two sensors were located at the same radial distance from the pile (6.5 ft); BG1 geophone was positioned on the surface and A5 accelerometer was installed 25.5 ft into a medium dense sand deposit. Figure 6-69 to Figure 6-71 illustrate peak particle velocities versus depth for these two sensors for the three monitored directions. For the vertical motions, the surface sensor has larger motion than the buried sensor until the pile tip reaches the depth of buried sensor A5, about 25 ft. At greater depths the buried sensor recorded higher amplitudes than the geophone on the surface because the shaft contribution becomes more important. For the longitudinal motions, the vibration pattern is similar for the two sensors, however the surface geophone recorded almost double the amplitudes of the buried sensor. For the transverse motions, ground motions were similar for both sensors with the surface sensor recording greater motion for most of the depth.

Figure 6-40 Bump created on the road close to pile driving operations at M-139 site

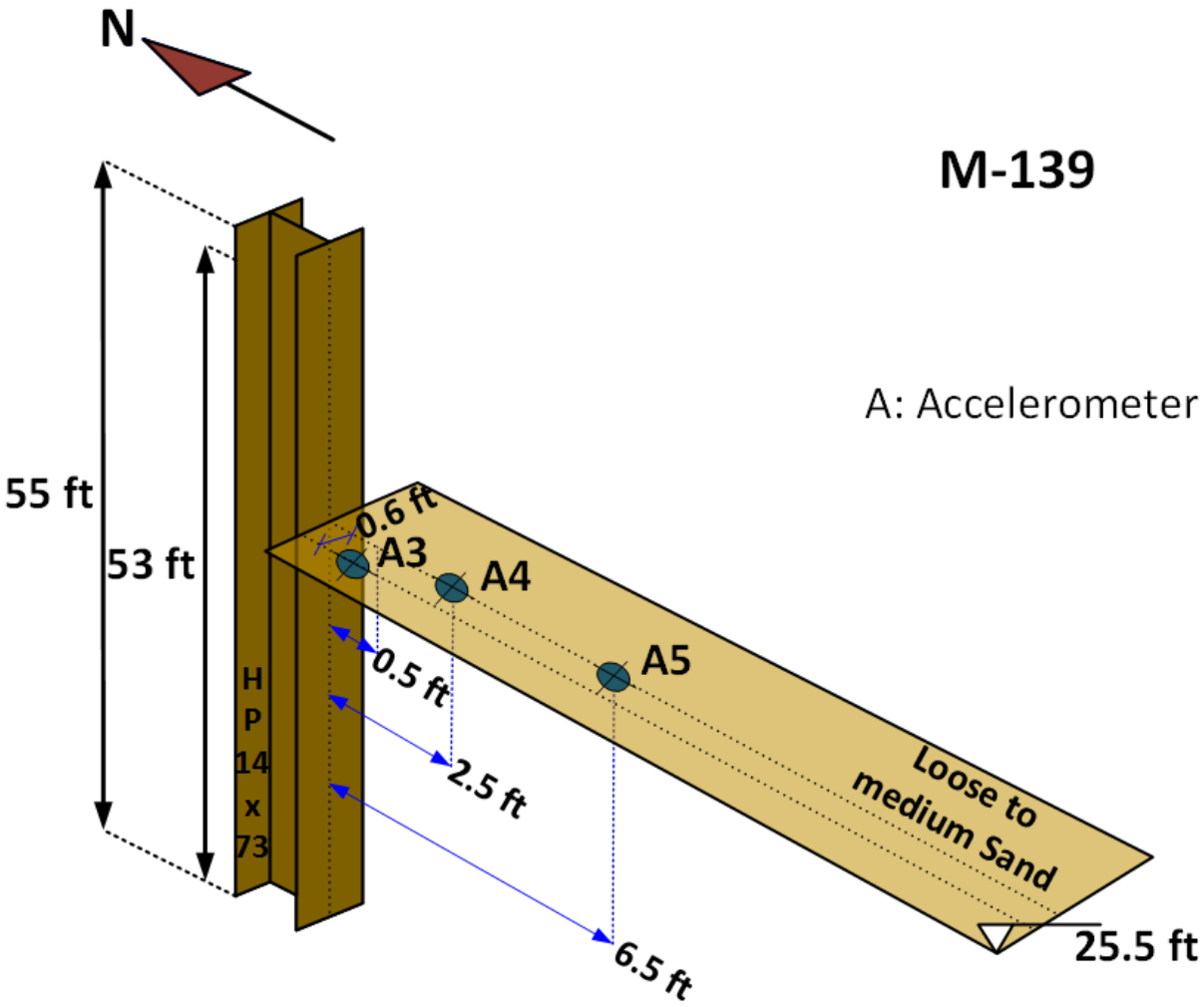

Figure 6-41 Perspective view of buried sensors at M-139 site (not to scale)

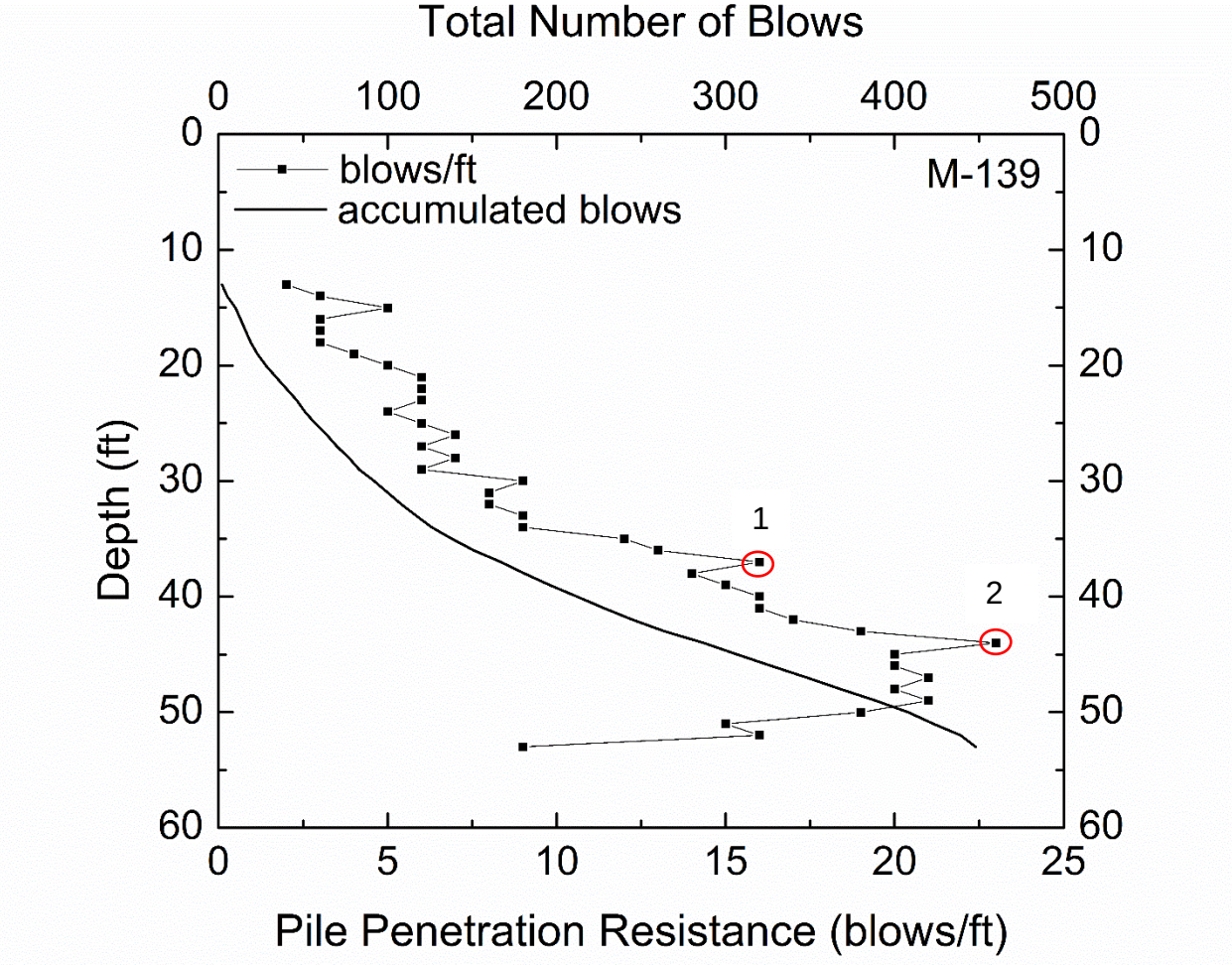

Figure 6-42 Driving Resistance and accumulated blows with depth – M-139 site

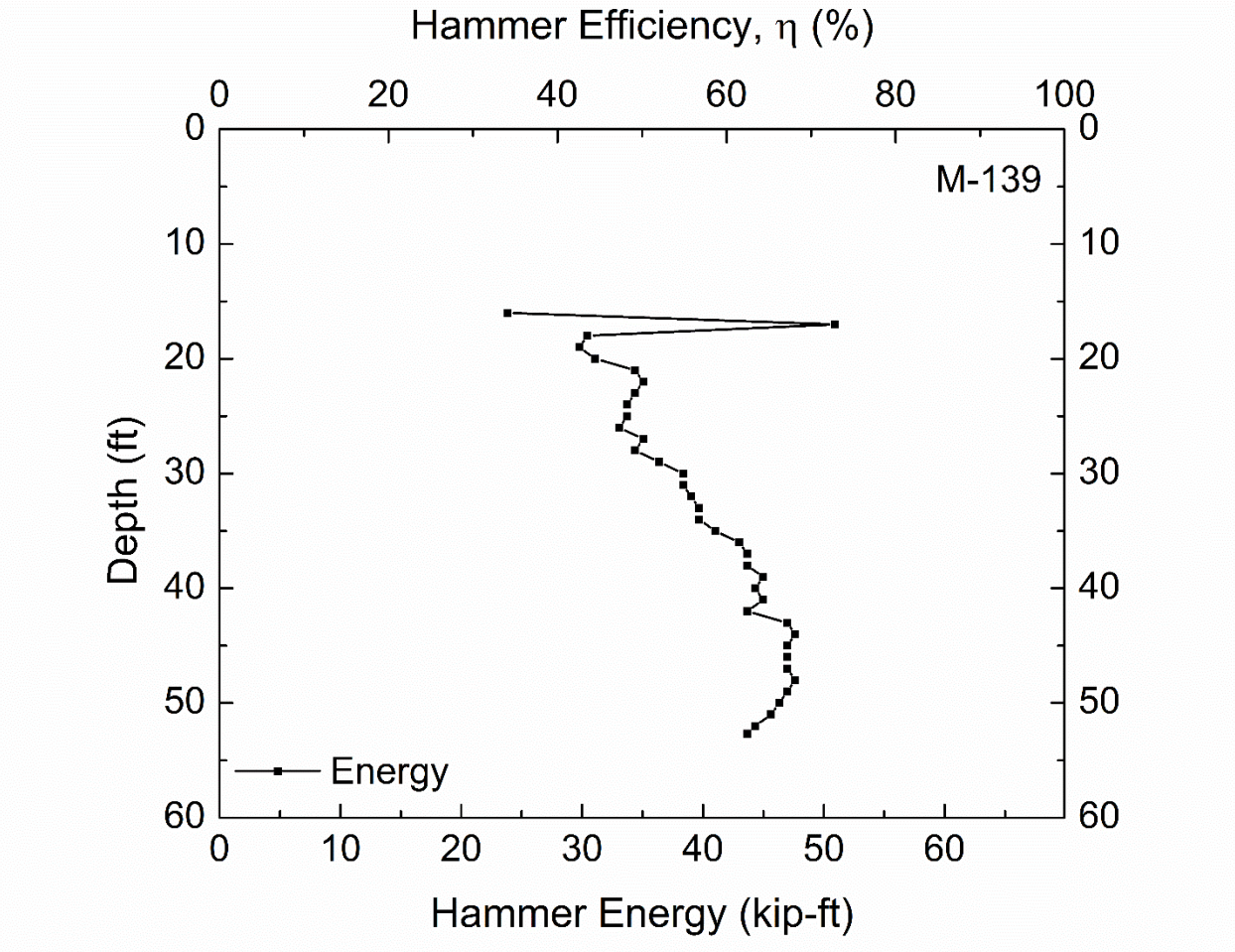

Figure 6-43 Hammer Energy and Hammer Efficiency with depth – M-139 site

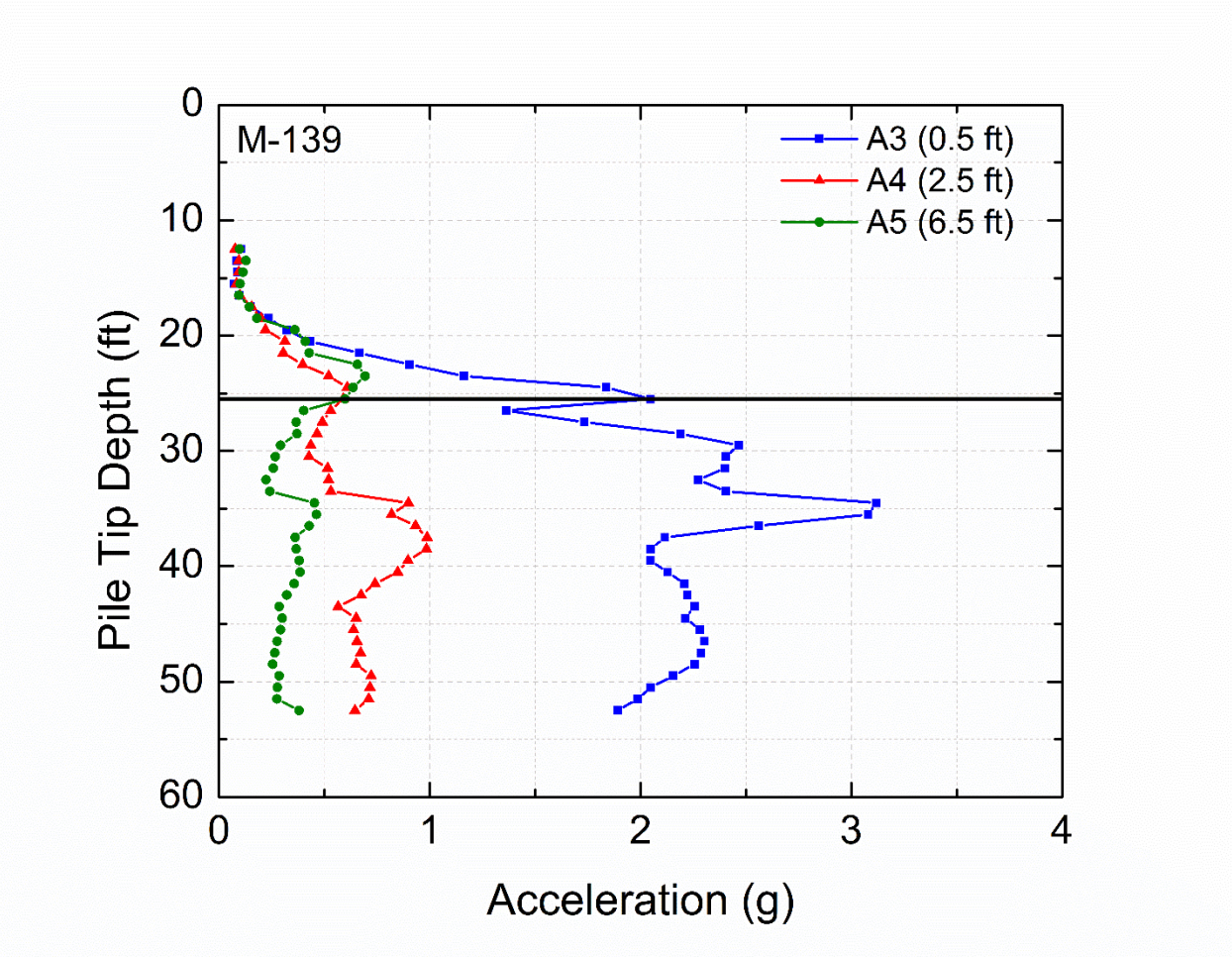

Figure 6-44 Acceleration of buried sensors at M-139 site – Vertical Direction

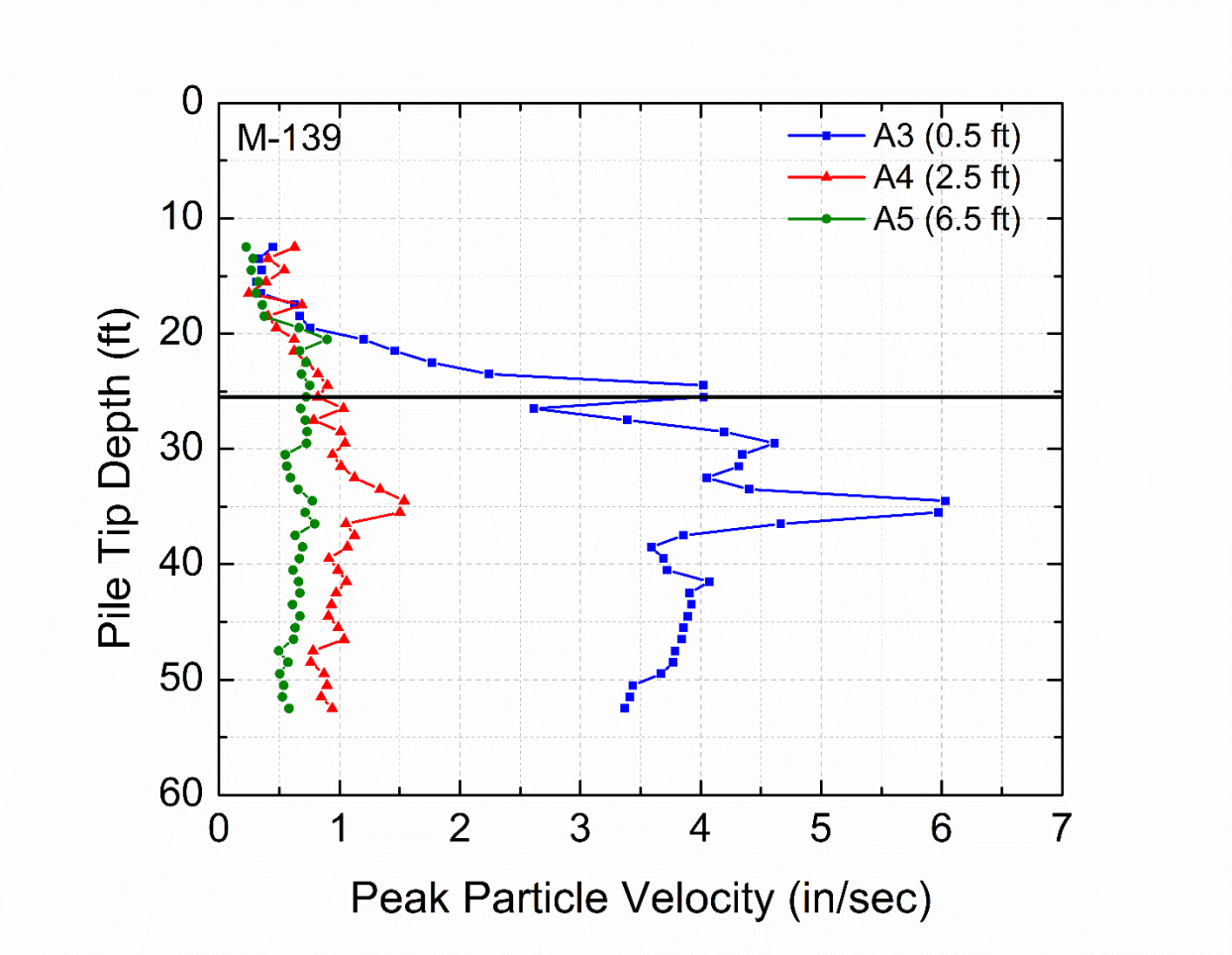

Figure 6-45 Peak Particle Velocity of buried sensors at M-139 site – Vertical Direction

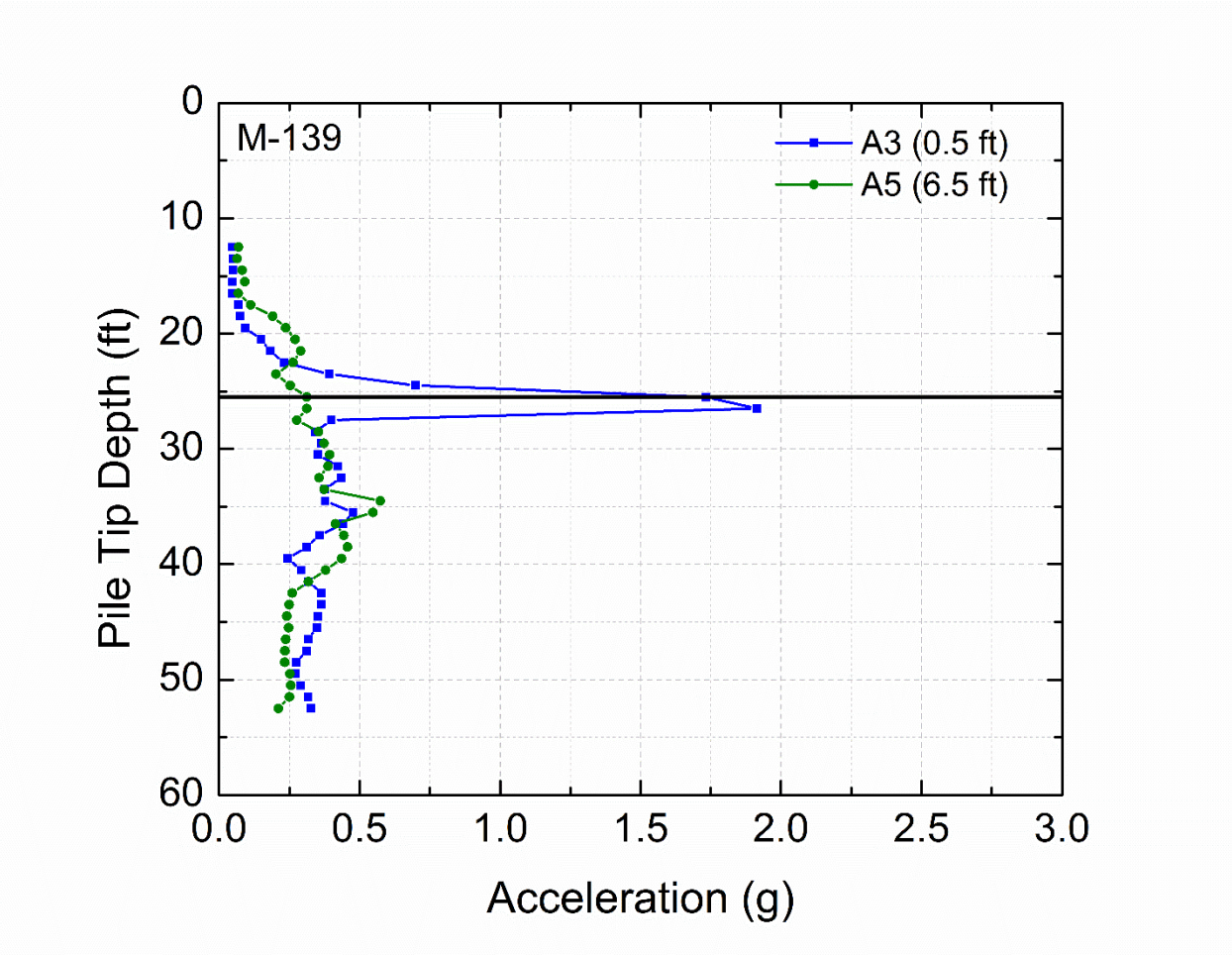

Figure 6-46 Acceleration of buried sensors at M-139 site – Longitudinal Direction

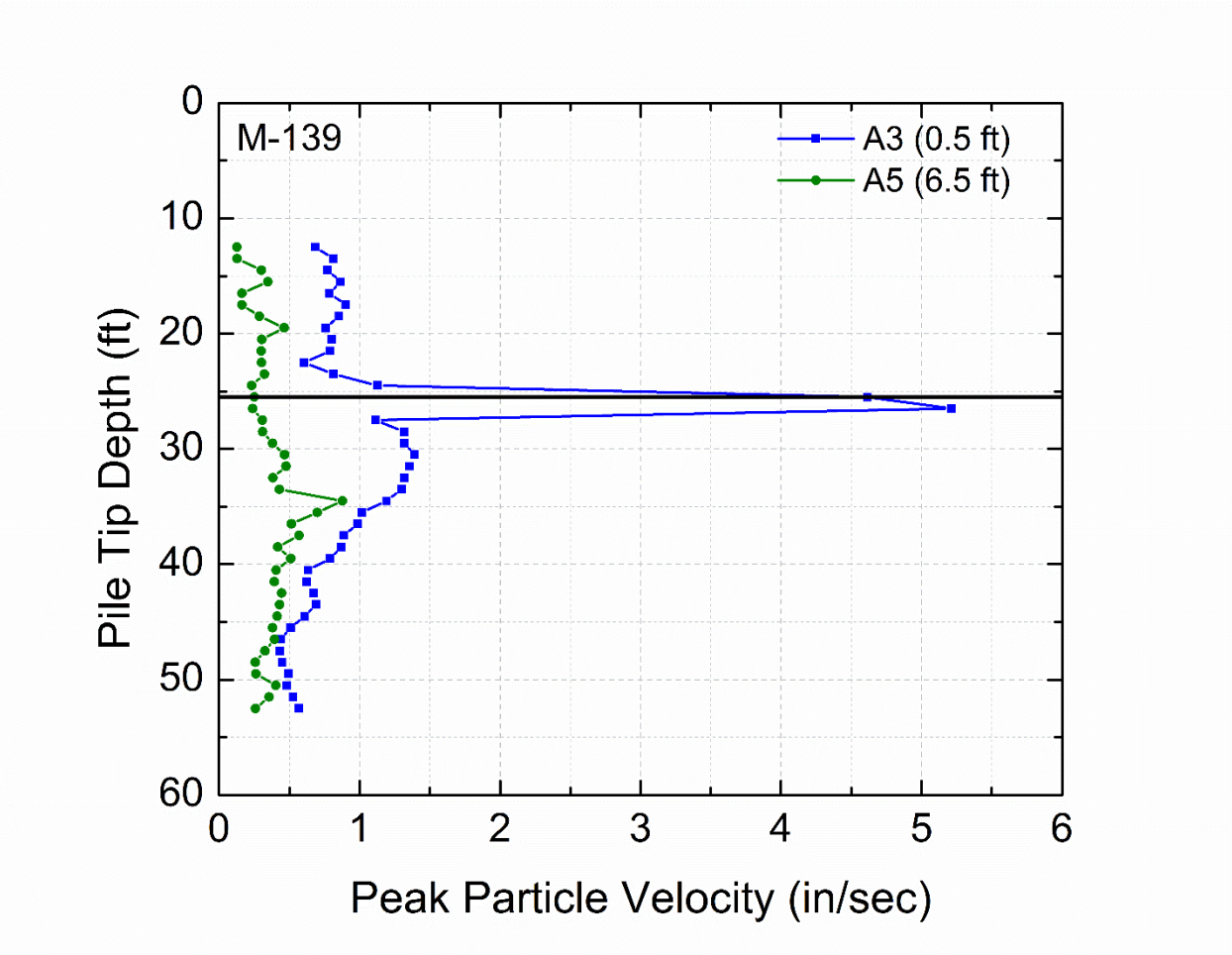

Figure 6-47 Peak Particle Velocity of buried sensors at M-139 site – Longitudinal Direction

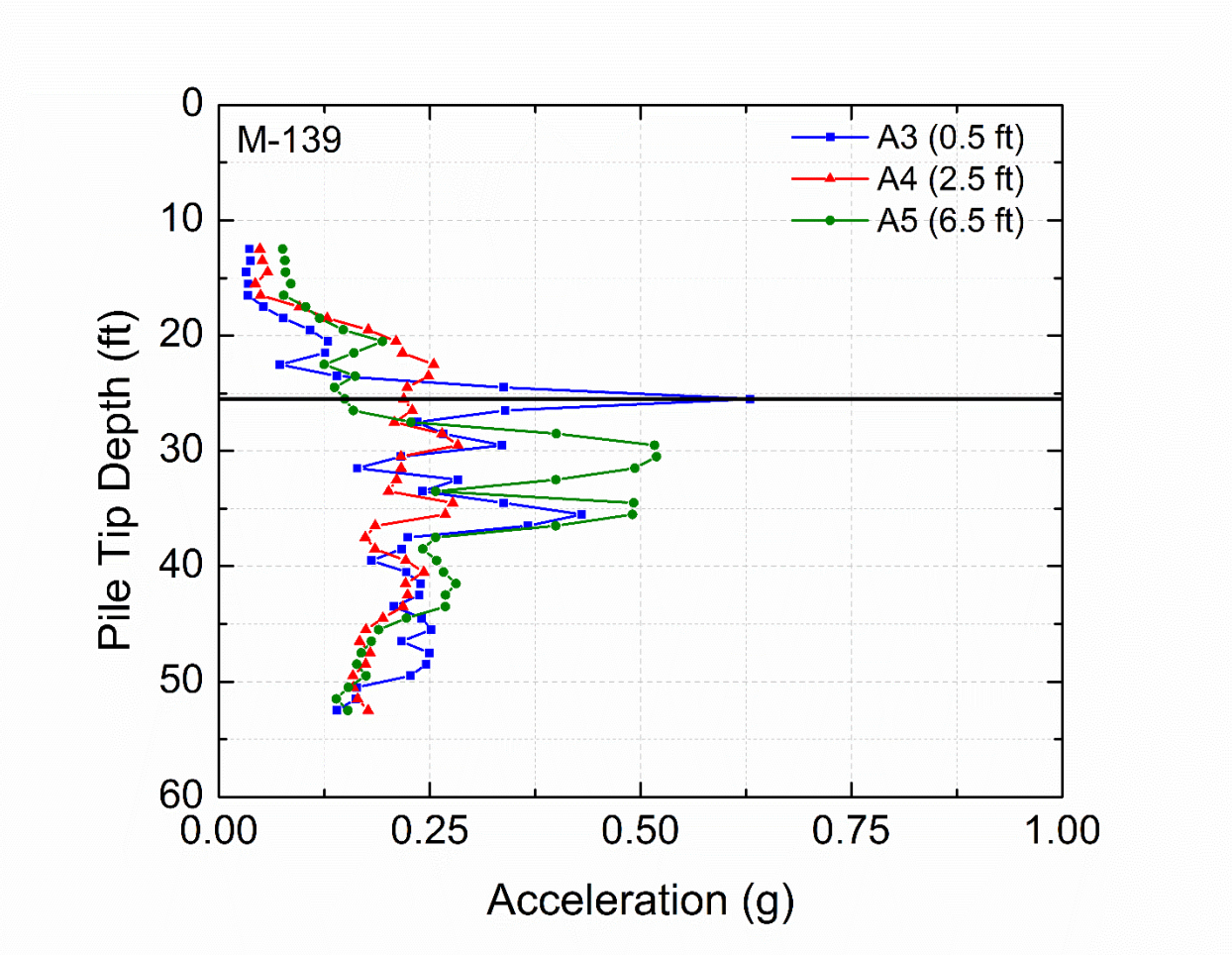

Figure 6-48 Acceleration of buried sensors at M-139 site – Transverse Direction

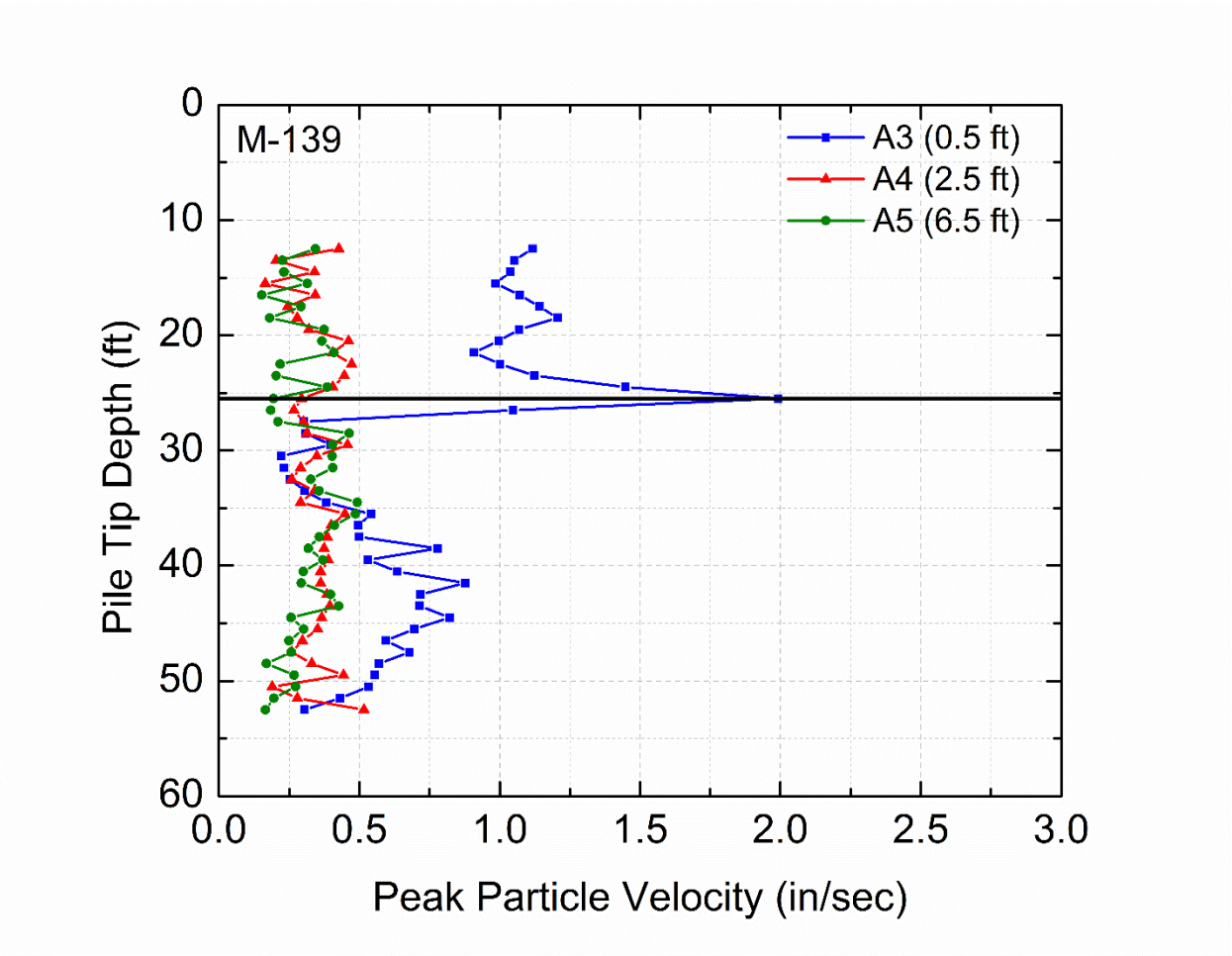

Figure 6-49 Peak Particle Velocity of buried sensors at M-139 site – Transverse Direction

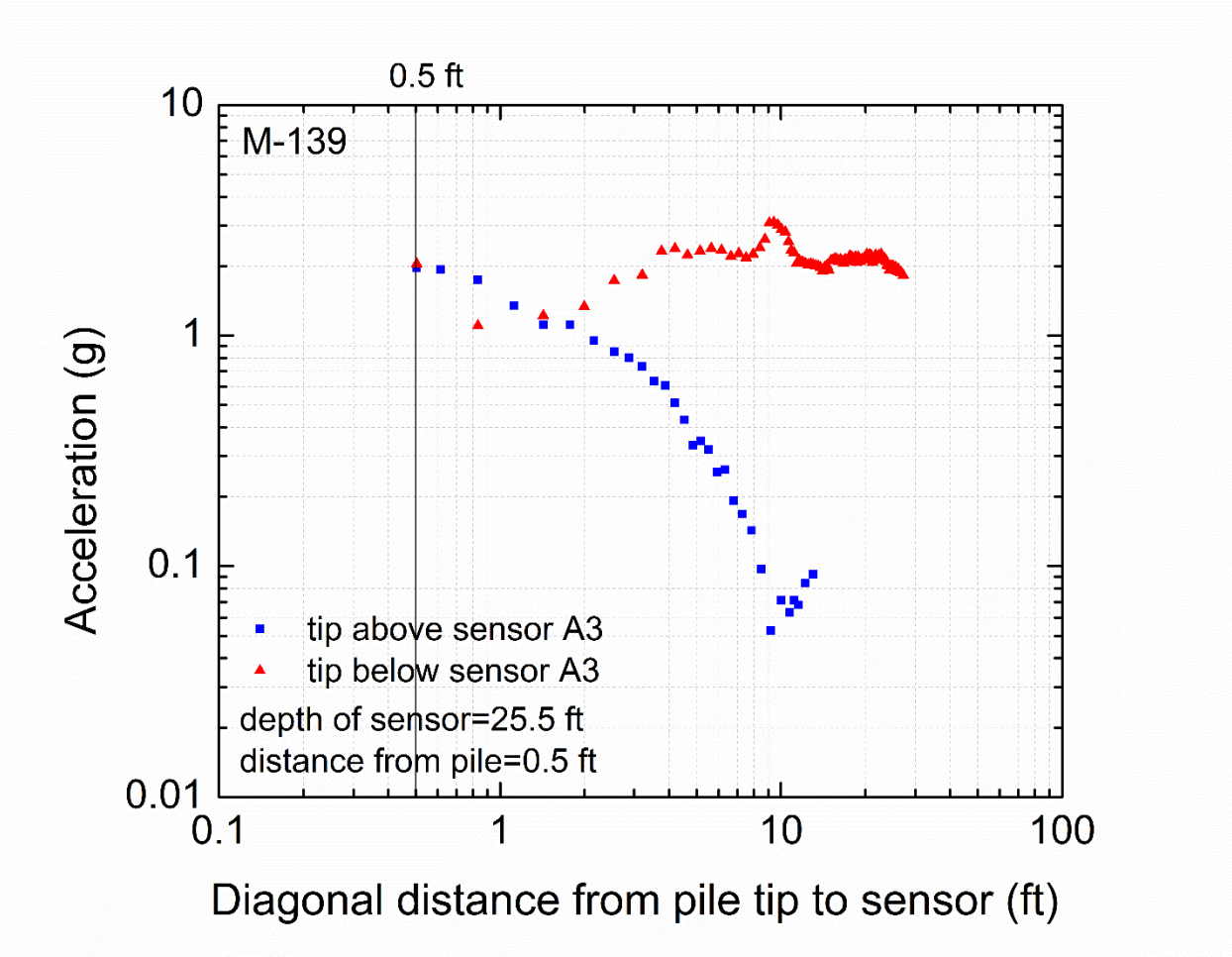

Figure 6-50 Acceleration versus diagonal distance from pile tip to sensor A3 at M-139 site – Vertical direction

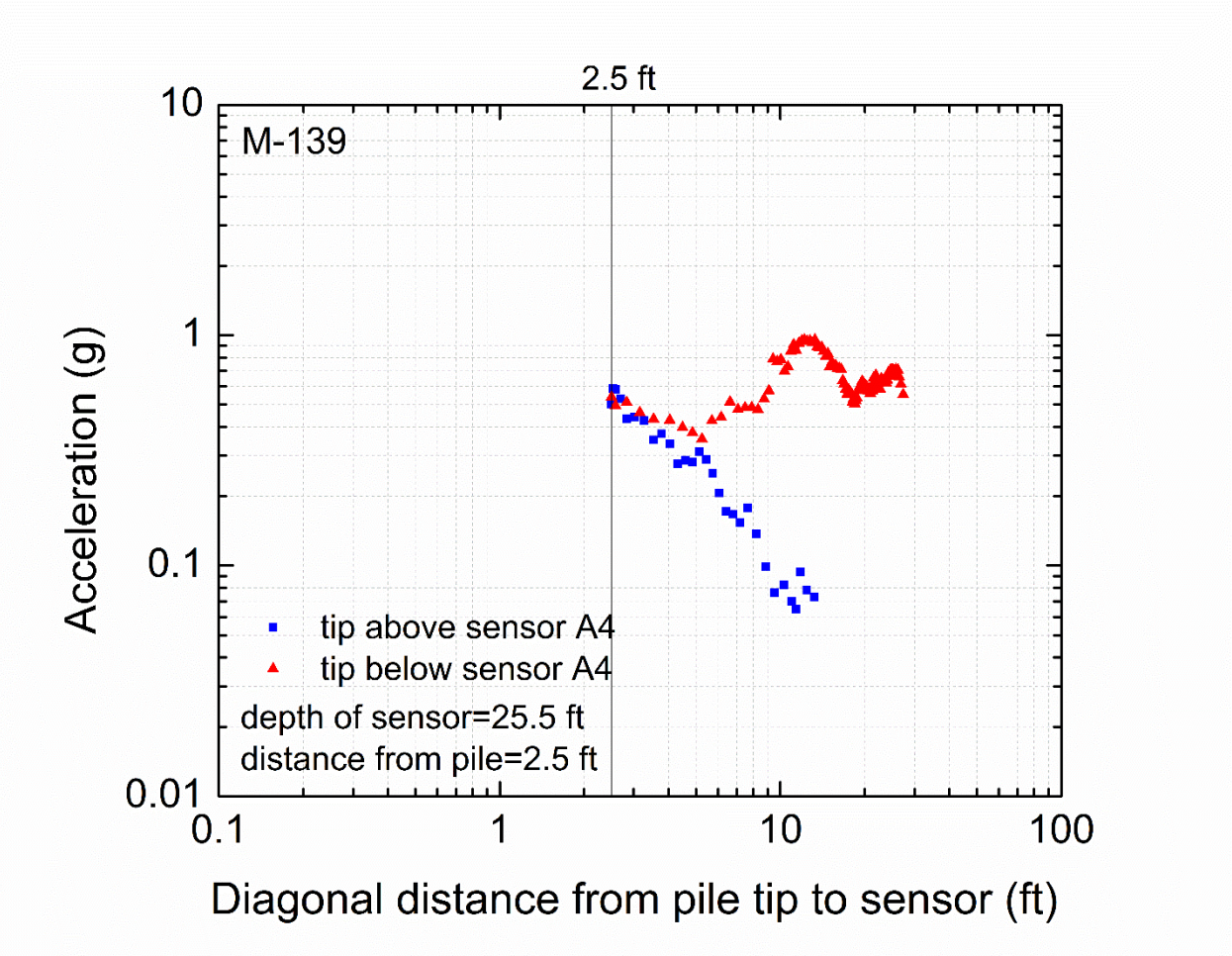

Figure 6-51 Acceleration versus diagonal distance from pile tip to sensor A4 at M-139 site – Vertical direction

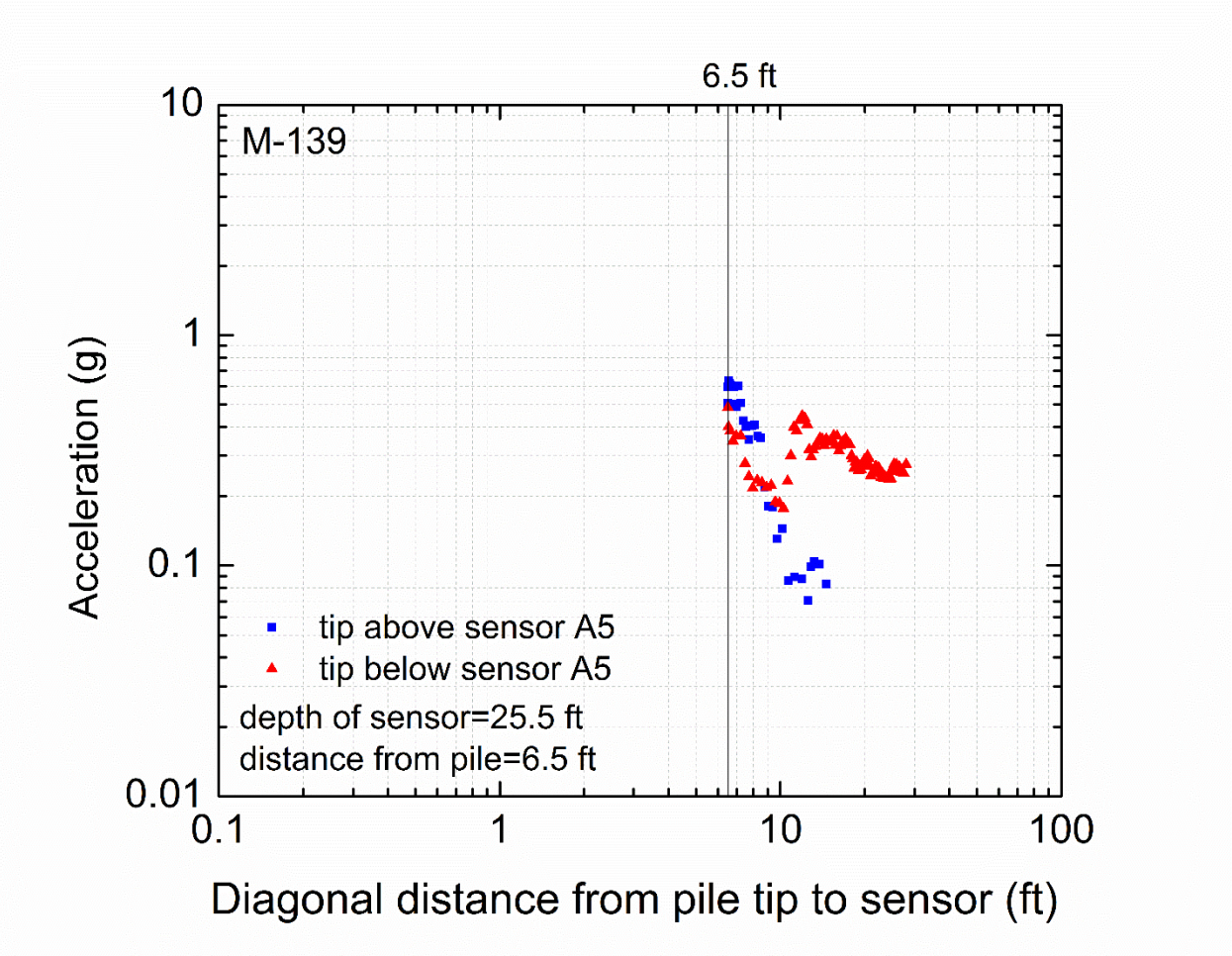

Figure 6-52 Acceleration versus diagonal distance from pile tip to sensor A5 at M-139 site – Vertical direction

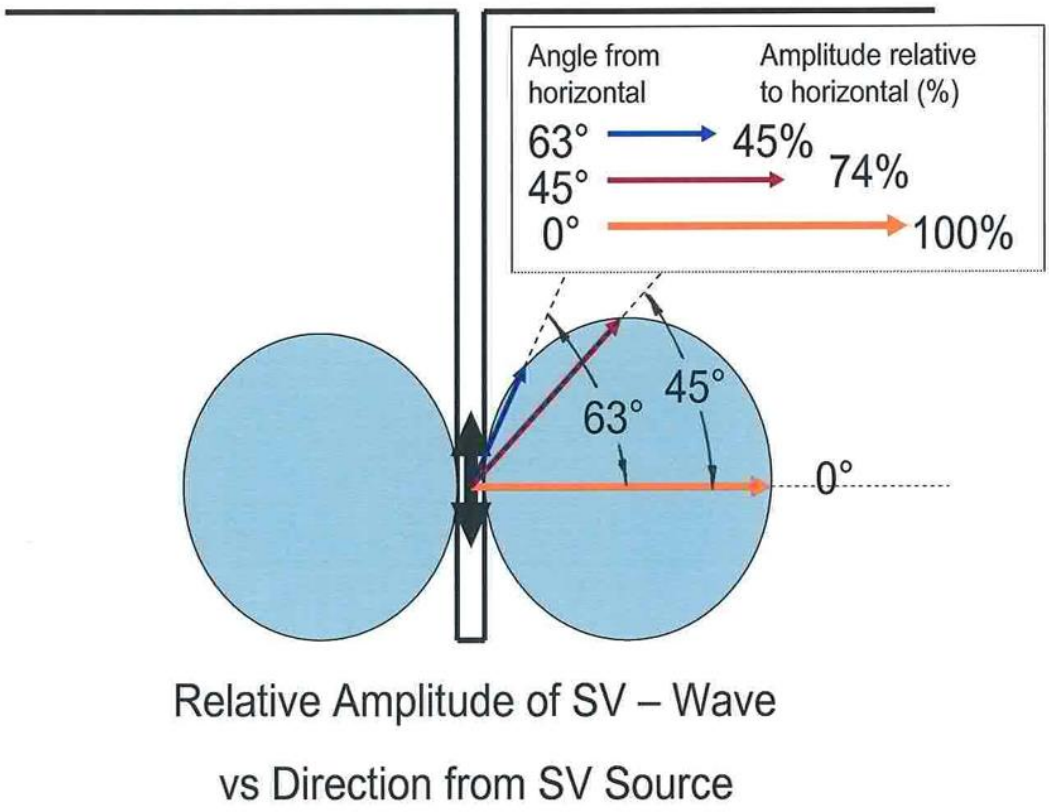

Figure 6-53 Amplitude distribution from shear traction in body of ideal medium (after Mooney 1974)

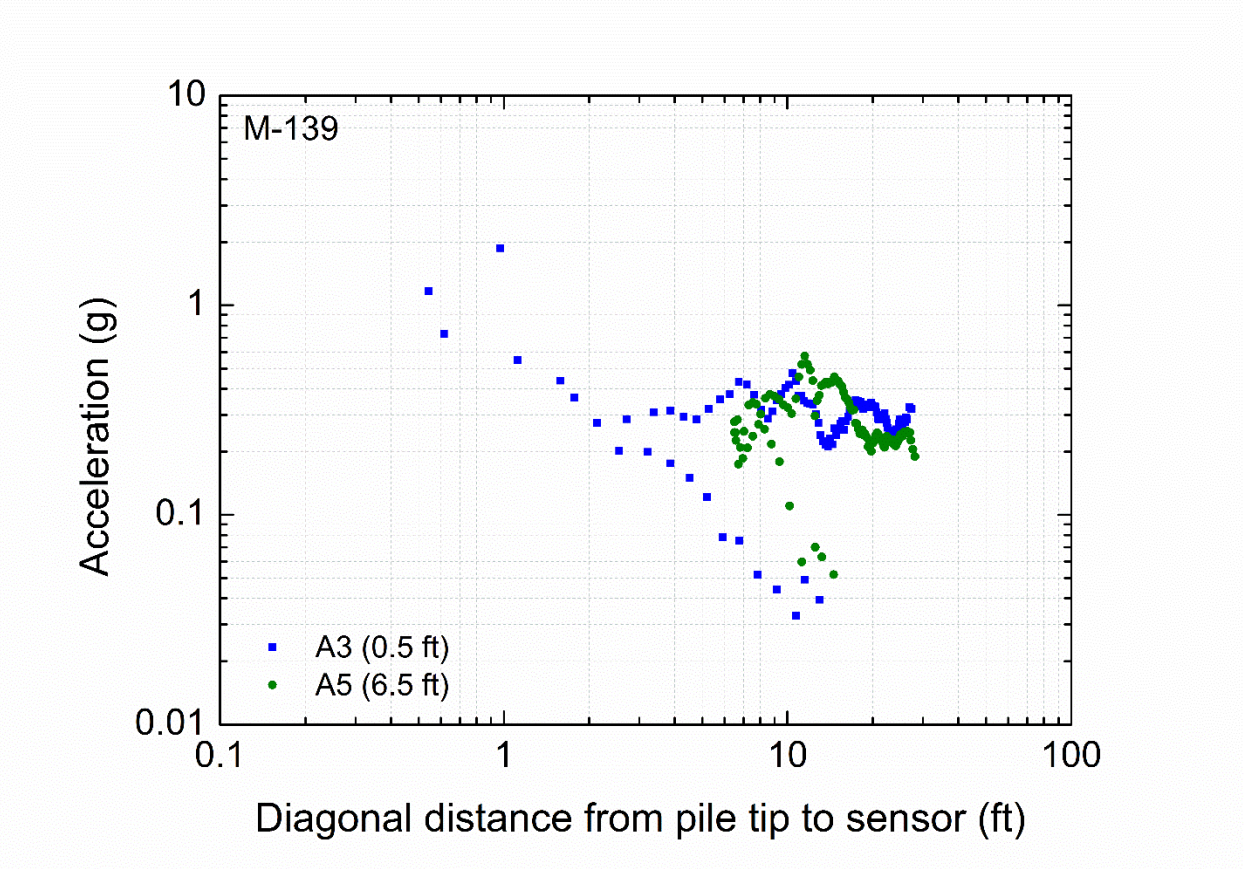

Figure 6-54 Acceleration versus diagonal distance from pile tip to buried sensors at M-139 site – Longitudinal direction, logarithmic scale

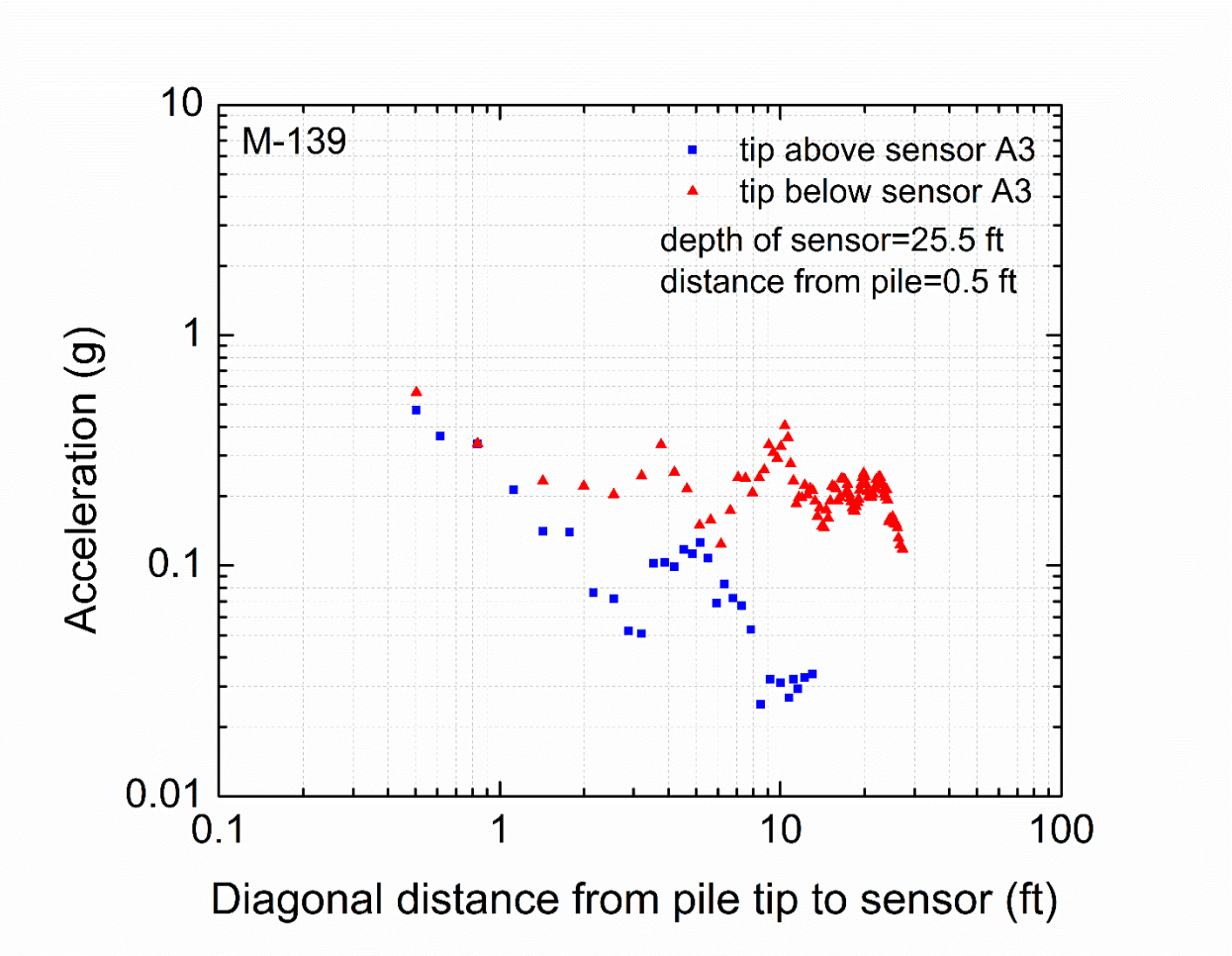

Figure 6-55 Acceleration versus diagonal distance from pile tip to sensor A3 at M-139 site – Transverse direction

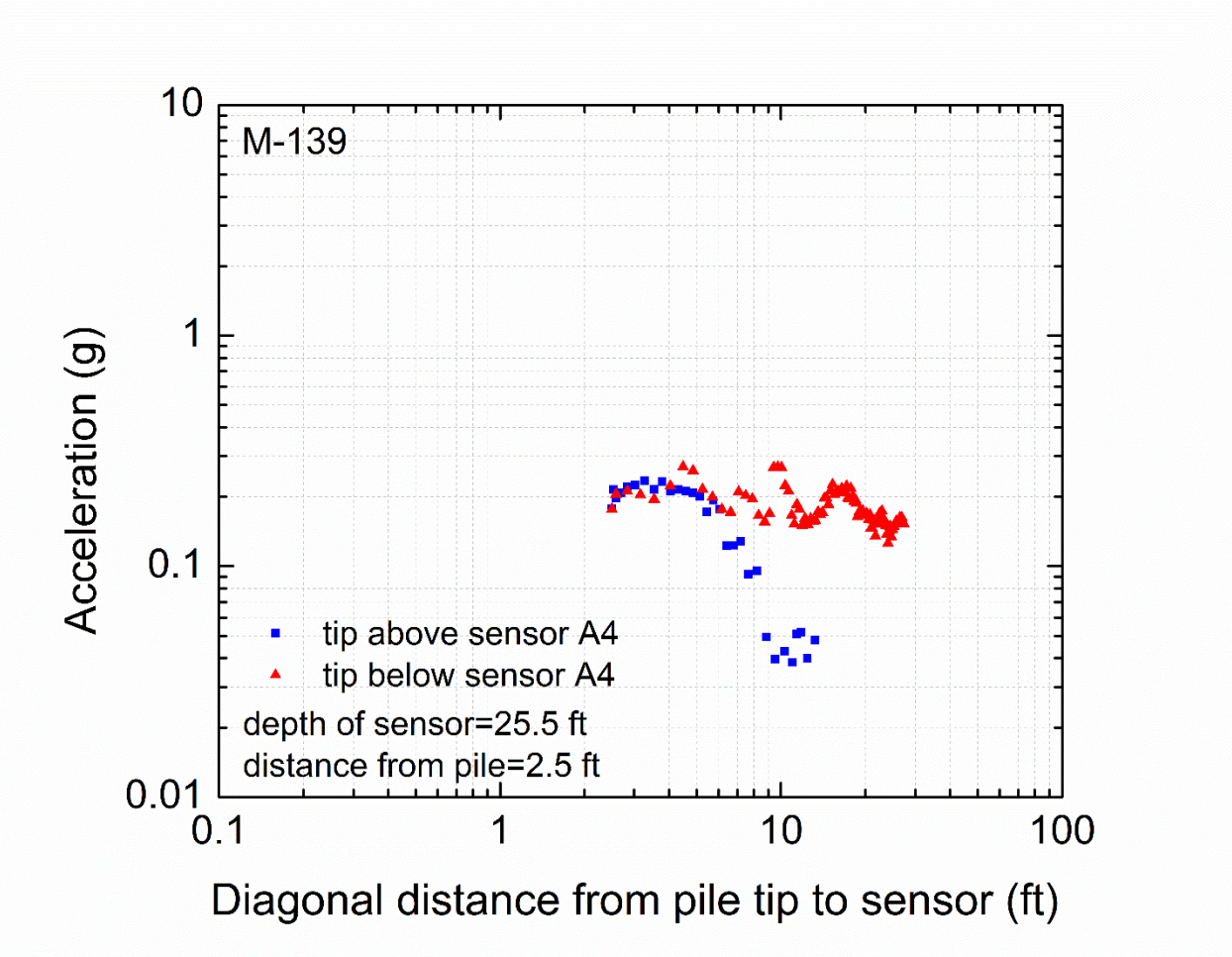

Figure 6-56 Acceleration versus diagonal distance from pile tip to sensor A4 at M-139 site – Transverse direction

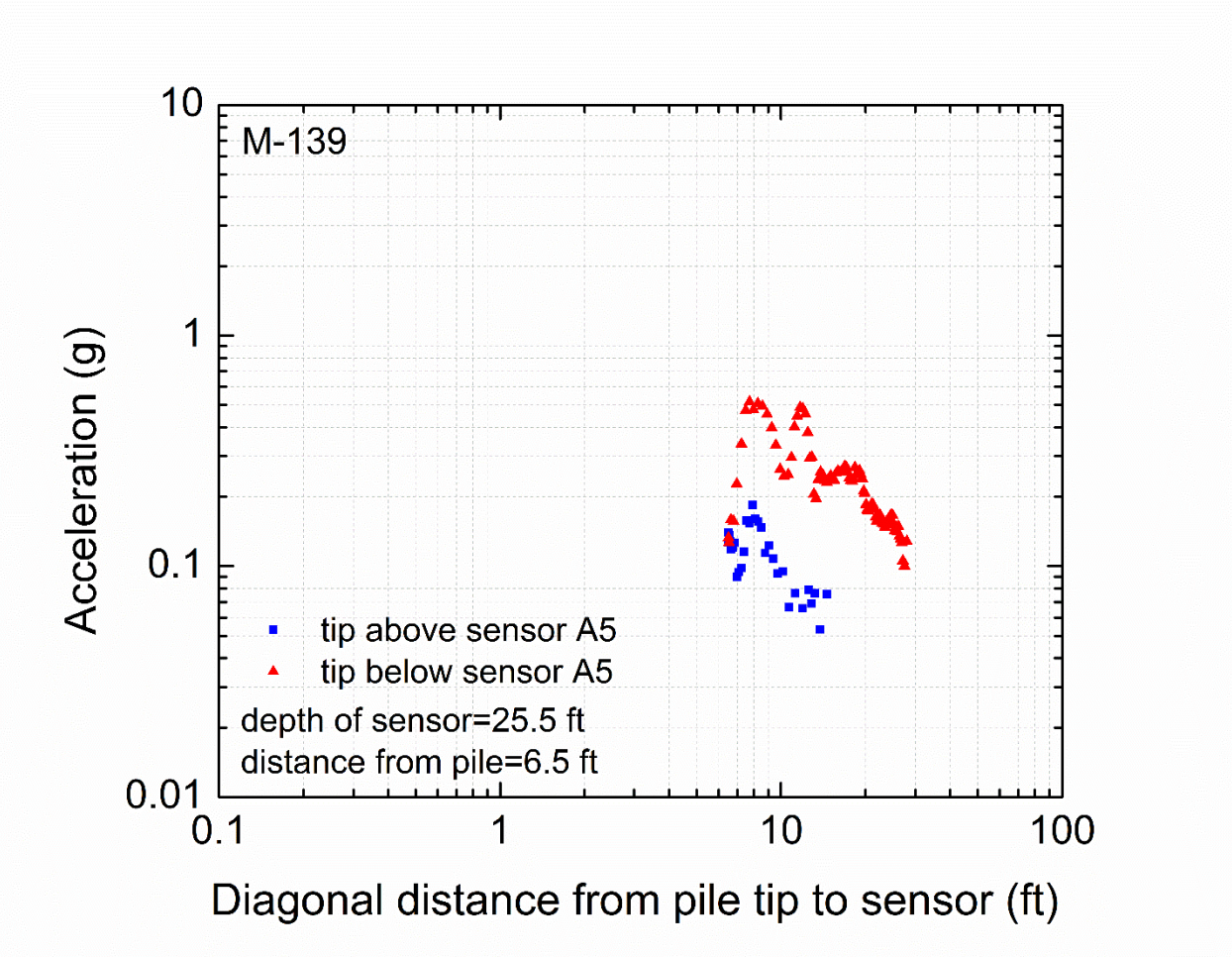

Figure 6-57 Acceleration versus diagonal distance from pile tip to sensor A5 at M-139 site – Transverse direction

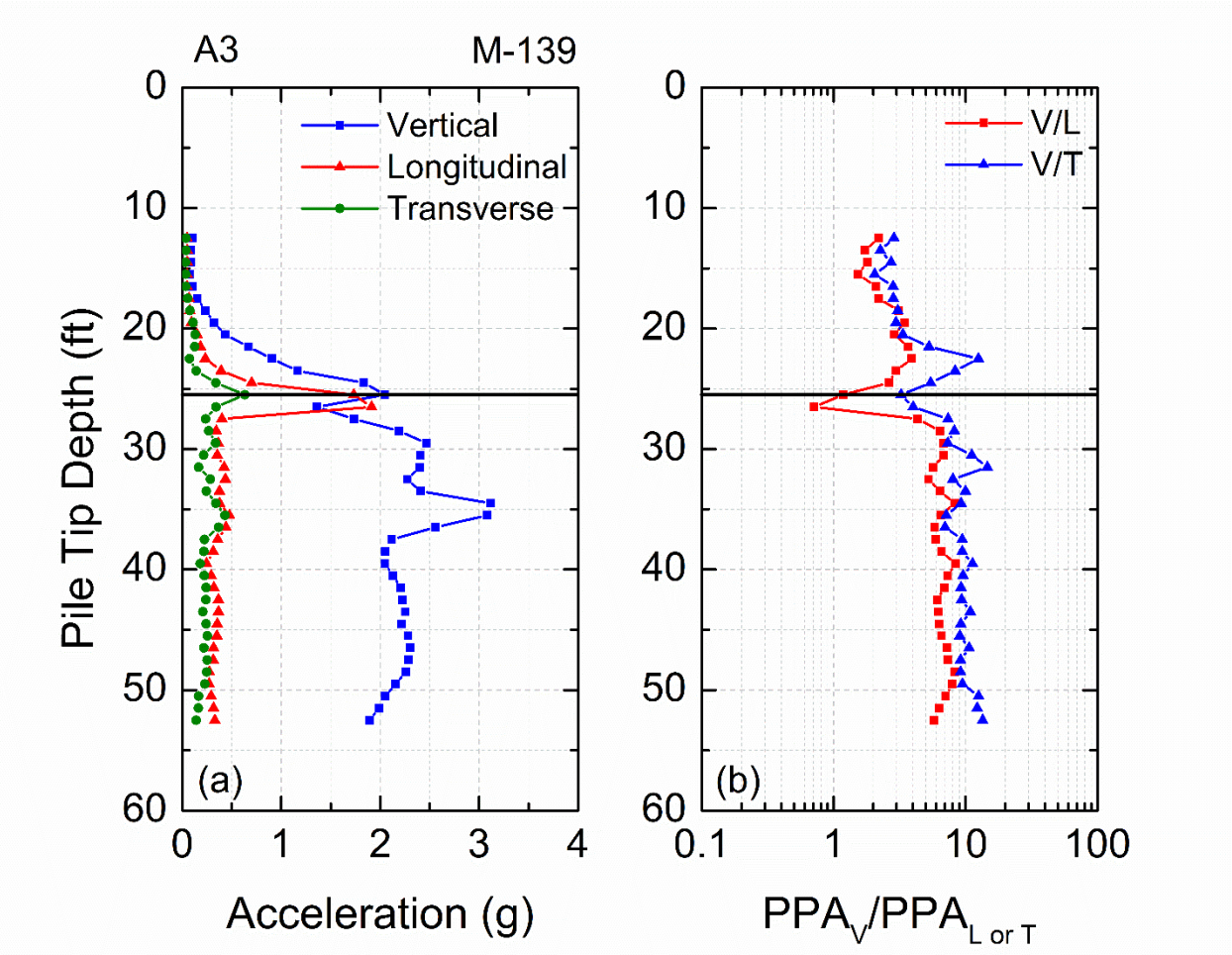

Figure 6-58 (a) Accelerations versus depth for the three components of sensor A3 and (b) vertical to longitudinal and vertical to transverse components of acceleration – M-139 site

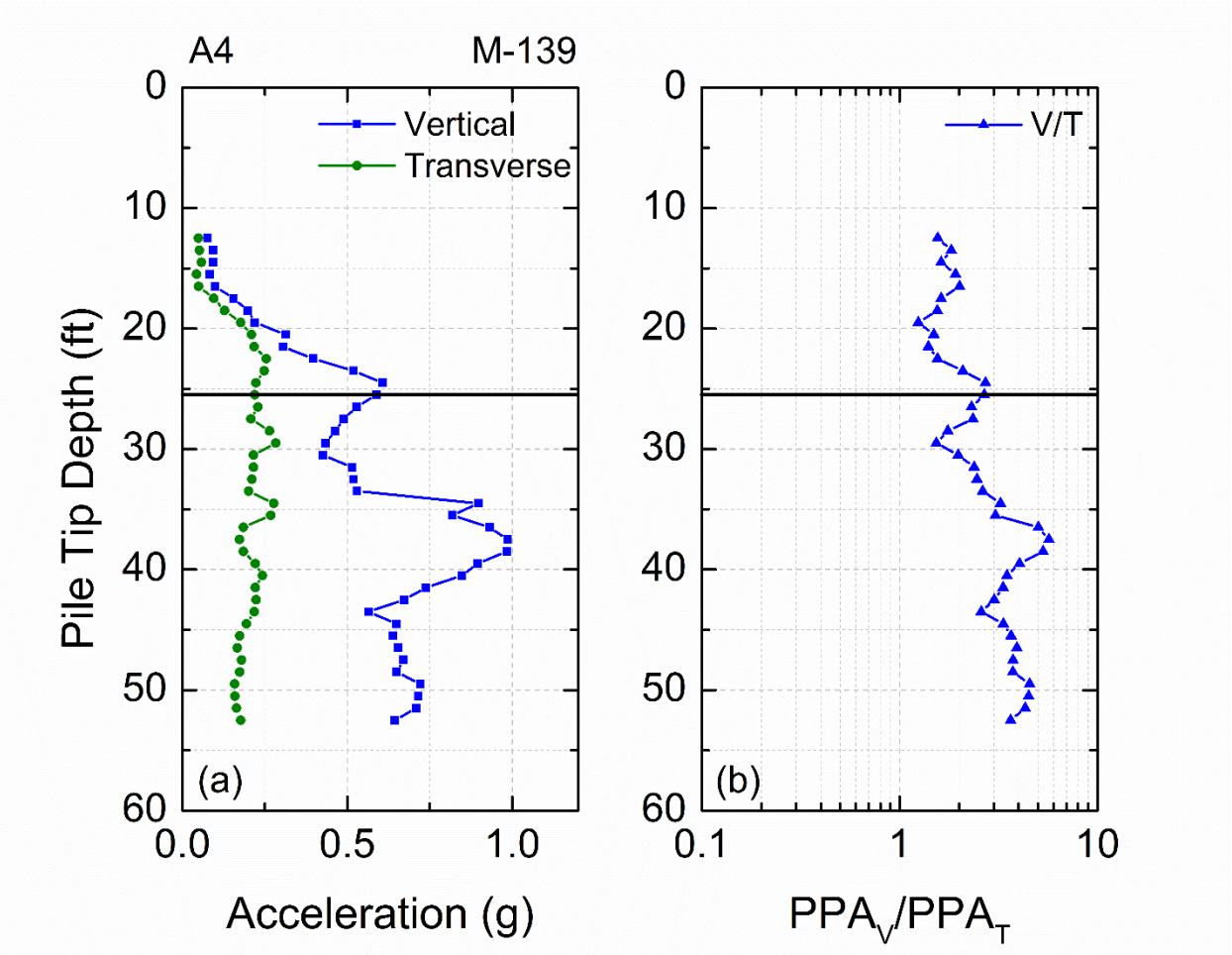

Figure 6-59 (a) Accelerations versus depth for the three components of sensor A4 and (b) vertical to transverse components of acceleration – M-139 site

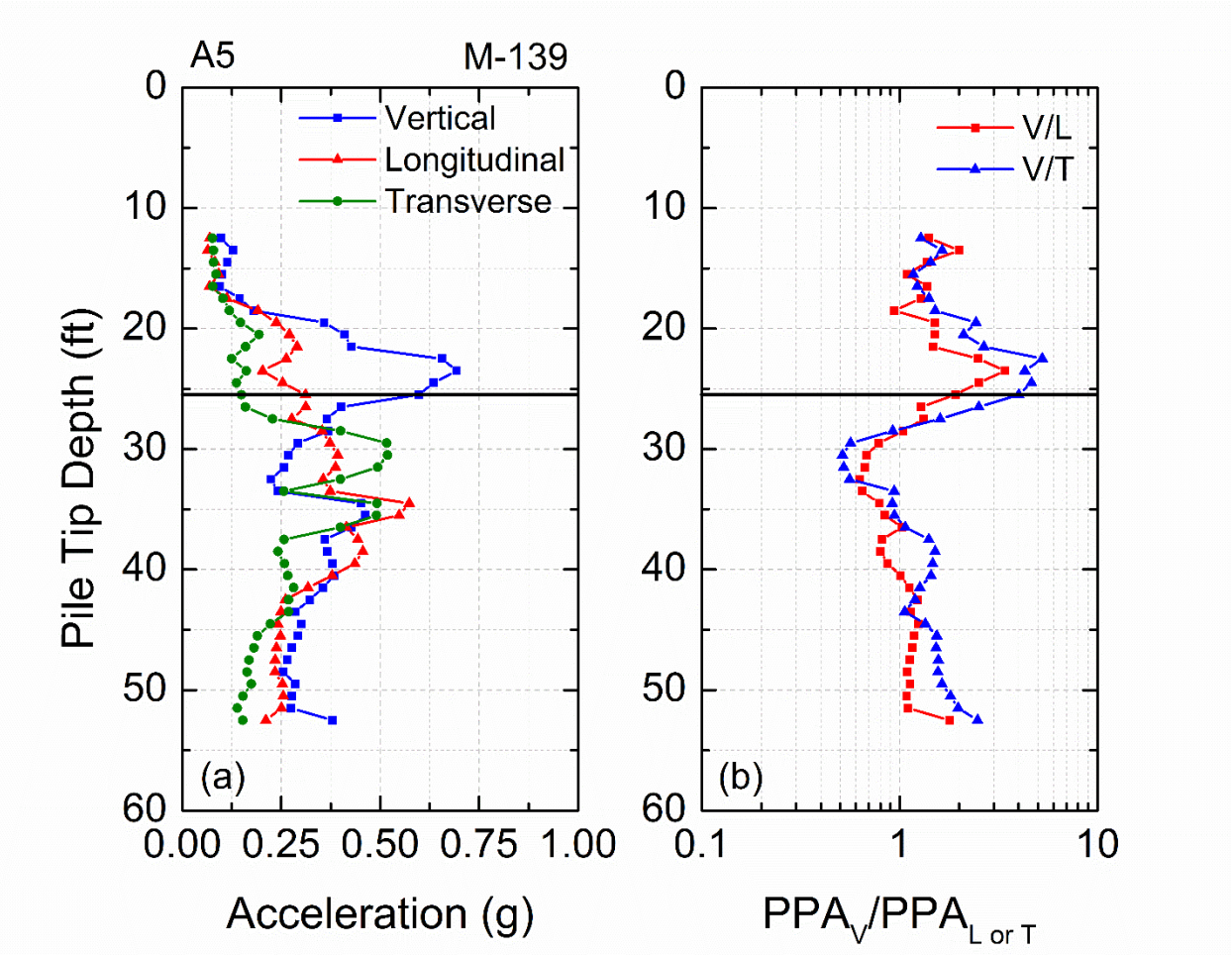

Figure 6-60 (a) Accelerations versus depth for the three components of sensor A5 and (b) vertical to longitudinal and vertical to transverse components of acceleration – M-139 site

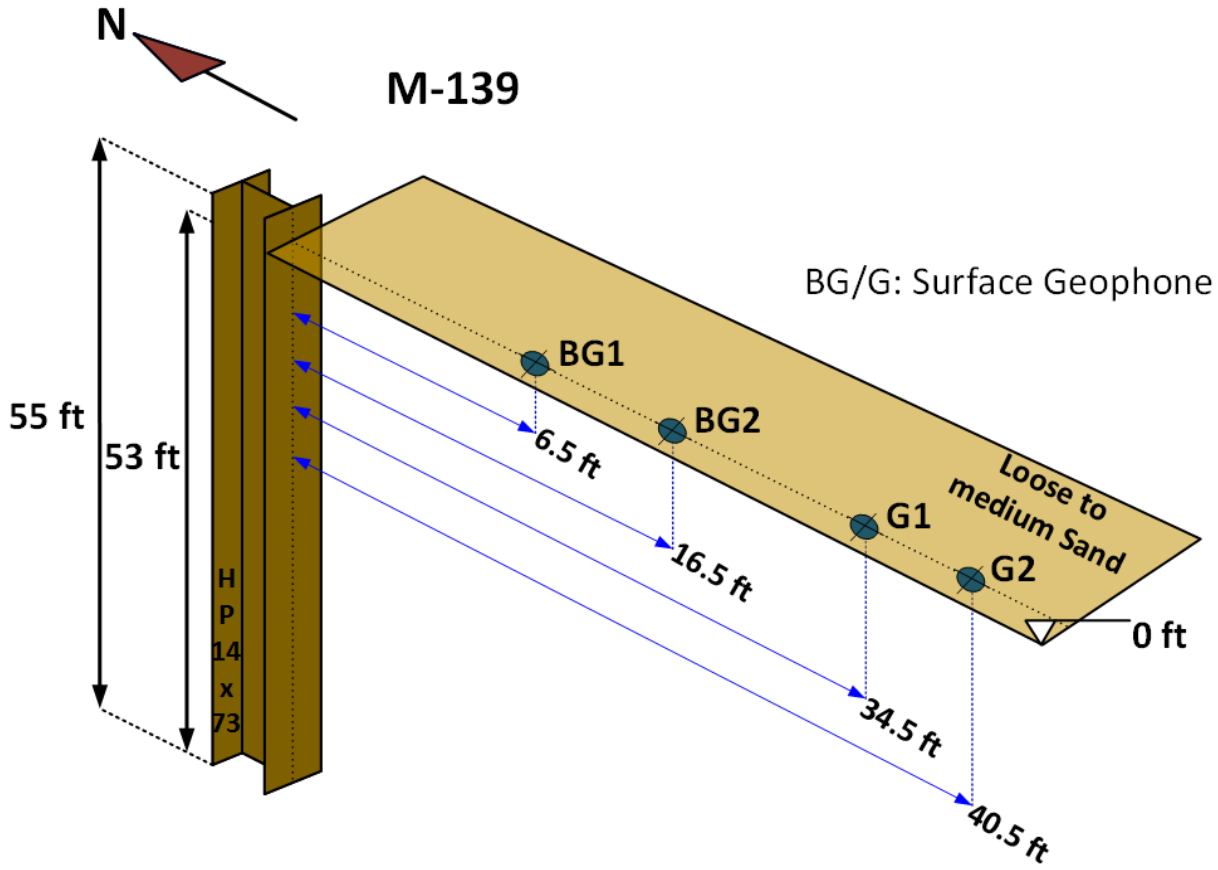

Figure 6-61 Perspective view of surface sensors at M-139 site (not to scale)

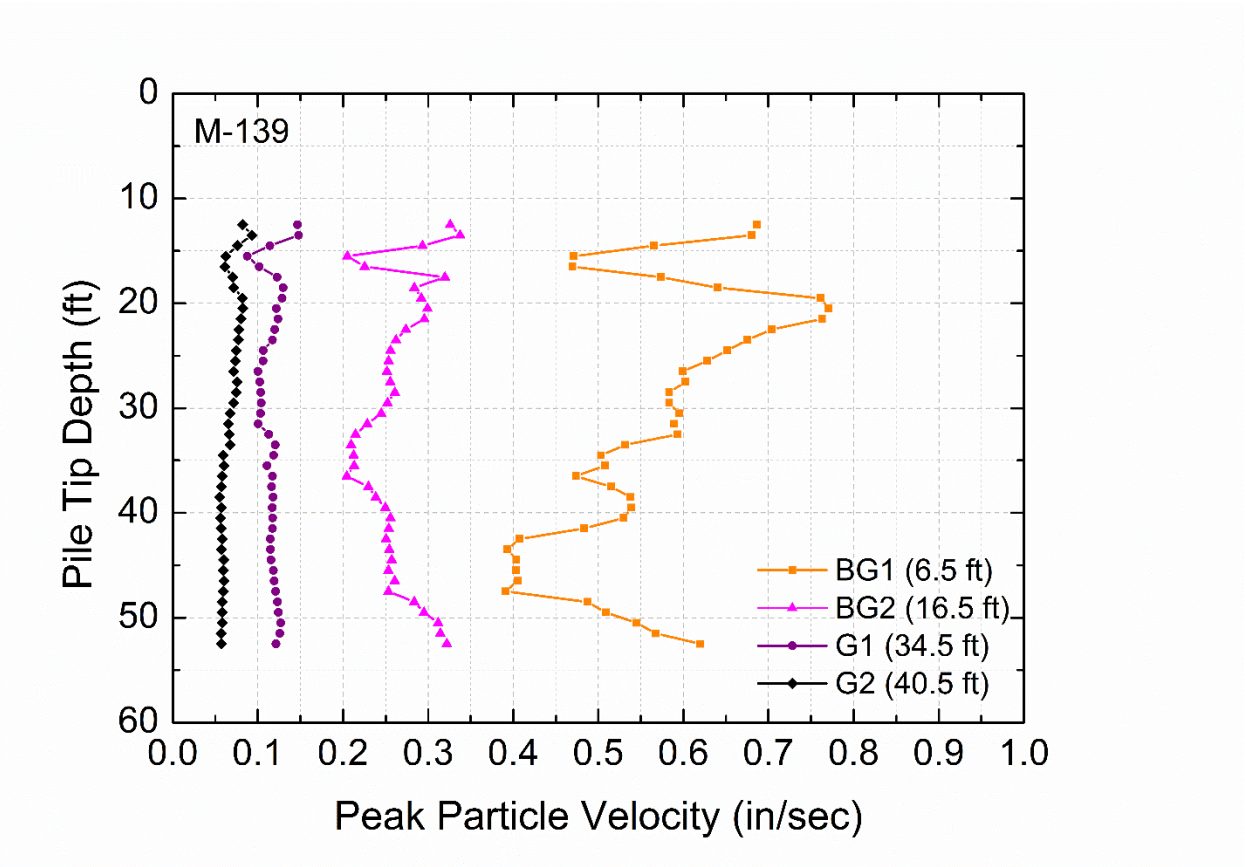

Figure 6-62 Peak Particle Velocity of surface geophones at M-139 site – Vertical Direction

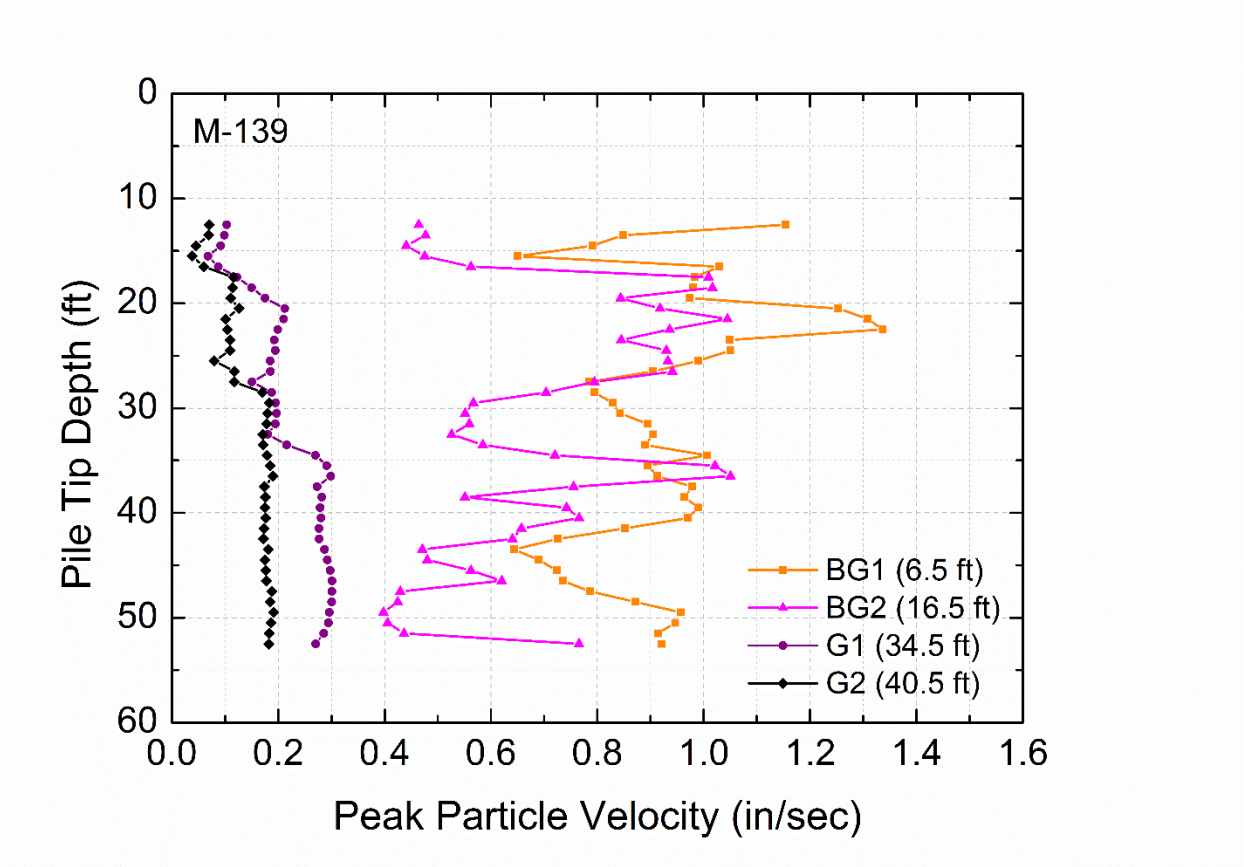

Figure 6-63 Peak Particle Velocity of surface geophones at M-139 site –Longitudinal Direction

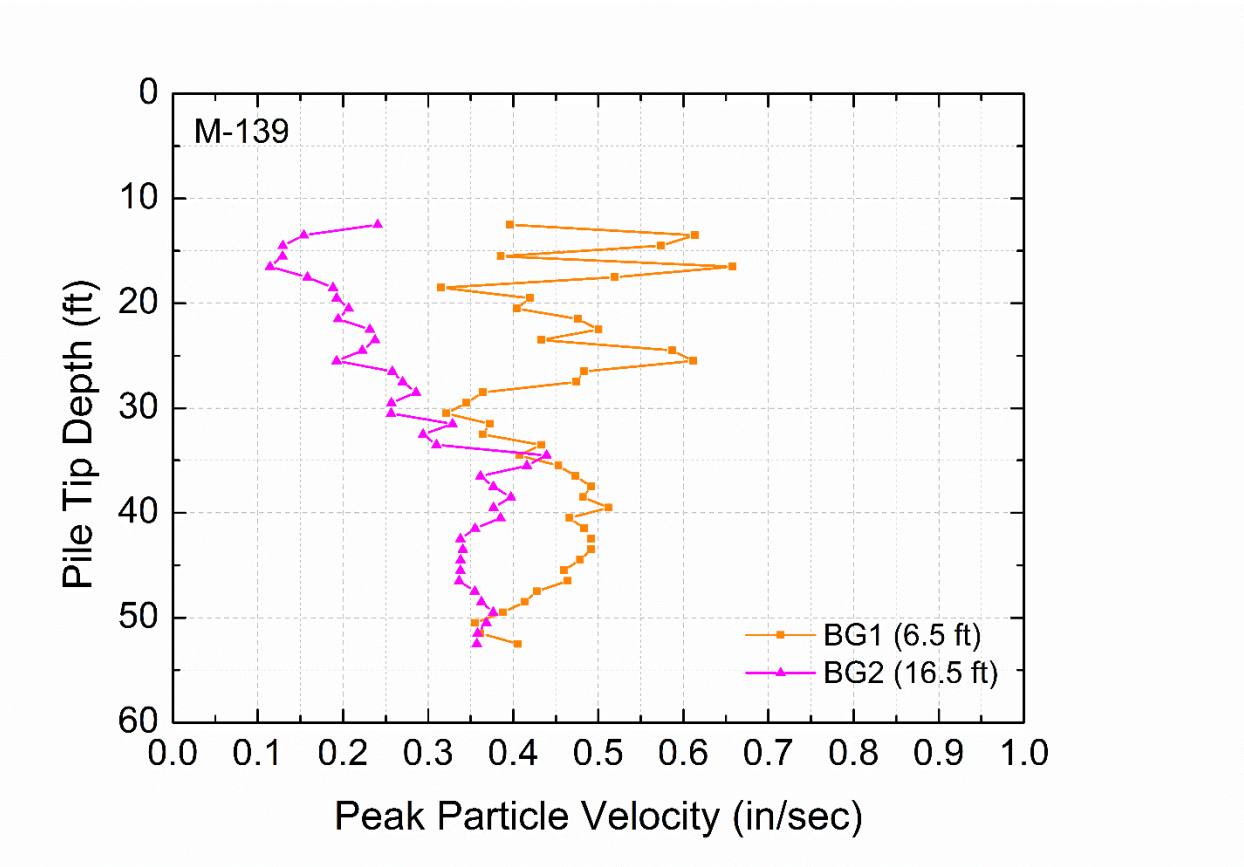

Figure 6-64 Peak Particle Velocity of surface geophones at M-139 site – Transverse Direction

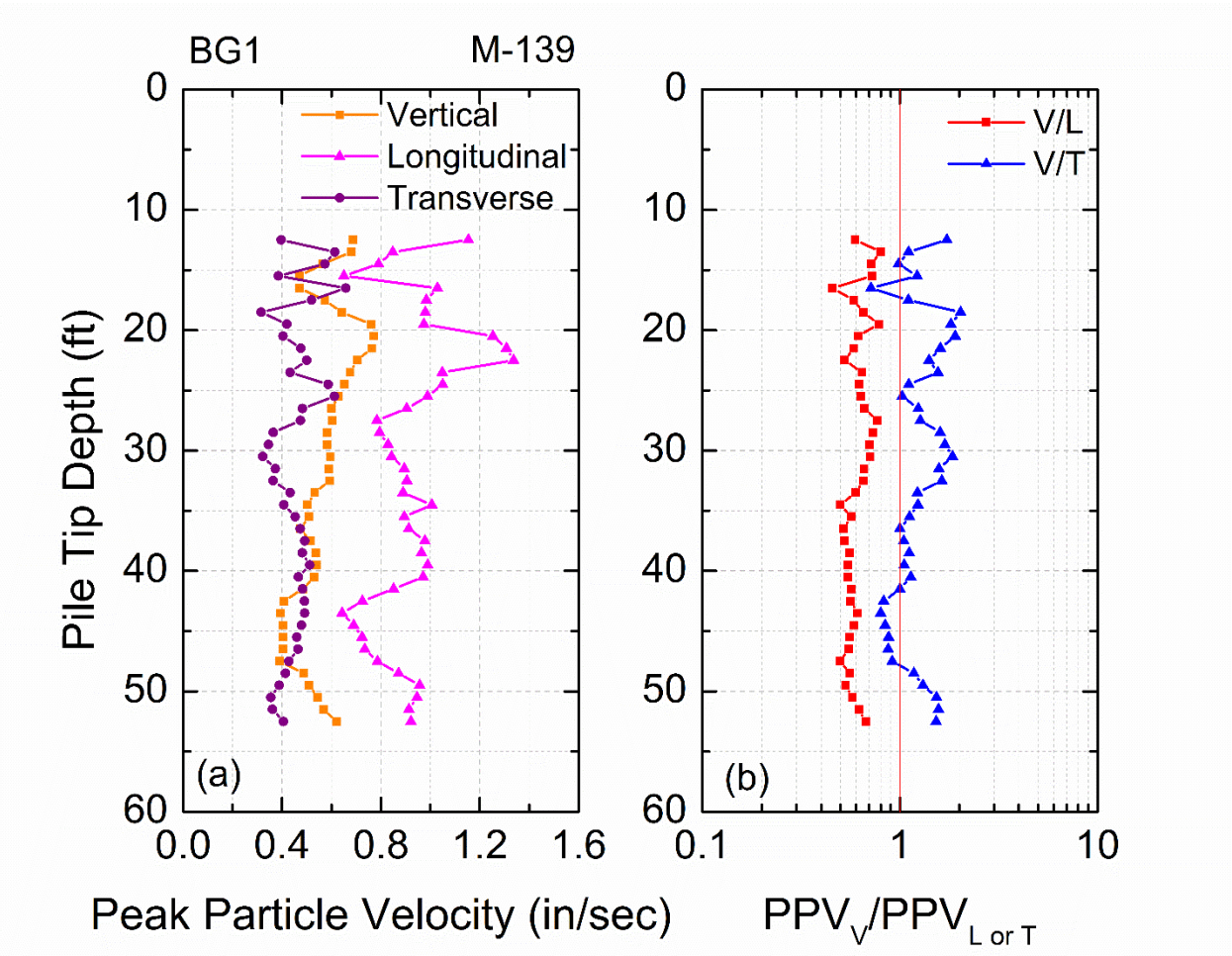

Figure 6-65 (a) Peak Particle Velocities of three directions of sensor BG1 and (b) vertical to longitudinal and vertical to transverse components of PPV – M-139 site

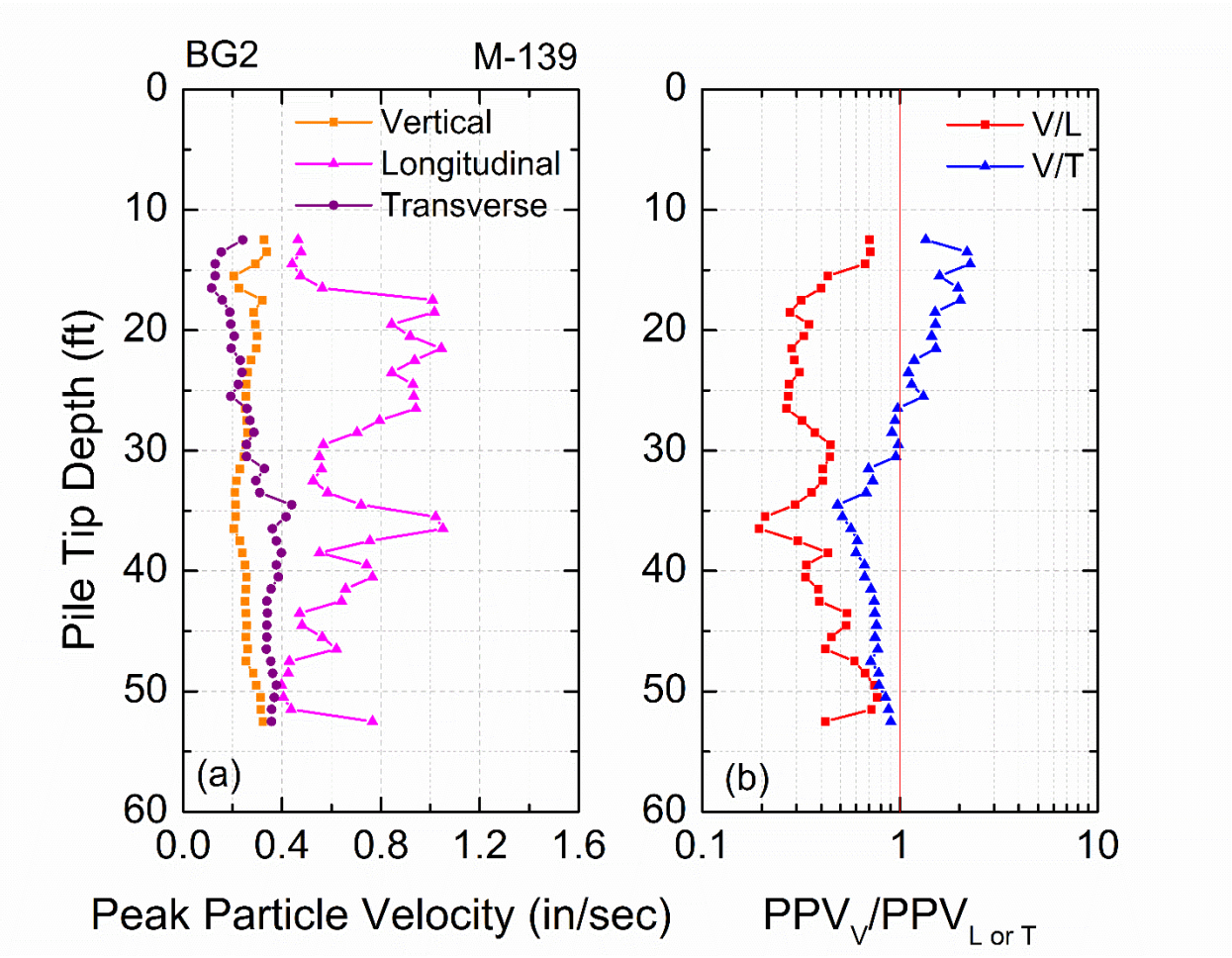

Figure 6-66 (a) Peak Particle Velocities of three directions of sensor BG2 and (b) vertical to longitudinal and vertical to transverse components of PPV – M-139 site

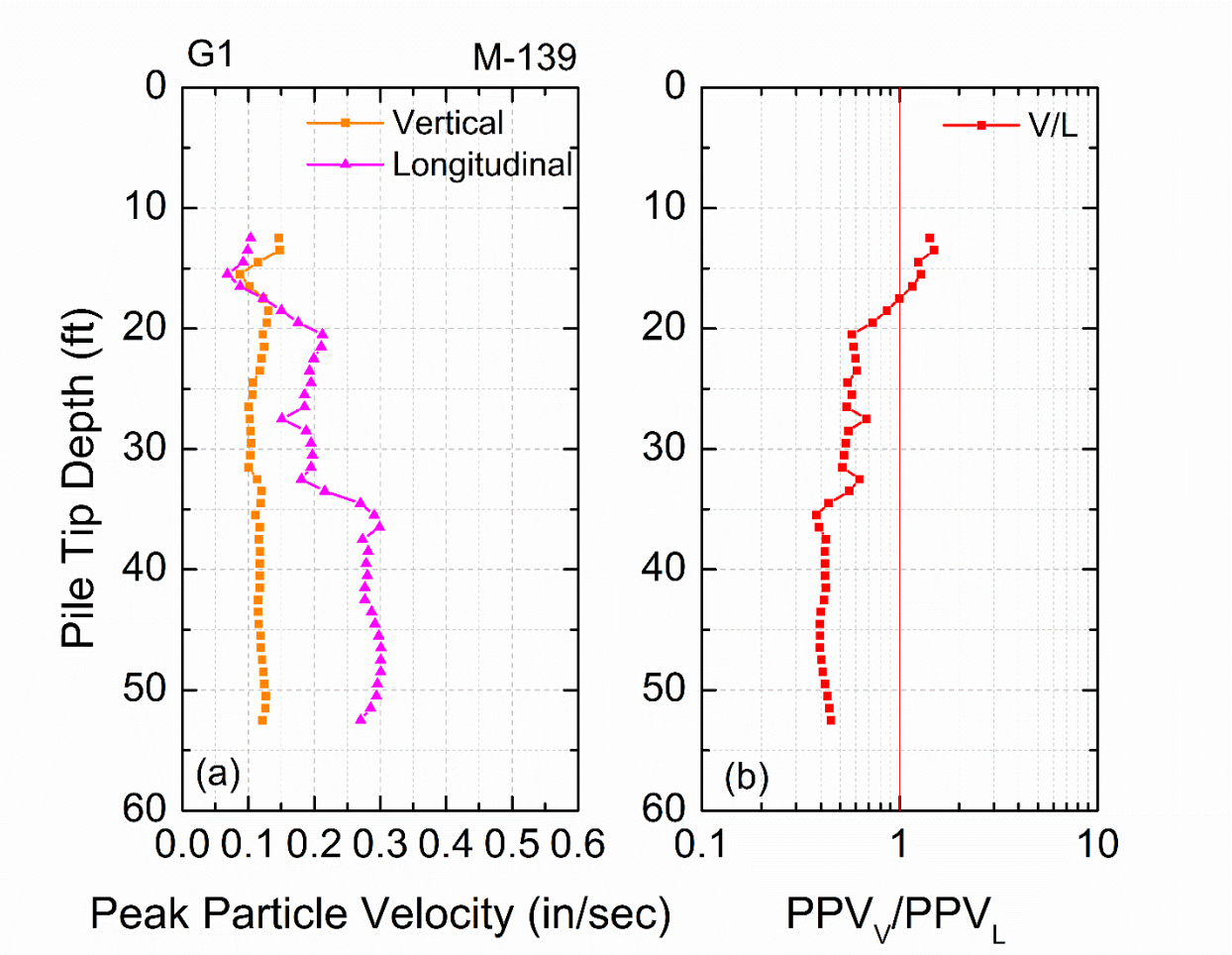

Figure 6-67 (a) Peak Particle Velocities of vertical and longitudinal directions of sensor G1 and (b) vertical to longitudinal components of PPV – M-139 site

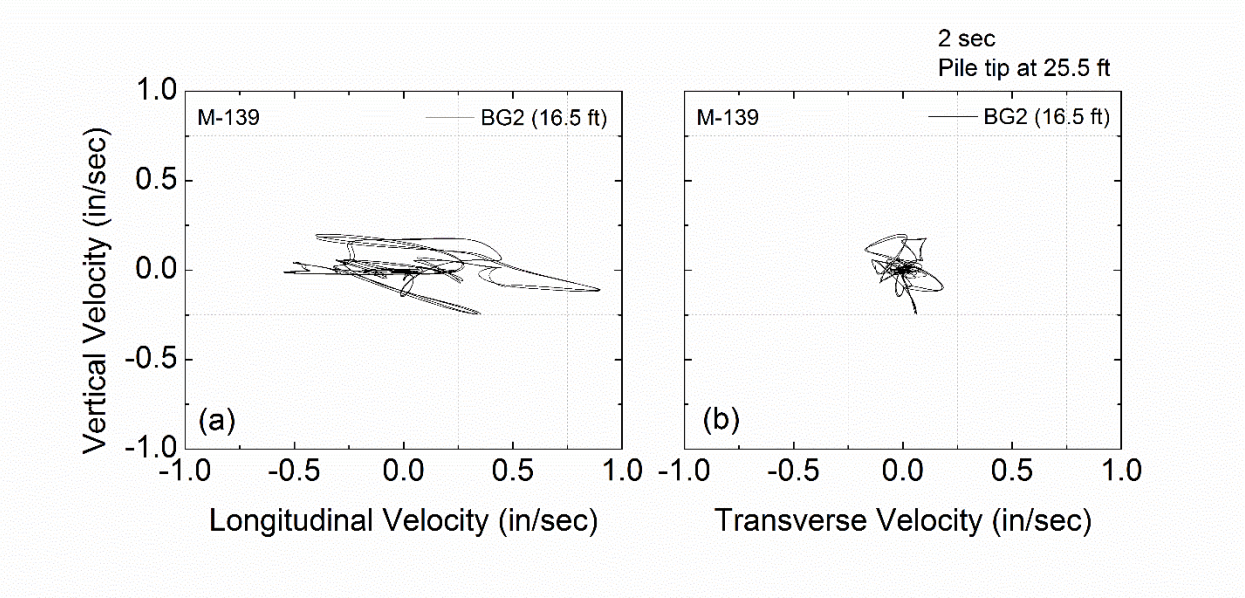

Figure 6-68 Particle motion paths during impact pile driving; 16.5 ft from pile face

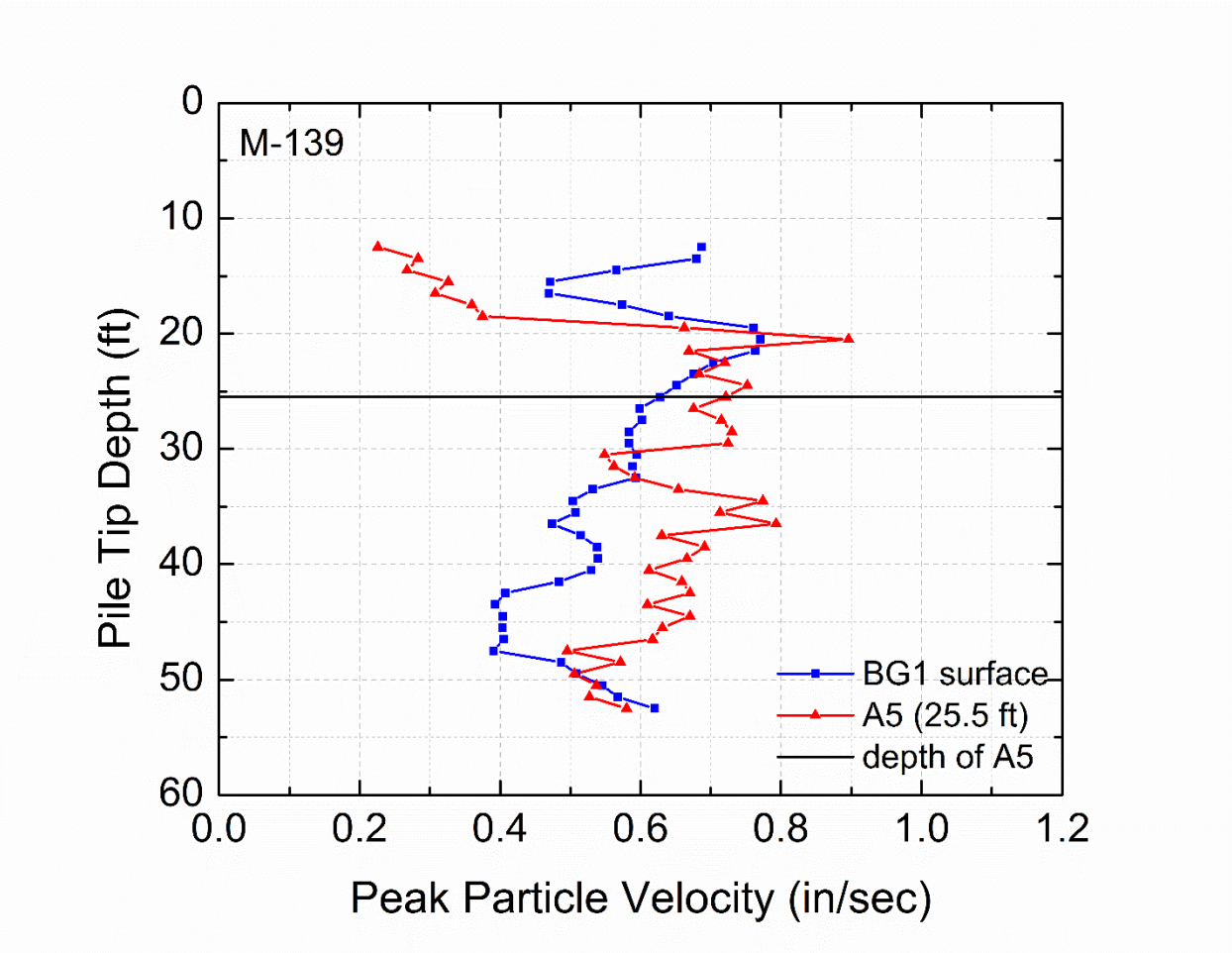

Figure 6-69 Peak particle velocity versus depth of sensors BG1 and A5 at M-139 site – Vertical direction

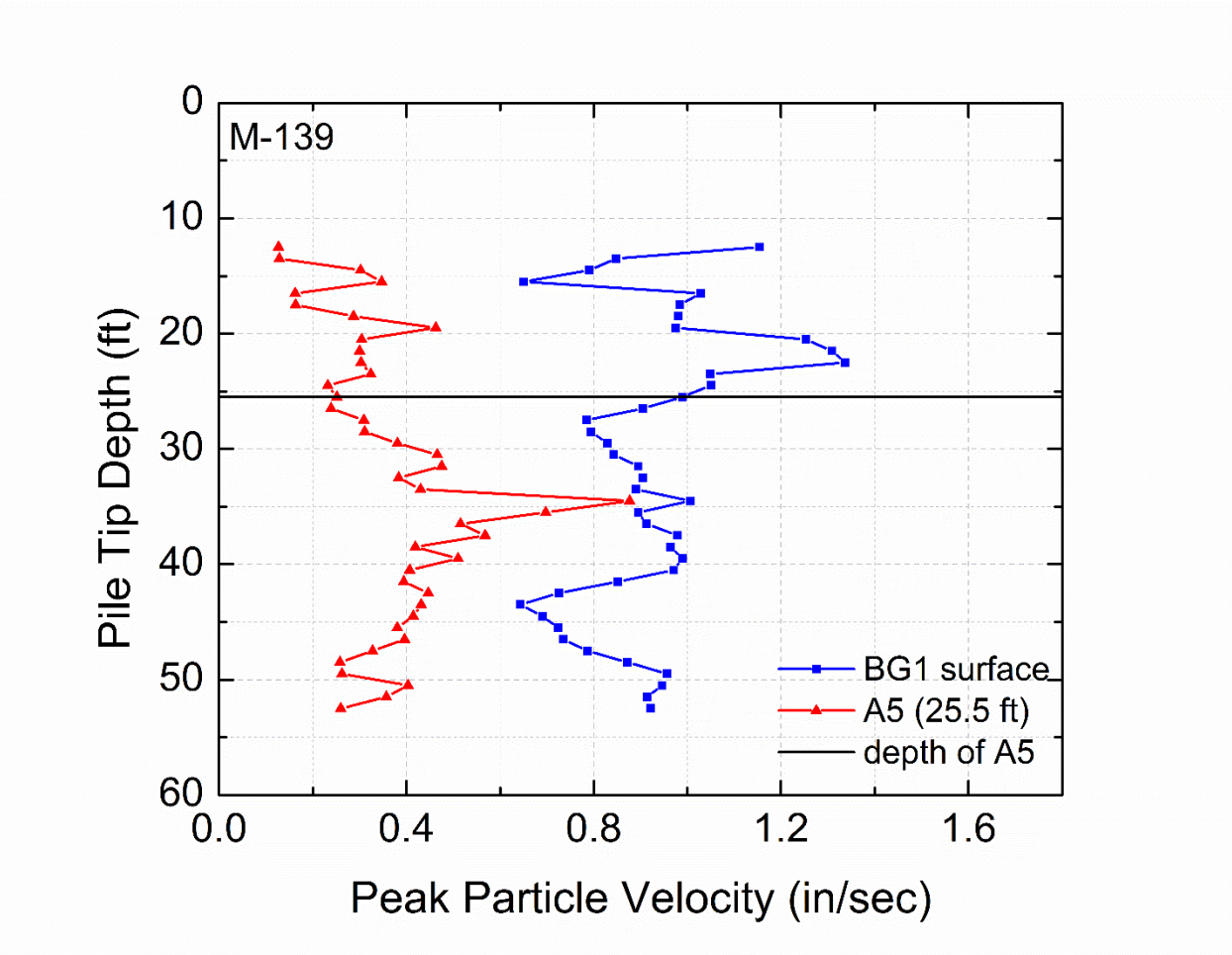

Figure 6-70 Peak particle velocity versus depth of sensors BG1 and A5 at M-139 site – Longitudinal direction

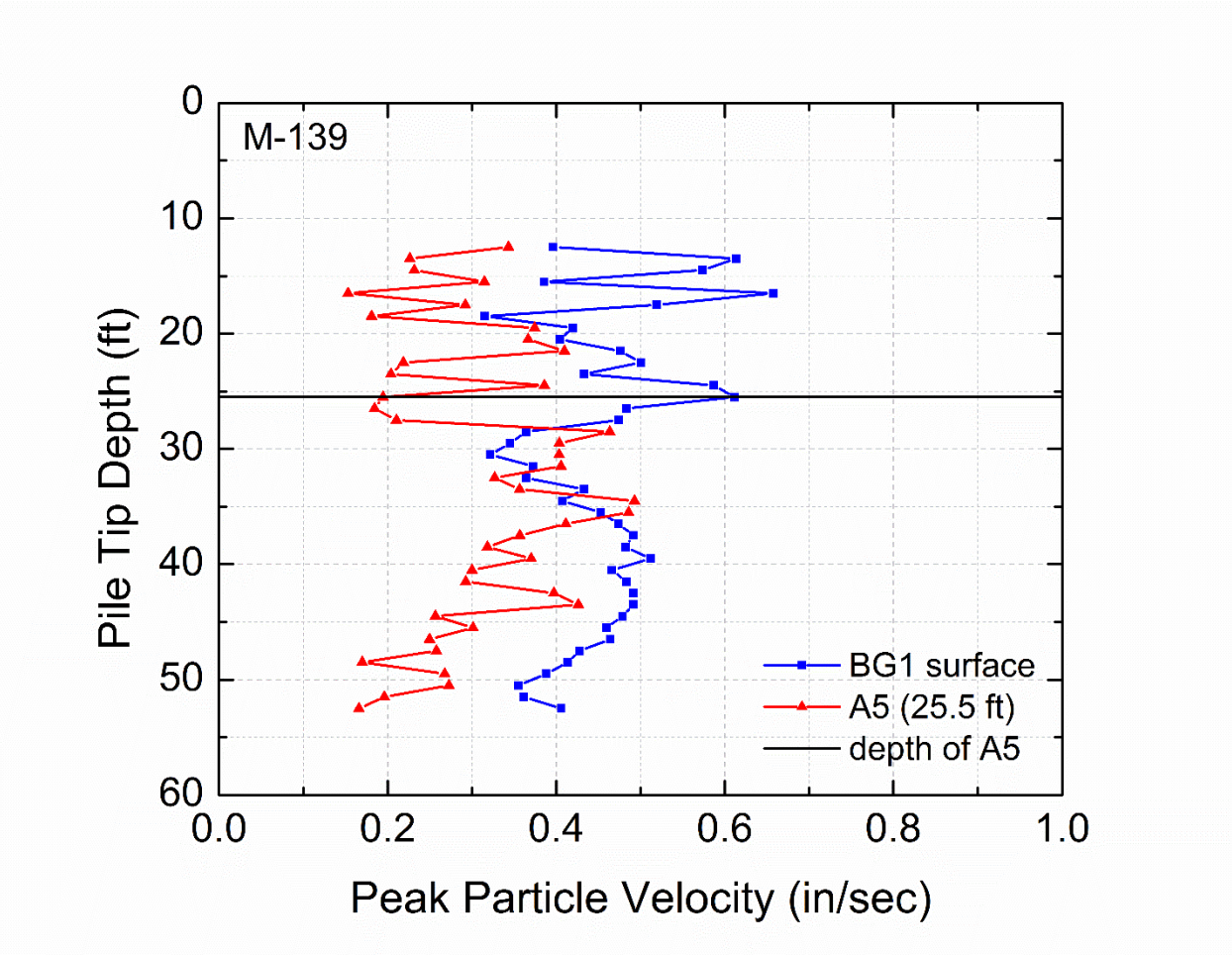

Figure 6-71 Peak particle velocity versus depth of sensors BG1 and A5 at M-139 site – Transverse direction

6.3.2 US-131 A Site

6.3.2.1 Test Pile 1

Ground vibration monitoring was performed during driving two test piles at the abutment A of US-131 site near Constantine, MI. A trench was prepared by the contractor for driving the piles. A perspective view of the in-depth sensor locations close to pile 1 is shown in Figure 6-72. At this site, sensor arrays were pushed to two different elevations; three sensors were installed at a depth of 35.3 ft into a hard sandy clay and four sensors were pushed to shallower depths of 15 ft to 17 ft into a loose to medium sand layer. One accelerometer (A3) and one geophone (SG1) were installed at approximately the same depth and distance from the pile, to confirm that their signals are comparable.

A 55 ft long HP 14x73 pile was driven using a Delmag D30-32 diesel hammer. The final depth of penetration of the pile was 43 ft. Figure 6-73 presents the pile driving penetration resistance as the number of blows per pile foot increment and the accumulated number of blows versus depth of pile tip penetration. The total blow count to drive pile 1 was 457. The driving resistance gradually increased with increasing penetration depth. Figure 6-74 illustrates the average actual hammer energy per pile foot increment and the hammer efficiency, η, versus depth. The rated energy of the Delmag D30-32 hammer is 75,970 lb-ft. The average hammer efficiency when driving pile 1 was around 43%.

Figure 6-75, Figure 6-77 and Figure 6-79 show the acceleration amplitudes of the three components of the shallow set of sensors versus depth of the pile tip, while Figure 6-76, Figure 6-78 and Figure 6-80 present the velocity amplitudes versus depth for the three measured directions, i.e. vertical, longitudinal and transverse. In a similar way, Figure 6-81, Figure 6-83 and Figure 6-85 show the acceleration amplitudes of the three components of the deep set of sensors versus depth of the pile tip, while Figure 6-82, Figure 6-84 and Figure 6-86 present the velocity amplitudes versus depth for the three measured directions. A black solid line indicates the sensors' elevation. Inspection of the data from the two arrays of sensors, reveals a similar vibration pattern as that of M-139 site; amplitudes increase as the pile tip reaches the sensor elevation with the trend being

more pronounced for the closest sensors to the pile (A1 and A2). The highest ground motion amplitudes are observed for the vertical component of the recorded values. Again as seen at M-139 site, a spike in amplitude is observed for all three directions as the pile tip reaches the sensor depth for the closest sensors to the pile (A1 and A2). An increase in amplitude is observed for the shallow set of sensors between 20 ft to 30 ft depths; the pile enters into the hard clay layer at 20 ft and the SPT blow counts increase (Figure 6-27). The peak particle velocities of sensors A3 and SG1, that were strategically pushed to approximately the same depth and same distance from the pile, showed similar response; the A3 sensor had a more scattered response due to noise in the signal and the integration processing that was required to convert acceleration amplitudes to velocities. The amplitudes of the longitudinal and transverse directions are not plotted for A3 sensor because of the noisy signal that was acquired.

Figure 6-87 to Figure 6-89 present the diagonal distance from pile tip to sensor location versus the ground motions for the set of the shallow sensors into the sand layer, for the three monitored directions. There are not many data points monitored when the pile tip was still above the sensors' elevation, however the responses after the pile reached the depth of the sensors is typical with those observed at M-139 site. Ground motions first increase, and then start to decay as the pile tip goes deeper than the sensors' elevation. Higher decrease rates are observed for the case of the longitudinal motions.

For the deeper set of sensors, the difference in vibration pattern when the pile tip is above and below the sensors' depth is more pronounced. Figure 6-90 and Figure 6-91 present vertical peak particle velocities versus diagonal distance, for the two closest sensors to the pile, A2 and A4, respectively. The amplitude increases smoothly to the level where the pile tip is at the same elevation as the sensors. The vibration levels after the tip passes the elevation of the sensors stays relative constant, suggesting that the pile tip which is getting further from the sensor contributes less and less to the vibration than the shaft. This behavior is again more evident for the closest sensor to the pile (A2), while for sensor A4 the amplitudes start to decrease close to the end of driving. Similar plots for the longitudinal and transverse motions are shown in Figure 6-92 and Figure

6-93, respectively. The same trend in amplitudes is observed for the two horizontal directions, as the pile tip approaches and departs from the elevation of the sensors.

A comparison of the three component response of the accelerometers for the three measured directions for each of the buried sensors is shown in Figure 6-94a to Figure 6-97a. The black dashed line indicates the sensors' depth. The vertical components generally showed higher ground motion amplitudes compared to the longitudinal and transverse directions. The transverse component values were found to be higher than the longitudinal values; this pattern was also observed at the M-139 site.

Figure 6-94b to Figure 6-97b show the vertical to longitudinal (V/L) and vertical to transverse (V/T) components of acceleration. For shallow sensor A1, nearest to the pile face, Figure 6-94b, the vertical component of motion is greater than either the longitudinal or transverse components except for one depth, 17 ft, i.e. ratios greater than one. The deep sensor A2, closest to the pile, has greater motions for the vertical component than the horizontal directions after the pile tip passes approximately a depth of 20 ft (Figure 6-96b). The furthest sensors from the pile, A5 and A4, revealed more depths that both the longitudinal and transverse components are greater than the vertical component, i.e. ratios (V/L) and (V/T) less than one.

Twelve ground surface geophones were also placed along the ground surface at the locations shown in Figure 6-98. The two closest geophones (BG1 and BG2) were triaxial configurations, while geophones G1 to G3 had single components of vertical, longitudinal and transverse axes and the further out (G4) was single vertical component geophone. Vertical peak particle velocity versus depth is shown for all the sensors in Figure 6-99. There is an increase in velocity amplitudes when the pile tip enters the dense sand at around 25 ft (Figure 6-27). Figure 6-100 and Figure 6-101 present the particle velocities for the longitudinal and transverse directions of these same surface sensors except G4 that did not have a longitudinal and transverse component transducer. An increase in amplitudes around 25 ft is also observed for the horizontal directions, while the transverse component of the closest sensor to the pile (BG1) showed an increase in particle velocities at around 38 ft depth.

Figure 6-102a to Figure 6-106a show the three velocity components versus depth and Figure 6-102b to Figure 6-106b show the ratios of vertical to longitudinal (V/L) and vertical to transverse (V/T) components for sensors BG1, BG2, G1, G2 and G3, respectively. As observed on the surface ground motions at M-139 site, the longitudinal directions recorded higher peak particle velocities. The red vertical line at the ratio value of 1 in Figure 6-102b to Figure 6-106b is the boundary below which vertical components of motion are smaller than either or both of the horizontal components of motion indicating that the wave motion at these sensors is not classical Rayleigh Wave form. It is interesting to notice that for the two furthest sensors from the pile, G2 and G3, the vertical components of motion are lower than the longitudinal and transverse components for almost the entire depth range of pile penetration. For the three closest geophones to the pile, the vertical components of motion are smaller than the longitudinal components, also for the entire depth range. This behavior indicates that these sensors did not record a classical Rayleigh wave.

Three sensors were located at the same radial distance from the pile (6.5 ft); BG1 geophone was positioned on the surface, A5 accelerometer was installed 15 ft into a medium dense sand layer and SG2 geophone was installed 35.3 ft into a hard clay deposit. Sensors BG1 and A5 recorded similar vibration amplitudes, while the deeper sensor, SG2, had lower peak particle velocities as shown in Figure 6-107. Interestingly, the surface geophone BG1 monitored much higher longitudinal ground motions than the accelerometer A5 (Figure 6-108). Finally, the transverse component responses of BG1 and A5 sensors are similar, except for a range of depths between 25 ft and 35 ft, where the accelerometer A5 captured higher vibrations (Figure 6-109). It should be noted that a hard clay layer extends from around 20 ft to 37 ft. Thus, higher amplitudes are expected to be recorded by the sensor that is buried to the ground when the pile tip reaches that clay layer. However, this behavior is not observed for the corresponding longitudinal motions, making the surface responses more complicated and harder to interpret.

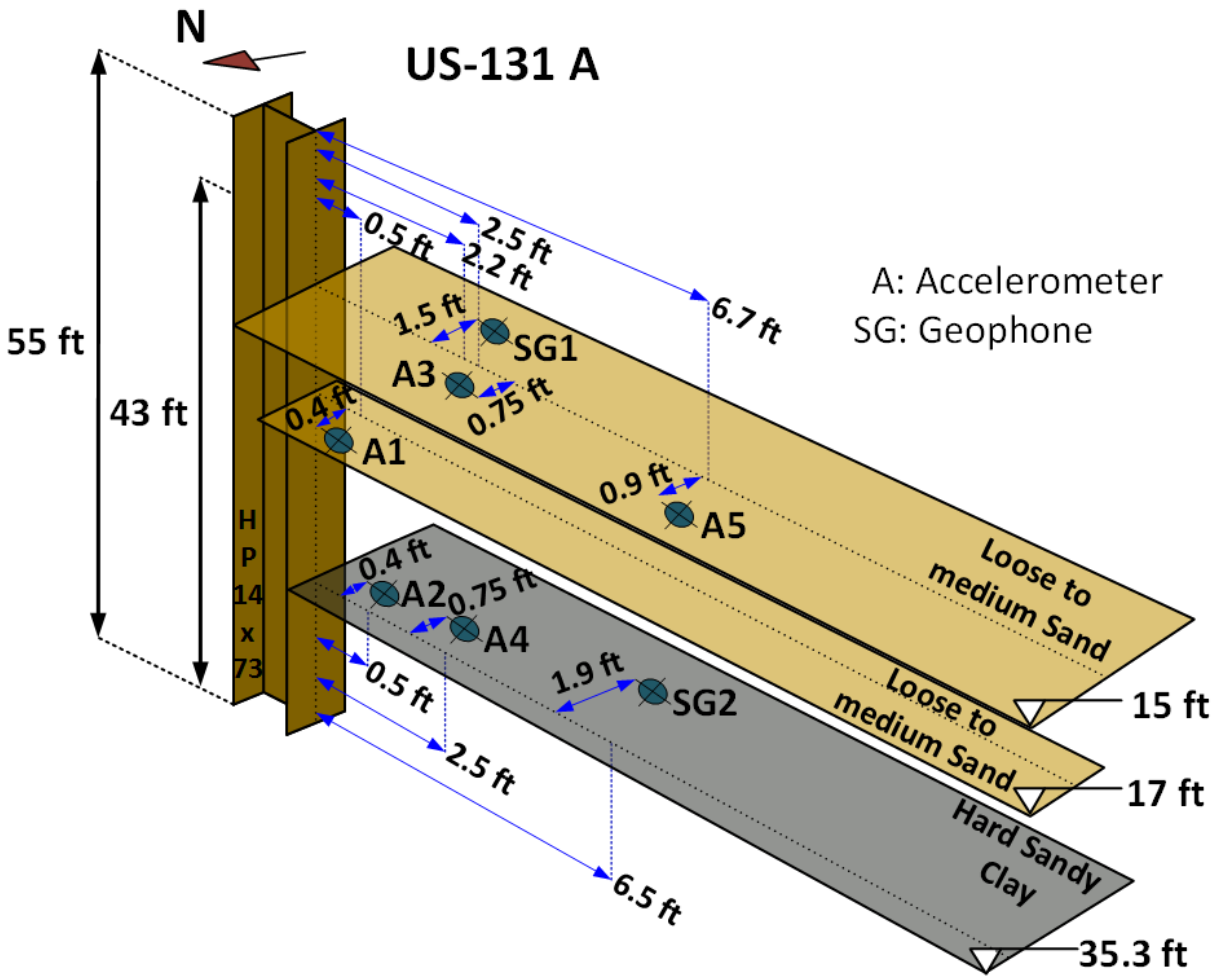

Figure 6-72 Perspective view of buried sensors at US-131 A site, Pile 1 (not to scale)

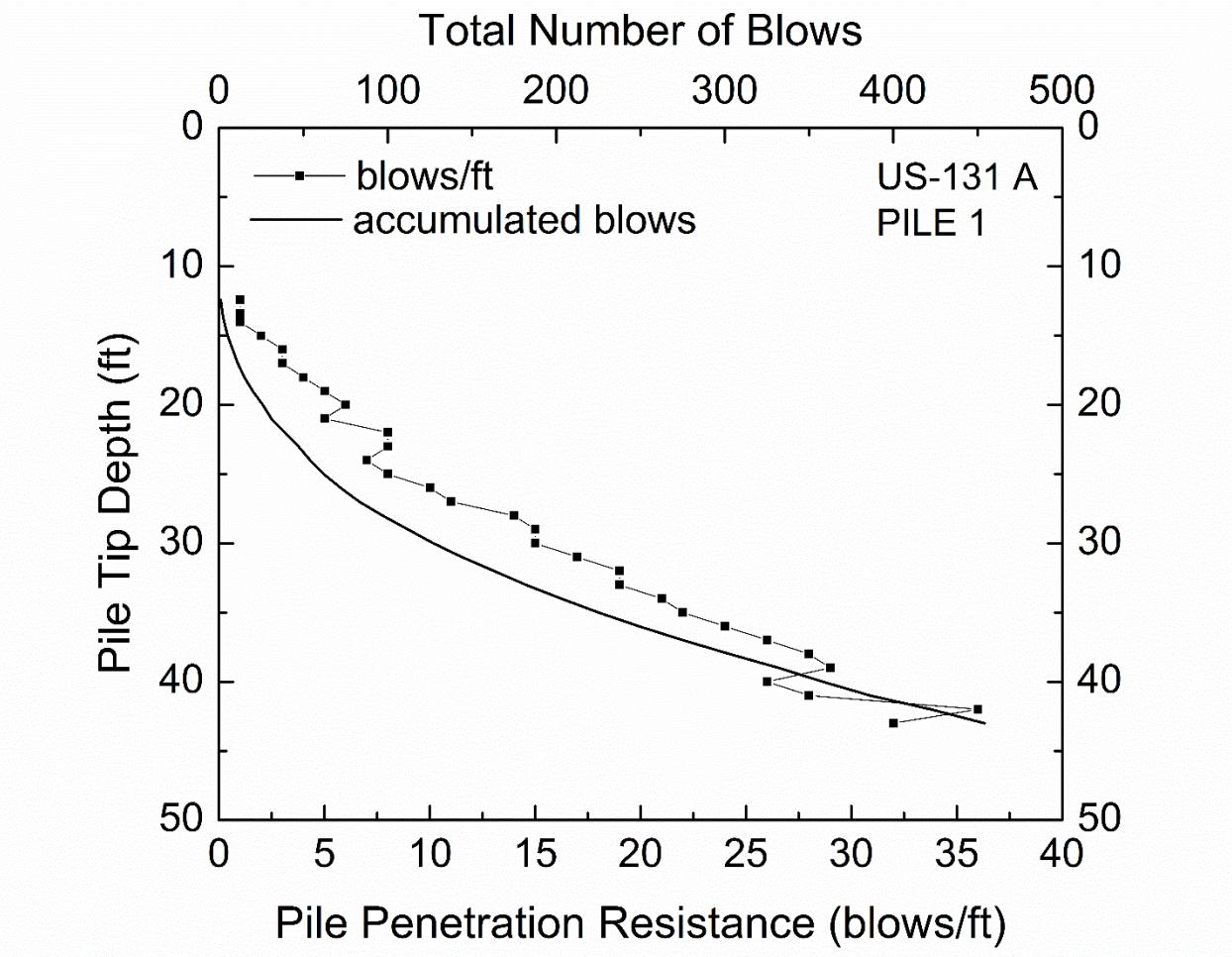

Figure 6-73 Driving Resistance and accumulated blows with depth – US-131 A site, Pile 1

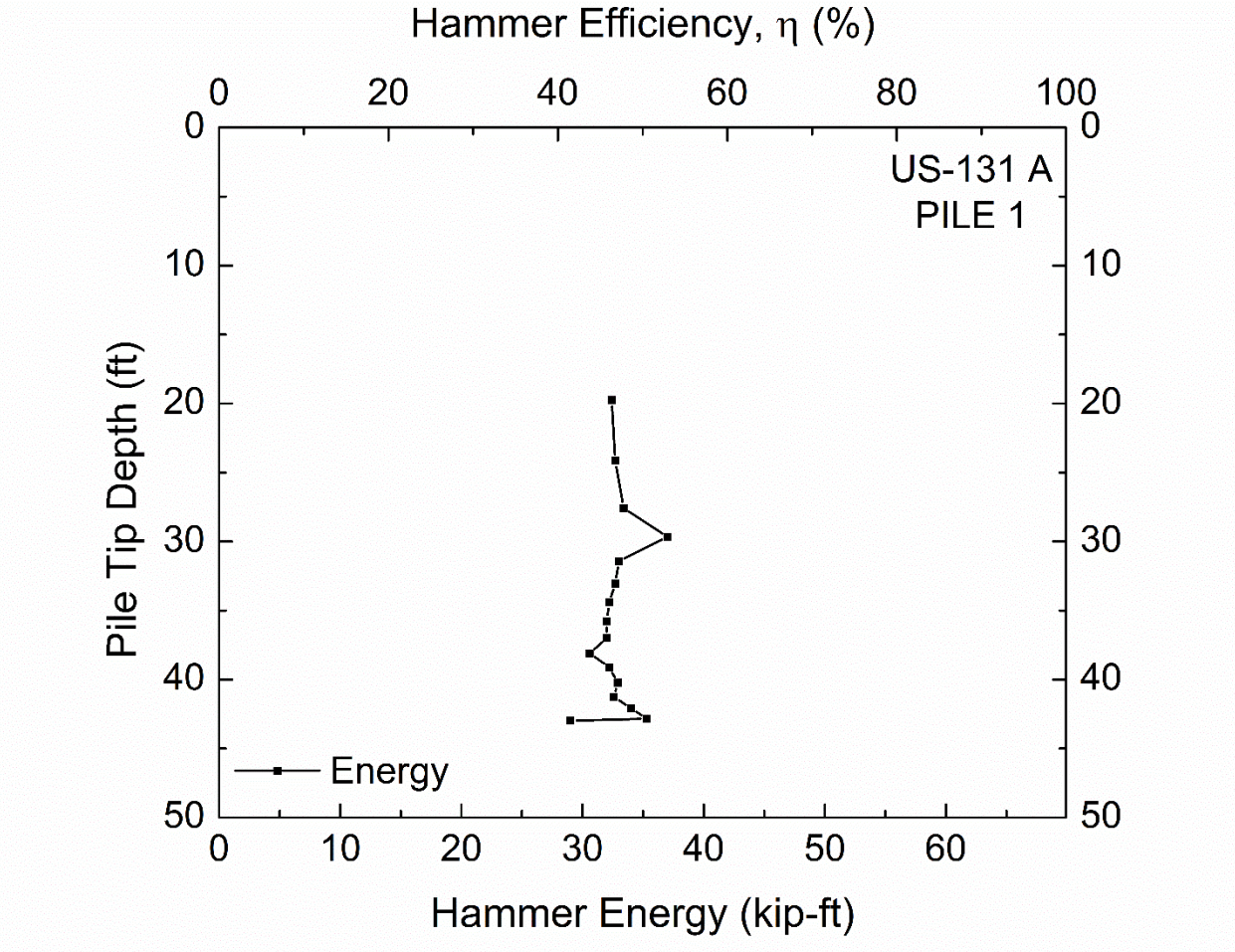

Figure 6-74 Hammer Energy and Hammer Efficiency with depth – US-131 A site, Pile 1

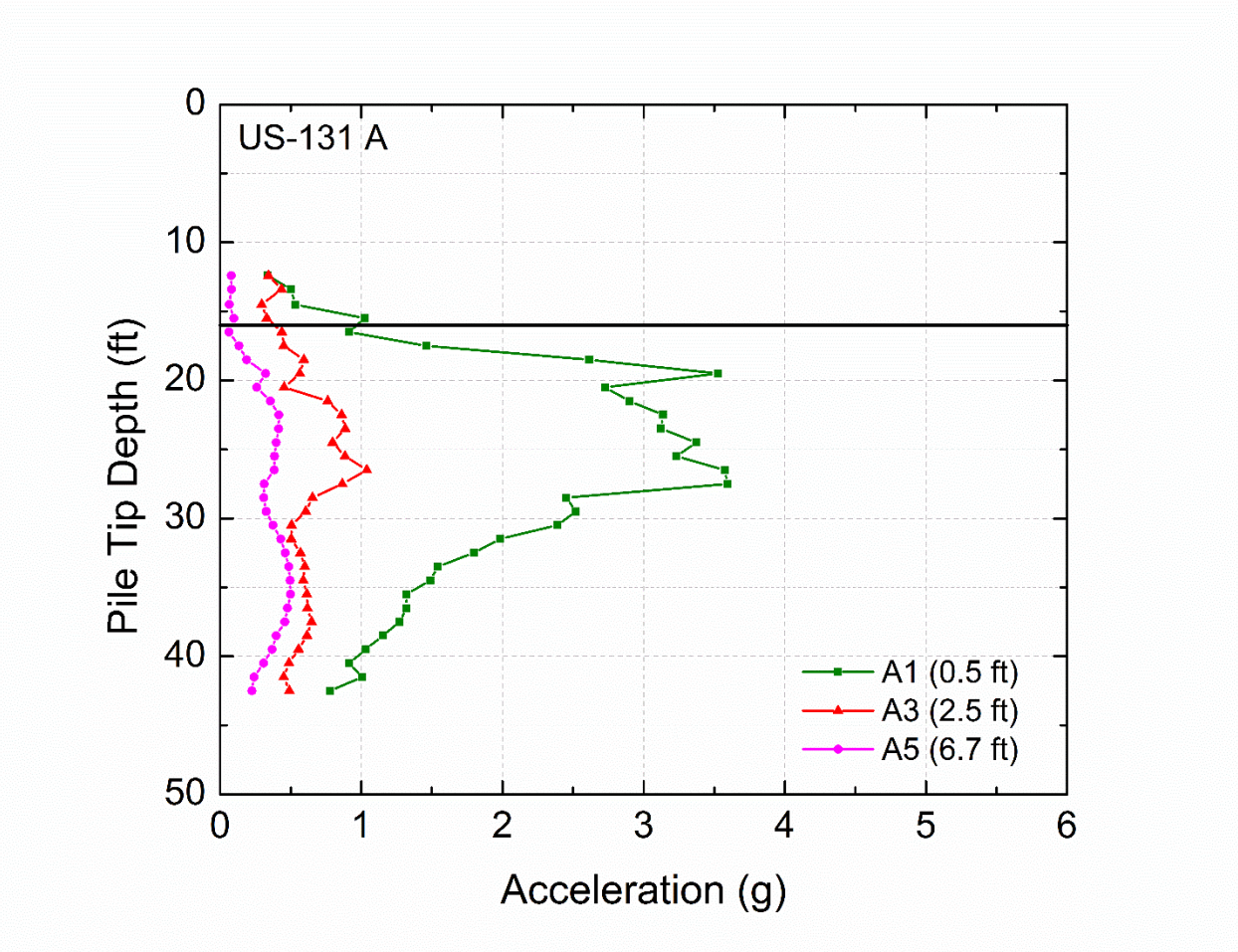

Figure 6-75 Acceleration of shallow set of buried sensors at US-131 A site – Pile 1, Vertical Direction

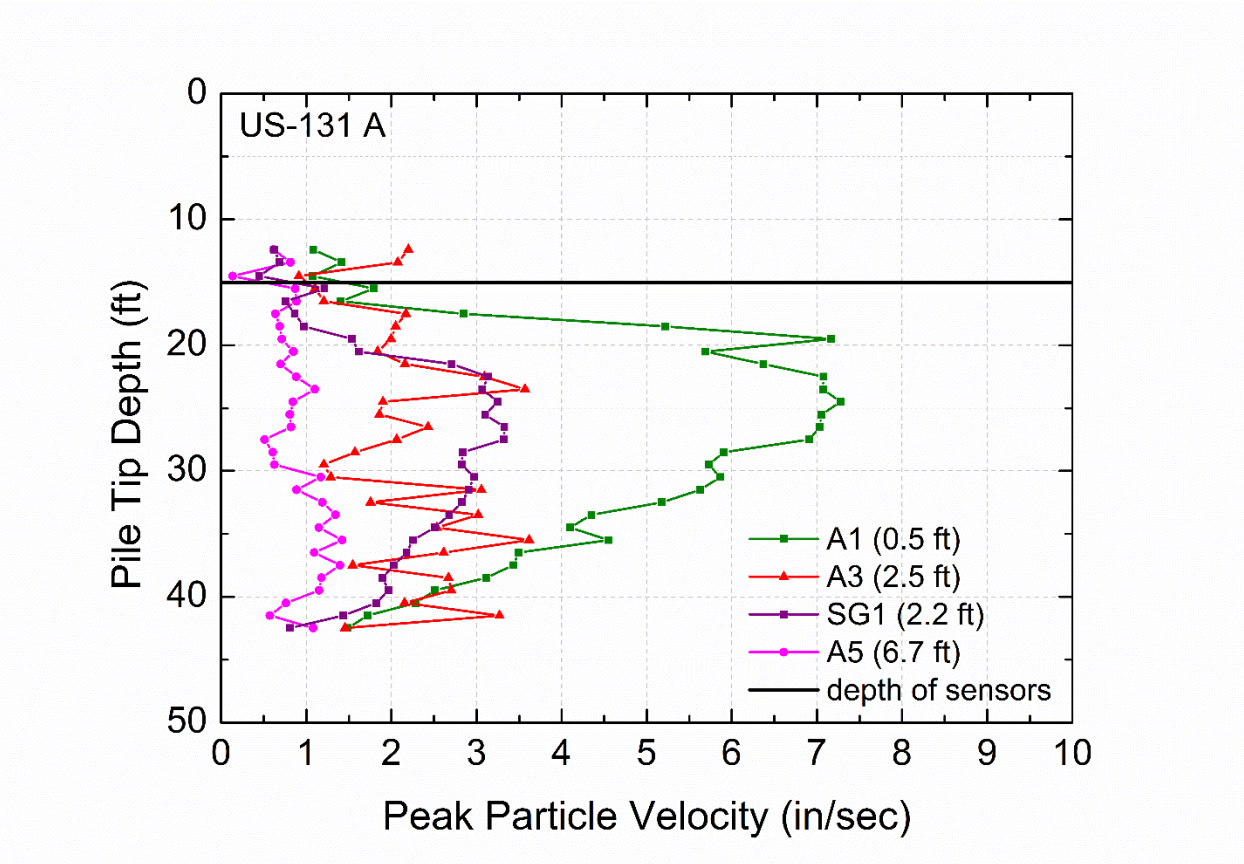

Figure 6-76 Peak Particle Velocity of shallow set of buried sensors at US-131 A site – Pile 1, Vertical Direction

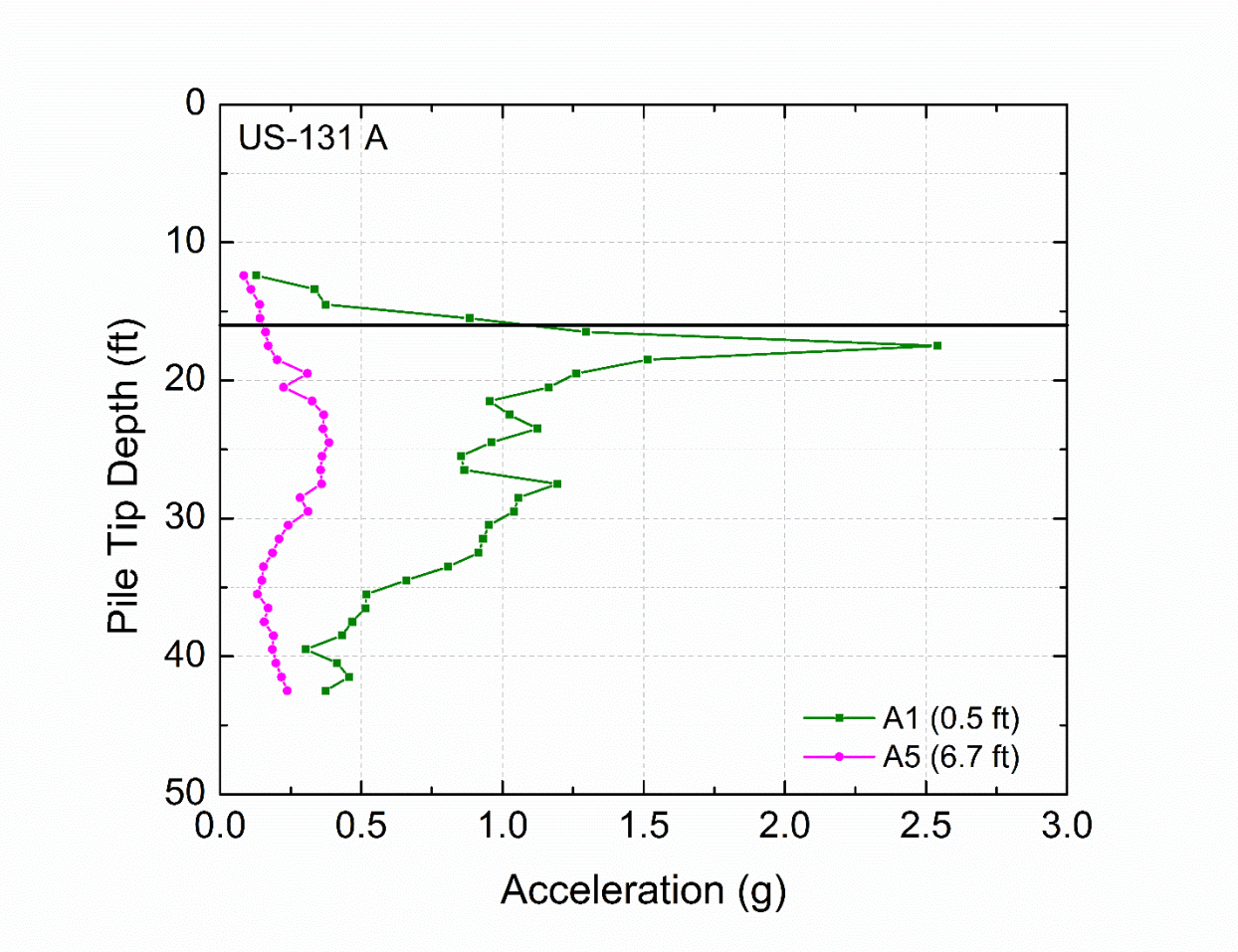

Figure 6-77 Acceleration of shallow set of buried sensors at US-131 A site – Pile 1, Longitudinal Direction

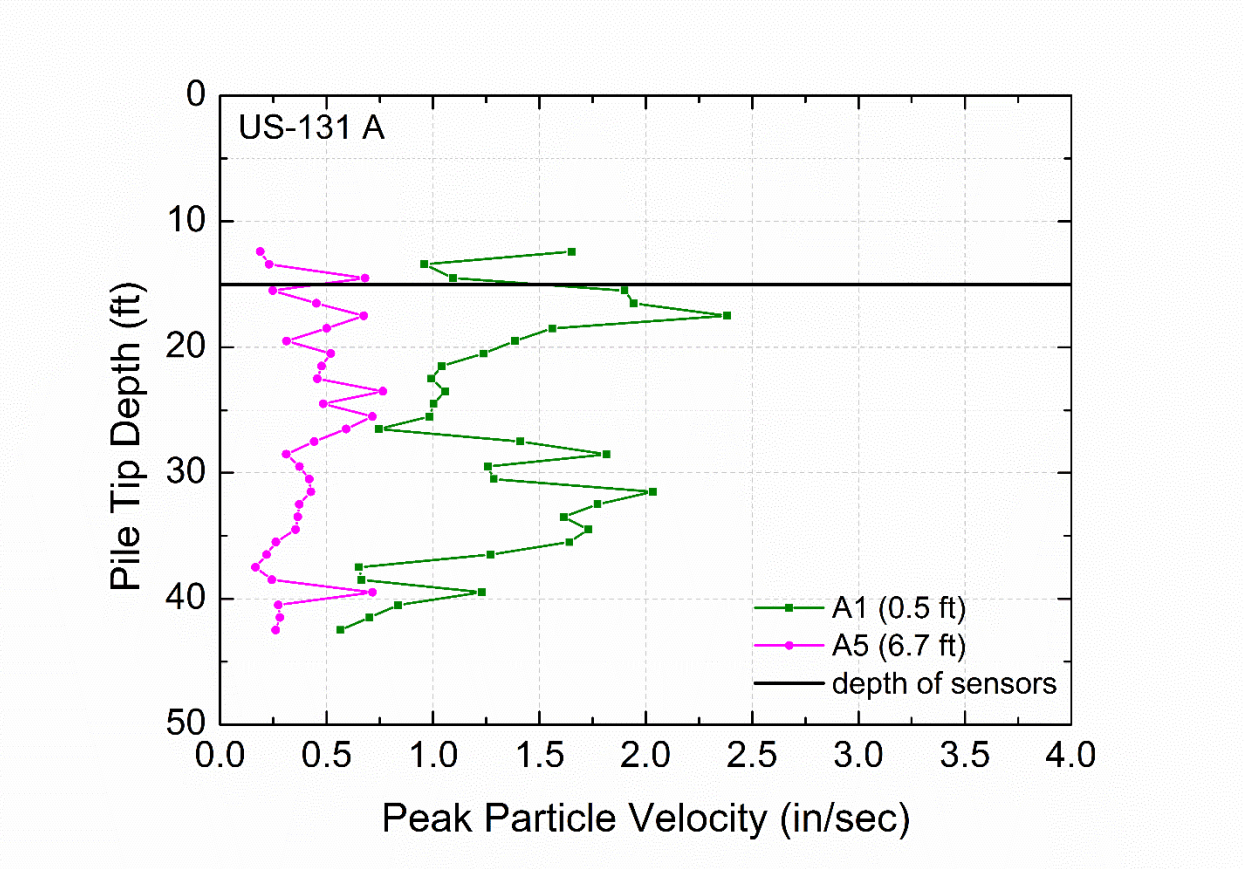

Figure 6-78 Peak Particle Velocity of shallow set of buried sensors at US-131 A site – Pile 1, Longitudinal Direction

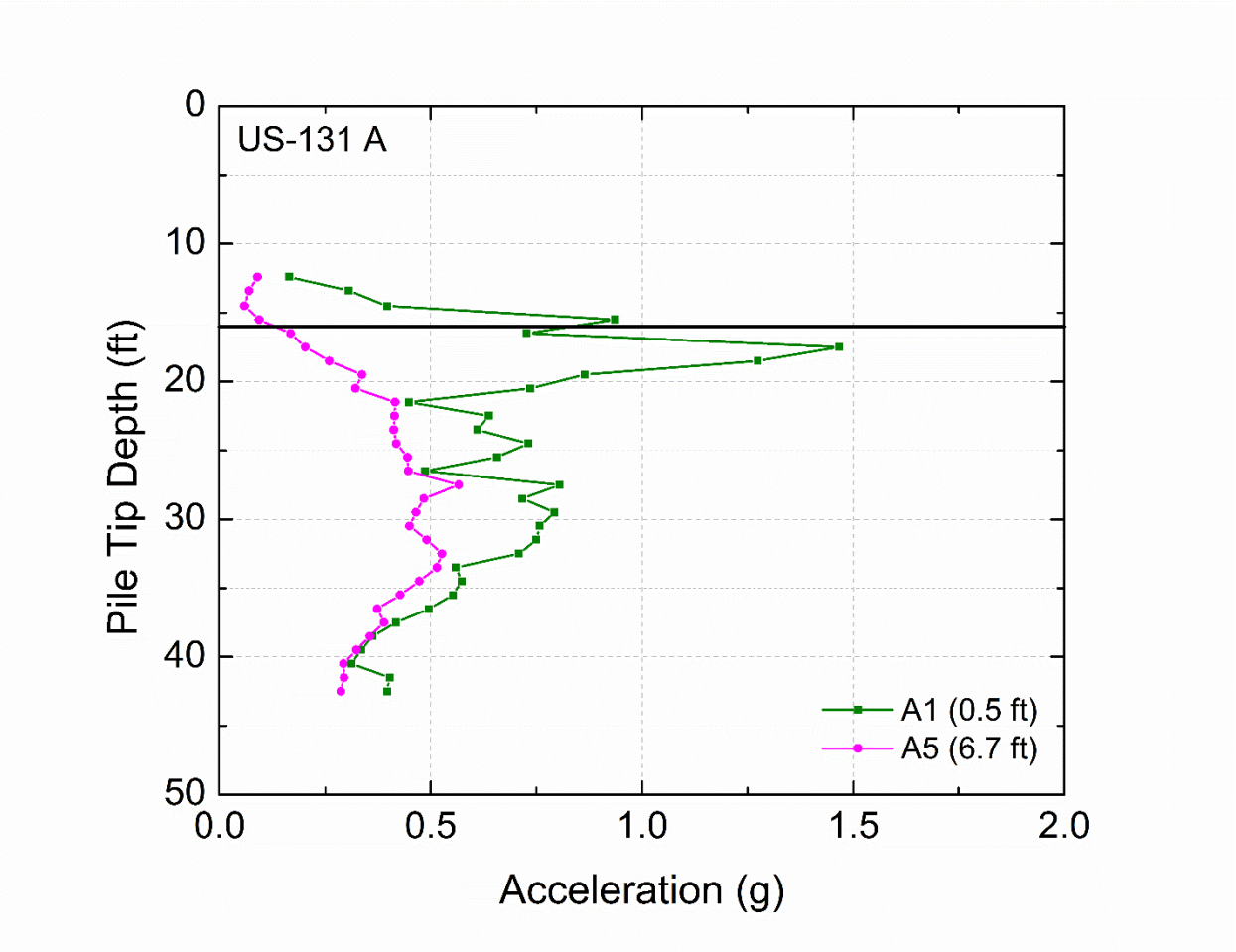

Figure 6-79 Acceleration of shallow set of buried sensors at US-131 A site – Pile 1, Transverse Direction

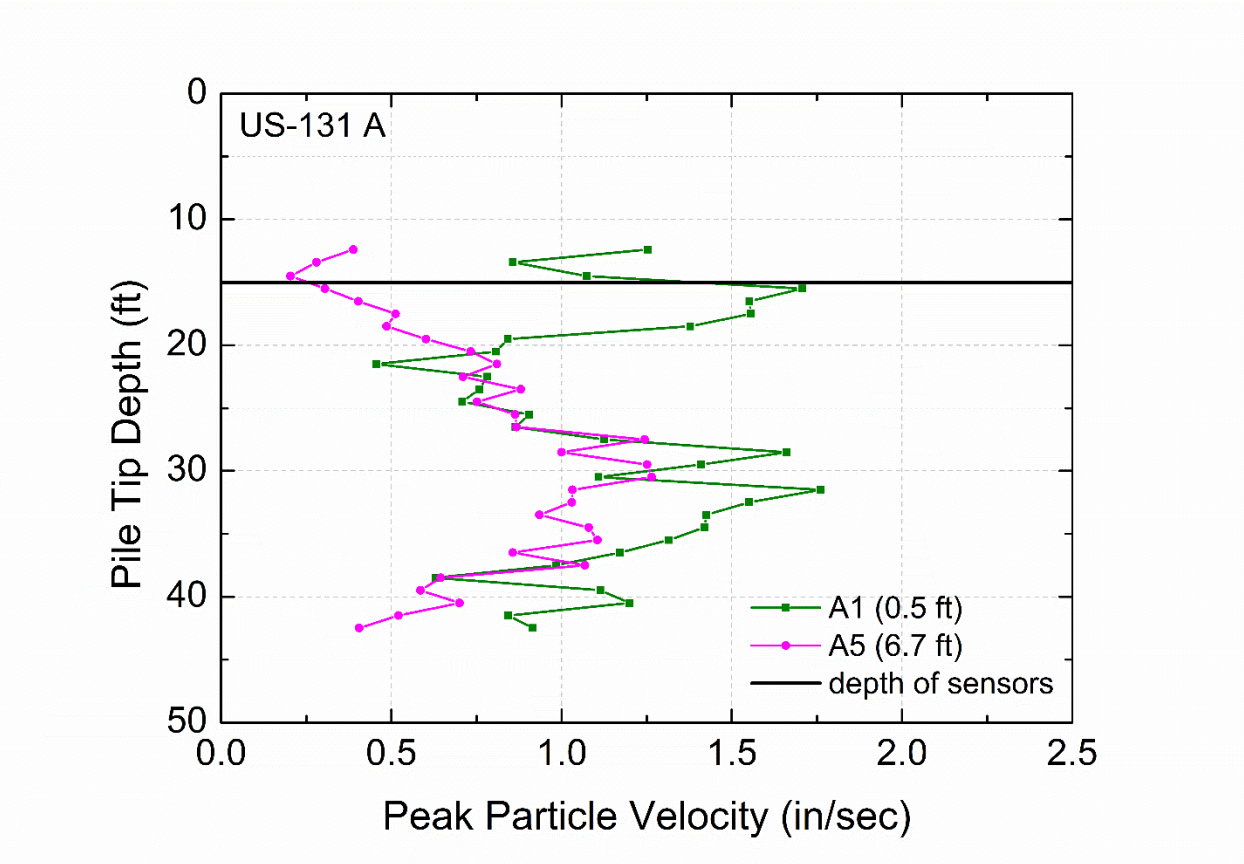

Figure 6-80 Peak Particle Velocity of shallow set of buried sensors at US-131 A site – Pile 1, Transverse Direction

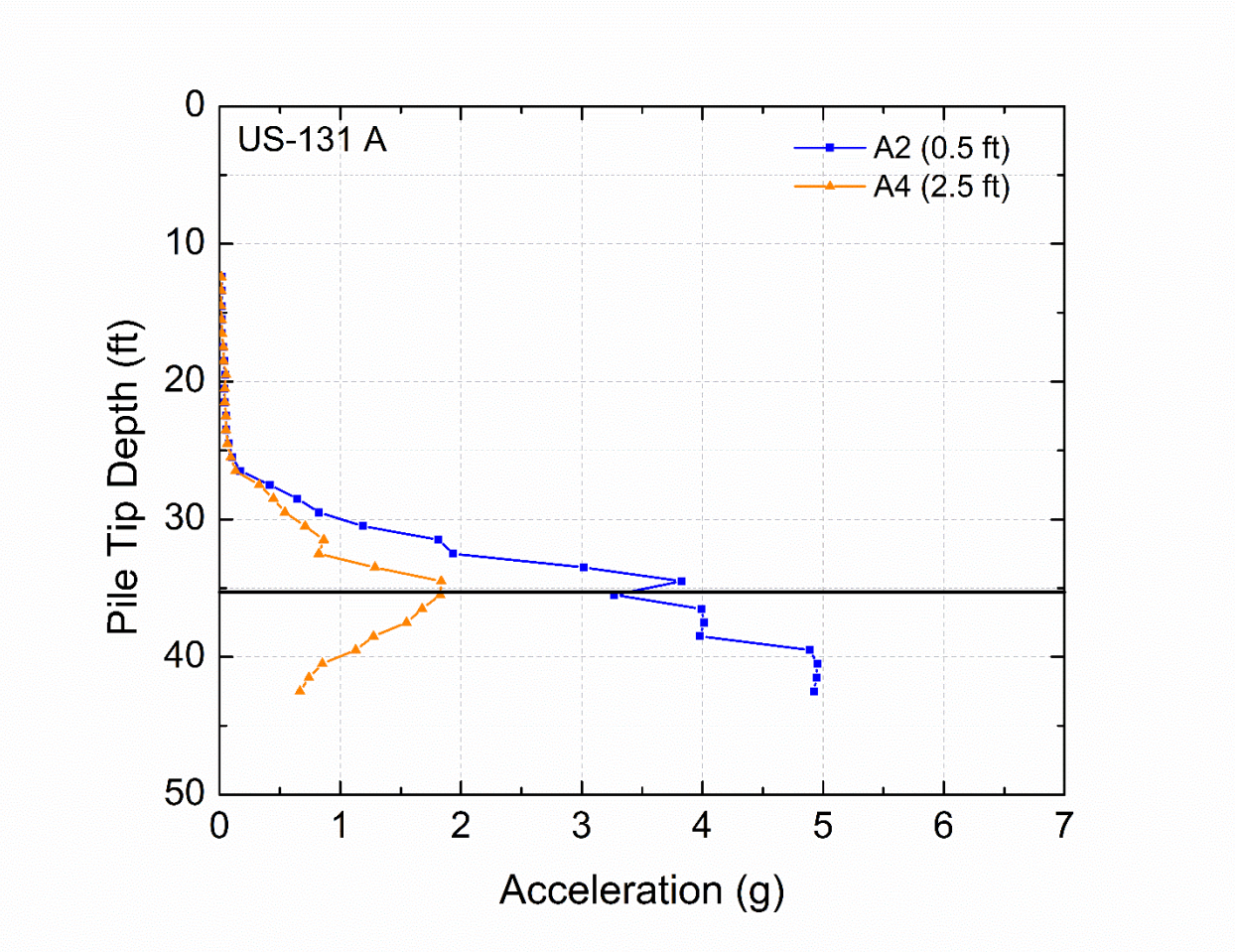

Figure 6-81 Acceleration of deep set of buried sensors at US-131 A site – Pile 1, Vertical Direction

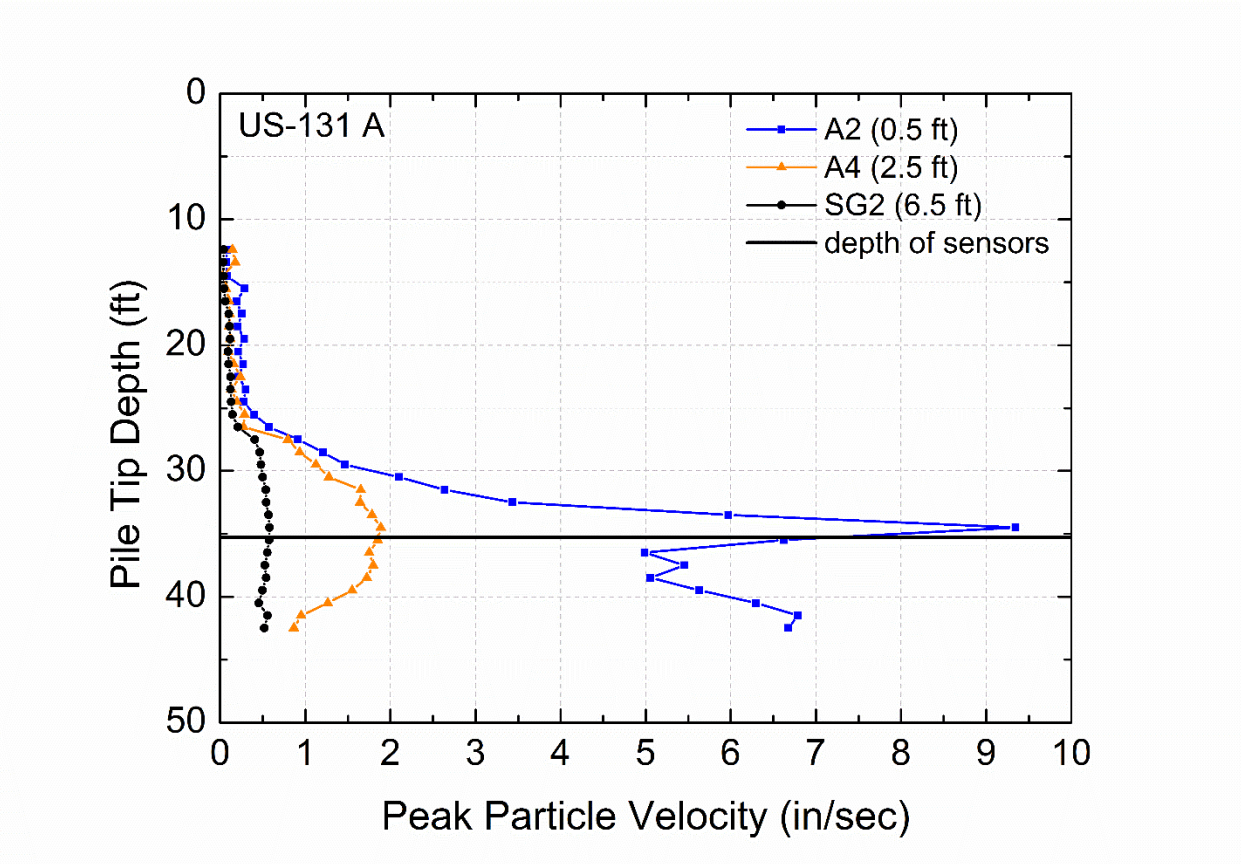

Figure 6-82 Peak Particle Velocity of deep set of buried sensors at US-131 A site – Pile 1, Vertical Direction

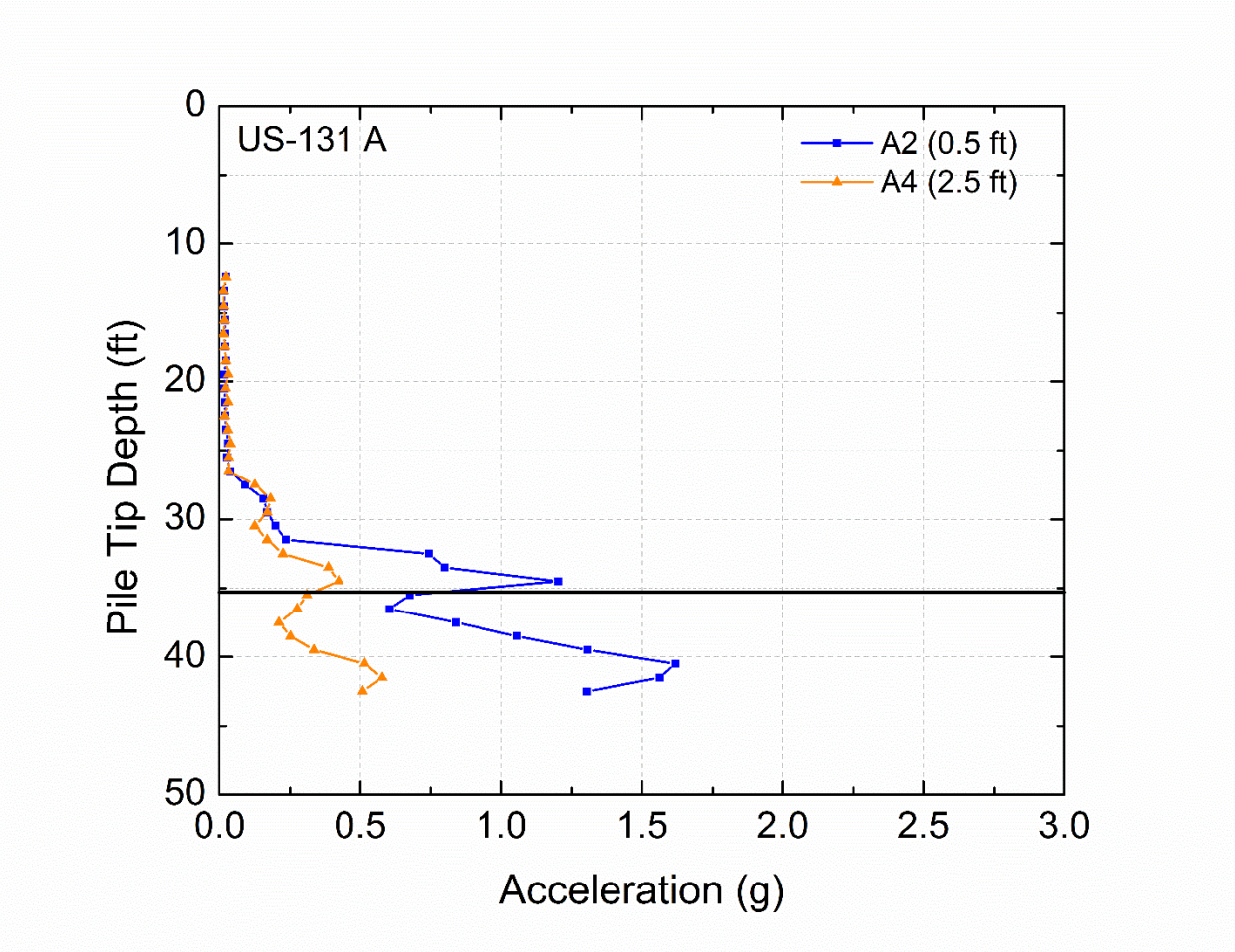

Figure 6-83 Acceleration of deep set of buried sensors at US-131 A site – Pile 1, Longitudinal Direction

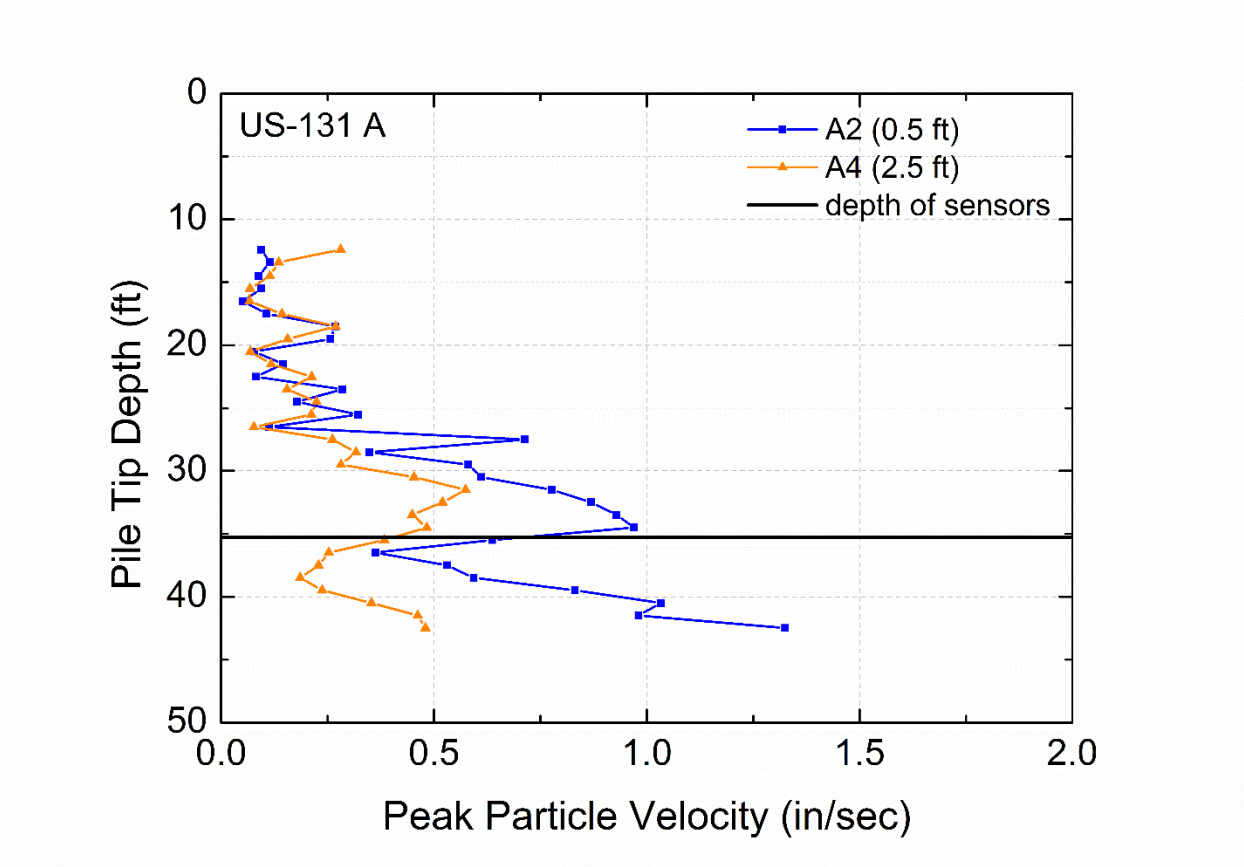

Figure 6-84 Peak Particle Velocity of deep set of buried sensors at US-131 A site – Pile 1, Longitudinal Direction

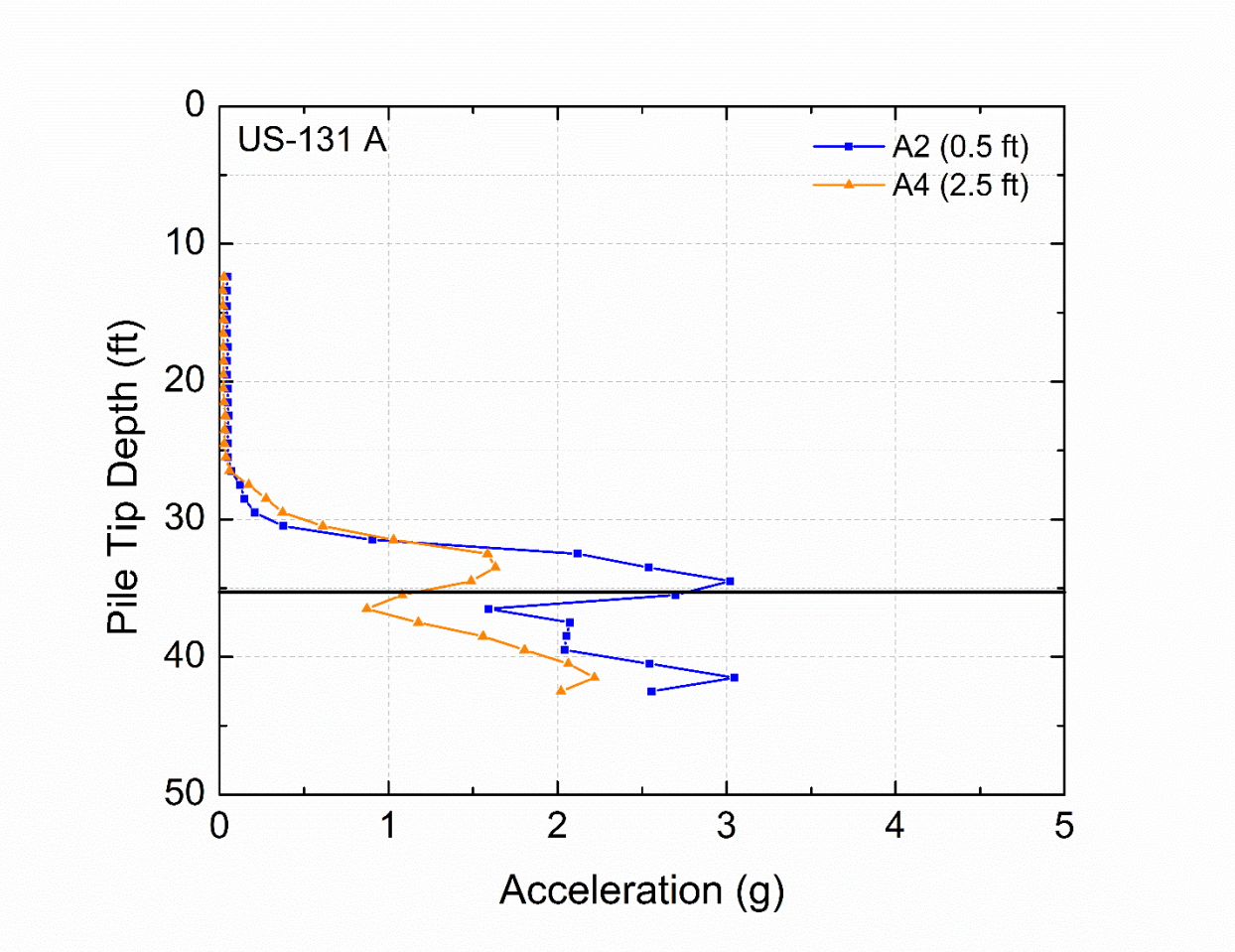

Figure 6-85 Acceleration of deep set of buried sensors at US-131 A site – Pile 1, Transverse Direction

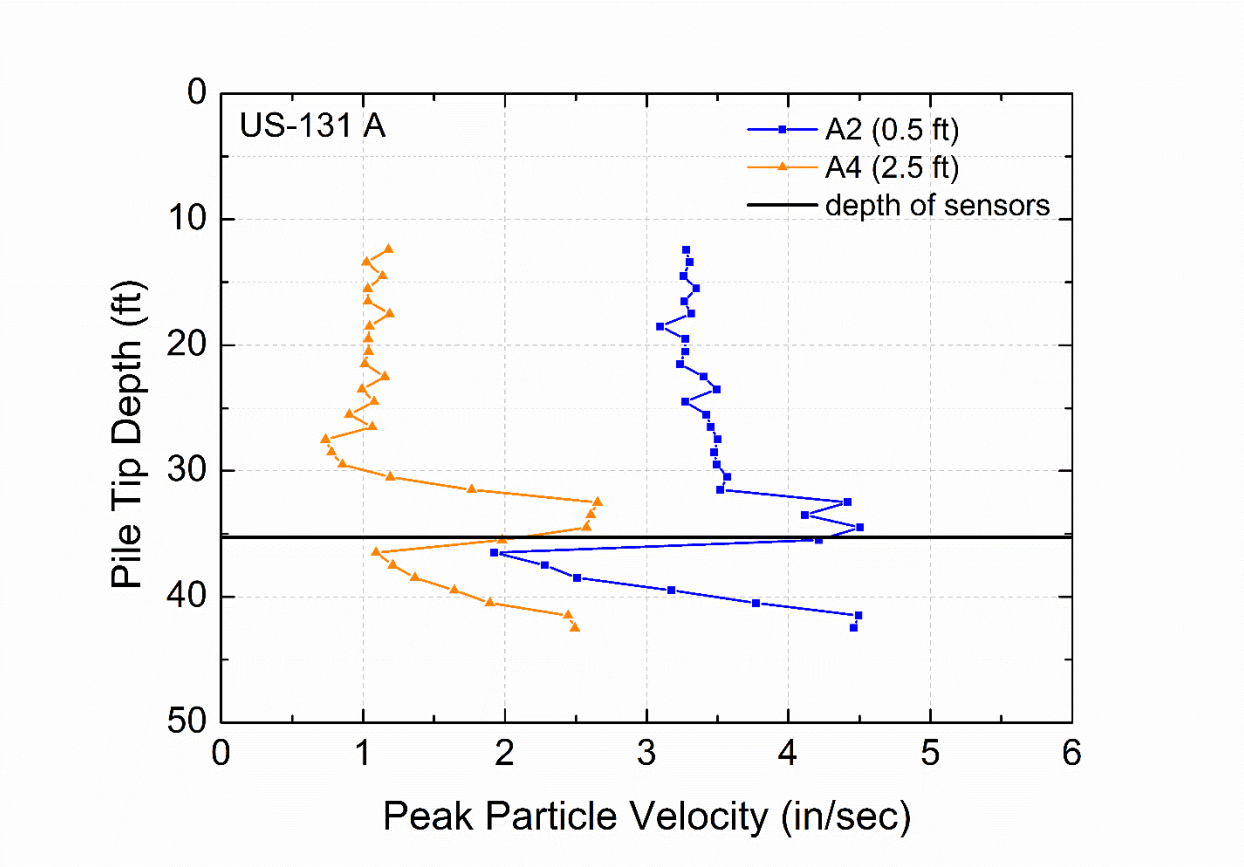

Figure 6-86 Peak Particle Velocity of deep set of buried sensors at US-131 A site – Pile 1, Transverse Direction

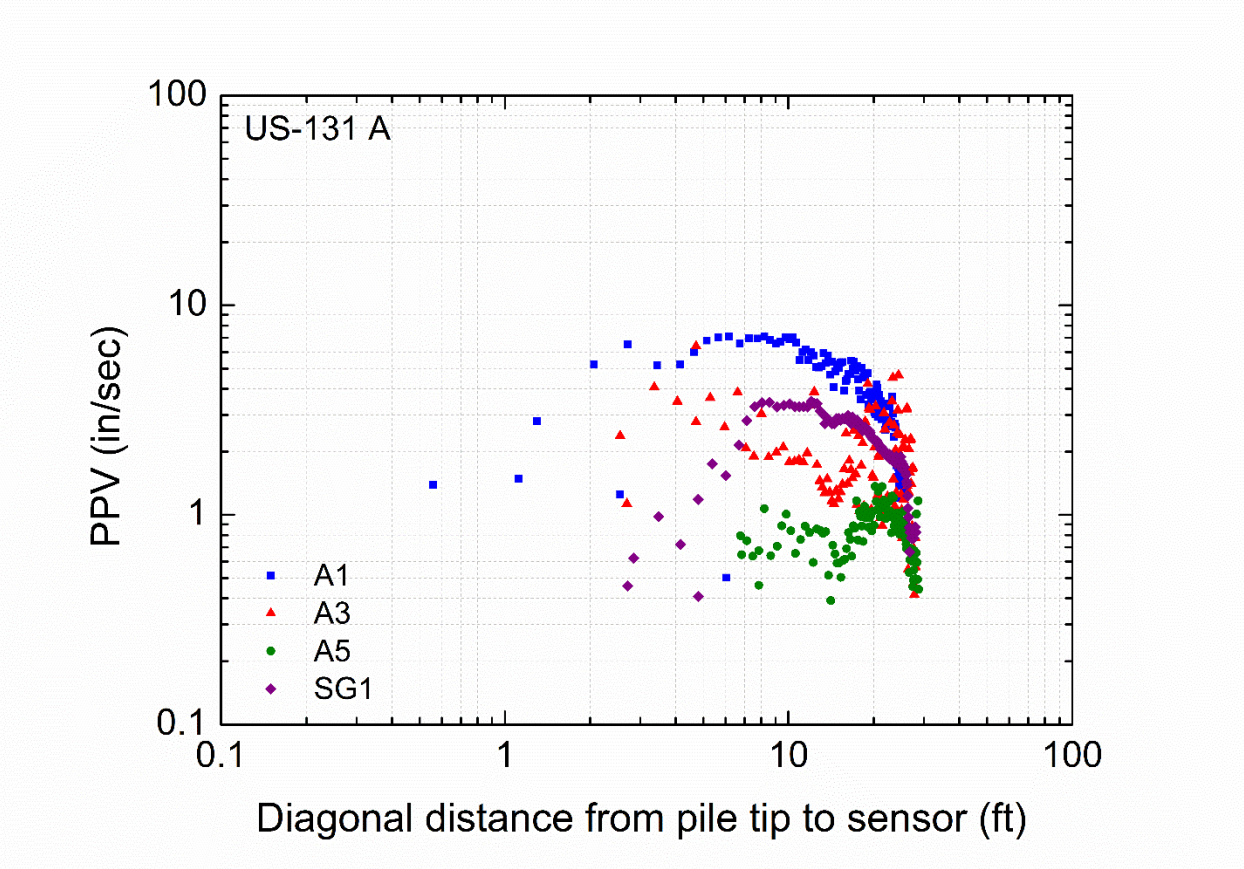

Figure 6-87 Peak particle velocity versus diagonal distance from pile tip to shallow set of sensors at US-131 A site, Pile 1 – Vertical direction, logarithmic scale

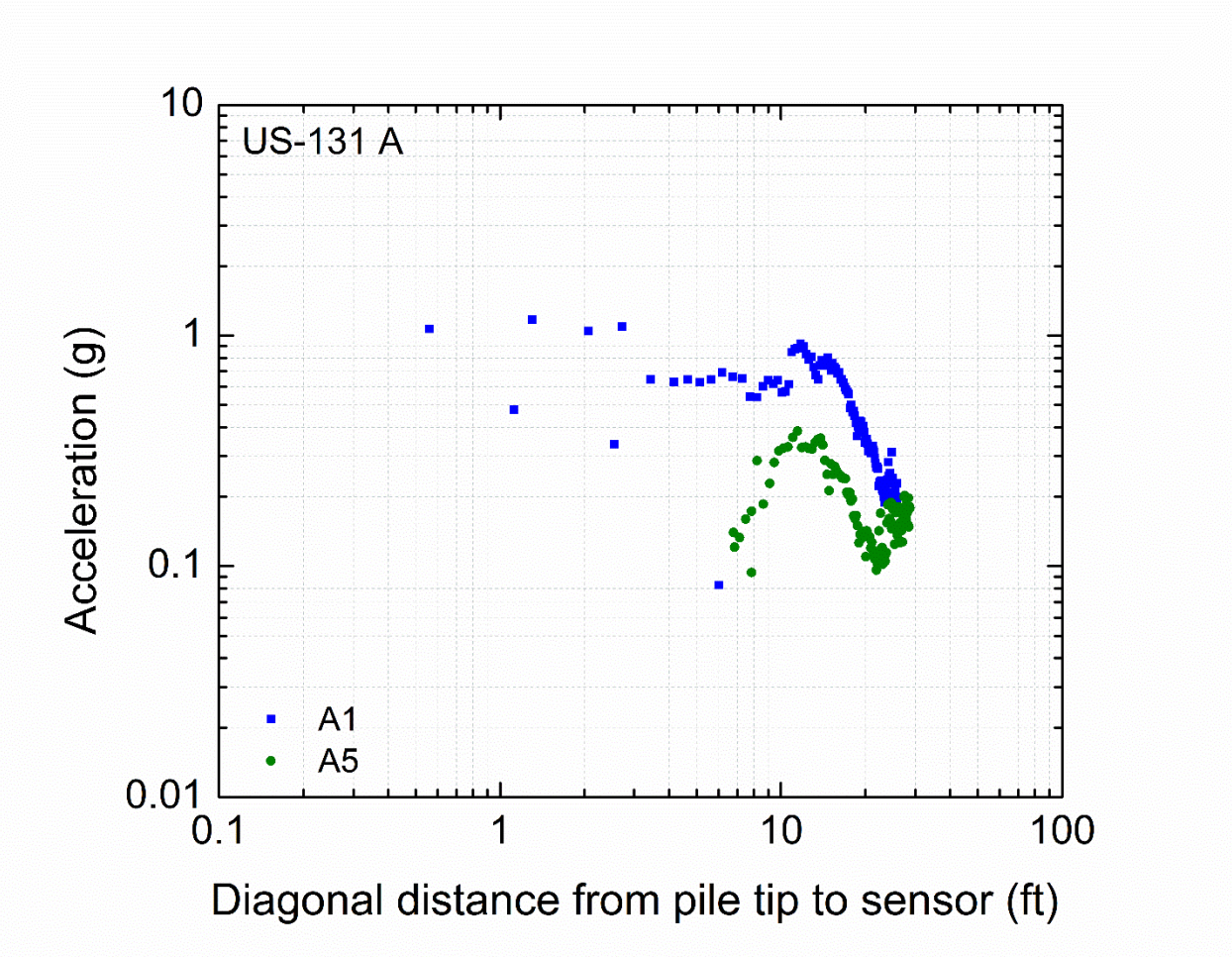

Figure 6-88 Acceleration versus diagonal distance from pile tip to shallow set of sensors at US-131 A site, Pile 1 – Longitudinal direction, logarithmic scale

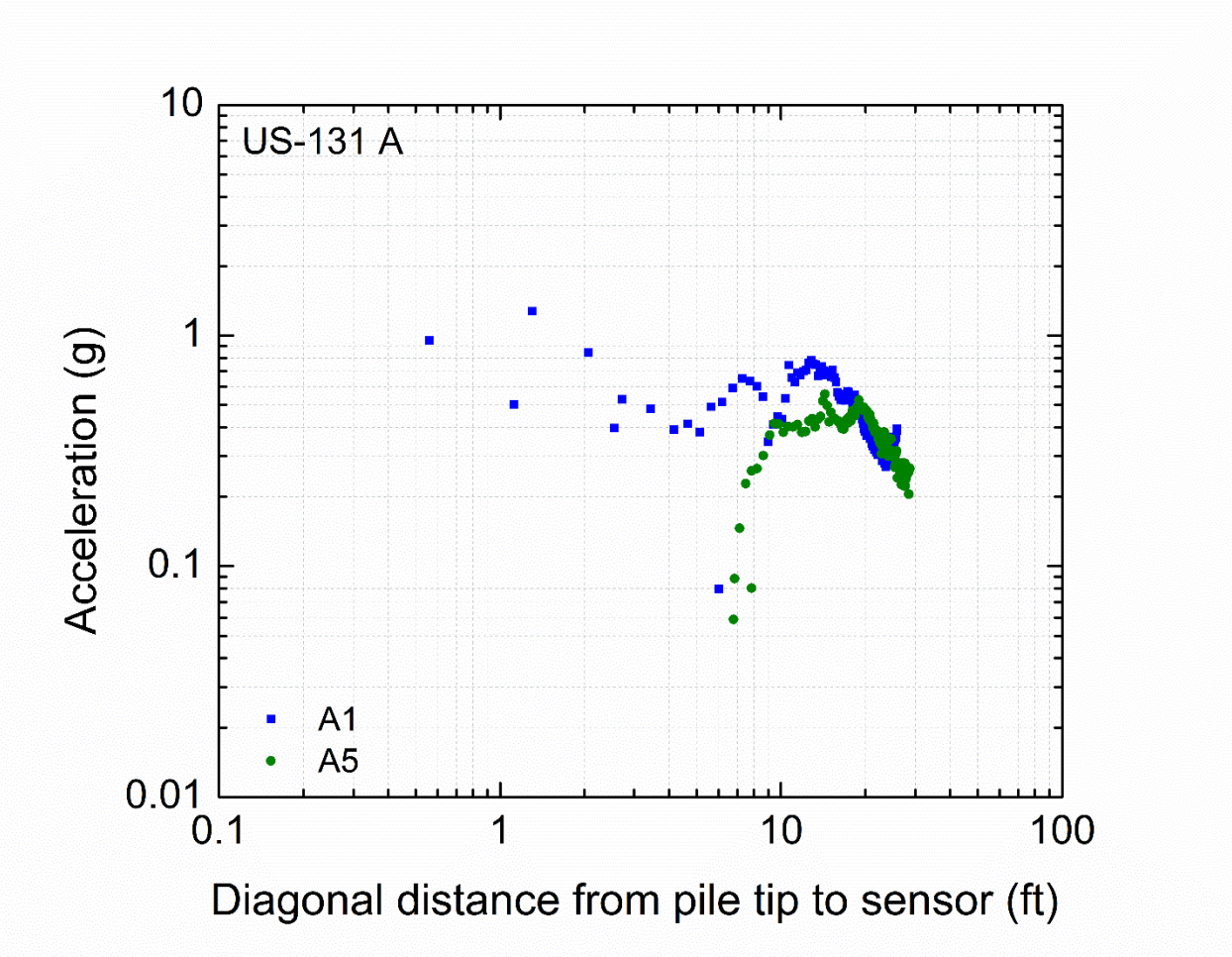

Figure 6-89 Acceleration versus diagonal distance from pile tip to shallow set of sensors at US-131 A site, Pile 1 – Transverse direction, logarithmic scale

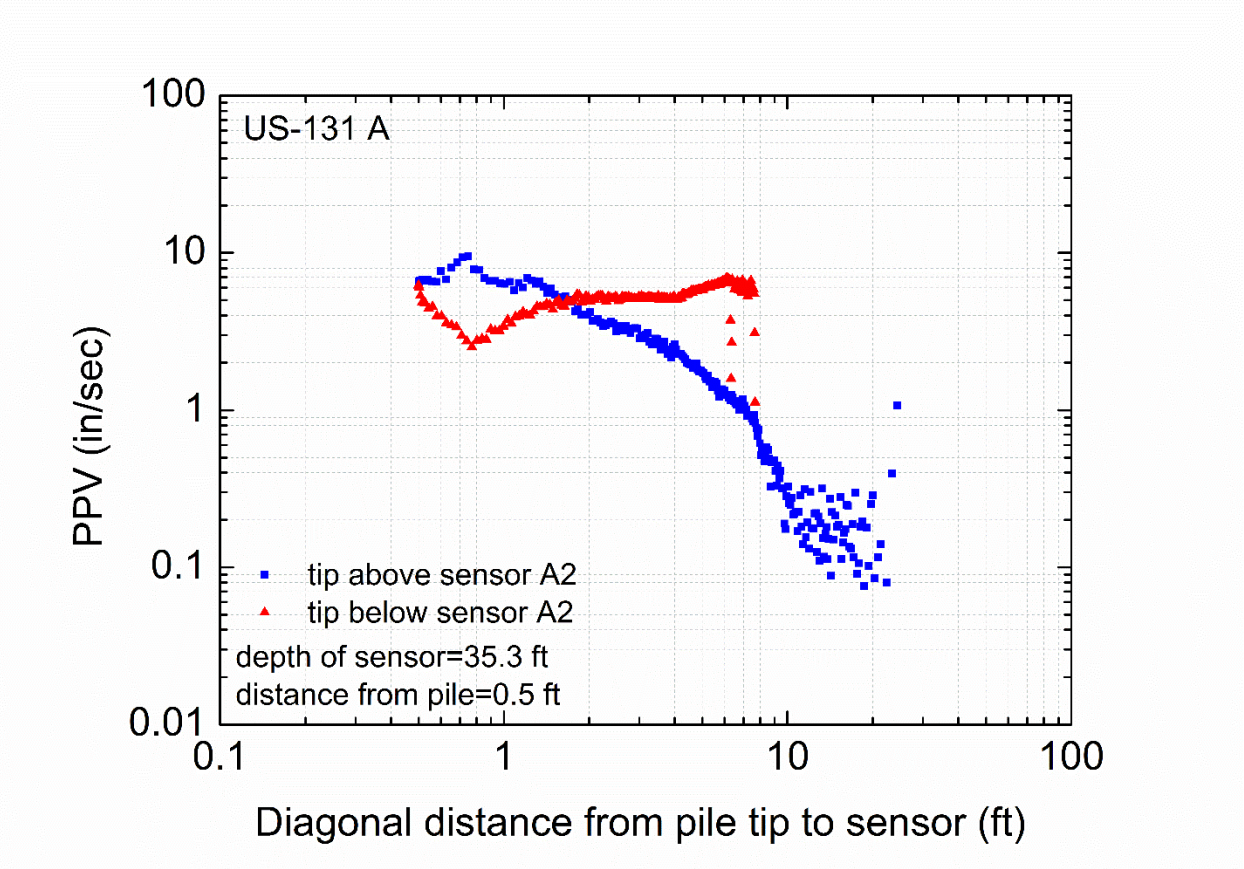

Figure 6-90 Peak particle velocity versus diagonal distance from pile tip to sensor A2 at US-131 A site, Pile 1 – Vertical direction

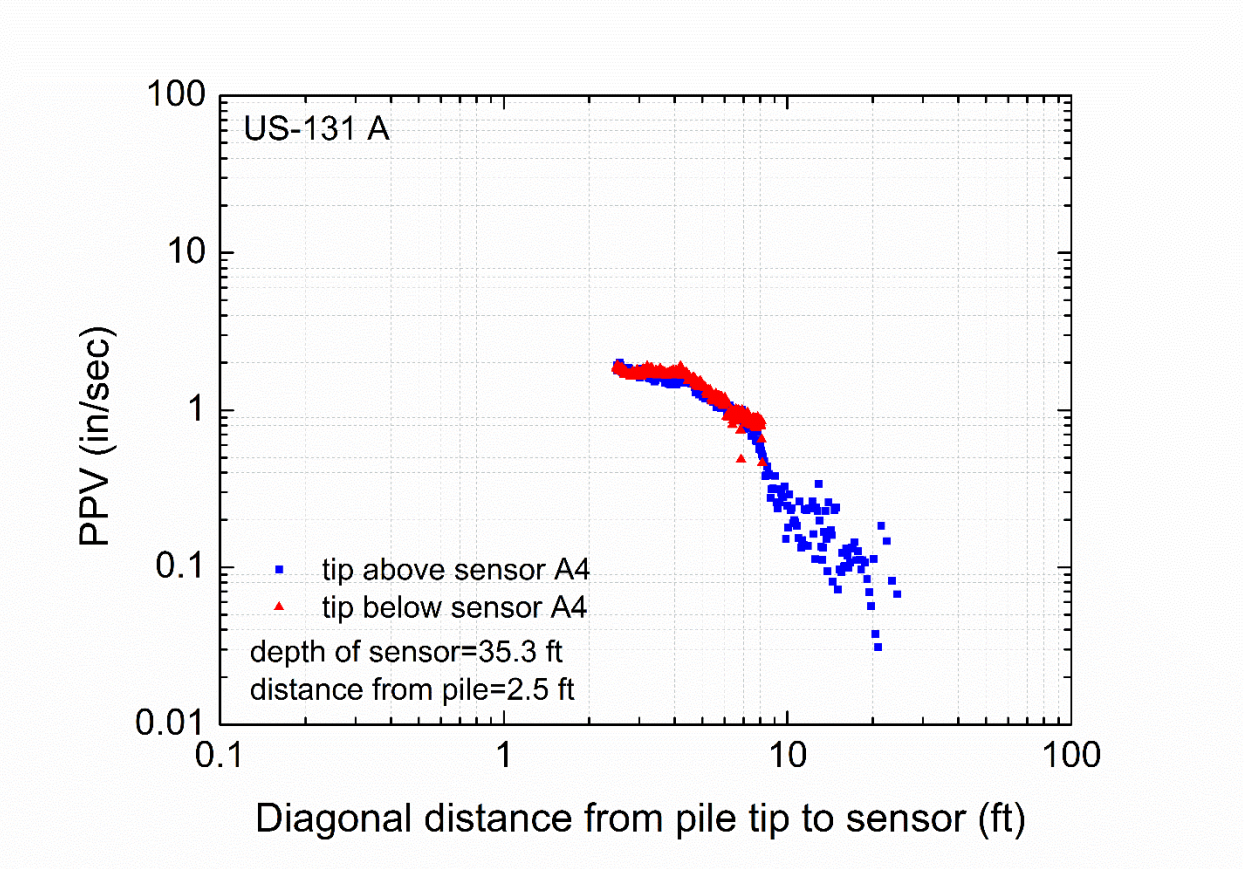

Figure 6-91 Peak particle velocity versus diagonal distance from pile tip to sensor A4 at US-131 A site, Pile 1 – Vertical direction

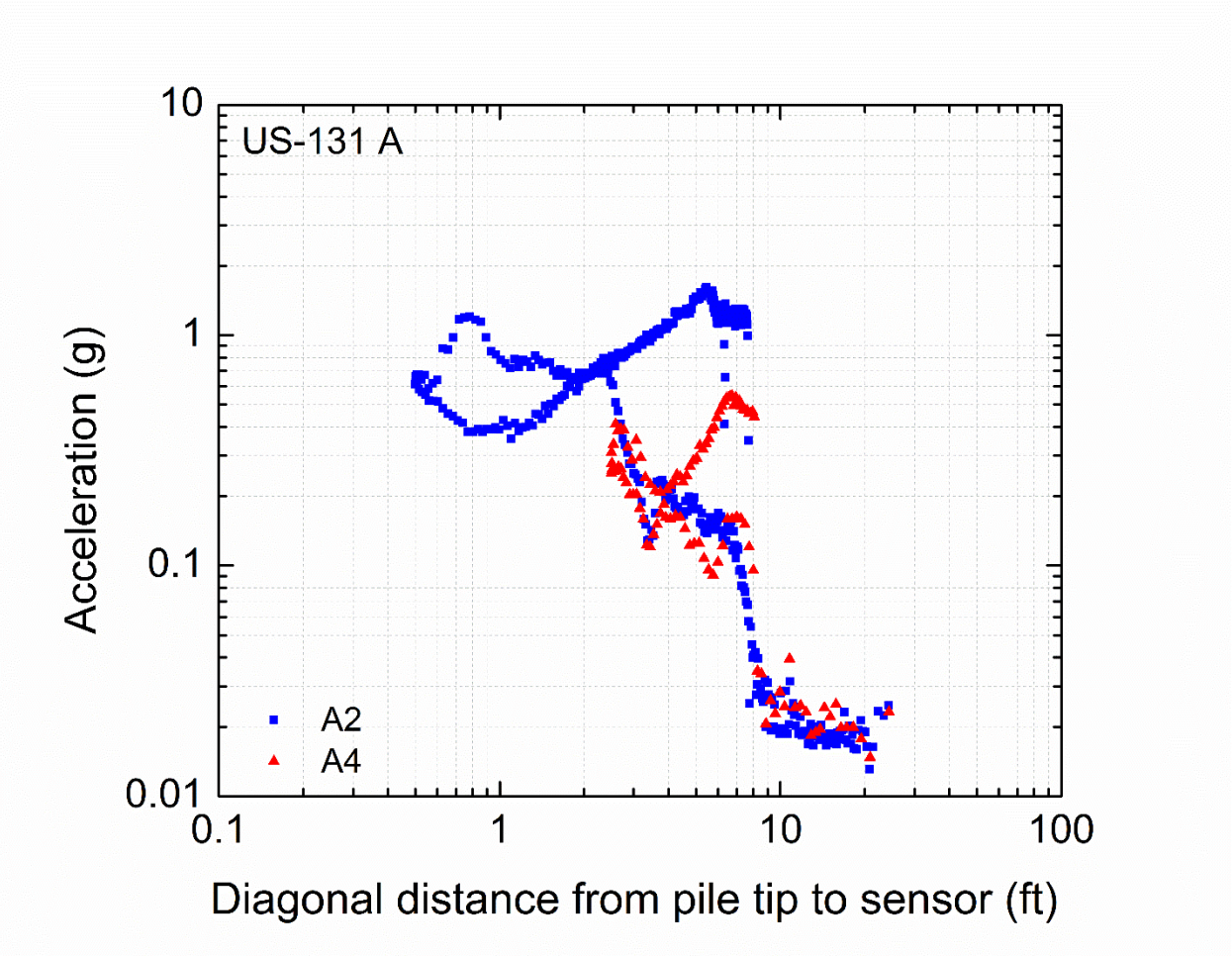

Figure 6-92 Acceleration versus diagonal distance from pile tip to deep set of sensors at US-131 A site, Pile 1 – Longitudinal direction, logarithmic scale

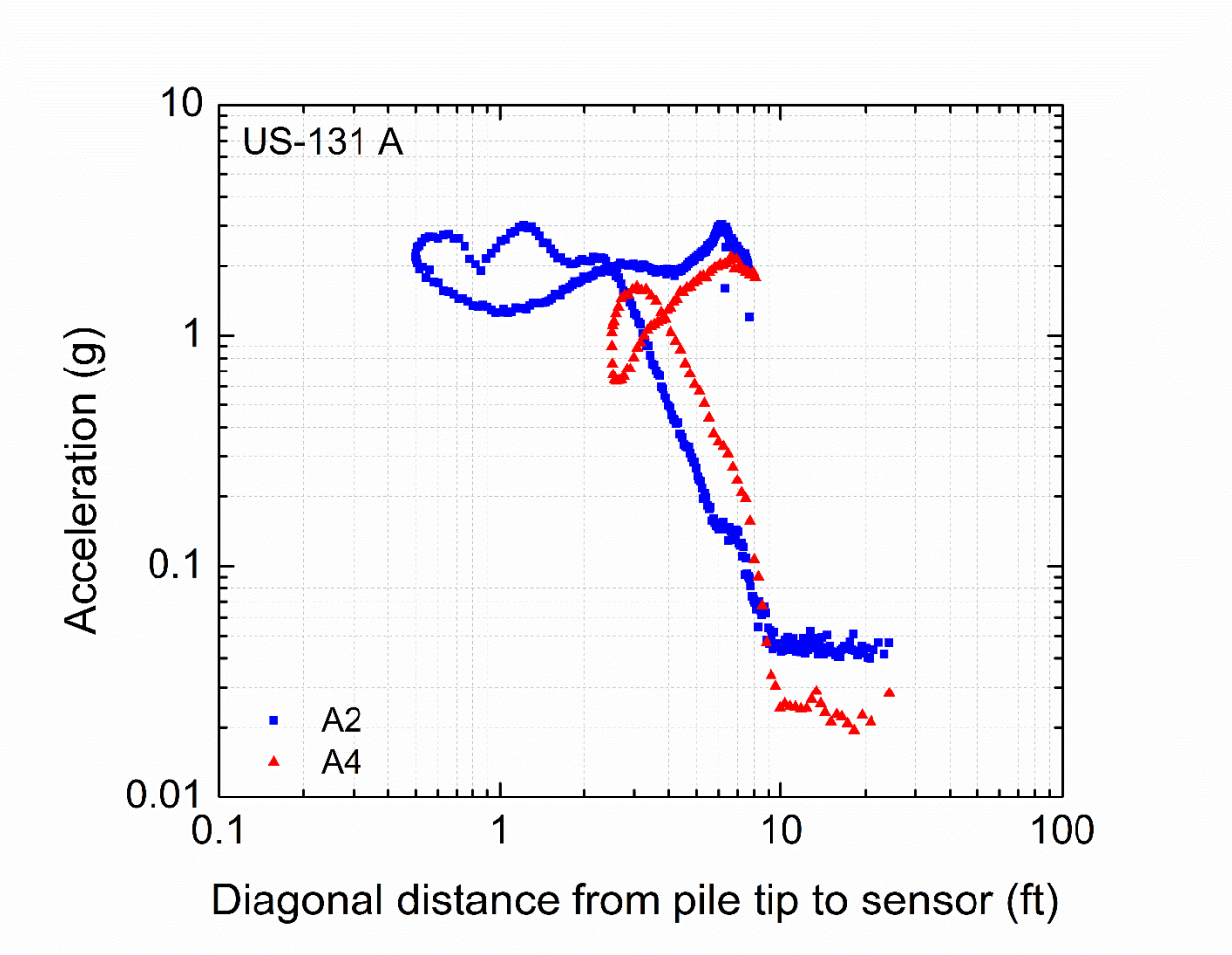

Figure 6-93 Acceleration versus diagonal distance from pile tip to deep set of sensors at US-131 A site, Pile 1 – Transverse direction, logarithmic scale

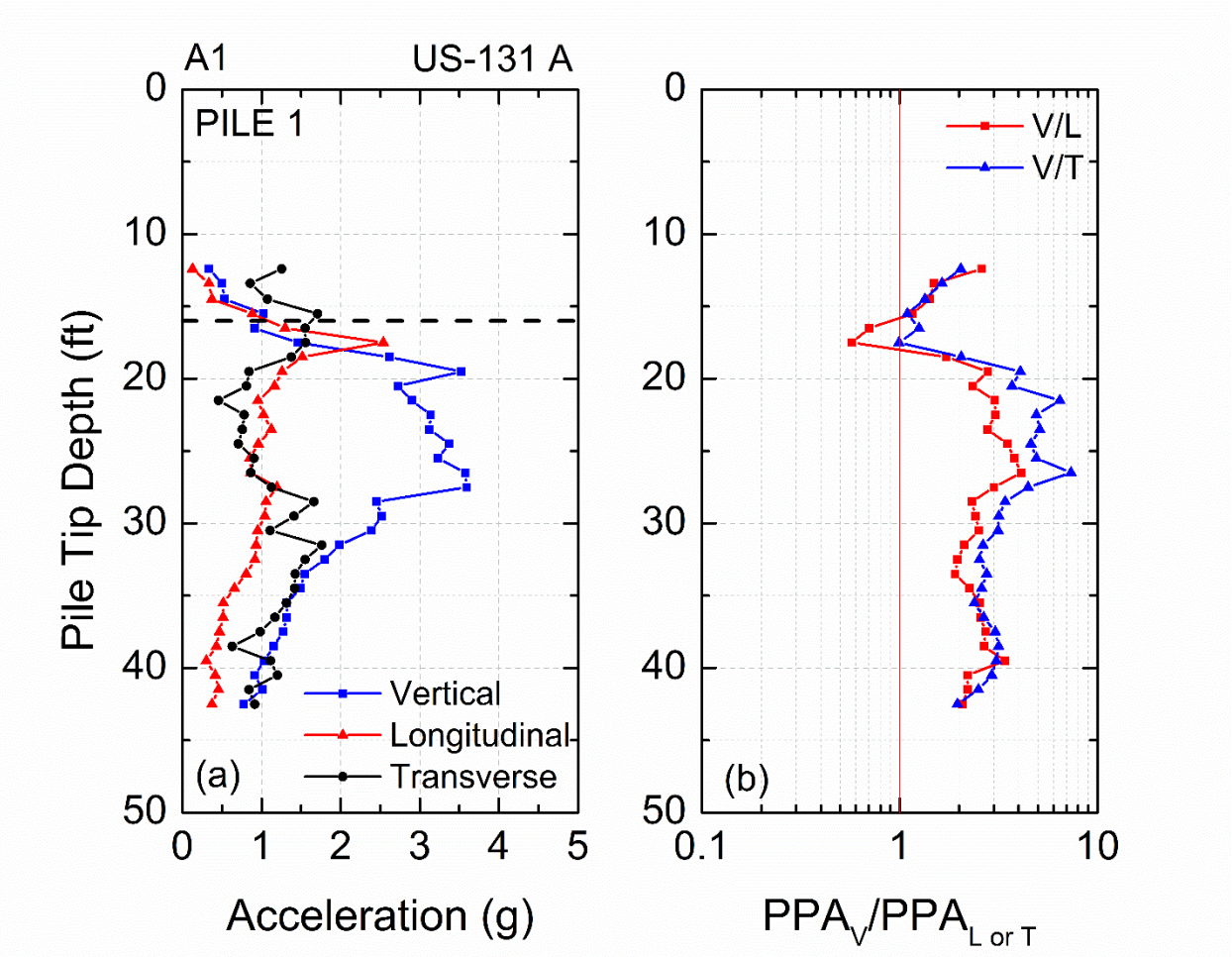

Figure 6-94 (a) Accelerations versus depth for the three components of sensor A1 and (b) vertical to longitudinal and vertical to transverse components of acceleration – US-131 A site, Pile 1

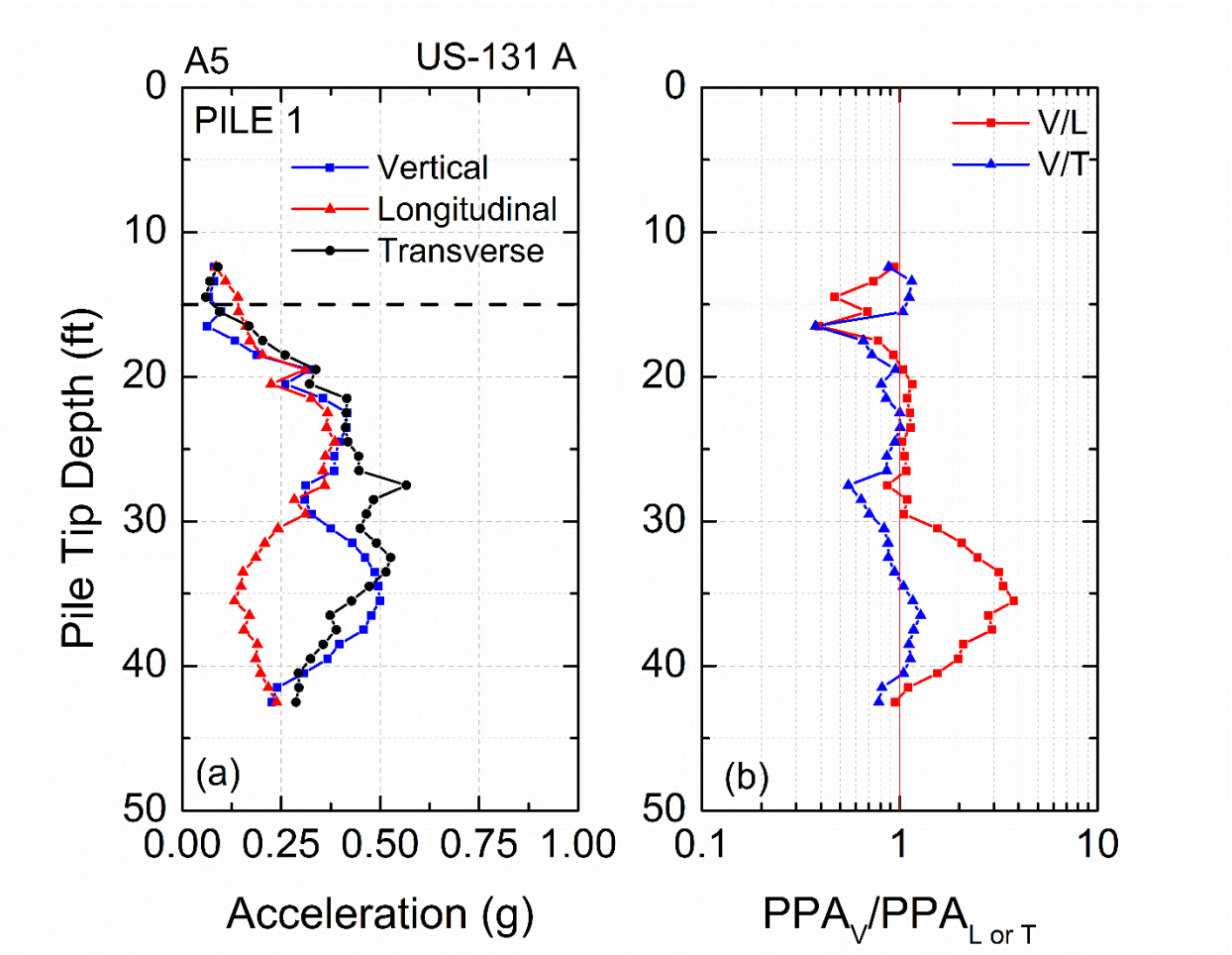

Figure 6-95 (a) Accelerations versus depth for the three components of sensor A5 and (b) vertical to longitudinal and vertical to transverse components of acceleration – US-131 A site, Pile 1

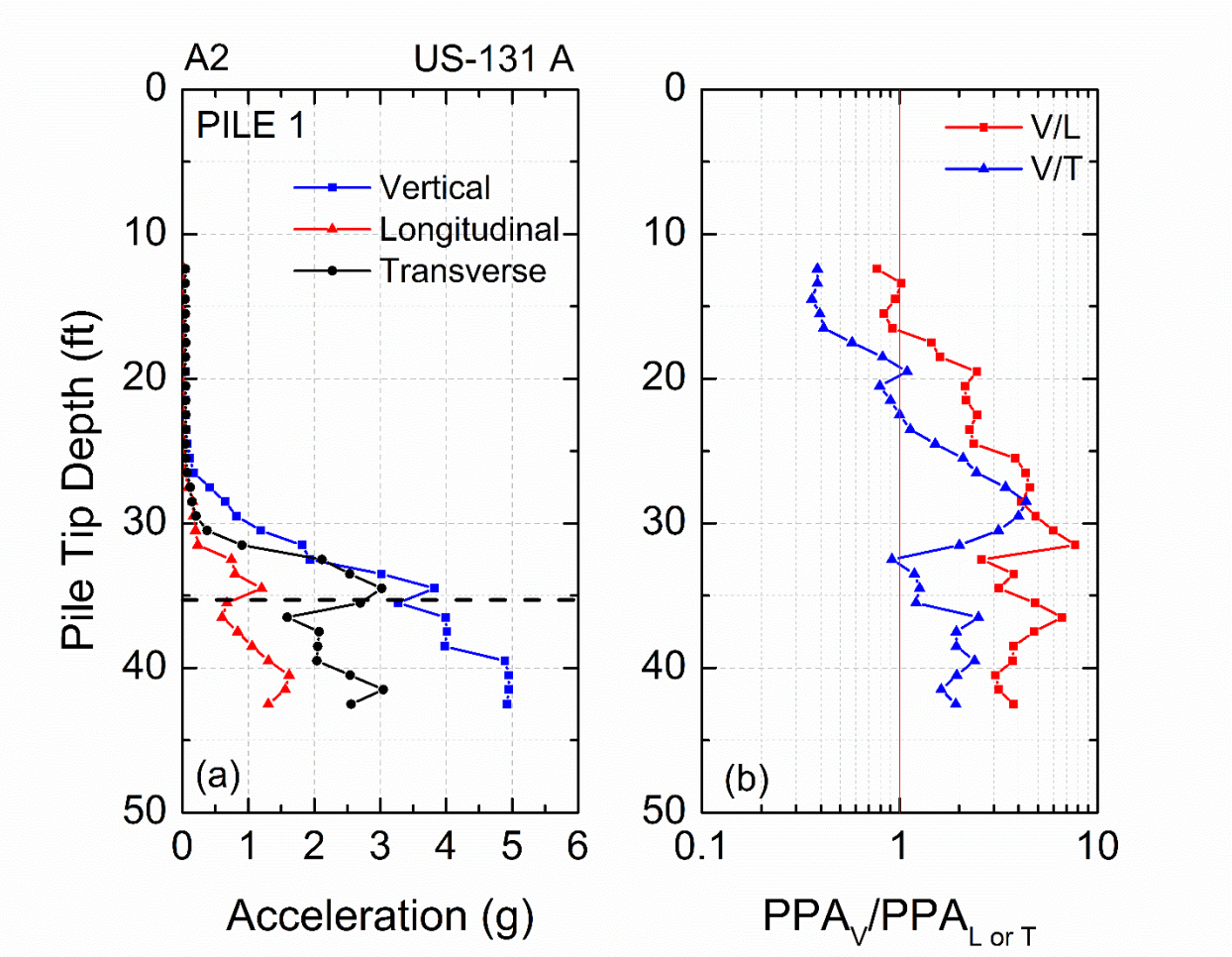

Figure 6-96 (a) Accelerations versus depth for the three components of sensor A2 and (b) vertical to longitudinal and vertical to transverse components of acceleration – US-131 A site, Pile 1

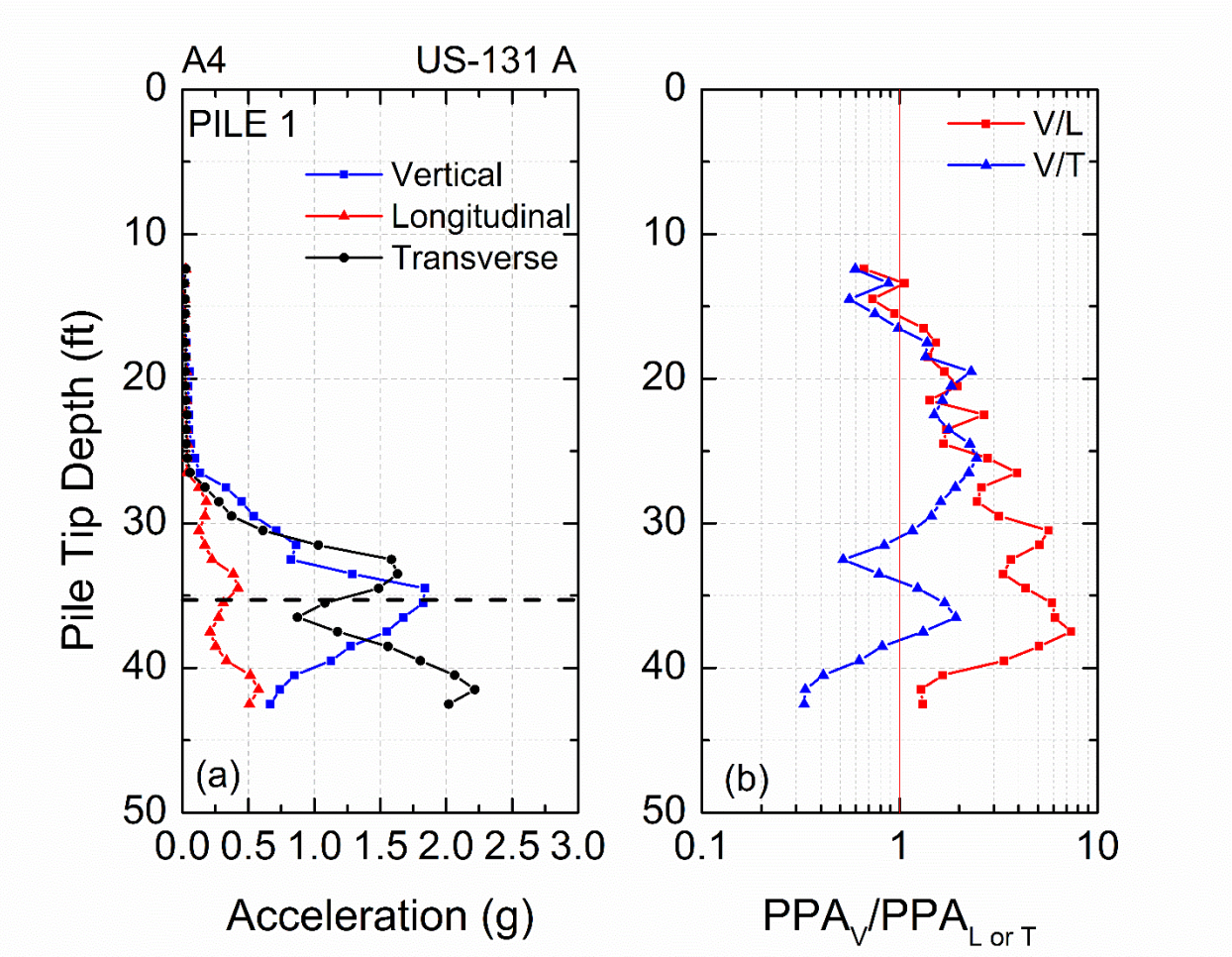

Figure 6-97 (a) Accelerations versus depth for the three components of sensor A4 and (b) vertical to longitudinal and vertical to transverse components of acceleration – US-131 A site, Pile 1

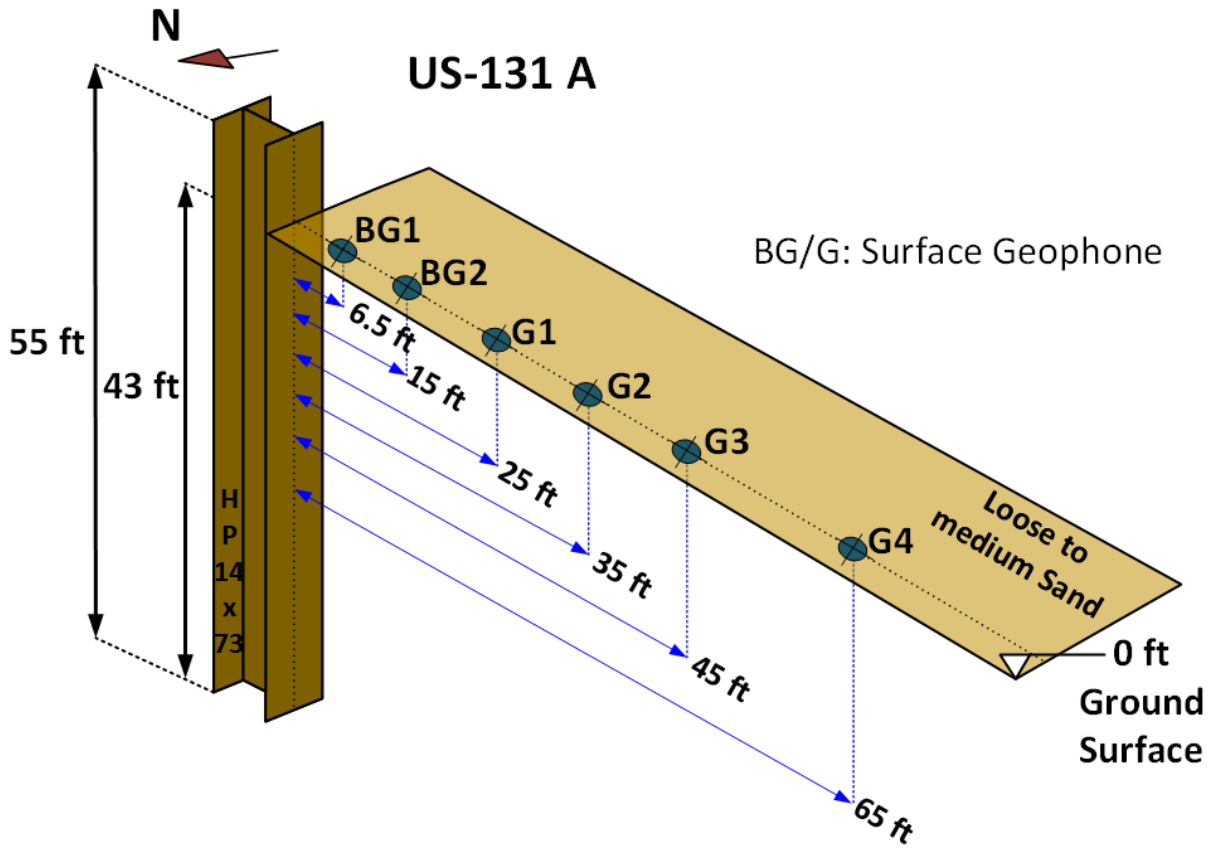

Figure 6-98 Perspective view of surface sensors at US-131 A site, Pile 1 (not to scale)

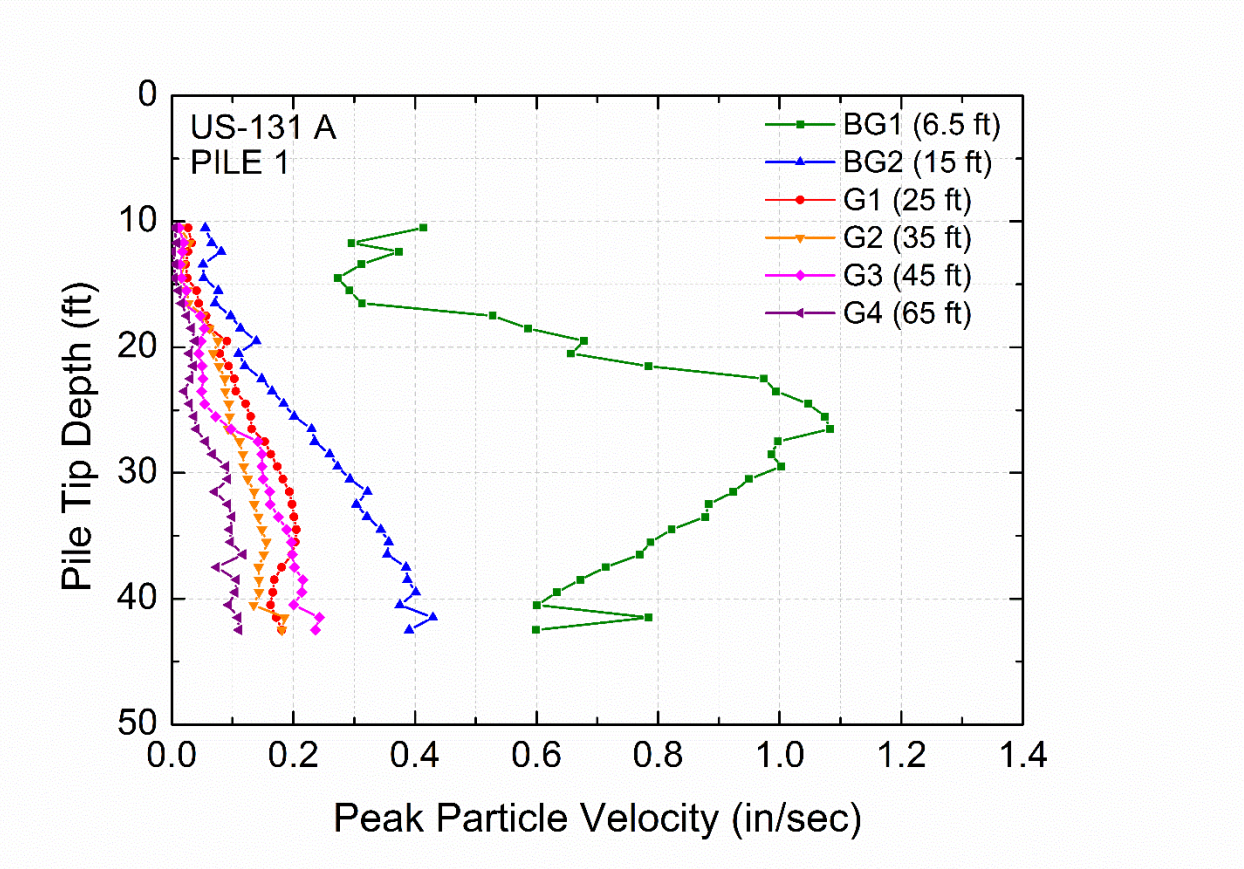

Figure 6-99 Peak Particle Velocity of surface geophones at US-131 A site – Pile 1, Vertical Direction

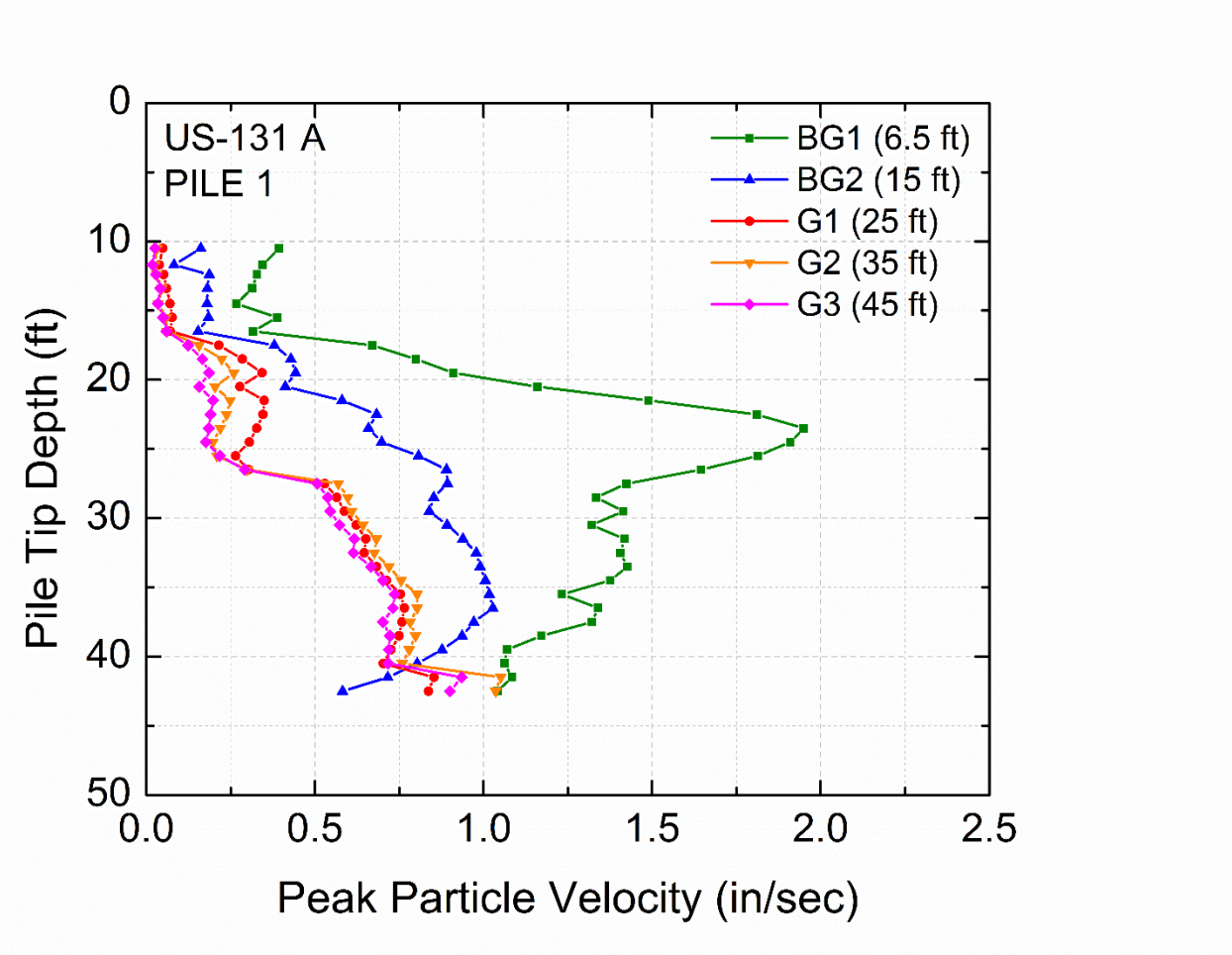

Figure 6-100 Peak Particle Velocity of surface geophones at US-131 A site – Pile 1, Longitudinal Direction

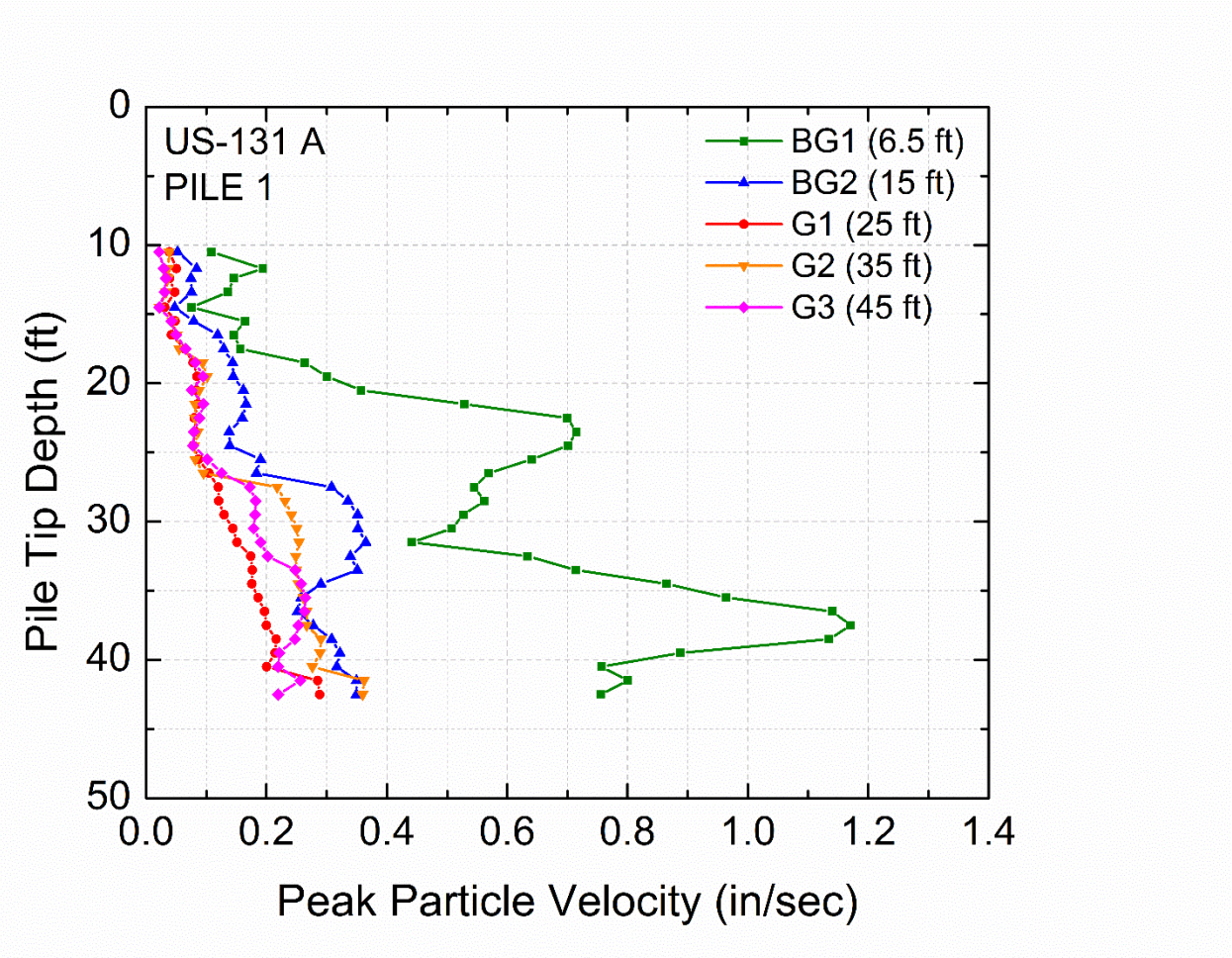

Figure 6-101 Peak Particle Velocity of surface geophones at US-131 A site – Pile 1, Transverse Direction

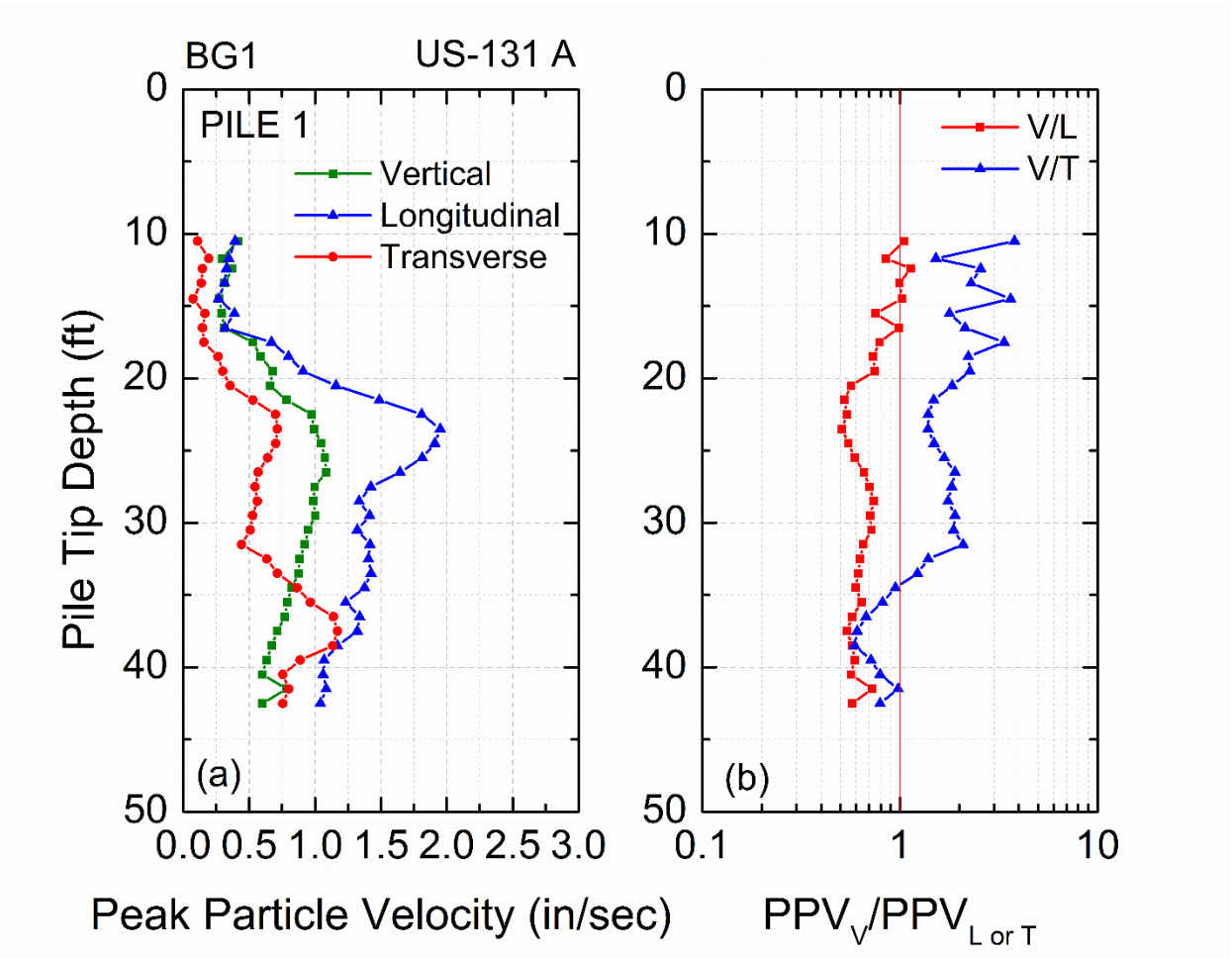

Figure 6-102 (a) Peak Particle Velocities of three directions of sensor BG1 and (b) vertical to longitudinal and vertical to transverse components of PPV– US-131 A site, Pile 1

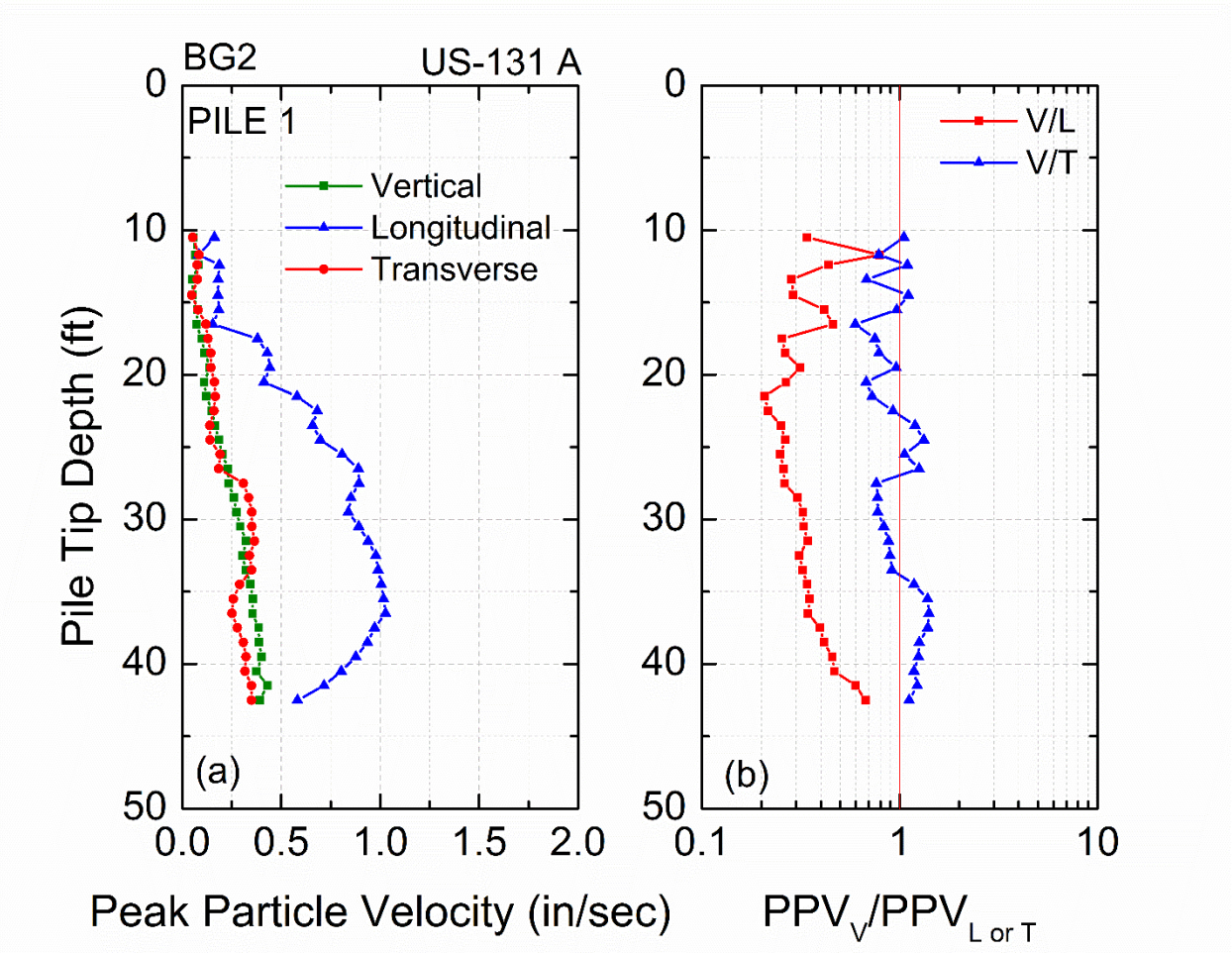

Figure 6-103 (a) Peak Particle Velocities of three directions of sensor BG2 and (b) vertical to longitudinal and vertical to transverse components of PPV– US-131 A site, Pile 1

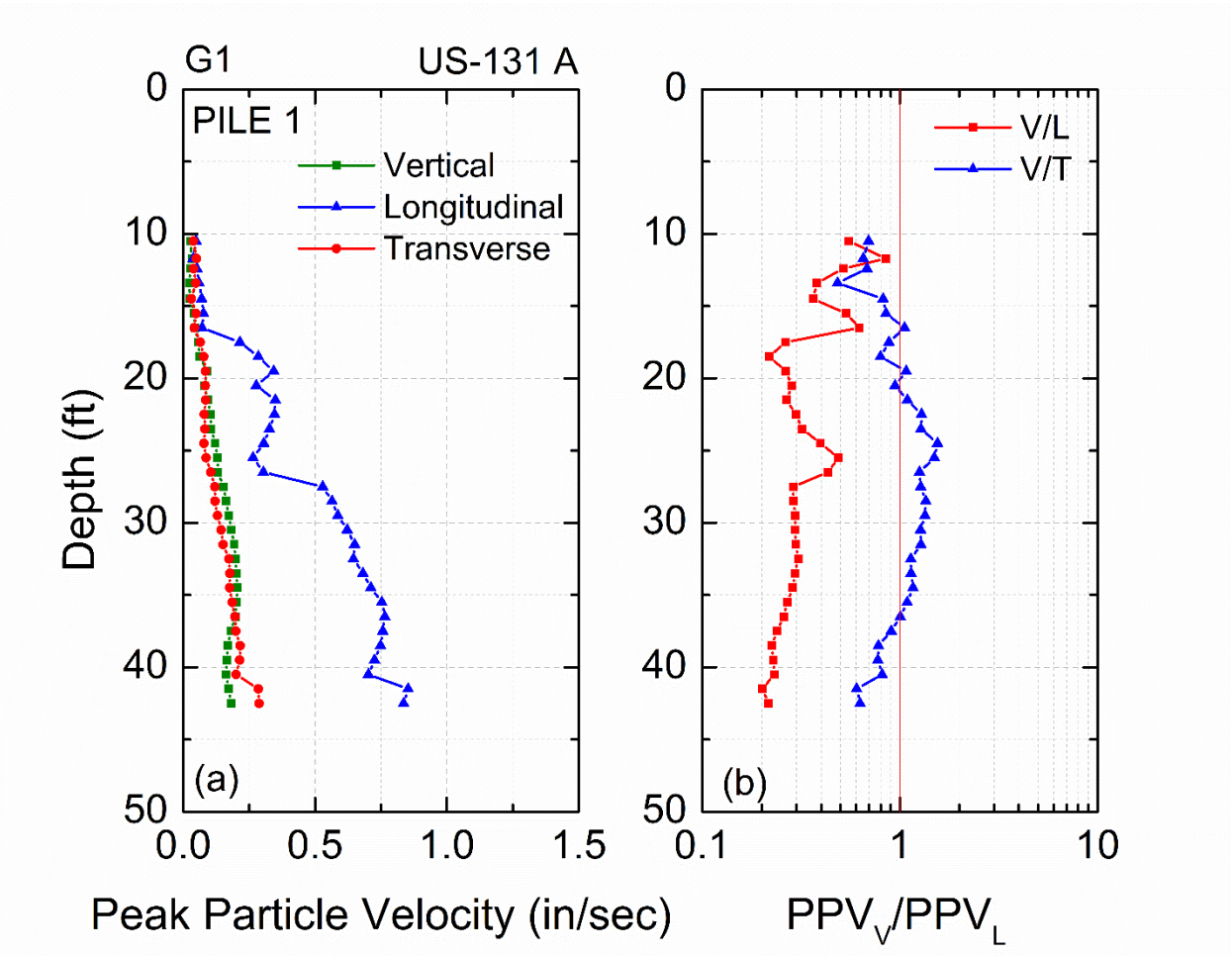

Figure 6-104 (a) Peak Particle Velocities of three directions of sensor G1 and (b) vertical to longitudinal and vertical to transverse components of PPV– US-131 A site, Pile 1

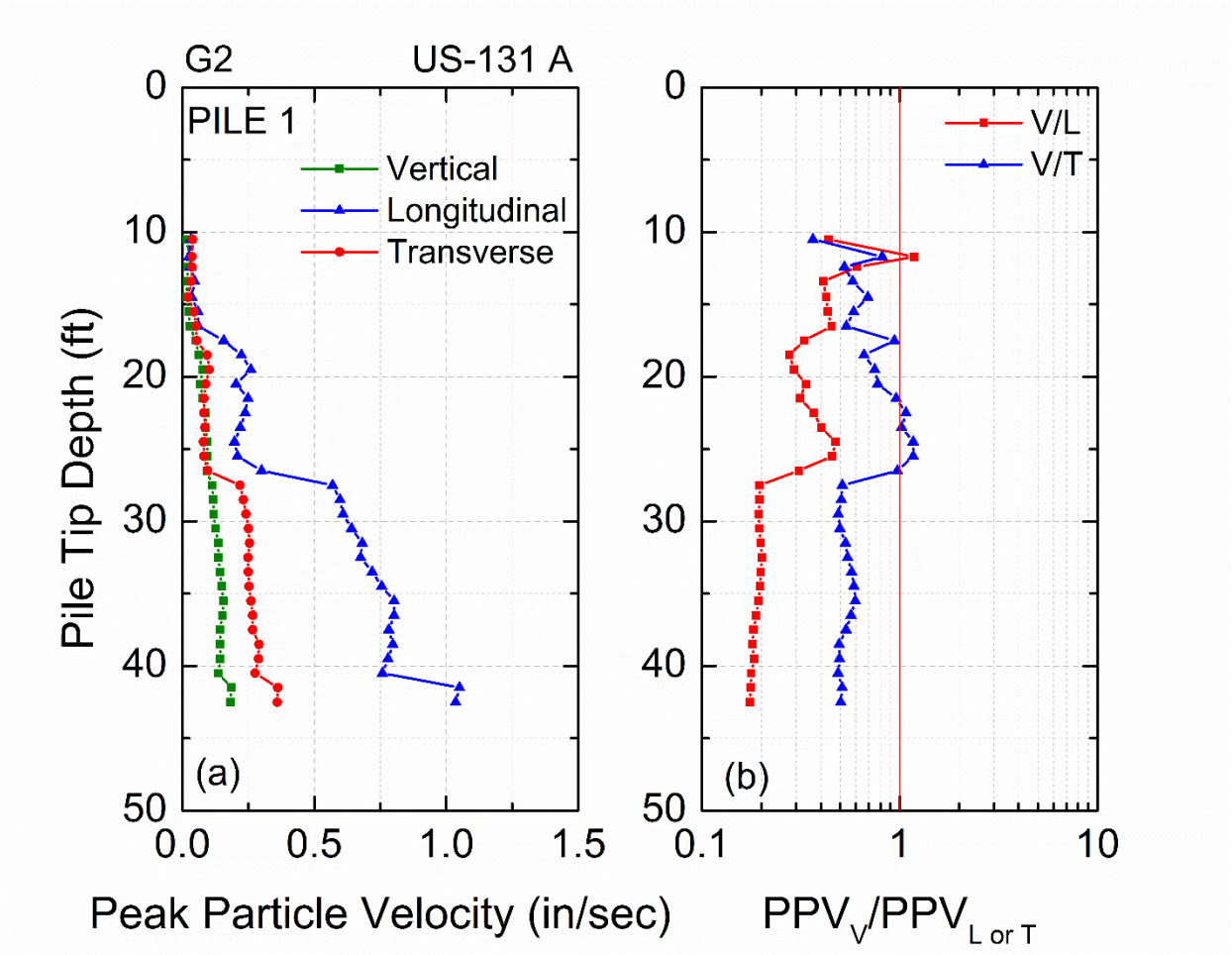

Figure 6-105 (a) Peak Particle Velocities of three directions of sensor G2 and (b) vertical to longitudinal and vertical to transverse components of PPV – US-131 A site, Pile 1

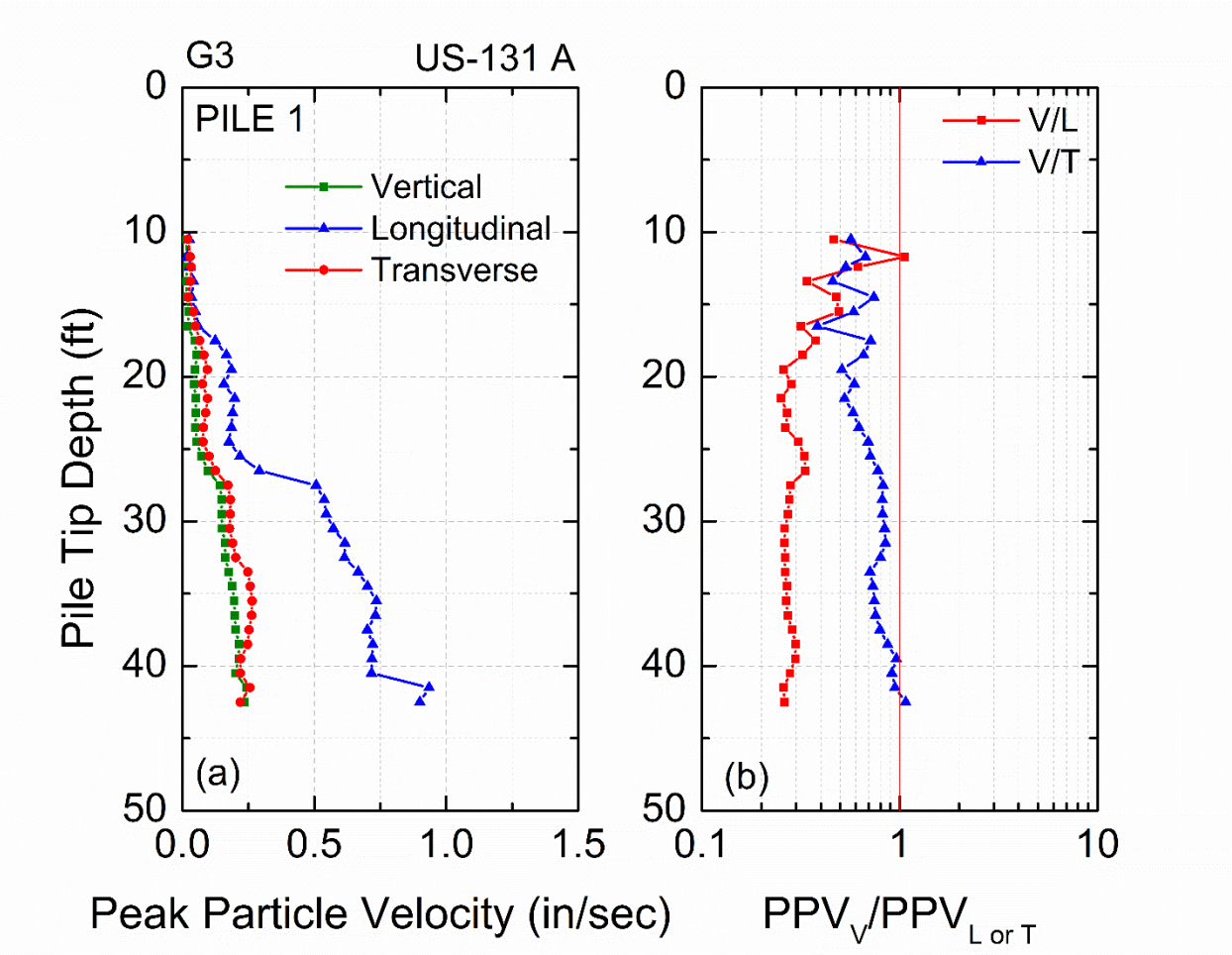

Figure 6-106 (a) Peak Particle Velocities of three directions of sensor G3 and (b) vertical to longitudinal and vertical to transverse components of PPV– US-131 A site, Pile 1

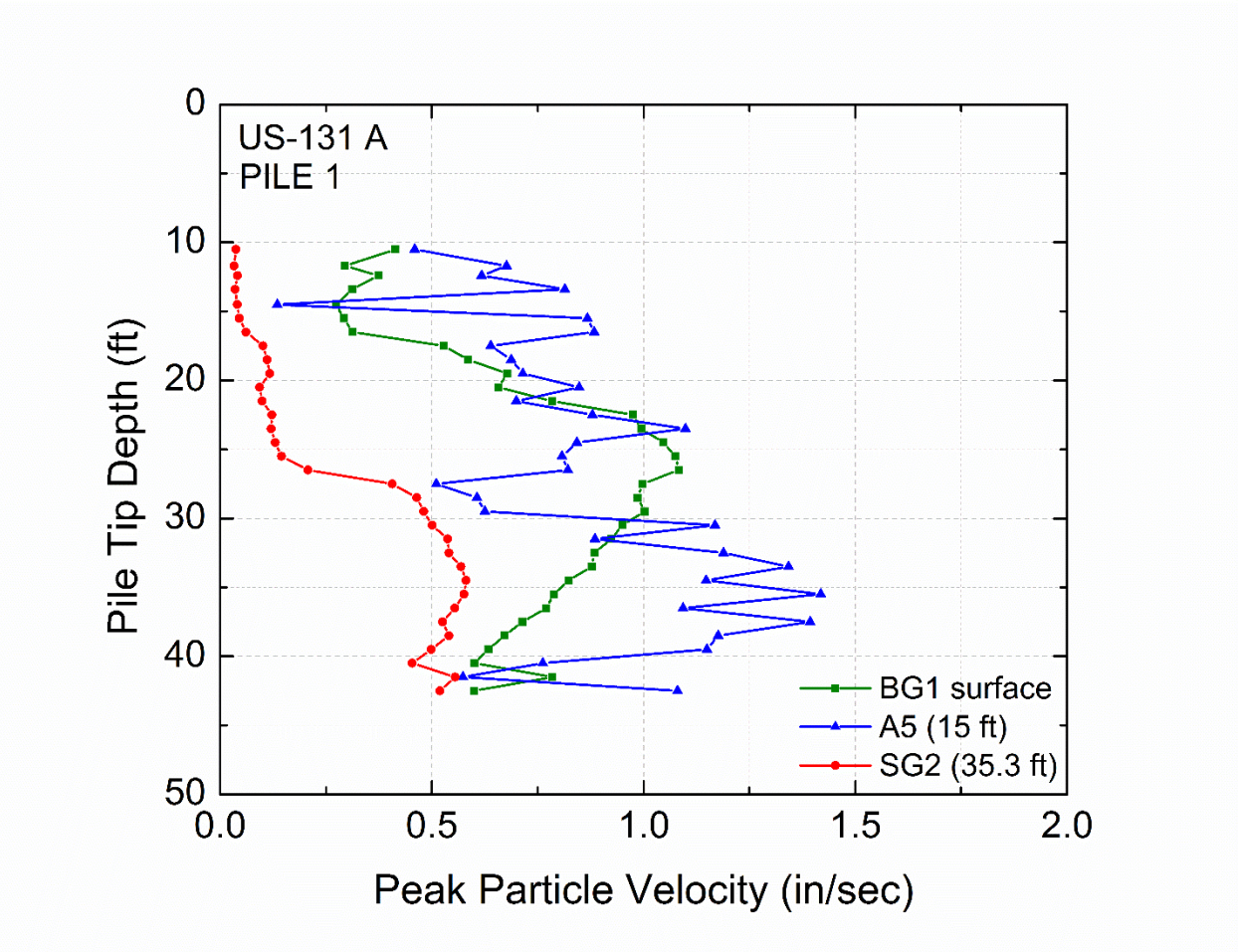

Figure 6-107 Peak particle velocity versus depth of sensors BG1, A5 and SG2 at US-131 A site, Pile 1 –Vertical direction

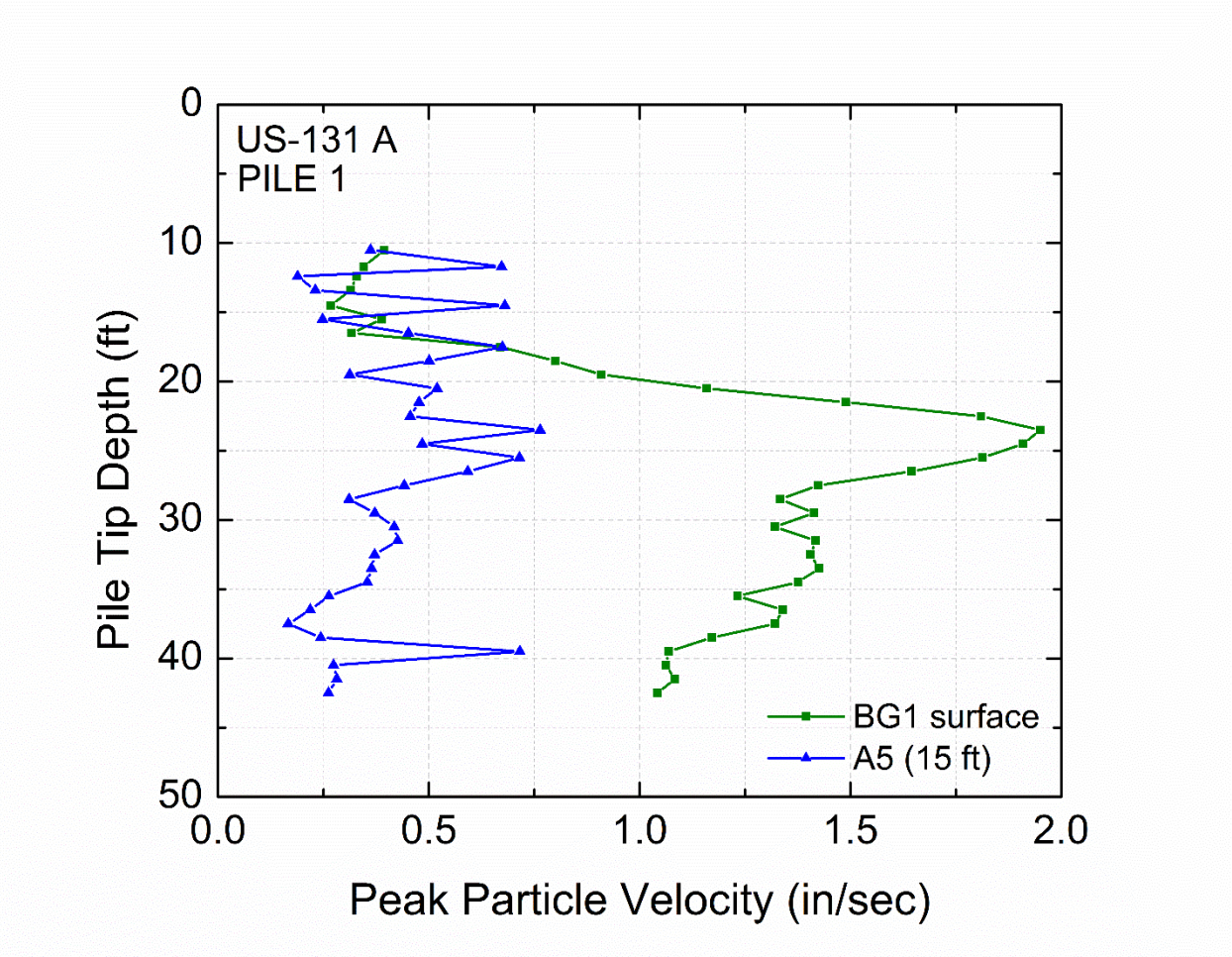

Figure 6-108 Peak particle velocity versus depth of sensors BG1 and A5 at US-131 A site, Pile 1 –Longitudinal direction

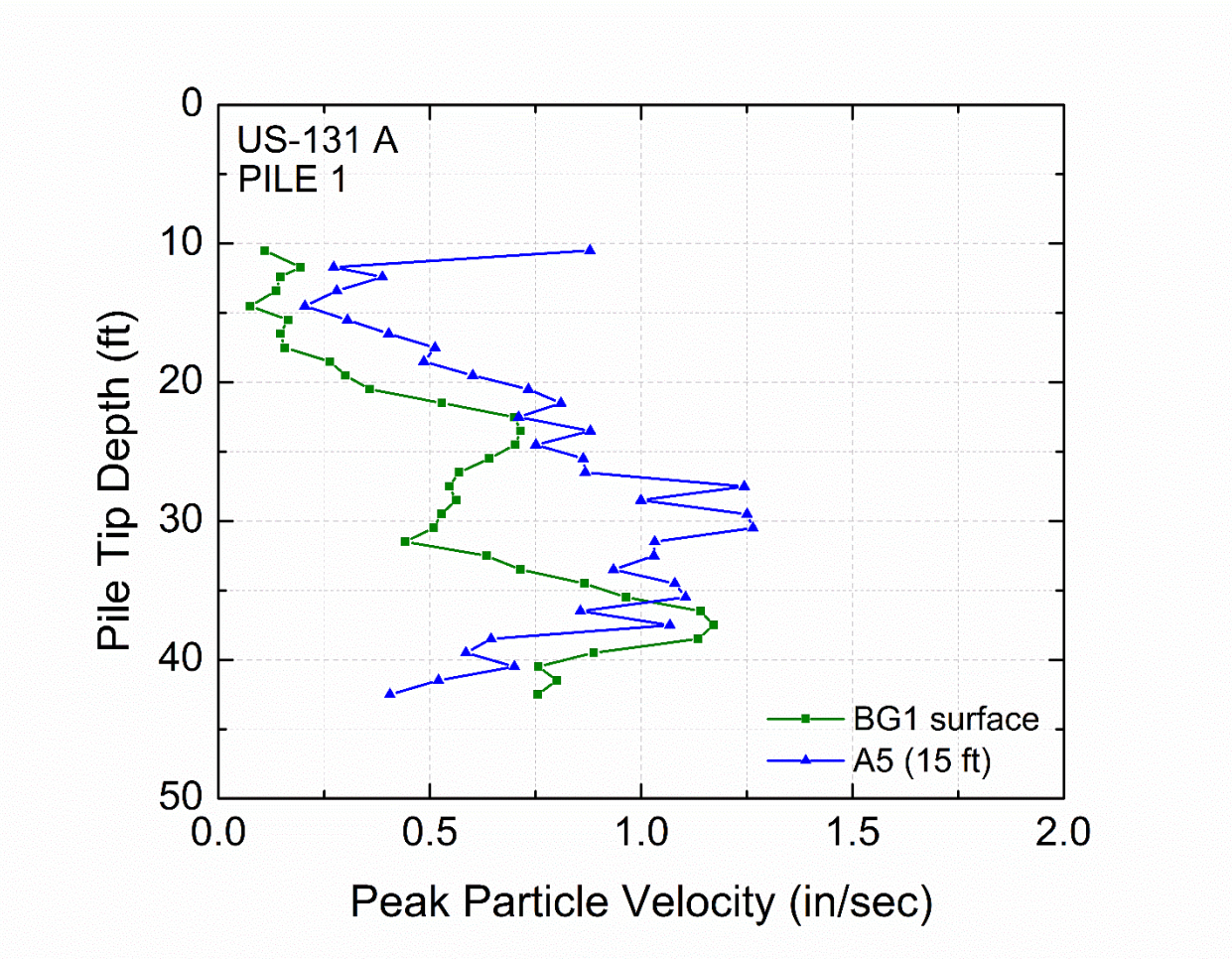

Figure 6-109 Peak particle velocity versus depth of sensors BG1 and A5 at US-131 A site, Pile 1 –Transverse direction

6.3.2.2 Test Pile 18

After recording ground motions during driving pile 1, the contractor prepared the hammer and continued to drive test pile 18. Both piles, were production piles that were on the schedule to be driven at abutment A. The ground surface geophones were placed in an array close to pile 18. Ground motion signals were acquired from the buried sensors close to pile 1; their values were much lower than when driving pile 1, since the two piles were around 100 ft apart, but their results will be discussed in the next Section along with the attenuation characteristics of the travelling waves.

A perspective view of the surface sensor locations close to pile 18 is shown in Figure 6-110. A 56.5 ft long HP 14x73 pile was driven using again the Delmag D30-32 diesel hammer. The final depth of penetration of the pile was 45.25 ft. Figure 6-111 presents the pile driving penetration resistance as the number of blows per pile foot increment and the accumulated number of blows versus depth of pile tip penetration. The total blow count to drive pile 18 was 576. The driving resistance gradually increased with increasing penetration depth, showing a higher rate of increase at a depth of 30 ft and below. Figure 6-112 illustrates the average actual hammer energy per pile foot increment and the hammer efficiency, η, versus depth. The average hammer efficiency when driving pile 18 was around 40%.

Vertical peak particle velocity versus depth is shown for all the sensors in Figure 6-113. There is an increase in velocity amplitudes when the pile tip enters the dense sand at around 15 ft and at 22 ft when the pile tip enters the clay deposit (Figure 6-28). Figure 6-114 and Figure 6-115 present the particle velocities for the longitudinal and transverse directions of these same surface sensors except G4 that did not have a longitudinal and transverse component transducer. It is of interest to note, that the two furthest geophones from pile 18 (BG2 and BG1) had a sharp increase in their recorded longitudinal component velocities around a depth of 30 ft, recording higher amplitudes than the closest sensors. This trend is also observed for the transverse components of motion of sensors G2 and G1, however geophones BG2 and BG1 have lower and almost identical response. The driving resistance begins to have a higher rate of increase at 30 ft (Figure 6-111), which explains the above behavior.

Figure 6-116a to Figure 6-120a show the three velocity components versus depth and Figure 6-116b to Figure 6-120b show the ratios of vertical to longitudinal (V/L) and vertical to transverse (V/T) components for sensors G3, G2, G1, BG2 and BG1, respectively. The three closest sensors to the pile (G3, G2 and G1) had higher transverse component peak particle velocities than the vertical component of motions for the entire depth range of pile installation. The ratio of vertical to longitudinal (V/L) is very close to one for the total depth range of installation. The furthest sensors from the pile (BG2 and BG1) had greater longitudinal component motions than the vertical components, again for the whole installations process. Also, the ratio of vertical to transverse (V/T) is very close to one for the total depth range of installation. So far, none of the surface recordings indicate a classical Rayleigh wave form.

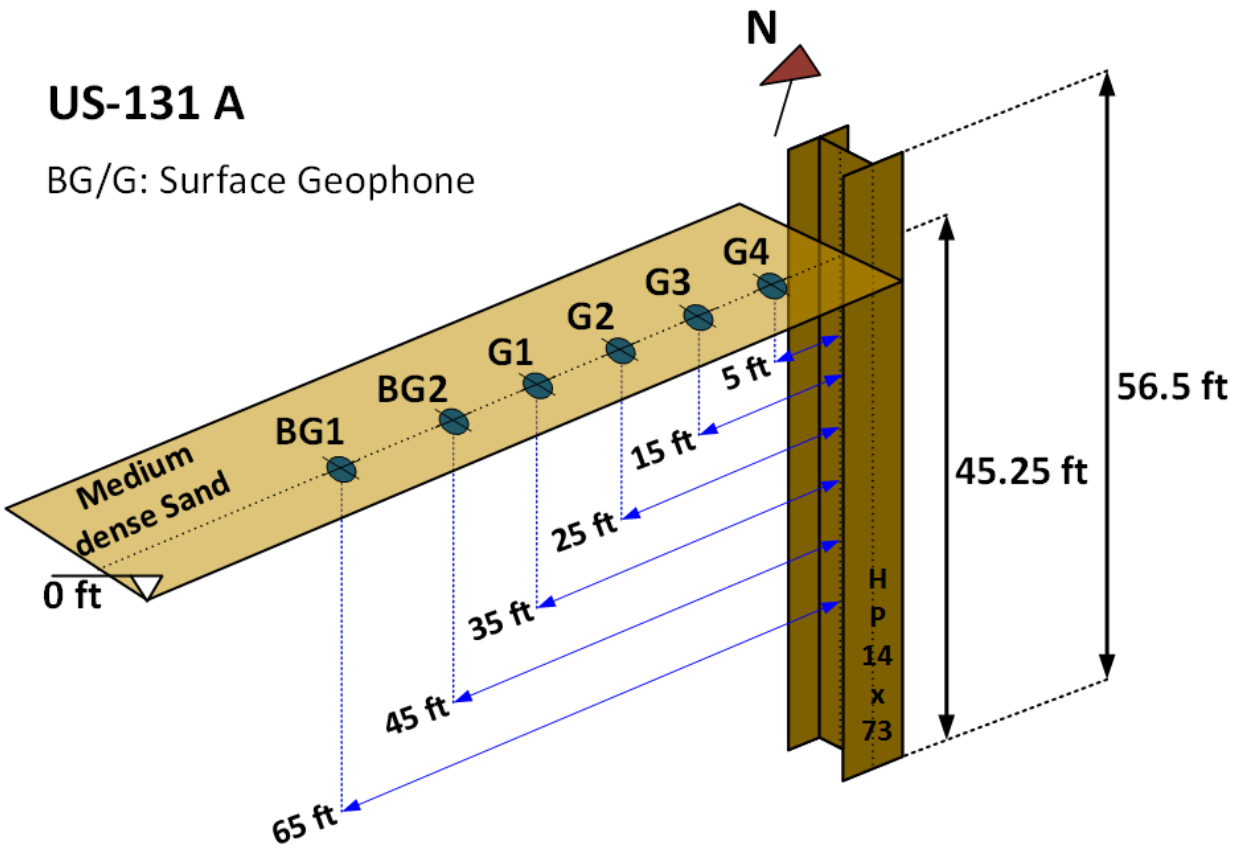

Figure 6-110 Perspective view of surface sensors at US-131 A site, Pile 18 (not to scale)

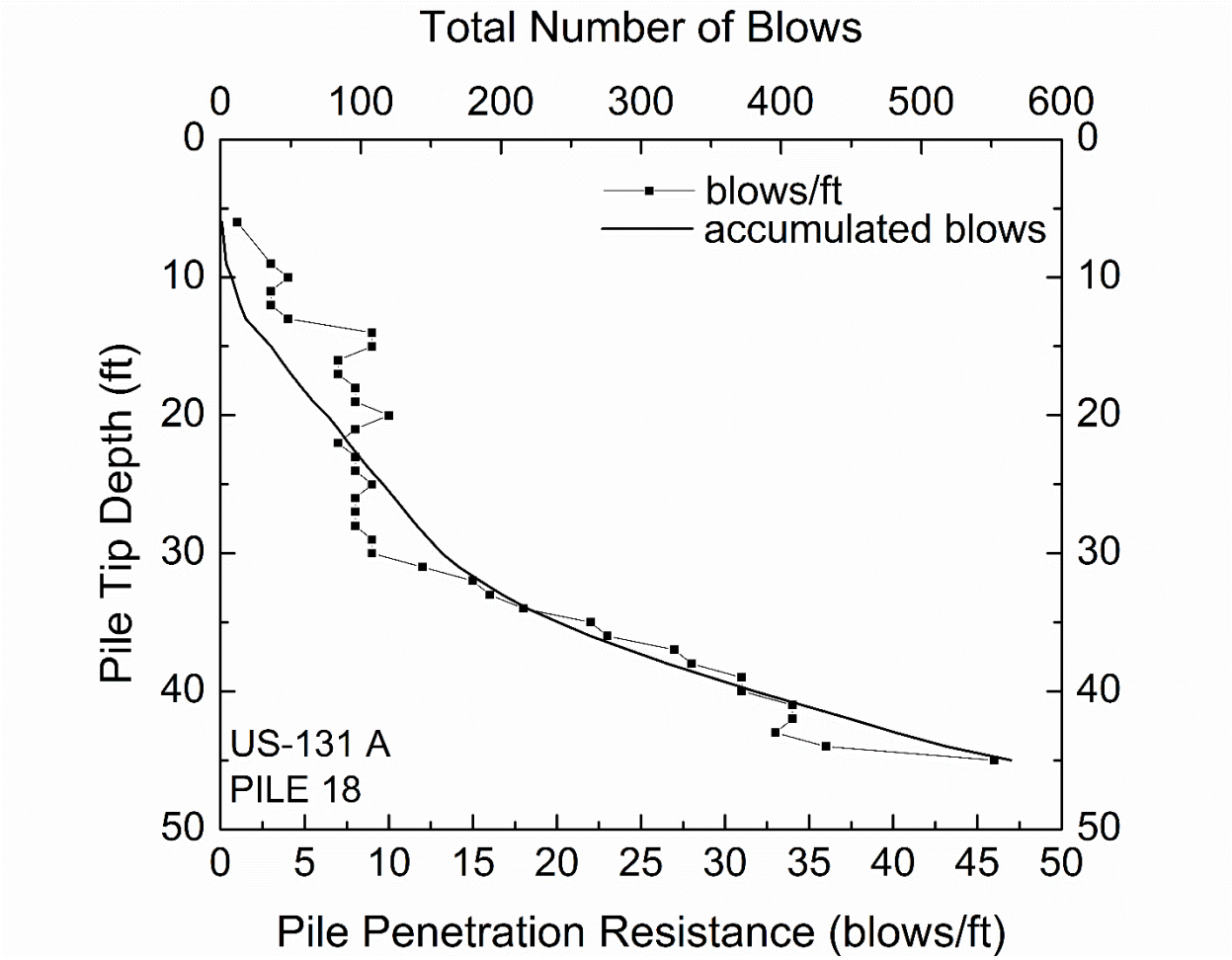

Figure 6-111 Driving Resistance and accumulated blows with depth – US-131 A site, Pile 18

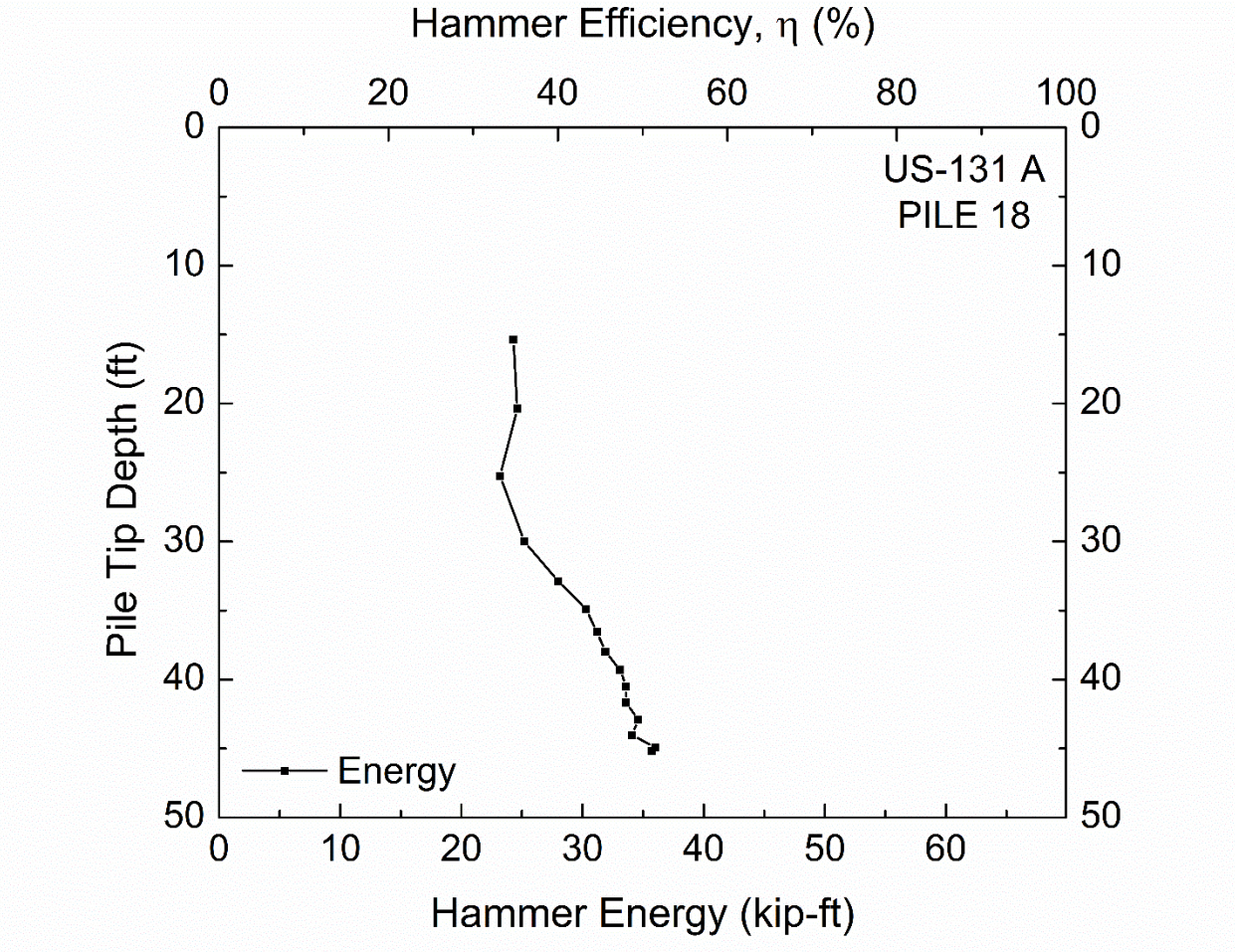

Figure 6-112 Hammer Energy and Hammer Efficiency with depth – US-131 A site, Pile 18

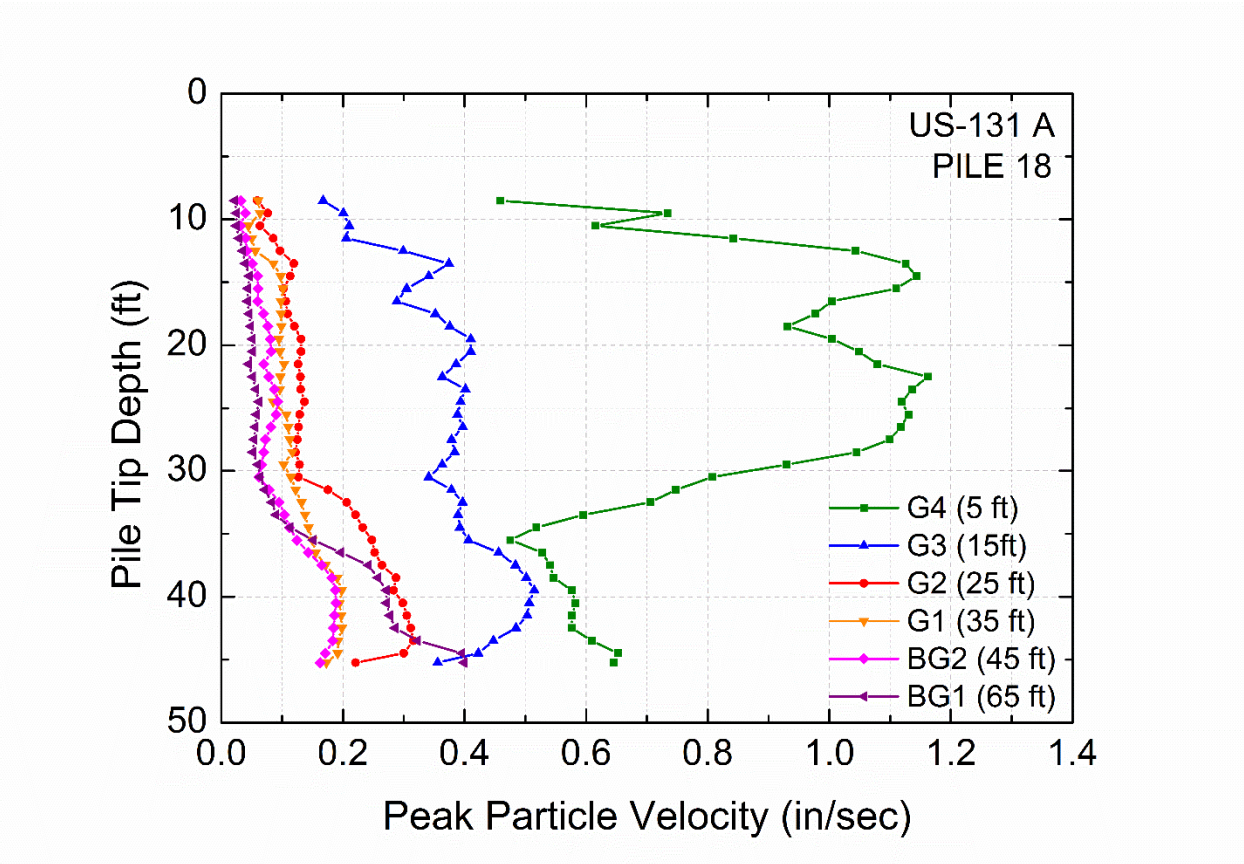

Figure 6-113 Peak Particle Velocity of surface geophones at US-131 A site – Pile 18, Vertical Direction

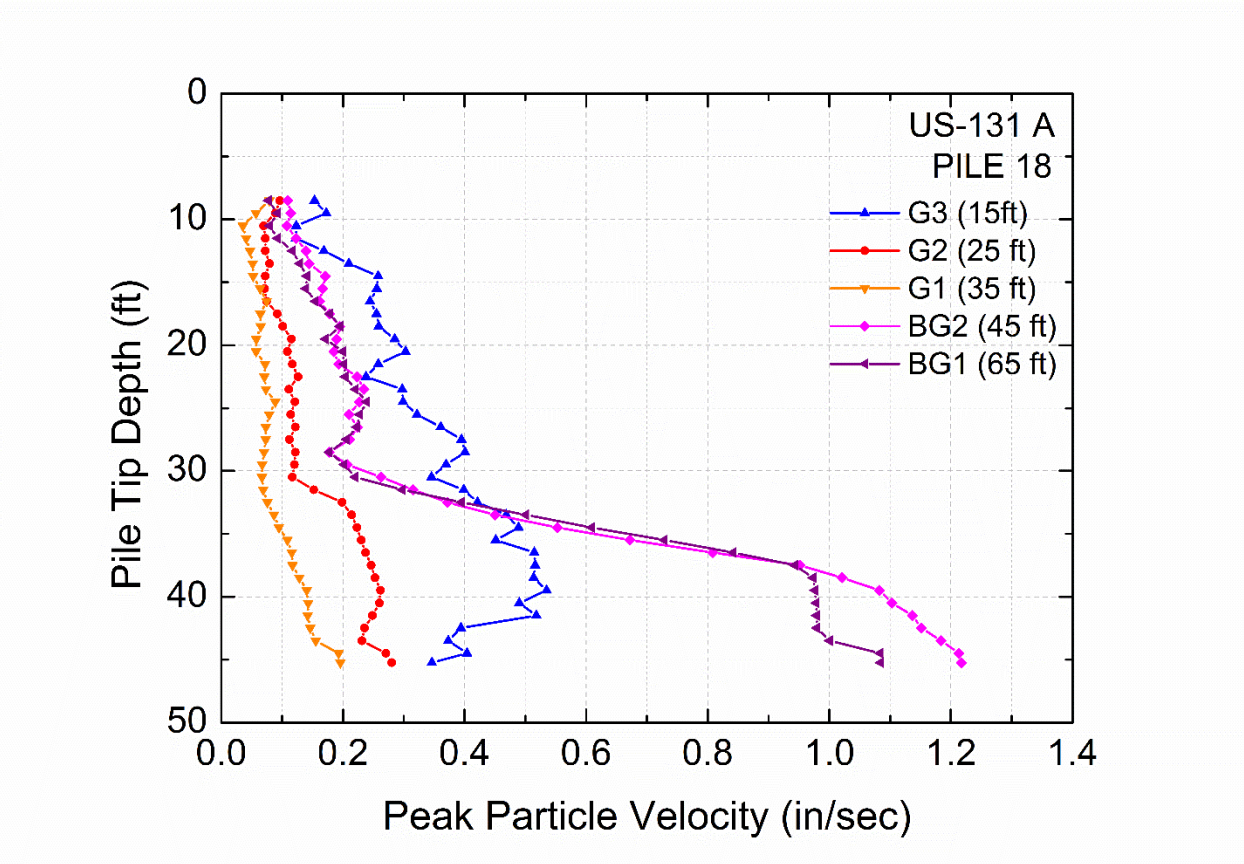

Figure 6-114 Peak Particle Velocity of surface geophones at US-131 A site – Pile 18, Longitudinal Direction

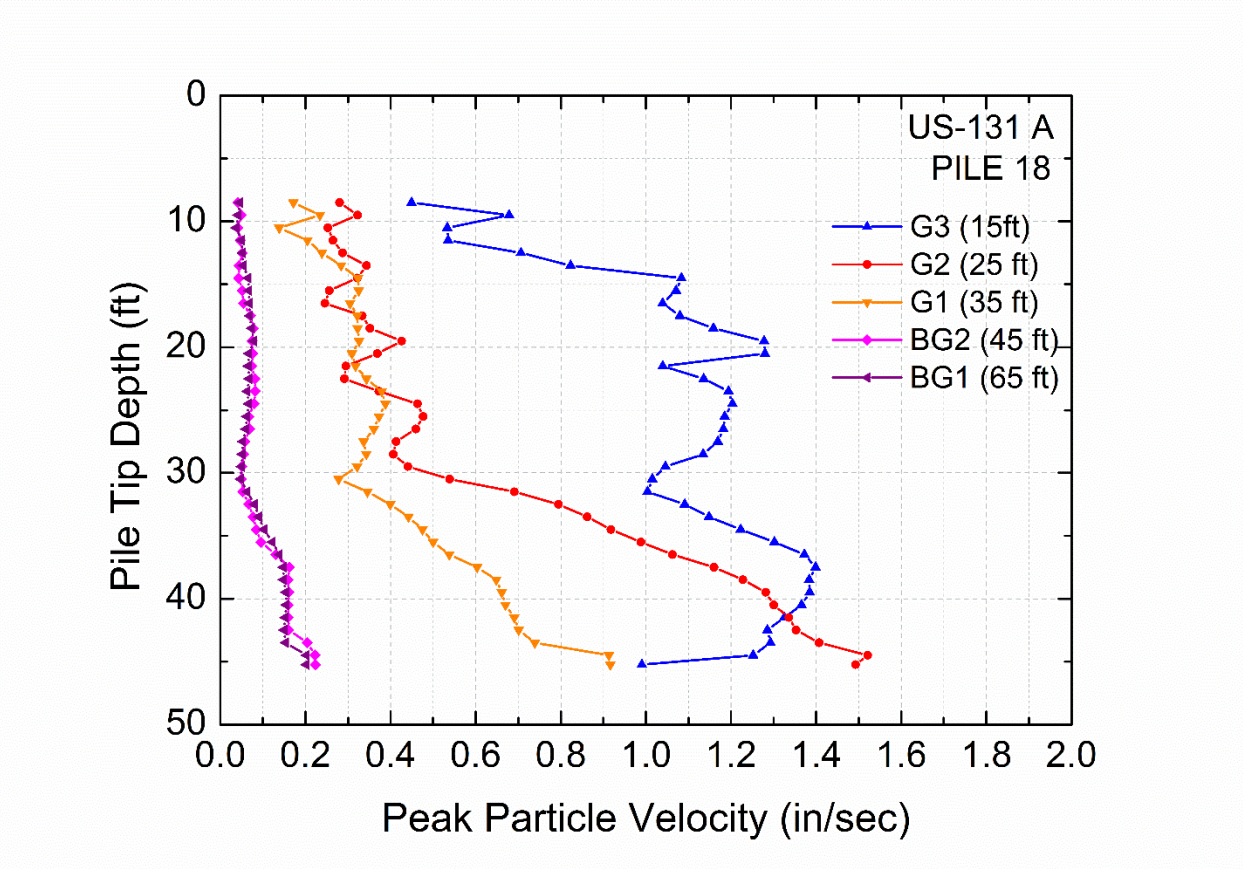

Figure 6-115 Peak Particle Velocity of surface geophones at US-131 A site – Pile 18, Transverse Direction

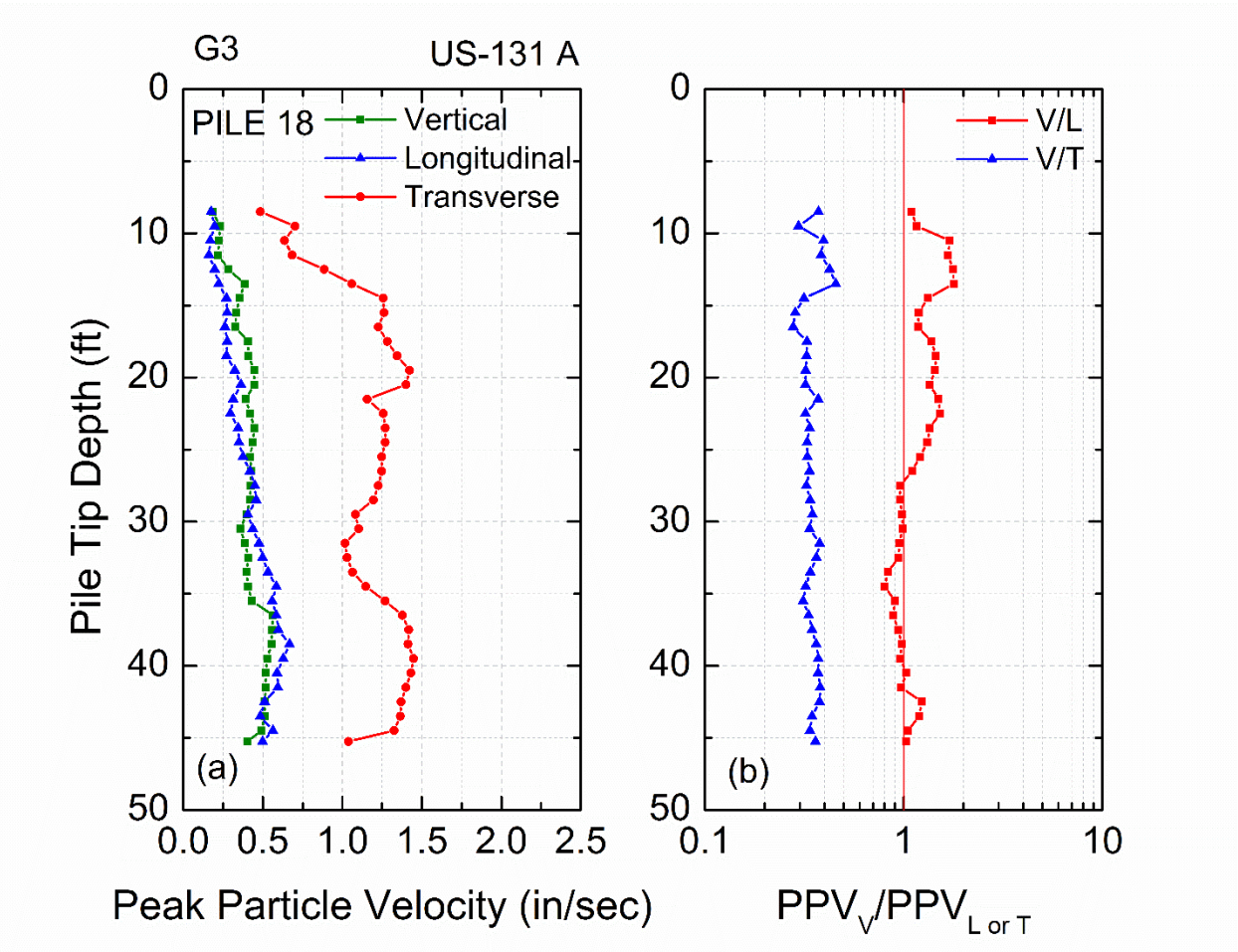

Figure 6-116 (a) Peak Particle Velocities of three directions of sensor G3 and (b) vertical to longitudinal and vertical to transverse components of PPV– US-131 A site, Pile 18

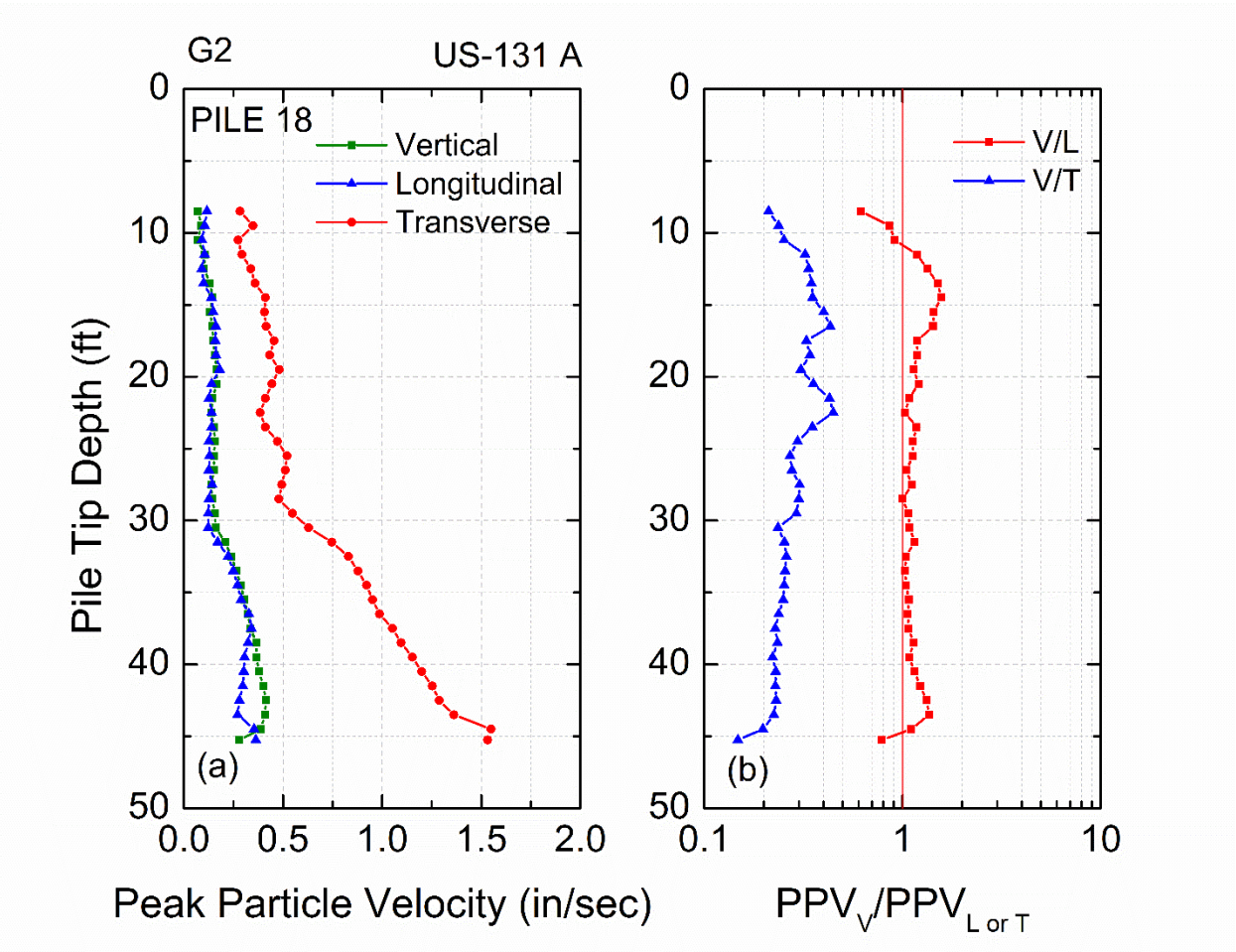

Figure 6-117 (a) Peak Particle Velocities of three directions of sensor G2 and (b) vertical to longitudinal and vertical to transverse components of PPV– US-131 A site, Pile 18

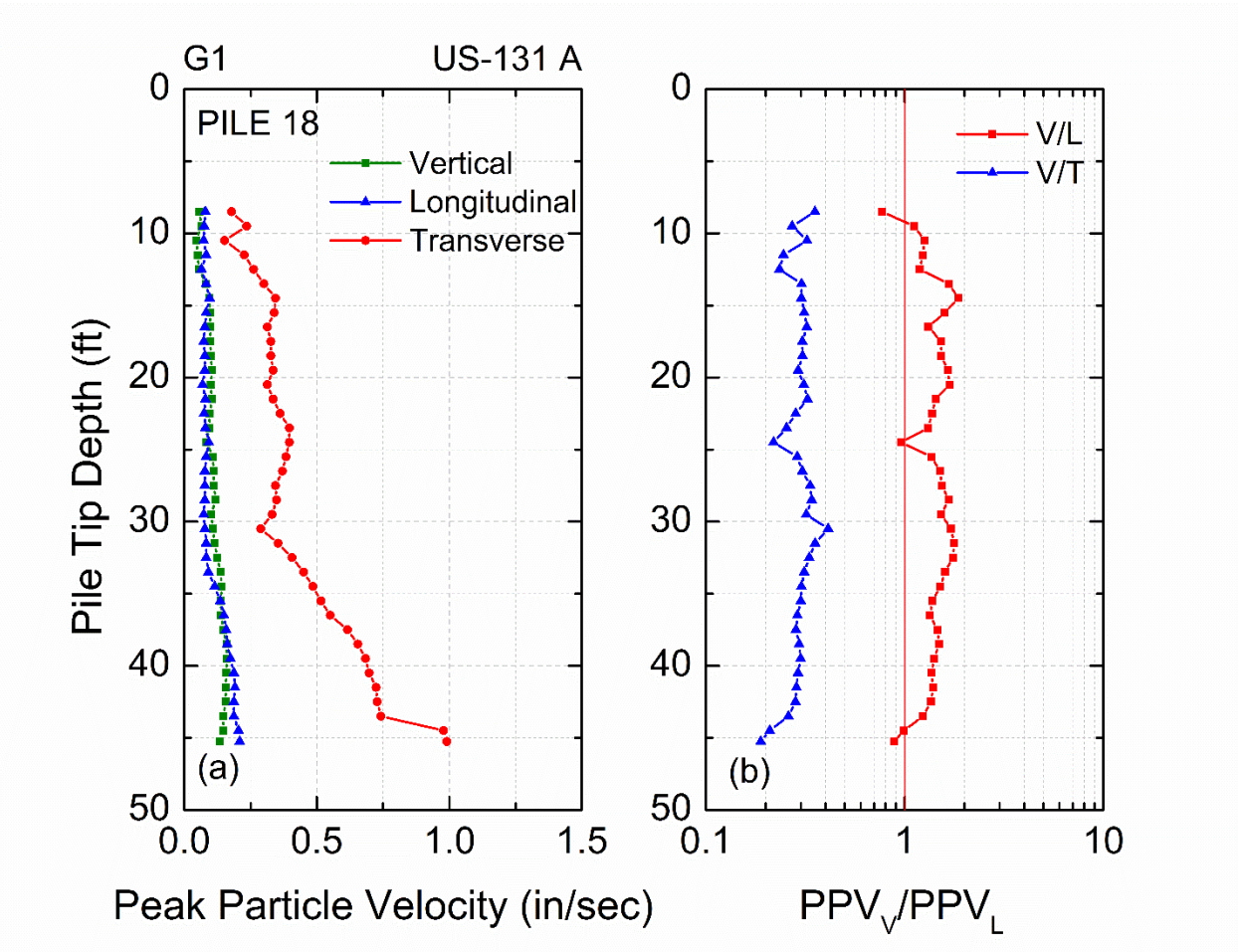

Figure 6-118 (a) Peak Particle Velocities of three directions of sensor G1 and (b) vertical to longitudinal and vertical to transverse components of PPV– US-131 A site, Pile 18

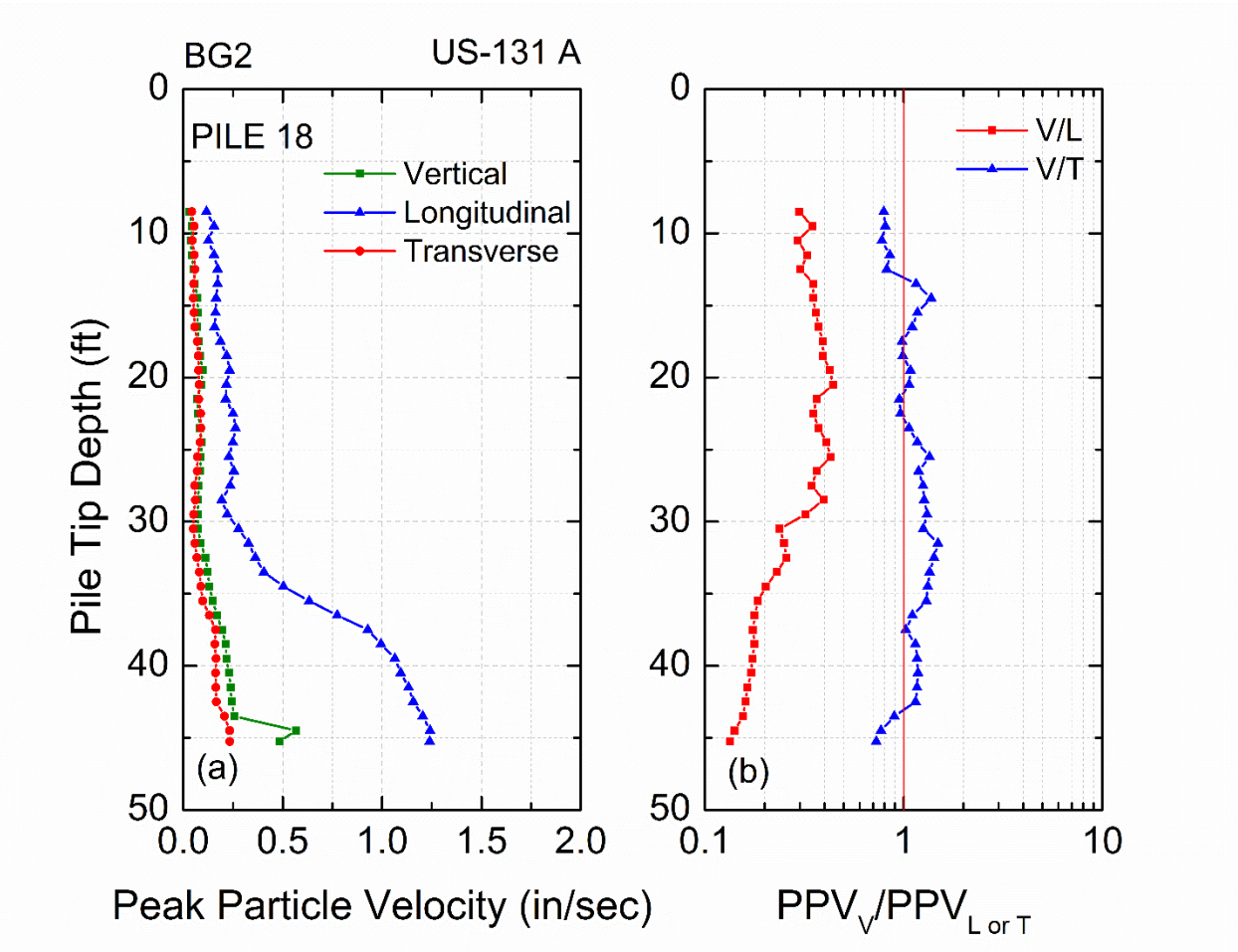

Figure 6-119 (a) Peak Particle Velocities of three directions of sensor BG2 and (b) vertical to longitudinal and vertical to transverse components of PPV– US-131 A site, Pile 18

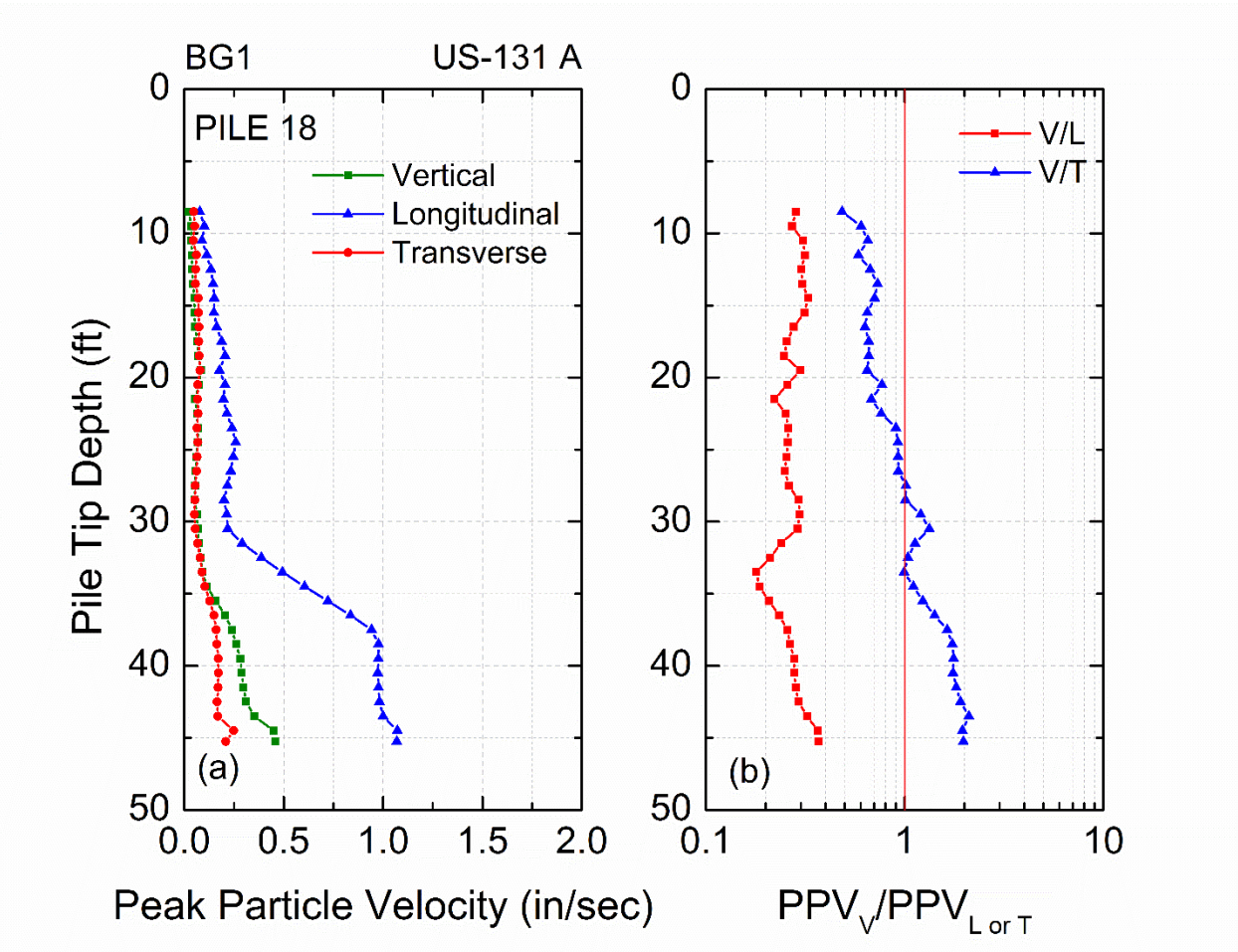

Figure 6-120 (a) Peak Particle Velocities of three directions of sensor BG1 and (b) vertical to longitudinal and vertical to transverse components of PPV– US-131 A site, Pile 18

6.3.2.3 Monitoring for surface settlement due to pile driving at US-131 A site

Two control points and one benchmark were established on the abutment A of site US-131 to monitor settlement around the pile driving area of the two tested piles. Control and mapping of this task was performed by the Michigan Department of Transportation Survey Unit. Differential leveling, Global Positioning System (GPS) and Total Station coverage were employed. The initial survey took place after the embedded sensors were installed and soil monitoring was conducted right after the end of driving pile 1 and pile 18. A Digital Terrain model (DTM) was created form the observed points which were compared to the base line DTM. Results from the observed points with distances from the pile centerline and the change in elevation are provided in Appendix F, for both test piles. Figure 6-121 shows a schematic of the triangle network of the points shot, after the end of driving piles 1 and 18. The maximum settlement after driving pile 1 was found to be 1.73 ft at 0.90 ft horizontal distance from the centerline of the pile. The maximum settlement after driving pile 18 was 1.35 ft and coincided with the pile centerline. Settlement was found to be a function of distance from the centerline of the pile; elevation change was negligible at a distance of around 20 ft from both piles. However, we should keep in mind that this survey was conducted after driving two piles, thus the affected area would extend further after driving all 54 piles planned for abutment A.

Figure 6-122 shows abutment A after the end of driving pile 1 and pile 18. In Figure 6-123 a close-up view of pile 1 after the end of driving and the observed settlement around the pile centerline are clearly shown. Figure 6-124 and Figure 6-125 present settlement contours after driving pile 1 and pile 18, respectively. The triangle indicates the pile location and the contour interval is 0.1 ft.

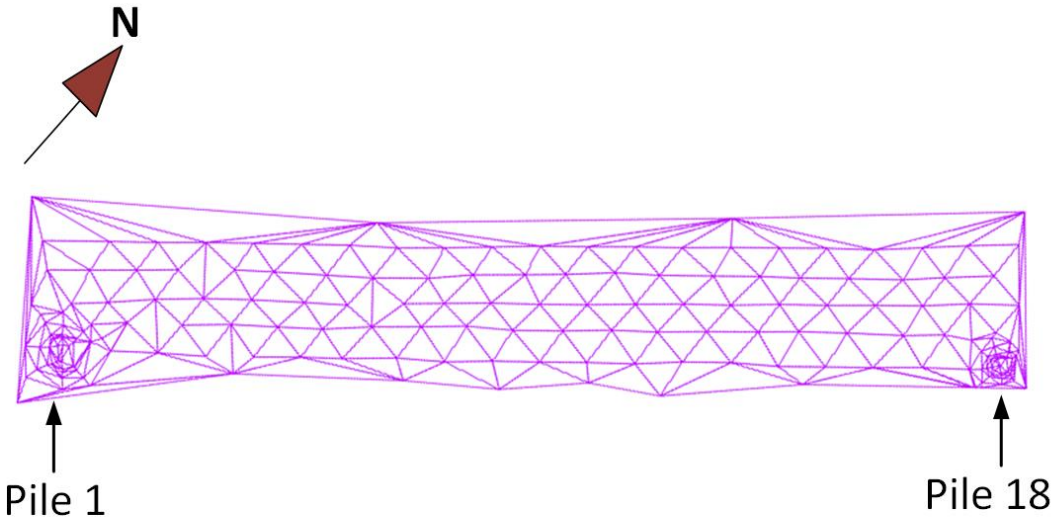

Figure 6-121 Triangle network of the points shot after driving pile1 and pile 18 at US-131 A site

Figure 6-122 Abutment A after the end of driving pile 1 (front) and pile 18 (back)

Figure 6-123 Settlement around pile 1 after the end of driving at US-131 A site

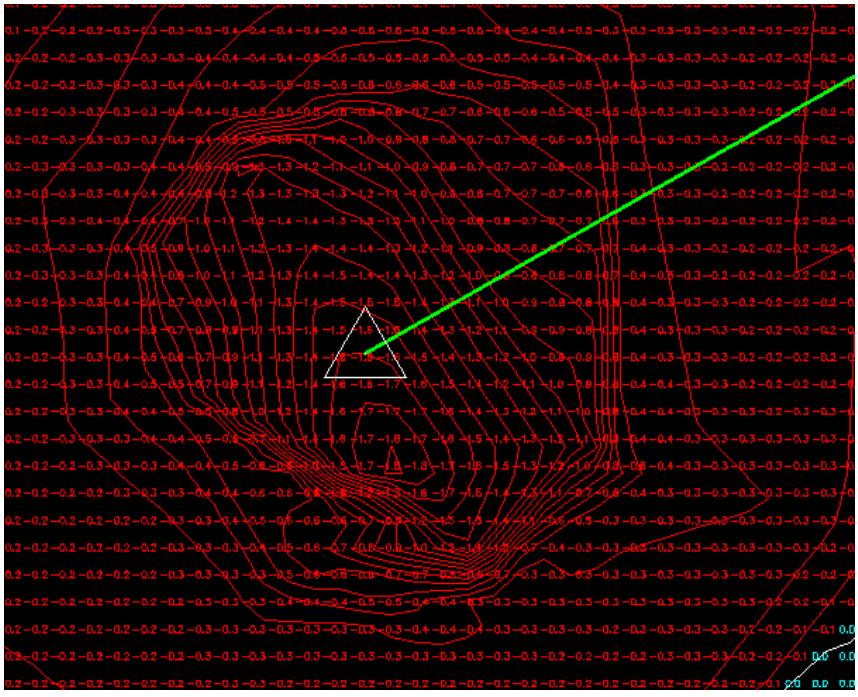

Figure 6-124 Settlement contours after driving Pile 1

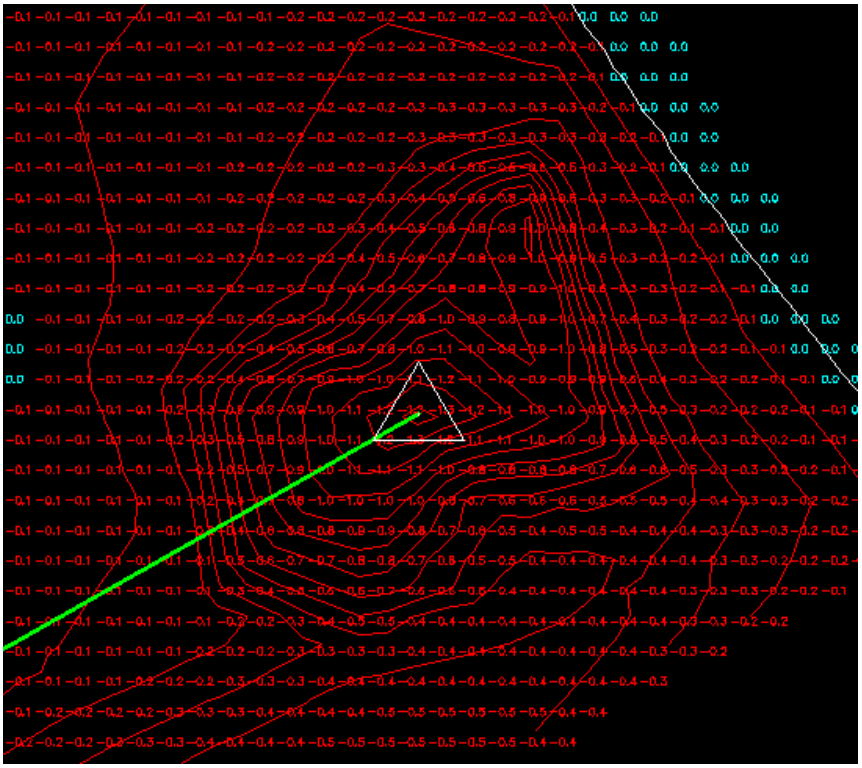

Figure 6-125 Settlement contours after driving Pile 18

6.3.3 US-131 B Site

6.3.3.1 Test Pile 54

Ground vibration monitoring was performed during driving two test piles at abutment B of US-131 site near Constantine, MI. A trench was prepared by the contractor for driving the piles. At this site an attempt was made to determine if there was any difference between energy transfer from the pile to the surrounding soil from the open face of the H-pile and the flange face of the H-pile. A perspective view of the in-depth sensor locations close to pile 54 is shown in Figure 6-126. Sensors were pushed into the hard clay deposit and into the shallower medium dense sand layer, in both the open face and flange face of the pile. The pile was accidentally driven askew of the intended orientation, which resulted to loss of the two close-in sensors from the open face of the pile (not shown in Figure 6-126), as the pile damaged the sensor package and/or cable while penetrating the ground.

A 64.5 ft long HP 14x73 pile was driven using a Delmag D30-32 diesel hammer. The final depth of penetration of the pile was 53.25 ft. Figure 6-127 presents the pile driving penetration resistance as the number of blows per pile foot increment and the accumulated number of blows versus depth of pile tip penetration. The total blow count to drive pile 54 was 793, almost twice the number that it took to drive pile 1 at US-131 A site with the same hammer. The driving resistance gradually increased with increasing penetration depth, with a higher increase rate when the pile tip entered the clay layer at 30 ft. Figure 6-128 illustrates the average actual hammer energy per pile foot increment and the hammer efficiency, η, versus depth. The rated energy of the Delmag D30-32 hammer is 75,970 lb-ft. The average hammer efficiency when driving pile 54 was around 39%.

Figure 6-129 and Figure 6-130, show the vertical peak particle velocity amplitudes versus depth for the shallow and deep set of sensors, respectively. For the shallow array of sensors, amplitudes increase as the pile tip approaches the sensor elevation with the trend being more obvious for the closest sensor to the pile (SG2). An increase in velocity values is observed at 30 ft depth where the pile enters the hard clay layer and around a

depth of 40 ft when the very dense silt starts in the soil profile (Figure 6-30). In addition, the SPT blow counts increased markedly at these two elevations, whereas a sharp increase in driving resistance can be seen in Figure 6-127. Accelerometer A3 and SG4 were pushed at approximately the same depth and distance from the pile and were compared for consistency. The vibration pattern of these sensors is very similar.

For the deep set of sensors, the amplitudes increased sharply when the pile tip reached the sensor depth. Also, sensor SG1 placed in the clay layer recorded twice as much particle velocities compared to sensor SG2 in the sand deposit and at approximately the same distance from the pile. The same response is observed for the second sensor in the array from the pile (SG3), which had double the values of peak particle velocity in comparison with sensor SG4 located at the shallow sand layer. Another important finding is observed when comparing the response of sensors A4 and SG3. Sensor A4 was pushed in front of the open face of the pile, while sensor SG3 was located on the side of the flange face of the pile at approximately the same distance and depth. Inspection of their signals in Figure 6-130, reveals that they follow the same trend. This observation strengthens the hypothesis that there is no significant difference between the energy transfer from the flange and the open face of the H pile.

Figure 6-131 presents vertical particle velocities versus diagonal distance, for the shallow set of sensors into the sand layer. When the pile tip reaches the sensor depth and continues below, the shaft has the primary contribution to the ground motion of the sensor and continues to have influence for the remainder of driving while the tip is getting further from the sensor and having lesser influence at the sensor. Sensors A3 and SG4 were located at the same horizontal distance from the pile (2 ft), at depths of 14.25 ft and 16.25 ft, respectively. As expected, their response is similar in terms of peak particle velocities. Figure 6-132 and Figure 6-133 show acceleration amplitudes recorded by sensor A3 for the longitudinal and transverse directions, respectively. Similar vibration trends are captured as for the vertical motions.

Figure 6-134 to Figure 6-136 show vibration amplitudes versus diagonal distance for the deep set of sensors, SG1, SG3 and A4, respectively. In all cases, when the pile tip is above the sensor, the ground motion amplitudes slowly increase with pile tip depth. As

the pile tip reaches the depth of the sensors, there are greater increases in particle velocities and the behavior is intense for all three sensors. The vibration levels after the tip passes the elevation of the sensors stay relative constant for the closest sensor to the pile face (SG1), while they rise and consequently reach constant values for the two sensors further away from the pile (A4 and SG3). This phenomenon may be attributed to the fact that the contribution of the spherical wave captured by the closest sensor (SG1) diminishes very fast compared to the furthest sensors from the pile. This behavior will be studied further from ground motions recorded in the laboratory tests. Figure 6-137 depicts vertical peak particle velocities versus the resultant distance for the three deep sensors. It is interesting to notice again, that sensors A4 and SG3 were located at approximately the same depth (~30.5 ft), with A4 at an horizontal distance of 1.94 ft from the open face of the pile and SG3 at an horizontal distance of 2.5 ft from the flange face of the pile. As seen in Figure 6-137, the two sensors have almost identical response; there is some scatter in the data of A3 but this is due to the integration of the accelerations to velocities. Figure 6-138 and Figure 6-139 show acceleration amplitudes recorded by sensor A4 for the longitudinal and transverse directions, respectively. Similar vibration trends are captured as for the vertical motions. For the horizontal directions, when the pile tip descends below the sensor depth there is initially a rise in acceleration amplitudes which is followed by a decrease when the pile tip is getting further from the sensor.

Twelve ground surface geophones were also placed along the ground surface at the locations shown in Figure 6-140. The two closest geophones (BG1 and BG2) were triaxial configurations, while geophones G1 to G3 had single components of vertical, longitudinal and transverse axes and the further out (G4) was single vertical component geophone. The peak particle velocities of the sensors versus depth are plotted in Figure 6-141 to Figure 6-143. There is an increase in the amplitudes when the pile enters the hard clay layer around 30 ft depth for all three directions. In addition, it is observed that after 30 ft some of the farthest sensors recorded higher amplitudes than the closest to the pile (BG1) for the longitudinal and transverse components.

Figure 6-144a to Figure 6-148a show the three velocity components versus depth and Figure 6-144b to Figure 6-148b show the ratios of vertical to longitudinal (V/L) and vertical to transverse (V/T) components for sensors BG1, BG2, G1, G2 and G3, respectively. The transverse component had higher amplitudes for all the sensors, with the trend being more obvious for the three sensor further away from the pile (G1, G2 and G3). The vertical to longitudinal or transverse component is either very close to one or less than one, contradicting the theory that the vertical component motion has always the greatest amplitude.

Two sensors were located at the same radial distance from the pile (6.5 ft); G4 geophone was positioned on the surface and SG5 geophone was pushed into a sand layer at a depth of 18.5 ft. Figure 6-149 shows vertical peak particle velocities versus depth for the two sensors, along with the response of the second sensor (BG1) on the surface line array, 15 ft away from the pile. It is interesting to note, that the second surface geophone recorded higher amplitudes than the closest one to the pile. In addition, the buried geophone SG5 has approximately the same vibration amplitudes as geophone BG2. Higher ground motions are recorded when the pile tip encounters the hard clay layer, around 30 ft.

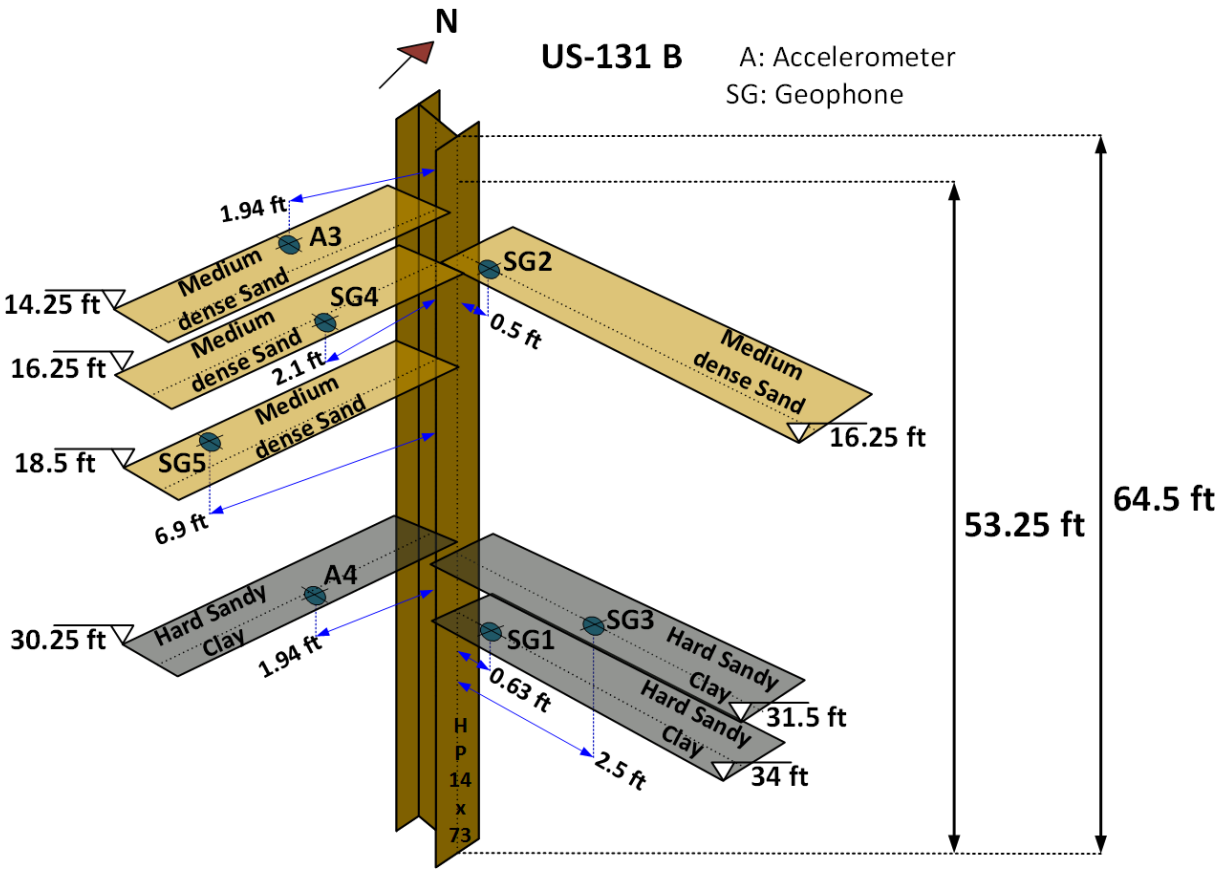

Figure 6-126 Perspective view of buried sensors at US-131 B site, Pile 54 (not to scale)

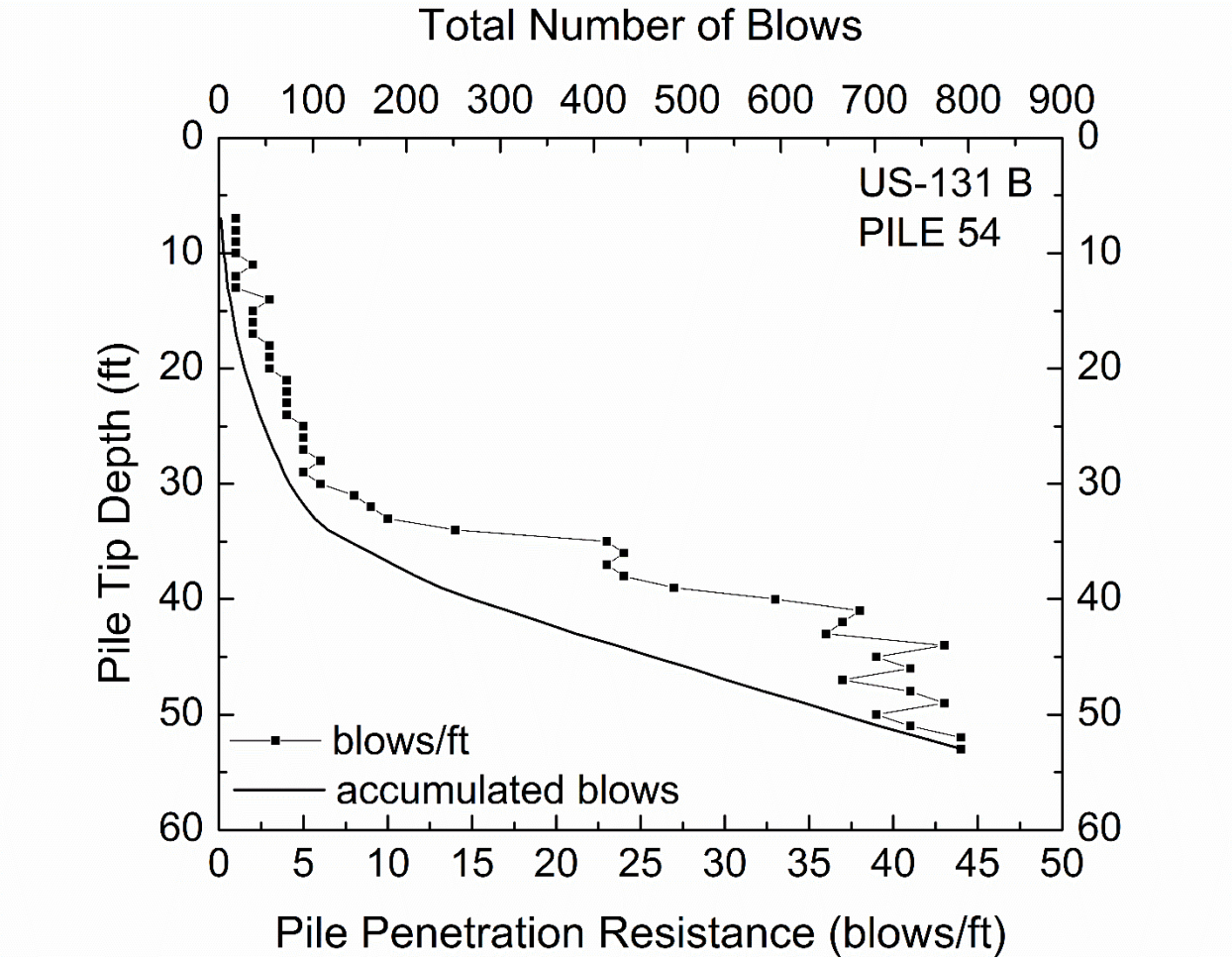

Figure 6-127 Driving Resistance and accumulated blows with depth – US-131 B site, Pile 54

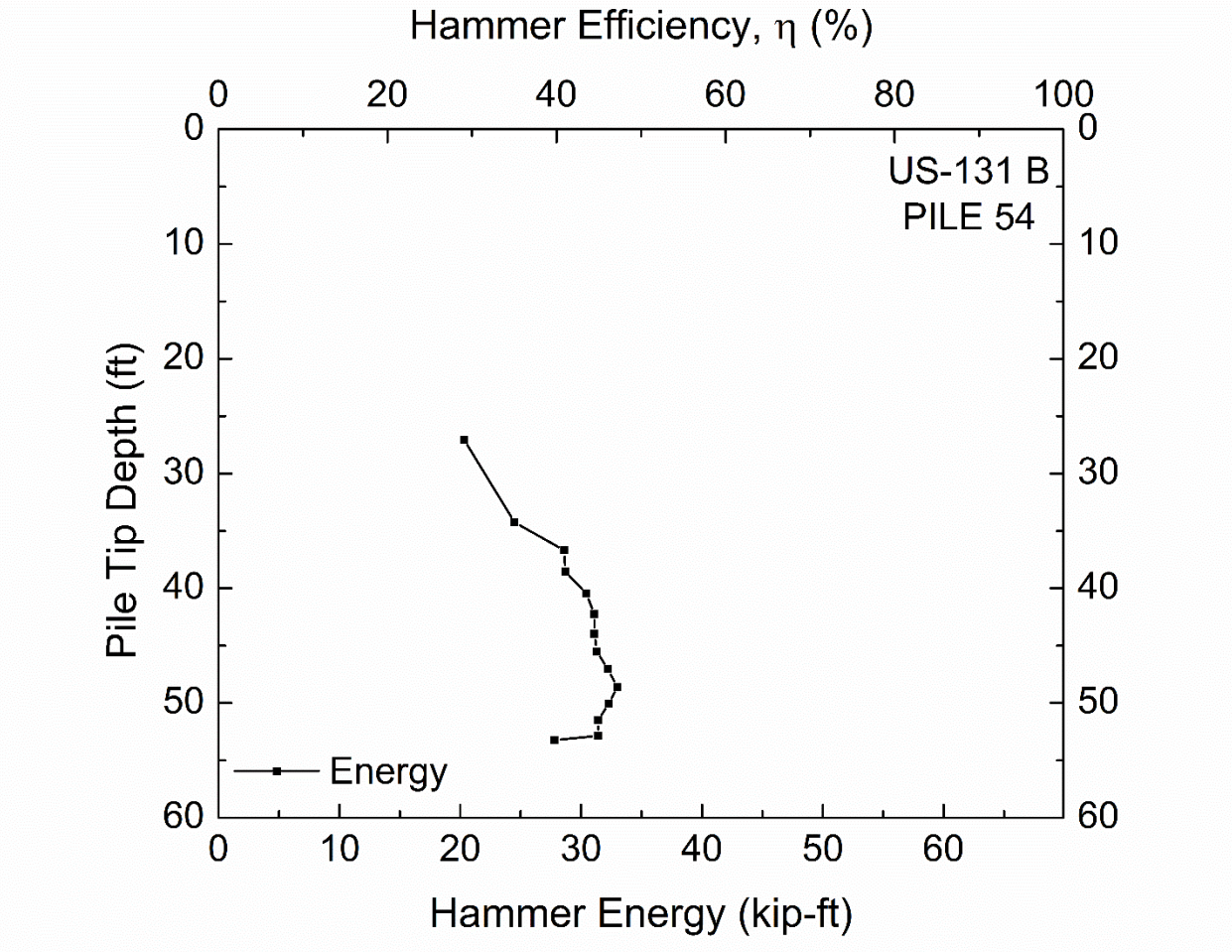

Figure 6-128 Hammer Energy and Hammer Efficiency with depth – US-131 B site, Pile 54

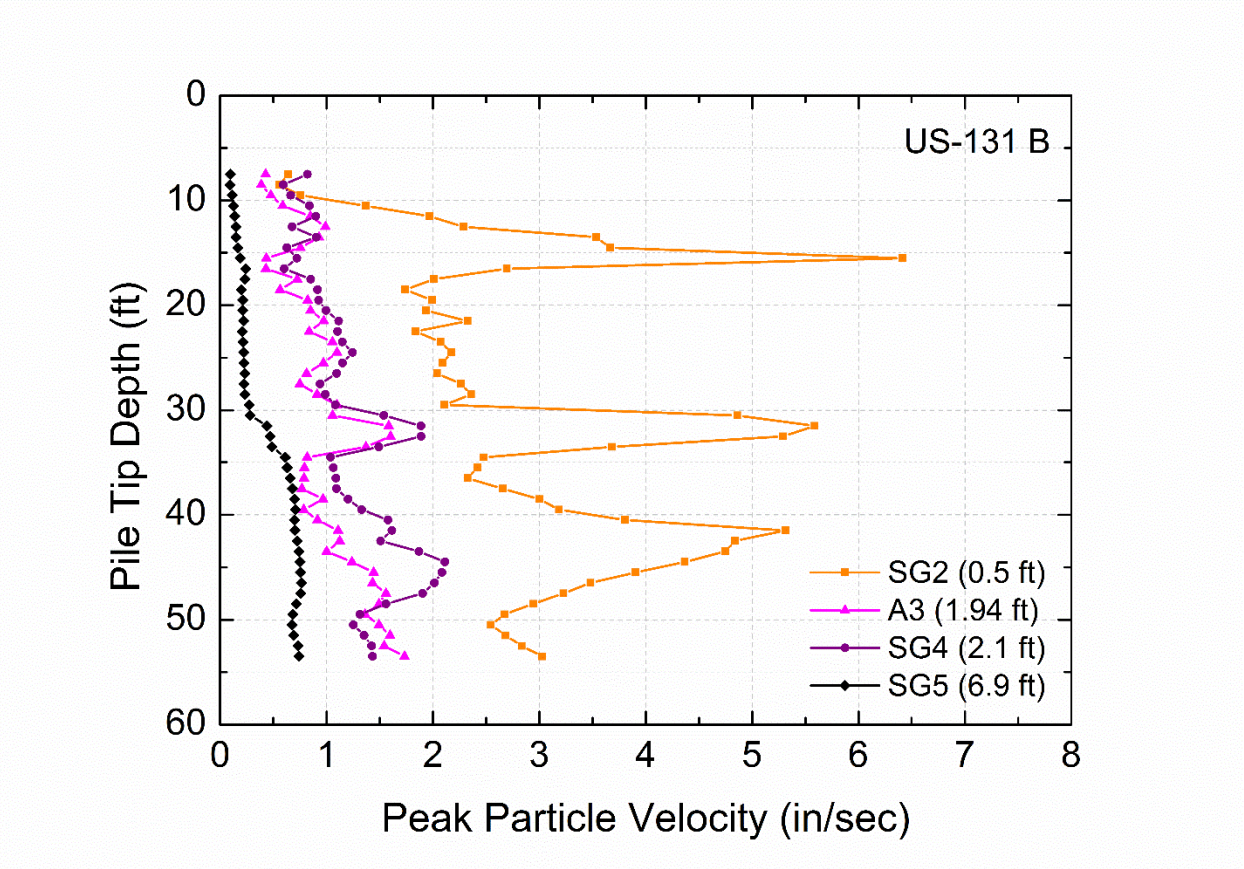

Figure 6-129 Peak Particle Velocity of shallow set of buried sensors at US-131 B site – Pile 54, Vertical Direction

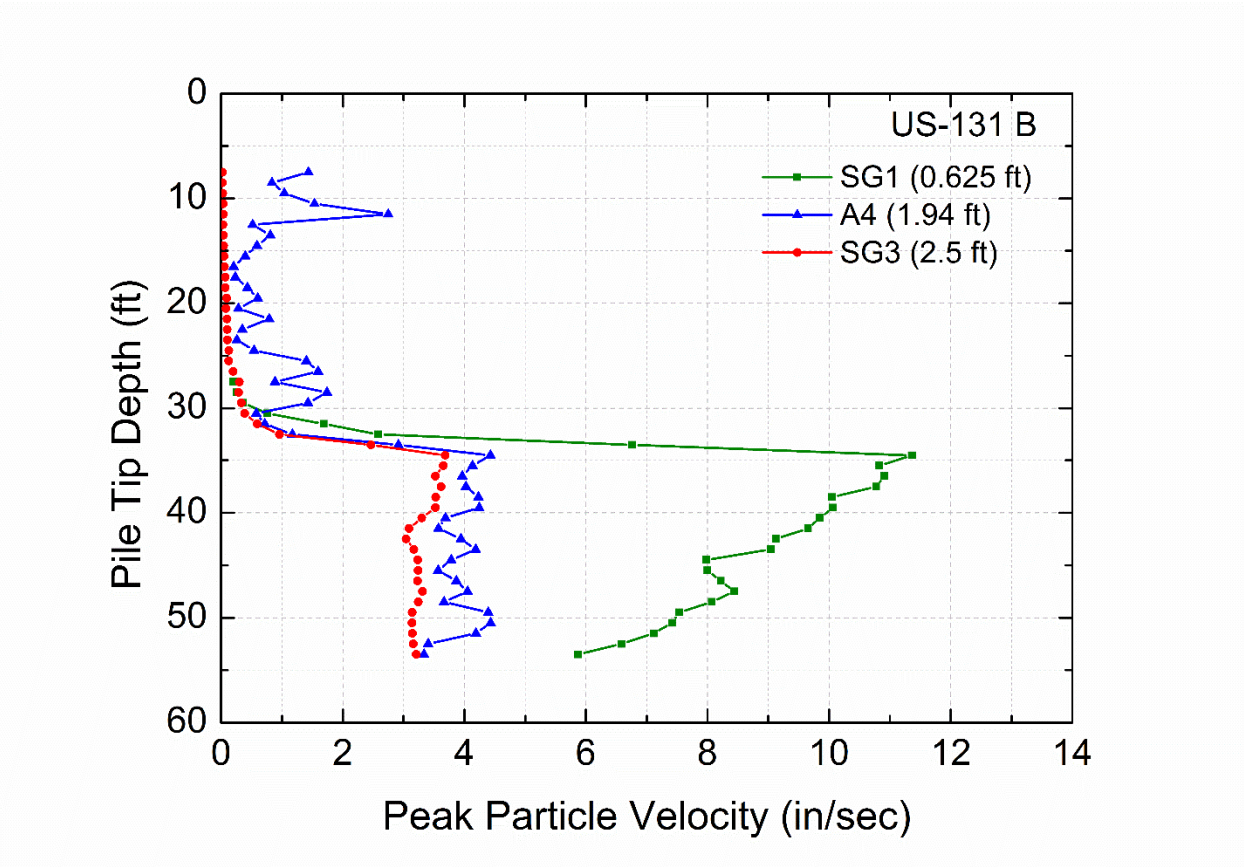

Figure 6-130 Peak Particle Velocity of deep set of buried sensors at US-131 B site – Pile 54, Vertical Direction

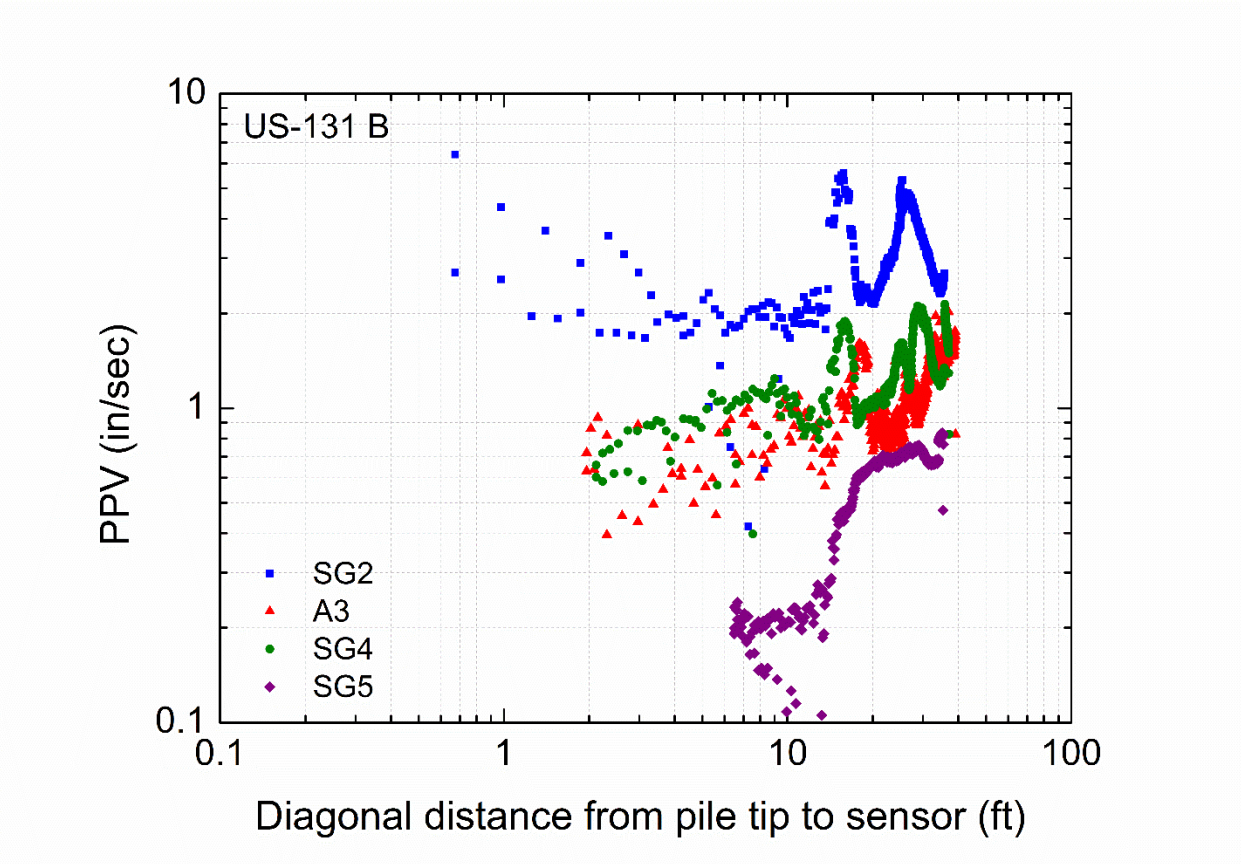

Figure 6-131 Peak particle velocity versus diagonal distance from pile tip to shallow set of sensors at US-131 B site, Pile 54 – Vertical direction, logarithmic scale

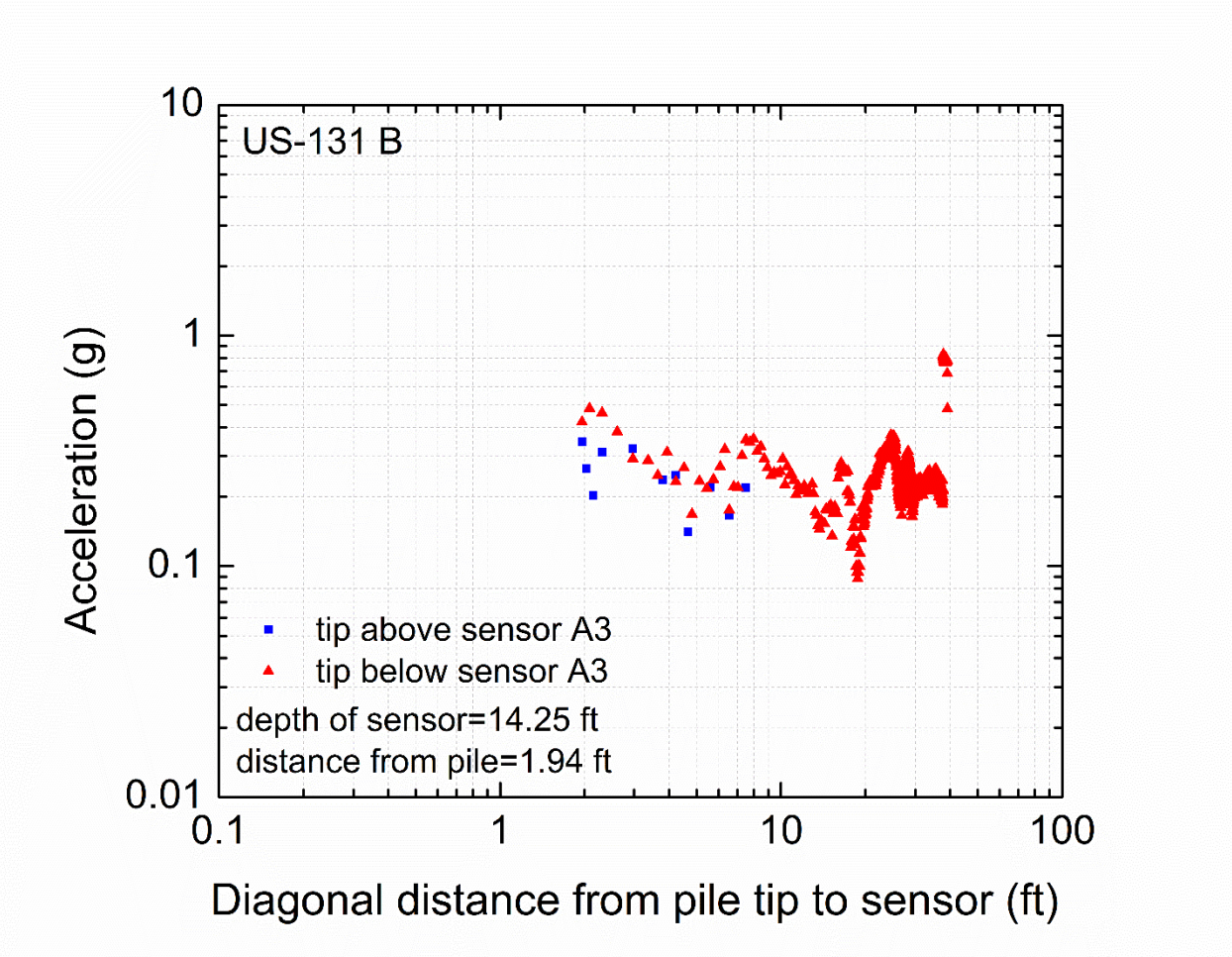

Figure 6-132 Acceleration versus diagonal distance from pile tip to sensor A3 at US-131 B site, Pile 54 – Longitudinal direction

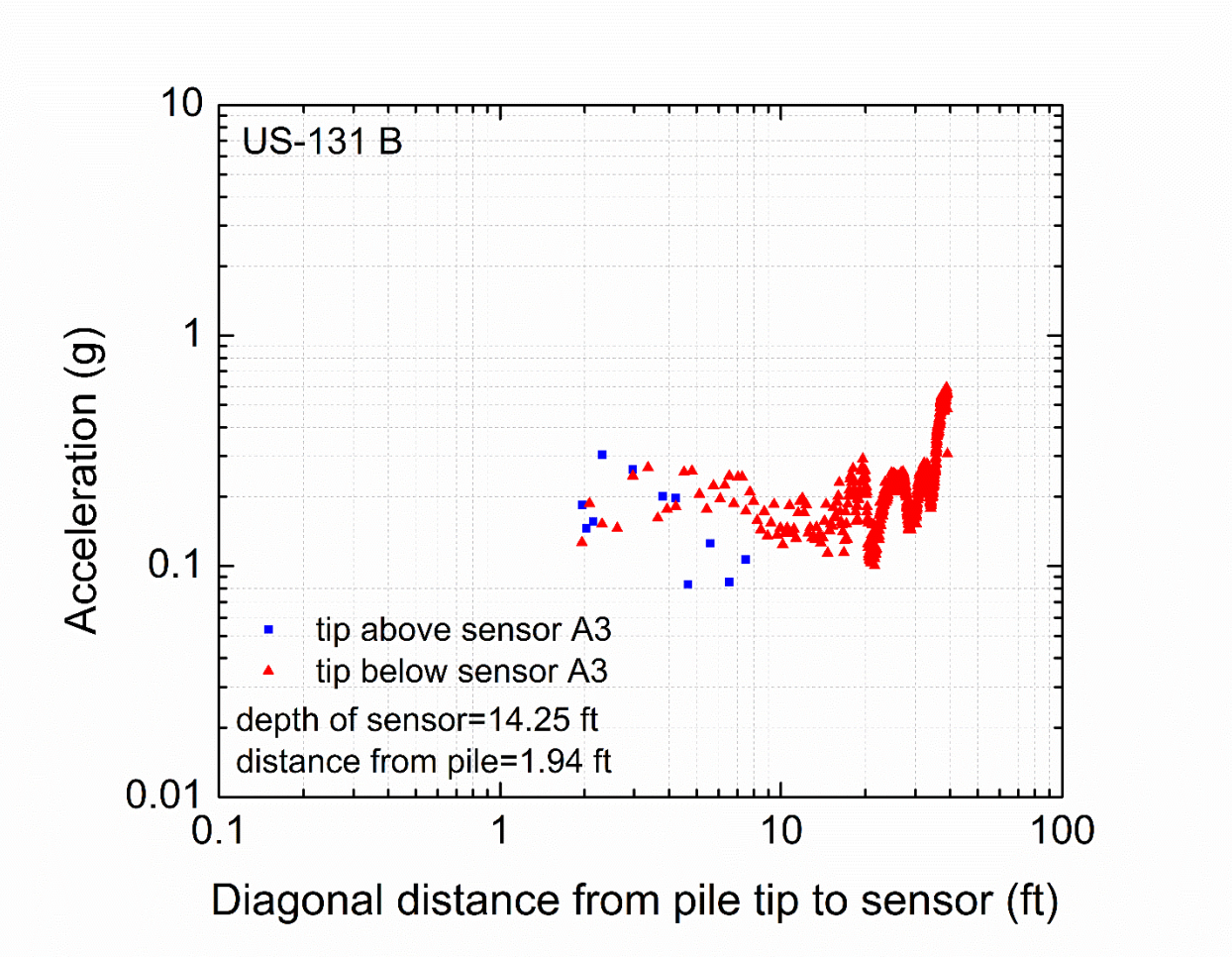

Figure 6-133 Acceleration versus diagonal distance from pile tip to sensor A3 at US-131 B site, Pile 54 – Transverse direction

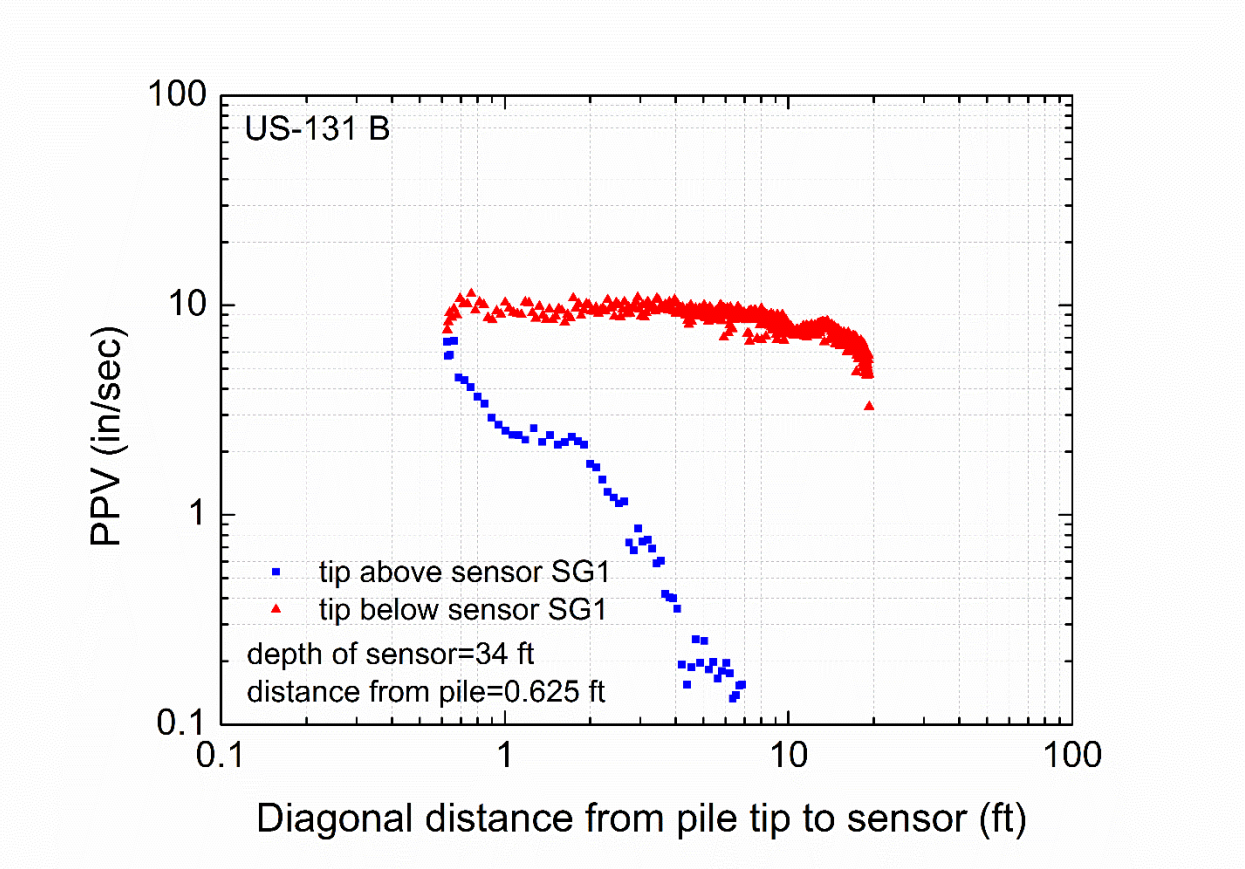

Figure 6-134 Peak particle velocity versus diagonal distance from pile tip to sensor SG1 at US-131 B site, Pile 54 – Vertical direction

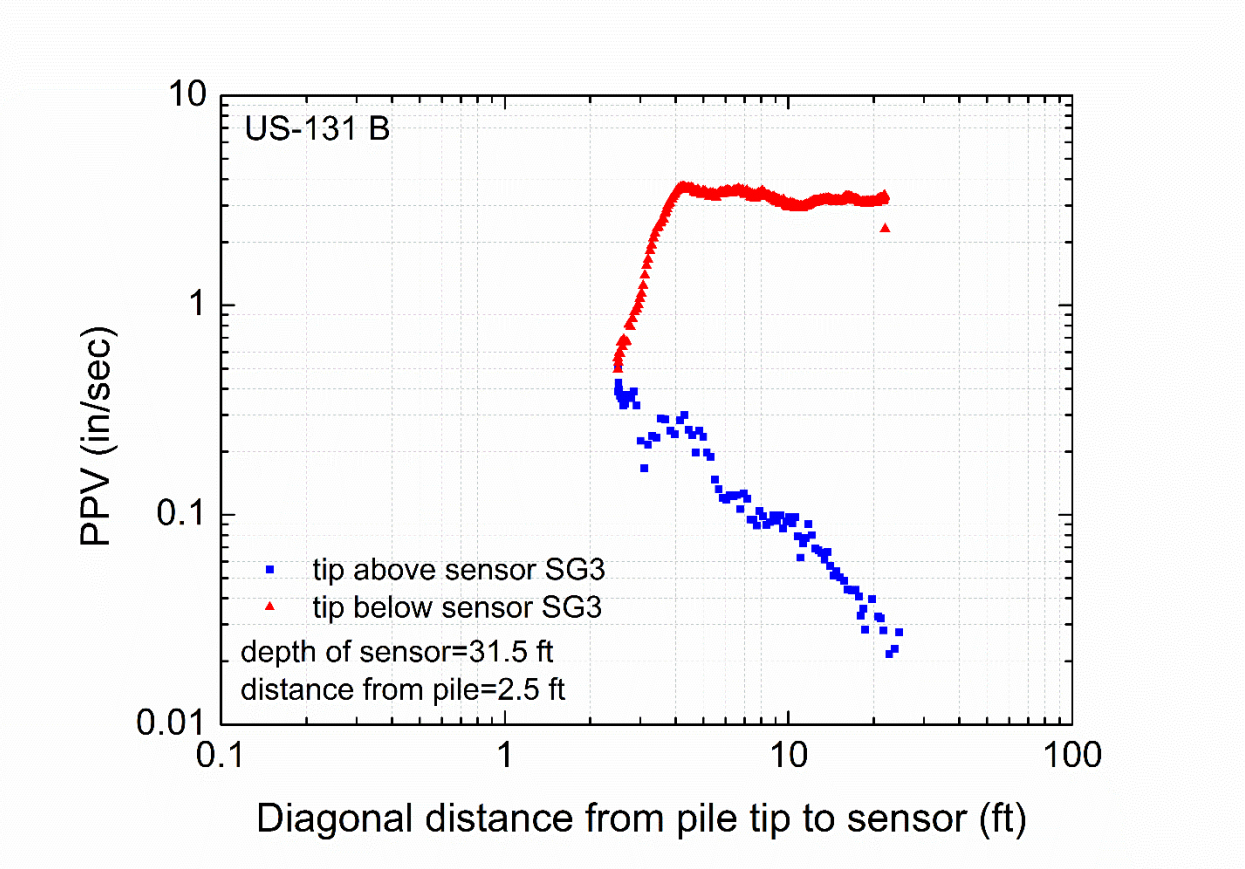

Figure 6-135 Peak particle velocity versus diagonal distance from pile tip to sensor SG3 at US-131 B site, Pile 54 – Vertical direction

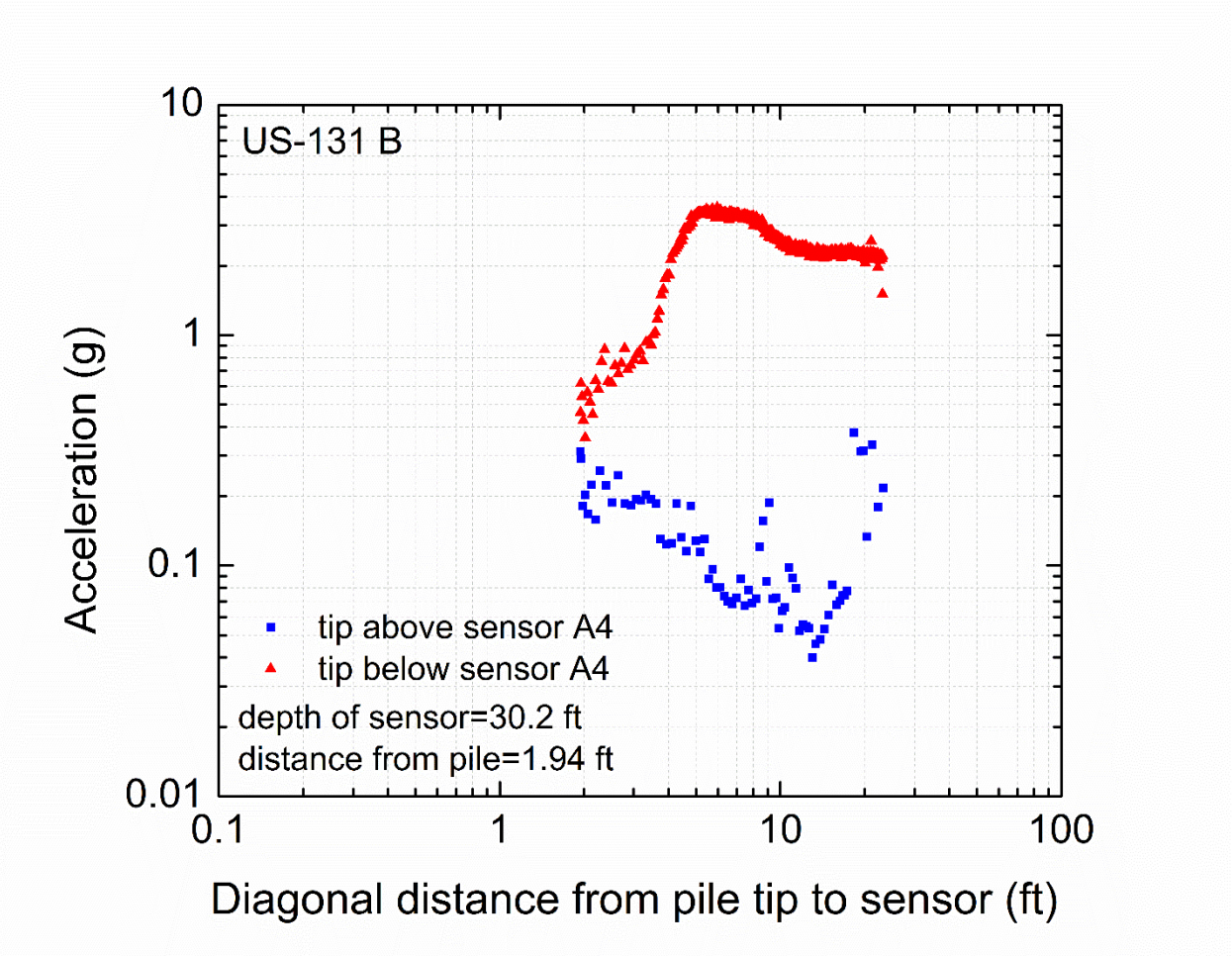

Figure 6-136 Acceleration versus diagonal distance from pile tip to sensor A4 at US-131 B site, Pile 54 – Vertical direction

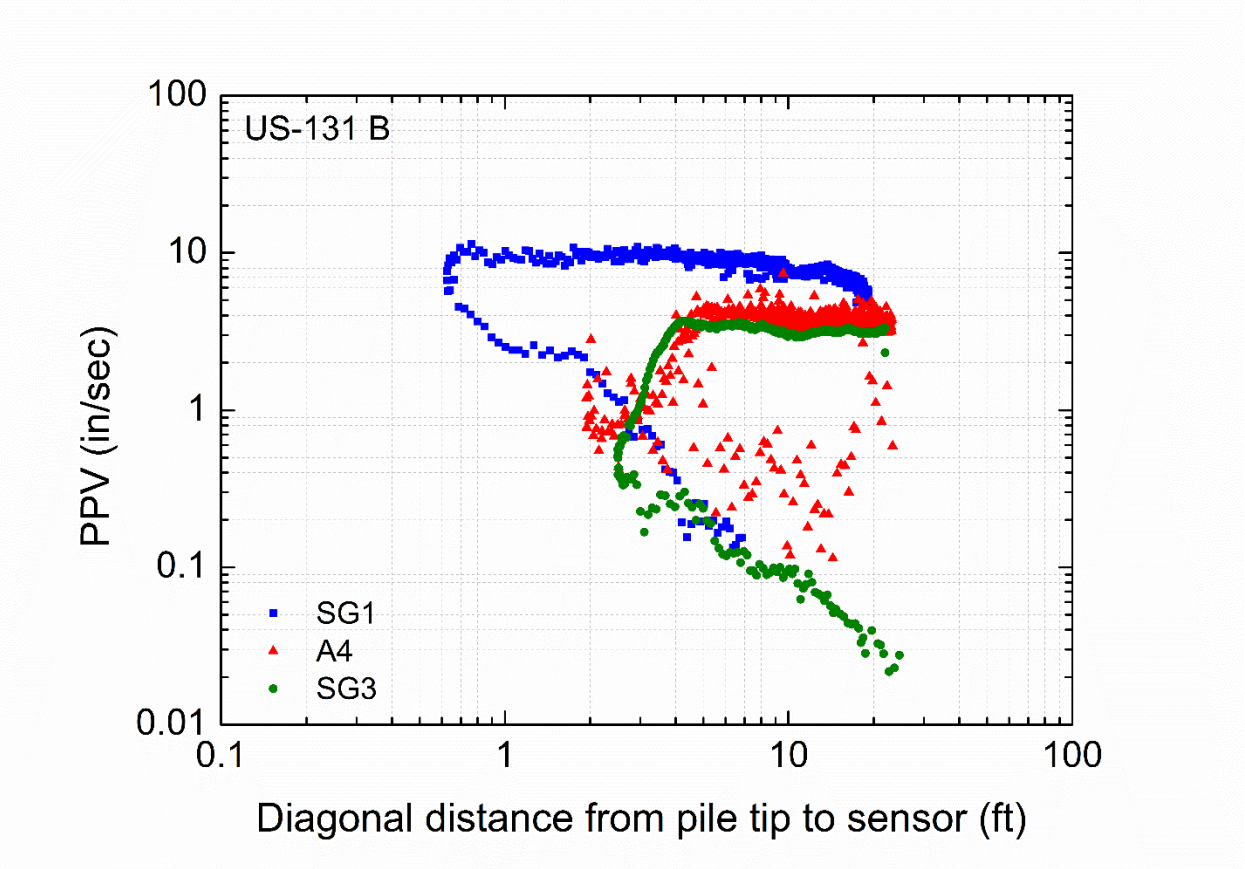

Figure 6-137 Peak particle velocity versus diagonal distance from pile tip to deep set of sensors at US-131 B site, Pile 54 – Vertical direction, logarithmic scale

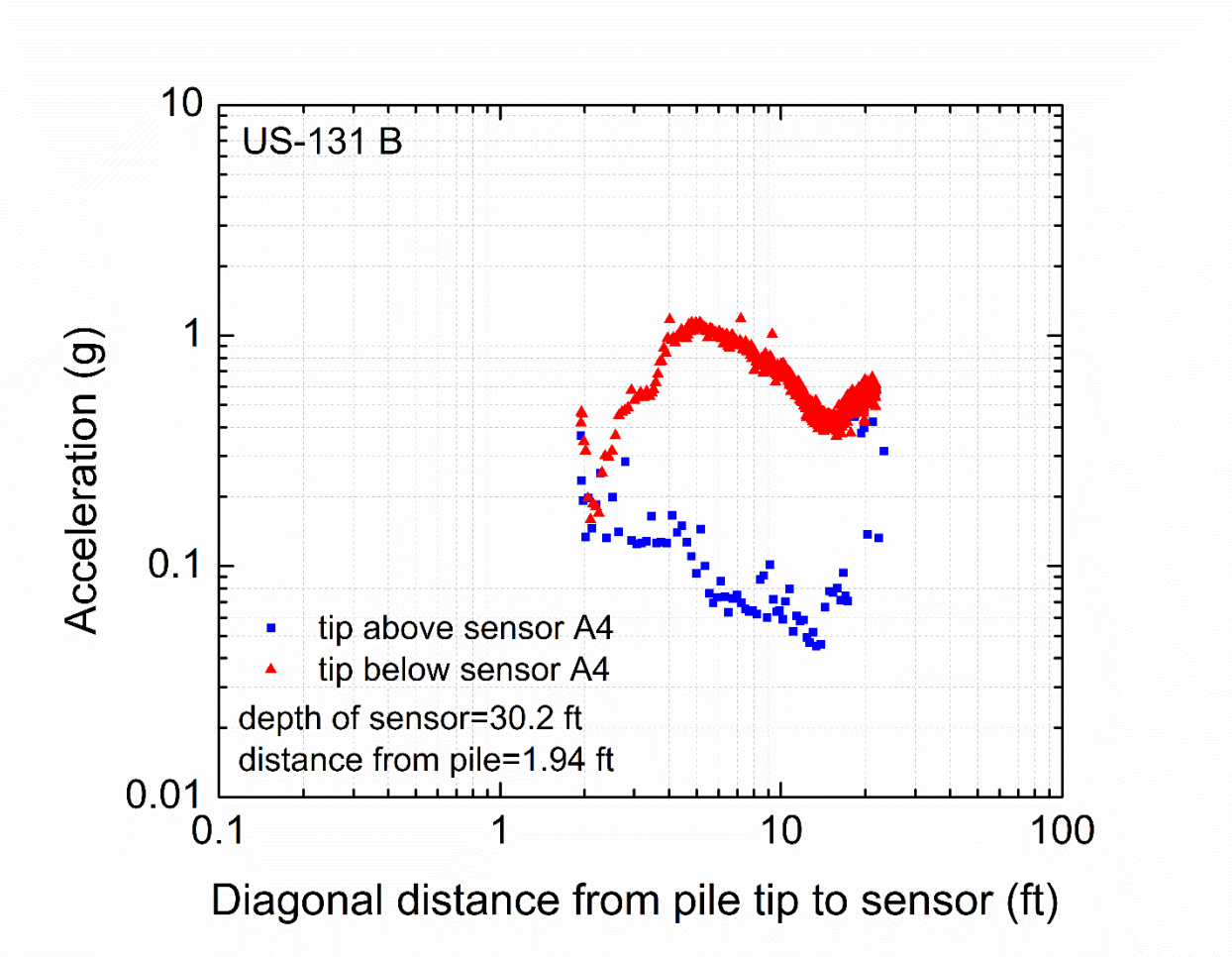

Figure 6-138 Acceleration versus diagonal distance from pile tip to sensor A4 at US-131 B site, Pile 54 – Longitudinal direction

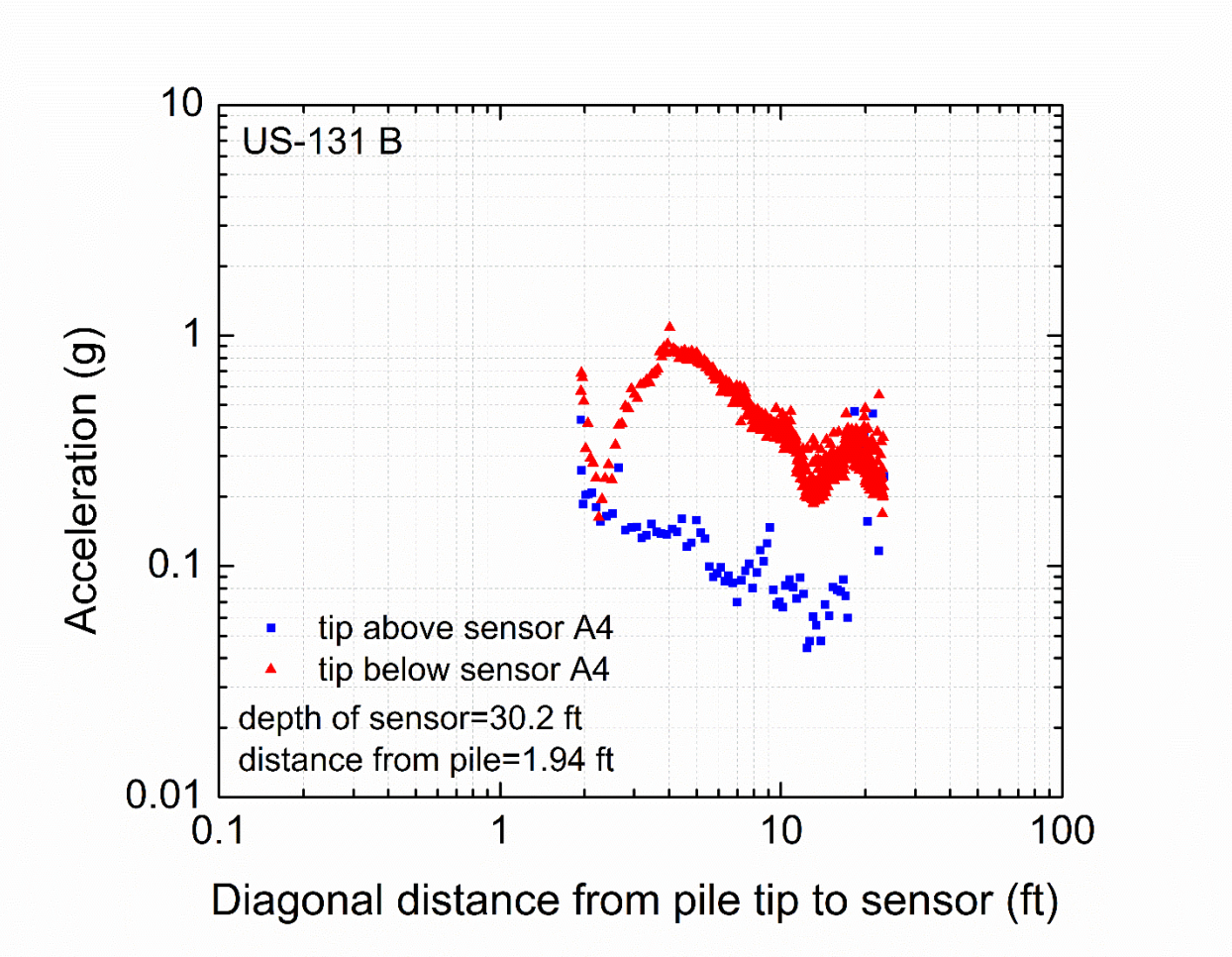

Figure 6-139 Acceleration versus diagonal distance from pile tip to sensor A4 at US-131 B site, Pile 54 – Transverse direction

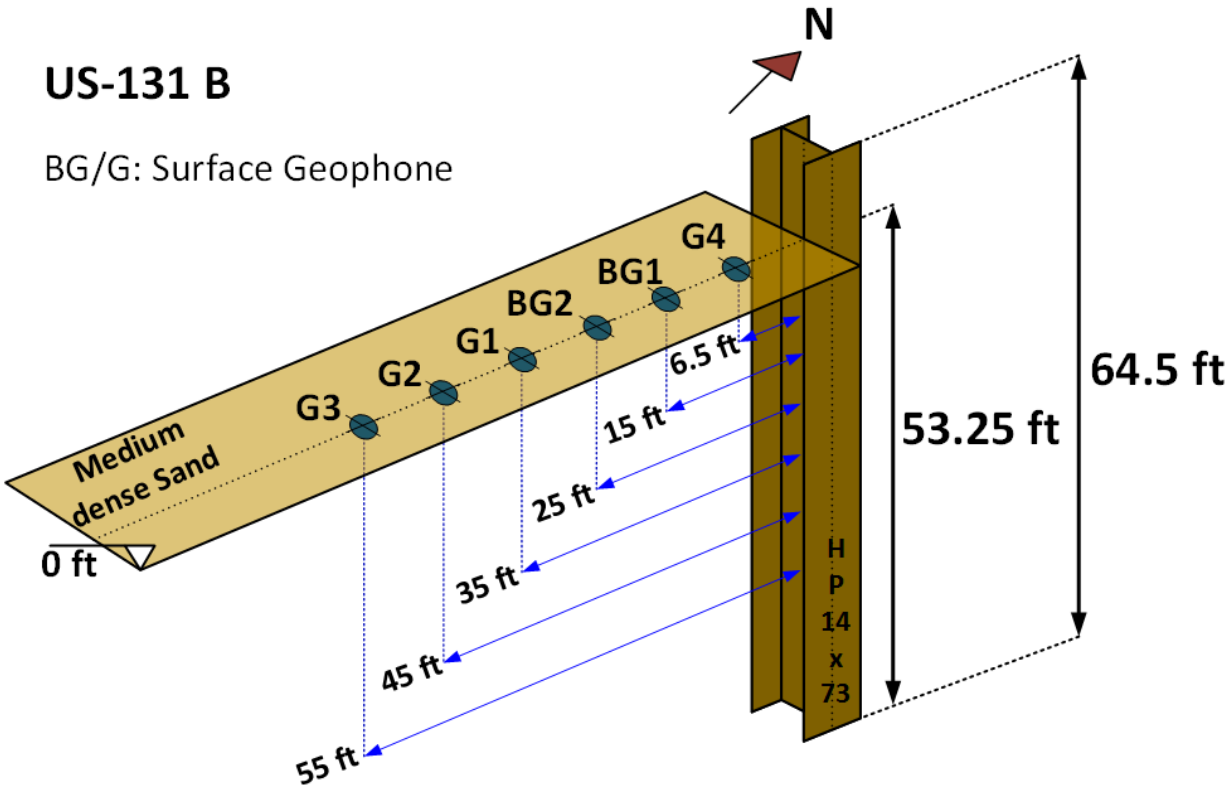

Figure 6-140 Perspective view of surface sensors at US-131 B site, Pile 54 (not to scale)

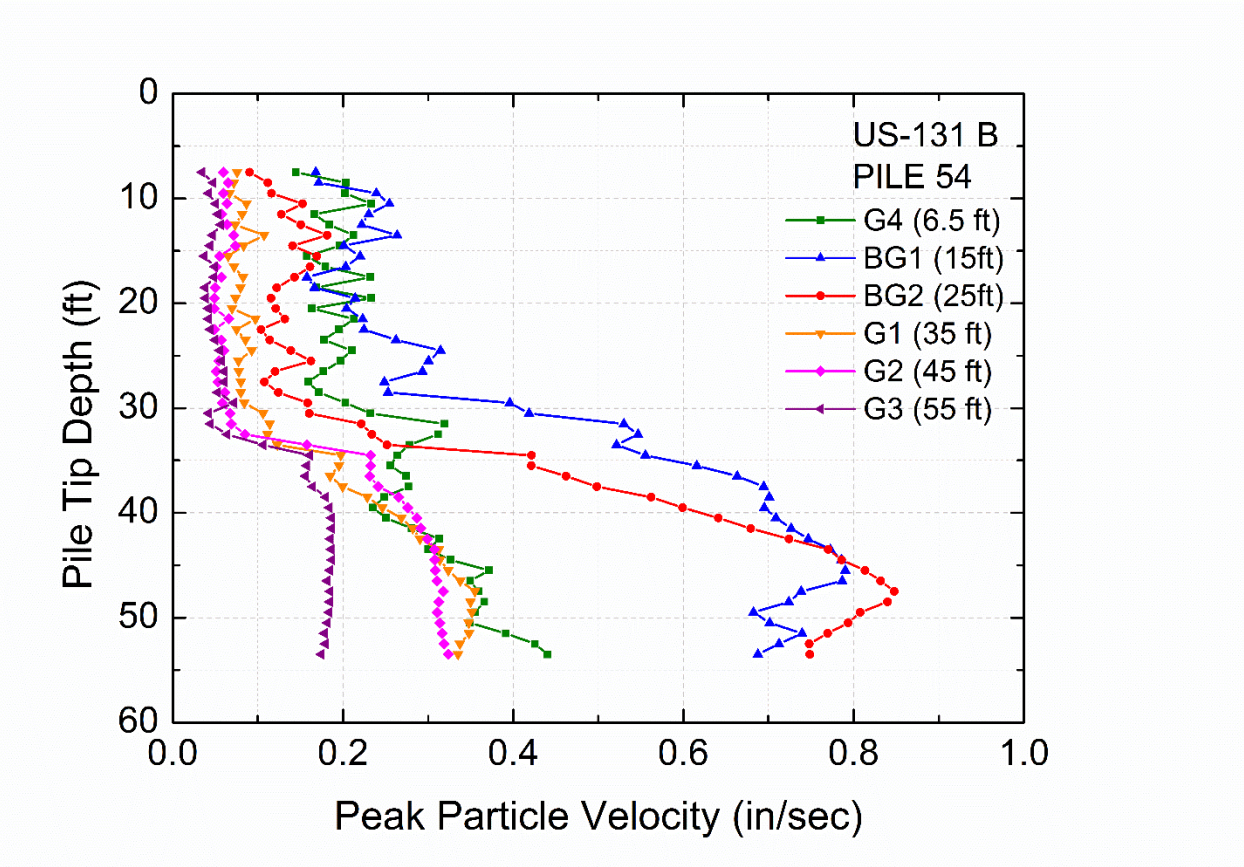

Figure 6-141 Peak Particle Velocity of surface geophones at US-131 B site – Pile 54, Vertical Direction

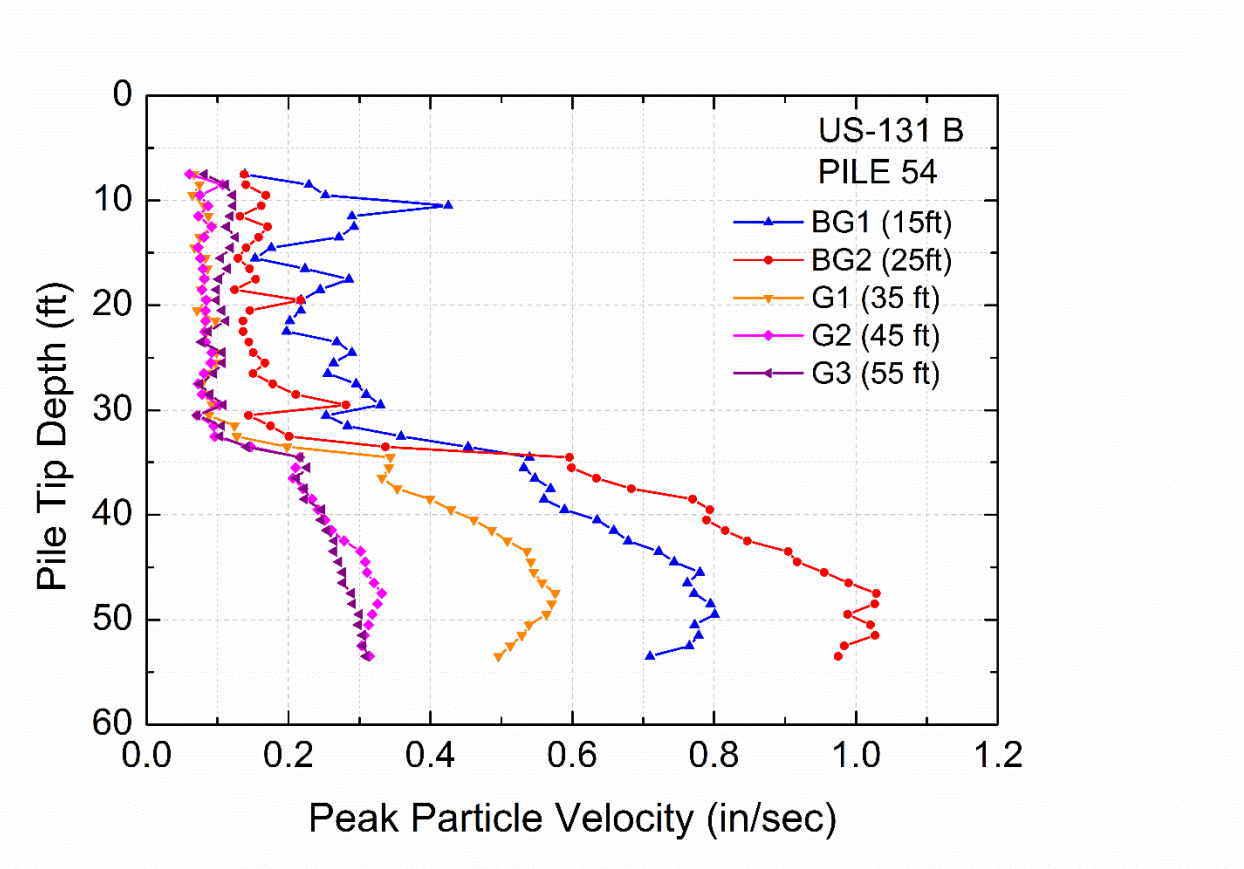

Figure 6-142 Peak Particle Velocity of surface geophones at US-131 B site – Pile 54, Longitudinal Direction

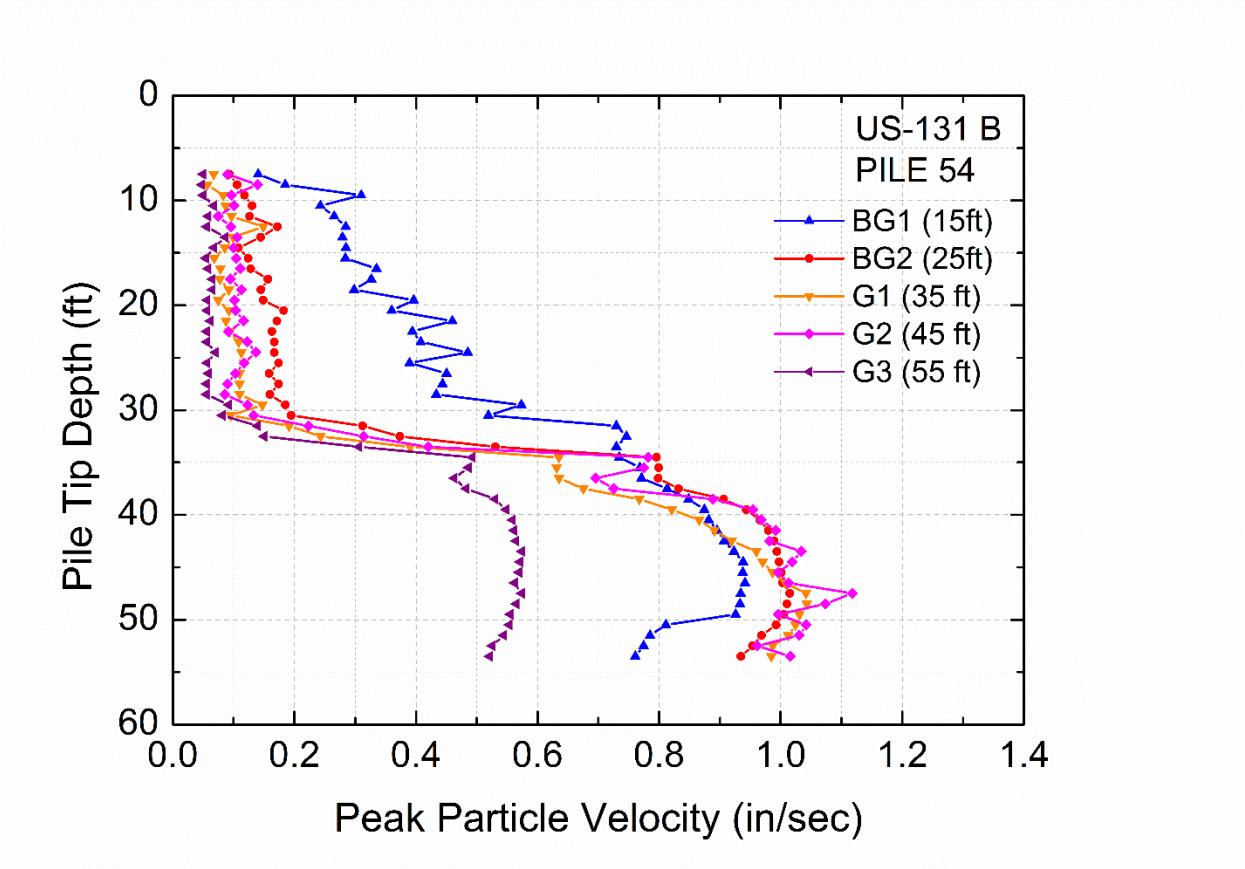

Figure 6-143 Peak Particle Velocity of surface geophones at US-131 B site – Pile 54, Transverse Direction

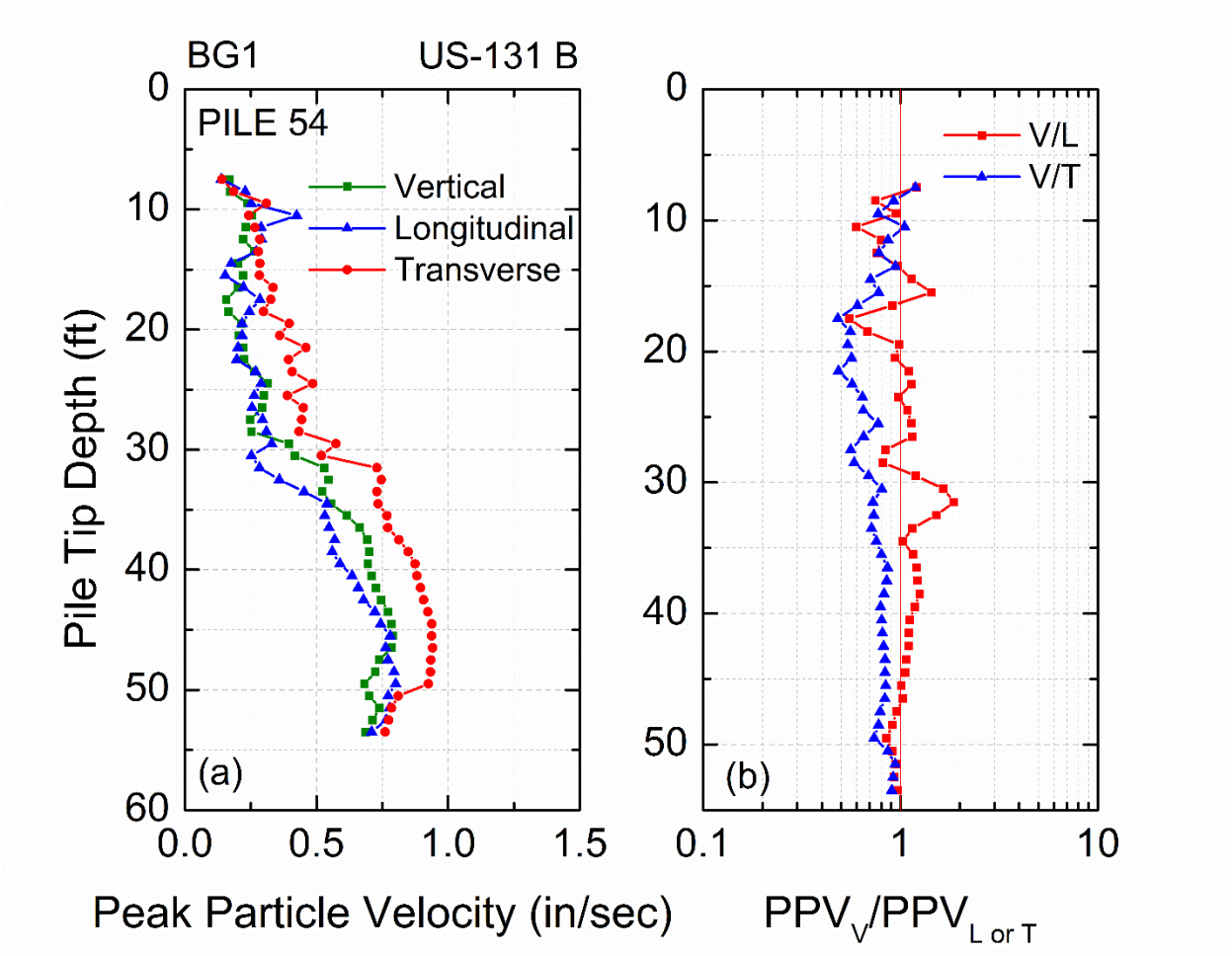

Figure 6-144 (a) Peak Particle Velocities of three directions of sensor BG1 and (b) vertical to longitudinal and vertical to transverse components of PPV – US-131 B site, Pile 54

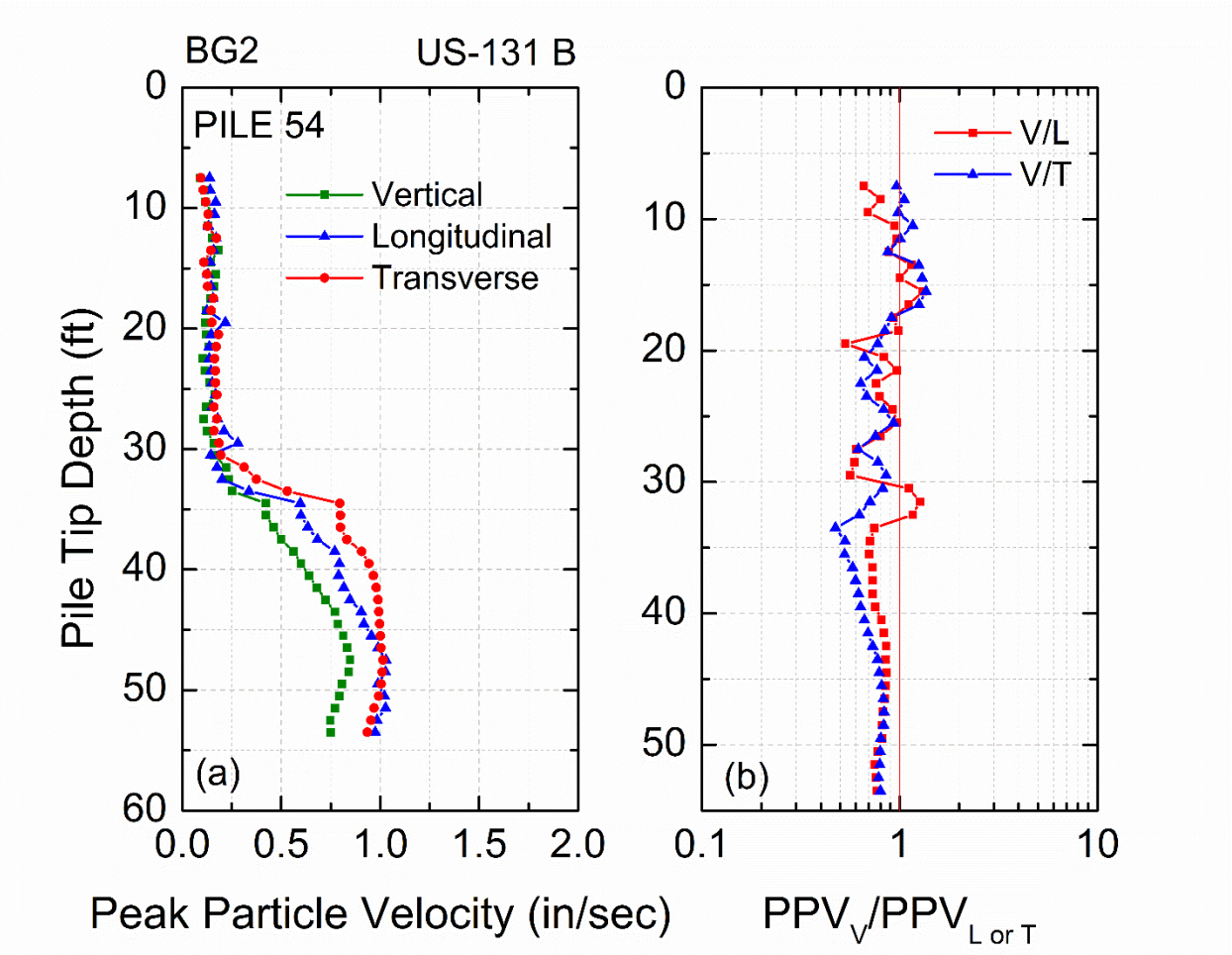

Figure 6-145 (a) Peak Particle Velocities of three directions of sensor BG2 and (b) vertical to longitudinal and vertical to transverse components of PPV – US-131 B site, Pile 54

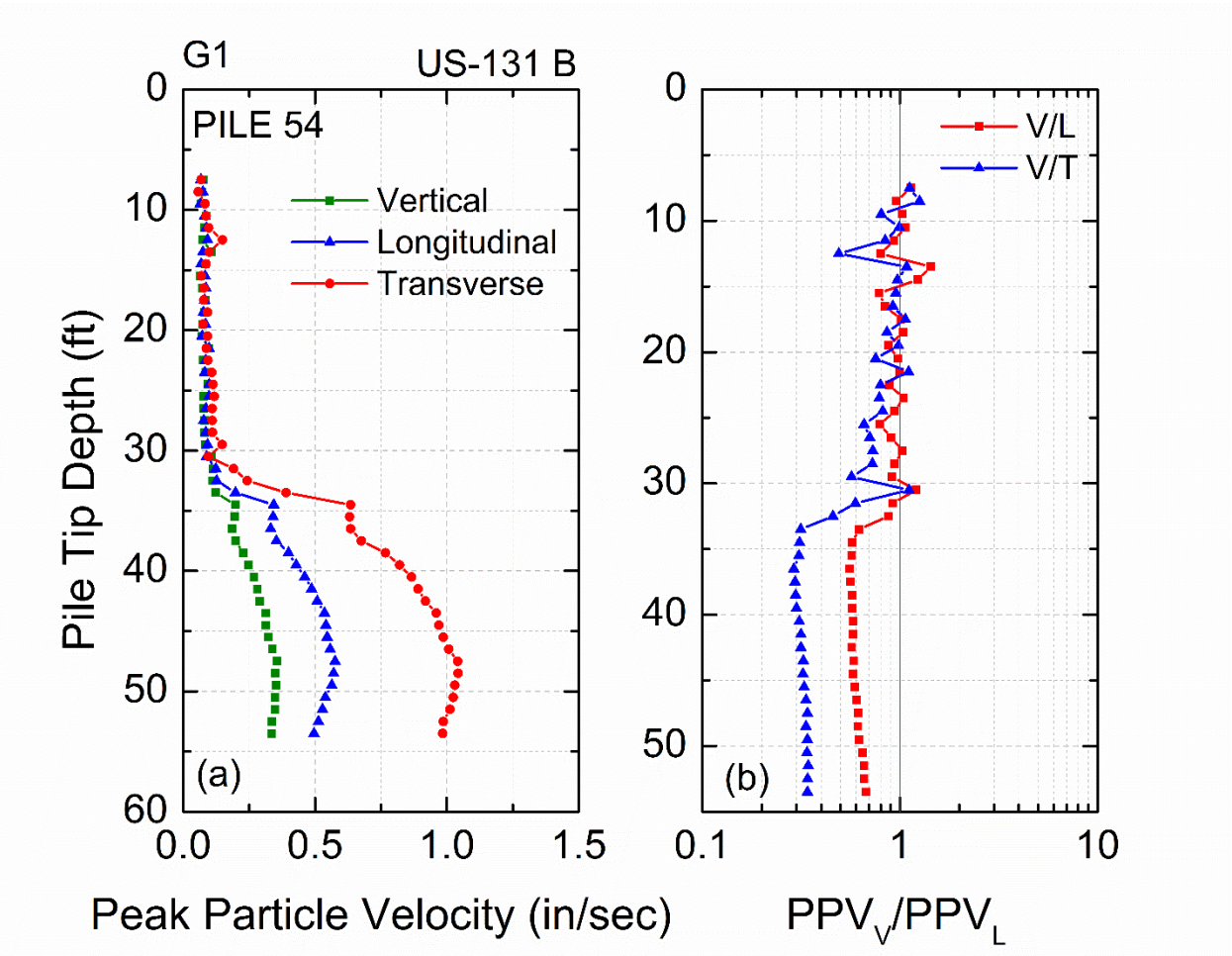

Figure 6-146 (a) Peak Particle Velocities of three directions of sensor G1 and (b) vertical to longitudinal and vertical to transverse components of PPV – US-131 B site, Pile 54

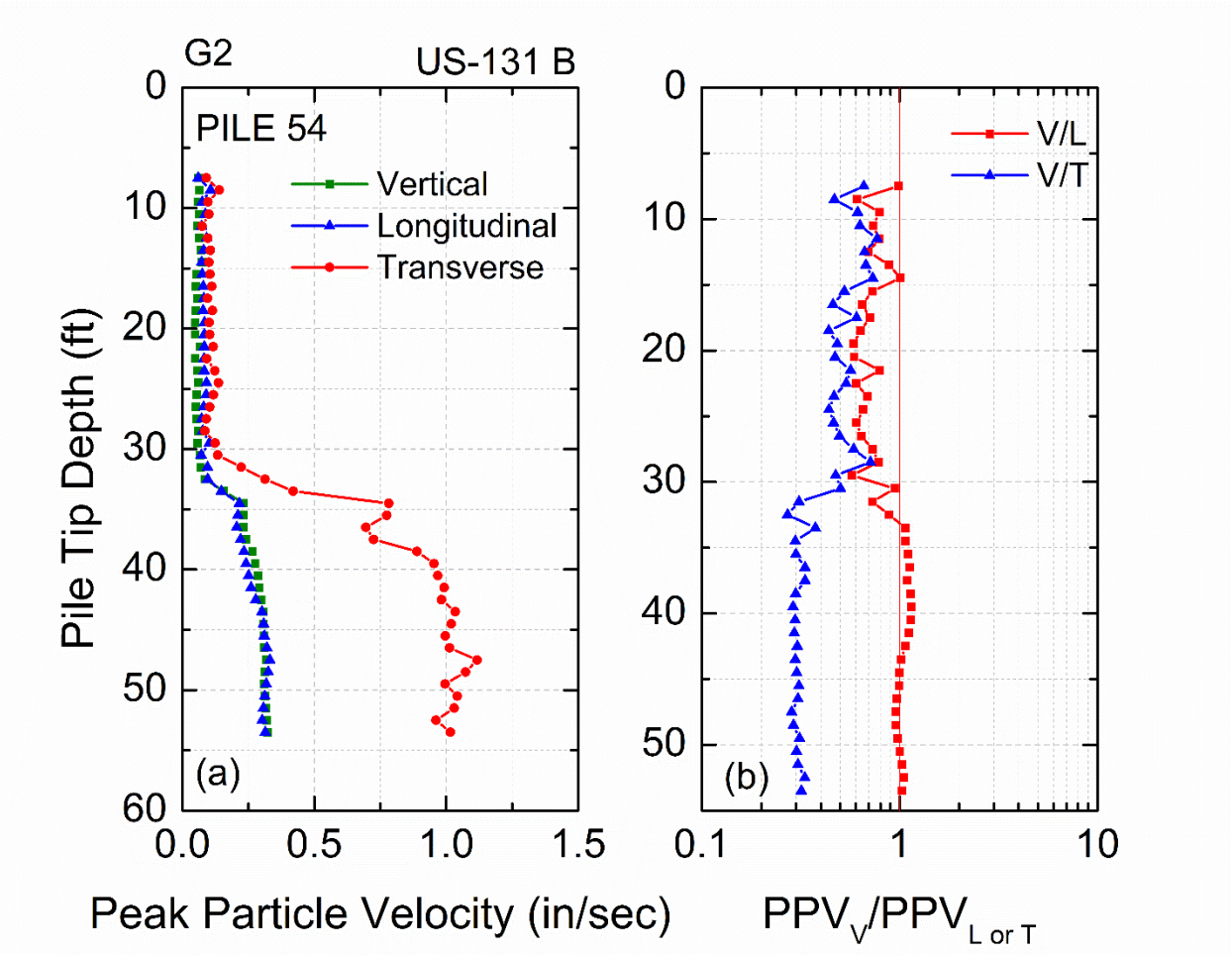

Figure 6-147 (a) Peak Particle Velocities of three directions of sensor G2 and (b) vertical to longitudinal and vertical to transverse components of PPV – US-131 B site, Pile 54

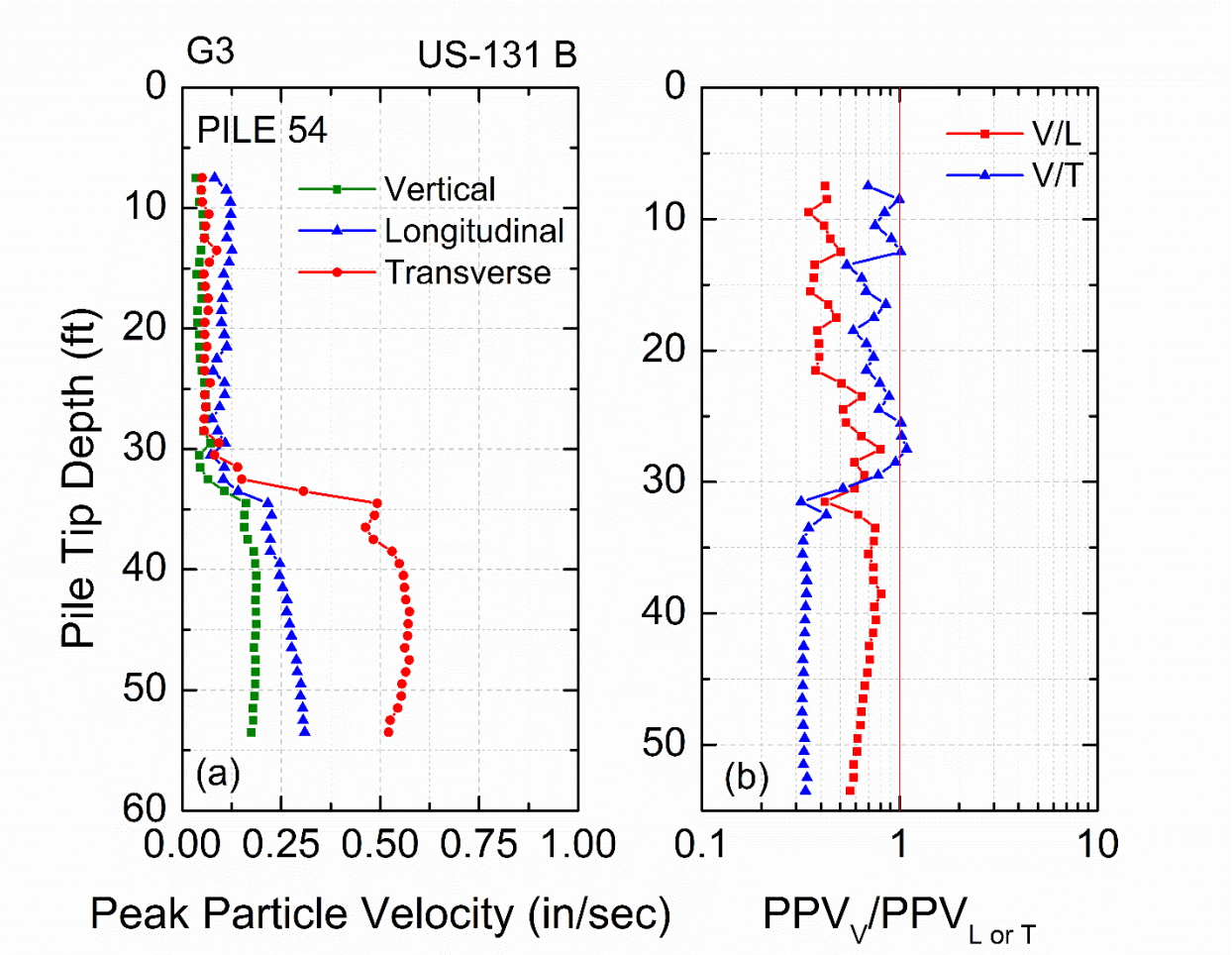

Figure 6-148 (a) Peak Particle Velocities of three directions of sensor G3 and (b) vertical to longitudinal and vertical to transverse components of PPV – US-131 B site, Pile 54

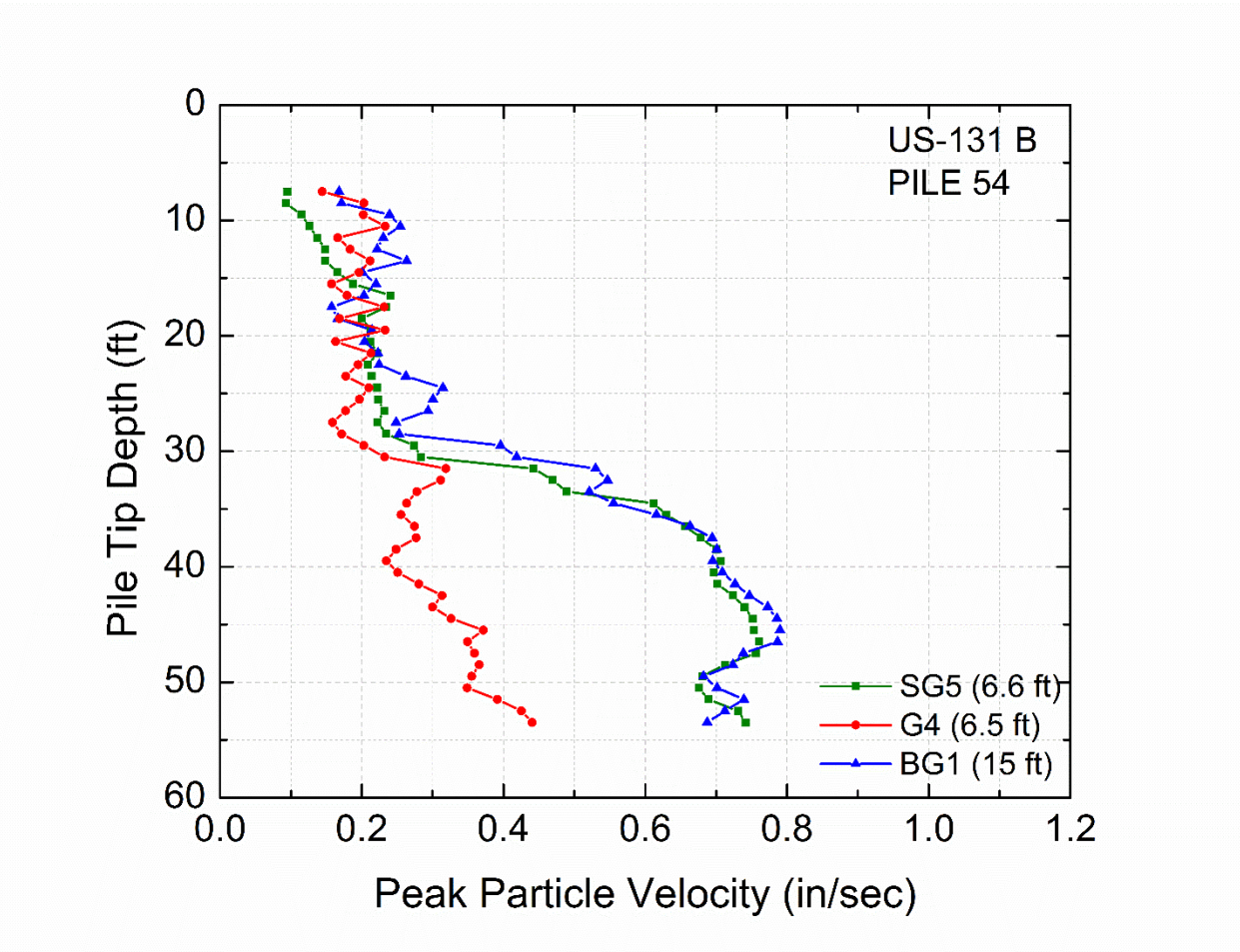

Figure 6-149 Peak particle velocity versus depth of sensors BG1, G4 and SG5 at US-131 B site, Pile 54 –Vertical direction

6.3.3.2 Test Pile 37

After recording ground motions during driving pile 54, the contractor prepared the hammer and continued to drive test pile 37. Both piles, were production piles that were on the schedule to be driven at abutment B. The ground surface geophones were moved and were positioned in an array close to pile 37. A perspective view of the surface sensor locations close to pile 37 is shown in Figure 6-150.

A 61 ft long HP 14x73 pile was driven using again the Delmag D30-32 diesel hammer. The final depth of penetration of the pile was 54.75 ft. Figure 6-151 presents the pile driving penetration resistance as the number of blows per pile foot increment and the accumulated number of blows versus depth of pile tip penetration. The total blow count to drive pile 37 was 882. The driving resistance gradually increased with increasing penetration depth, with a higher rate around 30 ft where the pile entered the hard clay. Figure 6-152 illustrates the average actual hammer energy per pile foot increment and the hammer efficiency, η, versus depth. The average hammer efficiency when driving pile 37 was around 42%.

Vertical peak particle velocity versus depth is shown for all the sensors in Figure 6-153. There is an increase in velocity amplitudes when the pile tip enters the dense clay deposit at around 30 ft (Figure 6-31); similar behavior as when driving pile 54. Figure 6-154 and Figure 6-155present the particle velocities for the longitudinal and transverse directions of these same surface sensors except G4 that did not have a longitudinal and transverse component transducer. The phenomenon is more pronounced for the transverse direction of all sensors.

Figure 6-156a to Figure 6-160a show the three velocity components versus depth and Figure 6-156b to Figure 6-160b show the ratios of vertical to longitudinal (V/L) and vertical to transverse (V/T) components for sensors BG2, BG1, G3, G2 and G1, respectively. The vertical component motions were higher for all sensors until the pile tip reached a depth of 30 ft where the transverse components of motion had higher amplitudes than the other two directions. The ratio of vertical to longitudinal (V/L) and vertical to transverse (V/T) components is either very close to one or less than one for the

total depth range of pile installation. As observed in surface ground motions in other sites, this is clearly not an indication of a Rayleigh wave development on the surface.

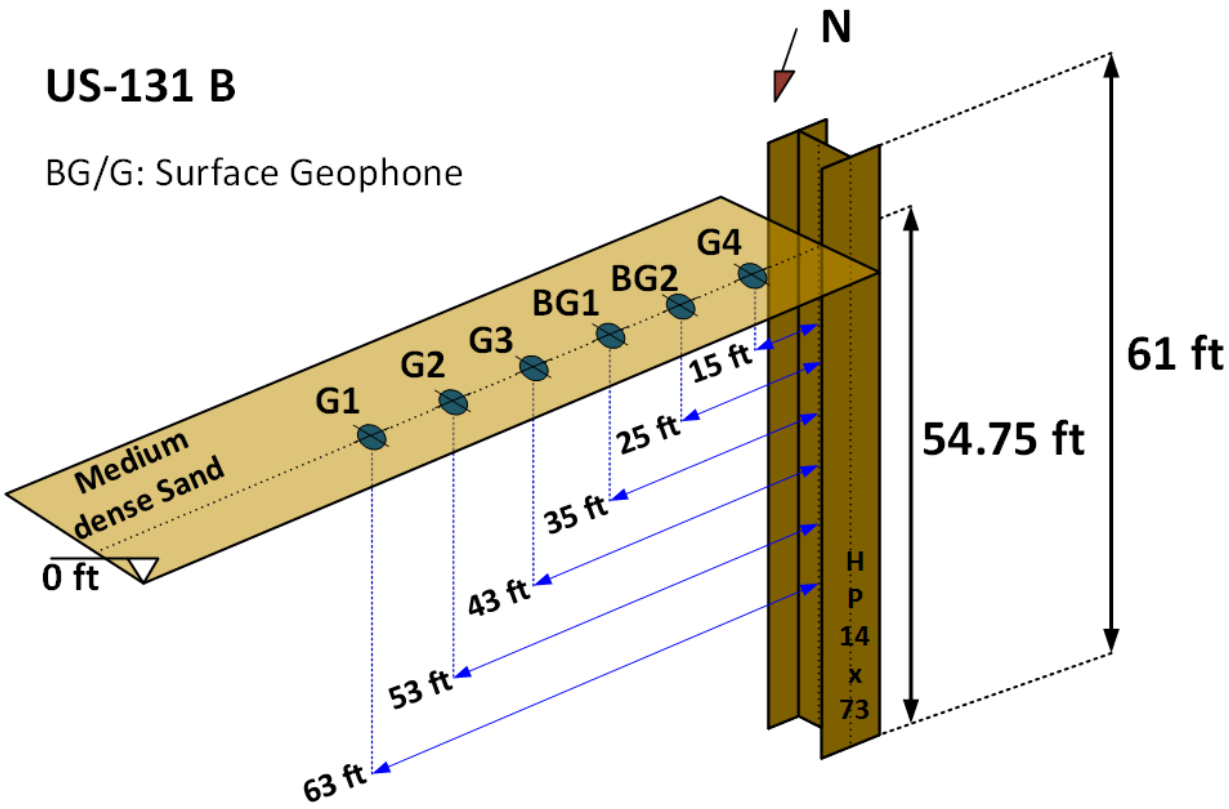

Figure 6-150 Perspective view of surface sensors at US-131 B site, Pile 37 (not to scale)

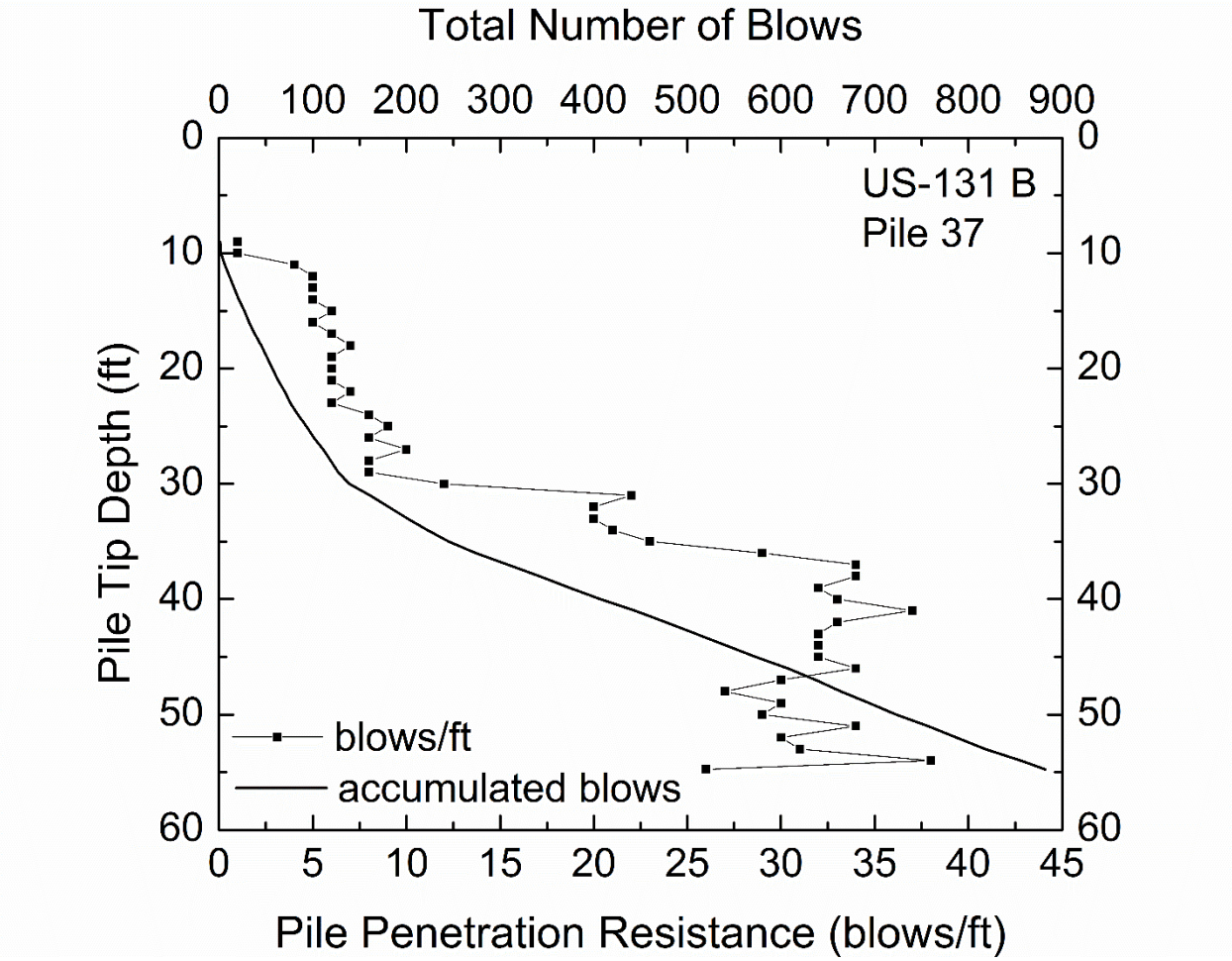

Figure 6-151 Driving Resistance and accumulated blows with depth – US-131 B site, Pile 37

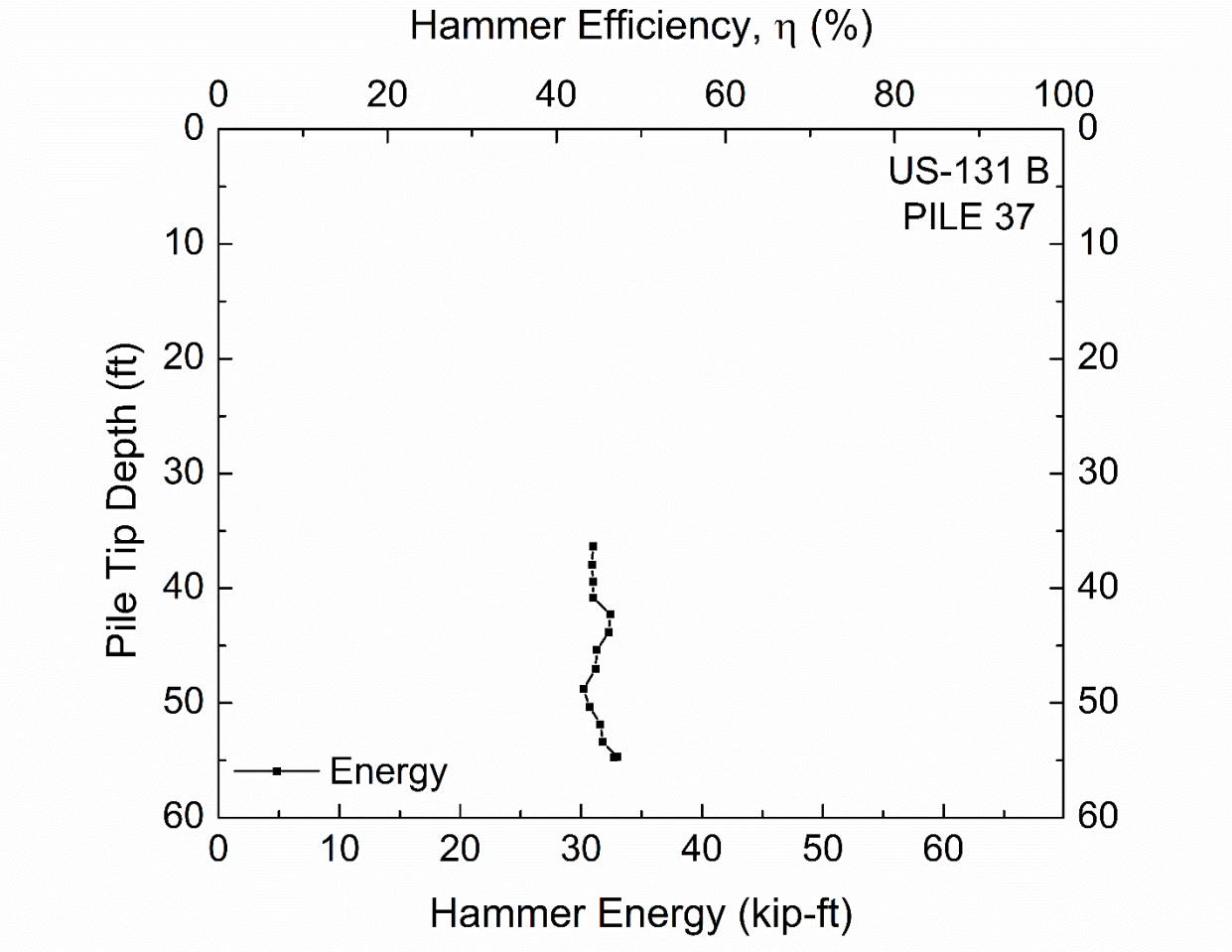

Figure 6-152 Hammer Energy and Hammer Efficiency with depth – US-131 B site, Pile 37

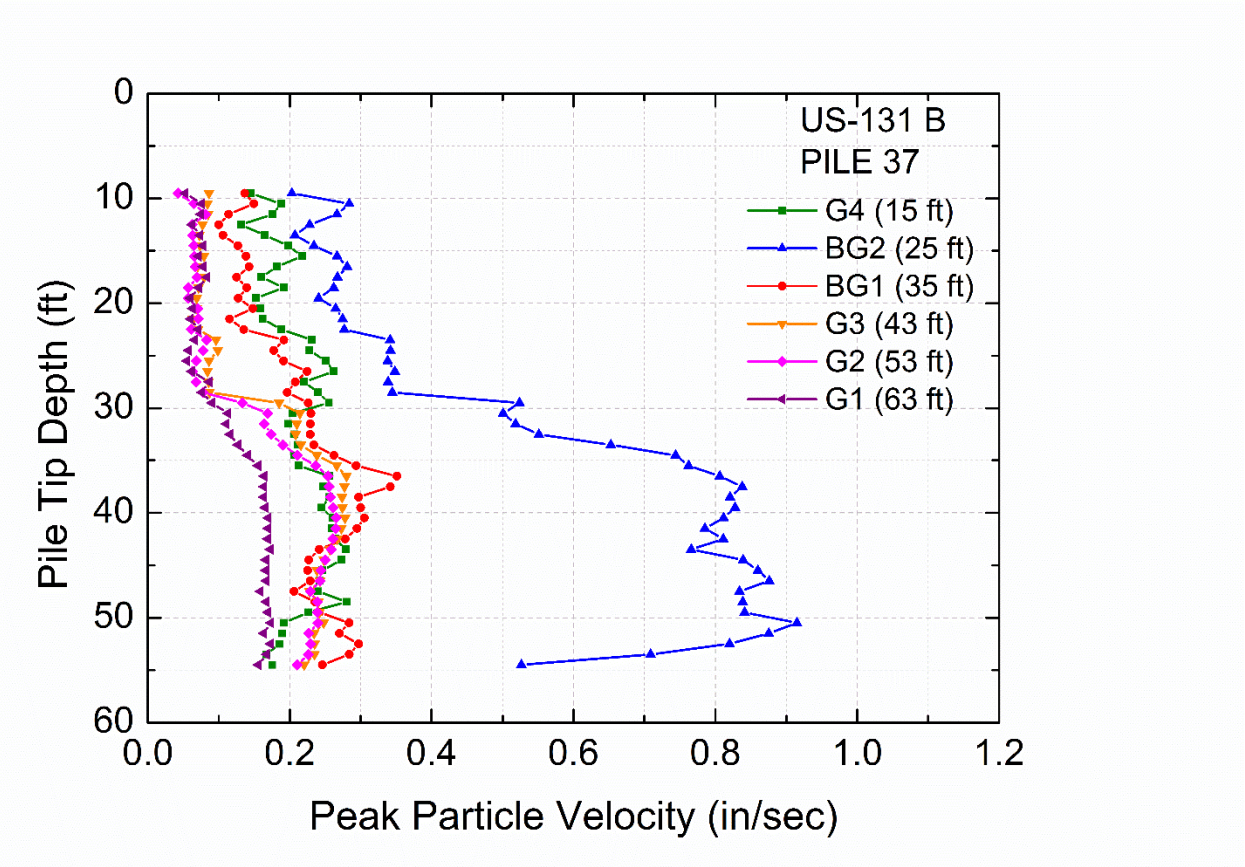

Figure 6-153 Peak Particle Velocity of surface geophones at US-131 B site – Pile 37, Vertical Direction

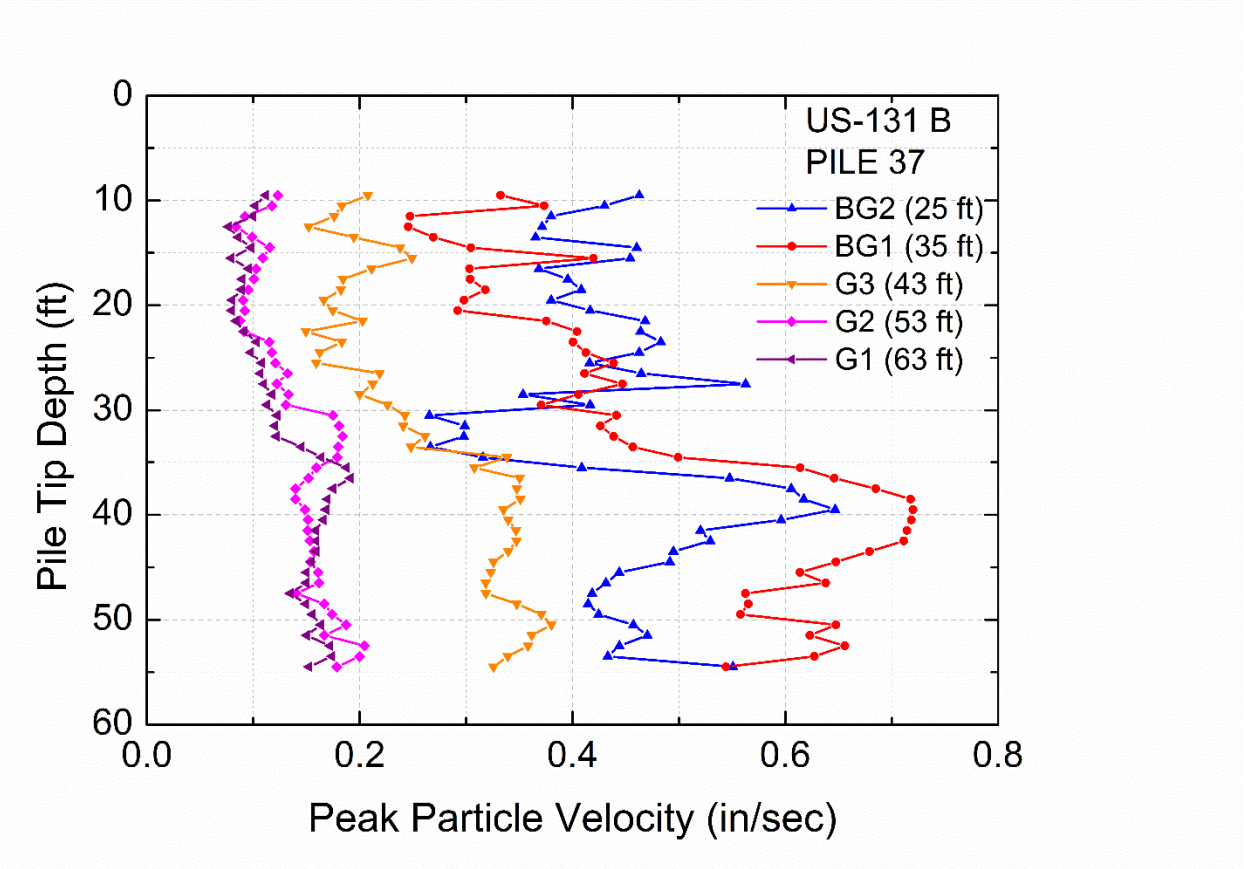

Figure 6-154 Peak Particle Velocity of surface geophones at US-131 B site – Pile 37, Longitudinal Direction

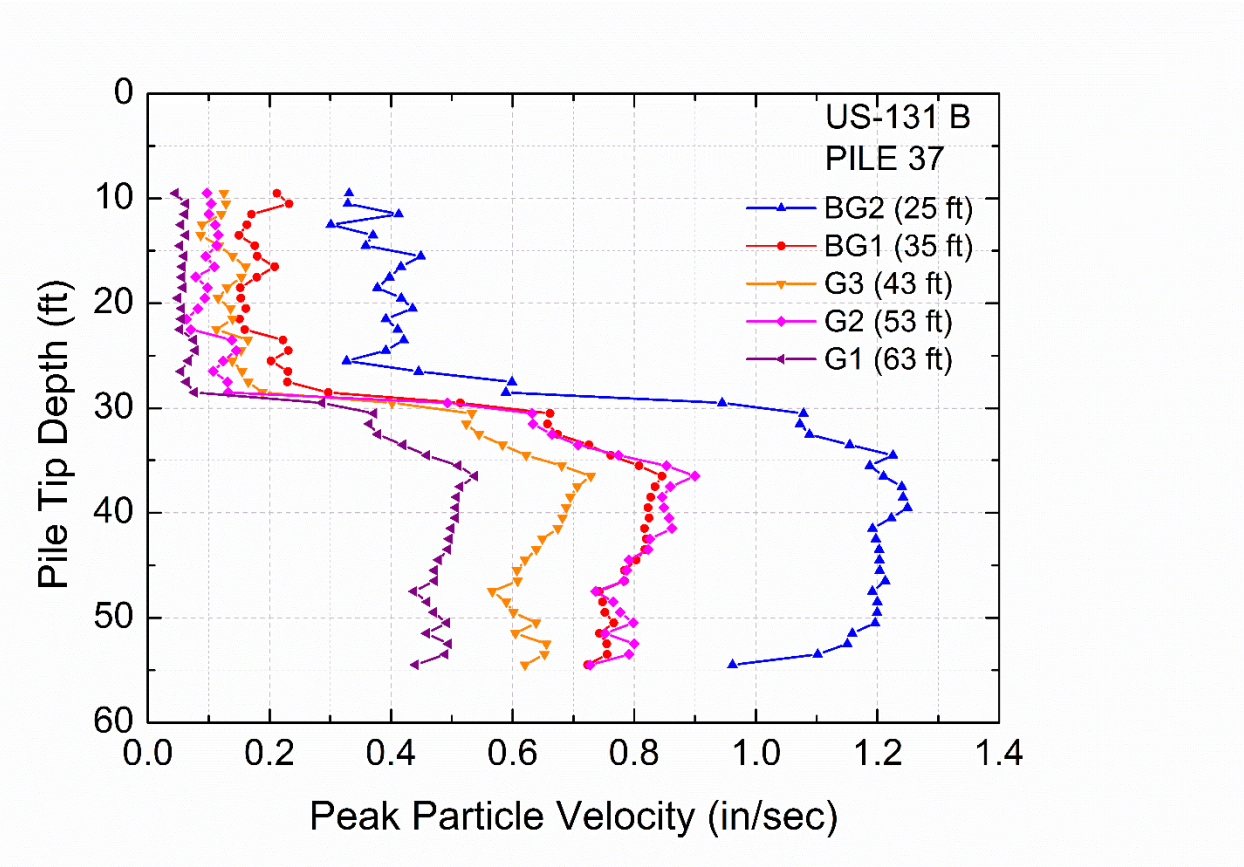

Figure 6-155 Peak Particle Velocity of surface geophones at US-131 B site – Pile 37, Transverse Direction

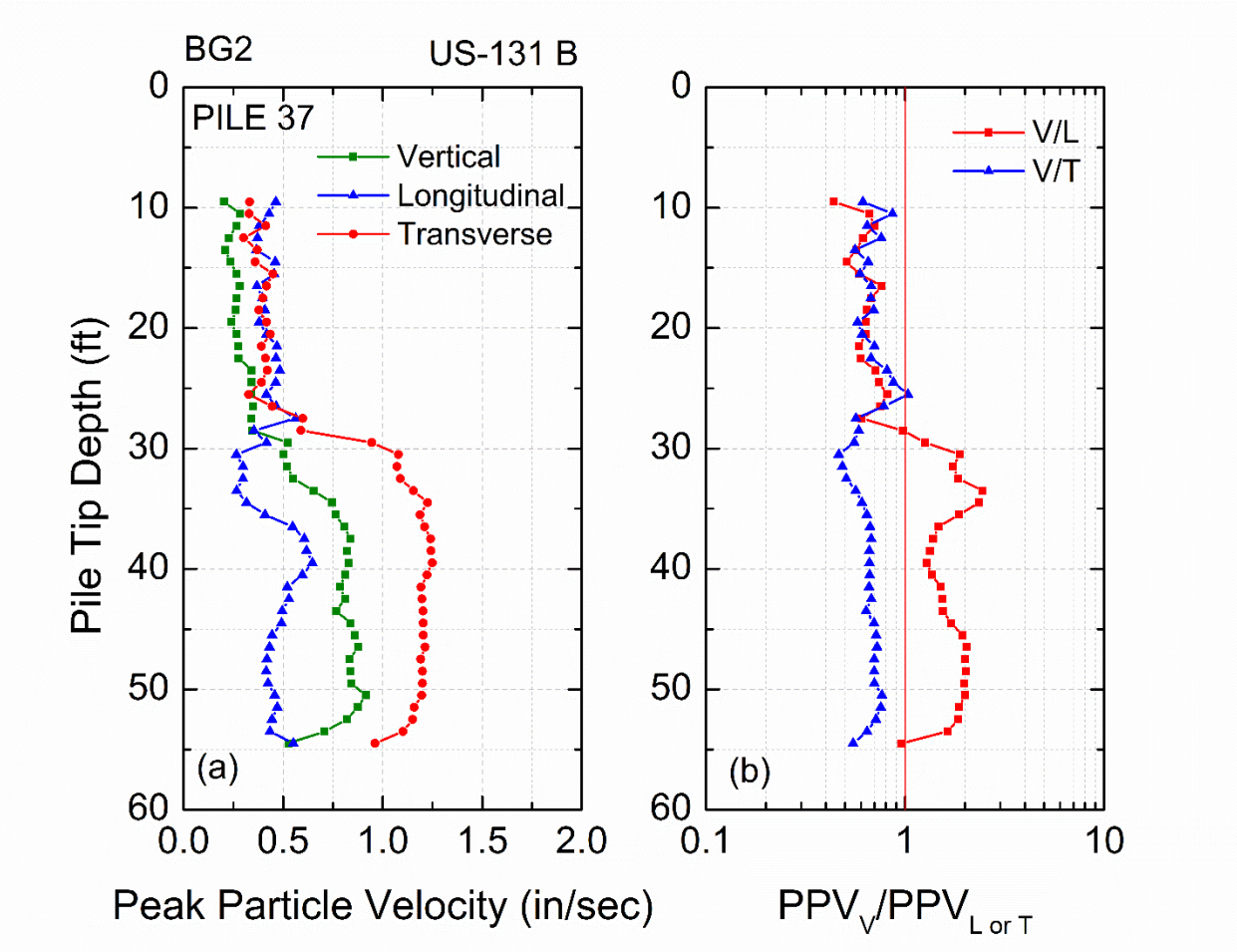

Figure 6-156 (a) Peak Particle Velocities of three directions of sensor BG2 and (b) vertical to longitudinal and vertical to transverse components of PPV – US-131 B site, Pile 37

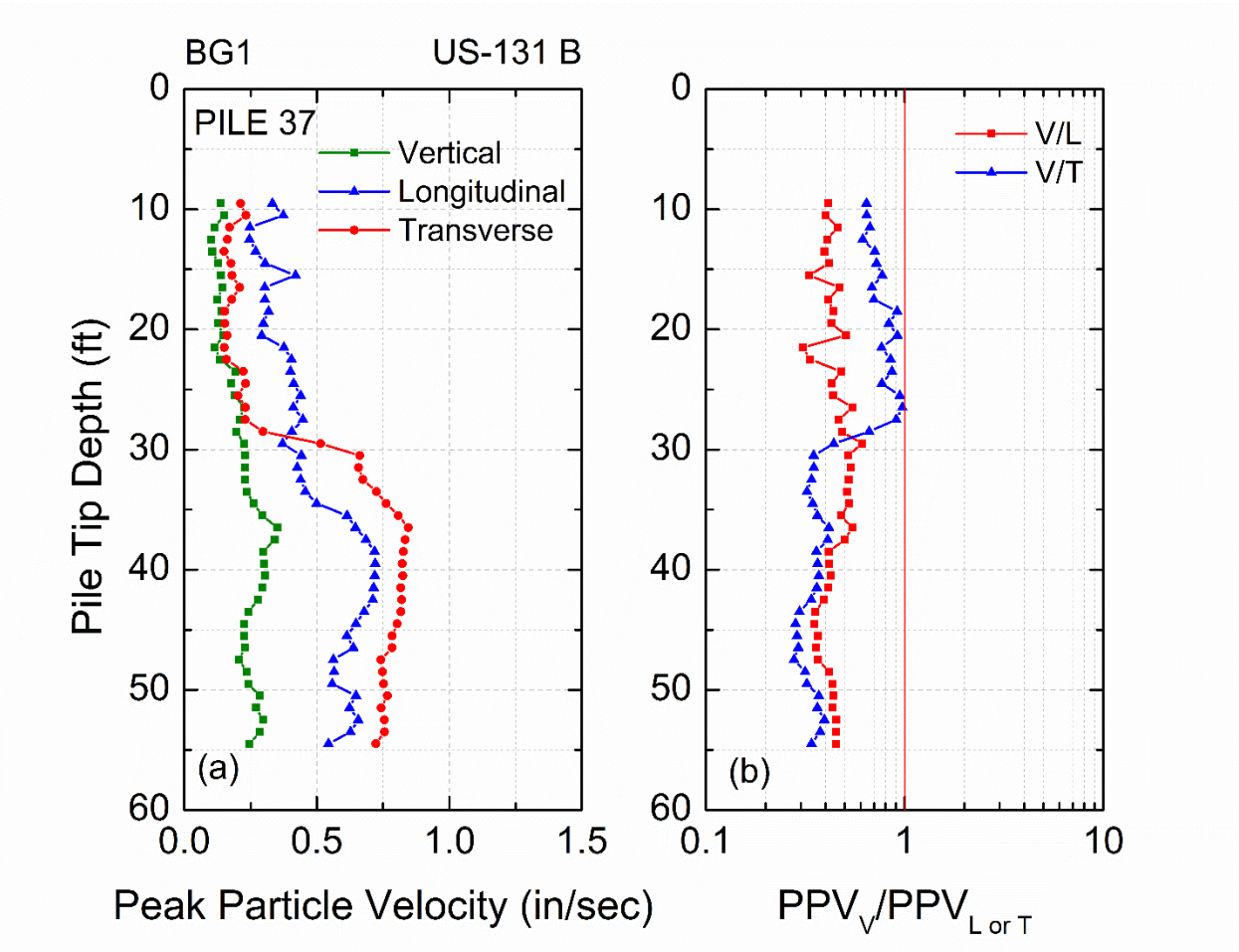

Figure 6-157 (a) Peak Particle Velocities of three directions of sensor BG1 and (b) vertical to longitudinal and vertical to transverse components of PPV – US-131 B site, Pile 37

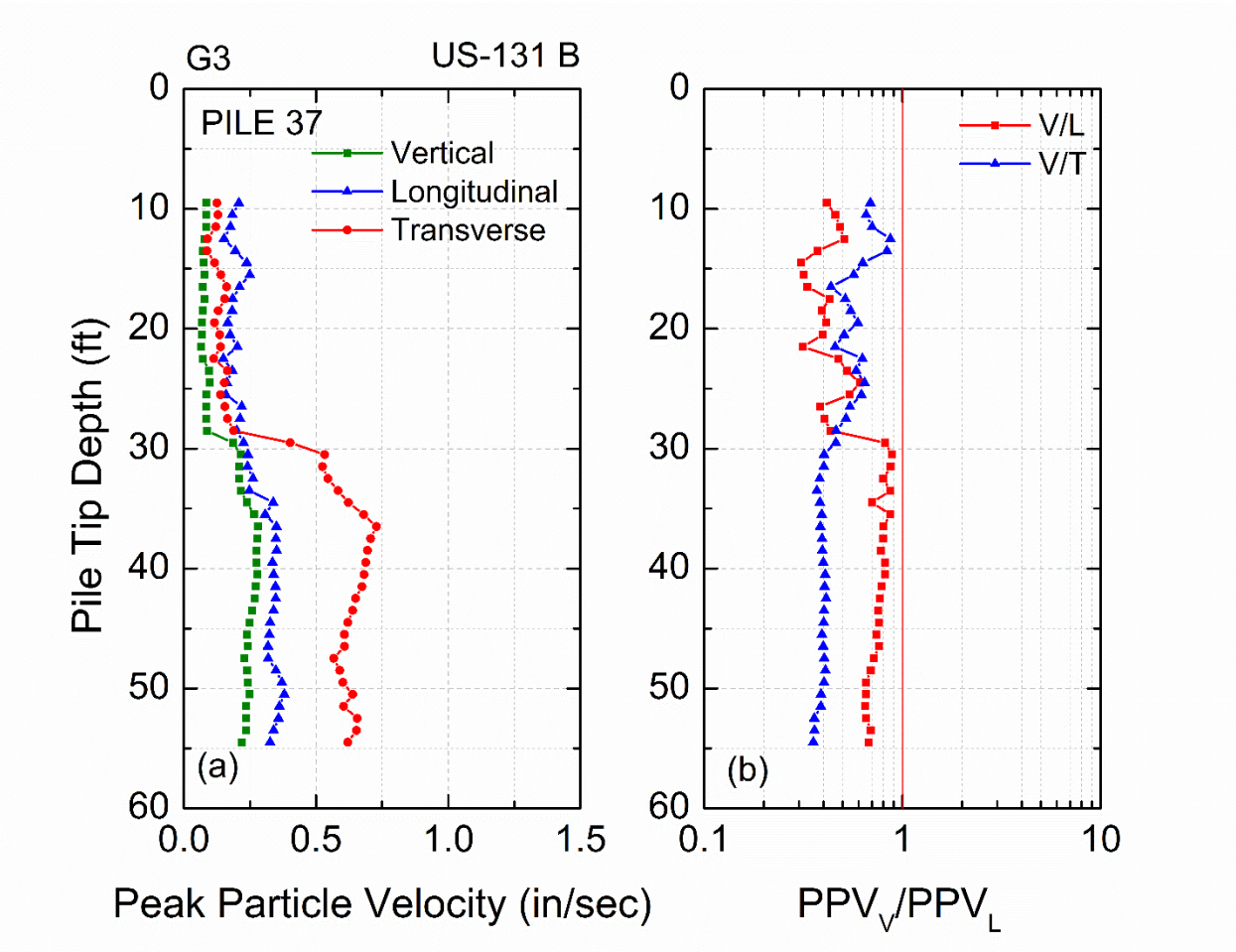

Figure 6-158 (a) Peak Particle Velocities of three directions of sensor G3 and (b) vertical to longitudinal and vertical to transverse components of PPV – US-131 B site, Pile 37

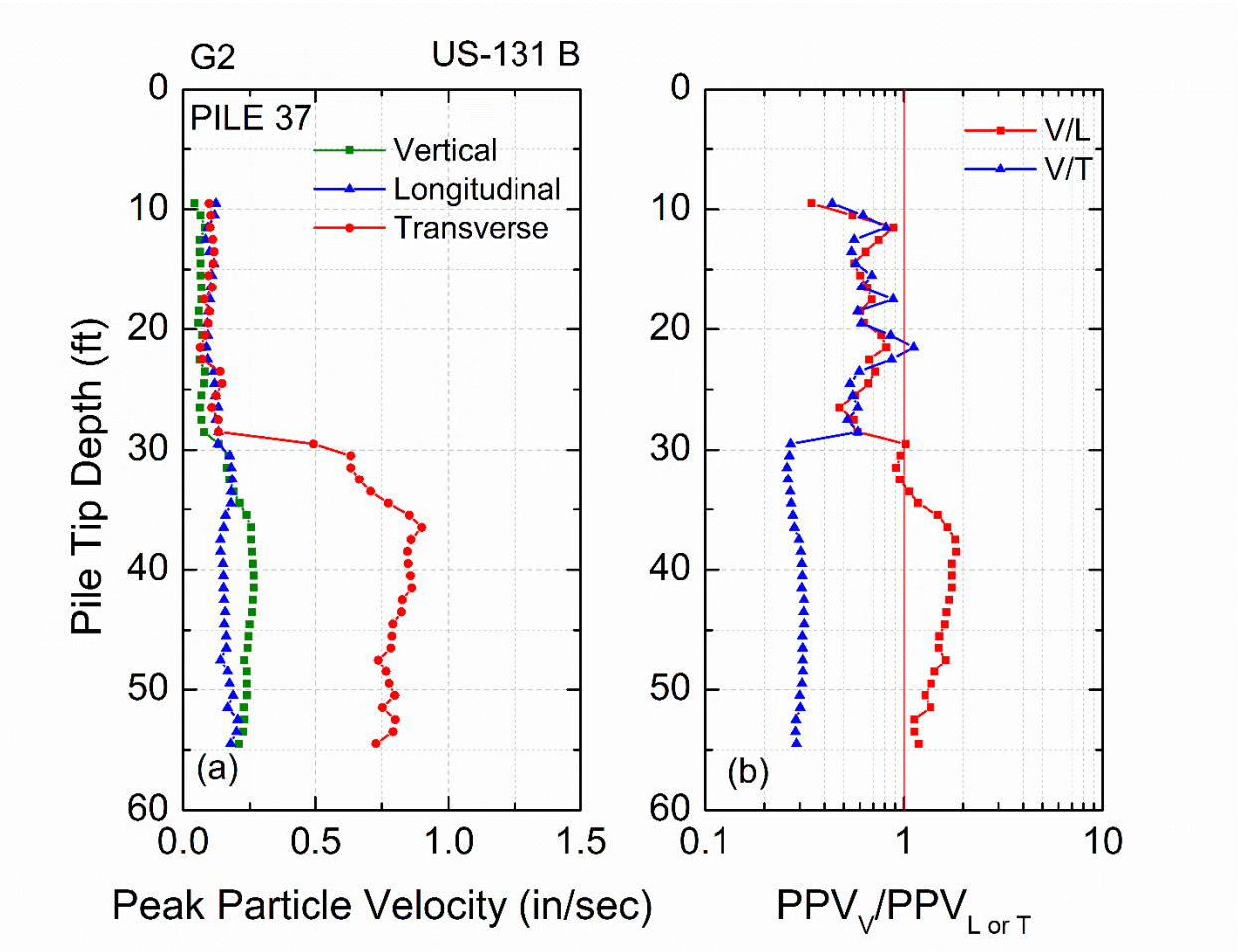

Figure 6-159 (a) Peak Particle Velocities of three directions of sensor G2 and (b) vertical to longitudinal and vertical to transverse components of PPV – US-131 B site, Pile 37

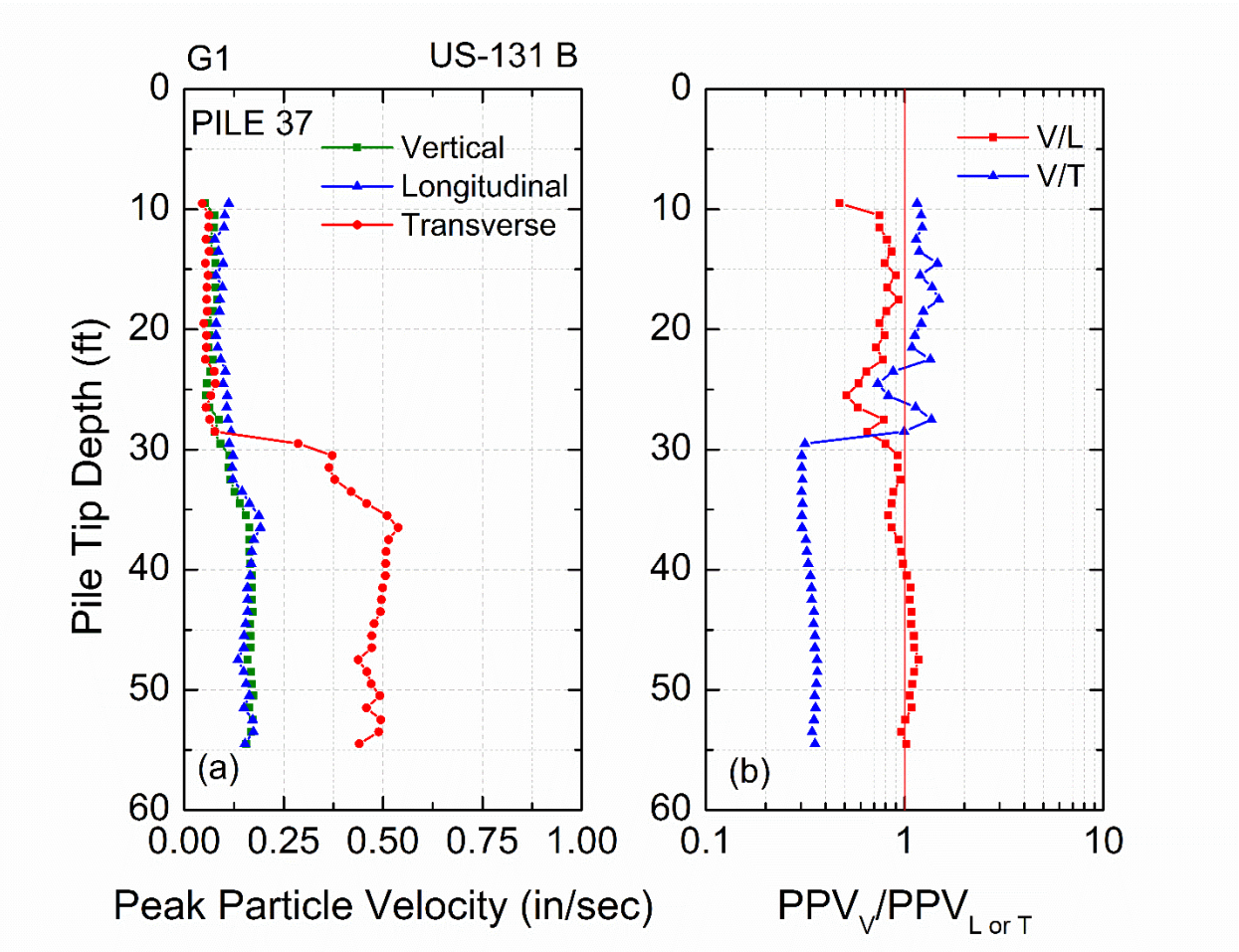

Figure 6-160 (a) Peak Particle Velocities of three directions of sensor G1 and (b) vertical to longitudinal and vertical to transverse components of PPV – US-131 B site, Pile 37

6.3.3.3 Monitoring for surface settlement due to pile driving at US-131 B site

Five control points and one benchmark were established on the abutment B of site US-131 to monitor settlement around the pile driving area of the two tested piles. Control and mapping of this task was performed by the Michigan Department of Transportation Survey Unit. Differential leveling, Global Positioning System (GPS) and Terrestrial Lidar Scanning collection techniques were employed for this abutment. The mapping of the abutment was performed by using a Leica C10 Terrestrial Lidar Scanner. The Scanner collects 50,000 points every second and rotates 360° to create a point cloud of the surveyed area. A digital camera was also attached on the scanner. Two scanners were utilized to speed up the collection process.

The initial survey took place after the embedded sensors were installed and soil monitoring was conducted right after the end of driving pile 54 and pile 37. One set of scan data was collected after pile 54 was driven and another set was collected after installation of pile 37 was completed. A Digital Terrain Model (DTM) was created from each set of scan data. After processing, the total points were limited to 16,317. The results provided the change in elevation with the distance of the points in relation to the center of pile locations. The maximum settlement after driving pile 54 was found to be 1.45 ft at 0.06 ft horizontal distance from the centerline of the pile. The maximum settlement after driving pile 37 was 1.22 ft at 0.04 ft horizontal distance from the pile centerline. Settlement was found again to be a function of distance from the centerline of the pile; elevation change was negligible at a distance of around 20 ft from both piles.

Figure 6-161 depicts a close-up view of pile 54 after the end of driving and the affected area around the pile centerline. Figure 6-162 and Figure 6-163 present settlement contours after driving pile 54 and pile 37, respectively; the contour interval is 0.1 ft. Figure 6-164 is a screen shot taken with the camera on the Lidar. Other screen captures during mapping abutment B at US-131 site, can be found in Appendix G.

Figure 6-161 Settlement around pile 54 after the end of driving at US-131 B site

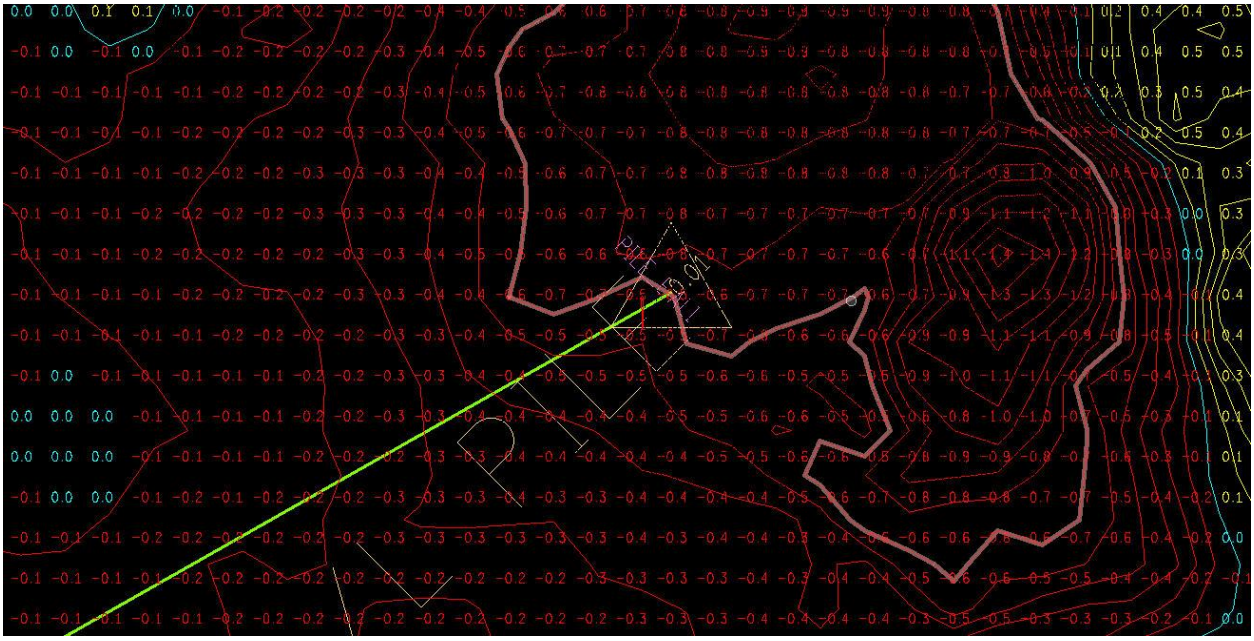

Figure 6-162 Settlement contours after driving Pile 54

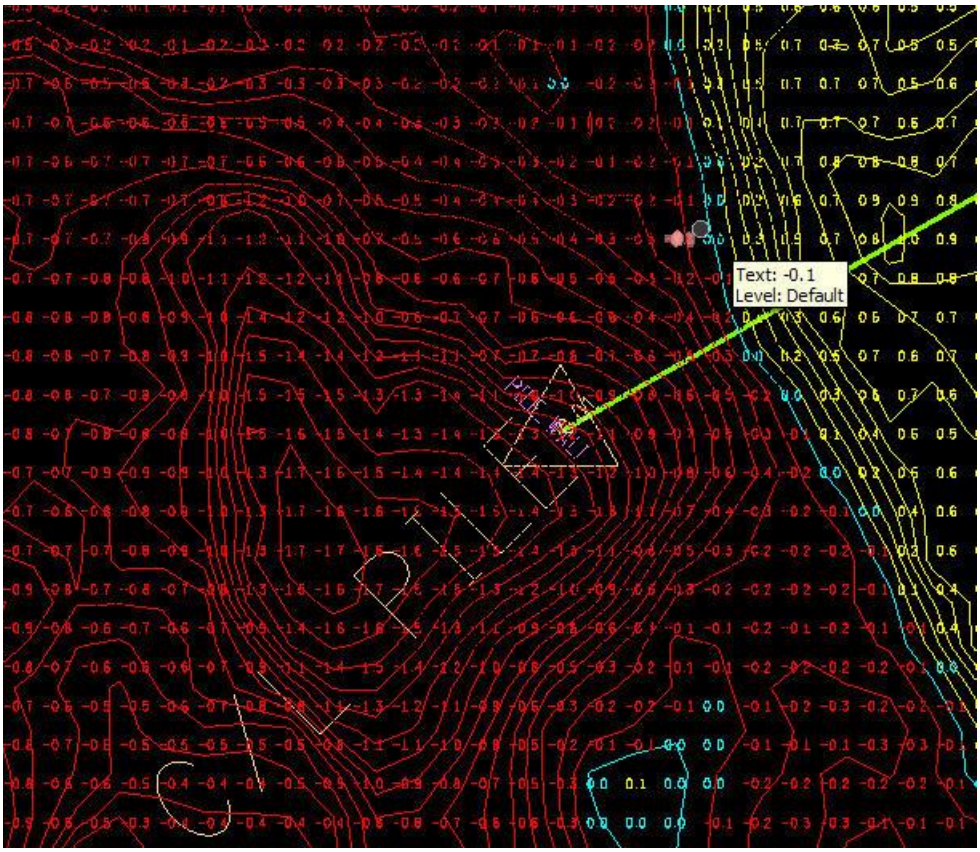

Figure 6-163 Settlement contours after driving Pile 37

Figure 6-164 Screen shot from Lidar camera of abutment B after the end of driving of the two test piles

6.3.4 M-25 Site

A perspective view of the in-depth sensor locations at the M-25 near Harbor Beach, MI is shown in Figure 6-165. Three vertical component accelerometers were pushed to depths 6 ft and 10.5 ft in the loose sand layer at three distances from the pile as shown in Figure 6-165. A 40 ft long HP 12x53 pile was driven to a depth of 32.5 ft using a Pileco D30-32 diesel hammer. Figure 6-166 presents the pile driving penetration resistance as the number of blows per pile foot increment, as well as the cumulative number of blows versus depth of pile tip penetration. It is observed that when the pile penetrates into the dense silt layer, that starts around 15 ft, the driving resistance increases. The total number of blows that were required to drive this pile section was 218. Figure 6-167 depicts the average actual hammer energy per pile foot increment and the hammer efficiency, η, versus depth. The rated energy of the Pileco D30-32 hammer is 69,923 lb-ft. The average hammer efficiency when driving the test pile at M-25 site was around 65%.

The loose condition of the sand near the ground surface resulted in driving the pile more than 12 ft with the first few blows (≈10). This precluded obtaining ground motion measurements at the three sensors installed at this site because the sensor packages were at depths of only 6 and 10.5 ft. However, ground motion data was recorded for the three embedded accelerometers for pile tip penetration depths from 13 ft to 33 ft. The maximum acceleration amplitude was extracted, with the procedure described earlier, and is plotted in Figure 6-168 at the mid-depth of each foot of pile penetration. The sensor closest to the pile face (A2) has the highest ground motion amplitudes, as expected. An increase at the acceleration amplitudes is also observed when the pile tip penetrated into the dense silt around 15 ft.

An array of surface geophones was placed along the ground surface at 10 ft intervals in a straight line from the pile. However, a different data acquisition system than the cDAQ was used to acquire the voltage amplitudes and the signals maxed out, i.e. exceeded the device’s measuring range capability. For this reason, the surface ground motions are not presented.

The contractor had installed sheet piling to form bulkheads on each side of the creek before ground motion monitoring of the test pile was conducted. Driving of the sheet piles was not monitored so contributions to settlement of the loose sand near the surface caused by driving 36 sheet-piles could not be assessed. Before and after driving elevations were determined at one established benchmark at the test pile only, showing no settlement.

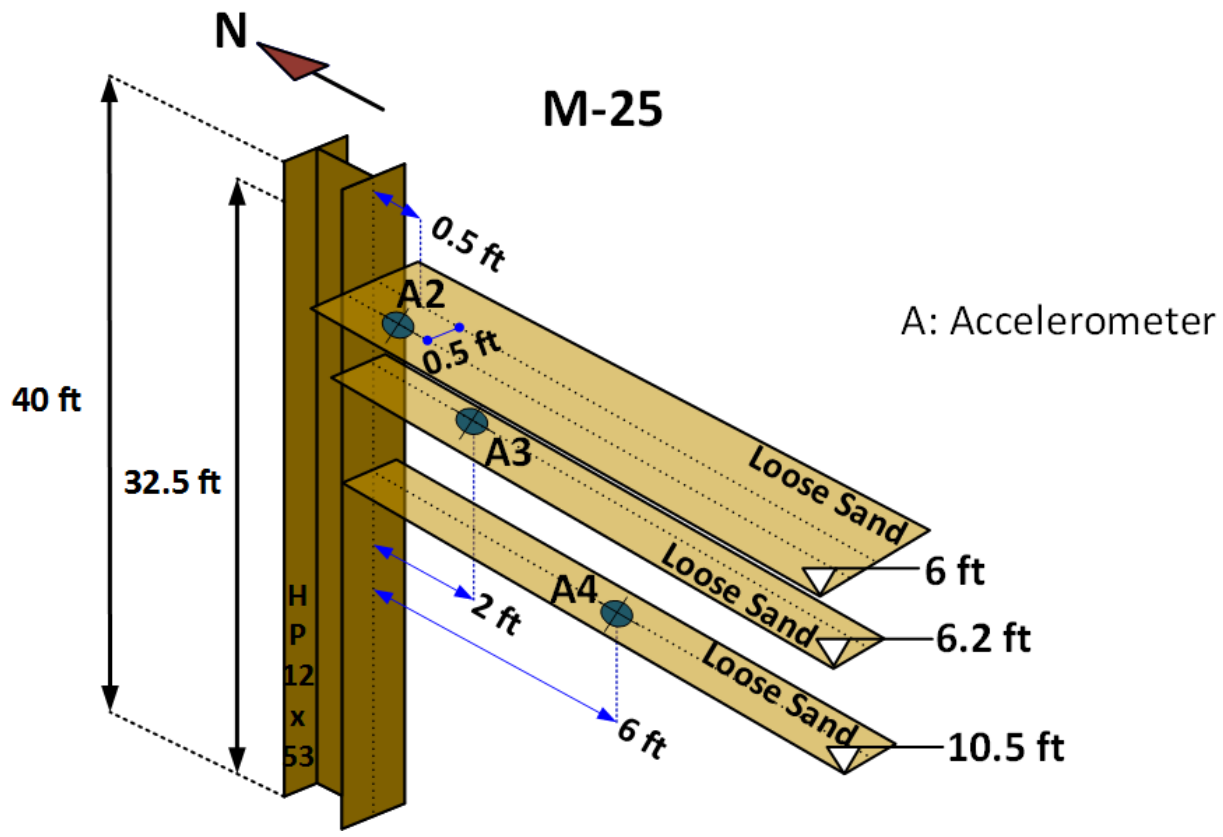

Figure 6-165 Perspective view of buried sensors at M-25 site (not to scale)

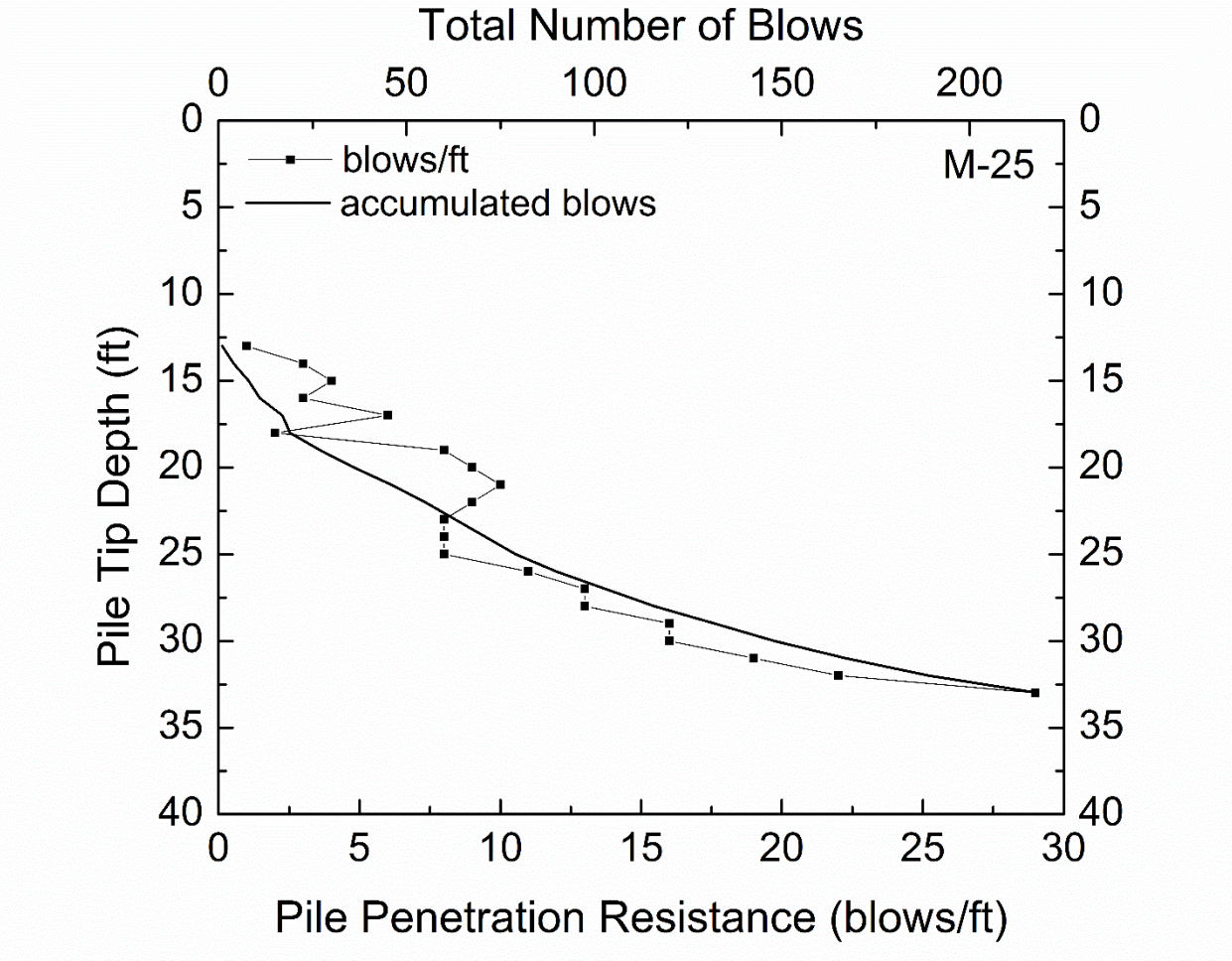

Figure 6-166 Driving Resistance and accumulated blows with depth – M-25 site

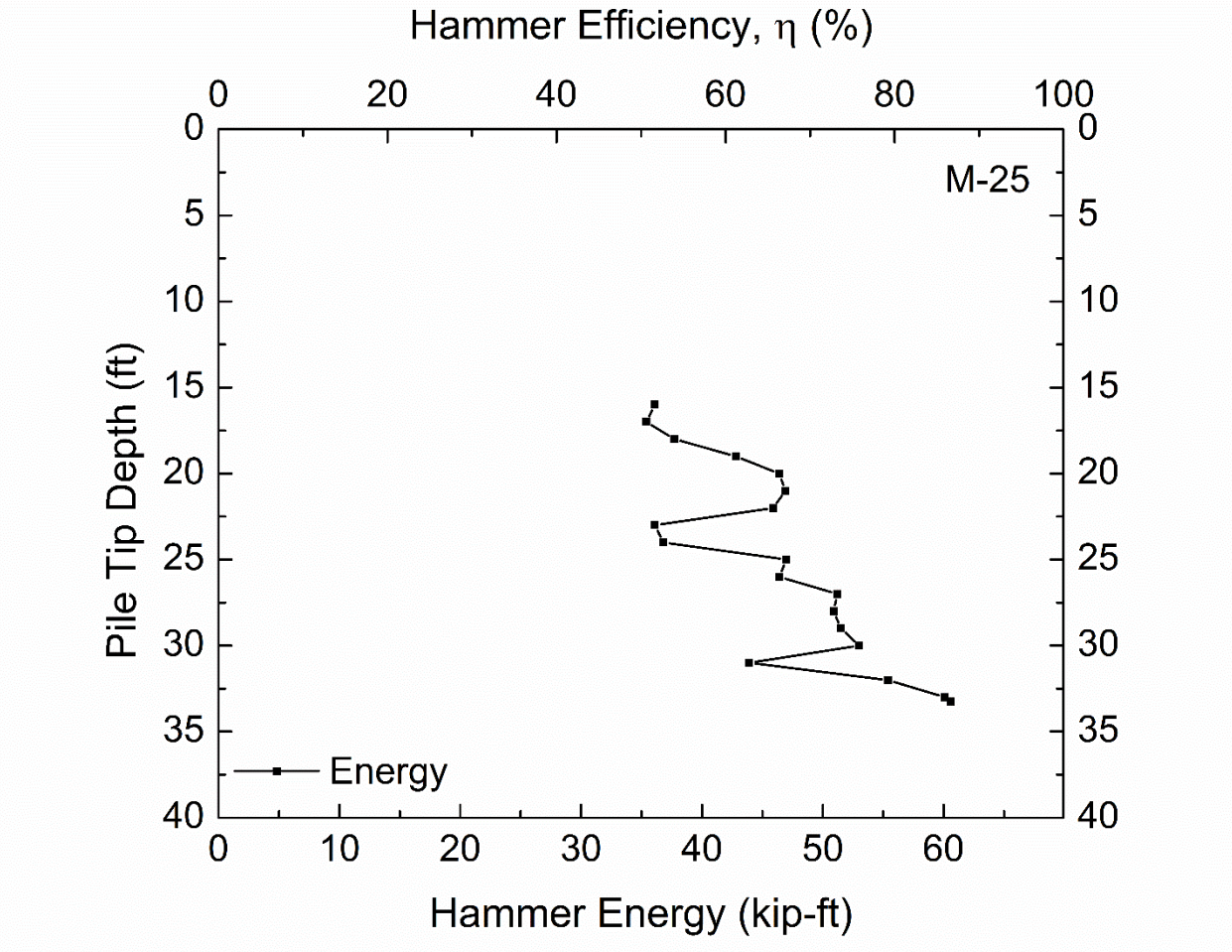

Figure 6-167 Hammer Energy and Hammer Efficiency with depth – M-25 site

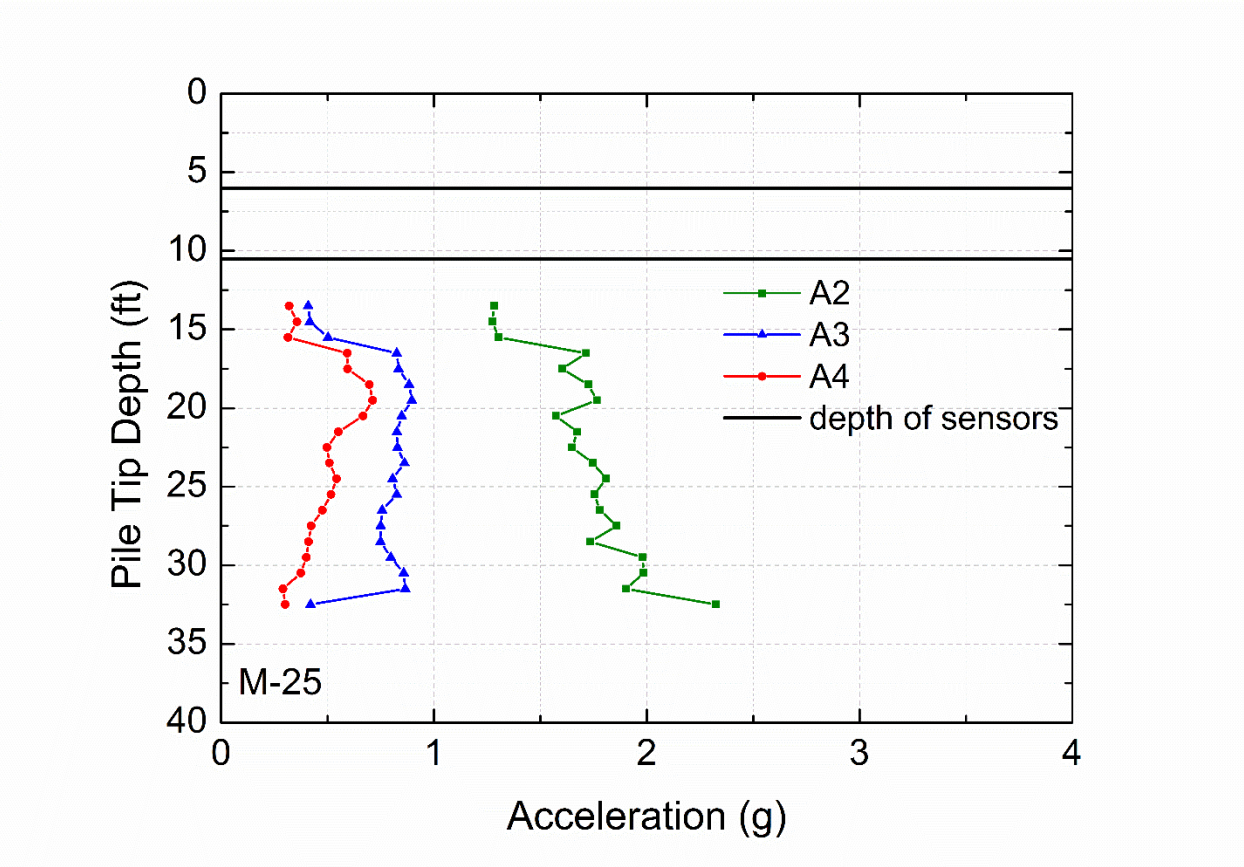

Figure 6-168 Acceleration of buried sensors at M-25 site – Vertical Direction

6.3.5 M-66 Site

A perspective view of the in-depth sensor locations at the M-66 near Battle Creek, MI is shown in Figure 6-169. Three triaxial accelerometers were pushed to a depth of 34.5 ft at three different distances from the pile flange, into a medium dense sand deposit. One geophone (SG) was installed in the very loose sand layer at a depth of 5.4 ft. A 40 ft long HP 12x53 pile was driven using a Delmag D16-32 diesel hammer. An additional pile section, of 9.5 ft length, was spliced on the pile when the pile tip was at a depth of about 36 ft, in order to achieve the predetermined ultimate pile capacity. The final depth of penetration of the pile was 47.5 ft. Figure 6-170 presents the pile driving penetration resistance as the number of blows per pile foot increment and the accumulated number of blows versus depth of pile tip penetration. The total blow count to drive this pile section was 430. The driving resistance gradually increased with increasing penetration depth into denser sand layers. Figure 6-171 illustrates the average actual hammer energy per pile foot increment and the hammer efficiency, η, versus depth. The rated energy of the Delmag D16-32 hammer is 39,830 lb-ft. The average hammer efficiency when driving the test pile at M-66 site was around 48%.

Figure 6-172, Figure 6-174 and Figure 6-176 show the acceleration amplitudes of the three components of the sensors versus depth of the pile tip, while Figure 6-173, Figure 6-175 and Figure 6-177 present the velocity amplitudes versus depth for the three measured directions, i.e. vertical, longitudinal and transverse. The peak particle velocities of the vertical component of the shallow geophone SG are also plotted in Figure 6-173. In each plot, the common depth of the sensors is shown by a solid horizontal line. A dashed horizontal line indicates the depth of the pile tip was (36.4 ft), when pile driving was paused to splice the pile. It was expected that the sensor closest to the pile face (A1) would record the largest ground motion amplitudes, which would attenuate for the next two sensors (A2 and A3). However, as can be seen on the Figures, the accelerometer nearest to the pile does not have much greater amplitudes than the further two until the pile driving is resumed after the splice. This phenomenon is more pronounced for the vertical component amplitudes. The reason for this anomalous behavior is not known, but it might be a function of poor coupling between the ground and the sensor packages.

When driving was resumed at 36.4 ft depth after the splice, the penetration resistance increased relative to the resistance before welding the additional pile section. The increase in pile capacity with time, known as soil set-up, is much faster for sands and silts than for clays because the pore pressures dissipate more rapidly in granular soils than in cohesive soils (Hannigan et al. 2006). Thus, this might be the reason that the increase in penetration resistance resulted in an increase of vibration amplitudes when pile driving resumed.

Figure 6-178 to Figure 6-180 present the diagonal distance from pile tip to sensor location versus the vertical peak particle velocity for the three buried accelerometers. It is evident that ground motions gradually increased as the pile tip reached the sensor elevation, thus the diagonal distance decreased. When the tip passed the sensor's depth and went below, with increasing diagonal distance, peak particle velocities were either constant or fell off when the pile tip was far away from the sensor. This behavior is more pronounced for the closest sensor to the pile (A1). This vibration pattern is another indication confirming the hypothesis that it is primarily spherical waves from the pile tip that impact the sensor. Cylindrical waves from the pile shaft do not travel on paths that could encounter the sensor up to this point. After the pile tip passes the depth of the sensor, both spherical waves from the pile tip and cylindrical waves from the pile shaft impact the sensors and the ground motion amplitude remains nearly constant until the pile tip is at considerable distance from the sensor.

Figure 6-181 and Figure 6-182 present acceleration amplitudes versus diagonal distance from the sensor for the three monitored directions of the buried accelerometers. The above behavior discussed for the vertical component is also observed for the two horizontal directions, with the phenomenon being more pronounced for the closest sensor to the pile (A1).

A comparison of the three component response of the accelerometers for the three measured directions for each of the buried sensors is shown in Figure 6-183a to Figure 6-185a . The black solid line indicates the sensors' depth, while the dashed line indicates the pile tip depth when pile driving was paused and an additional pile section was spliced.

The vertical components generally showed higher ground motion amplitudes compared to the longitudinal and transverse directions.

Figure 6-183b to Figure 6-185b show the vertical to longitudinal (V/L) and vertical to transverse (V/T) components of acceleration. For sensor A1, nearest to the pile face, Figure 6-183b, the vertical component of motion is greater than either the longitudinal or transverse components below a pile tip depth of around 13 ft. The next two sensors, A2 and A3, have ration of components, V/L and V/T, higher than one for almost the entire depth range of pile penetration.

Nine ground surface geophones were also placed along the ground surface at the locations shown in Figure 6-186. The two closest geophones (BG1 and BG2) were triaxial configurations, while geophones G1 to G3 had single components of vertical, longitudinal and transverse axes and the further out (G4) was single vertical component geophone. The peak particle velocities of the sensors versus depth are plotted in Figure 6-187 to Figure 6-189. There is an increase in velocity amplitudes when the pile tip enters the dense sand at around 25 ft.

Figure 6-190a and Figure 6-191a show the three velocity components versus depth and Figs. 6.3.1.26b to 6.3.1.28b show the ratios of vertical to longitudinal (V/L) and vertical to transverse (V/T) components for sensors BG1 and BG2, respectively. Both surface sensors had higher longitudinal component peak particle velocities than the vertical component of motions for the entire depth range of pile installation. For sensor BG2, the ratio of vertical to longitudinal (V/L) is less than one for the total depth range of installation. Also, the ratio of vertical to transverse (V/T) and vertical to longitudinal (V/L) is less than one for almost the total depth range of pile installation. This behavior does not indicate again a Rayleigh wave development.

Three sensors were located at the same distance from the pile (5.3 ft); BG1 geophone was positioned on the surface, SG geophone was installed 5.4 ft into a very loose sand layer and A3 accelerometer was installed 34.5 ft into a medium dense sand deposit. An interesting comparison can be made by plotting ground motions versus depth for the three monitored components (Figure 6-192 to Figure 6-194). For the vertical motions, the three

sensors, BG1, SG and A3, have a similar response until the pile tip reaches a depth of 25 ft. At greater depths, ground motion amplitudes increase for sensor A3 until the pile tip reaches the elevation of the sensor, following reduction in peak particle velocities after the pile tip departs downward from the sensor depth. Sensors SG and BG1 follow the same trend until the end of driving, with SG recording lower amplitudes after a depth of 20 ft. For the longitudinal motions, BG1 geophone on the surface recorded higher amplitudes than A3 accelerometer until a depth of 30 ft, where the two sensors have a similar response (Figure 6-193). For the transverse motions, the vibration pattern is similar for sensors BG1 and A3, with the in-depth sensor recording slightly lower amplitudes (Figure 6-194).

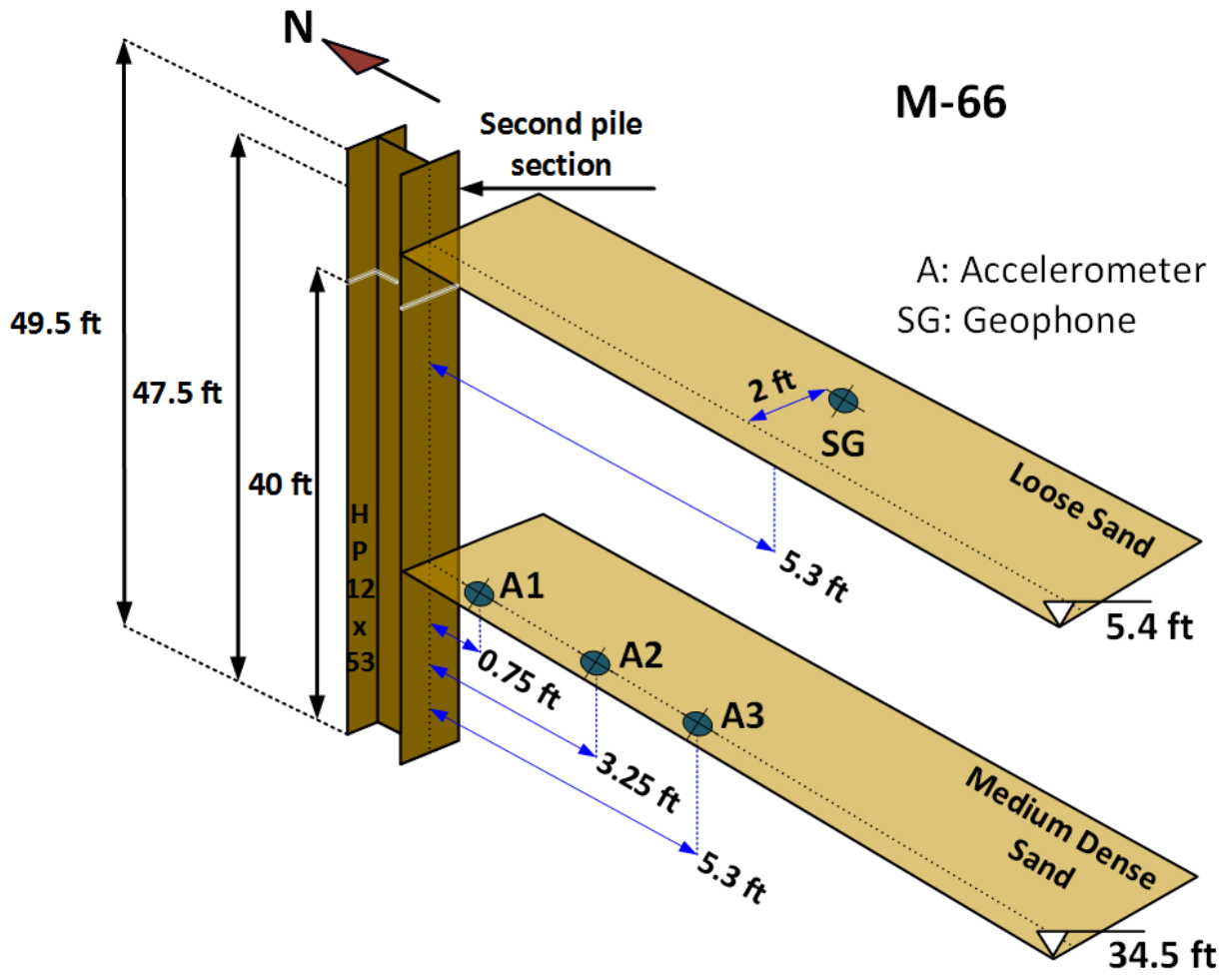

Figure 6-169 Perspective view of buried sensors at M-66 site (not to scale)

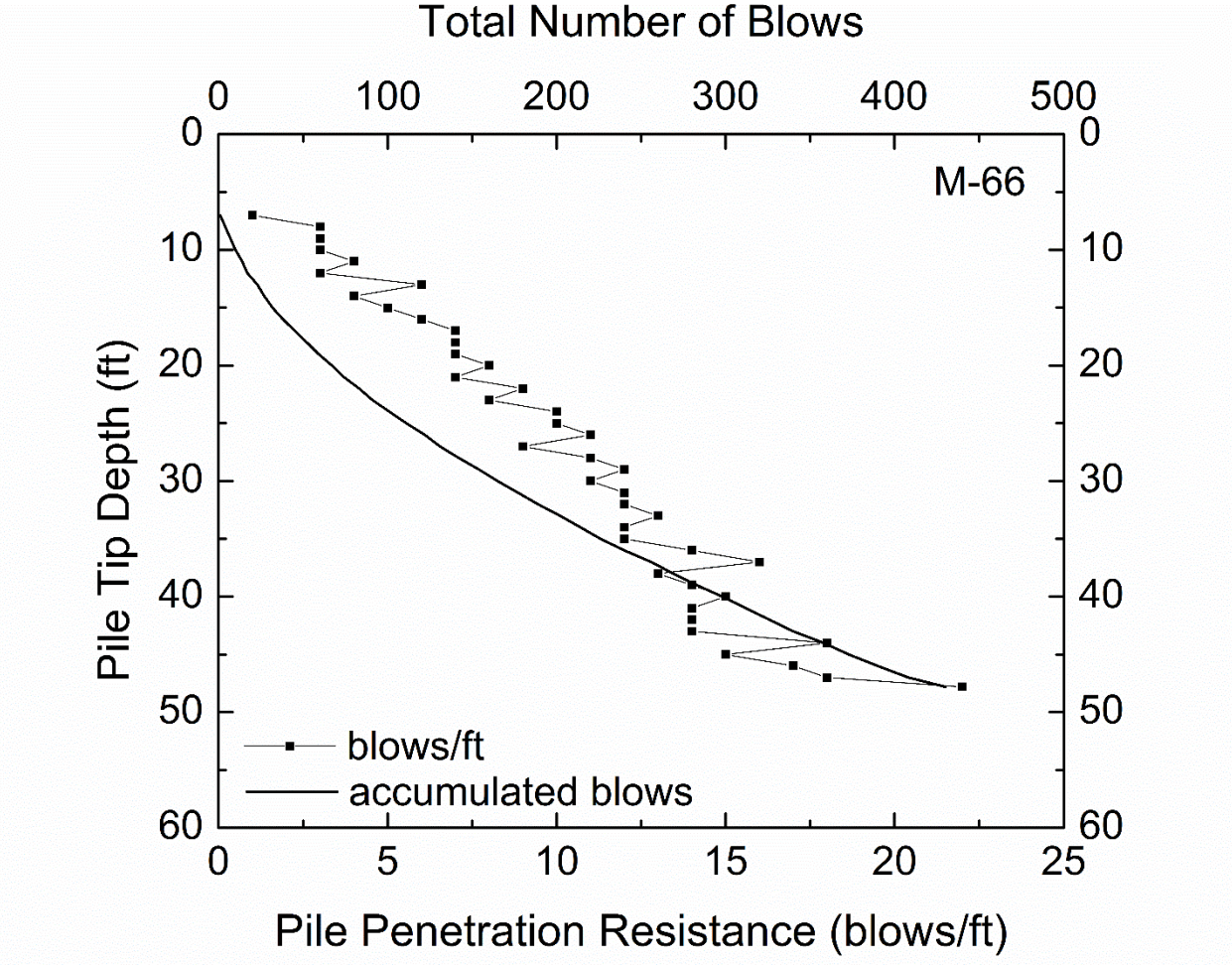

Figure 6-170 Driving Resistance and accumulated blows with depth – M-66 site

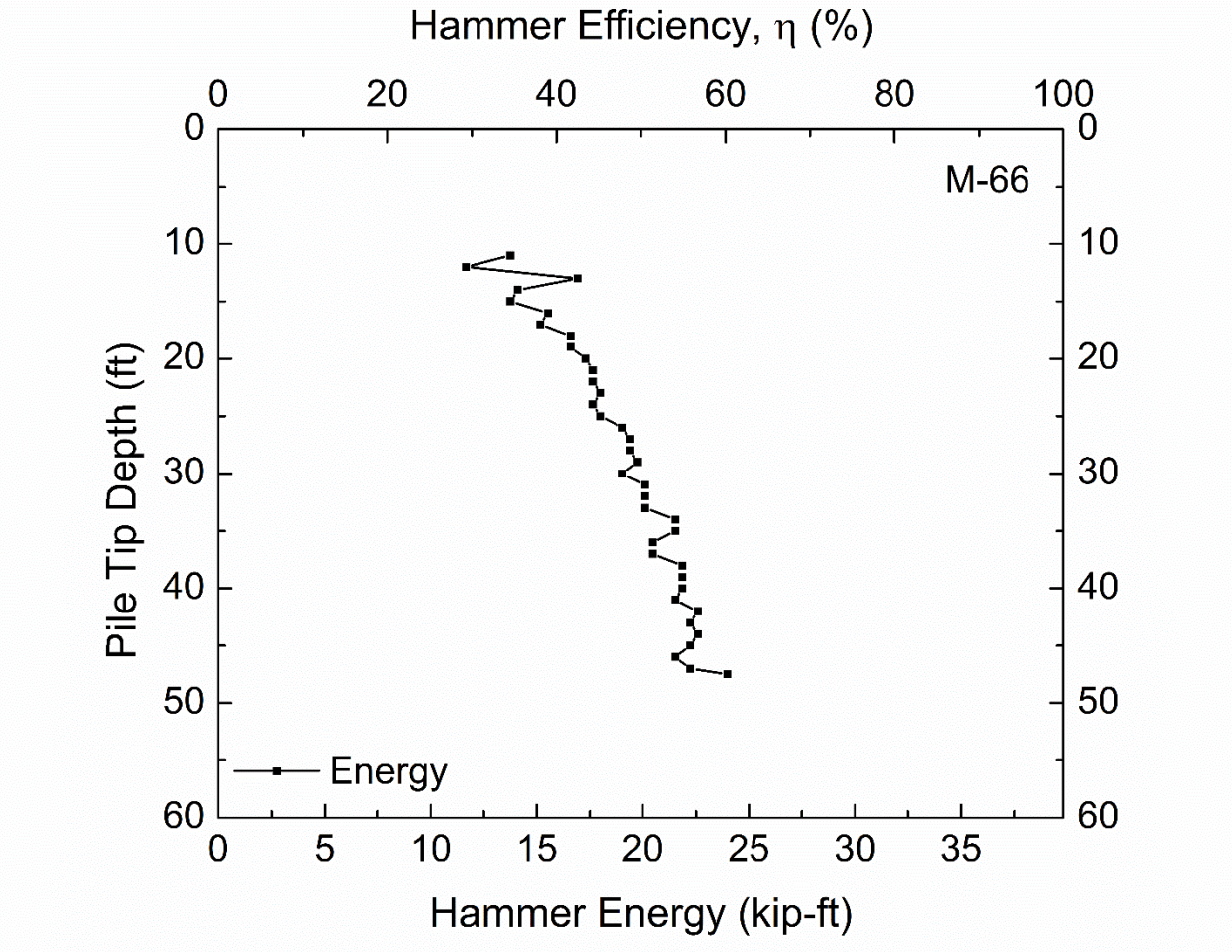

Figure 6-171 Hammer Energy and Hammer Efficiency with depth – M-66 site

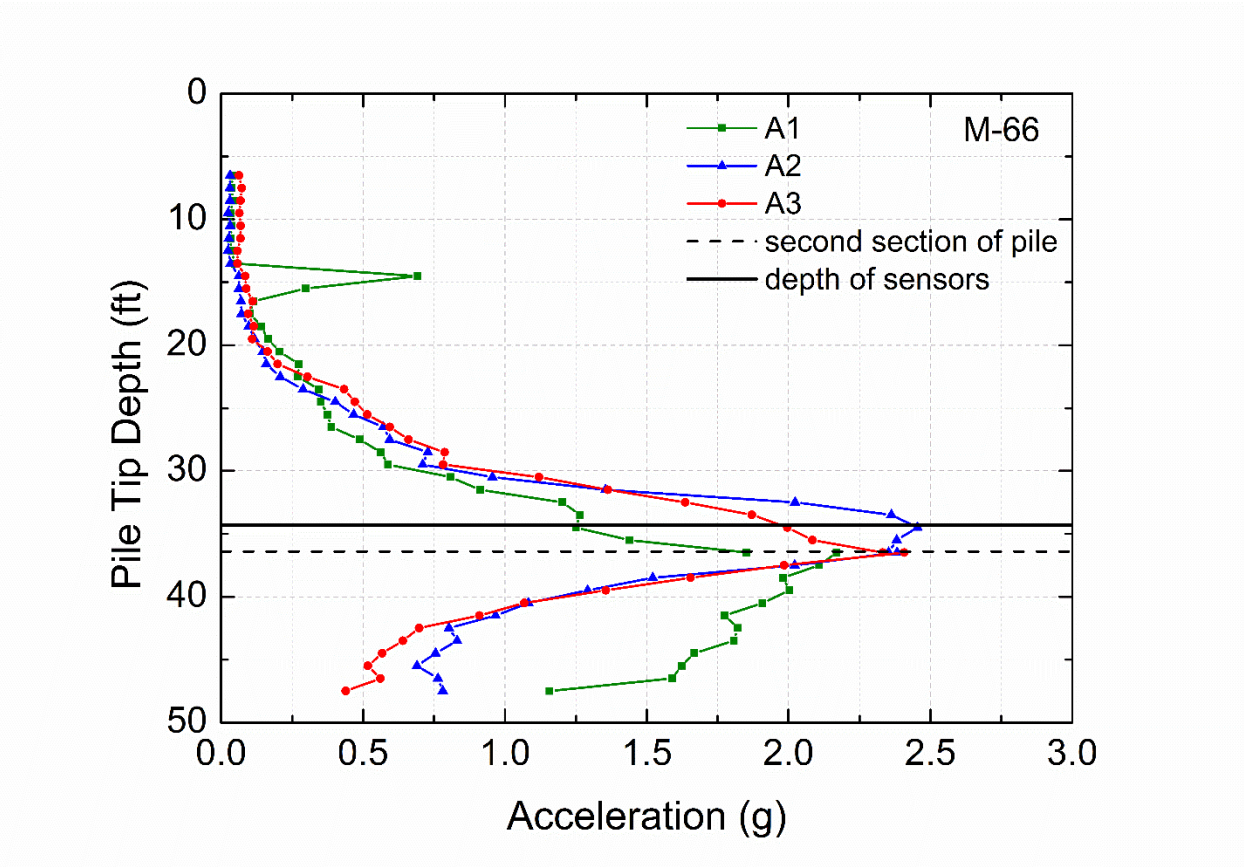

Figure 6-172 Acceleration of buried sensors at M-66 site – Vertical Direction

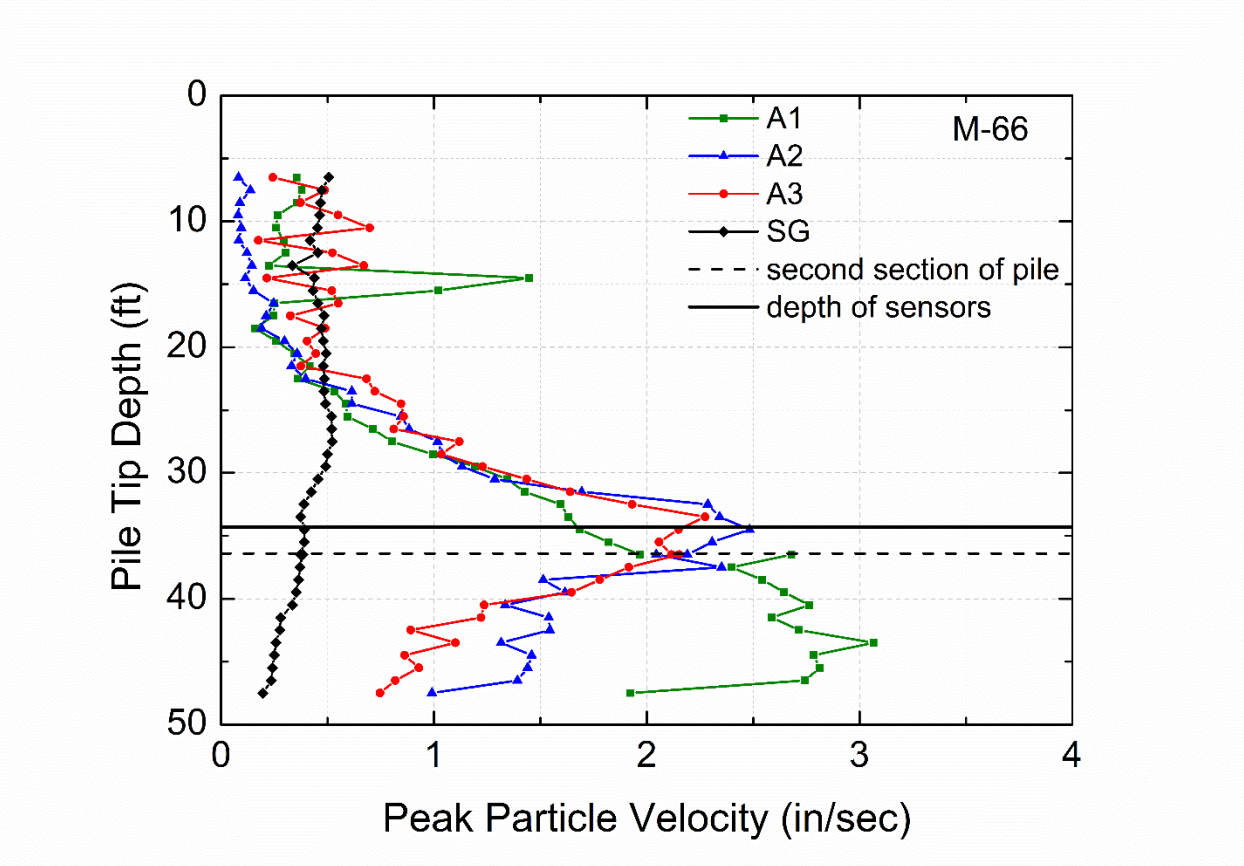

Figure 6-173 Peak Particle Velocity of buried sensors at M-66 site – Vertical Direction

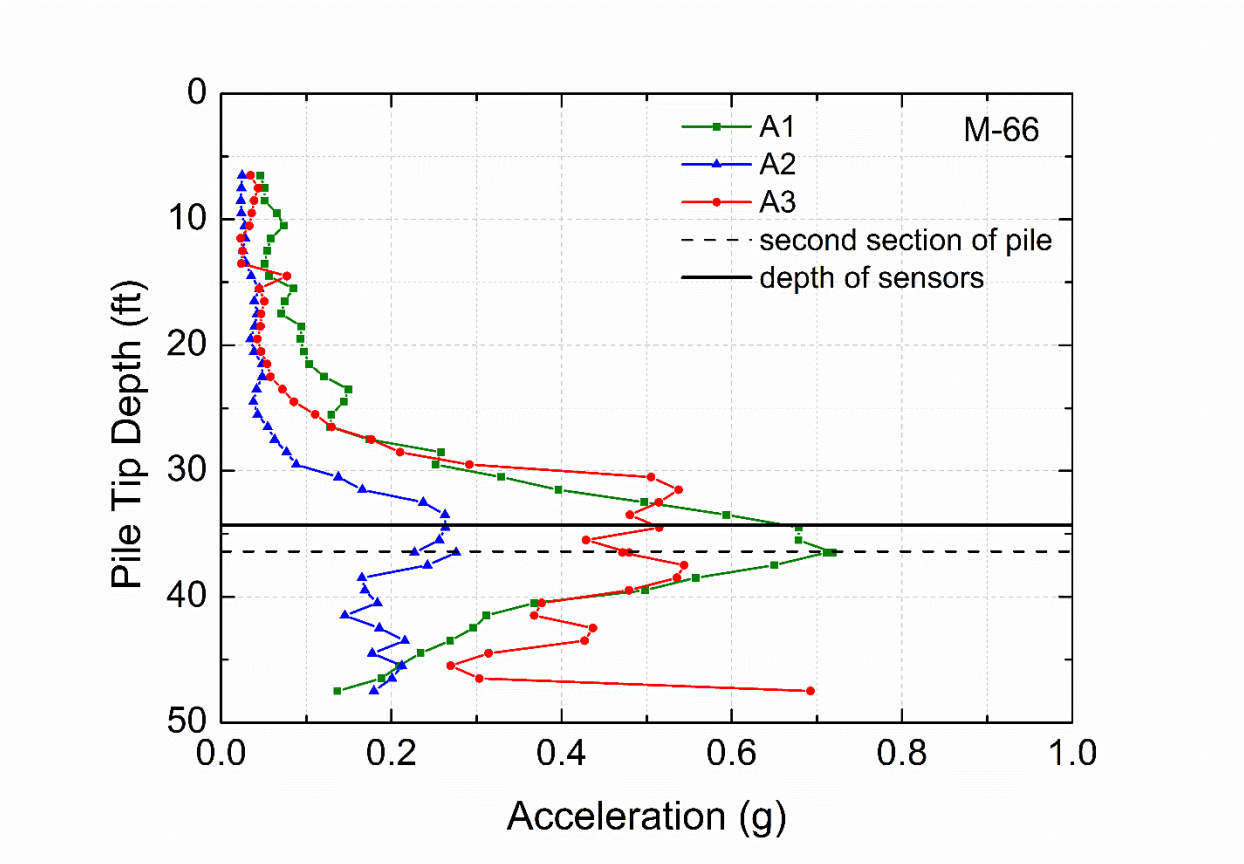

Figure 6-174 Acceleration of buried sensors at M-66 site – Longitudinal Direction

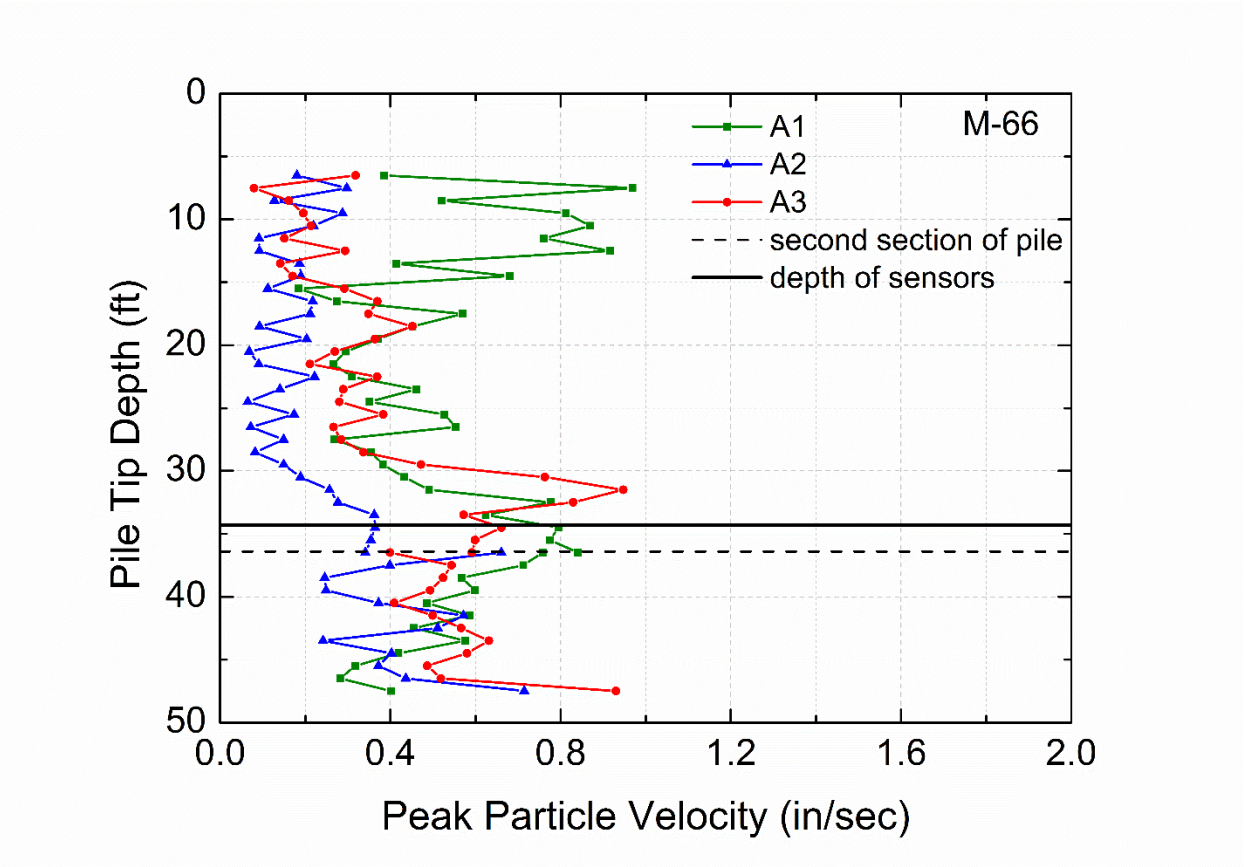

Figure 6-175 Peak Particle Velocity of buried sensors at M-66 site – Longitudinal Direction

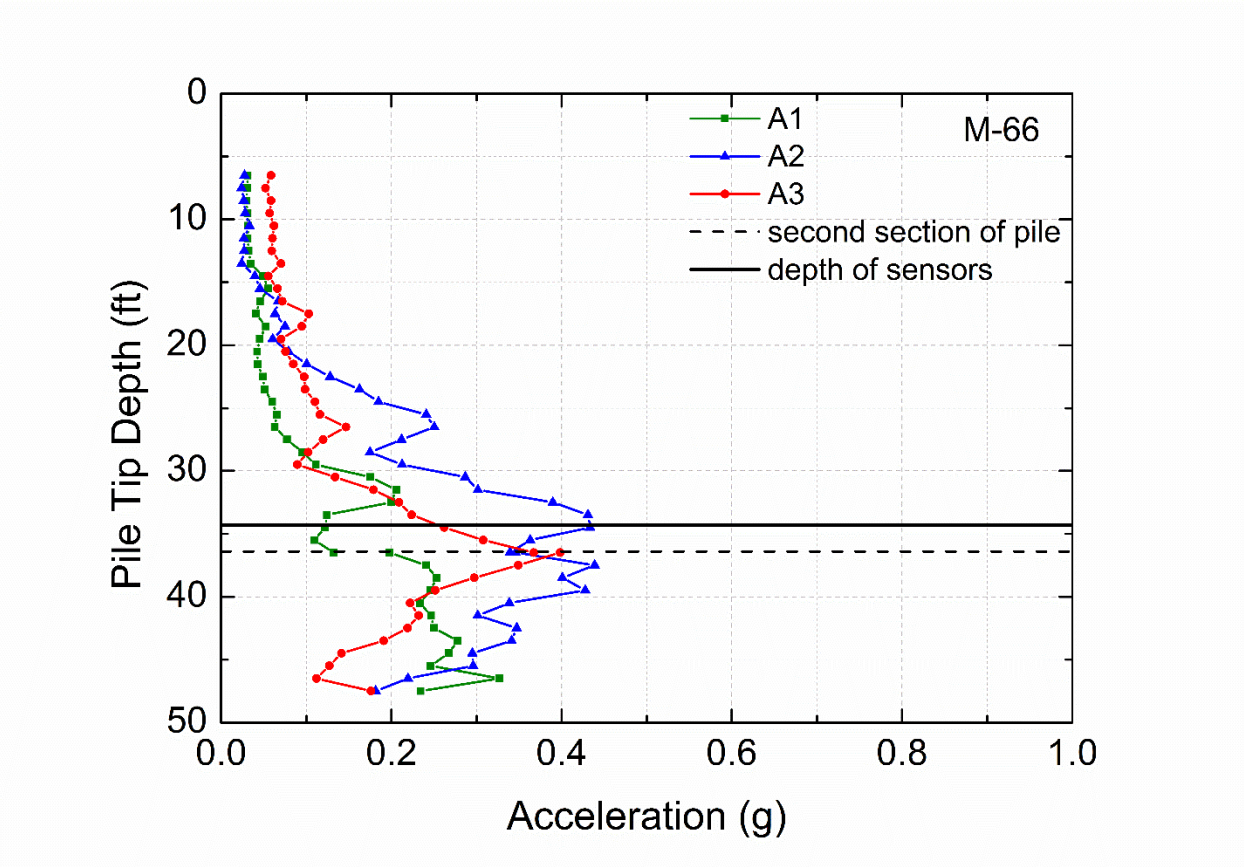

Figure 6-176 Acceleration of buried sensors at M-66 site – Transverse Direction

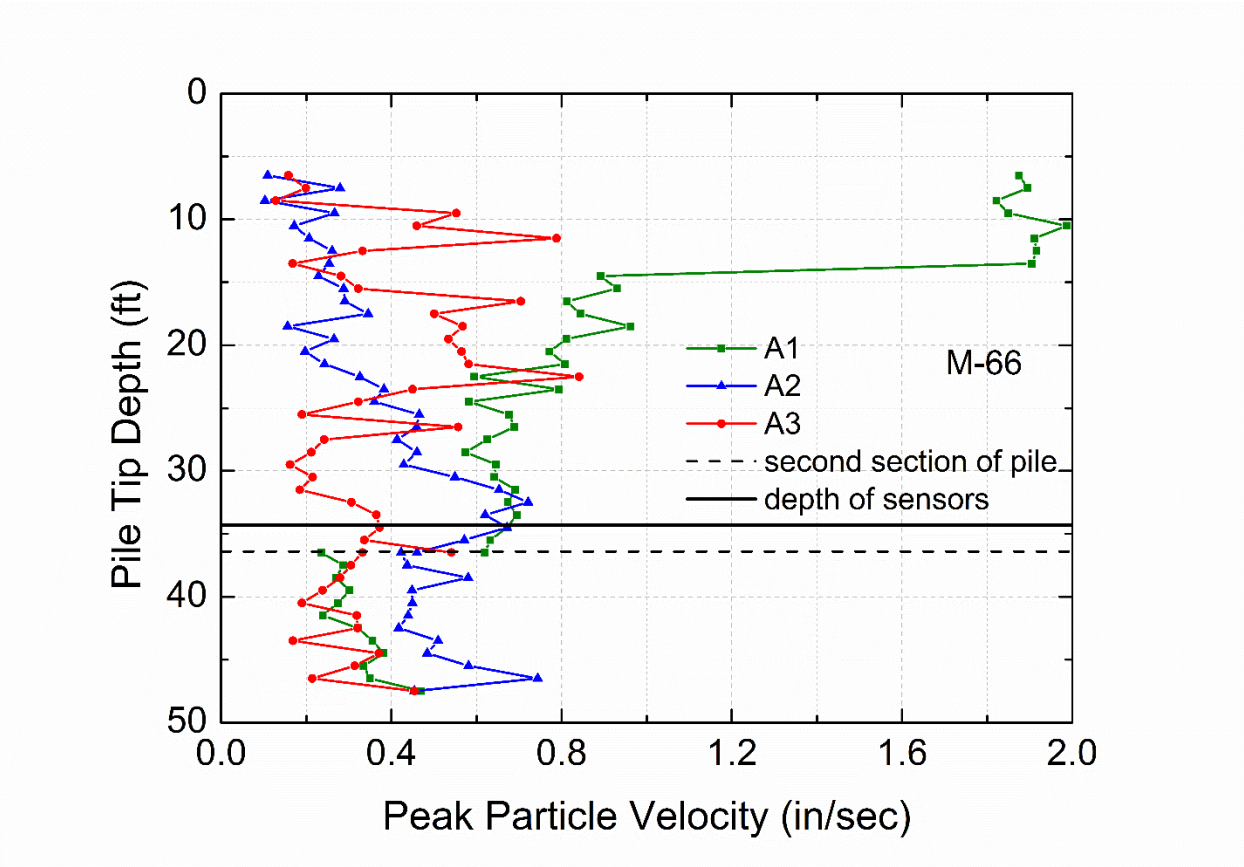

Figure 6-177 Peak Particle Velocity of buried sensors at M-66 site – Transverse Direction

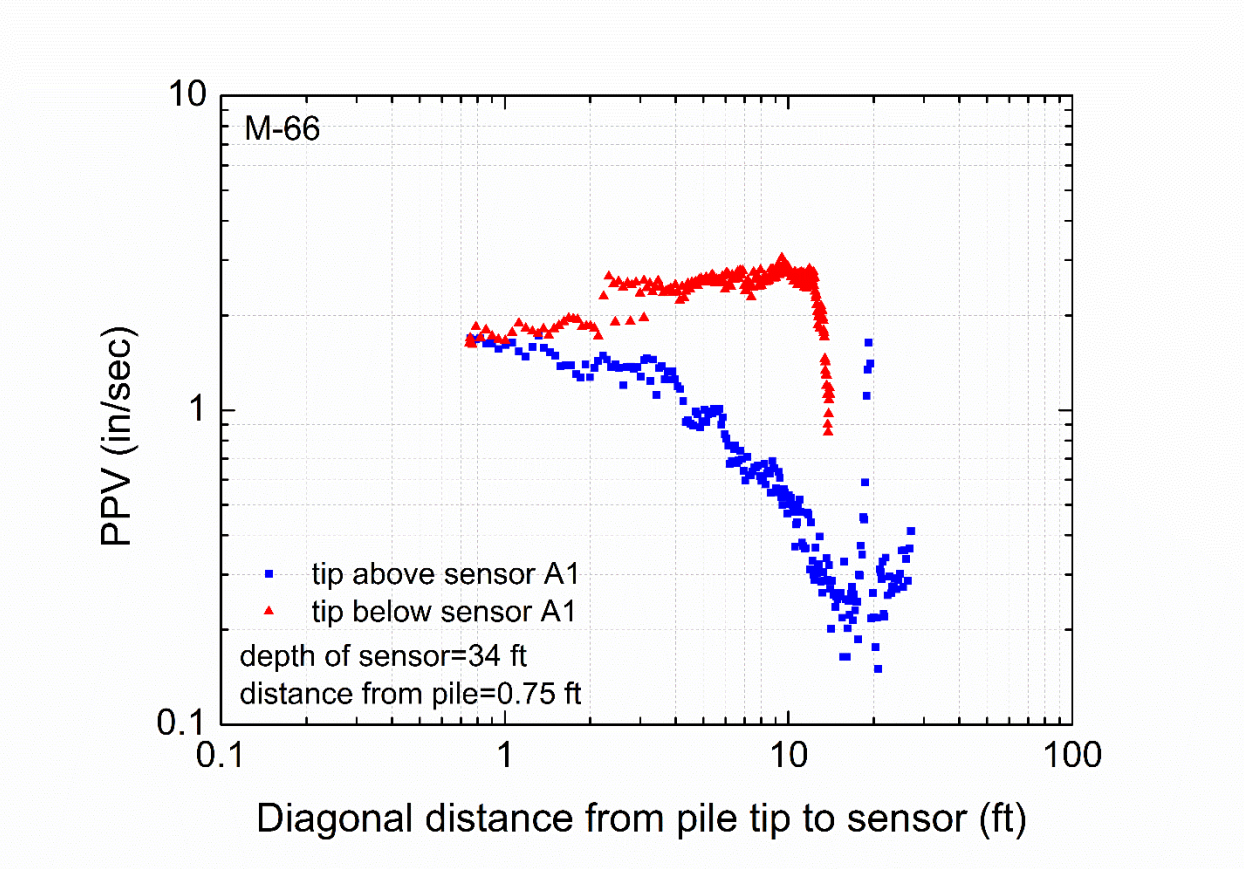

Figure 6-178 Peak particle velocity versus diagonal distance from pile tip to sensor A1 at M-66 site – Vertical direction

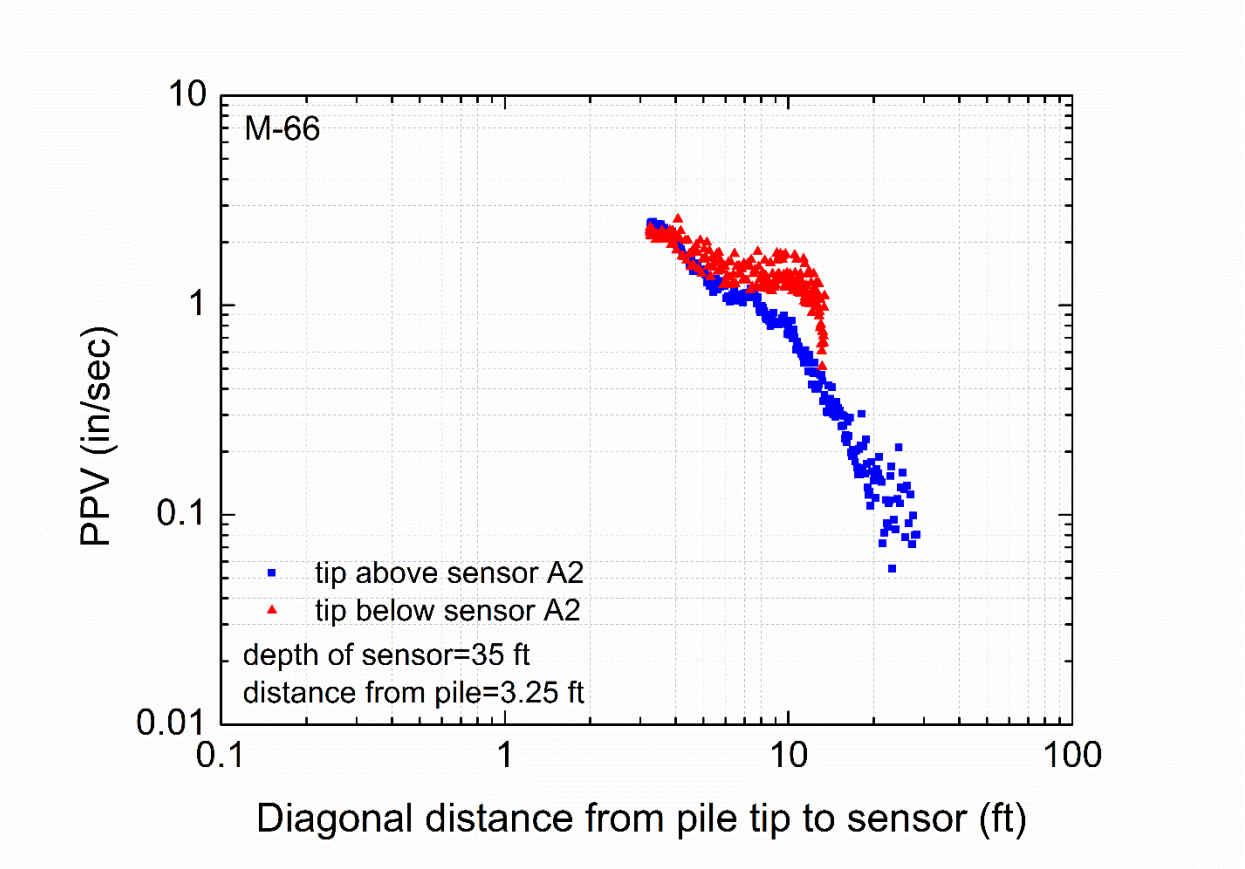

Figure 6-179 Peak particle velocity versus diagonal distance from pile tip to sensor A2 at M-66 site – Vertical direction

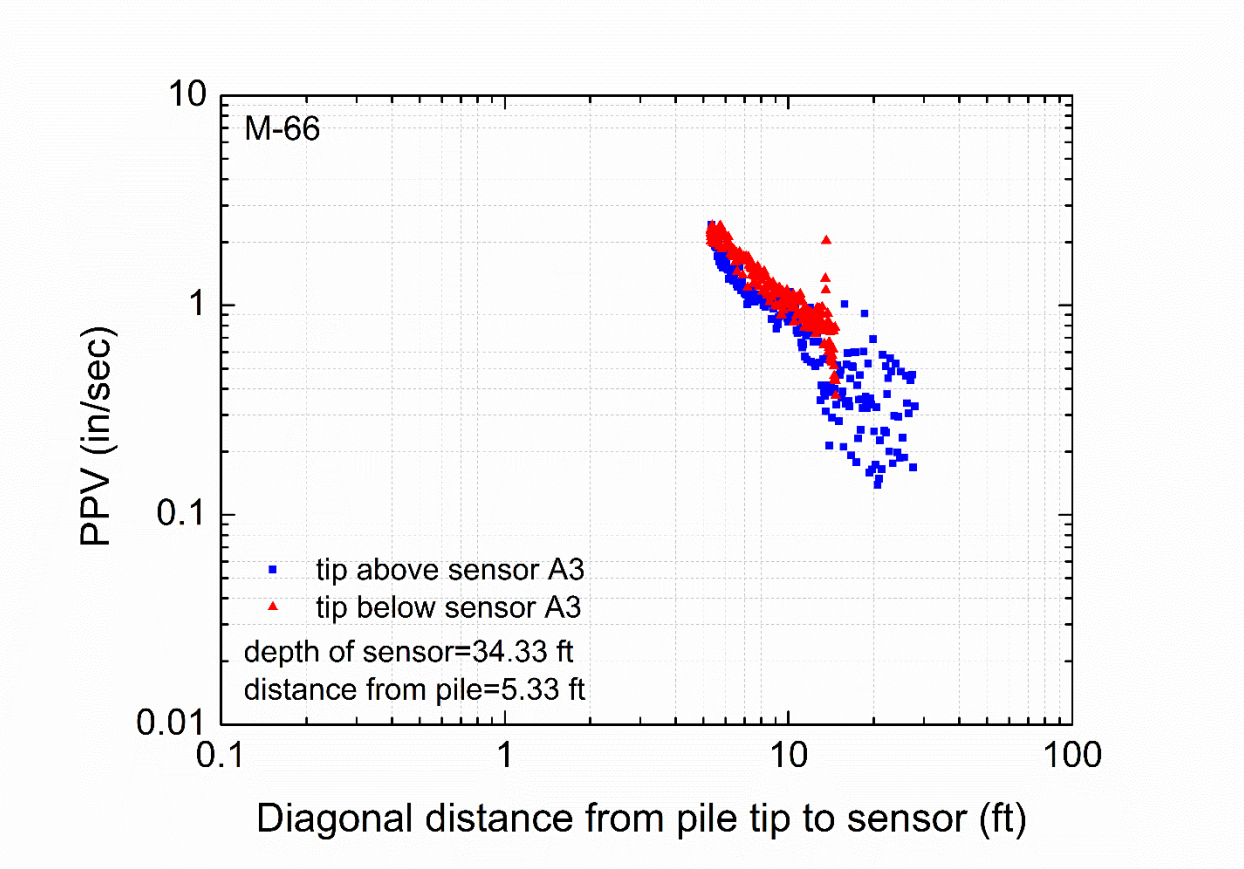

Figure 6-180 Peak particle velocity versus diagonal distance from pile tip to sensor A3 at M-66 site – Vertical direction

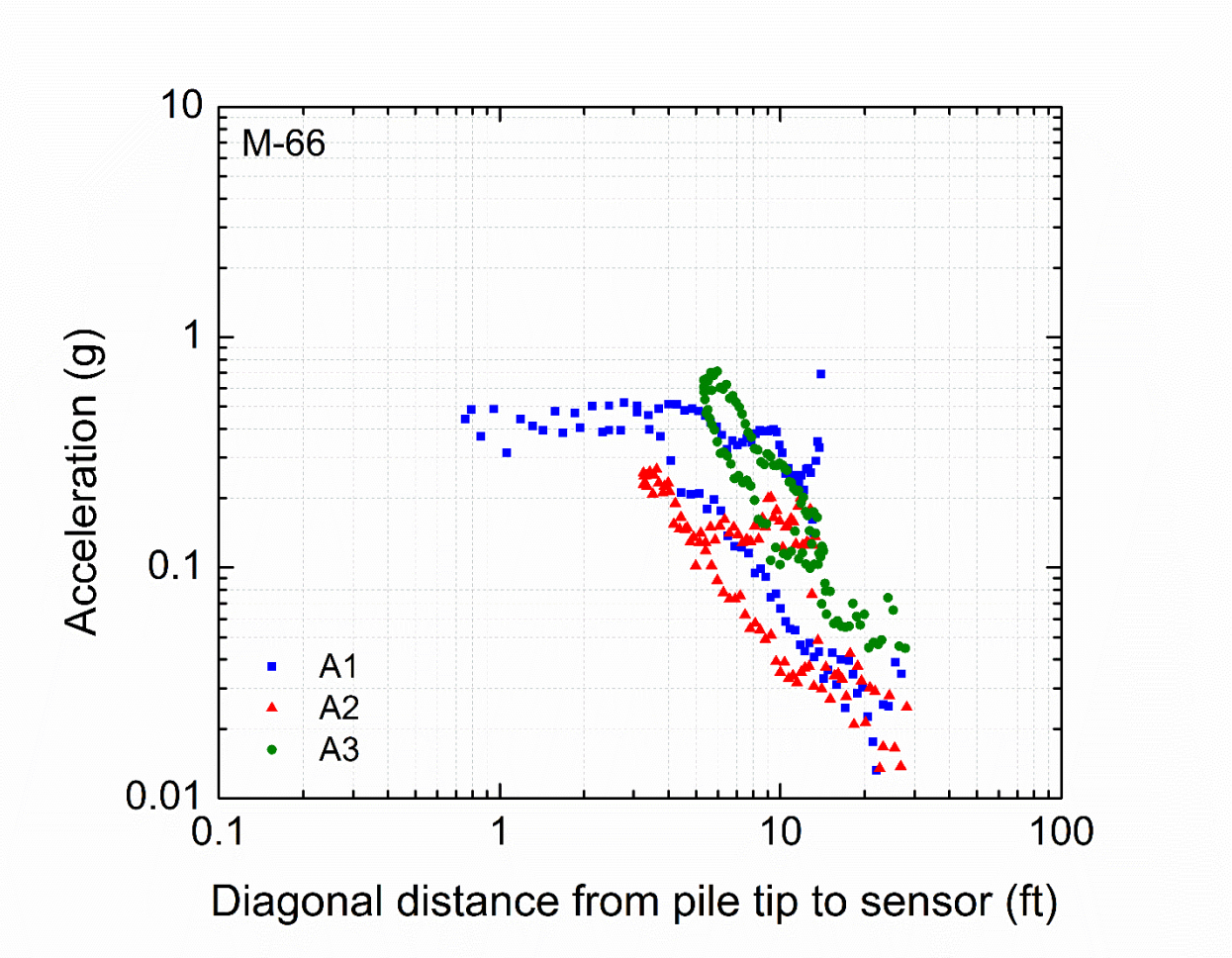

Figure 6-181 Acceleration versus diagonal distance from pile tip to buried sensors at M-66 site – Longitudinal direction, logarithmic scale

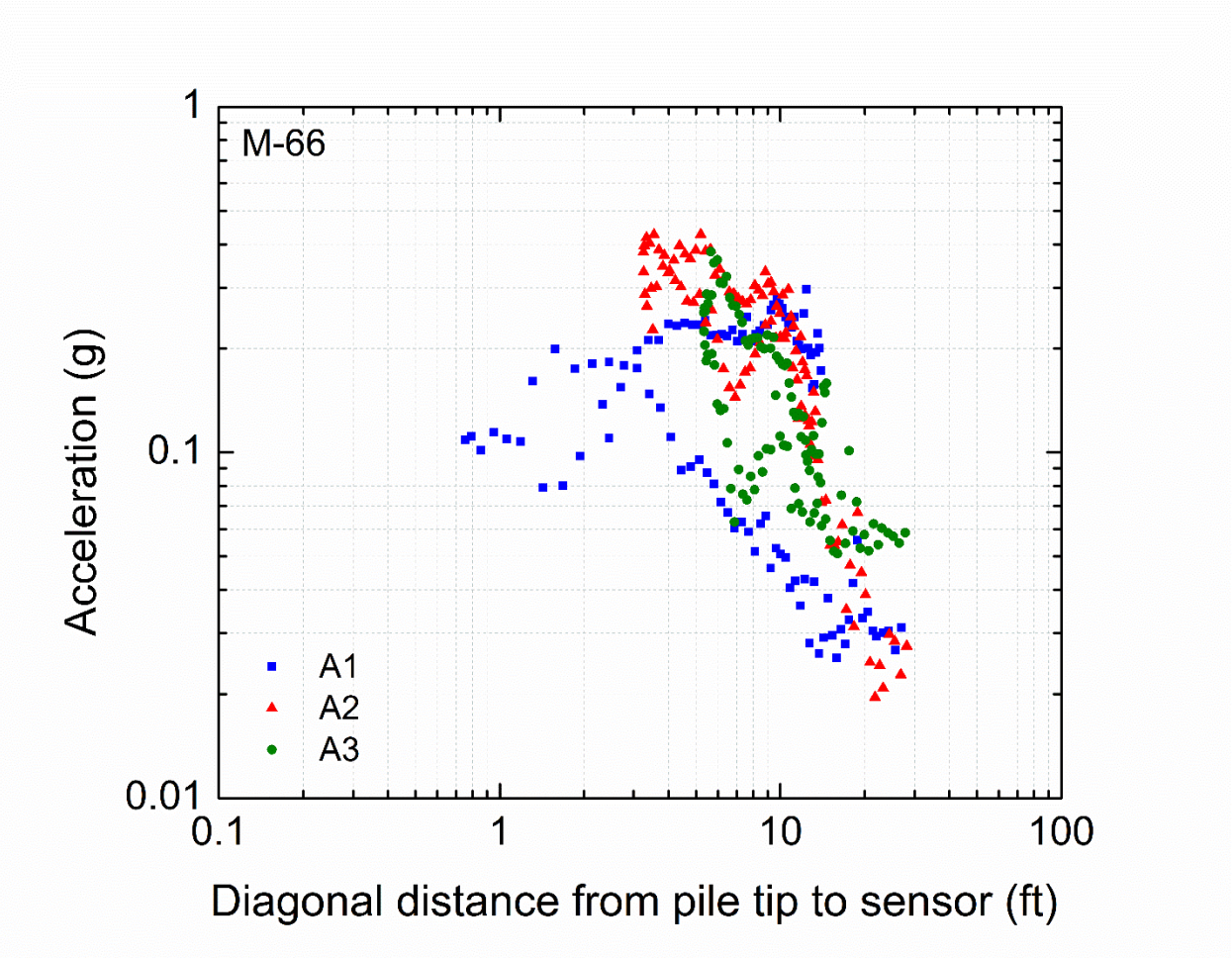

Figure 6-182 Acceleration versus diagonal distance from pile tip to buried sensors at M-66 site – Transverse direction, logarithmic scale

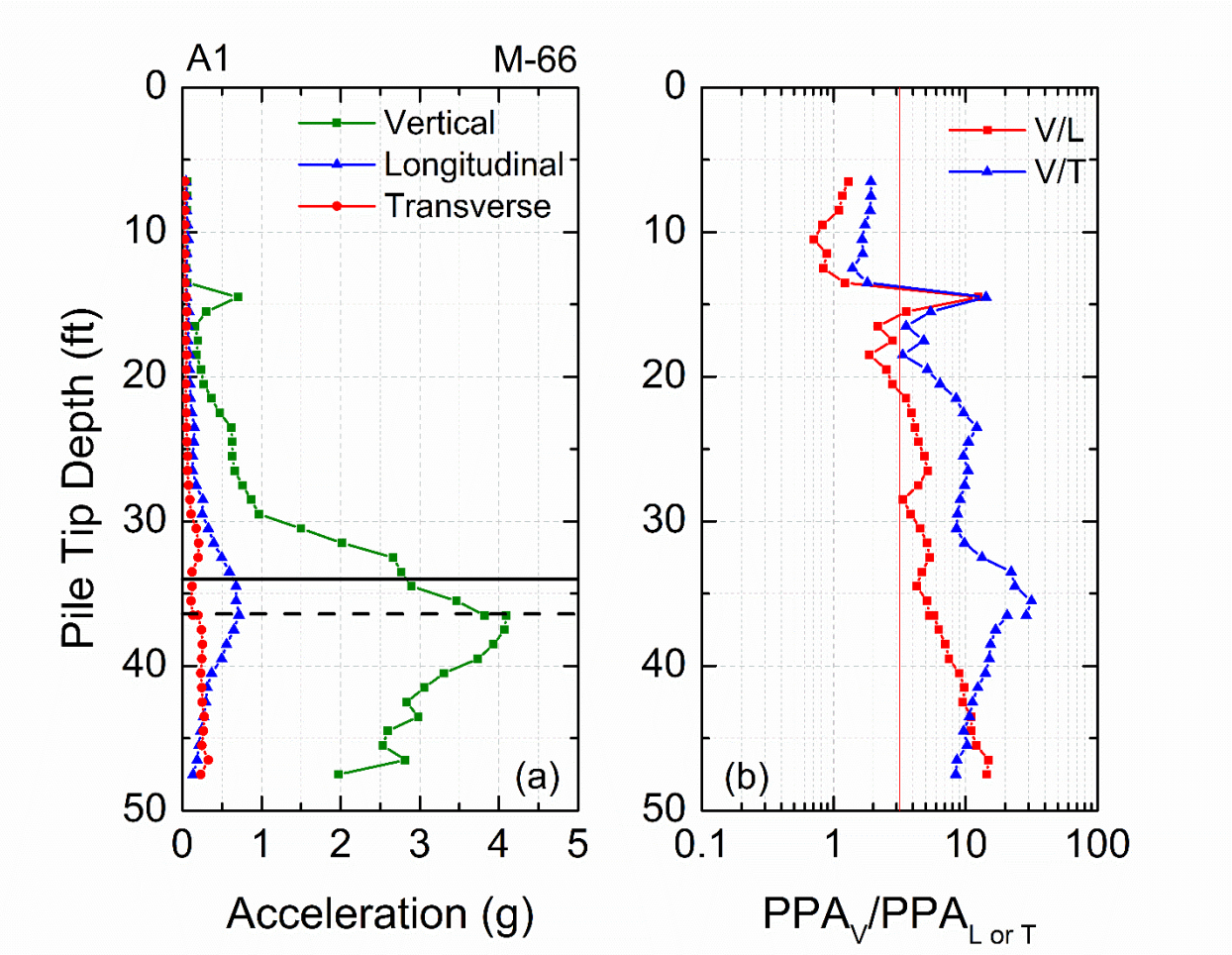

Figure 6-183 (a) Acceleration amplitudes of three directions of sensor A1 and (b) vertical to longitudinal and vertical to transverse components of accelerations – M-66 site

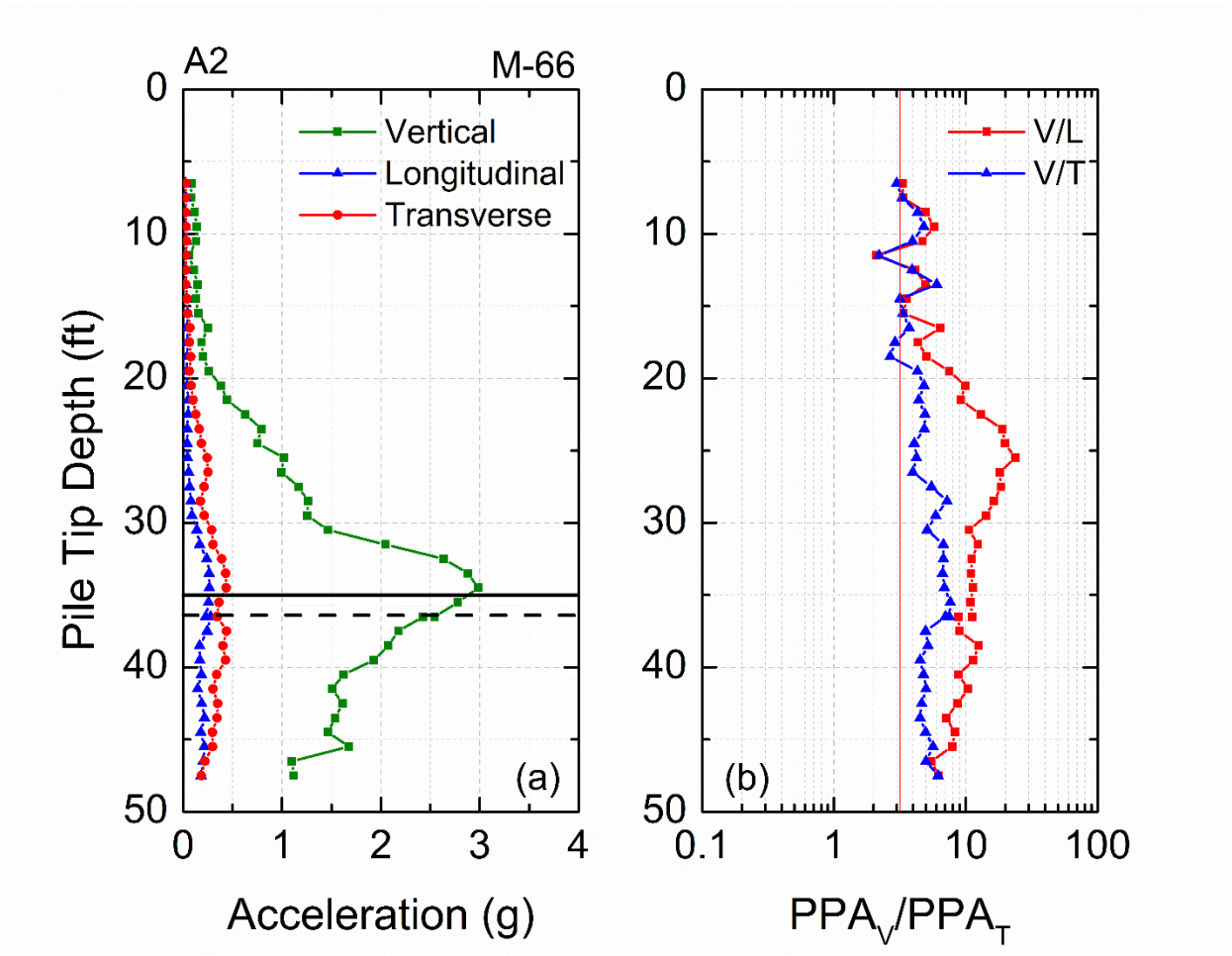

Figure 6-184 (a) Acceleration amplitudes of three directions of sensor A2 and (b) vertical to longitudinal and vertical to transverse components of accelerations – M-66 site

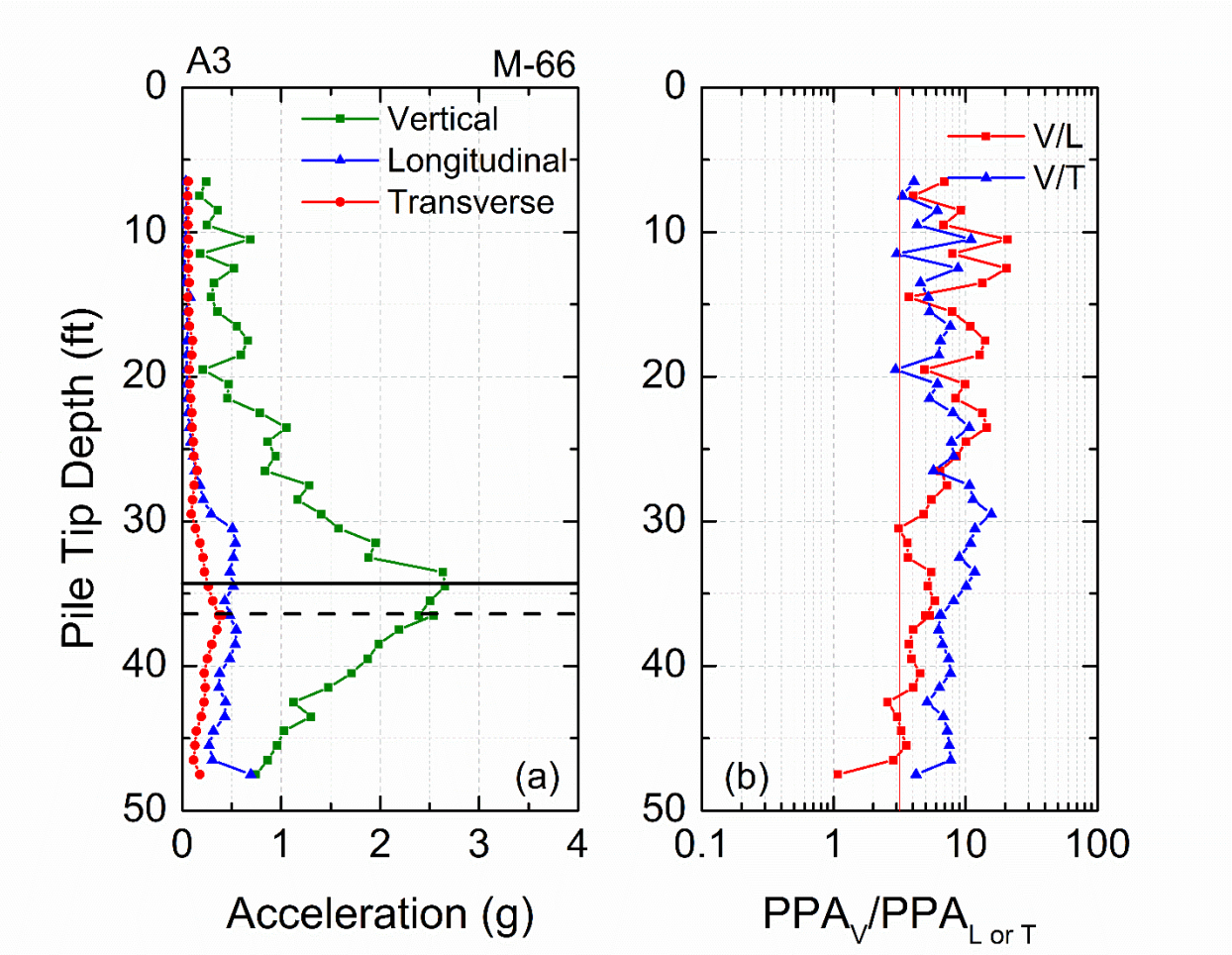

Figure 6-185 (a) Acceleration amplitudes of three directions of sensor A3 and (b) vertical to longitudinal and vertical to transverse components of accelerations – M-66 site

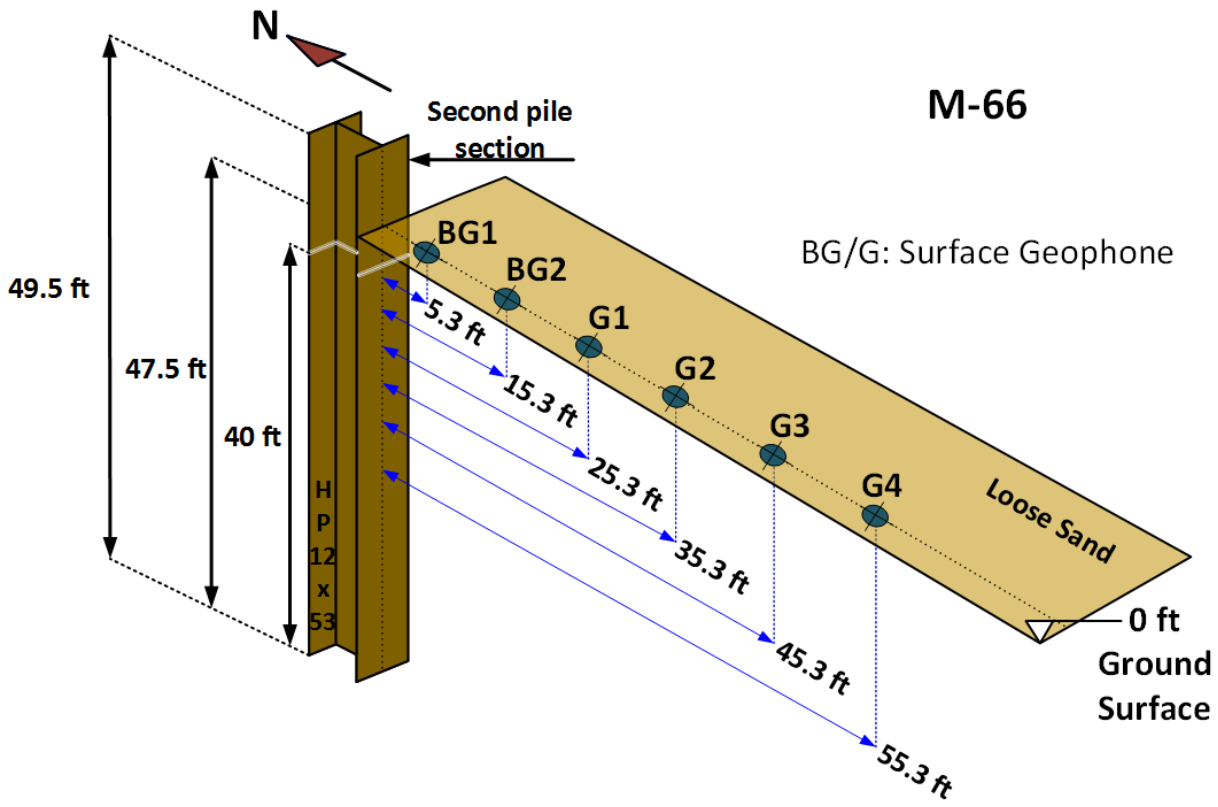

Figure 6-186 Perspective view of surface sensors at M-66 site (not to scale)

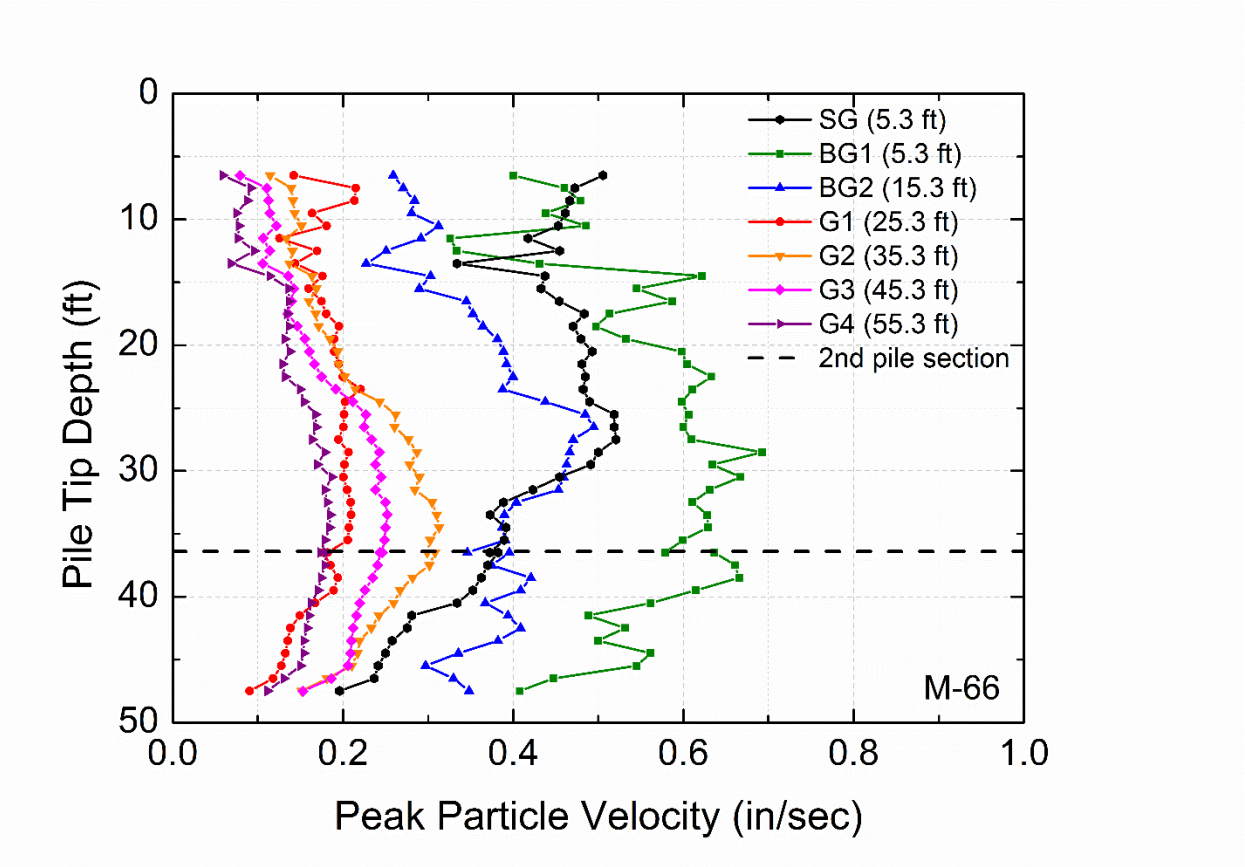

Figure 6-187 Peak Particle Velocity of surface and SG geophones at M-66 site – Vertical Direction

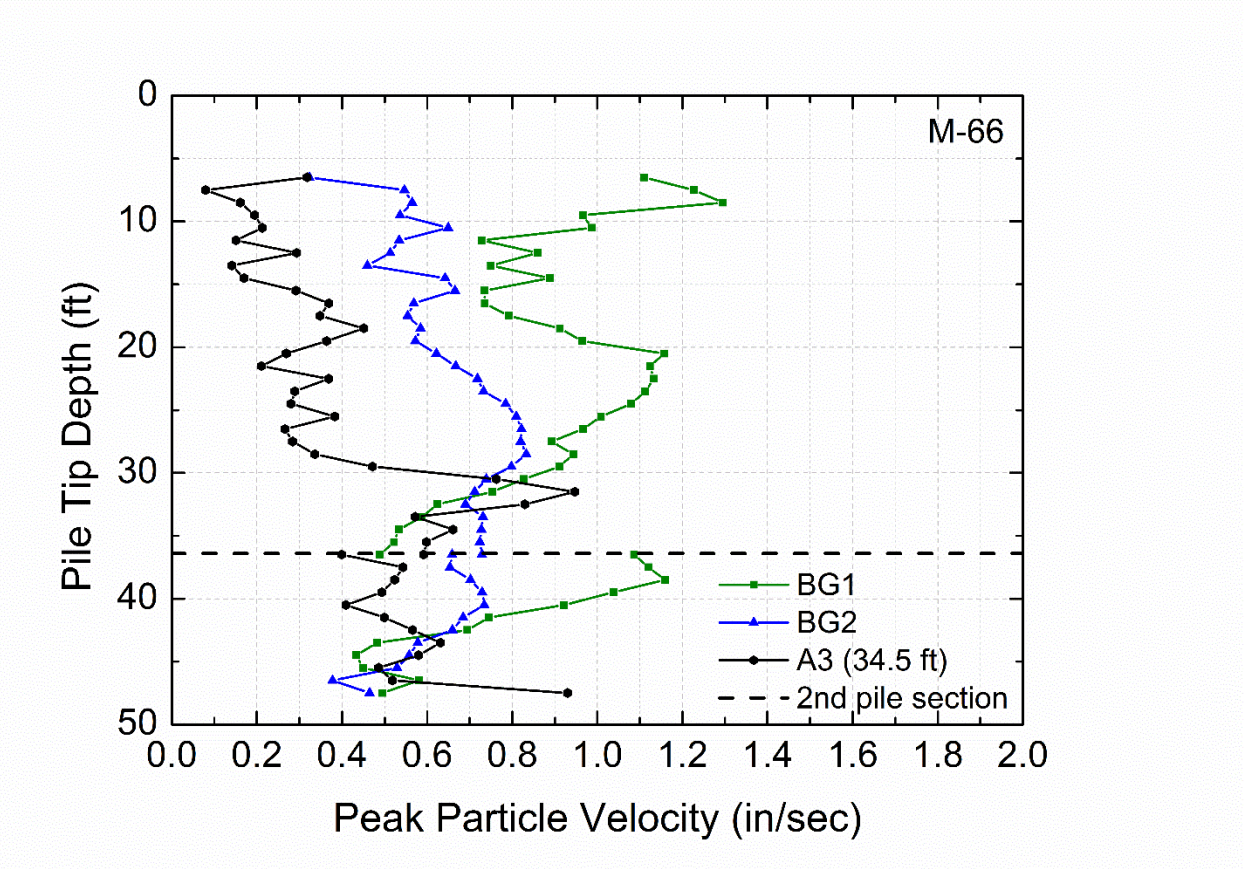

Figure 6-188 Peak Particle Velocity of surface and A3 sensors at M-66 site – Longitudinal Direction

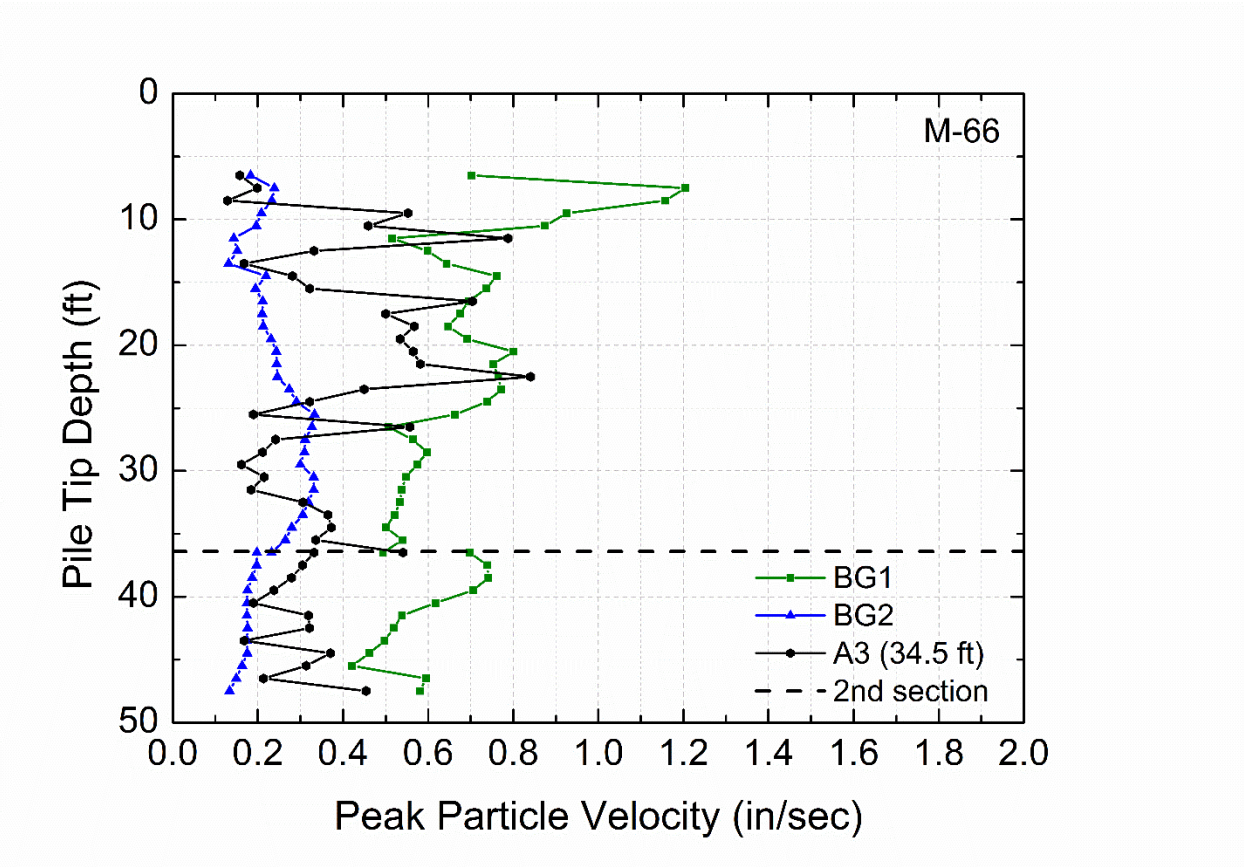

Figure 6-189 Peak Particle Velocity of surface and A3 sensors at M-66 site – Transverse Direction

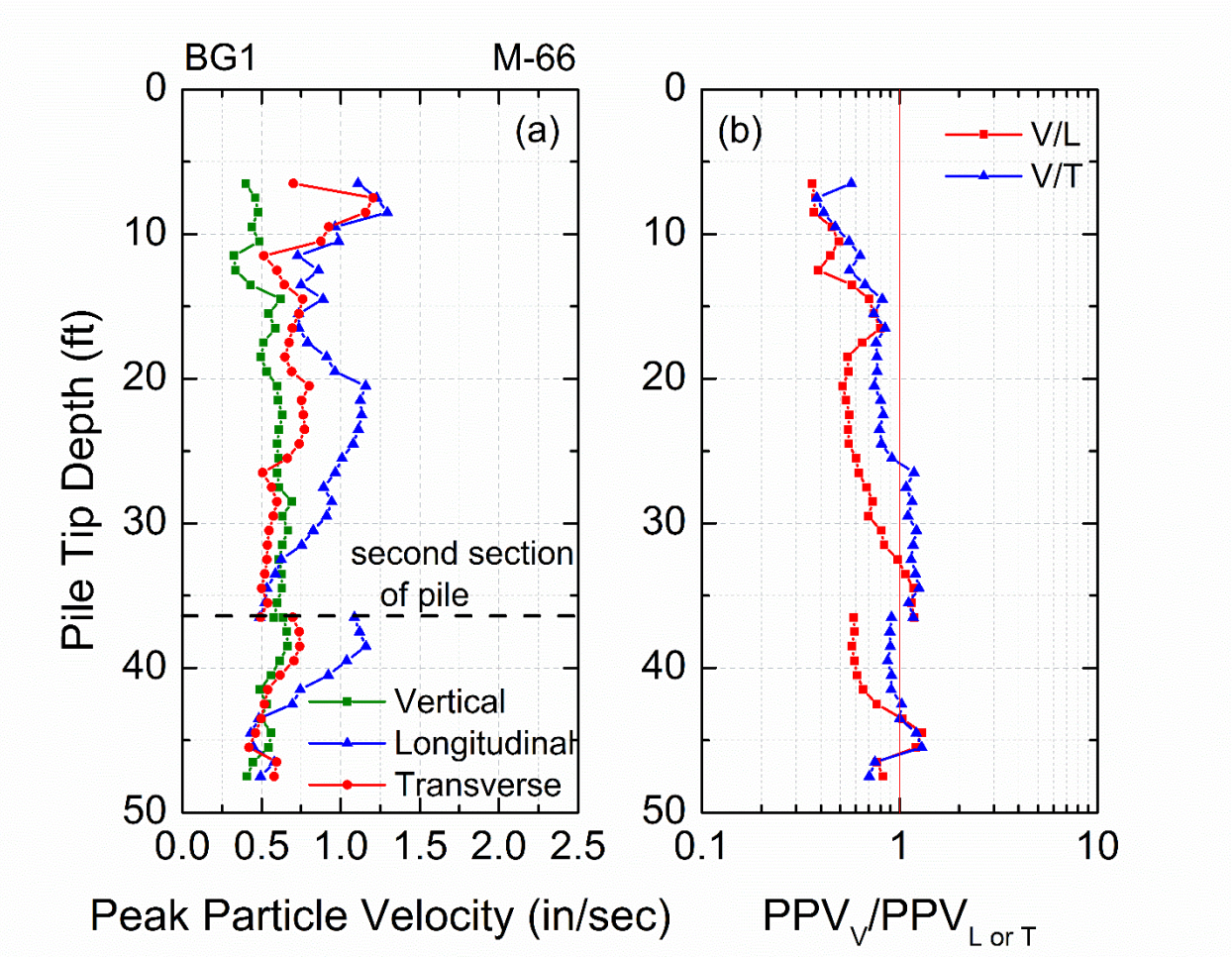

Figure 6-190 (a) Peak particle velocities of three directions of sensor BG1 and (b) vertical to longitudinal and vertical to transverse components of PPV – M-66 site

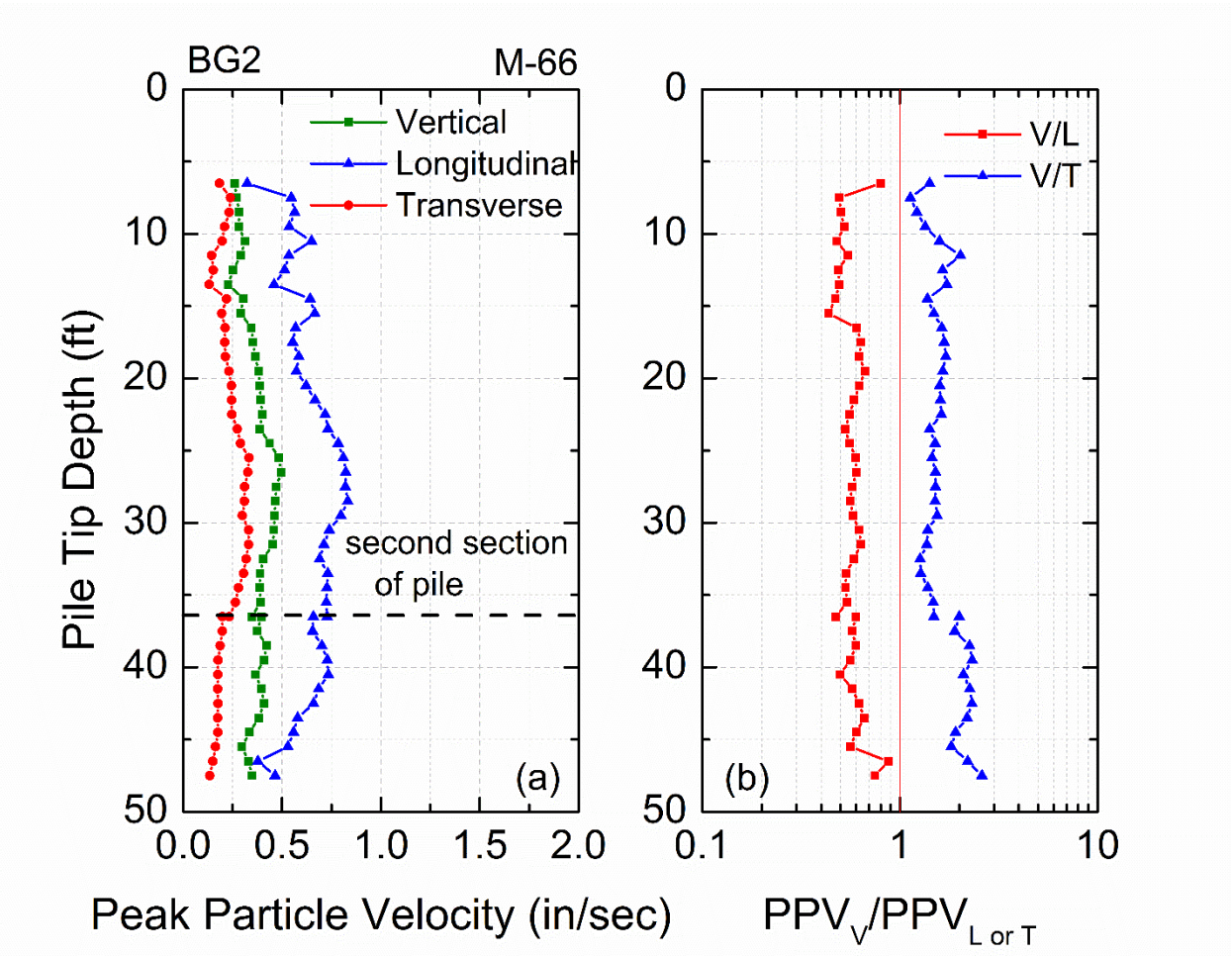

Figure 6-191 (a) Peak particle velocities of three directions of sensor BG2 and (b) vertical to longitudinal and vertical to transverse components of PPV – M-66 site

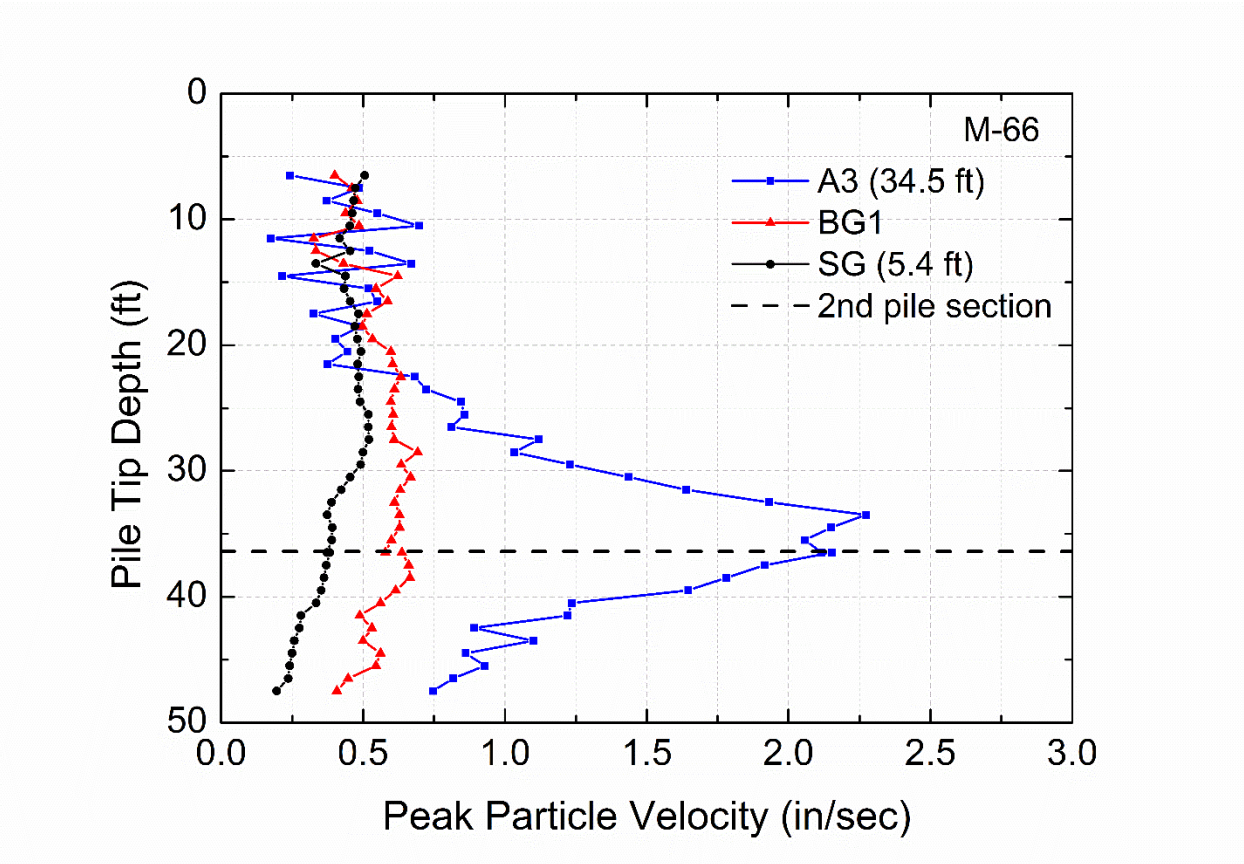

Figure 6-192 Peak particle velocity versus depth of sensors A3, BG1 and SG at M-66 site – Vertical direction

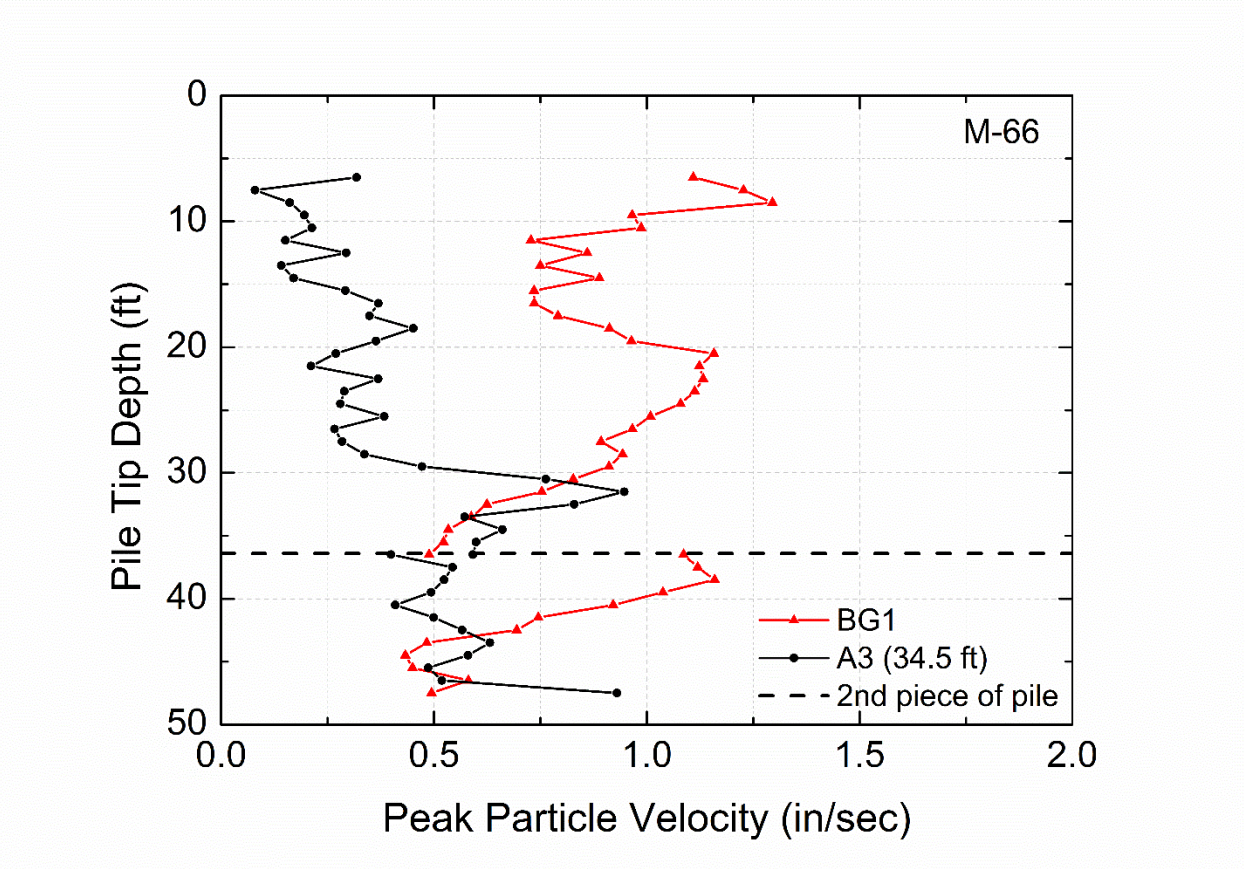

Figure 6-193 Peak particle velocity versus depth of sensors BG1 and A3 at M-66 site – Longitudinal direction

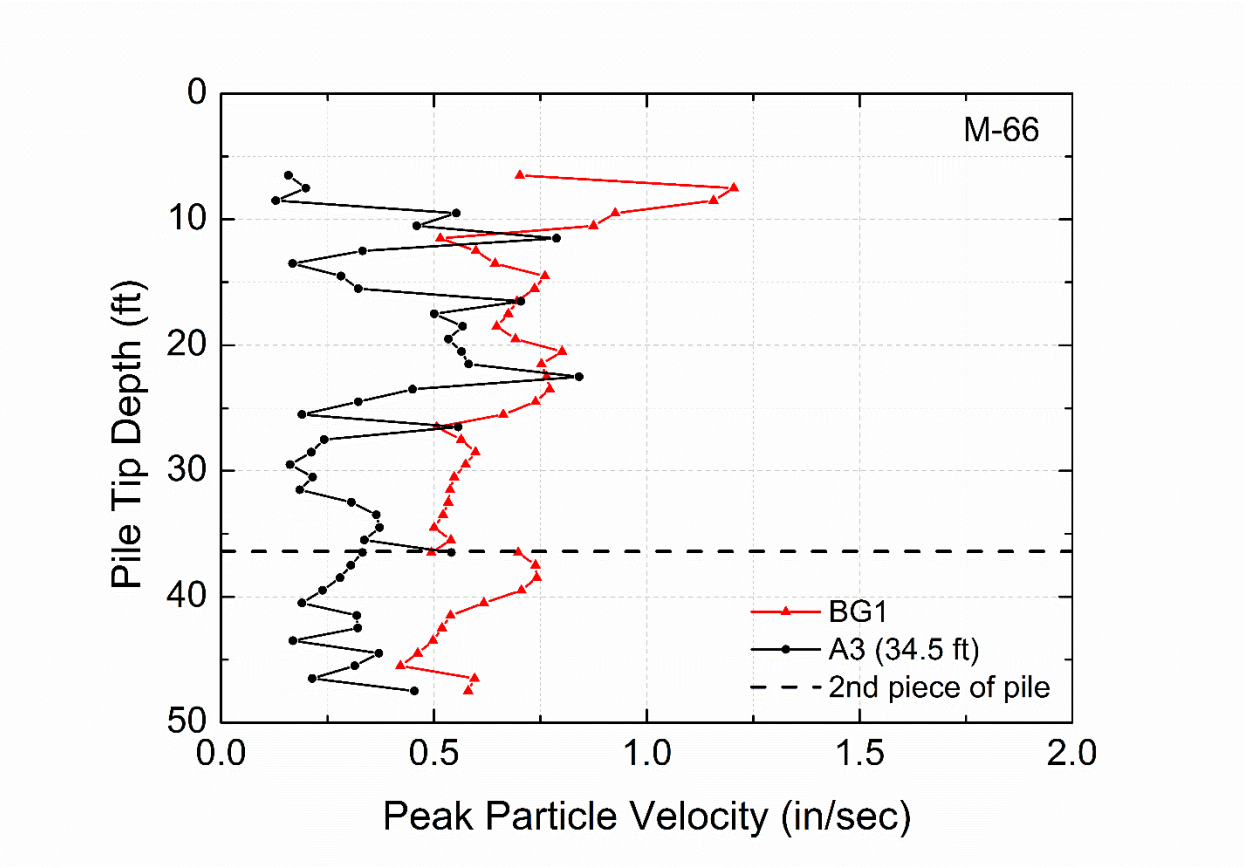

Figure 6-194 Peak particle velocity versus depth of sensors BG1 and A3 at M-66 site – Transverse direction

6.4 Shear Wave Velocity Calculation from Time Histories Wave Arrivals

At site M-139, three accelerometers were successfully installed at the same depth (25.5 ft) but different distances from the pile, providing a good database to investigate the time arrivals of the waves captured by the three sensors. This analysis will offer an opportunity to confirm (or not) the hypothesis of the much lower shear wave velocities in the close proximity of the pile due to the high strains that are developed in this plastic zone. Figure 6-195 presents an elevation view of the embedded sensors at M-139 site. Figure 6-196 shows vertical acceleration time histories, recorded by the three sensors, of one blow when the pile tip was 1.5 ft above the sensors (24 ft). Figure 6-197 depicts similar time histories of one hammer blow when the pile tip had penetrated below the sensors' elevation at 25.7 ft. A black line indicates the Vs arrival to each of the three sensors. A justification of the reason that this peak was chosen as the Vs arrival can be made by observing Figure 6-198. This Figure presents acceleration time histories of the three components of sensor A3 for the hammer blow that the pile tip reached 25.7 ft. The two horizontal components have the same first high peak as the vertical component. However, the second peak recorded by the vertical component of sensor A3 is not that pronounced, confirming that the first peak in the signal is not the Vs arrival.

It is important to remember that shear waves are not expected to be captured by a sensor until the pile shaft is nearly adjacent or below the sensor elevation. Calculation of the shear wave velocity by inspection of the signals and calculation of time arrivals was made by checking acceleration time histories right above and right below the sensors' depth. Figure 6-199 presents the evaluation of the shear wave velocity at the vicinity of the pile where the sensors were installed. The blue line indicates the calculated shear wave velocity using the time arrivals between the two closest sensors from the pile, A3 and A4. In a similar way, the red line depicts shear wave velocity using the time arrivals from the two furthest sensors from the pile, A4 and A5. Finally, the green line is the computed shear wave velocity using the first and the third sensor in the line array, A3 and A5. The black line is the shear wave velocity obtained for this layer by the MASW method

(far field). This analysis provided the shear wave velocity reduction factors in the vicinity of the pile (near field) as $0.4V_{smax}$, $0.6V_{smax}$ and $0.85V_{smax}$ for the three pairs of sensors, A3 to A4, A4 to A5 and A3 to A5, respectively. These reduction factors of shear wave velocity come as an important finding calculated from the acceleration time histories of the buried sensors, and confirm the large decrease of the shear wave velocity that is expected in the vicinity of the pile. As the closest sensor to the pile 0.5 ft away, it is expected that the shear wave velocity will decrease even more at the pile-soil interface where the soil experiences very high strains.

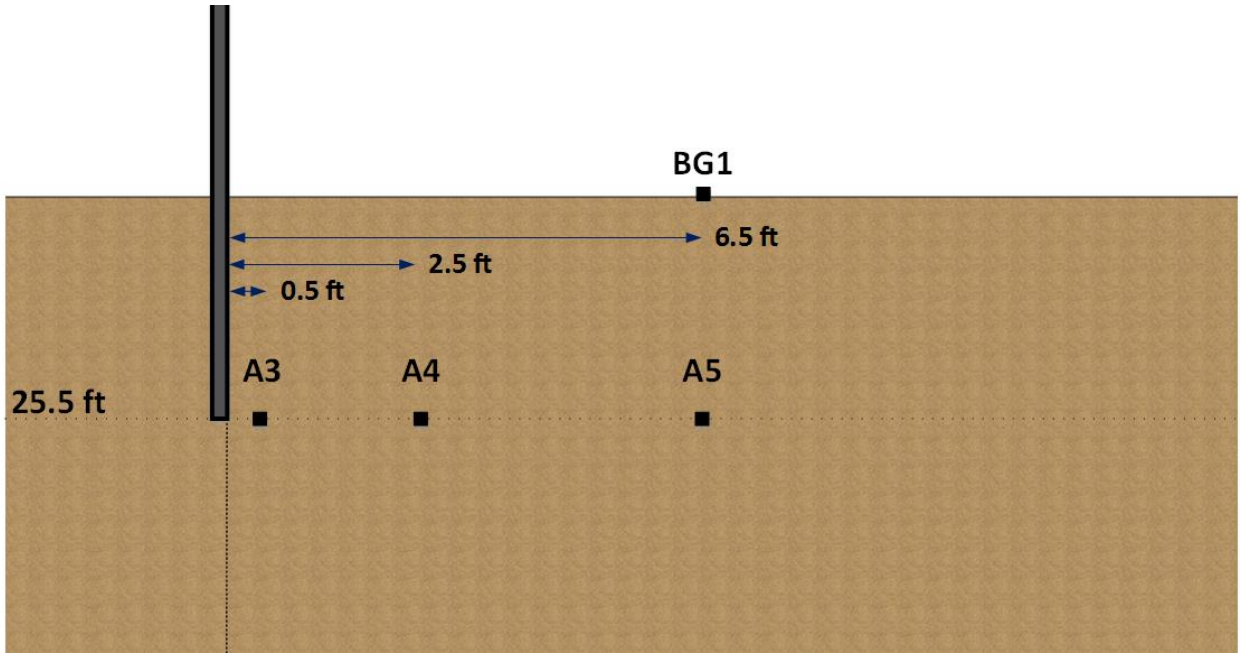

Figure 6-195 Elevation view of buried sensors at M-139 site

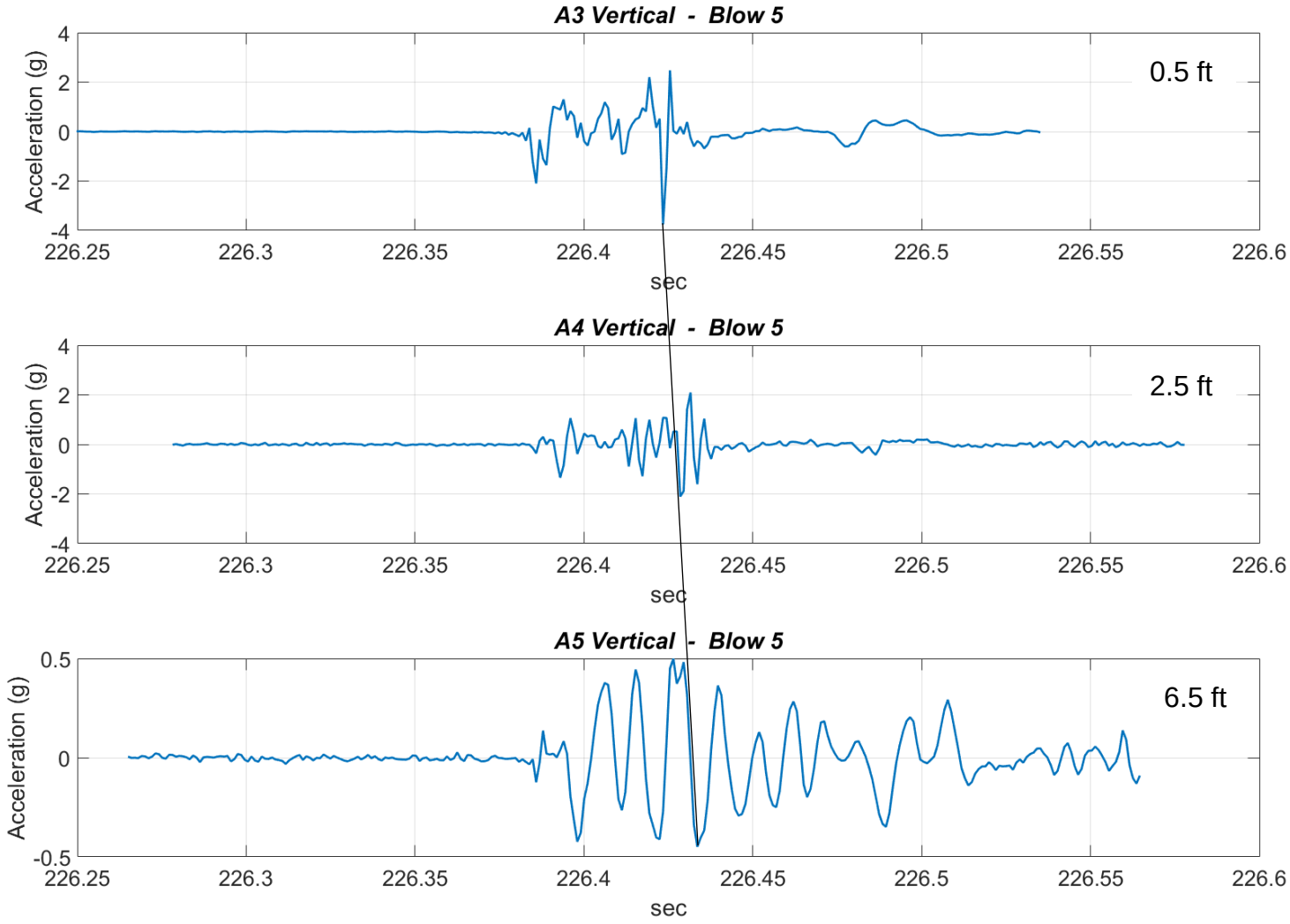

Figure 6-196 Acceleration time histories of buried sensors, pile tip at 24 ft

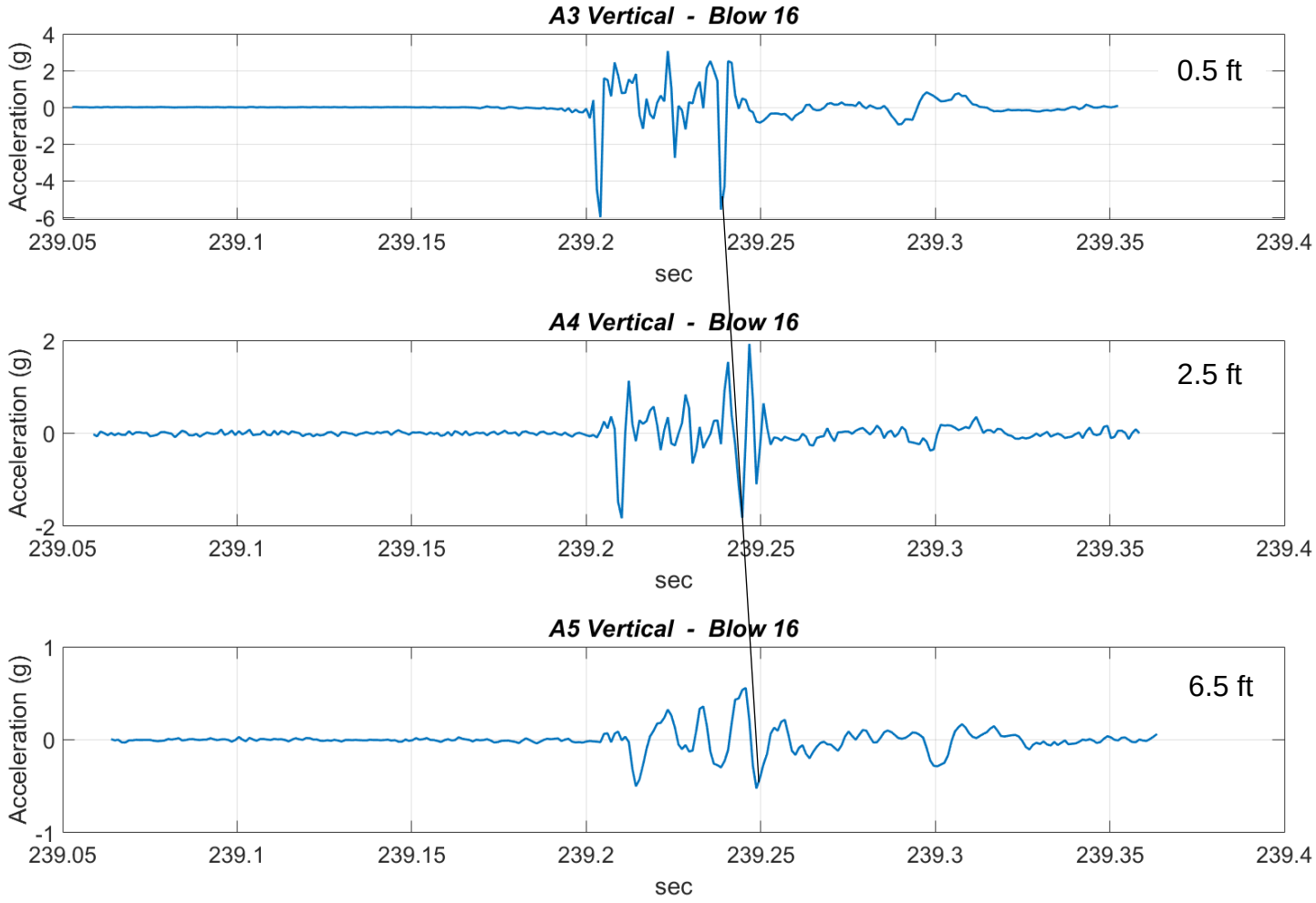

Figure 6-197 Acceleration time histories of buried sensors, pile tip at 25.7 ft

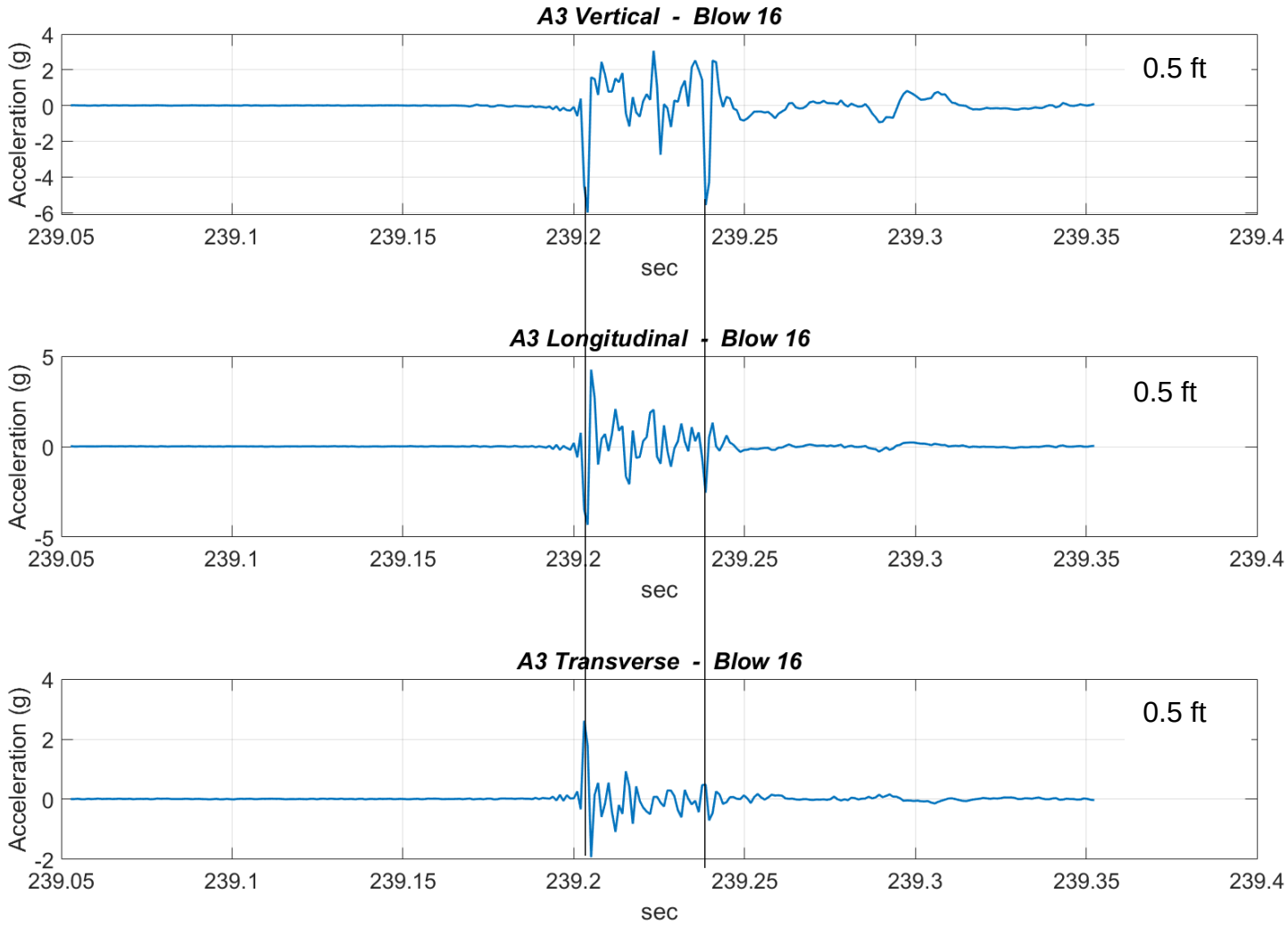

Figure 6-198 Acceleration time histories of three components of sensor A3, pile tip at 25.7 ft

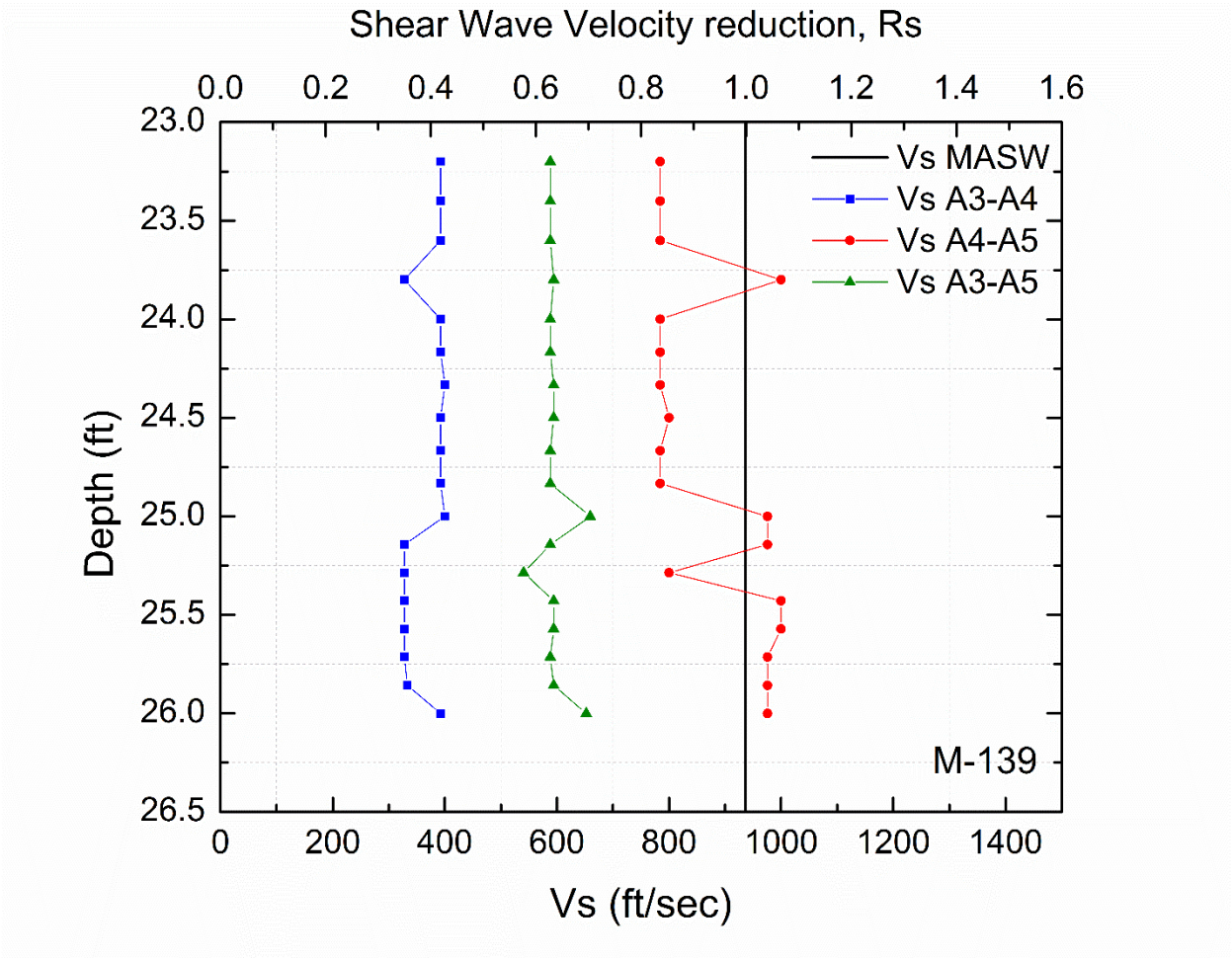

Figure 6-199 Evaluation of shear wave velocity by inspection of the signals; pile tip close to sensors' depth

6.5 Attenuation of waves from pile driving

As discussed in Section 3.2, researchers have used different ways to express attenuation of vibrations emanating from a pile while it is being driven. In this work, three different attenuation concepts were selected to be compared with the measured data in order to study how energy from the impact pile driving diminishes through the soil: the Caltrans equation (Hendriks 2002), the Bornitz equation (Richart et al. 1970), and the power pseudo-attenuation formula (Wiss 1981). The three equations are formulated as:

Caltrans $$A_2 = A_1 \left(\frac{r_1}{r_2}\right)^k$$ Eq. 6-3

Bornitz $$A_2 = A_1 \left(\frac{r_1}{r_2}\right)^n exp[-\alpha(r_2 - r_1)]$$ Eq. 6-4

Power $$A = cr^{-\beta}$$ Eq. 6-5

where:
r_1 = distance from source to point of known amplitude
r_2 = distance from source to point of unknown amplitude
A_1 = vibration amplitude at distance r_1 from source
A_2 = vibration amplitude at distance r_2 from source
n = geometric attenuation coefficient
- n = 0.5 for surface waves
- n = 1 for body waves in the ground
- n = 2 for body waves on the ground surface

α = material damping attenuation coefficient (units of 1/distance)
k = dimensionless soil parameter
r = distance from source
A = vibration amplitude at distance r from source
c, β = coefficients of the power law

It should be noted that the Bornitz equation was developed for sinusoidal motion at a single frequency. It is clear from Figure 6-35 that the ground vibration measurements from pile driving operations have a broad frequency content and are not sinusoidal waves. It is also evident that energy propagation during impact pile driving is composed of at least three different types of waves: spherical body waves from the pile tip, cylindrical waves emanating from the pile shaft and Rayleigh waves that propagate along the ground

surface also in a cylindrical wave form. Furthermore, the attenuation coefficient in Eq. 6-3, should not be thought of like the Bornitz, α, that results from the emergence along the free surface of a homogeneous half space by integration of primary and secondary waves from a point source. The Rayleigh waves travel through the same soil to all sensors. Alternatively, this coefficient of attenuation is derived from waves travelling through multiple soil types from the shaft and tip of the pile in a fan of waves arriving at surface sensors along directions from near vertical close to the pile to near horizontal at great distance from the pile. The path to each sensor is different and depends on the location of the observation point and the pile tip penetration depth as seen in Figure 6-200.

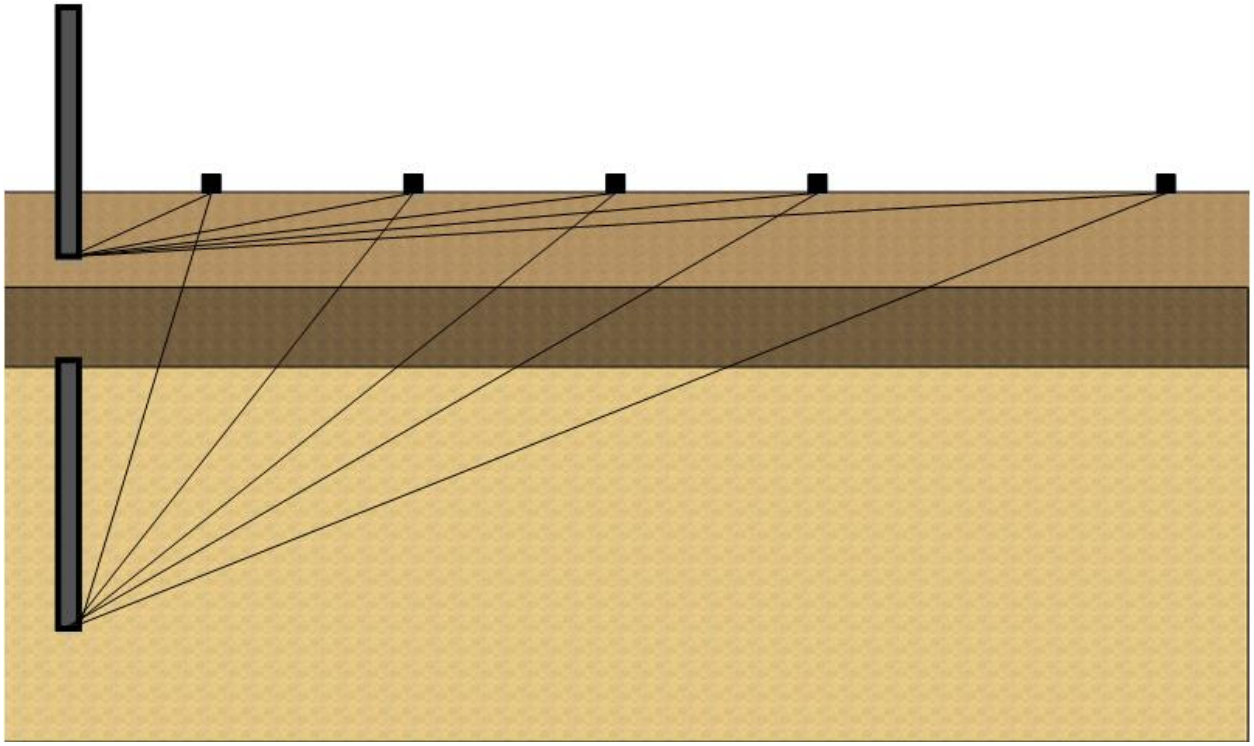

Figure 6-200 Surface ray paths at different pile tip penetration depths

The Rayleigh waves in this case are not developed from a point source on the surface, but from a buried vertical line source that is constantly lengthening as the pile is driven deeper. As discussed in Section 6.3, a combination of waves from the pile tip and shaft were captured by the line array of geophones on the surface, which was not the classic Rayleigh wave because of the vertical line source. However, it is possible to adopt the Bornitz equation to describe empirically attenuation of ground surface motion from pile driving induced vibrations.

For the buried sensors, spherical waves generated from the pile tip are only captured when the pile tip is at the depth of the sensors. When the pile tip descends below the elevation of the sensors, a combination of spherical waves from the tip and shear waves from the shaft are captured from the sensors. These phenomena are shown in a schematic in Figure 6-201.

The coefficient n, of the Bornitz equation depends on the wave type and is equal to 0.5 for the case of Rayleigh waves. The Bornitz equation was kept in this format even if the surface waves are not pure Rayleigh waves. In addition, ground motion amplitudes collected when the pile tip was in the ground at the same elevation as the buried sensors' array, were fitted to the Bornitz equation, again with the coefficient n=0.5 showing a very good fit. When the pile reached the depth at which the sensors were installed, cylindrical waves from the shaft were captured by the sensors with the height of cylinder being the embedded length of the pile.

The buried sensors were installed at different distances from the pile to investigate the attenuation phenomena during pile driving. The basic concept was to fit recorded vibration measurements when the pile tip was at the elevation of the sensors when tip dominates. In addition, the prediction equations were fitted to all the measurements from hammer blows collected when the pile tip was at the elevation of the sensor and also averaged wave paths about 1 ft above and 1 ft below the sensors' depth (Figure 6-202). In order to evaluate the goodness of fit of the formulas, prediction bounds with 95% confidence level are also plotted along with the attenuation curves. In addition, R-square values are calculated to evaluate how good the fit is. Curve fitting was conducted using a matlab code.

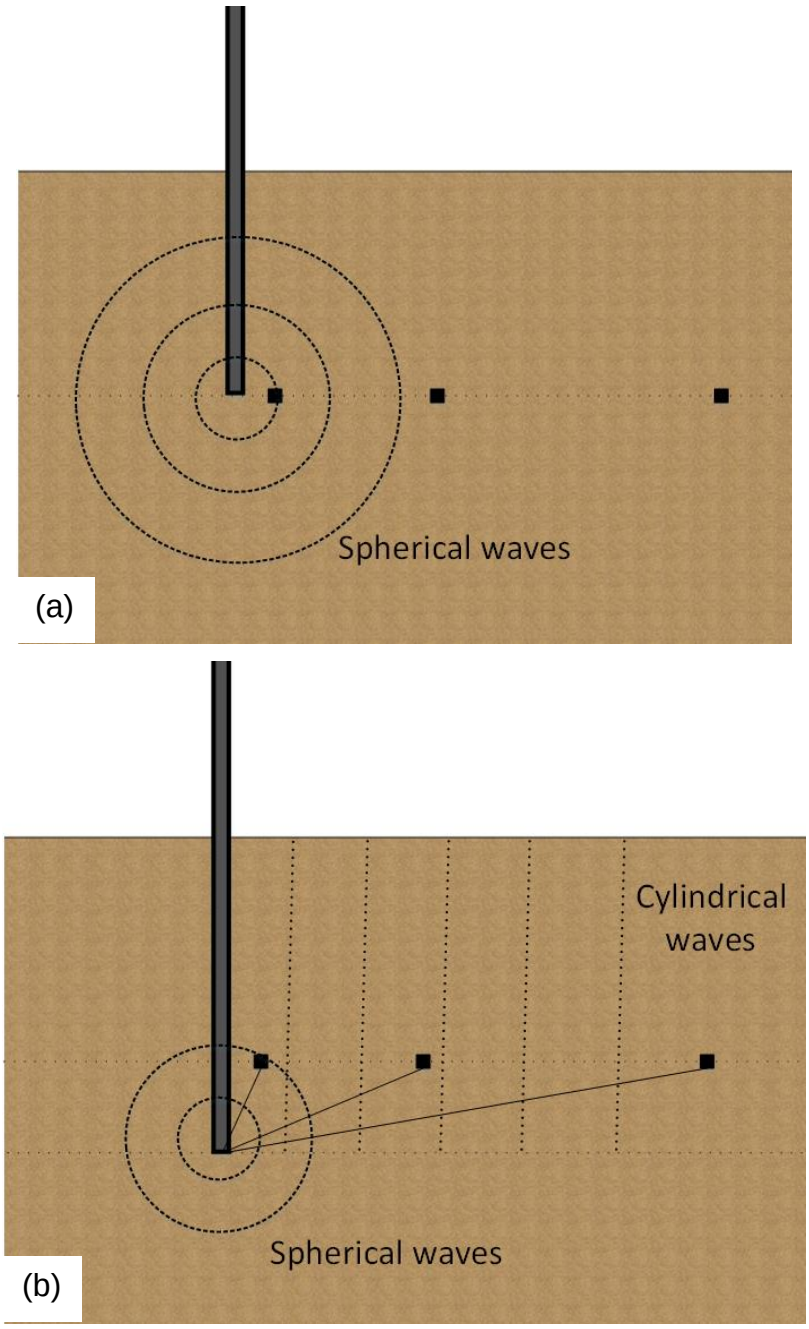

Figure 6-201 Wave paths reaching buried sensors when (a) pile tip is at sensors' elevation and (b) pile tip is below sensors' depth

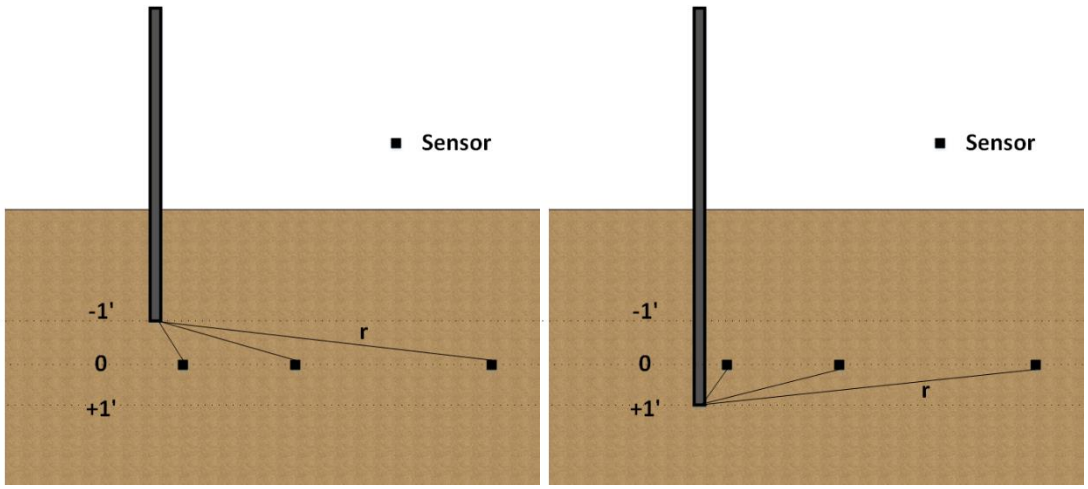

Figure 6-202 Pile tip to sensor locations diagonal distances for calculation of attenuation coefficients for a range of pile tip depths

The following procedure was used to fit the attenuation curves through data from buried sensors. First, the closest sensor to the pile was used as the reference point to fit the attenuation curves and calculate the attenuation coefficient. Then, the second sensor in the row was used as the reference point and a different attenuation coefficient was calculated by fitting the curves. Finally, the furthest sensor in the array was used as the fixed point to fit the data providing another attenuation coefficient. This analysis was employed to determine differences in the calculated coefficients as a function of the distance of the base sensor from the source. The Matlab routine was coded in a manner to find the attenuation coefficient, that would give the optimal fitting curve for all sensors in the row with the chosen reference point. An example of the above procedure is shown in Figure 6-203. Figure 6-204 presents an example of fitting the three attenuation curves to data recorded from buried sensors, with the closest sensor (A3) as the reference point. The distance from source, r, is taken as the diagonal distance from the pile tip to the point of measurement for calculation of average values from a range of pile tip depths, Figure 6-202. For the power equation, the matlab code fitted the curve using all data without interchanging the reference point. For this reason, only one coefficient was calculated using the data and fitting the power formula.

For the ground motion amplitudes collected from the surface geophones, attenuation curves were fitted using the closest sensor to the pile as the reference point in calculating the attenuation coefficients. The aforementioned procedures were conducted for all the surface and buried arrays of sensors and are provided below in graphical and tabular form.

An estimation of the vibration amplitude at the pile-soil interface was also made by fitting the three prediction equations to data from the buried sensors. The assumed distance, r, that was used as an estimate for the source distance was 0.01 ft from the pile shaft for the Bornitz equation, and 0.1 ft from the pile face for the Caltrans and power equations.

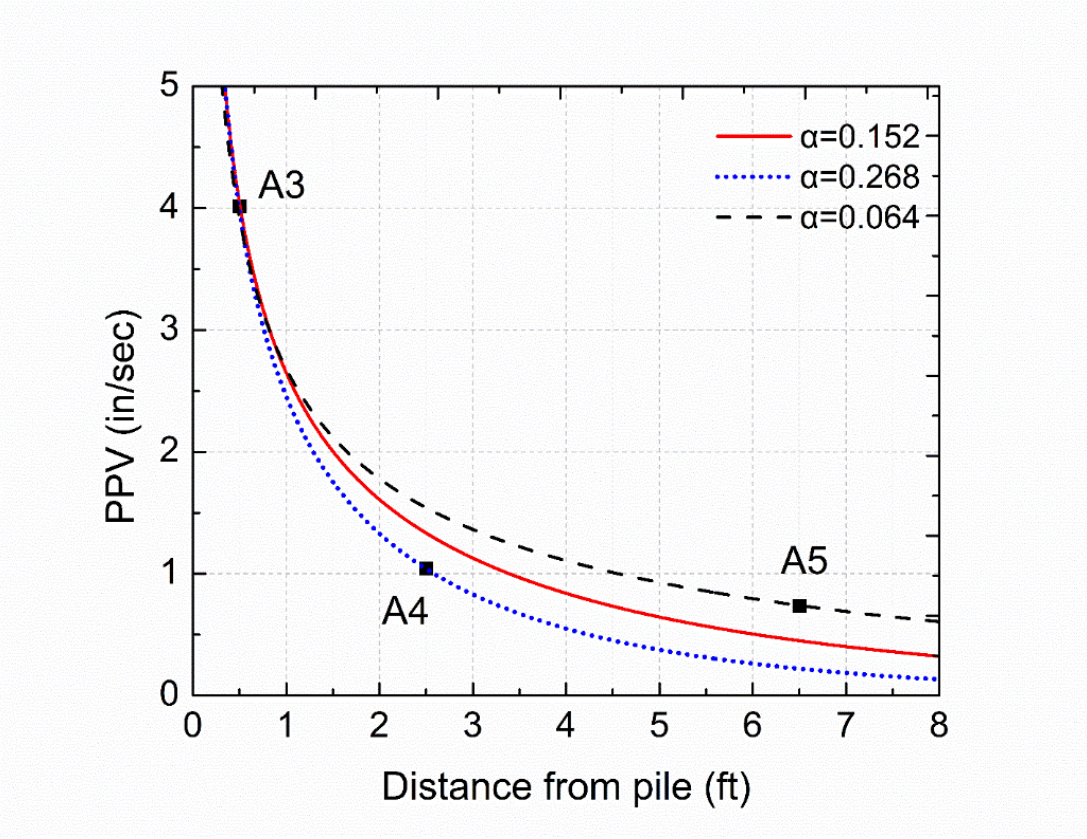

Figure 6-203 Example of attenuation curves with different fixed points

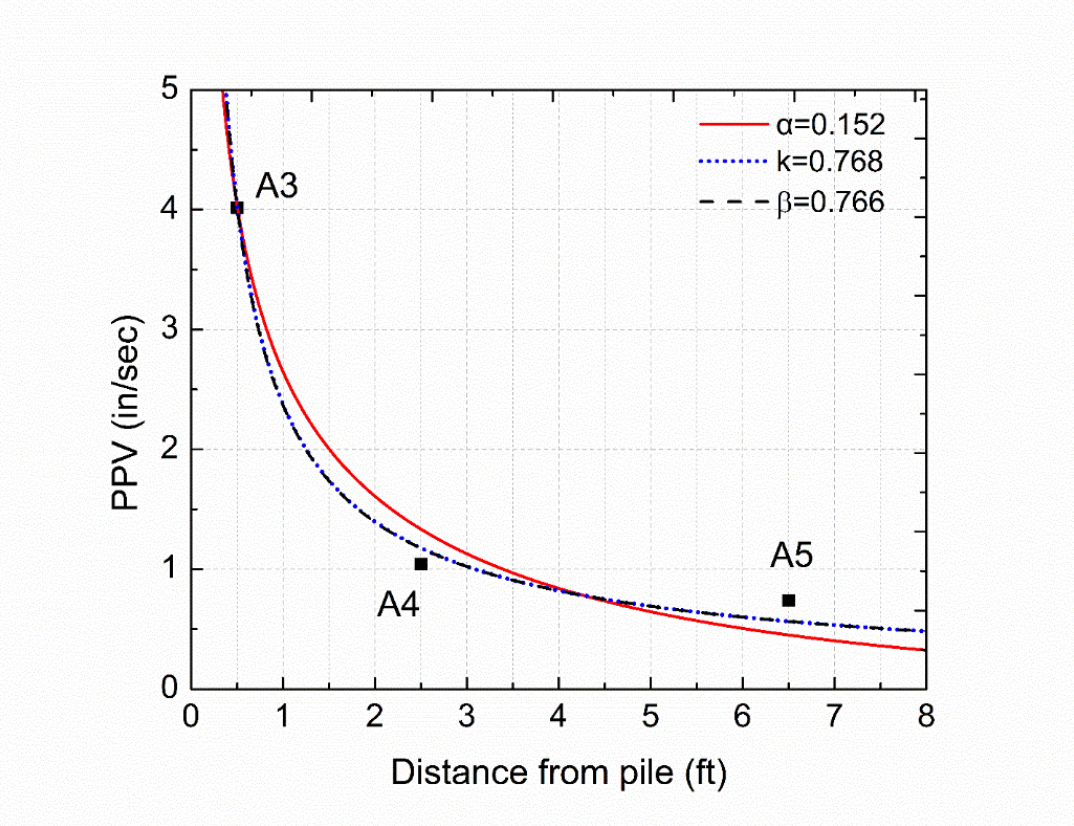

Figure 6-204 Example of different attenuation curves that were fitted to the collected measurements

6.5.1 M-66 Site

Due to site and pile contractor schedule problems, only surface sensor data was deemed reliable at this site. Using that data, attenuation curves were fitted to ground motion amplitudes recorded from surface geophones at the M-66 site, when the pile tip was at a depth of 9 ft where driving started at a constant rate. The results from the curve fitting are provided for the three component directions in Figure 6-205 to Figure 6-211. Data were measured for the longitudinal and transverse direction by the two geophones closest to the pile, providing only a crude curve fitting, however the results are displayed for reference. The ground motion amplitude reduction characterized by the three attenuation prediction equations shows very good fit for the vertical component, as shown in Table 6.3 to Table 6.9. The closest point/sensor to the pile was used as the reference point when fitting the three prediction equations in the matlab routine.

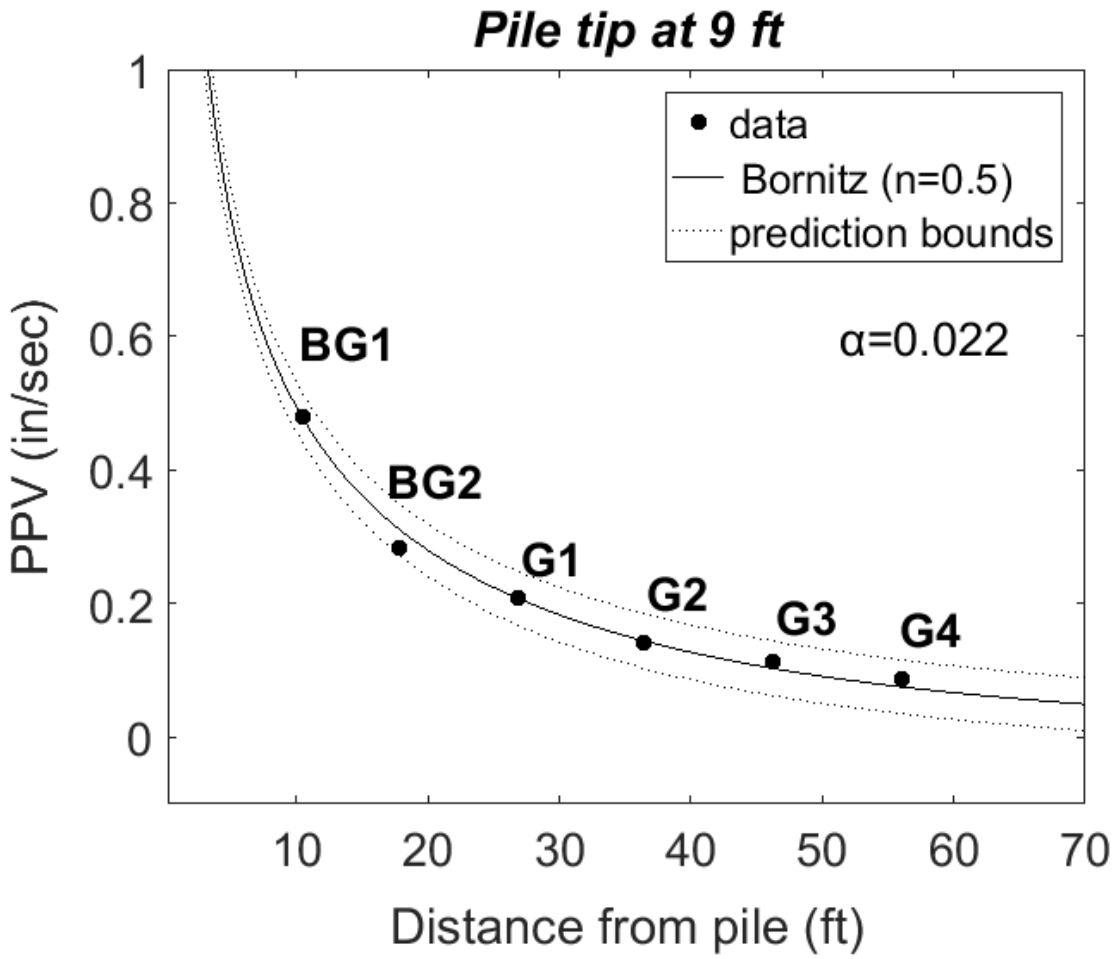

Figure 6-205 Attenuation curve for surface geophones at M-66 site – Bornitz Equation, Vertical Direction

Table 6.3 Data for attenuation coefficient using the Bornitz equation, M-66 site-Vertical

SENSOR	Distance from pile (ft)	α(1/ft) (n=0.5)	Diagonal distance from tip (ft)	PPV (in/sec)
BG1	5.30	0.022	10.4	0.479
BG2	15.30		17.8	0.284
G1	25.30		26.9	0.209
G2	35.30		36.4	0.141
G3	45.30	**R^2**	46.2	0.113
G4	55.30	0.990	56.0	0.086

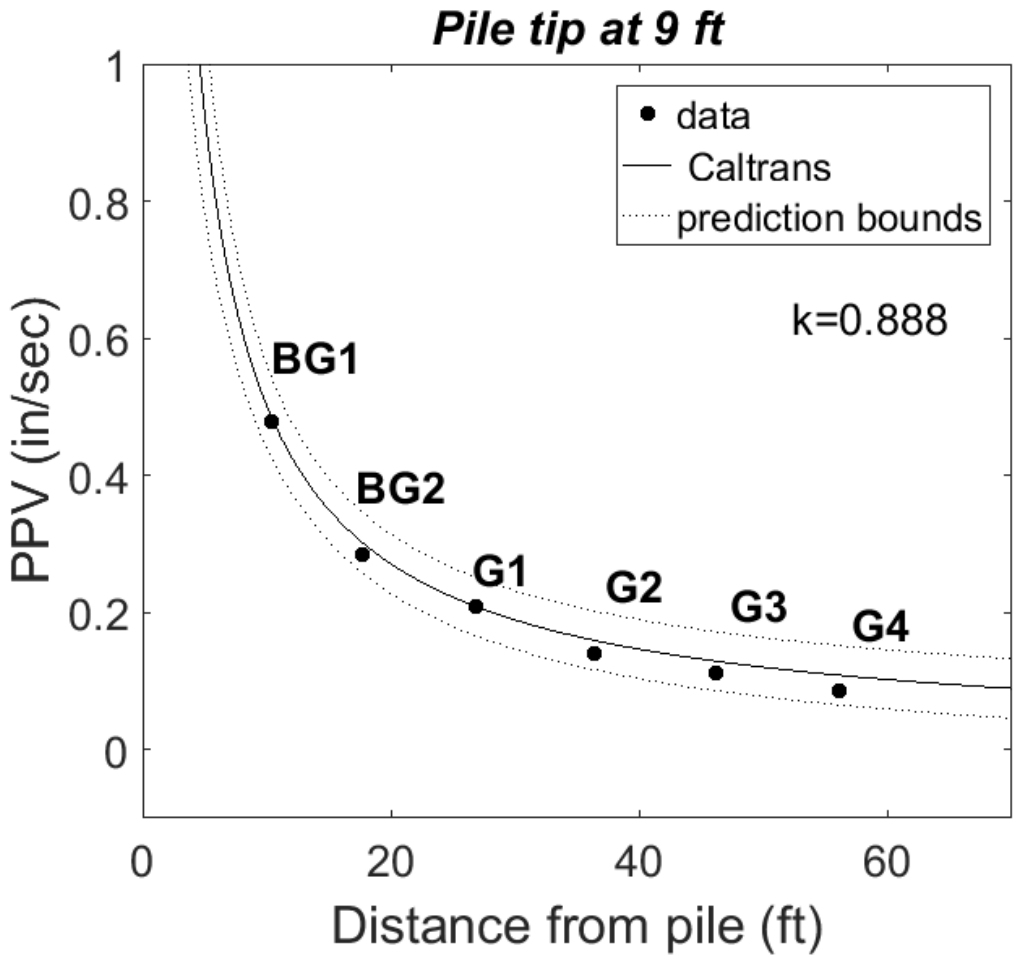

Figure 6-206 Attenuation curve for surface geophones at M-66 site – Caltrans Equation, Vertical Direction

Table 6.4 Data for attenuation coefficient using the Caltrans equation, M-66 site-Vertical

SENSOR	Distance from pile (ft)	k	Diagonal distance from tip (ft)	PPV (in/sec)
BG1	5.30	0.888	10.4	0.479
BG2	15.30		17.8	0.284
G1	25.30		26.9	0.209
G2	35.30		36.4	0.141
G3	45.30	**R^2**	46.2	0.113
G4	55.30	0.987	56.0	0.086

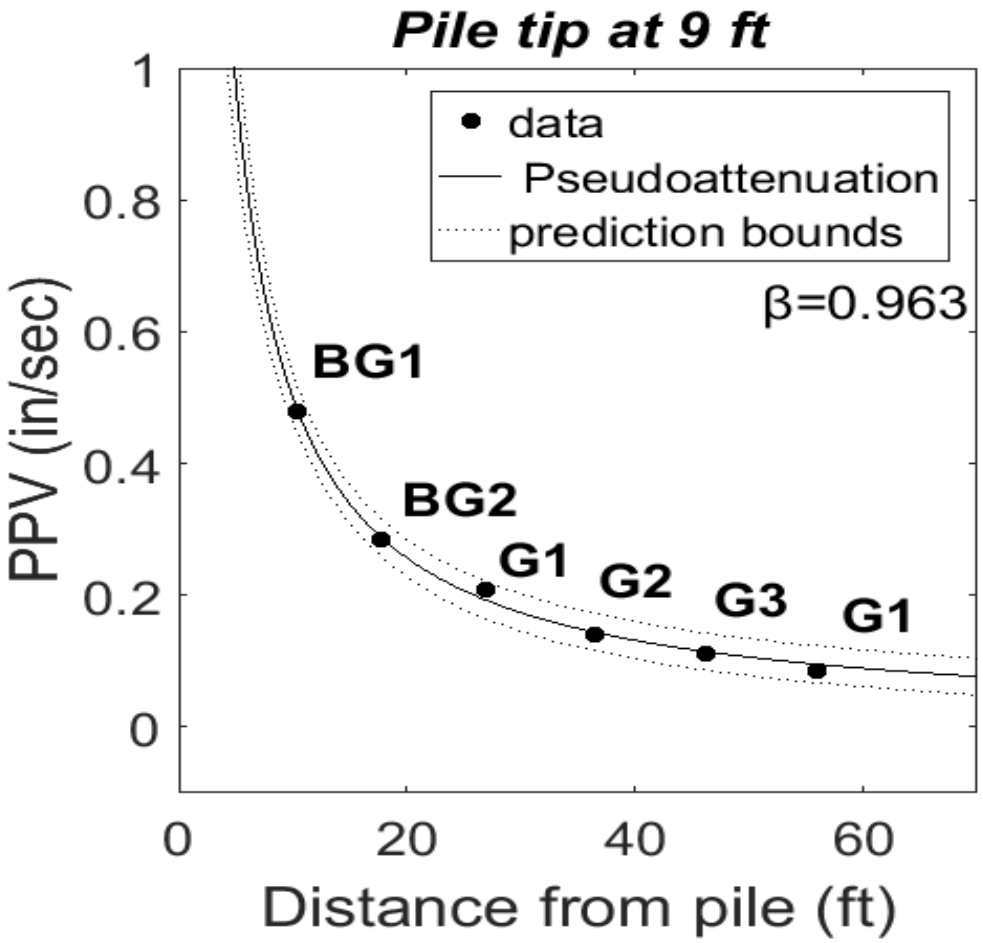

Figure 6-207 Attenuation curve for surface geophones at M-66 site – Power Equation, Vertical Direction

Table 6.5 Data for attenuation coefficient using the power equation, M-66 site-Vertical

SENSOR	Distance from pile (ft)	β	Diagonal distance from tip (ft)	PPV (in/sec)
BG1	5.30	0.963	10.4	0.479
BG2	15.30		17.8	0.284
G1	25.30		26.9	0.209
G2	35.30		36.4	0.141
G3	45.30	**R^2**	46.2	0.113
G4	55.30	0.997	56.0	0.086

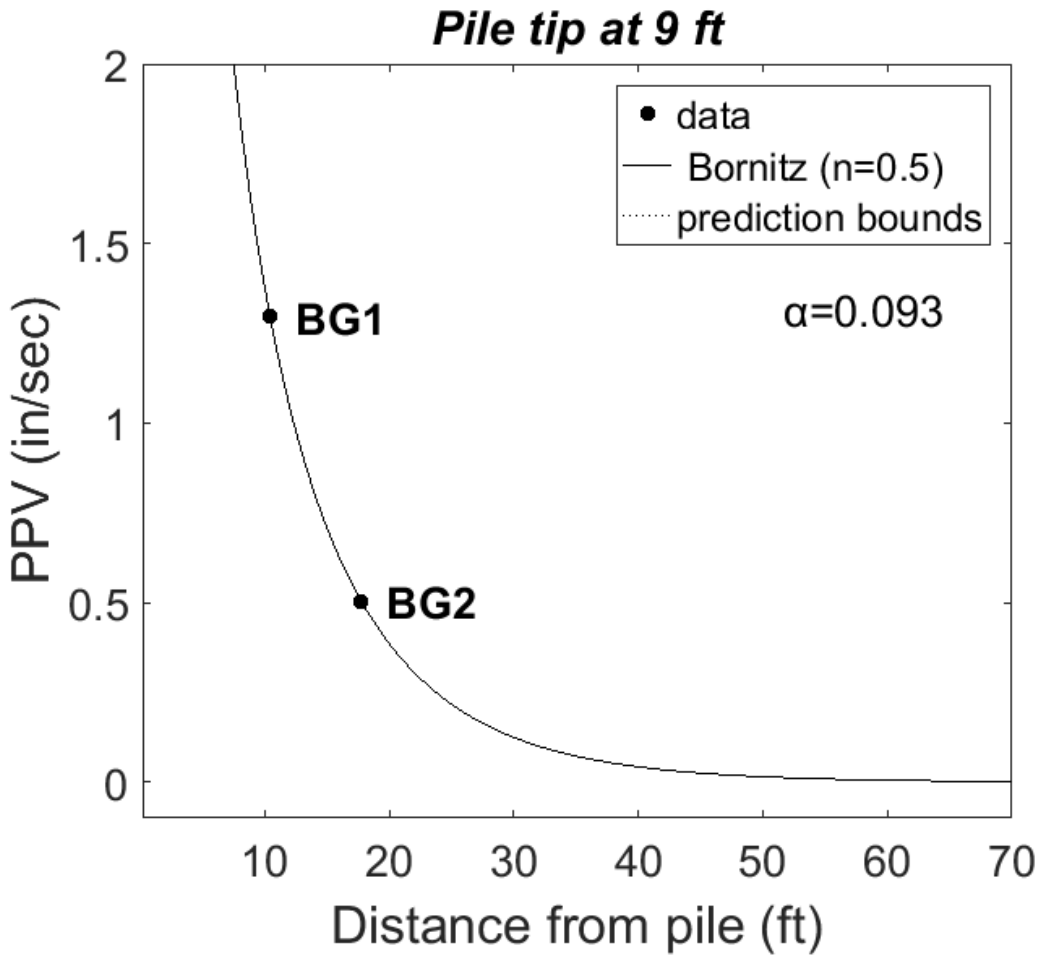

Figure 6-208 Attenuation curve for surface geophones at M-66 site – Bornitz Equation, Longitudinal Direction

Table 6.6 Data for attenuation coefficient using the Bornitz equation, M-66 site-Longitudinal

SENSOR	Distance from pile (ft)	α(1/ft) (n=0.5)	Diagonal distance from tip (ft)	PPV (in/sec)
BG1	15.00	0.093	10.4	1.296
BG2	25.00		17.8	0.505
		R^2		
		1.000		

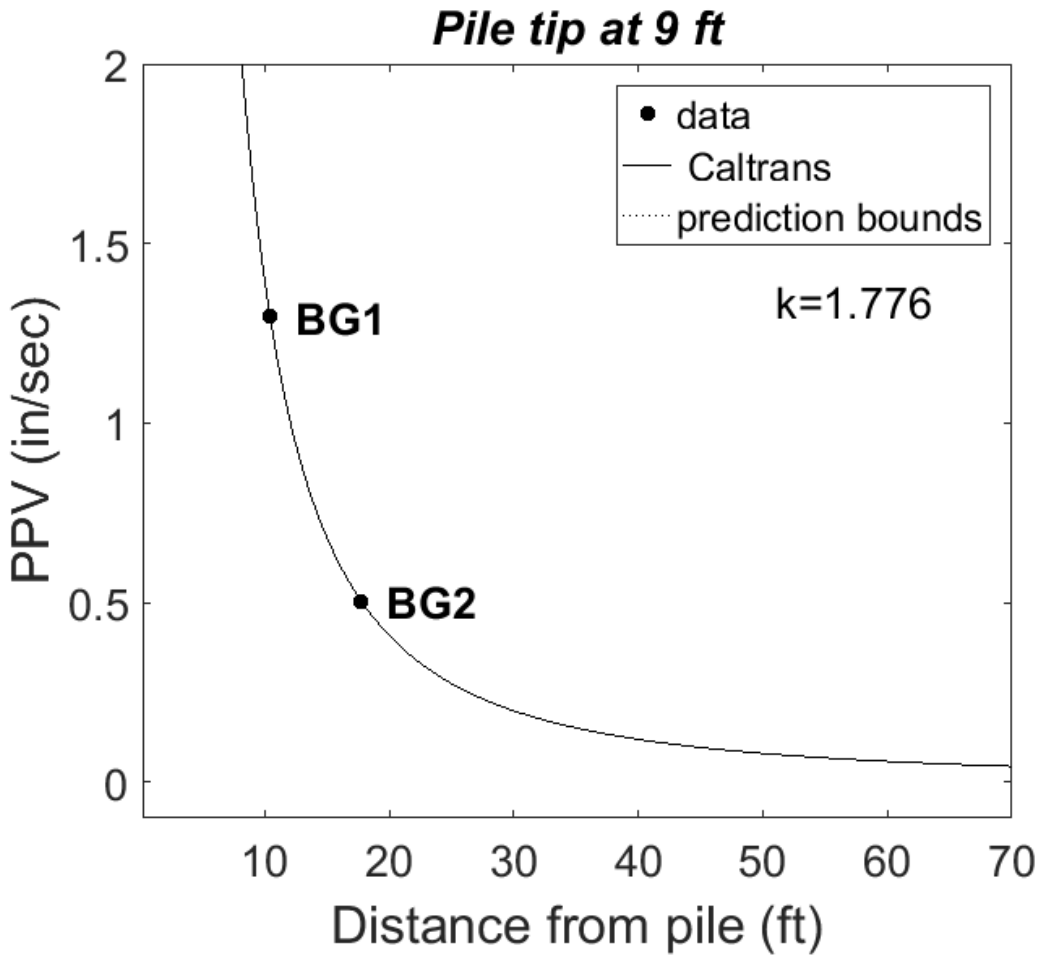

Figure 6-209 Attenuation curve for surface geophones at M-66 site – Caltrans Equation, Longitudinal Direction

Table 6.7 Data for attenuation coefficient using the Caltrans equation, M-66 site-Longitudinal

SENSOR	Distance from pile (ft)	k	Diagonal distance from tip (ft)	PPV (in/sec)
BG1	15.00	1.776	10.4	1.296
BG2	25.00		17.8	0.505
		R^2		
		1.000		

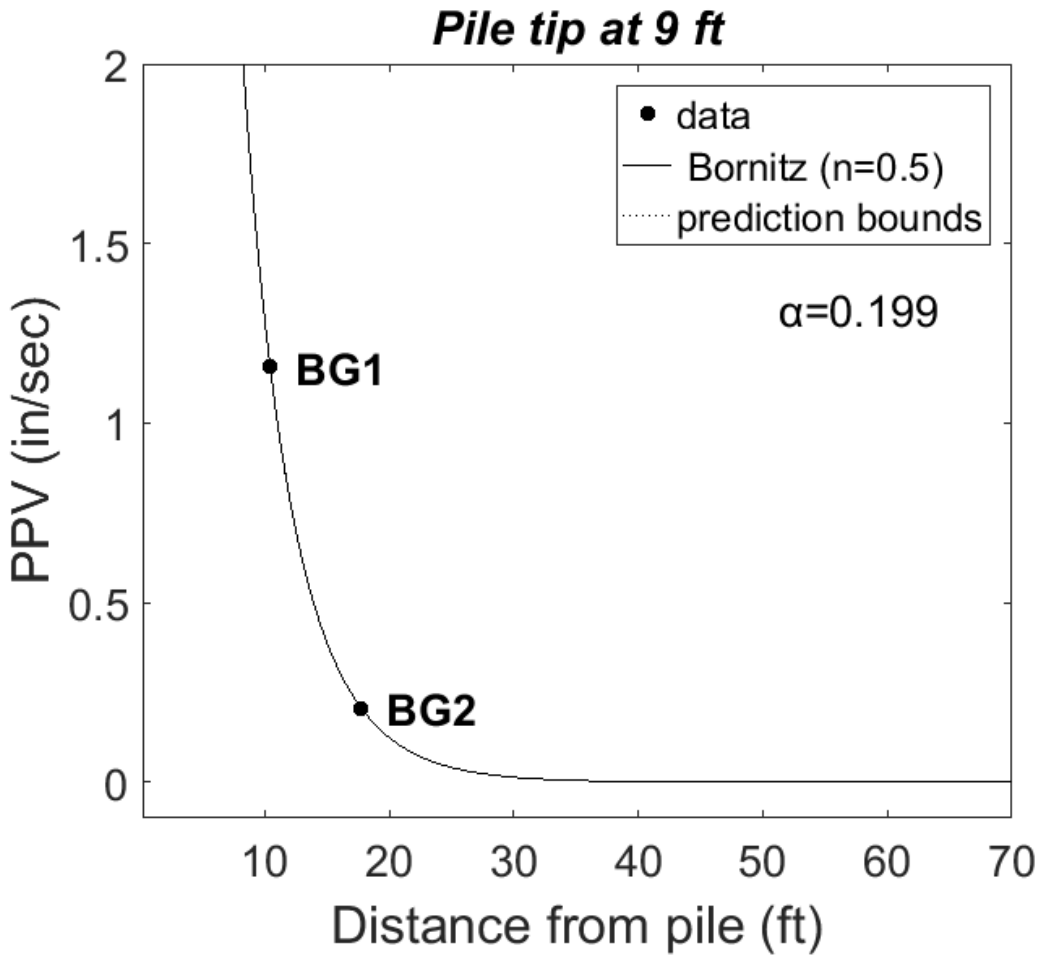

Figure 6-210 Attenuation curve for surface geophones at M-66 site – Bornitz Equation, Transverse Direction

Table 6.8 Data for attenuation coefficient using the Bornitz equation, M-66 site-Transverse

SENSOR	Distance from pile (ft)	α(1/ft) (n=0.5)	Diagonal distance from tip (ft)	PPV (in/sec)
BG1	15.00	0.199	10.4	1.157
BG2	25.00		17.8	0.207
		R^2		
		1.000		

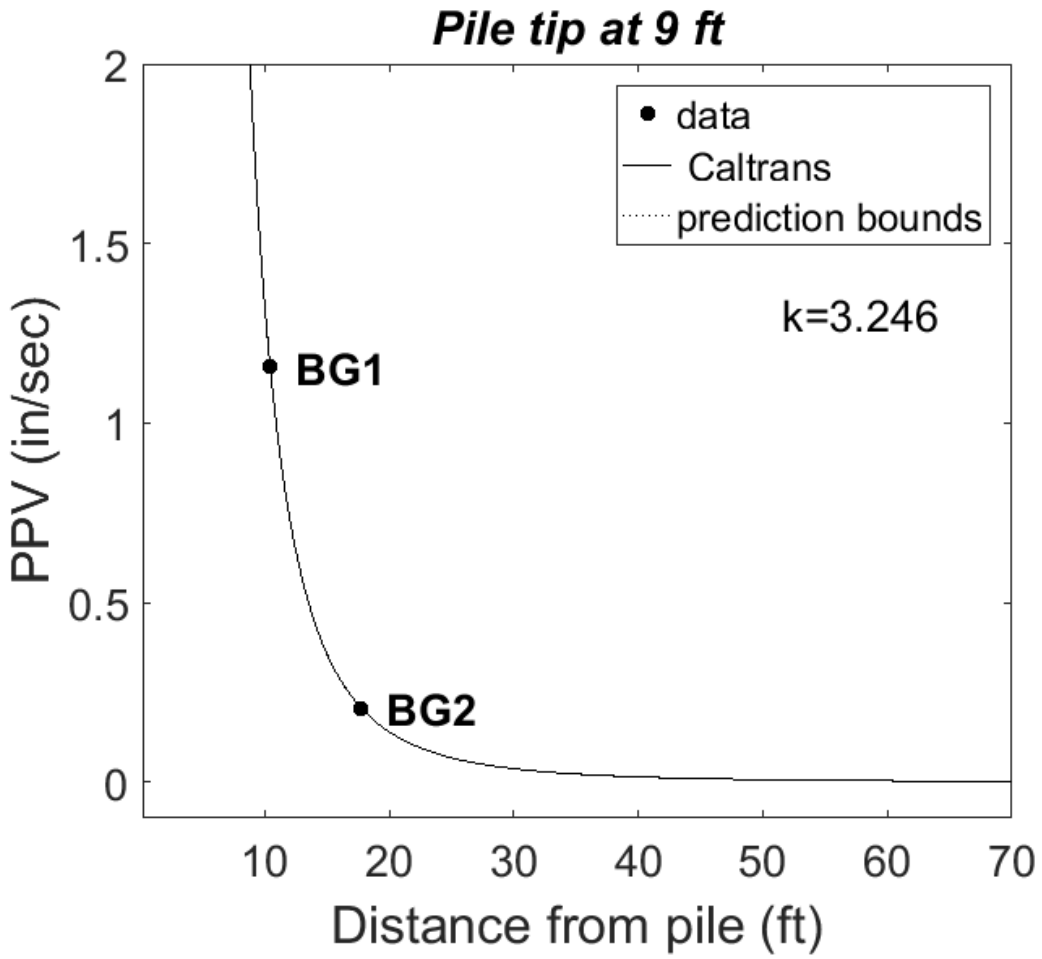

Figure 6-211 Attenuation curve for surface geophones at M-66 site – Caltrans Equation, Transverse Direction

Table 6.9 Data for attenuation coefficient using the Caltrans equation, M-66 site-Transverse

SENSOR	Distance from pile (ft)	k	Diagonal distance from tip (ft)	PPV (in/sec)
BG1	15.00	3.246	10.4	1.157
BG2	25.00		17.8	0.207
		R^2		
		1.000		

6.5.2 M-139 Site

Coefficients of attenuation were determined by fitting the three prediction equations to vibration amplitudes recorded from the buried accelerometers, when the pile tip was at their elevation depth (25.5 ft), Figure 6-212 to Figure 6-219. It is interesting to note for the case of the Bornitz equation, Table 6.10, that the attenuation coefficient decreases by a factor of 2.5, when fitting the curve using the closest sensor to the pile and subsequently when using the furthest sensor as the fixed point. For example, for the vertical component when having the A3 sensor, that is the closest to the pile, as the fixed point an attenuation coefficient of α=0.152 1/ft is calculated, while fixing the furthest sensor A5 provides an α=0.064 1/ft. This is an indication confirming the hypothesis that the energy diminishes very fast at a close zone around the pile (plastic zone). Attenuation of ground motions has a slower rate when measuring vibration amplitudes further away from the pile (elasto-plastic and nearly elastic zone). This is an important finding that was confirmed as sensors were successfully installed very close to the pile for the first time. Attenuation parameters, k, when fitting the Caltrans equation did not show a similar variation, Table 6.11. In addition, the calculated coefficients k and β are approximately the same, Table 6.11 and Table 6.12. The fit was again good for all three directions. Finally, attenuation coefficients were calculated for all the blow counts when the pile was being driven from 24 ft to 27 ft; 1.5 ft above and below the sensors' elevation. The average estimated coefficients for this range are shown in the data accompanying the Figures. For the vertical ground motions, the average values are slightly higher compared to the calculated coefficients when the pile tip was at the same depth that the sensors were installed (25.5 ft). For the transverse ground motion, the difference between the average coefficients and those calculated at 25.5 ft is inconsistent.

Attenuation curves were fitted to surface ground motion amplitudes when the pile tip was at 14 ft for the vertical and longitudinal directions, Figure 6-220Table 6.18 to Figure 6-222. In addition, the decay curves were fitted to recorded motions when the pile tip was at 50 ft, Figure 6-223 to Figure 6-225, close to the end of driving. For all three cases of prediction equations, the attenuation rate is much higher when fitting the curves for the deeper source. This is not surprising, since the diagonal distance from the pile to the

sensor, that is implemented in the equations, is different when the pile tip is at a shallow depth compared to when driving the pile at 50 ft. Comparable decay curves for the longitudinal component for the 14 ft and 50 ft source depths are shown in Figure 6-226 to Figure 6-228 and Figure 6-229 to Figure 6-231. Data points were again well fitted for the two different depths and the three prediction curves, with calculated R-square values very close to one because the physical phenomena are consistent.

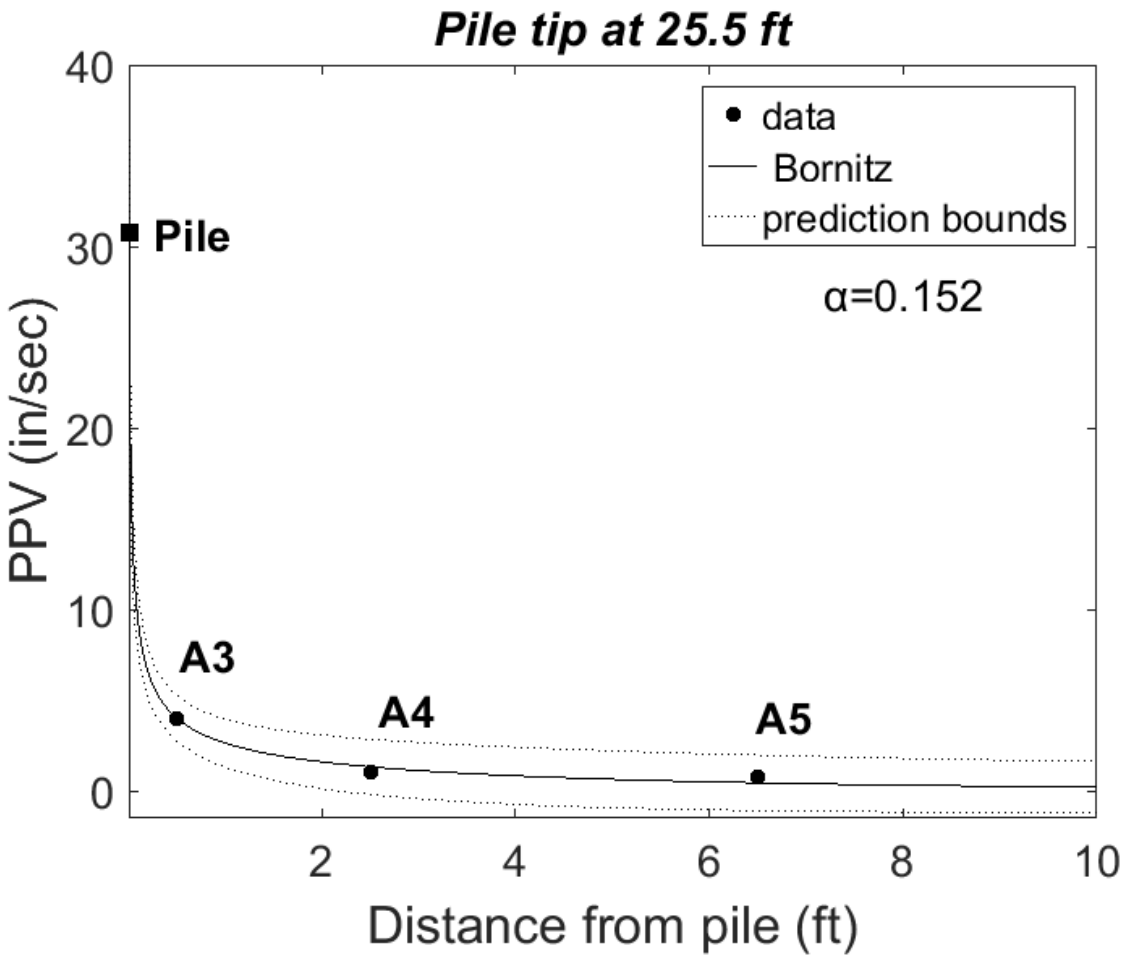

Figure 6-212 Attenuation curve for buried sensors at M-139 site – Bornitz Equation, Vertical Direction

Table 6.10 Data for attenuation coefficient using the Bornitz equation, M-139 site-Vertical

SENSOR	Distance from pile (ft)	α (1/ft) Pile tip at 25.5 ft	PPV (in/sec)	R^2	α (1/ft) Average Pile tip 24 - 27 ft	PPV (in/sec)	R^2
A3	0.50	0.152	4.02	0.975	0.249	3.17	0.916
A4	2.50	0.268	1.04	0.959	0.420	0.89	0.887
A5	6.50	0.064	0.74	0.960	0.072	0.72	0.875
PILE	0.01		30.76			39.54	

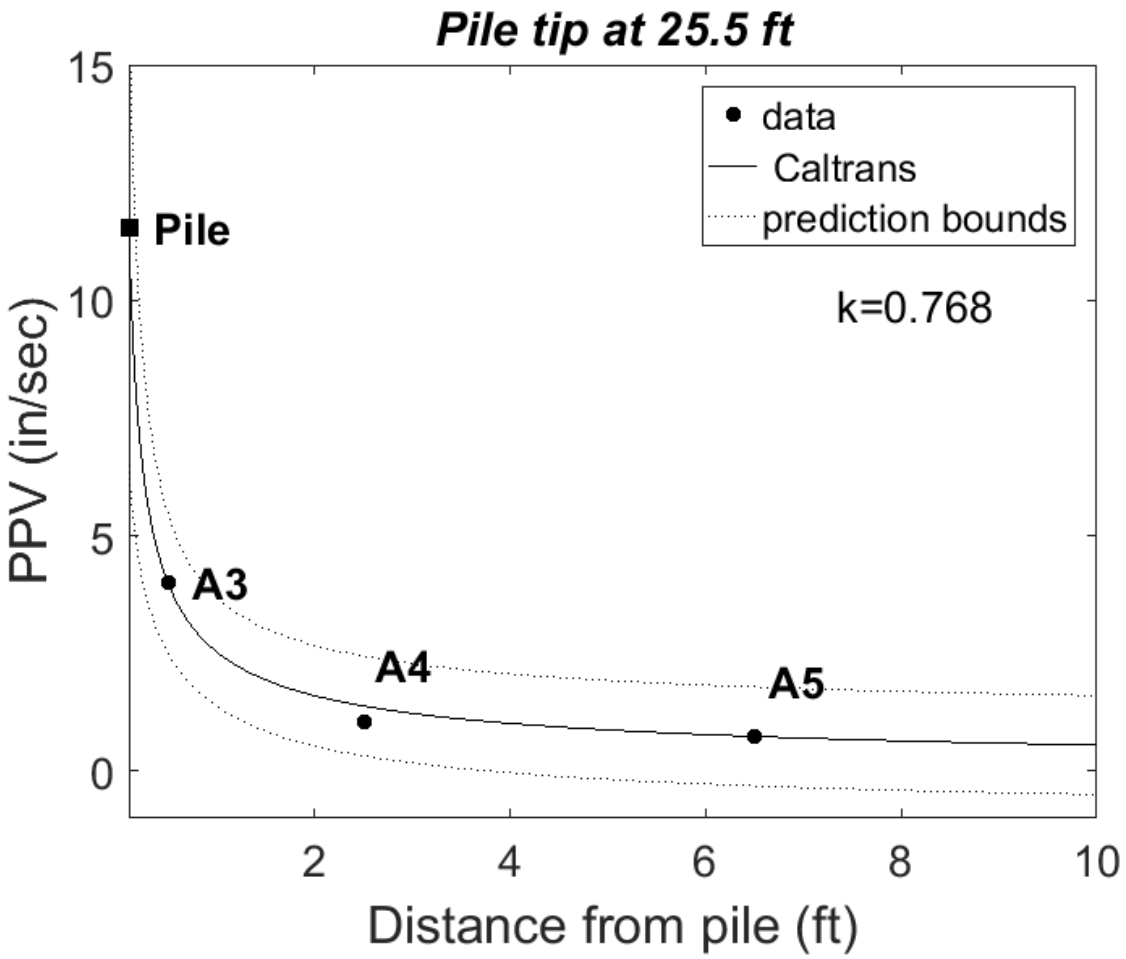

Figure 6-213 Attenuation curve for buried sensors at M-139 site – Caltrans Equation, Vertical Direction

Table 6.11 Data for attenuation coefficient using the Caltrans equation, M-139 site-Vertical

SENSOR	Distance from pile (ft)	k-Pile tip at 25.5 ft	PPV (in/sec)	R^2	k-Average Pile tip 24 - 27 ft	PPV (in/sec)	R^2
A3	0.50	0.768	4.02	0.993	1.016	3.17	0.961
A4	2.50	0.841	1.04	0.989	1.220	0.89	0.942
A5	6.50	0.659	0.74	0.982	0.733	0.72	0.917
PILE	0.10		13.94			41.40	

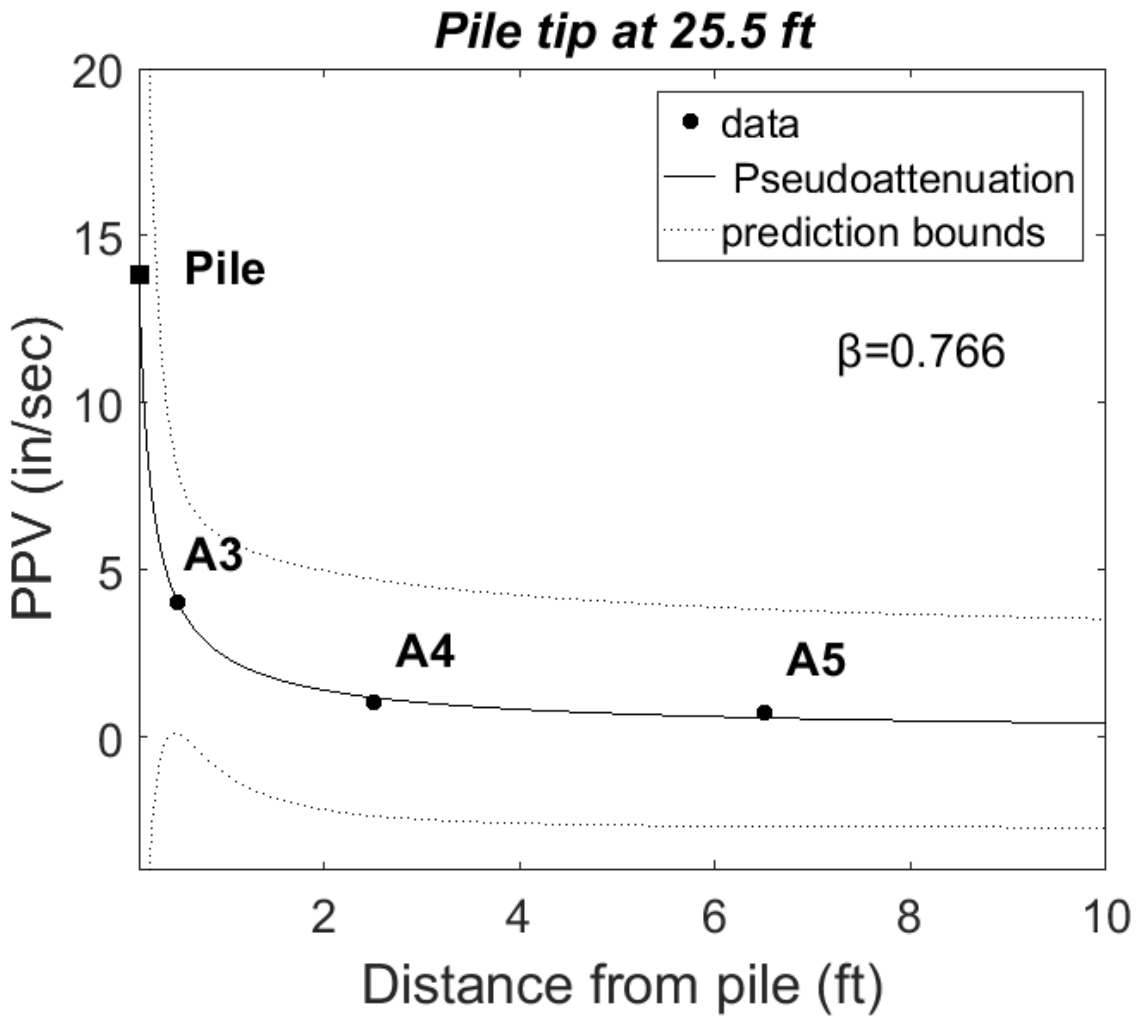

Figure 6-214 Attenuation curve for buried sensors at M-139 site – power Equation, Vertical Direction

Table 6.12 Data for attenuation coefficient using the power equation, M-139 site Vertical

SENSOR	Distance from pile (ft)	β-Pile tip at 25.5 ft	PPV (in/sec)	R^2	β-Average Pile tip 24 - 27 ft	PPV (in/sec)	R^2
A3	0.50	0.766	4.02	0.993	1.002	3.17	0.961
A4	2.50		1.04			0.89	
A5	6.50		0.74			0.72	
PILE	0.01		13.84			38.67	

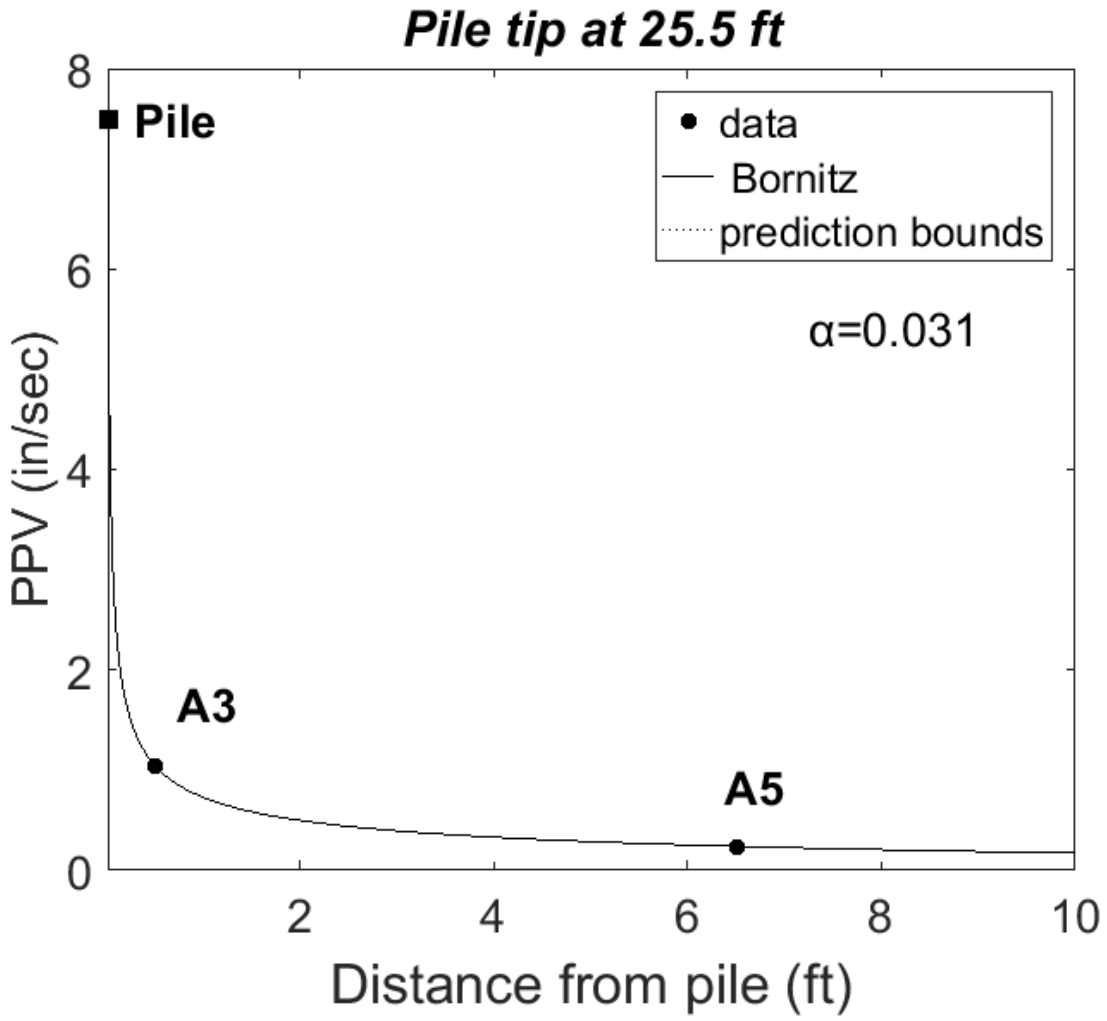

Figure 6-215 Attenuation curve for buried sensors at M-139 site – Bornitz Equation, Longitudinal Direction

Table 6.13 Data for attenuation coefficient using the Bornitz equation, M-139 site Longitudinal

SENSOR	Distance from pile (ft)	α (1/ft) Pile tip at 25.5 ft	PPV (in/sec)	R^2	α (1/ft) Average Pile tip 24 - 27 ft	PPV (in/sec)	R^2
A3	0.50	0.031	1.04	1.000	0.031	0.88	1.000
A4	2.50						
A5	6.50		0.24			0.24	
PILE	0.01		7.50			8.47	

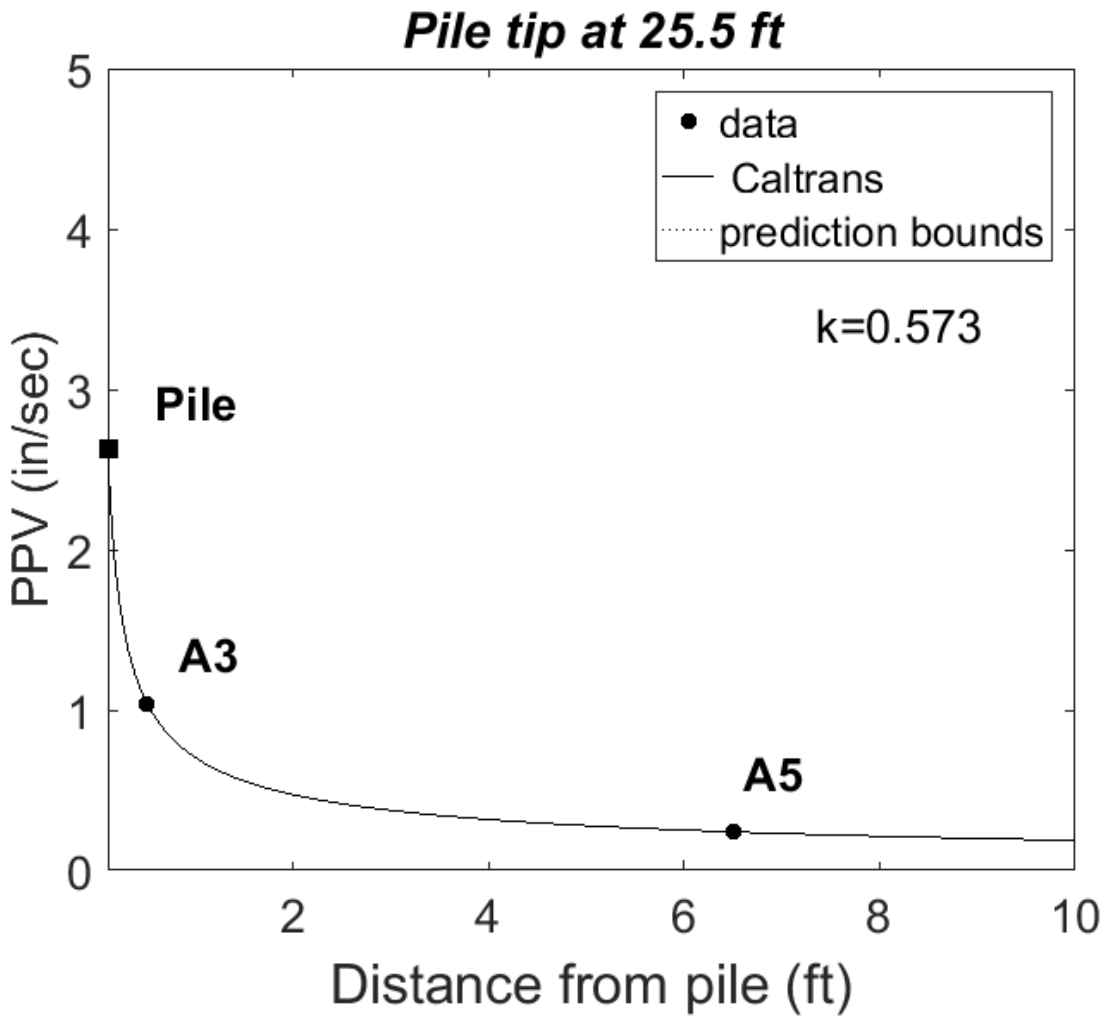

Figure 6-216 Attenuation curve for buried sensors at M-139 site – Caltrans Equation, Longitudinal Direction

Table 6.14 Data for attenuation coefficient using the Caltrans equation, M-139 site Longitudinal

SENSOR	Distance from pile (ft)	k-Pile tip at 25.5 ft	PPV (in/sec)	R^2	k-Average Pile tip 24 - 27 ft	PPV (in/sec)	R^2
A3	0.50	0.573	1.04	1.000	0.585	0.88	1.000
A4	2.50						
A5	6.50		0.24			0.24	
PILE	0.10		2.63			4.13	

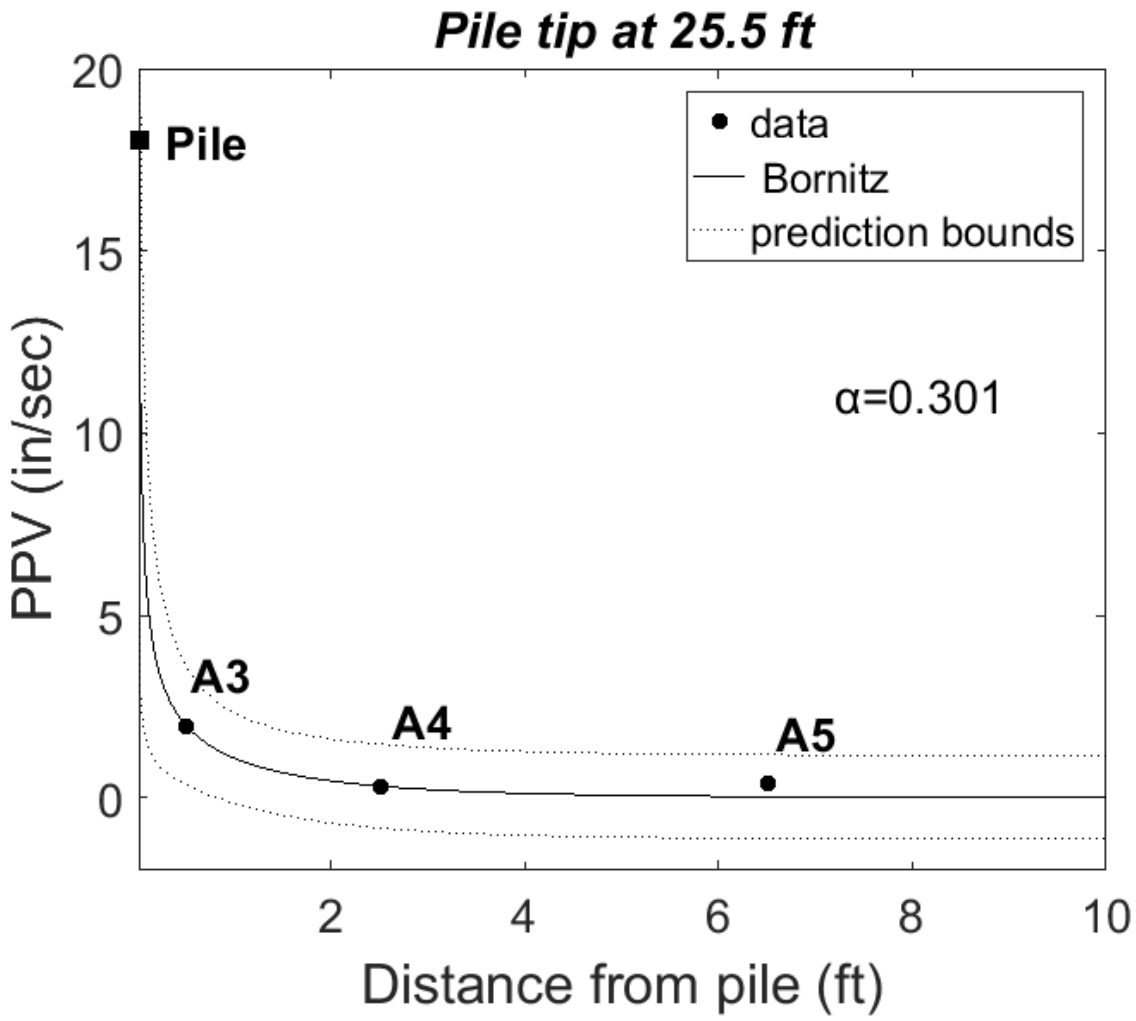

Figure 6-217 Attenuation curve for buried sensors at M-139 site – Bornitz Equation, Transverse Direction

Table 6.15 Data for attenuation coefficient using the Bornitz equation, M-139 site Transverse

SENSOR	Distance from pile (ft)	α (1/ft) Pile tip at 25.5 ft	PPV (in/sec)	R^2	α (1/ft) Average Pile tip 24 - 27 ft	PPV (in/sec)	R^2
A3	0.50	0.301	1.83	0.927	0.247	1.26	0.929
A4	2.50	0.520	0.40	0.918	0.374	0.34	0.896
A5	6.50	0.041	0.30	0.874	0.058	0.29	0.892
PILE	0.01		16.24			14.05	

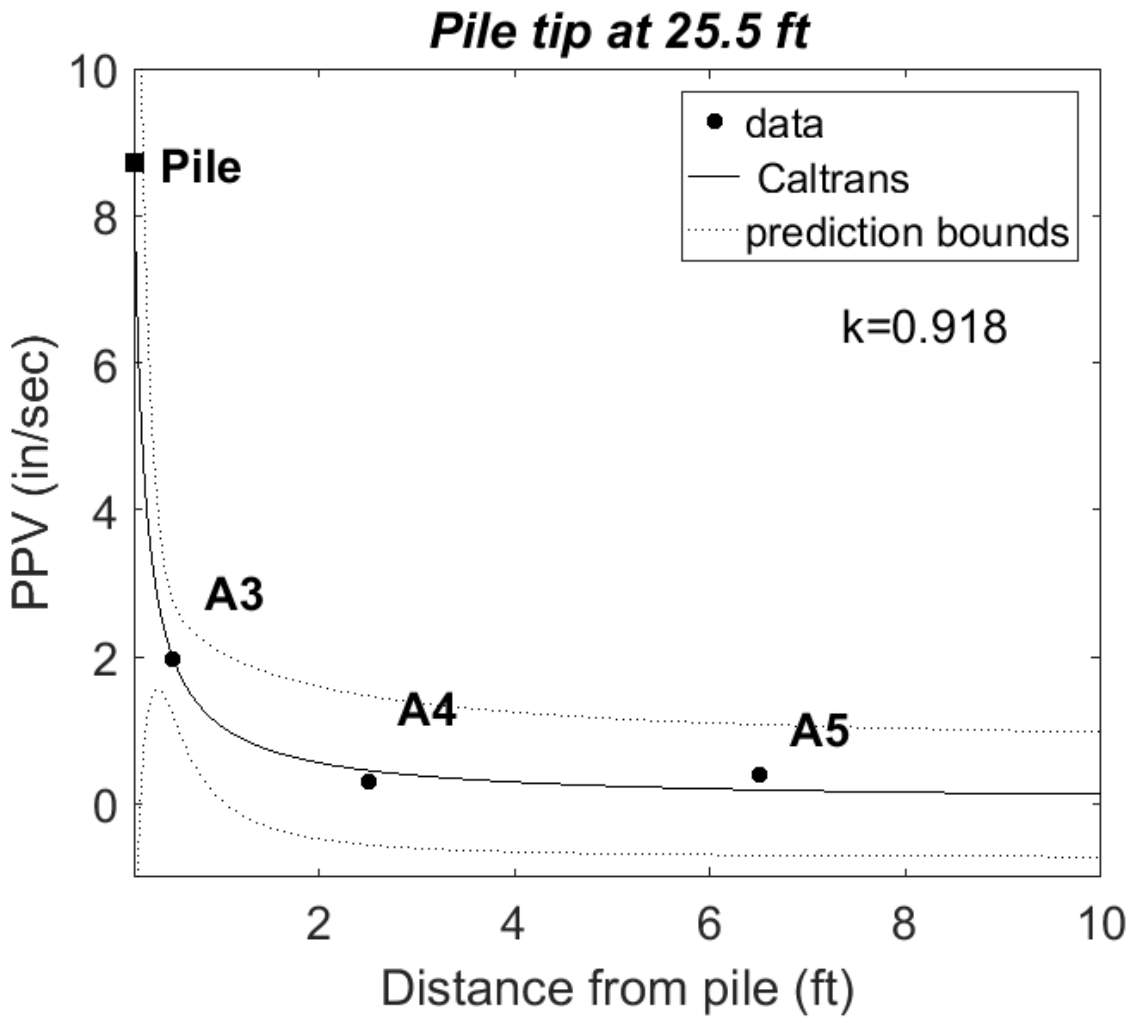

Figure 6-218 Attenuation curve for buried sensors at M-139 site – Caltrans Equation, Transverse Direction

Table 6.16 Data for attenuation coefficient using the Caltrans equation, M-139 site Transverse

SENSOR	Distance from pile (ft)	k-Pile tip at 25.5 ft	PPV (in/sec)	R^2	k-Average Pile tip 24 - 27 ft	PPV (in/sec)	R^2
A3	0.50	0.918	1.83	0.962	0.909	1.26	0.961
A4	2.50	1.149	0.40	0.949	1.081	0.34	0.937
A5	6.50	0.611	0.30	0.903	0.678	0.29	0.918
PILE	0.10		8.71			9.88	

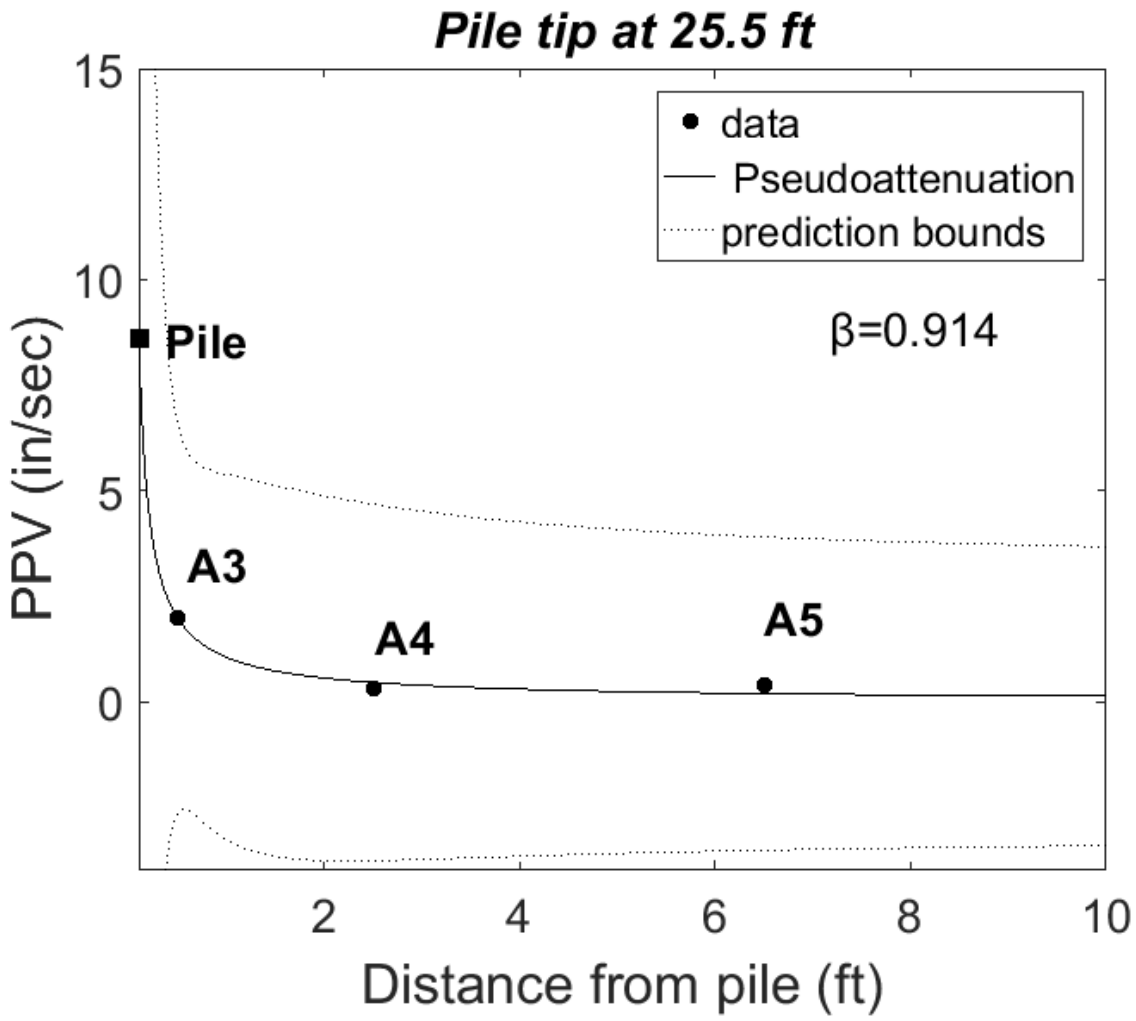

Figure 6-219 Attenuation curve for buried sensors at M-139 site – Power Equation, Transverse Direction

Table 6.17 Data for attenuation coefficient using the Power equation, M-139 site Transverse

SENSOR	Distance from pile (ft)	β Pile tip at 25.5 ft	PPV (in/sec)	R^2	β Average Pile tip 24 - 27 ft	PPV (in/sec)	R^2
A3	0.50	0.914	1.83	0.963	0.899	1.26	0.962
A4	2.50		0.40			0.34	
A5	6.50		0.30			0.29	
PILE	0.01		16.24			14.05	

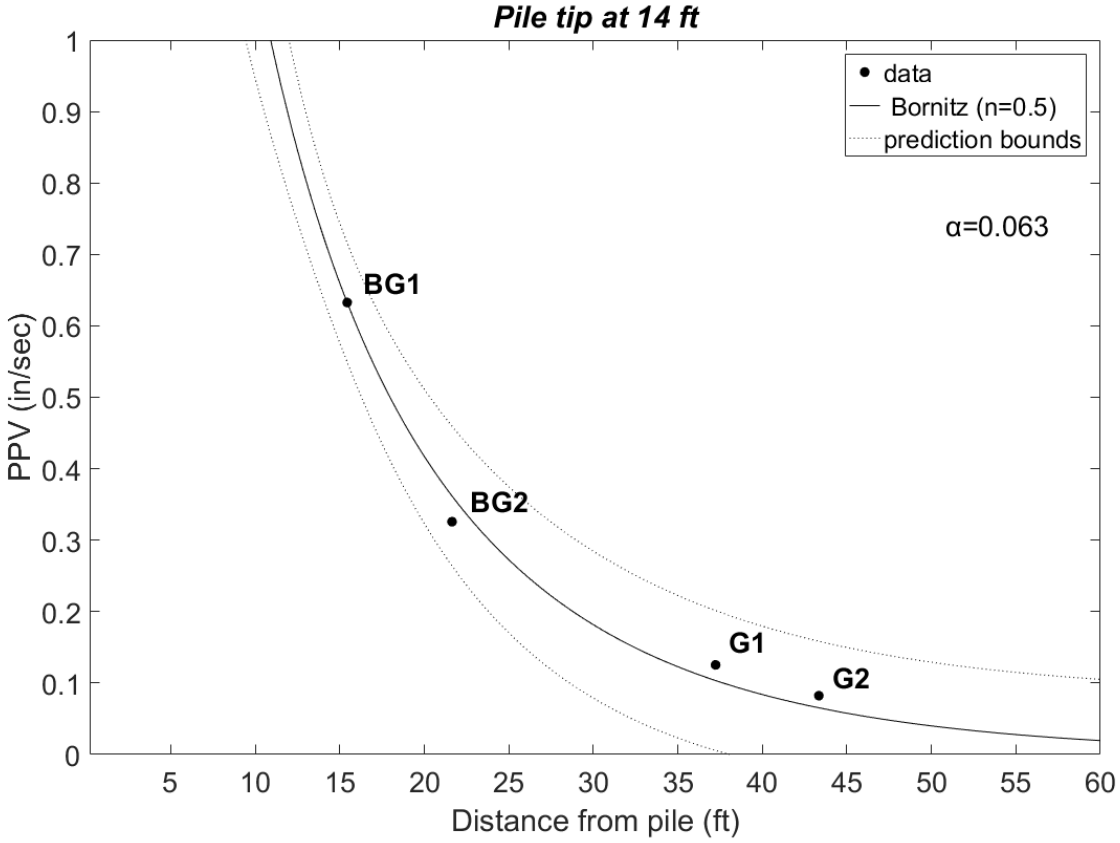

Figure 6-220 Attenuation curve for surface geophones at M-139 site – Bornitz Equation, Vertical Direction, Pile Tip at 14 ft

Table 6.18 Data for surface attenuation coefficient using the Bornitz equation, M-139 site Vertical, 14 ft

SENSOR	Distance from pile (ft)	α(1/ft) (n=0.5)	Diagonal distance from tip (ft)	PPV (in/sec)
BG1	6.50	0.063	15.4	0.63
BG2	16.50		21.6	0.33
G1	34.50	**R^2**	37.0	0.13
G2	40.50	0.989	43.3	0.08

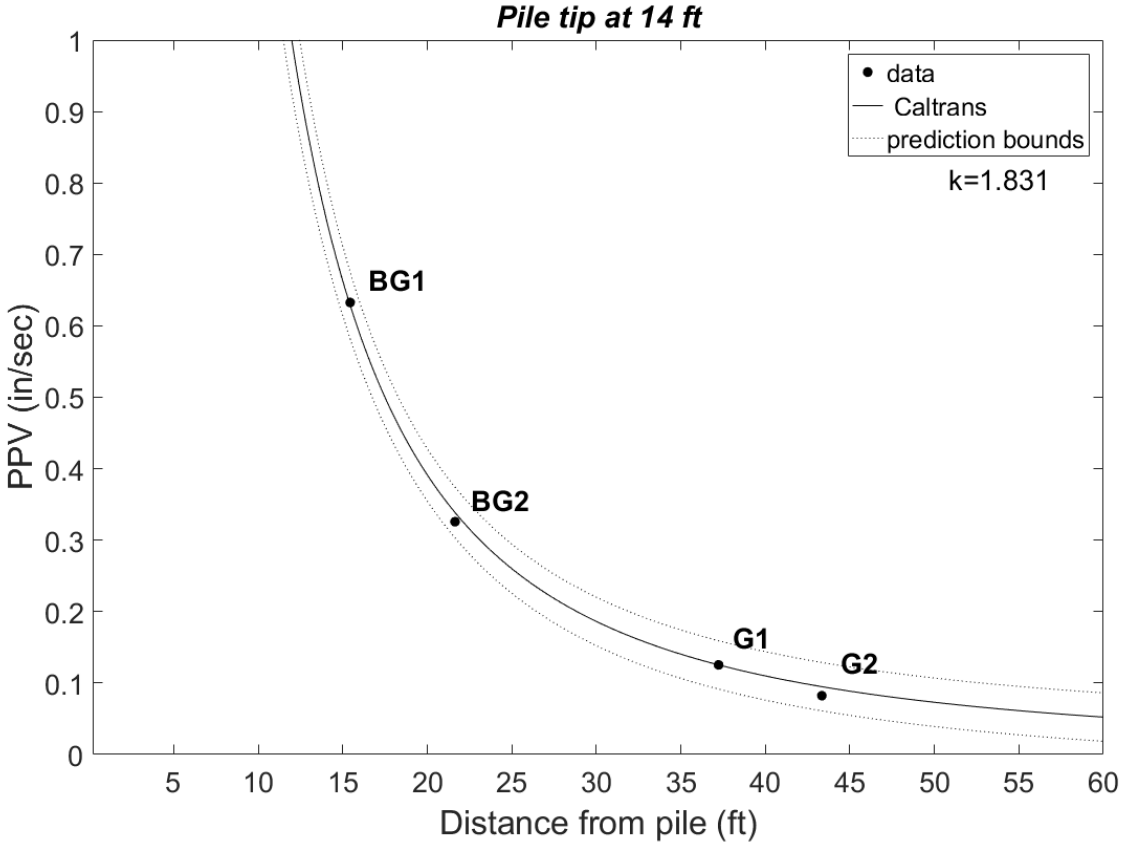

Figure 6-221 Attenuation curve for surface geophones at M-139 site – Caltrans Equation, Vertical Direction, Pile Tip at 14 ft

Table 6.19 Data for attenuation coefficient using the Caltrans equation, M-139 site-Vertical, 14 ft

SENSOR	Distance from pile (ft)	k	Diagonal distance from tip (ft)	PPV (in/sec)
BG1	6.50	1.831	15.4	0.63
BG2	16.50		21.6	0.33
G1	34.50	**R2**	37.0	0.13
G2	40.50	0.998	43.3	0.08

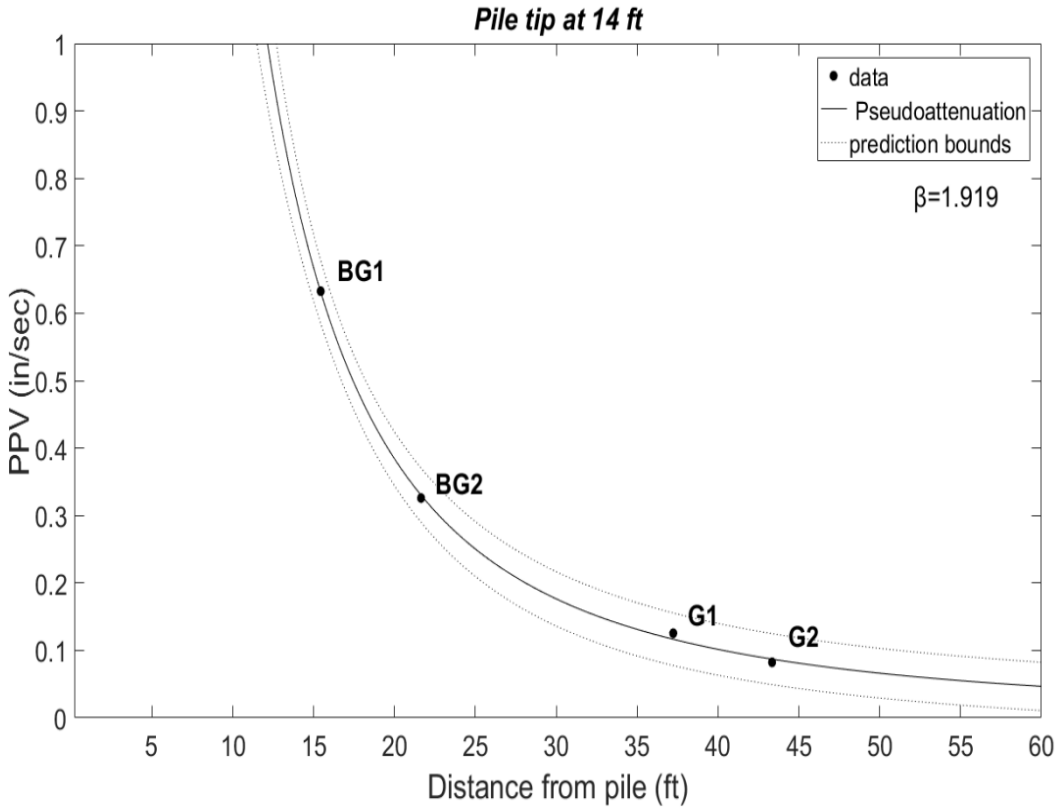

Figure 6-222 Attenuation curve for surface geophones at M-139 site – Power Equation, Vertical Direction, Pile Tip at 14 ft

Table 6.20 Data for surface attenuation coefficient using the power equation, M-139 site-Vertical, 14 ft

SENSOR	Distance from pile (ft)	β	Diagonal distance from tip (ft)	PPV (in/sec)
BG1	6.50	1.919	15.4	0.63
BG2	16.50		21.6	0.33
G1	34.50	**R^2**	37.0	0.13
G2	40.50	0.999	43.3	0.08

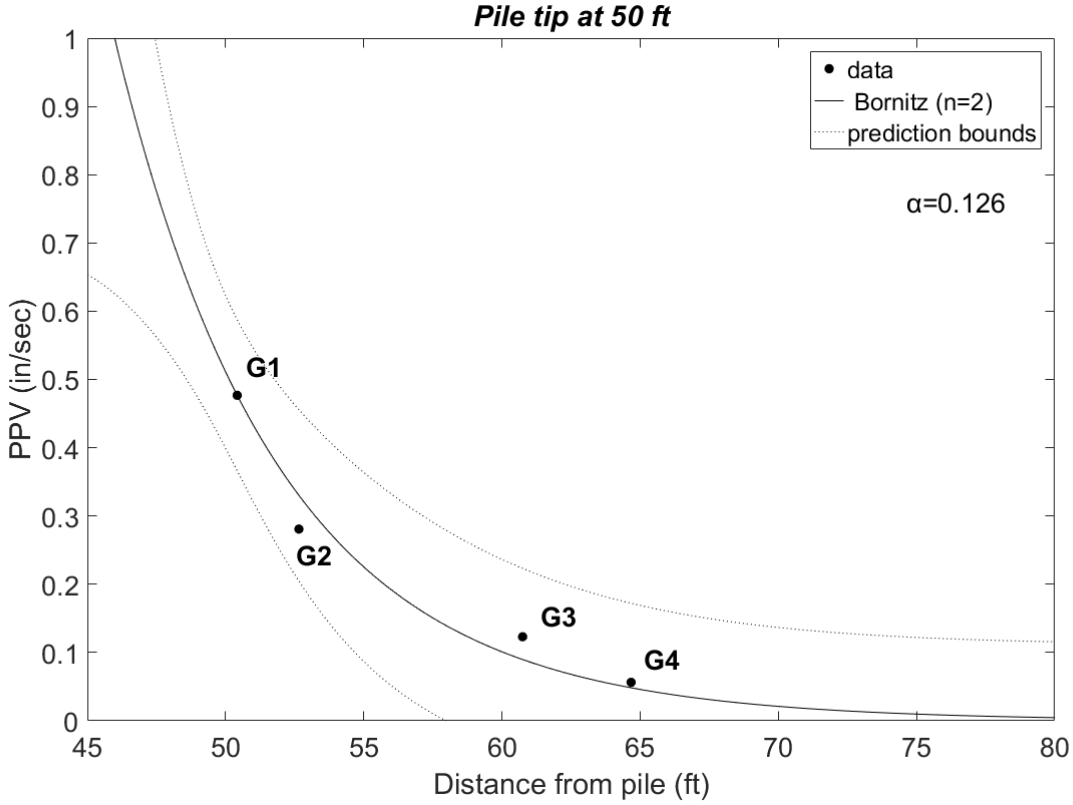

Figure 6-223 Attenuation curve for surface geophones at M-139 site – Bornitz Equation, Vertical Direction, Pile Tip at 50 ft

Table 6.21 Data for surface attenuation coefficient using the Bornitz equation, M-139 site-Vertical, 50 ft

SENSOR	Distance from pile (ft)	α(1/ft) (n=2)	Diagonal distance from tip (ft)	PPV (in/sec)
BG1	6.50	0.126	50.4	0.48
BG2	16.50		52.7	0.28
G1	34.50	R^2	60.7	0.12
G2	40.50	0.966	64.7	0.06

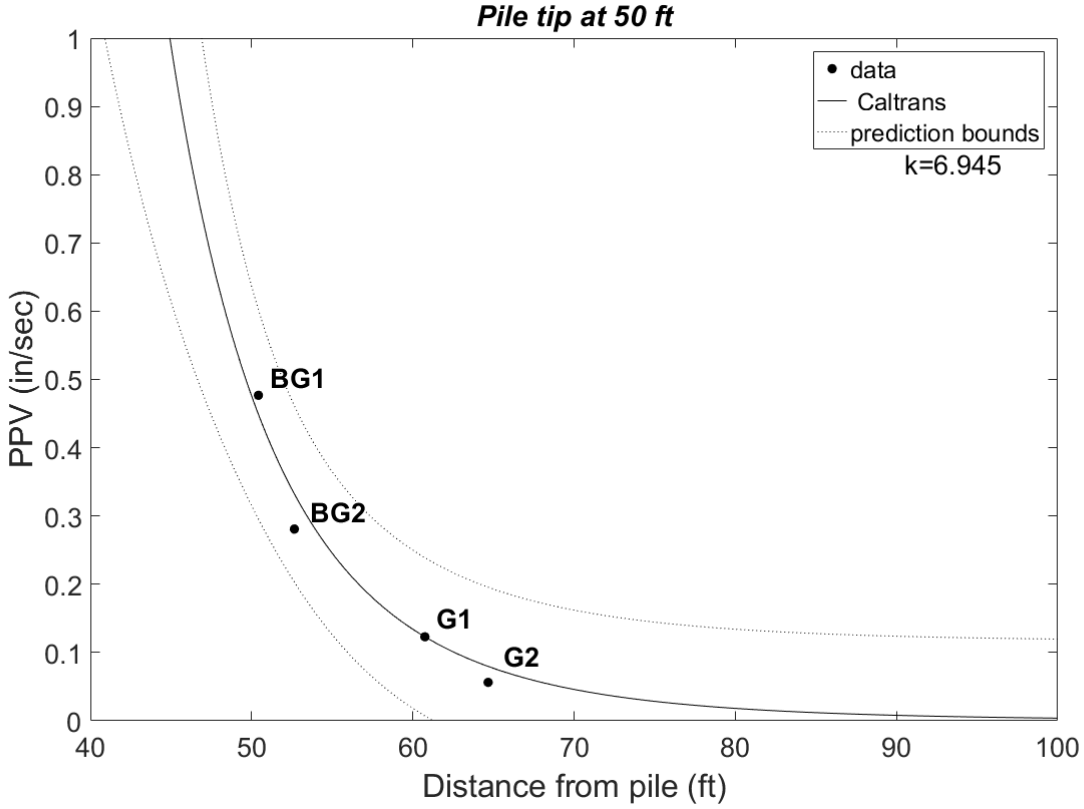

Figure 6-224 Attenuation curve for surface geophones at M-139 site – Caltrans Equation, Vertical Direction, Pile Tip at 50 ft

Table 6.22 Data for surface attenuation coefficient using the Caltrans equation, M-139 site-Vertical, 50 ft

SENSOR	Distance from pile (ft)	k	Diagonal distance from tip (ft)	PPV (in/sec)
BG1	6.50	6.945	50.4	0.48
BG2	16.50		52.7	0.28
G1	34.50	**R^2**	60.7	0.12
G2	40.50	0.962	64.7	0.06

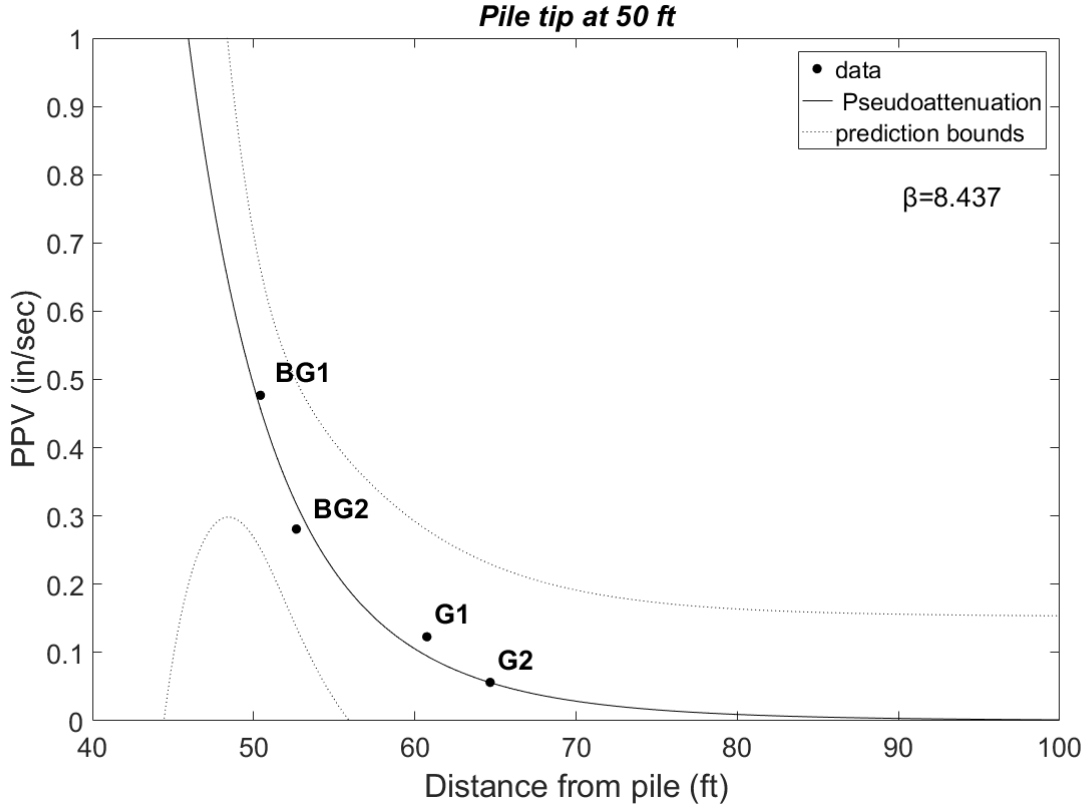

Figure 6-225 Attenuation curve for surface geophones at M-139 site – Power Equation, Vertical Direction, Pile Tip at 50 ft

Table 6.23 Data for surface attenuation coefficient using the power equation, M-139 site-Vertical, 50 ft

SENSOR	Distance from pile (ft)	β	Diagonal distance from tip (ft)	PPV (in/sec)
BG1	6.50	8.437	50.4	0.48
BG2	16.50		52.7	0.28
G1	34.50	R^2	60.7	0.12
G2	40.50	0.985	64.7	0.06

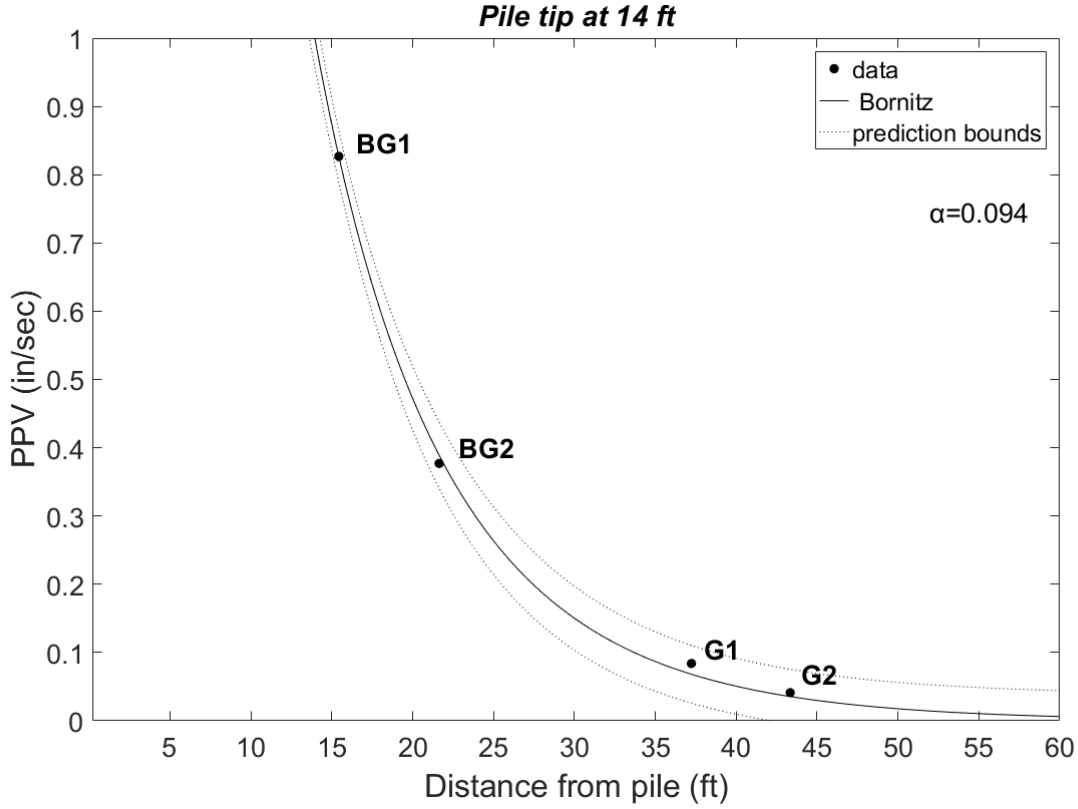

Figure 6-226 Attenuation curve for surface geophones at M-139 site – Bornitz Equation, Longitudinal Direction, Pile Tip at 14 ft

Table 6.24 Data for attenuation coefficient using the Bornitz equation, M-139 site-Longitudinal, 14 ft

SENSOR	Distance from pile (ft)	α(1/ft) (n=0.5)	Diagonal distance from tip (ft)	PPV (in/sec)
BG1	6.50	0.094	15.4	0.83
BG2	16.50		21.6	0.38
G1	34.50	R^2	37.2	0.08
G2	40.50	0.999	43.3	0.04

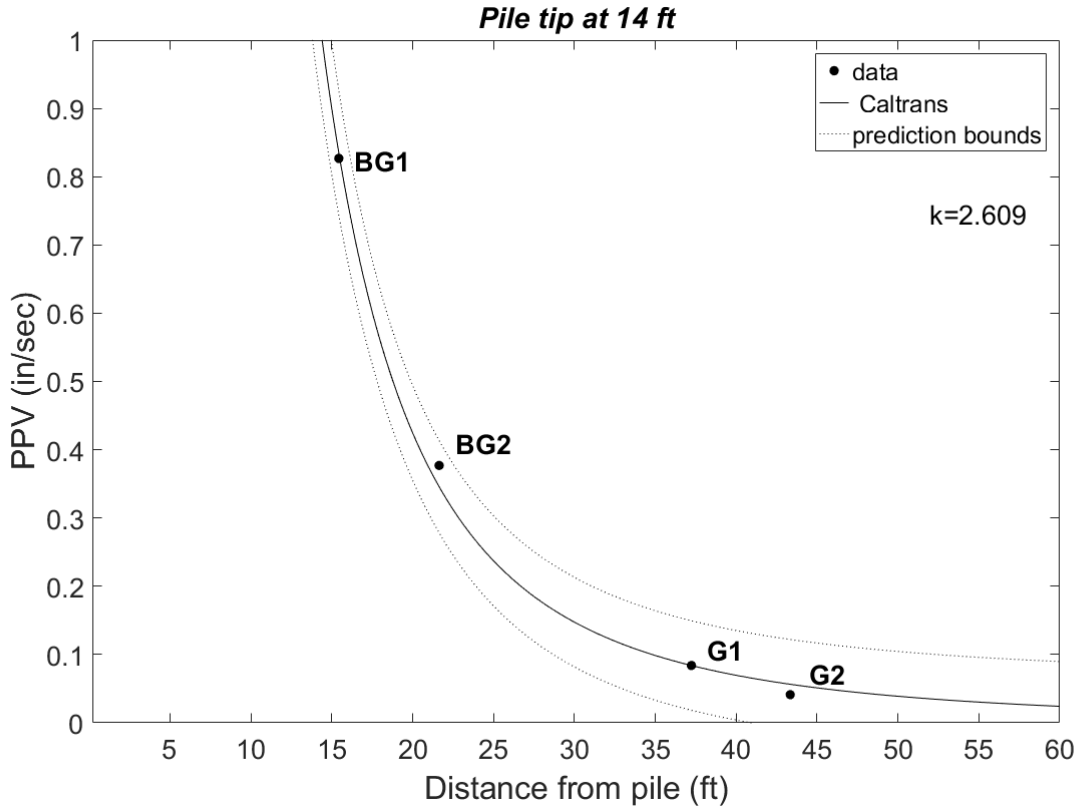

Figure 6-227 Attenuation curve for surface geophones at M-139 site – Caltrans Equation, Longitudinal Direction, Pile Tip at 14 ft

Table 6.25 Data for attenuation coefficient using the Caltrans equation, M-139 site-Longitudinal, 14 ft

SENSOR	Distance from pile (ft)	k	Diagonal distance from tip (ft)	PPV (in/sec)
BG1	6.50	2.609	15.4	0.83
BG2	16.50		21.6	0.38
G1	34.50	**R^2**	37.2	0.08
G2	40.50	0.997	43.3	0.04

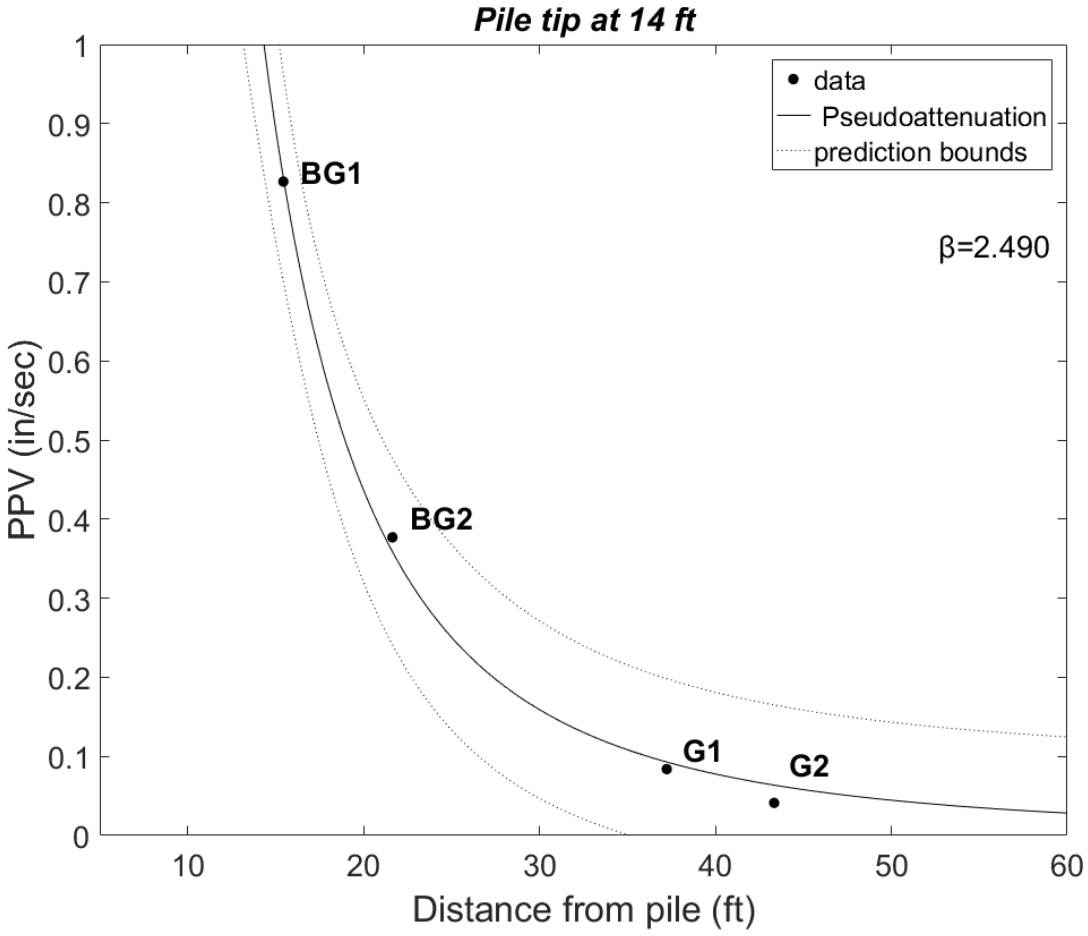

Figure 6-228 Attenuation curve for surface geophones at M-139 site – Power Equation, Longitudinal Direction, Pile Tip at 14 ft

Table 6.26 Data for attenuation coefficient using the power equation, M-139 site-Longitudinal, 14 ft

SENSOR	Distance from pile (ft)	β	Diagonal distance from tip (ft)	PPV (in/sec)
BG1	6.50	2.490	15.4	0.83
BG2	16.50		21.6	0.38
G1	34.50	**R^2**	37.2	0.08
G2	40.50	0.998	43.3	0.04

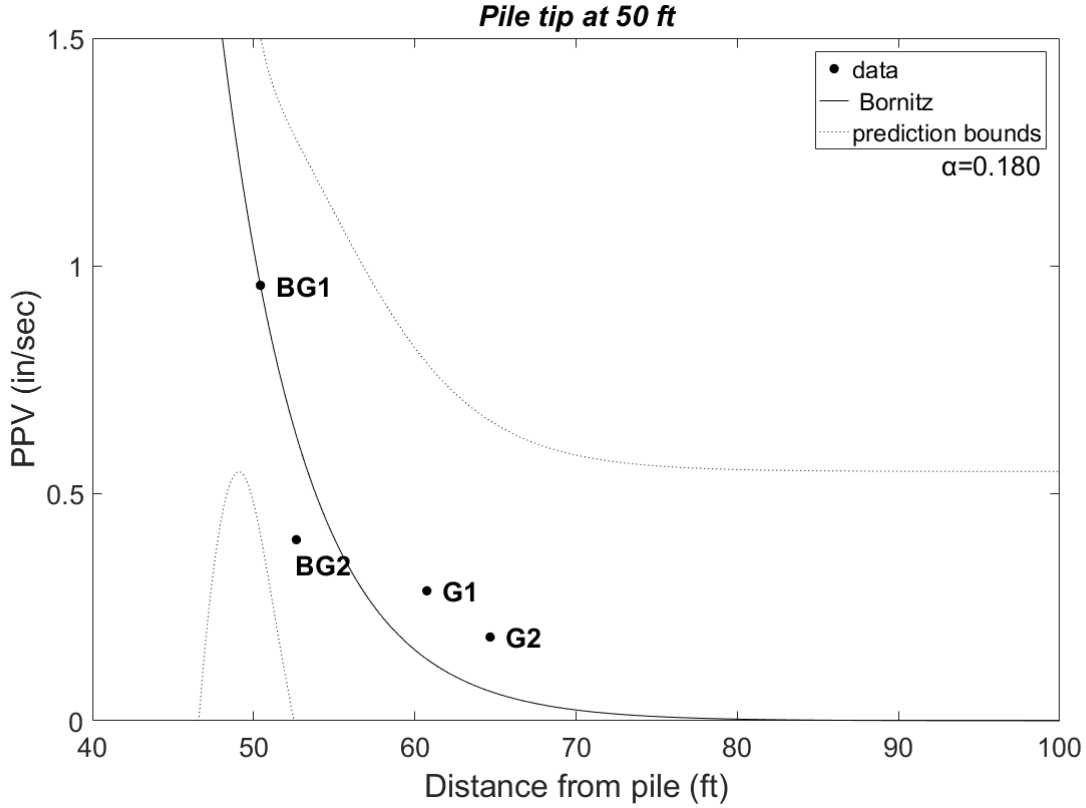

Figure 6-229 Attenuation curve for surface geophones at M-139 site – Bornitz Equation, Longitudinal Direction, Pile Tip at 50 ft

Table 6.27 Data for attenuation coefficient using the Bornitz equation, M-139 site-Longitudinal, 50 ft

SENSOR	Distance from pile (ft)	α(1/ft) (n=2)	Diagonal distance from tip (ft)	PPV (in/sec)
BG1	6.50	0.180	50.4	0.96
BG2	16.50		52.7	0.40
G1	34.50	**R^2**	60.7	0.29
G2	40.50	0.751	64.7	0.18

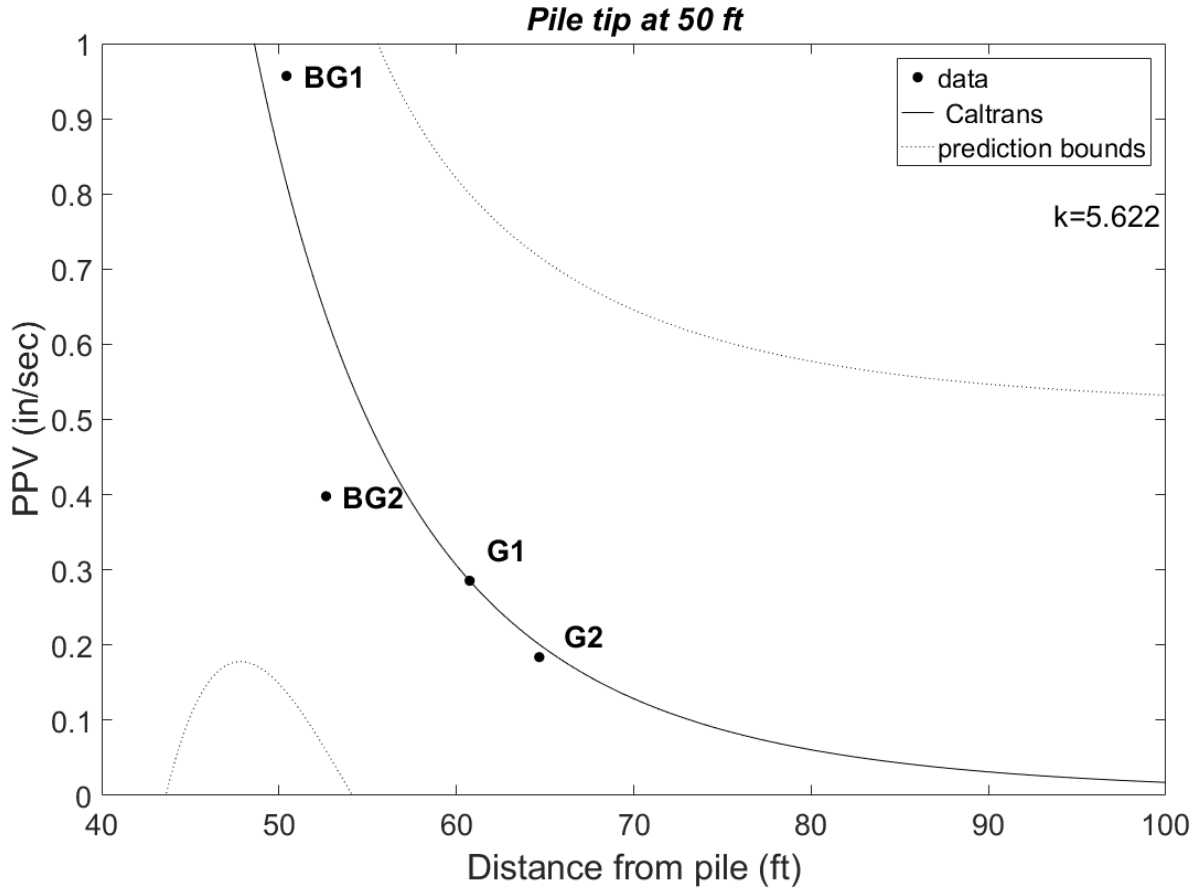

Figure 6-230 Attenuation curve for surface geophones at M-139 site – Caltrans Equation, Longitudinal Direction, Pile Tip at 50 ft

Table 6.28 Data for attenuation coefficient using the Caltrans equation, M-139 site-Longitudinal, 50 ft

SENSOR	Distance from pile (ft)	k	Diagonal distance from tip (ft)	PPV (in/sec)
BG1	6.50	5.622	50.4	0.96
BG2	16.50		52.7	0.40
G1	34.50	R^2	60.7	0.29
G2	40.50	0.781	64.7	0.18

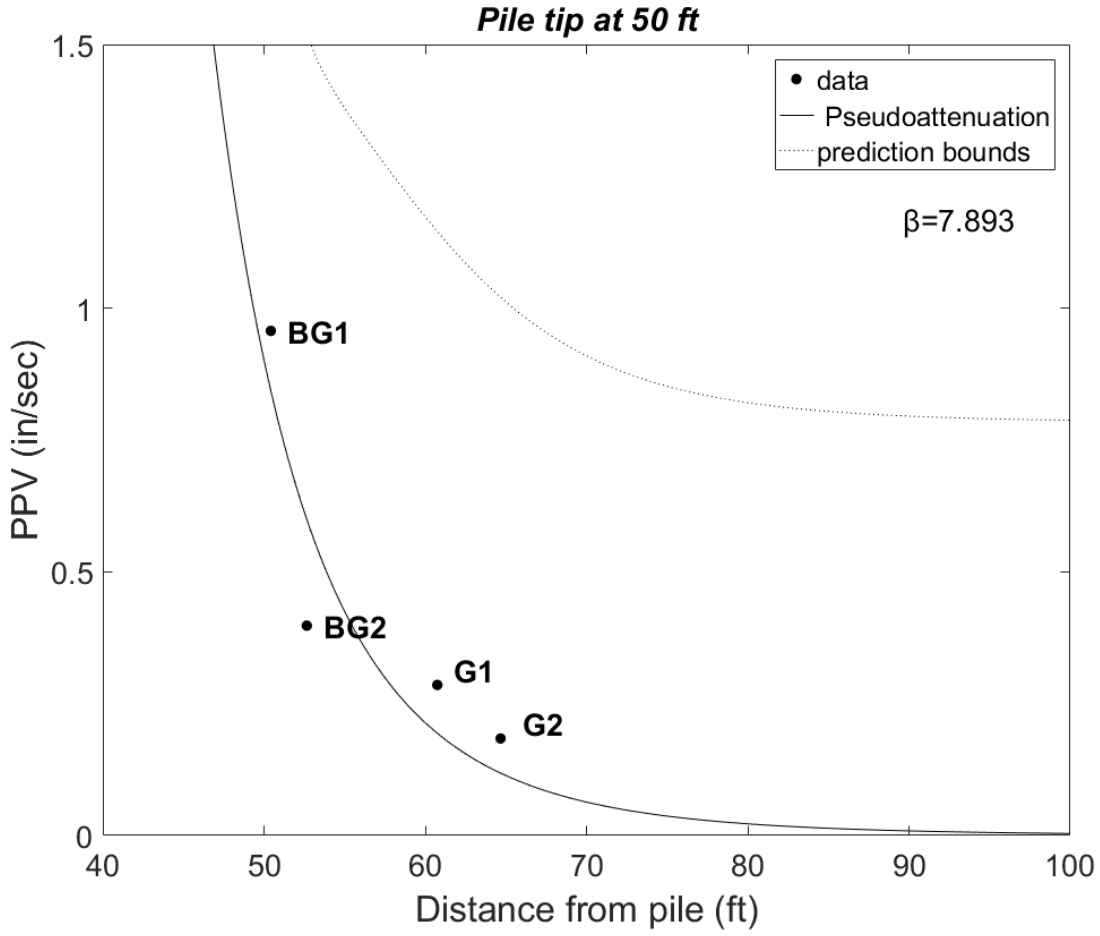

Figure 6-231 Attenuation curve for surface geophones at M-139 site – Power Equation, Longitudinal Direction, Pile Tip at 50 ft

Table 6.29 Data for attenuation coefficient using the power equation, M-139 site-Longitudinal, 50 ft

SENSOR	Distance from pile (ft)	β	Diagonal distance from tip (ft)	PPV (in/sec)
BG1	6.50	7.893	50.4	0.96
BG2	16.50		52.7	0.40
G1	34.50	**R^2**	60.7	0.29
G2	40.50	0.815	64.7	0.18

6.5.3 US-131 A Site

At this site, ground motions were recorded when driving two piles, Pile 1 and Pile 18. The two piles were 97.7 ft apart as shown in Figure 6-232 ,which happens to be about two pile lengths apart. The buried sensors were installed close to Pile 1 which was driven first, but ground motions were also recorded at these same sensors when the second pile was installed. This provided the opportunity to calculate attenuation coefficients for the far field, as the sensors were more than 90 ft away from the location of Pile 18. In addition, two sensor arrays were installed, one in a shallow sand layer and one in a deeper clay layer. The prediction curves were fitted in a similar way as shown for sites M-66 and M-139. Attenuation coefficients are presented only in tabular format in Table 6.30 to Table 6.35.

For the shallow sensors installed in the sand deposit, attenuation curves were fitted when the pile tip was at 18.4 ft; the closest sensor to the pile was installed 2 ft deeper (17 ft) than the next two furthest sensors (15 ft) and this depth was used as a reference, since the pile tip had passed the elevation depth of all three sensors. It is interesting to notice that when fitting the Bornitz formula with SG1 sensor as the reference point, when driving the second pile, the attenuation coefficient was decreased to one order of magnitude (α=0.027) compared to calculated coefficients when driving the first pile (α=0.285), Table 6.30; SG1 was 95.5 ft away from pile 18. A slower decrease in the attenuation rate is calculated when fitting the Caltrans equation through different fixed points, and no change is observed to the decay parameter when using the power equation. These phenomena are observed for the three directions that the data were recorded. Curve fitting is evaluated as very good for all the prediction equations and the three directions that ground motions were recorded.

For the deep sensors installed in the clay layer, attenuation coefficients were calculated for the vertical motions when the pile tip was at the depth of the sensors (35.3 ft). These decay parameters were found to be around half of the calculated coefficients for the sand layer. This is not surprising as similar observations have been reported by other researchers. Woods (1997) reported that softer soils have greater α values than

harder soils, for the case of fitting the Bornitz equation. The far field attenuation coefficient that was calculated using the SG2 sensor, 91.2 ft away from the pile, as the base point when driving pile18 was again around one order of magnitude lower (α=0.024) than the coefficients in the near field (α=0.127), when driving pile 1, for the case of the Bornitz equation (Table 6.30). Data points were well fitted for the three prediction equations.

Ground motions were recorded with surface geophones for both driven piles. For pile 1, decay parameters were calculated when the pile tip was at a depth of 13 ft. For pile 18, attenuation coefficients were determined when the pile tip was at 9 ft elevation. Given that the two piles are around 100 ft apart, the attenuation coefficients were expected to be similar. However, for the vertical and longitudinal ground motions, decay parameters were found to be much higher for pile 1 than pile 18. This is attributed to the fact, that the ground motions had similar values for the selected depth that data were fitted, for all geophones in the line array. For the case of transverse motions, similar attenuation coefficients were calculated when fitting prediction curves for the two different piles. Except for the case of the longitudinal motions when driving pile 18, the goodness of fit is evaluated very good for all cases. Results are presented in Table 6.33 to Table 6.35.

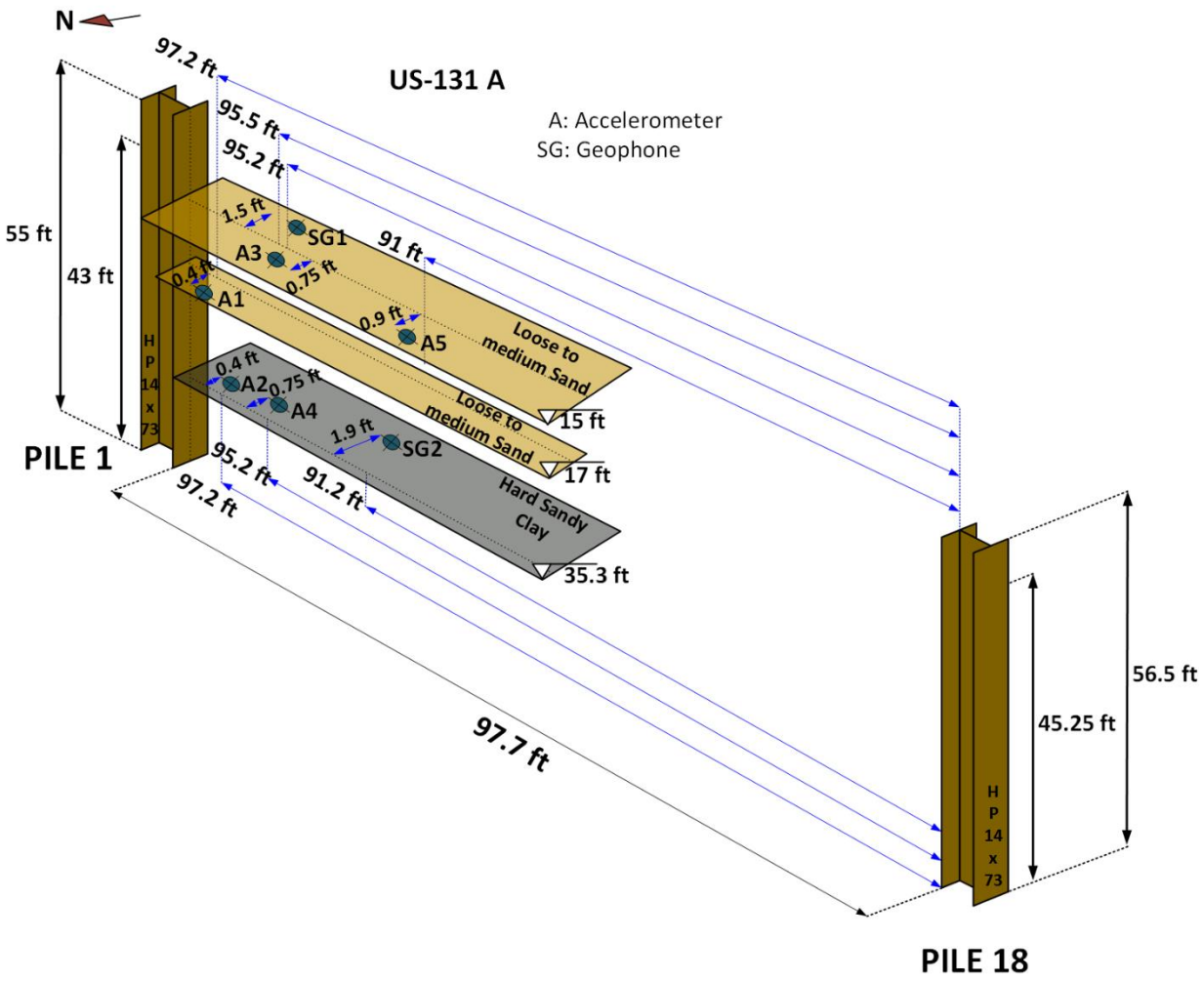

Figure 6-232 Perspective view of buried sensors at US-131 A site, Pile 1 and Pile 18 (not to scale)

6.5.4 US-131 B Site

This site included pile driving of two piles 97.7 ft apart, Pile 54 and Pile 37, as shown in Figure 6-233. The buried sensors were installed close to Pile 54 which was driven first. Data acquisition from the same buried sensors was conducted when driving the second pile in order to capture the attenuation response in the far field. Two sets of sensors were installed, one in a shallow sand layer and one in a deeper hard clay deposit. Only vertical component ground motions collected from the buried sensors were used to fit the equations because at this site most of the sensors were single axis vertical component geophones.

For the shallow sensors installed in the sand deposit, attenuation curves were fitted to vertical motions when the pile tip was at 17 ft. Again, the alpha value when fitting the Bornitz formula through the vibration amplitudes, with SG4 sensor as the reference point, when driving the second pile (far field), was more than one order of magnitude lower (α=0.023) compared to the attenuation coefficients calculated when driving the first pile (α=0.833, near field). A slower decrease in the attenuation rate is calculated when fitting the Caltrans equation through different fixed points, and no change is observed to the decay parameter when using the power equation (Table 6.30). Curve fitting is evaluated as very good for all the prediction equations.

For the deep sensors installed in the clay layer, attenuation coefficients were calculated for the vertical motions when the pile tip was at a depth of 34.1 ft. The attenuation coefficients were lower than those calculated for the sand layer, as observed at US-131 A site. The far field attenuation coefficient that was calculated using the SG3 sensor, 97.7 ft away from the pile, as the base point when driving pile 37 was again around one order of magnitude lower (α=0.021) than the coefficients in the near field (α=0.137), when driving pile 54, for the case of the Bornitz equation (Table 6.30). Data points were well fitted for the three prediction equations.

Ground motions were recorded with surface geophones for both driven piles. For pile 54, decay parameters were calculated when the pile tip was at a depth of 10.5 ft. For pile 37, attenuation coefficients were determined when the pile tip was at 10.75 ft elevation.

In contrast to the attenuation coefficients calculated for US-131 A site, the decay parameters calculated from the three prediction curves were not much different when driving pile 54 and pile 37. For the case of the Caltrans and power equations, the derived coefficients when driving pile 37 were found to be a bit higher. The goodness of fit is evaluated very good for all cases. Results for both piles are presented Table 6.33 to Table 6.35.

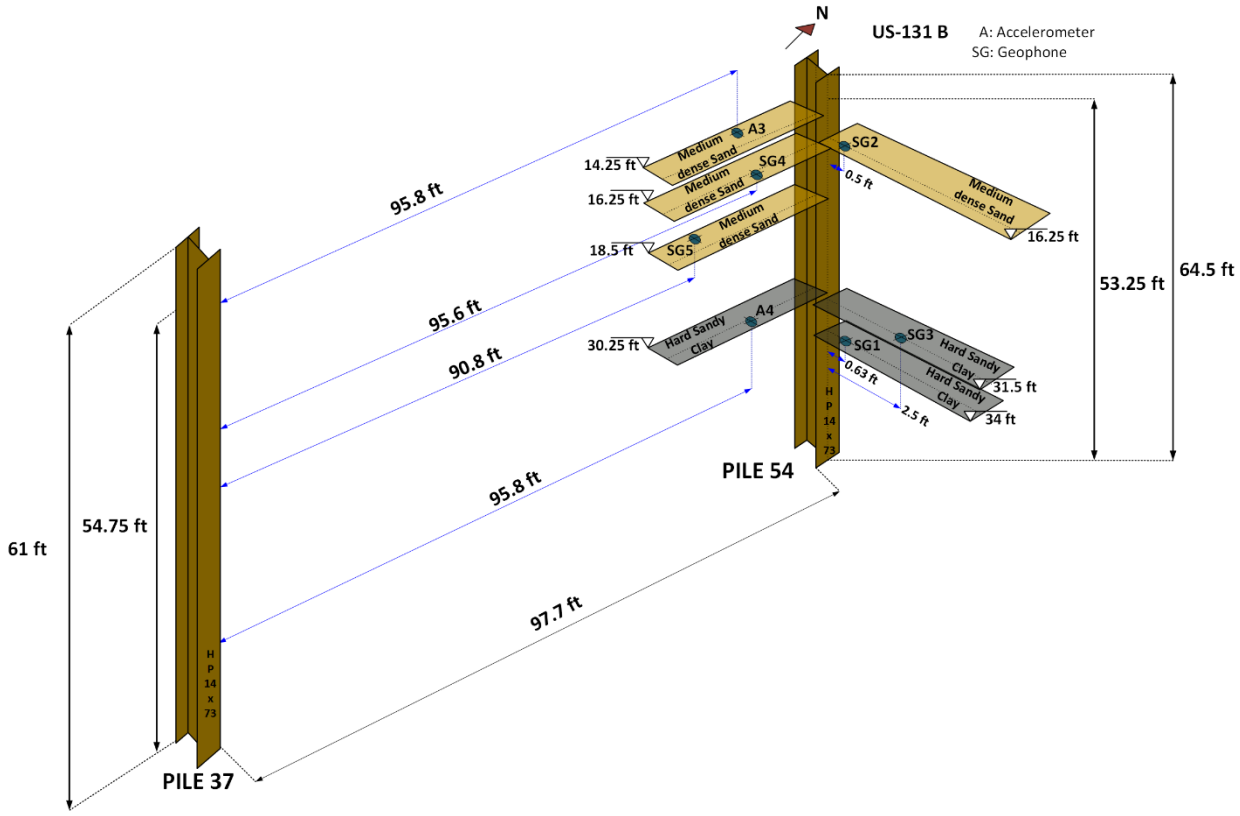

Figure 6-233 Perspective view of buried sensors at US-131 B site, Pile 54 and Pile 37 (not to scale)

A summary of the calculated coefficients evaluated for the buried and surface sensors for all the sites tested is provided in Table 6.30 to Table 6.35 . For the buried sensors, where the reference point was interchanged to fit the curves, the average attenuation coefficients when fixing different points in the matlab routine are only provided in these Tables; pile tip at the sensor depth. Frequency spectra from the sensors were observed and a frequency range for sensors in the same line array, data of which was used to calculate the coefficients, is provided in Table 6.30 to Table 6.35.

Some interesting conclusions can be derived by examining the results from different sites. The attenuation coefficients, α, were found to be consistent for ground motions in the ground and on the surface for the tested sites. This trend is not observed for the coefficients k and β, thus an average representative value cannot be easily selected. In addition, decay parameters calculated when fitting the Caltrans and power equations were similar for both recorded motions from the buried and surface sensors.

For the case of ground motions recorded from buried sensors, attenuation coefficients calculated for the far field are approximately one order of magnitude lower than those calculated in the near field. This trend is observed only when using the Bornitz formula. The Caltrans and power equations predict similar attenuation parameters in the near and the far field, thus overestimating the attenuation response in the elastic region. Therefore, the Bornitz equation seems to provide more realistic predictions. An average α value of 0.2 1/ft can be selected as representative value for vertical ground motion attenuation for the area close to the driven pile. For the far field, around two pile lengths from the driven pile, α=0.02 1/ft; one order of magnitude less than that in the near field.

For the case of surface ground motions, average α values of 0.05, 0.06 and 0.08 1/ft can be selected for the vertical, longitudinal and transverse directions, respectively. This is another important finding, as the current practice to monitor ground vibrations so far is by recording surface ground motions. The surface calculated coefficients are in the same order of magnitude as those calculated from the in-depth sensors in the far field.

The frequency range of ground motions, monitored from the buried sensors, was found to be between 6 and 113 Hz. Lower frequencies were found from the surface

ground motions, ranging from 3 to 60 Hz. Woods (1997) suggested an attenuation coefficient of 0.03 1/ft for a frequency of 25 Hz for most sandy soils. Most of the surface ground motions had a dominant frequency of 25 Hz, thus the calculated α=0.05 1/ft for the vertical ground motions is similar to that suggested by Woods.

Table 6.30 Attenuation coefficients from buried sensors' analysis – Vertical component

SITE	Soil Type	Depth of Pile Tip (ft)	Frequency Range (Hz)	Attenuation Coefficient, α (1/ft)		Pseudoattenuation factor, β		Dimensionless soil parameter, k	
				First Pile	Second Pile	First Pile	Second Pile	First Pile	Second Pile
M-139	Loose to medium dense sand	25.5	35-90	0.152	N/A	0.766	N/A	0.768	N/A
US-131 A	Loose to medium dense sand	18.4	20-92	0.285	0.027	1.336	1.337	1.337	1.140
US-131 A	Hard Sandy clay	35.3	26-104	0.127	0.024	0.724	0.728	0.724	0.937
US-131 B	Medium dense to dense sand	17	8-45	0.833	0.023	1.689	1.689	1.693	1.020
US-131 B	Hard Sandy clay	34.1	6-81	0.137	0.021	0.743	0.743	0.743	0.763

Table 6.31 Attenuation coefficients from buried sensors' analysis – Longitudinal component

SITE	Soil Type	Depth of Pile Tip (ft)	Frequency Range (Hz)	Attenuation Coefficient, α (1/ft)		Pseudoattenuation factor, β		Dimensionless soil parameter, k	
				First Pile	Second Pile	First Pile	Second Pile	First Pile	Second Pile
M-139	Loose to medium dense sand	25.5	35-92	0.031	N/A	0.572	N/A	0.573	N/A
US-131 A	Loose to medium dense sand	18.4	24-97	0.191	0.010	1.192	1.192	1.214	0.730
US-131 A	Hard Sandy clay	35.3	29-104	N/A	N/A	N/A	N/A	N/A	N/A
US-131 B	Medium dense to dense sand	17	22-67	N/A	N/A	N/A	N/A	N/A	N/A
US-131 B	Hard Sandy clay	34.1	18-50	N/A	N/A	N/A	N/A	N/A	N/A

Table 6.32 Attenuation coefficients from buried sensors' analysis – Transverse component

SITE	Soil Type	Depth of Pile Tip (ft)	Frequency Range (Hz)	Attenuation Coefficient, α (1/ft), n=0.5		Pseudoattenuation factor, β		Dimensionless soil parameter, k	
				First Pile	Second Pile	First Pile	Second Pile	First Pile	Second Pile
M-139	Loose to medium dense sand	25.5	34-101	0.301	N/A	0.914	N/A	0.768	N/A
US-131 A	Loose to medium dense sand	18.4	21-97	0.139	0.008	0.994	0.994	1.019	0.697
US-131 A	Hard Sandy clay	35.3	28-113	N/A	N/A	N/A	N/A	N/A	N/A
US-131 B	Medium dense to dense sand	17	27-78	N/A	N/A	N/A	N/A	N/A	N/A
US-131 B	Hard Sandy clay	34.1	30-87	N/A	N/A	N/A	N/A	N/A	N/A

Table 6.33 Attenuation coefficients from surface sensors' analysis – Vertical component

	SITE	Soil Type	Rated Energy of Pile Driver (lb-ft)	Frequency Range (Hz)	Attenuation Coefficient, α (1/ft), n=0.5	Pseudoattenuation factor, β	Dimensionless soil parameter, k
	M-66	Very loose sand	39,830	8-38	0.022	0.963	0.888
	M-139	Loose to medium dense sand	69,923	12-38	0.063	1.919	1.831
Pile 1	US-131 A	Loose to medium dense sand	75,970	15-41	0.244	4.616	3.969
Pile 18	US-131 A	Loose to medium dense sand	75,970	14-57	0.085	1.844	2.337
Pile 54	US-131 B	Loose to medium dense sand	75,970	16-45	0.040	1.627	1.726
Pile 37	US-131 B	Medium dense sand	75,970	4-23	0.053	2.345	2.454

Table 6.34 Attenuation coefficients from surface sensors' analysis – Longitudinal component

	SITE	Soil Type	Rated Energy of Pile Driver (lb-ft)	Frequency Range (Hz)	Attenuation Coefficient, α (1/ft), n=0.5	Pseudoattenuation factor, β	Dimensionless soil parameter, k
	M-66	Very loose sand	39,830	11-52	0.093	1.753	1.776
	M-139	Loose to medium dense sand	69,923	21-41	0.094	2.490	2.609
Pile 1	US-131 A	Loose to medium dense sand	75,970	18-57	0.089	2.303	2.839
Pile 18	US-131 A	Loose to medium dense sand	75,970	13-54	-0.007	0.225	0.872
Pile 54	US-131 B	Loose to medium dense sand	75,970	14-45	0.011	0.795	0.625
Pile 37	US-131 B	Medium dense sand	75,970	17-60	0.036	1.868	1.806

Table 6.35 Attenuation coefficients from surface sensors' analysis – Transverse component

	SITE	Soil Type	Rated Energy of Pile Driver (lb-ft)	Frequency Range (Hz)	Attenuation Coefficient, α (1/ft), n=0.5	Pseudoattenuation factor, β	Dimensionless soil parameter, k
	M-66	Very loose sand	39,830	9-37	0.199	3.202	3.246
	M-139	Loose to medium dense sand	69,923	5-23	N/A	N/A	N/A
Pile 1	US-131 A	Loose to medium dense sand	75,970	3-39	0.074	1.904	2.475
Pile 18	US-131 A	Loose to medium dense sand	75,970	14-41	0.055	1.943	2.939
Pile 54	US-131 B	Loose to medium dense sand	75,970	20-51	0.022	1.099	1.249
Pile 37	US-131 B	Medium dense sand	75,970	12-54	0.044	2.076	1.892

CHAPTER 7 SUSCEPTIBILITY OF GROUND SETTLEMENT DUE TO PILE DRIVING

In this Chapter, a process to evaluate the potential for a soil to undergo shakedown settlement from pile driving is presented. The two sources of the energy emanating from the driven pile are taken into account, i.e. spherical waves from the pile tip and cylindrical waves from the pile shaft. For the case of the pile shaft, the maximum shear stress of the soil between the pile and soil interface controls the transfer of the energy. For the case of the pile tip, the relative impedance between the soil and the pile is employed as part of the mechanism of the energy transfer. The transferred energy attenuates travelling through the soil mass, thus particle motion and consequently shear strain decrease at increasing distances from the driven pile. Particle motion and shear strains calculated from the shaft and the tip of the pile can be summed giving the total particle motion amplitude and shear strain. The total shear strain is then compared with an accepted threshold cyclic shear strain to determine the potential of settlement due to impact pile driving.

The shear wave velocity measured in the far field at low shear strains, should be decreased significantly for the plastic zone around the pile where large levels of shear strains occur. The calculation of the shear wave velocity from the time histories for one of the field tests confirmed this (Figure 6-199). As another approach, an iterative procedure is implemented to find the shear wave velocity reduction factor according to measured particle velocities at different distances from the pile, from the tested sites. A value of shear strain is assumed for the observed points where particle velocity data was collected. The reduction factor of shear wave velocity is obtained by available relations between shear strain and shear wave velocity reduction for similar soils. The G/G_{max}

versus cyclic shear strain curve proposed by Vucetic and Dobry (1991) was modified as shown in Figure 7-1 to get the shear wave velocity reduction for sands (PI=0) and silty sands (PI=15) which are susceptible to densification. The value of shear strain is calculated and is compared with the assumed for the point of interest. If the two values are close the iteration stops. If not, the calculated shear strain value from the previous step is assumed as the shear strain at the point of interest. The value of the shear wave velocity reduction factor of the last step is the appropriate reduction factor for the observed point. The calculation of the shear strain is performed as follows:

$$\gamma = \frac{\dot{z}}{R_S V_{Smax}} \qquad \text{Eq. 7-1}$$

where: γ = shear strain at the observed point
$\dot{z}$ = peak particle velocity measured at the observed point
V_{Smax} = maximum shear wave velocity at low strains
R_S = reduction factor of shear wave velocity

The above procedure was conducted for the measured particle velocities at sites M-139, US-131 A and US-131 B. The layers of interest to find the shear wave velocity reduction factor, are the granular soils that the embedded sensors were installed and are susceptible to settlement. The maximum shear wave velocity profile at low strains was obtained with MASW testing for all sites. The iteration process was performed for the complete soil profile that the pile was penetrated, however only the sandy soil layers close to the buried sensors are of interest to calculate shear strains and corresponding reduction factors. The shear strain profiles for the three tested sites are provided in Figure 7-2 to Figure 7-4. The range of depths that are of interest for each site are: 20 ft to 30 ft for M-139 site and 10 ft to 20 ft for US-131 A and US-131 B sites.

Table 7.1 presents the calculated shear wave velocity reduction factors and the corresponding shear strains at different distances from the driven pile that particle velocities were measured. It is obvious that the closer to the pile, the more the shear wave velocity is reduced. However, a common reduction factor for the shear wave velocity cannot be derived from the tested sites. For a distance of 0.5 ft from the pile the reduction

factor for the shear wave velocity, R_S, ranges from 0.36 to 0.54. This value should be even lower at the pile-soil interface.

It should be emphasized that the above procedure is based on the assumption of the shear strain and iteration process to estimate a shear wave velocity reduction factor. However, if we compare these estimated reduction factors with those calculated from the wave arrivals from the time histories (Figure 6-199), the agreement is good. This indicates that the reduction of the shear wave velocity in the proximity of a driven pile should be expected to be in the range shown in Table 7.1.

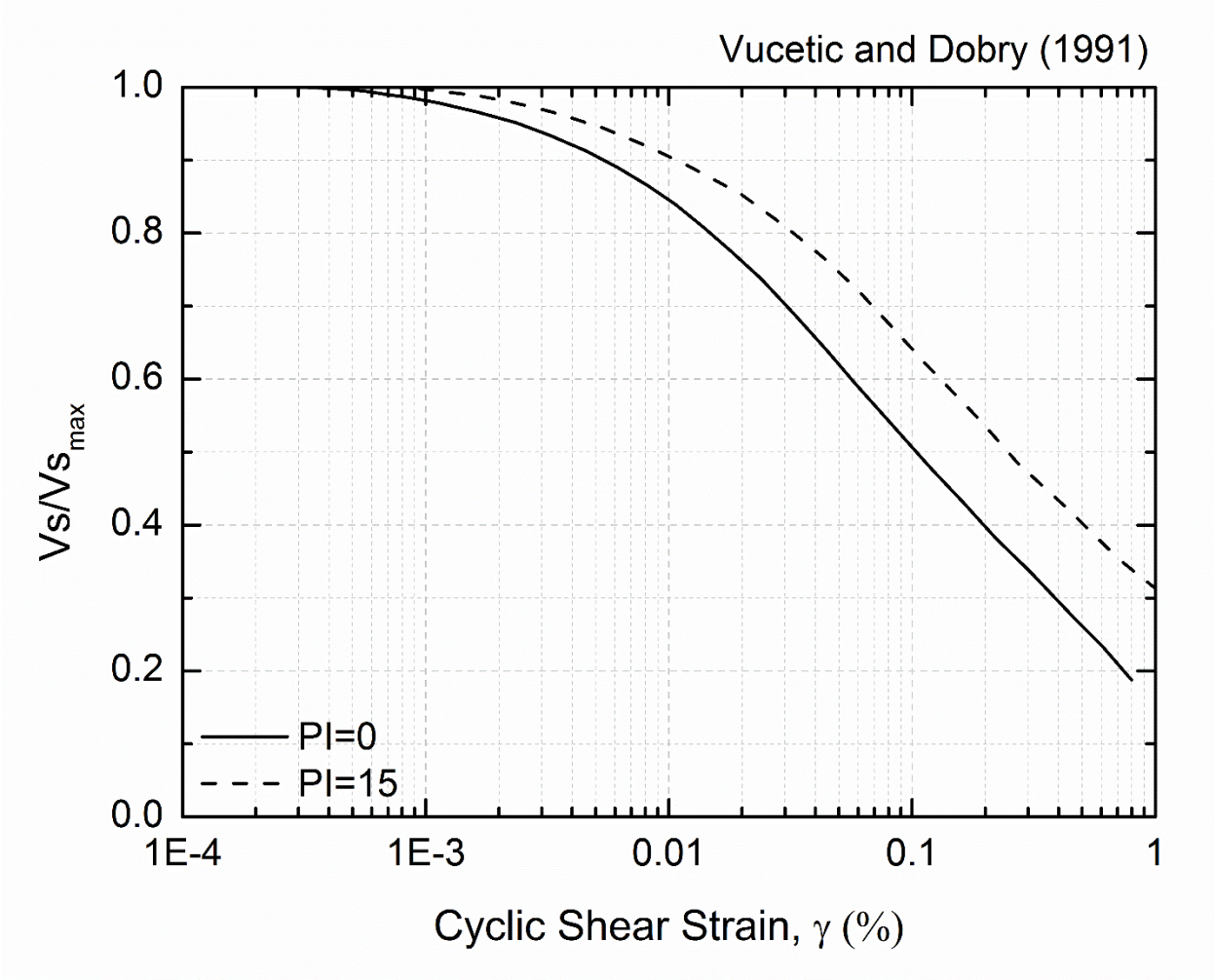

Figure 7-1 Shear wave velocity reduction for different shear strains for sands and silty sands (modified after Vucetic and Dobry 1991)

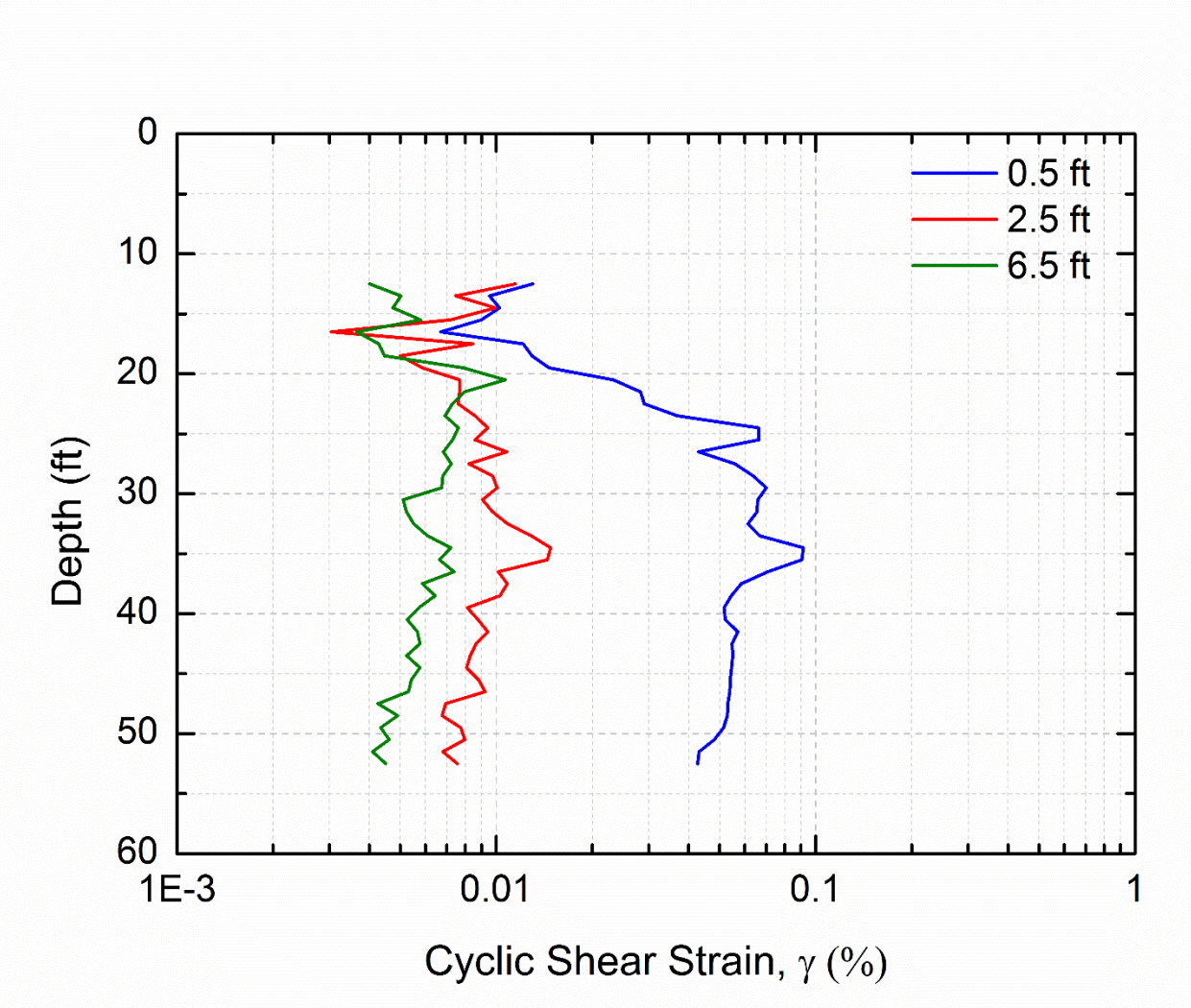

Figure 7-2 Shear strain profile at different distances from the driven pile – M-139 site

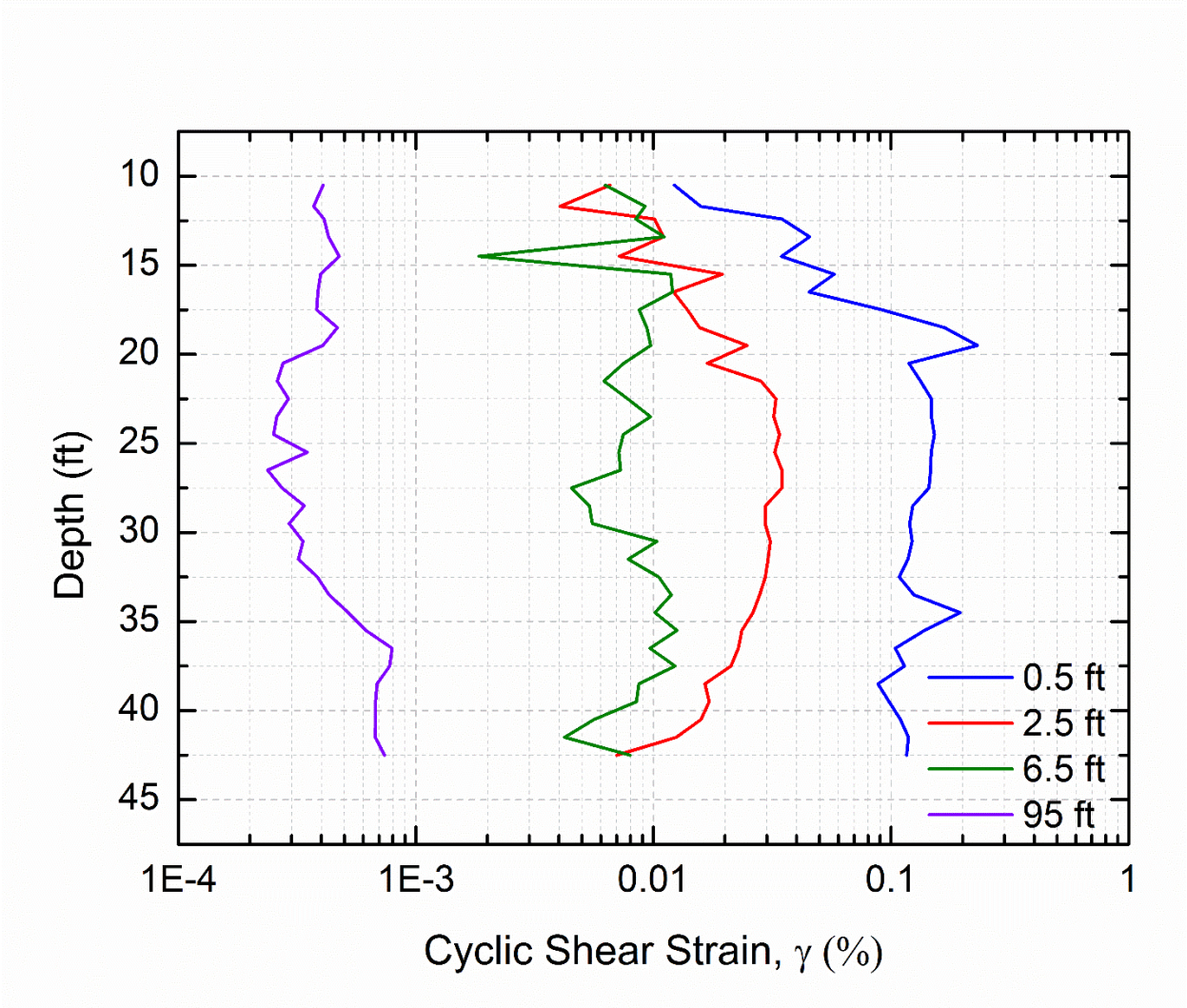

Figure 7-3 Shear strain profile at different distances from the driven pile – US-131 A site

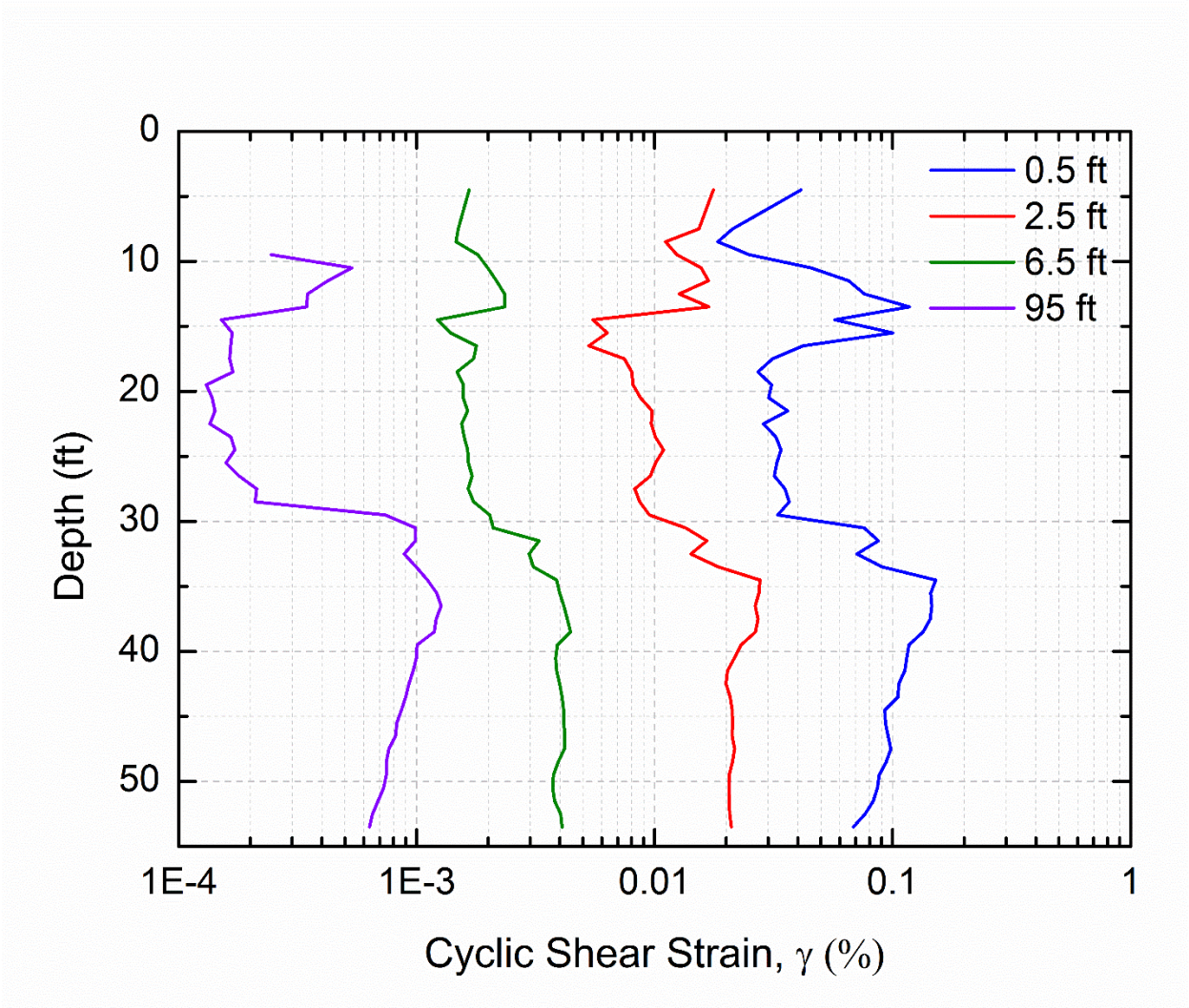

Figure 7-4 Shear strain profile at different distances from the driven pile – US-131 B site

Table 7.1 Calculated shear wave velocity reduction factors and shear strains for different distances from the pile for the tested sites

Distance from pile	0.5 ft		2.5 ft		6.5 ft		95 ft	
Site	γ (%)	R_S	γ (%)	R_S	γ (%)	R_S	γ (%)	R_S
M-139	0.07	0.54	0.009	0.85	0.007	0.88	N/A	N/A
US-131 A	0.23	0.36	0.028	0.72	0.012	0.85	0.0005	1
US-131 B	0.118	0.45	0.018	0.8	0.0023	0.95	0.0005	1

7.1 Process for estimation of susceptibility to ground settlement due to pile driving

7.1.1 Energy coupled into the ground from pile shaft

Prediction of the maximum particle velocity generated by shear between the shaft and the soil can be estimated by the following equation proposed by Massarsch and Fellenius (2008):

$$\dot{z}_{shaft} = \frac{\tau}{\rho V_S^*} \qquad \text{Eq. 7-2}$$

where: $\dot{z}_{shaft}$ = peak particle velocity in the soil at the pile-soil interface (ft/sec)
τ = shear strength of soil (lb/ft^2)
ρ= mass density of the soil (lb-sec^2/ft^2)
V_S* = shear wave velocity of soil at the contact with the pile (ft/sec)

Table 7.2 presents typical values of unit weight for a range of soils that can be used to determine the vertical stress in absence of values derived from laboratory tests. To determine the consistency of granular soils which are of primary interest, values for the relative density, Dr, correlated with the SPT N values can be used as shown in Table 7.3.

Table 7.4 presents a correlation of undrained shear strength with SPT N values that can be used for cohesive soils.

Table 7.2 Typical unit weights for various soils (from Coduto 2001)

Soil Type	**Classification (in this study)**	**Dry unit weight, γ_d (pcf)**	**Saturated unit weight, γ_s (pcf)**
GP, Poorly graded gravel	Sand	110-130	125-140
GW, Well graded gravel	Sand	110-140	125-150
GM, Silty gravel	Sand	100-130	125-140
GC, Clayey gravel	Sand	100-130	125-140
SP, Poorly graded sand	Sand	95-125	120-135
SW, Well graded sand	Sand	95-135	120-145
SM, Silty sand	Sand	80-135	110-140
SC, Clayey sand	Clay	85-130	110-135
ML, Low plasticity silt	Clay	75-110	80-130
MH, High plasticity silt	Clay	75-110	75-130
CL, Low plasticity clay	Clay	80-110	75-130
CH, High plasticity clay	Clay	80-110	75-125
PT, Peat	Clay	30	70

Table 7.3 Relative density of granular soils versus N (from Terzaghi and Peck (1967) and Lambe and Whitman (1969))

N Value (Blows/ft)	Classification	Relative Density, Dr (%)
0-4	Very Loose	0-15
4-10	Loose	15-35
10-30	Medium Dense	35-65
30-50	Dense	65-85
>50	Very Dense	85-100

Table 7.4 Approximate values of undrained shear strength versus N for cohesive soils (from Terzaghi and Peck 1967)

N Value (Blows/ft)	Consistency	Su (psf)
<2	Very Soft	<250
2-4	Soft	250-500
4-8	Medium	500-1000
8-15	Stiff	1000-2000
15-30	Very Stiff	2000-4000
>30	Hard	>4000

The shear strength, τ, can then be estimated from the SPT blow count N. Friction angle can be calculated using a correlation equation between N and φ as proposed by Kulhawy and Mayne (1990):

$$\varphi = \tan^{-1}\left[\frac{N}{12.2 + 20.3\frac{\sigma'_v}{P_a}}\right]^{0.34} \qquad \text{Eq. 7-3}$$

where: φ = effective stress friction angle (degrees)
N = field standard penetration number (blows/ft)
σ_v' = vertical effective stress (psf)
P_a = atmospheric pressure (2116 psf)

To determine the shear wave velocity at low strains in the absence of measured values in the field, the correlation between shear wave velocity and SPT blow count suggested by Imai and Tonouchi (1982) can be used:

$$V_S = 318N^{0.314} \qquad \text{Eq. 7-4}$$

where: V_S = shear wave velocity at low strains (ft/sec)
N = field standard penetration number (blows/ft)

The shear wave velocity at low strains should be decreased for observed points close to the pile, i.e. higher shear strains. As discussed in the previous section, an attempt was made to back calculate the reduction factor that should be applied for the shear wave velocity from the recorded particle velocities. The monitored data closer to the pile (0.5 ft) indicated that an average R_S would be equal to 0.4. Shear wave velocity at the pile-soil interface should be decreased even more, thus a reduction factor of R_S=0.2 may be applied in Eq. 7-5. The reduced shear wave velocity can generally be calculated as follows:

$$V_S^* = R_S V_S \qquad \text{Eq. 7-5}$$

where: V_S* = reduced shear wave velocity (ft/sec)
R_S = reduction factor
V_S = shear wave velocity at low strains (ft/sec)

7.1.2 Energy coupled into the soil from pile tip

The energy coupled into the ground at the tip of the pile during driving is a function of the ratio of impedance of the pile and the soil at the level of the tip. Saximeter and PDA analysis from the test sites of this project and recommended values of efficiencies for diesel hammers indicate that about 50% of the rated energy of the hammer reaches the top of the pile. As a conservative approach, it is assumed that this energy reaches the tip of the pile as well. Particle velocity in the soil in contact with the tip of the pile depends on the relative impedances of the pile and the soil at the tip and the energy reaching the pile tip. The equation is modified by a concept proposed by Massarsch and Fellenius (2008):

$$\dot{z}_{tip} = 2R_R \frac{Z_S}{Z_P} (E_o)^{0.5} \cos\theta \qquad \text{Eq. 7-6}$$

where: $\dot{z}_{tip}$ = vertical particle velocity in the soil at pile tip (ft/sec)
R_R = dimensionless correction factor accounting for soil compaction in granular soils and remolding in cohesive soils
R_R = 2 for loose to medium dense sand
0.2 < R_R <0.5 for normally consolidated to overconsolidated clay
$Z_S = A_c \rho_S V_{SP}$*, impedance of soil at pile tip (lb-sec/ft)
$Z_P = A_c \rho_P V_P$, impedance of pile at tip (lb-sec/ft)
A_c = contact area between pile and soil (ft^2)
V_{SP}* = velocity of Biot wave of the second kind in soil (ft/sec)
V_P = compression wave velocity in pile (ft/sec)
E_o = 0.5 times rated energy of hammer (ft-lb)
θ = angle between any ray of spherical wave and vertical (radians)

Wave velocity used in the soil impedance term (Z_S) in Eq. 7-6 is the Biot wave of the second kind. This wave velocity is slightly slower than the primary wave velocity in the soil (Richart et al. 1970). For this analysis the primary wave velocity (V_{SP}) can be used. This wave velocity in the soil will also be used to calculate strain caused by penetration of the pile at the tip at any point in the surrounding soil zone. The wave velocity V_{sp} can be calculated as follows:

$$V_{SP} = kV_S \qquad \text{Eq. 7-7}$$

$$k = \left[\frac{2(1-\nu)}{(1-2\nu)}\right]^{0.5} \qquad \text{Eq. 7-8}$$

$$V_{SP}{}^{*} = R_S V_{SP} \qquad \text{Eq. 7-9}$$

where: V_{SP} = primary wave velocity in the soil (ft/sec)
V_S = shear wave velocity at low strains (ft/sec)
k = dimensionless ratio
v = Poisson's ratio for soil
v = 0.2 for granular soils, yielding k = 1.63
v = 0.45 for cohesive soils, yielding k = 3.32
V_{SP}* = reduced primary wave velocity in the soil based on strain amplitude (ft/sec)
R_S = dimensionless reduction factor as in Eq. 7-5

7.1.3 Attenuation of seismic waves

Multiple cycles of strain exceeding a threshold in a soil mass will cause volume change resulting in settlement of the soil. Using the above Equations, the particle velocity in the soil next to the pile can be estimated. As the wave travels away from the pile, the amplitude of particle velocity decreases from both geometric and hysteretic damping.

The rate of attenuation of the shear wave travelling from the shaft of the pile (cylindrical) is different than the rate of attenuation of the primary wave travelling from the tip of the pile (spherical). Analysis of the field data of this work revealed that the Bornitz equation can best decribe the energy attenuation through the soil. A modified formula of

the Bornitz equation (Richart et al, 1970) will be used to express the attenuation of both types of waves:

$$\dot{z}_2 = \dot{z}_1 \left(\frac{r_1}{r_2}\right)^n exp[-\alpha(r_2 - r_1)] \qquad \text{Eq. 7-10}$$

where: $\dot{z}_2$ = particle velocity amplitude at point 2 (ft/sec)
$\dot{z}_1$ = particle velocity amplitude at point 1 (ft/sec)
r_1 = distance from source to point 1 = 0.1 in = 0.0083 ft
r_2 = distance from source to point 2
n = power exponent depending on wave type
n = 0.5 for cylindrical wave coming from the pile shaft
n = 1 for spherical wave coming from the pile tip
α = coefficient of attenuation (1/ft)

The distance r_1=1 in. (≈0.1 ft.) represents the first point where the maximum amplitude of soil motion right next to pile shaft for cylindrical waves and below the pile tip for spherical waves is estimated. Based on the analysis of the measured field data, the attenuation coefficient, α, from the pile face up to distances of 10 ft may be taken as α=0.2. Beyond 10 ft distances from the pile, α=0.02, also found from fitting the Bornitz formula to measured amplitudes of the tested sites. The amplitude of particle velocity at any point in the soil mass can then be determined when the amplitude of particle velocity at the pile shaft or tip is known.

7.1.4 Calculation of shear strain at points in soil mass

Strain associated with the seismic waves can be calculated as particle velocity divided by wave velocity. For shear waves travelling from the shaft and primary waves coming from the tip, the shearing strain is calculated as follows:

$$\gamma_{shaft} = \frac{\dot{z}_{shaft}}{V_S^*} \qquad \text{Eq. 7-11}$$

$$\gamma_{tip} = \frac{\dot{z}_{tip}}{V_{SP}^*} \qquad \text{Eq. 7-12}$$

$$R_S' = R_S + 0.05 \qquad \text{Eq. 7-13}$$

where: γ_{shaft} = shear strain of soil for waves coming from shaft
γ_{tip} = shear strain of soil for waves coming from tip
$\dot{z}_{shaft}$ = vertical particle velocity in the soil at pile shaft
$\dot{z}_{tip}$ = vertical particle velocity in the soil at pile tip
R_S' = reduction factor for shear wave velocity

The reduced wave velocities, V_S* and V_{SP}*, are calculated from Eq. 7-5 and Eq. 7-9, respectively. The reduction factor, R_S, is equal to 0.2 at the pile shaft and is increased by 0.05 for every 5 ft distance from the pile. The basis for this reduction for the shear wave velocity every 5 ft distance from the pile was made upon trial using the recorded data, while providing a conservative estimation.

Summation of shaft and tip contributions of shear strain give the total shear strain which is the compared with the threshold strain, γ_t=0.01%, for granular soils. With increased distances from the pile, it is possible to determine the distance beyond which strain amplitude is less than the threshold. The threshold shear strain should be increased if information for the fines content is available. Borden and Shao (1995) performed a regression analysis (Figure 3-76) taking into account the fines content, and calculated a dynamic settlement factor, R_{Strain}, by which the total shear strain threshold should be divided as:

$$R_{Strain} = 8.311(fc)^{-1.381} \qquad \text{Eq. 7-14}$$

where: fc = fines content (in %)

For the case of clays and silts, a default value of 50% fines can be used if no other information is available.

7.2 Comparison of Measured and Predicted Ground Motion

The above concept was used to predict ground motions using the SPT information from sites M-139, US-131 A and US-131 B. Comparisons between the predicted peak particle velocity amplitudes and the measured ground motion data from the embedded sensors are presented. It should be noted that prediction of ground motions was made for two cases: unplugged and plugged condition. When the space between the flanges and web of an H-pile is packed hard with soil near the tip of the pile due to driving, the pile is called *plugged* for these analyses. If that space is not packed with soil, the condition is called *unplugged*. The unplugged condition was surmised from comparative calculations of ground vibration when the pile tip was in sandy soils with blow counts (N) less than about 40 but may have been plugged when the tip was in clay soils and sands with blow counts higher than 40. There was no way to tell from the measured vibrations alone whether or not the pile was plugged or not.

In general, the correlation between measured and predicted ground motion was good for sensor elevations where the soil was loose to medium dense sand. The correlation was less good when the soil was medium dense to dense sand and was not good when the soil at the elevation of the sensor was classified as clay. The latter condition is not surprising because the prediction model is based on the soil behaving as sand. It is also important to note, that the comparison between the predicted and measured data is valid when the pile tip is close to the elevation of the sensors. This is because when the pile tip is way above the sensors' depth, not much ground motion is captured by the instruments.

Figure 7-5a presents comparisons between measured and predicted ground motion for the unplugged H-pile condition for site M-139. The predicted vibration amplitude is about 4% lower than the measured amplitude at the closest sensor (0.5 ft) and at the sensors' elevation (25.5 ft). The predicted amplitude is slightly over-predicted (7%) than the measured amplitude at the second distance from the pile (2.5 ft) and 4% lower than the measured particle motion at the third distance from the pile (6.5 ft). Figure 7-5b presents measured and predicted ground motions for the plugged condition. It is obvious

that the predicted amplitude is 40% higher than the measured amplitude at the closest sensor (A3), 19% higher than the measured amplitude at the second sensor from the pile (A4) and about the same for the third sensor from the pile (A5).

Figure 7-6a and Figure 7-6b show predicted and measured particle velocities for the closest sensors (0.5 ft) to the pile for site US-131 A. For the unplugged condition, the shallow measured velocity at the sensor's elevation (17 ft) matches the predicted motion, however for the plugged condition the predicted amplitude is 50% higher than the measured. In general, the plugged condition gives a more conservative prediction for a range of depths of 10 ft to 20 ft. For the deep sensors embedded into the clay deposit, the predicted amplitude is 50% higher than the measured amplitude at the sensors' elevation (35.3 ft). Similar behavior with the closest sensors to the pile is observed for the measured and predicted amplitudes for the next two distances from the pile, 2.5 ft and 6.5 ft, as shown in Figure 7-7a and Figure 7-7b. The unplugged and plugged cases were found to be very close for the prediction of the particle motions, thus only results for the unplugged condition are presented. Figure 7-8 illustrates the comparison between predicted and measured ground motion when driving the second test pile at US-131 A site; the sensor being at a distance of 94.5 ft from the pile and at a depth of 15 ft into the loose to medium dense sand. The predicted amplitude slightly over-predicts the ground motion for the sand deposit and is greatly over-predicted for the clay layer.

Figure 7-9a and Figure 7-9b show predicted and measured particle velocities for the closest sensors (0.5 ft) to the pile for site US-131 B. For the unplugged condition, the shallow measured velocity at the sensor's elevation (16.25 ft) is about 25% higher than the predicted motion, however for the plugged condition the predicted amplitude matches the measured. The predicted values for the unplugged case give a very good match for the shallow loose to medium dense sand layer, except for a peak in amplitudes around 15 ft. For the deep sensors embedded into the clay deposit, the predicted amplitude is 50% higher than the measured amplitude at the sensors' elevation (34 ft). For the intermediate distance sensor (SG4) at the sand layer and a depth of 16.25 ft, the measured amplitude is much higher (130%) than the predicted at the sensor's elevation, as seen in Figure 7-10a. The prediction for the furthest sensor (SG5) at a depth of 18.5 ft

matches very well the measured amplitudes when the pile tip was penetrating the sand layer (Figure 7-10b). Figure 7-11 depicts the comparison between predicted and measured ground motion when driving the second test pile at US-131 B site; the sensor being at a distance of 95.1 ft from the pile and at a depth of 16.25 ft into the loose to medium dense sand. The predicted amplitude slightly over-predicts the ground motion for the sand deposit and the clay layer.

Considering the many variables necessary for the prediction model and the heterogeneity of each soil profile tested, the agreement between predicted and measured ground motion is considered good. It is recognized though that this concept was developed using ground motion measurements from the sites studied in this project, thus it is not surprising that the agreement between recorded and predicted motions for the granular soils is good.

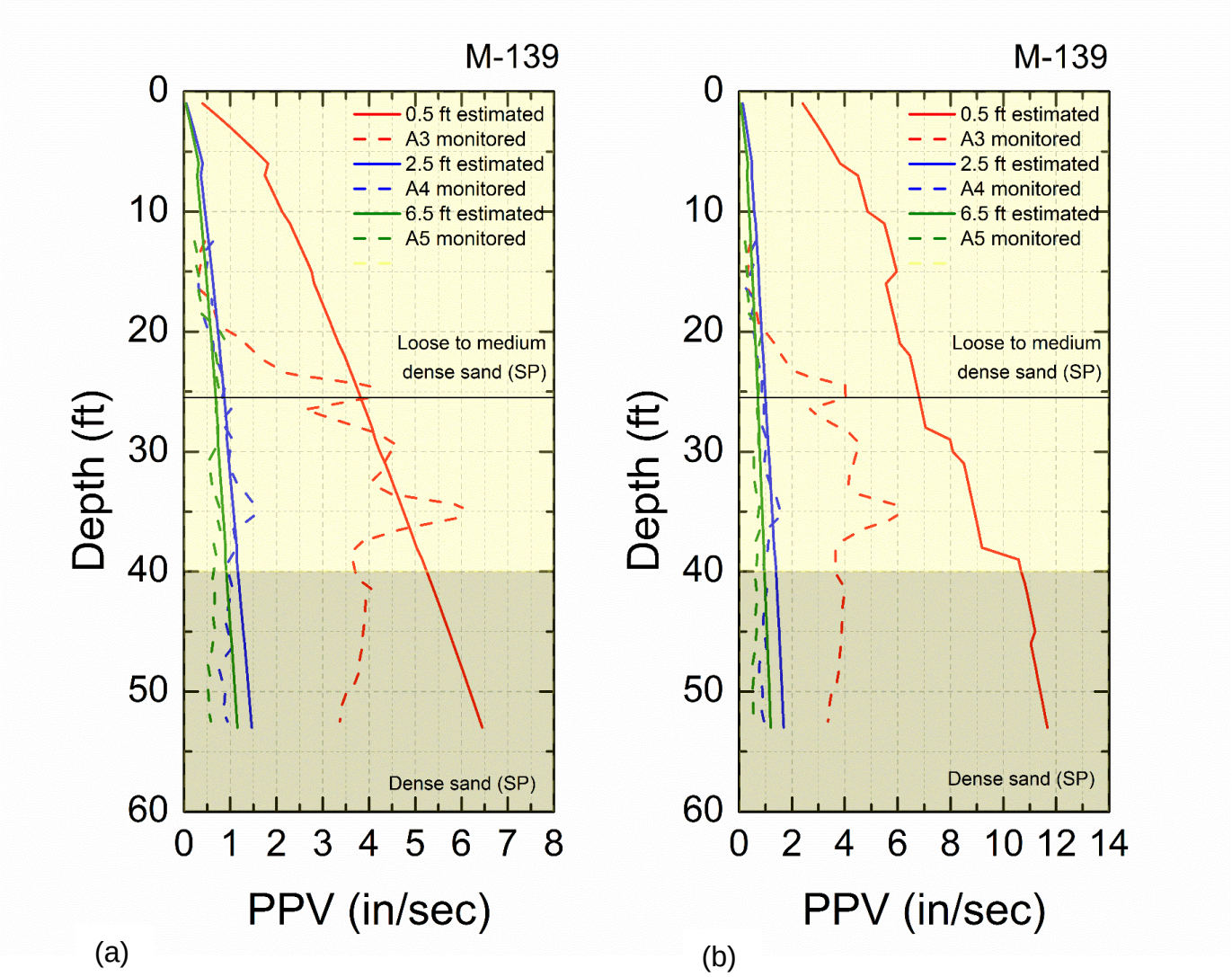

Figure 7-5 Measured and predicted ground motion for the (a) unplugged condition and (b) plugged condition – M-139 site

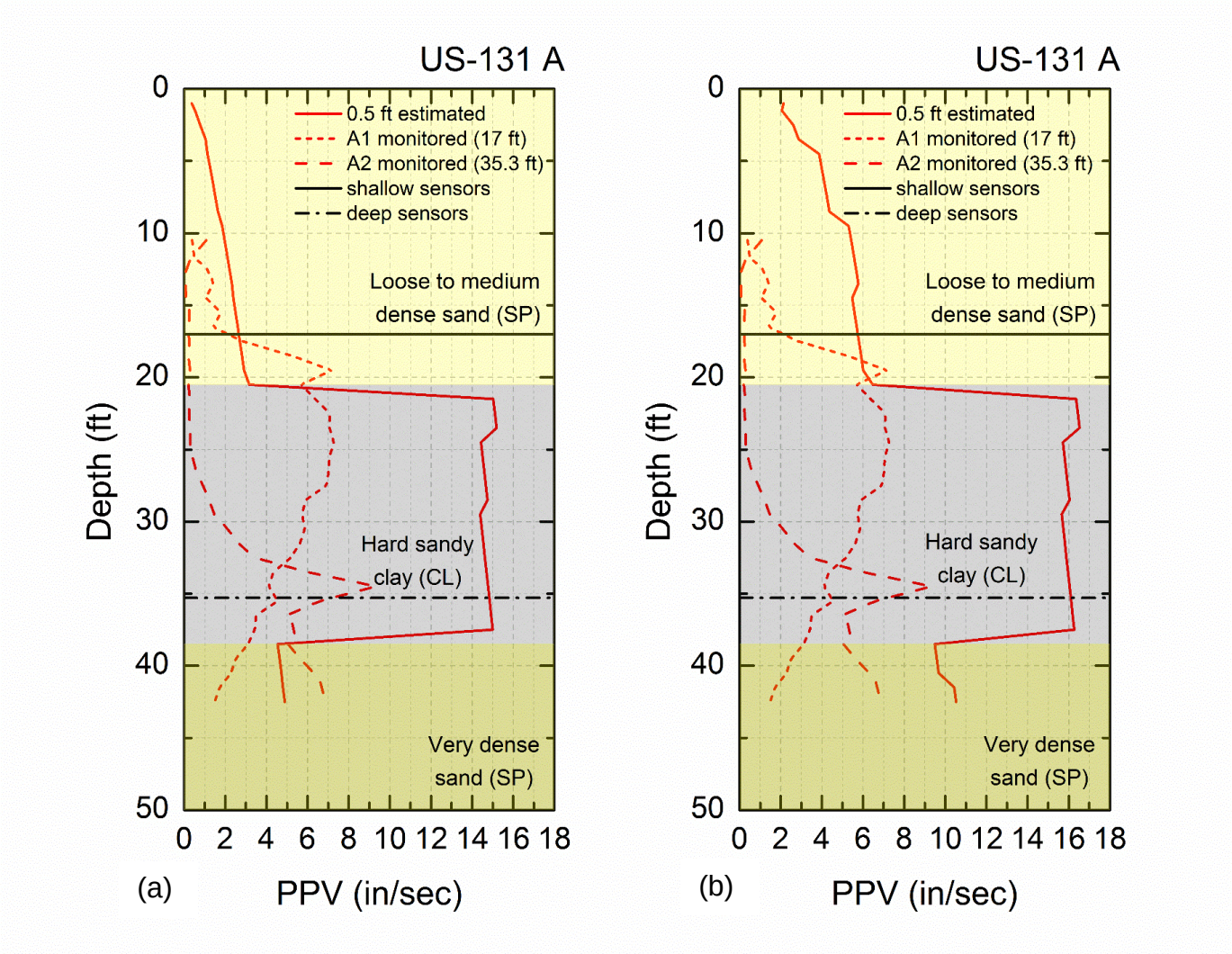

Figure 7-6 Measured and predicted ground motion for the (a) unplugged condition and (b) plugged condition at 0.5 ft distance from the pile – US-131 A site

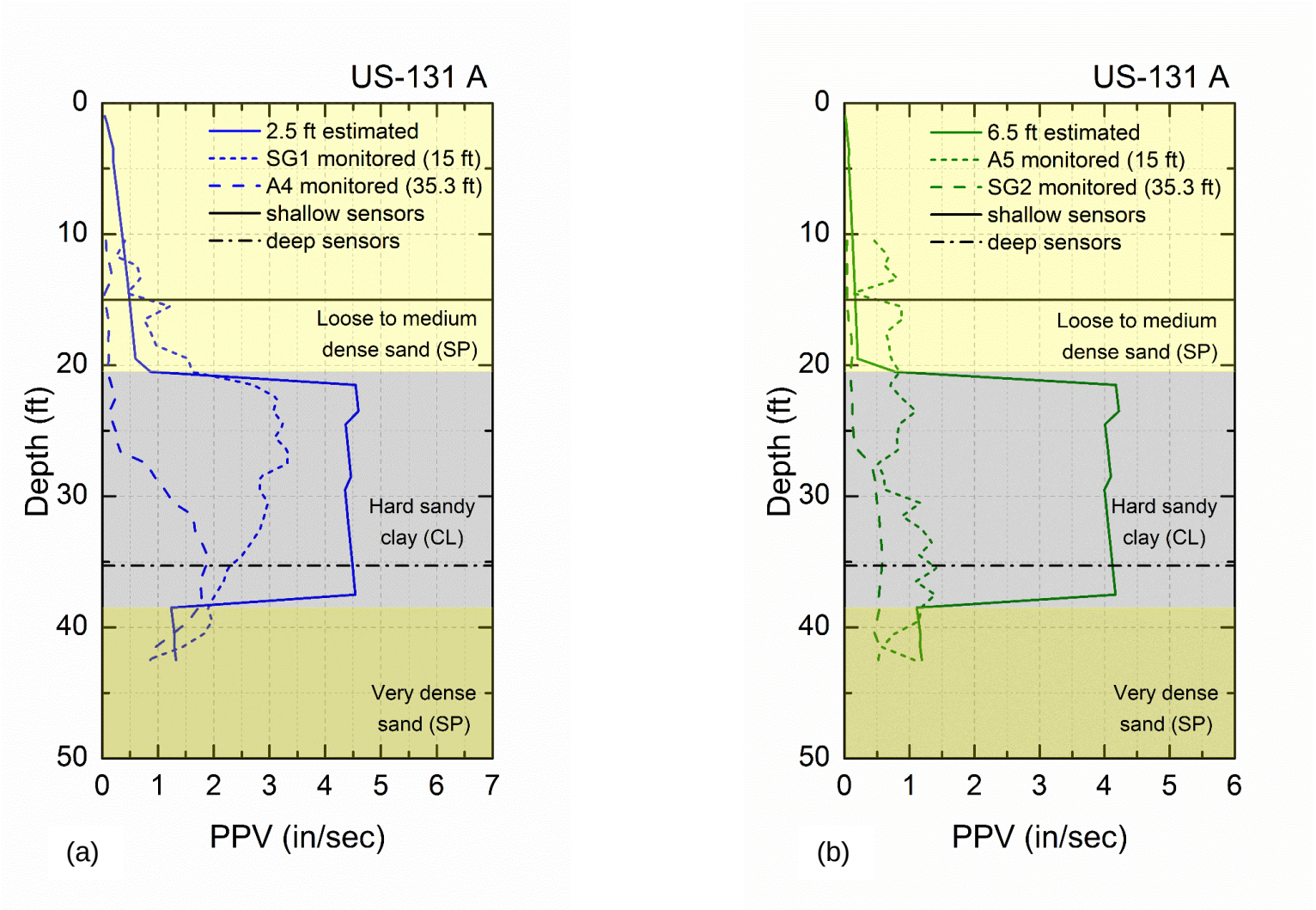

Figure 7-7 Measured and predicted ground motion at (a) 2.5 ft from pile and (b) 6.5 ft from pile – US-131 A site

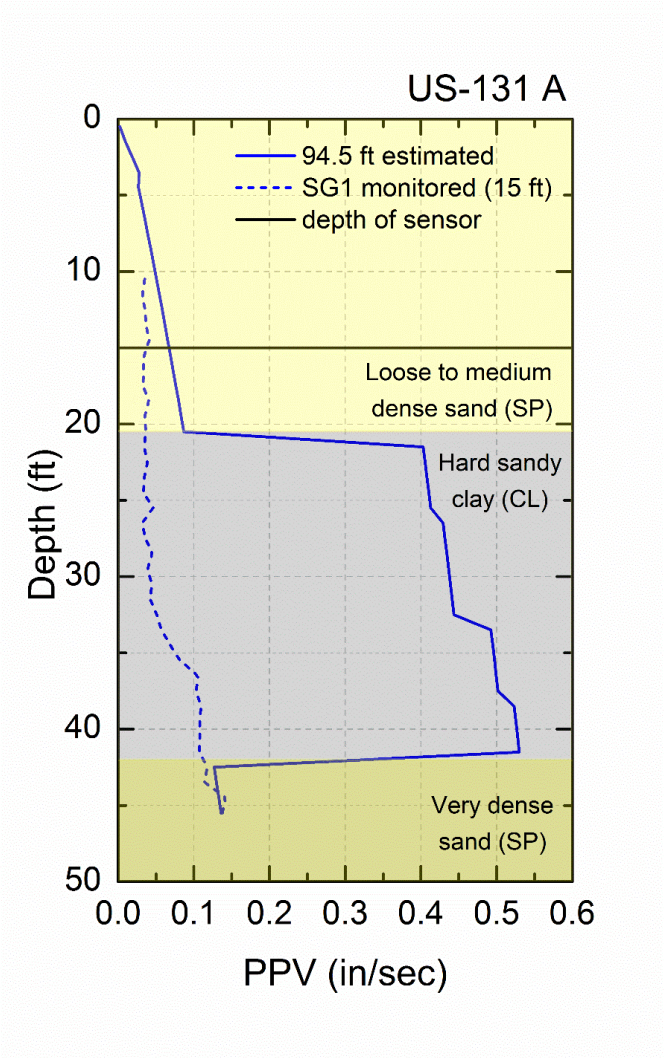

Figure 7-8 Measured and predicted ground motion at 94.5 ft distance from the pile – US-131 A site

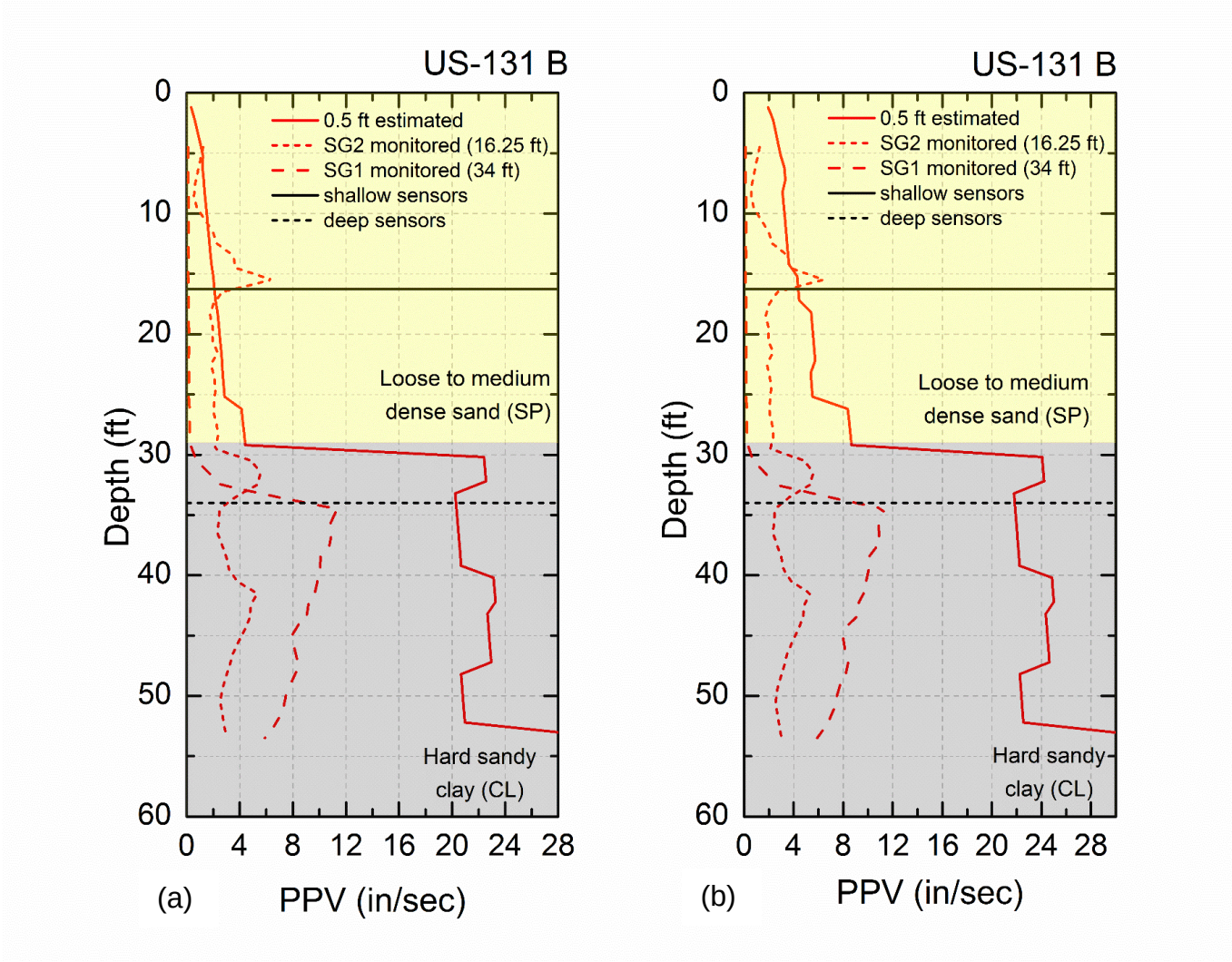

Figure 7-9 Measured and predicted ground motion for the (a) unplugged condition and (b) plugged condition at 0.5 ft distance from the pile – US-131 B site

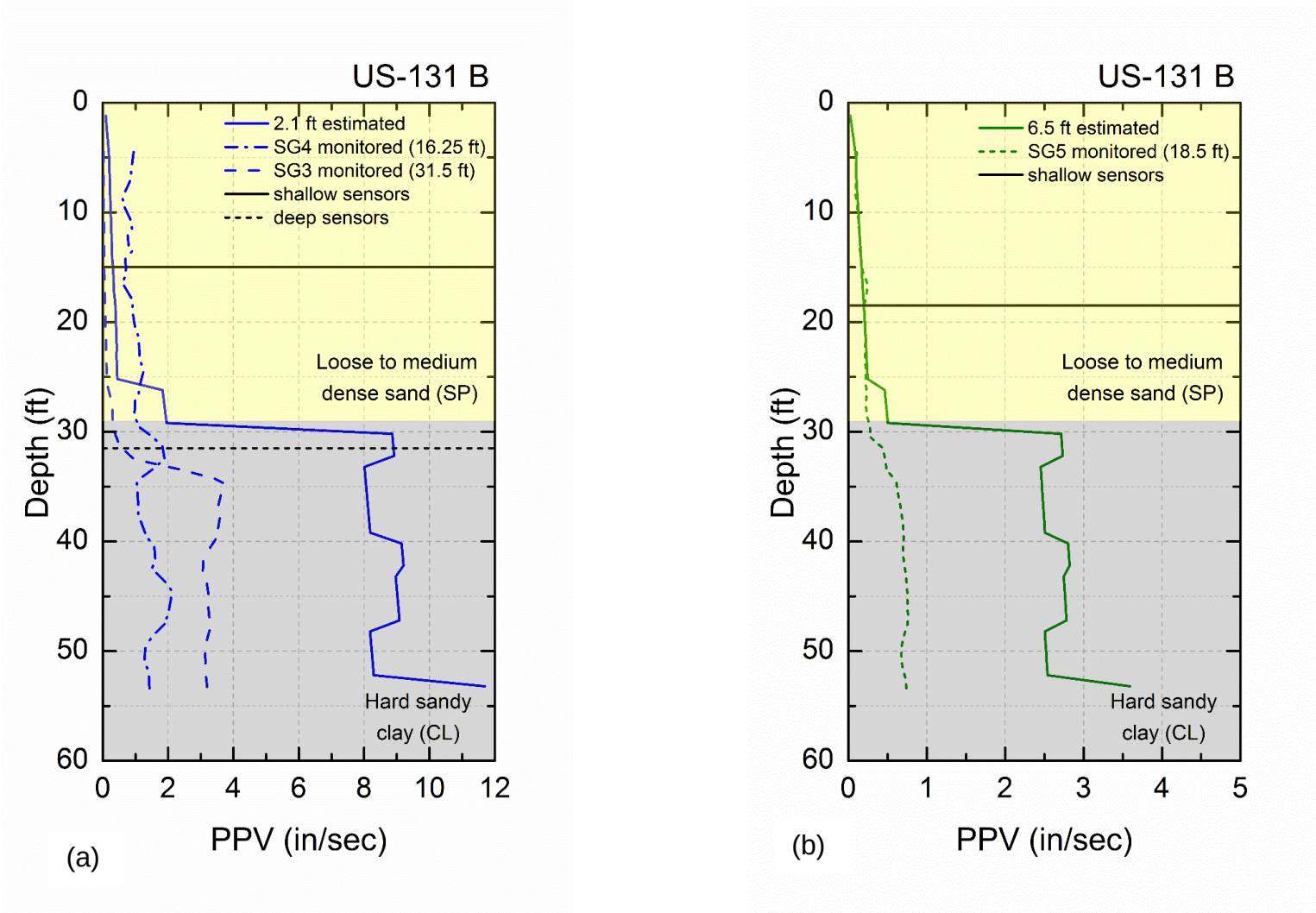

Figure 7-10 Measured and predicted ground motion at (a) 2.5 ft from pile and (b) 6.5 ft from pile – US-131 B site

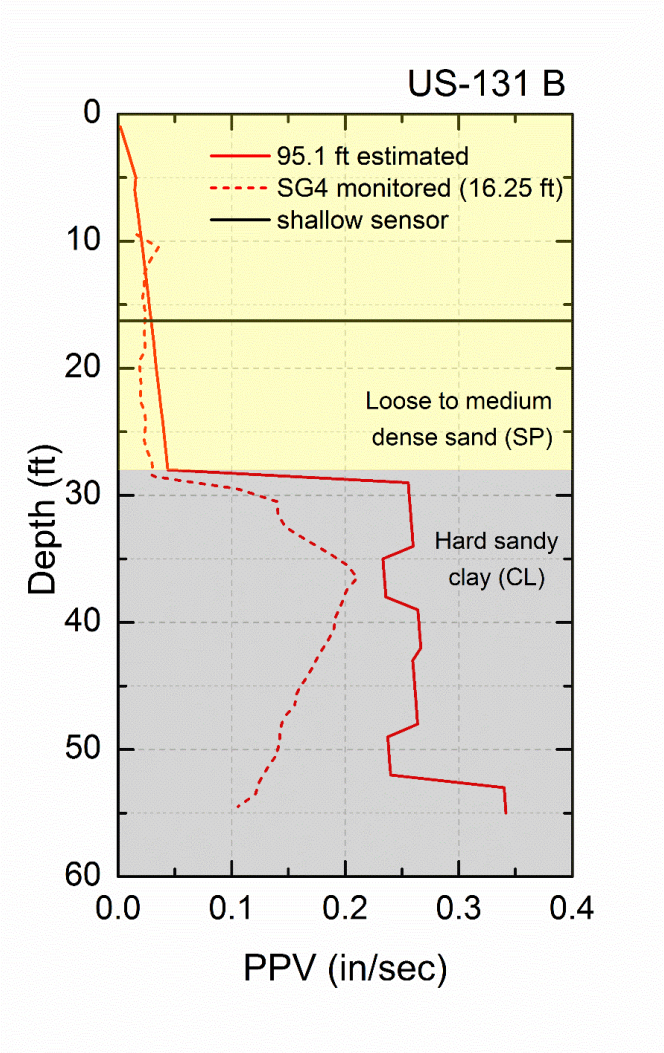

Figure 7-11 Measured and predicted ground motion at 95.1 ft distance from the pile – US-131 B site

7.3 Prediction of shear strain

As discussed previously, a prediction for the total shear strain can be calculated using the presented concept. Figure 7-12 to Figure 7-14 present comparisons between the predicted shear strain using the concept and the estimated shear strain using monitored vibration data for sites M-139, US-131 A and US-131 B, respectively, as discussed in the beginning of this Chapter. It is observed that the prediction for the shear strain when using the concept is highly over-predicted than when evaluating the estimated shear strain using the recorded ground motions. This is not surprising if we consider that many of the assumptions made for the concept of the energy transmission through the ground, are on the conservative side. In addition, the calculated shear strain when using the recorded particle velocities are estimations and not the exact values, since the sensors were buried at one elevation into the sand layer.

For site M-139, the predicted amplitude of the total shear strain is around 70% to 80% higher than the calculated shear strain using the monitored data, for the three distances from the pile (Figure 7-12). The calculated shear strain for the furthest distance from the pile (6.5 ft) is close to the threshold of 0.01%. The predicted shear strain for the same distance from the pile is higher than the threshold value. This is not surprising since for soil profiles than include loose sand layers, it is expected that the susceptibility to settlement would extend further than the longest observed point monitored at this site.

For site US-131 A, the predicted amplitude of the total shear strain is closer to the calculated shear strain using the recorded data (Figure 7-13); 25% to 35% higher amplitude for the four observed distances from the pile, into the sand layer deposit that is of interest in this research. The predicted and calculated shear strain for the furthest observed point from the pile (6.5 ft) fall close to the threshold shear strain of 0.01%. The predicted and calculated shear strain for about two pile lengths away from the pile (95 ft) are approximately one order of magnitude less than the threshold strain, indicating that no settlement is expected.

For site US-131 B, the predicted amplitude of the total shear strain ranges between 30% to 90% higher than the calculated shear strain for the four monitored distances from the pile (Figure 7-14). The calculated shear strain for the furthest distance from the pile (6.5 ft) is lower the threshold of 0.01%. The predicted shear strain for the same distance from the pile is higher than the threshold value.

The predicted and calculated shear strain for the closest distance to the pile is around one order of magnitude higher than the threshold shear strain. Again, the agreement between the predicted and calculated shear strain using the recorded data is considered good, if we consider the many variables, assumptions and heterogeneity of the soil profiles.

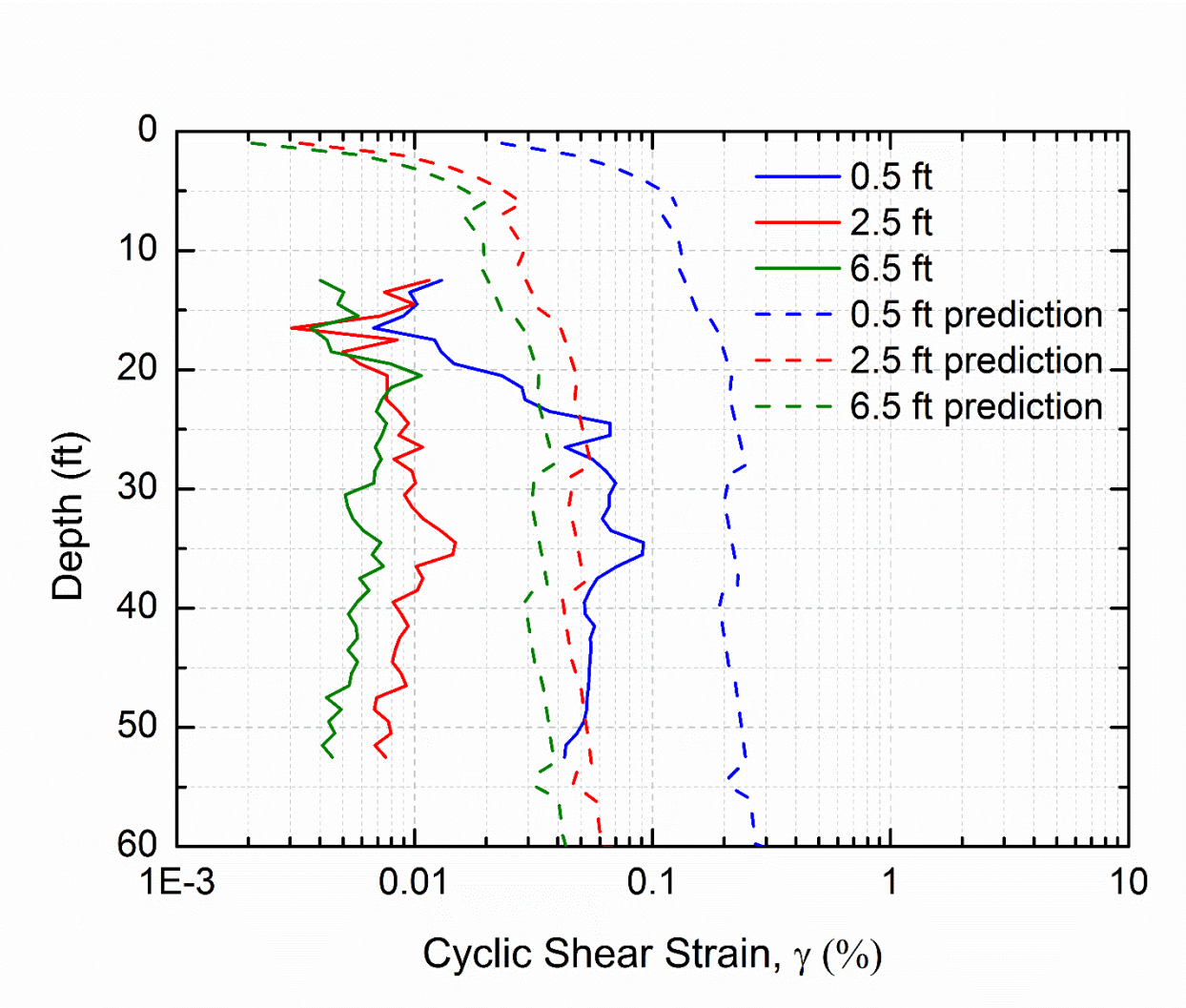

Figure 7-12 Predicted and calculated shear strain for three distances from the pile – M-139 site

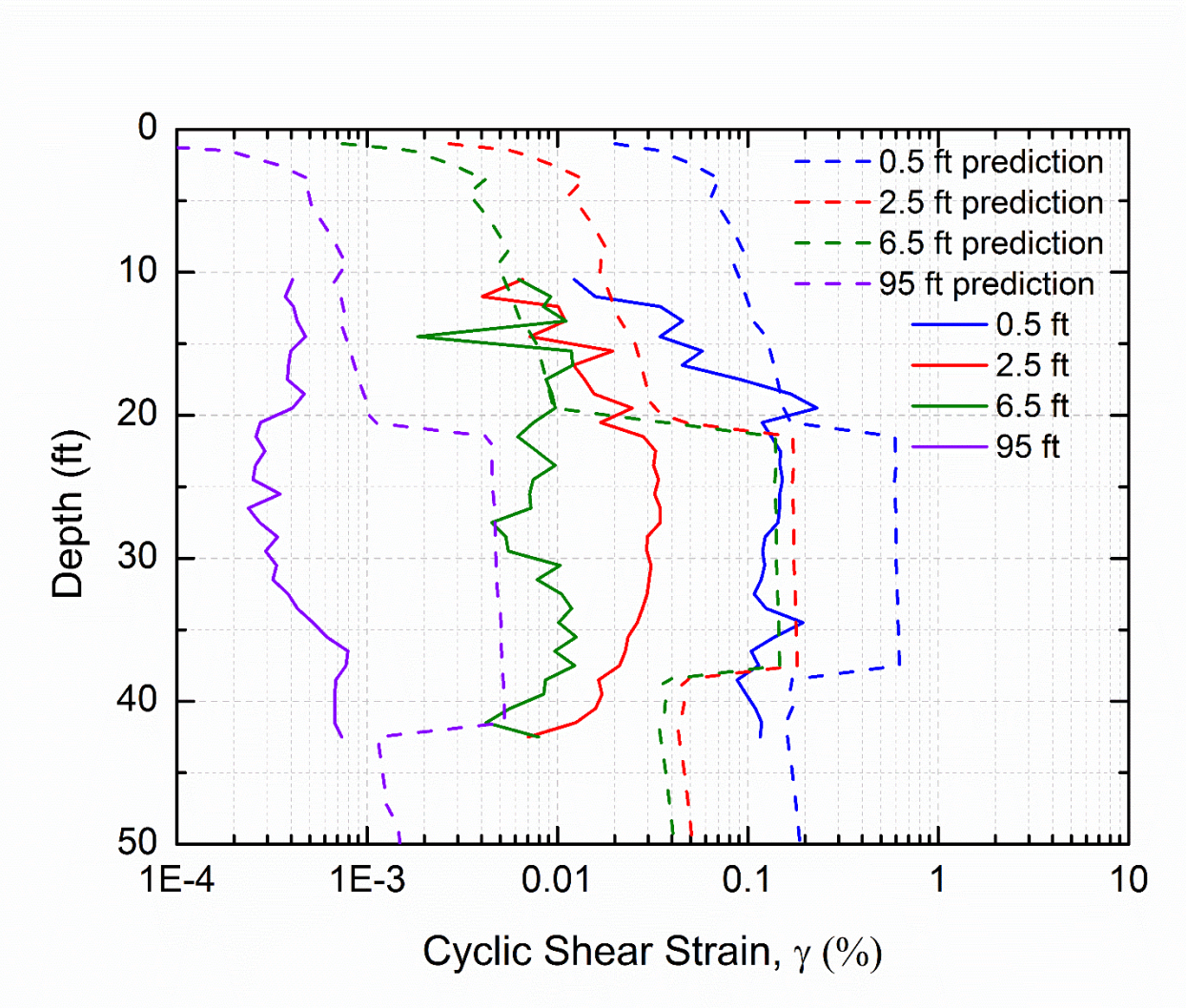

Figure 7-13 Predicted and calculated shear strain for four distances from the pile – US-131 A site

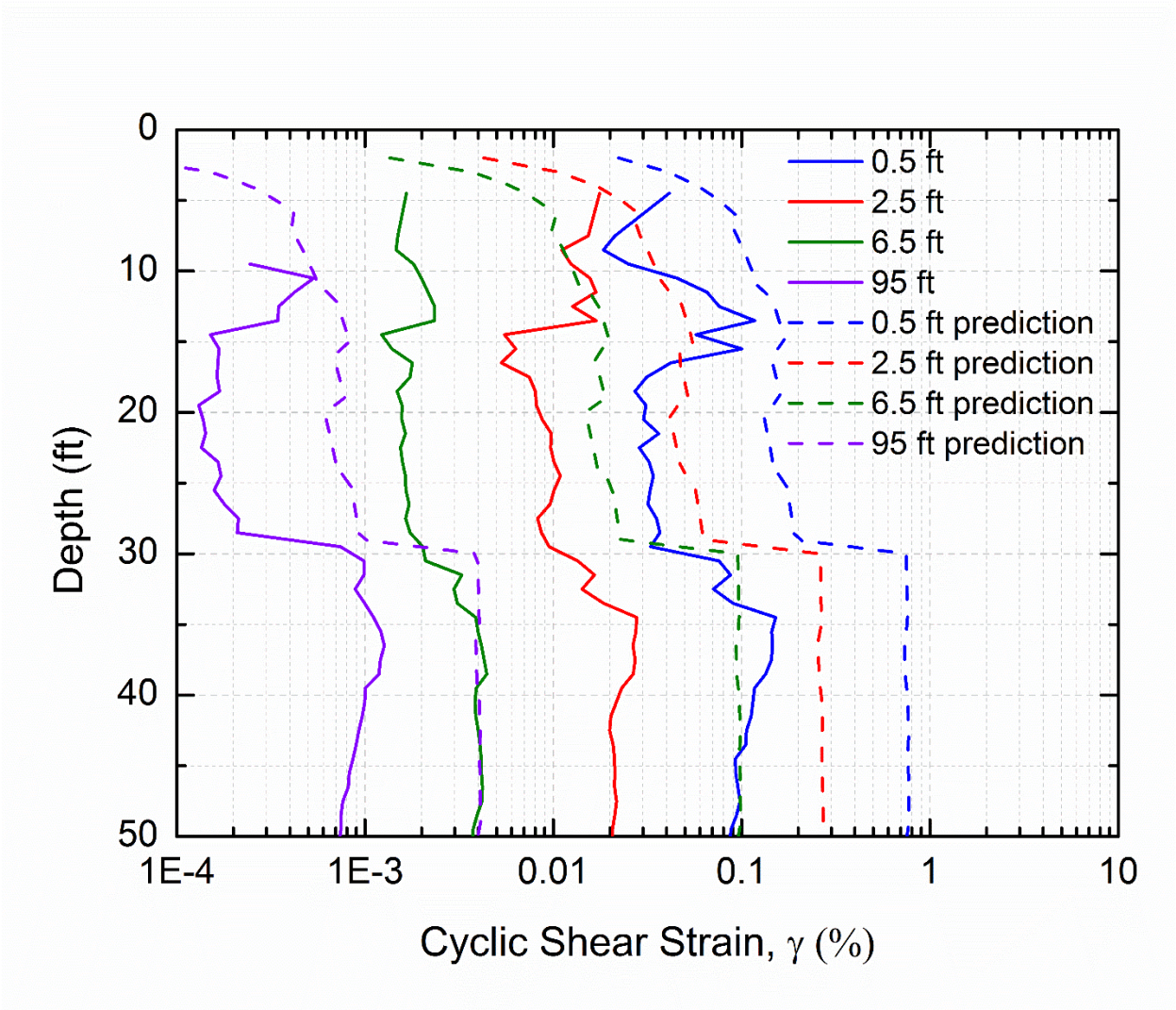

Figure 7-14 Predicted and calculated shear strain for four distances from the pile – US-131 B site

CHAPTER 8 SMALL-SCALE PHYSICAL EXPERIMENTS OF PILE DRIVING IN THE LABORATORY

There are several challenges with interpreting the data collected at the field testing sites, as has been discussed in the previous chapter. The intention of the small-scale laboratory pile driving tests, was to monitor ground vibrations in a controlled environment with a homogeneous and well-characterized soil profile. The laboratory testing of driving a smaller scale pile and recording the ground motion amplitudes, was conducted in the sand bin, one of the Geotechnical Engineering laboratory facilities in G.G. Brown Laboratories at the University of Michigan. The sand bin is a 22 ft diameter and 6 ft deep cylindrical container. It was constructed by driving interlocking Z-shaped steel sheet piles down to a depth of 7 ft (Al-Shayea 1994). The original soil deposit, which is a dense clayey silt with sands, was excavated to a depth of approximately 7 ft and was replaced by graded mortar sand of glacial origin (Glazier Way sand) by Hassini (1990). Al-Shayea (1994) removed the Glazier Way sand and replaced it with a silica sand, which is the sand that forms the sand bin today (Figure 8-1).

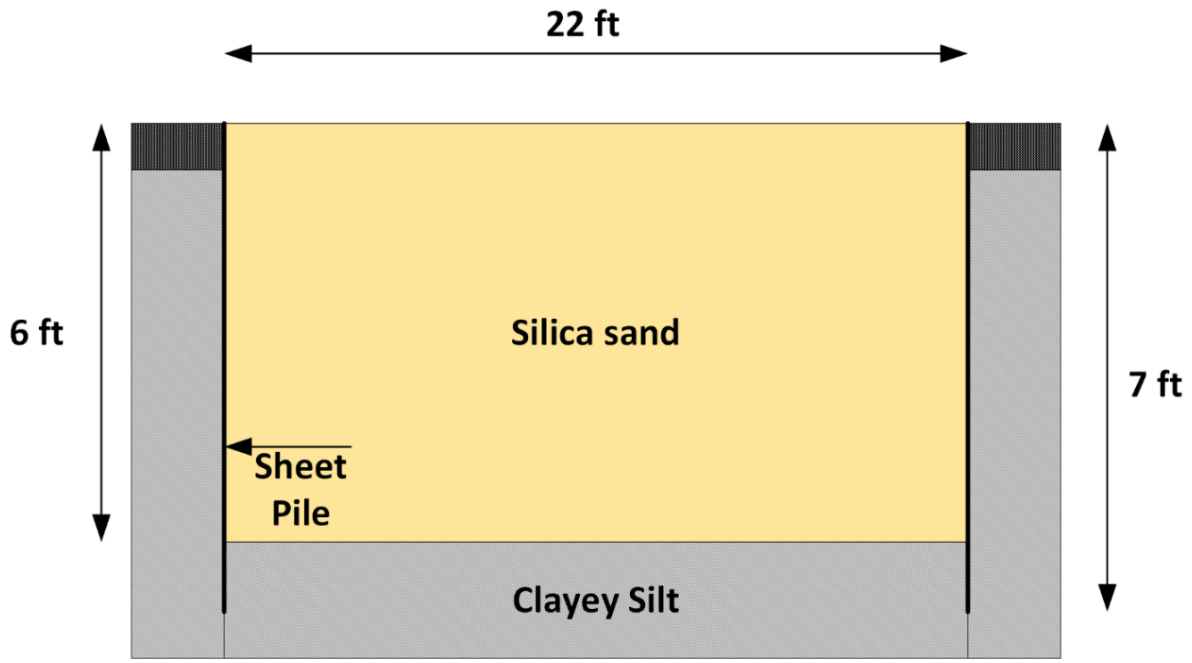

Figure 8-1 Cross section of the sand bin (not to scale)

8.1 Soil Properties of Silica Sand

The sand bin was filled with a silica sand for a previous research project by Al-Shayea (1994). The R-50 Foundry silica sand was supplied by U.S. Silica. The product data sheet of the sand is provided in Appendix H. Chemical analysis shows that this sand consists mainly of silicon dioxide (or quartz) (99.8 % SiO2). The grain size distribution curve is illustrated in Figure 8-2. The silica sand is a white, rounded, fine, uniform clean sand with a Specific Gravity of G_S=2.65. The coefficient of curvature, C_c, is 1.05 and the coefficient of uniformity, C_u, is 1.69; where D_{10}=0.176, D_{30}=0.234 and D_{60}=0.297. According to the Unified Soil Classification System, ASTM D2487-11, this soil is a clean poorly graded sand (SP). The unit weight of the silica sand is γd_{max}=104 pcf for the dense condition and γd_{min}=96 pcf for the loose condition (U.S. Silica). This corresponds to minimum void ratio of e_{min}=0.59 and a maximum void ratio of e_{max}=0.72. This sand has a tendency to keep its moisture content unchanged over a long period of time (Al-Shayea 1994).

In order to determine the strength parameters of the silica sand in the sand bin, direct shear tests were performed using the ShearTrac II direct shear device by Geocomp (Figure 8-3) in six specimens in accordance with ASTM D3080-11; three specimens were prepared loose and three specimens were prepared dense. The sand was placed in the shear box using a funnel to prepare the loose sand specimens. The dense soil specimens were prepared again by using the funnel to pour the sand in the shear box, and were then densified with vibrating rods. The square metal shear box has dimensions of 4 in x 4 in with a height of 1.675 in. The specimens were tested under three different normal stresses, 5.08 psi, 10.15 psi and 15.23 psi, in order to get the failure envelopes of the silica sand. The direct shear test reports of each test can be found in Appendix H. Figure 8-4 depicts a summary of the consolidation phase of the six tests. Figure 8-5 illustrates the change in height of specimens versus shear displacement for the loose and dense condition; the negative axis indicates expansion. Figure 8-6 shows the shear stress versus horizontal displacement for the tested specimens. It is obvious that the dense specimens reached a peak shear strength before the shear stress decreased until it finally reached the post-peak (ultimate) shear strength. The loose sand specimens, reached a

peak shear strength close to the post peak strength of the corresponding dense specimen, tested under the same normal stress. The above shear strengths are plotted in Figure 8-7 along with the Mohr-Coulomb failure envelopes. For the dense state, the peak friction angle was found to be equal to 36°, whereas the post-peak friction angle was found to be equal to 28° without any cohesion. The peak friction angle of the sand at the loose state was found to be equal to 27°, close to the post-peak friction angle at the dense state.

Zekkos et al. (2014) performed shear wave velocity measurements in the sand bin using the MASW method. The same system that was used for the field MASW testing was implemented. The shear wave velocity profile of the soil in the sand bin is shown in Figure 8-8. The silica sand has a shear wave velocity of 357 ft/sec for the top 3.5 ft and increases to 636 ft/sec for the next 3 ft. This phenomenon will be discussed in the next Section. The original clayey silt deposit below 6 ft has a shear wave velocity of 868 ft/sec. Table 8.1 has a summary of the properties of the silica sand discussed above.

Table 8.1 Properties of silica sand

Parameter		**Value**
Specific Gravity	G_S	2.65
Minimum unit weight	γd_{min}	96 pcf
Maximum unit weight	γd_{max}	104 pcf
Peak friction angle	φ_p	36°
Post-peak friction angle	φ_{p-p}	28°
Shear wave velocity (0-3.5 ft)	V_s	357 ft/sec
Shear wave velocity (3.5-6 ft)	V_s	636 ft/sec

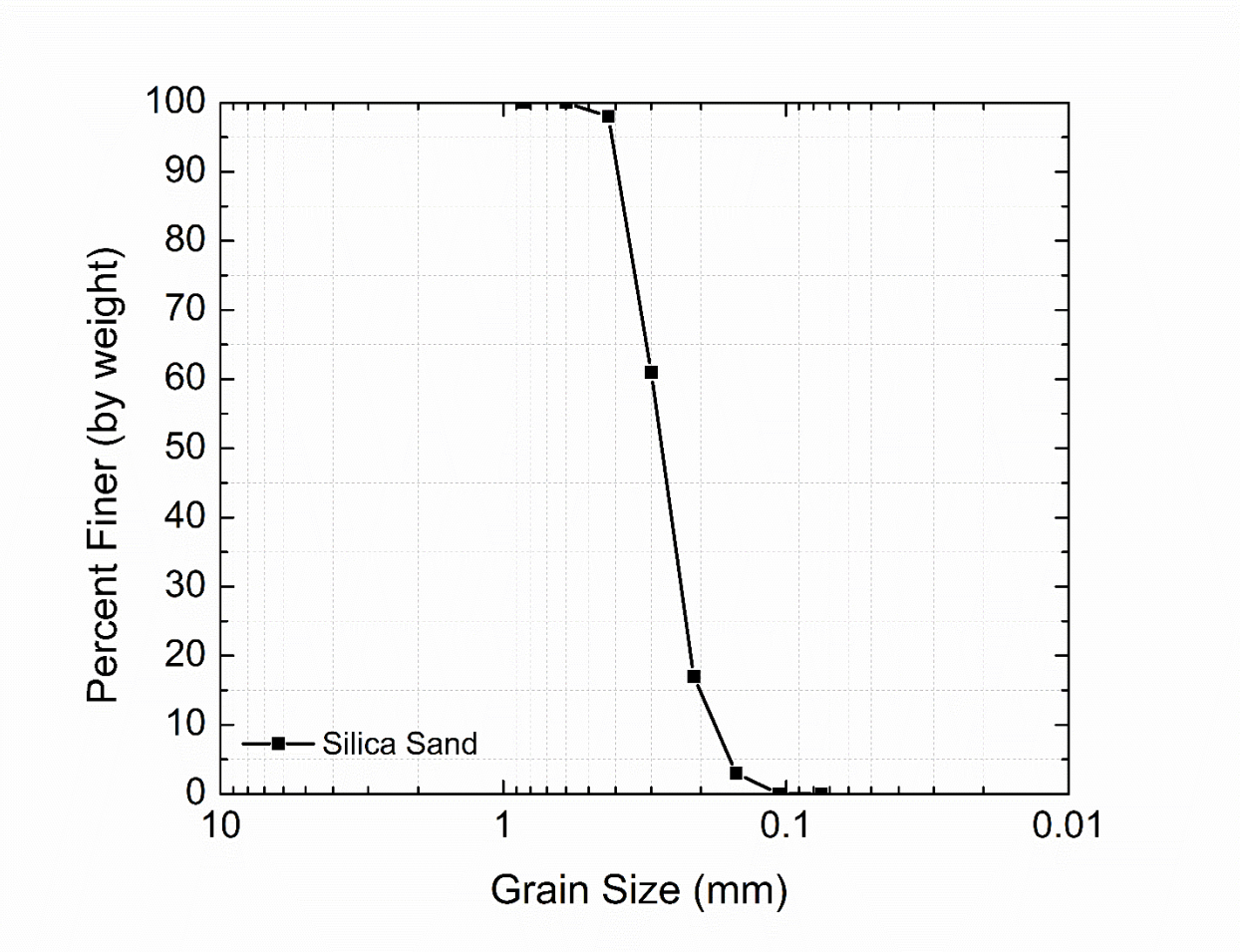

Figure 8-2 Grain size distribution curve of silica sand (from U.S. Silica)

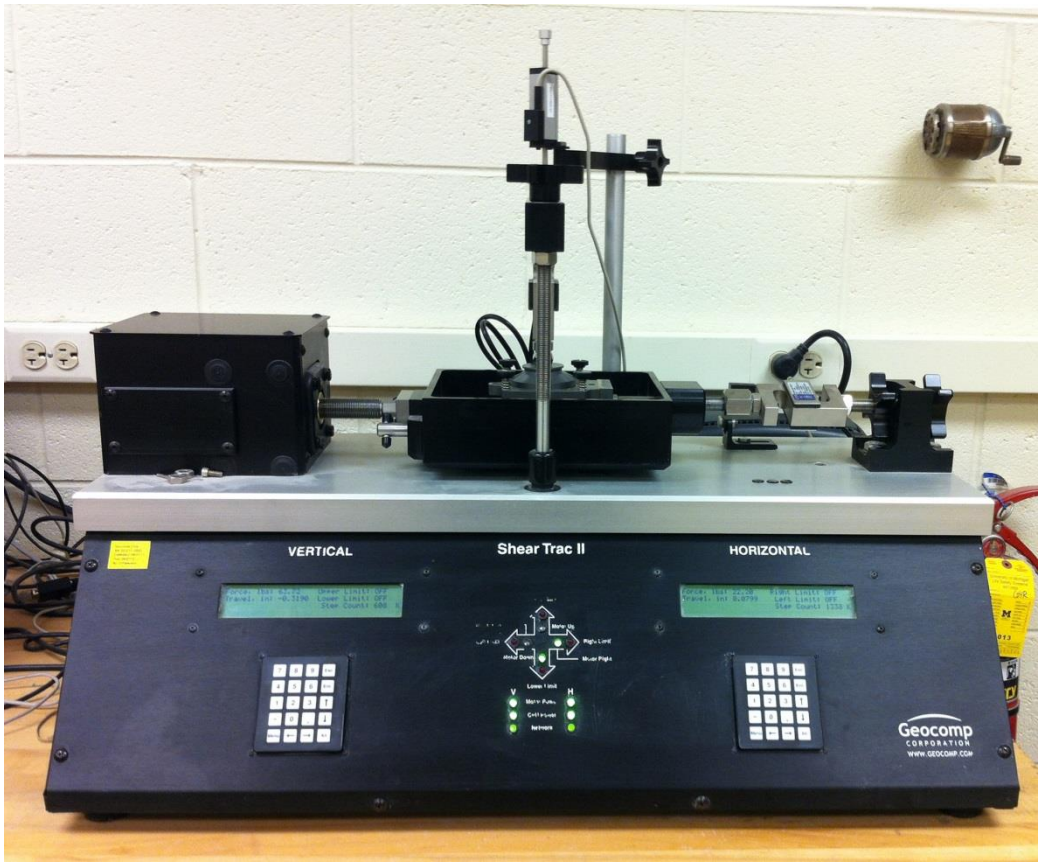

Figure 8-3 Direct shear apparatus

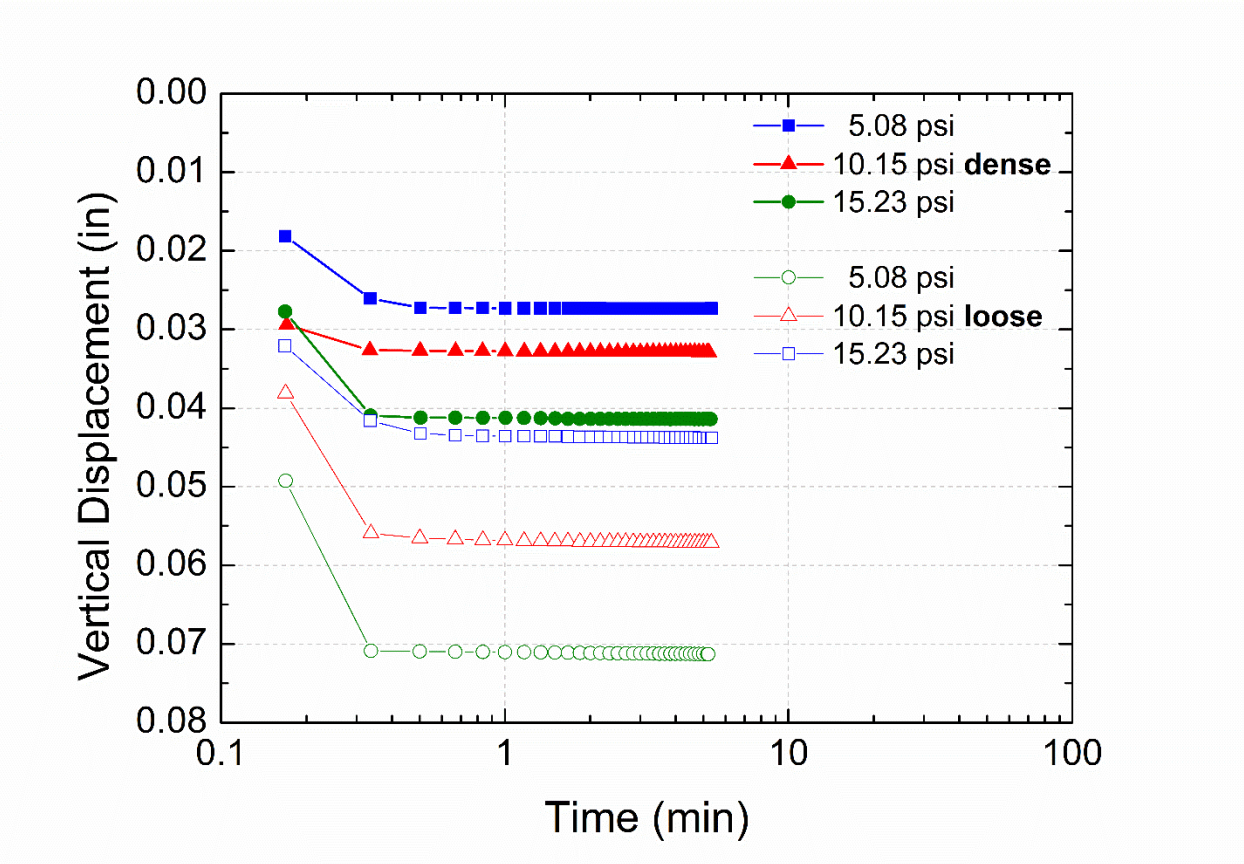

Figure 8-4 Vertical displacement versus time during the consolidation phase of direct shear tests

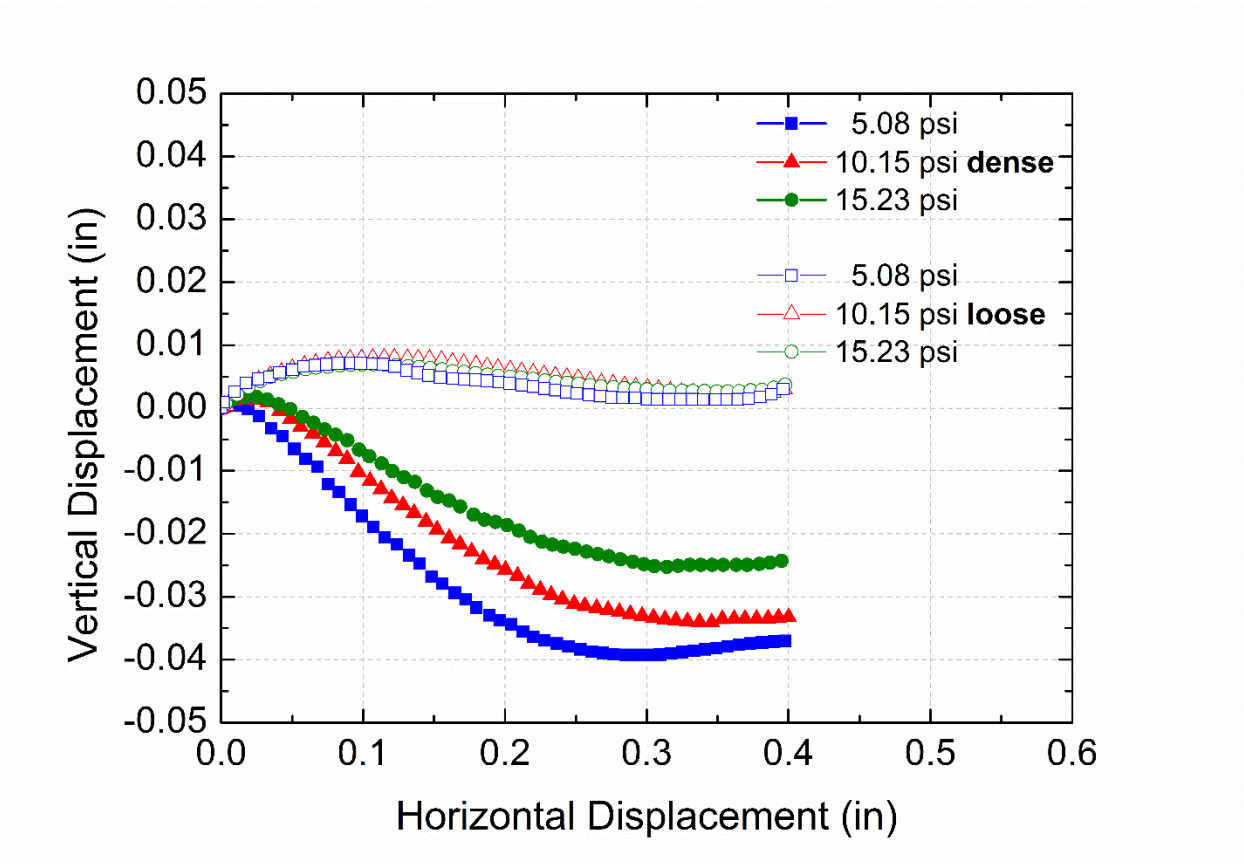

Figure 8-5 Vertical displacement versus horizontal displacement during the shear phase of direct shear tests

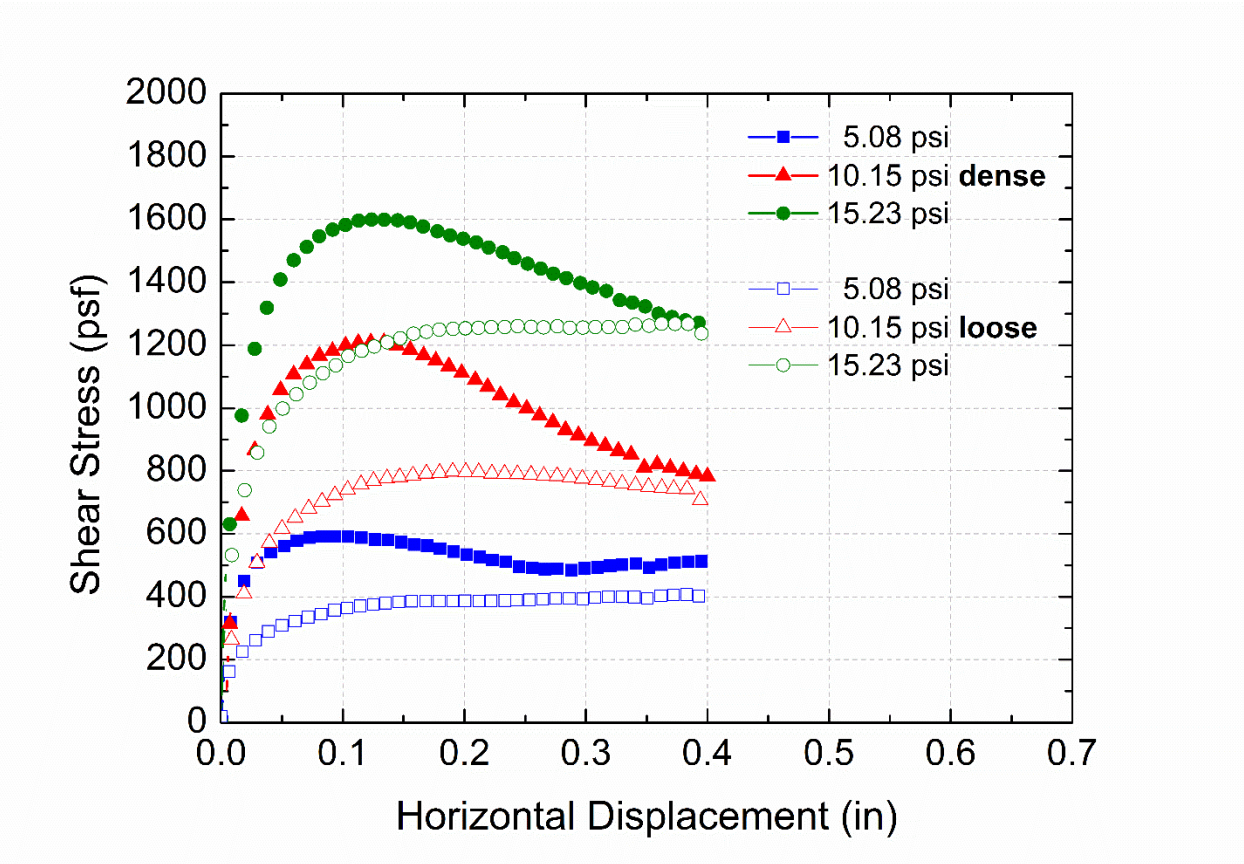

Figure 8-6 Shear stress versus horizontal displacement during the shear phase of direct shear tests

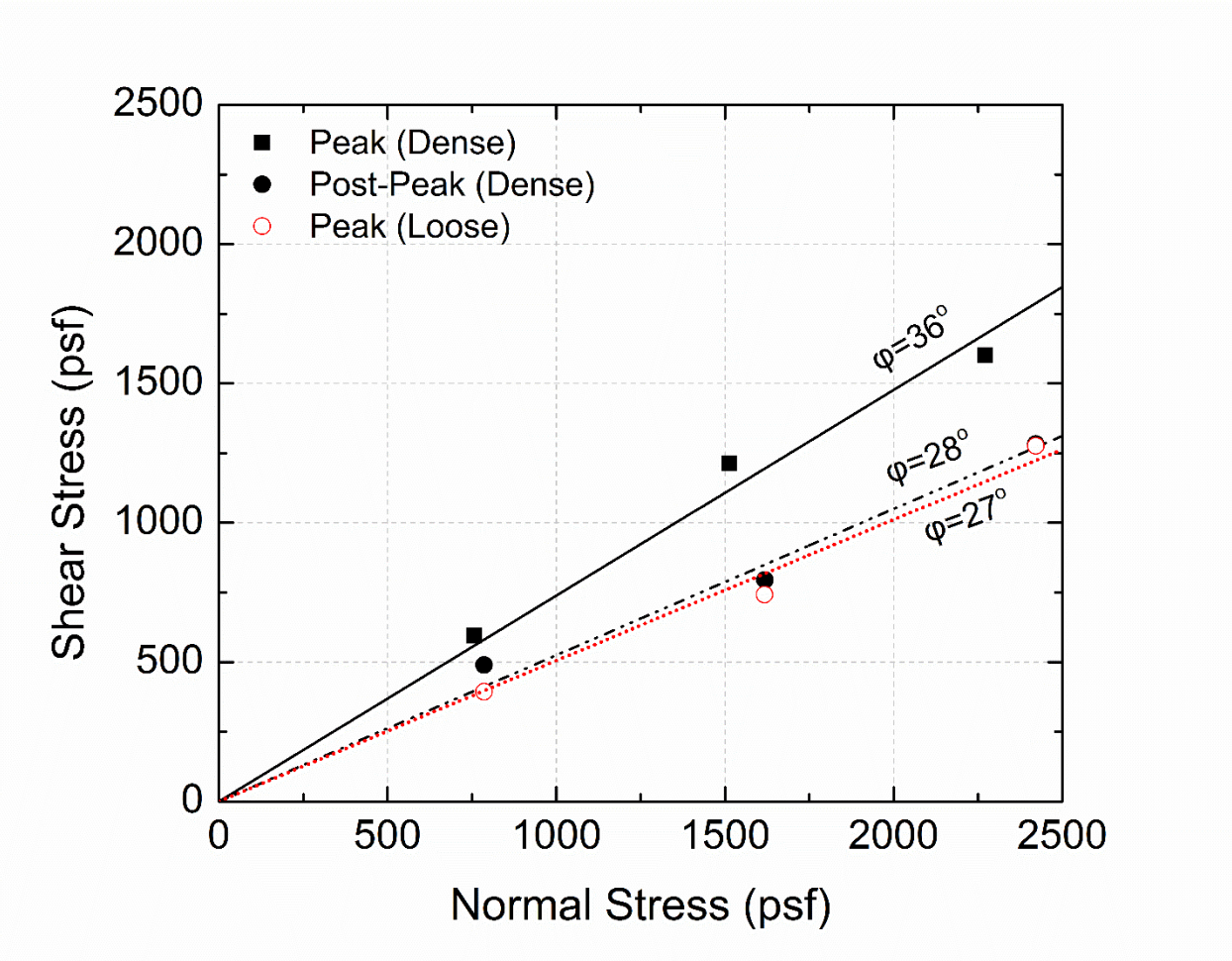

Figure 8-7 Failure envelopes of direct shear tests and friction angles for silica sand

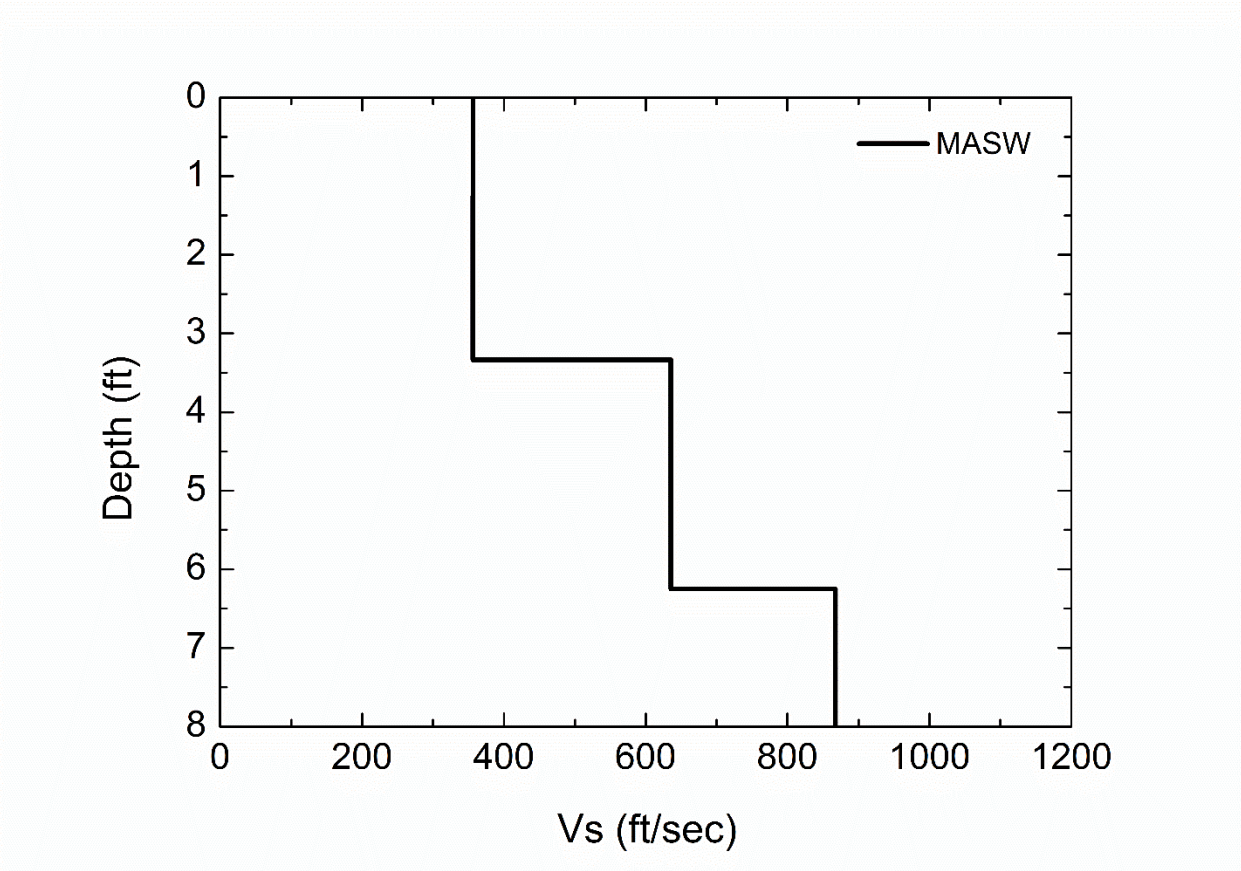

Figure 8-8 Shear wave velocity profile at the sand bin

8.2 Lab Set-Up and Methodology

Al-Shayea (1994) filled the sand bin with the silica sand described previously, using two different sand deposition methods. The bottom 2 ft of the silica sand were compacted using a small motor-driven plate vibrator. The sand deposition was then continued using the pluviation technique. The optimum height of fall (30 in) that resulted in maximum density was found after trials, and the sand was rained free-falling from this height using a special designed apparatus. As discussed in the previous Section, the shear wave velocity changes at 3.5 ft depth. This can be attributed to the two different sand deposition methods that were used in the past.

The research project of Al-Shayea (1994) included the placement of a void at the center of the bin, buried 2 ft below the ground surface, in order to investigate the influence of the surface waves with the void in place. A styrofoam box with dimensions 4 ft x 2 ft x 1 ft (length x width x height) was placed in the sand bin as shown in Figure 8-9. After driving a model pile for the current research project, and when trying to recover the buried sensors, the styrofoam box was found to be still there. The sand was excavated down to 2 ft and the box was removed. After placing the sand back in the bin, the ground surface was moistened and a vibratory plate compactor supplied by WEN (model 56035) was used to densify the top layer of the sand as shown in Figure 8-10. The compactor has a plate size of 24 in x 18 in and weighs 240 lb. It has a 4-stroke overhead valve engine of 7 HP that can deliver 4,496 lb of force at 90 Hz. A similar compactor was used in the sand bin by Hassini (1990).

The Vs was measured again using the MASW method, to ensure the properties were similar to before. Figure 8-11 shows the configuration set-up for the MASW technique. The shear wave velocity profile was found to be close to that measured by Zekkos et al. (2014) as shown in Figure 8-12.

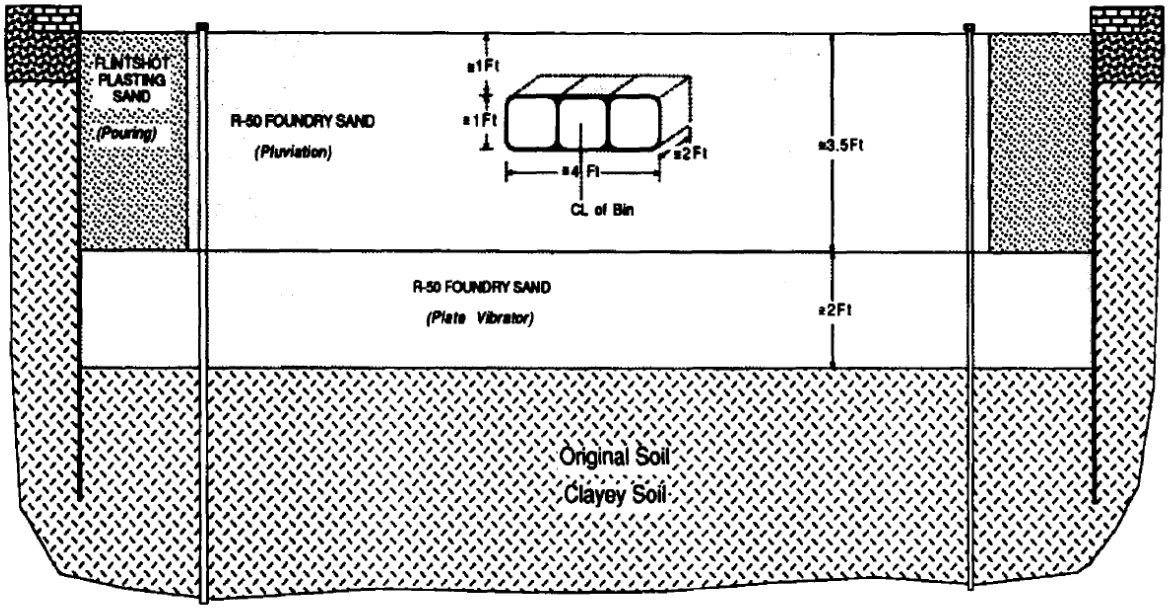

Figure 8-9 Deposition methods and void location in the sand bin used by Al-Shayea (1994)

Figure 8-10 Compaction of silica sand using a vibratory plate compactor

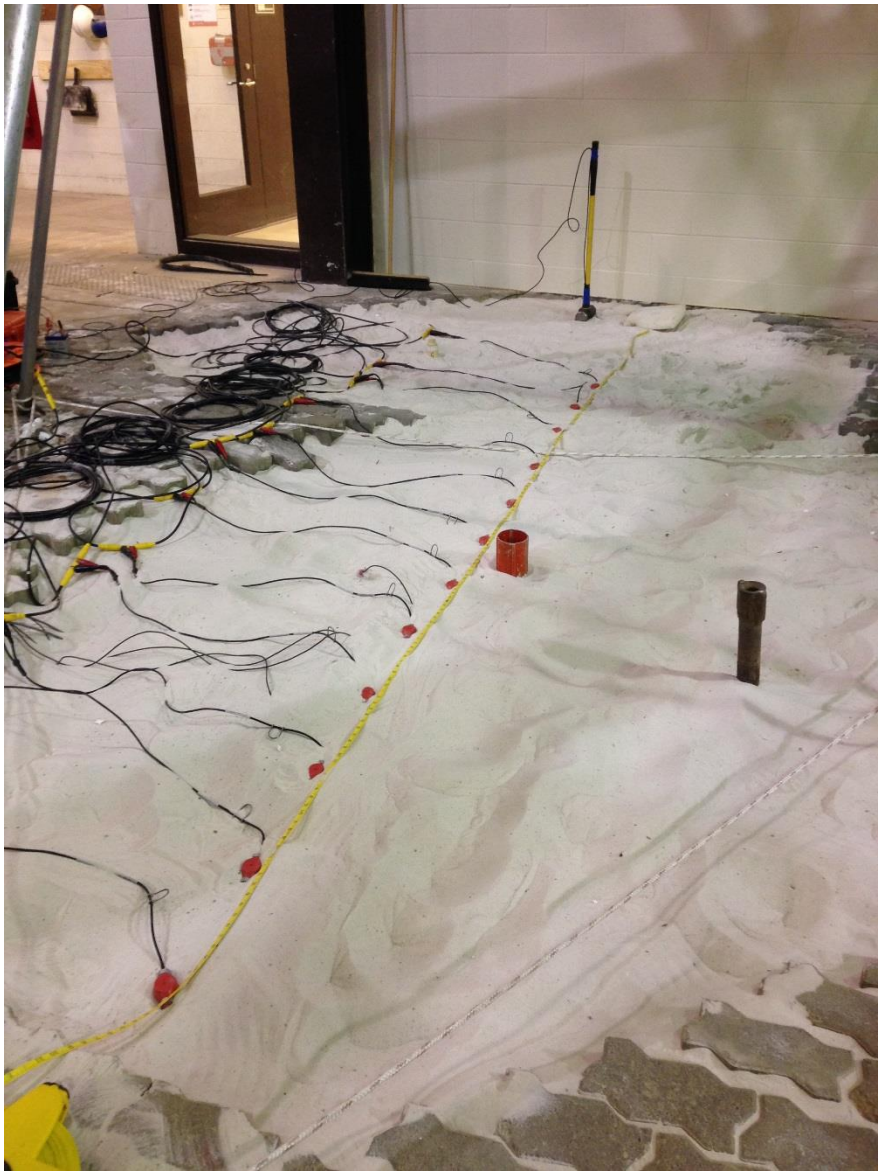

Figure 8-11 Configuration of the MASW testing in the sand bin

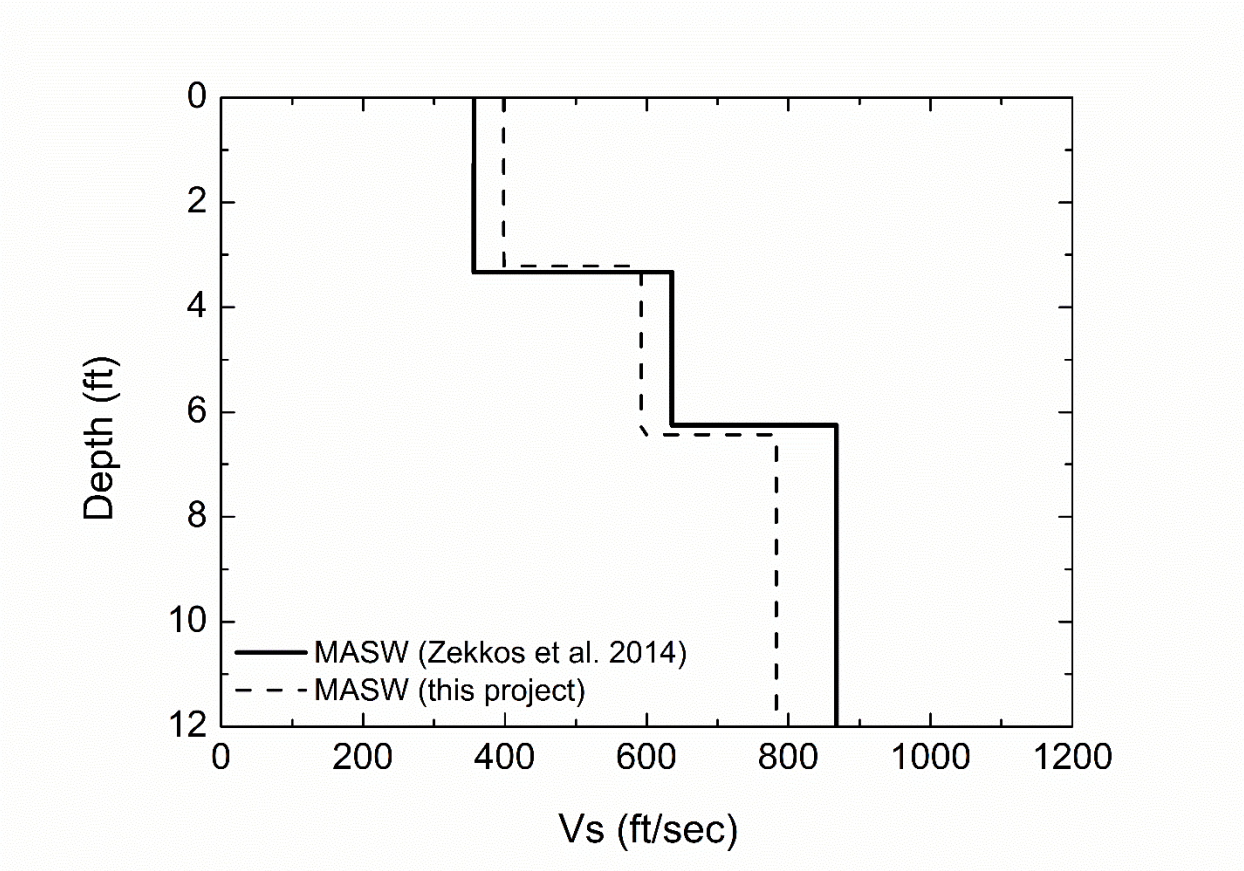

Figure 8-12 Shear wave velocity profile of the sand bin compared with a previous test

8.2.1 Model Pile and Driver

An American standard steel S 3x5.7 section, supplied by Alro Steel, was selected to be driven in the bin. The properties of S-beam types are provided in Appendix I. The S 3x5.7 beam has a depth of 3 in, a flange width of 2.33 in and a web thickness of 0.17 in with a sectional area of 1.67 in^2. The length of the beam is 8 ft and its weight is 45.6 lb (5.7 lb/ft). A view of the beam is shown in Figure 8-13. The beam was marked every half foot in order to investigate the driving resistance during driving in the sand.

A fence post type driver was used as the drop hammer to drive the pile into the silica sand layer. A cross section and a view of the driver are shown in Figure 8-14. The maximum stroke that could be achieved with this driver was 23 in, and with a hammer weight of 44.55 lb, this provided a potential energy of 85.39 lb-ft. In one of the tests in the sand bin, PDA measurements were recorded providing the transferred energy to the pile and other important outputs, which will be discussed in a following Section. The inner diameter of the cylindrical driver is 4 in, adequate to fit and drive the 3 in depth of the pile.

A tripod stand, commonly used for Standard Penetration Tests, was placed in the center of the bin with the tripod head over the location that the pile would be driven. A rope was tied on the top handle of the driver which was then passed over the pulley at the tripod head. The rope was pulled down raising the driver, which was then released to drop freely on the pile head. The driver was carefully lifted up to a height, so as the pile head would not be detached from the driver. A schematic of the driving process of the pile is illustrated in Figure 8-15. After the pile was driven to approximately 3 ft, the handles that are attached on the driver were used to raise it, allowing it again to fall freely on the pile head. Caution was taken to lift the driver and keep almost the same stroke every time in order to have equivalent energy delivered to the pile after every blow. Figure 8-16 shows the process of driving the pile by raising the driver by its handles.

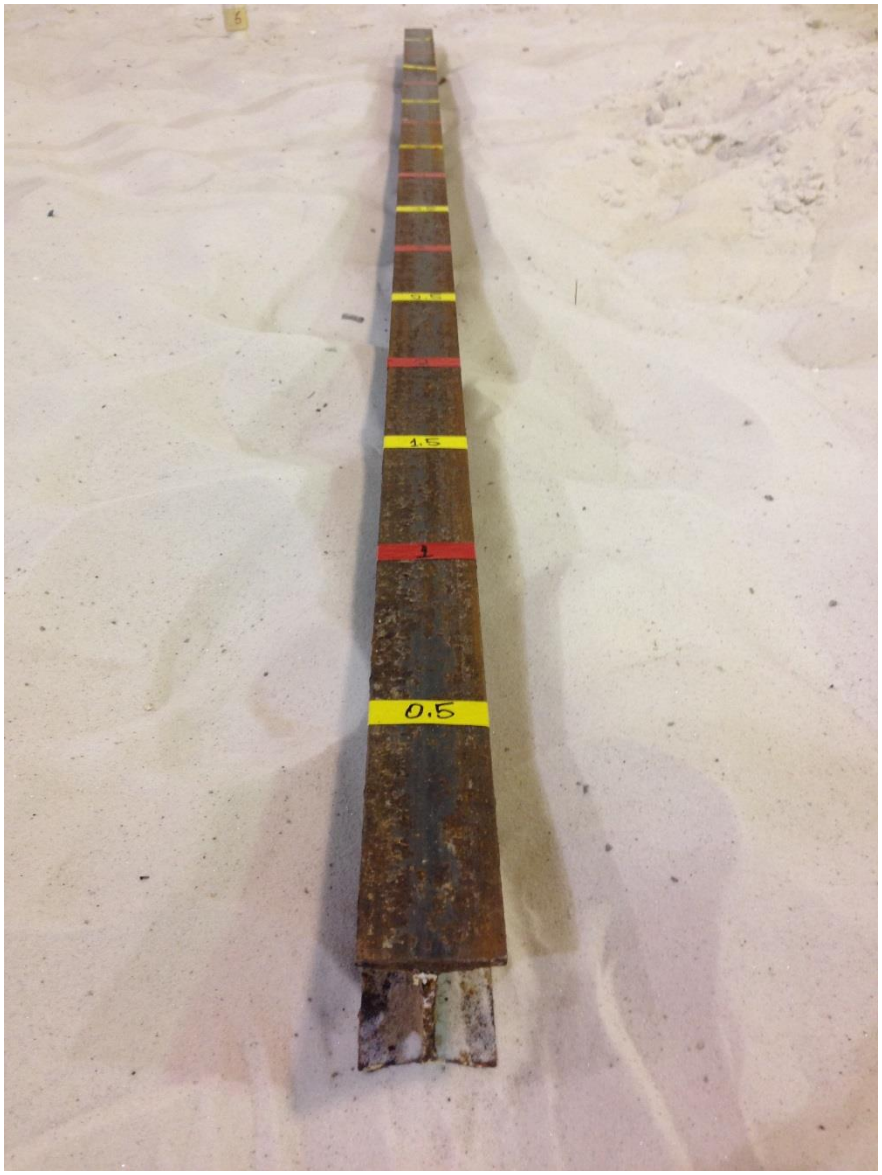

Figure 8-13 View of S 3x5.7 section

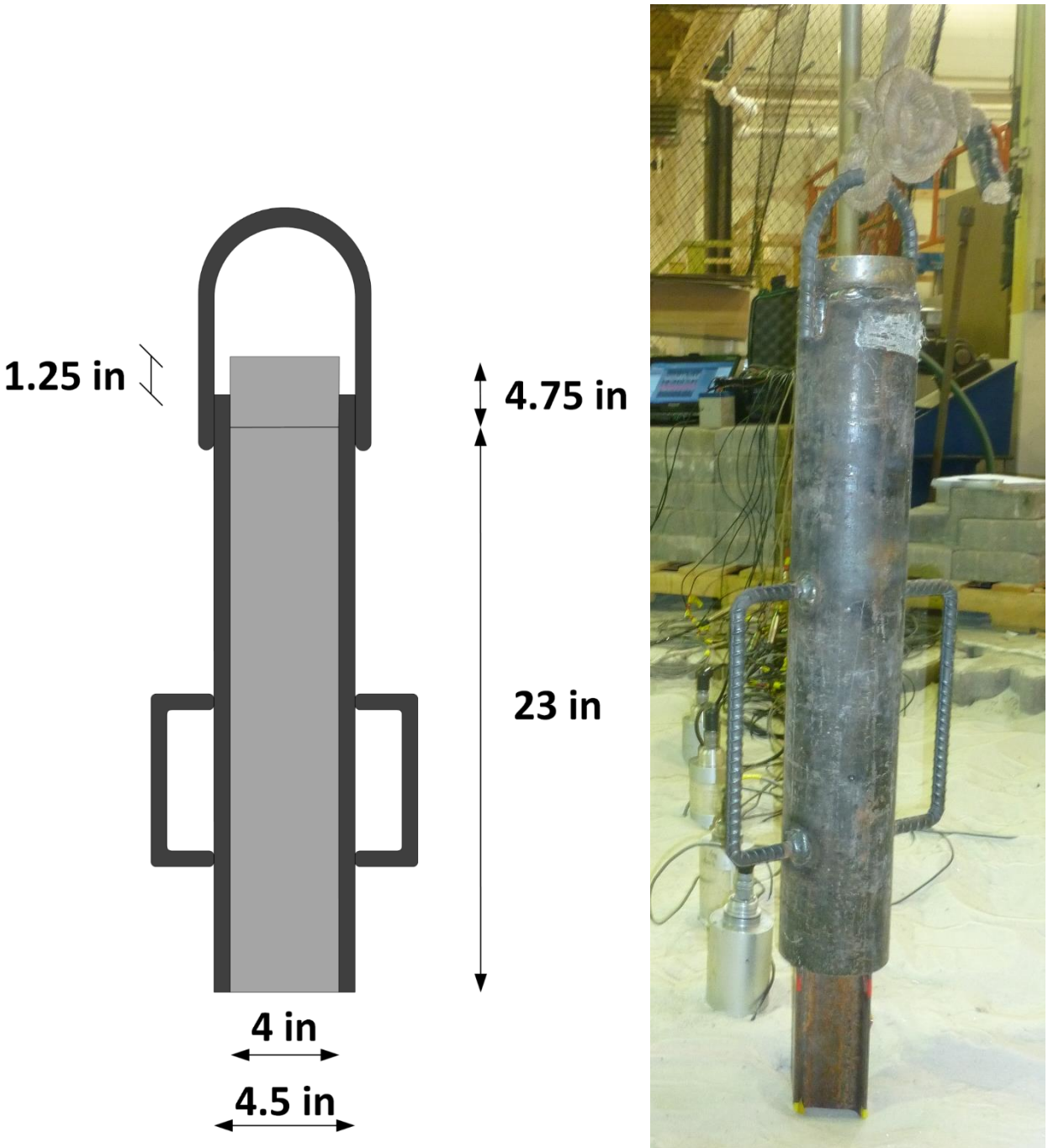

Figure 8-14 Cross section and view of fence post driver used to drive the pile in the sand bin (not to scale)

Figure 8-15 Driving of the pile in the sand bin using the tripod system

Figure 8-16 Driving the pile by lifting the driver by its handles

8.2.2 Sensors' Installation Process

The steel cone casings that were used to house the sensors that were installed in the ground for the field tests, were also used to push the embedded transducers in the sand bin. In addition, plastic cone casings of the exact same dimensions as the steel sensor packages were designed and were used to push the sensors in the sand. Figure 8-17a shows an accelerometer being fitted into the plastic cone cavity and Figure 8-17b depicts the same cone after filling the cavity with epoxy resin. The SPT rods, with the rod to cone adaptor used in the field testing, were pushed into the sand by dropping the same driver that was implemented to drive the pile, on the SPT rods. Another adaptor was used on the top of the rod that was hit by the hammer, in order to protect the rod and the conductor cable from damage. After making sure that the sensor package was left in place at the desired depth, the rods were removed from the ground by a special designed system by the lab technicians. Figure 8-18 presents the installation of one of the sensor casings.

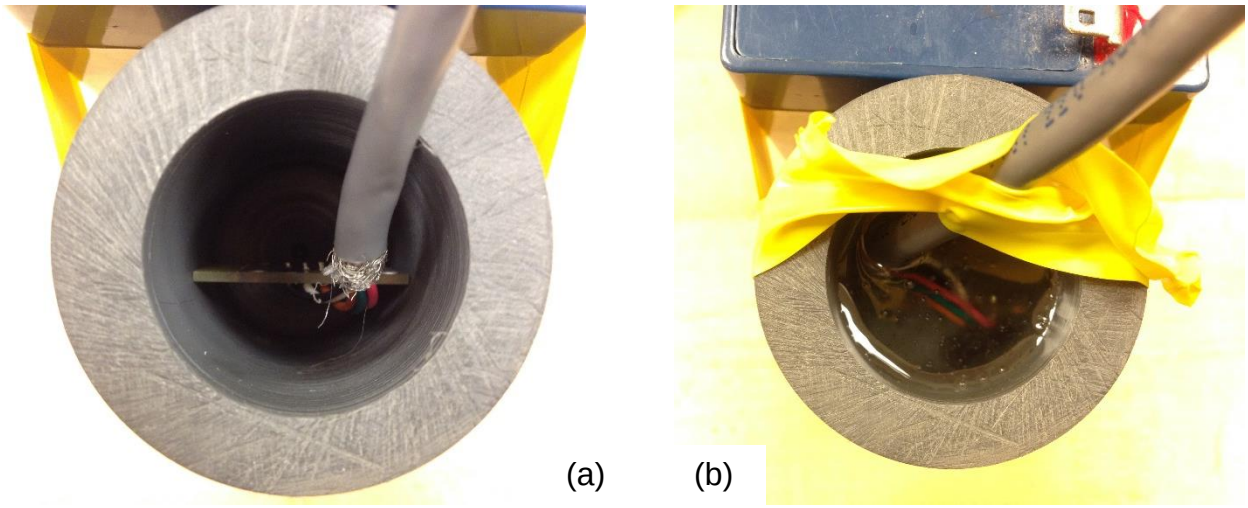

Figure 8-17 (a) Accelerometer fitted into the plastic cone cavity and (b) casing after being filled with epoxy

Figure 8-18 Pushing a sensor package to the desired depth in the sand bin

For the laboratory test program, it was decided that some of the sensors would be pushed into the sand without being fitted in the cone casing. By employing this technique, it would be feasible to assess the impact of the casing on the recorded vibrations.

The following procedure was used to install the sensors in the sand bin without a casing. A special designed wooden cone tip was attached at the bottom of a 10 ft long 1-1/4 schedule 40 PVC pipe, supplied by Alro Plastics. The pipe has an outside diameter of 1.66 in and a wall thickness of 1/8 in; the inner diameter is 1.38 in. The geophones supplied by Racotech Geophysical Instruments have a diameter of 1 in and could fit inside the pipe. The pipe was pushed first, with the wooden tip at its bottom, to the depth that the sensor was to be placed with the fence post driver. The geophone was then lowered into the pipe. Sand was poured on top of the geophone inside the pipe and a 10 ft long PVC rod with a diameter of 5/8 in was used to compact the sand inside the pipe. The pipe was gradually extracted from the ground, leaving the sensor and the wooden cone tip in place, while the backfilling and the compaction was continued up to the ground surface in phases. The installation process described above is shown in the schematic of Figure 8-19.

Three tests were performed in the sand bin, recording ground motions during driving the pile in the silica sand. Table 8.2 presents the penetration depth of the pile and the embedded and surface sensors that were used at each test. A PDA test was performed during driving the pile for LT-4 test. A pair of strain transducer and accelerometer were mounted near the top of the pile as shown in Figure 8-20. Figure 8-21 illustrates the configuration of one of the tests after the end of the driving; four vertical component surface geophones are aligned at different distances from the driven pile. Figure 8-22 depicts a close-up of the driven pile with the cables of the three closest buried sensors from the pile coming out on the ground surface.

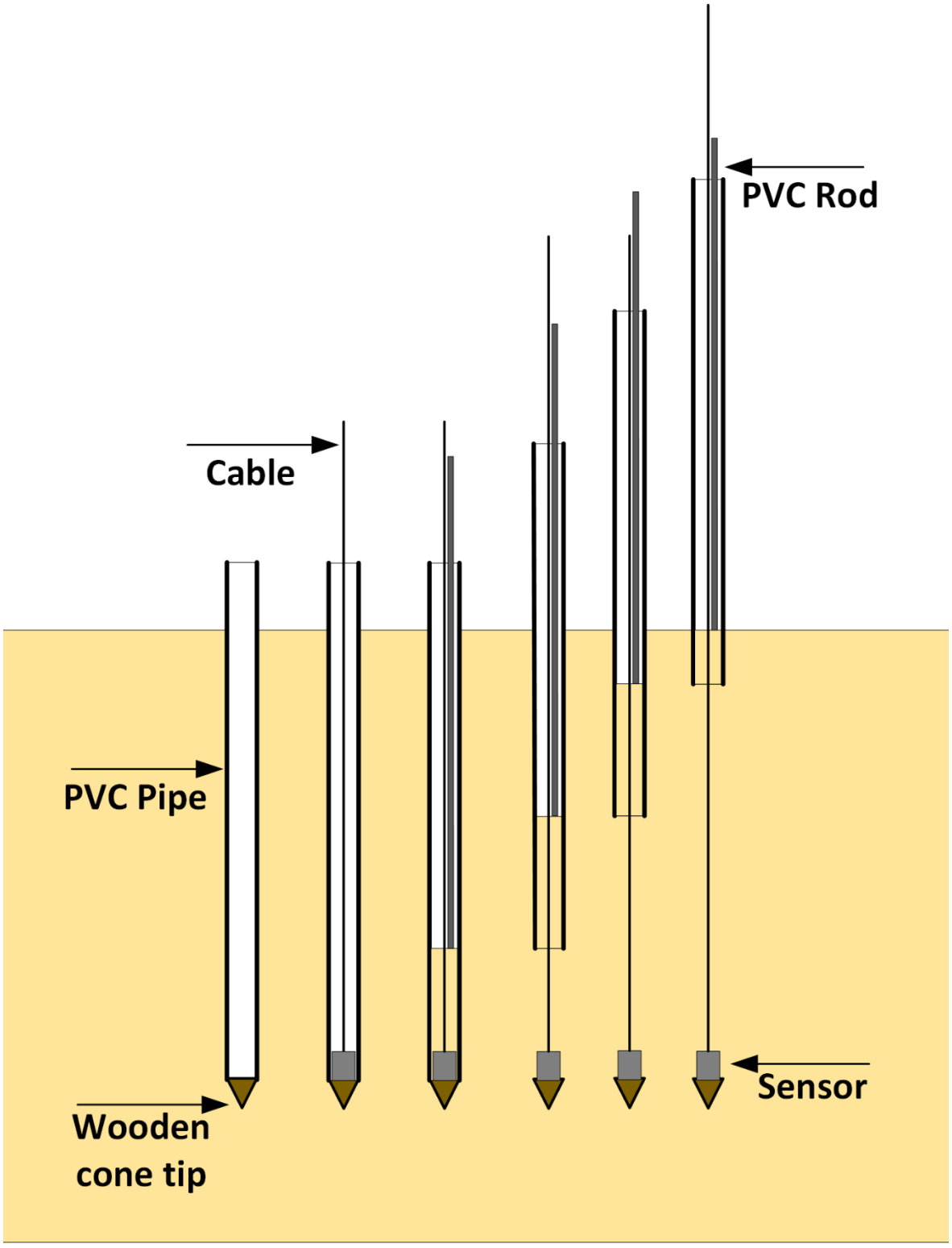

Figure 8-19 Installation steps for geophone without casing package

Table 8.2 Laboratory test program

Test	Penetration Depth (ft)	Surface Geophones, G	Buried Geophones, SG	Buried Accelerometers, A
LT-2	5.5	4	5	1
LT-3	5.6	4	9	
LT-4	5.5	4		

Figure 8-20 Accelerometer and strain gage mounted near the top of the pile

Figure 8-21 Set up of lab test after the end of driving

Figure 8-22 Pile, driver and wires of closest buried sensors on the ground surface

8.3 Ground Motion Measurements

Three tests were performed in the sand bin, recording ground motions during driving a model pile. The cDAQ data acquisition system was employed again to record and store ground motions from embedded and surface geophones. The sampling rate was kept at 1 kHz, as in the field tests. Signal processing was conducted using a Matlab code. A video was recorded during the whole duration of the pile installation, to determine the number of blows per 0.5 ft pile increments and evaluate the pile penetration resistance. Thus, the model pile was marked every 0.5 ft. Table 8.3 has a summary of the accumulated number of blows required to drive the pile, the final penetration depth and the total number of buried sensors for every test. After the end of test LT-1 and when trying to excavate the sand to the sensors' elevation, a styrofoam box that was placed in the sand bin from a previous research project was revealed. The bottom of the box was approximately found at a depth of 2 ft, where the shallow set of sensors was installed. The box was removed, the sand was compacted and test LT-2 was conducted. Test LT-3 was performed for repeatability purposes, having the maximum amount of installed sensors. Finally, test LT-4 was done to record the PDA measurements when the buried sensors had been removed from the sand bin. Since, tests LT-2 and LT-3 provided similar results, but LT-3 had the most installed sensors, results from LT-3 test will only be presented in the following sections.

Table 8.3 Information about the three laboratory tests

Test	Penetration Depth (ft)	Total Blow Count	Buried Sensors
LT-2	5.5	373	6
LT-3	5.6	446	9
LT-4	5.5	942	N/A

8.3.1 Test LT-3

A perspective view of the in-depth sensor locations for LT-3 test is shown in Figure 8-23. Four vertical component geophones were installed to a depth of 2 ft and five vertical component geophones were placed deeper at 4 ft. Geophones SG2 and SG3 were located 0.25 ft from the pile face, with SG2 being housed to a cone casing while SG3 was installed into the sand without a casing. In a similar way, sensors SG4 and SG6 were located 1.1 ft and 1.2 ft from the pile, respectively. SG4 was potted in a cone casing while SG6 was installed without a casing. The pile was driven to a penetration depth of 5.6 ft. Figure 8-24 presents the pile driving penetration resistance as the number of blows per half pile foot increment, as well as the cumulative number of blows versus depth of pile tip penetration. The total number of blows required to drive the pile was 446. Driving resistance is observed to have an increasing rate around 2.5 ft.

Figure 8-25 shows vertical peak particle velocity amplitudes versus depth for the four shallow geophones. A dashed horizontal line indicates the common depth of the geophones. Peak particle velocities gradually increased as the pile descended and reached the sensors' elevation. Decrease in ground motions is noticed when the pile tip passed the depth of 3 ft, for the two closest sensors to the pile (SG2 and SG3). In addition, for these two sensors, it is evident that their response is very close when the pile tip is above their elevation (2 ft), but when the pile reached their installation depth the sensor without a casing (SG3) recorded lower motions. This behavior continued until the pile reaches a depth of 3.5 ft where the sensor inside a casing (SG3) had lower amplitudes than SG3. This behavior may be attributed to poor geophone and ground coupling for the case of SG3 sensor. In general, the monitored vibration pattern is similar for both sensors. This is an important finding to keep in mind, because the primary reason for installing a sensor without a casing was to examine if there are any differences in signals compared to those recorded by the one potted in a casing. It was much easier to install geophones without a casing into the sand bin than employing this installation procedure in the field. However, it is clear that the cone casings that the sensors were housed for field and laboratory testing, do not have a significant effect to the recorded ground motions.

Figure 8-26 to Figure 8-29 illustrate the diagonal distance from pile tip to sensor location versus the vertical peak particle velocity for the four shallow sensors, SG2, SG3, SG5 and SG9, respectively. When the pile tip is still above the sensors' depth (2 ft), spherical waves coming from the tip are only captured from the geophones, with an increasing rate as the tip gets closer to their elevation. After this elevation, cylindrical waves emanating from the shaft start to contribute and impact the sensors. The amplitudes increase, reach a plateau and finally decrease close to the end of driving, where the pile tip is getting further away from the sensors' elevation. However, the sensors located closer to the pile (SG2 and SG3) seem to have a higher decreasing rate when the pile tip descends below their elevation. This phenomenon will be discussed further in one of the next sections. Figure 8-30 shows a comparison of the responses of all four geophones located at 2 ft.

Figure 8-31 depicts vertical peak particle velocities versus depth recorded from the deep row of geophones located at 4 ft. The dashed line indicates the common depth of the sensors. Ground motions increased gradually as the pile penetrated further into the sand, with a maximum response at 3.5 ft for the closest geophone to the pile (SG1). The furthest sensors from the pile had an increasing or constant rate until the end of driving, capturing lower amplitudes than geophone SG1. A comparison of the two sensors installed with (SG4) and without (SG6) a casing, reveals a similar behavior as noted for the corresponding shallow sensors. The geophone without a casing tends to have lower amplitudes until the pile tip reaches their elevation. Then, the geophone with the casing recorded lower ground motions than SG6. These differences are not considered significant, since the plotted values are peak particle velocities for every half foot increment. In general, signals from the two sensors with and without a casing are quite similar if we take into account all the blows.

Figure 8-32 to Figure 8-36 present the diagonal distance from pile tip to sensor location versus the ground motions for the five deep sensors, SG1, SG4, SG6, SG7 and SG8. As expected, ground motions gradually increase and reach constant values as the pile tip gets closer to the sensors' location (4 ft). After this depth, velocities continue to have relatively constant values until the end of driving, with a slight decrease for the case

of the closest geophone (SG1). Figure 8-37 has a summary of the responses of the five deep sensors. In addition, the similar vibration pattern of sensors SG4 and SG6, with and without a casing, is also evident in this plot.

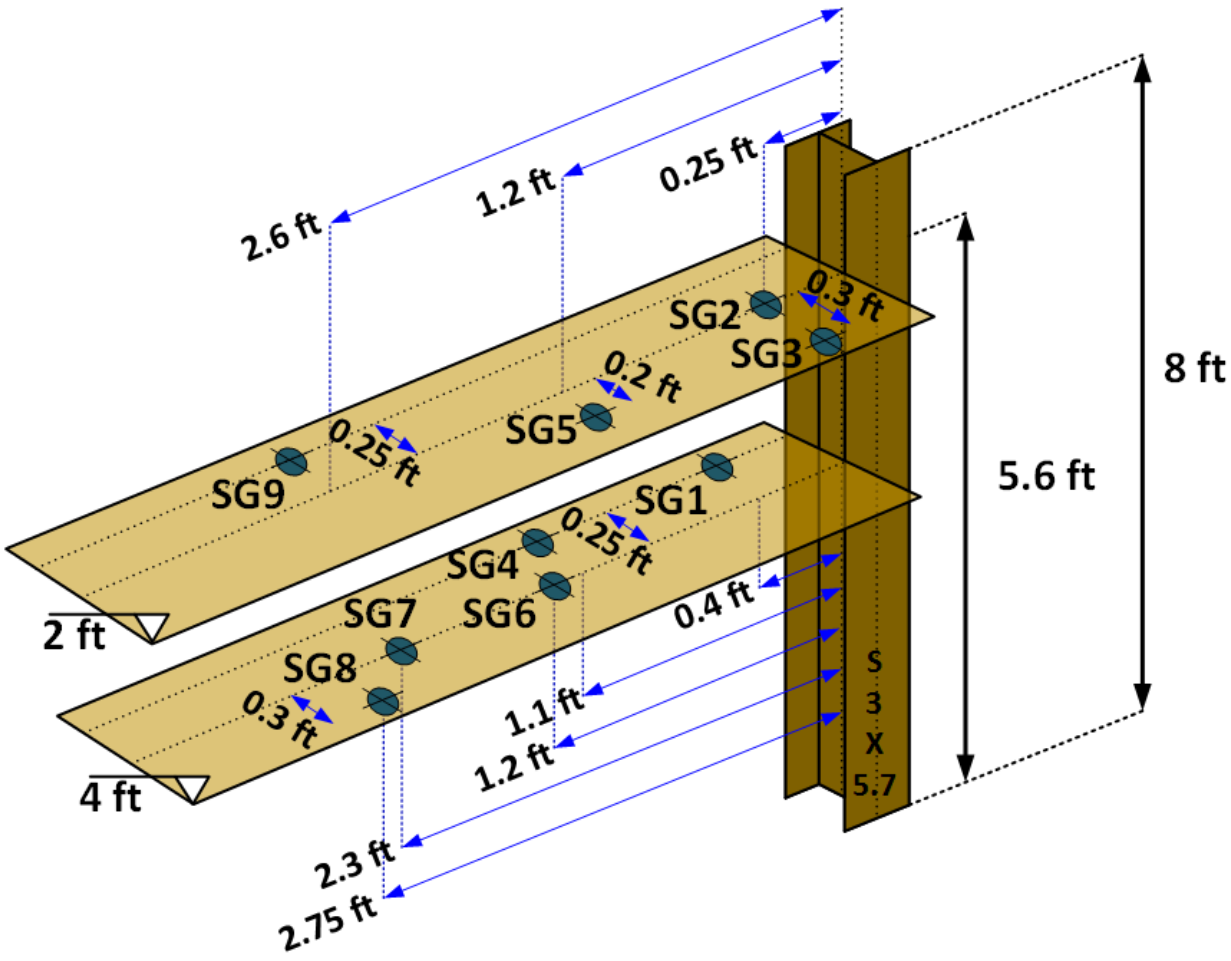

Figure 8-23 Perspective view of buried sensors for LT-3 test (not to scale)

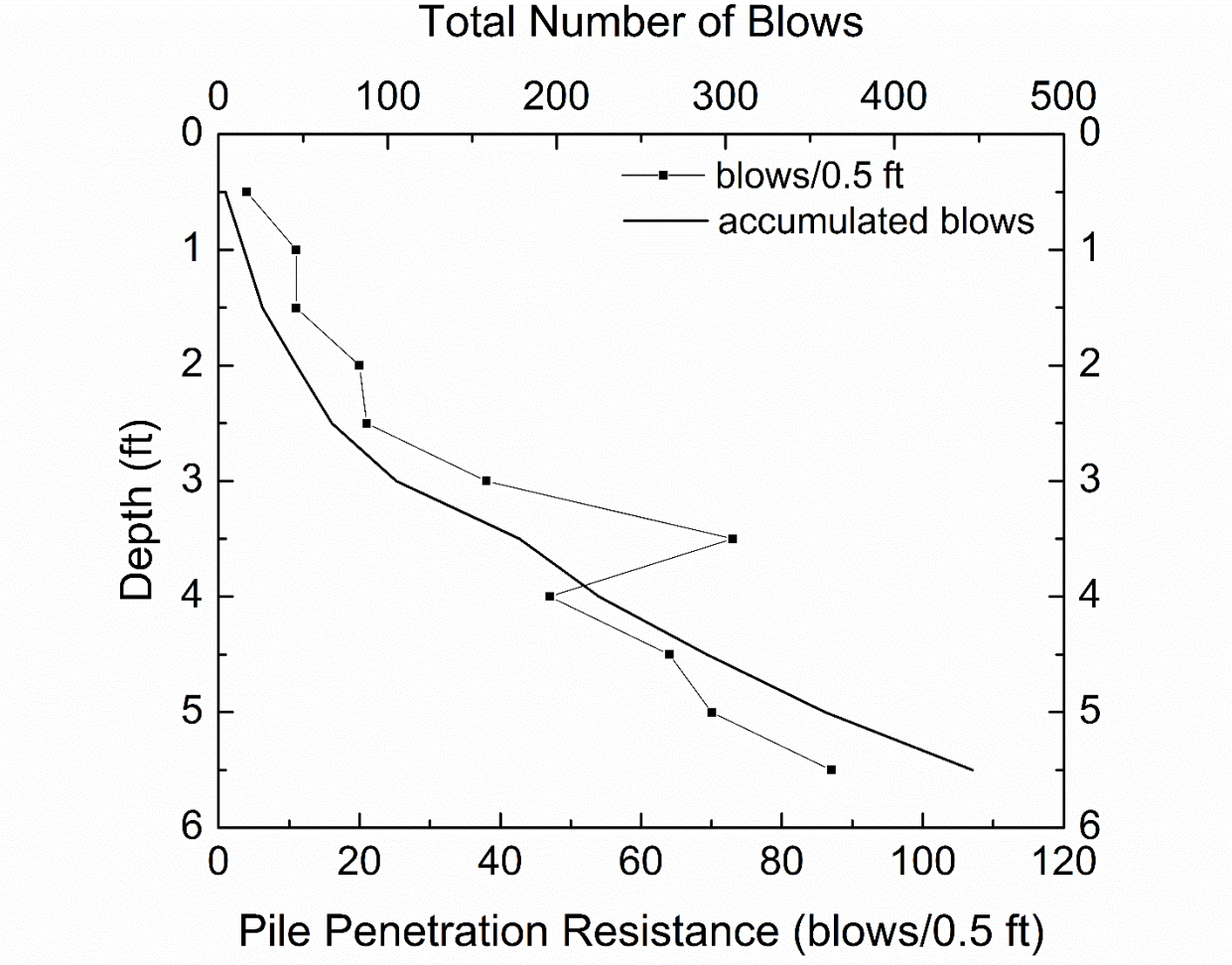

Figure 8-24 Driving Resistance and accumulated blows with depth – LT-3 test

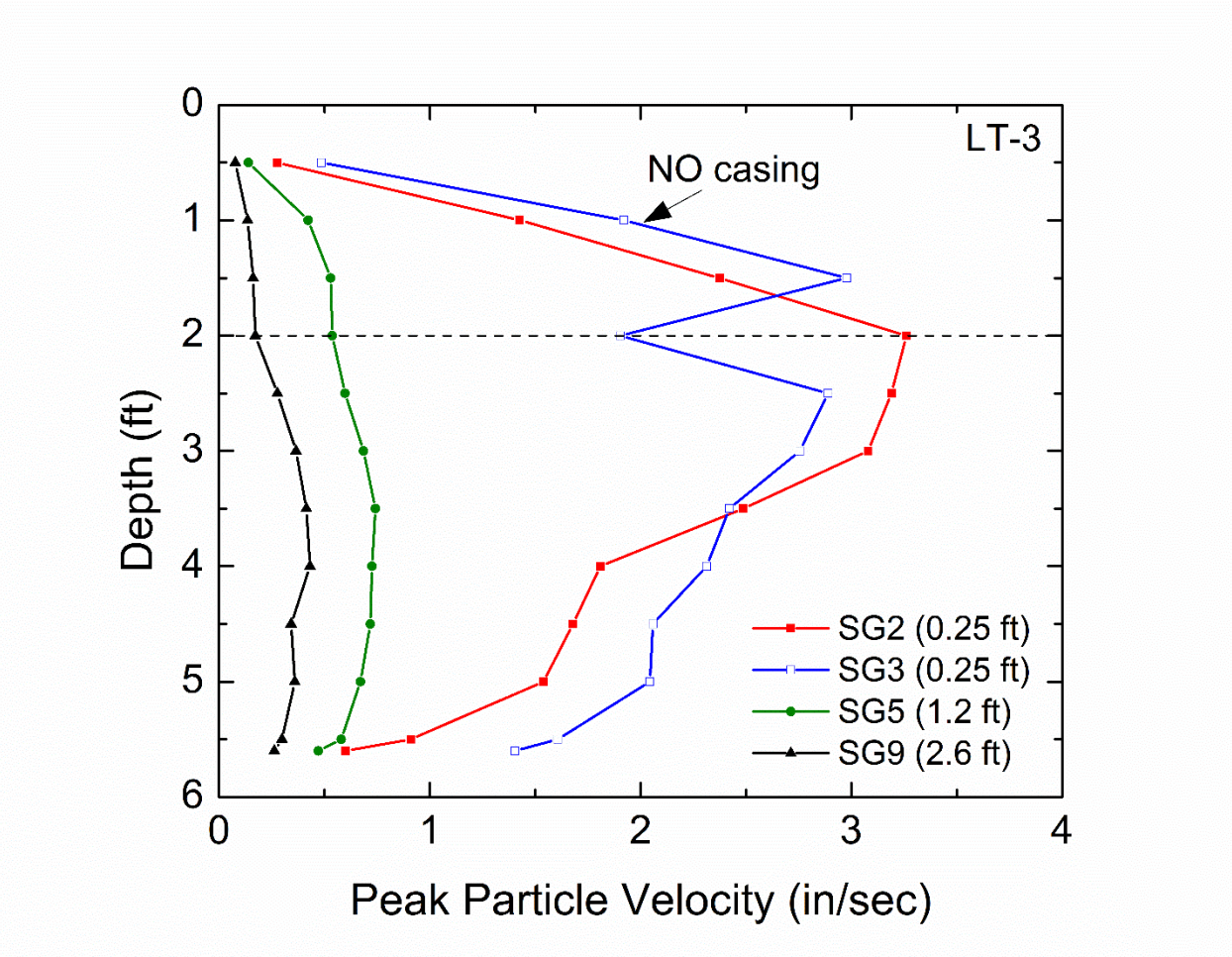

Figure 8-25 Peak Particle Velocity of shallow set of buried geophones - LT-3 test

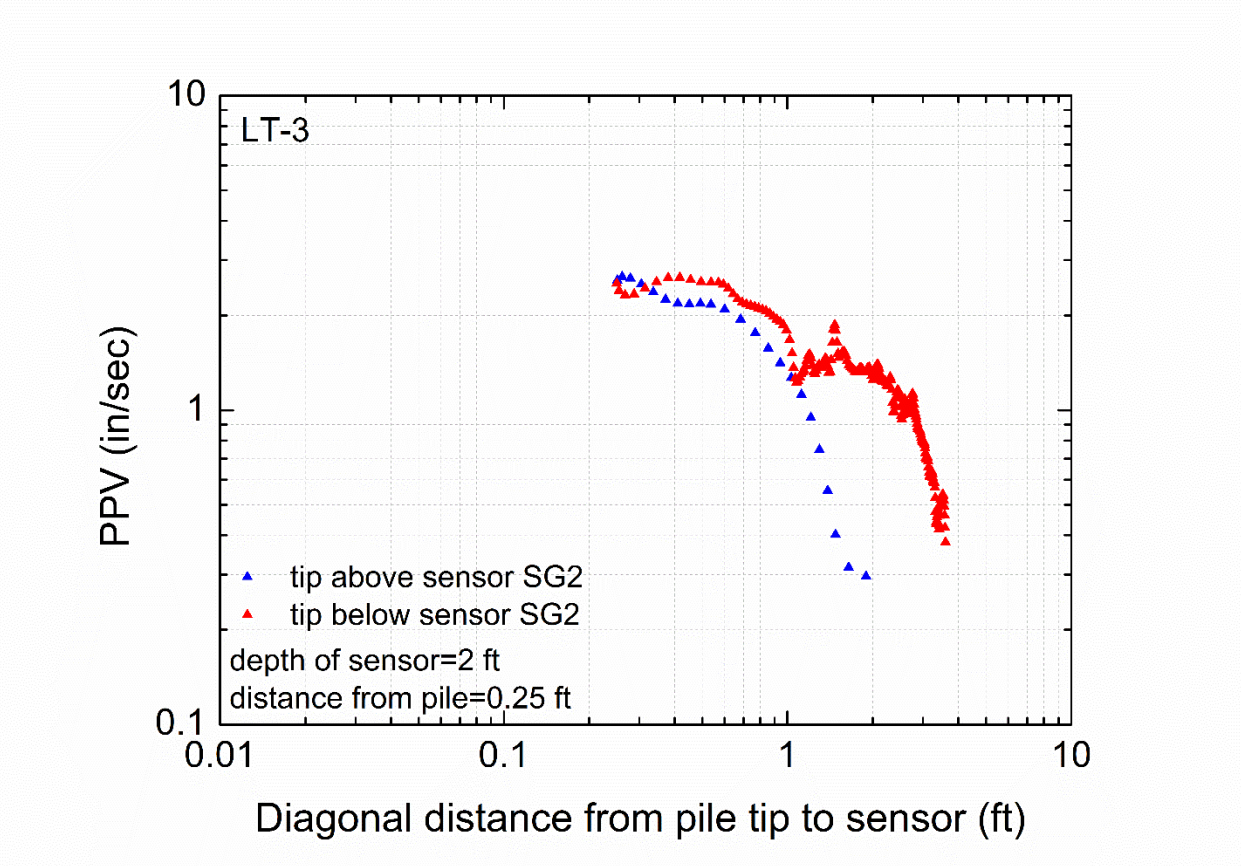

Figure 8-26 Peak Particle Velocity versus diagonal distance from geophone SG2 - LT-3 test

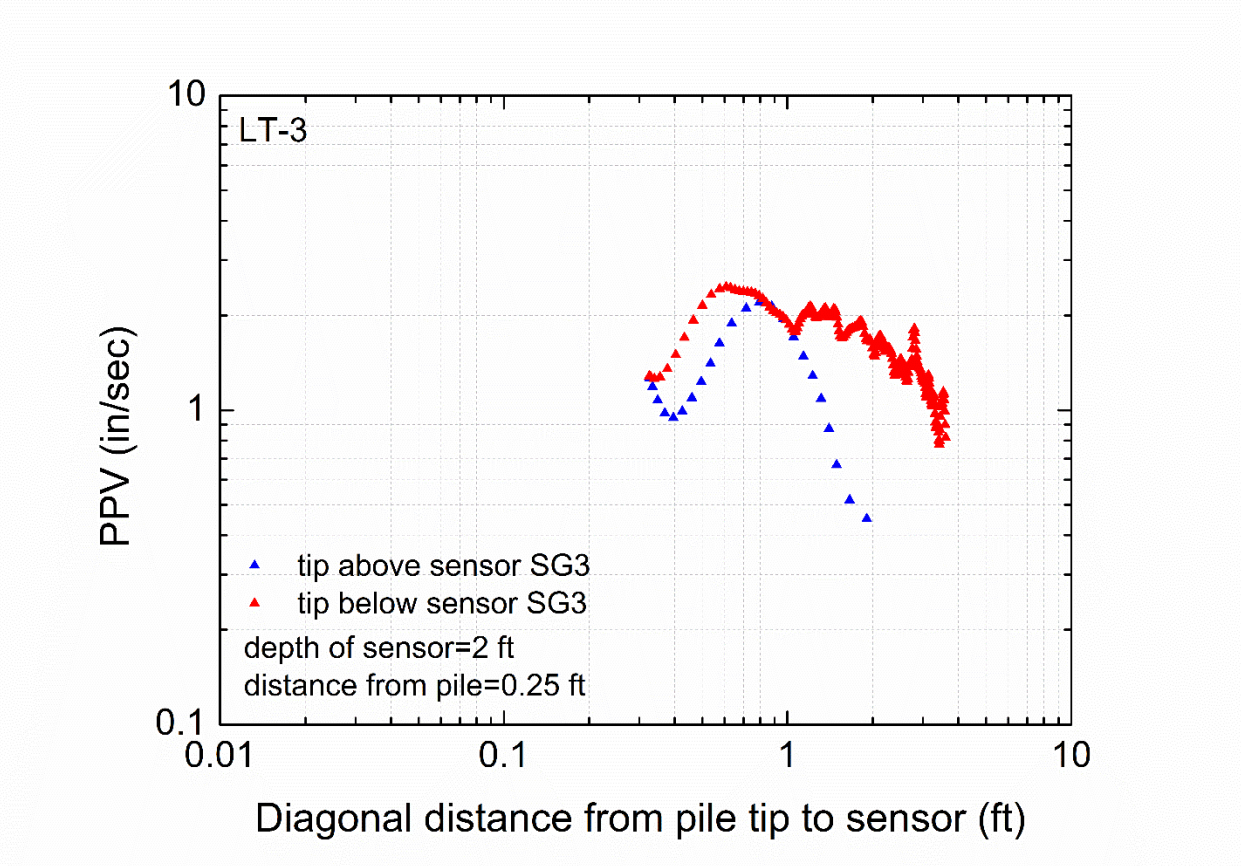

Figure 8-27 Peak Particle Velocity versus diagonal distance from geophone SG3 - LT-3 test

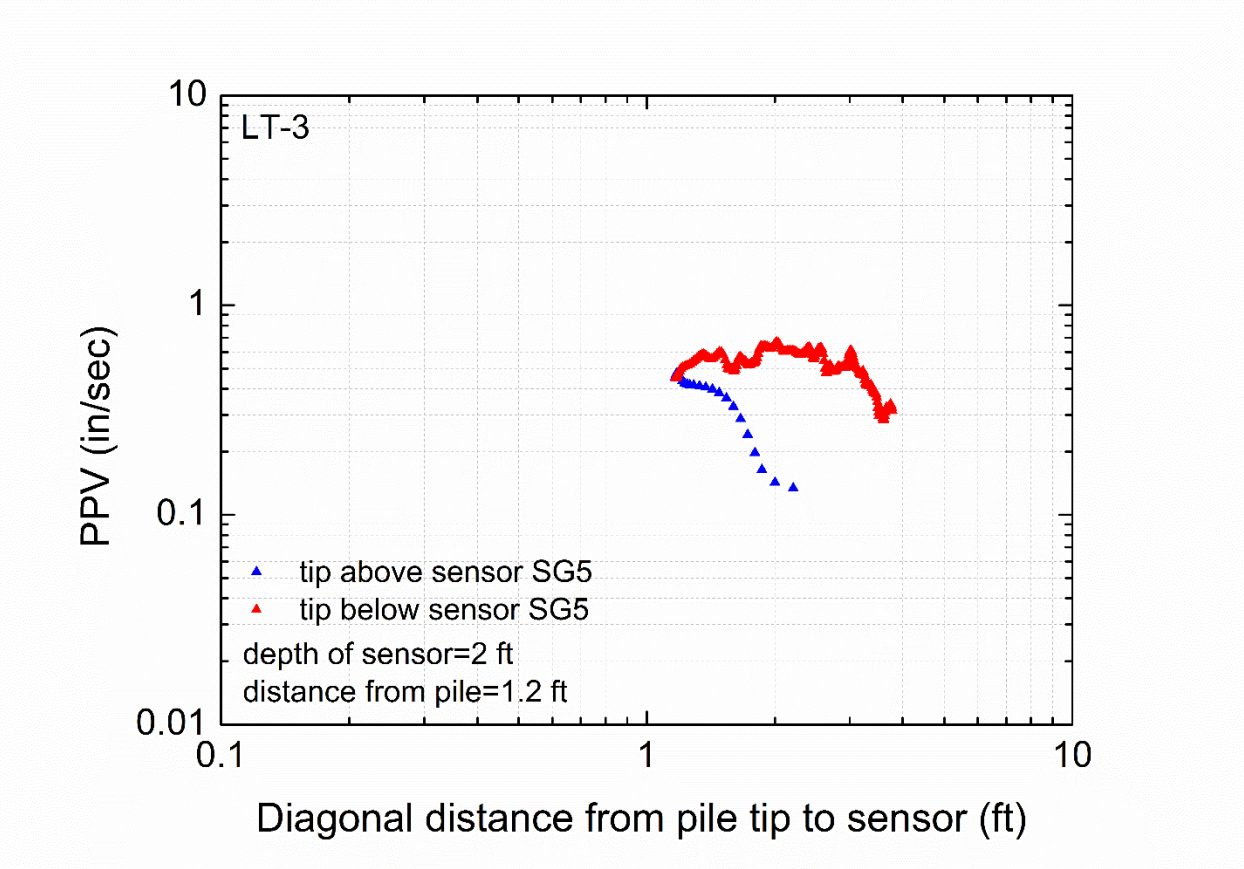

Figure 8-28 Peak Particle Velocity versus diagonal distance from geophone SG5 - LT-3 test

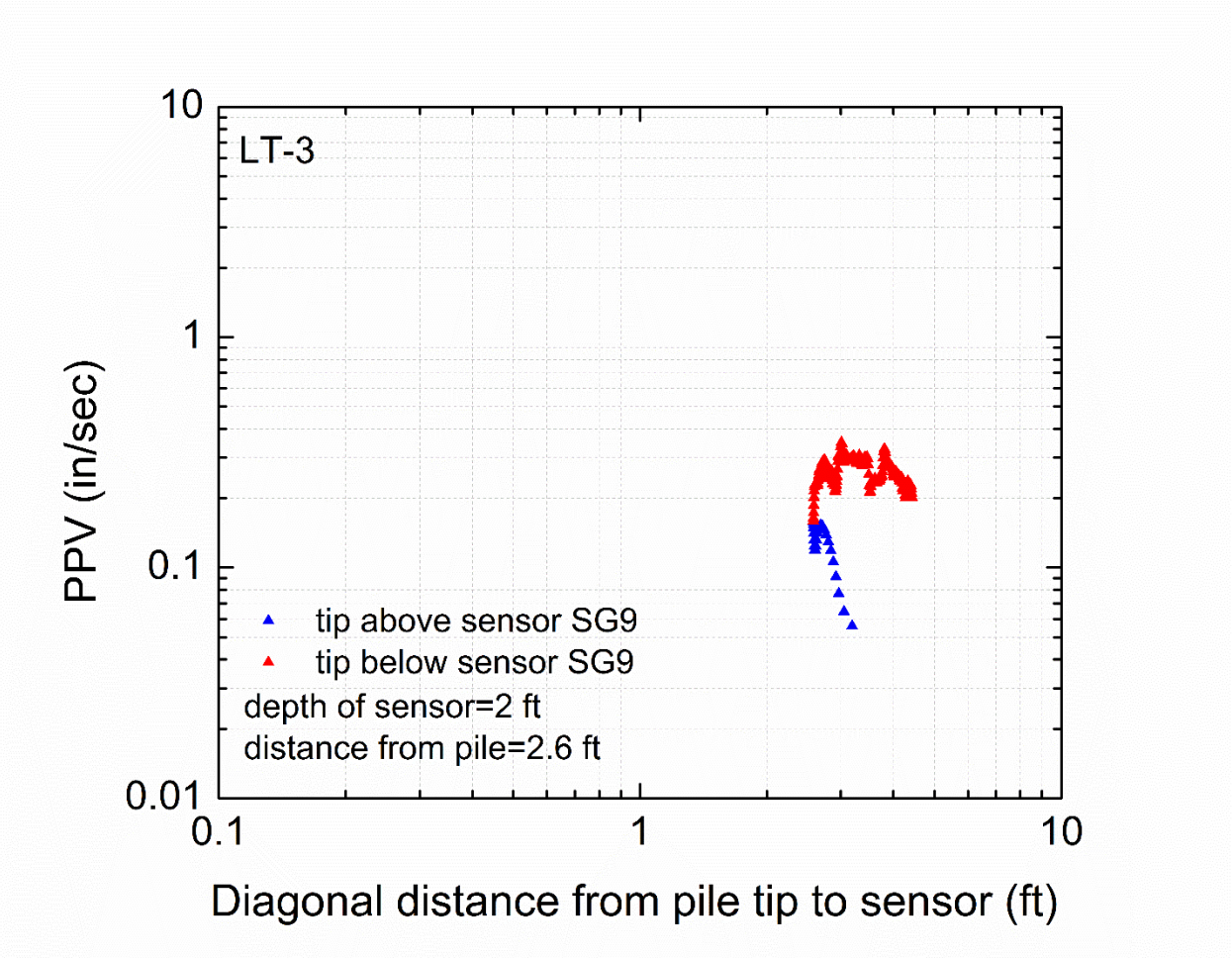

Figure 8-29 Peak Particle Velocity versus diagonal distance from geophone SG9 - LT-3 test

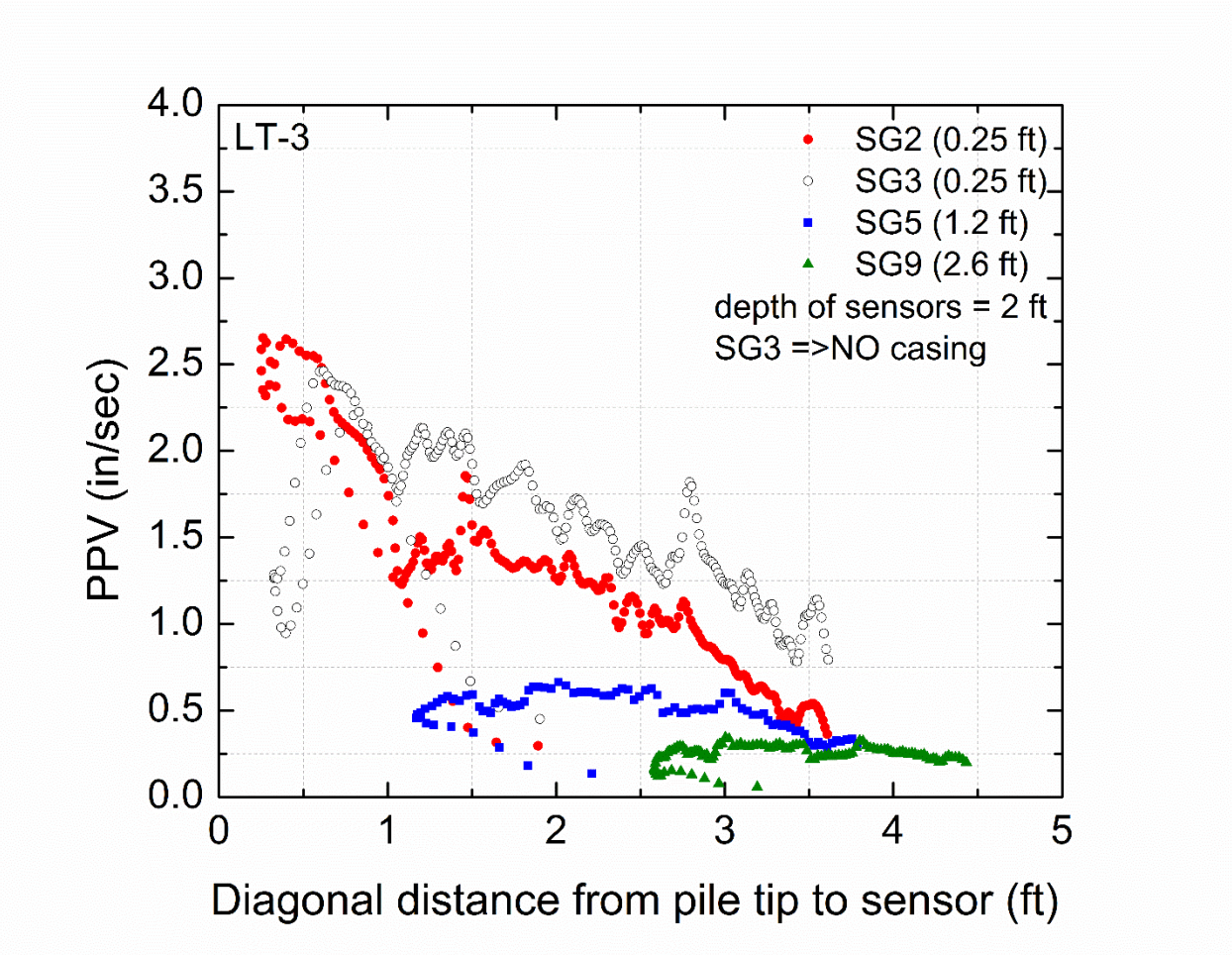

Figure 8-30 Peak Particle Velocity versus diagonal distance from shallow geophones - LT-3 test, arithmetic scale

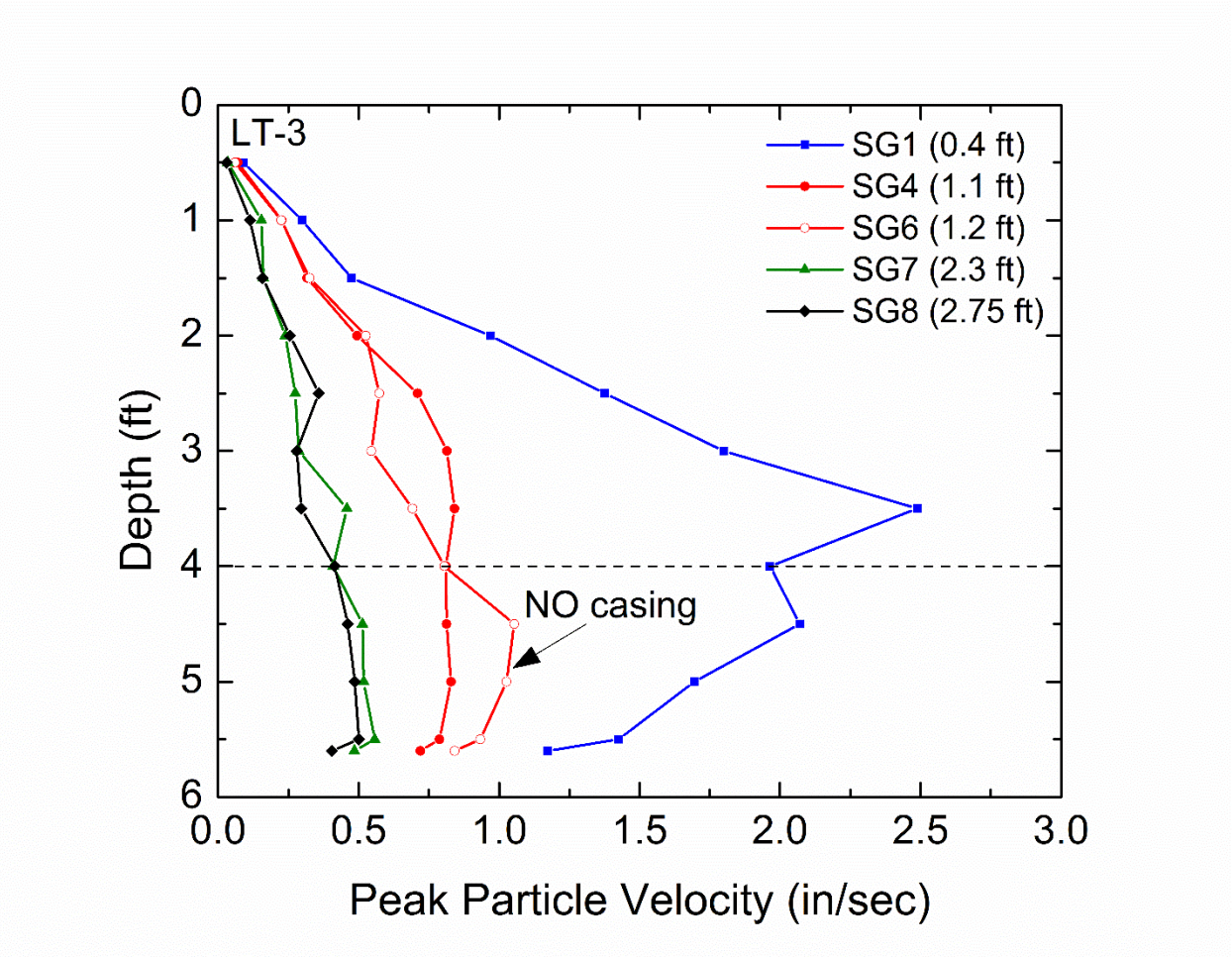

Figure 8-31 Peak Particle Velocity of deep set of buried geophones - LT-3 test

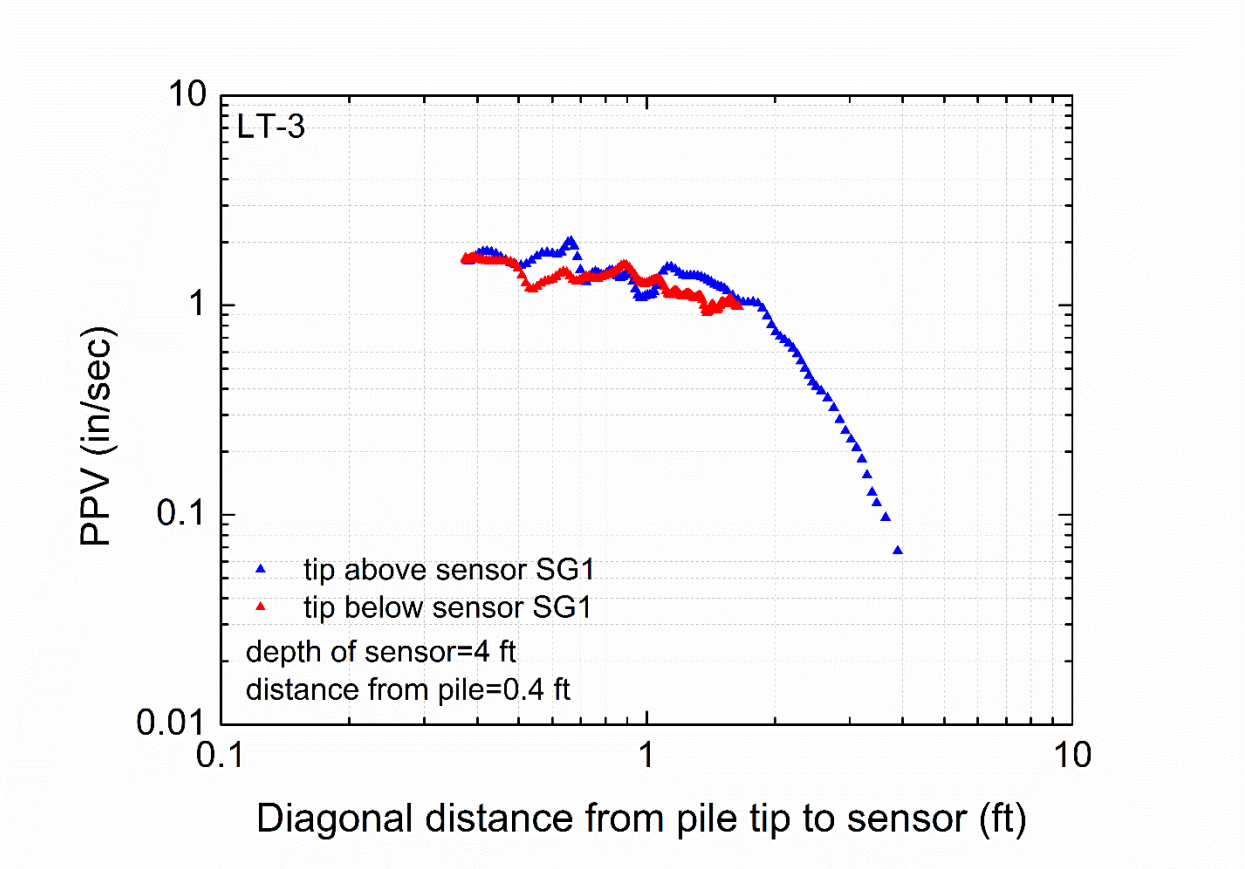

Figure 8-32 Peak Particle Velocity versus diagonal distance from geophone SG1 - LT-3 test

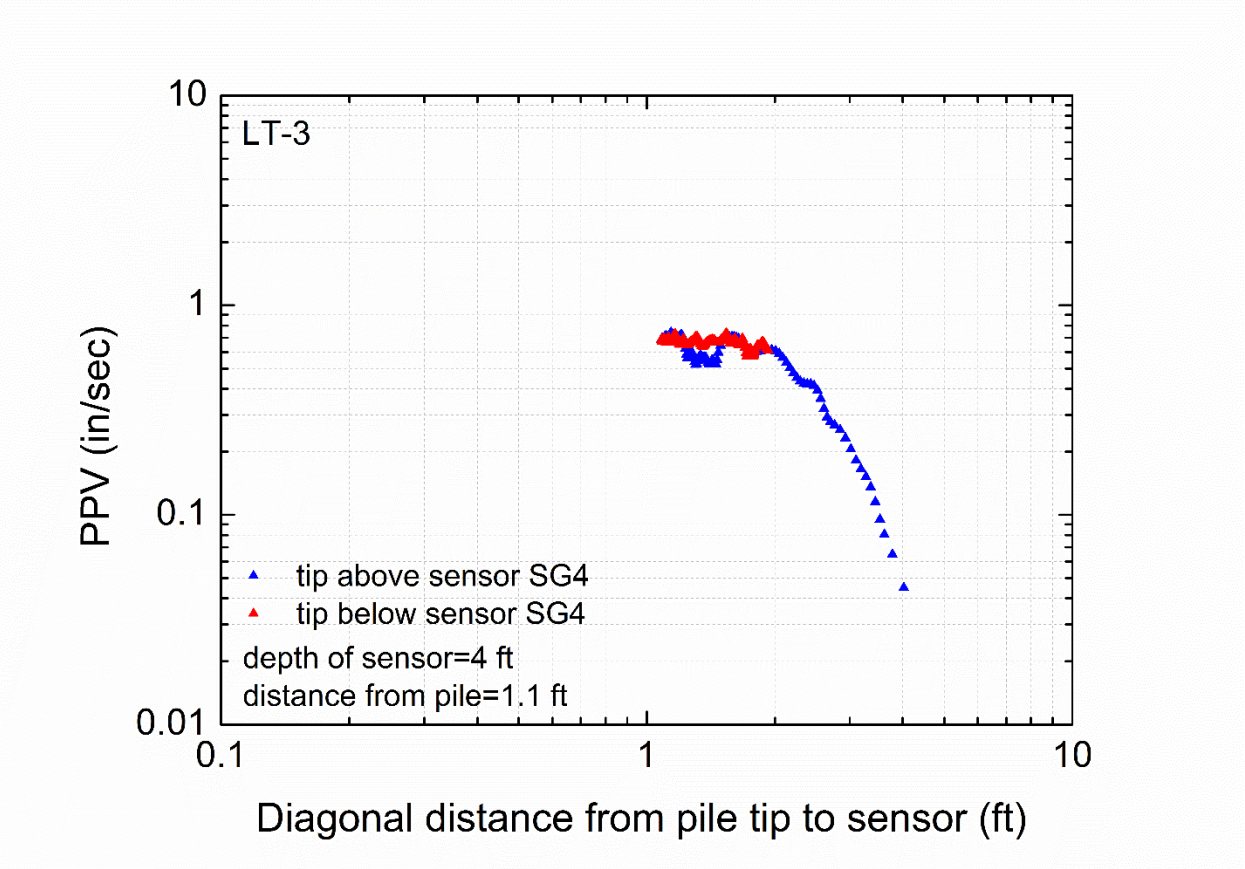

Figure 8-33 Peak Particle Velocity versus diagonal distance from geophone SG4 - LT-3 test

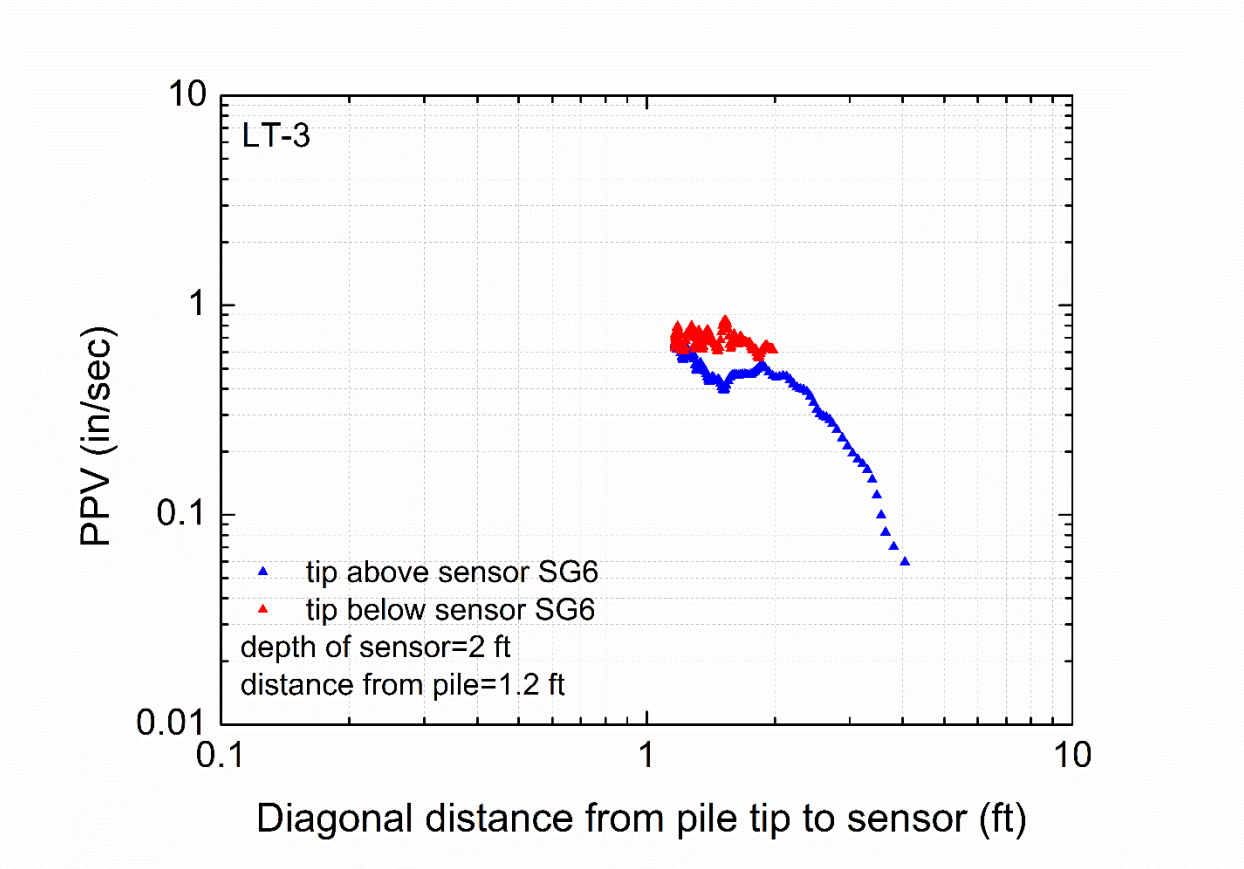

Figure 8-34 Peak Particle Velocity versus diagonal distance from geophone SG6 - LT-3 test

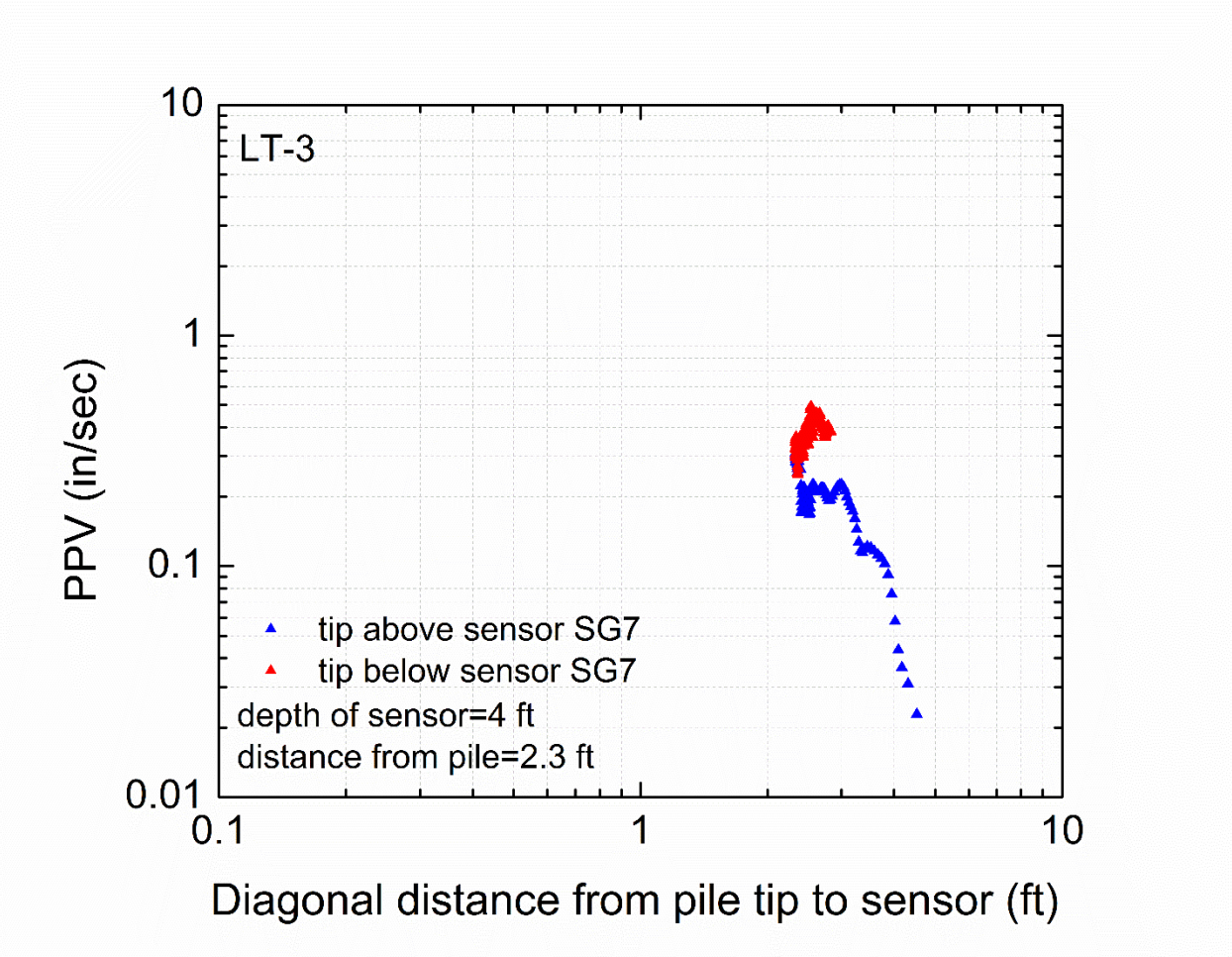

Figure 8-35 Peak Particle Velocity versus diagonal distance from geophone SG7 - LT-3 test

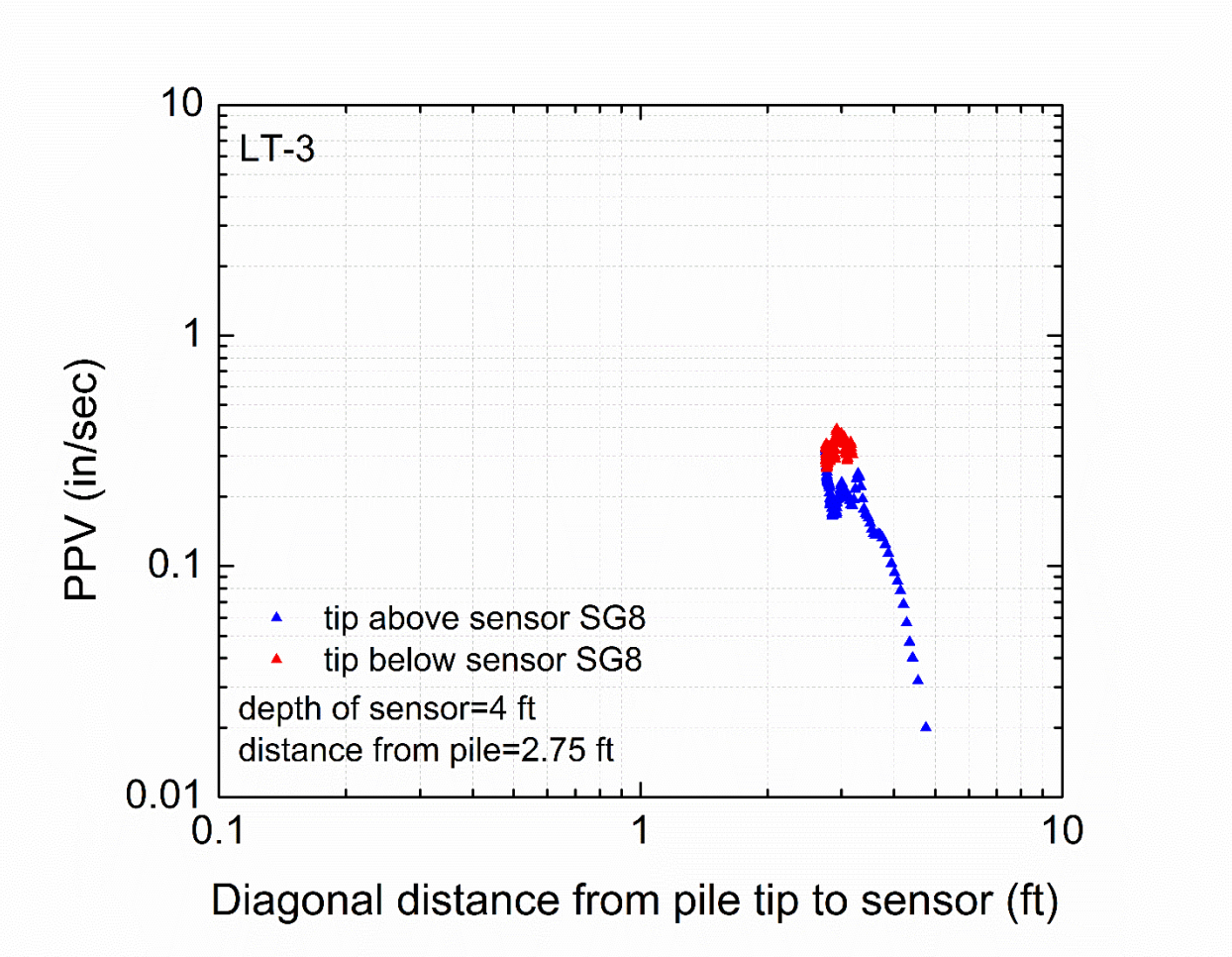

Figure 8-36 Peak Particle Velocity versus diagonal distance from geophone SG8 - LT-3 test

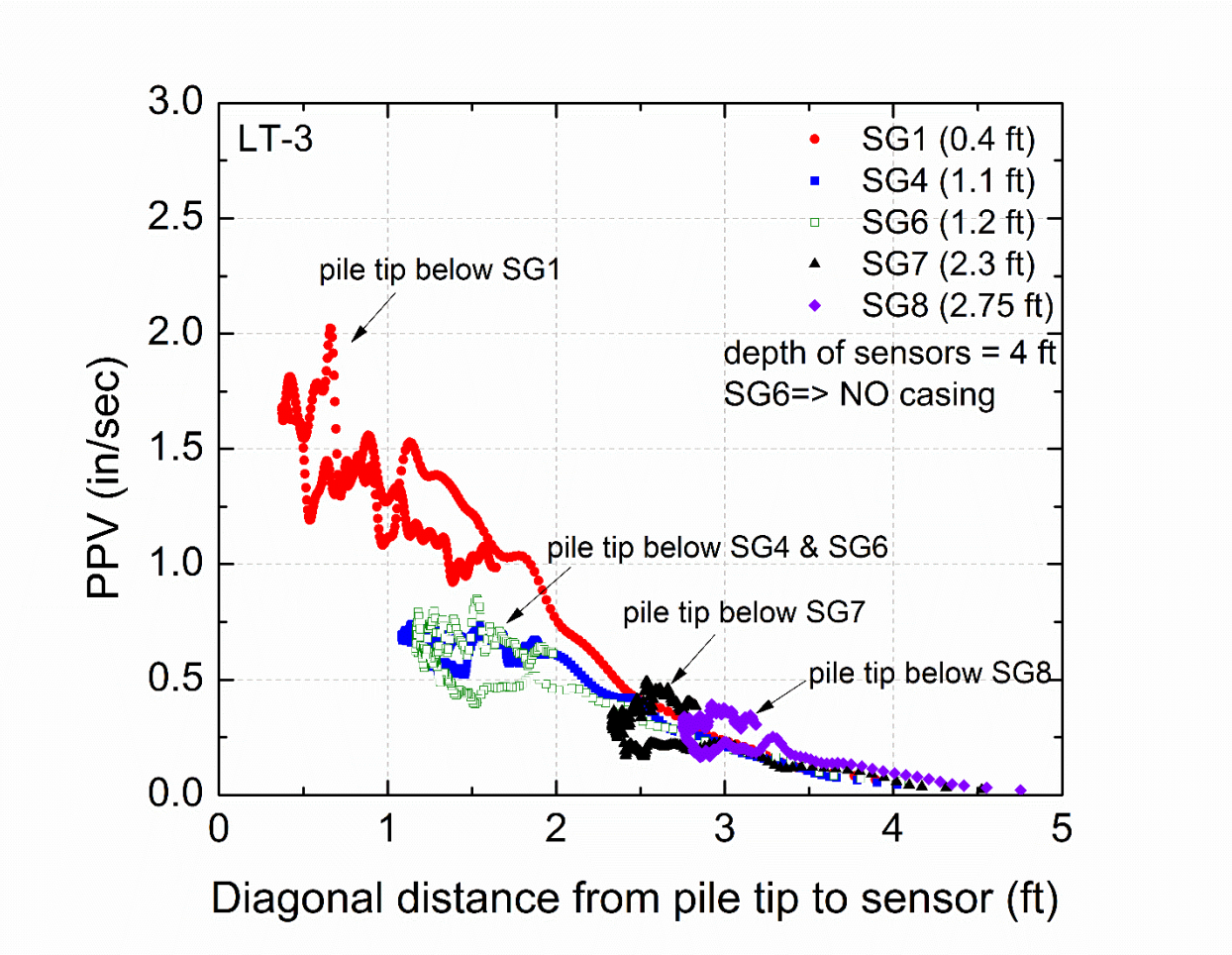

Figure 8-37 Peak Particle Velocity versus diagonal distance from deep geophones - LT-3 test, arithmetic scale

Four vertical component surface geophones were placed in a line array along the surface at the locations shown in Figure 8-38. Vertical peak particle velocity amplitudes versus depth for the four geophones are presented in Figure 8-39. The three geophones placed further from the pile, G2, G3 and G4, have increasing ground motions until a depth of 2.5 ft and then the amplitudes stay relatively constant or slightly decrease. Ground motions recorded from the closest geophone to the pile (G1) decrease slowly until the pile tip reaches a depth of 3 ft and then have a sharp decrease in their amplitudes until the end of driving, while their values are comparable to the three further geophones from the pile. These behaviors will be discussed and analyzed in a different way in one of the next sections.

In Figure 8-40 the peak particle velocities versus depth are plotted for the closest surface and buried sensors to the pile face, G1 on the surface, SG2 at 2 ft and SG1 at 4 ft. The buried geophones (SG2 and SG1) recorded similar amplitudes when the pile tip passed the depth of 3.5 ft, where there is a change in the shear wave velocity. The surface geophone (G1) recorded lower amplitudes from both buried sensors after the pile tip passed a depth of 2.5 ft. This is not surprising, as its distance from the pile is only 0.4 ft which indicates that is not enough for the potential Rayleigh wave to develop. Thus, geophone G1 monitored only waves coming from the tip and the shaft of the pile.

Figure 8-41 shows peak particle velocities versus depth for the next three sensors that have a common distance from the pile (1.2 ft), G2, SG5 and SG4. The three sensors recorded similar ground motions, with the surface geophone (G2) having higher amplitudes than the two buried geophones, until a depth of 2.5 ft. After the pile tip passed a depth of 3 ft, the deeper geophone (SG4) recorded larger motions. Finally, Figure 8-42 presents a comparison of ground motions recorded from geophone G3 on the surface, SG9 at 2 ft, and SG7 and SG8 at 4 ft depth. Again, the surface geophone has higher amplitudes until the pile tip descends and reaches a depth of 4 ft. Then the deeper sensors (SG7 and SG8) have slightly higher amplitudes. In general, the three buried sensors recorded similar values until reaching the elevation of the deep sensors (4 ft), where amplitudes from the shallow buried sensor (SG9) started to decrease. To conclude, the surface geophone (G3) seems to sense a combination of surface waves, spherical

waves from the tip and cylindrical waves from the shaft, and as a result recorded slightly higher motions than the buried sensors. This behavior will also be discussed further in a following section.

It is also important to mention that the ratios between the horizontal distance from sensors to pile face to the pile length are comparable to those of the field tests. Thus, this parameter does not affect the interpretation of the results between the full-scale and small-scale tests.

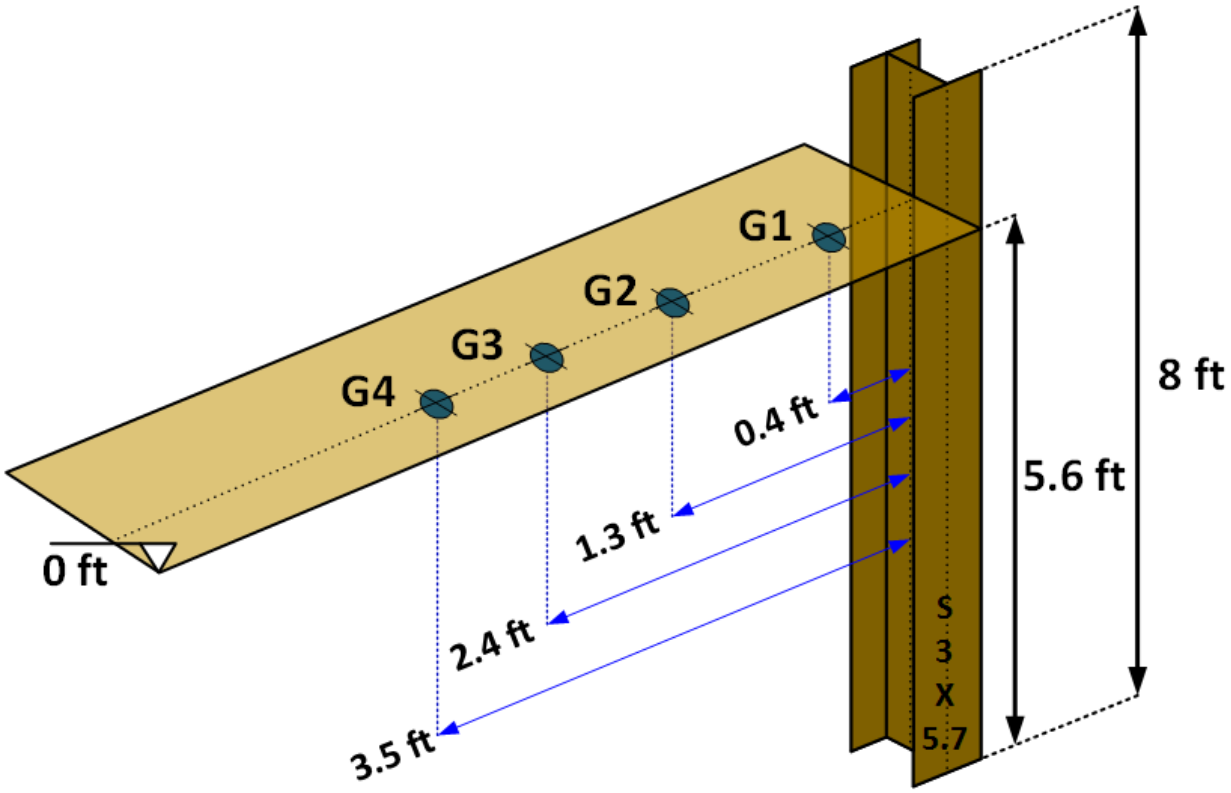

Figure 8-38 Perspective view of surface sensors for LT-3 test (not to scale)

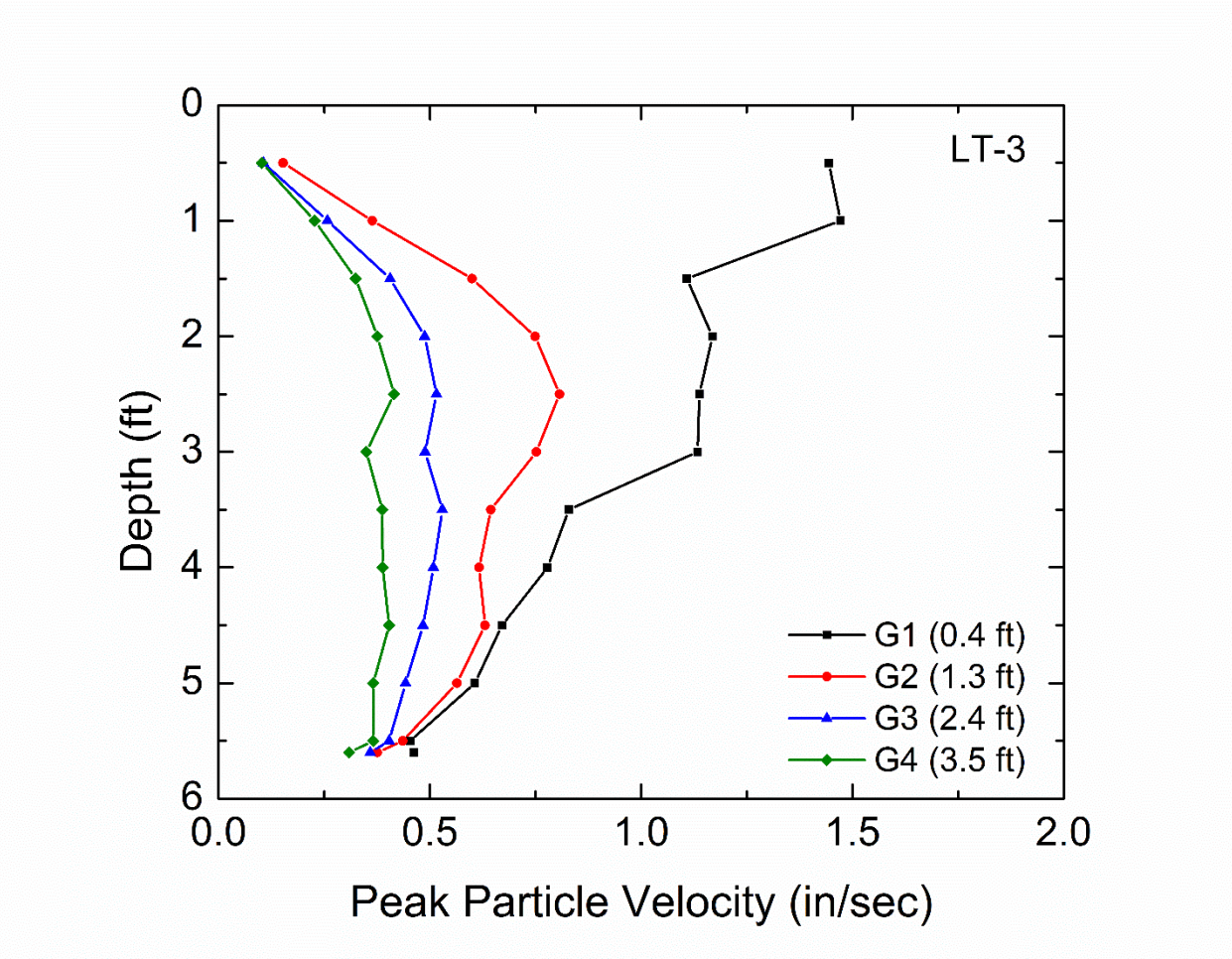

Figure 8-39 Peak Particle Velocity of surface geophones - LT-3 test

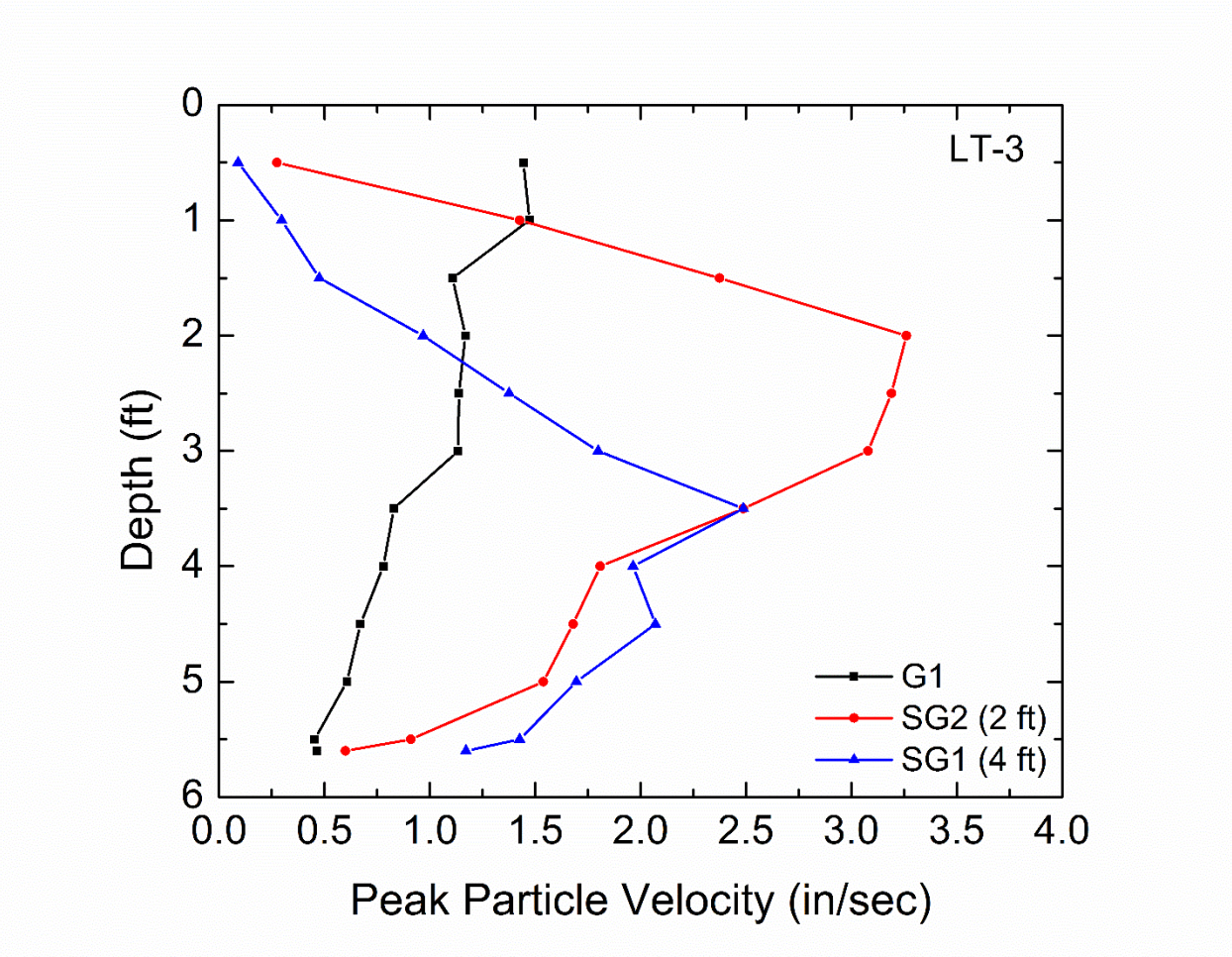

Figure 8-40 Peak Particle Velocity of G1, SG2 and SG1 geophones - LT-3 test

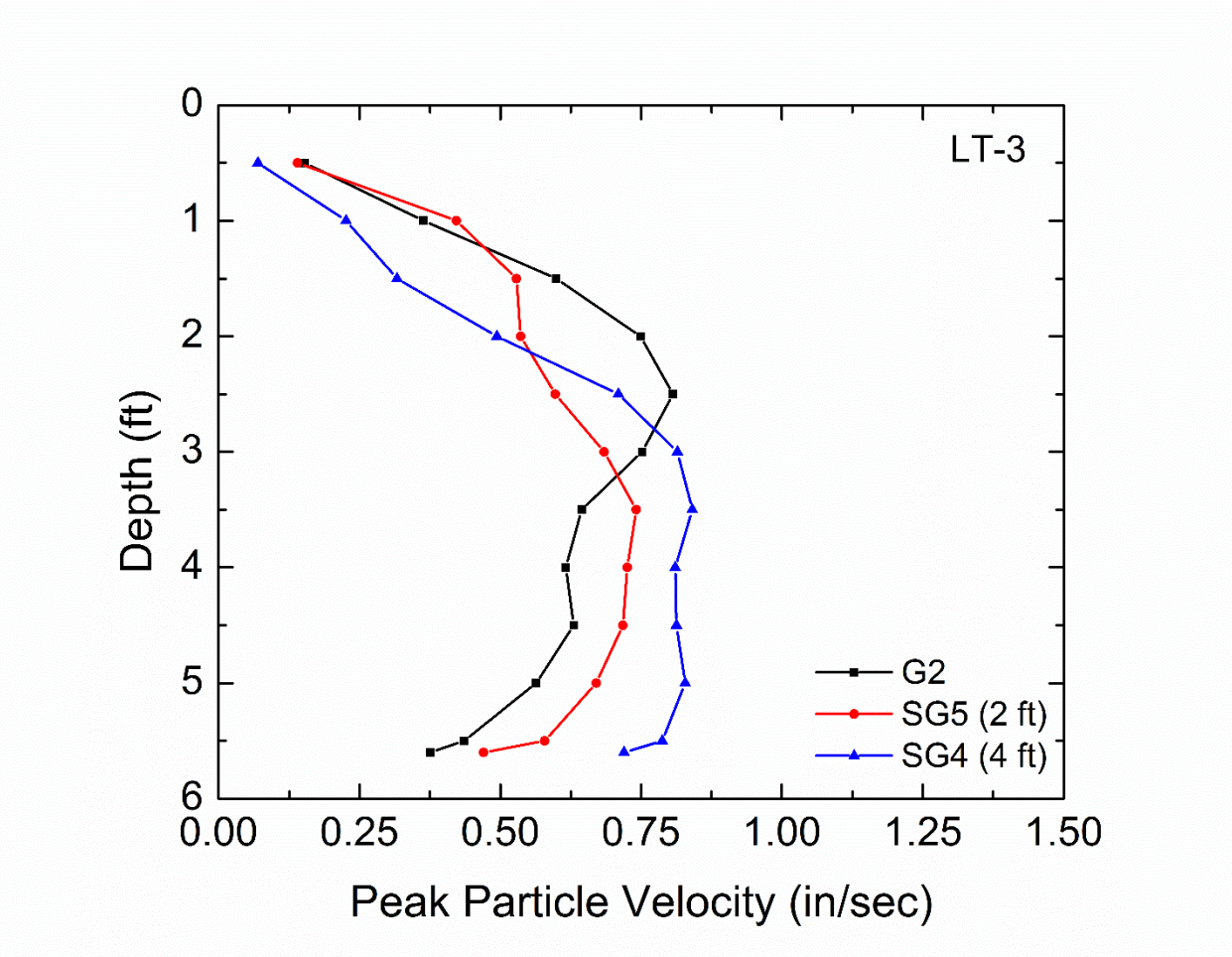

Figure 8-41 Peak Particle Velocity of G2, SG5 and SG4 geophones - LT-3 test

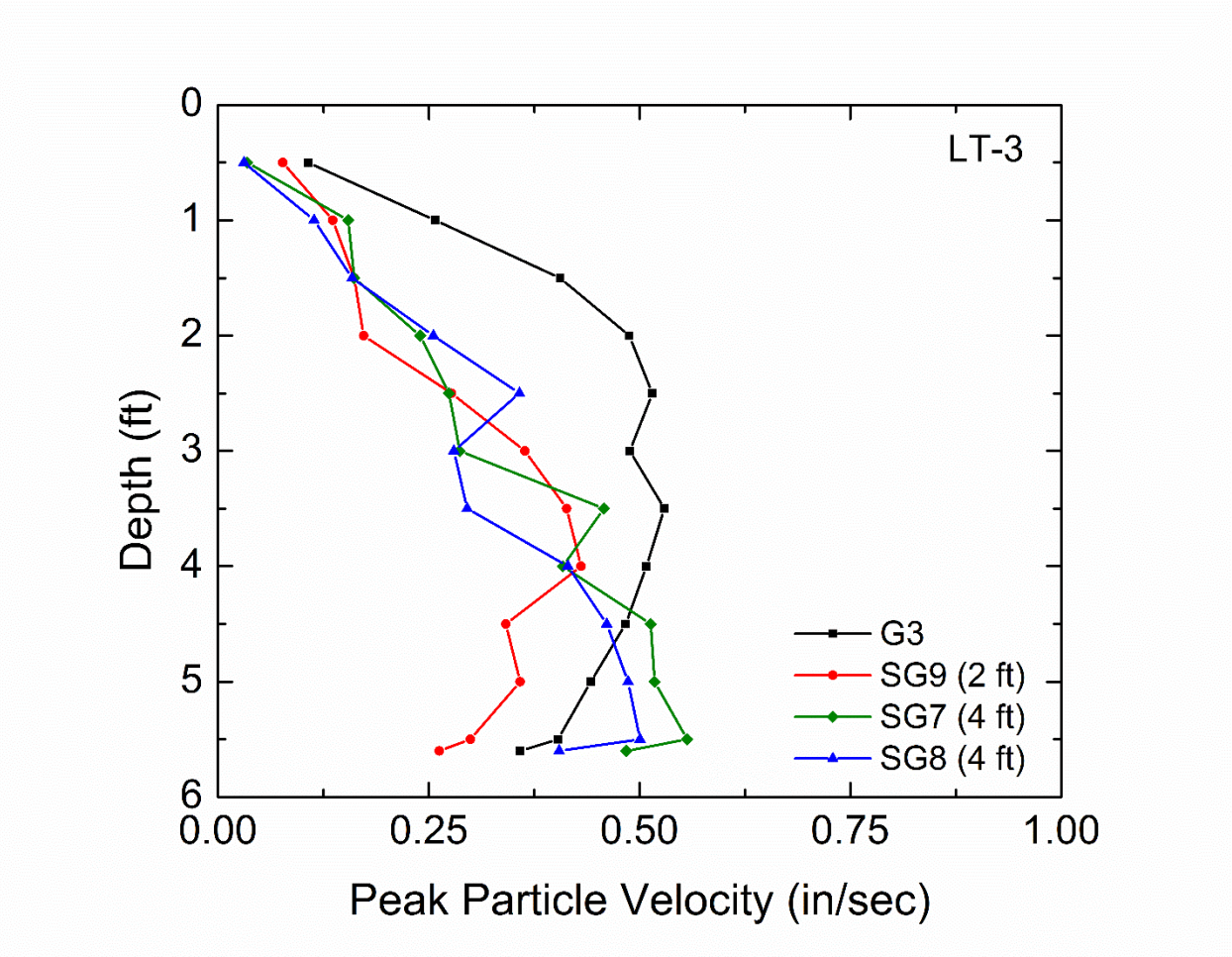

Figure 8-42 Peak Particle Velocity of G3, SG9, SG7 and SG8 geophones - LT-3 test

8.4 Understanding the energy transfer mechanism from impact pile driving

In this section, ground motions recorded during driving a small scale pile in the sand bin will be analyzed in a different way, in an attempt to understand how different types of waves emanate from a linear source. Wave propagation can be easier investigated in a controlled environment like the sand bin, which consists of a uniform sand, and simplifies the problem. In addition, sensors were placed at different distances from the pile and three different elevations; surface, 2 ft and 4 ft. Examination of the responses from sensors located in the same row (same depth), but also in the same column (same horizontal distance from the pile) will be discussed. Interesting trends are revealed from the laboratory recordings, which are hard to be captured in the field where the soil stratification makes the problem more complicated.

Test LT-3 was performed with 13 sensors recording simultaneously ground motions while driving the pile into the sand. Figure 8-43 presents a cross section view of the buried and surface sensors located at approximately the same distance from the pile but different depths. The geophones were strategically placed as shown in Figure 8-43, in order to investigate changes in ground motions as the pile penetrated further into the sand. This is because the pile is not a point source vibrating on the ground, but a linear source which constantly changes position into the ground.

Figure 8-44 to Figure 8-46 present peak particle velocities versus penetration depth for sensors located at different depths but approximately the same distance from the pile. Peak particle velocities of all the blows, and not the maximum from every half foot, are plotted. It is interesting to notice how the surface sensors recorded ground motions as the distance from the pile increases. Obviously, the closest column of sensors to the pile (Figure 8-44) recorded the higher amplitudes compared to the next two sets of sensors (Figure 8-45 and Figure 8-46). However, surface geophone G3, which is located at 2.4 ft distance from the pile, recorded higher amplitudes than the embedded sensors, SG9 and SG7, located almost right below G3 (Figure 8-46) until the end of driving. This behavior

is seen for sensors located at the second furthest distance from the pile (Figure 8-45), but motions recorded from surface geophone G2 started to decrease around 3.5 ft depth and were lower than those recorded from the deepest sensor (SG4) of this set. Interestingly, sensor G1 which is the closest surface sensor to the pile recorded lower ground motions than both the closest embedded sensors at 2 ft and 4 ft (Figure 8-44). This behavior is an indication of a Rayleigh wave development that may have been captured from the furthest surface geophones, G2 and G3, but not from the very close one, G1.

Another important parameter that needs to be examined is the inclination of the pile tip to the sensor distance, with the horizontal. Since the pile tip changes elevation constantly during driving, this inclination will also constantly change for an observation point as the pile penetrates further into the sand. Spherical waves emanating from the tip will be distributed differently if we compare different observation points. Figure 8-47 shows the difference in inclinations for the four surface geophones when the pile tip is at 1.7 ft. As the pile driving proceeds, the inclination from the horizontal increases for all four locations, however the closer the observation point to the pile, the steeper the angle. Figure 8-48 depicts the response of the four surface geophones versus the increasing inclination. The peak particle velocities recorded when the pile tip is at different depths, are normalized to the amplitude at surface. For sensor G1, which is closer to the pile, pile driving starts and the inclination increases very fast to 77° when the pile tip reaches a depth of 1.7 ft (Figure 8-47). The amplitudes are almost constant until this elevation, with a slight decrease and increase, but after reaching the depth of 1.7 ft, and consequently an angle of 77°, the amplitudes have a constant decreasing rate until the end of driving, where the peak particle velocity is 20% of the amplitude recorded at the beginning of driving at surface.

A totally different behavior is observed for the next three surface geophones in the array. As pile driving proceeds, the ground motions increase until the pile tip is at an elevation of 1.7 ft. The corresponding angles at this depth are 54° for G2, 35° for G3 and 26° for G4 (Figure 8-47). Then, the particle velocities stay constant and after the pile tip reaches a depth (different for each sensor) the amplitudes start to decrease. The phenomenon is less obvious for the furthest sensor (G4) from the pile. However,

amplitudes are still higher even at the end of driving than the PPV recorded when the driving started, in contrast to the behavior of sensor G1. This trend can be attributed to the fact that the closer sensor to the pile, G1, not only is very close for the Rayleigh wave development, but also cannot sense the spherical waves emanating from the tip with the steep angle of the horizontal to its location. The inclination of the two furthest geophones from the pile, G3 and G4, has a much lower increasing rate, and even with the geometric damping that takes place due to the constantly increasing distance from the pile tip, the amplitude is around 300% of the amplitude recorded when pile driving started.

Figure 8-49 presents the velocity time history of one blow when the pile tip was at 1.18 ft, recorded by sensors G3, SG9 and SG7. These sensors are approximately at the same distance from the pile (~2.5 ft) and at three different elevations, surface, 2 ft and 4 ft, respectively. Sensors G3 and SG9, captured different wave types while the deepest sensor, SG7, sensed only one wave type, having one peak. This behavior was expected as cylindrical waves travelling from the shaft were not captured yet by the deep sensor when the pile tip was still at shallow depths. To conclude, the wave propagation model from impact pile driving into a uniform soil is supported by the above observations.

Investigation of the wave propagation captured by the buried sensors will be discussed in terms of the inclination change of the horizontal and the pile tip to sensor distance. For the shallow set of sensors at 2 ft, pile driving starts with the inclination decreasing until the pile reaches the sensors' depth where the inclination is zero for all the sensors in the row. After the pile tip passes the elevation of the sensors, the inclination increases until the end of driving. The decreasing and increasing rate of the inclination is different for the three sensors at 2 ft. Figure 8-50 shows the angles with the horizontal when the pile tip is at 1.4 ft and 2.6 ft; i.e. 0.6 ft above and below the sensors' depth respectively.

Figure 8-51 presents the normalized responses of the three shallow sensors to the motion recorded when the pile tip was at the sensors' depth (2 ft) versus the inclination change during driving. The black line indicates driving when the pile tip is above the elevation of the sensors and the blue line corresponds to responses after the pile tip passed the depth of 2 ft. As pile driving starts, black line at bottom left side of graphs, the

inclination decreases reaching a value of zero at 2 ft. Then, follow the blue line from top to bottom with the inclinations increasing until the end of driving.

For sensor SG2, which is the closest to the pile, pile driving starts with a very steep angle around 82°. At a depth of 1.4 ft and 67° with the horizontal (Figure 8-50), and still above the sensor's depth, the amplitude reaches 80% of the amplitude recorded at 2 ft. Then, the ground motion stays relatively constant and when the pile tip is at 2.6 ft and 67° again, the peak particle velocities start to decrease, being almost 15% of the PPV at 2 ft at the end of driving. This behavior can be explained again with the energy distribution of the body waves coming from the tip. There is a maximum inclination from the horizontal as the pile tip penetrates into the sand, where the spherical wave front can be captured at its maximum from the sensor.

Examining the behavior of the furthest sensor from the pile, SG9, in a similar way reveals a different behavior. At the beginning of pile driving, the inclination is around 35°, much lower than the steep angle that the first sensor had (82°). When the pile tip reaches a depth of 1.4 ft and 13° with the horizontal (Figure 8-50a), sensor SG9 recorded almost 100% of the motion recorded when the pile tip reached the sensor's elevation (2 ft). After the tip passed the latter depth, amplitudes stayed relatively constant until a depth of 4.8 ft (47°) where they started to decrease. However, the ground motions were higher than the record at 2 ft even at the end of driving. It is important to understand that this sensor being further away from the pile recorded much lower amplitudes than SG2 that was very close to the pile, but the responses never got lower than the amplitude recorded at 2 ft. This is attributed to the fact that SG9 geophone can still sense waves coming from the tip at deeper penetration depths in comparison with the close sensor, SG2, which gets to steep angles very fast, above and below its depth, and body waves do not contribute anymore. Thus, when the pile tip is below sensor SG2, it is primarily the shear waves from the shaft that are recorded at this close distance from the pile.

Sensor SG5, which is the intermediate sensor of the shallow array follows the trend of the furthest sensor. Again, amplitudes increased as the pile tip reached the depth of the sensor and stayed relatively constant after the tip passed the 2 ft depth until a depth of 4.8 ft (67°) where they started to decrease falling at around 65% of the PPV at 2 ft at

the end of driving. This phenomenon is also observed in Figure 8-30 where the peak particle velocities versus diagonal distance from the tip to the sensor are plotted. It is evident that after the pile tip passes the sensors' depth the amplitudes stay constant but then start to decrease. The trend is more evident for the observation point closest to the pile (SG2).

Figure 8-52 presents velocity time histories of one blow recorded from the three shallow sensors when the pile tip was at a depth of 2.05 ft. Figure 8-53 depicts similar time histories of one blow when the pile tip is deeper at 3.9 ft. By comparing these two Figures, it is evident that when the pile tip is at the sensors' elevation, the geophones can capture different types of waves. When the pile tip descends deeper, it is the furthest sensor from the pile (SG9) that can still see different wave fronts. The contribution of the shaft dominates for the two closest sensors to the pile (SG2 and SG5).

A similar analysis with the change in inclination can be made for the deep set of sensors at 4 ft depth. Figure 8-54 shows the normalized responses of the three sensors to the record when the pile tip was at their elevation. The difference in inclination depths for the three observation points when the pile tip was at a depth of 3` ft is shown in Figure 8-55. The amplitudes again increase as the penetration proceeds. At around 3 ft depth, the amplitude is at its maximum for the two closest sensors to the pile, SG1 and SG4. This means that after the pile tip reached this depth, the sensors can capture the maximum amount of energy coming from the tip. After the pile tip passed the elevation of the sensors, the amplitudes stay constant with a slight decrease observed for sensor SG1 which is closer to the pile. Sensor SG7, which is the furthest from the pile face, has increasing amplitudes after the pile tip passed its elevation until the end of driving. As observed in the shallow set of sensors, the amplitudes are higher than the response recorded at 4 ft until the end of driving. With end of driving at 5.6 ft, a decrease in responses of the blue line were not able to be developed.

Figure 8-56 and Figure 8-57 present velocity time histories of the three sensors when the pile tip was at 4.06 ft and 2.26 ft, respectively. It is obvious that when the pile tip is at the sensors' depth, the geophones capture similar wave types. Also, it is observed that

the period is larger, thus the frequency decreases as the distance from the pile increases (Figure 8-57).

To conclude, the above discussion supports the wave propagation mechanism and explains the decrease in particle motions that is happening after the pile tip passes the sensors' elevation located very close to the pile. This behavior was also observed in the field responses but of course is much harder to be interpreted due to the reflections and refractions that take place along with the above phenomena. The energy distribution from the spherical waves depends on the inclination of the tip to the observation point distance with the horizontal which has steeper angles the closer we are to the pile. Therefore, after the pile tip passes the point of observation, cylindrical waves are captured travelling from the shaft, but spherical waves from the tip will have a lower contribution the closer we are to the pile.

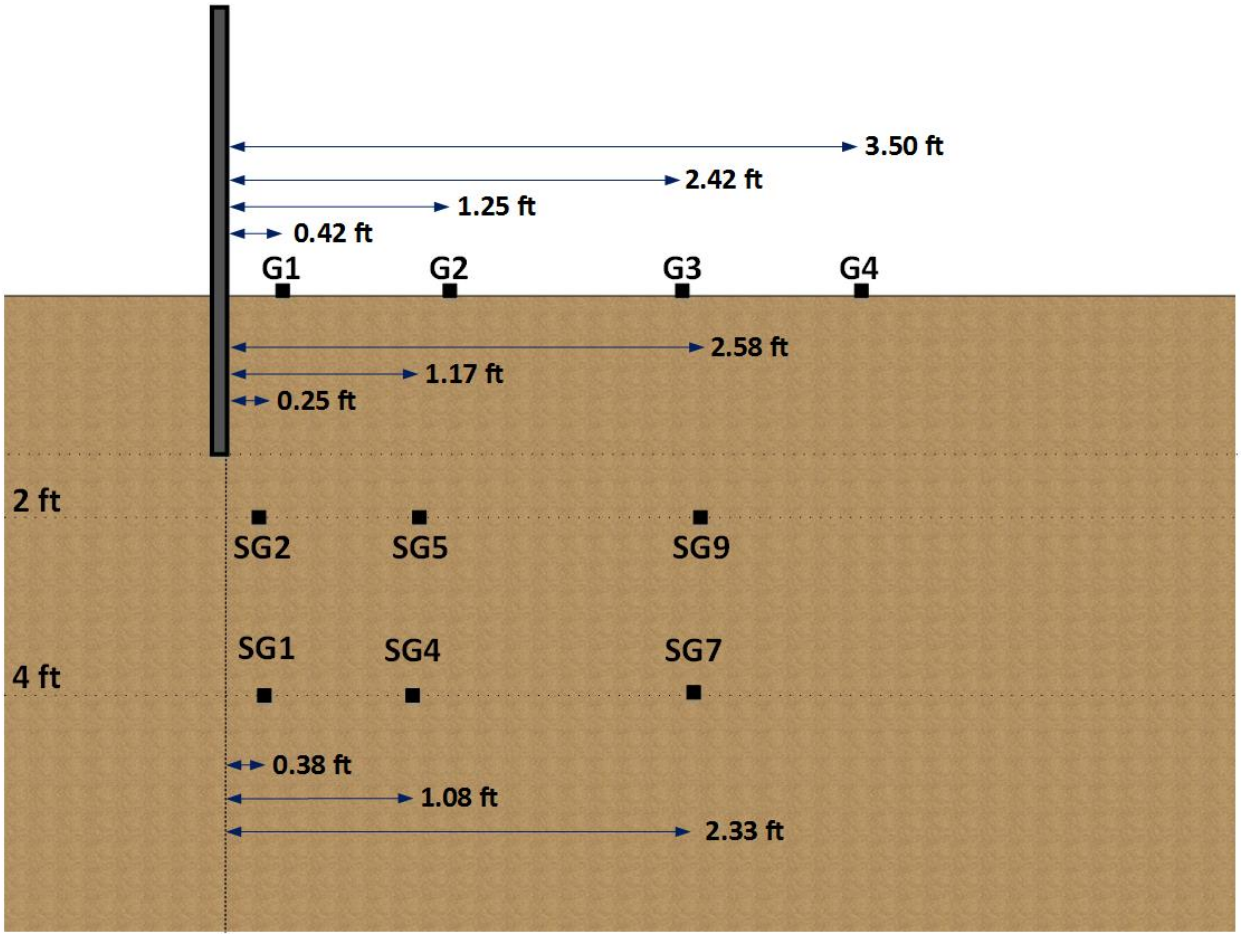

Figure 8-43 Surface and embedded sensors at LT-3 test

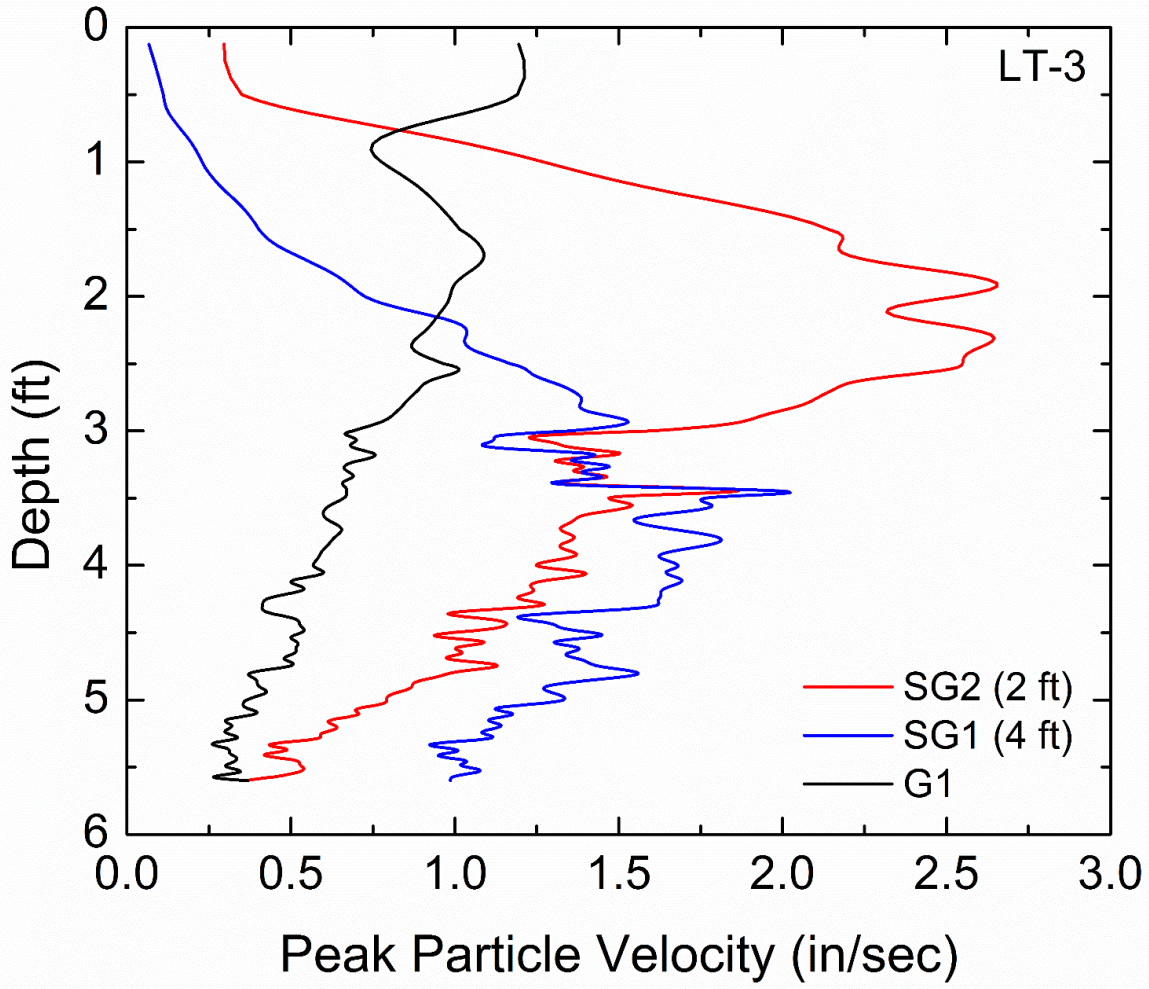

Figure 8-44 Peak particle velocities recorded by G1, SG2 and SG1 geophones – LT-3 test

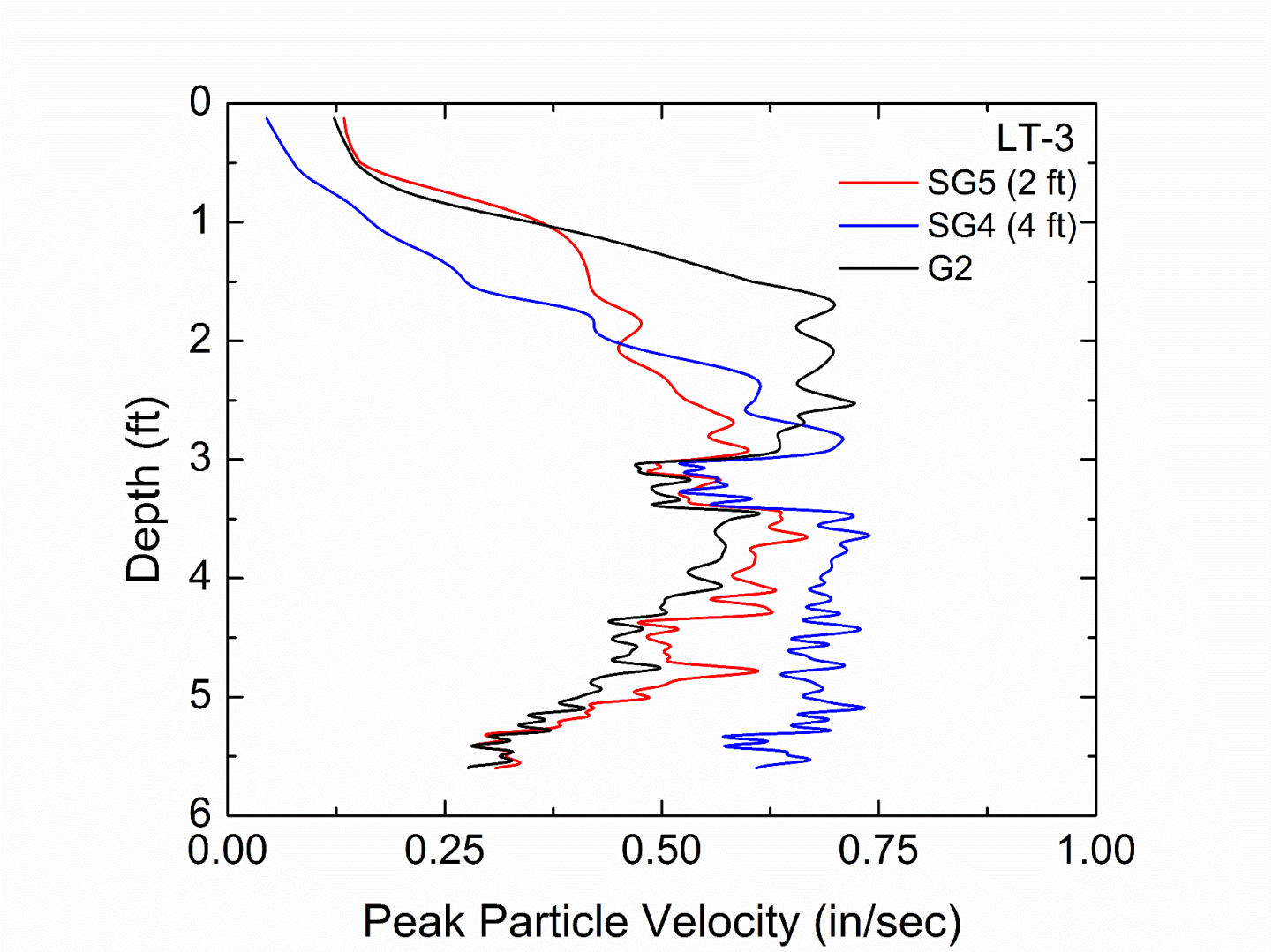

Figure 8-45 Peak particle velocities recorded by G2, SG5 and SG4 geophones – LT-3 test

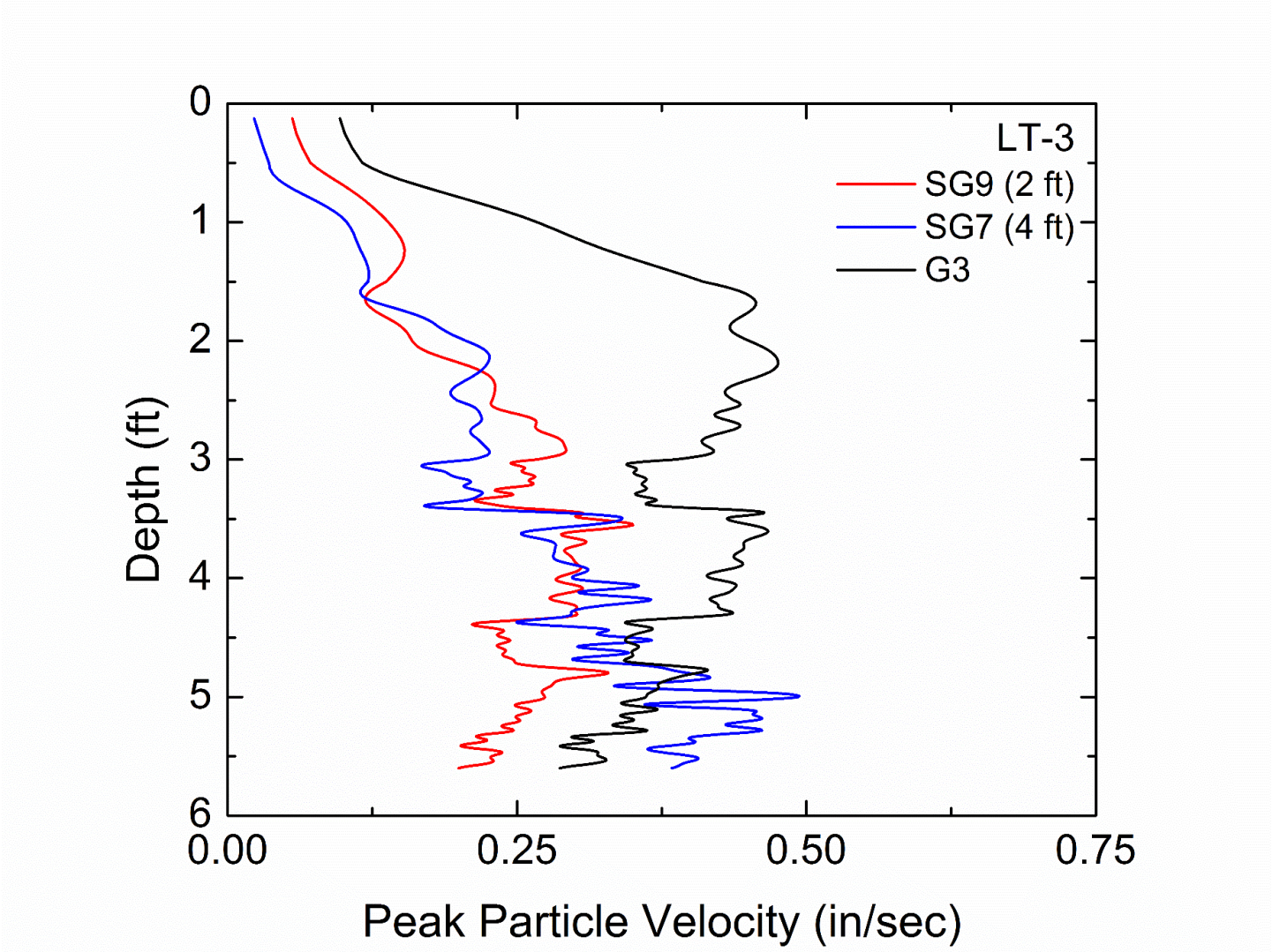

Figure 8-46 Peak particle velocities recorded by G3, SG9 and SG7 geophones – LT-3 test

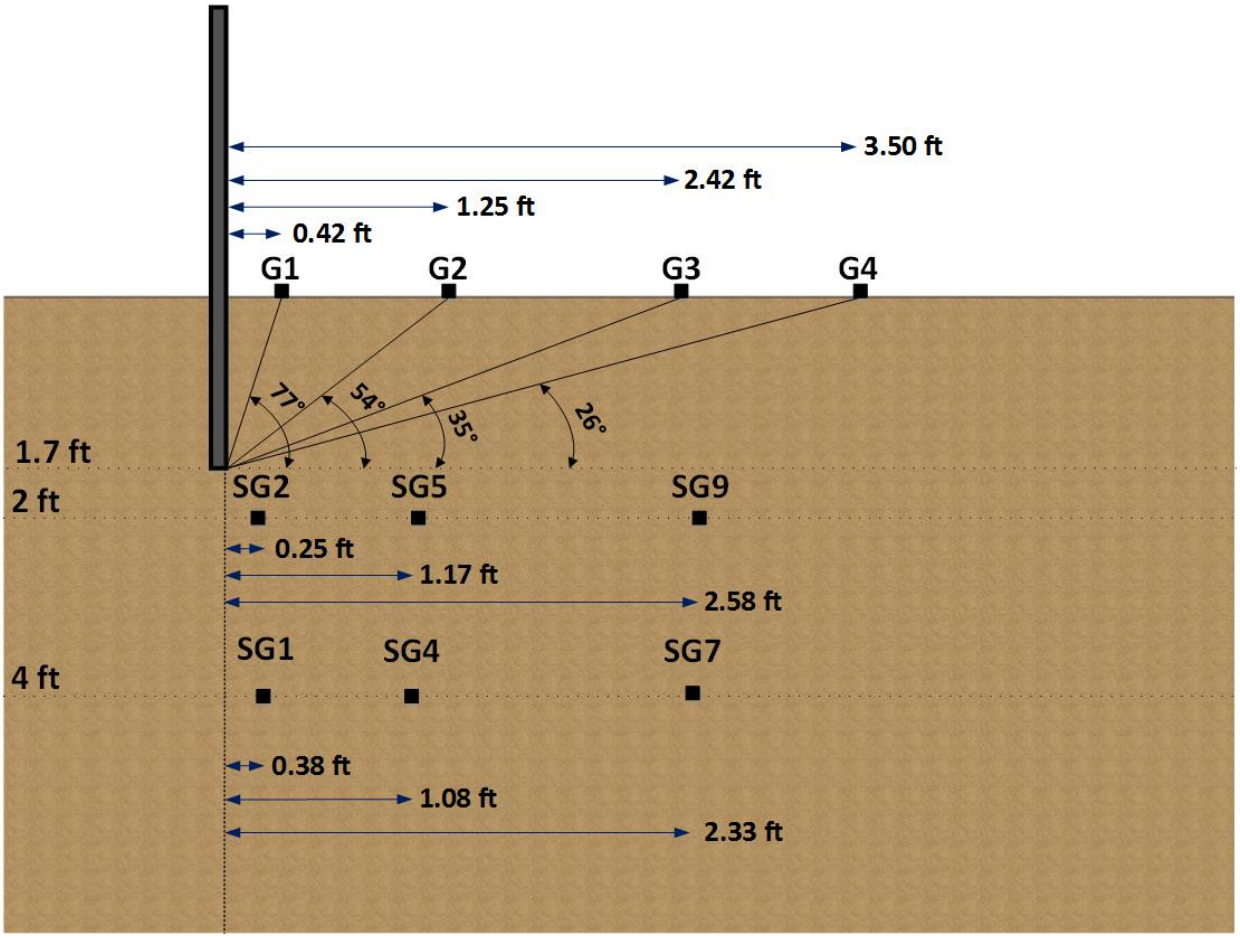

Figure 8-47 Inclination of pile tip to surface sensor distance with the horizontal – pile tip at 1.7 ft

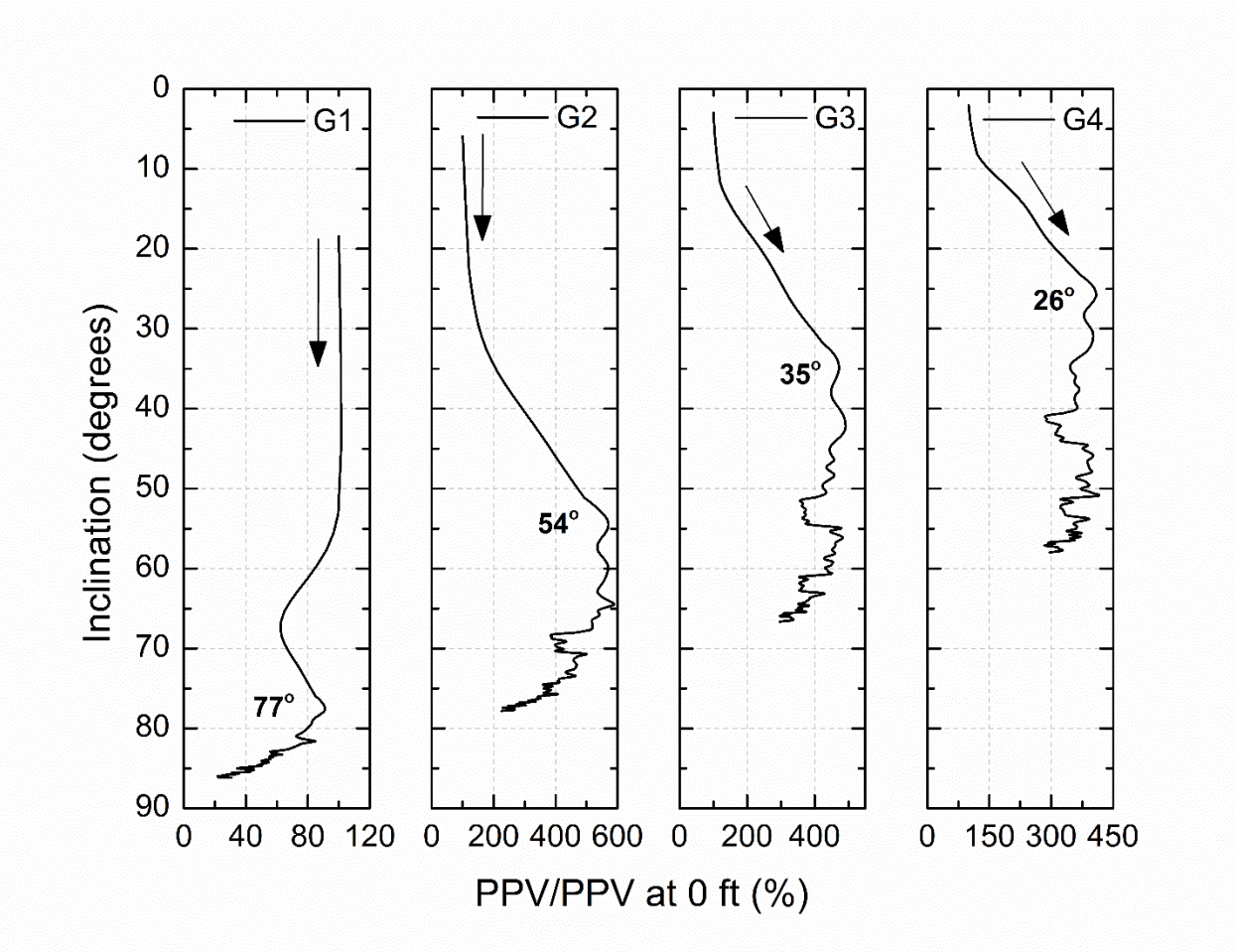

Figure 8-48 Normalized PPVs with PPV at surface versus change in inclination – Surface geophones

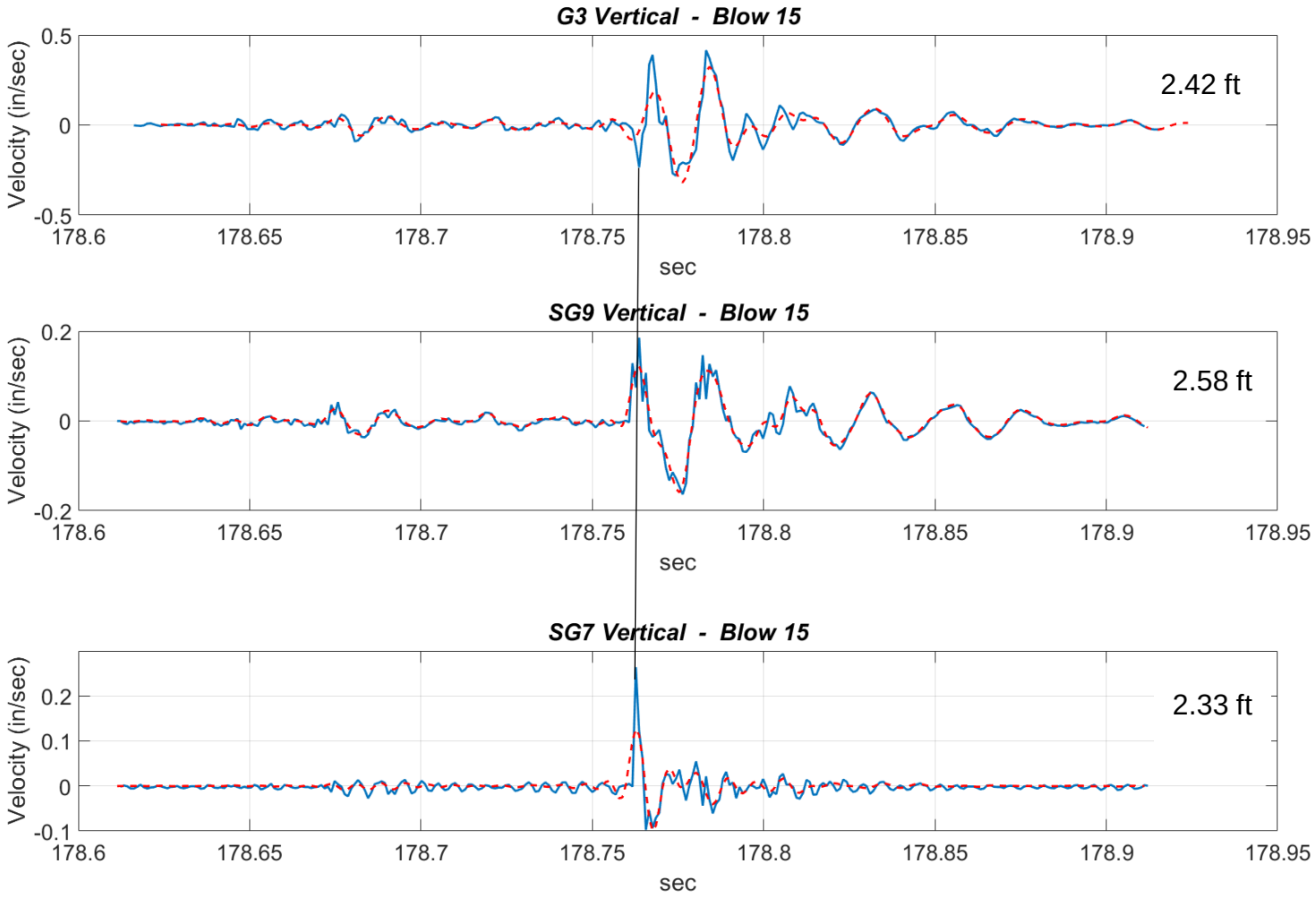

Figure 8-49 Velocity time history of one blow recorded by sensors G3, SG9 and SG7 – pile tip at 1.18 ft

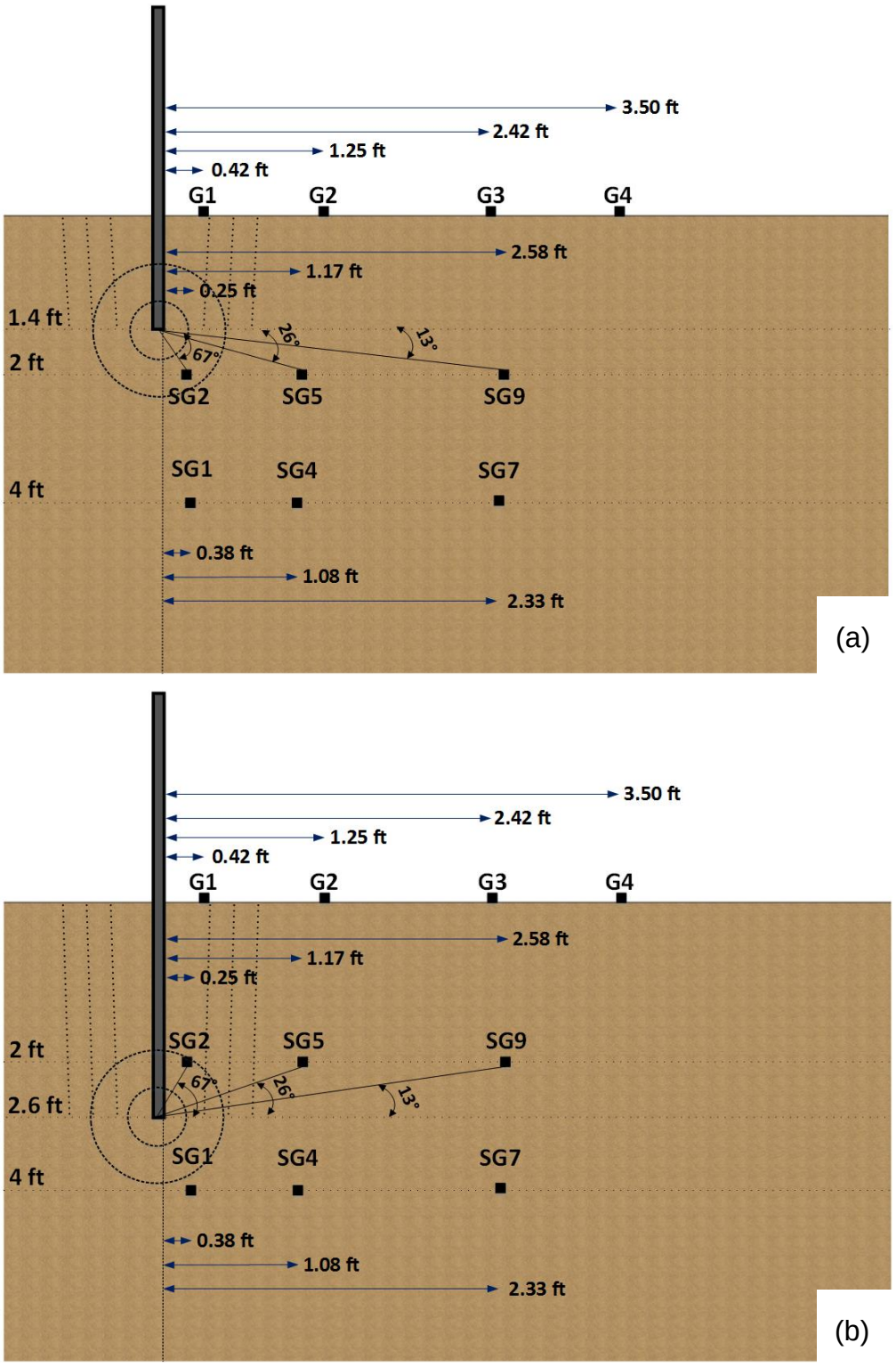

Figure 8-50 Difference in inclinations for shallow set of sensors when pile tip is (a) 0.6 ft above and (b) 0.6 ft below sensors' elevation

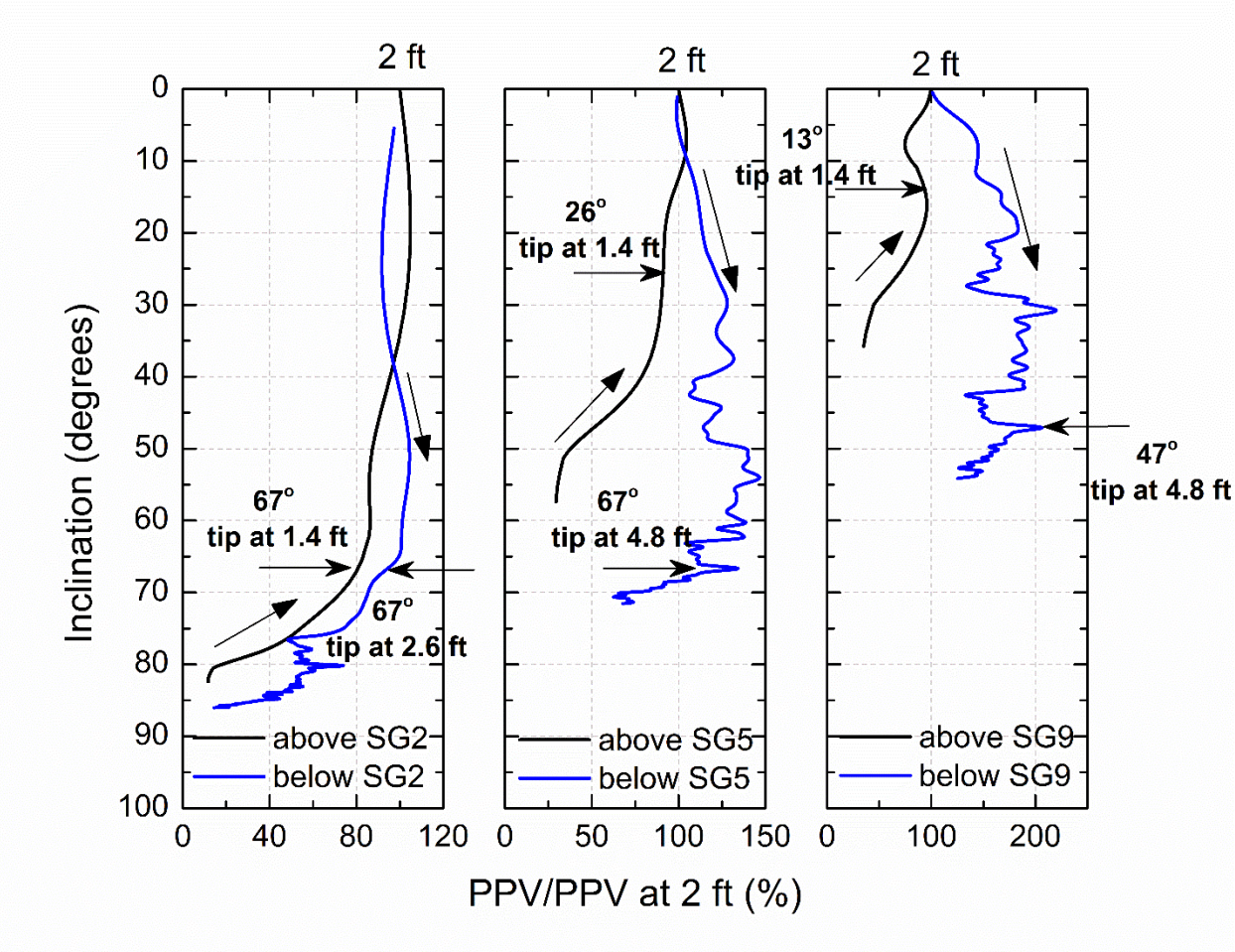

Figure 8-51 Normalized responses of shallow set of sensors with motion when pile tip was at sensors' elevation versus change in inclination

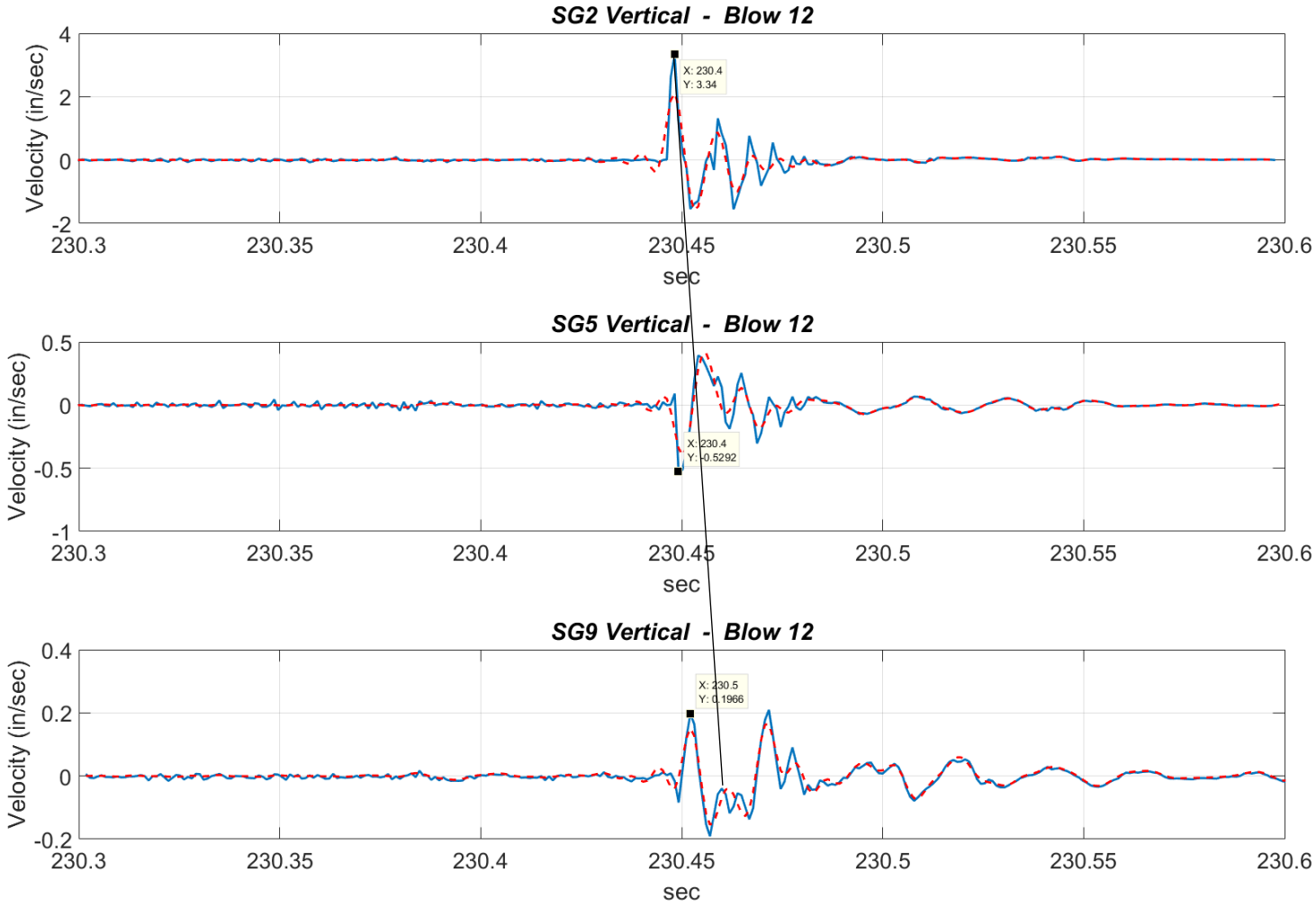

Figure 8-52 Velocity time history of one blow recorded by sensors SG2, SG5 and SG9 – pile tip at 2.05 ft

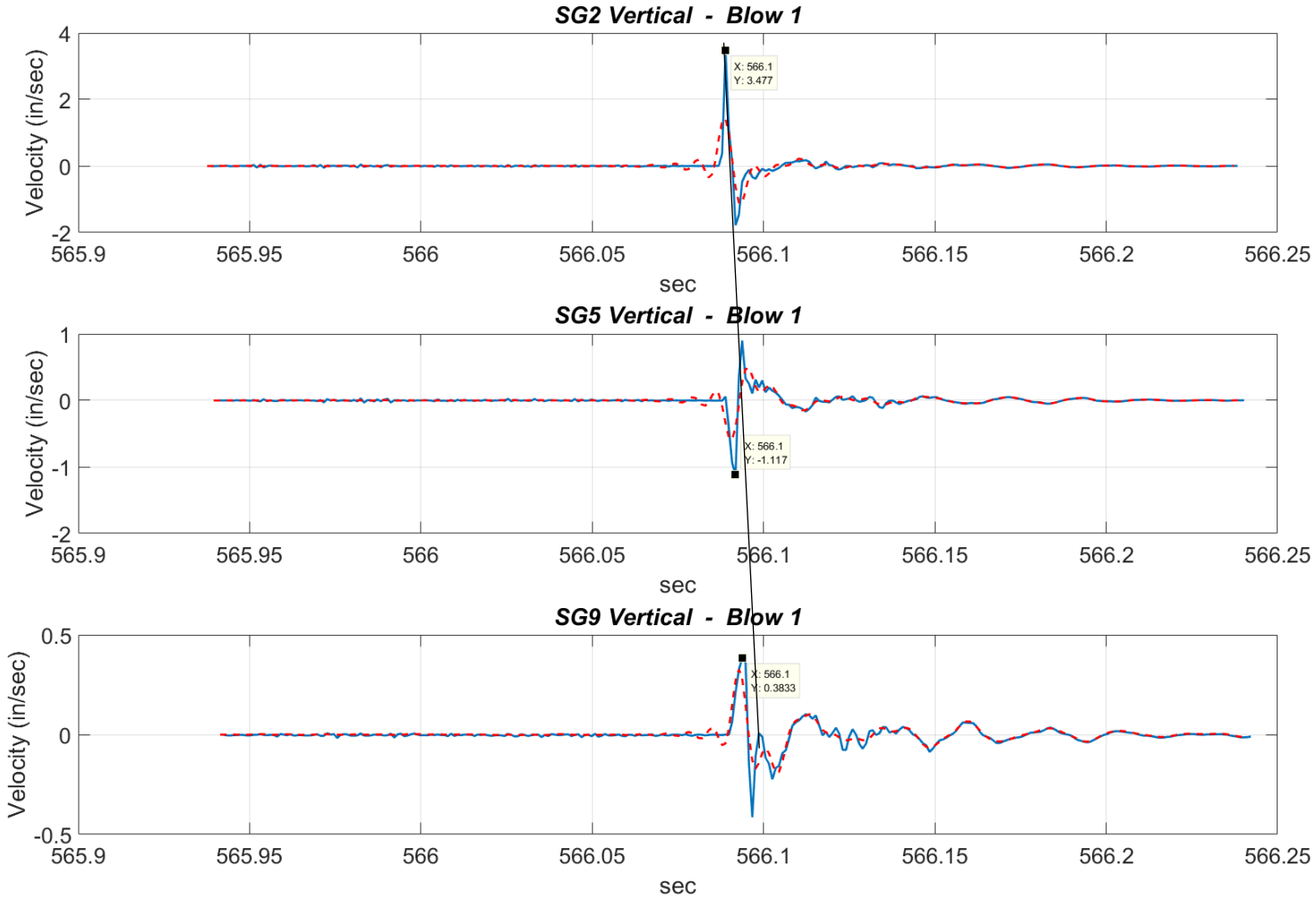

Figure 8-53 Velocity time history of one blow recorded by sensors SG2, SG5 and SG9 – pile tip at 3.9 ft

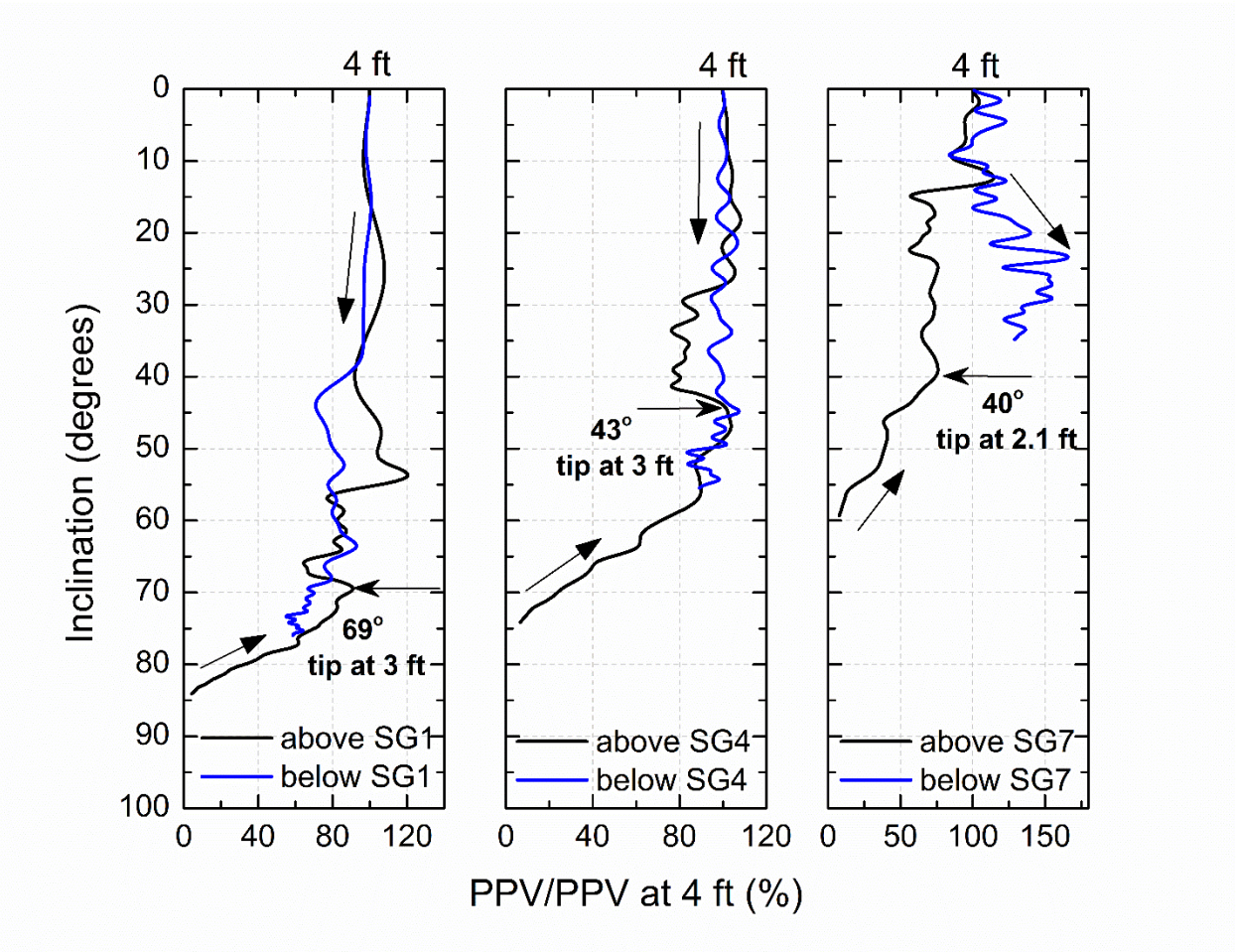

Figure 8-54 Normalized responses of deep set of sensors with motion when pile tip was at sensors' elevation versus change in inclination

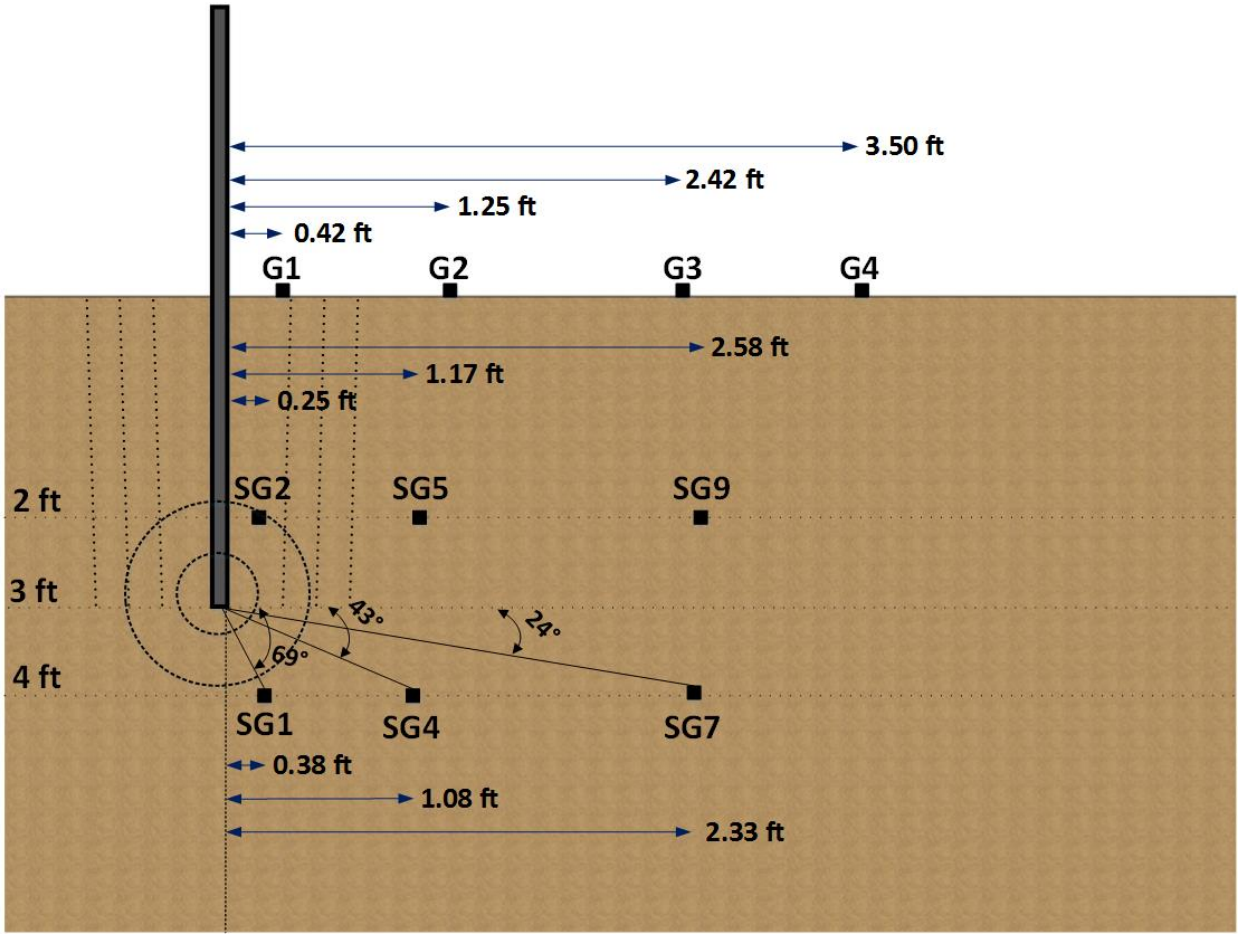

Figure 8-55 Difference in inclinations for deep set of sensors when pile tip is at 3 ft

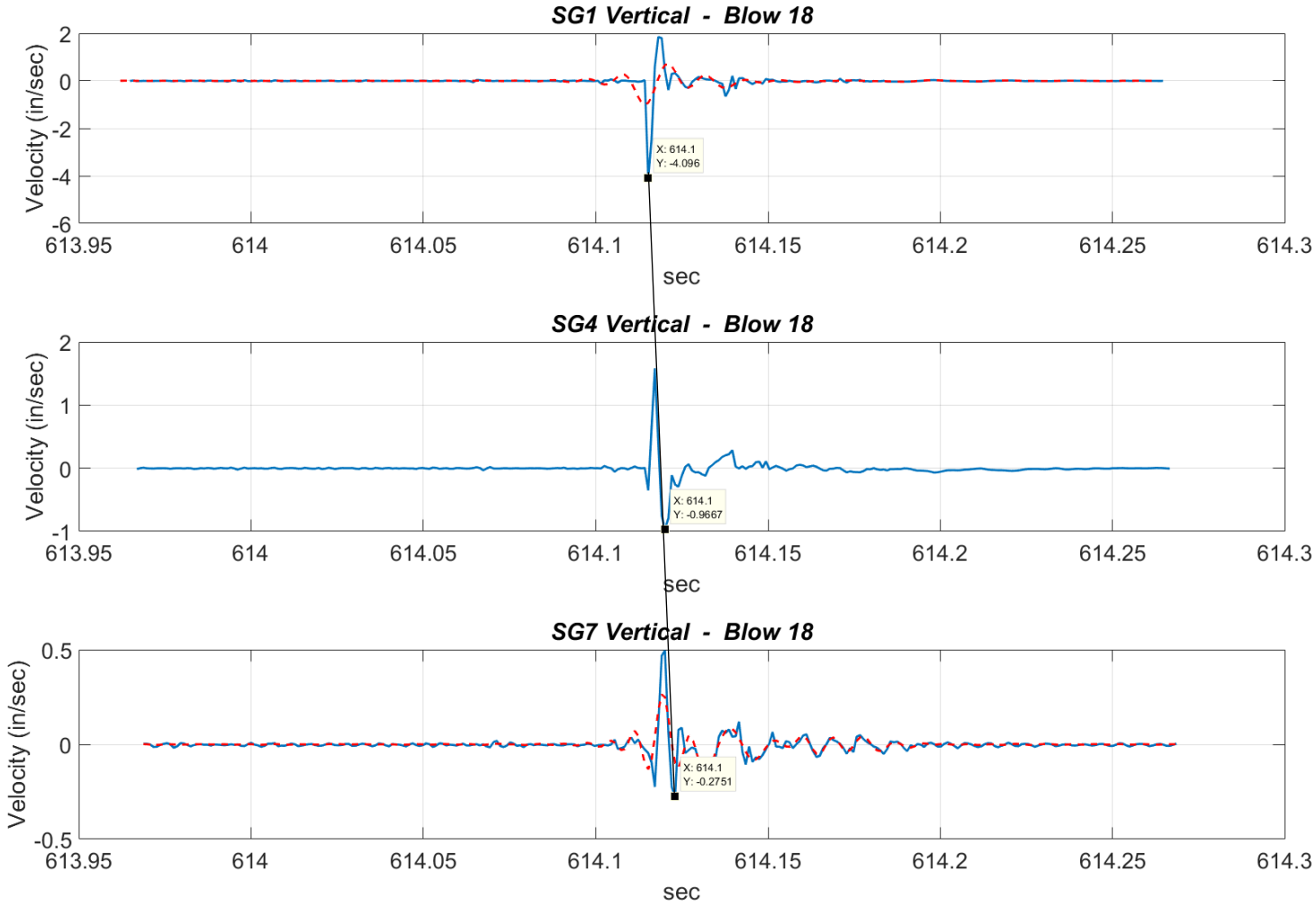

Figure 8-56 Velocity time history of one blow recorded by sensors SG1, SG4 and SG7 – pile tip at 4.06 ft

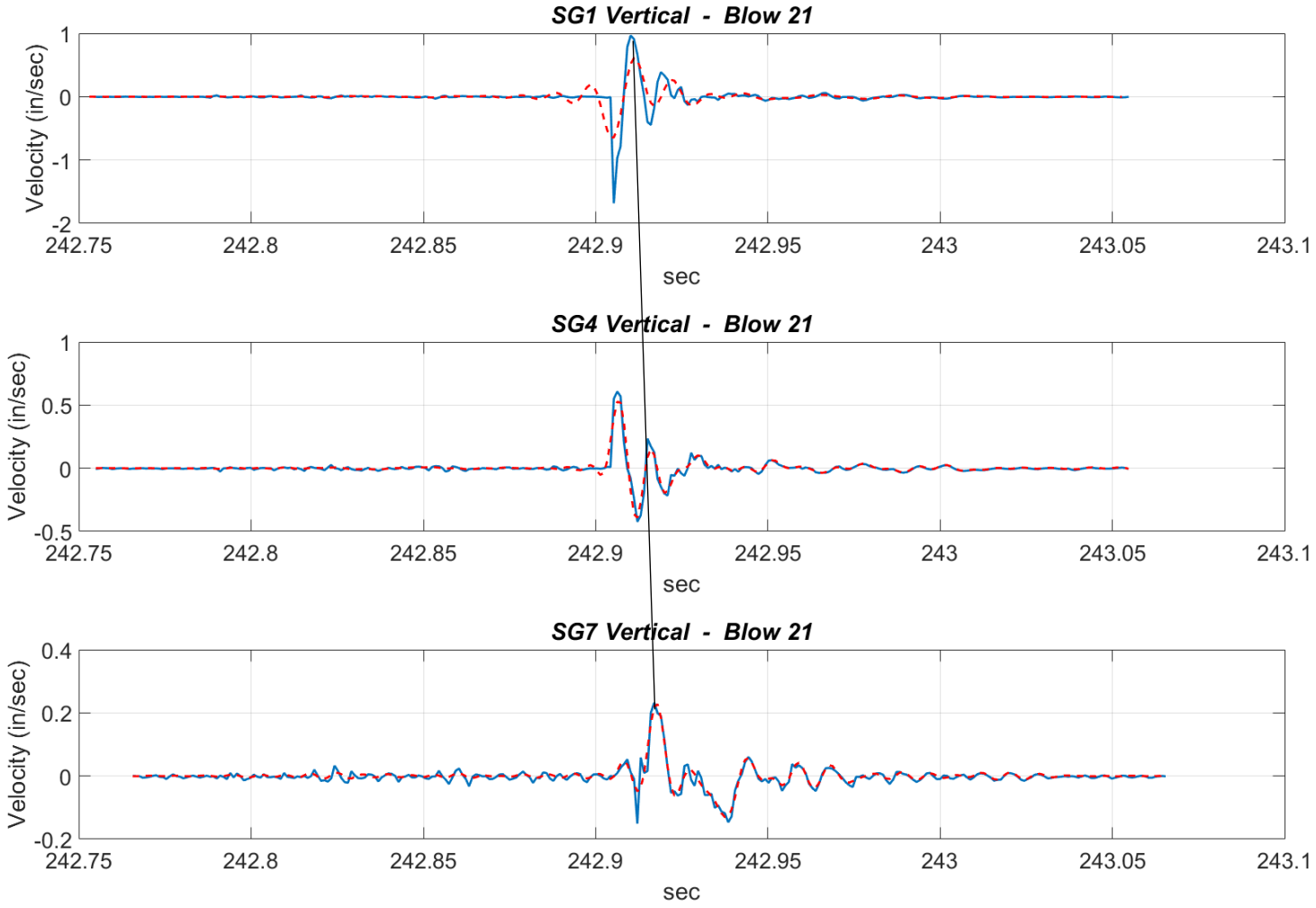

Figure 8-57 Velocity time history of one blow recorded by sensors SG1, SG4 and SG7 – pile tip at 2.26 ft

8.5 Attenuation of waves from model pile driving

The same formulas that were fitted to field ground motions were used to study the attenuation of vibrations emanating from the small-scale pile driving test in the laboratory. Specifically, the Bornitz, the Caltrans and the power pseudo-attenuation equations were employed in the form they were used to analyze the field test results.

The same procedure as for the field data processing was followed for the buried sensors in sand bin. The three prediction equations were fitted to all the laboratory measurements when the pile tip was at the elevation of the sensors and half foot above and half foot below the sensors' depth. An average attenuation coefficient was calculated from the latter procedure. The calculated attenuation coefficients when the pile tip was at the exact depth of the sensor will be presented in graphical and tabular form. Prediction bounds with 95 % confidence level are also plotted to evaluate the goodness of curve fitting. Furthermore, R-square values are provided for each plot and for the average calculated attenuation coefficients. Curve fitting was performed using a Matlab code.

Again, each of the measurement points in a row, that the attenuation coefficients were calculated, was used as a reference point to fit the curves for the cases of the Bornitz and Caltrans formulas. The Matlab routine was coded in a manner to find the attenuation coefficient, that would give the optimal fitting curve for all sensors in the row with the chosen reference point. Thus, a sensitivity analysis was conducted as the reference points were interchanged for each fitting. For the power equation, the Matlab code fitted the curve using all data without interchanging the reference point. For this reason, only one coefficient was calculated using the data and fitting the power formula. The distance from source, r, is taken as the diagonal distance from the pile tip to the point of measurement. An estimation of the vibration amplitude using the prediction curves was also conducted to calculate the peak particle velocity at the pile-soil interface. For the ground motion amplitudes collected from the surface geophones, attenuation curves were fitted using the closest sensor to the pile as the reference point, to calculate the attenuation coefficients.

8.5.1 Third Test – LT-3

For the shallow set of sensors, the three prediction equations were fitted to the measuring data when the pile tip was at the sensors' elevation, and are plotted in Figure 8-58 to Figure 8-60. For the case of the Bornitz equation, the estimated alpha parameter that was calculated when using the furthest sensor from the pile (SG9), was almost half in magnitude compared to coefficients evaluated when using the closest sensors (SG2 and SG5) to the pile as fixed points to fit the curve. The variation in calculated coefficients from fitting the Caltrans equation is not significant. The Caltrans and power attenuation coefficients are exactly the same when fitting the curves to measurements recorded when the pile tip was at the elevation of the sensors. The goodness of fit is considered very good for all three prediction formulas. Attenuation coefficients were calculated for every hammer blow when the pile tip was half foot above and half foot below the sensors' elevation (2 ft). The average estimated coefficients for this range are shown in Table 8.4 to Table 8.6 below. Average decay parameters are found to have similar magnitudes as the coefficients calculated when the tip was at the same elevation as the sensors (2 ft).

For the deep set of sensors, the prediction formulas were fitted to ground motion data when the pile tip was at the sensors' elevation (4 ft) and are plotted in Figure 8-61 to Figure 8-63. For the case of the Bornitz formula, the estimated attenuation coefficient slightly decreases, when fitting the curve using the furthest sensor to the pile (SG7) as the fixed point, in comparison to the parameter calculated with the closest observation points (SG1 and SG4) as the reference. Significant variation in the estimated parameters for the different references points (SG1, SG4, SG7) using the Caltrans equation is not observed. Curve fitting is evaluated as very good for all the prediction equations. Attenuation parameters were calculated for all the hammer blows, when the pile tip was in the range between 3.5 ft and 4.5 ft. Average values are provided in Table 8.7 to Table 8.9. Projections at the pile-soil interface estimated by the three prediction equations are also provided in the Tables.

Attenuation curves were fitted to surface ground motion amplitudes when the pile tip was at 0.5. Figure 8-64 to Figure 8-66 present prediction curves using the three formulas.

Table 8.10 to Table 8.12 show attenuation parameters calculated when the pile tip was at depths of 0.5 ft, 1.5 ft and 3 ft. The diagonal distance implemented in the equations, is constantly increasing as the pile penetrates deeper. It is observed, that when the pile tip is at 1.5 ft and 3 ft, the alpha coefficients calculated from Bornitz formula are close. The attenuation coefficient when the pile tip is at 0.5 ft is about five times higher than the latter. For the case of Caltrans and power formulas, the decay parameter when the pile tip is at 0.5 ft is again higher than when the tip has penetrated at 1.5 ft and 3ft, but the increase is less than when using the Bornitz equation; k increases by a factor of 0.7 and β by a factor of 1 when the pile tip is at 0.5 ft. Evaluation of fitting the three formulas to the measured data is considered very good.

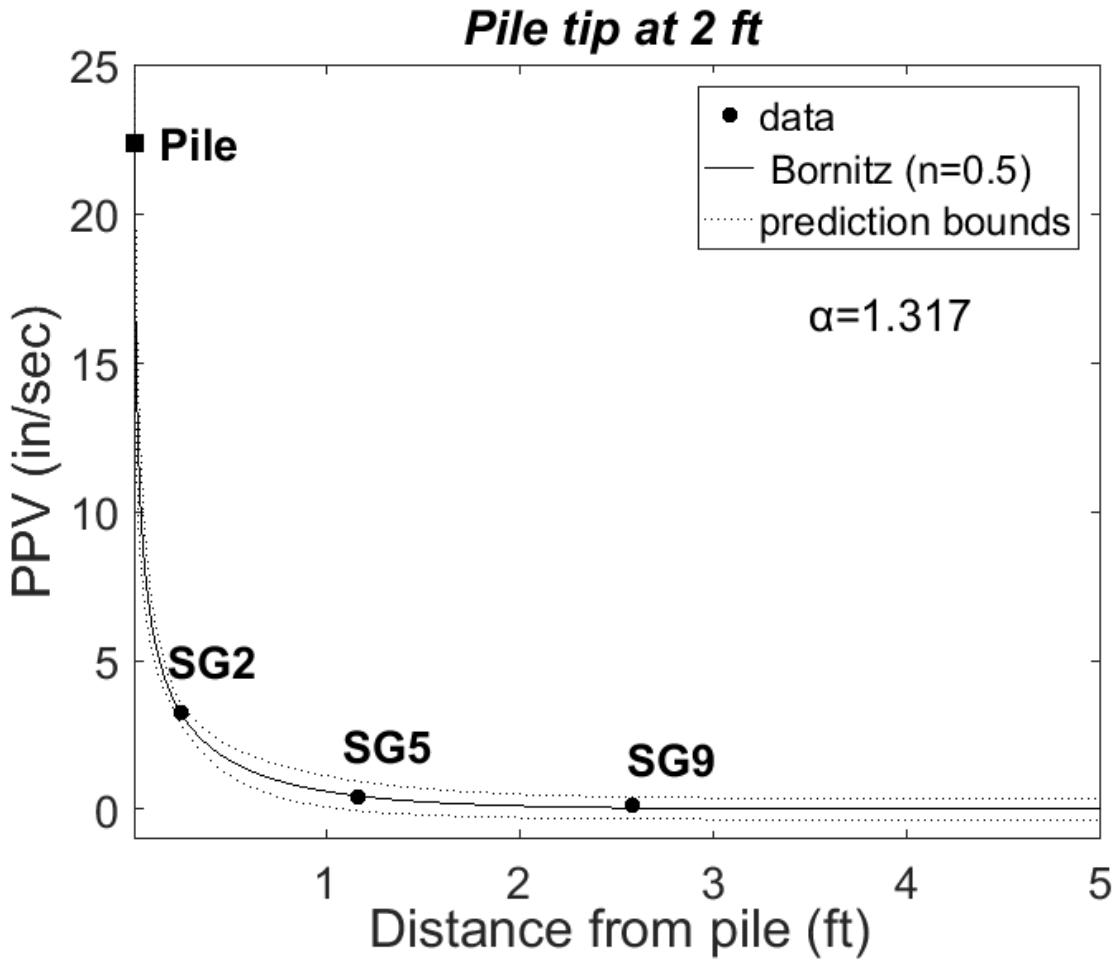

Figure 8-58 Attenuation curve for shallow sensors for LT-3 test – Bornitz Equation

Table 8.4 Data for attenuation coefficient using the Bornitz equation-2 ft

SENSOR	Distance from pile (ft)	α (1/ft), Pile tip at 2 ft	PPV (in/sec)	R^2	α (1/ft), Average Pile tip 1.5 – 2.5 ft	PPV (in/sec)	R^2
SG2	0.25	1.317	3.26	0.998	1.171	2.43	0.996
SG5	1.20	1.391	0.42	0.998	1.253	0.47	0.995
SG9	2.60	0.786	0.16	0.984	0.747	0.17	0.978
PILE	0.01		22.37			23.85	

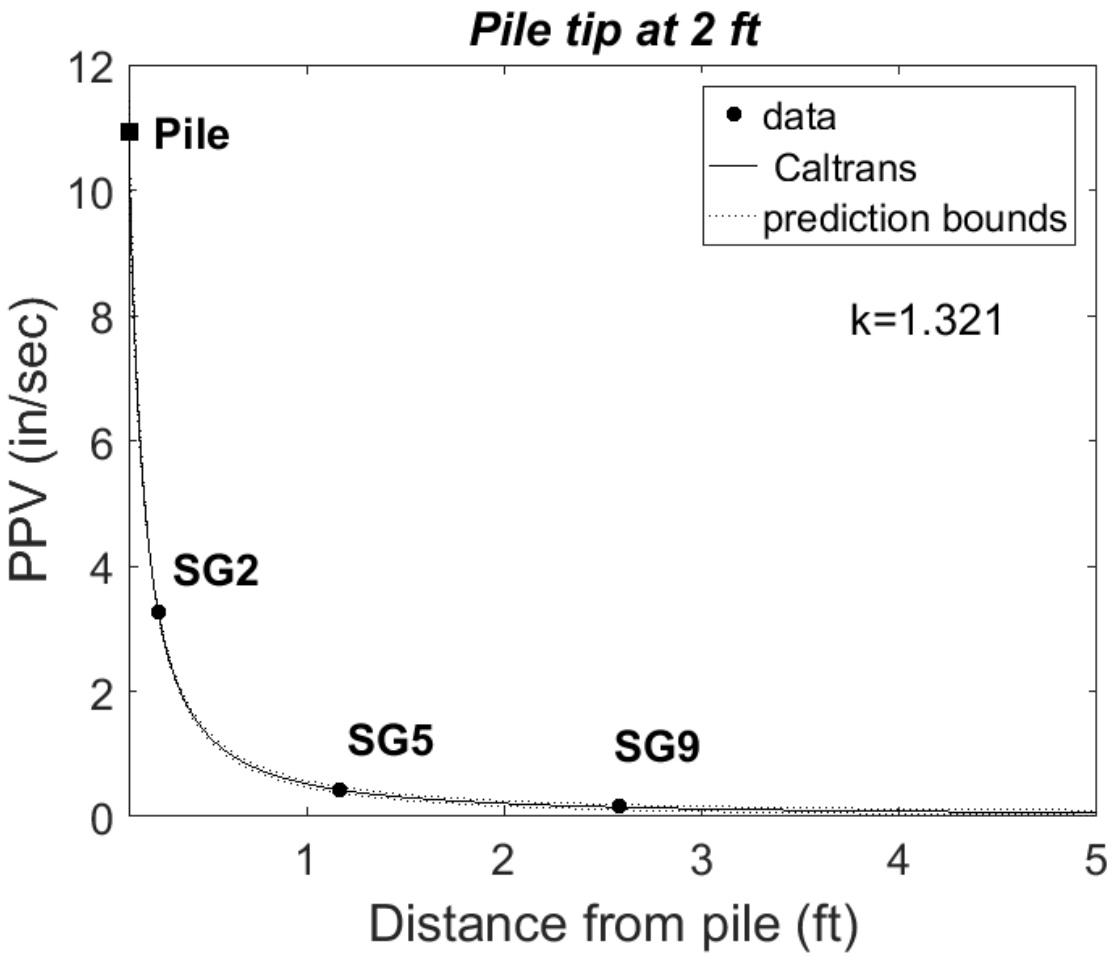

Figure 8-59 Attenuation curve for shallow sensors for LT-3 test – Caltrans Equation

Table 8.5 Data for attenuation coefficient using the Caltrans equation- 2 ft

SENSOR	Distance from pile (ft)	k, Pile tip at 2 ft	PPV (in/sec)	R^2	k, Average Pile tip 1.5 – 2.5 ft	PPV (in/sec)	R^2
SG2	0.25	1.321	3.26	1.000	1.391	2.43	0.999
SG5	1.20	1.330	0.42	1.000	1.400	0.47	0.999
SG9	2.60	1.291	0.16	1.000	1.365	0.17	0.997
PILE	0.10		10.94			19.48	

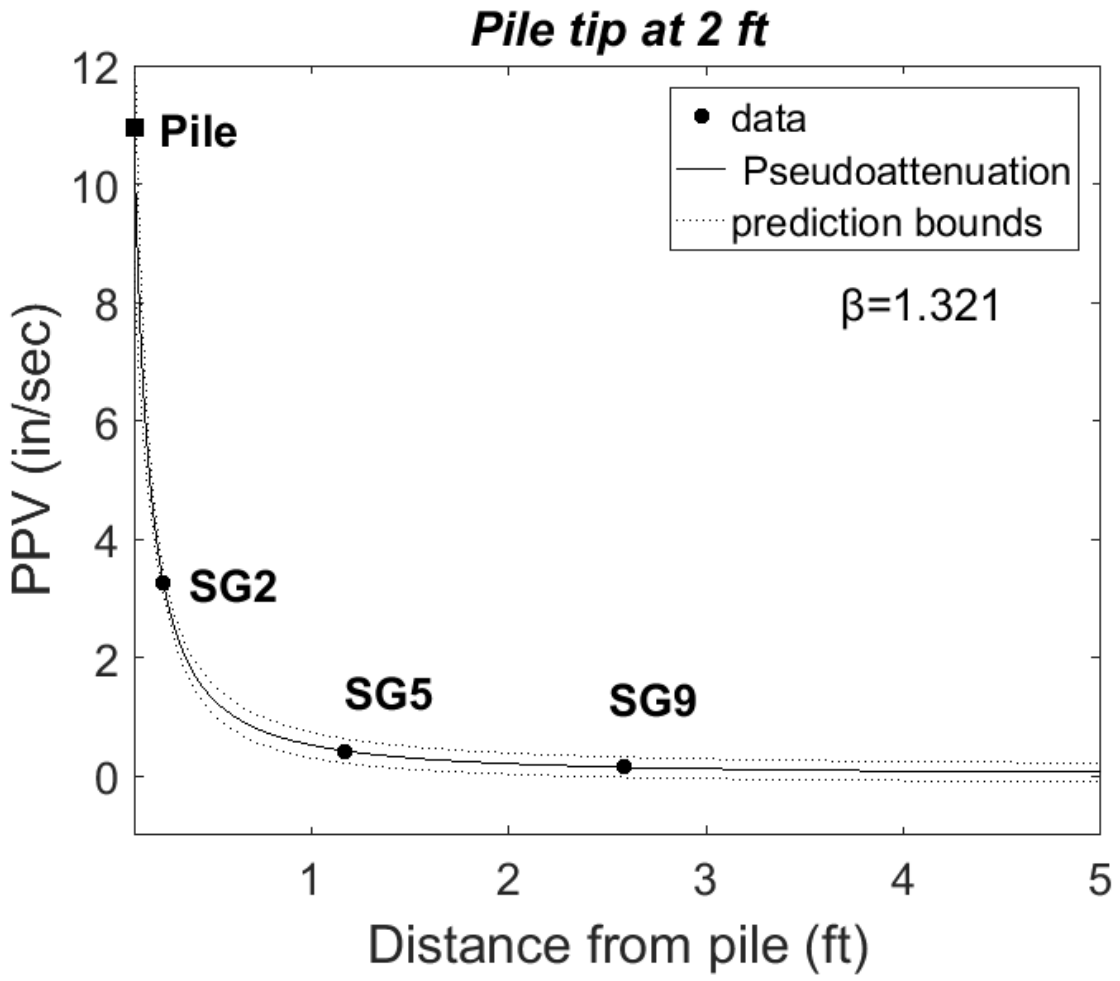

Figure 8-60 Attenuation curve for shallow sensors for LT-3 test – power Equation

Table 8.6 Data for attenuation coefficient using the power equation-2 ft

SENSOR	Distance from pile (ft)	β, Pile tip at 2 ft	PPV (in/sec)	R^2	β, Average Pile tip 1.5 – 2.5 ft	PPV (in/sec)	R^2
SG2	0.25	1.321	3.26	1.000	1.407	2.43	0.999
SG5	1.20		0.42			0.47	
SG9	2.60		0.16			0.17	
PILE	0.10		22.37			23.85	

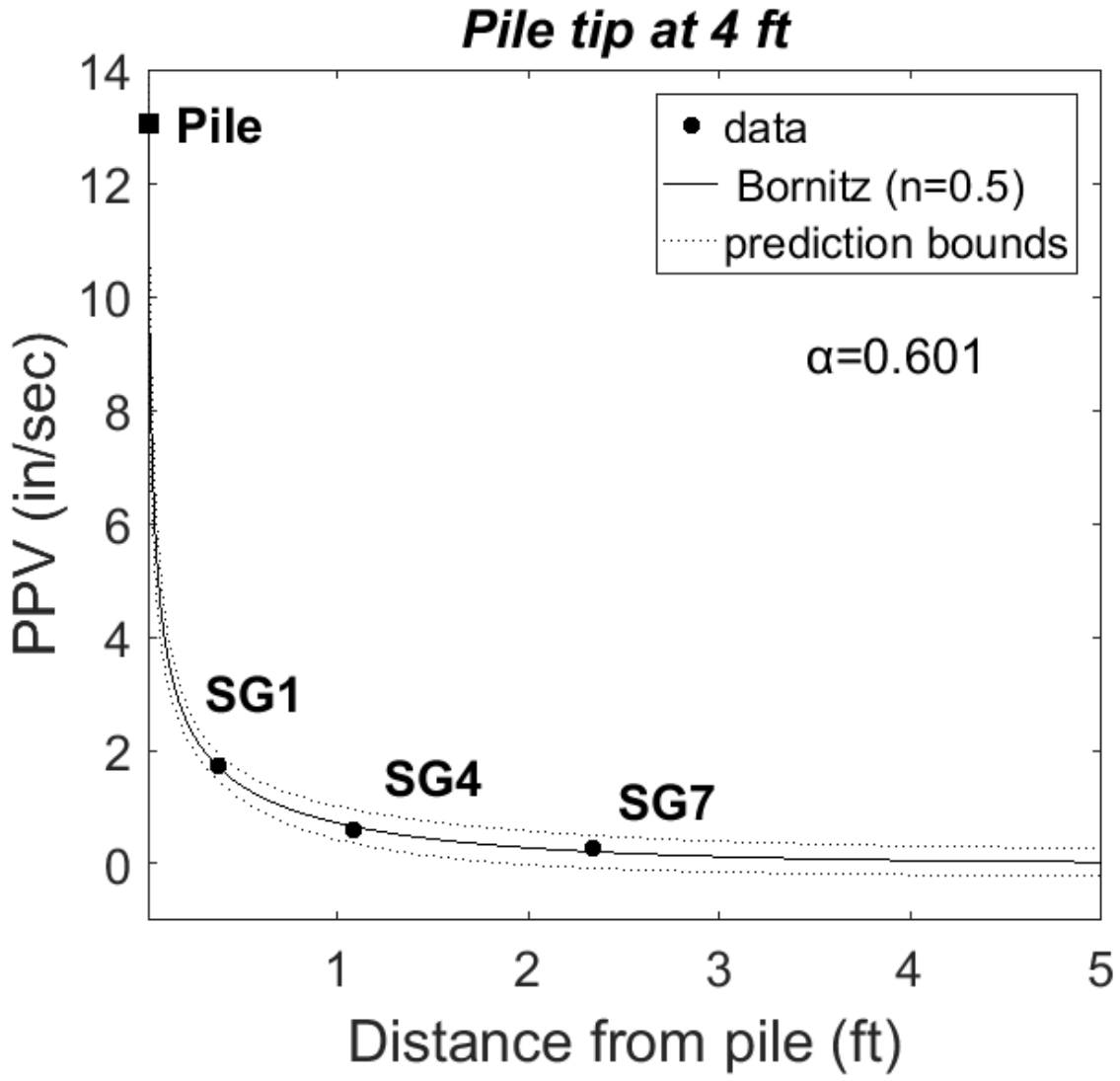

Figure 8-61 Attenuation curve for deep sensors for LT-3 test – Bornitz Equation

Table 8.7 Data for attenuation coefficient using the Bornitz equation-4 ft

SENSOR	Distance from pile (ft)	α (1/ft), Pile tip at 4 ft	PPV (in/sec)	R^2	α (1/ft), Average Pile tip 3.5 – 4.5 ft	PPV (in/sec)	R^2
SG1	0.40	0.601	1.71	0.995	0.519	1.59	0.988
SG4	1.10	0.703	0.61	0.991	0.584	0.69	0.976
SG7	2.30	0.467	0.27	0.989	0.450	0.30	0.980
PILE	0.01		13.06			14.03	

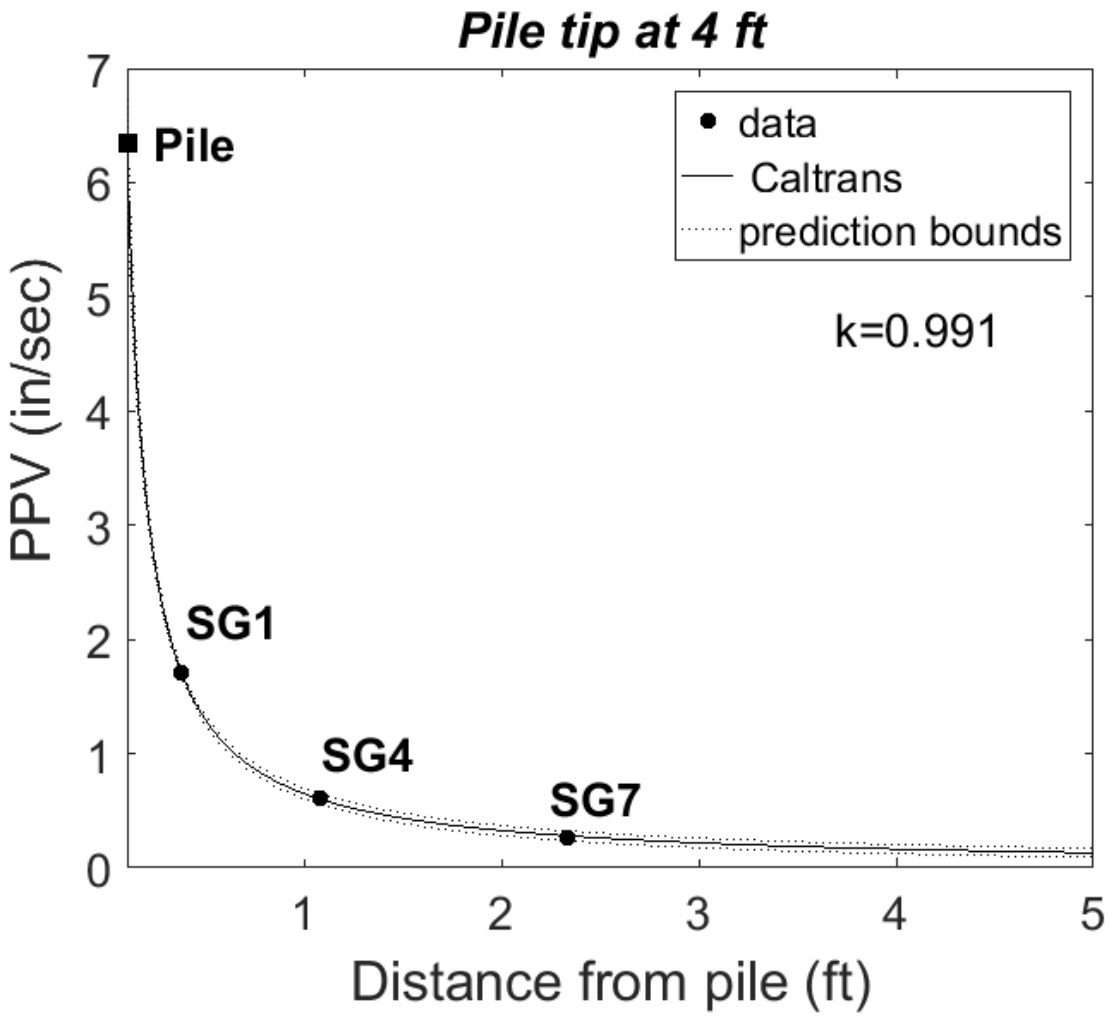

Figure 8-62 Attenuation curve for deep sensors for LT-3 test – Caltrans Equation

Table 8.8 Data for attenuation coefficient using the Caltrans equation-4ft

SENSOR	Distance from pile (ft)	k, Pile tip at 4 ft	PPV (in/sec)	R^2	k, Average Pile tip 3.5 – 4.5 ft	PPV (in/sec)	R^2
SG1	0.40	0.991	1.71	1.000	0.978	1.59	0.988
SG4	1.10	0.980	0.61	1.000	0.952	0.69	0.978
SG7	2.30	1.010	0.27	1.000	1.037	0.30	0.976
PILE	0.10		6.35			7.92	

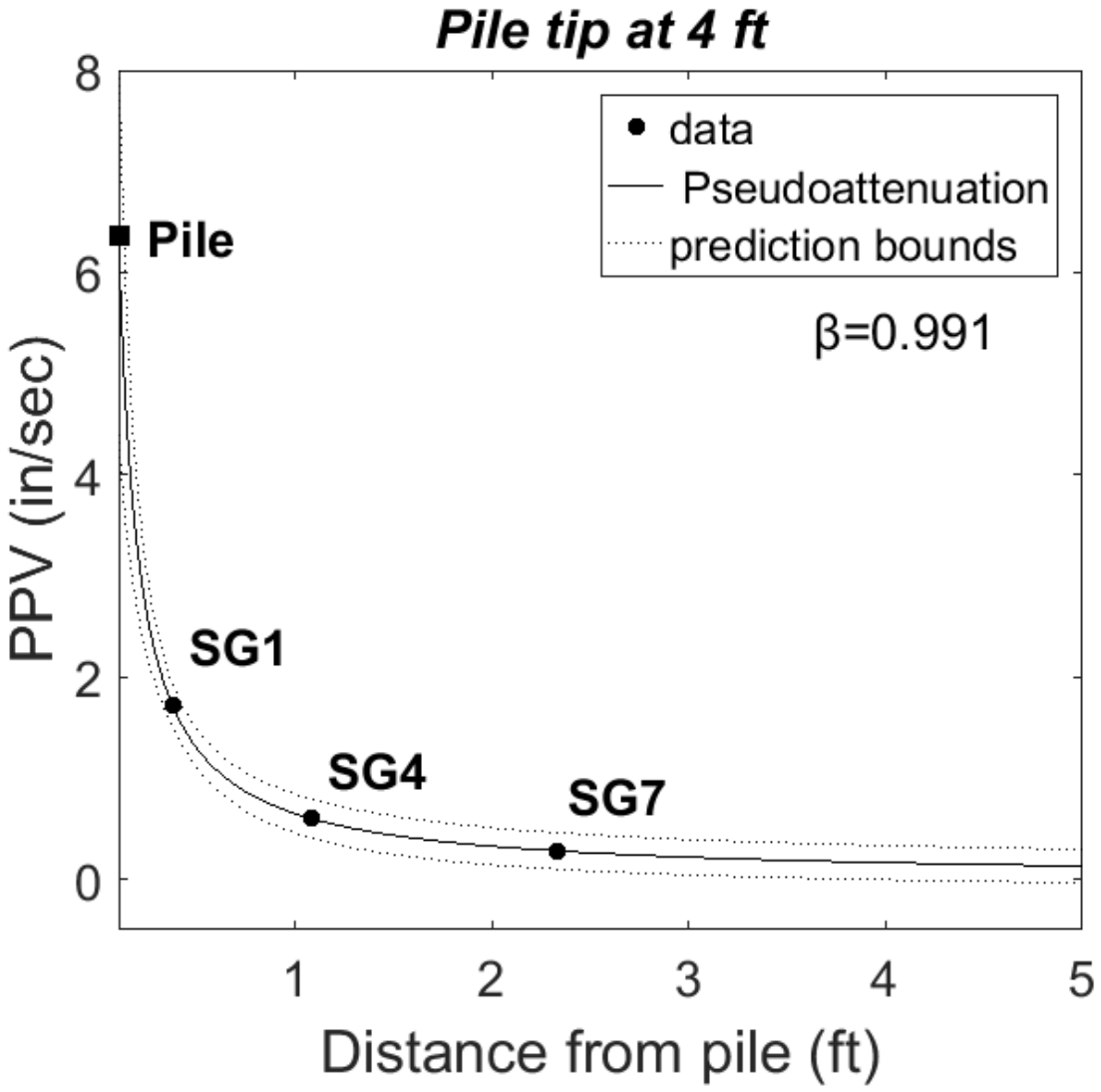

Figure 8-63 Attenuation curve for deep sensors for LT-3 test – power Equation

Table 8.9 Data for attenuation coefficient using the power equation-4 ft

SENSOR	Distance from pile (ft)	β, Pile tip at 4 ft	PPV (in/sec)	R^2	β, Average Pile tip 3.5 – 4.5 ft	PPV (in/sec)	R^2
SG1	0.40	0.991	1.71	1.000	0.981	1.59	0.989
SG4	1.10		0.61			0.69	
SG7	2.30		0.27			0.30	
PILE	0.10		6.35			7.92	

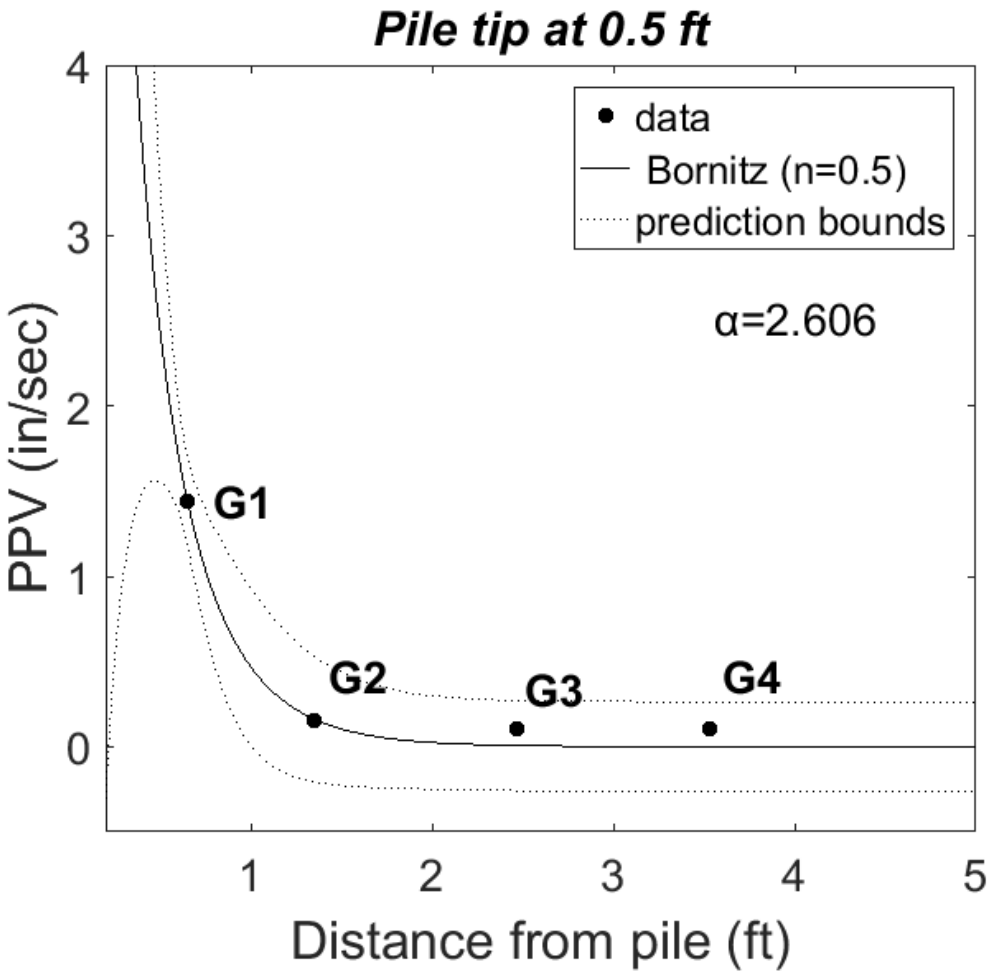

Figure 8-64 Attenuation curve for surface sensors for LT-3 test – Bornitz Equation

Table 8.10 Data for attenuation coefficient using the Bornitz equation

		α (1/ft)					
SENSOR	**Distance from pile (ft)**	**Pile tip at 0.5 ft**	**PPV (in/sec)**	**Pile tip at 1.5 ft**	**PPV (in/sec)**	**Pile tip at 3 ft**	**PPV (in/sec)**
G1	0.40	2.606	1.44	0.439	0.99	0.406	0.70
G2	1.25		0.15		0.60		0.65
G3	2.50	**R^2**	0.11	**R^2**	0.40	**R^2**	0.41
G4	3.50	0.984	0.10	0.892	0.32	0.970	0.32

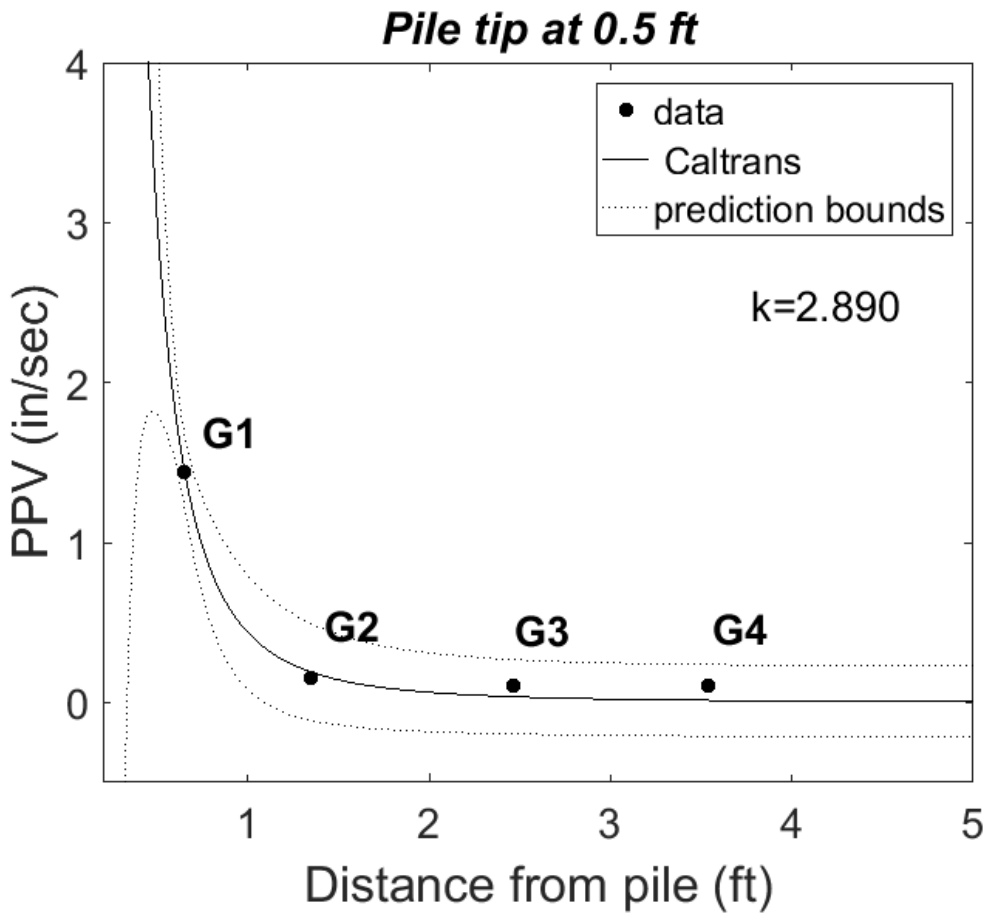

Figure 8-65 Attenuation curve for surface sensors for LT-3 test – Caltrans Equation

Table 8.11 Data for attenuation coefficient using the Caltrans equation

		k					
SENSOR	**Distance from pile (ft)**	**Pile tip at 0.5 ft**	**PPV (in/sec)**	**Pile tip at 1.5 ft**	**PPV (in/sec)**	**Pile tip at 3 ft**	**PPV (in/sec)**
G1	0.40	2.890	1.44	1.708	0.99	2.084	0.70
G2	1.25		0.15		0.60		0.65
G3	2.50	**R^2**	0.11	**R^2**	0.40	**R^2**	0.41
G4	3.50	0.995	0.10	0.956	0.32	0.949	0.32

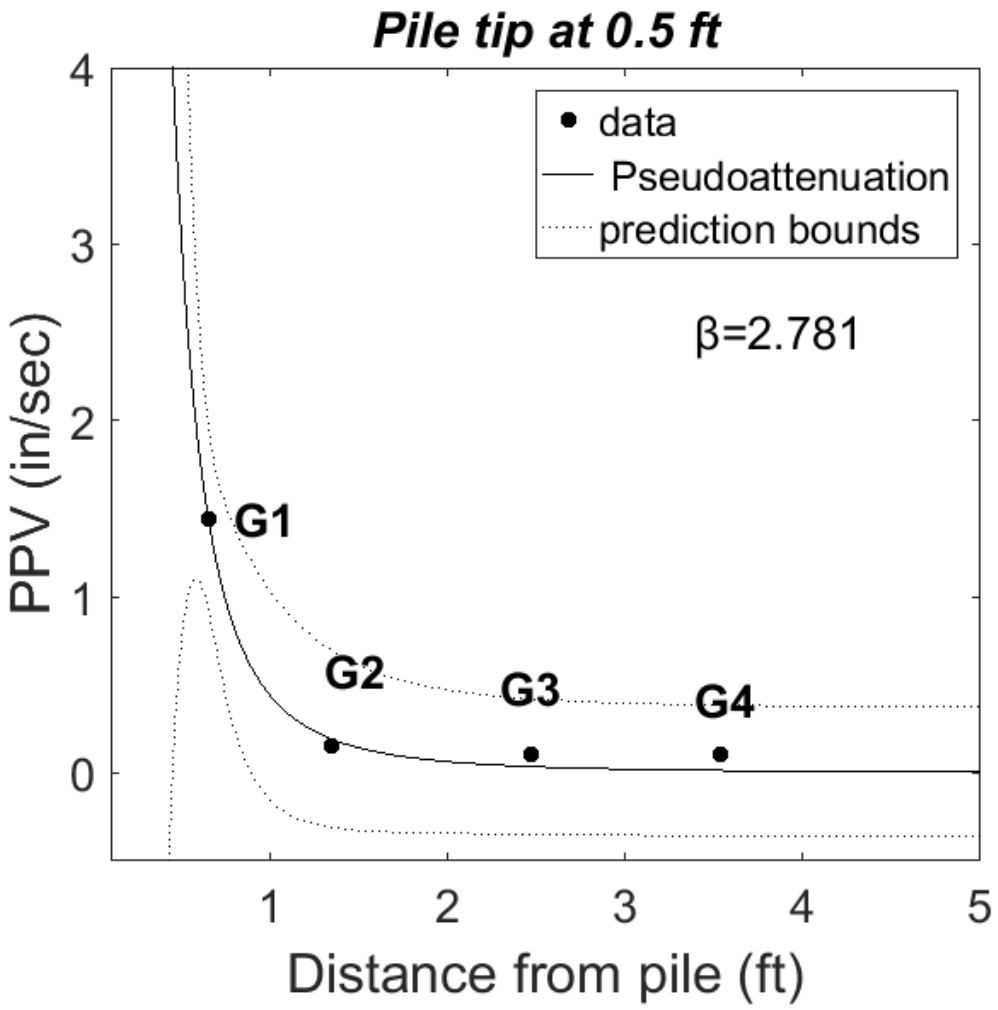

Figure 8-66 Attenuation curve for surface sensors for LT-3 test – power Equation

Table 8.12 Data for attenuation coefficient using the power equation

		β					
SENSOR	**Distance from pile (ft)**	**Pile tip at 0.5 ft**	**PPV (in/sec)**	**Pile tip at 1.5 ft**	**PPV (in/sec)**	**Pile tip at 3 ft**	**PPV (in/sec)**
G1	0.40	2.781	1.44	1.401	0.99	2.037	0.70
G2	1.25		0.15		0.60		0.65
G3	2.50	**R^2**	0.11	**R^2**	0.40	**R^2**	0.41
G4	3.50	0.989	0.10	0.952	0.32	0.975	0.32

A summary of the calculated coefficients evaluated for the buried and surface sensors for all the sites tested is provided in Table 8.13 to Table 8.16. Table 8.13 presents attenuation parameters calculated when using the closest sensor to the pile as the reference point to fit the curve, for the case of buried sensors. Table 8.14 shows decay coefficients evaluated for the buried sensors, when using the furthest sensor form the pile as the reference point. For the Bornitz formula, a decrease in the attenuation values is observed for the second case. This trend is not surprising, as when we go further from the driven pile and closer to the elastic zone, the vibration attenuation rate decreases. A similar decay vibration pattern is not noticed for the case of fitting the Caltrans and the power equations. Consequently, a distinction for the attenuation behavior in the near field region and the far field region is not easy when using the Caltrans and the power equation.

Table 8.15 shows attenuation coefficients calculated from surface ground motion data when the pile tip was at 0.5 ft. Table 8.16 presents similar parameters when the pile tip was at a depth of 1.5 ft. It is noticed that for tests LT-3 and LT-4 the decay coefficients decrease for all prediction formulas when the pile tip is deeper than the ground surface. The diagonal distance from the measuring point to the pile tip is constantly increasing as the pile penetrates deeper, which means that the contribution of the surface waves is not that evident whereas attenuation due to geometric damping from waves emanating from the tip is greater.

The frequency range of ground motions, monitored from the buried sensors, was found to be between 6 and 113 Hz. Lower frequencies were found from the surface ground motions, ranging from 22 to 88 Hz. These frequencies are comparable to those obtained from the signals during full scale pile driving.

Table 8.13 Attenuation coefficients from buried sensors' analysis with closest sensor to the pile as the reference point

TEST	Sensors' Elevation	Frequency Range (Hz)	Attenuation Coefficient, α (1/ft)	Pseudoattenuation factor, β	Dimensionless soil parameter, k
LT-2	2 ft	30-99	0.487	0.858	0.858
	4 ft	20-93	0.526	0.826	0.826
LT-3	2 ft	32-87	1.317	1.321	1.321
	4 ft	39-110	0.601	0.991	0.991

Table 8.14 Attenuation coefficients from buried sensors' analysis with furthest sensor to the pile as the reference point

TEST	Sensors' Elevation	Frequency Range (Hz)	Attenuation Coefficient, α (1/ft)	Pseudoattenuation factor, β	Dimensionless soil parameter, k
LT-2	2 ft	30-99	0.417	0.858	0.902
	4 ft	20-93	0.526	0.826	0.826
LT-3	2 ft	32-87	0.786	1.321	1.291
	4 ft	39-110	0.467	0.991	1.010

Table 8.15 Attenuation coefficients from surface sensors' analysis with pile tip at 0.5 ft

TEST	Frequency Range (Hz)	Attenuation Coefficient, α (1/ft)	Pseudoattenuation factor, β	Dimensionless soil parameter, k
LT-2	25-88	0.344	0.986	1.021
LT-3	22-81	2.606	2.781	2.890
LT-4	25-87	3.035	2.836	2.848

Table 8.16 Attenuation coefficients from surface sensors' analysis with pile tip at 1.5 ft

TEST	Frequency Range (Hz)	Attenuation Coefficient, α (1/ft)	Pseudoattenuation factor, β	Dimensionless soil parameter, k
LT-2	25-88	0.416	1.332	1.457
LT-3	22-81	0.439	1.401	1.708
LT-4	25-87	0.518	1.680	1.621

8.6 Pile Driving Analyzer test for the model pile

The fourth test (LT-4) of driving a model pile in the sand bin included a dynamic pile testing with the use of Pile Driving Analyzer (PDA) equipment. The test was conducted by Soil and Materials Engineers, Inc. (SME). A pair of a strain transducer and an accelerometer were mounted near the top of the pile. During driving, the PDA unit records, analyzes and stores data obtained from these two gages for every hammer blow; force and velocity time records are acquired. During pile driving, the PDA uses the Case Method capacity equations for estimates of the ultimate pile capacity. Additional Case Method equations are used to calculate driving stresses, pile integrity and hammer performance quantities. The pile was driven to a depth of 5.5 ft. A case damping factor, Jc, of 0.35 was used. Table 8.17 provides results for selected blow counts, covering different depths when driving the pile. Definitions of the quantities are as follows:

BLC – blows per foot

CSX – max average compression stress at gage location (from both gages)

CSB – max computed compression stress at toe of pile

EMX – max transferred energy to pile

AMX – max acceleration at gage location

DMX – max displacement at gage location

VMX – max velocity at gage location

ETR – Energy transfer ratio

FMX – max compressive force at gage location

Table 8.17 PDA output quantities for different blows during pile driving

Blow #	Depth	BLC	CSX	CSB	EMX	AMX	AMX	DMX	VMX	ETR	FMX
	ft	bl/ft	ksi	ksi	kip-ft	g's	ft/sec^2	in	ft/sec	%	kips
9		18	10.4	2.38	0.041	1477	47557		12.5	48.0	17.4
10	0.67	18	10.6	1.74	0.038	1513	48733	0.96	12.6	44.6	17.7
13		18	8.2	1.81	0.028	-1117	-35964		12.2	32.8	13.6
33		80	14.2	1.85	0.059	769	24761		9.6	70.0	23.8
34	1.24	80	13.5	1.60	0.054	817	26299		10.1	63.4	22.6
35		80	14.3	2.70	0.061	815	26258	0.37	10.2	71.8	23.9
58		54	6.6	3.18	0.016	633	20397		8.5	19.2	11.0
59	1.56	54	7.1	3.57	0.017	594	19134	0.21	8.3	20.1	11.8
60		54	6.6	2.89	0.015	647	20827		8.6	18.1	11.0
396		226	8.5	5.29	0.028	1099	35376		6.8	32.7	14.2
397	3.78	226	8.0	5.26	0.030	908	29231	0.07	6.7	35.5	13.3
398		226	8.0	4.92	0.027	909	29272		6.6	31.8	13.3
444		226	8.1	2.28	0.024	-999	-32157		6.9	28.5	13.6
445	4	226	8.4	2.55	0.026	-997	-32115		7.1	30.4	14.0
446		226	7.7	2.53	0.023	-939	-30240	0.07	6.6	27.0	12.9
585		280	8.9	2.63	0.033	-1085	-34935		7.5	39.1	14.8
586	4.53	280	9.0	2.80	0.038	-915	-29478		7.0	44.2	15.0
587		280	8.3	2.79	0.034	-890	-28671	0.06	7.1	39.9	13.8
733		446	7.2	1.67	0.018	-787	-25334		6.1	21.6	12.0
734	5.03	446	7.6	2.73	0.027	711	22883	0.06	5.9	32.2	12.6
735		446	7.0	3.20	0.036	682	21951		5.9	42.7	11.7
934		446	8.4	3.34	0.029	-853	-27451		6.2	33.6	14.0
935	5.48	446	6.4	3.15	0.029	625	20119		5.3	34.1	10.6
936		446	7.2	6.49	0.033	776	24977	0.1	6.2	39.2	12.1

It is observed that the average energy transferred to the pile is around 40 % of the potential energy. Figure 8-67 illustrates an example of the force and velocity time histories for one of the hammer blows. Table 8.18 presents parameters of the model pile that were used in the calculations. Table 8.19 depicts the hammer quantities of interest for this analysis.

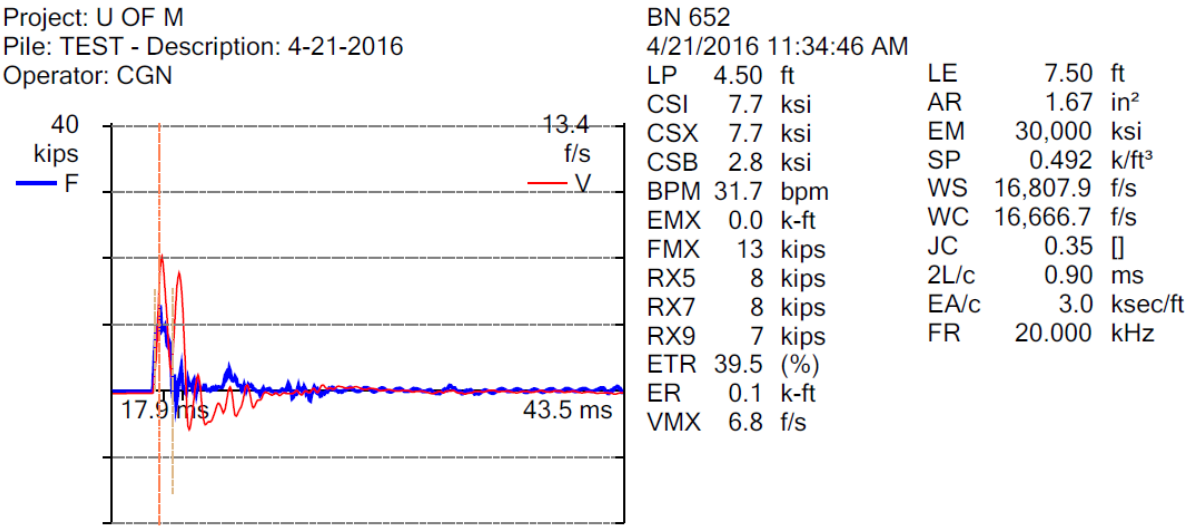

Figure 8-67 Force and velocity time histories from PDA unit

Table 8.18 Model pile parameters

Depth	3	in
Width	2.33	in
Web Thickness	0.17	in
Area	1.67	in^2
Weight	5.7	lb/ft
Length, L	7.5	ft
Modulus of Elasticity	30,000	ksi
Density	490	pcf
Wave Travel Speed, c	16,800	ft/sec
Impedance	2.98	k/ft/sec
2L/c	0.893	msec

Table 8.19 Hammer quantities of interest

Weight (lb)	**Max stroke, h (in)**	**Potential Energy, W*h (lb-ft)**	**Impact velocity, vi (ft /sec)**
44.55	23	85.4	11.1

CHAPTER 9 NUMERICAL MODELING

In recent years, some progress has been made in terms of developing computational finite element models in an attempt to better understand the pile response and wave propagation during impact pile driving. A complete pile driving model, however, should consider the sliding at the pile-soil interface and soil plasticity around the pile (Masoumi et al. 2008). Ramshaw et al. (1998) developed a model based on finite and infinite elements using the commercial package Abaqus. Infinite elements were employed to model the outgoing waves in the far field. Results of vibratory and impact pile driving were in good agreement with field data. During pile driving, the transmitted energy through the soil causes plastic deformations in the near field. Masoumi et at. (2008) presented a non-linear coupled finite element-boundary element approach for the prediction of free field vibrations due to vibratory and impact pile driving. Considering a non-linear constitutive behavior for the soil around the pile resulted in predictions in good agreement with experimental results

Acurately modelling the pile installation procedure with numerical analysis is still very difficult to achieve due to limited knowledge of the soil behavior and the development of large displacements during the installation process (Dijkstra et al. 2006). Thus, it is very important to choose an appropriate model to simulate the soil behavior and the pile-soil interaction.

In this study, the commercial Finite Element (FE) package PLAXIS 3D (Brinkgreve et al. 2016) is used to simulate the installation process. The Dynamics module of this software allows analysis of the soil vibrations and their influence on nearby structures. Advanced constitutive models are available for the simulation of the non-linear, time dependent and anisotropic behavior of soils. The combination of ground vibration

monitoring data along with records of the impact force from PDA testing collected from the small-scale laboratory pile driving tests, offer a great opportunity to validate the numerical code. Preliminary results of these FE models will be presented in this Chapter.

9.1 Geometry of the model

Plaxis 3D has a database with input parameters for several commercially available profiles for beams used commonly in geotechnical projects. Thus, a beam close to the size of the model pile that was driven in the sand bin, was chosen to simulate the structural element. Specifically, beam IPE A 80 was used as an input in the FE model. A comparison of the model pile driven in the sand bin (S 3x5.7) and the beam used in the numerical analysis (IPE A 80) is presented in Table 9.1

Table 9.1 Comparison of model pile used in pile driving test and beam used in model simulation

Beam	Depth (mm)	Width (mm)	Web thickness (mm)	Area (cm^2)	Weight (kg/m)	Ixx (cm^4)	Iyy (cm^4)
S 3x5.7	76.2	59.2	4.3	10.8	8.5	104.9	18.9
IPE A 80	78	46	4.2	6.2	5	62.35	6.8

For the simulation of the soil behavior, the Hardening Soil model (HS) is used. This model is an advanced hyperbolic soil model. In addition, the HS model uses the theory of plasticity rather than the theory of elasticity, includes soil dilatancy and takes into account the stress dependency of soil stiffness (Schanz et al. 1999). The soil is described more accurately than the Mohr-Coulomb model, by using three different stiffness values: secant stiffness in drained triaxial loading, E_{50}, tangent stiffness for primary oedometer loading,

E_{oed}, and unloading/reloading stiffness, E_{ur}. Detailed information about the model and how it is implemented in PLAXIS can be found in Brinkgreve et al. (2016).

In order to account for the shear wave velocity change of the sand in the bin at a depth of around 3.5 ft, two different soil layers were defined as shown in Figure 9-1. Extensive wetting of the sand took place before the PDA test, as part of other laboratory activities in the sand bin, and excavation revealed the ground water level being around 3.5 ft below the surface. The natural clay deposit below the silica sand is not included in the model, instead an appropriate boundary condition is applied at the bottom of the sand layer. In a dynamic analysis, model boundaries should be far away from the region of interest to avoid disturbances due to possible wave reflections. Viscous boundaries are specified at Xmin, Xmax, Ymin, Ymax and Zmin, to avoid these spurious reflections during the dynamic calculation phases. The ground surface (Zmax) was set free to vibrate.

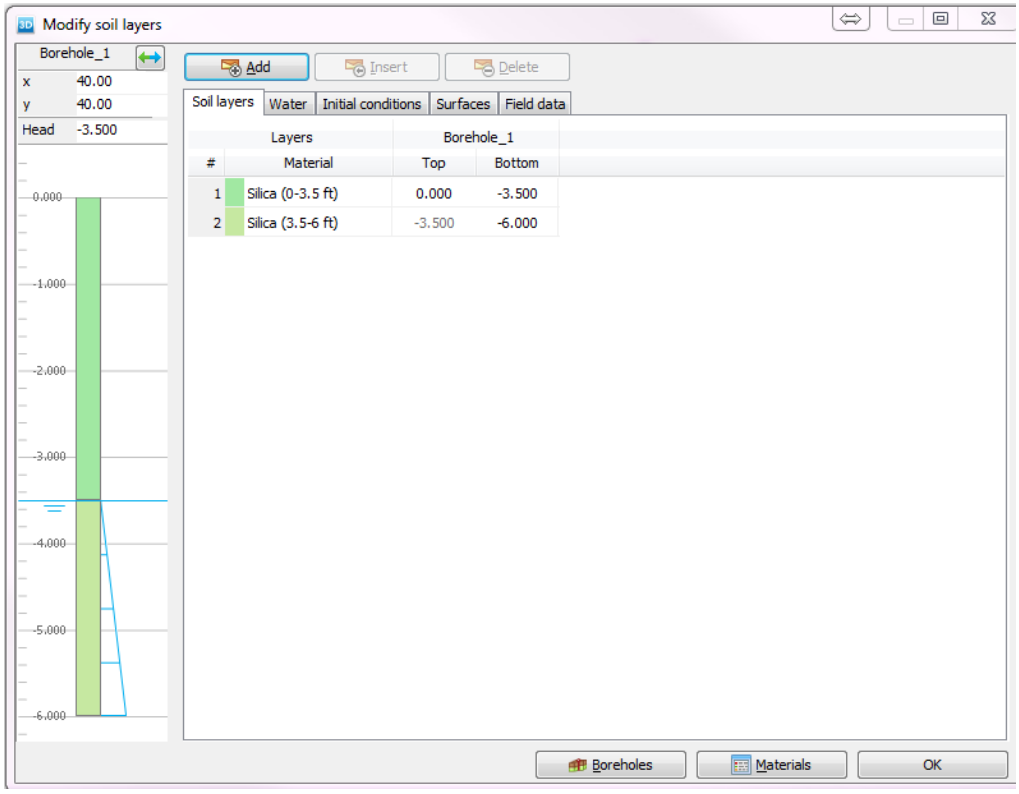

Figure 9-1 Soil stratigraphy definition

The soil-structure interface behavior, which captures the plastic behavior between pile and soil during impact is important to be modeled. The interface element between the pile and the soil that is suggested by Plaxis was employed but led to numerical difficulties when the pile was dynamically loaded. As an alternative approach, a material data set with reduced strength parameters and shear wave velocity was created, and was used as an input in the vicinity of the pile. This plastic zone extended as a cylindrical soil cluster element with a radius of 0.5 ft around the pile and 0.5 ft below the tip of the pile. The selection of this diameter for the plastic zone around the pile, was based on the ground motions monitored in this sand in the laboratory. This was done to make sure that the non-linear deformations along the shaft and below the tip of the pile would be properly modeled. Figure 9-2 shows a zoom-in view of the volume element with the reduced strength parameters around the pile.

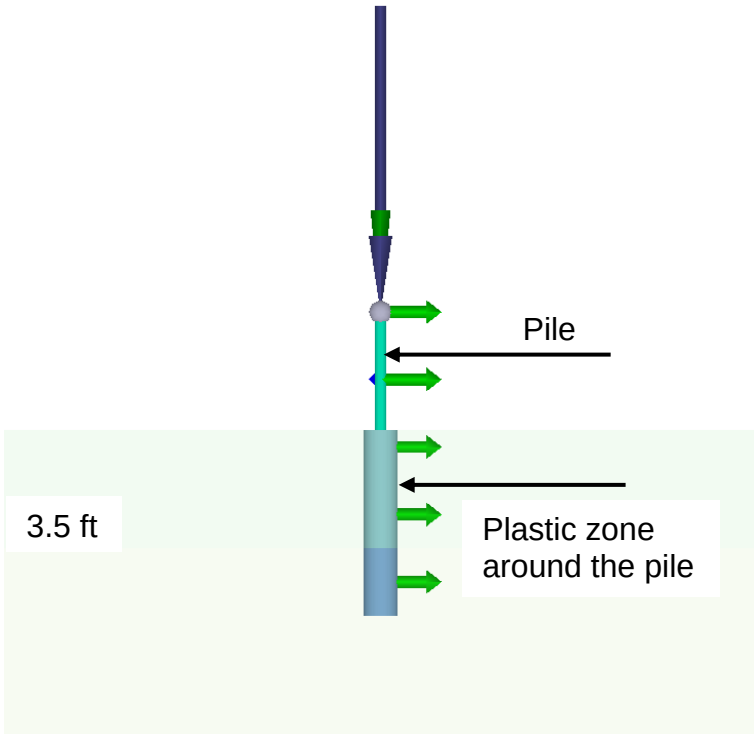

Figure 9-2 Zone with reduced strength parameters around the pile

Table 9.2 presents the soil properties of the silica sand that were used as input in the model. The sand has been properly characterized with tests presented in Chapter 8. The reduced strength material properties applied in the vicinity of the pile are also presented in Table 9.2. A value of R=0.5 was chosen as a strength reduction factor in this zone after trials. For the shear wave velocity reduction factor, a value of R_S=0.2 was selected based on the findings of the dissipation of shear wave velocity of the soil near the pile, derived from the field tests.

Element size is another important parameter that needs special attention in dynamic FE calculations. Large elements are not able to transmit high frequencies. Element sizes must be sufficiently small relative to wavelength in order for the finite element mesh to properly propagate induced waves. The basic soil elements of the 3D finite element mesh are the 10-node tetrahedral elements. The medium mesh option in Plaxis, with further refinement along the pile shaft and tip, was found to be sufficient. Figure 9-3 depicts the generated mesh and the mesh refinement around the pile. The model is 80 ft wide and 80 ft long, with the pile located in the center as shown in Figure 9-3. Two different models were analyzed in terms of the height of the silica sand. The first had a height of 6 ft as shown in Figure 9-1, with an appropriate boundary condition at the bottom. The second, had an extended height of 40 ft (Figure 9-4) to determine if a change of height would have an effect on the ground vibration results. The ground motions after applying the impact hammer were found to be similar for both models.

The hammer blow is simulated by the recorded force measurements during a PDA test when driving the model pile in the sand bin. The pile was modeled at different installed depths with a single blow applied on the top of the pile, corresponding to the force measurements collected from the PDA at that time. It is recognized that the stresses and strains that change continuously during pile driving cannot be modeled realistically with the aforementioned model. However, since it is impossible to model the complete pile installation process, calculated ground motions when hitting the pile with a single blow at different installation depths can provide some insight when they are compared with measured data.

Table 9.2 Soil properties for Hardening Soil model

				Reduced strength parameters - Plastic Zone		
		Sand (0-3.5 ft)	**Sand (3.5-6 ft)**	**Sand (0-3.5 ft)**	**Sand (3.5-6 ft)**	
Material model	**Model**	Hardening Soil	Hardening Soil	Hardening Soil	Hardening Soil	
Type of behavior	**Type**	Drained	Undrained (A)	Drained	Undrained (A)	
Unit weight above phreatic line	**γunsat**	110	110	110	110	pcf
Unit weight below phreatic line	**γsat**	125	125	125	125	pcf
Secant stiffness in drained triaxial test	**E50ref**	1.30E+06	2.87E+06	5.19E+04	1.15E+05	psf
Tangent stiffness for oedemeter loading	**Eoed**	1.20E+06	2.30E+06	5.19E+04	1.15E+05	psf
Unloading/Reloading stiffness	**Eur**	3.90E+06	8.62E+06	1.56E+05	3.45E+05	psf
Power for stress-level dependency of stiffness	**m**	0.5	0.5	0.5	0.5	-
Poisson's ratio	**v'**	0.2	0.2	0.2	0.2	-
Cohesion	**c**	21	21	11	11	psf
Friction angle	**φ**	37	37	19	19	degrees
Dilatancy parameter	**ψ**	7	7	4	4	degrees
Shear Wave Velocity	**Vs**	398	592	80	118	ft/sec
Shear Wave Velocity reduction factor	**Rs**			0.2	0.2	
Strength Reduction Factor	**R**			0.5	0.5	
Ko determination		Automatic	Automatic	Automatic	Automatic	
Lateral earth pressure coefficient	**Ko,x**	0.3982	0.3982	0.691	0.691	

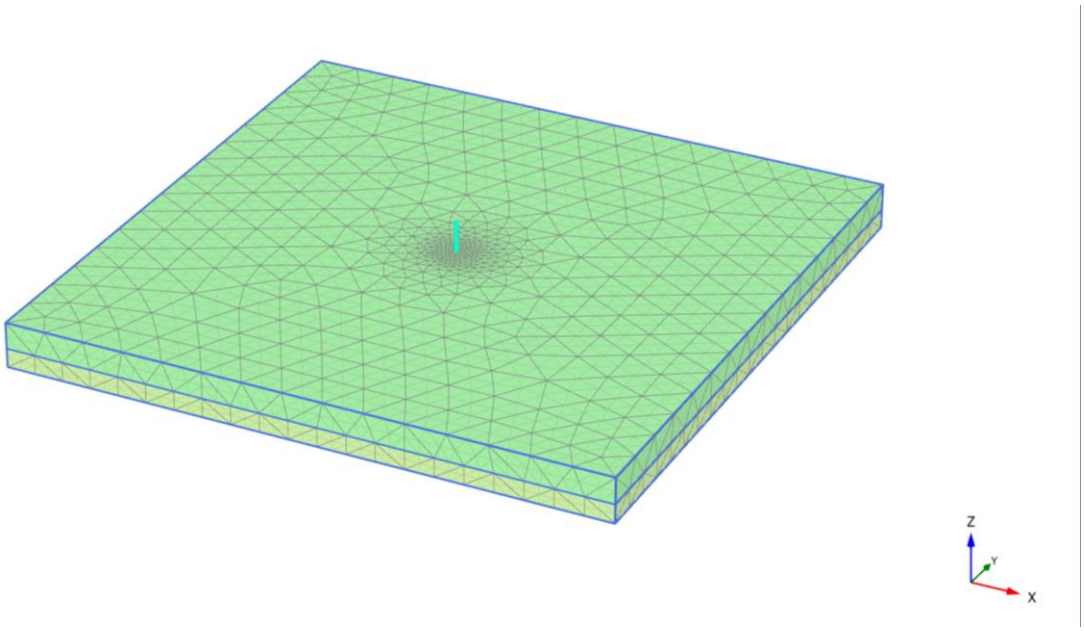

Figure 9-3 Generated mesh and refinement around the pile

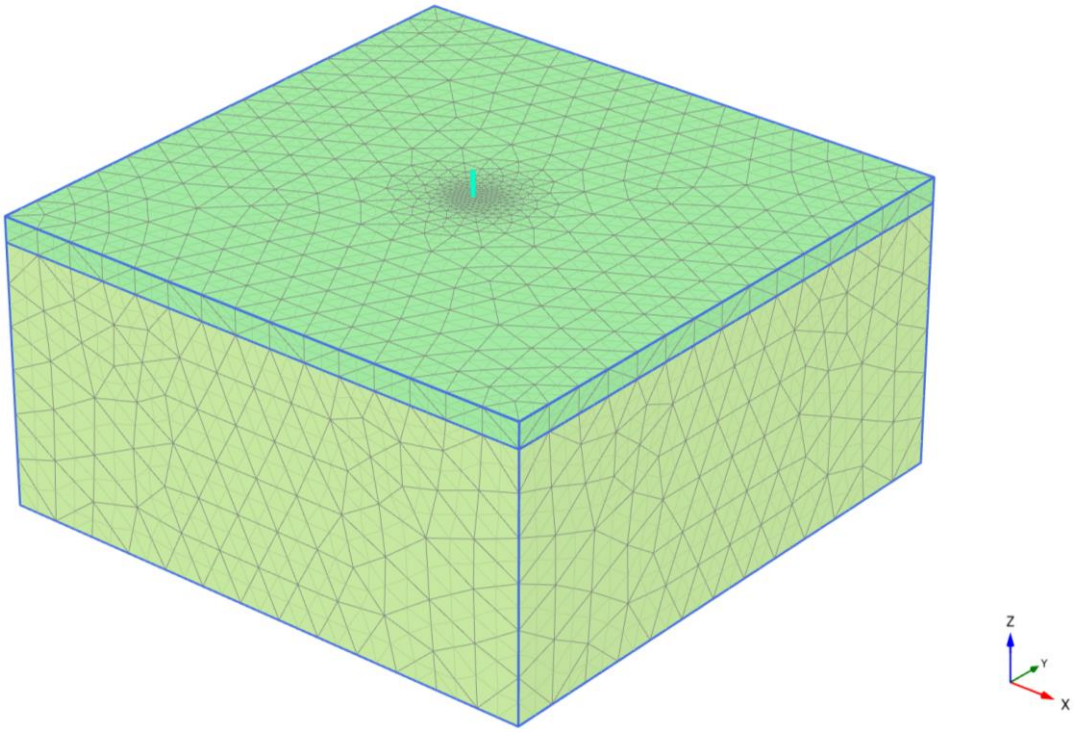

Figure 9-4 Generated mesh and refinement around the pile (extended height)

In Plaxis 3D, a dynamic load can be specified by load input values and a multiplier. The actual dynamic value at each time step equals the input value times the multiplier. Signals collected by the PDA tests were imported as text files. Figure 9-5 presents a single blow imported as a load multiplier.

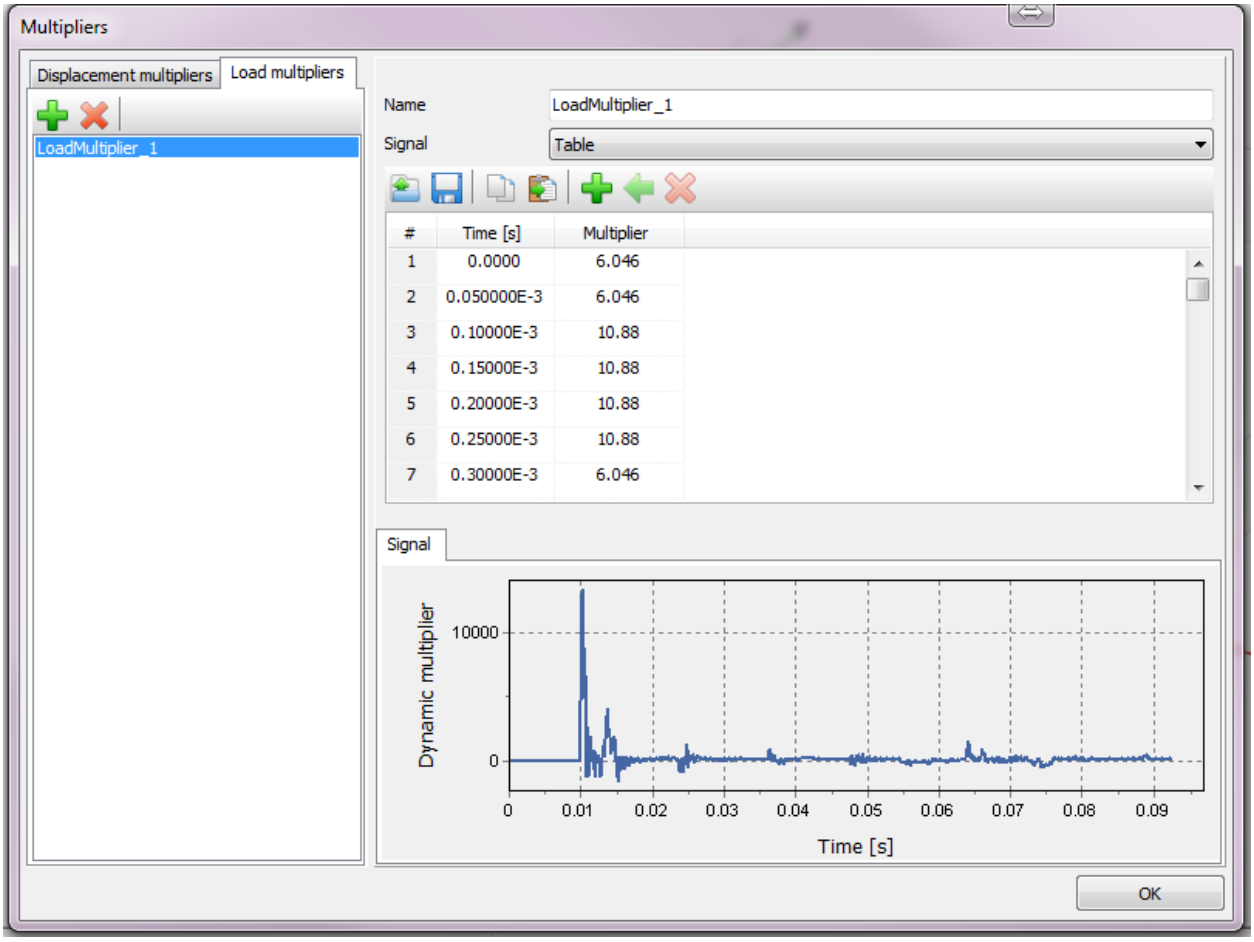

Figure 9-5 Importing dynamic load in PLAXIS

The calculation consists of four individual phases. First, the initial stresses are calculated. Then, the pile is introduced in the model at the desired depth. The hammer blow is applied on top of the pile in the next phase, while the soil cluster with the reduced strength parameters is activated. This is a dynamic phase with the dynamic time interval being set at 0.02 sec. In the last phase, the dynamic load is deactivated and the dynamic response of the pile and soil is analyzed in time. The dynamic time interval is set a t=0.08 sec.

The above calculation phases were performed for seven single hammer blows at seven different pile penetration depths. A representative blow per half foot pile driving was used as an input. The sensors mounted on the pile top were loosened due to the impact pulses between 2 ft and 3.5 ft depths, thus recorded force impulses from this depth range were not used. The results from the numerical simulation will be compared with the recorded ground motions during driving the model pile in the sand bin.

9.2 Numerical Results

Wave propagation over time can be plotted for the dynamic phases in PLAXIS in terms of displacements, velocities and accelerations. Figure 9-6 to Figure 9-11 illustrate the total displacements in the soil at three different times, with the pile tip being at a depth of 3.75 ft. In Figure 9-6, the impact load is initiated (t=0 sec). The shear wave along the shaft is generated in a conical wave form. High values of total displacements are observed at the tip of the pile where a P-wave is generated in a spherical wave form. A zoomed-in view of this time step is shown in Figure 9-7. presents the wave propagation at the end of impact (t=0.02 sec). The spherical wave front at the tip is more pronounced, while the shear wave along the shaft propagates even further from the pile face. A zoomed-in view of this time step is shown in Figure 9-8. In Figure 9-10 the soil vibrates after the impact force has been removed (t=0.1 sec). At the pile tip, the spherical wave front has expanded further compared to the previous time step. The amplitude decreases quickly with the

distance from the pile tip. A Rayleigh wave can also be seen propagating on the surface. A zoom-in view of this time step is shown in Figure 9-11.

In Plaxis it is possible to select different nodes in the soil or structure clusters and display the dynamic time history of load, acceleration, velocity and displacement. Points close to the location of the sensors from the pile face placed for the laboratory test were selected in the ground and on the surface. This was done when applying the impact load with the pile tip being at different depths. The vertical velocity time histories were calculated at these points and peak particle velocities were extracted from the calculated signals from Plaxis in order to compare them with the recorded ground motion amplitudes.

Figure 9-12 shows a comparison between measured and calculated vertical peak particle velocities at observation points located at a depth of 4 ft and at different distances from the pile. SG1, SG4 and SG7 are the sensors placed at a depth of 4 ft. It is observed that at a distance of 0.4 ft from the pile, where the plastic zone is assumed to be and was modeled with reduced strength parameters, the agreement between the calculated and measured peak particle velocities is very good. It should be reminded that no results could be derived between 2 ft and 3.5 ft in Plaxis, because of the bad signals of the force transducer during the PDA test, which were not used as an input in the model. For distances 1 ft and 2.35 ft away from the pile, Plaxis underestimates the peak particle velocity with an exception at 4.5 ft to 5.5 ft where the agreement is quite good.

Figure 9-13 depicts a similar comparison between measured and calculated vertical peak particle velocities at observation points located at a depth of 2 ft and at different distances from the pile face. SG2, SG5 and SG9 are the sensors placed at a depth of 2 ft. For the top 1.5 ft, the agreement is very good for a distance of 0.35 ft from the pile, while Plaxis overestimates the ground motions below 3.5 ft. Again, no results could be calculated when the pile tip was between 2 ft and 3.5 ft. However, it is anticipated that the calculated results would be close to the recorded values since the ground motion vibration pattern for the rest of the pile tip depths is similar for the measured and calculated values. Beyond the plastic zone (0.5 ft), the Plaxis model underestimated the measured ground motions.

Figure 9-14 presents measured and computed vertical peak particle velocities for surface points located at different distances from the pile. For the closest distance from the pile (0.35 ft), the model overestimated the measured ground motions on the surface when the pile tip was below 1.5 ft depth. For the surface points further away from pile the model underestimates the recorded peak particle velocities.

As mentioned before, velocity time histories may be plotted in Plaxis for various pre-selected points. Figure 9-15 to Figure 9-19 present computed velocity time histories from Plaxis and recorded time histories when driving the model pile in the sand bin. It is reminded that the records collected from the geophones were filtered in order to remove the high frequency noise, thus the signals are smoother compared to those calculated from Plaxis. In addition, Plaxis underestimates measured amplitudes that are not in the close vicinity of the pile. However, it is observed that the shape of the recorded and computed signals is similar.

To conclude, the availability of a dataset of recorded ground motions, at different distances and depths from an impact driven pile, in a controlled environment like the sand bin, allowed validation of a numerical FE code. A zone with reduced strength parameters that was introduced around the vicinity of the pile, worked very well in capturing the plastic behavior and the soil-structure interaction. In addition, wave propagation at different dynamic time steps resemble the theoretical model for an impact driven pile; a spherical wave emanates from the pile tip while a cylindrical conical wave form propagates from the pile shaft.

Since the pile installation process is difficult to model, the preliminary results presented in this Chapter, where a single blow was applied on the top of the pile at different pile penetration depths, are promising. Further tests and simulation models will be needed to provide a better insight of the impact pile installation.

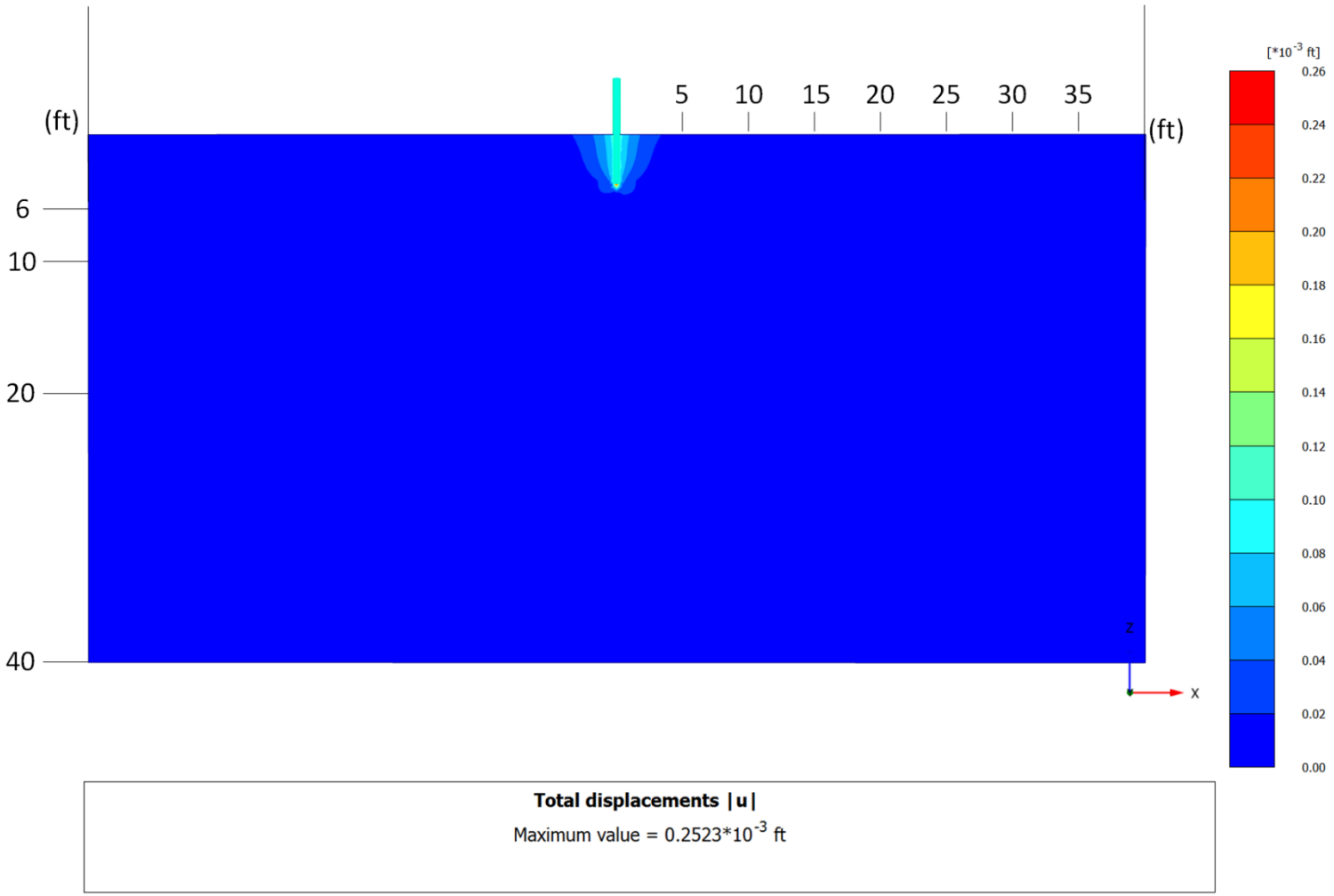

Figure 9-6 Wave propagation at impact initiation, t=0 sec – pile tip at 3.75 ft depth

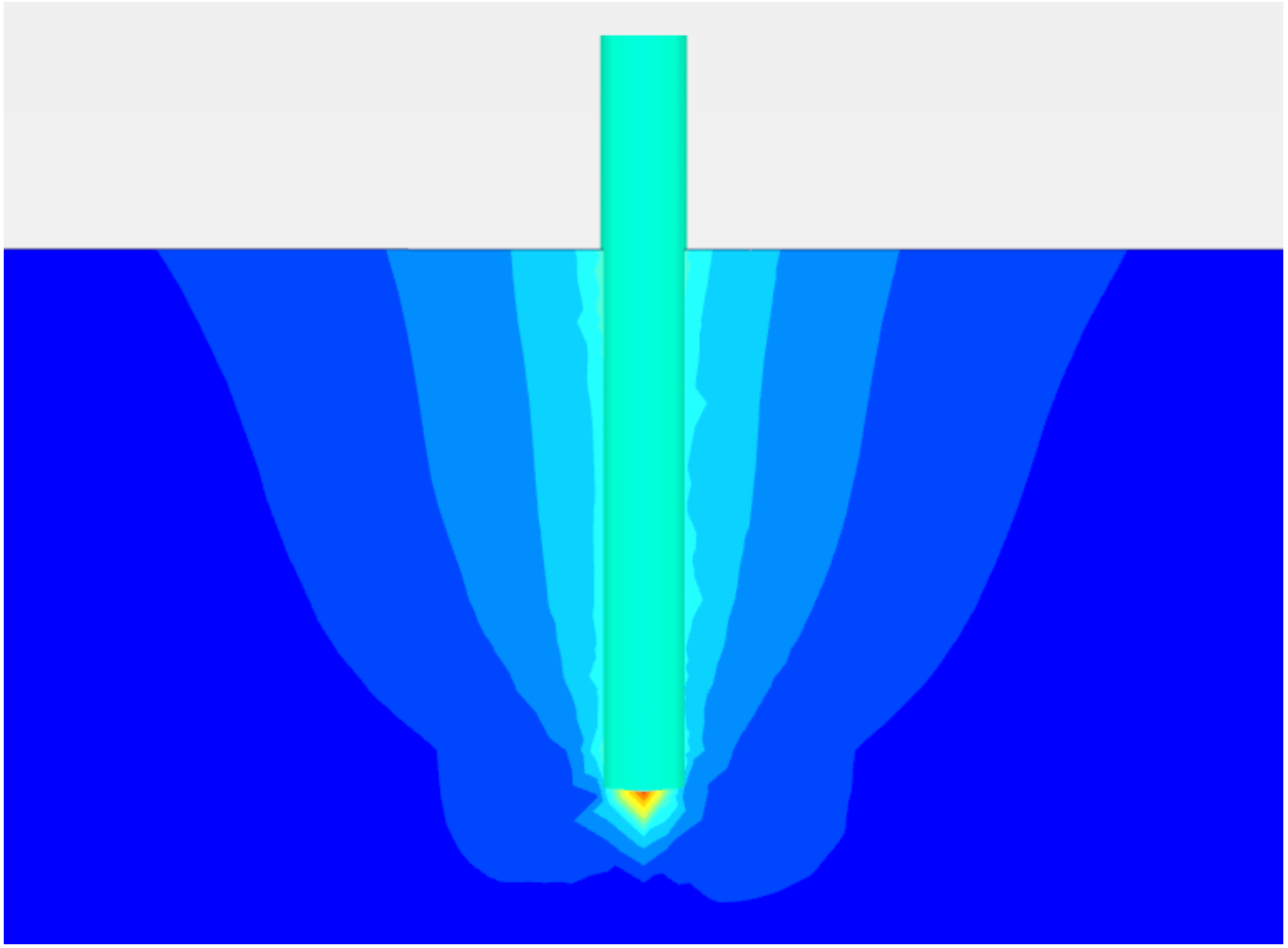

Figure 9-7 Zoom-in view of wave propagation at impact initiation, t=0 sec – pile tip at 3.75 ft depth

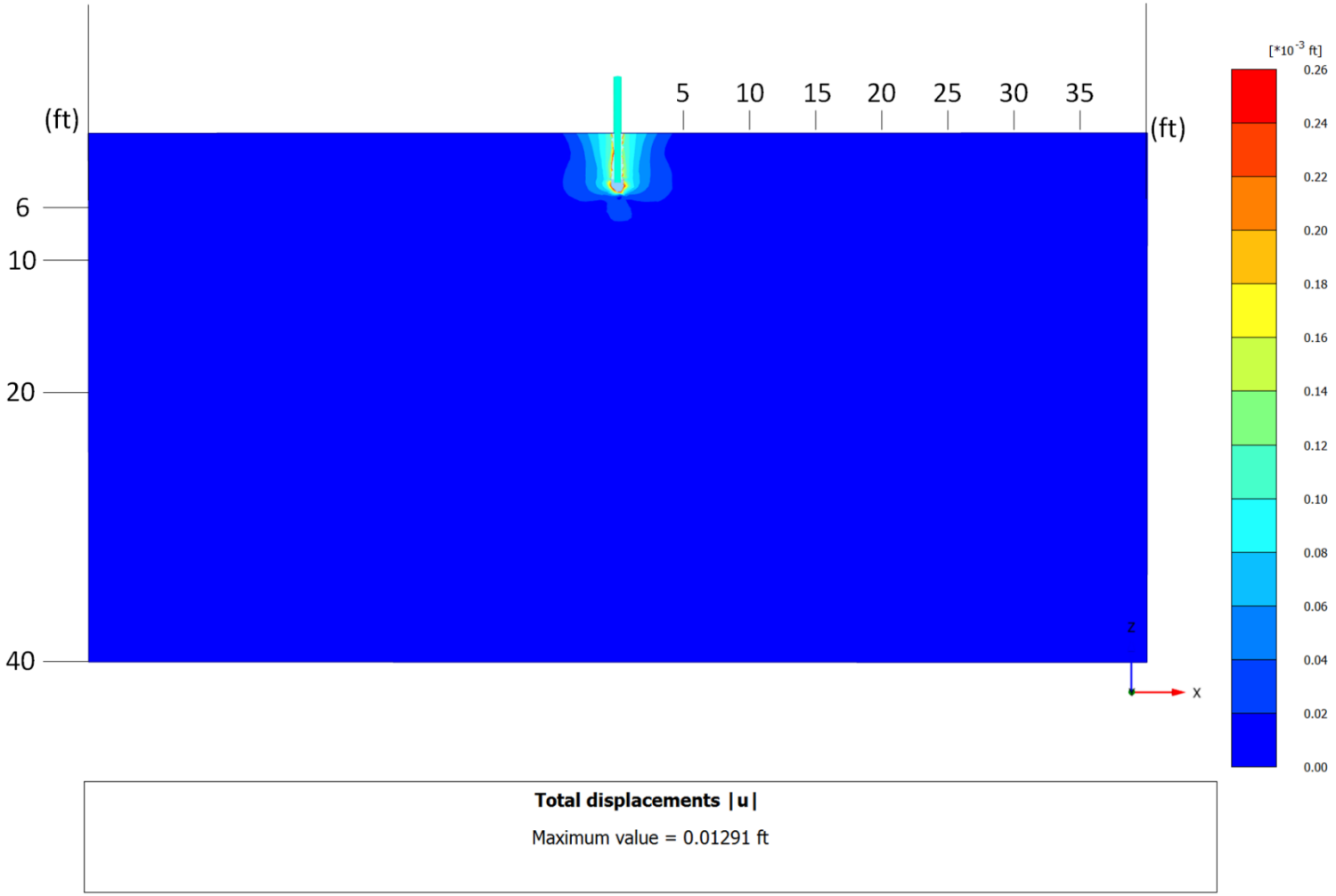

Figure 9-8 Wave propagation at end of impact load, t=0.02 sec – pile tip at 3.75 ft depth

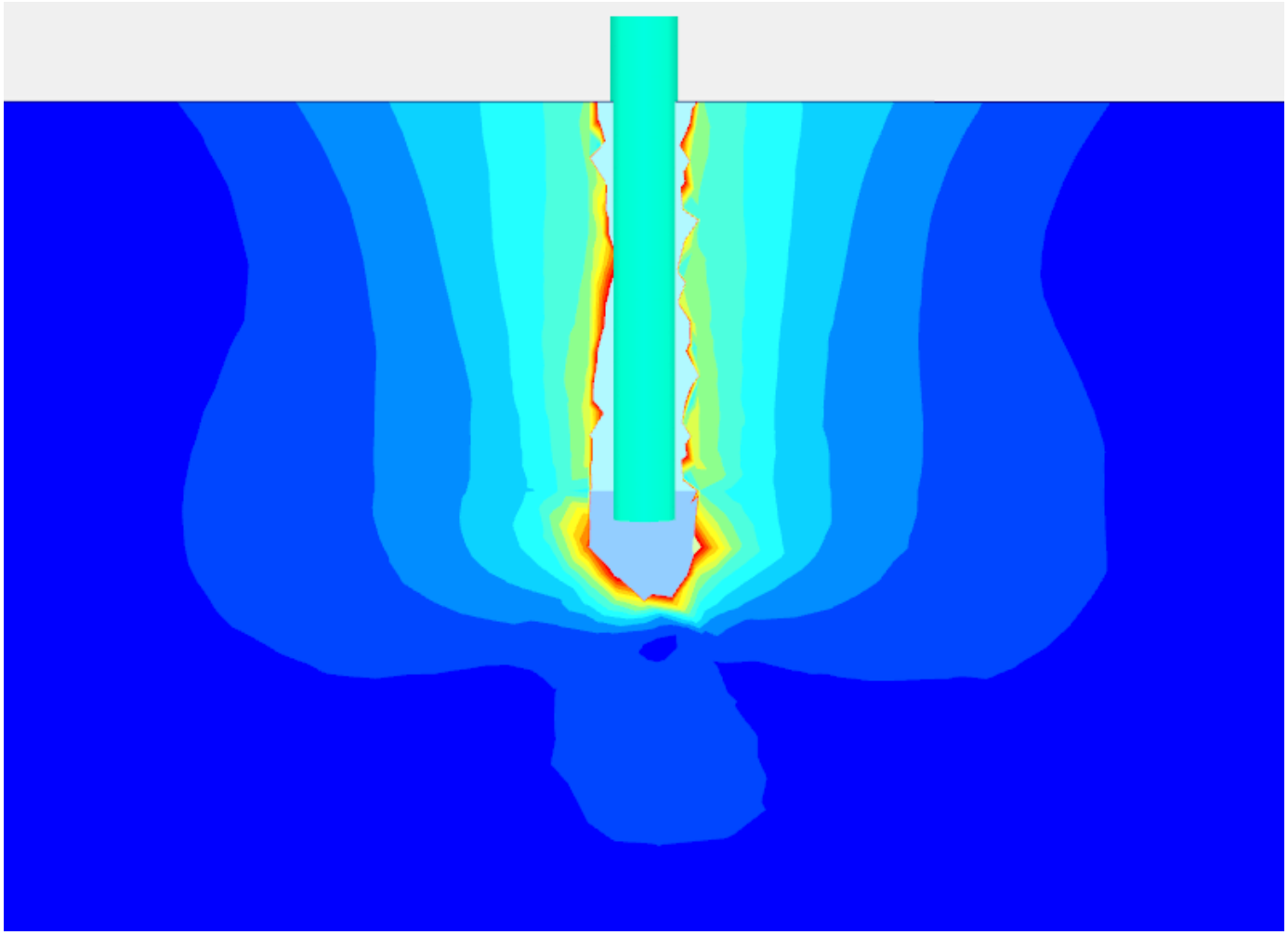

Figure 9-9 Zoom-in view of wave propagation at end of impact load, t=0.02 sec – pile tip at 3.75 ft depth

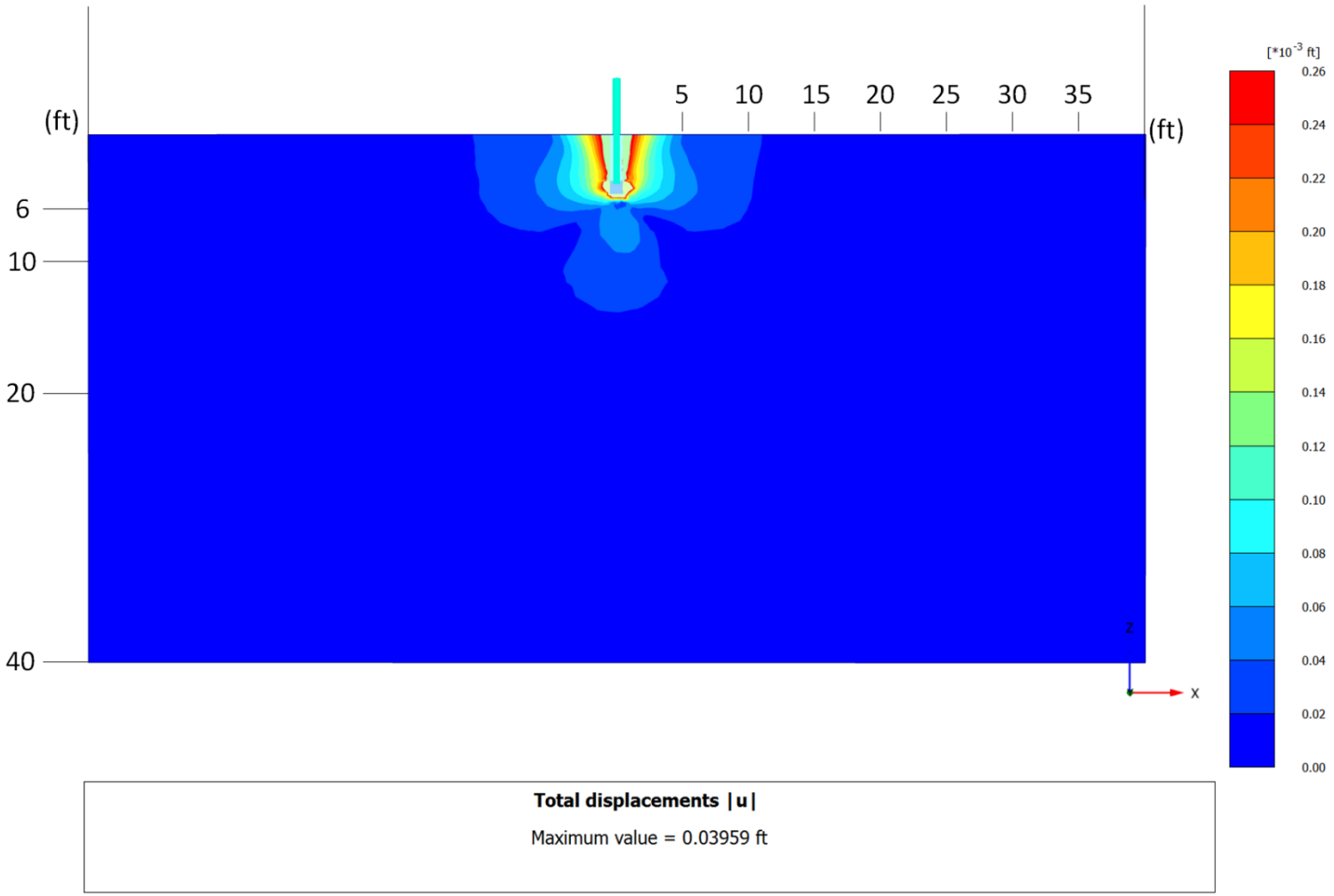

Figure 9-10 Wave propagation after impact load, t=0.1 sec – pile tip at 3.75 ft depth

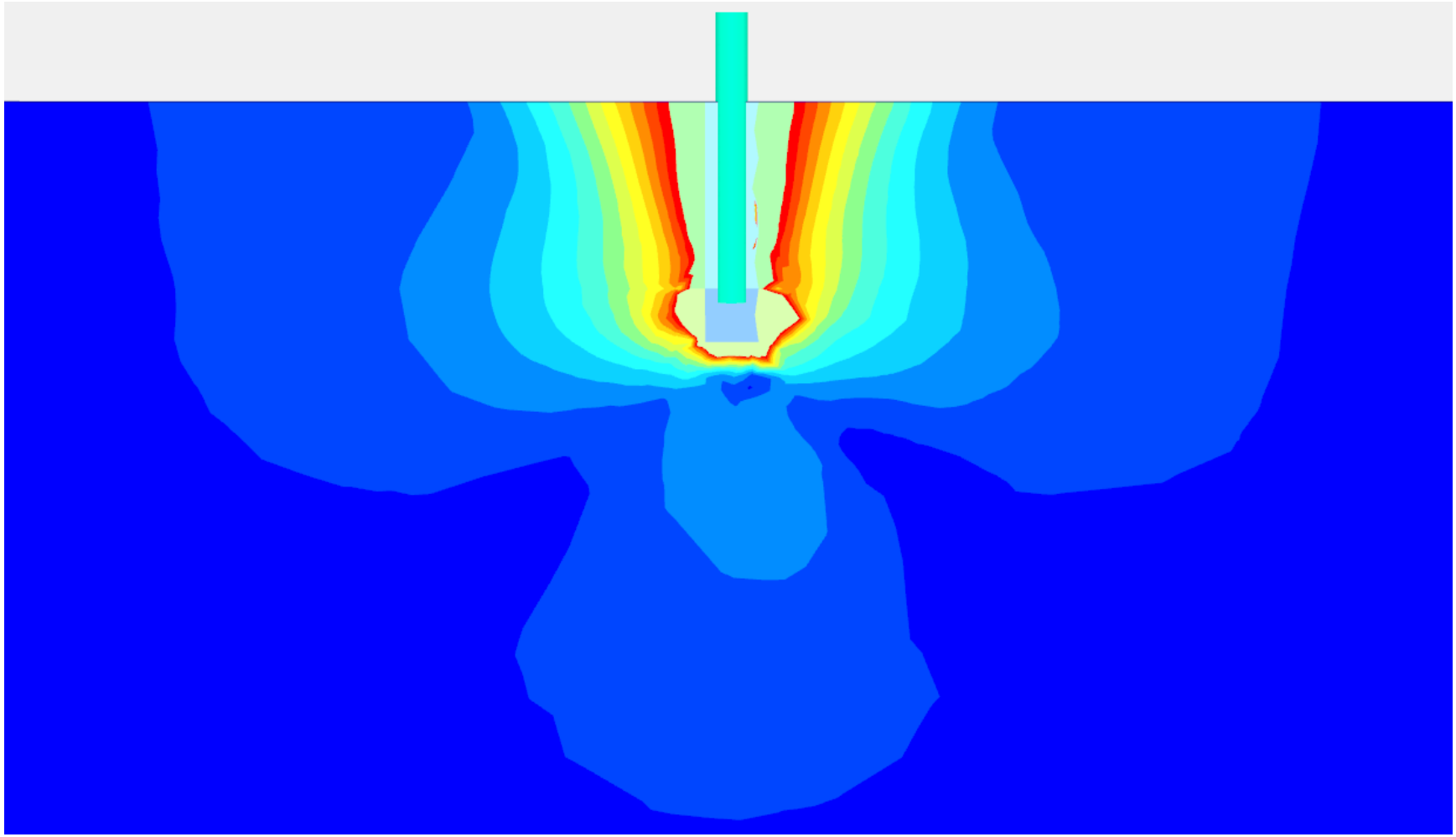

Figure 9-11 Zoom-in view of wave propagation after impact load, t=0.1 sec – pile tip at 3.75 ft depth

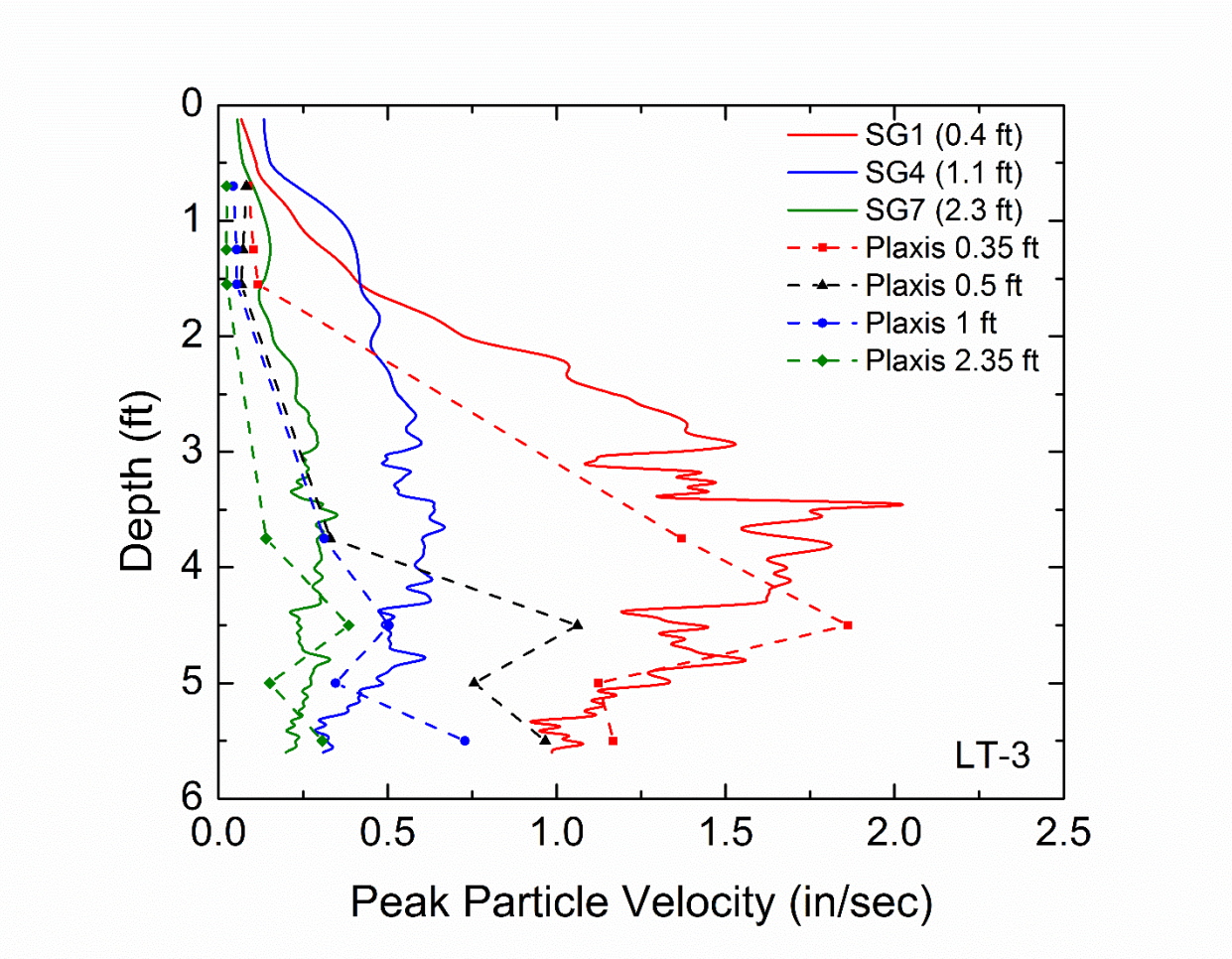

Figure 9-12 Comparison between measured and predicted peak particle velocities for observation points at 4 ft depth

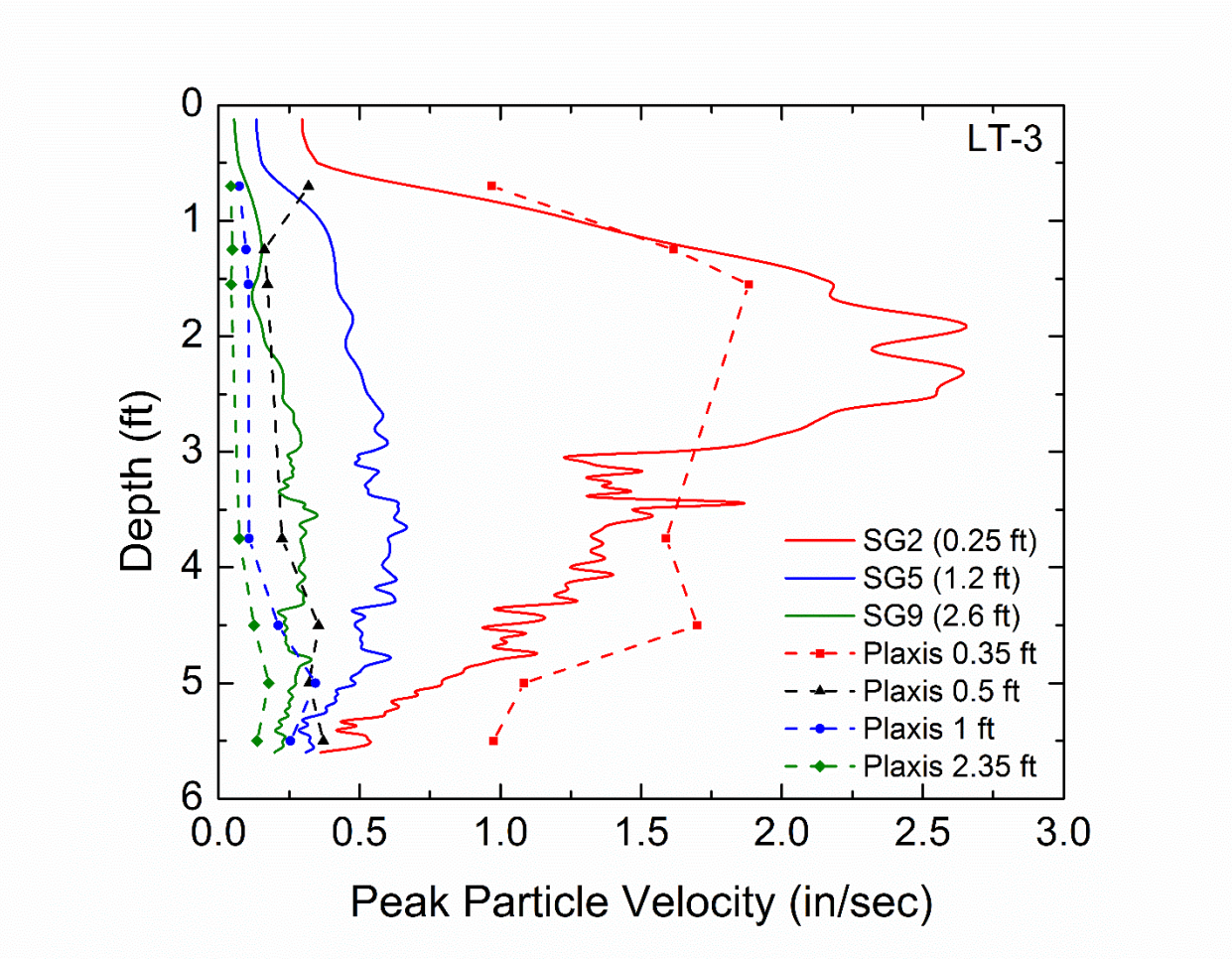

Figure 9-13 Comparison between measured and predicted peak particle velocities for observation points at 2 ft depth

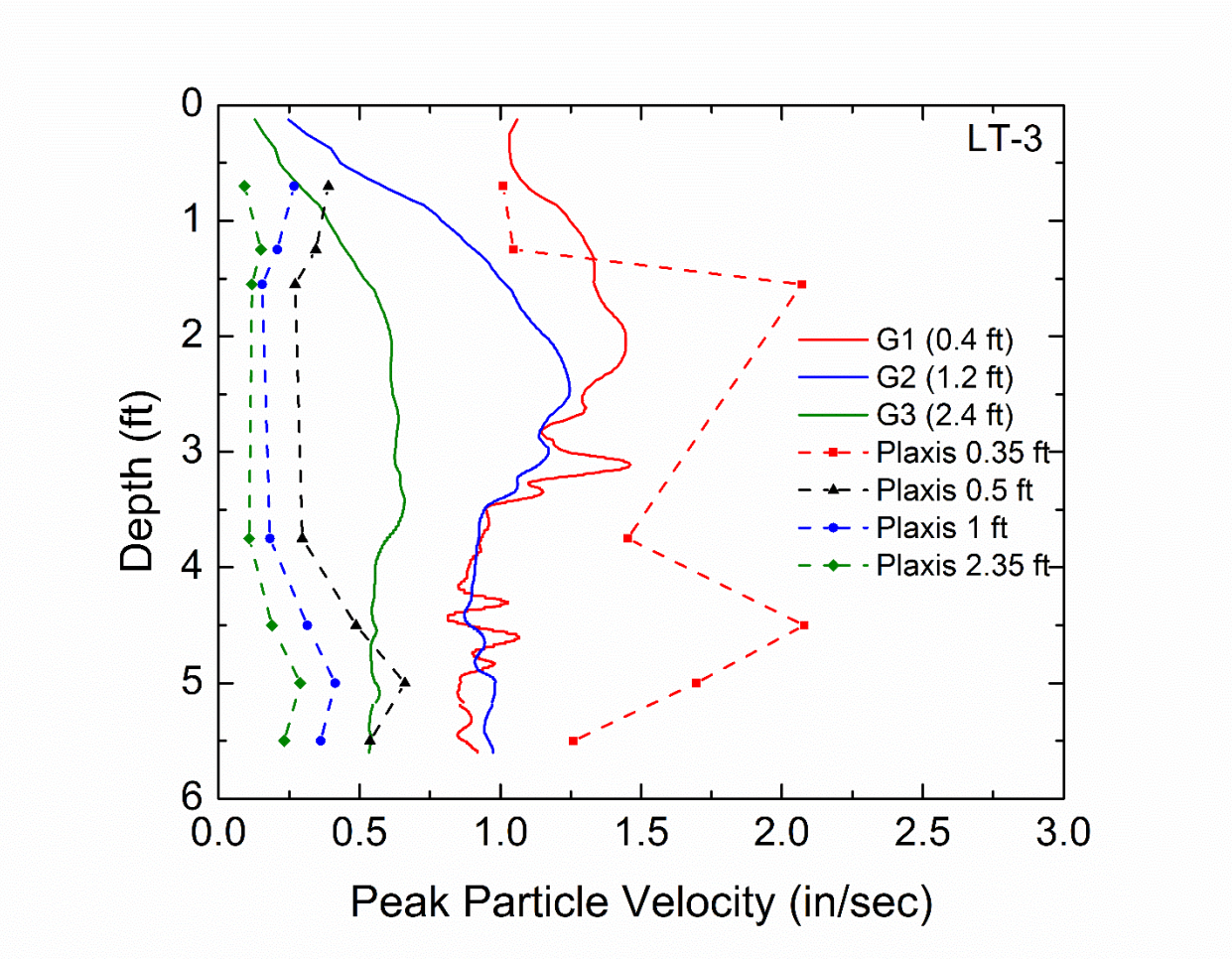

Figure 9-14 Comparison between measured and predicted peak particle velocities for observation points on the ground surface

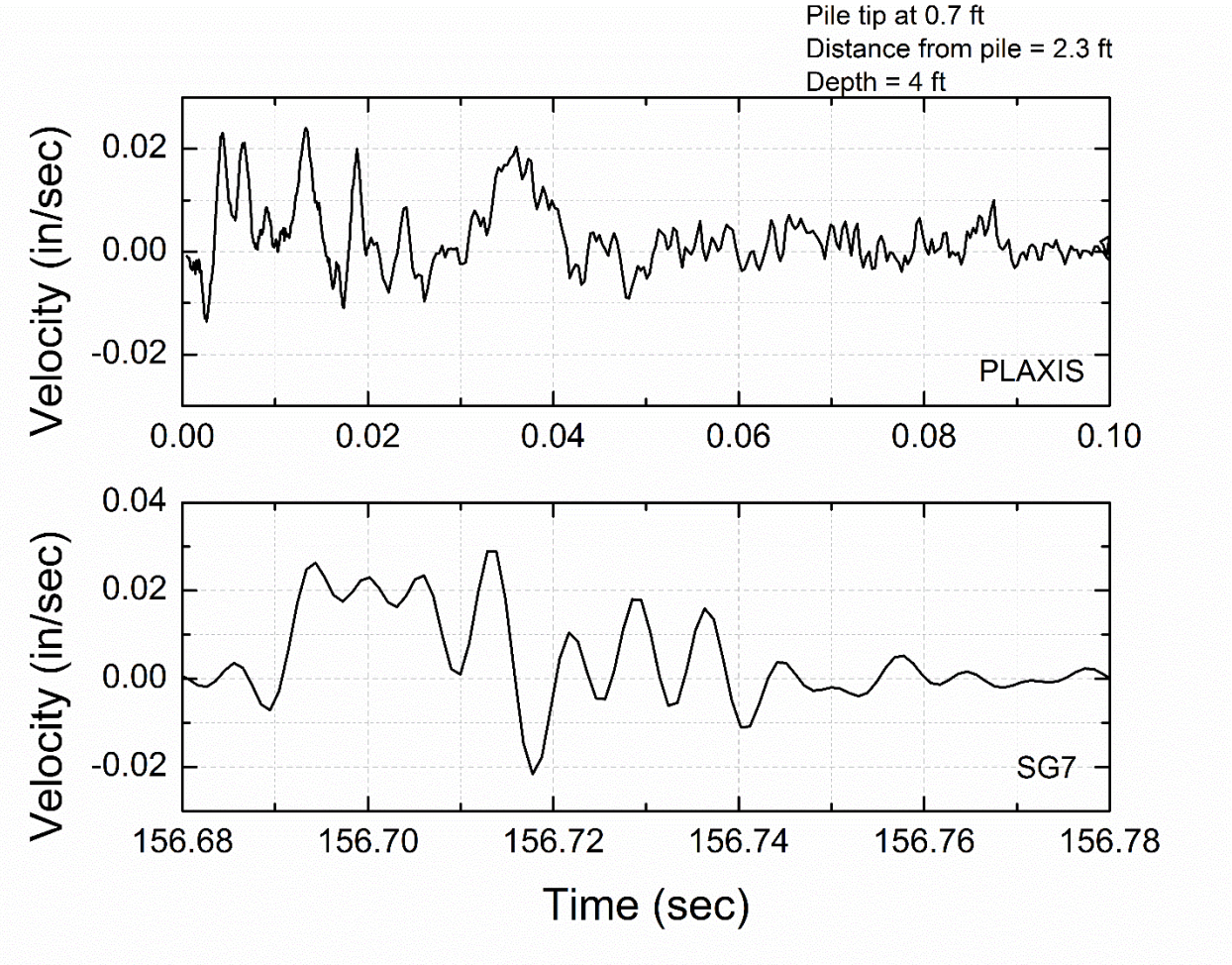

Figure 9-15 Measured and computed velocity time histories – Pile tip at 0.7 ft, observation point (x, z) = (2.3, 4)

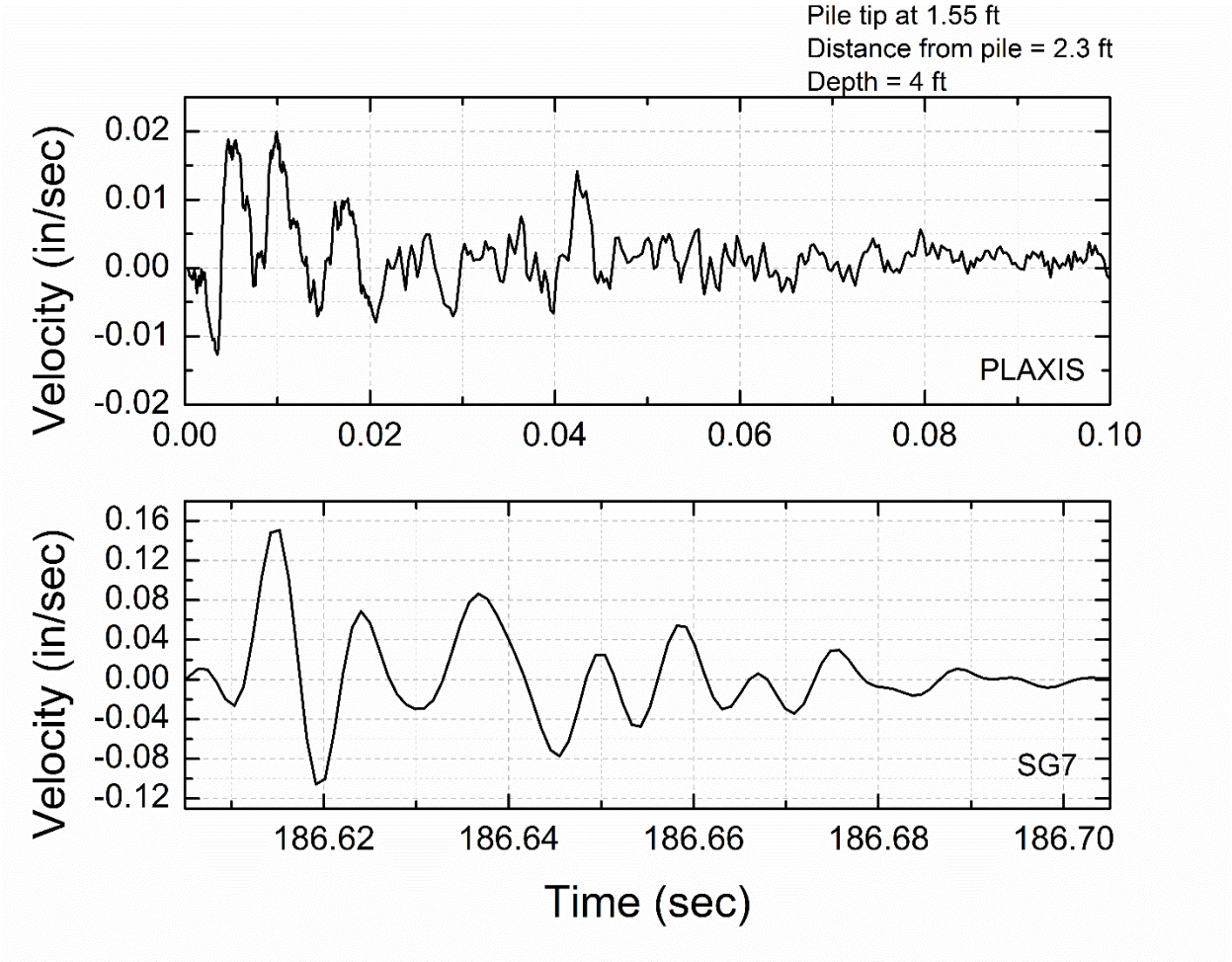

Figure 9-16 Measured and computed velocity time histories – Pile tip at 1.55 ft, observation point from pile (x, z) = (2.3, 4)

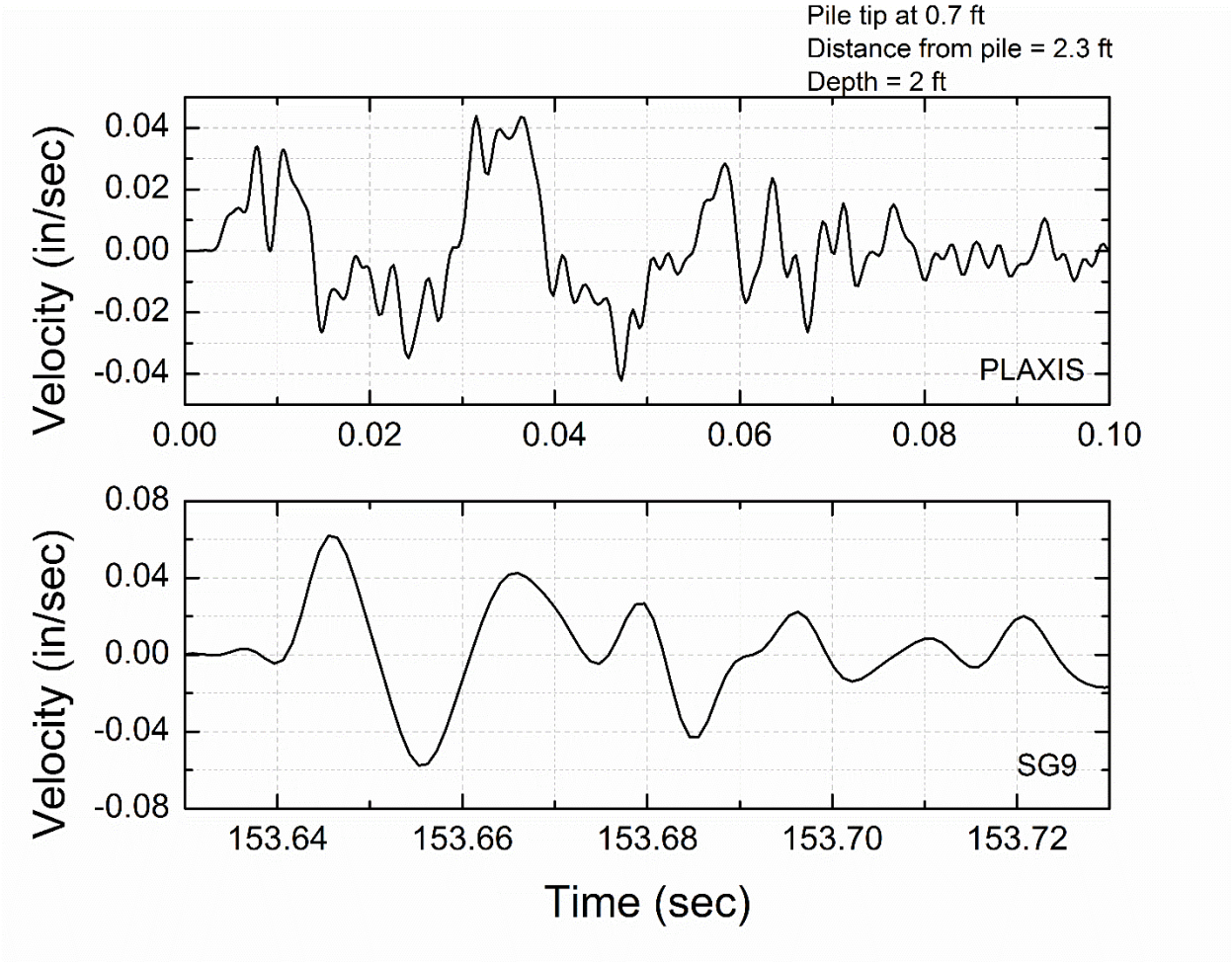

Figure 9-17 Measured and computed velocity time histories – Pile tip at 0.7 ft, observation point from pile (x, z) = (2.3, 2)

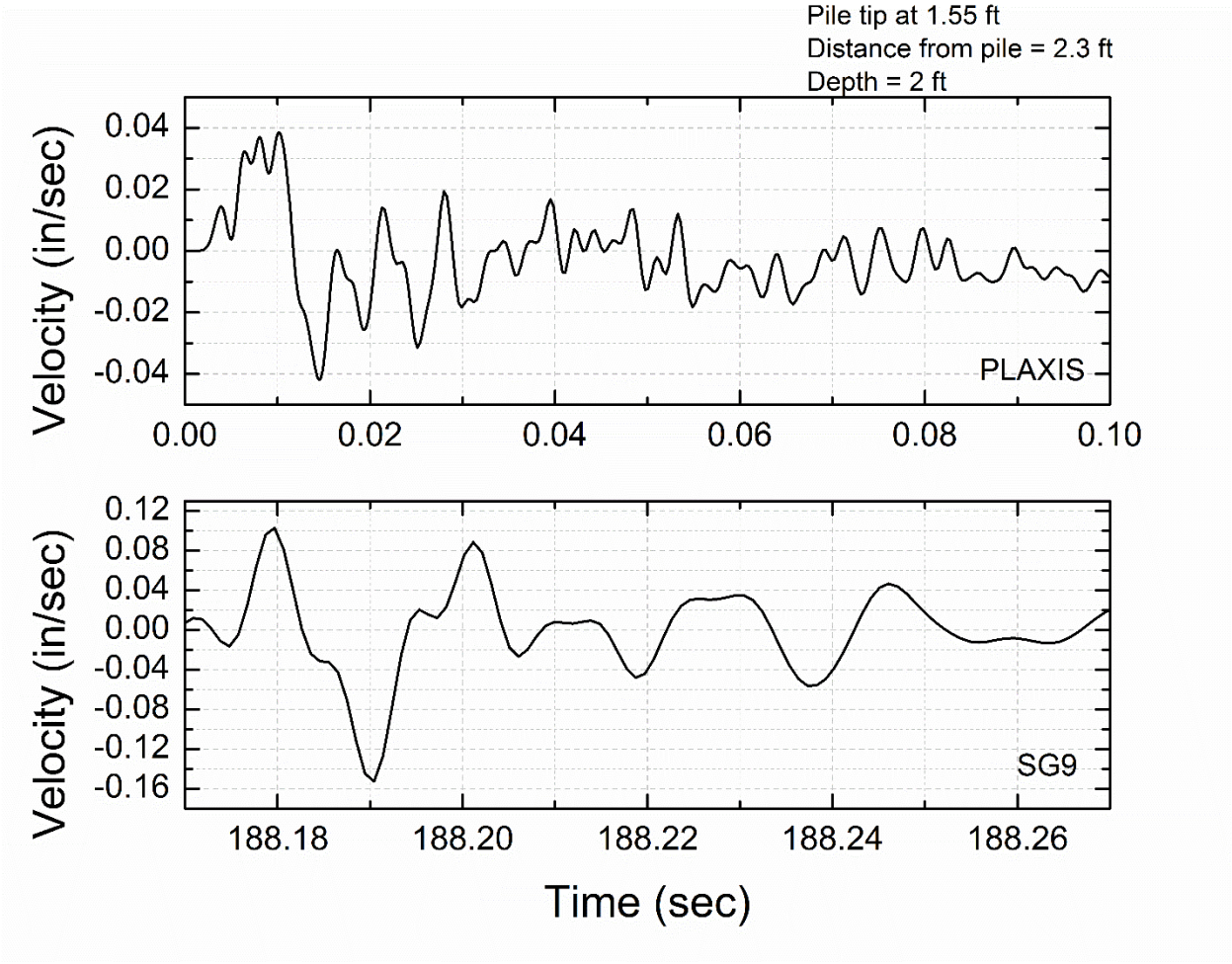

Figure 9-18 Measured and computed velocity time histories – Pile tip at 1.55 ft, observation point from pile (x, z) = (2.3, 2)

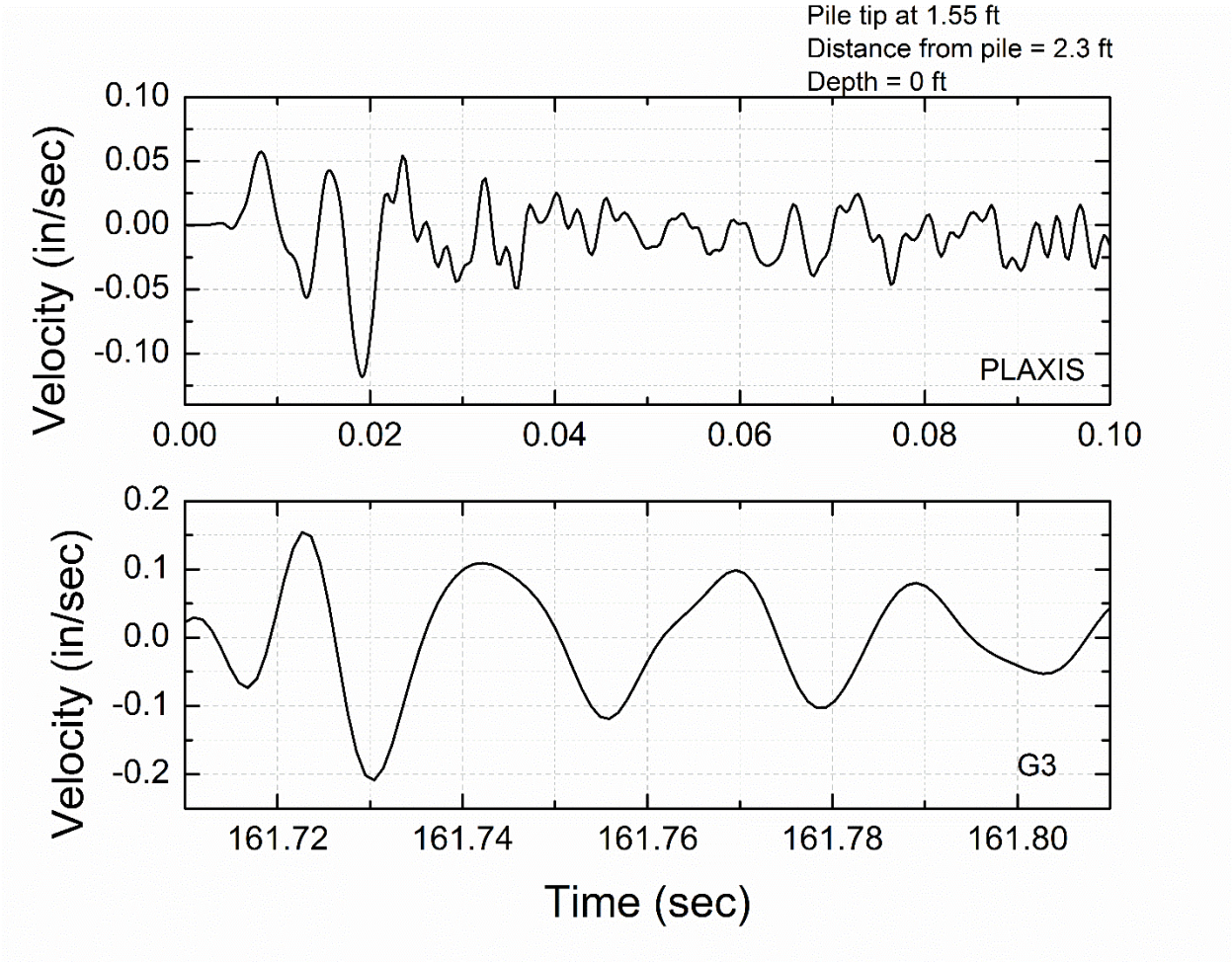

Figure 9-19 Measured and computed velocity time histories – Pile tip at 1.55 ft, observation point from pile (x, z) = (2.3, 0)

CHAPTER 10 CONCLUSIONS AND RECOMMENDATIONS

Ground vibrations due to impact pile driving operations become a major concern when influencing nearby structures and underground utilities. These vibrations can cause direct structural damage and damage due to settlement of granular soils. In an effort to better understand coupling, transmission and attenuation of energy into the ground during impact pile installation, a study comprised of three significant components was conducted: (a) full-scale ground motion monitoring during H-pile driving in the field, (b) small-scale pile driving testing in a controlled laboratory environment and (c) numerical modeling of the impact pile driving process using 3D finite element analysis.

The first portion of this research focused on collecting vibration data from pile driving projects in collaboration with the Michigan Department of Transportation (MDOT). The current practice to measure ground motions due to pile driving, is to place a line array of sensors on the ground surface. However, this approach cannot capture the complexity of the energy transfer mechanisms as the pile penetrates deeper into the ground. For the first time, ground motion measurements were made in the close proximity of driven H-piles, as close as 0.5 ft. Sensors were installed at different horizontal distances from the driven pile and at various depths into the ground. A surface array of sensors was also used. It is commonly accepted by various researchers that a Rayleigh wave is developed on the surface when the pile is being driven into the ground. The triaxial surface ground motion sensors, unlike to single component vertical axis sensors traditionally used in the literature, gave some insight to this theory. Having both buried and surface sensors collecting ground motion data during impact pile driving, refined many aspects concerning the energy coupling from pile to ground and the wave propagation patterns away from the pile. In addition, attenuation concepts that are used in the literature were compared with the measured data to study the energy decay through the soil.

The second task of this research project, included small-scale pile driving laboratory tests conducted in an in-doors sand bin to supplement the data obtained during full-scale testing. The sand bin consists of a uniform clean sand that was properly characterized. The uniform soil profile in the laboratory was ideal to characterize the wave field in a controlled environment. Ground motion sensors were installed in the ground at two different elevations, again starting very close to the model pile (0.2 ft) and continuing at further radial distances from the pile. Surface sensors were also placed in a line array providing useful outcomes. Furthermore, a PDA test was conducted when driving the pile with a special impact hammer in order to quantify the amount of the energy that reaches the top of the pile.

Finally, ground motion data collected in the laboratory were implemented to validate the 3D numerical finite element model. Comparing actual measurements to numerical analyses results is unique for pile driving projects. The combination of knowledge of the soil properties, the energy that is transmitted on the top of the pile (PDA test) and the vibration data were invaluable in validating the non-linear and time dependent modeling process.

Analysis of all three components presented in this study led to many conclusions as well as ideas for further investigation of the assessment of impact pile driving induced vibrations. The following sections present these points.

10.1 Conclusions

The conclusions of this study are discussed in two groups below. The first group deals with findings from the analysis of the field ground motion measurements during driving of H-piles. The second group deals with findings drawn from the laboratory tests and their implementation in the numerical code.

10.1.1 Outcomes from ground motion field measurements

Based on the experimental work on monitoring impact pile driving operations during actual projects the following conclusions can be drawn:

- The hypothesis of two different wave fronts emanating from a driven pile has been confirmed (Figure 10-1). Specifically, spherical body waves are generated from the tip of the pile and shear waves move outwards from the pile shaft in a cylindrical wave front. This behavior was captured by the buried sensors in the proximity of the pile. As the pile tip is still above the elevation of the sensors, only spherical waves are captured by the sensors. When the pile tip passes below the sensor, the shear waves from the shaft start to contribute and the sensors “see” a combination of spherical and cylindrical waves. As the pile tip moves further below the sensor’s depth, body waves from the tip diminish and only cylindrical waves are seen by the sensors. These phenomena are clearly observed when analyzing ground motion amplitudes in terms of the diagonal distance from pile tip to the sensor (Figure 10-2). The characterization of the wave field during impact pile driving was not proven with physical ground motion measurements until now.
- The surface ground motion measurements revealed that the surface waves are not the classical Rayleigh waves that researchers have assumed. Traditionally, only vertical component amplitudes have been measured on the surface during impact pile driving. This work showed that ratios of vertical to horizontal component amplitudes versus depth were below one for many depth ranges. This observation is a firm indication that the surface wave motion that was assumed to be a Rayleigh wave is not right. That is because the layered soil profile makes the wave propagation more complex than the assumed uniform isotropic half-space upon which the mechanisms of energy transfer are based.
- The Bornitz equation was compared to the measured data and was found to provide realistic predictions in terms of the energy dissipation through the soil. This outcome was found after fitting the Bornitz and two more formulas, suggested in the literature, to the ground motion measurements collected from both buried and surface sensors. It is recognized that the Bornitz equation was developed for sinusoidal motion at a single frequency for a point source on the surface. The pile is a linear source which is constantly lengthening as it penetrates deeper into the ground. However, the Bornitz formula was well fitted in the measured data and representative attenuation coefficients for the near field and the far field are presented based on the tested sites.

It should be recognized that the alpha coefficients derived from the Bornitz equation are different for each site, but this was expected because of the layered stratification. The decay parameters are in a range found by other researchers.

- Velocity degradation in the near field of an impact driven pile was evaluated by studying the shear wave time arrivals to the different observation points/sensors in the ground. It was found that the shear wave velocity at 0.5 ft radial distance from the pile is about 0.4 times of the shear wave velocity in the far field (Figure 10-3). It is expected that the degradation of the shear wave velocity will be even more at the pile-soil interface where the soil experiences high strains. This quantification of the shear wave velocity reduction in the non-linear, plastic zone very close to the pile, where the soil is sheared with high strains, was not proven with physical ground motion measurements until now.
- The hypothesis of three different soil behavior zones in terms of shear strain is also supported by the calculation of the reduced shear wave velocity at the points were buried sensors were installed at different distances from the pile (Figure 10-4). Definitive distances from the pile to distinguish these soil behavior zones are not established, but an approximation can be evaluated.
- A process to evaluate the potential for a granular soil to undergo shakedown settlement is presented based on the field measurements from the tested sites. This concept takes into account both sources of the energy emanating from the driven pile, i.e. spherical waves from the pile tip and cylindrical waves from the pile shaft. The order of magnitude of shear coupling assumed for soil behavior zones in the proximity of the pile is confirmed. No firm confirmation of tip coupling was established but the model seems to provide good prediction values. Particle motion and shear strains calculated from the shaft and the tip of the pile are summed giving the total particle motion amplitude and shear strain. The total shear strain is then compared with an accepted threshold cyclic shear strain (γ=0.01%) to determine the potential of settlement due to impact pile driving. This simplified procedure should be taken as a first guidance for identifying potentially troublesome sites with similar site conditions.

10.1.2 Outcomes from ground motion laboratory measurements and their implementation to the finite element code

Based on the experimental work on monitoring ground motions during driving a model pile and using the data to validate a finite element method numerical code, the following conclusions can be drawn:

- The wave propagation during driving a model pile into a uniform soil profile was better characterized and quantified compared to the complex behavior of a driven pile into a realistic soil profile. It was found that the amount of energy that is transmitted to different observation points depends on the inclination of the pile tip to the sensor distance with the horizontal. The pile tip changes elevation constantly, thus this inclination also changes for a specific observation point. The closer the observation point to the pile, the steeper the inclination and the less amount of energy is transmitted to that point. This pattern was observed by studying the normalized amplitudes of peak particle velocities at different depths of the pile tip to the response when the pile tip was on the surface (Figure 10-5). As the pile driving proceeds, the inclination from the horizontal increases for all observation points, however the rate of increase is higher for the closest point to the pile. For this reason, the furthest sensors from the pile had a much lower decreasing rate of peak particle velocities compared to the closest one, i.e. the amplitudes of the furthest sensors started falling off close to the end of driving. This is a very important finding that was investigated because of the uniformity of the soil in the laboratory tests.
- The above pattern was also observed for the buried observation points. As the pile tip reaches the depth of the sensors, the inclination of the diagonal distance from pile tip to sensor location with the horizontal, decreases. The ground motion amplitudes increase up to that point and after the pile tip passes below the sensor, where the contribution of the waves from the shaft starts, the amplitudes stay constant or slightly increase. When the pile tip is further below the sensors' elevation, the contribution from the spherical waves are not captured anymore from the sensor and there is a decrease in ground motions. This phenomenon is more pronounced for the closest observation point as seen in Figure 10-6. This trend serves as a firm confirmation of

the characterization of the wave field, as first observed in the complicated case of impact pile driving in the field.

- The validation of the finite element code using the measured ground motions from the laboratory tests provided promising results in terms of characterizing the vibration field around the pile, comparison of the recorded and calculated velocity time histories and peak particle velocity versus depth profiles. The pile was modeled at different installed depths with a single blow applied on the top of the pile, corresponding to the force measurements collected from the PDA at that depth. This was done because it is impossible to simulate the whole installation process of an impact driven pile. It is recognized that this is not a realistic simulation of a pile driving installation but the preliminary results gave some insight to the concepts of pile driving that are still in question. A plastic zone with reduced strength parameters was introduced around the pile to simulate the pile-soil interface and the high strains that develop very close to the pile. The calculated ground motions in nodes selected at locations where the sensors were installed had a good agreement for the case of the plastic zone. The model underestimated the recorded peak particle velocity amplitudes at further distances from the driven pile. Figure 10-7 shows the wave propagation pattern in the soil after the impact load has been removed and the soil vibrates freely. It is evident that a spherical wave front radiates from the pile tip, while a cylindrical wave front expands from the pile shaft. Also, a surface wave propagates on the surface. All these observations are in agreement of the hypothesis of the energy transfer through the ground during impact pile driving.

10.2 Recommendations for Future Research

Based on the findings of this research the following recommendations are proposed for future research:

- A more appropriate formula predicting the energy dissipation through the ground needs to be introduced. The attenuation coefficients calculated from the sites and laboratory tests are site specific and it is recognized the Bornitz equation that was

employed was derived for a homogeneous half space and sinusoidal motion happened to work well in this study. However, because of the nature of this formula and the infinite possibilities for soil layering, a more appropriate decay curve needs to be developed. This task can be only achieved with more physical ground motion measurements.

- There is a need for re-evaluation of the currently accepted thresholds of strain from pile driving activities. It was found in this work that shear strains can be much lower than the accepted threshold of 0.01 % in the close proximity of a driven pile. A project can include installation of hundreds of piles, i.e. thousands of loading cycles, leading to a much lower threshold of shear strain. The proposed concept to estimate the distance from a pile that a soil layer exceeds the threshold for volume reduction is a first step towards this goal, but quantification of the magnitude of settlement is important.
- Quantification of ground settlement at impact pile driving sites is a significant aspect that has not been studied for pile driving operations. Careful incremental settlement measurements need to be made in association with impact pile driving. Baseline ground elevations need to be established before any construction work is done and measurements repeated after each major step of construction. For example, before and after any operations like site excavation, after operation of any heavy equipment, after vibratory sheet-pile driving and after impact pile driving. It is only in this way that an estimate of the amount of settlement due to impact pile driving can be identified and separated from all other contributions to settlement. The vibration measurements were recorded in this work after significant amount of sheet piles were installed and shakedown settlement was observed.
- Parametric numerical analysis should be performed to examine the effect of pile type, hammer type and soil conditions. The time schedule of this work allowed only for validation of the finite element code using the laboratory ground motion measurements. At this time, realistic simulation of the pile driving installation is very difficult but the continuous progress of the already advanced finite element software will make this feasible soon.

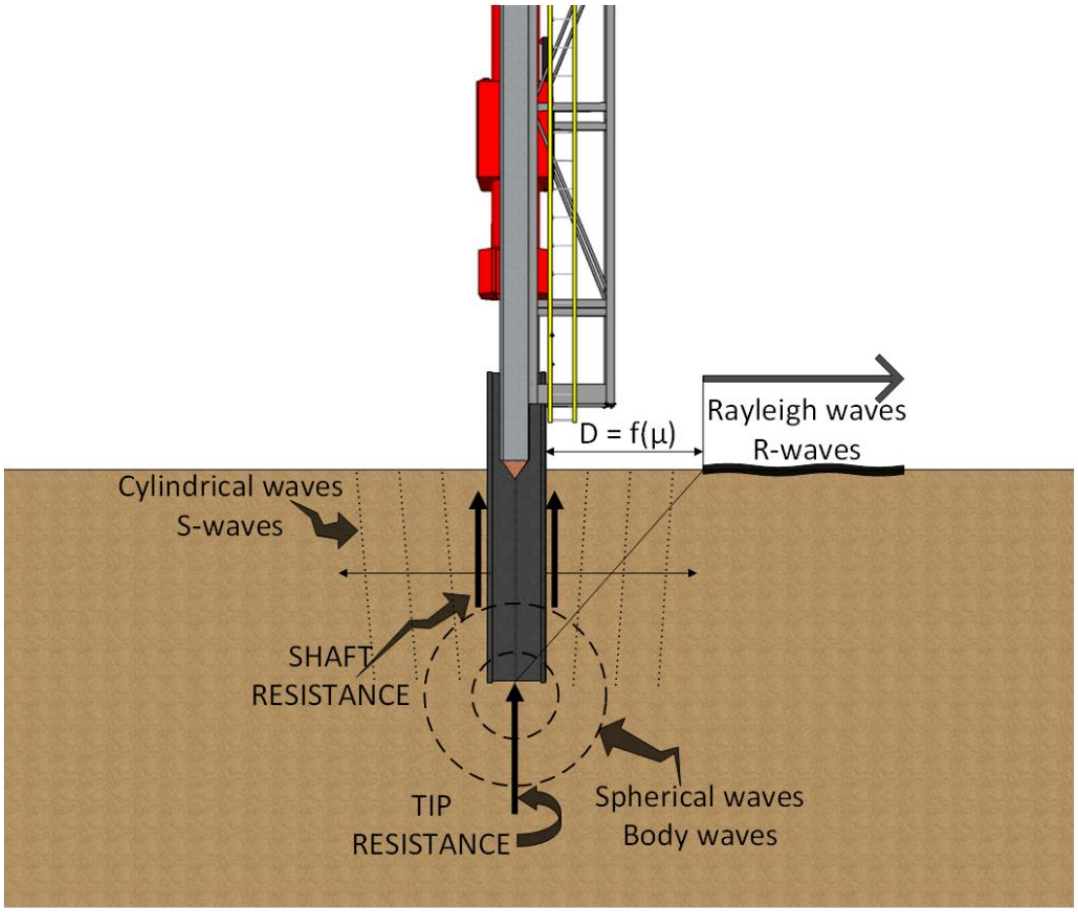

Figure 10-1 Mechanisms of energy transfer from impact driven pile to surrounding ground (from Grizi et al. 2016)

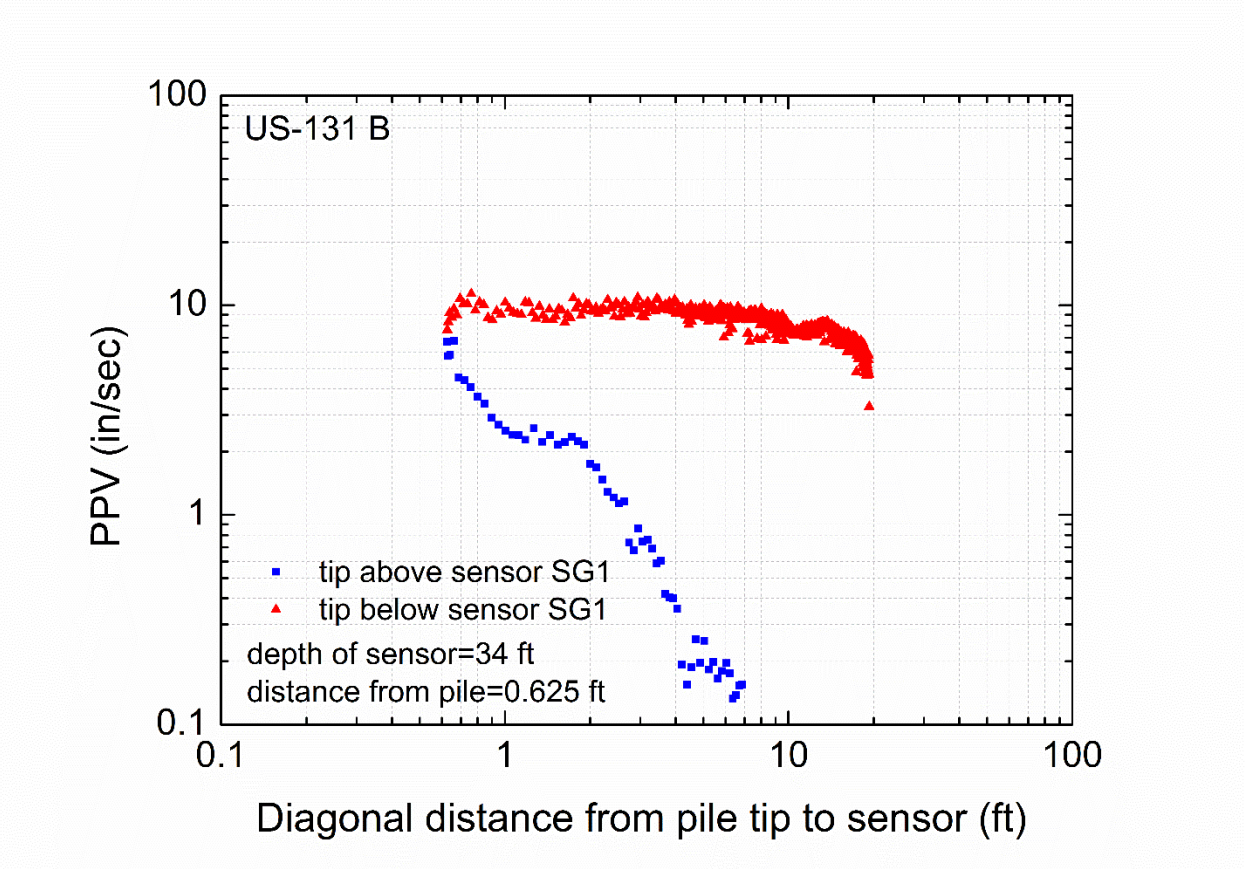

Figure 10-2 Analysis of PPV recorded for pile tip above and below the sensor in terms of diagonal distance to the sensor

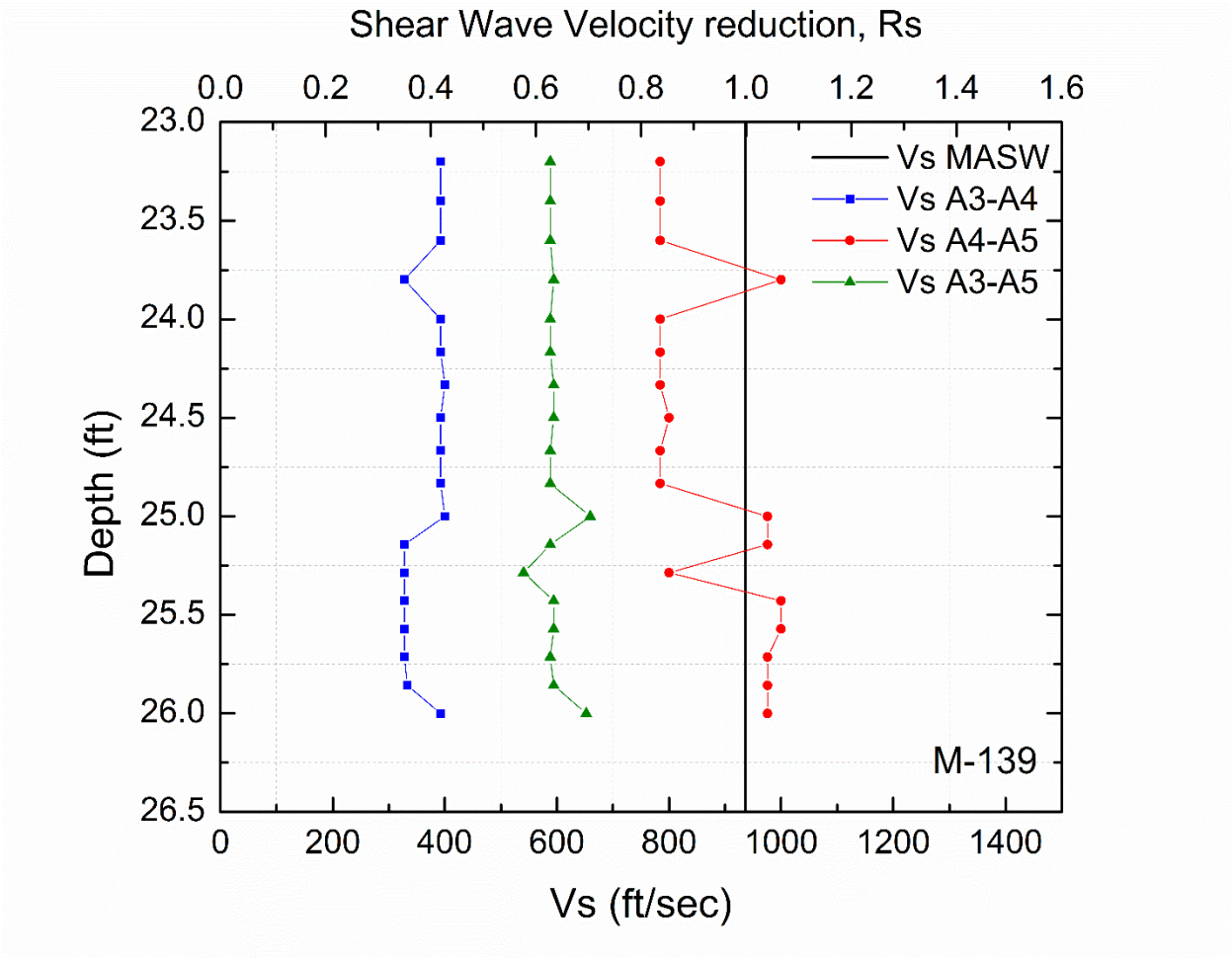

Figure 10-3 Shear wave velocity degradation in the close proximity of a driven pile

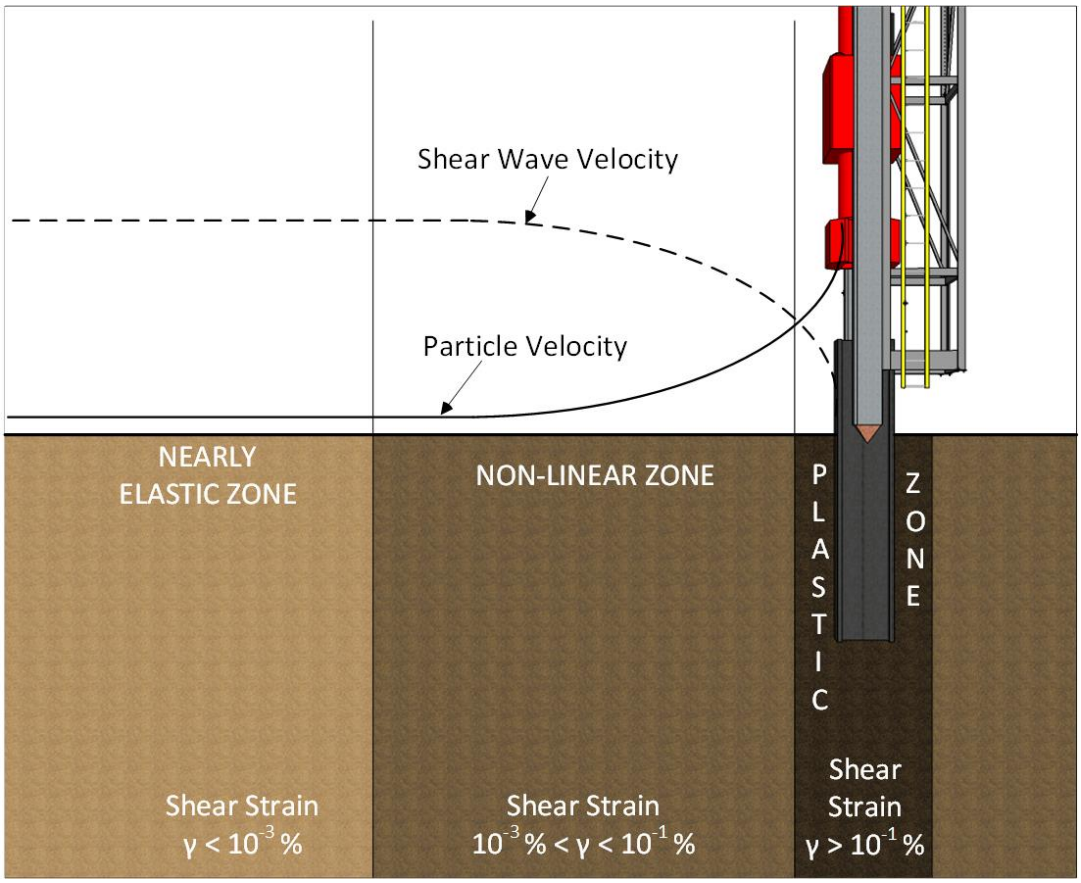

Figure 10-4 Assumed soil behavior zones near impact driven pile (from Grizi et al. 2016)

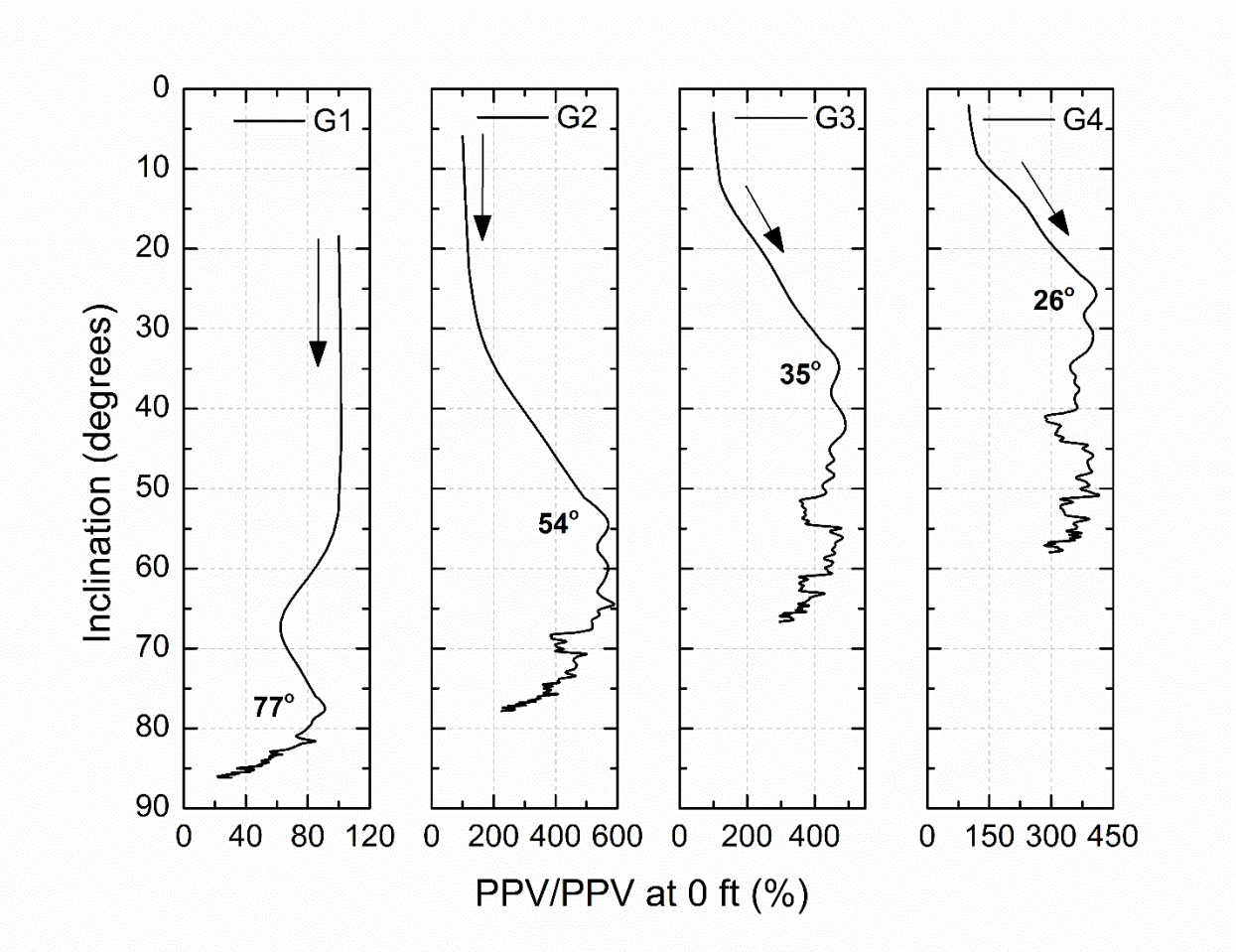

Figure 10-5 Normalized responses of sensors placed on the ground surface of the sand bin at different distances from the pile; G1 at 0.4 ft, G2 at 1.3 ft, G3 at 2.4 ft and G4 at 3.5 ft

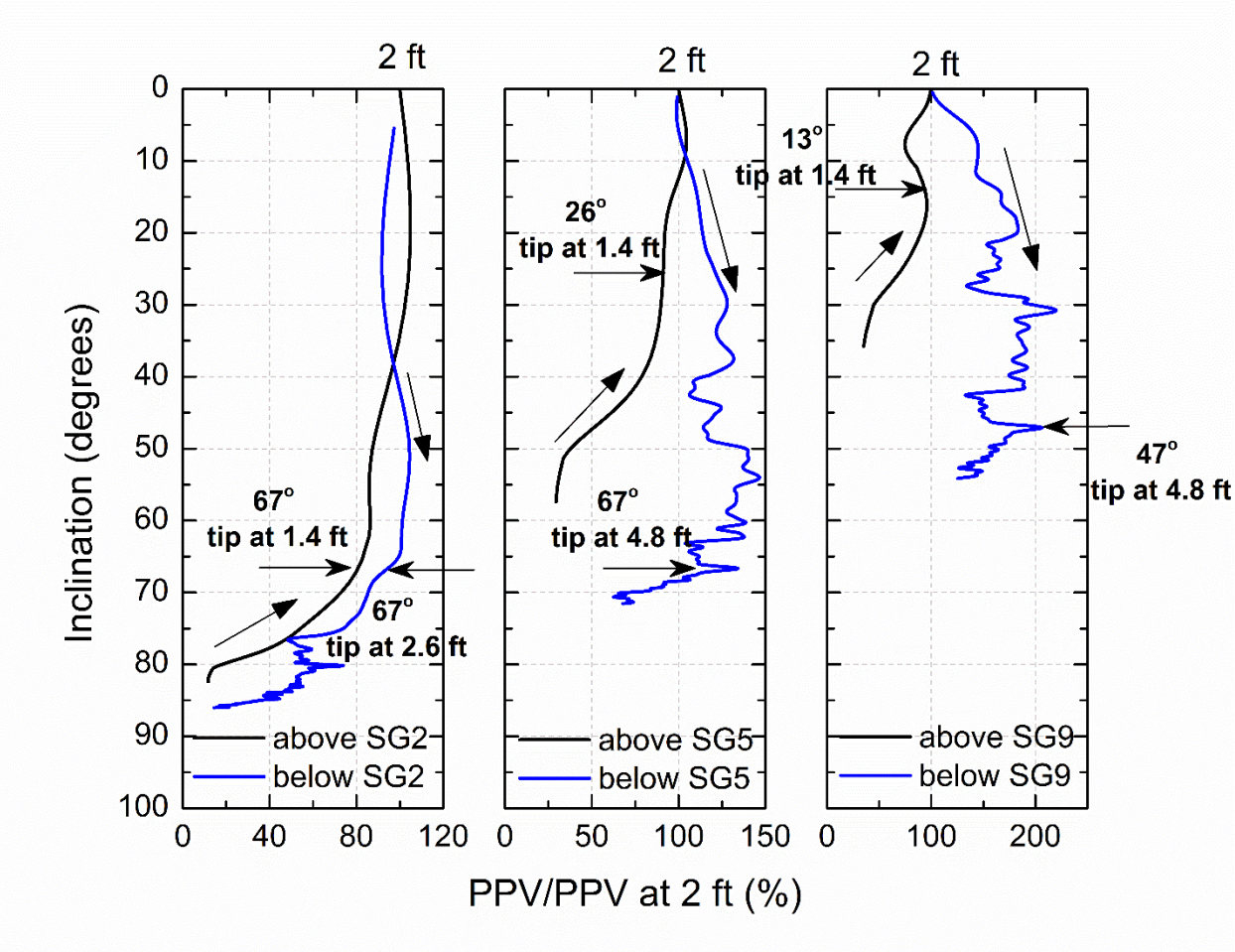

Figure 10-6 Normalized responses of sensors installed in the sand bin at 2 ft and different distances from the pile; SG2 at 0.25 ft, SG5 at 1.2 ft and SG9 at 2.6 ft

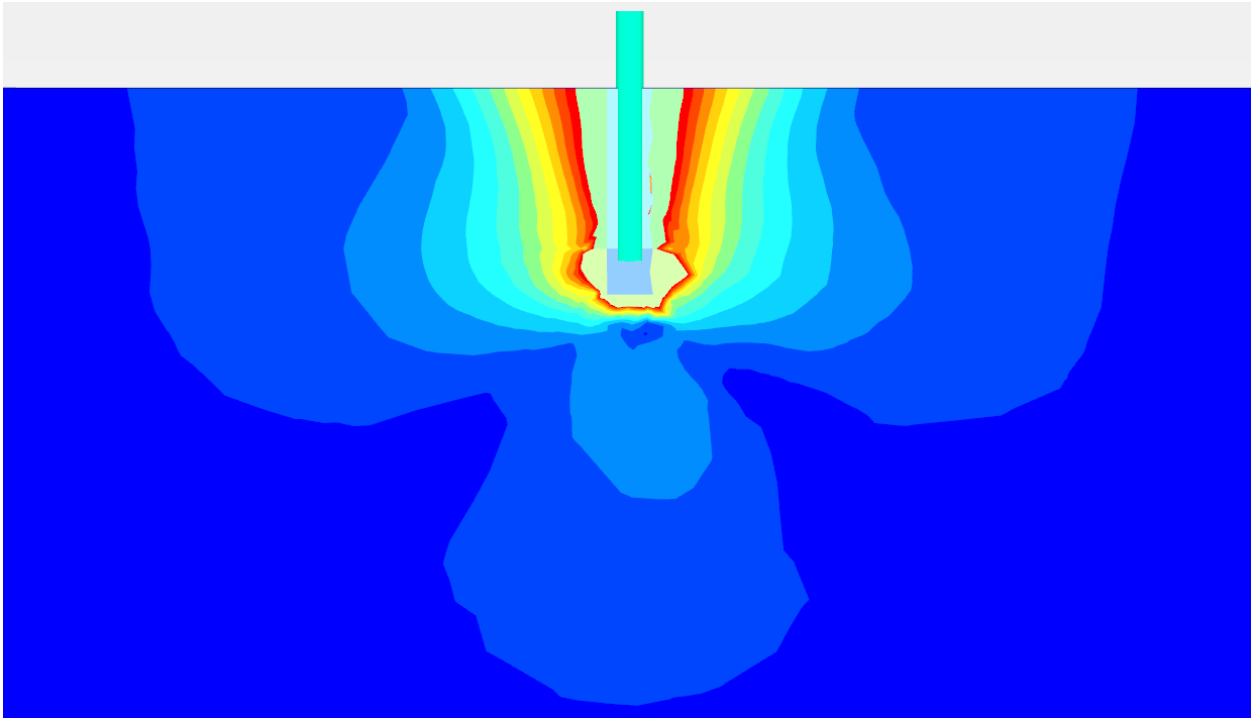

Figure 10-7 Wave propagation after impact load – numerical simulation